MILITARY HANDBOOK

DESIGN OF AERODYNAMICALLY STABILIZED FREE ROCKETS

AMSC N/A

AREA GDRQ

MIL-HDBK-762(MI)

FOREWORD

1. This military handbook is approved for use by the US Army Missile Command, Department of the Army, and is available for use by all Departments and Agencies of the Department of Defense.

2. Beneficaial comments (recoomendations, additions, deletions) and any pertinent data that may be of use in improving this document should be addressed to: Commander, US Army Missile Command, ATTN: AMSMI-RD-SE-TD-ST Redstone Arsenal, AL 35809, by using the self-addressed Standardization Document Improvement Proposal (DD Form 1426) appearing at the end of this document or by letter.

3. This handbook was developed under the auspices of the US Army Materiel Command's Engineering Design Handbook Program, which is under the direction of the US Army Management Engineering College. Research Triangle Institute was the prime contractor for the preparation of this handbook, which was prepared under Contract No. DAAG34-73-C-0051.

CONTENTS

CHAPTER 1
INTRODUCTION

CHAPTER 2
SYSTEM DESIGN

MIL-HDBK-762(MI)

CONTENTS (cont'd)

MIL-HDBK-762(MI)

CONTENTS (cont'd)

CHAPTER 3
PERFORMANCE

CHAPTER 4
ACCURACY

v

MIL-HDBK-762(MI)

CONTENTS   (cont'd)

MIL-HDBK-762(MI)

CONTENTS (cont'd)

CHAPTER 5
AERODYNAMICS

CONTENTS (cont'd)

CHAPTER 6
PROPULSION

MIL-HDBK-762(MI)

CONTENTS (cont'd)

MIL-HDBK-762(MI)

CONTENTS (cont'd)

Page

Paragraph

CHAPTER 7
STRUCTURES

MIL-HDBK-762(MI)

CONTENTS (cont'd)

CHAPTER 8
LAUNCHER CONSIDERATIONS

MIL-HDBK-762(MI)

CONTENTS (cont'd)

APPENDIX A
ATMOSPHERIC DATA

APPENDIX B
COMPUTER PROGRAMS

MIL-HDBK-762(MI)

CONTENTS (cont'd)

APPENDIX C
HEAT TRANSFER EQUATIONS

CONTENTS (cont'd)

MIL-HDBK-762(MI)

LIST OF ILLUSTRATIONS

MIL-HDBK-762(MI)

DOD-HDBK-762(Ml)

LIST OF ILLUSTRATIONS (cont'd)

MIL-HDBK-762(MI)

LIST OF ILLUSTRATIONS (cont'd)

MIL-HDBK-762(MI)

LIST OF ILLUSTRATIONS (cont'd)

MIL-HDBK-762(MI)

LIST OF ILLUSTRATIONS (cont'd)

DOD-HDBK-762(MI)

LIST OF ILLUSTRATIONS (cont'd)

MIL-HDBK-762(MI)

LIST OF ILLUSTRATIONS (cont'd)

MIL-HDBK-762(MI)

LIST OF ILLUSTRATIONS (cont'd)

MIL-HDBK-762(MI)

LIST OF ILLUSTRATIONS (cont'd)

MIL-HDBK-762(MI)

LIST OF TABLES

MIL-HDBK-762(MI)

LIST OF ABBREVIATIONS AND ACRONYMS

AFRPL = Air Force Rocket Propulsion Laboratory
AP = ammonium perchlorate
ARDC = Air Research and Development Command
BF = biaxial improvement factors
cal = calibers
CEP = circular error probable
CG = center of gravity
CI = configuration item
COESA = Committee on Extension of the Standard Atmosphere
COSPAR = Committee on Space Research
CP = center of pressure
= circular port
CTPB = carboxy terminated polybutadiene
DEP = deflection error probable
DoD = Department of Defense
DOF = degrees of freedom
FAMAS = Field Artillery Meteorological Acquisition System
FE = finite element
FS = factor of safety
HEAT = high explosive antitank
HTPB = hydroxyl-terminated polybutadiene
IR = infrared
IRIG = Inter-Range Instrumentation Group
JMSNS = Justification of Major System New Starts
KP = potassium perchlorate
LOA = Letter of Agreement
MEOP = maximum expected operational pressure
MHX = cyclotetramethylene tetranitramine
MIL-STD = Military Standard
MLRS = Multiple Launch Rocket System
MOC = method of characteristics
MS = margin of safety
MSFC = Marshall Space Flight Center
NASA = National Aeronautics and Space Administration
NC = cellulose hexanitrate
NG = glycerol trinitrate
PADA = prespin automatic dynamic alignment
PBAA = butadiene acrylic acid copolymers
PE = probable error
QE = quadrant elevation
RDX = cyclotrimethylene trinitramine
REP = range error probable
ROC = Required Operational Capability
rps = revolutions per second
SOSR = spin on straight rail
SUDS = slowly uniformly decreasing spin
TE = trailing edge
TMO = transition metal oxide
WAF = wraparound fins

MIL-HDBK-762(MI)

C H A P T E R   1
I N T R O D U C T I O N

This chapter introduces the handbook. Rocket systems are presented in two broad classes: military rocket systems and research rocket systems. Military rocket systems are discussed in terms of their application in a battle environment. Research rocket systems are discussed in terms of the application to provide the means of placing data gathering equipment into a desired environment. Operational modes for the rocket systems are described. Finally, brief descriptions of the remaining chapters and the appendices are given.

1-1 PURPOSE OF HANDBOOK

Aerodynamically stabilized free rockets offer relatively simple, reliable, small, low-cost means for delivering payloads and, when great accuracy is not required, are often the optimum systems. This handbook provides engineering design information and data for such rockets. Primarily, this handbook is intended to cover the conceptual and preliminary design phases; however, reference is made to the technical approaches and computer programs required for the system development phase. The material includes operational and interface requirements as they influence the design of the total weapon system. The handbook provides

1. The preliminary design engineer with specific design information and data useful in the rapid response situations required of preliminary design activities

2. The specialist in each technical area an introduction to the other disciplines in terms of data requirements and trade-off studies that must be performed.

Free flight rockets are those rockets that do not have an in-flight guidance system; they are aimed, guided, or directed by the launching device. These launchers usually have a launching rail or tube to provide initial direction to the rocket. Free flight rockets are of two basic kinds—spin stabilized and aerodynamically stabilized. The spin stabilized rocket, as the name implies, depends upon a high rate of spin and resulting gyroscopic moments to oppose disturbances. The aerodynamically stabilized rocket depends upon aerodynamic forces on the body and fins to oppose disturbing forces. The aerodynamically stabilized rocket generally employs some spin to minimize dispersion caused by nonsymmetrical body characteristics (body asymmetries, fin misalignment, thrust misalignment, etc.). The data and concepts presented in this handbook are limited to aerodynamically stabilized free flight rockets.

1-2 CLASSES OF FREE FLIGHT ROCKETS

For the purposes of this handbook, rockets are discussed as either military rocket systems or research rocket systems.

1-2.1 MILITARY ROCKET SYSTEMS

1-2.1.1 General

In general, military rockets are used to deliver some form of destructive warhead or other military payload such as smoke canisters or electronic beacons to a target. There are some exceptions, which will be discussed as logistic rockets. The types of military rockets most frequently used are described in the paragraphs that follow.

1-2.1.2 Field Artillery

Field artillery rocket systems are used in the same manner as artillery gun systems. They have

medium- and long-range capabilities and vary in size from small to very large rockets requiring heavy equipment for handling and loading. Indirect fire is the primary function of most artillery rocket systems. Examples of free flight field artillery rockets are Multiple Launch Rocket System (MLRS), HONEST JOHN, and LITTLE JOHN shown in Fig. 1-1.

1-2.1.3 Infantry

Infantry rocket systems are generally man-portable, direct-fire weapons usually smaller than field artillery rockets. Antitank rockets are the most common infantry rocket systems. They are designed to be carried by the individual soldier and fired from the shoulder. Many special factors must be considered in such systems because the man and rocket are in such close proximity. The weapon must be light yet effective, and must be safe to handle and fire without endangering the user. Simplicity of operation is also a requirement of infantry systems. Examples of free flight infantry rockets are the LAW and VIPER shown in Fig. 1-2.

1-2.1.4 Air Defense

Air defense rocket systems are used primarily to protect the ground soldier and/or land areas from attack by enemy aircraft. Unlike air defense missiles, which are guided to enable the missile to maneuver, air defense free rockets are fired into an area in which the aircraft is or is expected to be. Sufficient numbers are fired to produce a lethal pattern. An example of a free flight air defense rocket is the LOKI shown in Fig. 1-1.

1-2.1.5 Armor

Rocket systems used by the armored forces are, in many instances, the same as those used by the infantry. The tank, armed with a direct-firing gun or rocket system, is the primary weapon fo the armored elements. Because tank weapons are used against may types of targets, a tank will carry ammunition mixes suitable to the type targets anticipated.
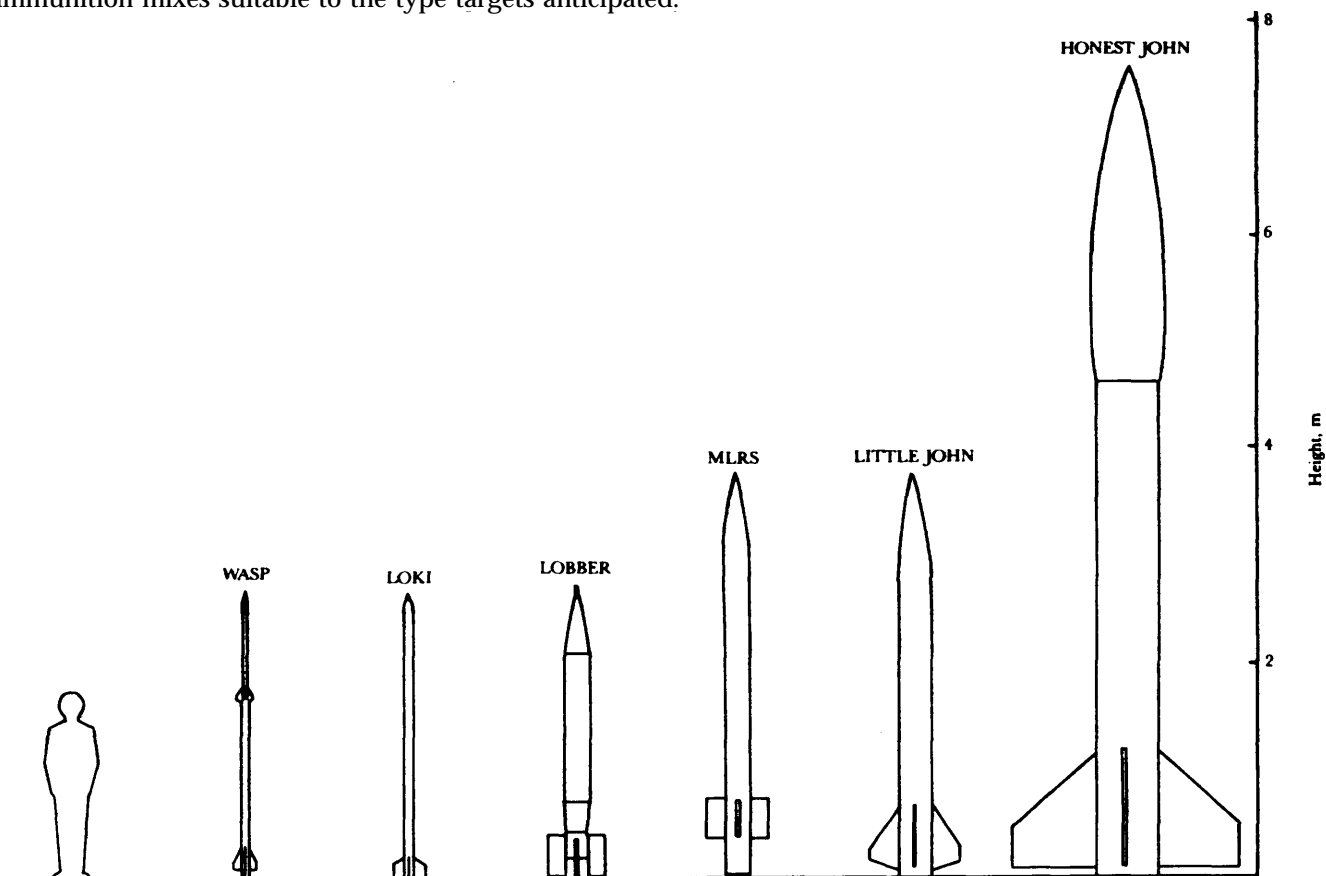
Figure 1-1. Examples of Midsize Free Flight Rockets
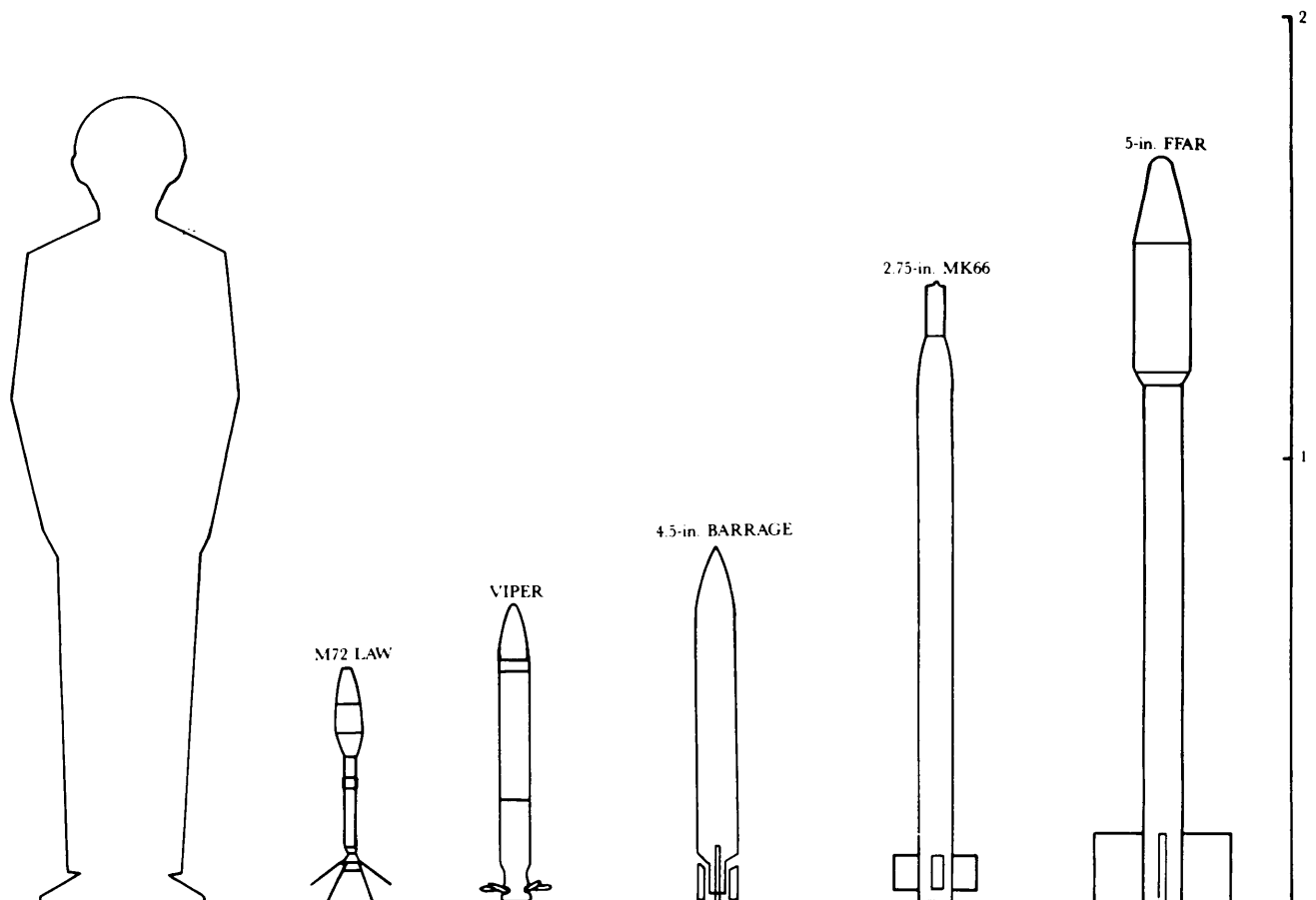
Figure 1-2. Examples of Small Free Flight Rockets

1-2.1.6 Aviation

Rocket systems are mounted on and fired from fixed- and rotary-wing aircraft, usually for close support of the ground soldier. The rockets may also be used for the defense of the attack aircraft. Design of airborne rockets is complicated by the fact that these rockets are fired from an elevated platform that is unstable and, in many instances, moving rapidly. Many additional factors must be considered in the design of aircraft rocket systems to permit the tactical performance desired without endangering the aircraft or crew. An example of a free flight aviation rocket is the 2.75-in. rocket shown in Fig. 1-2.

1-2.1.7 Logistic

The development of logistic rockets has not been significant to date. The role of the logistic rocket is to provide a fast, direct method of delivering supplies to a specified point. In concept, the payload, instead of being a destructive mechanism, is ammunition, medical. or other supply items. The payload separates and parachutes to the ground at the destination. An example of a logistic rocket is the LOBBER shown in Fig. 1-1.

1-2.1.8 Other

There are military applications of free flight rockets in addition to those just described. These include

1. Tactical meteorological rockets for obtaining data necessary in artillery fire control

2. Rockets for delivery of some type of electronic equipment to a specific point to mark a location or to transmit intelligence

3. Rockets that produce smoke or other means of spotting or obscuring a target.

1-2.2 RESEARCH ROCKET SYSTEMS

1-2.2.1 General

Research rockets have the same general group of components as military rocket systems; the notable difference is the payload. Research rockets usually are designed to accomplish a mission from which technical data will be obtained. The purpose of the data is to further the understanding of some scientific discipline or phenomena. In this role, the payload becomes a device to gather data. Evaluation of the gathered data is often done at a later date. It may be necessary to recover the payload, thereby making a recovery system necessary. Means to prevent payload damage or destruction must be designed into the rocket system.

1-2.2.2 Meteorological

Aerodynamically stabilized free flight rocket systems are used to place sensing devices at various altitudes. Data providing information about the air, winds, temperature, radiation, and atmospheric moisture content of the Earth and other phenomena are obtained for use by the researcher. An example of a meteorological rocket is the WASP shown in Fig. 1-1.

1-2.2.3 High-Altitude Sounding

High-altitude sounding rockets are used to obtain specific information at altitudes ranging to several hundred miles above the surface of the Earth. These rocket systems and most meteorological rocket systems fly near vertical trajectories. The principal design goal for this type rocket is efficient attainment of altitude. The BLUE SCOUT JR. rocket shown in Fig. **1-3** is an example of a high-altitude sounding rocket.

1-2.2.4 Satellites

Aerodynamically stabilized free flight rockets may be- used to place a payload into Earth orbit. Rocket systems capable of placing a payload in orbit are usually multistage. Design and analysis of multistage rocket systems are not addressed in this handbook. The first stage and perhaps the second stage operate as unguided free rockets. The later stages are guided to permit maneuvering to attain the desired orbital path. The unguided phase of flight places the vehicle at some altitude from which the orbital phase can be initiated. The use of unguided rocket systems for the lower phases of flight can result in considerable savings in guidance hardware when very precise positioning is not required. The SCOUT shown in Fig. 1-3 is an example of a rocket capable of placing a satellite into orbit.

1-2.2.5 Dispensing

Dispensing rocket systems dispense materials—either for research or military purposes-at some point in the trajectory of the rocket. Examples are chaff-dispensing rockets, leaflet-dispensing rockets, smoke-dispensing rockets, and rockets to disseminate crystals of various substances for cloud seeding to induce rain. The chaff dispensers are used to put large quantities of very small metallic wires or strips in an area at some height above the ground. Leaflet rockets are used to deliver propaganda leaflets to areas not accessible from the ground. Although not in general use, cloud seeding rockets have been proposed, e.g., a rocket to dispense small pellets of dry ice into fog banks for fog removal over airports and similar areas. The rocket offers the advantage of delivering materials quickly, and its intrusion cannot be easily detected. The LOBBER shown in Fig. 1-1 can be used as a dispensing rocket.

1-3 OPERATIONAL MODES

1-3.1 GENERAL

Aerodynamically stabilized free flight rockets may be designed for use in a number of ways. It is not the purpose of this handbook to discuss all the uses of rockets, but to present the most common uses of military systems. Accordingly, the paragraphs that follow will briefly describe the modes normally used for military rocket systems. Classification by operational mode is normal military practice and also provides a useful alternative and supplement to the classifications used in par. 1-2.
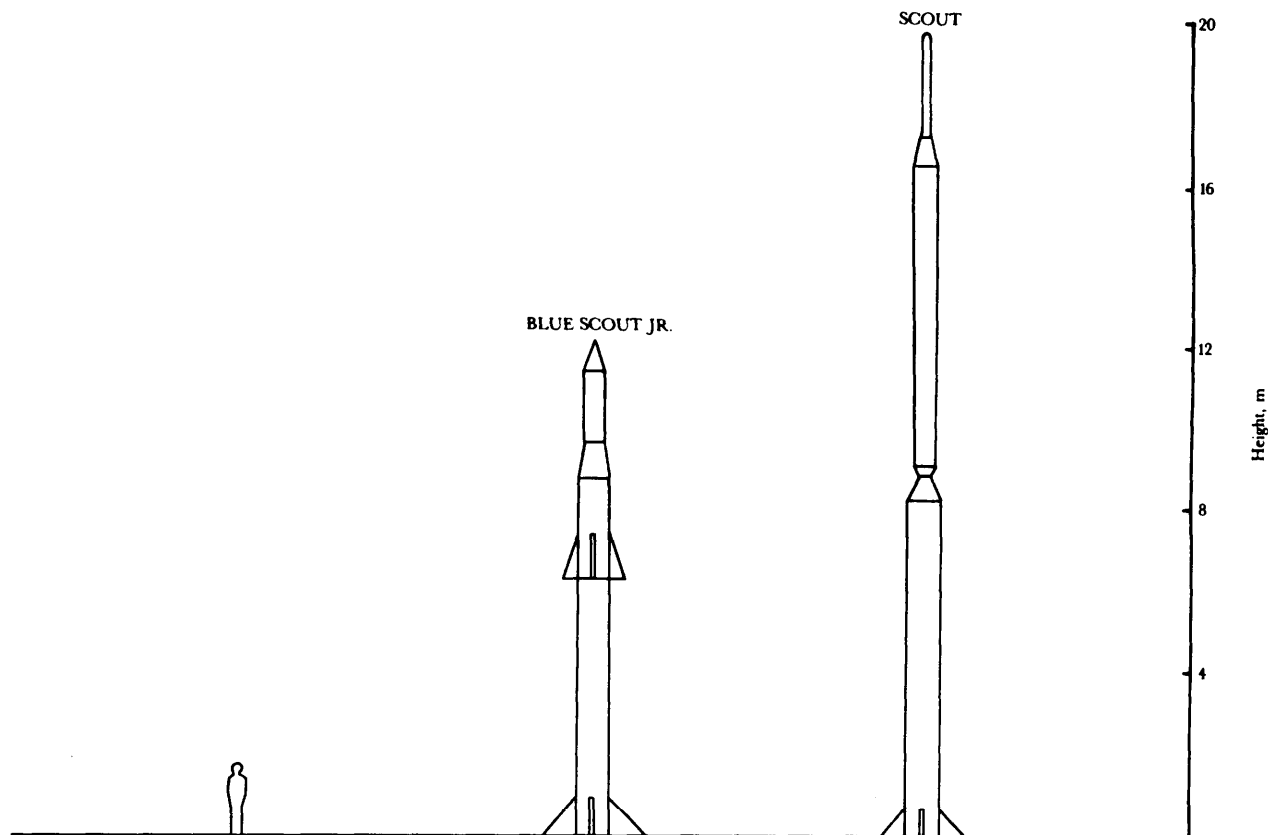
Figure 1-3. Examples of Large Free Flight Rockets

1-3.2 SURFACE TO SURFACE

Surface-to-surface aerodynamically stabilized free flight rockets are launched from a point on the surface of the Earth to a target also on the surface. Most artillery, infantry, and armor rocket systems are used in this mode. They can range from small shoulder-fired rocket systems to large rockets fired from launchers requiring heavy transport equipment.

1-3.3 SURFACE TO AIR

Surface-to-air rockets are usually employed in the defense of ground troops or equipment. The rocket is launched from the surface against an airborne target—e.g., a manned aircraft, an unmanned drone, another rocket or missile, or simply a point in space. Air defense, meteorological, high-altitude sounding, and dispensing rocket systems operate in this mode.

1-3.4 AIR TO SURFACE

Air-to-surface rocket systems are used for suppressive fire over areas and to deny the enemy a specific position. Air-to-surface rockets are fired from fixed-wing or rotary-wing aircraft, usually from low altitudes because of accuracy limitations, and usually are relatively short range.

1-3.5 UNDERWATER LAUNCH

Rocket systems have been built to be fired from beneath the water and to continue flight after emerging into the atmosphere. The design considerations after entry into the atmosphere are similar to any other atmospheric rocket. This handbook will only address the atmospheric phase of rocket flight.

1-3.6 SURFACE OR AIR TO UNDERWATER

These systems are fired from the air or surface, experience a phase of atmospheric flight, enter the water, and continue through the water to the target. A rocket of this type must be designed for travel through the atmosphere and through the water. This handbook will only address design considerations for the atmospheric phase of flight.

1-4 GENERAL ROCKET SYSTEM DESCRIPTION

A rocket system is made up of a number of subsystems, or elements, each of which performs a function necessary to the successful performance of the system. In general, the system is composed of three main elements—i.e., rocket, launcher, and fire control equipment. Each of these elements is, in turn, composed of subelements or components. This handbook will discuss the rocket in considerable detail and will discuss the other elements only insofar as they interact with the rocket. The reader should consult other handbooks for the details of the other system elements.

The basic components of an aerodynamically stabilized free flight rocket area are a payload or warhead, a propulsion motor, and an airframe. The airframe provides structural rigidity and the physical envelope for the internal components. The airframe shape is also important in determining the flight dynamic characteristic of the rocket. A typical rocket configuration and its components are shown in Fig. 1-4. The functions and major characteristics of each component will be discussed in Chapter 2.
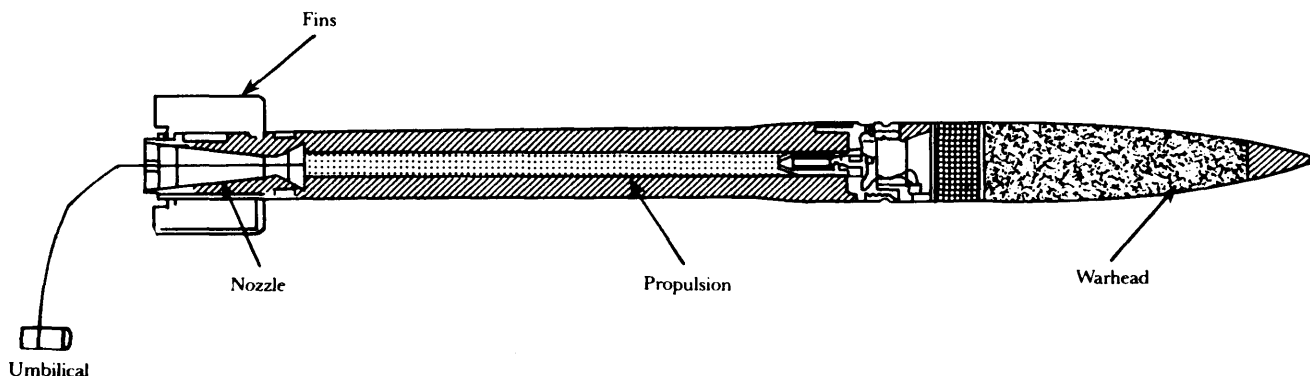
Figure 1-4. Typical Free Flight Rocket Configuration

1-5 OVERVIEW OF CONTENT OF THE HANDBOOK

The applications of this handbook are limited to atmospheric flight of aerodynamically stabilized free flight rockets employing solid propellant motors. The handbook is organized into chapters subsequently described, that are each self-contained and applicable to a particular technical area. Conceptual and system design phases of development are discussed in some detail, but the primary emphasis is on the preliminary design phase. The technical areas are System Design, Performance, Accuracy, Aerodynamics, Propulsion, Structures, Heat Transfer, Launcher Considerations, Atmospheric Considerations, and Computer Programs. A synopsis of these chapters follows:

1. Chapter 2, "System Design", introduces the system design process and illustrates the type of data inputs and outputs for each of the engineering disciplines.

2. Chapter 3, "Performance", presents data describing the performance of various design concepts. Material is provided which will permit consideration of trade-offs to maximize range for a given mass or optimize mass for a given range.

3. Chapter 4, "Accuracy", presents data pertinent to estimating the accuracy of a given concept. Launch, powered flight, and ballistic phase errors are considered. The effects that errors during each of the flight phases have on impact dispersion are presented.

4. Chapter 5, "Aerodynamics", presents design curves, equations, and data that will permit the prediction of stability and drag characteristics for commonly used aerodynamic bodies or combinations of bodies, including various types of fins and other stabilizing devices.

5. Chapter 6, "Propulsion", presents concepts and data necessary to predict propulsion system performance, as well as important considerations in conceptual and preliminary design.

6. Chapter 7, "Structures", presents data and methods pertinent to structural design, mass estimating techniques for preliminary design considerations, and heat transfer considerations.

7. Chapter 8, "Launcher Considerations", discusses launchers and delineates interfaces and interactions between the launcher and the rocket. Constraints placed on the launcher by the rocket system requirements are also discussed.

Three appendixes—located at the rear of the handbook—are included to assist the designer, namely:

1. Appendix A, "Atmospheric Considerations", presents climatological information pertinent to free flight rocket design.

2. Appendix B, "Computer Programs", presents a brief description of representative computer programs that can be used in the design of aerodynamically stabilized free flight rockets.

3. Appendix C, "Heat Transfer Equations", presents calculation methods for conductive and convective heat flow.

C H A P T E R   2
S Y S T E M   D E S I G N

This chapter- describes the process of designing an aerodynamically stabilized free rocket. The acqui-sition process for development of a rocket system is discussed briefly. The emphasis is on the concept selection and preliminary design. The system validation phase is discussed since this effort is involved in the testing and verification of hardware through prototype development and testing. Production engineering, manufacturing, and deployment are mentioned briefly.

2-1 G E N E R A L

This handbook, which is primarily intended for conceptual and preliminary design, divides system design into three phases: (1) concept selection, (2) preliminary design, ant! (3) systems validation. The Department of Defense (DoD) acquisition process for weapon systems, as defined by DoD Directives (Refs. 1 through 4), is essentially the same for all branches of service. In general, this acquisition process involves a conceptual phase, a validation phase, a full-scale development phase, and a produc-tion and deployment phase.

The concept selection and preliminary design activities described in this handbook are encompassed by the conceptual phase in the DoD acquisition process; the described system validation phase activi-ties correspond to the validation phase of the DoD acquisition process. However, the full-scale devel-opment phase and the production and deployment phase of the DoD acquisition process are not emphasized. The terminology used is that commonly employed by engineers to define the technical activities involved in a system design. Fig. 2-1 depicts the three phases of activities discussed in this chapter. The feedback shown for each of the three blocks is to emphasize the iterative nature of the technical activities involved in the system design process. Fig. 2-1 is discussed further in the paragraphs that follow.

2-1.1 CONCEPT SELECTION PHASE

The concept selection phase begins with the identification of a needed mission or operational requirement or the identification of new technology; it usually ends with the submission and approval of the Justification of Major System New Starts (JMSNS). The JMSNS is the official document used to describe the mission and to justify the initiation of a new major system acquisition. The major activi-ties of concept selection are studies performed to establish system or component constraints, parametric trade-off studies for selection of candidate integrated systems, and system concept definitions. For example, component constraints may require the rocket to operate with an existing piece of equip-ment, to be man rated and shoulder mounted, or to fit on a specific rocket launcher. The parametric studies may include accuracy requirements for kill, guided versus unguided, warhead lethality versus dispersion, size of warhead, propellant selection, propellant design, operational range, type of target, accuracy, fire control technique selection, etc. The concept selection phase ends

1. When the mission and performance envelopes are adequately defined

2. When the system is deemed to be technically feasible and capable of achieving the stated objec--tives within reasonable cost and schedule constraints

3. When the military objectives, technical requirements, and economic costs are determined to be sound, reasonable, and well defined

4. When the JMSNS document, to allow the study to progress into preliminary design, is approved.
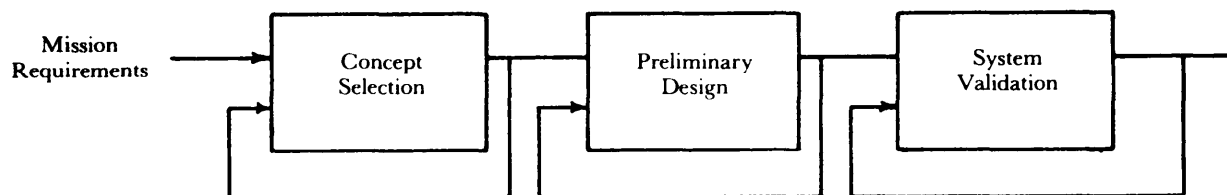
Figure 2-1. System Design Phases

2-1.2 PRELIMINARY DESIGN PHASE

Preliminary design phase activities begin with the output of the concept selection phse and end with the creation of fuctional baseline specifications. All interfaces between the rocket and other equipment should have been defined at the end of preliminary design. The advanced development studies begin during the preliminary design phase. Activities in this phase include trade-off studies and breadboarding for key subsystems and components to show feasibility and to demonstrate capability. For systems exceeding spedified levels of development cost, an official required document called Letter of Agreement (LOA) is prepared by the combat developer, corrdinated with the material developer, and submitted through official channels to support further development work. The preliminary design phase is a highly iterative process with activities performed either simultaneously or sequentially. This phase requires a continuous system integration effort to provide updated requirements and data inter-faces to all technical disciplines and design efforts involved. The preliminary design system integration effort compares and makes trade-offs between the known altermatives, determines the status of technol-ogy for each alternative, evaluates the environmental impact of each alternative, and recommends specific actions that should be followed to meet the required capablity. Usually, the task of exploring and identifying alternative system concepts is made into a competitive activity to facilitate the selection of the best possible solutions from industry, the academic community, and Government sources, including foreign developments. The validation and updating of the JMSNS includes initiating and conduction studies that involve system analysis trade-offs, cost-effectiveness, and evaluation of techni-cal approaches. A primary objective of the preliminary design effort is to compare alternative system design approaches before selection of the single approach that best meets the need. The preliminary design data are basic to the accomplishment of parallel support studies such as risk assessment, cost estimates, utility analysis, and energy effictiveness studies. Government sources usually are involved in the technical and cost risk assessment and trade-off analysis studies as state-of-the-art experts. Part of the preliminary design activities usually are performed as parallel advanced development efforts by competing industrial and Government sources.

Major design or technological uncertainties are identified during preliminary design for further investigation during the system design (validation) phase. Planning for testing to eliminate these uncertainties begins during preliminary design. Estimated test costs, schedules, and facility support requirements are also and output of the preliminary design phase.

Production feasibility assessments, producibility problems, production processes, tolling develop-ments, production tests, and demonstrations identified during preliminary design are evaluated to determine overall production risk, production cost, and schedule impacts. This assessment is used to identify prototype tests and demonstrations that must be performed in the system development phase.

The functional baseline (program baseline requirement) is established by the end of the preliminary design phase and includes broad system performance objectives and operational concept, a logistic concept, and cost estimates. The system specification defines the technical portion of the baseline.

2-1.3 SYSTEM VALIDATION

Activities performed in the system validation phase include a definition of the program charac-teristics—i.e., performance, cost, and schedule. These parameters are validated and refined through extensive study and analysis, hardware development, or prototype testing. The quantity and level of prototype and hardware validation depend on the nature of the program and the risks and trade-offs involved.

The end objective of the system validation phase is to determine whether to proceed with full-scale development. The ultimate goal of the system development phase, in which the development is to be performed (usually by a contractor), is to establish firm and realistic equipment performance specifications that meet the operational and support requirements.

The test hardware produced during this phase is usually produced by other than production methods and probably is a prototype in form. Although qualification testing is performed in the full-scale development phase, the testing performed at this point should be conducted to check the design for functional performance. Development, test, and evaluation of training simulators, test equipment, tools, and other support equipment parallel the development of system prototypes.

The baseline design requirement is established during the system development phase and is the basis for detailed design and development of the system during the full-scale development phase. This baseline incorporates the technological approaches developed to satisfy the objectives in the functional baseline (program requirements). During the system development phase, these objectives are translated into system segment, subsystem, and configuration items (CIs) performance requirements and decision constraints.

The system validation phase should produce a more precise and detailed definition of the systtvn as the functional baseline grows into the design requirements baseline. Documentation resulting from the system development phase should include the following technical reports:

1. System engineering studies and analysis information
2. Updated system specification
3. Detailed specifications for prime item equipment, real property facility items, computer programs, and critical identifiable engineering components
4. Data requirements or recommendations.

System end-items or components requiring hardware proofing are identified in the system development phase. Prototypes of systems or components requiring hardware proofing also are produced and tested in the system development phase. Development prototypes produced will vary from a breadboard of a system or subsystem to complete flying prototypes.

A major effort in the system validation phase is performing trade-off studies to ensure that a configuration being defined for full-scale development addresses tactical needs and is the best possible balance among total costs, schedule, and operational effectiveness.

A document called the Required Operational Capability (ROC) is written during the system validation phase. The ROC is the requirement document that supports the work to be undertaken in the full-scale engineering development effort. The remainder of this chapter addresses the various technical activities, data requirements, and data interfaces involved in the system design of an aerodynamically stabilized free rocket.

2-2 REQUIREMENTS

The development of any new rocket system begins with a specific requirement the user believes must be met, i.e., requirements start with the definition of some mission objective by the user. Mission objectives can be stated in a wide variety of terms and even in very broad terms, For example, a need may start simply as the desire to provide the infantry with some defense against armor. The statement of this mission objective could be very broad—provide a weapon that is transportable by an infantry-man and capable of destroying armor at a particular range. The ability to place a particular payload at a point at specified ranges within certain accuracy requirements is another example of a broad mission objective. The general requirements to meet some particular need establish broad requirements on the rocket system. The broad requirements then are the genesis of more detailed requirements, i.e.,

1. Operational requirements to meet a broad mission objective usually hav the effect of placing more detailed requirements on the system.
2. Compatibility with other systems and subsystems places additional restraints on a system.
3. Weight and size usually are physical constraints imposed upon a system.
4. Performance objectives place certain requirements on a system that are incompatible with the

physical requirements of weight and size. Thus compromises must be made.

    5. Safety factors influence system design.

    6. Reliability and maintainability must be given serious consideration.

    7. Environmental factors, such as temperature and humidity operating ranges, place requirements on system design.

    8. Finally, costs—development, production, and operating and support-placr additional constraints on system design.

    Thus, detailed design requirements are the result of the many general requirements placed on the rocket system. The final design of the system to achieve the overall mission objective is the result of trade-offs among requirements. The remainder of this chapter discusses trade-off and design studies to be performed in the system design of an aerodynamically stabilized free rocket.

2-3 CONCEPT SELECTION

    Concept selection is the process of identifying a system or systems that have a reasonable chance of satisfying the user's needs. The selection of a concept can be as simple as identifying an existing system that meets the user requirements. However, the usual case requires that a complete, new system be designed or at least that some of the system components be redesigned to meet the new requirements. The process of designing a new or imposed system usually evolves from either the determination of a need or the development of new technology that allows previously established needs to be met. Fig. 2-2 depicts the steps and information flow for the concept selection phase activities. User needs enter the system as general requirements. Data on the capabilities of existing systems are an input to be compared to the general requirements. The technology base information-originating from industrial and/or Government sources-consists of inputs on state of the art in component and system designs. The comparison of mission needs and the technology base will yield information on the feasibility}' of developing a new rocket system to meet the general requirements. Mission objectives and system and/or components constraints that meet the user's general requirements are developed during the concept selection process. The mission objectives and system and or component requirements and constraints are then used in the parametric trade-off study. By using the results of the analyses performed, the selection of a concept or concepts is made. The concept selection process also will identify technology areas that require improvement or further development to meet the requirements. Estimates will be made of the costs and times required to develop this required new or upgraded technology, and attendant risks will be identified. Information on costs and times required to develop new or upgraded technology then is compared to mission needs to determine whether the new system can be developed within the time frame required and be cost effective. This comparison could result in changes in mission objectives and the repetition of the concept selection process. The process of concept selection
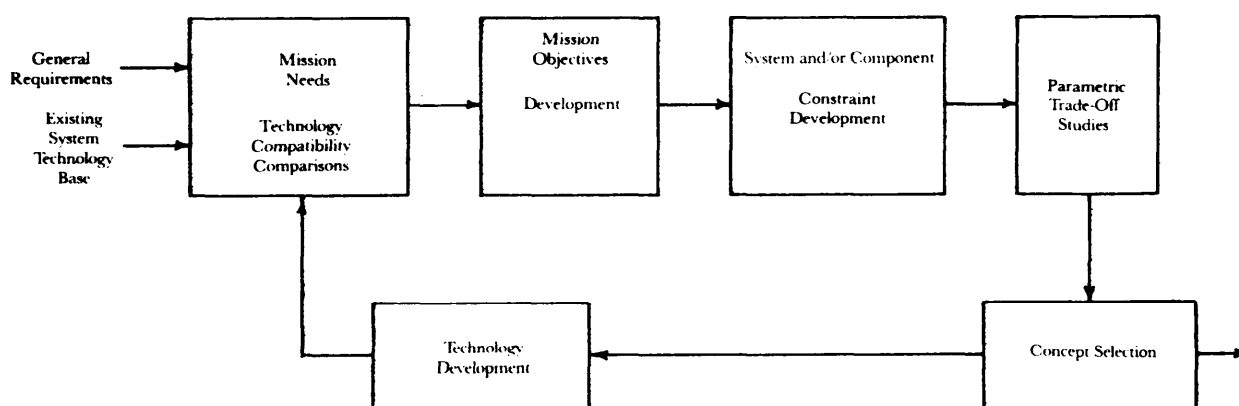
Figure 2-2. Concept Selection Phase Activities

is iterative in nature and is a continual process until timing, cost, and technology are properly balanced to meet the mission needs as defined by the user.

The mission objectives development in the concept selection phase are usually the result of closely examining the needs as determined by the user and intelligence sources, and refining these needs into technically feasible and definable objectives. The constraint development, parametric studies, and system selection process are discussed in more detail in the paragraphs that follow.

2-3.1 COMPONENT CONSTRAINTS

Constraints are imposed on a free flight rocket due to its use, lethality requirements, and method of launch. A man-launched direct fire free rocket must be small. A rocket launched from a slow speed rotary-wing aircraft may require a special design to provide stability at low speeds. Coverage of area targets and suppressive fire against personnel may be provided by high velocity fragmentation and blast, flechette, and white phosphorus smoke warheads. The desired effect against wheeled vehicles, parked aircraft, materiel targets, bunkers, and light armored vehicles may be provided by high-velocity fragmentation and high explosive antitank (HEAT) warheads. To defeat a tank, it may be necessary that the rocket impact at an angle nearly normal to the surface and near the center of a tank. Another type of constraint is that the propellant be essentially smokeless to minimize visual and infrared (IR) signatures.

Helicopter fired rockets have the constraint that the thrust profile must be staged or must progressively increase as the rocket moves away from the launcher. Low thrust levels at launch reduce the launcher motion on subsequent firings in a ripple fire mode, and the increased thrust levels are required during the boost period to reduce dispersion.

Thus the mission and operational environments place constraints on the rocket system. For example, if the same rocket is to defeat different target types, it may be desirable to have several types of warheads available. The operational utility of having several types of warheads then is constrained by the logistic problems of providing the various type warheads.

Mobility and transportability requirements of the system will place constraints on the physical dimensions of the rocket. The rocket will be required to fit within prescribed physical dimensions. Mass restrictions determined by the mode of transport certainly place constraints on the rocket. A rocket to be transported by man must meet the mass lifting limits and portability criteria of Military Standard (MIL-STD) 1472.

2-3.2 PARAMETRIC STUDIES

2-3.2.1 General

Parametric studies and trade-offs conducted during the concept selection phase are discussed in this paragraph. The mission objectives and constraints on system and component characteristics will, in most cases, define the class of rocket required and the operational mode, e.g., a military versus a research rocket. Military use for the rocket—such as air defense, artillery, or antiarmor-is determined from the mission objectives. Further, the mission objective establishes the type of launcher required and defines the target kill requirements. First-cut payload or warhead sizing usually is based on the characteristics of the target; however, first-cut propulsion system sizin,g can be made by using (1) range considerations and (2) payload mass and vehicle propulsion to structure mass fractions from similar rockets. Accuracy requirements determine whether the rocket is guided or unguided.

The determination of performance parameters is a necessary first step in designing a rocket. This step defines the relationship between the performance requirements and physical characteristics of the rocket. The parametric study results will show the sensitivity of the physical parameters of the rocket to variations in performance requirements, propulsion system characteristics, aerodynamic characteristics, and energy management techniques. Studies that need to be performed after the performance trade-off study include aerodynamic characteristics, warhead sizing, structural analysis, and accuracy.

Based on a knowledge of similar rockets, an experienced design engineer can estimate sufficient

parameters to determine, in an iterative manner, the rocket performance and propulsion requirements. Chapter 3 presents data that can be used to provide estimates of propulsion system sizing.

The parameters that are sized or considered in the performance trade-off studies involve aerodynamic and propulsion considerations as well as performance interactions. The perfomrance type parameters that are determined in these studies are payload mass, burnout velocity, range, time of flight, and launch angle. Determination of these performance patameters requires knowledge of aerodynamic characteristics, primarily drag, as a function of length, diameter, nose shape, and stabilizing surfaces.

Propulsion-type parameters identified in the performance calculations are specific impulse, motor propellant mass fraction, total impulse, burning time, and thrust to initial rocket mass ratio.

The aerodynamic design of a rocket involves trade-off studies of small variation in component performance for different candidate comfigurations. The aerodynamic design goal is to select an integrated rocket configuration that provides tailored aerodynamic stability and lowest drag consistent with other design constraints to achieve minimum dispersion and maximum range performance. To estimate the aerodynamic stability characteristic for different configurations, it is necessary to know the aerodynamic coefficients of each major rocket component and interference relationships between the components. The aerodynamic trade-off studies are defined in detail in Chapter 5. The aerodynamicist must know how to combine these component coefficients to arrive at values for the complete configurations.

2-3.2.2 Motors

The primary function of the rocket motor is to accelerate the rocket with its payload to the required velocity to achieve the desired flight range. In the conceptual phase, the initial effort to define the rocket motor is directed toward establishing nominal values—those which meet the user and operational requirements and restraints—for all essential parameters. For instance, if limitations are given for impulse, chamber pressure, burning time, size, and mass, then a set of advantage values can be derived for motor physical design characteristics, propellant ballistic mass flow, and other properties.

Often in the comceptual phase the performance characteristics of solid propellant rocket motors are scaled from motors with similar characteristics. The parameters suitable for scaling or simple calculations are rocket thrust, nozzle throat or exit area, motor mass, specific impulse, total impulse, chamber pressure, burning rate, and burn duration.

2-3.2.3 Warheads

Warhead trade-off studies involve many factors and considerstions. For example, there are trade-offs between warhead weight and overall rocket weight, and trade-offs between warhead types for various target mixes. Reload and or resupply situations also will influence the types of launchers and personnel handling requirements in warhead trade-off studies. Other trade-offs will address the problem of packaging various available ordnance into allowable physical dimensions to establish the most effective configuration from a target kell probability point of view. These studies consider rocket delivery accuracy, warhead lethality, and target vulnerability to determine the size, number, and type of warhead required.

The specific type of warheads wused in the trade-off studies will depend on the target characteristics and the kill effectiveness of the various warheads against the targets. The types of warheads that would be considered are blast fragmentation, kinetic energy peretrators, shaped charge, self-forging gragments, and duel purpose. Each type of submunition can be considered as a warhead and trade-offs made to determine the type required.

2-3.2.4 Error Sources

Accurate free flight rocket systems are achieved by either reducing the magnitude of the error source or the sensitivity of the rocket to the error. The most significant error sources influencing the accuracy of free flight rockets are malaim, mallaunch, total impulse reproducibility, thrust misalignment, dynamic unbalance, surface wind, ballistic coefficient, air density, and ballistic wind.

The dispersions for these error sources are calculated using a 6-degree-of-freedom (DOF) and a point-mass trajectory program. After error free baseline trajectory is established, each error source is usually

considered independently in preliminary design studies to determine the contribution to dispersion due to that error. The dispersions for the various error sources are then root sum squared, and the circular error probable (CEP) is calculated for a particular rocket design. It should be recognized that in some cases error sources are interdependent and cannot be root sum squared. The error source trade-off studies will show the relative merit of competing aerodynamic tailoring techniques for reduction of dispersion during the burn phase. The accuracy studies will also identify the important error sources. The error analysis trade-off studies coupled with warhead lethality studies can provide data for use in the cost-effectiveness studies. The dispersion sensitivities to error sources determined in the error analysis studies also provide input to the design of a rocket system. Monte Carlo methods can be used to provide data for system accuracy analysis and are often used when the assumptions for calculating miss by applying the root-sum-squared method to individual errors are invalid.

2-3.3 SYSTEM SELECTION

The system selection process consists of applying the given requirements and constraints (boundary conditions) to the parametric trade-off studies and selecting the concept(s) that best meets the user and operational requirements.

The concept selection process will include all technical disciplines necessary to establish the interaction between rocket components, and the interaction between rocket components and the environment to ascertain that rocket user and operational requirements are met. The rocket system selection process begins with performance parametric trade-off studies. These studies establish the interaction-with certain rocket aerodynamic factors and propulsion parameters—of payload mass, burnout velocity, range, time of flight, and launch angle.

The parametric studies provide information for the selection of the proper aerodynamic shape, thrust energy management, total impulse, warhead type(s), and fin deployment. The class of rocket needed and its operational mode are primarily determined by user needs and mission objectives. The parametric trade-off studies will determine whether accuracy requirements are comparable with a free rocket. Launcher considerations are influenced by the rocket class, accuracy requirements, and operational mode. The launcher, in turn, initially influences the rocket drag because of shoes, sabots, spin lugs, umbilical, etc. Operational environments also place constraints on the launcher type considered for the system.

The system selection process should result in the definition of a rocket system concept(s) that has a high probability of meeting the mission objectives and operational effectiveness criteria. New technology development requirements are identified, and the time frame for meeting the development requirements is established. Estimates of system development costs and life cycle costs also are made. Finally, system effectiveness studies are made to determine the overall cost-effectiveness of the selected concept(s).

Data of the type described in this paragraph are used in deciding whether to proceed into the preliminary design phase.

2-4 PRELIMINARY DESIGN

The development of a new rocket system proposed in the conceptual design phase reaches a formal status with the start of the preliminary design phase. The JMSNS has now been prepared and received appropriate approval. The output of the conceptual design phase is available to start the preliminary design. The mission objectives and requirements developed in the conceptual design phase provide the basis for starting the preliminary design, and the concept(s) selected for further analysis is refined and analyzed in the preliminary design phase. All information and data developed in the conceptual design phase are input data to the preliminary design phase.

Fig. 2-3 depicts the technical activities that take place in the preliminary design phase. Subsystems are designed and optimized in an iterative fashion. The results of the parametric studies and trade-offs are used in the subsystem design and, in conjunction with the mission objectives, are amalgamated into an overall system design. The system design is then translated into a set of specifications, interface
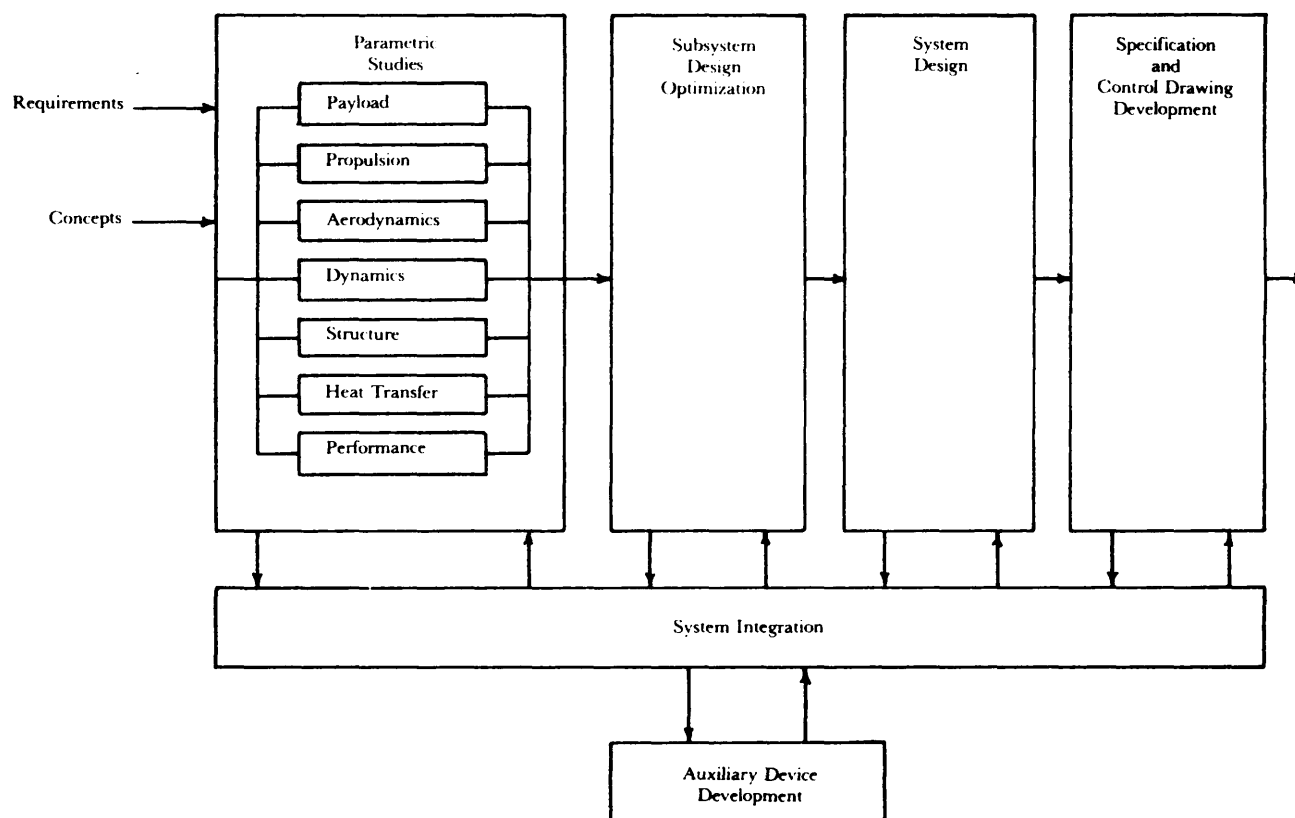
Figure 2-3. Preliminary Design Phase Activities

control documents, and design drawings from which the prototype or engineering development can proceed. Fig. 2-3 illustrates a system integration function that accepts inputs and provides feedback to all the other activities. The system integration function is illustrated this way to stress the importance of information exchange among the activities, and it is assigned this strong role to stress the importance of maintaining balance and a single sense of purpose for the other activities. System integration also provides the interface with other activities involved in the development of auxiliary devices.

The preliminary design phase explores alternative system concepts to evaluate the effects of various trade-offs in minimizing the major design and technological uncertainties. A test and evaluation plan is developed at the end of the preliminary design phase for use during the system design phase. Testing is pm-formed during the system validation phase to verify that all major uncertainties identified during the preliminary design phase have been eliminated.

The preliminary design phase concept selection process is an iterative process. Further detail on each of the preliminary design activities is provided in the paragraphs that follow.

2.4-1 PAYLOAD

The class of rocket and the operational mode largely determine the type payload required for an aerodynamically stabilized free rocket.   The payload for most military rockets is a warhead.   A general description of a warhead was presented in par. 1-4.2 and will not be repeated here.   This paragraph briefly defines the engineering analyses and trade-off studies involved in the preliminary design of a warhead.   The detailed mission objectives will define the function of the warhead.   Questions to be resolved before detailed warhead design begins include type of target(s), hardness of target(s), rocket accuracy, and number of rockets expendable per target.   Probability of kill for a particular target is a consideration in establishing the requirements for the warhead.   Probability of kill analysis involves target vulnerability studies and detailed information on the destructive effects of the warheads.   Proba-

bility of kill assessments and velnerability analysis are beyond the scope of this handbook but are presented in other handbooks in the Engineering Handbook series. The remainder of this paragraph will discuss the warhead kill mechanisms, performance characteristics, physical characteristics, and safing, arming, and fuzing. Each of these items will be discussed in general terms. The reader should consult Refs. 5 through 13 for detailed analysis techniques and parametric data.

2-4.1.1 Kill Mechanism

A rocket for artillery or infantry use may have a requirement for a variety of warheads. The need may be to destroy a point tar-get, e.g., a tank, or provide wide area coverage for the neutralization or suppression of area targets consisting of personnel and unarmored materiel. The kill mechanism employed will depend on the target characteristics, system delivery errors, range, mission, etc.

Blast fragmentation warheads and submunitions are employed against targets such as perso]]ncl; supply dumps; ammunition dumps; petroleum, oil, and lubricant dumps; groups of buildings; and other soft materials. The lethal effect is provided by thousands of small high velocity fragments.

Warheads with small arrow- or dart-like elements (flechettes) have some advantages over unitary blast/fragmentation warheads in use against personnel provided the spray angle can be concentrated onto the target such that a larger portion of the fragments (flechettes) is more effectively used, i.e., more hits.

Penetration-type warheads must have sufficient energy to pierce a target. One technique for achieving the required momentum is to accelerate a slender warhead to a hypersonic velocity with a blunt rocket. The warhead separates from the rocket at motor burnout because of the greater ballistic coefficient of the warhead. Once the warhead impacts the target—depending on the warhead-the kill mechanism will result from blast, fragments, spall, penetration, or a combination of these effects.

Self-forging fragment warheads and shaped-charge warheads are used to neutralize tanks and other armored targets. The warheads penetrate the armor and scatter high velocity metal particles that affect the occupants, ammunition, fuel, etc.

Warheads can be designed to contain various chemical agents. The function of the warhead will differ depending, for example, on whether the chemical agent employed has a lethal effect or only a disabling effect.

2-4.1.2 Performance Characteristics

A rigorous system analysis to establish performance characteristics for a warhead requires a detailed knowledge of certain parameters, namely, functioning mode, delivery accuracy, fuzing system errors and correlation, target vulnerability considerations, and detailed warhead performance characteristics and fragmentation properties. If this information is not available, warhead kill-studies are conducted on a lethal area basis alone. Assumptions made for the area studies are dispersal full-cone angle, shape and drag factors, angle of fall, velocity at burst, and burst height. Lethal area computations for all rounds are made on the basis of a uniform hit density across the target width at all ranges. The lethal area for a single warhead is obtained from test data. An analysis is then performed to evaluate the fraction of warheads or submunitions which will impact inside a circular target from multiple rocket firings. All rockets are assumed to be aimed at the center of the target. The number of rockets required to achieve the desired damage or casualty effect is then calculated by using predetermined data on target hardness, target density, blast overpressure, and the number of fragments expected in a given area from the rocket warhead.

The percent of casualties and damage effect will increase both (1) as the ratio of the target radius to the effective kill radius is decreased and (2) as the ratio of the CEP error distance to the effective kill radius is decreased.

2-4.1.3 Physical Characteristics

The physical characteristics of a warhead will vary depending on its intended target and on the rocket delivering the warhead. The external shell of the warhead is designed to provide the aerodynamic and structural properties needed for performance, accuracy, launching flight dynamics, and

handling of the overall rocket. The internal physical characteristics depend upon the type of warhead—i.e., whether the warhead or submunition is a high explosive, a flechette, a chemical, a penetrating, self-forging or shaped-charge type, and on the fuze type.

2-4.1.4 Safing, Arming, and Fuzing

The safing, arming, and fuzing of a warhead are functions that must be performed properly or the effectiveness of the total rocket can be drastically degraded. Safing is the process that makes the warhead and rocket sfe to handle—i.e., the warhead is prevented from a unwanted detonation caused by storage, handling, launching, and other considerations. arming is the process of preparing the warhead for detonation. During arming, the safing functions are neutralized and the warhead is prepared for detonation upon receiving the proper signal from the fuze. Safing and arming are functions designed into the fuze.

Fuzes can be super quick, delay, proximity, etc. The super quick (point-detonating) fuze initiates the explosive charge immediately upon striking an object. a proximity fuze, which activates when the warhead passes near the target, can be used for in-flight fuzing; this type of fuze function when the warhead passes whing some predetermined distance of the target. Delay fuzes provide a delay after target impact before the warhead is detonated. Often this is done to give the warhead time to penetrate the target before exploding. Delay fuzes may use the burning characteristics of primer cord to create a delay or use a mechanical device that requires a specific period of time to initiate. Electronic time delays can be created by the charging or discharging time constant in resistive and capacitive networks. Timers created by integraged circuit technology can be very small lightweight. Either electronic or mechanical timers can produce delay times that allow detonation of the warhead at some specified time after the occurrance of a particular event. Whatever method is used, the amount of delay time should be known, repeatable, and reiable. See Refs. 14 through 19 for fuze design information.

2-4.2 PROPULSION

This paragraph introduces the parameters, engineering analyses, and design processes involved in the preliminary design of propulsion systems for an aerodynamically stabilized free rocket. A solid propellant motor is used for a number of reasons to propel aerodynamically stabilized free rockets. Solid propellants are safer to handle, cheaper to buy, simpler to use, storable for longer periods, and more reliable in the operational environment.

The parameters to be determined in the preliminary design include propellant masss (total impulse), propellant mass consumption rate (thrust profile), combustion pressure and temperature, the ratio of propellant surface area to nozzle throat area, and nozzle expansion ratio. These parameters usually are determined through trade-off studies at both the motor and system levels. Analyses are perfomed to develop methods of obtaining the desired thrust versus time profiles. The obtaining of an axisymmetric thrust vector and repeatable burnout weights ad velocities are problems to be solved in the preliminary design phase. See Refs. 20 and 21 for propulsion data

2-4.2.1 Propulsion Energy Management

Energy management techniques can be used to (1) reduce the rocket dispersion sensitivity to the boost phase and ballistic phase error sources and (2) reduce the error source value and the sensitivity of the rocket to these error sources. Some energy management techniques that have been used to impart propulsive energy to a rocket system are boost, boost-sustain, staged boost, and shaped thrust-profiles.

Once ignited, a solid rocket motor ususaly burns continuously until all propellant is expended. Shaping of the propellant is the motor case creates various burn areas as a function of the amount of propellant remaining. The burning characteristics are termed progressive, neutral, or regressive depending upon whether the burning area increases, remains constant, or decreases with time, respectively. Thus it is possible to shape the thrust profile through the geometric configuraation of the propellant.

The boost-sustain approach consists of an initial, high thrust of the booster motor which is followed by either a constant or varying sustaining thrust of lesser magnitude. The boost or boost-sustain energy

management techniques are used in most military aerodynamicaly stabilized free flight rockets. Sour-ding rockets sometimes use the staged boost method of energy management.

Aerodynamically stabilized free rockets require high thrust and high acceleration during the boost phase to minimize dispersion. Plumes from underexpanded motor exhausts induce boundary layer separation; the net effect on aerodynamic characteristics is a reduction in the static stability margin. Considerate ion should be given to plume effects on the aerodynamic characteristics in order to prevent instabilities. However, the desirable situation to reduce sensitivity to wind is to have a rocket very near to neutral stability. The results published in Ref. 22 show how plume effects call be beneficially used to tailor static margin.

A boost-sustain configuration can reduce dispersion due to all ballistic phase error sources if the sustainer thrust matches the ballistic drag variation. The maximum to minimum thrust ratio required to reproduce this thrust variation is on the order of 10 or more. This variation in thrust is not within the present state of the art of solid rocket motors without significant system level trade-offs. This energy management technique loses its potential advantage in accuracy over a boost-only configuration because of this constraint, and the added error sources of sustainer total impulse, thrust level variation, and increased base drag during sustainer operation. Based on Ref. 23, the boost-sustain configuration does not reduce dispersion over that for a boost-only configuration due to state-of-the-art performance constraints placed on the boost-sustain motor.

2-4.2.2 Motor Design

2-4.2.2.1 Motor Physical Characteristics

A solid propellant rocket is made up of two major components-a loaded motor case assembly and a nozzle assembly. The motor case assembly consists of a head closure, cylinder, propellant, liner or inhibitor, insulation, aft closure, slivers, and igniter. A nozzle normally is composed of a convergent section, a throat, and an expansion section. Nozzles are designed to provide the proper expansion ratio depending upon the flight regime of operation (see Ref. 21). Nozzles for operation at sea level are different from nozzles for high altitude operation. If the rocket is to operate over a mixed flight regime (sea level and high altitude), the nozzle is designed to obtain the best compromise in overall performance.

Motor cases may be made of a medium alloy steel, a hardened alloy steel, a maraging steel, titanium, aluminum, or composites. Life cycle costs are important considerations in the choice of a motor case. Chapter 6 provides more detail of the physical characteristics of a rocket motor.

2-4.2.2.2 Performance Characteristics

The rocket performance characteristics are determined primarily by the motor performance, specifically by the propellant performance characteristics. For an acrodynamically stabilized free rocket to function properly it is important that the motor performance be predictable and repeatable. Minimizing variations in total impulse (the integral of the thrust with respect to time) and specific impulse (the impulse developed in burning one unit of propellant mass) are of fundamental importance in most rocket motor applications. Variation in impulse is typically the second or third largest source of range dispersion error in free flight rockets. Sources that contribute to impulse variation are burning rate variation, throat area variation, grain asymmetry, propellant mass variation, grain temperature, surface area variations, etc. (Ref. 24).

A rocket motor preliminary designer's usual goal, which is to select a propellant with the highest value of specific impulse and specific mass, is not as important for free flight rockets as obtaining a formulation that provides reproducibility of specefic impulse and specific mass. The major source of specific impulse variation can be reduced by reducing burning rate variations. It is shown in Ref. 25 that the composite propellant burning rate reproducibility was far superior to the other propellant families. Care should be taken in the preliminary design to select propellants that have burning rates as consistent as possible for the expected operational environment. Motor case, propellant grain, and nozzle variations produce variations in nozzle performance, propellant symmetry (thrust misalign-

ment), or propellant surface area (combustion pressure)—all of which also affect overall propulsion reproducibility.

2-4.2.2.3 Propellants

Two types of propellants have been used in solid propellant rockets—double base propellants and heterogeneous composite propellants. Recent propellant technology development incorporates aspects of these two propellant types into a new heterogeneous propellant that employs an energetic binder. A double base propellant is a homogeneous, plastic, solid monopropellant comprised of three principal ingredients—a polymer, an oxidizer-plasticizer, and a fuel plasticizer. The heterogeneous composite propellants also have three principle ingredients—a fuel that is an organic polymer called binder; a finely powdered oxidizer; and additives for catalyzing the combustion process, increasing the density, incrasing the specific impulse, improving physical properties, and increasing storage life. Considerations in the coice of type of propellant to use include exhaust plume smoke, impulse reproducibility, type of case insert needed, and cost. Free rockets are usually produced in large quantity; therefore, life cycle costs are an important consideration in the selection of a propellant.

2-4.3 AERODYNAMICS

The aerodynamic design of a rocket involves the study of the effect of variations in components on the dynamics, accuracy, and performance of the different candidate configurations. The aerodynamic design goal is to select an integrated rocket configuration that provides stable flight with minimum drag while it maintains insensitivity to outside disturbances. To determine the aerodynamic drag and stability characteristics for different configurations, it is necessary to estimate the aerodynamic coefficients of each major rocket component and each interference between components. The aerodynamicist must know how to combine these component coefficients to arrive at values for the complete configuration. The remainder of this paragraph will discuss methodology for estimating drag, calculating stability, and determining the effects of nonlinear aerodynamics. Each of these subjects will be discussed in general terms. The reader should refer to Chapter 5, "Aerodynamics", and Ref. 26 for more detailed discussions.

2-4.3.1 Drag

Drag forces on an aerodynamic surface are fundamentally the result of the horizontal components of the normal and tangential forces transitted from the air to the body. Estimation of drag for free rockets can be restricted to zero-lift because the rocket follows a ballistic path. The total drag on the rocket is the summation of wave drag, skin-fiction drag, and base drag. Wave drag is the result of pressure forces acting normal to all surfaces except teh base. Skin-friction drag is the result of viscous forces acting tangential to the surfaces. Base drag is produced by pressure forces acting normal to the base. Each drag force is discussed in teh paragraphs that follow.

The aerodynamic drag of the complete rocket is the most important foactor affecting accuracy and performance during the sustain the ballistic flight phases. Minimizing drag, for example, is more important for an indirect fire rocket since the sustain and or ballistic flight times are much greater than those of the boost phase.

2-4.3.1.1 Wave Drag

Wave drag is present on the rocket nose, the afterbody (boattail or flare), and the fins or other stabilizing surfaces. Nose wave-drag is influences primarily by the fineness ratio, nose shape, and Mach number. For preliminary design estimates, the family of nose shapes-of-interest for free rocket is bounded by cones and ogives. Data on these basic shapes are given in Chapter 5 and 7.

Various techiques can be used to reduce the drag on a rocket vehicle in flight. For example, if the exit diameter of the rocket nozzle is smaller than the body-cylinder diameter, the afterbody of the rocket may be tapered to form a boattail to reduce the base drag. This technique, however, increases the wave drag on the configuration. Therefore, an optimum boattail configuration results from balancing the increase in wave drag with the reduction of base drag.

Flared afterbodies are used sometimes to provide inherent restoring moments for which precise sta-

bility margin control is required. The drag on flares, however, is higher than the drag on fins giving equivalent stabilization. The wave drag on fins is slight compared to the total rocket drag, and it is influenced strongly by the thickness-to-chord ratio and sectional shape.

2-4.3.1.2 Skin-Friction Drag

Friction drag results from the boundary layer airflow over the rocket surface. Shear stress is imposed on the external surface of rockets due to the velocity gradient in the boundary layer. The magnitude of this shear stress is a function of the position of transition from laminar to turbulent flow, and, therefore, it is Reynolds number and Mach number dependent. Correlation of experimental data and analytical techniques has shown that the skin-friction coefficient for bodies of revolution is approximately 73% higher for laminar flow and 17% higher for turbulent flow than that on a flat plate (Ref. 27). The aerodynamicist must make appropriate transformations to available data to account for body shape.

2-4.3.1.3 Base Drag

The base drag is caused by the pressure forces resulting from airflow separation at rearward-facing steps such as body bases and fin trailing edges. The geometry of the rearward-facing step and the properties of the boundary layer approaching the step affect the drag.

2-4.3.2 Stability

Static stability is defined as the condition in which a disturbance of the system creates forces or restoring moments in the proper sense to drive the system toward equilibrium at zero angle of attack. If the subsequent motion finally restores the equilibrium, the system is termed dynamically stable. However, if the motion—although starting the system brick toward the initial equilibrium, never restores equilibrium-the system is termed dynamically unstable. The natural frequency of the system is proportional to the restoring moments anti inversely proportional to the inertia.

For a rocket to possess flight stability, a restoring moment must be produced when the longitudinal axis of the rocket is rotated away from the flight direction, i.e., when an angle of attack exists. This flight stability is achieved in aerodynamically stabilized free rockets by designing the external configuration so that the center of pressure of aerodynamicaatvx)(i}mamic forces acting normal to the longitudinal axis is located aft of the center of gravity. When the center of pressure is aft of the center of gravity, the rocket is said to be statically stable.

The degre of aerodynamic stability, or the static margin requirement, varies with the desired accuracy of each rocket and the design approach. For example, a rocket designed for minimum dispersion during powered free flight requires special tailoring of the static margin over the expected Mach number regime; however, a high-acceleration rocket, which achieves most of its velocity prior to release from the launcher, only has a requirment that the stability margin remains within certain upper and lower bounds. The width of this stability band is governed primarily by the requirement to maintain a suitable spread between roll and pitch-yaw frequencies.

2-4.3.3 Nonlinear Aerodynamics

The aerodynamicist must consider nonlinear aeridynamic forces and moments under certain situations. The basic aerodynamic coefficients of a free flight rocket design are nonlinear when very high thrust levels exist during boost. The resulting plumes are underexpanded at the nozzle exit and continue to expand until they are 1.5 to 2.0 missile diameters in size. These plumes can cause nonsymmetrical flow separation that changes the center of pressure location and results in a loss of stability. The degree of nonlinearity is also a function of the angle-of-attack magnitude. Nonlinear aerodynamics can increase the dispersion errors caused by crosswinds. If the nonlinear effects cause side forces and moments greater than those predicted by linearized aerodynamics, the dispersions cause by the crosswind can be larger than anticipated. Nonlinear normal force and pitching moment test data can be used to provide better estimates of the effects. If computer simulations are used, actual coefficients as functions of angle of attack and Mach number can be input into the simulation.

Nonlinear aerodynamics are also introduced if a fin is damaged or torn off during flight. The nonlinear aerodynamic coefficients have to be determined from wind-tunnel or free flight testing for each

configuration considered. Primarily, there is a need for nonlinear data for range safety analyses, but this tipic is not addressed since it is not of great concern in preliminary design.

2-4.4 DYNAMICS

Dynamic consideration involved in the preliminary design of an aerodynamically stabilized free flight rocket can be divided into problems encountered in two phases of the operation, i.e., launch phase at the flight phase of a rocket system. The motions of the launcher and/or rocket are calculated according to Newton's laws by equation the forces and moments acting on these systems to the resulting system response. The dynamic response during the launch phase considers teh coupled transient dynamic response behavior of the launcher, the rocket system, and the time dependent constraints between teh rocket and the launcher.

Calculation of the dynamic response fo the system is called simulation. Rocket simulations are most commonly performed using 2-, 3-, or 6-DOF. A DOF is a coordinate along which a rocket may translate (range, altitude, or crossrante) or aout which it may rotate (pitch, yaw, or roll). Sumulations using various combinations or all of the DOF are useful during each phase of rocket design and development. Par. 4-5 contains information about the equations used to simulate rockets and the use of such simulation in accuracy computation and estimation.

Tip-off rates and other paramters defnging the initial state of the reocket are used in accuracy calculations. Simulations often ae used to define the initial state of the rocket at the time it leaves the launcher. These simulations vary in complexity, dependign upon the degree of accuracy desired and the sophistication of the launcher. The more precise simulations consider the flexibility effects of the launcher and the rocket.

The dynamic motion of a rocket in free flight is determined by the propulsive forces supplied by the motor, the force due to gravity, the inertia characteristics of the rocket, and the aerodynamic forces. The flight dynamic calculations are called trajectory analysis. See Refs. 28 and 29 for additional information on trajectories.

This paragraph will address the use of trajectory analysis to calculate dispersions and the accuracy of a free flight rocket. The dispersion of a rocket to a particular parameter is determined by first finding the trajectory for an undisturbed rocket. Next, a disturbance (error source) is inserted into the trajectory calculations, and a new trajectory is calculated. Chapter 4, "Accuracy", presents data—given error source values—useful in calculating dispersions. The dispersions fro the various error sources are then root sum squared to determine the CEP for the free flight rocket system. Error contributors can be grouped as precision (random) errors or bias errors. Precision errors are those associated with the desigh of a rocket and vary randomly from round-to-round. Bias errors are rocket errors created by the bias of an outside influence, such as the atmosphere, and they tend to remain constant for all rounds fired over a short period of time.

Design (precision) error include the categories of mallaunch, malaim, thrust misalignment, total impulse variation, static margin variation, and ballistic coefficient variation. Bias errors include, but are not limited to, the categories of surface wind, ballistic wind, and ballistic air density variations.

2-4.4.1 Accuracy Trade-Offs

Accuracy trade-offs are addressed in terms of the errors associated with the various rocket component designs (precision errors) and the errors associated with the environment (bias errors). Precision errors include those of the propulsion system, launcher, stabilizing devices, spin methods, and manufacturing tolerance buildup. Cross products of inertia (dynamic unbalance) contribute to errors in spinning rockets. Bias errors include errors in the assumed winds and atmospheric density.

Propulsion accuracy trade-offs are discussed in par. 2-42. Chapter 6 presents a detailed description of propulsion system design and trade-off considerations. There are primarily three precision errors associated with motor design and manufacture—total impulse variation, thrust misalignment, and ballistic coefficient variation. A discussion of each error follows:

1. Total Impulse Variation. The total impulse variation results from the failure of a rocket motor to deliver a specified total impulse under flight conditions. This failure results from variations in one

or more of the following parameters: total loaded propellant, propellant specific impulse, and specific impulse due to physical quantities such as nozzle throat diameter. Total impulse variations cause velocity errors at burnout, resulting in range errors at warhead event or impact.

2. Thrust Misalignment. Thrust misalignment is defined as the failure of the thrust vector to pass through the rocket center of mass. This condition is caused primarily by nozzle eccentricities or thermal bow in the motor case and the displacement of the center of mass away from the rocket centerline. The error from thrust misalignment is inversely proportional to the static stability margin; it is also a function of the transverse radius of gyration. If axial spin is employed to reduce thrust misalignment error, the error is reduced as the axial spin velocity increases. The optimum axial spin must be determined for each design. Thrust misalignment causes an angular variation about the nominal velocity vector of the rocket which contributes to both range and deflection errors.

3. Ballistic Coefficient Variation. Ballistic coefficient variations, which cause perturbation in the coast phase trajectory, can be attributed to three factors: external shape variations, induced drag changes, and nonrepeatable rocket mass.
Causes that produce these variations are

a. External shape variations caused by inaccuracies resulting from manufacturing, or damage in assembly or handling

b. Induced drag changes caused primarily by variation in fin-to-body alignment, rocket body bow, and roll-yaw coupling resulting in different angle-of-attack histories

c. Nonrepeatable rocket mass due primarily to inaccuracies resulting from manufacturing errors in inert parts as well as variations in residual propellant slivers.
The ballistic coefficient variation also contributes to the range error.

Launcher accuracy trade-off studies include the firing platform, suspension system, rocket spin rate, nontip-off versus tip-off, firing rate, aim system, and motor exhaust gas impingement on the launcher. The details of these trade-off studies are included in Chapter 9. The errors associated with the launcher are malaim and mallaunch.

Aiming errors are deviations between the intended launch direction and the actual launch direction. This angular variation can result from surveying errors, laying and sighting equipment errors, firing table errors, and computational errors. This error source contributes to both range and deflection errors. The effects of rocket-launcher interaction result in a transverse angular velocity of the rocket at launch and cause angular variation about the nominal velocity vector. Also, when the rocket is spun on the launcher and is constrained to it, dynamic unbalance results in a mallaunch effect that increases with an increasing spin rate. Dynamic unbalance is the angular difference between the geometric axis of the rocket and its principal longitudinal axis of inertia. Thus dynamic unbalance, when the rocket is spun, results in angular variation (coning) about the nominal velocity vector of the rocket; this variation contributes to both range and deflection errors.

The aerodynamic stability of a rocket is the measure of its ability to align itself with the relative wind. The greater the stability margin designed into the rocket, the faster it will attempt to weathercock into the wind. Therefore, trade-offs are made between stability and accuracy. Various physical elements contribute to the static stability. The detailed stability trade-off studies performed for design of a free rocket are included in Chapter 5.

One of the more effetite methods of controlling rocket dispersion caused by thrust misalignment is to spin the rocket so that the spin rate of the system remains more or less constant during the burning period. Trajectory errors caused by thrust misalignment are inversely proportional to the spin rate. For most rocket systems, little reduction in errors can be achieved for rates greater than 20 revolutions per second (rps). The principal objection to spinning the rocket before launch is the increase in launcher complexity; prespinning also increases the errors caused by the dynamic unbalance of the rocket. Trade-off studies must be performed to balance the launcher requirements and the free flight rocket requirements to achieve the error reduction and improved accuracy desired. Types of spinning devices to be considered include the autospin device (Ref. 30), a radial propulsion spin motor (Ref. 23), a motor nozzle spin vane (Ref. 31), various belt-driven launcher spinning devices, and an eroding spin turbine.

Manufacturing tolerances should be considered during the preliminary design phase because (1) tolerances that are too tight result in high manufacturing costs, and (2) manufacturing tolerance build-up can create rockets with asymmetries in internal mass distribution and external configuration. Inter--nal mass distribution asymmetrics produce center-of-gravity offsets, whereas external configuration asymmetries can cause aerodynamic force unbalance. Center-of-gravity offsets and aerodynamic force imbalance both produce moments that cause aerodynamic angle of attack. Rockets flying at angles of attack have higher drag, thus performance losses. The offset center of gravity causes coning in a spinning vehicle. Therefore, trade-offs must be made between manufacturing tolerances and manufacturing costs.

Two of the major contributor-s to artillery-type free flight rocket dispersion are ballistic wind and atmospheric density variations. The errors due to these sources are greatest during ballistic flight. Drag reduction reduces the sensitivity to atmospheric density. Variations, and improved or updated meteorological data can provide information for firing table corrections in the artillery rocket system. The wind sensitivity during the boost phase can be reduced by tailoring the static margin. Wind and density trade-off studies are performed to desensitize the rocket to these effects during launch and ballistic flight.

Error budgets are usually established for particular components and system errors. A typical error budget will include one-sigma component error values and burnout angular errors for range and deflection for several error sources. These sources are usually malaim, mallaunch, thrust misalignment, surface wind, total impulse, ballistic coefficient, density, and ballistic wind. Based on these data, a CEP in meters and roils is calculated. Table 24, Ref. 23, presents several error budgets for different ranges and different age meteorological data.

Table 2-1 is presented to illustrate a typical error budget for an artillery rocket.

TABLE 2-1. ERROR BUDGET EXAMPLE

Type Error	One-Sigma Component Error Values		Burnout Angular Errors		Range × 12.21 km		Range × 14.65 km	
	Range	Deflection	Range, mrad	Deflection, mrad	Range Error, m	Deflection Error, m	Range Error, m	Deflection Error, m
Malaim	0.5 mrad	0.5 mrad			38	6	32	7.3
Mallaunch	5 mrad/s	5 mrad/s	1.9	1.9	144	24	122	27
Thrust								
Misalignment	0.5 mrad	0.5 mrad	1.9	1.9	144	24	122	27
Surface Wind	1.789 m/s	1.789 m/s	0.5	0.5	4	5	6	7
Total Impulse	0.2%	0			51	0	47	0
Ballistic								
Coefficient	0.74%	0			29	0	41	0
Density	1%	0			39	0	55	0
Ballistic Wind	4.18 m/s	4.18 m/s			27	19	41	29
Root Sum Square					220.5	39.7	198.6	49
CEP, m					153.2		145.7	
CEP, mrad					12.5		9.9	

2-4.4.2 Dynamic Loads

Dynamic loads are the result of accelerations of the rocket, which can arise from a number of external or internal forces acting upon the vehicle. Some typical acceleration- or disturbance-producing quantities are shock, thrust, acoustics, handling, aerodynamic forces, and launcher-induced accelerations. The shock environment may be produced by one or more of the following events: truck transportation; rail transportation; ship transportation; handling during transit, including drops; propulsion unit ignition, boost-sustain transition, and shutdown; fin opening or abrupt stabilizing surface area

change; operation of mechanical or electroexplosive devices; and rail launch tip-off. High-intensity acoustic-producing events occur during free or powered flight and the firing of adjacent rockets.

2-4.4.3 Rocket Vibrational and Bending Considerations

Vibration and bending of the rocket may be caused by either external forces and moments or induced by accelerations. Sources of disturbances which can produce bending are transportation by truck, rail, ship, and aircraft; handling or transfer operations; launcher operations; launch-to-target sources such as turbulent boundary layer, propulsion unit, rotating devices; and any unusual protrusion into the airflow. Simplified solutions of the equations of motion are available for the flexible launcher and rocket interaction problem, for example, Ref. 32. Detailed vibration studies often involve finite element modeling and usually are deferred to the advanced development phase. The information needed to develop a finite element model often is not available until the advanced development phase.

2-4.5 STRUCTURES

The rocket structure provides a specific external shape, a protective envelope, and a platform for the delivery of a payload to a target. The structure must be designed with minimum mass and sufficient strength to withstand ground handling, launch, and flight loads. Producibility and aerodynamic heating are also considerations in structural design.

The strength of a structure depends upon the physical and mechanical properties of the materials and the geometric configurations of the structural members. The proportional limit, elastic limit, yield point, ultimate strength, modulus of elasticity, ductility, anti hardness are the significant material properties considered in the preliminary design.

The physical dimensions, moments of inertia, and cross-sectional area are the significant geometric factors of the structural members.

2-4.5.1 Materials

The structural engineer must not only be concerned with the elastic constants, yield and breaking strength, and fatigue characteristics but also the temperature, creep and plasticity, notch sensitivity, moisture, and dielectric characteristics of the materials. The compatibility of dissimilar materials that are physically connected must be considered because materials with different coefficients of expansion could produce undesirable stresses; also the problem of gait'anic corrosion of metals exists. Rockets require a broad spectrum of materials ranging from explosives, propellants, metals, to plastics— however, this paragraph will address only the load-carrying, structural materials. The main load-carrying structures for a rocket are the rocket case and motor case.

Rocket motor cases frequently have been made of high strength steels. These materials have high yield and ultimate strength, are not notch sensitive, and are elastic. They can be cycled to 75% of full load several times without hoop strength failure, and they have been proven to be safe for man-launched rocket applications. However, steel cases are heavy, and therefore, structural designers also have used aluminum and composites. Several rockets using other materials have been designed; for example, the VIPER motor case is made of a composite material with an 8-mil aluminum liner. The aluminum liner is included to eliminate gas leaks and to provide a moisture barrier for the combustion chamber. The PERSHING II motor case is another example; it is made of Kevlar®. Special aluminum alloys have been developed which have high yield and ultimate strength in the 620 to 685 MPa range. However, these materials are relatively notch sensitive and brittle. The composite motor cases offer high strength to mass properties. However, proof test procedures and environmental protection must be considered before these materials are selected for use in structural components.

2-4.5.2 Structural Sizing

The structural designer must develop loads and moment data in order to calculate the stresses and deformations sustained by candidate materials. The equations used for calculating the stresses and deformations of rocket and motor cases are those applicable to unreinforced thin shells. The detailed stress and deformation calculations for rocket structures are provided in Chapter 7.

2-4.5.3 Mass and Balance.

The mass and balance calculations performed are mass and center-of-gravity estimation, pitch iner-tia, and roll inertia.   The equations for evaluating the volumes of typical reccket sections are presented in Chapter 7.   The volumes are calculted for homogeneous sections, and the masses are then calculated by multiplying by assumed densities.   Equations for calculating the center-of-gravity location also are provided by Chapter 7.   For convenience, these locations are identified as rocket station numbers, i.e., distance from the nose tip.   The location of the center of gravity of the complete configuration can be estimated by summing moments of the section masses about the nose tip and dividing by the total rocket mass.   Thi pitch and roll inertias fo the rocket are calculated by similar methods.

2-4.6 HEAT TRANSFER

The depth of heat transfer analysis performed in the preliminary design phase of an aerodynamically stabilized free rocket is highly dependent upon the type of rocket.   Some rockets may require consider-able heat transfer analysis, wheras for others extrapolation from similar rocket may suffice.   The description of analyses and studies in this paragraph covers those analyses for a completely new rocket vehicle design.   Details for carrying out the analysis are described in Chapter 8, "Heat Transfer".   Tra-jectory and configuration data are required to define aerodynamic heating.   Velocity, attitude, and altitude data versus time; configuration data; and a selected heating rate option are the usual inputs to an aerodynamic heating rate program such as the one given i nRef. 33.   A heating rate indicator pro-gram will calculate the integrated aerodynamic heating rate versus trajectory time for any point on the conceptual body.   The integrated heating rates for various designs provide the designer with data to use in the preliminary design process.

During the preliminary design phase, system component temperatures are calculated by using closed-form solutions of the general energy equation.   The internal heat transfer solutions are obtained by applying the aeroheating boundary conditions to known exponential form Laplace solutions given in Ref. 34 or to temperature response chart solutions given in Ref. 35.

The rocket motor case must case must meet structural load requirements while bing heated both internally and externally.   Calculation of internal heating requires knowledge of the combustion gaseous equili-brium composition and flow rate for the expected conbustion chamber pressure and termperature con-ditions.   The exposed propellant grain surface and downstream flow restriction areas determine the chamber pressure.   Propellant composition determines the equilibrium termerature.   For the prelimi-nary design phase, chamber conditions can be estimated from previous similar rockets or test pro-grams.   Rocket duct and nozzle propellant gas flow solutions to the momentum equation are obtained by useing ideal gas flow relationships.   There relationships involve duct area change, energy subtraction from and addition to the flow, momentum loss, mass addition to or subtraction from the flow, or combinations of these changes in the form of influence factors (Ref. 36).   Once the combustion chamber pressure and temperature time histories are known, the convection coefficients in the rocket ducting and nozzle can be calculated by using Bartz's relationship given in Ref 37.   The heat transfer from the combustion chamber to the rocket skin can be calculated by using relatively simple computer pro-grams, such as the on in Ref. 38, that couple a one-dimensional surface ablator analysis to backup layers of nonablative materials.   This analysis accounts for both the ablative heating on the combution chamber side and the aerodynamic heating on the rocket mold line side.

Design analysis includes determining the effect of the rocket on the launcher, e.g., is the launcher purely structural or a shoulder-fired weapon.   The heat effects of the launcher ususally result from plume impingement.   Plume temperature and velocity flow fields must be defined before the plume impingement heating calculations can be performed.   Flow field solutions must be provided for both the gaseous and condensed phase.   Computer programs are available for calculating the gaseous flow field through the nozzle and into the atmosphere.   No simple methods are available for calculating the condensed phase trajectories resulting from a body being submerged in a rocket plume.   Convective and radiative heat transfer contributions from both the gaseous and condensed phase must be included in the analysis.   The convective heat transfer between the gaseous phase and structure is dependent on the

gas recovery temperature and convection conductance values. The conductance values can be calculated by using standard relationships for different shapes. The convective heat transfer between the condensed phase and the structure is characterized in terms of accommodation coefficients that express the ratio of particle impingement heating to the energy content of the particle. The particle heating, including contributions from both the thermal and kinetic energy fluxes, is computed based on the particle trajectory data.

2-4.7 PERFORMANCE ESTIMATES

The determination of performance parameters is a necessary first step in the preliminary design of a rocket system. Performance trade-off studies are made to determine the sensitivity of the physical parameters to variations in performance requirements, aerodynamic drag and static margin tailoring, and propulsion energy management techniques. The performance calculations are used to size the overall dimensions.

The parameters that are considered in this evaluation can be divided into three categories:

1. Factors associated with performance-such as payload, velocity, range, altitude, time of flight, and launch angle

2. Factors associated with the propulsion system—such as energy management technique, specific impulse, thrust, burning time, and propellant mass fraction

3. E-actors affecting aerodynamics—such as shape, stabilization devices, length, and diameter.

The performance factors, with the exception of launch angle and time of flight, usually are fixed for the solution of a given problem.

Determination or selection of optimum values of the propulsion-system variables is called energy management. Energy management determines the thrust magnitude for the boost and sustainer phases, and also considers the duration of coast periods. The objective of energy management is to deposit the payload at the target with a minimum expenditure of propellant while meeting accuracy and cost goals.

Drag is of main concern for aerodynamic sizing of a free flight rocket. The drag and its resultant effect on the ballistic coefficient have a direct effect upon the ballistic trajectory flown by a rocket using a particular energy management system.

Performance parameters provide data relating performance to physical characteristics. Mass is the principal physical characteristic of concern to the rocket designer, although such physical characteristics as length, diameter, or volume may sometimes be limiting factors also, e.g., in considering transportability.

The reader is referred to Chapter 3, "Performance", for detail on estimating performance.

2-4.8 SUBSYSTEM DESIGN OPTIMIZATION

The preliminary design phase is a highly iterative process with actitities performed either simultaneously or sequentially to meet the user need requirements. The primary objective of the preliminary design effort is to compare all competing alternative subsystem design approaches that best meet the needs for an integrated system. Subsystem design optimization is the process by which the proper trade-offs among the physical parameters, the accuracy requirements, the manufacturing tolerances, the interfaces between rocket and other equipment, life cycle cost, and the technology availability to achieve mission objectives are made. The name usually assigned to this function is system integration. Par. 2-4.10 presents in some detail the process used to coordinate the activities just described.

2-4.9 AUXILIARY DEVICES

Auxiliary devices are used in aerodynamically stabilized free rocket systems. The requirement for these devices is defined in the preliminary design phase. Although they are necessary for its operation, these devices are not considered a part of the primary rocket system.

2-4.9.1 Wind and Density Measuring Devices

Major contributors to the dispersion of artillery-type free flight rockets are ballistic wind and atmospheric density errors. This is particularly true for medium and long-range rockets. These two error

sources and their effects on the trjectory are discussed in Chapter 4, "Accuracy". Also discussed in that chapter are methods that can be used to desensitize the rocket to these error sources. Ballistic winds and atmospheric density are quantities that produce bias-type errors, i.e., if the correct values were known, one could compensate by changing the launch conditions. Obviously, more current and more accurate meterorological data can reduce the bias errors. A new upper atmosphere sounding system named the Field Artillery Meteorological Acquisition System (FAMAS) has been developed to replace the AN/GMD-1 Rawin set which has been in use for over 20 yr. The FAMAS system in automated and provedes a digital readout after the sounding equipment in launched. The system will automatically acquire and track the flight equipment, handle and process the received meteorological intelligence, compute the various meteorological messages, and send the data to user elements.

2-4.9.2   Temperature Control Devices

Temperature control problems can orrucr while the rocket is on the launcher and during flight. For example, a rocket component may be so sensitive to temperature that its performance is seriously degraded above and below some limiting temperature range, and failures can occur if temperatures are not kept within some specified range. Some parts generate heat internally which must be dissipated to the external evironment. These environments can be quite severe; thus it is sometimes necessary to proved auxiliary devices to effect the heat transfers.

Various temperature control devices are available for handling these situations. For example, a local-ized over-temperature problem can be handled with a change of phase material that melts above a certain threshold temperature; insulation can be used to protect warheads and fuxed from aeordynamic heating; thermal batteries can be used to supply electrical power for heating various components; and thermoelectric devices used in combination with thermal bvatteries can cool components. The specific temperature control device used will depend on the component limit temperature, the available sink temperature, the amount of heat to be removed, available energy sources for adding removing heat, and the duration of the critical temperature situation.

2-4.9.3   Firing and Firing Control Equipment

Rocket motors can be fired with pyrotechnic igniters, pyrogenic ignition systems, squibs, and igniter safe-arm mechanisms. The main components of a rocket motor igniter are the primary initiating device, the main ignition charge, and the case. The operational requirements are a driver in determin-ing the firing mechanism. The firing mechanism and the propellant must function together to achieve proper motor ignition. The paragraphs that follow briefly describe some of the firing mechanisms and systems.

In pyrotechnic igniters, the main ignition charge consists of a mixture of metallic fuel and an oxidizer, which is designed to react chemically and produce heat. Organic binders that also function as fuel frequently are added to metal-oxidant mixtures to maintain intimate contact between the powered fuel and oxidizer. These mixtures are used in the form of pressed pellets, as sheet coatings, and as loose powders.

The pyrogenic ignition system can either be mounted at the head end of the motor or on the aft end nozzle adapter with its exhaust gases directed across the propellant surface, or it can be mounted as part of the launching equipment at the nozzle end.

Hypergolic ignition is achieved when at least two materials are brought together physically, and spontaneous ignition occurs upon their contact. In solid rockets, hypergolic ignition has been demon-strated by using a composite propellant as one of the reactants and a powerful gaseous oxidizer, such as chlorine trifluoride, as the other reactant.

An electric igniter-squib, or initiator. contains one or more resistance wires called bridge wires which are surrounded by readily ignitable pyrotechnics or primary explosives. The bridge wire is heated by an electric current to ignite the heat-sensitive explosive.

Requirements sometimes specify that a safe-arm device be used in the ignition systems. There are two basic approaches for a safe-arm dm'ice: (1) an electric block that will not permit current to be supplied to the squibs or initiators, and (2) a mechanical block that usually is a barrier across the face

of the squibs or initiators. The electrical and mechanical blocks often are incorporated into a single mechanism.

2-4.9.4 Fuze Setting Equipment

Every rocket warhead has a safe and arm, and fuze setting system. The rocket may be launched by a remote management system that sets the fuze in the warhead and activates the rocket igniters. Fuzes can be super quick, time delay, or proximity.

The electronic time fuze is one of the more accurate delay fuzes available; it can be set to initiate the detonation process at any time after a specific event. It can also be designed for remote setting.

2-4.9.5 Shipping Containers

The rocket shipping container must be designed to absorb shock; isolate the rocket from rain, hail, sand, and dust; and insulate the rocket from diurnal temperature variations. Some shipping containers also serve as part of the launch system. See Ref. 39 for information on container design.

2-4.9.6 Other Devices Unique to a Given System

Other devices unique to a given system may be a laying and aiming system; target acquisition, discrimination, tracking, and engagement systems; etc.

2-4.10 SYSTEM INTEGRATION

The preliminary design phase requires continuous system integration effort to provide updated requirements and to maintain interfaces on a daily basis with all technological disciplines and design areas involved. System integration during this phase expedites the exchange of data among the different disciplines and design areas. This is to insure that all subsystems and components intermesh physically and functionally in an acceptable manner. The system integration process also must consider component performance, reliability, availability, and maintainability Manufacturing techniques and life cycle costs are also of concern to the engineers involved in system integration. Each of these areas is discussed in the paragraphs that follow.

2-4.10.1 Performance

The system integration process continuously compares the updated performance characteristics and the design requirements of the rocket components to those required to satisfy the mission need.

The warhead performance requirement may be antipersonnel and have a specified kill probability within a certain area. Other interfaces could create an updated design requirement that a certain size wire bundle be carried through the warhead section or that the warhead skin carry the structural loads in a certain manner.

The propulsion performance requirement may be that the propellant provide a progressive thrust in a manner that minimizes low velocity crosswind-induced dispersions at the warhead delivery point. A design requirement may be that a rocket motor or auxiliary device impart a spin rate to the rocket while it is still on the launcher.

Aerodynamic performance often requires that trade-offs be made between the shape of the warhead and drag characteristics. Static margin tailoring and fin design require trade-offs. The types of fins and the launcher sometimes pose compatibility problems. The rocket and launcher interface must be considered when defining the drag.

An accuracy performance requirement may be that the CEP of the rocket be no greater than 300 m at a 30-km range. From a total system integration design standpoint, the accuracy of a rocket can be improved by using a better meteorological data sounding system such as FAMAS as is discussed in par. 2-4.9. Thus, the use of the FAMAS system could be an accuracy design requirement.

It may be required that the rocket structure be formed to minimize thrust misalignment, i.e., a performance requirement. A design requirement would be the imposed load distribution for handling, launch, and flight. Cost for manufacture must be considered in the structure design.

A requirement that impacts on heat transfer studies is the rocket thermal protection system requirements. A design requirement may be that the motor case structure be maintained below some specified temperature.

The system integration engineer must trade off the individual discipline or subsystem requirements with that of the rocket mission. He nust keep in mind that the important performance requirements are those associated with payload, velocity, range, altitude, time of flight, and launch angle.

2-4.10.2 Reliability

A reliability assurance program must be established and maintained in accordance with military standards such as MIL-STD-790 for electronics. The systems engineer must not only be concerned with whether a component will perform satisfactorily but also whether the component has a satisfactory reliability history. A reliability failure analysis must be performed on each component. Government supplied parts, reiability data are beneficial in this analysis. Once component reliability is established, the reliability engineer must determine whether the differnet components of a subsystem are compatible. He must determine whether materials are dissimilar, whether stress concentrations are created by different materials having different doefficients of thermal expansion, etc. Once a reliable subsystem has been configured, the reliability engineers must evaluate the interplay amont the different subsystems to perform a total system reliability analysis.

2-4.10.3 Cost

A life cycle cost-effectiveness analysis models a total weapon system for a specified life cycle in terms of logistics, ammunition, training, personnel, and costs. The total recket system next would be deployed against a specified battle scenario in a computer-simulated battle. Then a quantities of diferent types of rockets and associated equipment are adjusted until the battle is won-i.e., all targets have been attacked or a specified number destroyed. In this manner a parameter can be varied within the weapon system, the system adjucted to be successful, and the total cost determined. This is a life cycle cost analysis that could be applied in preliminary design to a total weapon system; however, all types of cost studies are necessary from the time the component selection process begins, until the total system selection process is completed. Cost and performance versus quality assurance are trade-offs made at each level of weapon system design. These cost studies not only apply to the design of systems but also to the verification of that system through an enviromental quality assurance program.

2-4.10.4 Availability Data

Literature searches must be performed to gather information on the availability of the different types of systems which are bing considered. Contracts made through use of vendors' supplier lists are also good sources of availability data. The system engineer must continue to evaluate his proposed system until he is certain that it will be state of the art and producible within the time frame of his contract.

2-4.10.5 Manufacturing Considerations

The system engineer must consider manufacturing processes from the forming, assembly, and cost-effectiveness standpoints. He may machine, spin, shear, form, stamp, deep draw, tube draw, roll bend, host extrude, cold extrude, hydrostatically extrude, or expand the part in the forming process. He may assemble the parts by using rivets, quick disconnects, or an array of welding and brazing process. Available processes are arc, electron beam, tungsten inert gas, and plasma welding; or vacuum, hydrogen, inert gas, and retort hydrogen atmosphere brazing. Ref. 40 provides information on producibility

From a cost-effectiveness and minimum weight standpoint, the substitution of advanced composite for metals must be considered. This is particularly true for large, nonload-carrying structural members. Generally speaking, epoxy graphite composites, although light in weight and relatively easy to process, are costly. The system engineer must constantly monitor advancements completed by materials laboratories such as the Air Force Materials Laboratory at Wright Patterson Air Force Base. Refs. 41 through 44 provide useful information on composites.

2-4.11 SPECIFICATIONS

The functional baseline (baseline of program requirements) and interface control specifications are established by the end of the preliminary design phase. The functional baseline includes broad system performace objectives, an operational concept, a logistic concept, and cost estimates. The system

specification defines the technical portion of the baseline program requirements. An interface control specification establishes the physical, functional, safety, inspection, and test interfaces among rocket components, and between the rocket and launcher subsystem.

2-5 SYSTEM VALIDATION

The system validation phase serves to validate and refine program characteristics through extensive study and analysis, prototype hardware development, and prototypte testing. The objective of this phase is to establish firm and realistic performance specifications that impose the operational and support requirements. Hardware that will meet the functional and performance requirements is defined and designed during this phase. Prototype models are fabricated and tested to verify the ability of the system to meet these requirements.

Fig. 2-4 depicts the technical activities that take place in the system validation phase. The prelininary design functional requirement baseline is translated into a design requirement baseline during system validation phase. The functional baseline during this phase is redefined in terms of performance requirements, decision constraints, and physical configurations. The parametric trade-off studies performed during the preliminary design phase are refined further. These studies lead into the demonstration and validation of concept tests and studies. These tests and studies are performed to insure that a configuration being defined for the full-scale development phase meets the updated mission needs and is the best possible balance among the alternatives, considering total cost, schedule, and operational effectiveness. The quantity and level of prototype modeling and hardware validation per-- formed during the validation phase depend on the nature of the program and the risks and trade-offs involved. It must be remembered that the hardware tested in this phase is produced by other than production methods. Testing is performed to determine whether a design is functional and meets performance requirements. Complete qualification testing is performed in the full-scale development phase.

Overall program office management activity increases in the system validation phase. Usually at the time of the system validation phase, a somewhat definitive contract has been written. New data, the results of technology studies, test results, or changing needs may alter the functional requirements defined as output of the preliminary design. Any changes in the requirements placed on a weapon supplier must be coordinated through official channels. Thus program office management must coordinate its changing requirements through the contract organization.
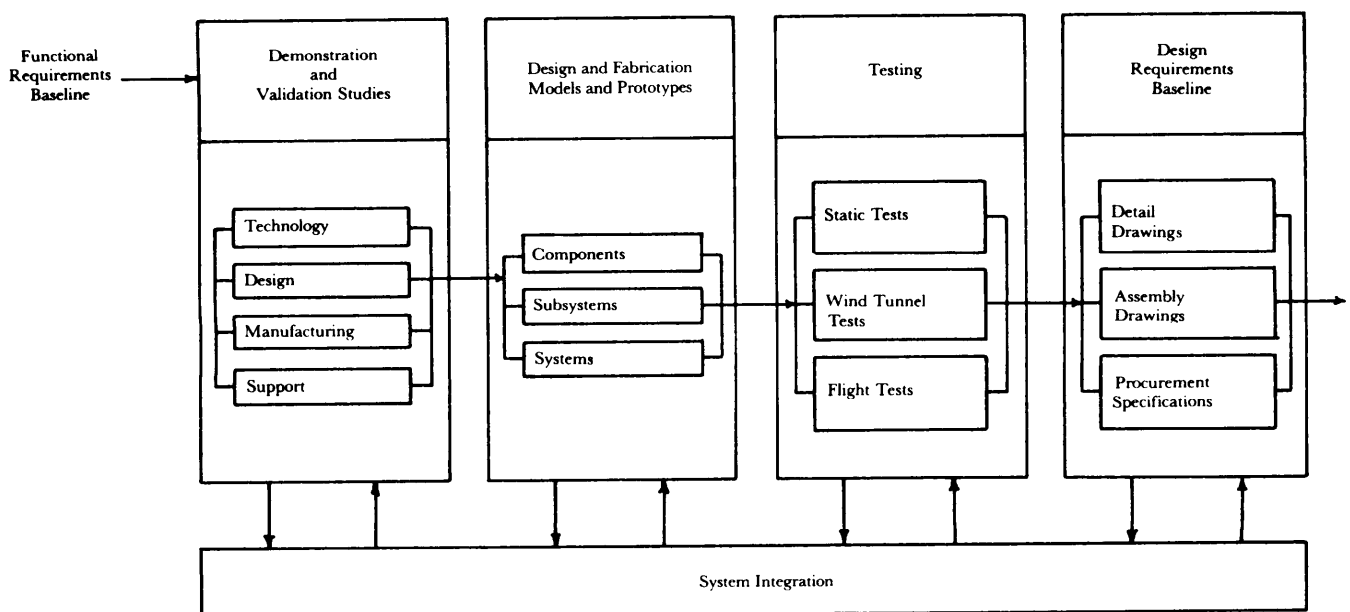
Figure 2-4. System Validation Phase Activities

2-5.1 DESIGN AND DOCUMENTATION

The process involed in developing any design consists of four steps, i.e.,

1. Program requirements translated into functional requirements.

2. Functions analyzed and translated into requirements for design, facilities, personnel training, and prodedural data.

3. Requirements integrated into contract end items, training course, and procedural publications.

4. System and design engineering trade-off studies to determine requirements and design approach. The process is a method for defining the system on a total basis so that the design will reflect requirements for hardware, software, and personnel in an integrated fashion. It provides the source requirement data for the development of specifications, test plans, and procedures. It also provides the backup data required to define, contract, design, develop, produce, install, check, and test the system.

2.5.1.1 Detailed Hardware Design

Detailed hardware design proceeds after the functional and performance requirements are defined. The functional and performance spedifications with the interface constraints set the bounds for the detailed hardware design. The detailed design must meet specific functioal and performance requirements, interface properly with the rest of the system, and meet the physical constraints. Environmental contraints also impact the hardware design and must be considered. The design for equipment for military use also must meet several standardized spedifications. Thes spedifications serve to standardize drawings and otherwise assist in maintaining proper relationships between engineering and manufacturing data and the manufactured configuration items. The reader is cautioned to refer to the proper military standards and specifications for standards and practices applicable to hardware design and documentation. Examples of standard practices and specifications are

1. Engineering drawings and associated lists will be prepared in accordance with Spedification MIL-D-1000.

2. Drawing practices will follow MIL-STD-100.

The weapon supplier is required to submit drawings that comply with the standards and practices of the user. The configuration management function is responsible for the quality control of drawings. Engineering drawings will provide complete information to assure design integrity relative to interchangeability and replaceability by showing detail and assembly information, material identification, critical reference points, lines or surfaces, including related dimensions and tolerances, plus delineation of c ritical surfaces. Configuration mansgement also establishes a document control system to record, release, and maintain document usage data to assure adequate and accurate records for effective baseline control.

2-5.1.2 Weights and Balances

The weight and balance calculations performed are mass and center-of-gravity estimation, and pitch and roll inertias. The weight and balance calculations performed in the system validation phase will be similar to those performed in the preliminary design phase but in much greater detail. The reader is referred to Chapter 7 for more details on this analysis.

2-5.1.3 Fabrication Drawings

Detailed drawings and fabrication (assembly) drawings were discussed in par. 2-5.1.1.

2-5.1.4 Specifications

Specifications are written to accomplish a number of objectives, i.e.,

1.   Define the functional and performatnce requirements.
2.   Define the physical dimensions.
3.   Define interfaces with other equipment.
4.   Specify testing to demonstrate reliability and maintainability.
5.   Provide definitive documentation on contractural items.

The allocated baseline specifications are developed in the preliminary design, updated, and further defined during the system validation phase. The specifications incorporate the technological ap-

preaches developed to satisfy the objectives in the functional baseline (baseline of program requirements). The allocated specification, defined in Ref. 45, is a document intended primarily for use in procurement. Ref. 45 clearly and accurately describes the essential technical requirements for items, materials, or services, including the procedures by which it will be determined that the requirements have been met. Specifications for items and materials may also contain preservation packaging, packing, and marking requirements.

Specifications for procurement should state only the actual minimum needs of the Government. They should describe the supplies and services in a manner that will encourage maximum competition and eliminate, insofar as possible, any restrictive features that might limit acceptable offers.

The specification should state the necessary requirements—description, systems, design materials, performance characteristics, processes, reliability, workmanship, etc.—to obtain the product for which the specification is prepared. The requirements shall represent the actual minimum practical needs of the Government to satisfy the intended use and application. The specification should include quality assurance provisions, including examinations and tests to be performed, to determine that the item or service to be offered for acceptance conforms to the design requirements.

2-5.2 TESTING

Testing is performed in the system validation phase to determine whether the design meets the functional and performance requirements. Included in the reliability testing is that performed on components subjected to some environmental or dynamic cycling. Testing programs are structured to verify technical approaches, resolve technical risks, verify interface compatibility, validate producibility through hardware proofing, and to assess the impact of the environment on reliability and performance. System validation testing includes static **or** laboratory-type tests, ballistic range tests, wind-tunnel-scale model tests, and full-scale flight tests.

2-5.2.1 Types of Tests

Static tests as discussed here represent those tests that are not flight tests or wind-tunnel tests. Static testing is conducted to evaluate all rocket components and subsystems and is performed to determine or verify system component performance, structural integrity, sensitivity to climatic extremes, measurement techniques, and applicability of analysis techniques used to evaluate data. Tests are also performed to provide data for improving and upgrading simulation models.

For an aerodynamically stabilized free rocket, the rocket motor is one of the more important components; therefore, tests are conducted to verify motor performance characteristics. Motor properties, either measured or derivable from data obtained during the tests, include burn rate, thrust, specific impulse, and the characteristic velocity. Quantities are measured as a function of time to allow definition of the thrust profile.

Structural tests are performed on propellant samples to determine their capability to function after being stored at specified temperature ranges. Conducted tests include stress-strain modulus, thermal conductivity, thermal expansion, density, and burn rate.

The environmental climatic extreme tests are qualification tests during which the rocket motor is subjected to a series of these environments and then fired to evaluate performance characteristics. The environmental tests include salt spray, humidity, rain, temperature cycling, acceleration, accelerated aging, etc. Refs. 46 through .50 provide worldwide environmental data. In addition to these climatic environments, the rocket is submitted to in-service environments such as helicopter, vibration and spin rate. After a motor is subjected to these climatic and in-service environments, it may be soaked at an extreme temperature and fired. The instrumentation used in these tests includes uniaxial and biaxial strain gages, motor pressure transduces, sound level analyzers, and thermistors.

The measurement techniques used and the analysis performed are inseparable and wi11 be discussed as a single item. The propellant and insulation weights are measured before and after the tests. The total pressure of the chamber and rocket thrust variations as functions of time are measured during the test. By knowing the nozzle throat area, nozzle area ratio, and nozzle half angle before the test and after the test, the nozzle mass-flow rate can be obtained by using the measured propellant and inert mass loss

data and burn time. since all other parameters are known, the variation of the cahracteristic velocity with time is obtained. The specific impulse is determined by dividing the measured thrust by the calculated average nozzle mass-flow rate.

The theoretical rocket thrust, spedifica impulse, and characteristic velocity are calculated. The ratio of the measured values to theoretical values provides the designer with the characteristic velocity and specific impulse efficiencies.

The motor case structuarl tests are performed to demonstrate that a motor case design of minimum dimensions and material strength will carry a specified pressure without yielding and to demonstrate location and type of failure during burst pressure test. Microtensile specimens can be taken from the case failure region for use in further determination of the minimum ultimate strength and minimum yield strength of the case. These determinations are make in the circumferential and longitudinal directions.

Wind-tunnel tests are perfomed to measure and determine aerodynamic force and moment coefficients, aerodynamic heating parameters, and heat transfer characteristics. The aerodynamic tests measure forces, moments, and pressure loads. The aerodynamic heating tests are conducted to measure heating rates and recovery temperatures. Heat transfer tests are performed to measure ablation rates and temperatures at critical locations throughout the rocket. The aerodynamic force, moment, and derived stability data are used in computer simulations of the boost phase and the coast phase. Wind-tunnel tests are conducted at subsonic, transonic, supersonic, and hypersonic speeds to cover the entire spectrum of flight velocity. Thus no one tunnel can be expected to cover this range, and it may be necessary to use several tunnels to establish a complete aerodynamic data base. The tunnels should have a high Reynolds number in order to yield reliable data. The models ussed to obtain basic 6-component aerodynamic data are sized by the facility to be used for the test and can range from 5% of full scale to full scale. The model scale must be of sufficient size so that the component parts normally exposed are not submerged in the boundary layer of the test model. Coefficeints for forces along, and moments about, three orthogonal axes are obtained by using a sting- or strut-support internal force balance. Pressure taps can be placed on the model to determine pressures at selected locations. For each Mach number tested, the angle of attack of the model in the vertical plane may be varied. Each model configuration incorportating tail fins is tested at various roll angles. The force and moment data are reduced to coefficient form and plotted versus appropriate a ngle of attack. Those parameters showing nonlinear vatiation with angle of attack are noted to further study. The resulting coefficient data are normal force, side force, axial force, pitching moment, yawing moment, and rolling moment. Pressure data are used in aerodynamic load analysis.

Flight profiles for some rockets indicate that aerodynamic heating must be considered in the design of the external surfaces. Therefore, erodynamic heating tests are conducted for rockets with flight regimes that cause significant aerodynamic heating. Wind-tunnel tests are conducted to measure undisturbed, interference, and protuberance heating of a rocket. Tests are performed at supersonic and hypersonic Mach numbers, and at Reynolds numbers characteristic of severe heating flight regimes. The undisturbed heating tests use scale models of the clean body configurations of the entire rocket, but interference and protuberance heating tests use scale models of the intire rocket including fins, bourrelets, etc. The ratio of the heating measured on the interference and protuberance model to that measeured on an undisturbed model, and the calculated clean body heating for the full-scale flight rocket are used to calculate total heating rate of the rocket. Heat transfer tests normally are conducted wieh a full-scale model that will have an adiabatic wall and heat transfer convection coefficeint equivalent to that existing on the rocket at some Mach number and Reynolds number during the flight time of interest. Thermographic phosphors and external thermocouples are used to show the natural boundary layer transit on these full-scale models. Heat flux gages can be used to verify that the correct surface heat flux is simulated at a particular location on the rocket, whereas internal thermocouples are used to evaluate system component performance.

Flight tests are used to verify component and system performance, aerodynamic stability and drag characteristics, overall accuracy characteristics of the rocket, structural load, moment and vibration

environments, and rocket roll rate. The primary purpose of a flight test program is to obtain engineering data on the rocket during the launch, boost, and ballistic flight phases, and during flight to impact. In addition to evaluating total functional performance of the system, the objective of a flight test program may be to gather specific data on velocity and spin rate profiles, rocket and launcher interaction, tip-off or nontip-off characteristics, rocket stability, structural integrity of the rocket and launcher, detent release, motor performance, fin dynamics, and blast pressure effects of a rocket. During these tests, the rockets are ballasted so that their masses and centers of gravity will simulate the tactical weapon.

The instrumentation used in flight test programs includes everything described under static tests plus that required to monitor the flight dynamics of the vehicle. The instrumentation to monitor flight dynamics can be an on-board package or a range setup. On-board packages will have inertial instrumentation and either a telemetry system or a recording system. Range instrumentation usually involves a variety of cameras, radars, and other tracking equipment to record the position and orientation of the rocket. The decision to use on-board or range instrumentation, or a combination of both, varies with the types of rockets, range equipment available, and specific data requirements.

Flight test programs allow different component configurations to be demonstrated and the best configuration to be verified for use in the final configuration selection process.

2-5.2.2 Test Plan

A test—whether a static test, a wind-tunnel test, or a flight-test- should have a specific set of clearly defined objectives. These objectives are best accomplished by a carefully planned test. Testing procedures may vary for different types of tests, but the fundamentals of planning, conducting, and analyzing the results of any test are similar. Data required to determine whether the test objective is met must be specified. The models or equipment needed to provide test data are then determined, and instrumentation required to measure and record data is identified. The method of reducing and analyzing the data is then determined. Once all this information is available, the test plan can be written. The test plan is the documentation to support and define the operations to accomplish the test objectives. The next paragraph describes the essential contents of a test plan.

A test plan should include an introduction, a model description, instrumentation requirements, operation requirements, data reduction and presentation requirements, a run schedule, and model drawings. Each element is discussed further:

1. Introduction. Presents information about test location, test date, and the objective of the testing to be performed. It also names the test engineer and delineates distribution of the test data.

2. Model Description. Includes a description of the model construction, a reference to the rocket configuration represented by the model, and a description of the coordinate system used to identify instrumentation. The model description includes dimensional data showing a comparison between full-scale rocket dimensions compared to model dimensions.

3. Instrumentation Description. Delineates the number and types of instrumentation to be used in the test program. The locations of all instrumentation on the model are defined by coordinate location and by sketches of the model.

4. Operations. Required sequence of events to conduct the test and the delineation of responsibilities for model preparation, test preparation, instrumentation, test conduction, data reduction, and data analysis. Operations includes specifying which instrumentation fits into which data set and describes the process of conducting the test. The definition of the test conditions and parameters to be measured and recorded is part of operations. Specific data requirements such as photographs are part of the operations portion of the test plan.

5. Data Reduction. Specifics the procedure for transforming the raw instrumentation data into useful engineering parameters. Specific algorithms for transforming data are supplied in the test organization. Data formats for returning test data to the designer or other ultimate user are specified.

6. Run Schedule. Includes model geometry and altitude data, tunnel Mach number and Reynolds number, and instrumentation set to be used for each test run. The run schedule also defines all runs to be performed.

7. Model Drawing. Provided for use in manufacturing the models. The drawings spedify material requirements, surface finish requirements, machining operations, method of attachment of parts, and instrumentation installation processes.

The conduct of a successful test program requires considerable consideration between the requesting organization and the organization conducting the tests. For the user to receive the desired information from a test program, it is necessary for him to know the quantities that can be instrumented, the accuracy of the data that can be obtained, the test conditions available to obtain the data, and what is required of the model or test item. Information exchange or system integration is very important for the conduct of a successful test program.

2-5.3 SYSTEM INTEGRATION

System integration is an important function in all phases of the development of a rocket system; it is to assure compatibility of all elements of the system. All the functions performed in the preliminary design phase continue in the system validation phase. Integration and coordination of activities and data increase in importance in the system validation phase. This is the phase during which prototype hardware is fabricated, testing and final system designs are performed, and manufacturing require- ments and field support and training needs are defined. During the system validation phase, the system design becomes sufficiently firm and detailed; accordingly, changes may be difficult and very costly to implement.

Simulations are used to aid in the integration of the various system components into an overall functional system. As subsystems are designed and tested, simulations can be updated to reflect actual hardware dynamics and functional responses. The overall system is simulated to assure the ability of the system to meet the requirements.

Costing for the overall system is updated. Life cycle costing is performed to provide data for the cost-effectiveness trade-offs performed before commitment to production. Manufacturing processes and availability considerations feed into the design.

Materials for the fabrication of particular items are considered. The cost and availability of mate- reals, manufacturing processes, availability of tooling, and reiablility of the finished product all are considerations for system integration in the system validation phase.

The reliability of the system, as expected in the field, is determined in the system validation phase. Failure rates for the components, subsystems, and the system are determined and used in life cycle costing and overall system effectiveness studies. Maintainability and logistic requirements for support- ing the system in the field are determined. Training requirements for operation and maintenance are defined and furnish information into the life cycle costing studies.

The configuration management aspects of system integration continue in the system validation phase, and additional emphasis is placed on interface and change controls. Any changes to the system must be properly cooridated and evaluated to determine the effect on any and all elements of the system. The impact of the change of performacne, reliability, producibility, maintainability, cost, etc., must be evaluated before any changes can be allowed.

In summary, the system integration function is very important in the development, manufacture, and fielding of a cost-effective rocket system.

REFERENCES

1. DoD Directive No. 5000.1, *Major System Acquisition,* 29 March 1982.

2. DoD Directive No 5000.2, *Major System Acquisition Process,* 8 March 1983.

3. DoD Directive No. 5000.3, *Test and Evaluation,* 26 December 1979.

4. DoD Directive No. 5000.4, *OSD Cost Analysis Improvement Group,* 13 June 1973.

5. DARCOM-P 706-101, *Engineering Design Handbook, Army Weapon Systems Analysis, Part One,* November 1977.

6. DARCOM-P 706-102, Engineering Design Handbook, *Army Weapon Systems Analysis, Part Two,* October 1979.

7. AMCP 706-160, Engineering Design Handbook, *Elements of Terminal Ballistics, Part One, Kill Mechanisms and Vulnerability,* November 1962.

8. DARCOM-P 706-163, Engineering Design Handbook, *Basic Target Vulnerability* (U), July 1977, (THIS DOCUMENT IS CLASSIFIED CONFIDENTIAL.)

9. AMCP 706-170, Engineering Design Handbook, *Armor and Its Applications* (U), November 1973, (THIS DOCUMENT IS CLASSIFIED SECRET.)

l0. AMCP 706-181, Engineering Design Handbook, *Explosions in Air, Par-t One,* July 1974.

11. AMCP 706-182, Engineering Design Handbook, *Explosions in Air, Part Two* (U), August 197.5, (THIS DOCUMENT IS CLASSIFIED SECRET-RESTRICTED DATA.)

12. AMCP 706-210, Engineering Design Handbook, *Fuzes,* November 1969.

13. AMCP 706-290, Engineering Design Handbook, *Warheads—General,* July 1964.

14. AMCP 706-205, Engineering Design Handbook, *Timing Systems and Components,* December 1975.

15. AMCP 706-211, Engineering Design Handbook, *Fuzes, Proximity, Electrical, Part One,* July 1973.

16. AMCP 706-212, Engineering Design Handbook, *Fuzes, Proximity, Electrical, Part Two* (U), August 1963, (THIS DOCUMENT IS CLASSIFIED SECRET.)

17. AMCP 706-213, Engineering Design Handbook, *Fuzes, Proximity, Electrical, Part Three* (U), August 1963, (THIS DOCUMENT IS CLASSIFIED SECRET.)

18. AMCP 706-214, Engineering Design Handbook, *Fuzes, Proximity, Electrical, Part Four* (U), August 1963, (THIS DOCUMENT IS CLASSIFIED SECRET.)

19. AMCP 706-215, Engineering Design Handbook, *Fuzes, Proximity, Electrical, Part Five,* August 1963.

20. AMCP 706-175, Engineering Design Handbook, *Solid Propellants, Part One,* September 1964.

21. AMCP 706-285, Engineering Design Handbook, *Elements of Aircraft and Missile Propulsion,* July 1969.

22. R. A. Deep, J. H. Henderson, and C. E. Brazzel, *Thrust Effects on Missile Aerodynamics,* Report No. RD-TR-71-9, US Army Missile Command, Redstone Arsenal, AL, May 1971.

23. B. W. Douglas, L. W. Lee, M. B. Morrow, C. W. Dahlke, J. H. Henderson, D. R. Combs, and R. G. Canard, *Free Flight Rocket Technology Program, Aeroballistic Directorate FY74 Activity Report,* MIRADCOM TR-RD-75-3, US Army Missile Command, Huntsville, AL, July 1974.

24. A. R. Maykut, *Technology for Improving Solid Rocket Motor Reproducibility,* MICOM Report TR-RK-77-2, US Army Missile Command, Huntsville, AL, October 1976.

25. A. R. Maykut, *An Analysis of Impulse Variations in Solid Propellant Rocket Motors* (U), MICOM Report TR-RK-72-20, US Army Missile Command, Huntsville, AL, September 1972, (THIS DOCUMENT IS CLASSIFIED CONFIDENTIAL.)

26. AMCP 706-283, Engineering Design Handbook, *Aerodynamics,* April 1965.

27. D. L. Mattox, *Laminar and Turbulent Divergence Factor Calculations for Use on the Space Shuttle External Tank (ET) and Solid Rocket Booster (SRB),* NSI Report TN-230-1350, Northrop Services, Inc., Huntsville, AL, October 1974.

28. AMCP 706-107, Engineering Design Handbook, *Elements of Armament Engineering, Part Two, Ballistics,* August 1960.

29. AMCP 706-284, Engineering Design Handbook, *Trajectories,* May 1962.

30. R. W. Forgey, J. J. McDermatt, and D. W. Holder, Free *Rocket Technology, Autospin Accuracy lmprovement,* MIRADCOLM Report TR-RD-75-36, US Army Missile Command, Huntsville, AL, 30 June 1975.

31. H. T. Clark, *Low Cost Integrated Motor Program Part 1. Motor Development,* MIRADCOM Report T-SR-79-12, US Army Missile Command, Huntsville, AL, 10-12 October 1978.

32. J. E. Cochran, Jr., and D. E. Christensen, *A Simp!e Model for Estimating Mallaunch Due to Rocket Flexibility,* MIRADCOM Report T-SR-79-12, US Army Missile Command, Huntsville, AL, 10-12 October 1978.

33. D. L. Mattox and C. W. Hurst, *Sphere and Plate Heating Indicator Program,* NSI Report TR-224-1795, Northrop Service, Inc., Huntsville, AL, May 1977.

34. D. L. Mattox, *Method of Thermal Analysis for Flight Test Vehicle,* NSI Memorandum Y4522-78-086, Northrop Services, Inc., Huntsville, AL, 28 February 1978.

35. P. J. Schneider, *Temperature Response Charts,* John Wiley & Sons, Inc., New York, NY, 1963.

36. A. H. Shapiro, *The Dynamics and Thermodynamics of Compressible Fluid Flow,* The Ronald Press Company, New York, NY, 1953.

37. D. R. Bartz, *A Simple Equation for Rapid Estimation of Rocket Nozzle Convection Heat Transfer Coefficients,* JPL External Pub. 351, Jet Propulsion Laboratory, Pasadena, CA, January 1957.

38. V. A. Dauro, *Heat Transfer and Fluid Flow Computer Program (NHEAT),* NSI Memorandum M9230-78-05, Northrop Services, Inc., Huntsville, AL, 15 December 1978.

39. DARCOM-P 706-298, Engineering Design Handbook, *Rocket and Missile Container Engineering Guide,* January 1982.

40. MIL-HDBK-727, *Design Guidance for Producibility, 5* April 1984.

41. AMCP 706-313, Engineering Design Handbook, *Short Fiber Plastic Base Composites,* July 1975.

42. DARCOM-P 706-314, Engineering Design Handbook, *Discontinuous Fiberglass Reinforced Thermoplastics,* March 1981.

43. DARCOM-P 706-315, Engineering Design Handbook, Dielectric *Embedding of Electrical or Electronic Components,* April 1979.

44. DARCOM-P 706-316, Engineering Design Handbook, *Joining of Advanced Composites,* February 1979.

45. MIL-STD-961A, *Military Specification and Associated Documents, Preparation of, 30* April 1981.

46. AMCP 706-115, Engineering Design Handbook, *Environmental Series, Part One, Basic Environmental Concepts,* October 1969.

47. AMCP 706-116, Engineering Design Handbook, *Environrnental Series, Part Two, Natural Environmental Factors,* April 1975.

48. AMCP 706-117, Engineering Design Handbook, *Environmental Series, Part Three, Induced Environmental Factors,* January 1976.

49. AMCP 706-118, Engineering Design Handbook, *Environmental Series, Part Four, Life Cycle Environments,* March 1975.

50. AMCP 706-119, Engineering Design Handbook, *Environmental Series, Part Five, Glossary of Environmental Terms,* July 1975.

C H A P T E R   3
P E R F O R M A N C E

The chapter prevents information for use in determining the free rocket physical characteristics that result from mission range and payload requirements. Idealized velocity requirement estimates are presented in equation form. Also included are equations and figures useful in the estimation of additional velocity requirements resulting from aerodynamic drag and gravitationale effects. Data for several classes of rockets are presented.

Figures depicting parametric relationships useful to the performance design function are presented. These parametric data are useful in design trade-offs and in establishing limits on some parameters for several classes of free rockets.

A numerical example is presented to illustrate the use of the information and data presented in the chapter.

3-0 LIST OF SYMBOLS

$A_{ref} = \pi d_{ref}^2/4,$, aerodynamic reference area, m^2

$B = m/(C_d A_{ref})$, ballistic coefficient, kg/m^2

$B_{bo} = m_{bo}/(C_{DbO} A_{ref})$, ballistic coefficient immediately after motor burnout, kg/m^2

$C_D = F_D/(q A_{ref})$, aerodynamic drag coefficient, dimensionless

C_{D_B} = instantaneous drag coefficient during rocket flight (boost), dimensionless

$C_{D_{bO}}$ = aerodynamic drag coefficient immediately after rocket motor burnout, dimensionless

C_{D_C} = instantaneous drag coefficient during rocket unpowered flight (coast), dimensionless

$(C_{D_B})_{bo}$ = aerodynamic drag coefficient immediately before rocket motor burnout, dimensionless

d_{ref} = aerodynamic reference length, m

F_B = thrust of rocket booster motor, N

F_D = aerodynamic drag force, N

F_s = thrust of rocket sustainer motor, N

$G = F_B/(m_0 g_0)$, initial acceleration level of rocket, dimensionless

$g_0 = 9.80665$ m/s^2, reference acceleration due to gravity

H = altitude, m

H_{max} = maximum altitude of sounding rocket, m

† $I_{sp} = F_B/(m g_0)$, rocket motor specific impulse, s

I_S/I_B = ratio of sustainer motor total impulse I_S to booster motor total impulse I_B, dimensionless

---

†In this chapter, the specific impulse is defined in the traditional sense, i.e., $I_{sp} = F_B/(\dot{m} g_0)$ with units newton/(newton/second) or second. The equations herein use this definition. In Chapter 6, I_{sp} is defined in a manner consistent with the International System of Units (SI).

$(I_{SP})_S / (I_{SP})_B =$ ratio of sustainer motor specific impulse to booster motor specific impulse X 100, %

K = a function accounting for variation of C_D, mass, and gravity during boost, kg/m·s²

M = Mach number, dimensionless

m = rocket mass, kg

$\dot{m}$ = rocket motor mass flow rate, kg/s

$m_{bo} = m_0 - m_p$, rocket mass at motor burnout, kg

m_p = mass of usable propellant, kg

m_{pld} = payload mass, includes all mass not associated with the rocket motor, kg (Usually taken to mean all mass forward of the motor.)

m_0 = rocket gross mass at ignition, kg

$PMF = m_p / (m_0 - m_{pld})$, propellant mass fraction, the ratio of propellant mass to the mass associated with the motor, dimensionless

P_a = atmospheric pressure, Pa

P_c = rocket motor chamber pressure, Pa

P_c / P_a = ratio of rocket motor chamber pressure to standard atmospheric pressure, dimensionless

$Q = m_0 / m_{pld}$, growth factor, the ratio of rocket gross mass to payload mass. dimensionless

QE = quadrant elevation angle, measured positive above horizon, deg or rad as noted

$q = pV^2/2$, instantaneous dynamic pressure, Pa

R = range, m or km

R_{max} = maximum range, km

$r_b = m_0 / (m_0 - m_p)$, booster mass ratio, the ratio of rocket gross mass to burnout mass, dimensionless

t = time, s

t_{alt} = time to altitude, s

t_b = rocket motor burn time, s

t_{bo} = time of rocket motor burnout, s

t_{imp} = time of rocket flight termination, s

t_t = time to target, s

t_0 = time of rocket ignition, s

V = velocity, m/s

V_B = estimate of rocket velocity requirement without drag and gravity losses, m/s

v_{bo} = burnout velocity, m/s

$V_{ideal} = g_0 I_{SP} \ln(r_b)$ = rocket velocity determined by the ideal velocity equation, m/s

V_{prop} = total rocket motor propulsive velocity requirement including estimates of drag and gravity effects, m/s

ΔV_{boost} = estimate of velocity increment lost to drag during powered flight (boost), m/s

ΔV_{coast} = estimate of velocity increment lost to drag during unpowered flight (coast), m/s

ΔV_{grav} = estimate of velocity increment lost (or gained) due to gravity effects, m/s

p = atmospheric density, kg/m^3

p_0 = 1.2250 kg/m^3, atmospheric density at standard sea-level conditions

3-1 INTRODUCTION

Performance in the context of this handbook, and specifically in this chapter, relates to velocity and impulse characteristics of the rocket. The analysis and determination of performance requirements involve the determination of the velocity and impulse requirements to deliver a given payload to the target at a specific range. Accuracy requirements are not considered part of the performance discussions; accuracy is the subject of Chapter 4.

In the design of any rocket, the study of performance parameters is a necessary early step in the trade-off studies of the concept because the parametric performance data

1. Relate the performance to rocket physical characteristics

2. Serve as the basis for trade-off considerations among competing requirements and characteristics

3. Show the sensitivity of the rocket physical characteristics to variations in performance requirements, propulsion system efficiency), aerodynamic characteristics (primarily drag), and energy management technique.

Flight performance characteristics are developed using the simple, 2-degrees-of-freedom (DOF), trajectory computer programs. The forces acting on the rocket are considered to be thrust, drag, and that due to gravity. In addition, the thrust and drag forces are assume-d to be aligned with the instantaneous flight path angle. Flight performance data can be determined fairly easily by applying these approximations with relatively small computers. The only input data required are the initial mass, propellant consumption rate, burn time, thrust history, and drag coefficient versus Mach number.

Performance trade-off studies generally start with the requirement to deliver a specified payload mass to a specified range or altitude. Additional payload requirements that can be imposed include velocity and approach angle at the target or other warhead requirements. General operational requirements may include a total mass limitation, initial boost thrust limits, and overall length limits. The effects of geometry and packaging may also be included in the flight performance analysis. Other data in the form of propulsion data, mass-estimating relationships, and sizing methodologies may be required.

The parametric flight performance data for this chapter have been developed by use of a simple computer program. The computer program is described in par. 3-3; a sample methodology for sizing rockets is presented in par. 3-9. Other data in this chapter are presented to show the relationships among the various rocket motor parameters, rocket mass parameters, and rocket performance.

The rocket performance and sizing methodology presented in this chapter is meant to be used for preliminary design estimations. The methodology allows the relatively rapid assessment of several rocket configurations in order to narrow the choice among such configurations. More detailed and precise analyses can then proceed on a more limited number of configurational options that are more likely to meet system specifications.

'Ihe preliminary rocket design effort must be supported by information from several rocket discipline. Achievable thrust and specific impulse estimates, reasonable mass densities for typical rocket sections, and rough estimates of aerodynamic drag coefficients are required in selecting such rocket parameters as length and diameter. These estimates can be found in other chapters of this handbook, from the available rocket literature, and from experience.

Approximation techniques are presented that allow the determination of the propulsive velocity requirements. The required propulsive velocity requirement V_{prep} is presented in terms of an ideal propulsive velocity requirement V_B. V_B is the velocity at motor burnout in the absence of drag and gravitational effects. Approximate methods of determining the drag and gravity losses are presented. These losses are presented in terms of a velocity requirement due to drag for boost $\Delta V'_{boost}$ and coast $\Delta V'_{coast}$, and a gravity requirement $\Delta V'_{grav}$. The total propulsive requirement is calculated from an equation of the form:

$$V_{prop} = V_B + \Delta V'_{boost} + \Delta V'_{coast} + \Delta V'_{grav} \qquad (3\text{-}1)$$

where

V_{prop} = estimate of total propulsive evlocity requirement including drag and gravity effects, m/s

V_B = velocity requirements noglecting drag and gravity effects, m/s

$\Delta V'_{boost}$ = velocity increment lost to drag during powered flight (boost), m/s

$\Delta V'_{coast}$ = velocity increment lost to drag during unpowered flight (coast), m/s

$\Delta V'_{grav}$ = velocity increment lost (or gained) due to gravity effects, m/s.

Parametric data and approximation techniques are presented for each of the following types of rockets:

1. Indirect fire of surface-to-surface artillery rockets
2. Direct fire rockets of the type normally employed in antitank or similar roles
3. Sounding rockets that are launched vertically for the purpose of reading extreme altitudes
4. Surface-to-air rockets for an interceptor role
5. Air-to-surface rockets launched from aircraft.

Finally, a numerical example is presented to show how the flight performance requirements are used to develop an estimate of the rocket propulsion system and physical sizing.

3-2 PERFORMANCE PARAMETERS

The parameters, or variables, that are considered in the evaluation of the flight performance can be divided into three major categories:

1. Those factors such as payload, velocity, range, altitude, time of flight, and launch angle associated with performance.

2. factors such as energy-management technique, specific impulse, thrust, burning time, and propellant mass fraction associated with the propulsion system.

3. Aerodynamic considerations such as shape, means of stabilization, drag characteristics, diameter, and payload density.

3-2.1 PERFORMANCE FACTORS

Performance requirements such as delivery of a given payload mass to a specified range are generally considered as fixed conditions for the solution of a given problem. Actual performance requirements are more involved, e.g., the requirements could be stated in terms of delivering the maximum payload for ranges between 10 and 40 km for a launch mass of 90 kg and a total missile length of 5 m. Performance requirements in this chapter will be addressed in a simplified form to allow the significance of the important variables to be easily demonstrated.

Mass ratios are of major importance in parametric performance studies and can be considered exchange ratios relating basic rocket mass parameters. The mass ratios of interest are

1. Q = growth factor, ratio of rocket gross mass m_0 to payload mass, m_{pld} (mass forward of the motor), dimensionless

2. r_b = booster mass ratio, ratio of rocket gross mass m_0 to rocket mass at burnout m_{bo}, dimensionless,

3-2.2 PROPULSION SYSTEM FACTORS

The performance factor of interest is the growth factor Q. The propulsion system influences the value of Q through the basic propulsive system parameters I_{SP} and PMF where

I_{SP} = spedific impulse delivered by the rocket motor, s

PMF = propellant mass fraction, the ratio of usable propellant mass to the mass associated with the motor, dimensionless.

The growth factor Q is also influenced by the energy management technique. The energy management factors are

1. G = ratio of booster motor thrust F_B to rocket takeoff weight $m_0 g_0$, normalized to the acceleration due to gravity, a measure of boost phase acceleration, dimensionless
2. F_s/F_B = ratio of sustainer motor thrust F_s to booster motor thrust F_B, dimensionless
3. I_s/I_B = ratio of sustainer motor total impulse is to booster motor total impulse I_B, dimensionless
4. Time and duration of propulsive force application, s.

Energy management is the control of the propulsion system variables in terms of boost, sustain, and coast modes to meet performance requirements most efficiently. One objective of energy management is to minimize the propulsive mass requirements by tailoring the propulsive system to overcome the retarding drag and gravity effects. Procedures to determine the energy management parameters, such as boost and sustain thrust and their duration, are discussed in this chapter.

3-2.3 AERODYNAMIC CONSIDERATIONS

Generally, the most significant retarding influence that the propulsive system must overcome is the aerodynamic drag effect. Drag effects can increase the propulsive energy requirements by significant amounts. As discussed in Chapter 5, the drag force on the rocket is described by the drag coefficient C_D, the trajectory dynamic pressure q, and the aerodynamic reference area A_{ref}. The drag coefficient varies with Mach number and generally is described by two curves, a boost or power-on curve C_{D_B} and a coast or power-off curve C_{D_C}. The parameter for the deceleration influence of drag is the ballistic coefficient B, a measure of the ability of a rocket to overcome the drag effect. The larger the value of the ballistic coefficient B, the smaller the deceleration influence of drag and the propulsive energy requirements for the rocket. The ballistic coefficient B varies with time as a result of mass variations during boost and variations of the aerodynamic drag coefficient C_D with Mach number. Motor burnout is a significant flight condition for the drag deceleration effect because the rocket mass is a minimum and the flight dynamic pressure is generally at a maximum; thus the drag force per unit mass is the largest. Accordingly, conditions at burnout are used in this chapter to specify the ballistic coefficient of the rocket. Boost effects are described by the ballistic coefficient at burnout by using the burnout mass and the power-on drag coefficient at burnout. Coast drag effects are described by the burnout mass and the power-off drag coefficient at burnout.

3-3 APPROXIMATION TECHNIQUES AND APPLICABLE EQUATIONS

Approximation techniques are available for estimating the velocity requirements and propulsive size requirements including the influence of drag and gravity. A discussion of the approximation techniques for each type of rocket is described in the paragraphs that follow.

3-3.1 ESTIMATION OF VELOCITY REQUIREMENT

The velocity requirement, which includes drag and gravitational effects, is developed in terms of the velocity required to achieve a given range or altitude. The approximation techniques include drag losses during boost and during coast. The data presented have been developed by integrating the velocity loss from parametric trajectory data. These data are applied by using an impulsive velocity summation technique to determine the total propulsive requirements.

The velocity summation technique approach of this chapter is used for estimating all propulsive requirements-regardless of whether the rocket is direct-fire, indirect-fire, air defense, etc. The data are presented in a manner which allows consistent application of Eq. 3-1 to all types of rockets. The data also are presented in terms of the basic rocket performance parameters of par. 3-2 and other well defined parameters such as motor burn time t_b. The paragraphs that follow will show how the velocity summation technique is applied to the several types of rockets. Par. 3-9 contains a detailed numerical example and also presents a methodology for applying the velocity summation technique and determination of the rocket performance parameters.

3-3.1.1 Indirect Fire Rockets

Range and velocity relationships as a function of B_{bo} and quadrant elevation (QE) for selected indirect fire rockets are presented in Figs. 3-1, 3-2, and 3-3 for 130-mm, 762-mm, and 321-mm rockets, respectively.
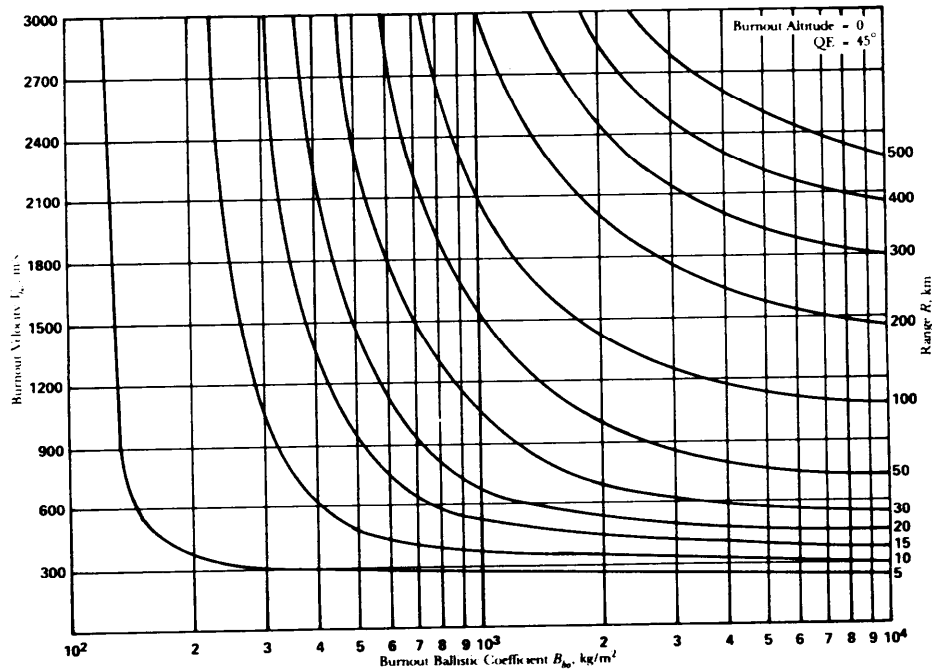
Figure 3-1. **Effect of Burnout Ballistic Coefficient and Burnout Velocity on Range-133-mm Rocket**
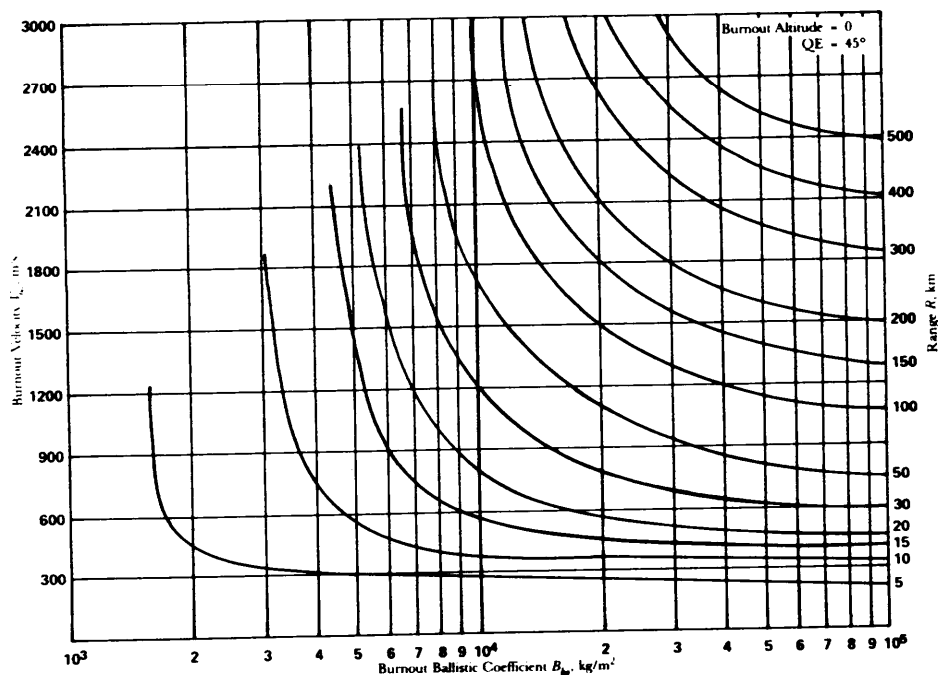
Figure 3-2. **Effect of Burnout Ballistic Coefficient and Burnout Velocity on Range-762-mm Rocket**

MIL-HDBK-762(MI)
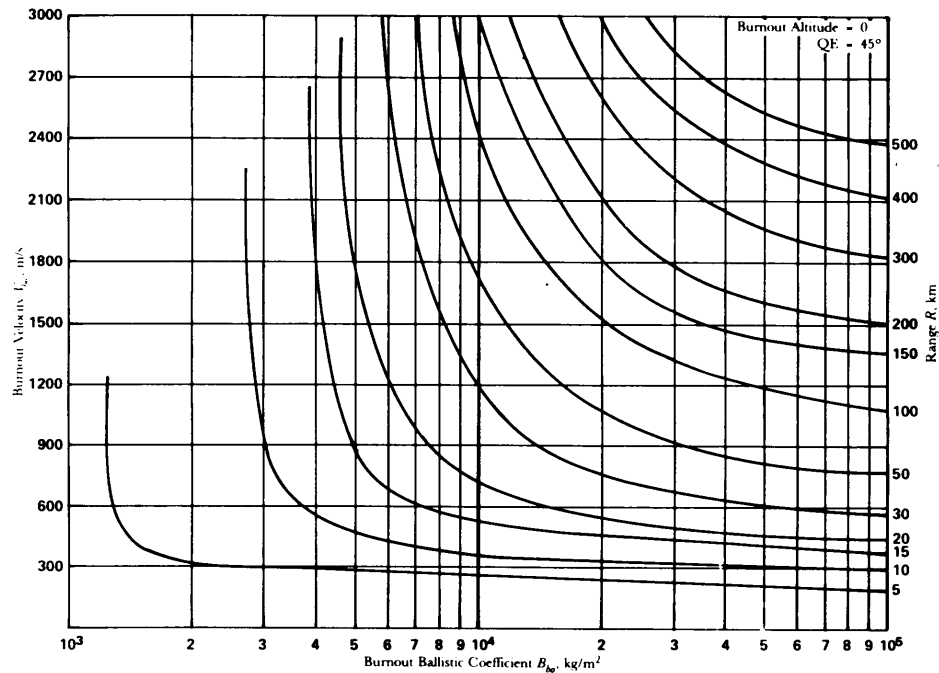
Figure 3-3. Effect of Burnout Ballistic Coefficient and Burnout Velocity on Range-321-mm Rocket

These data were generated by use of a simple, 2-DOF computer program. The program contained a US Standard atmosphere and gravity as a function of altitude over a flat earth. A more complete discussion of equations of motion for a rocket is found in Chapter 4, "Accuracy". From these figures, the burnout velocity V_{bo} requirement is shown to be a strong function of the ballistic coefficient B_{bo} immediately after burnout. The larger the value of B_{bo}, the lower the burnout velocity V_{bo} requirement for a given range. The aerodynamic drag coefficient C_D for each of the selected rockets is presented in Figs. 3-4 through 3-6, along with a line drawing of each rocket.

The boost velocity V_B requirement, neglecting drag and gravity effects, is given by

$$V_B = \sqrt{\frac{Rg_0}{\sin(2QE)}} \qquad , \text{m/s} \tag{3-2}$$

where

R = range from launcher to target, m
g_0 = 9.80665, m/s², reference acceleration of gravity
QE = quadrant elevation angle, measured positive above horizontal, rad.

This equation is usable for ranges less than .500 km in which a flat earth approximation is acceptable. Equations for longer ranges, including an oblate rotating earth, can be obtained from Ref. 1. The burnout velocity that would be required in a drag-free environment can be determined from Figs. 3-1 through 3-3 as B_{bo} approaches infinity.

The velocity loss ΔV_{coast}, due to drag during the coast phase is developed by the following equation:

$$\Delta V_{coast} = \int_{t_{bo}}^{t_{imp}} \left(\frac{C_{D_C}\, q\, A_{ref}}{m_{bo}} \right) dt, \text{m/s} \tag{3-3}$$

Rewriting,

$$\Delta V_{coast} = \frac{1}{B_{bo}} \int_{t_{bo}}^{t_{imp}} \left(\frac{C_{D_C}\, q}{C_{D_{bo}}} \right) dt, \text{m/s} \tag{3-4}$$

3 - 7

where

$$B_{bo} = \frac{m_{bo}}{C_{D_{bo}} A_{ref}}, \text{ kg} / \text{m}^2 \qquad (3\text{-}5)$$

ΔV_{coast} = velocity lost to drag during the coast phasse, m/s

t_{bo} = time of rocket motor burnout, s

t_{imp} = time of flight termination due to impact or warhead detonation, s

C_{D_c} = instantaneous drag coefficient during coast, dimensionless

q = instantaneous dynamic pressure, Pa

A_{ref} = rocket reference area, m^2

m_{bo} = rocket mass at motor burnout, kg

B_{bo} = rocket ballistic coefficient immediately after rocket motor burnout, kg/m^2

$C_{D_{bo}}$ = aerodynamic drag coefficient, immediately after rocket motor burnout, dimensionless.

Eq. 3-4 shows ΔV_{coast} to be the product of the reciprocal of B_{bo} multiplied by the integral of the drag coefficient variation from burnout to impact multiplied by the dynamic pressure. The velocity loss during coast for the 130-mm rocket is presented in Fig. 3-7. Fig.3-7 shows that a rocket with a burnout ballistic coefficient B_{bo} of $10^4 \text{kg}/\text{m}^2$ will lose approximately half or more of the boost velocity V_{bo} as a result of drag. This maximum drag loss reduces the range to approximately 70% of the drag-free range.

An additional velocity loss resulting from drag occurs during boost. The boost velocity loss is described
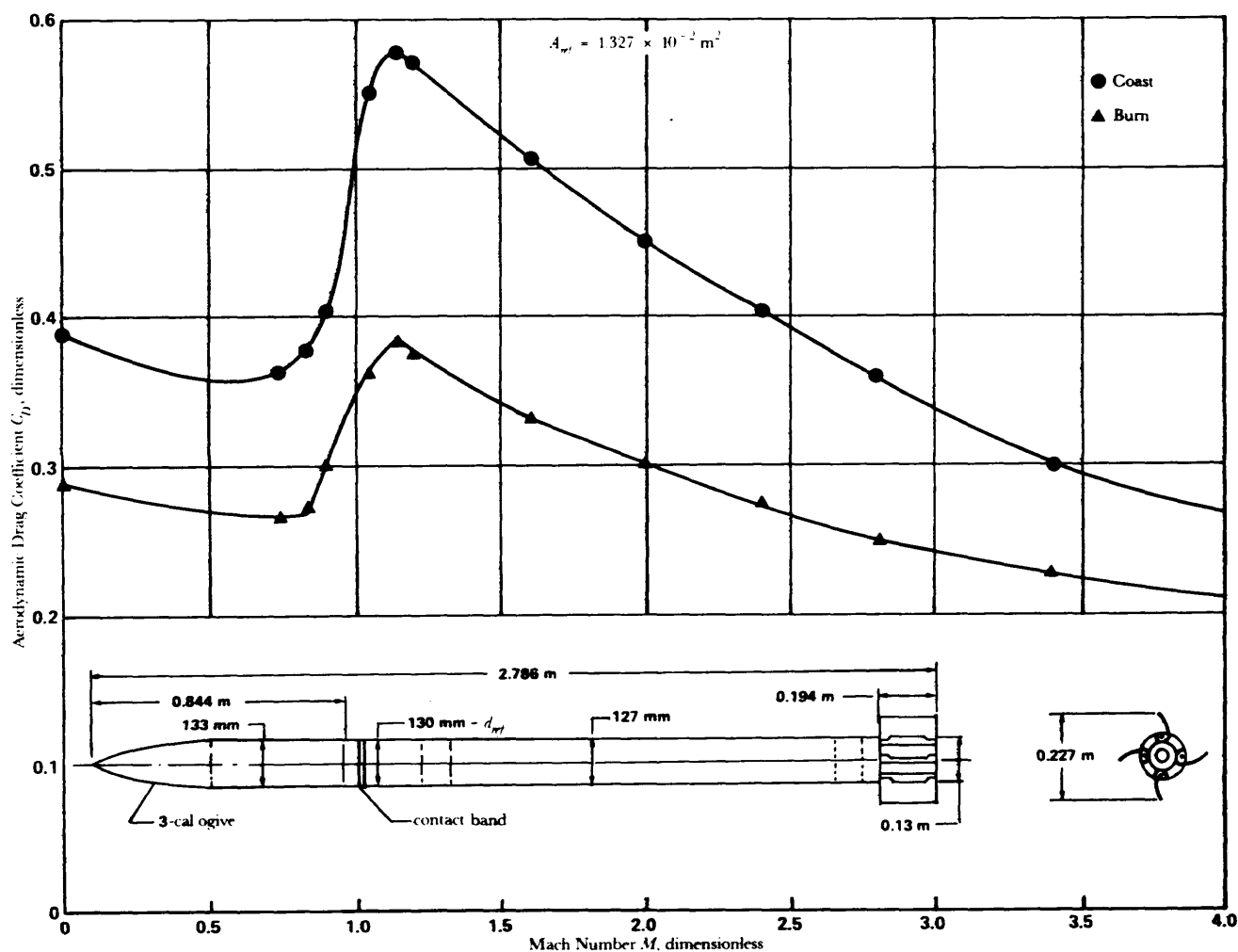
Figure 3-4. Drag Coefficient vs Mach Number-HO-mm Rocket
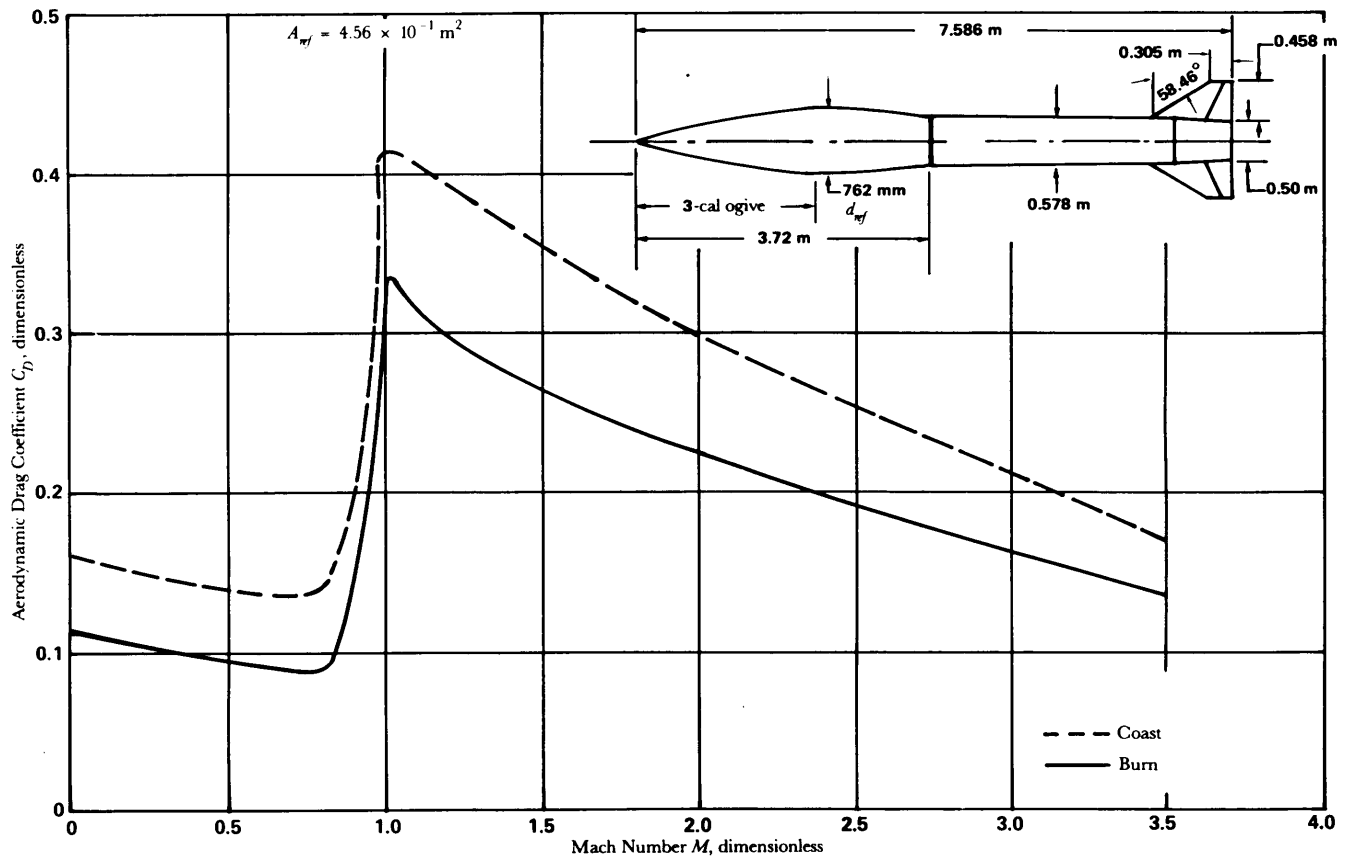
Figure 3-5. Drag Coefficient vs Mach Number—762-mm Rocket

by an equation similar to Eq. 3-3 with the integration limits now being time of ignition t_0 to time of motor burnout t_{bo}. The drag coefficient becomes C_{D_B}, i.e., that for the power-on rocket. The drag acceleration term $(C_{D_C} q A_{ref})/m_{bo}$ is changed to $[(C_{D_B})_{bo} A_{ref}/m_{bo}]f(K)$. The function K accounts for the variations in C_D, q, mass, and gravity. Thus $\Delta V_{boost} = 1/B_{bo} \int f(K)dt$. The function of K is dependent on t_{bo} and G such that

$$\frac{\Delta V_{boost}}{t_{bo}} = f(B_{bo}, Gt_{bo}), \text{ m/s}^2 \tag{3-6}$$

where

ΔV_{boost} = velocity lost to drag during boost, m/s

G = $F_b/(m_0 g_0)$, initial acceleration ratio of the rocket, dimensionless

t_0 = time of rocket motor ignition, s

B_{bo} = $\dfrac{m_{bo}}{(C_{D_B})_{bo} A_{ref}}$ = ballistic coefficient immediately after motor burnout, kg/m².

The boost drag loss is presented in Fig. 3-8. The figure shows that a rocket with a burnout ballistic coefficient of 3000 kg/m², an acceleration ratio G of 100, and a motor burn time t_b of 1 s will have a velocity loss during boost ΔV_{boost} of 100 m/s.

The velocity ΔV_{grav} lost to gravity during the boost phase may be estimated by

$$\Delta V_{grav} = g_0 t_b \sin(QE), \text{ m/s} \tag{3-7}$$

where

t_b = rocket motor burning time, s.
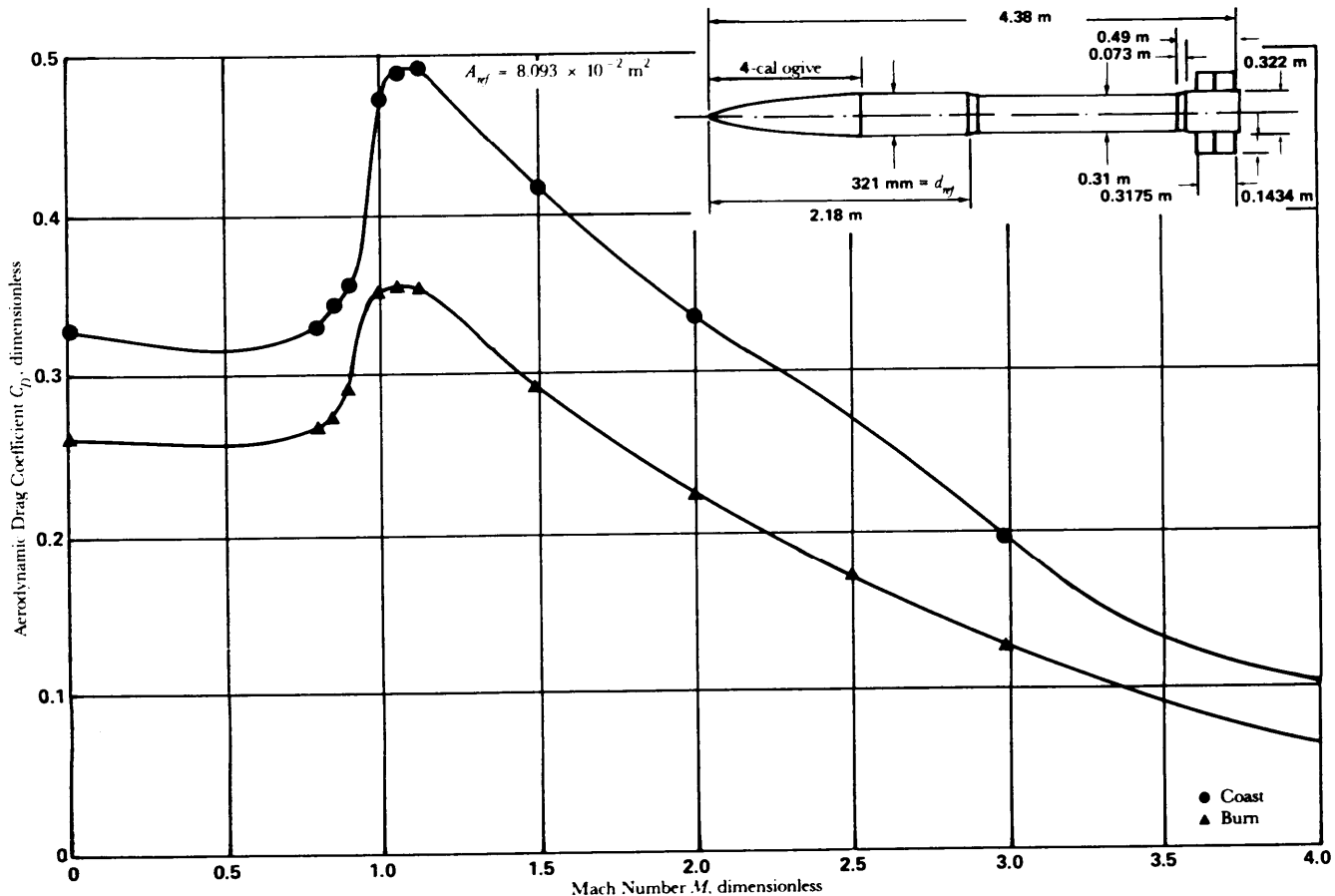
Figure 3-6. Drag Coefficient vs Mach Numbr-321-mm Rocket

The change in the total propulsive velocity V_{prop} requirements due to gravity effects during coast may be considered negligible for indirect fire rockets in the ranges of interest.

The velocity required from the propulsion system for indirect fire rockets is then the summation of the no-loss velocity V_B and the boost, coast, and gravity velocity losses, i.e.,

$$V'_{prop} = V'_B + \Delta V'_{coast} + \Delta V'_{boost} + \Delta V'_{grav}, \text{ m s.} \tag{3-8}$$

The calculation of the propulsion system velocity requirement is similar to the method used in Ref. 2, which presents working charts for the determination of the propulsive velocity requirements for rockets with a range from 15 to 200 km including the infleence of boost and coast drag.

3-3.1.2 Direct Fire Rockets

The drag-free boost velocity V_B requirement for direct fire rockets can be estimated from the following equation:

$$V'_B = \frac{R}{t_t - (t_b \, 2)}, \text{ m s} \tag{3-9}$$

where

  R = range from launcher to target, m
  t_t = estimated or required time to target, s.

The velocity loss $\Delta V'_{coast}$ during coast can be estimated from the following equation:

$$\Delta V_{coast} = V_B \{1 - \exp[\, -\rho_0 \, R/(2B_{bo})]\}, \text{ m/s} \tag{3-10}$$

3-10

MIL-HDBK-762(MI)
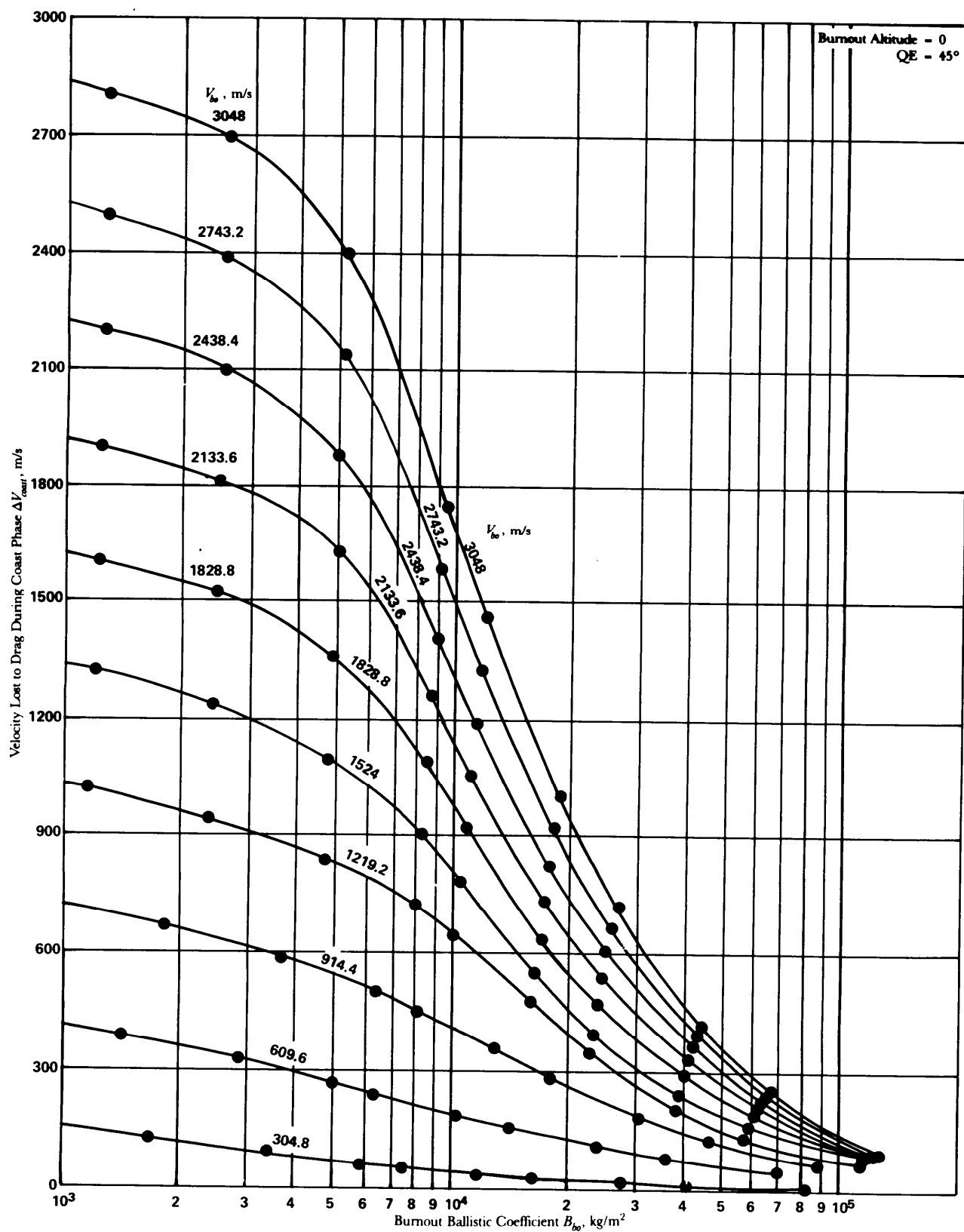
Figure 3-7. Coast Drag Velocity Loss-130-mm Indirect Fire Rocket
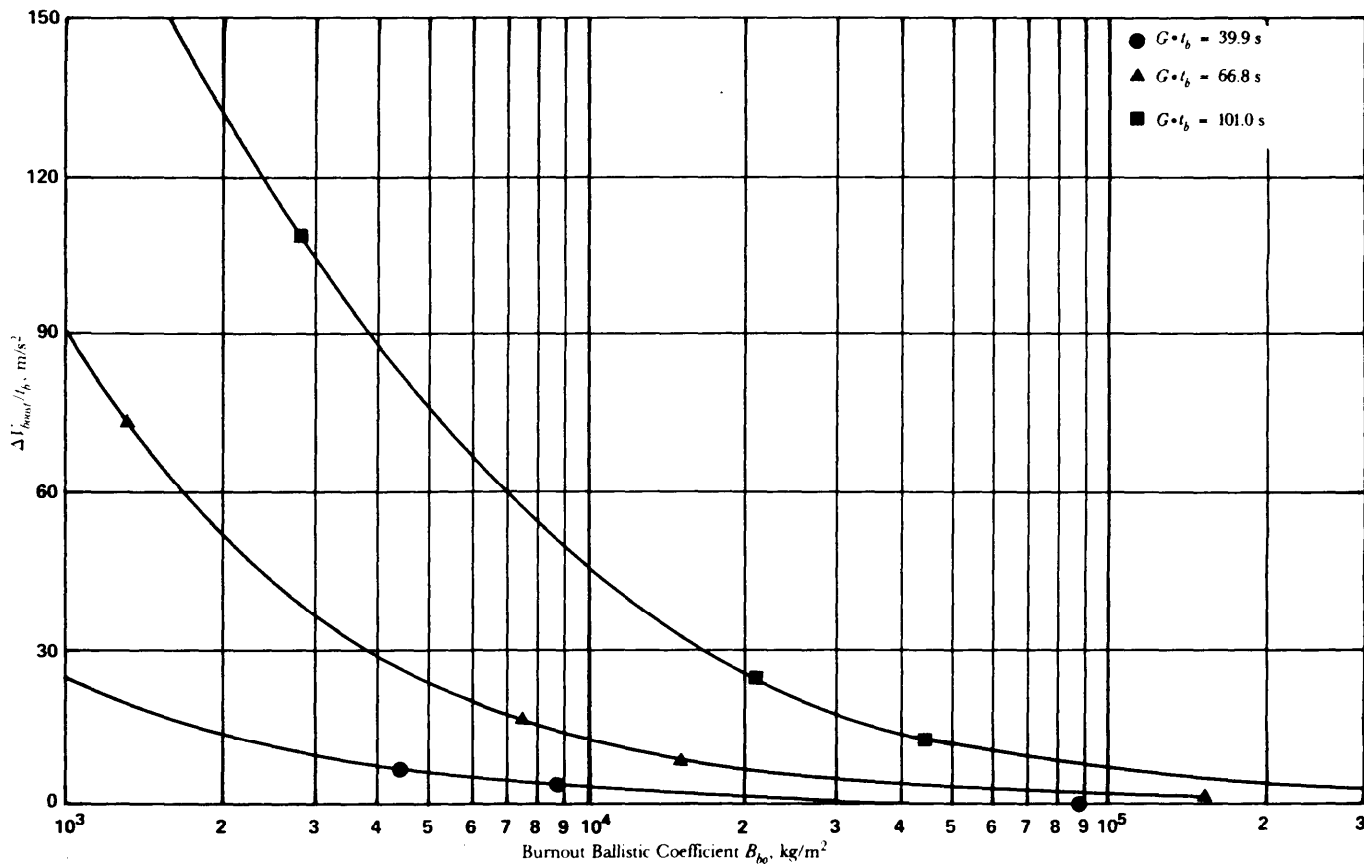
Figure 3-8. Boost Drag Velocity Loss-Indirect Fire Rocket

where

V_B = no-loss boost velocity from Eq. 3-9, m/s

p_0 = 1.2250 km/m³, atmospheric density at sea level

R = range traversed during the coast (unpowered) portion of direct fire flight, m.

The effects of gravity are not insignificant, but a small positive flight path angle can compensate for the losses at the ranges usually encountered in direct fire rockets. The boost velocity loss $\Delta V'_{boost}$ for typical direct fire rockets is presented in Fig. 3-9.

The propulsive velocity requirement V_{prop} for typical direct fire rockets, neglecting gravity, is

$$V'_{prop} = V'_B + \Delta V'_{coast} + \Delta V'_{boost}, \text{ m/s.} \tag{3-11}$$

3-3.1.3 Sounding Rockets

The drag-free boost velocity requirement V_B for a vertically launched rocket is a function of the maximum altitude H_{max} and is given by

$$V'_B = \sqrt{2g_0 H_{max}}, \text{ m/s} \tag{3-12}$$

where

H_{max} = maximum altitude to be achieved, m.

The drag loss ΔV_{coast} during coast is presented in Fig. 3-10. The drag loss ΔV_{boost} during boost is presented in Fig. 3-11. Eq. 3-7 given an additional loss term $\Delta V'_{grav}$ required in the calculation of boost velocity which is the velocity loss caused by gravity.

3-12
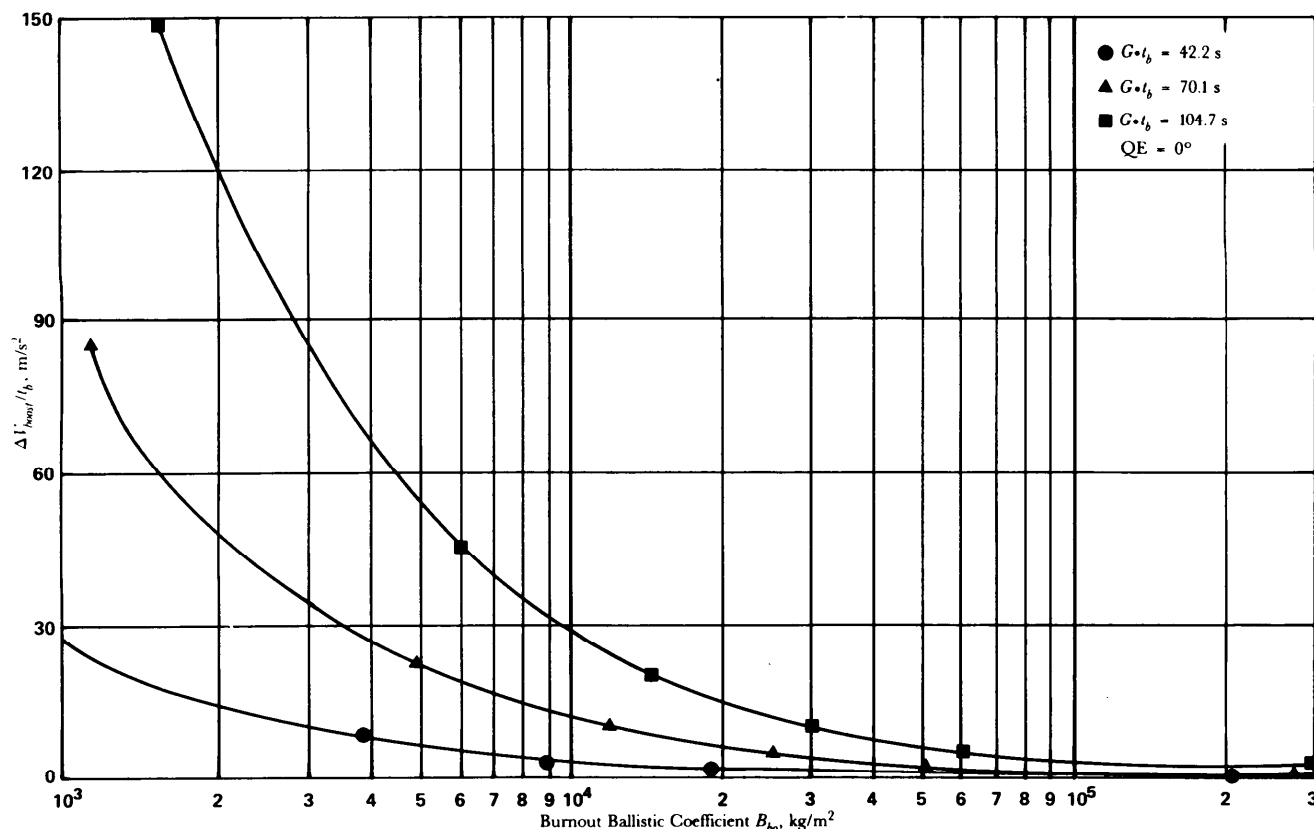
Figure 3-9. Boost Drag Velocity Loss-Direct Fire Rocket

The total propulsive velocity requirement V_{prop} for the sounding rocket is given by

$$V_{prop} = V_B + \Delta V_{coast} + \Delta V_{boost} + \Delta V_{grav}, \text{ m/s.} \qquad (3\text{-}13)$$

3-3.1.4 Surface-To-Air Rockets

The drag-free boost velocity V_B for vertically launched rockets to a given altitude is given by

$$V_B = \frac{H + (g_0/2)(t_{alt} - t_b)^2}{t_{alt} + (t_b/2)} , \text{ m/s} \qquad (3\text{-}14)$$

where

H = altitude desired, m

t_{alt} = estimated or required time to altitude, s.

The velocity loss ΔV_{coast} from drag during coast is presented in Fig. 3-12. The boost velocity loss ΔV_{boost} from drag is presented in Fig. 3-13. The boost velocity loss ΔV_{grav} from gravity is approximated by Eq. 3-7. Thus, the total propulsive velocity requirement V_{prop} for surface-to-air rockets may be expressed as

$$V_{prop} = V_B + \Delta V_{coast} + \Delta V_{boost} + \Delta V_{grav}, \text{ m/s.} \qquad (3\text{-}15)$$

3-3.1.5 Air-To-Surface Rockets

Air-to-surface rockets are similar to direct fire rockets except they are fired from airplanes or helicopters. The altitude of fire for free rockets is generally less than 2 km. The velocity requirement V_B for air-to-surface rockets can be estimated from the direct fire Eq. 3-9, except that R is now interpreted as the slant range from aircraft to target. The velocity loss ΔV_{coast} during coast can be estimated from Eq. 3-10, where R is again interpreted as the coast slant range from aircraft to target. Air-to-surface rockets generally have a range of less than 8 km.

3-13
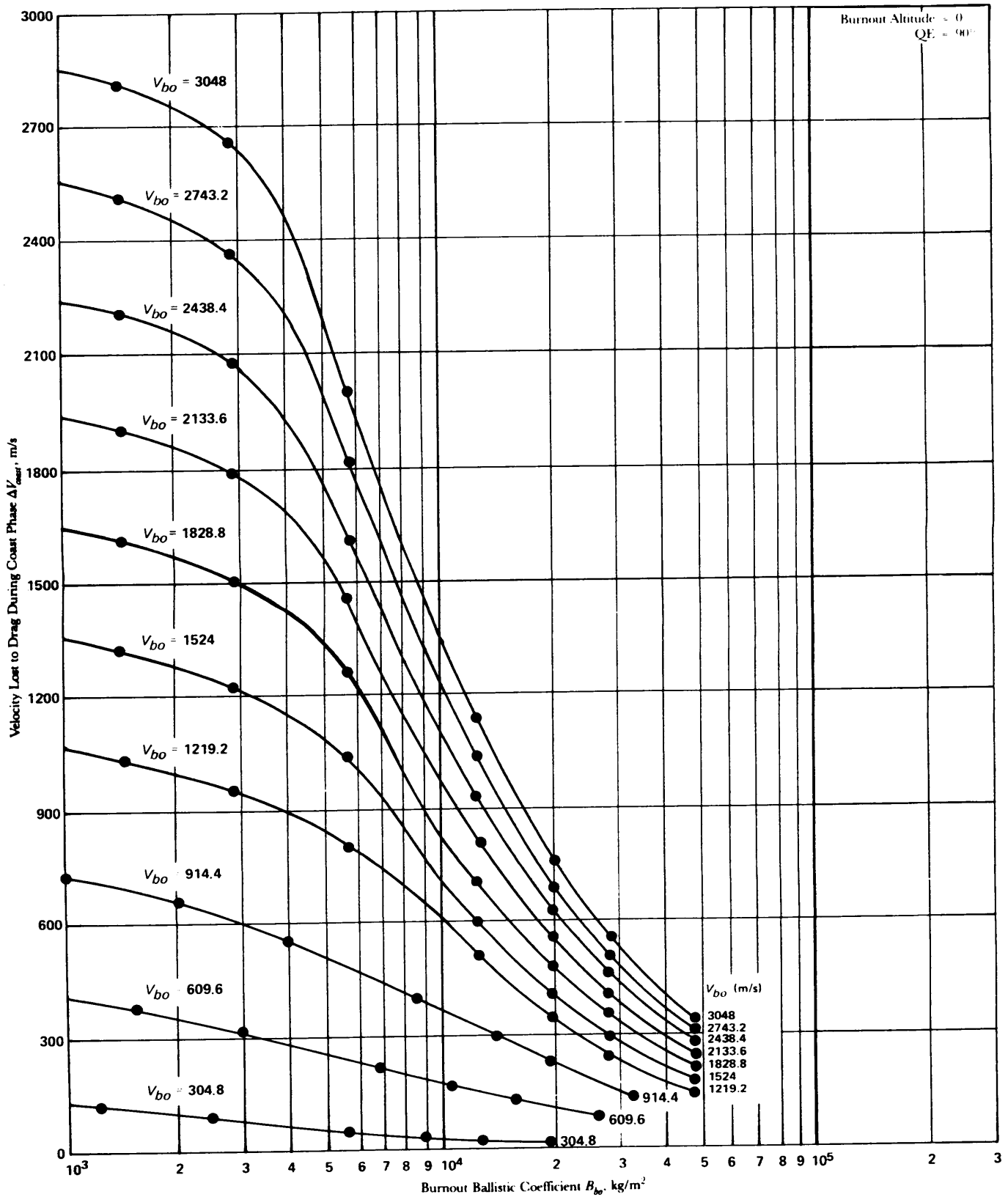
Figure 3-10. Coast Drag Velocity Loss-Sounding Rocket
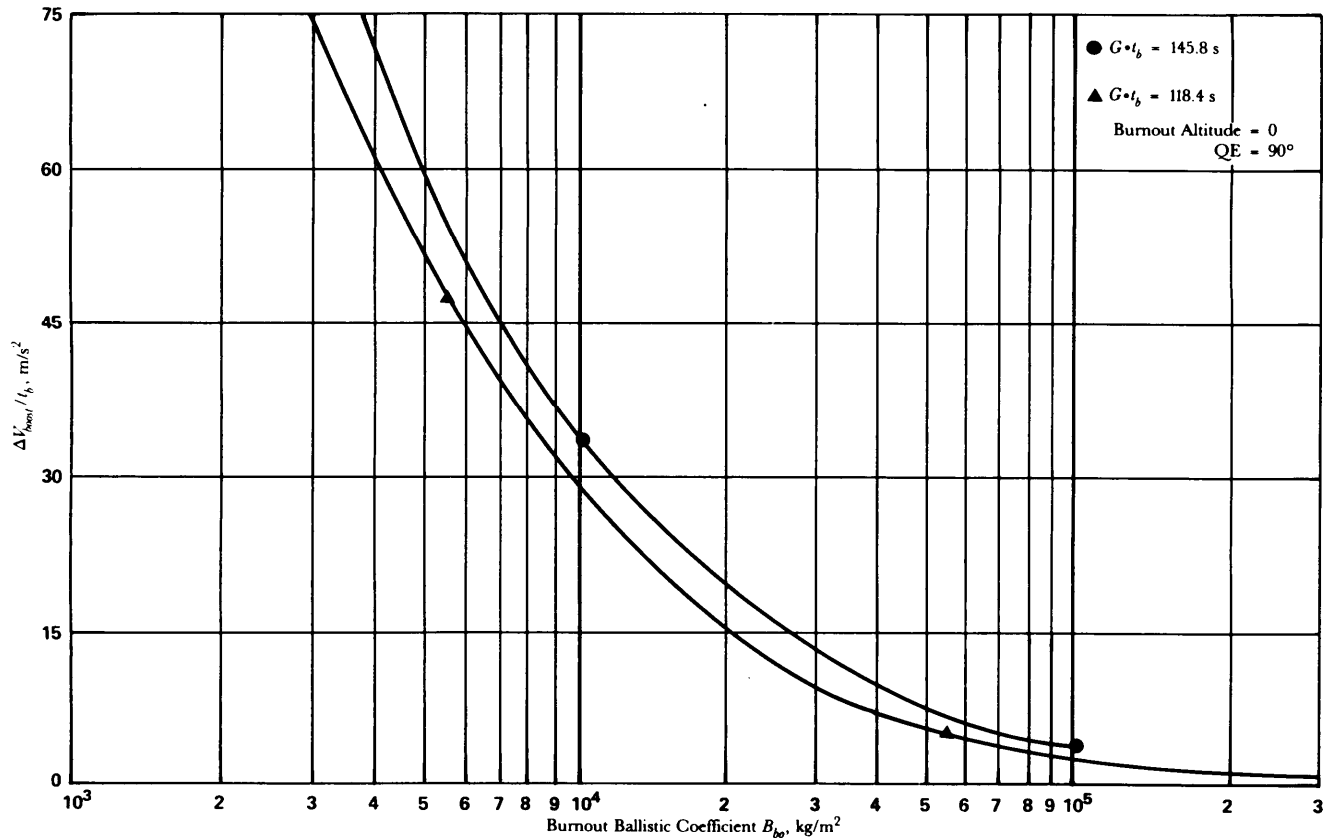
Figure 3-11.   Boost Drag Velocity Loss-Sounding Rocket

Although the atmospheric density over the slant range will not be constant, the variation from sea-level conditions will not be significant.

The boost velocity loss ΔV_{boost} is presented in Fig. 3-13, i.e., the figure for surface-to-air rockets.

Gravity effects cause a small velocity gain that is a function of the initial negative QE and flight time. The gravity velocity gain increment ΔV_{grav} is approximated by

$$\Delta V_{grav} = g_0 t_t \sin(QE), \text{ m/s} \tag{3-16}$$

where t_t = time to target, s.

The propulsion system velocity requirement V_{prop} including the losses and gains is

$$V_{prop} = V_B + \Delta V_{coast} + \Delta V_{boost} - \Delta V_{grav}, \text{ m/s}. \tag{3-17}$$

Note that Eq. 3-17 is the velocity requirement when the velocity of the launching aircraft is zero, i.e., a hovering helicopter. Any forward velocity of the aircraft would reduce the V_{prop} given by Eq. 3-17. Par 3-8.2 will point out that the aircraft velocity is negligible for performance estimate purposes in many cases. When it is not negligible, factors and influences other than just performance parametric must be considered. Other methods for estimating the propulsion system velocity requirements for air-to-surface rockets can be obtained from Ref. 3.

3-3.2 ESTIMATION OF ROCKET MOTOR REQUIREMENTS

The equations of par. 3-3.1 identified methods of obtaining the propulsive velocity V_{prop} required to perform the mission requirements. The velocity requirement is a function of the mass of the payload, mass of the rocket at burnout, size of the rocket, drag characteristics, and type of trajectory. The mass of the rocket at burnout and the size of the rocket may not be known until preliminary mass and sizing trade-offs
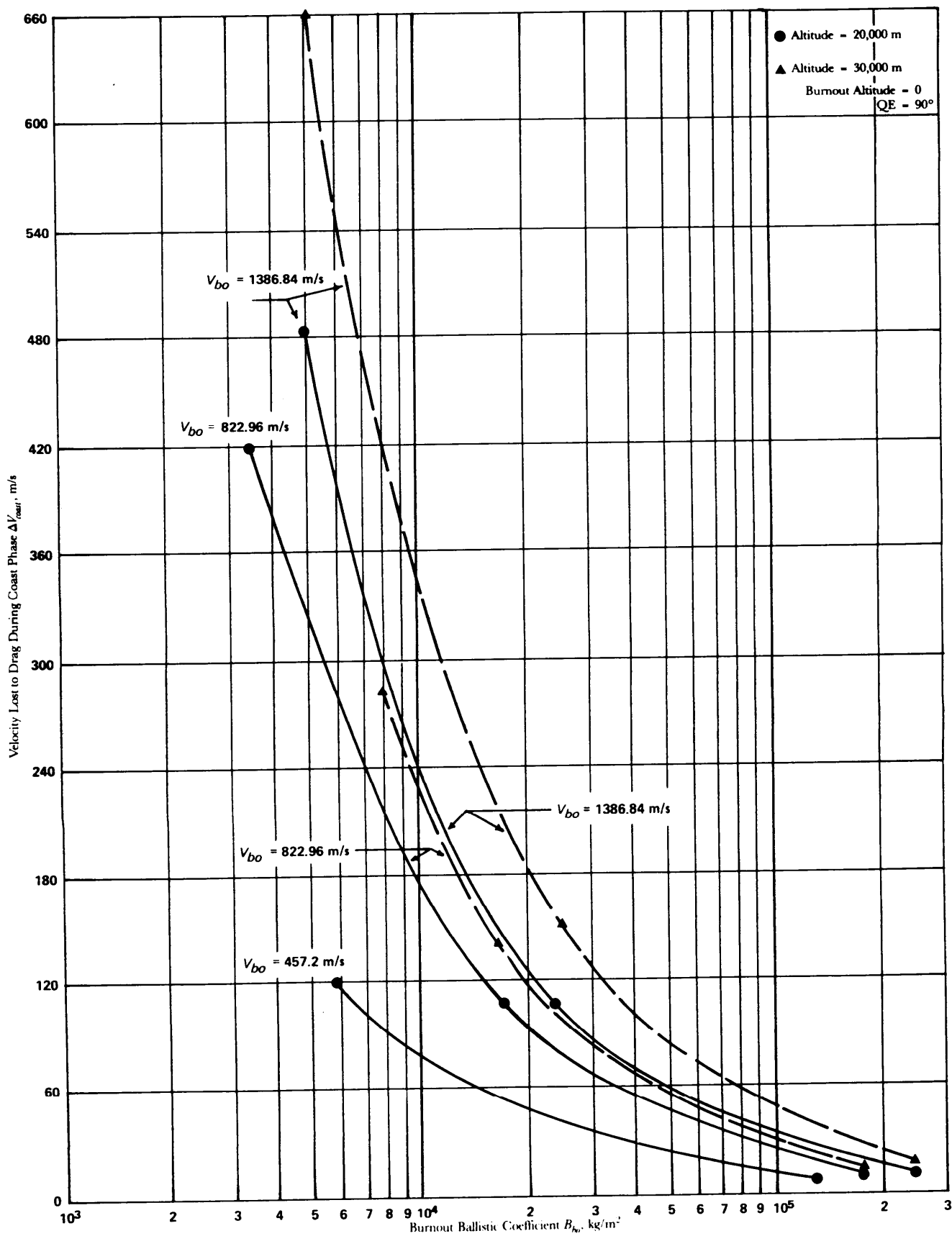
Figure 3-12. Coast Drag Velocity Loss-Surface-to-Air Rocket
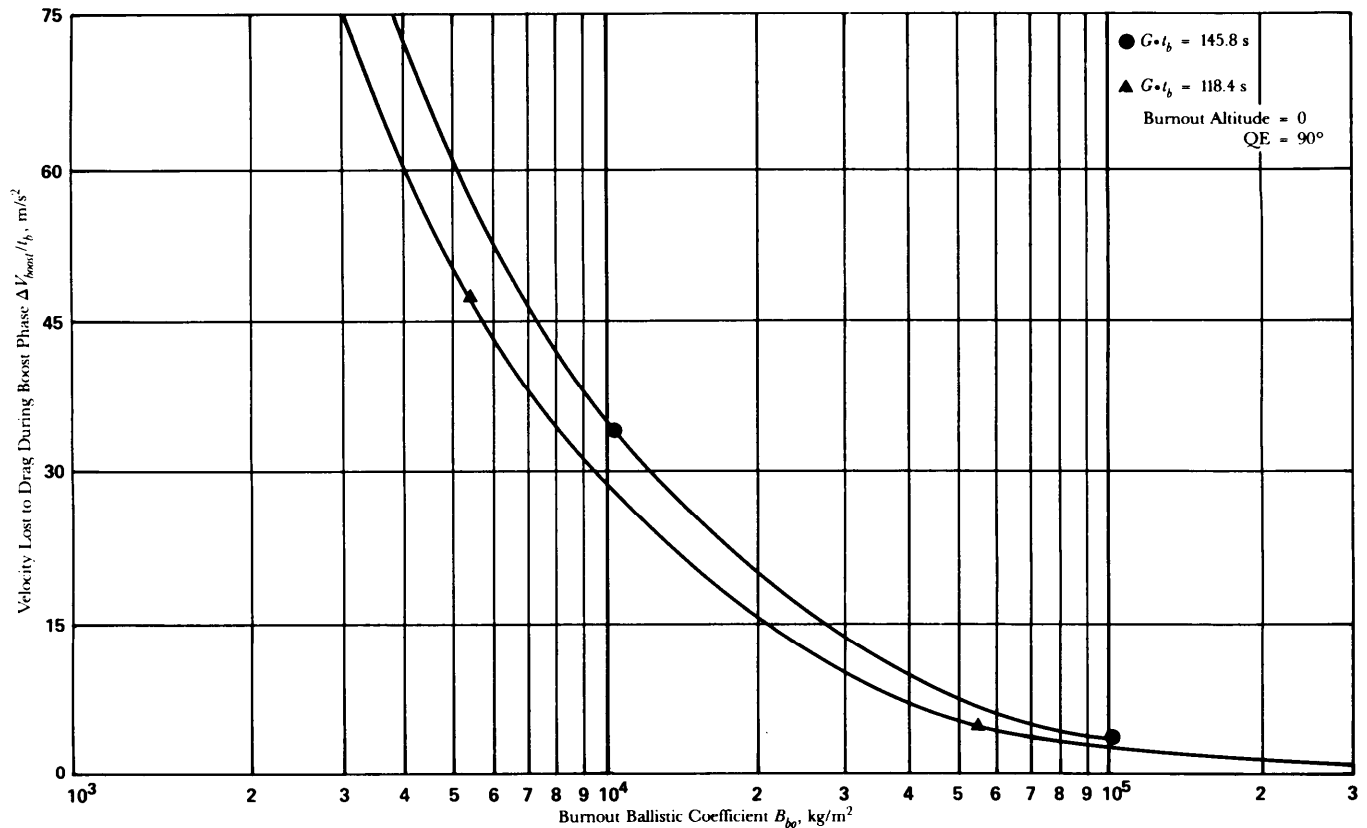
Figure 3-13. Boost Drag Velocity Loss-Surface-to-Air Rocket

are performed. An iteration procedure may be required unless the velocity requirements are developed parametrically in terms of the burnout ballistic coefficient B_{bo}. The paragraphs that follow will develop the mass characteristics of the rocket by using the velocity requirement and propulsive system parameters.

For the purposes of this chapter, rocket mass will be grouped into two major components, i.e.,

1. Payload mass m_{pld}, i.e., all mass forward of the forward motor-closure

2. Motor mass m_m, i.e., all mass aft of the forward motor-closure.

The relationship between the propulsion system ideal velocity V_{ideal} and the rocket gross mass is given by the Ideal Velocity Equation

$$V_{ideal} = g_0 I_{sp} \ln \frac{m_0}{m_0 - m_p}, \text{m/s} \tag{3-18}$$

or

$$V_{ideal} = g_0 I_{sp} \ln(r_b), \text{m/s} \tag{3-19}$$

where

I_{SP} = rocket motor specific impulse, s

m_0 = rocket gross mass at ignition, kg

m_p = usable propellant mass of motor, kg

r_b = $m_0 / (m_0 - m_p)$, booster mass ratio, dimensionless.

The Ideal Velocity Equation relates the burnout velocity of a rocket to specific rocket motor parameters, i.e., I_{sp} and r_b. Note that gravity and aerodynamic velocity effects are not included, hence the name ideal. The propulsive velocity of a multistage rocket can be developed in a manner similar to Eq. 3-19. Ref. 4 presents the equations for calculating the ideal velocity of a propulsion system for a multiple stage rocket system.

The booster mass ratio r_b and the specific impulse I_{SP} determine the ideal burnout velocity of the

propulsion system. The ideal burnout velocity is presented in Fig. 3-14 for various values or r_b and I_{SP}. The variation in mass of the rocket may be estimated from the propellant consumed by using Eq. 3-21. The specific impulse I_{SP} of the motor is related to the thrust F_B of the rocket booster motor and propellant
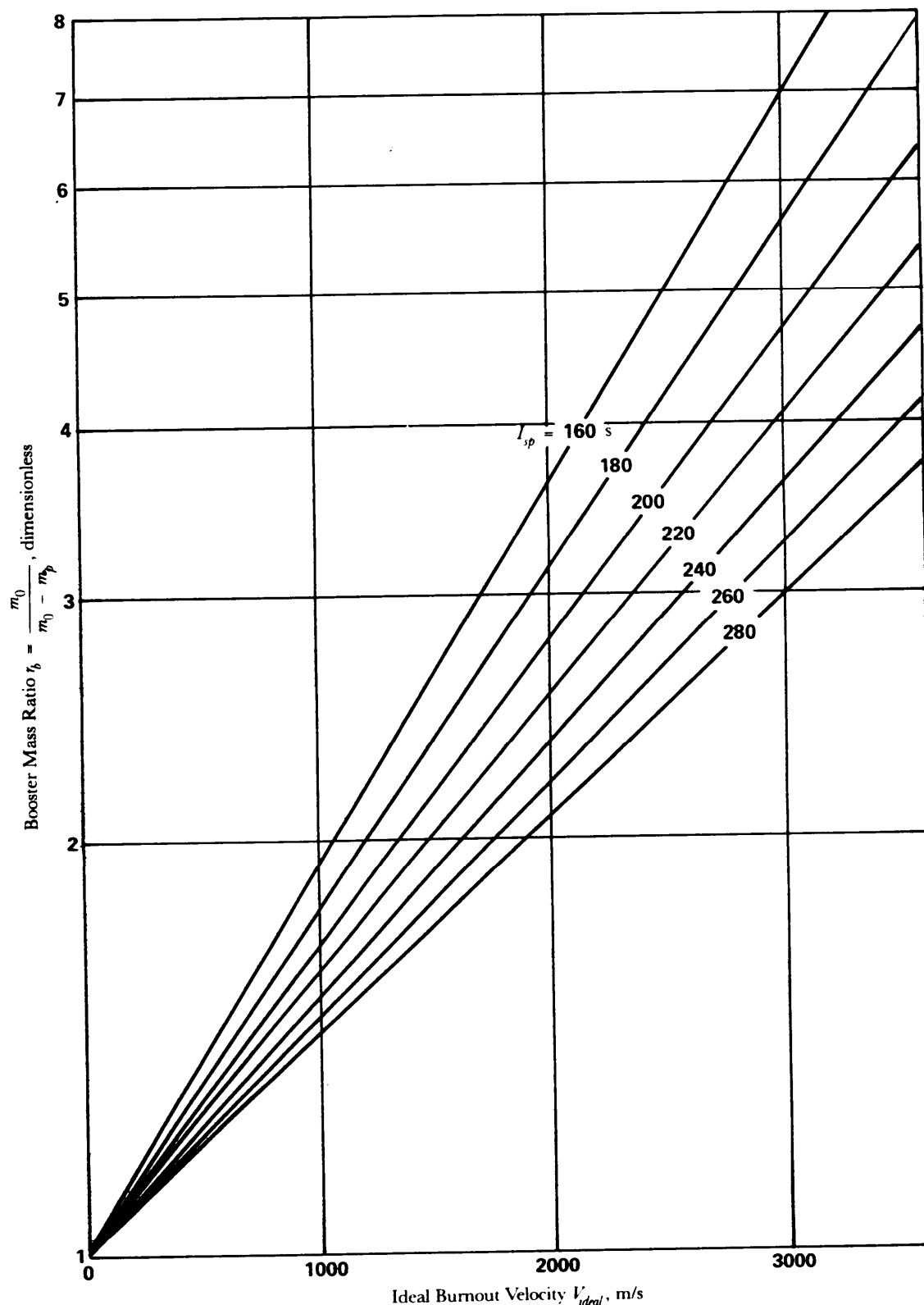
Figure 3-14. Effect of Ideal Burnout Velocity on Booster-Mass Ratio

consumption rate $\dot{m}$ by the following equation:

$$I_{sp} = F_B/(\dot{m}g_0), \text{ s}^*$$ (3-20)

. where

$$\dot{m} = m_p/t_b, \text{ kg/s}.$$ (3-21)

Estimates of rocket motor I_{sp} values achievable can be obtained from Chapter 6, "Propulsion". Other sources for rocket motor I_{sp} values are the rocket literature. The mass of the rocket m at time t may then be given by

$$m = m_0 - \dot{m}t, \text{ kg}$$ (3-22)

or, substituting the expression for $\dot{m}$ from Eq. 3-21,

$$m = m_0 - m_p t/t_b, \text{ kg}.$$ (3-23)

The propellant mass m_p is used in defining one figure of merit for the rocket, i.e., propellant mass fraction PMF. The defining equation for PMF is

$$PMF = \frac{m_p}{m_0 - m_{pld}}, \text{ dimensionless}$$ (3-24)

where

m_{pld} = rocket payload mass, kg.

The payload mass m_{pld} including warhead, nose fairing, and supporting structure—is interpreted to mean all rocket mass forward of the rocket motor. Thus PMF is the ratio of propellant mass to the remaining rocket mass aft of the payload, including fins, motor case, nozzle, and supporting structure.

A second figure of merit is the growth factor Q, defined as the ratio of the rocket gross mass to the payload mass, and is related to the booster mass ratio r_b and the propellant mass fraction PMF by

$$Q = \frac{m_0}{m_{pld}} = \frac{r_b(PMF)}{1 - r_b[1 - (PMF)]}, \text{ dimensionless}.$$ (3-25)

The name "growth factor" arises from the consideration that this ratio indicates to the rocket designer how much his rocket must "grow in mass" to accommodate unit increases in payload mass m_{pld}.

Fig. 3-15 presents the relationship among Q, PMF, and V_{ideal}/I_{SP}. Note that V_{ideal}/I_{SP} is relatable to r_b via Eq. 3-19. Therefore, Fig. 3-15 shows the relationship among Q, PMF, and indirectly, r_b.

3-3.3 SUMMARY

Eqs. 3-18 through 3-25 relate the mass ratios of the rocket and the propellant efficiency I_{SP} to the ideal velocity V_{ideal} that the motor will impart to the rocket at burnout. The value of the growth factor Q is determined from r_b and estimates of PMF, and relates the rocket gross mass m_0 to payload mass m_{pld}. Since the value of m_{pld} is generally part of the initial performance requirement, m_0 is determined. If values of rocket motor booster thrust F_B are known in terms of initial acceleration ratio G, the rocket motor thrust values may then be estimated since

$$F_B = G m_0 g_0, \text{ N}.$$ (3-26)

The propellant consumption rate rate may be calculated from

$$\dot{m} = F_B/(I_{sp}g_0), \text{ kg/s}$$ (3-27)

and the burn time t_b is

$$t_b = m_p/\dot{m}, \text{ s}.$$ (3-28)

---

*See discussion of units for I_{SP} in List of Symbols.
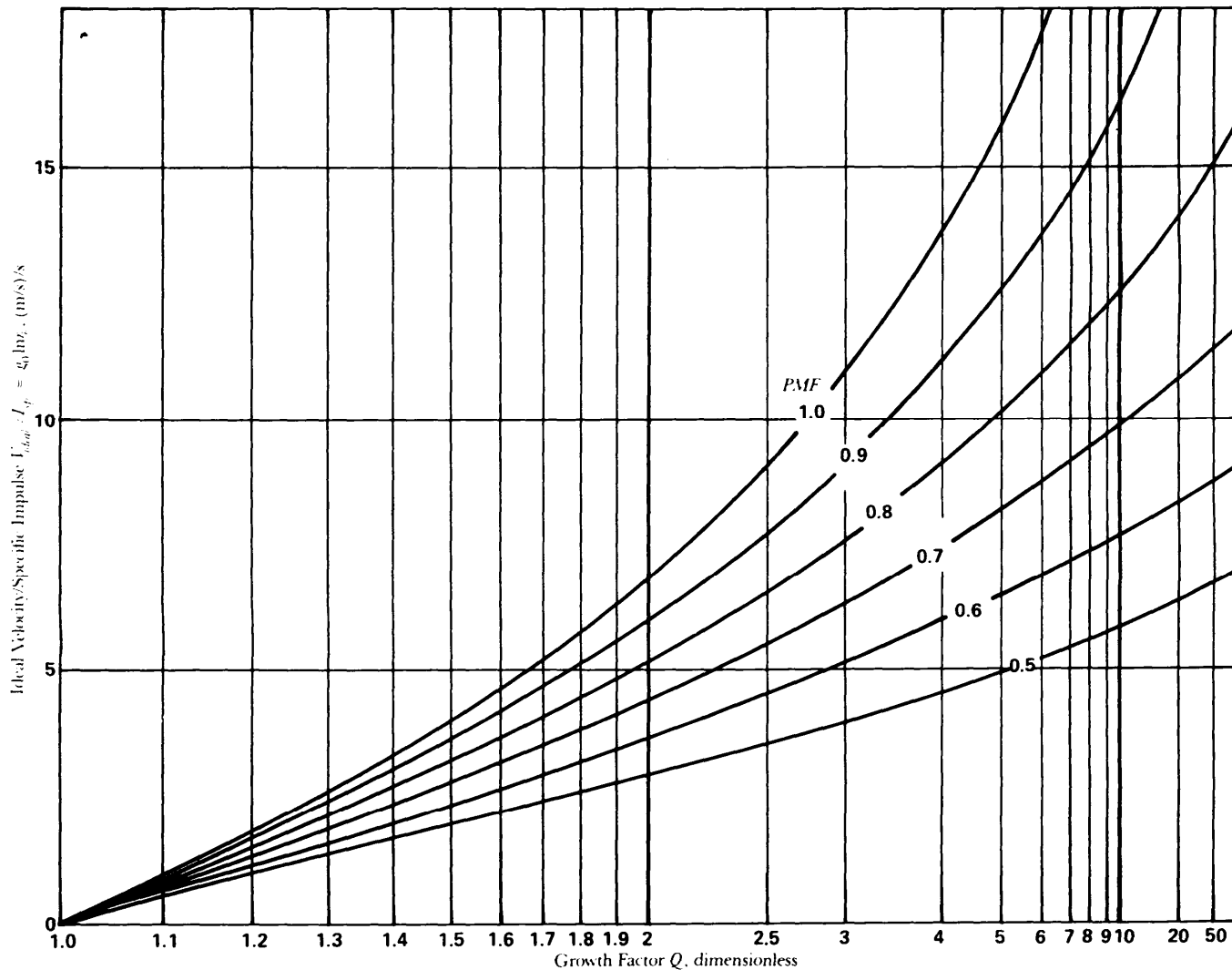
Figure 3-15.   Effect of Growth Factor on Ideal Burnout Velocity

From the preceding it is evident that a considerable amount of information is known or determinable about the rocket system in terms of a few simple mass parameters. However, the preceding equations are only approximations, and the actual defining equations for rockets are more complex than these equations imply. Nevertheless, the equations are useful in the preliminary design phase. As will be demonstrated in the numerical example at the end of this chapter, these relationships may be used in the early phases of design to establish the approximate values of the important rocket parameters such as I_{SP} and Q. These rocket parametric values can be used to determine whether the design requirements are consistent with the state of the art. In addition, these approximate values will establish the region of interest for a more detailed analysis.

3-4 PARAMETRIC PERFORMANCE DATA FOR INDIRECT FIRE SYSTEMS
3-4.1 DELIVERY TECHNIQUES

The trajectory profile for an unguided surface-to-surface rocket (ballistic rocket) is shaped somewhat like a parabola, with an initial QE of between 45 deg and 60 deg for maximum range. Once the rocket is designed, range is controlled by the QE—the shorter ranges requiring either lower or higher angles of fire. The trade-offs between low and high QE for the shorter ranges are governed by accuracy, warhead effects, and tactical requirements.

Some large ballistic rockets are launched vertically; however, they require a maneuver to tilt the rocket onto a ballistic path. The discussion that follows will be limited to the nonmaneuvering types of rockets.

Among the methods that have been used to impart propulsive energy to indirect-fire rocket systems are

1. Boost
2. Boost/sustain
3. Staged boost.

Each method is briefly discussed in the paragraphs that follow.

In the boost method, the booster motor fires for a portion of the flight time after which there is a coast phase to the target. This approach is the least complex of the three and has been used extensively in the field of unguided ballistic rockets.

The boost! sustain method consists of an initial thrust by the booster motor, followed by a sustaining thrust of lesser magnitude. Although this approach offers performance advantages over the boost approach for some applications, it requires a more complex and costly motor construction.

In the staged-boost method, the total thrust is delivered by a series of booster motors, each of which is jettisoned upon burnout. This is the most efficient means of energy management, but its use is limited to those cases for which mass considerations override the cost and reliability penalties of staging, and for which the hazards of falling motor cases can be tolerated. The staged-boost approach is most efficient for very long-range and extreme velocity applications. As the range increases, the growth factor Q increases. An all-boost system would require a larger growth factor than that of the first stage of a staged-boost system. This is so because the m_{pld} of the first stage is the mass of the second stage rocket motor and the second stage m_{pld}.

3-4.2 PARAMETRIC PERFORMANCE DATA

The relationship between growth factor and range for an indirect fire rocket system is a function of the following parameters:

QE = launch elevation angle, deg

I_{SP} = rocket motor specific impulse, s

PMF = propellant mass fraction, dimensionless

B_{bo} = burnout ballistic coefficient immediately after burnout, kg/m^2

G = initial boost acceleration ratio, dimensionless

F_S/F_B = ratio of sustainer motor to rocket booster motor thrust, dimensionless

I_S/I_B = ratio of sustainer motor total impulse to booster motor total impulse, dimensionless.

The angle at which the rocket must be launched to achieve maximum range is of initial interest to the designer. Fig. 3-16 presents the effect of initial acceleration ratio G and growth factor Q on the optimum launch angle for an all-boost system with fixed values of I_{SP}, PMF, and B_{bo}. Although the data would be different if these parameters were varied, the trends of the curve are worth noting. Low G-rockets require higher launch angles to achieve maximum range. Higher growth factors Q also require higher launch angles (QE) because the Qs are equivalent to longer boost burning times at any given G. For a boost/sustain system, as shown in Fig. 3-17, the optimum launch angle will be slightly greater than for an all-boost system. As the ratio F_S/F_B is decreased and/or the ratio I_S/I_B is increased, an increase in the optimum launch angle is indicated. One noteworthy point about Fig. 3-17—and other figures where F_S/F_B or I_S/F_B are depicted—is that when either ratio is zero, the all-boost case is indicated.

Fig. 3-18 presents the relationship between Q and range R for an all-boost system with the QE optimized and PMF, I_{SP}, and B_{bo} held constant. Note that the lower accelerations permit more efficient energy management because they require a lower growth factor for any specified range. In this sense, the selection of G is also an energy-management technique. Although Fig. 3-18 is constructed for only one value each of I_{SP}, PMF, and B_{bo}, it is indicative of trends. Therefore, we may say that the growth factor Q for a given range will be inversely proportional to I_{SP}, PMF, and B_{bo}. The designer would, of course, examine trade-offs among these parameters as discussed later in this chapter. Another trend of significance to the designer or to the originator of requirements may be noted on Fig. 3-18. Examination of the curve shows that significant increases in range can be obtained for relatively minor rocket mass increases. For example, a
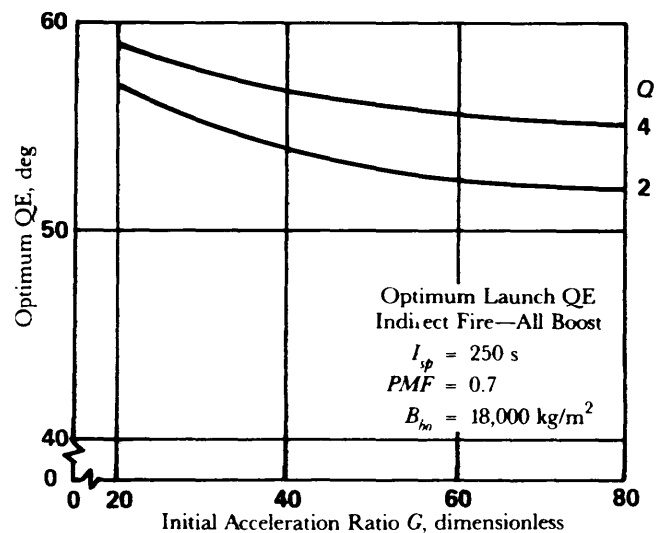
Figure 3-16. **Indirect Fire—Roost; Effect of Initial Acceleration Level on Optimum Launch Quadrant Elevation**
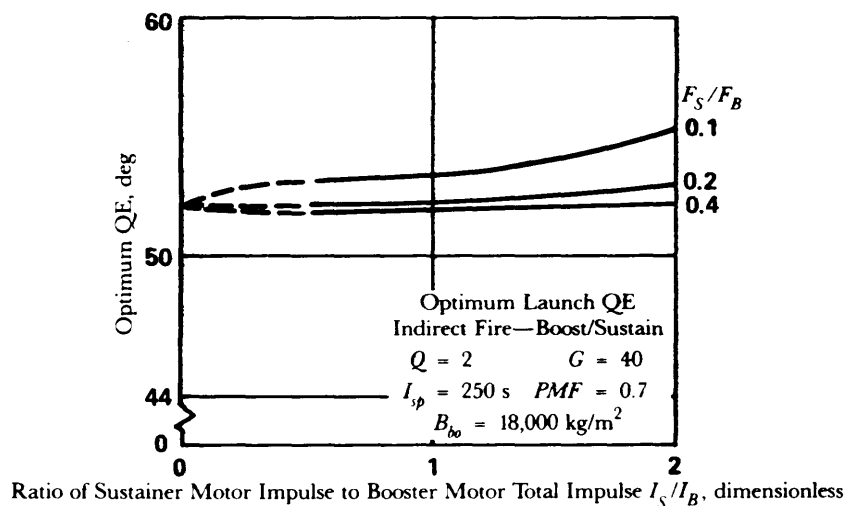
Figure 3-17. Indirect Fire—Boost/Sustain; Effect of Impulse Ratio on Optimum Launch Quadrant Elevation

growth factor of about Q = 2 is required for a range of 30 km; however, a 25% increase in rocket mass (an increase of Q from 2.0 to 2.5) doubles the range to 60 km.

The relationship between Q and range R for a boost sustain system will be dependent upon the choice of sustainer parameters in addition to the parameters discussed for the all-boost system. There is no unique method for determining optimum sustainer parameters since the choice will depend upon which characteristics, e.g., mass or accuracy, of the rocket the designer is attempting to optimize.

The designer has a choice of methods to provide the sustainer impulse. This can be accomplished with separate booster and sustainer motors or by one motor with two thrust levels. In the case of separate motors, it is possible to achieve high specific impulse with each motor, but the propellant mass fraction of the combination is usually lower than for a single motor. In the case of a single motor with two thrust levels, the specific impulse of the sustainer motor will be less than that for the booster motor if a constant-geometry nozzle is used (due to decreased chamber pressure during the sustainer phase). For this discussion it will be assumed that a single motor with two thrust levels and fixed nozzle geometry is used. The relationship between the ratio of F_S/F_B and the resulting ratio $I_S I_B$ of specific impulses is presented in Fig. 3-19; both ratios are expressed as percent.
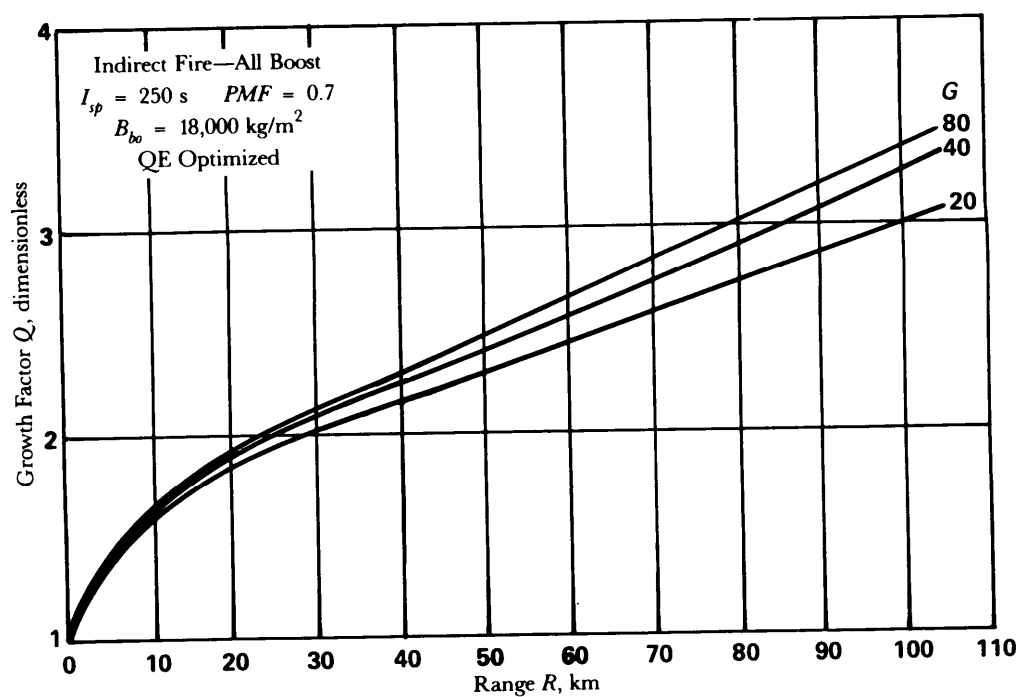
Figure 3-18. Indirect Fire—Boost; Effect of Range on Growth Factor
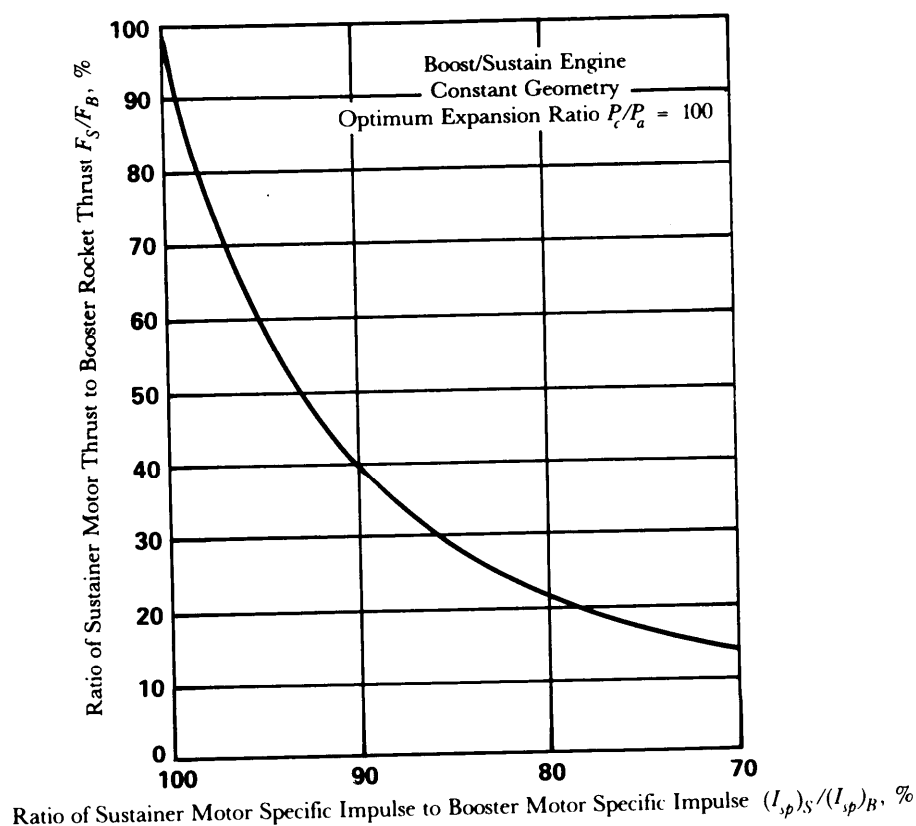
Figure 3-19. Boost/Sustain Engine; Variation of Specific Impulse with Thrust

Fig. 3-20 indicates the type of parametric data that should be generated for optimization of sustainer parameters when minimizing mass is the primary concern.

Fig. 3-21 presents the relationship between Q and range R for a boost/sustain system, for which the sustainer parameters are assumed to have been fixed by considerations other than minimum mass. A
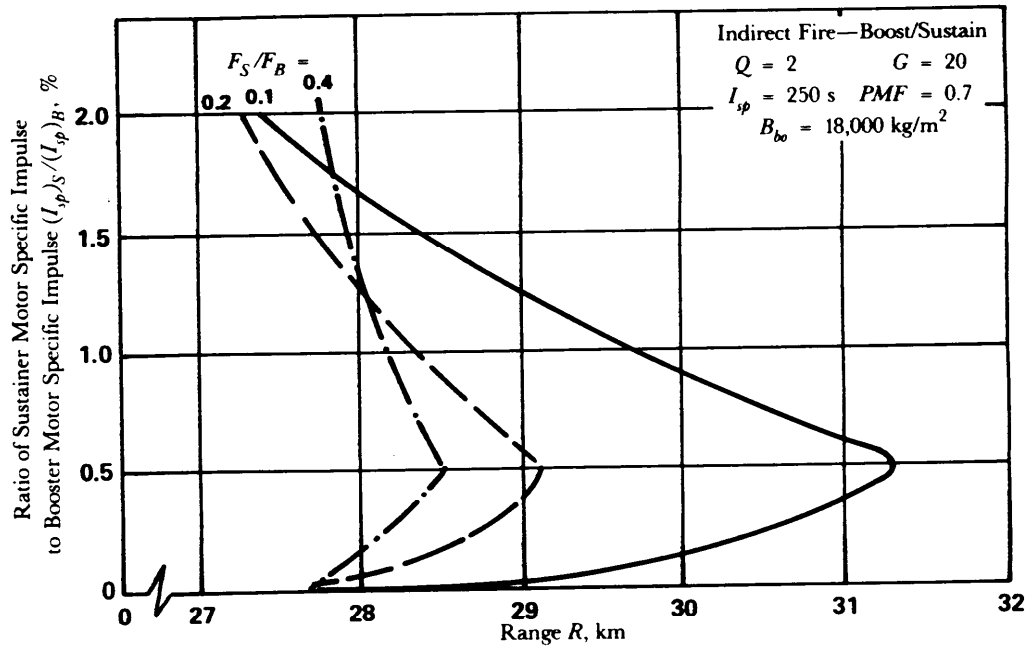
Figure 3-20.   Indirect Fire—Boost/Sustain; Effect of Range on Impulse Ratio
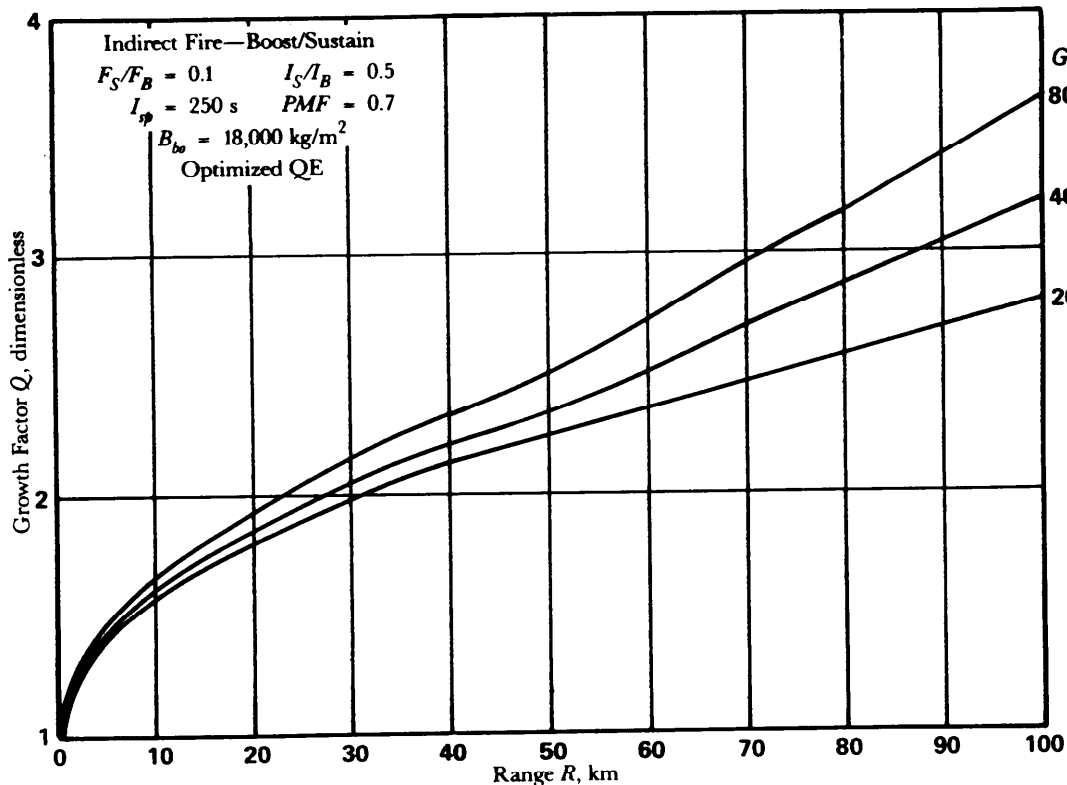
Figure 3-21. Indirect Fire-Boost/Sustain; Effect of Range on Growth Factor

comparison of these data with the data for the all-boost system will show that there are conditions for which the boost/sustain system is heavier than an all-boost system. These conditions are a result of the reduction in sustainer specific impulse mentioned earlier.

The range R versus Q data have been presented for only one value each of I_{SP}, PMF, and B_{bo}. It is of interest to know the sensitivity of the rocket mass to variations in these parameters. Fig. 3-22 presents the effects of I_{SP} and PMF on Q for a specific range, acceleration ratio G, and B_{bo}. Fig. 3-23 presents a similar trade-off with G and B_{bo} as variables.

The data presented in the cited figures were not intended to cover every situation. They are an indication of trends and serve to illustrate several trade-offs the designer should consider.
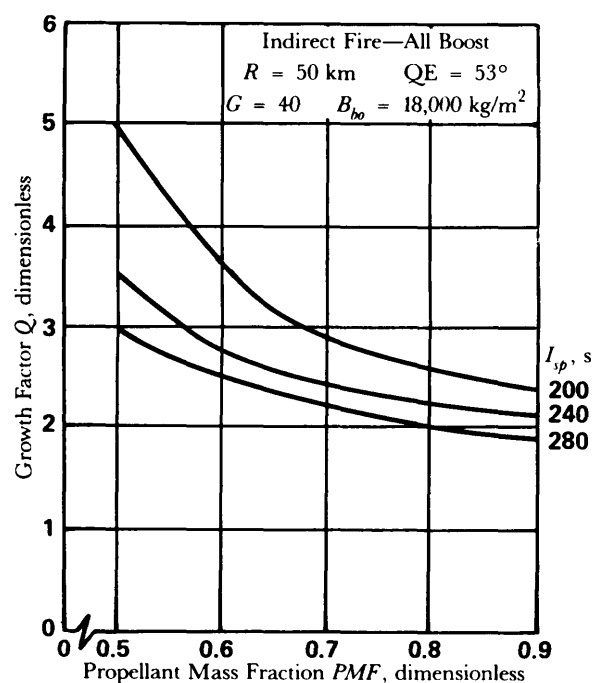
Figure 3-22. Indirect Fire-Boost; Effects of Propellant Mass Fraction on Growth Factor
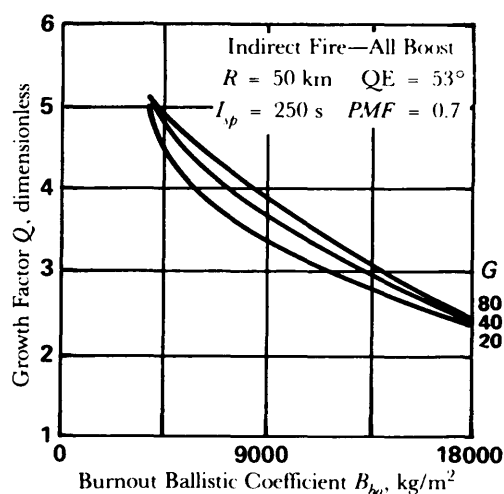
Figure 3-23. Indirect Fire-Boost; Effect of Ballistic Coefficient on Growth Factor

MIL-HDBK-762(MI)

3-5 PARAMETRIC PERFORMANCE DATA FOR DIRECT-FIRE SYSTEMS
3-5.1 DELIVERY TECHNIQUES

When the free rocket is used as a direct fire weapon, the ballistic trajectory flown is essentially flat. For example, a ballistic trajectory with a maximum altitude of 30 m at its apex has about the same range versus time relationship as a line-of-sight trajectory for ranges to 5 km. The relationships presented in this paragraph may be used for guided, direct fire rockets because the degree of maneuvering is usually small.

Among the commonly employed energy-management techniques for direct fire rockets are

1. Boost
2. Boost/sustain
3. Boost/coast/sustain.

The choice here will depend to some extent on the level of performance required and on the intended method of use. Considering the method of use, one must determine whether burning outside the launch tube can be permitted. In the case of direct fire infantry weapons, this usually cannot be permitted, whereas for weapons to be employed on armored vehicles, burning outside the launch tube is no problem aside from accuracy considerations. If burning outside the launch tube is permitted, either the boost or the boost/sustain approaches will be applicable. However, where burning outside the tube is not permitted, the choice is between the boost and the boost/coast/sustain approaches, with the boost approach generally limited to low performance systems by the maximum velocity that can be attained within the limitations of the tube length and the rocket acceleration.

Of the three energy-management techniques mentioned, the all-boost technique is the simplest to implement. The boost/sustain requires a more complex motor involving the ignition of the sustainer propellant after the boost propellant is consumed. The boost coast sustain possesses a similar sustainer ignition problem plus an added source of dispersion due to the timing uncertainties associated with the coast phase. In most applications, the coast period is short and the technique approaches the boost sustain technique as a limit. The major application of the boost coast sustain technique would be in a role in which a high impulse is imparted to the rocket within the launch tube, followed by a brief coast period during which the rocket is allowed to move away from the launcher. The high performance is achieved by the sustainer burn. This technique protects the launcher (infantryman or aircraft) from the effects of the rocket plume.

3-5.2 PARAMETRIC PERFORMANCE DATA

The relationship among growth factor, range, and time of flight is a function of the following parameters:

I_{SP} = rocket motor specific impulse, s

PMF = propellant mass fraction, dimensionless

B_{bo} = ballistic coefficient immediately after motor burnout, kg/m^2

G = initial boost acceleration ratio, dimensionless

F_S/F_B = ratio of sustainer motor thrust to booster motor thrust, dimensionless

I_S/I_B = ratio of sustainer motor total impulse to booster motor total impulse, dimensionless.

Fig. 3-24 presents the relationship among target range, time of flight, and energy-management technique for a given set of rocket characteristics. The energy-management technique of choice is noted to be all boost, i.e., $I_S/I_B = 0$, in cases where a minimum time of flight is desired. This is usually the case for aerodynamically stabilized free rockets. It is desirable to concentrate, for the remainder of this discussion, on the boost system that has the minimum time of flight.

Fig. 3-25 presents trade-offs with respect to growth factor Q, time-to-target t_t, range R, and boost acceleration ratio G. Note that the dashed lines of Fig. 3-25 represent the locus of rocket motor burnout points. A performance limit appears to be reached at a growth factor of about 3. Increases beyond this point reduce the time of flight by an insignificant amount. Increasing the boost acceleration ratio G reduces the time of flight, but decreases the percentage of powered flight. For example, from Fig. 3-25(A) at a growth factor of 1.7 and G = 20, the burning distance is about 1.2 km, and 3 km is attained in 7.5s. If G is increased
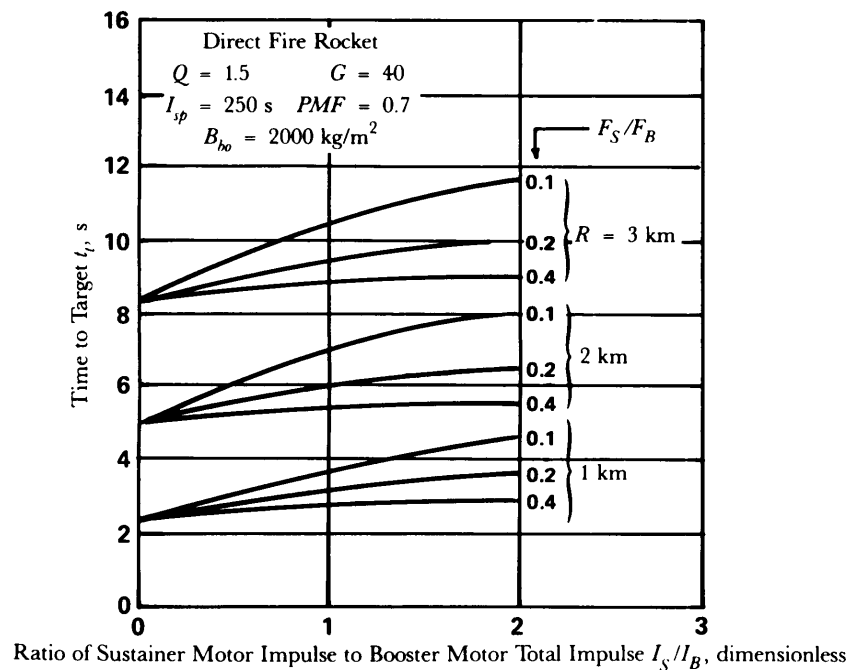
Figure 3-24. Direct Fire—Boost/Sustain; Effect; of Impulse Ratio on Time to Target

to 80, Fig. 3-25(C) shows the burning distance is reduced to about 0.5 km, and 3 km is attained in 6.5s. This illustration points out another of the choices facing the designer, i.e., the trade-off between time to target and percentage of powered flight.

Once the designer has examined the trade-offs between range and time to target, he may wish to determine the effects of various design parameters on the rocket mass (growth factor) for a specified performance level. For example, Fig. 3-26 shows the trade-oft among B_{bo}, G, and Q for a specified performance level of achieving 2 km range in 3s. Fig. 3-27 illustrates the trade-off among PMF, I_{SP}, and Q for the same performance level.

In the preceding subparagraphs an attempt has been made to illustrate the types of trade-offs of concern to the designer of direct fire rockets. From the preceding discussion, the following conclusions can be drawn:

    1. For minimum time to target, the all-boost system is superior to the boost/sustain system.

    2. The choice of boost acceleration must result from a consideration of the trade-off between time to target and the percentage of powered flight desired.

    3. Increasing PMF, I_{Sp}, B_{bo}, or G results in decreased rocket mass for a given payload weight and specified time to target.

    4. Increasing the growth factor beyond about 3.0 results in a negligible performance increase for the range of parameters presented.
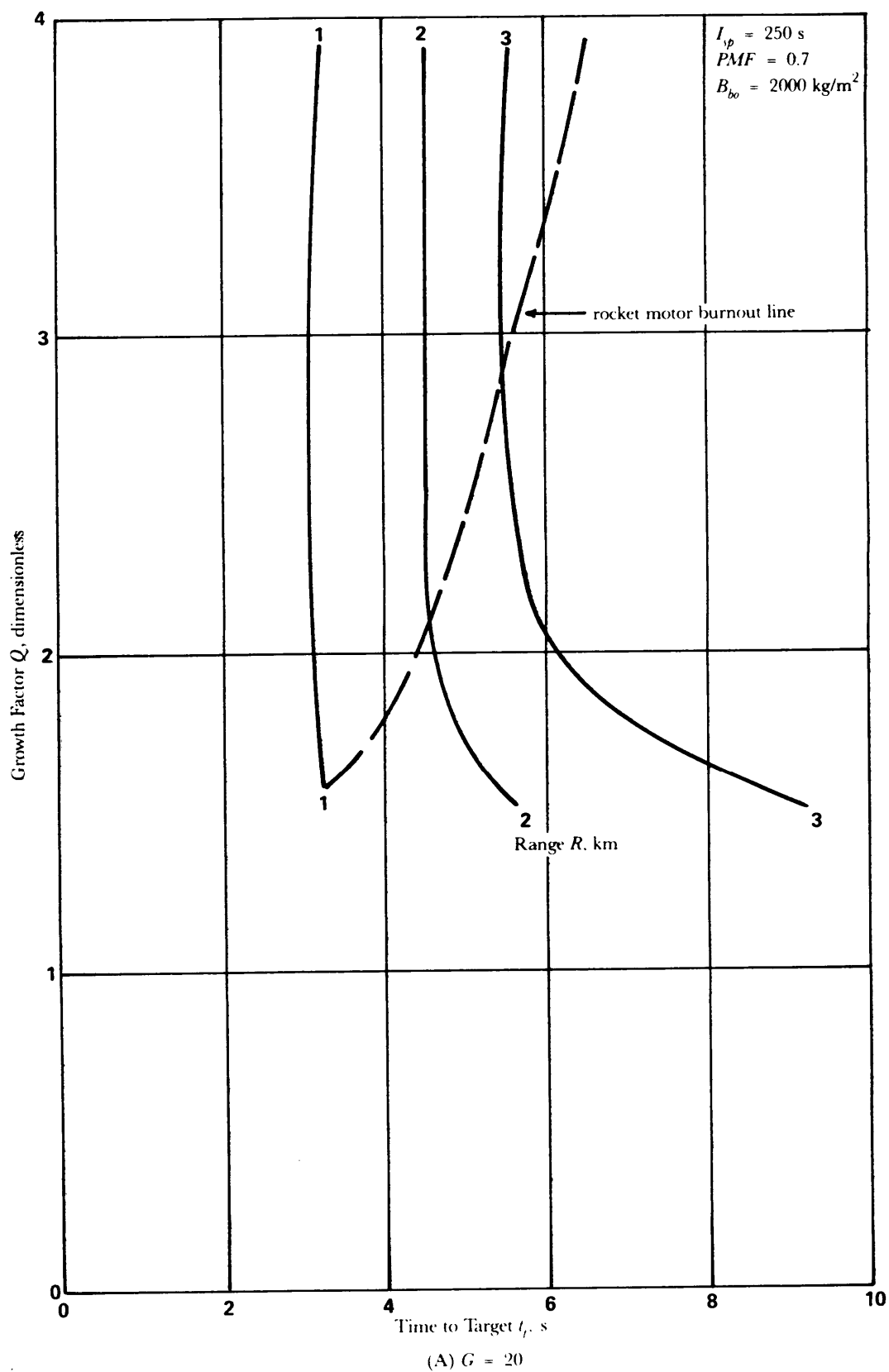
Figure 3-25. **Direct Fire—Boost; Effect of Growth Factor on Time to Target for Various G Values**
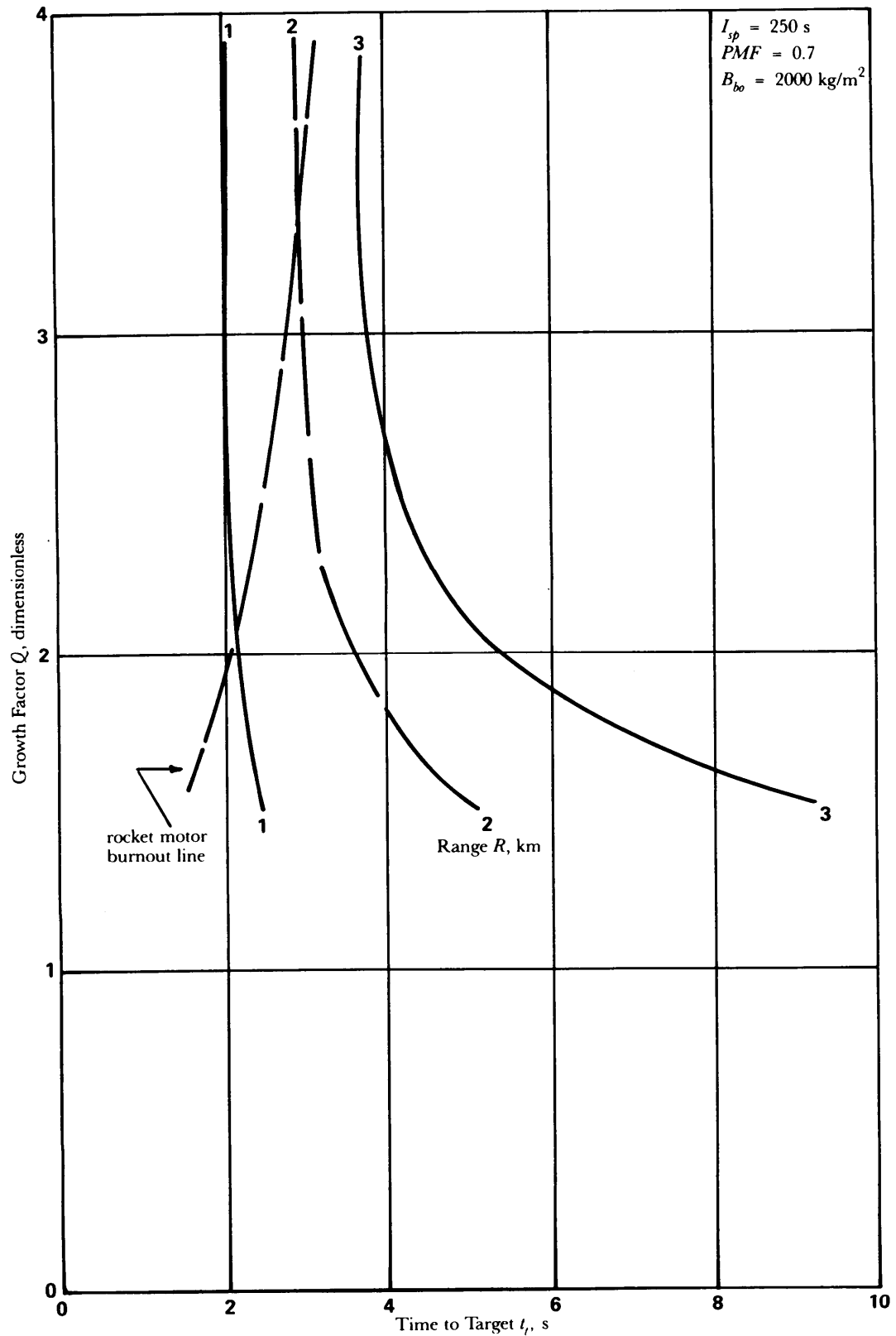
MIL-HDBK-762(MI)

(B) $G = 40$

Figure 3-25 (cont'd)

MIL-HDBK-762(MI)
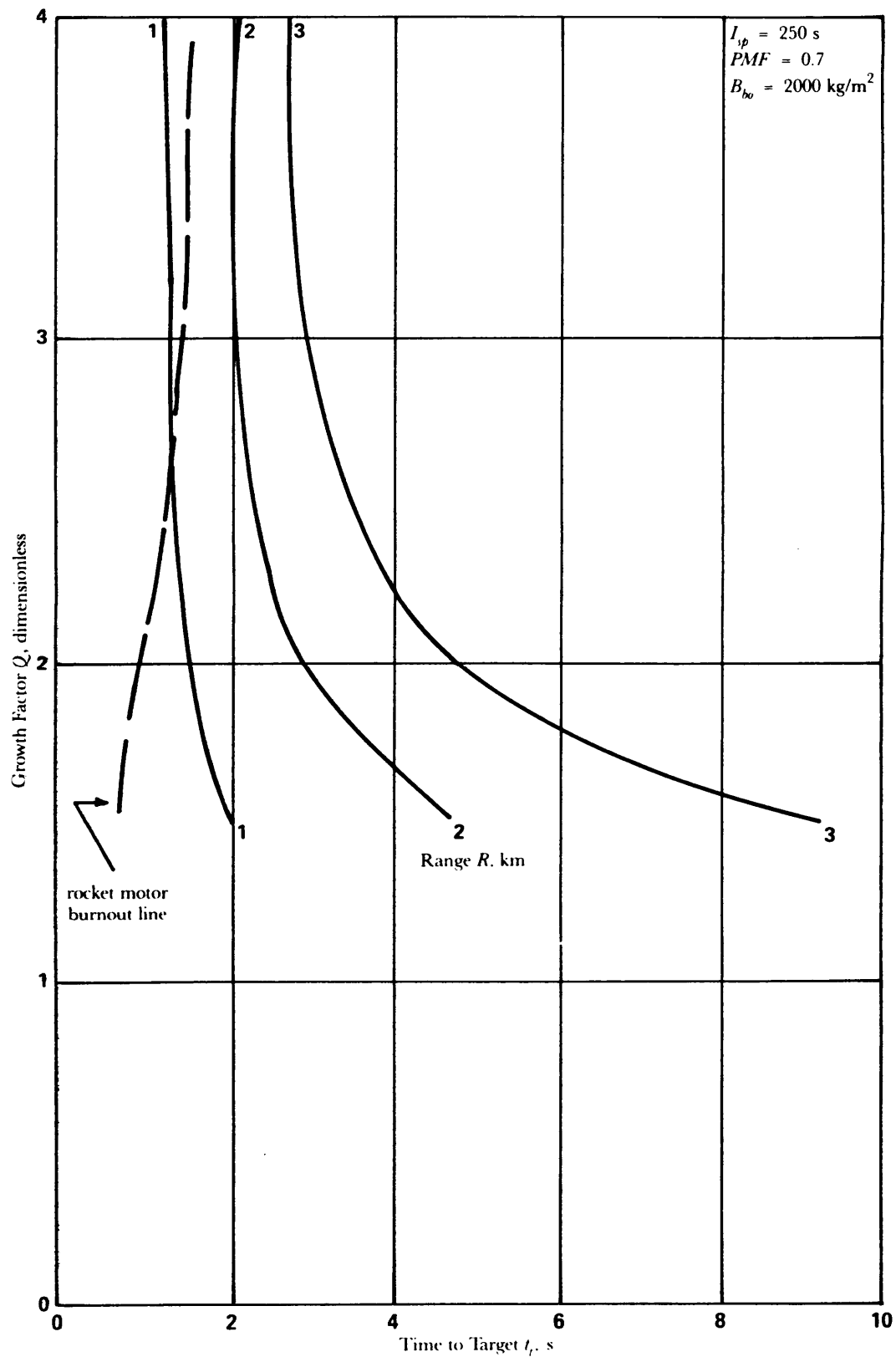
(C) $G = 80$

Figure 3-25 (cont'd)
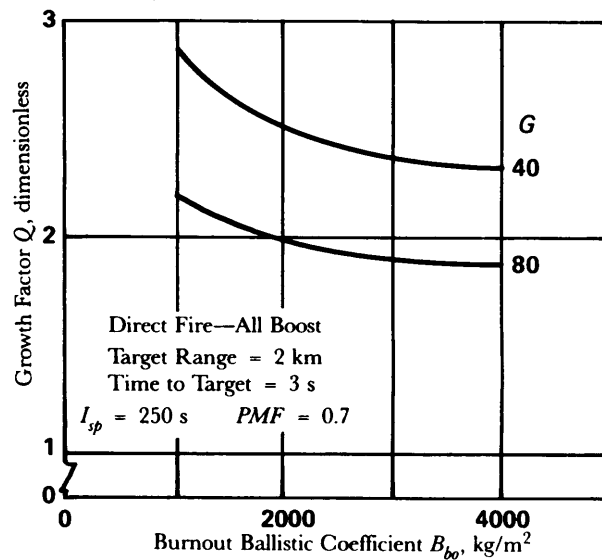
Figure 3-26.   Direct Fire—Boost; Effect of Ballistic Coefficient on Growth Factor
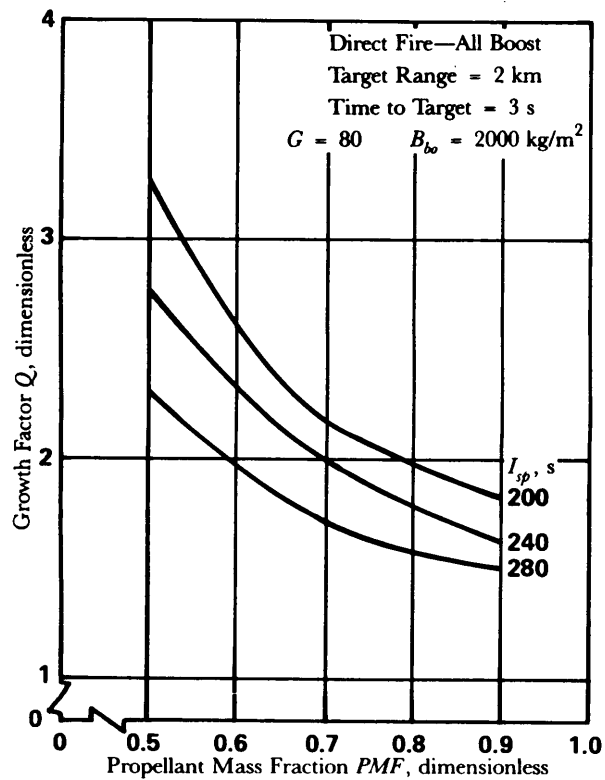
Figure 3-27.   Direct Fire—Boost; Effect of Propellant Mass Fraction on Growth Factor

3-6 PARAMETRIC PERFORMANCE DATA FOR SOUNDING ROCKETS

3-6.1 DELIVERY TECHNIQUES

Sounding rockets are generally launched at quadrant elevation angles (QE $\approx$ 85 deg) near the vertical. To simplify data presentation of the significant parameters, a vertical launch is considered.

The energy-management techniques that are most commonly used for sounding rockets are

1. Boost
2. Staged boost.

Boost/sustain is seldom used. The all-boost system generally is used for low altitude (under 40 km) sounding rockets, and staged boost generally is used for high altitudes (greater than about 90 km). For intermediate altitudes, trade-off studies should be made considering cost and reliability. Fig. 3-28 presents velocity versus summit altitude relationships for the all-boost sounding rocket.

The advantages of the all-boost system are simplicity of design and higher reliability. The staged boost will out perform the all-boost system at higher altitudes, but suffers from the disadvantage of being more complex and potentially less reliable. The dropped stages must also be considered a disadvantage because they will also impact the ground.

3-6.2 PARAMETRIC PERFORMANCE DATA

The relationship between Q and peak altitude for a sounding rocket is a function of the following parameters:

I_{SP} = rocket motor specific impulse, s

PMF = propellant mass fraction, dimensionless

B_{bo} = ballistic coefficient immediately after motor burnout, kg/m²

G = initial boost acceleration ratio, dimensionless

F_S/F_B = ratio of sustainer motor thrust to booster motor thrust, dimensionless

I_S/I_B = ratio of sustainer motor total impulse to booster motor total impulse, dimensionless.

In Fig. 3-29 the relationship among Q, energy-management technique G, and peak altitude is presented. The boost/sustain approach for a given altitude, would provide a slight reduction in Q. Although Fig.
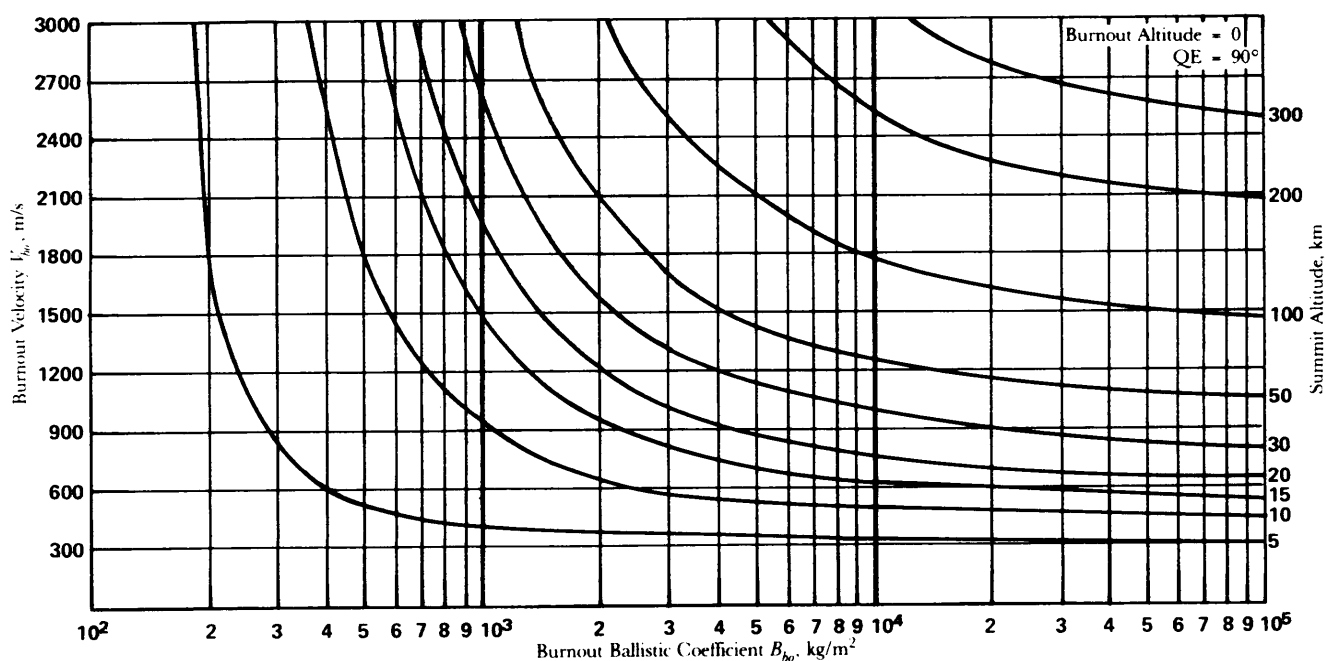
Figure 3-28. **Effect of Burnout Ballistic Coefficient and Burnout Velocity on Summit Altitude—133-mm Rocket**

3-32
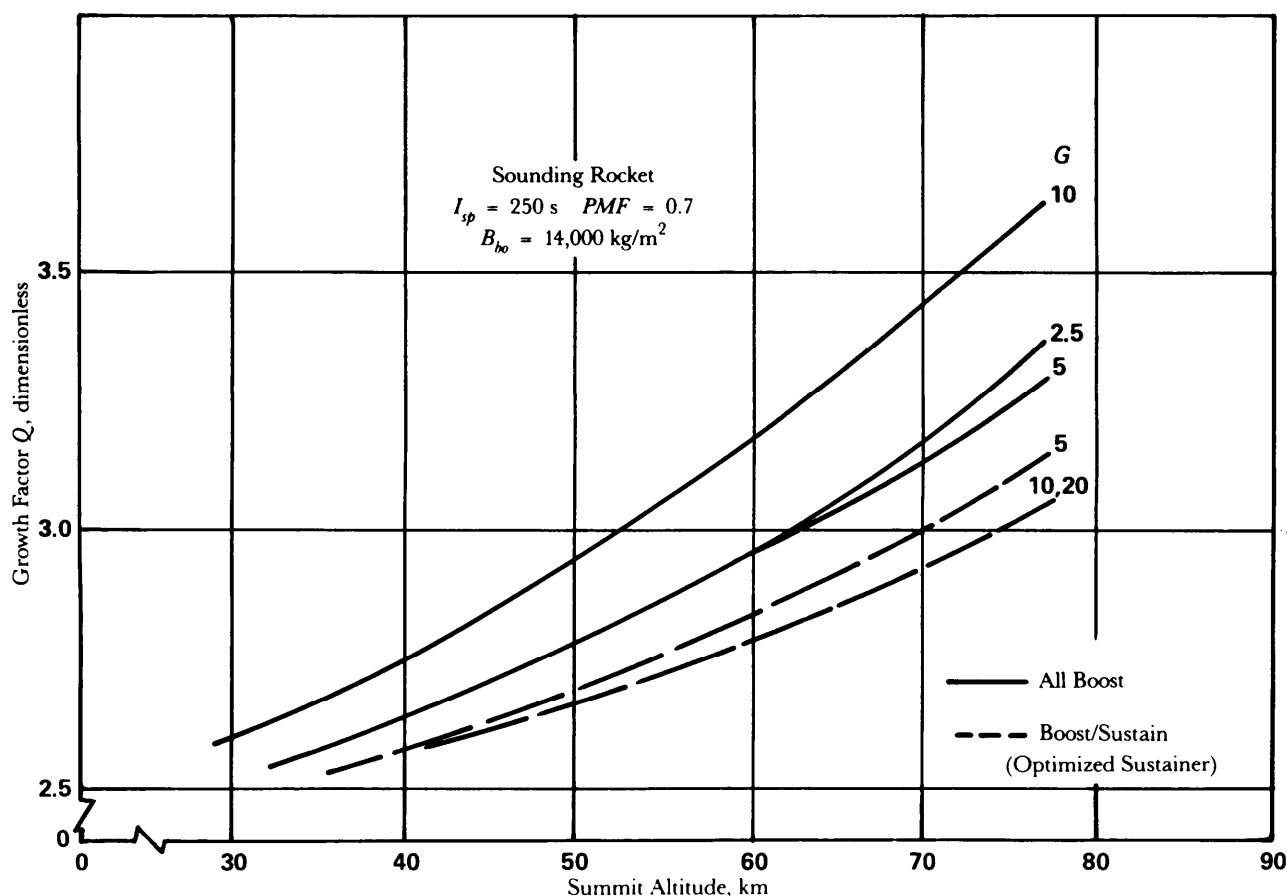
Figure 3-29.   Sounding Rocket—Boost; Effect of Growth Factor on Summit Altitude

3-29 presents only one value each of I_{SP}, PMF, and B_{bo}, a reduction in any of these parameters will result in an increase in the growth factor Q.

For a given maximum altitude, Q will be inversely proportional to PMF, I_{SP}, and B_{bo}. This is shown in Figs. 3-30 and 3-31 for peak altitudes of approximately 45 and 75 km. Although these curves depict the boost/coast case, the boost/sustain curves would be similar at slightly lower Q. The figures indicate that the minimum rocket gross mass m_0 results from a high performance motor (high PMF and I_{SP}) and a large burnout ballistic coefficient B_{bo} for the same payload mass m_{pld}—i.e., results in a low Q.

Parametric performance data for staged-boost sounding rockets can be obtained from Ref. 5. Typical performance data for staged-boost sounding rockets are available from Refs. 6 through 8.

3-7 PARAMETRIC PERFORMANCE DATA FOR SURFACE-TO-AIR ROCKETS
3-7.1 DELIVERY TECHNIQUES

The unguided surface-to-air rocket flies a ballistic trajectory and may be launched at any QE angle necessary for intercept of the target. Usually, the rocket will be required to attain a given altitude in a given time, and, therefore, the ascent is of interest for parametric data presentation.

Energy-management techniques applicable to surface-to-air rockets are
1. Boost
2. Boost/sustain
3. Staged boost.

If we consider that minimum time to altitude will be desired for the surface-to-air rocket and that achievable accuracy will limit this type of rocket to low altitude application, typically under 9 km, the boost approach usually will be the most attractive. For this reason the discussion will be limited to the

Sounding Rocket—All Boost

$G = 10 \qquad B_{bo} = 14,000 \text{ kg/m}^2$

(A) Altitude ≈ 45 km max

(B) Altitude ≈ 75 km max
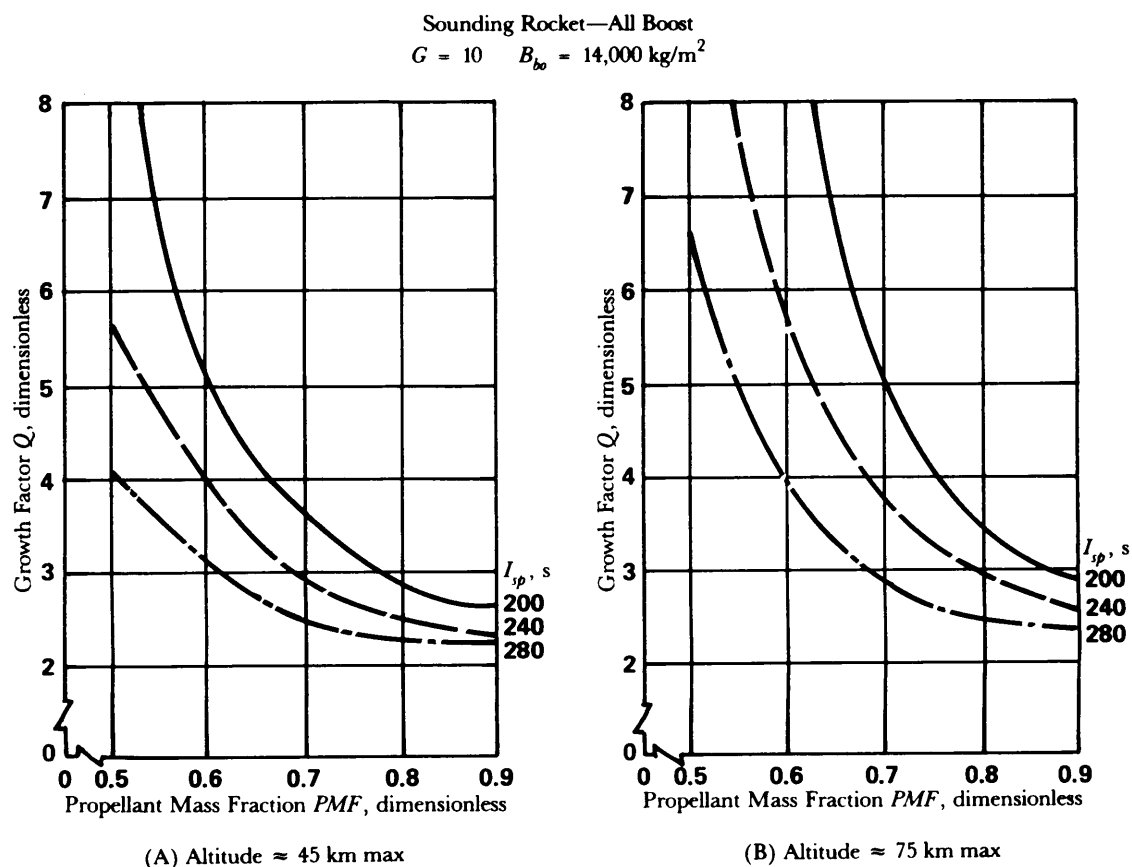
Figure 3-30.   Sounding Rocket—Boost; Effect of Propellant Mass Fraction on Growth Factor

Sounding Rocket—All Boost

$I_{sp} = 250 \text{ s} \qquad PMF = 0.7$

(A) Altitude ≈ 45 km max

(B) Altitude ≈ 75 km max
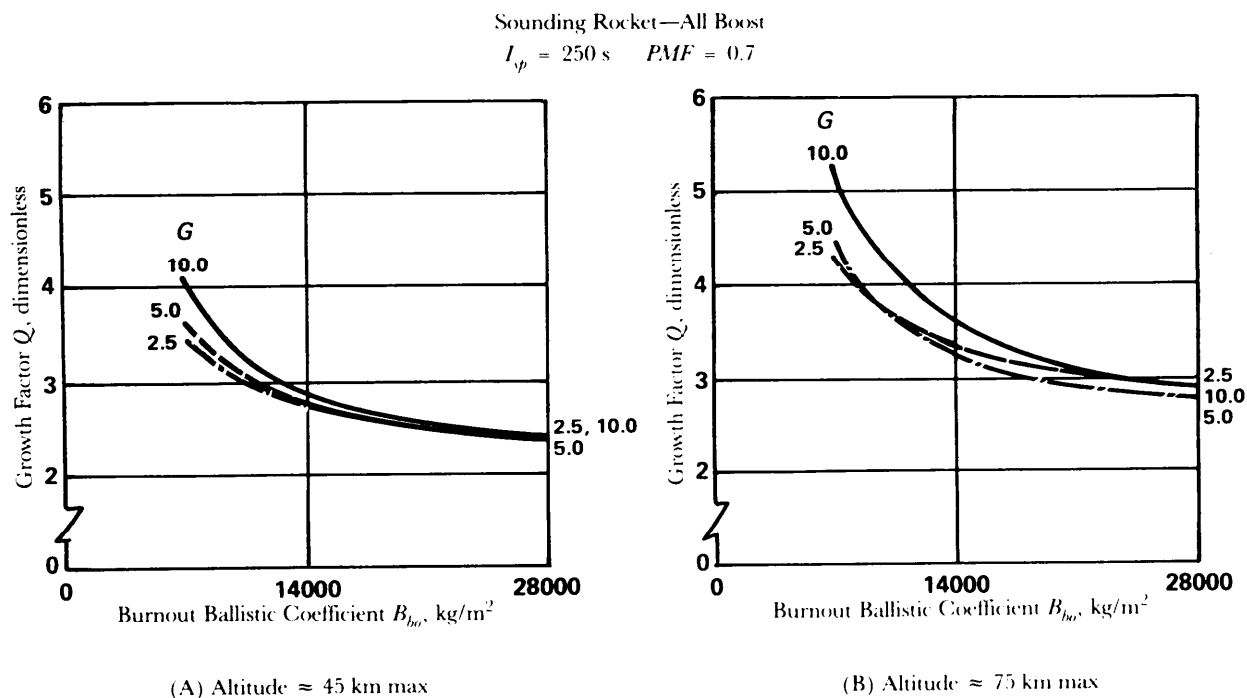
Figure 3-31.   Sounding Rocket—Boost; Effect of Ballistic Coefficient on Growth Factor

boost approach. Surface-to-air rockets for greater altitudes, such as those that require minimum flight time to attack reentry vehicles, generally use the staged boost approach with very high boost acceleration levels.

The advantages and disadvantages of each energy management technique have been previously discussed in pars. 3-5.1 and 3-6.1.

3-7.2 PARAMETRIC PERFORMANCE DATA

The relationship between growth factor and the time-to-altitude performance requirement is a function of the following parameters:

I_{SP} = rocket motor specific impulse, s

PMF = propellant mass fraction, dimensionless

B_{bo} = ballistic coefficient immediately after motor burnout, kg/m^2

G = initial boost acceleration ratio, dimensionless.

Fig. 3-32 presents the relationship between growth factor Q, boost acceleration ratio G, and time to altitude t_{alt} for a target altitude of approximately 6 km. It is noted that an increase in G reduces the t_{alt} significantly. An increase in Q above 5 has little influence on t_{alt} for the range of parameters depicted.

The trade-off among I_{SP}, PMF, and Q for a specified performance level of approximately 6 km in 5 s is given in Fig. 3-33. Fig. 3-34 illustrates the trade-off among Q B_{bo}, and G for the same t_{alt}.

From the previous discussion, the following conclusions may be drawn:

1. Increasing the growth factor above 5 results in a negligible performance increase for the range of parameters presented.

2. Increasing PMF, I_{SP}, and B_{bo} results in decreased rocket mass m_0 for a given payload mass m_{pld}.
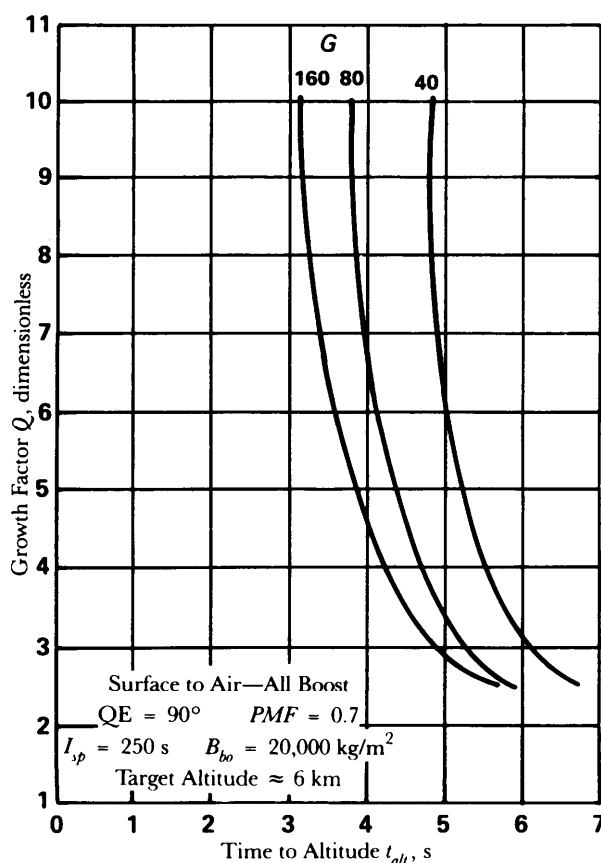
Figure 3-32. Surface to Air—Boost; Effect of Time to Altitude on Growth Factor
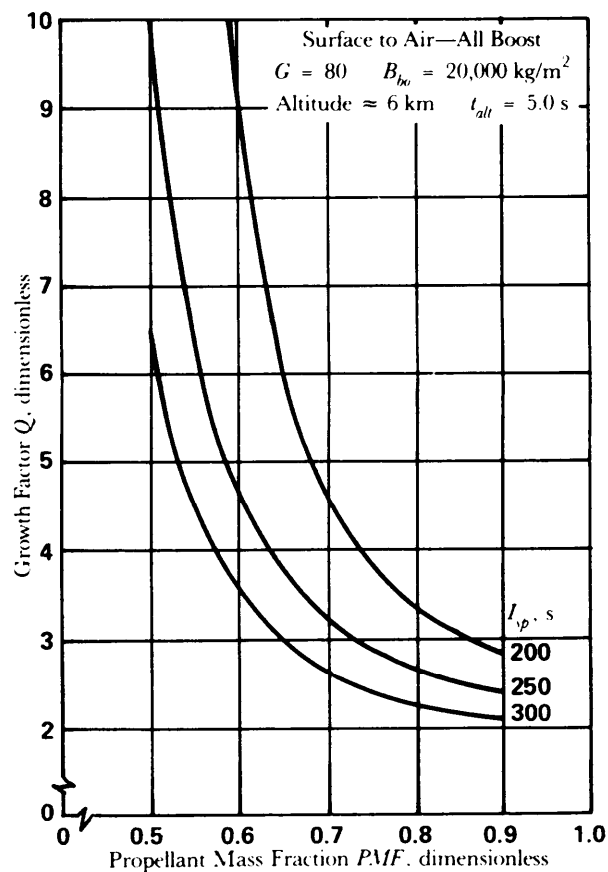
Figure 3-33.   Surface to Air—Boost; Effect of Propellant Mass Fraction on Growth Factor
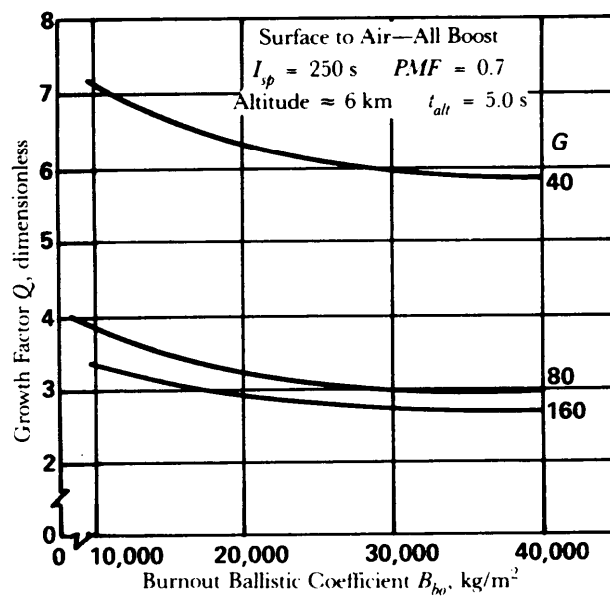
Figure 3-34.   Surface to Air—Boost; Effect of Ballistic Coefficient on Growth Factor

3-8 PARAMETRIC PERFORMANCE DATA FOR AIR-TO-GROUND ROCKETS
3-8.1 DELIVERY TECHNIQUES

Air-to-ground rockets are carried by fixed-wing and rotary-wing aircraft and are used to attack ground targets generally from low altitudes (generally less than 1 km) in a direct fire mode. Air-to-ground rockets are, therefore, very similar to the direct fire type of weapon. The difference is that they can burn both outside the launch tube and all the way to the target. Additional differences include the effects of the velocity, altitude, and flight path angle QE of the launching aircraft; the details of these effects are discussed in par. 3-8.2.

Limitations to the operational performance exist because of the rocket exhaust effects and other disturbances to the launching aircraft. A major concern of the air-to-ground rocket designer is the effect of the rocket motor exhaust upon the launching aircraft aerodynamics. This exhaust can be a potential threat to the aircraft stability. Par. 9-2.3 discusses the effect of rocket exhaust on launch aircraft in more detail.

Energy-management techniques include
1. Boost
2. Boost/sustain
3. Staged boost.

Boost is generally the preferred technique because the range and time requirement usually can be met with the boost mode and because this mode has a significant advantage in both cost and simplicity. Other advantages and disadvantages were discussed in pars. 3-5.1 and 3-5.2.

3-8.2 PARAMETRIC PERFORMANCE DATA

The relationship among the maximum range, rocket release altitude and flight path angle is shown in Fig. 3-35. The figure shows that the limiting range is approximately 8 km for direct fire air-to-ground rockets at a maximum altitude of release of 600 m. These data are for initial flight path angles QE that are zero or negative; lofted trajectories are not considered. The influence of release altitude is significant. Increasing the release altitude from 300 m to 600 m almost doubles the range. The influence of the initial flight path angle is also important.
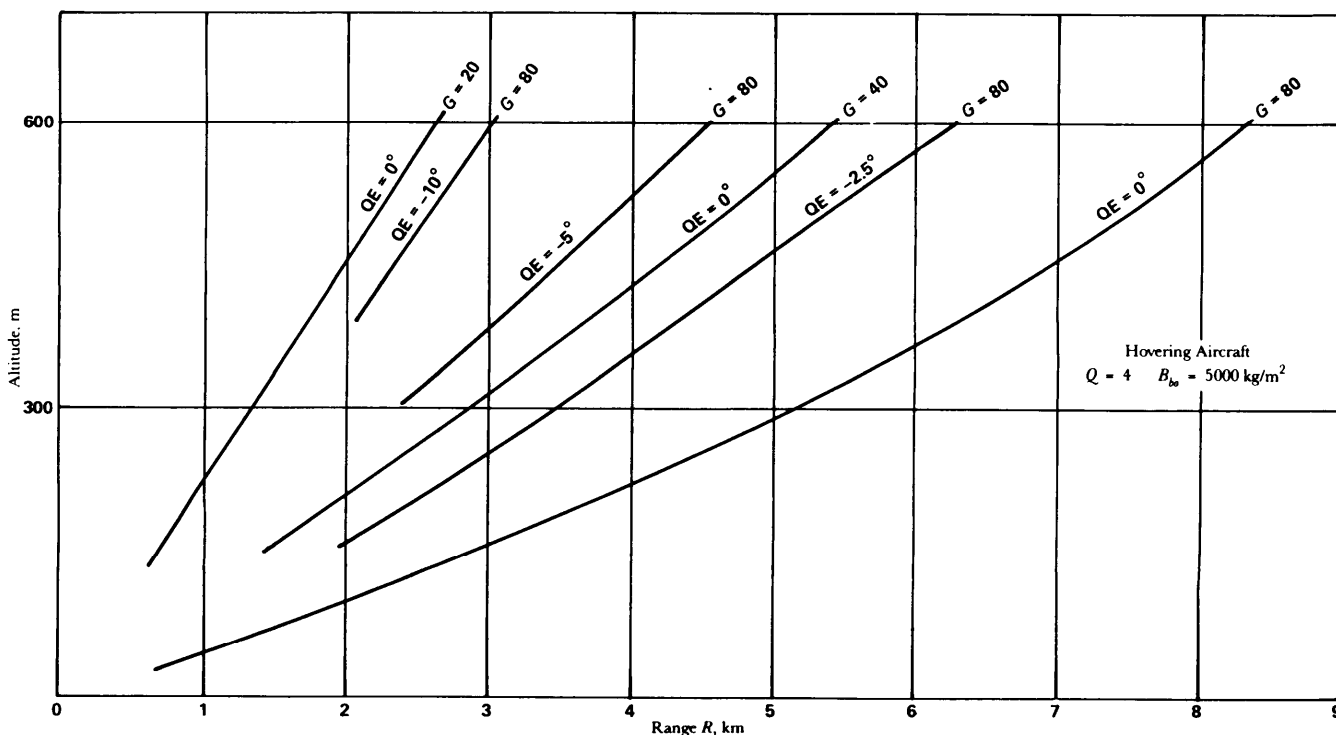
Figure 3-35. Effect of Altitude and Flight Path Angle on Maximum Range 3-37

Changing the initial flight path angle by 2.5 deg will change the range by approximately 50%. The influence of the initial boost acceleration ratio is also significant. Increasing the initial boost acceleration ratio from 40 to 80 increases the range by approximately 100%. The curves presented in Fig. 3-35 are for a rocket released from a helicopter with zero forward velocity (hovering); no helicopter downwash is included. The influence of the for-ward velocity of the launching aircraft on maximum range is small for rockets with Q values greater than 2. The increase in rocket range will be less than 10% for launching aircraft traveling with a forward velocity of 100 m s. High-speed aircraft firing air-to-ground rockets generally are at altitudes above 1000 m to insure that the aircraft is not hit by the warhead fragments. High explosive warhead fragments can reach an altitude of 600 m within 3 s after the warhead has detonated. Thus the aircraft trajectory and warhead fragment trajectories must be evaluated when considering air-to-surface rockets delivered from high-speed jet aircraft. The influence of aircraft forward velocity is only significant for rockets with Q values less than 2 in combination with delivery aircraft speeds around 200 m/s. Therefore, results are presented for air-to-ground rockets launched with zero initial velocity, i.e., simulating launch from a hovering helicopter.

The influence of maximum range on the Q required is shown in Fig. 3-36 for hovering aircraft. A maximum range of 8 km will requires value of Q near 4; a maximum range of 4 km will requires growth factor Q of approximately 2.5.

A comparison of the trajectories for a 3-km range from three release altitudes is shown in Fig. 3-37. This figure shows that the times to a given ground range are almost identical and are independent of the release altitude. A direct fire trajectory at zero altitude is also shown for comparison at the bottom of the figure. Note that the three air-to-ground trajectories compare well with the direct fire trajectory that is at zero altitude and has no gravity influence. Despite the fact that the influence of gravity and the launch angle QE is to increase the velocity of the air-to-ground rocket, the increased velocity is such that the resulting
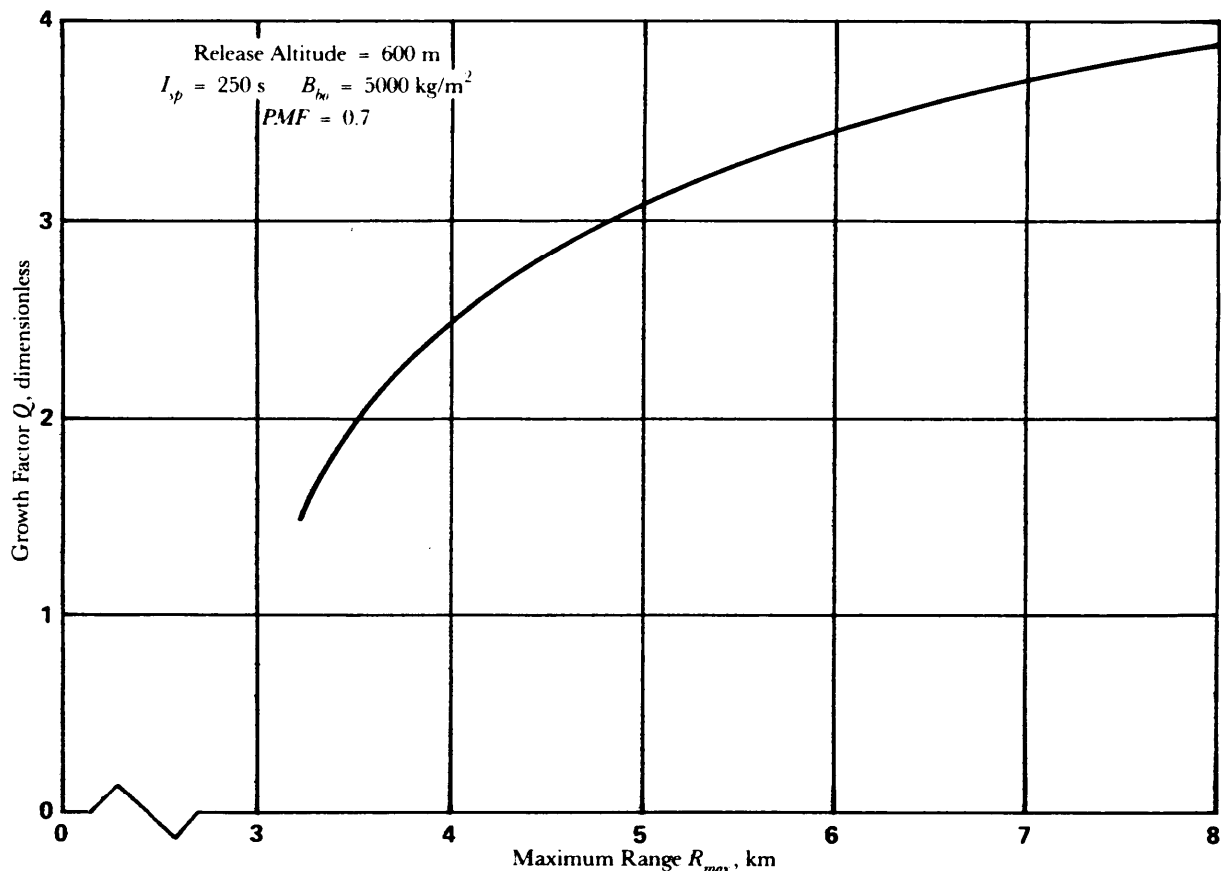
Figure 3-36. Effect on Maximum Range on Growth Factor
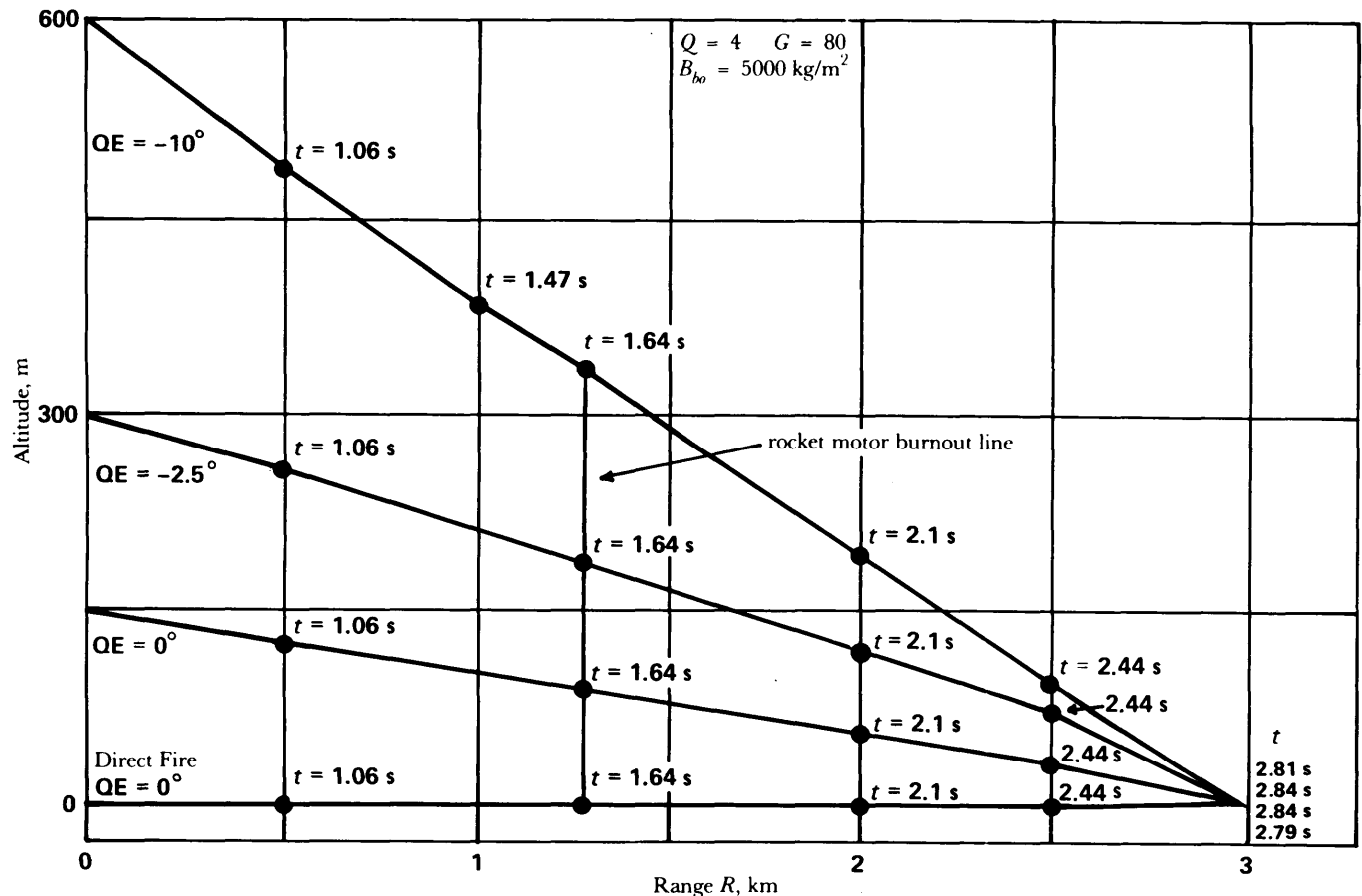
Figure 3-37.   Effect of Release Altitude and Flight Path Angle on Air-to-Ground Trajectory

ground range versus time plot is almost identical to the direct fire rocket. Consequently, direct fire parametric data are suitable for evaluation of air-to-ground rocket performance characteristics.

The basic differences between direct fire and air-to-ground rockets are the influence of initial altitude and flight path angle on the maximum range attainable. If the range of interest is less than the maximum, then direct fire data can be used to evaluate the range and time parameters of air-to-ground rockets. The relationship between growth factor and time of flight for ranges less than the maximum are determined by

I_{SP} = rocket motor specific impulse, s

PMF = propellant mass fraction, dimensionless

B_{bo} = ballistic coefficient immediately after motor burnout, kg/m^2

G = initial boost acceleration ratio, dimensionless

F_S/F_B = ratio of sustainer motor to booster motor thrust, dimensionless

I_S/I_B = ratio of sustainer motor total impulse to booster motor total impulse, dimensionless.

Fig. 3-38 presents the relationship among target range, time of flight, and energy-management tech-nique for a given set of rocket characteristics (recall that $I_S/I_B = 0$ is the all-boost technique). The desired energy-management technique is noted to be all-boost where a minimum time of flight is desired. This is usually the case for aerodynamically stabilized free rockets. The remainder of this discussion will concen-trate on the all-boost mode.

Fig. 3-39 presents the influence of time of flight on growth factor for various initial boost acceleration ratios. A time of flight performance limit appears to be reached at a growtly factor of about 3. Increasing the growth factor beyond this value does not significantly reduce the time of flight for a range of 3 km. The major influence of increasing the initial boost acceleration ratio is to reduce the percentage of powered flight along the trajectory. For an initial boost acceleration ratio of 20 and a growth factor of 2.1, the end of

3-39
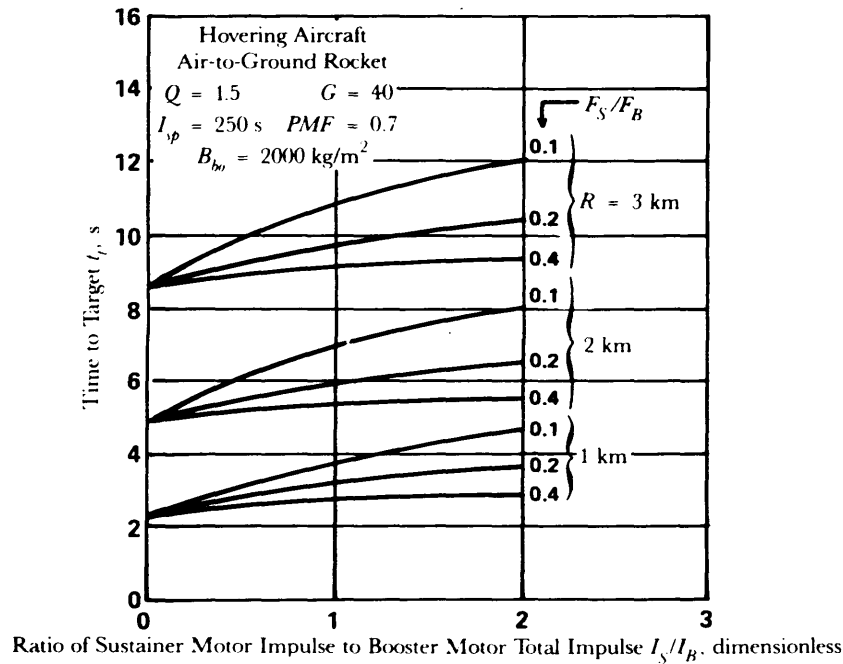
Figure 3-38. **Air to Ground—Boost/Sustain; Effect of Impulse Ratio on Time to Target**

boost occurs at a 2-km range in 4.5 s (see Fig. 3-39(A)). Burnout occurs at a range of less than 1 km for an initial boost acceleration ratio of 80 (see Fig. 3-39(C)).

The influence of B_{bo}, I_{SP}, and PMF on Q are shown in Figs. 3-40 and 3-41. Note that reduction in B_{bo} I_{SP}, and PMF all result in a larger Q.

3-9 NUMERICAL EXAMPLE

An indirect fire surface-to-surface rocket preliminary design problem is presented to illustrate the iterative steps in developing the propulsion system and physical characteristics to meet the required performance. The problem involves determining the rocket system weight characteristics, dimensions, and propulsion system parameters which will deliver a given payload mass m_{pld} to a desired range R.

The graphs previously cited indicate the complexity of the relationships among the performance parameters. These relationships have no closed form solution for a rocket configuration that will satisfy all the required relationships and still meet the performance requirements. The only alternative is to assume some of the important rocket or motor parameters and to calculate the performance for these assumed conditions. The calculated performance data are then compared with the desired values. The original assumptions are then modified and the procedure is repeated until the desired results are obtained. The accuracy of the original assumptions determines the amount of effort required to reach the final solution.

Fig. 3-42 is a flow diagram illustrating the steps of the design procedure. Block 1 indicates the design performance requirements; in this case R and m_{pld} are specified. Block 2 shows the parameters that are being assumed and their values, i.e., the first guess at the design configuration with no losses considered. The ideal velocity requirement is calculated in Block 3. The next sequence of blocks (4 through 7) illustrates the iterative procedure that must be followed until the initial assumptions are verified. The procedure shown for an indirect fire rocket uses the coast drag ΔV_{coast} as the main iteration parameter because ΔV_{coast} represents the major additional velocity increment to be included for a typical indirect fire rocket. After the iterative process is complete, enough is known about the system to define its performance parameters. Estimates of the boost drag ΔV_{boost} and gravity ΔV_{grav} losses can now be made, resulting in final improvements in the velocity requirement estimate.

3-40
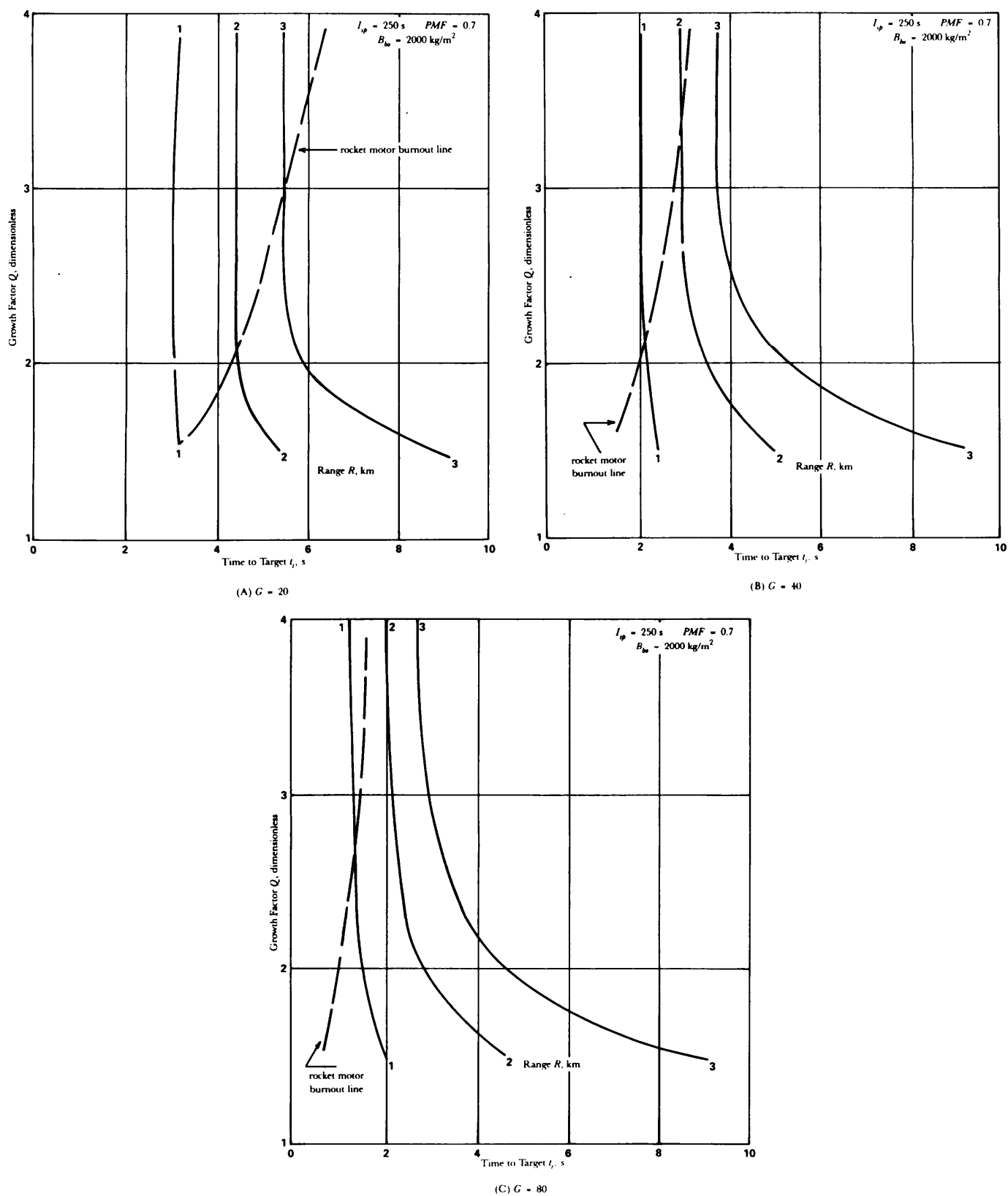
Figure 3-39. Air to Ground—Boost; Effect of Growth Factor on Time to Target for Various G Values
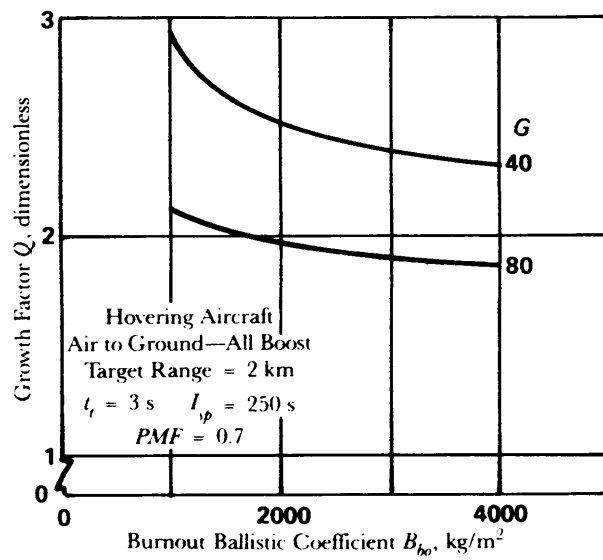
Figure 3-40. Air to Ground—Boost; Effect of Ballistic Coefficient on Growth Factor
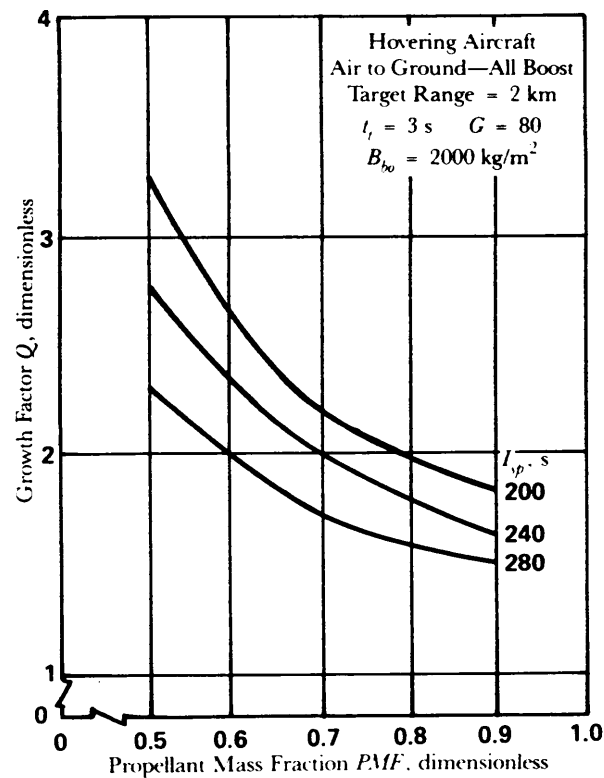
Figure 3-41. Air to Ground—Boost; Effect of Propellant Mass Fraction on Growth Factor

It is procedurally correct and permissible to include Blocks 8 through 11 in the iteration loop between Blocks 6 and 7. However, the accuracy achievable from the graphs and the additional computation involved may or may not justify such a change. Factor that would influence such a change in procedure would be the rocket parameters themselves, i.e., G, Q, r_b, PMF, and t_b; the fire mode, i.e., direct, indirect, etc.; and the accuracy required at this stage of the rocket design. The data of this chapter are meant to be used in basic sizing, not for precise or exact computation.

The numerical example that follows outlines the procedure. The results of all calculations are rounded to four significant digits. This is consistent with the accuracy of the graphical data used and the accuracy implied by this estimating method.

The procedure of other fire modes is similar to that shown in Fig. 3-42. The designer should select the appropriate equations to be used under the guidance of par. 3-3.1.

EXAMPLE 3-1 (The numbers in parentheses correspond to the steps indicated in Fig. 3-42.):

(1) The problem assumes the performance requirement is to deliver a 400-kg mass m_{pld} to a 30-km range R.

(2) Assume:

QE = 45 deg
PMF = 0.7
I_{SP} = 250 s
g_0 = 9.80665 m/s^2.

(3) By use of the assumed QE = 45 deg. Eq. 3-2 gives the drag-free velocity V_B requirement

$$V_B = \frac{30\times10^3\times9.80665}{\sin(2\times45°)} = 542.4 \text{ m/s.}$$

(4)

(4a) By use of the assumed I_{SP} = 250 s, Eq. 3-19 gives the booster mass ratio r_b

$$r_b = \exp[(542.4/(9.80665\times250)] = 1.248.$$

(4b) By use of the assumed PMF = 0.7, Eq. 3-25 gives the growth factor Q

$$Q = \frac{1.248\times0.7}{1 - 1.248(1 - 0.7)} = 1.396.$$

Methods for estimating values of PMF are presented in par. 7-4.2.6, "Mass and Size Estimating Relationships".

(4c) By use of Eq. 3-25, the gross mass m_0 is

$$m_0 = 1.396\times400 = 558.4 \text{ kg.}$$

(4d) By use of Eq. 3-24, the usable propellant mass m_p is

$$m_p = 0.7\times(558.4 - 400) = 110.9 \text{ kg.}$$

(4e) The burnout mass m_{bo} is

$$m_{bo} = m_0 - m_p = 558.4 - 110.9 = 447.5 \text{ kg.}$$

The next step in the procedure requires the calculation of B_{bo}. To do this, $C_{D_{bo}}$ and A_{ref} must be determined or estimated. The rocket diameter maybe specified as a requirement, or a few diameters may be assumed and the performance parameters calculated for each. For the purposes of this example, a 0.3048-m reference diameter will be assumed. The aerodynamic reference area A_{ref} is then, by definition,

$$A_{ref} = \pi(0.3048)^2/4 = 0.07297 \text{ m}^2.$$

MIL-HDBK-762(MI)

1 Require:
a. $R =$
b. $m_{pld} =$

2 Assume:
a. $QE =$
b. $PMF =$
c. $I_{sp} =$

3 $V_B =$ from appropriate Eq

4
a. $r_b = \exp\left[V_B/(I_{sp}\,g_0)\right]$

b. $Q = \dfrac{r_b\,(PMF)}{1 - r_b\,[1 - (PMF)]}$

c. $m_0 = Q\,m_{pld}$

d. $m_p = (PMF)(m_0 - m_{pld})$

e. $m_{bo} = m_0 - m_p$

f. $B_{bo} = m_{bo}/(C_{D_{bo}}A_{ref})$

5 From Fig. 3-7:
$\Delta V_{coast} =$

6 $V_{prop} = V_B + \Delta V_{coast}$

7 Compare ΔV_{prop} with previous value

Disagree

Agree

8 Assume:
$G =$

9
a. $F_B = G g_0 m_0$
b. $\dot{m} = F_B/(I_{sp}\,g_0)$
c. $t_b = m_p/\dot{m}$

10 From Fig. 3-8:
$\Delta V_{boost} =$ drag during boost

11 Calculate
$\Delta V_{grav} =$ gravity loss during boost

12 Calculate
ΔV_{prop} by summing ΔV_B and all losses

Figure 3-42. Flow Diagram

Chapter 5, "Aerodynamics", discusses considerations relating to rocket nose shape and volume drag efficiencies (par. 5-5.1, "Wave Drag") and other data and methods for determining drag. A $C_{D_{bo}}$ of 0.38 will be assumed for this example.

Chapter 7, "Structures", presents methods for estimating the lengths of the payload and motor sections. Par. 7-4.2.6, "Mass and Size Estimating Relationships", takes up the sizing problem from the mass estimates calculated here.

(4f) By use of the assumed A_{ref} and $C_{D_{bo}}$, Eq. 3-5 gives the required burnout ballistic coefficient B_{bo}

$$B_{bo} = 447.5/(0.38 \text{X} 0.07297) = 1.614 \text{X} 10^4 \, kg \backslash m^2.$$

(5) Fig. 3-7 allows a refinement to the burnout velocity V_{bo} by giving the drag velocity losses during coast. By use of $V_{bo} = 542.4$ m/s and $B_{bo} = 1.614 \text{X} 10^4 \, kg/m^2$, the drag loss ΔV_{coast}, is about 140 m/s.

(6) The first iteration of V_{prop} at the required burnout velocity is then

$$V_{prop} = V_B + \Delta V_{coast} = 542.4 + 140 = 682.4 \text{ m/s}.$$

Repeating Steps 4 through 6 continues the iteration process with V_B now being 682.4 m/s as determined by Step 6. Therefore, from

(4a) $r_b = 1.321$

(4b) $Q = 1.532$

(4c) $m_0 = 612.8$ kg

(4d) $m_p = 149$ kg

(4e) $m_{bo} = 463.8$ kg

(4f) $B_{bo} = 1.673 \text{X} 10^4 \, kg/m^2.$

(5) By use of $V_{bo} = 682.4$ m/s and $B_{bo} = 1.673 \text{X} 10^4 \, kg/m^2$, Fig. 3-7 gives a drag loss of about 200 m/s.

(6) The second iteration of V_{prep} at the required burnout velocity is $V_{prop} = V_B \Delta V_{coast} = 542.4^* + 200 = 742.4$ m/s.

(7) Comparing the V_{prop} from this iteration with that from earlier computation shows an increase of some 9%. The iteration procedure should continue until the current V_{prop} agrees with the V_{prop} obtained in a previous iteration.

Three additional iterations yield the following converged data:

$r_b = 1.382$	$Q = 1.652$	$m_{bo} = 478.3$ kg
$m_0 = 661$ kg	$m_p = 182.7$ kg	$V_{coast} = 258$ m/s.
$B_{bo} = 1.725 \text{X} 10^4 \, kg/m^2$	$V_{prop} = 800$ m\s	

(8) The initial acceleration ratio G is assumed to be $G = 40$.

(9) The initial thrust F_B is calculated from Eq. 3-26

$$F_B = 40 \text{X} 9.80665 \text{X} 661 = 2.593 \text{X} 10^5 \, N.$$

The mass flow rate $\dot{m}$ is determined from Eq. 3-27

$$\dot{m} = 2.593 \text{X} 10^5/(250 \text{X} 9.80665) = 105.8 \text{ kg/s}.$$

From Eq. 3-28 the motor burn time t_b is

$$t_b = 182.7/105.8 = 1.727 \text{ S}.$$

(10) To determine the drag velocity loss during boost, first form the product $G \check{Z} t_b = 69.08$ s. From Fig. 3-8, using $G \check{Z} t_b = 69.08$ s and $B_{bo} = 1.725 \text{X} 10^4 \, kg/m^2$, the boost drag loss parameter is $\Delta V_{boost}/t_b$ approximately 10 m/s². The velocity loss ΔV_{boost} during boost is, therefore,

$$\Delta V_{boost} = 10 \text{ m/s}^2 \text{X} 1.727 = 17.27 \text{ m/s}.$$

(*Note the use of V_B from Step 3, and not V_{prop} of 682.4 in from the previous Step 6.) **3-45**

(11) The velocity loss ΔV_{grav} due to gravity during boost is determined from Eq. 3-7

$$\Delta V_{grav} = 9.80665 \times 1.727 \times \sin 45° = 11.98 \text{ m/s.}$$

(12) Finally, the total velocity requirement estimate V_{prop} determined from Eq. 3-8 is

$$V_{prop} = 542.4 + 258 + 17.27 + 11.98 = 829.7 \text{ m/s.}$$

REFERENCES

1. A. D. Wheelon, "Free Flight of a Ballistic Missile", American Rocket Society Journal 29, 915-26 (December 1959).
2. J. W. Reese, R. D. Joseph, and D. Shaffer, "Ballistic Missile Performance", Jet Propulsion 26,251-5 (April 1956).
3. L. Davis, Jr., J. W. Follin, Jr., and L. Blitzer, *The Exterior Ballistics of Rockets,* Van Nostrand Company, New York, NY, 1958.
4. W. C. Nelson and E. E. Loft, *Space Mechanics,* Prentice-Hall, Inc., Englewood Cliffs, NJ, 1962.
5. J. J. McKay and R. J. Wehen, *Performance Charts for Multistage Rocket Boosters,* NASA Technical Note D-582, National Aeronautics and Space Administration, Lewis Research Center, Cleveland, OH, January 1961.
6. H. E. Newell, Jr., *Sounding Rockets,* McGraw-Hill Book Co., New York, NY, 1959.
7. G. G. Wilson and W. A. Willard, "Performance and Flight Characteristics of the Sandhawk Family of Rocket Systems", J. of Spacecraft 8, 783-9 (July 1971).
8. *AIAA Sounding Rocket Vehicle Technology Specialist Conference, A Volume of Technical Papers,* American Institute of Aeronautics and Astronautics, Williamsburg, VA, February-March 1967.

BIBLIOGRAPHY

AMCP 706-140, Engineering Design Handbook, *Trajectories, Differential Effects, and Data for Projectiles.*

N. J. Bowman, *The Handbook of Rockets and Guided Missiles,* Perastadion Press, Chicago, IL, 1963.

C. D. Baker and J. J. Hart, "Maximum Range of a Projectile in a Vacuum", American J. of Physics 23, 253-5 (May 1955).

L. Blitzer and A. D. Wheelon, "Maximum Range of a Projectile in a Vacuum on a Spherical Earth", American J. of Physics 25, 21-4 (January 1957).

B. D. Fried and J. M. Richardson, "Optimum Rocket Trejectories", J. of Applied Physics 27, 955-61 (August 1956).

W. E. Frye, "On the Accuracy of the Long Range Ballistic Rocket", J. of Applied Physics 22, 585-9 (May 1951).

B. E. Kalensher, *Equations of Motion for a Missile and a Satellite for an Oblate-Spheroidal Rotating Earth,* JPL Memo 20-142, Jet Propulsion Laboratory, Pasadena, CA, 1957.

A. J. Kelly, "Effect of Thrust Termination Process Upon Range Dispersion of a Ballistic Missile", American Rocket Society Journal 29, 432-40 (June 1959).

D. F. Lawdon, "Minimal Rocket Trajectories", American Rocktet Society Journal 23, 360-7 (November-December 1953).

S. F. Singer and R. C. Wentworth, "A Method of Calculating Impact Points of Ballistic Rockets", Jet Propulsion 27, 407-9 (April 1957).

J. Levine, *Performance and Some Design Aspects of the Four-Stage Solid Propellant Rocket Vehicle Used in the RAM A1 Flight Test,* NASA Technical Note D-1611, National Aeronautics and Spare Adminis-tration, Langley Research Center, Langley Station, Hampton, VA, March 1963.

J. L. Raper *et al., Detailed Description and Flight Performance of the RAM B Vehicle,* NASA Technical Note D-2037, National Aeronautics and Space Administration, Langley Research Center, Langley Station, Hampton, VA, September 1964.

R. T. Mayhue, *NASA Scout ST-1 Flight Test Result and Analysis, Launch Operations, and Test Vehicle Description,* NASA Technical Note D-1240, National Aeronautics and Space Administration, Langley Research Center, Langley Station, Hampton, VA, June 1962.

R. B. Jenkins, *NIKE Apache Performance Handbook,* NASA Technical Note D-1699, National Aeronautics and Space Administration, Goddard Space Flight Center. Greenbelt, MD, March 1963.

R. H. Hertholler, *Flight Investigation of the Performance of a Two-Stage Solid Propellant NIKE-Deacon (PAN) Meteorological Sounding Rocket,* NACA TN-3739, National Advisory Committee for Aeronautics, Goddard Space Flight Center, Greenbelt, MD, July 1956.

C H A P T E R   4

A C C U R A C Y

Accuracy is defined as the measure of the ability of a rocket system to position the payload at a given point at the warhead event. Error sources are defined, discussed, and categorized by flight phase. Methods are given for relating the dispersions from the flight phases to errors at the war-head event. General consideration is given to and specific methods are presented for reduction of the effects of error sources. Simulation of and statistical topics concerning the estimation and calculation of free rocket accuracy are presented and include equations of motion, statistical methods, and an example problem.

4-0 LIST OF SYMBOLS

$A_{ref} = \pi d^2/4$, aerodynamic reference area, m^2

$B = m/(C_D A_{ref})$, ballistic coefficient, $kg\backslash m^2$

$C_D = drag/(0.5 p V^2 A_{ref})$, aerodynamic drag coefficient, dimensionless

$C_{m_q} = \partial M_t/\partial[(qd)/(2V)] \times 1/(0.5 \rho V^2 A_{ref} d)$, aerodynamic damping moment coefficient, dimensionless

$C_{N\alpha} = \partial F_N/\partial\alpha \times 1/(0.5 \rho V^2 A_{ref})$, aerodynamic normal force coefficient gradient, rad^{-1}

CEP = circular error probable, m

DEP = deflection error probable, m or mrad

d = rocket diameter, aerodynamic reference length, m

$F_N = C_{N\alpha}\alpha(0.5 \rho V^2 A_{ref})$, aerodynamic normal force, N

F_T = thrust, N

F_X, F_Y, F_Z = external force components along the X-, Y-, and Z-inertial axes, respectively, N

F_x, F_y, F_z = external force components along the x-, y-, and z-body-centered axes, respectively, N

F_{gx}, F_{gy}, F_{gz} = force components due to gravity along the x-, y-, and z-body-centered axes, respectively, N

$G = G'/g_0$, acceleration level, g-units

$G' = F_T/m$, rocket acceleration due to thrust, m/s^2

$G'(0)$ = average rocket acceleration while on launcher, m/s^2

$g_0 = 9.80665$, reference acceleration due to gravity, m/s^2

h = altitude, m

I = transverse moment of inertia, $kg\check{Z}m^2$ (For a symmetrical rocket, $I = I_{YY} = I_{ZZ}$.)

I_{SP} = specific impulse, s

I_{xx}, I_{yy}, I_{zz} = principal moments of inertia, $kg{=}m^2$

I_{xz}, I_{xy}, I_{yz} = cross-products of inertia, $kg\check{Z}m^2$

I'_x, I'_z = transformation parameters, used to uncouple the rotational equations of motion, dimensionless

K = constant relating CEP to elliptical distributions, dimensionless. (Alternately, K $= (\text{CEP})/[0.5(\sigma_x + \sigma_y)]$ or $K = (\text{CEP})/\sigma_{max.}$)

K_1, K_2 = transformation parameters used to uncouple the rotational equations of motion, rad/s^2

k = $\sqrt{I/m}$, rocket radius of gyration, m

L = thrust misalignment distance, m

$\ell_s = d\partial C_{m\alpha}/\partial C_{N\alpha}$ static margin, distance from CG to point where normal force is assumed to act, m

ℓ_t = distance from CG to point of thrust application, m

M_x, M_y, M_z = external moments about x-, y-, and z-body-centered axes, respectively, NŽm

m = rocket mass, kg

$\dot{m}$ = mass flow rate, kg/s

n = number of sample values taken from a universe of statistical values, dimensionless

n_δ = number of revolutions made by a spinning rocket in the first wavelength of yaw; $n_\delta = p\sigma/(2\pi V)$ for p expressed in rad/s; nó = pó/V for p expressed in rev/s

P = launcher length/a, dimensionless launcher length

P_{HIT} = probability y of hit, dimensionless or %

PE = probable error

p = rotational rate of rocket about x-body-centered axis, rad/s or rev/s

q = rocket angular velocity component about y-body-centered axis, rad/s

q_{equiv} = pe, equivalent initial angular rate about the y-body-centered axis due to spin with dynamic imbalance, rad/s

QE = quadrant elevation, deg or rad

R = range, km

R = maximum range, km

REP = range error probable, m or mrad

r = rotational rate of rocket about the z-body-centered axis, rad/s

r_b = booster mass ratio, dimensionless

Y_t = effective radius of a target; used in calculation of P_{HIT}, m

S^2, s = estimate of universal variance and standard deviation, respectively, computed from a sample of statistical values taken from universe of values

t = Student's t statistic, dimensionless

t = time, s

At = time-of-flight error, m

u = rocket velocity component along x-body-centered axis, m/s

$u_p = \sqrt{2P\overline{G'(0)}\sigma}$, rocket velocity at the end of launcher, m/s

V = rocket velocity, m/s

V_B = rocket velocity at end of boost, m/s

V_I = rocket velocity with respect to inertial earth, m/s

V_R = rocket velocity relative to wind, m/s

V_W = velocity of wind with respect to inertial coordinates, m/s

V_0 = rocket initial velocity, m/s

v = rocket velocity component along y-body-centered axis, m/s

w = rocket velocity component along z-body-centered axis, m/s

W_z = wind velocity component along z-body-centered axis, m/s

X = burning distance, m

X, Y, Z = inertial-coordinate system axes and distances measured in that system, m

X = component of rocket velocity along the aiming direction, m/s

AX = range error, m

x, y, z = body-coordinate system axes

$\overline{x}$ = estimate of universal mean computed from a sample of statistic values taken from universe of values

ΔY = crossrange (deflection) error, m

$\dot{Z}$ = component of rocket velocity normal to the aiming direction, m/s

ΔZ = attitude error, m

α = $\text{Tan}^{-1}(w/u)$, angle of attack, rad ($\alpha = w/u$ for linearized equations of motion; $\alpha = (w + w_z)/u$ when wind effect is included.)

α = confidence level for statistical estimation, dimensionless

α_{ss} = steady state trim angle of attack of rocket with thrust misalignment, rad

β = (dispersion with reduction method) /(dispersion, without method), dispersion reduction factor, dimensionless

$\gamma = \tan\text{-l}\left(\dfrac{\sqrt{\dot{Y}^2 + \dot{Z}^2}}{\dot{X}}\right)$, where $V = \sqrt{\dot{X}^2 + \dot{Y}^2 + \dot{Z}^2}$, general expression for rocket flight path angle, rad

γ_{TS} = steady state postboost dispersion angle from linearized equations of motion, mrad

$\Delta\theta_0, \Delta\psi_0$ = elevation and azimuth aiming error, respectively, mrad

θ = elevation aiming angle, rad

$\Delta\theta, \Delta\psi$ = errors in rocket pitch and yaw, respectively, which are introduced by any error source, mrad

δ = thrust misalignment angle, mrad

δ_f = aerodynamic misalignment angle, mrad

ϵ = dynamic imbalance, angle between rocket geometric and principal inertia axes, mrad, $(\tan(2\epsilon) = 2I_{xz}/(I_{zz} - I_{xx}))$

θ = Euler angle in pitch or rocket pitch angle, rad

$\dot{\theta}$ = rocket transverse (lateral) rotational rate, rad/s

θ_0, ψ_0 = initial aim directions in elevation and azimuth, respectively, deg or rad

$\Delta\theta_0, \Delta\psi_0$ = errors in elevation and azimuth, respectively, mrad

$(\theta_0)_{std}$ = aiming quadrant elevation for standard trajectory, deg or rad

μ = mean of a universe of statistical values

ρ = atmospheric density, kg/m^3

$\sigma = 2\pi[2I/(\rho A_{ref}\ell_s C_{N\alpha})]^{1/2}$, yaw oscillation distance (wavelength of yaw), m

$$= \text{stability parameter}$$

$\sigma_D = $ standard deviation in deflection, m or mrad

$\sigma_{D_{tot}} = $ total standard deviation in deflection, m or mrad

$= $ total one-sigma dispersion in deflection, mrad

$\sigma_{max} = $ larger of the two standard distributions for an elliptical distribution, m

$\sigma_{opt} = $ optimum value of ó to minimize total dispersion from thrust misalignment and boost phase wind, m

$\sigma_{R_{tot}} = $ total standard deviation in range, mrad or rad

$= $ total one-sigma dispersion in range, mrad

$\sigma_{range} = $ standard deviation in range, m or mrad

$\sigma_{tot} = $ total error, m

$\sigma_x, \sigma_y = $ standard deviation of impact points in x- and y-directions, respectively, (usually range and deflection), m or mrad

$\sigma_{x_{tot}}, \sigma_{y_{tot}} = $ total standard deviation of impact points in x- and y-directions, respectively, m or mrad

$\sigma^2, \sigma = $ variance and standard deviation, respectively, of a universe of statistical values

$\sigma_{D_i}^2 = $ variance due to individual error sources in deflection, m or mrad

$\sigma_{R_i} = $ variance due to individual error sources in range, m or mrad

$\phi = $ Euler angle in roll or rocket roll angle, rad

$\dot{\phi} = $ rocket angular velocity component about x-body-centered axis, rad/s

$\chi^2 = $ chi-square statistic

$\psi = $ Euler angle in yaw or rocket yaw angle, rad

$= $ aximuth aiming angle, rad

$(\psi_0)_{std} = $ aim direction in azimuth for standard trajectory, mrad

4-1 INTRODUCTION

Accuracy is the measure of the ability of the rocket system to position the payload at a given point at warhead event. Various error sources inherent in the rocket system and external conditions, such as winds, cause the payload to disperse from its intended path. To calculate dispersion errors, the actual flight paths of the rockets are compared to an idealized trajectory. The error sources are identified and then categorized as to whether they are predictable, i.e. , allow compensations to be made, or random. The most significant factors that influence the accuracy of free rockets have been identified by extensive comparisons of experimental tests and theory.

This chapter contains a detailed discussion of error sources and the effects of the errors on free rocket flight. The error sources are discussed for the prelaunch, launch, boost, and ballistic flight phases. Techniques for the reduction of dispersion through control of the error sources and their effects are presented. These techniques describe how the designer can compensate for the errors to achieve the level of accuracy required by the mission specifications. Both the reduction of the error sources themselves and the reduction of rocket sensitivity to error sources are treated.

The remainder of the chapter deals with topics related to accuracy estimation and calculation. Equations of motion are presented that enable the designer to analyze error effects on rocket accuracy. Also discussed are statistical methods for defining measures of central tendency and dispersion. Finally, a sample problem with a sample error budget and calculation for determining the free rocket accuracy is included.

4-2 ERROR SOURCES

4-2.1 GENERAL

For the purpose of this chapter, error source is defined as any device, procedure, or accident of assemblage which causes a free rocket to deviate from an ideal, intended trajectory. If a number of free rockets of a given type are launched, their impact points will not coincide, but the points will create some pattern in the intended target area. This pattern will possess some central tendency point, which is the "average" of the impacts, and a measure of the dispersion of the rockets from the average. Methods of calculating the central tendency and dispersion of the pattern are presented in par. 4-5.4. The pattern is caused by error sources that are discussed in pars. 4-2.2 through 4-2.5. Error sources maybe categorized by their effect on the pattern of impact points. In this chapter, they will be categorized as producing either bias errors or random (sometimes referred to as precision) errors. Bias errors affect all of the rockets in the same manner; consequently, bias errors move the average impact point. Random errors tend to affect the dispersion of the rocket pattern but have little effect on the average impact point. Often, individual sources of error may be of either the bias or random type, and the designer should assess each source as it applies to the rocket system under consideration.

To aid in further understanding this categorization of errors, the following definitions are useful:

1. Fixed Bias Errors. Assume that, because of a manufacturing error, the sight for a particular rocket launcher is misaligned with the launcher rail. This will result in a center of impact that is not in line with the intended direction as established by the sight. This type of error is called a fixed bias error. Fixed bias errors will not be considered in this chapter because it is assumed that they can always be discovered, by systematic testing, and compensations can be made.

2. Random Bias Errors. Errors that exist for a specific set of shots fixed at the same elevation and deflection setting, such as the misreading of an unchanging wind or the missetting of the quadrant elevation (QE) angle, are called random bias errors. Methods will be described for computation of these errors; however, in the description of dispersion the errors will not be considered because, when prior knowledge of these disturbances exists, correction can be made through such methods as prelaunch computation and adjusted aiming.

3. Random Errors. The computation of these errors is the main topic of pars. 4-2 through 4-4. These errors are due to thrust misalignment, mass variations, incomplete compensation for random bias errors, and many other causes.

An informative approach to the description of error sources is to separate the flight of a rocket into phases, consider each phase separately, and identify the major contributors to the total error from each phase. In each flight phase different forces predominate: therefore, the important parameters change. In the paragraphs that follow the important parameters for each phase will be discussed.

Consideration of the errors in each flight phase separately has two advantages: (1) the equations can be simplified by including only the forces that predominate during the phase and (2) the simplified equations can be manipulated to provide analytical solutions. The availability of analytical solutions is of great benefit to the designer because the effects of the important variables or combinations of variables that determine the error call be easily identified. These results can then be combined with computer calculations that provide the required accuracy.

The flight of a rocket will be divided into four phases:

1. Prelaunch Phase. Includes all preparations up to the time of rocket ignition

2. Launch phase. Includes the time from motor ignition to that point in time at which the rocket and launcher are considered to be no longer interacting through mechanical or motor exhaust effects.

3. Boost Phase. The time during which the rocket is free of the launcher and the propulsion system is burning.

4. Ballistic Phase. Includes that portion of flight from the time of motor burnout to detonation (warhead event) that occurs either by impact or other types of fuzing.

The errors associated with each of these phases are discussed in the paragraphs that follow.

4-2.2 PRELAUNCH PHASE ERRORS

When preparing to launch a rocket at a target, the launch angle QE in the vertical plane and the azimuth angle under standard conditions must be established first. The term "standard" applies to a flight that exists under arbitrarily chosen meteorological, positional, and material conditions. Corrections must then be made to this standard aiming for variations from the standard of the existing conditions for a given flight. Both the standard aiming and the corrections generally are obtained from a firing table that is a catalog of standard trajectories and corrections for nonstandard conditions. These tables are usually cataloged in a fire control computer. For example, the usual rocket firing table includes

 1. Pertinent data for the standard trajectories of the rocket

 2. Corrections to the standard aiming to compensate for rotation of the earth

 3. Corrections to the standard launch elevation (QE) to compensate for variations in propellant temperature; uninhibited propellant weight; atmospheric pressure, density, and temperature; inert weight; and wind

 4. Corrections to the standard aiming azimuth for wind.

The sources of error in the prelaunch phase can be described us errors in the aiming of the rocket. Aiming errors are caused by any combination of the following sources:

 1. <u>Inexact Knowledge of Location of Launcher and Target.</u> These errors may be caused by either survey errors or an incorrect map grid determination of the target. This type of error is categorized as a bias error because each round will be affected in an identical manner.

 2. <u>Errors in Positioning Launcher.</u> These errors are sometimes called laying and sighting errors. These also are bias errors and result from the inability to level exactly the launcher and from the inability to align exactly the launcher along the desired QE and azimuth.

 3. <u>Incorrect Determination of Trajectory Corrections to be Applied for Nonstandard Flight.</u> This bias error can be caused, for example, by inexact knowledge of the true wind azimuth or by the incorrect use of the firing tables.

Although caused by different sources, these errors all result in physical displacement of the launcher from the orientation required for the rocket to impact the target. The errors are determined by calculating the difference between a flight with an error and the standard trajectory at warhead event.

Fig. 4-1 illustrates the coordinate system and errors at payload disposition. The choice of error parameters ΔX, ΔY, and ΔZ may be any convenient orthogonal set since the error magnitudes are usually much less than X.
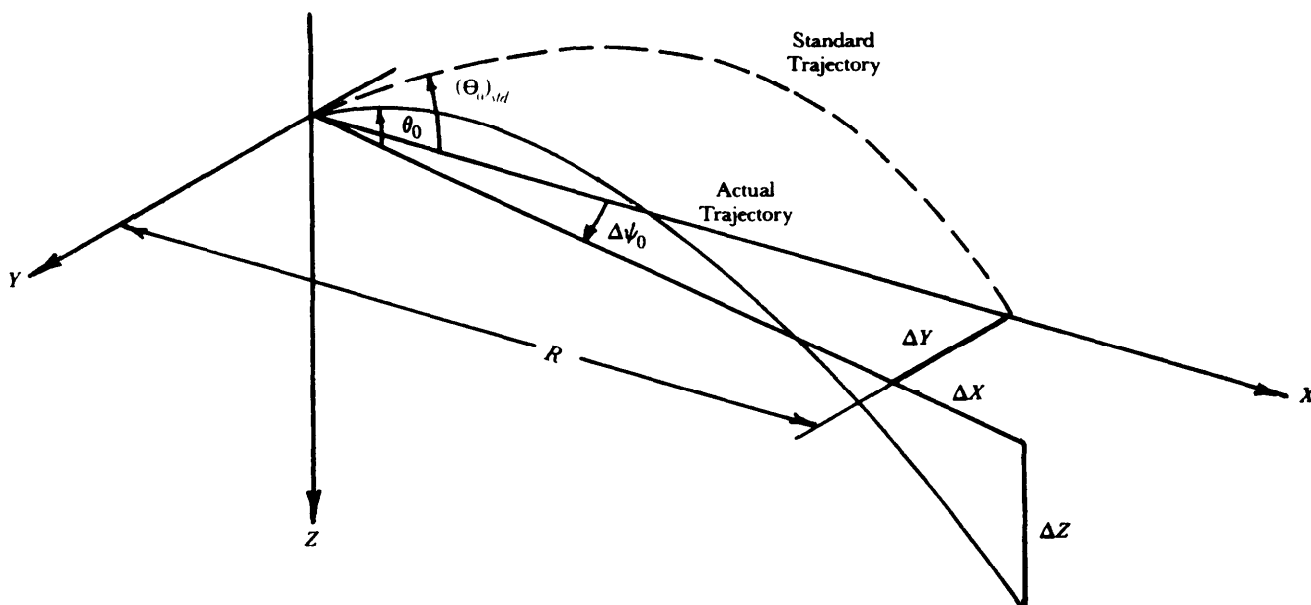
Figure 4-1. Aiming Errors

The errors at payload disposition which result from aiming errors of the launcher are

$$\Delta Y = \Delta \psi_0 R, \text{ m} \tag{4-1}$$

$$\Delta X = (\Delta \theta_0) \left. \frac{\partial R}{\partial \theta} \right|_{Y = \text{const}}, \text{m} \tag{4-2}$$

$$\Delta t = (\Delta \theta_0) \left. \frac{\partial t}{\partial \theta} \right|_{R = \text{const}}, \text{s} \tag{4-3}$$

$$\Delta Z = (\Delta \theta_0) \left. \frac{\partial Z}{\partial \theta} \right|_{t = \text{const}}, \text{m} \tag{4-4}$$

$$\Delta \psi_0 = (\psi_0)_{std} - \psi_0, \text{ mrad} \tag{4-5}$$

$$\Delta \theta_0 = (\theta_0)_{std} - \theta_0, \text{ mrad} \tag{4-6}$$

where

$\Delta Y =$ crossrange (deflection) error, m
$\Delta X =$ range error, m
$\Delta t =$ time-of-flight error, s
$\Delta Z =$ altitude error, m
$R =$ standard range, km
$t =$ time, s
$\psi_0 =$ initial aim direction in azimuth, mrad
$(\psi_0)_{std} =$ aim direction in azimuth for standard trajectory, mrad
$\theta_0 =$ initial aim direction in elevation, QE, rad
$(\theta_0)_{std} =$ aim direction in elevation QE for standard trajectory, rad
$\Delta \psi_0 =$ azimuth aiming error, mrad
$\Delta \theta_0 =$ elevation aiming error, mrad.

The partial derivatives $\partial R/\partial \theta$, $\partial t/\partial \theta$, and $\partial Z/\partial \theta$ will be discussed in more detail in par. 4-5.

4-2.3 LAUNCH PHASE ERRORS

The launch phase begins with the ignition of the rocket and terminates when forces imparted to the rocket by the launcher become insignificant. During this flight phase the rocket and launcher can be thought of as an interacting system. Asymmetries resulting from manufacture and assembly tolerances will cause a rocket to produce forces normal to the intended line of flight. These forces are transmitted to the launcher which moves in a manner dictated by its design. Because the launcher cannot compensate for all rocket errors, each rocket is launched with some finite velocity normal to the aim line and some finite angular rate about a transverse axis. Further, if the launching device is attached to an aircraft, such as a helicopter, additional transverse angular velocities and angular rates will exist which are caused by aircraft-induced motions. These finite velocities and rates are referred to as mallaunch; in practice, mallaunch is usually taken to mean only angular rates because they are potentially larger sources of error than the translational velocity. Another cause of angular rate at launch is a rocket supported in the launcher by devices located fore and aft. As the front device leaves its launcher support, gravity will tend to "tip" the rocket downward about the aft support. This effect is known as rocket tip-off and is not usually considered a part of the mallaunch effects.

For analysis purposes, launch-phase error effects are reduced to errors in angular rate, translational velocity, and changes in speed. The principal sources of rocket errors during launch are

1. <u>Acceleration Level.</u> This is a random error whose effect on speed is usually accounted for in the boost phase of flight. It is mentioned here because the acceleration level of a rocket determines both the magnitude and time history of the forces imparted to the launcher. It can affect launcher motion directly through starting shock and nonsteady burning and through the frictional force between the rocket and launcher.

2. <u>Thrust Misalignment.</u> These random errors are depicted in Fig. 4-2. Although angular misalignment is depicted, similar disturbances can be caused by the thrust being parallel to the rockot longitudinal axis but being displaced radially.
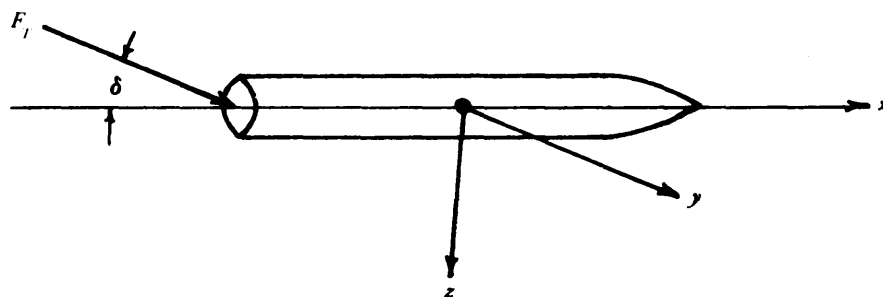
Figure 4-2. Thrust Misalignment

3. <u>Static and Dynamic Imbalance.</u> These random errors are caused by the geometric longitudinal axis being noncoincident with the principal axis of inertia. Fig. 4-3 shows examples of static and dynamic imbalance. The figure shows massless rods, which may be considered to be the geometric axis of a rocket, with identical masses fixed at some point off the axis. Spinning either of these rockets about the geometric axis will impart unwanted motions to the launcher which lead to mallaunch. However, the launcher may be designed so that the inherent motion of it could help compensate for this rocket motion. Also, at the instant of release from the launcher, the motion of the spinning rocket will be that of a body exhibiting the characteristics of a force-free precession of a rigid body. This introduces a second error effect caused by the imbalance which is separate from the induced launcher motions. This precessional motion is equivalent to an angular velocity at launch. The magnitude of this initial angular velocity will be discussed in par. 4-3.3.

(A) Statically Imbalanced
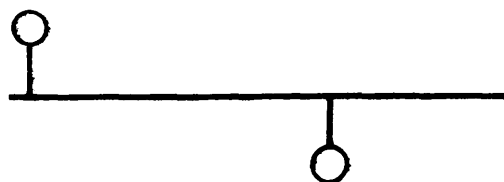
(B) Dynamically Imbalanced

Figure 4-3. Static and Dynamic Imbalance

4. Flexible Rocket. The rocket, not being a perfectly rigid body, will have an angular rate as it exits the launcher tube because it is bending and flexing due to launcher and rocket interaction forces.

4-2.4 BOOST PHASE ERRORS

Error sources associated with the boost phase of flight can produce errors in the speed of the rocket and angular errors in the flight direction.

The speed change errors are usually random and are characterized by a change from the nominal velocity attained at propellant burnout. These errors, which result in an error in the plane of the trajectory, are primarily the result of the variability present in the propulsion system. Any variation in a parameter that influences the delivered total impulse will obviously result in a different burnout velocity for the rocket. These include variations in

1. Total loaded propellant
2. Propellant specific impulse due to chemical composition
3. Specific impulse due to physical quantities, e.g., the ratio of nozzle throat diameter to nozzle exit diameter
4. Inert mass.

In addition to propulsion system variability effects, the burning time and thrust of solid propellant rockets are affected by propellant temperature. Even though the temperature has a negligible effect on total impulse, it does affect the burnout velocity because the rocket is then subjected to a different drag history.

Speed change errors are a function of mechanical design, manufacturing control, and propellant selection. Angular errors associated with the boost phase of flight are primarily caused by thrust misalignment and a wind normal to the intended flight path. Fig. 4-4 illustrates how thrust misalignment produces errors during boost. The thrust-induced moment causes the rocket to rotate until it is balanced by a stabilizing aerodynamic restoring moment. The rocket then has a component of thrust normal to the intended flight path. Because thrust is invariably the largest force acting during the boost phase, errors caused by thrust misalignment can be quite large. As was mentioned previously, angular and laterally-displaced thrust misalignments would have similar effects, and both are random in nature.
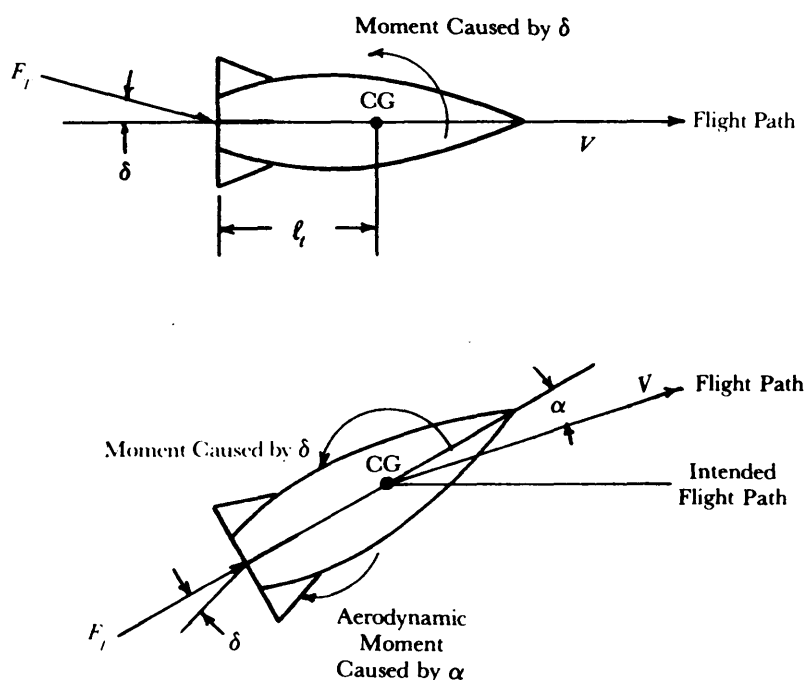
Figure 4-4. Effect of Thrust Misalignment on an Aerodynamically Stable Rocket

4-9

Depending on its variability and other factors, wind error may be of either the bias or random type. An aerodynamically stable free rocket will turn toward the direction from which the wind is blowing. Fig. 4-5 illustrates the effect. As with the thrust misalignment error, wind causes a component of thrust normal to the intended flight path.
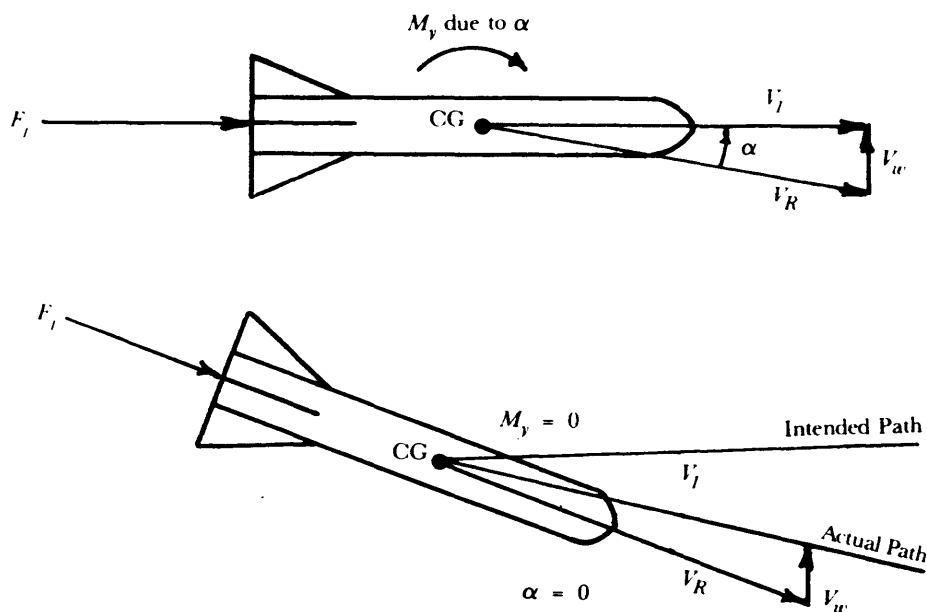
Figure 4-5. Effect of Wind on an Aerodynamically Stable Rocket

A steady, constant velocity wind is effectively a bias error, i.e., it will affect identical rockets in the same manner. Winds often have a variable component either in magnitude and/or direction which produces random-type errors in the rocket flight path. For a rocket launched from an aircraft local airflow effects, such as downwash from helicopter blades, are one source of steady and transient winds. The effects of steady and transient winds on the unpowered portion of rocket flight will be discussed in par. 4-2.5.

From the preceding discussion it is apparent that the degree of stability of the reocket will be of primary importance to the designer. The degree of stability will determine the angle through which the missile will turn in response to thrust misalignment or wind. This, in turn, determines the magnitude of the thrust component normal to the intended path and the ultimate error.

The aerodynamic stability of a rocket is the measure of the tendency of the rocket to align itself with the relative wind. If an aerodynamically stable rocket in steady flight with no aerodynamic moments should be given a disturbance such as a sudden increase in the angle of attack α, the aerodynamic forces caused by the disturbance direct the rocket back to its original state. The motion of the rocket immediately following the disturbance is generally a sinusoidal oscillation about a lateral axis. One of the most important parameters in the study of the behavior of free rockets is the distance the rocket travels during one such oscillation. The yaw oscillation distance ó (Refs. 1 and 2) is related to the aerodynamic stability of the rocket by the static margin ℓ_s (the moment arm of the corrective aerodynamic forces

$$\sigma = 2\pi \sqrt{\frac{2I}{\rho A_{ref}\ell_s C_{N_\alpha}}} \text{, m} \qquad (4\text{-}7)$$

where

σ = yaw oscillation distance or wavelength of yaw, m

I = moment of inertia of the rocket about a lateral axis, kgŽm^2

ρ = atmospheric density, kg/m^3

A_{ref} = aerodynamic reference area, m^2

ℓ_s = rocket static margin, m

$C_{N\alpha}$ = rocket normal force coefficient gradient, rad^{-1}.

Fig. 4-6 illustrates the sign conventions associated with thrust misalignment and static margin (arrow tips are pointed in the positive direction). Because ó depends on the aerodynamic coefficients, mass distribution of the rocket, and air density, it is subject to change during flight as the mass, velocity, and altitude of the rocket change.
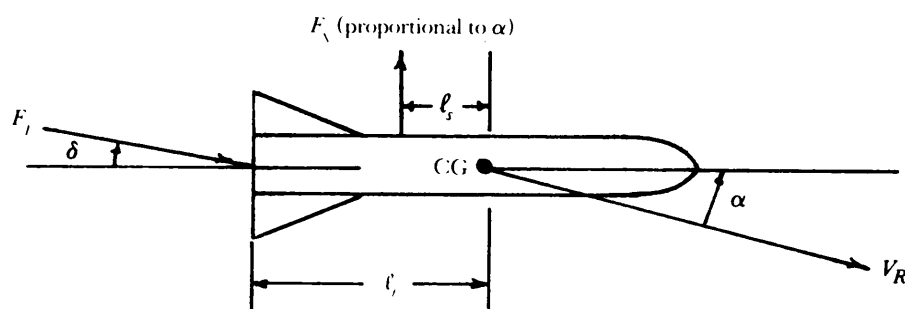
Figure 4-6. Static Margin

Fig. 4-7 shows the variation of ó and the buildup of angular dispersion for a typical flight. From the figure, it is seen that most of the dispersion takes place during the first yaw oscillation. During this time, ó does not change appreciably; this has been found to be generally true. Therefore, the dependence of dispersion on ó is mainly determined by the initial wavelength of yaw. This initial value will be used to describe the wavelength of a flight for the remainder of the chapter. As can be seen from Fig. 4-6 and Eq. 4-7, the larger the static margin, the more stable the rocket, and the smaller the yaw oscillation distance.

Other sources of error during the boost phase are fin misalignments and aerodynamic variations that cause errors in the static margin. Both of these errors, functions of assembly tolerances and mishandling of the rocket, are usually of the random type.

4-2.5 BALLISTIC PHASE ERRORS

The ballistic phase of rocket flight begins at motor burnout and continues to the warhead event. During this phase, the rocket is only under the influence of aerodynamic and gravity forces.

The aerodynamic forces may be separated into drag forces and those forces acting normal to the standard trajectory. If only drag is considered in calculating the standard trajectory, any change in either the normal force or the drag force will introduce dispersions at the warhead event. In addition to dispersion of the flight path, errors associated with warhead fuzing must also be considered.

During the ballistic phase, the largest potential error source is normally that caused by winds. Winds acting on a free rocket during the ballistic phase generate three perturbing forces that affect the missile trajectory (see Fig. 4-8), namely,

1. <u>Change in Drag Magnitude.</u> Magnitude. Ballistic wind will cause a change in airspeed and, consequently, in dynamic pressure and drag force magnitude.

2. <u>Lift Forces.</u> A change in wind velocity normal to the ballistic flight path will cause an angle of attack and, consequently, the development of a lift force. Because this is a transient effect, it is usually very small.
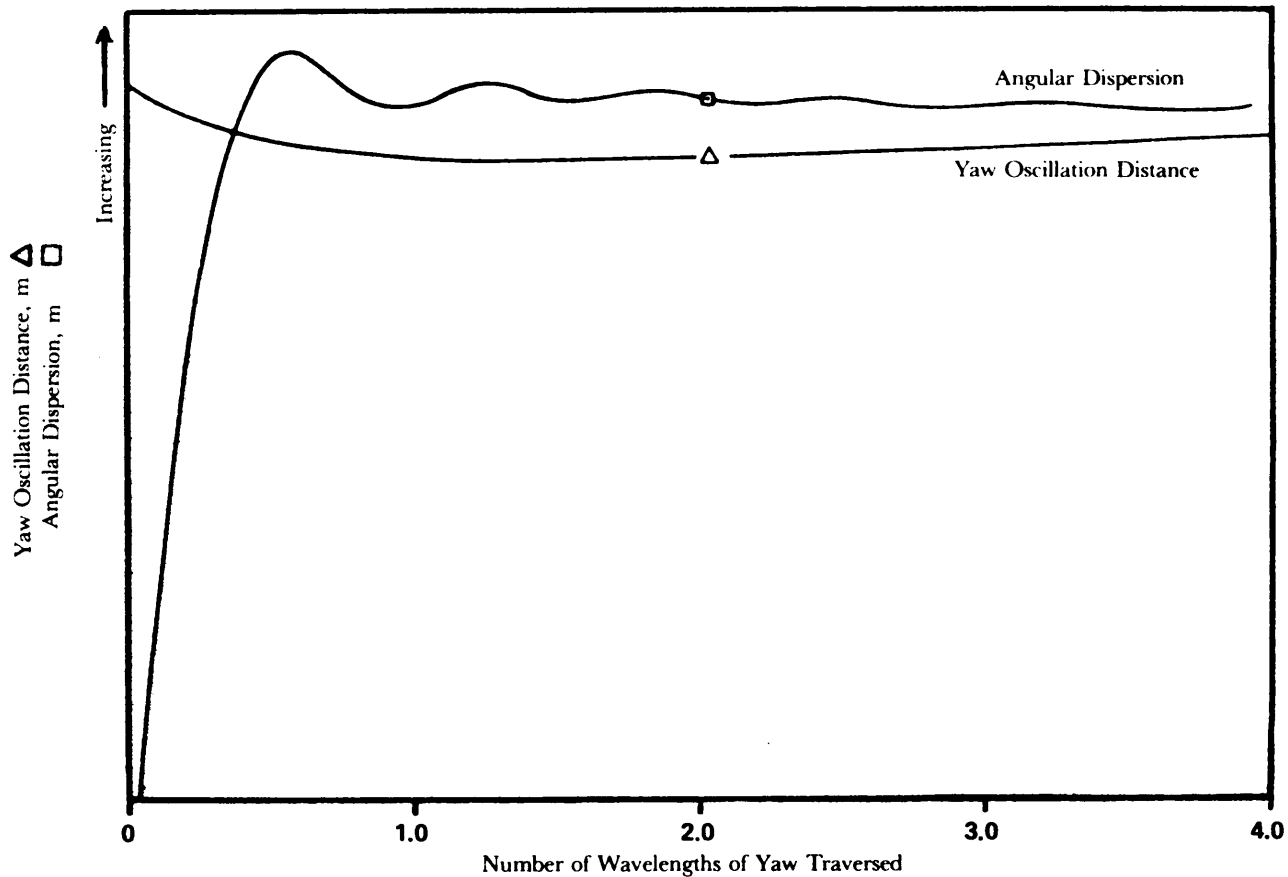
Figure 4-7. Variation of Angular Dispersion and Wavelength of Yaw During Flight

3. Change in Drag Direction. In its transient response to a normal wind, a stable missile will be oriented at some angle with respect to its zero-wind flight path. The drag force vector still lies along the missile axis and, therefore, causes an acceleration in the downwind direction until the missile dispersion velocity reaches the wind velocity. This is the predominant force causing ballistic wind error. High-altitude winds can reach high velocities; therefore, frequently an attempt is made to compensate for the winds in the aiming process. This can be accomplished by the use of data from firing tables and some remeasurement of the predominant wind.

Fig. 4-8 illustrates the effects of transient and steady wind-induced forces. The transient condition may be caused by the first entry of the rocket into a steady wind field or by a wind gust of relatively short duration compared to the total flight time. The instantaneous action is a force normal to the trajectory, resulting from the wind-induced angle of attack a. A stable rocket will then cock into and, eventually drift with, the wind. Rotation of the rocket will produce an axial drag component that is normal to the intended path. The drag component is in a direction to cause the rocket to drift with the wind.

The standard trajectory assumes some nominal set of atmospheric data such as density; however, the atmosphere experienced by a given rocket may be quite different. Atmospheric data for a given site changes with the season, time of day, temperature, humidity, and other factors. These effects will cause a nonstandard drag history to be experienced by a given rocket. This error effect is usually accounted for as an error in atmospheric density and is considered a bias-type error because it affects all rockets in a given fire mission in the same manner.

Fuzing errors result from inaccuracies in the warhead detonation device. With impact fuzing, the errors are those associated with the dispersion of the trajectory. There are, however, no errors introduced by the fuzing technique itself.

4-12

(A) Transient Condition

(B) Steady State Condition
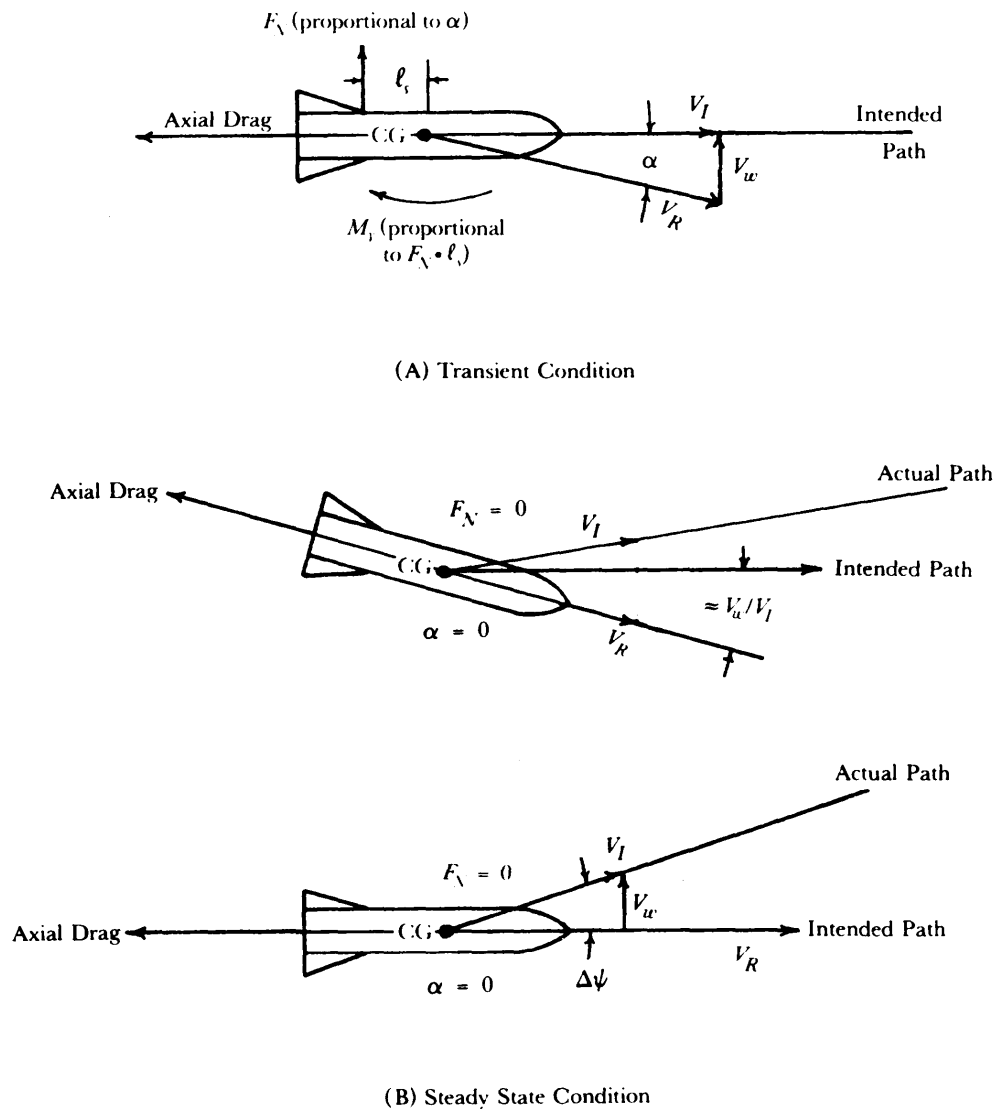
Figure 4-8. Effect of Wind on a Ballistic Free Rocket (After Burnout) (Top View)

With time fuzing, variations in fuze action time introduce errors in addition to those associated with the dispersion of the trajectory. The result is additional range and altitude dispersions of the warhead at the time of detonation. With altitude fuzing, variations in the altitude sensing device cause error effects similar to time fuzing. Fuzing errors usually are considered to be of the random type.

The remainder of the ballistic phase error sources discussed are considered to be equivalent to changes in the standard atmospheric density and to changes in the rocket ballistic coefficient. The ballistic coefficient B is a measure of the ability of a ballistic vehicle to overcome the effects of drag. The ballistic coefficient B was defined in Chapter 3 to be

$$B = \frac{m}{C_D A_{ref}}, \text{kg/m}^2 \tag{4-8}$$

where

    B = rocket ballistic coefficient, kg/m^2

    m = rocket mass, kg

   C_D = aerodynamic drag coefficient, dimensionless.

The error sources that follow usually are grouped into errors in B and usually are considered to be random-type errors. This association with B is done so that the errors can be equated to a change in either the mass or drag coefficient C_D when compared to those values in the standard trajectory. The error sources are

    1. A projectile seldom has an actual drag history exactly like the one used in the calculation of the standard trajectory. Inaccuracies inherent in the methods of determining drag-as well as inaccuracies resulting from manufacturing and damage in handling—are typical causes of these drag deviations.

    2. Projectiles with fins that have become misaligned or bent as a result of careless handling or manufacturing error will cause aerodynamic forces and will result in dispersion. However, fin misalignment will also cause a slow spin that will reduce the effect of the error (Ref. 1, p. 60).

    3. Manufacturing tolerances usually cause the projectile c-enter of gravity to be located off the longitudinal axis (static imbalance). The aerodynamic forces will then produce a moment resulting in an angle of attack. This, in turn, produces a net normal force and a small change in drag along the trajectory.

    4. Manufacturing tolerances plus the unavoidable unsymmetric placement of small components or uneven propellant burning will result in the inertial spin axis being displaced from the projectile centerline (dynamic imbalance). If the rocket is spinning, this will cause the missile to precess in a coning motion about the velocity vector at some angle of attack.

    5. The trajectory of the projectile during the ballistic phase will approximate a parabolic arc. An aerodynamically stable vehicle will attempt to keep its axis aligned with the flight path. However, the inherent resistance of the body to rotation (aerodynamic damping) will cause the projectile axis to lag behind the changing flight path direction. This phenomenon is called the yaw of repose (Ref. 1, p. 58) which causes a small dispersion unaffected by spin.

    6. Variations in the burnout mass due to manufacturing tolerances and unburned propellant are additional error sources.

The preceding paragraphs have identified the major sources of error in each of the defined phases of rocket flight. Par. 4-3 will detail the calculation of dispersions caused by these identified error sources.

4-3 EFFECTS OF ERROR SOURCES

4-3.1 GENERAL

Each of the error sources previously described produces dispersions in the rocket at the warhead event. For the purpose of this paragraph, dispersion means any deviation of the detonation location from the standard trajectory. The dispersions occurring in each flight phase will be presented in terms of angular errors $\Delta\theta$ and $\Delta\psi$ where possible; therefore, the actual linear dispersion is assumed to propagate linearly with range. The total dispersion from all the individual error sources is then calculable. The combining of individual dispersions will be discussed in more detail in par. 4-5. Accepted practice has been to measure the dispersion in units of milliradians (mrad) which is often called roils; mrad will be used in the chapter.

The angular error of a rocket is obtained by solving the differential equations of motion throughout the flight. The equations can be solved on a computer to any desired accuracy. Values are chosen for the error sources, and a number of parametric runs are made. The results can then be combined statistically as outlined in par. 4-5.

If symmetry about the longitudinal axis of the rocket is assumed (see Fig. 4-9) so that normal small-angle approximations are valid and the gyroscopic effects due to missile roll are omitted, then the six-degree-of-freedom equations of motion become decoupled in the vertical and horizontal planes. Furthermore, motion in the two planes is identical except for the gravity terms in the vertical plane.
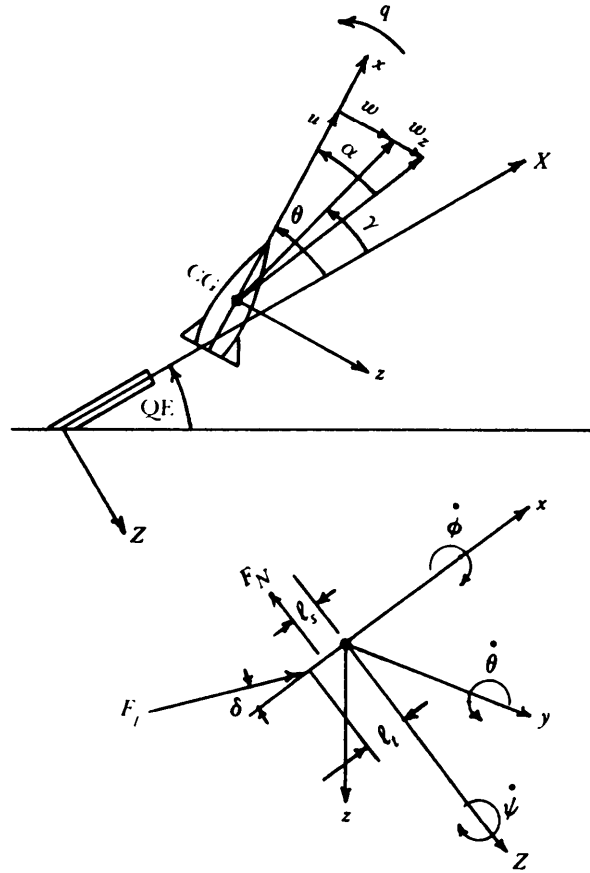
Figure 4-9. Definitions of Sign Conventions for Dispersion Equations of Motion

(The effect of gravity is equivalent to a bias error and will not be considered in these equations.) A useful solution of the equations of motion in only one plane can then be obtained. This greatly simplifies the study of dispersion while maintaining sufficient accuracy of results for the purposes of this paragraph. A more detailed discussion of these equations is found in par. 4-5.3.

The uncoupled, pitch-plane equations to be solved can be written

$$\dot{u} = [G'] - \frac{\rho u^2}{2} \left[\frac{C_D A_{ref}}{m} \right], \text{ m/s}^2 \tag{4-9}$$

$$\dot{w} = qu - \frac{\rho u}{2} \left[\frac{C_{N\alpha} A_{ref}}{m} \right] (w + w_z) + [G']\delta\cos\phi, \text{ m/s}^2 \tag{4-10}$$

$$\dot{q} = - u \left[\frac{4\pi^2}{\sigma^2} \right] \left\{ w + w_z - \left[\frac{C_{m_q} d^2}{2 C_{N\alpha} \ell_s} \right] q + \delta_f u \cos\phi \right\}$$

$$+ \frac{G' \ell_t}{k^2} \ \delta\cos\phi, \text{ rad/s}^2 \tag{4-11}$$

$$\dot{X} = u \text{ , m/s} \tag{4-12}$$

$$\dot{Z} = w - u\theta \text{, m/s} \tag{4-13}$$

$$\dot{\theta} = q \text{ , rad/s} \tag{4-14}$$

$$\phi = f(t), \text{rad} \text{ (This is specified by the spin program.)} \tag{4-15}$$

where

u, w = components of rocket velocity in direction of x- and z-body-centered axes, respectively, m/s

$q, \dot{\phi}$ = components of rocket angular velocity about the y- and x-body-centered axes, respectively, rad/s

θ = rocket pitch angle, rad

ϕ = rocket roll angle, rad

$\dot{X}, \dot{Z}$ = components of rocket velocity along and normal to aiming direction, respectively, m/s

G' = rocket acceleration due to thrust, m/s^2

C_{m_q} = aerodynamic damping moment coefficient, dimensionless

ℓ_t = distance from center of gravity to point of thrust application, m

d = reference body diameter, m

k = rocket radius of gyration, m

δ = thrust misalignment angle, rad

δ_f = aerodynamic misalignment angle, rad

w_z = component of wind velocity in direction of negative z-body-centered axis, m/s

γ = rocket flight path angle deviation from reference direction, rad, $\tan\gamma = \dot{Z}/\dot{X}$ (since $\dot{Y} = 0$)

ρ = atmospheric density, kg/m^3

$\cdot$ = derivative with respect to time.

For this set of equations

1. X, Y, Z are the inertial (reference)-coordinate system axes; the X-coordinate is along the launcher axis, and the Z-coordinate is normal to X in the vertical plane.

2. x, y, z are the body-centered coordinate system at the rocket CG; the x-coordinate is directed along the longitudinal axis of symmetry.

The six expressions in square brackets completely specify all the rocket characteristics needed to calculate its motion. Threfore, if the rocket motion is tabulated for variations in each of the six expressions, the results will be applicable to any configuration for which these expressions are known.

For Eqs. 4-9 through 4-15, the launcher affects the motion of the rocket only through the initial conditions. For convenience a dimensionless expression for the launcher length P will be used

$$P = \frac{\text{launcher length}}{\sigma} \text{ , dimensionless} \tag{4-16}$$

Launcher length in this context means the point on the launcher (or in the launch tube) at which the rocket is no longer effectively constrained by the launcher, i.e., the distance traveled by the rocket before it enters free flight. This distance is usually referred to as effective launcher guided length or end of launcher guidance. Also, this expression assumes a rigid launcher and a rigid rocket. The effect of launcher length, then, is represented by an initial value of velocity

$$u_p = \sqrt{2P\overline{G'(0)}\sigma} \text{ , m/s} \tag{4-17}$$

where

UP = rocket velocity at end of launcher, m/s

$\overline{G'(0)}$ = average rocket acceleration while on launcher, m/s².

Throughout this chapter it is important to remember that the parameter P is essentially an initial velocity effect, and, unless specifically noted, a perfectly rigid launcher is assumed.

Examination of the solutions of Eqs. 4-9 through 4-15 for typical rocket systems indicates that only a relatively few parameters have first-order effect on the angular dispersion. These are the rocket acceleration $\overline{G'(0)}$, the wavelength of yaw ó, and the dimensionless launcher length P. The burning distance X also will have a first-order effect. These equations can now be solved on an analog or digital computer and the dispersion at the end of flight determined for any given error source.

As mentioned previously, a more informative approach for the rocket designer is to consider each flight phase separately and to identify the major contributors to dispersion during each phase. This representation allows rapid evaluation of the accuracy of the rocket without resorting to the complex methods of accounting for ballistic phase errors.

The rocket equations were solved, using an automatic computer, for the burning phase of flight. The angular dispersion γ_{TS} at the end of the boost phase is approximated by the following expression (Ref. 3)

$$\gamma_{TS} = \theta - \frac{w}{u} + \frac{qk^2}{u\ell_s} - \left(\frac{\rho d^2 A_{ref} C_{m_q}}{4mu\ell_s}\right)(w + w_z), \text{ mrad} \tag{4-18}$$

where the values of θ, w, u, q and the aerodynamic parameters are those at burnout; and γ_{TS} is determined by computing $\lim_{t \to \infty} \frac{\dot{z}}{u}\Big|_{u = \text{const}}$ which is the steady state, postboost angular dispersion of the direction of the velocity. Thus for calculating the effect of the boost-phase errors on dispersion at warhead event, γ_{TS} may be treated as an aiming error. Then the missile is assumed to be launched with the initial conditions taken from booster burnout for the ballistic phase.

Par. 4-3.2 will present angular dispersion at flight termination in terms of the defined parameters. For convenience the rocket acceleration term used will be normalized to gravity, namely, $G = G'/g_0$, which is measured in units of g's.

4-3.2 PRELAUNCH PHASE

Prelaunch-phase error effects on dispersion can most easily be seen from Eq. 4-18. In effect, an aiming error during prelaunch is experienced as an initial value of θ. If no other errors are present, the terms involving q, w, and w_z in Eq. 4-18 are zero. From this, the prelaunch dispersion is

$$\gamma_{TS} = \theta_0, \text{ mrad.} \tag{4-19}$$

4-3.3 LAUNCH PHASE

Launch-phase error sources were defined and discussed in par. 4-2.3. During the launch phase, the rocket is constrained to its intended path by the launcher. Random motion induced by rocket forces and torques are controlled by the launcher structure. The phasing of the launcher reactions to these forces and torques will determine conditions at the beginning of the boost phase. These conditions are separated into three modes of motion, i.e.,

1. Initial angular velocity about a lateral axis
2. Initial translational velocity normal to the launcher axis
3. Angular velocity resulting from rocket dynamic imbalance when some form of spin on the launcher is used.

The angular dispersion at flight termination caused by these initial conditions is presented here.

The analysis that follows is presented for a rigid launcher and a rigid rocket; however, flexible launcher and flexible rocket effects should be included if they contribute significantly to motion at launcher release.

Figs. 4-10(A), (B), and (C) show the angular dispersion caused by an initial angular velocity of 100 mrad/s for various P values. The launcher length P, the wavelength of yaw ó, and the rocket
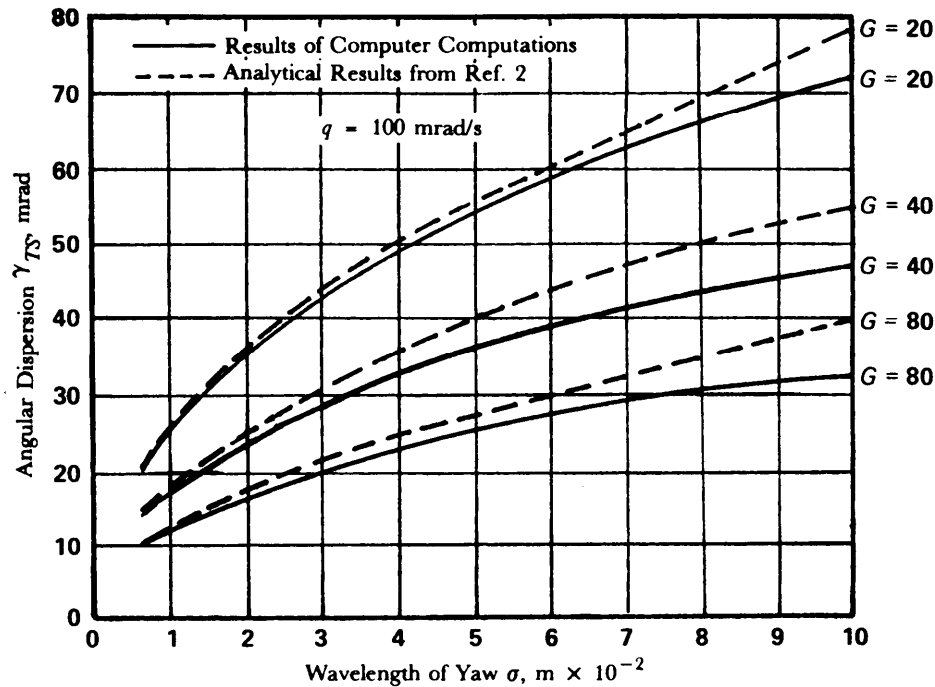
(A) $P = 0$
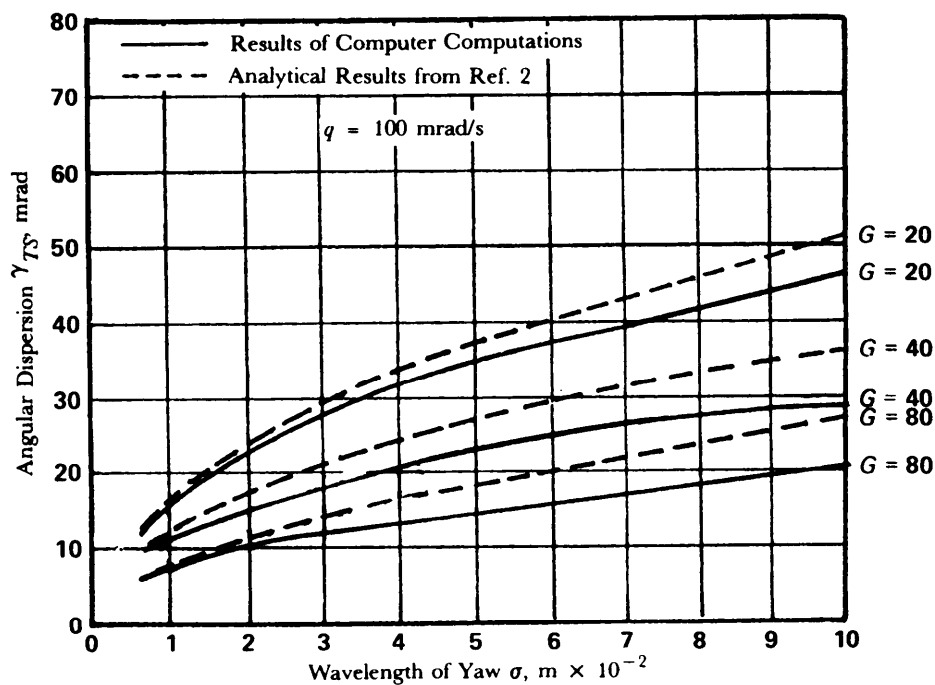
(B) $P = 0.01$

Figure 4-10.   Angular Dispersion Due to Initial Angular Rate for Various P Values

(cont'd on next page)

(C) $P = 0.10$
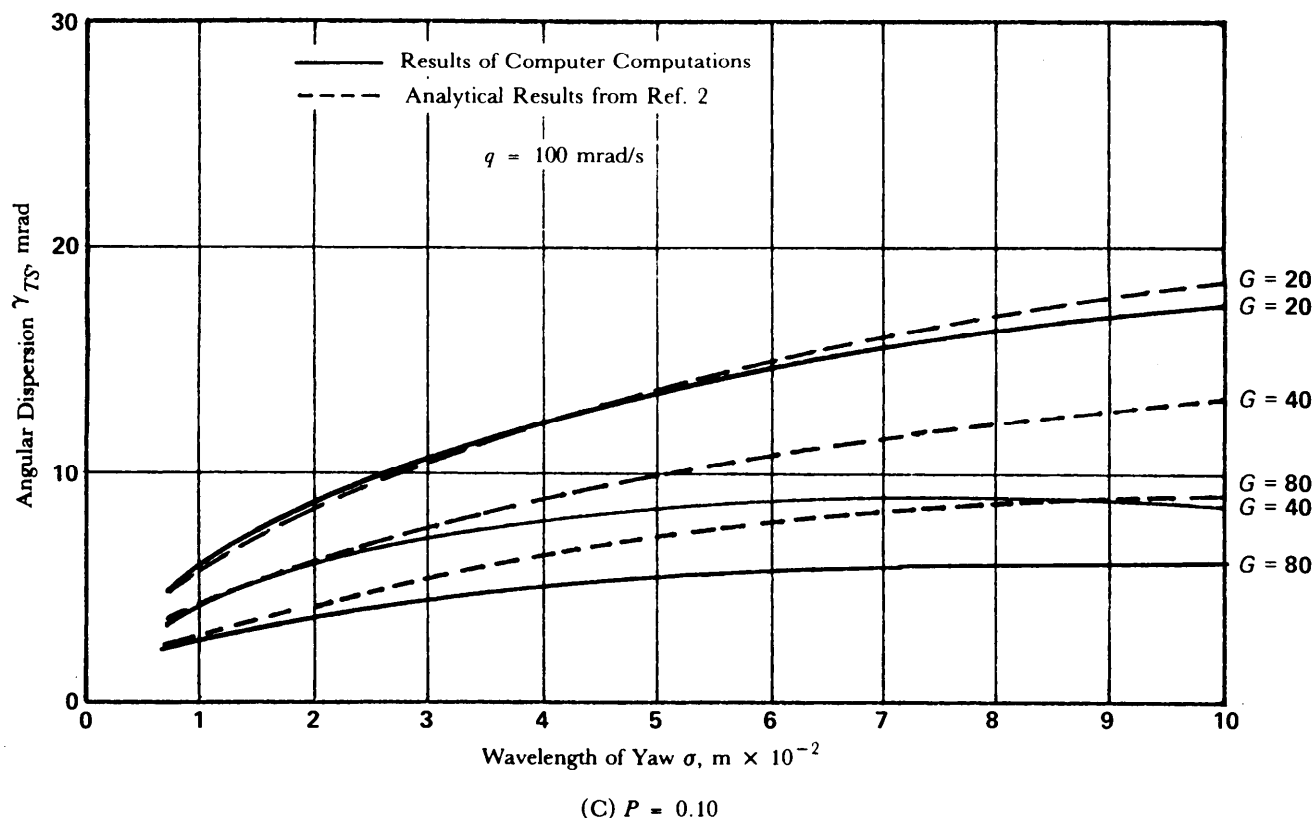
Figure 4-10. (cont'd)

acceleration level G all have substantial effects on the dispersion. The figures indicate that the dispersion is minimized by increasing the launcher length and the acceleration level while keeping the aerodynamic stability as high as possible, i.e., a small value of ớ.

Figs. 4-1 l(A), (B), and (C) show the effect of an initial translational velocity of 0.3 m/s, normal to the launcher line, on the angular dispersion for various values of P. The figures indicate that the launcher length P does not significantly affect the dispersion. An increase in the wavelength of yaw has a significant, beneficial effect on rockets with high aerodynamic stability. Increasing the acceleration level causes a decrease in the dispersion for all cases considered. Thus the angular dispersion γ_{TS} due to initial translational velocity is minimized by making the rocket acceleration as high as possible and the aerodynamic stability low.

Dynamic imbalance is the result of the longitudinal axis of inertia not being the same as the geometric longitudinal axis, i.e., the weight distribution is not uniform about the geometric axis and, thereby, displaces the axes a finite amount. When the rocket is spun on the launcher, release of the launcher constraints will result in a motion characteristic of the force-free precession of a rigid body unless the rocket is spinning about its principal axis of inertia.

The resulting precessional motion is equivalent to an initial angle velocity at launch. The magnitude of this angular velocity is

$$q_{equiv} = p\epsilon, \text{ rad/s} \qquad (4\text{-}20)$$

where

p = rocket spin rate about x-axis of body, rad/s

q_{equiv} = equivalent initial angular rate about y-axis of body due to spin with dynamic imbalance, rad/s

ϵ = angle between geometric and principal inertial axes of the rocket, rad.

After determining the equivalent angular rate by Eq. 4-20, the angular dispersion γ_{TS} can be assessed from Fig. 4-10.

(A) $P = 0$

(B) $P = 0.01$
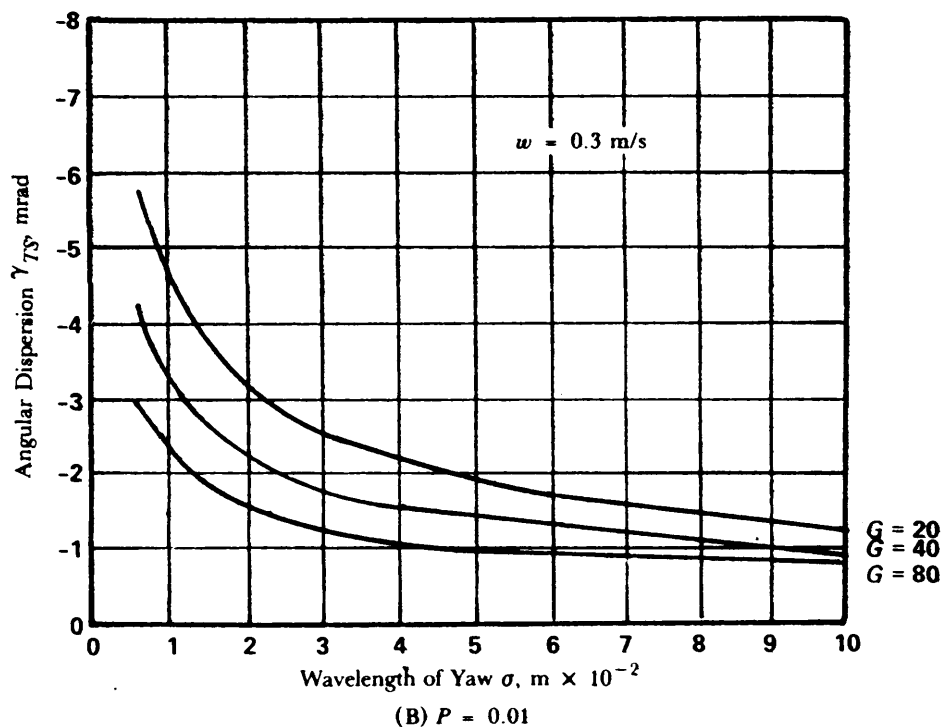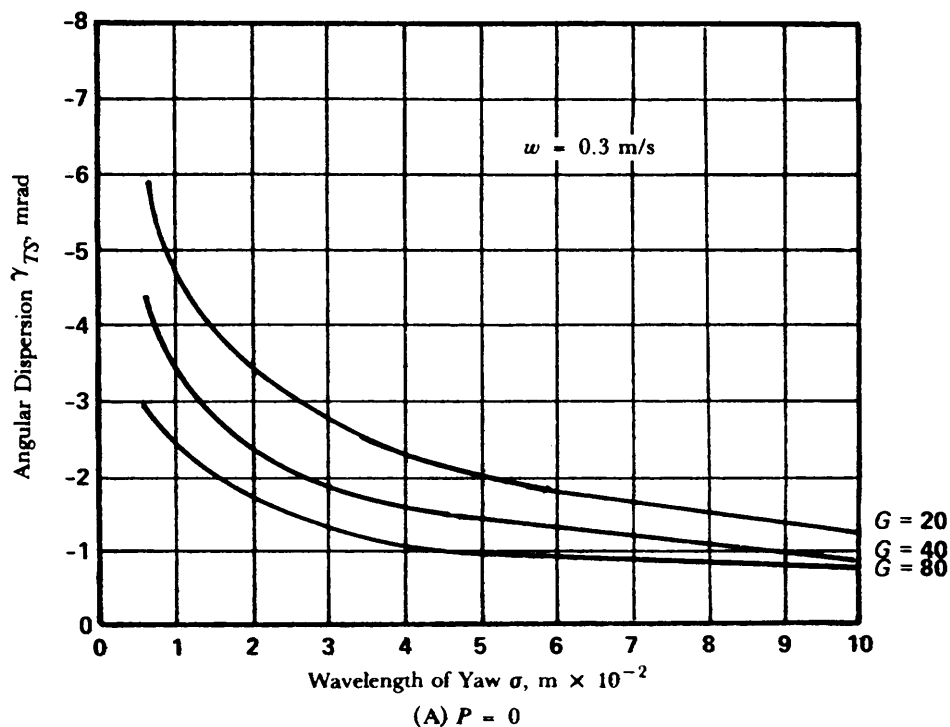
Figure 4-11.   Angular Dispersion Due to Initial Translational Velocity for Various P Values

(cont'd on next page)
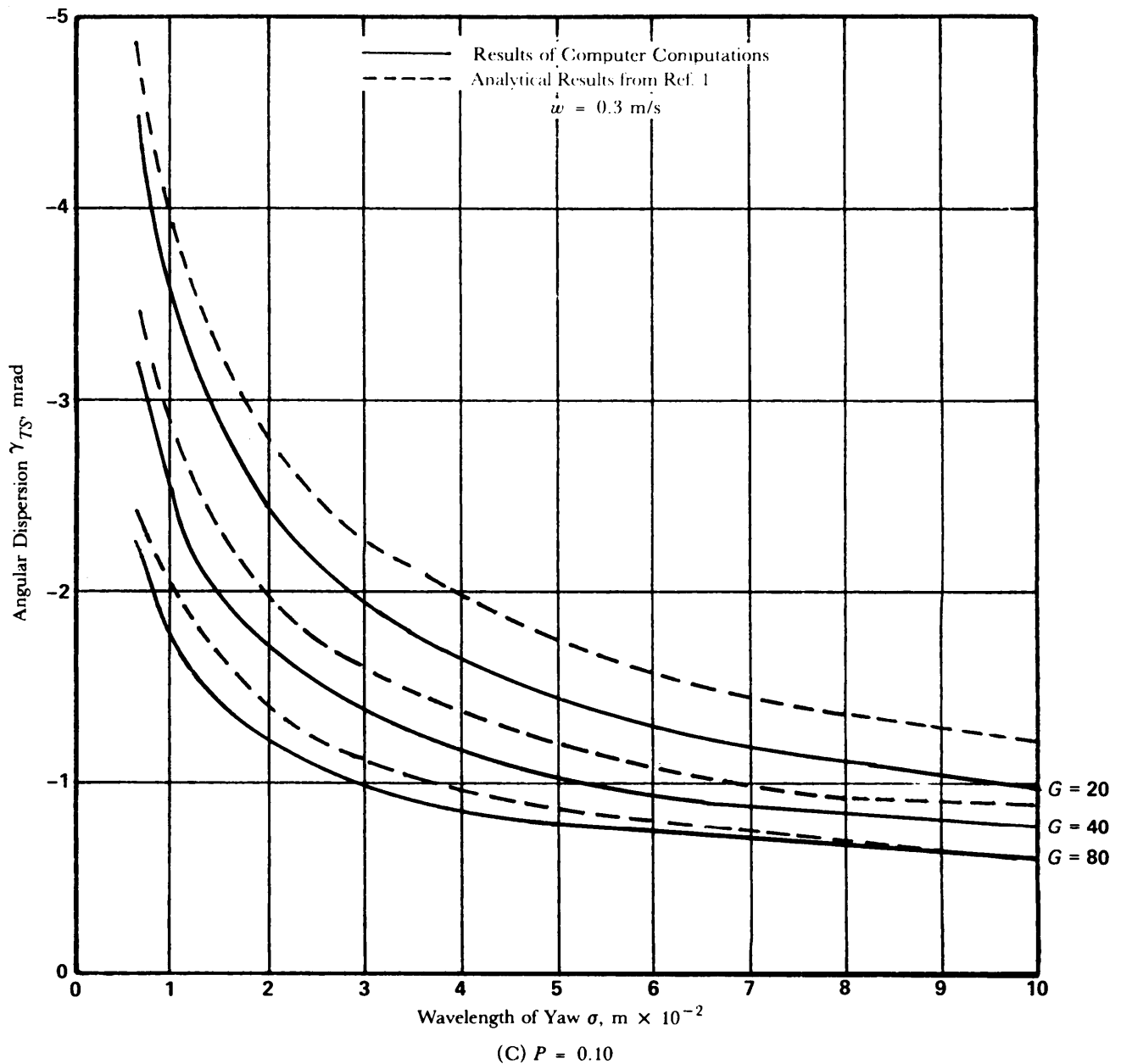
Figure 4-11. (cont'd)

The angular dispersion (see Fig. 4-10) due to dynamic imbalance is minimized by increasing the launcher length and the rocket acceleration while maintaining a high level of aerodynamic stability. In addition, the dynamic imbalance angle ϵ should be kept as small as possible by careful design and care in manufacturing. Also, the lower the spin rate, the less the effect of dynamic imbalance.

From the discussion of the launch-phase error effects on angular dispersion, conflicting design goals are seen to exist among some of the error sources. Note, for example, the conflict in desired stability between Figs. 4-10(A) and 4-1 1(A). Other conflicts will become apparent in par. 4-3.4 on the boost phase. Par. 4-4 on dispersion reduction techniques contains information on balancing the conflicting design requirements.

4-3.4 BOOST PHASE

Angular errors that originate during the boost phase of flight are primarily caused by wind normal to the direction of flight and by thrust misalignment. A qualitative description of the effect of wind and thrust misalignment was given in par. 4-2.4. Par. 4-3.4, however, presents some quantitative results that describe the effects of the important rocket parameters on the angular dispersion caused by these same two error sources, i.e. , wind and thrust misalignment. These results can be used for preliminary accuracy estimates.

This paragraph will present results for the nonspinning rocket. Spinning the rocket is effective in reducing the dispersion caused by thrust misalignment. Dispersion reduction for thrust misalignment is presented in par. 4-4.2.

Figs. 4-12 and 4-13 show the angular error γ_{TS} caused by a 3-m/s wind (u'_z) normal to the flight path of the rocket and by a 0.5-mrad thrust misalignment angle (δ'), respectively, on a nonrotating rocket for various P values.

Since the wind force on a symmetrical rocket does not depend on the roll orientation, spin does not affect the dispersion caused by wind. Therefore, Figs. 4-12(A), (B), and (C) are applicable to a spinning rocket system.

The angular dispersion caused by wind is reduced by keeping the aerodynamic stability as low as possible. Fig. 4-12 indicates that launcher length P has very little effect on the wind dispersion, provided the rocket acceleration is large.

Refer to Fig. 4-13. The dispersion due to thrust misalignment is reduced by keeping the aerodynamic stability as high as possible. The effect of acceleration level is most significant for rockets with low stability. The angular dispersion increases with an increasing acceleration level. The effect of launcher length is significant under all conditions. Since the launcher is assumed to be perfectly rigid, a long launcher would be desired. For a flexible launcher, the length would be tuned to the launcher stiffness to give the minimum dispersion.

4-3.5 BALLISTIC PHASE

The sources of ballistic-phase error were identified in par. 4-2.5 together with a discussion of the numerous and complex ways in which these errors are introduced. Since the ballistic phase of indirect fire rockets is usually much longer than the launch and boost phases, an assumption of constant aerodynamic and atmospheric conditions is no longer valid. Thus the forces acting on the rocket can no longer be considered only a function of the missile attitude, and the velocity-altitude history of the rocket becomes increasingly significant. Also small changes in the ballistic coefficient exert an integrative effect along the trajectory and may also cause significant changes in range and deflection. For these reasons, dispersion during the ballistic phase is usually developed through parametric data by using both standard and perturbed trajectories. The error effects are then linearized with respect to the magnitude of the perturbation in a given parameter of interest. This method of accounting for ballistic-phase dispersion is demonstrated in par. 4-.5.5 in which figures are presented that depict typical dispersions in range and deflection for a unit change in ballistic error source.

For purposes of analysis, the ballistic phase errors are grouped into four independent effects, i.e.,

1. Ballistic winds
2. Ballistic coefficient
3. Atmospheric density
4. Fuzing.

Ballistic winds and fuzing were discussed in par. 4-2.5. Ballistic coefficient dispersions include all effects caused by drag changes and burnout mass. Density dispersions include all effects caused by static atmospheric variations.

The dispersions caused by ballistic-error effects are quite linear with respect to range when depressed QE's are used for ranges less than maximum. However, the dispersions increase dramatically when lofted trajectories are used because the flight time and total path length are greatly increased, and the
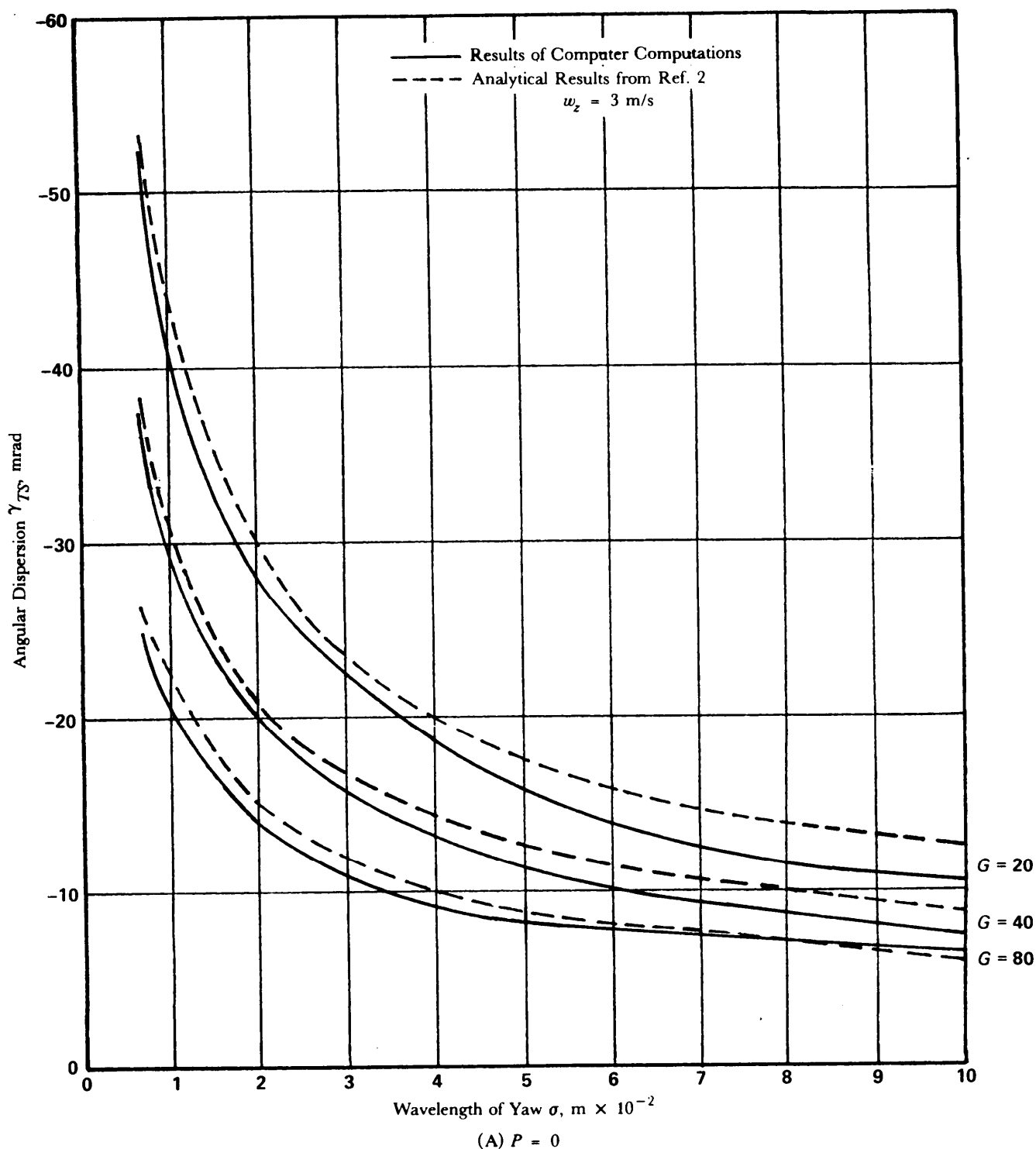
Figure 4-12.   Angular Dispersion Due to Wind for Various P Values

(cont'd on next page)

error source then has a potentially longer action period. The relative magnitudes of the dispersions of the stated independent effects are functions of the magnitudes of the error sources and the selection of a lofted or depressed QE.
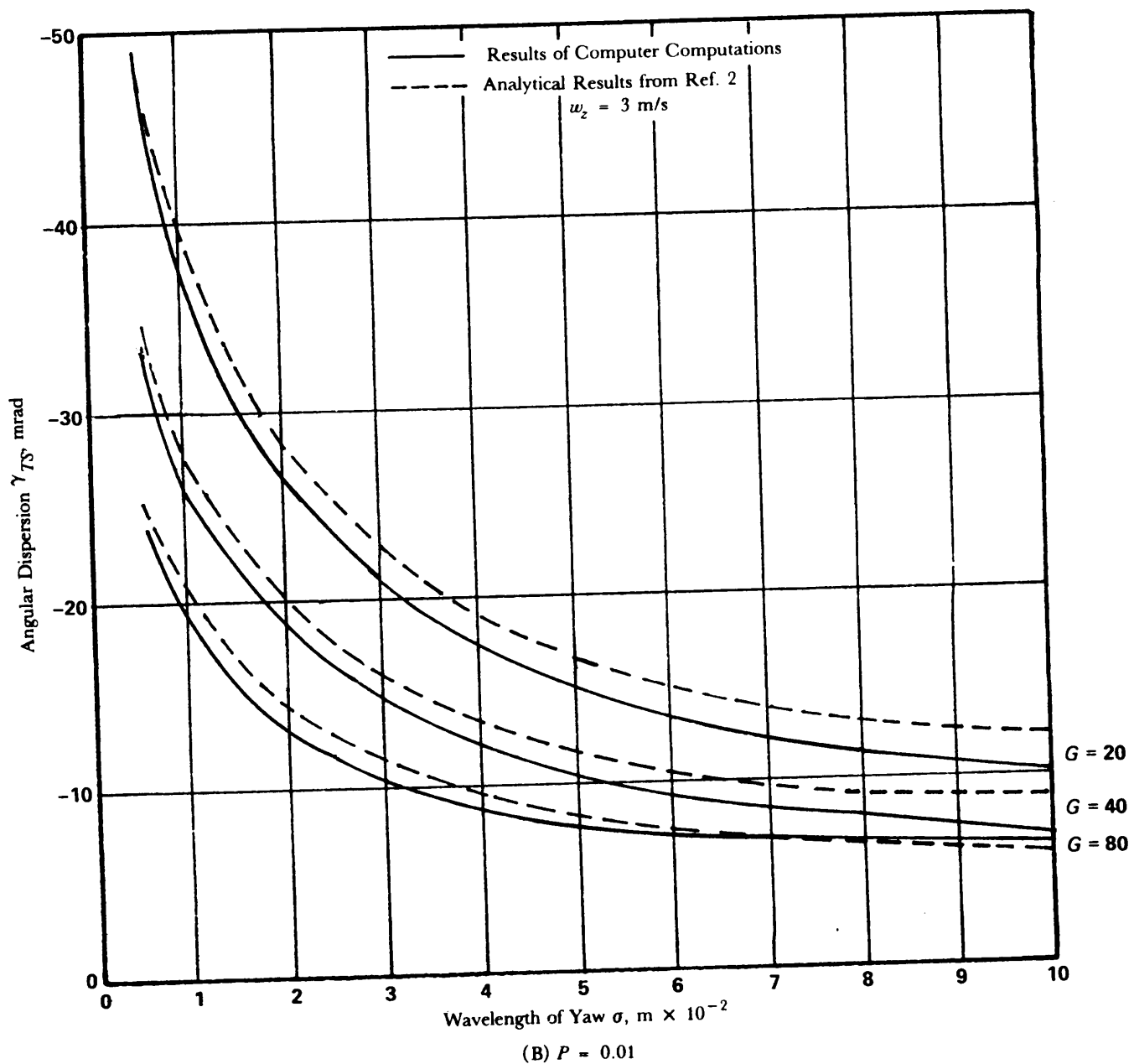
Figure 4-12. (cont'd)

4-4 DISPERSION REDUCTION

4-4.1 GENERAL

Par. 4-3.3 identified one of the conflicting design requirements on rocket parameters that occur when the designer attempts to reduce the dispersion of a given rocket. This paragraph presents information pertinent to the reduction of free rocket dispersion.

Generally, dispersion reduction techniques can be classified into two principal methods. The first method is to reduce the magnitude of the error source. This can be accomplished by careful attention to manufacture and assembly of the rocket, by protection of the rocket from mishandling in transport and use, and by increased attention to launcher design and manufacture. The second method is to

(C) $P = 0.10$
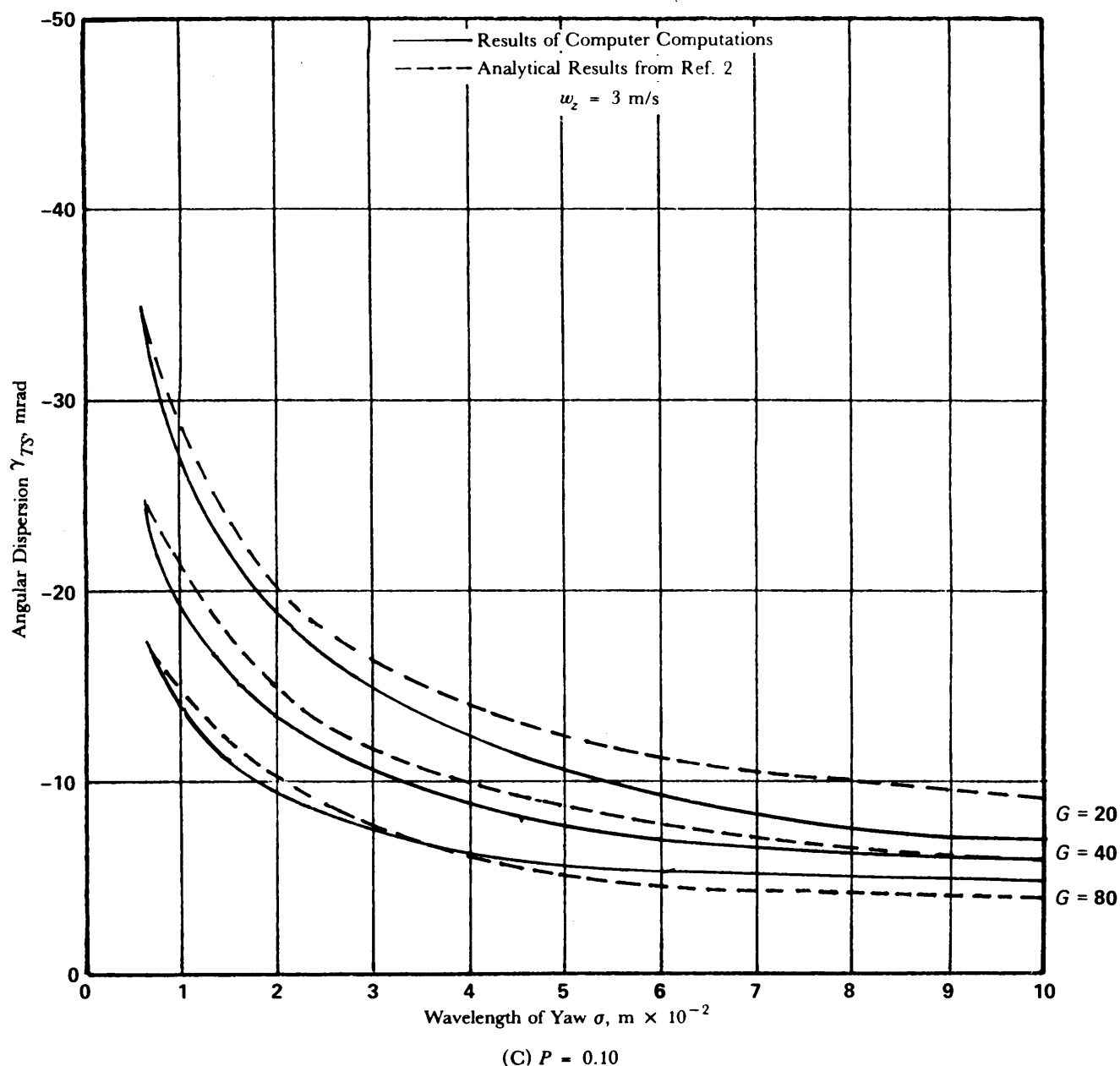
Figure 4-12. (cont'd)

design the rocket to reduce its sensitivity to error source magnitudes. Most of the topics in this paragraph fall within this second method.

Several important considerations that the rocket designer must bear in mind while using the techniques and data contained in this chapter are

1. Attempts to reduce manufacture and assembly tolerances can become prohibitively expensive beyond a specific point. The effectiveness of free rockets generally requires firing several at a target; therefore, relatively large numbers of rockets must be manufactured. Accordingly, the cost per rocket should be an important consideration in the selection of a dispersion reduction technique.

2. Some of the techniques discussed impose additional complexity on the rocket or launching device. This complexity can affect both cost and reliability.

MIL-HDBK-762(MI)
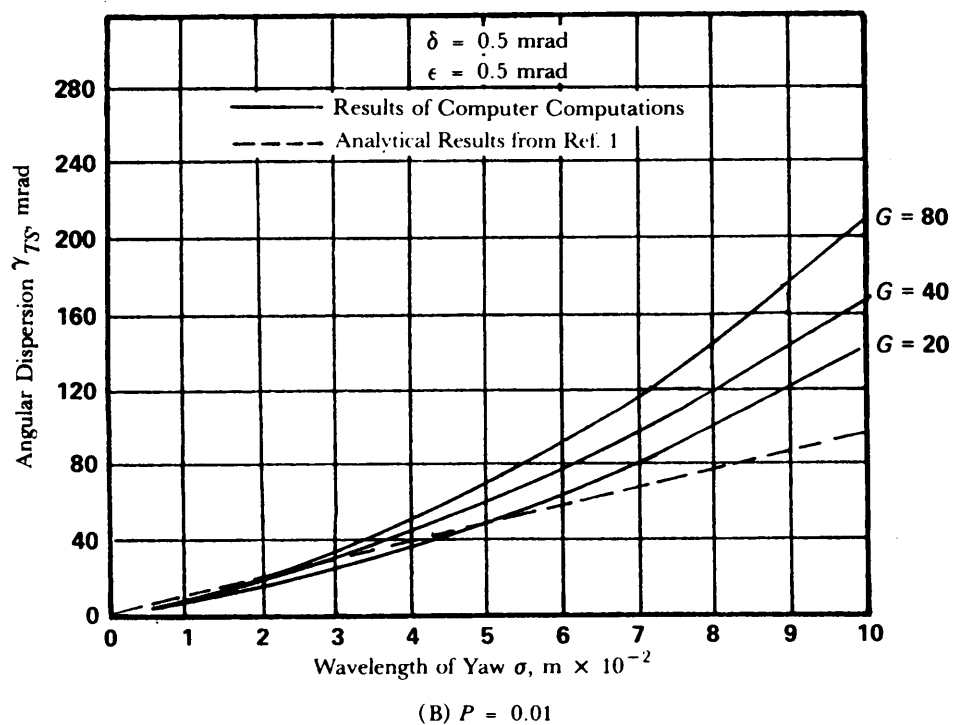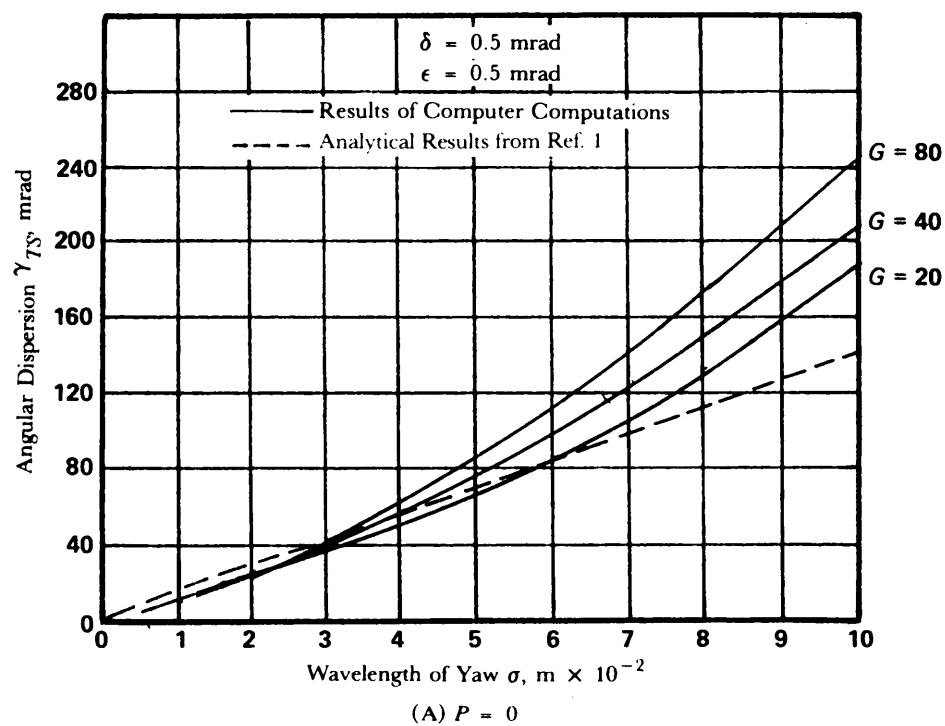
Figure 4-13. Angular Dispersion Due to Thrust Misalignment for Various P Values—
Zero Spin

(C) $P = 0.10$
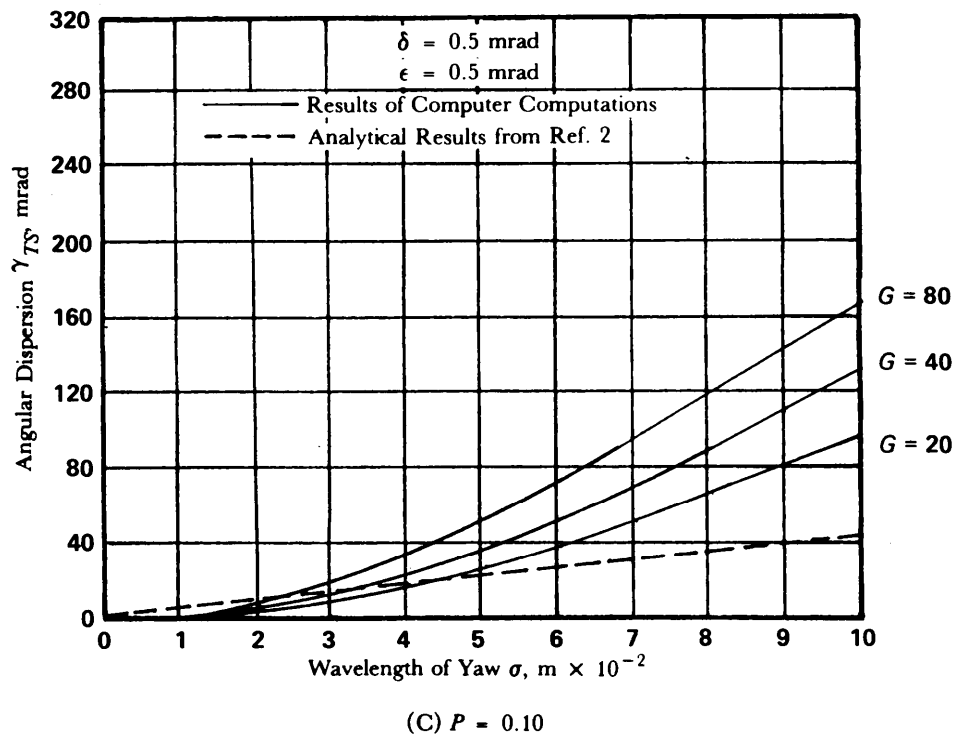
Figure 4-13. (cont'd)

3. A proper perspective in the reduction of error sources should be maintained. Complete elimination of, or reduction of sensitivity to, only one error source may not appreciably affect the overall accuracy of a rocket system; however, moderate reduction of several of the error sources may produce better results at less design and manufacturing expense.

4. Balanced attention should be given to the rocket system bias errors as they relate to the random or precision errors. Par. 4-2.1 pointed out that bias errors affect the center of a group of rocket impacts, whereas precision errors affect the dispersion of impacts away from the center of the group. Reducing precision errors without effective reductions in bias errors would result in grouping rocket impacts away from the target area. Efforts to reduce precision error below a given value (dependent on the bias errors of the system) would be counterproductive.

5. Finally, the designer must be aware of the possibility of introducing a source of dispersion while attempting to reduce another source of dispersion. As an example, the paragraph on rocket spin effects will point out that while spinning a rocket is effective in reducing certain types of errors, very high spin rates introduce complex dynamic motion of the rocket, aerodynamic effects, and increasingly complex motions of the rocket and/or launcher systems. The paragraphs that follow introduce dispersion reduction methods and their effects.

4-4.2 THE EFFECT OF SPIN

Par. 4-3 pointed out a conflict on aerodynamic stability and wavelength of yaw caused by winds and thrust misalignment. The conflicting requirements on the wavelength of yaw are a result of an attempt to decrease two different types of errors by using the same technique, namely, changing the aerodynamic stability. The combination of the two error sources resulted in Fig. 4-14 which suggests an optimum value of ó.

However, a different method, i.e., spinning the rocket about its longitudinal axis, for reducing the dispersion caused by thrust misalignment is introduced in this paragraph. Rocket spin is effective in reducing all errors that are body-fixed—e.g., thrust and fin misalignments, and thrust and CG offsets.
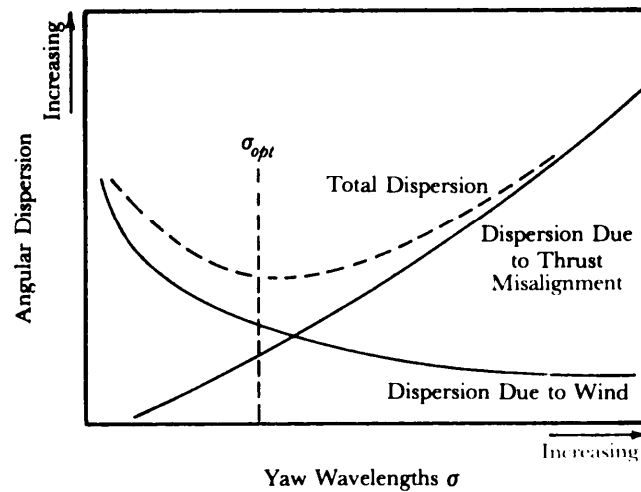
Figure 4-14. Optimum Wavelength of Yaw for Minimum Total Dispersion

Fig. 4-15 illustrates the buildup of the dispersion of a nonrotating rocket with a thrust misalignment. Because the thrust is applied in an unchanging direction, the dispersion grows steadily with time. Fig. 4-16 shows the effect of giving the rocket a slow spin about its longitudinal axis. Slow spin is defined as a spin during which gyroscopic moments are not yet significant. In this case the direction of the thrust changes as the body rotates. The result is a reduction in total angular dispersion.
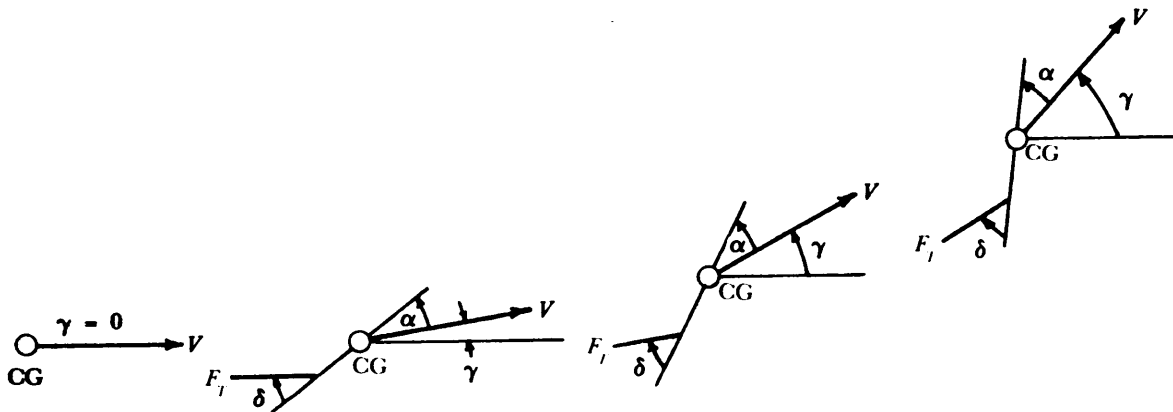
Figure 4-15. Growth of Angular Dispersion For A Rocket With A Thrust Misalignment and No Spin
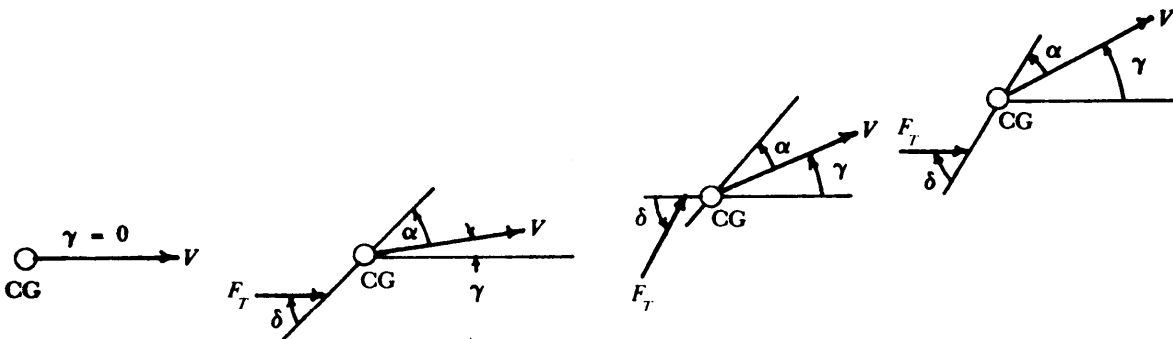
Figure 4-16. Growth of Angular Dispersion For A Rocket With A Thrust Misalignment and Slow Spin

4-28

Fig. 4-17 shows the variation of the angular dispersion with distance for a typical rocket with and without a slow spin.

Refs. 1 and 2 contain extensive treatments of the effects of spin on dispersion. Many of the analytic results presented herein for spin result from these works.

From these previous figures and discussion, it follows that spin of any kind will have some effect on the angular dispersion of a rocket. The rotational motion of the rocket has been shown to be characterized by the wavelength of yaw; therefore, it is to be expected that this parameter will have a strong influence on the effectiveness of any spin program.

As was shown in Figs. 4-7 and 4-17, most of the angular dispersion takes place during the first yaw oscillation; therefore, the spin motion during this period will have the most influence on the angular dispersion.

If the spin is constant or increasing in the same direction, the error will tend to accumulate because the acceleration of the rocket causes the influence of the misalignment to decrease as the rocket momentum increases. Therefore, the dispersion occurring in the first half of the spin cycle is not completely compensated for during the second half. Accordingly, a uniform spin program will always result in some finite error.

These considerations have led investigators to study nonuniform spin programs with the intention of developing techniques that would achieve zero angular dispersion. The simplest program to visualize is the instantaneous, 180-deg rotation of the vehicle at some point in the trajectory. The point is chosen so that the accumulation of angular dispersion to that point is completely eliminated by reversing the direction of the error for the remainder of the flight. This concept has been incorporated
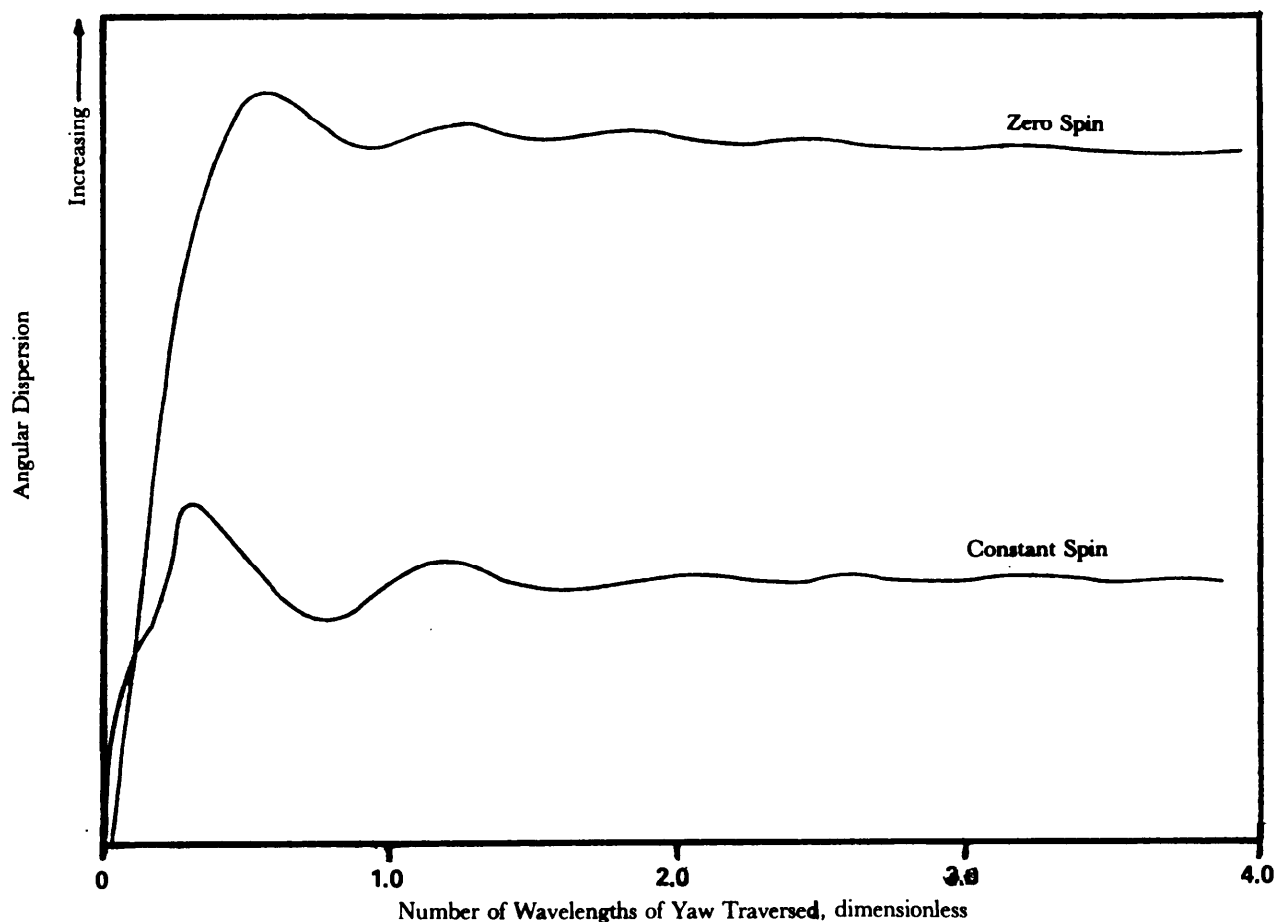
Figure 4-17. Effect of Spin on Buildup of Angular Dispersion Due to Thrust Misalignment

into the Spin-Buck Program discussed in par. 4-4.2.4. Several spin programs that have been of interest to designers of free rockets are discussed in the paragraphs that follow.

The amount of dispersion reduction obtained from any given spin program is measured by the parameter β which is the ratio of the dispersion with a spin program to the dispersion with no spin program, i.e.,

$$\beta = \frac{\gamma_{TS} \text{ (with spin program)}}{\gamma_{TS} \text{ (no spin)}} \text{, dimensionless} \tag{4-21}$$

where

    β = dispersion reduction factor, dimensionless.

Other paragraphs in this chapter indicate values of β for several spin programs. The concept of a dispersion reduction factor is not limited to spin but may be extended to include any dispersion reduction technique.

Once estimates of β are known, the optimum value of ó (see Fig. 4-14)—which accounts for the combined effects of the spin program on thrust misalignment and the effects of winds—can be determined. Ref. 4 gives, for short launcher lengths,

$$\sigma_{opt} = \left(\frac{4\pi k^2 V_w}{\sqrt{G'} L\beta} \right)^{2/3} \text{, m} \tag{4-22}$$

where

    σ_{opt} = optimum wavelength of yaw, m

    V_w = wind velocity with respect to inertial coordinates, m/s

    L = thrust misalignment distance, m.

The dispersion for this value of σ_{opt} is given by

$$\gamma_{TS} = \frac{\sqrt{3}}{8} \left[\frac{(4\pi)^2 L\beta V_w^2}{G'k^2} \right]^{1/3} \text{, rad.} \tag{4-23}$$

For the purposes of this chapter the effect of angular thrust misalignment distance L may be estimated by the approximate relationship

$$L \approx l_i\delta \text{, m.} \tag{4-24}$$

The paragraphs that follow indicate the optimum design depends on yaw oscillation wavelength, launching technique, and error source magnitude. To evaluate these items, these paragraphs present a more detailed discussion of the errors and the means by which dispersion under varying conditions is computed.

Fig. 4-17 indicated that, with constant spin, thrust misalignment has its greatest effect during the first wavelength of yaw but is almost negligible during the remainder of the flight. This observation leads to the use of the number of revolutions made by the rocket during this initial wavelength as an important spin parameter. n_o is the number of revolutions that rocket makes during the first wavelength of yaw. Fig. 4-18 shows the dependence of the dispersion reduction factor β on n_σ. The dashed line is the theoretical value taken from methods in Ref. 2.

Various techniques can be used to achieve spin, but any method used must be capable of spinning the rocket without imparting unwanted motions. The importance of spin during the early portion of
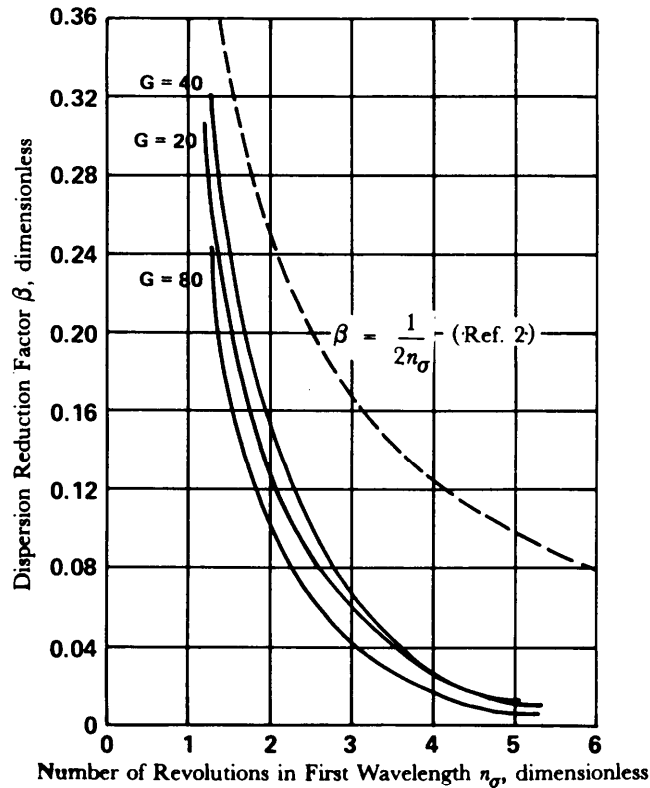
Figure 4-18. Effect of Constant Spin on Dispersion Reduction Factor

flight eliminates aerodynamic fins as a means of obtaining spin since fins are least effective during this time. One common method of providing spin is through auxiliary rockets fired in a circumferential direction.

The importance of early spin has led to the development of systems in which spin is accomplished while the rocket is still on the launcher. These systems involve many mechanical problems because of the difficulties involved in clearing the rocket fins and in releasing the launcher constraints without introducing translational or angular motion to the rocket. Further consideration of launcher-associated problems is presented in par. 4-4.2.6 and Chapter 8.

Fig. 4-18—together with Eq. 4-23—shows that the angular dispersion decreases as the number of revolutions in the first wavelength increases. On the other hand, the dispersion due to dynamic imbalance increases with spin. These two effects result in an optimum spin rate, beyond which the dispersion reduction associated with thrust misalignment is lost to the dynamic imbalance effect.

4-4.2.1 Constant Spin Rate

In practice, constant spin is not achieved. The programs referred to as constant spin actually are composed of a period of high angular acceleration from spin rockets or from other spin-producing technique, followed by a slow deceleration caused by aerodynamic forces on the fins.

Figs. 4-19(A), (B), and (C)—for the case of constant spin rate—present the effects of rocket acceleration level G, dimensionless launcher length P, and wavelength of yaw ó on the dispersion reduction factor β. As shown in the figures, the wavelength of yaw has the greatest influence on the dispersion reduction. The spin rates used for the constant-spin results are the optimum values for a dynamic axis misalignment (dynamic imbalance ϵ) of 0.5 mrad.

4-31
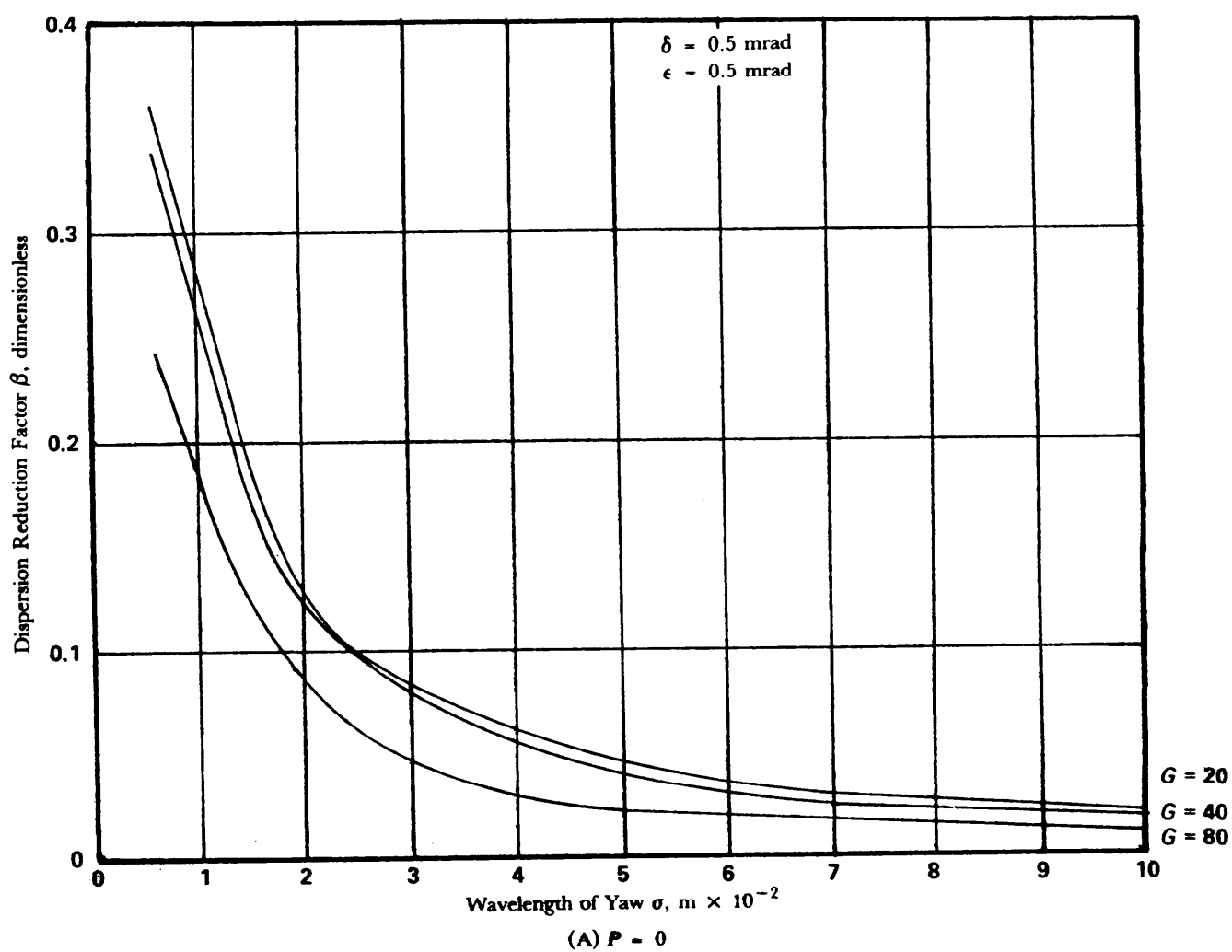
Figure 4-19. Constant Spin Rate; Various P Values
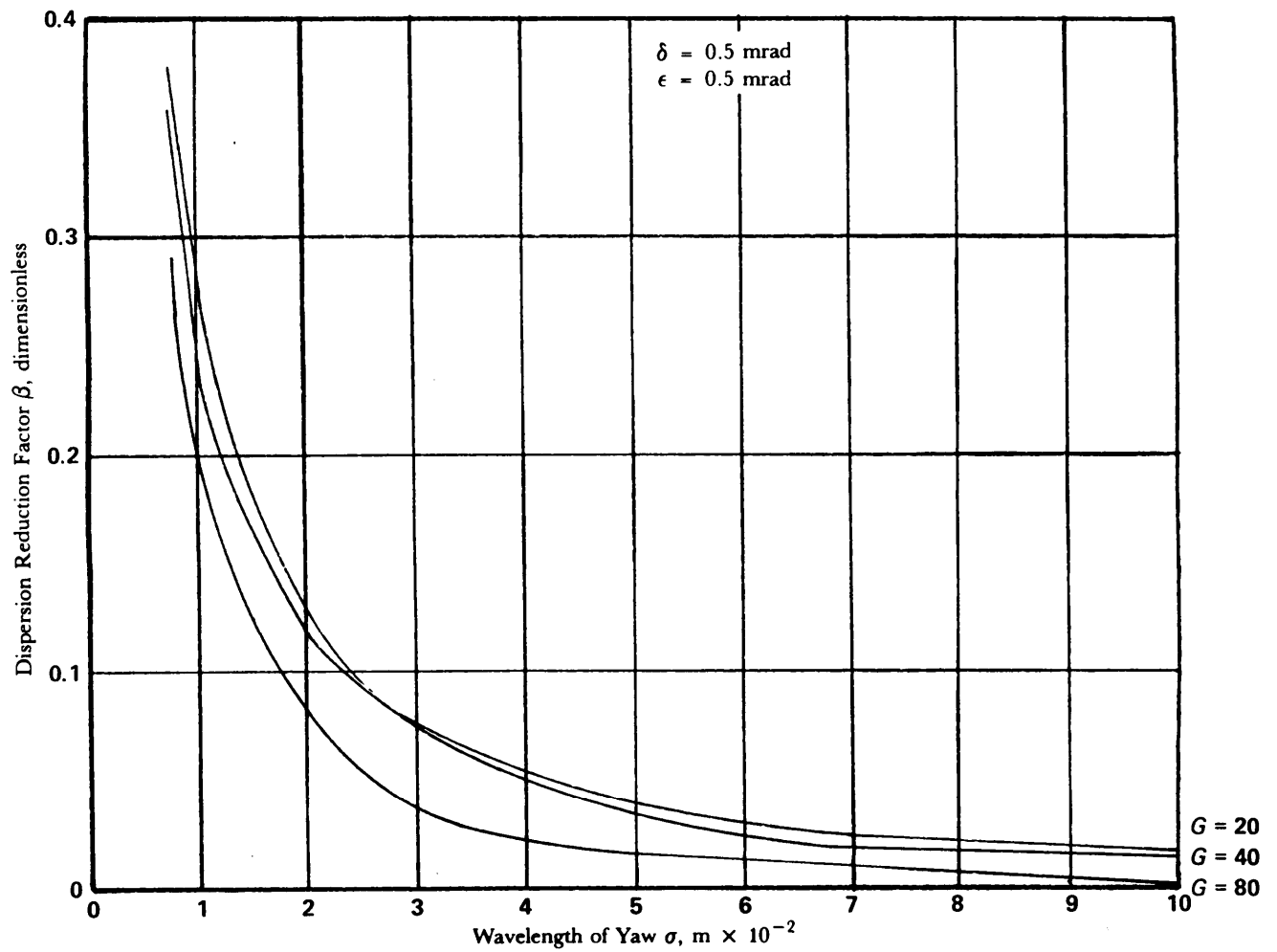
(B) $P = 0.01$
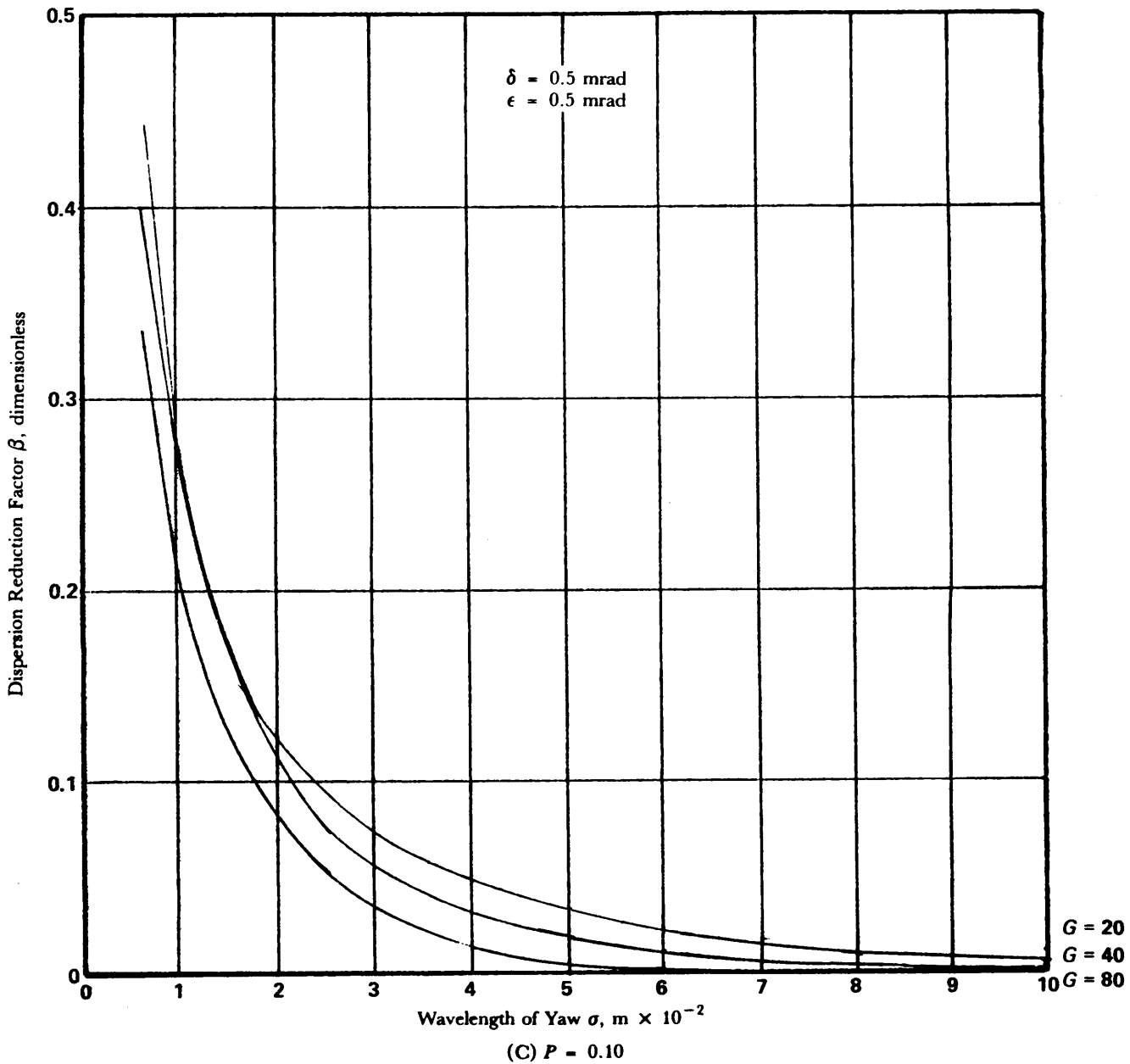
Figure 4-19. (cont'd)

Figure 4-19. (cont'd)

4-4.2.2 Constant Acceleration

The dispersion reduction technique that is the easiest to implement is the constant spin acceleration. It can be achieved by canting the nozzles of the rocket motors (if more than one motor is used), by placing fins in the rocket exhaust, or by fluting the exhaust nozzle to produce spin of the exhaust gases. Unfortunately, due to the slow initial spin, the technique is not as effective as the constant spin.

Figs. 4-20(A), (B), and (C) present the effects of the rocket variables on the dispersion reduction factor for constant spin acceleration. The most significant variable is the wavelength of yaw which should be long to minimize the dispersion.

(A) $P = 0$

(B) $P = 0.01$
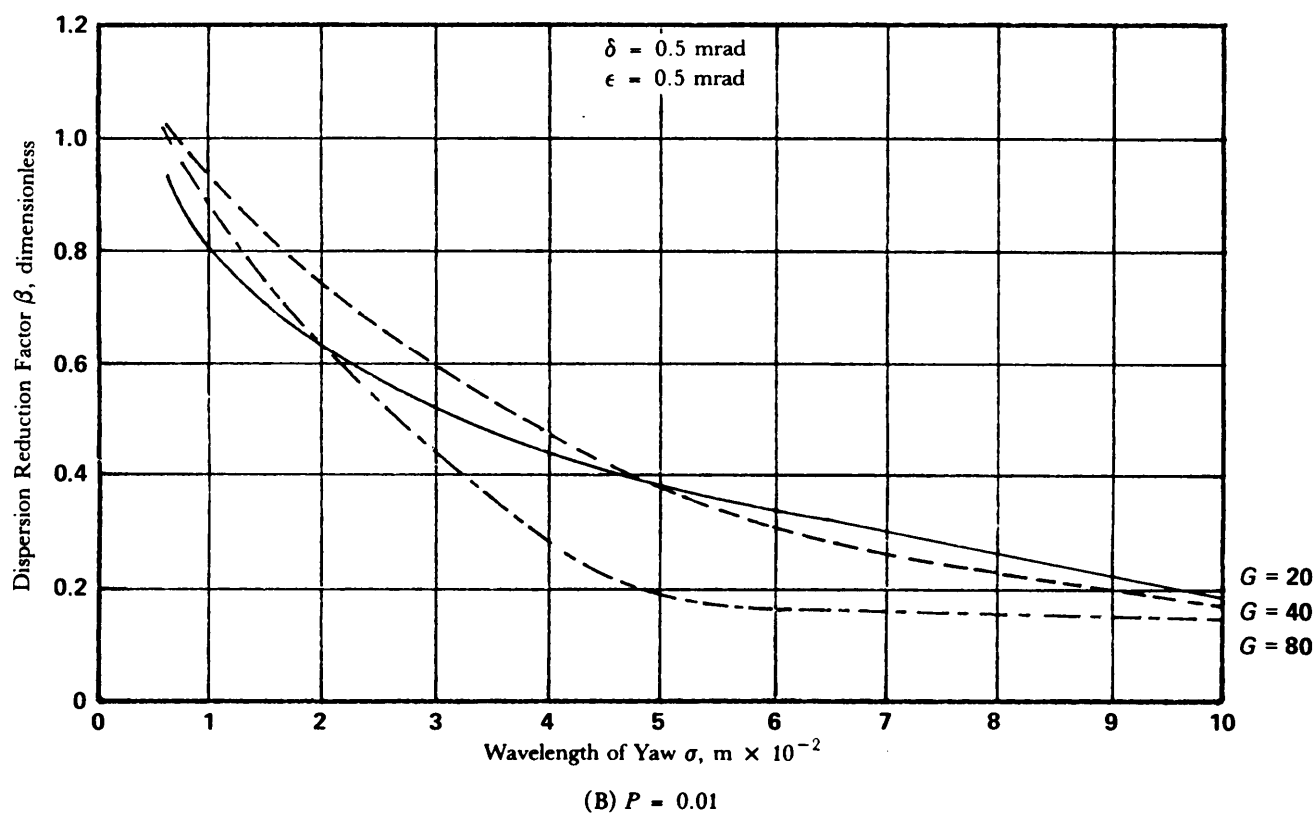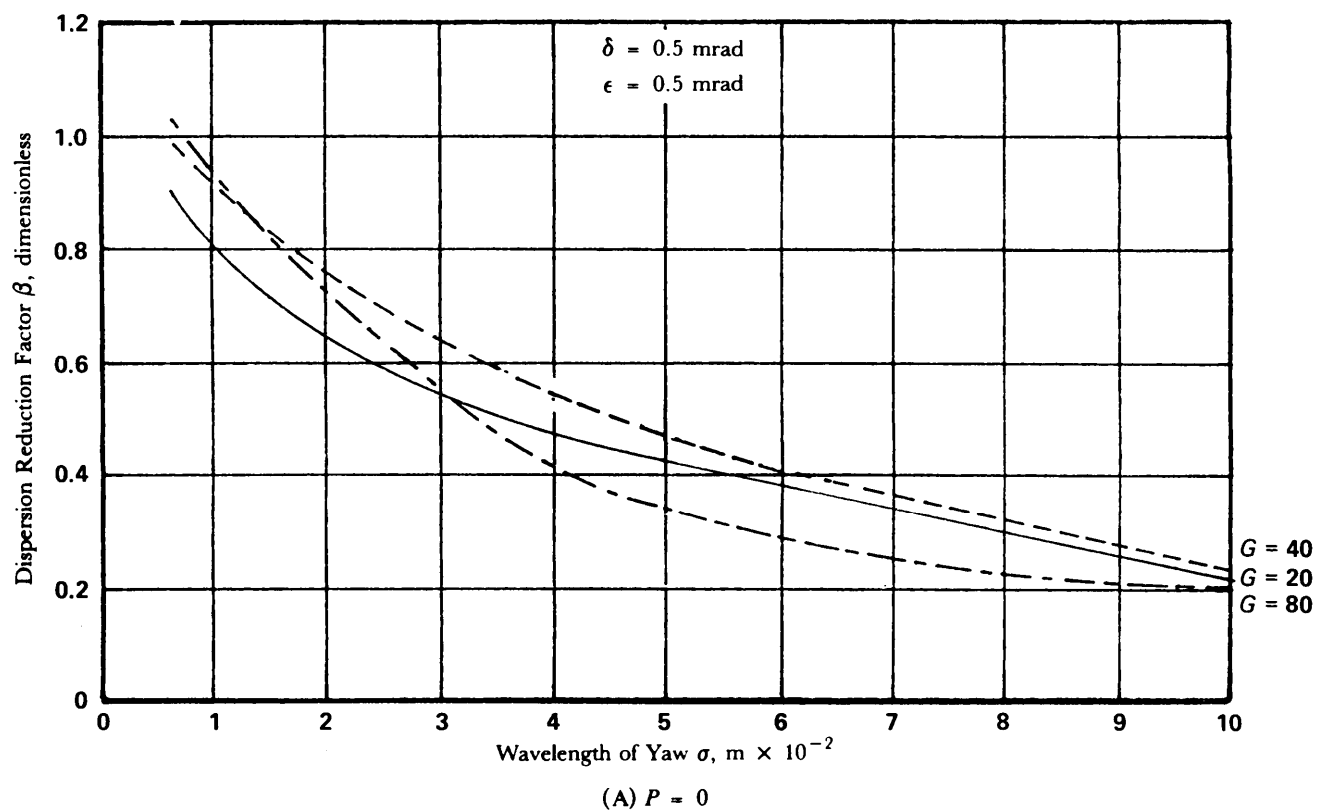
Figure 4-20. Constant Spin Acceleration; Various P Values

(C) $P = 0.10$
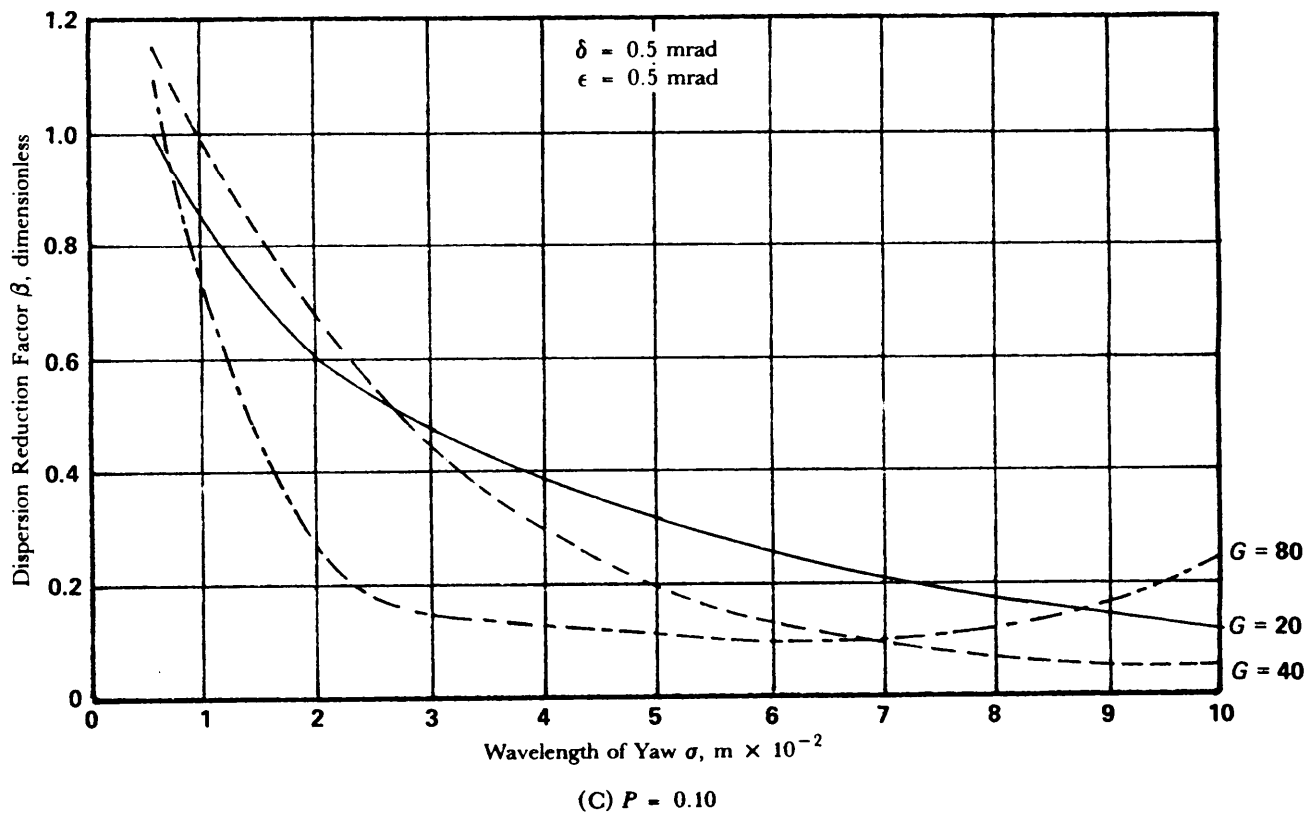
Figure 4-20. (cont'd)

4-4.2.3 Constant Deceleration—Slowly Uniformly Decreasing Spin (SUDS)

The preceding spin programs always result in some finite dispersion. According to the mathematical theory of rocket flight (see Refs. 5, 6, and 7), it is possible to devise spin programs that result in zero angular dispersion. One such program is that of a Slowly Uniformly Decreasing Spin (SUDS); another is the Spin-Buck program (par. 4-4.2.4).

The SUDS program begins with an initial spin rate that is followed by a constant deceleration; both of these are functions of the rocket parameters. The angular error is very sensitive to changes in the spin rate or the deceleration. For this reason it is not possible to achieve zero dispersion in practice. Also, the limitations of rocket theory make the zero dispersion result invalid. Figs. 4-21(A), (B), and (C) present the dispersion reduction for SUDS for various P values when the assumptions of the rocket theory are removed.

(A) $P = 0$

(B) $P = 0.01$
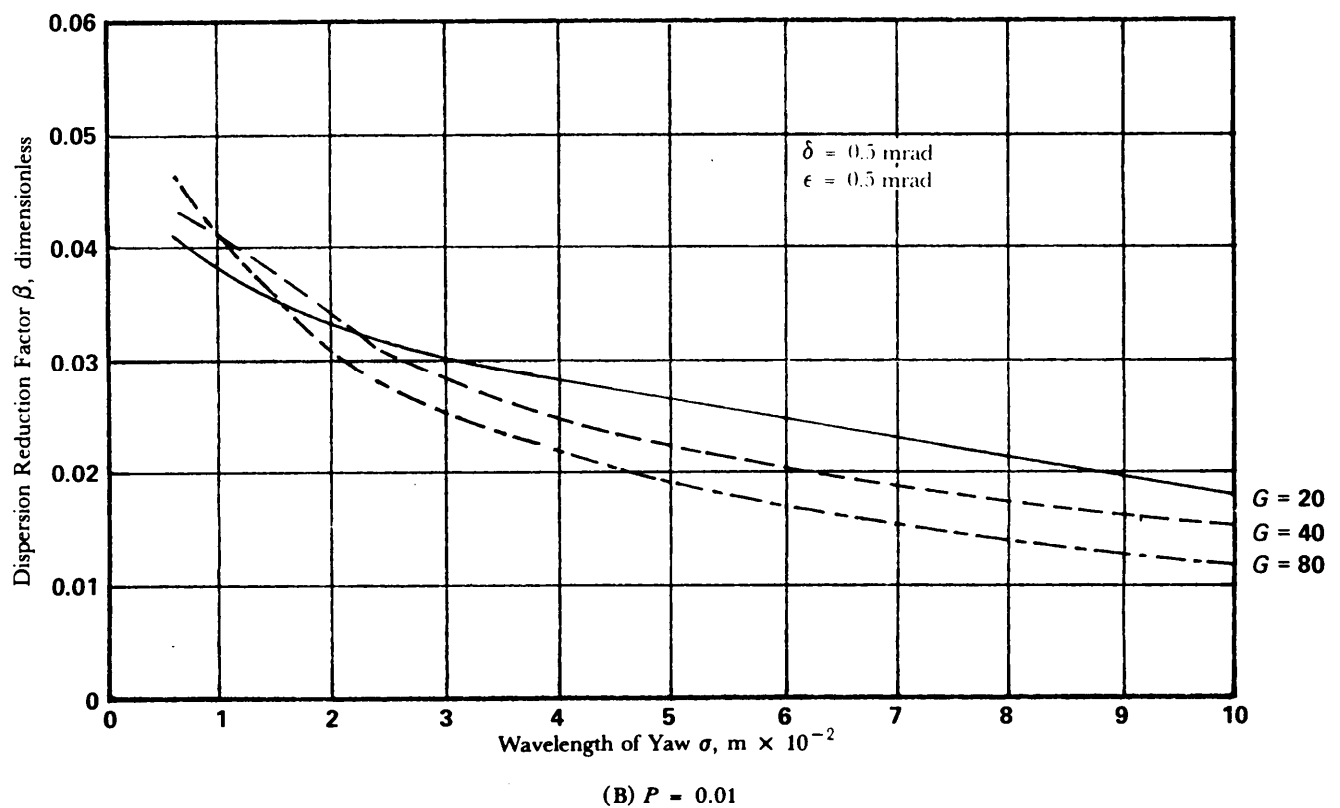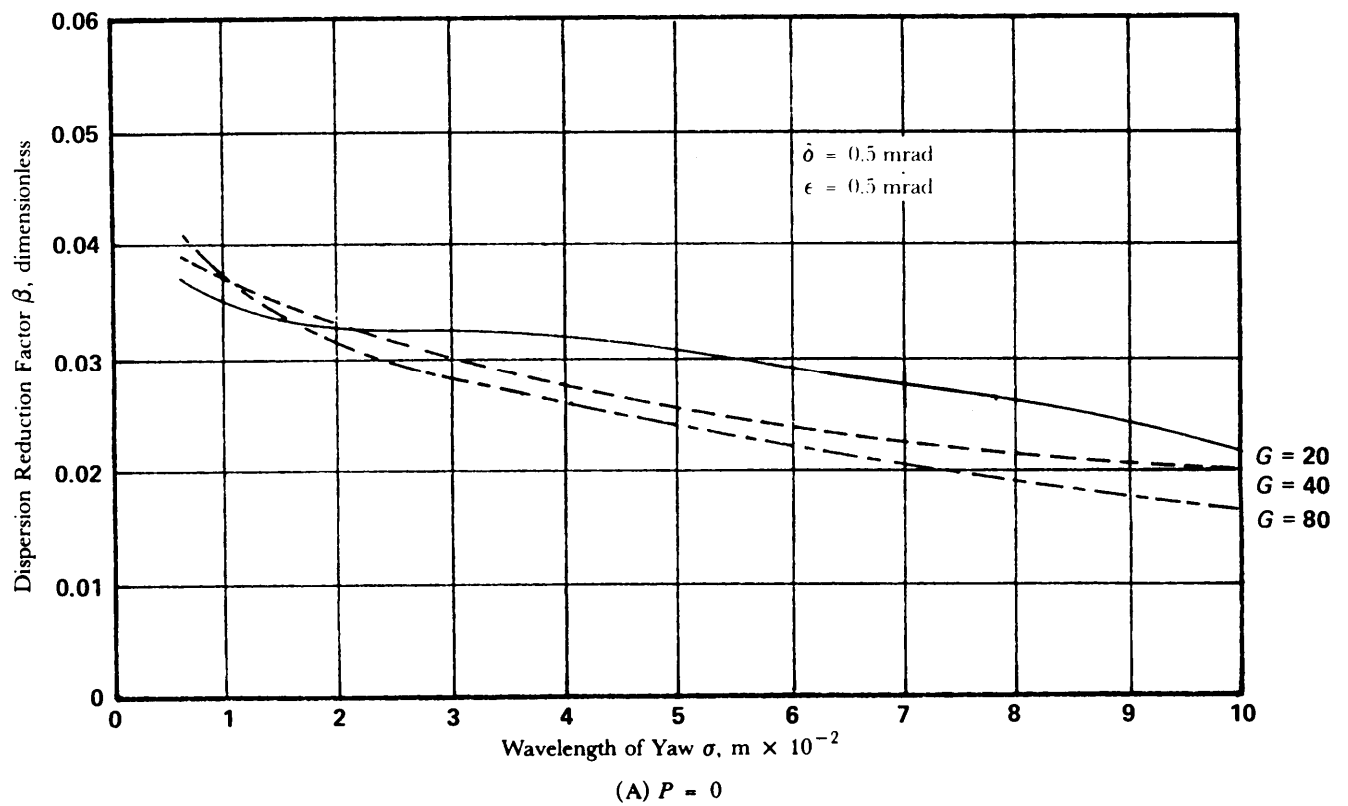
Figure 4-21. Slowly Uniformly Decreasing Spin (SUDS)

(C) $P = 0.10$
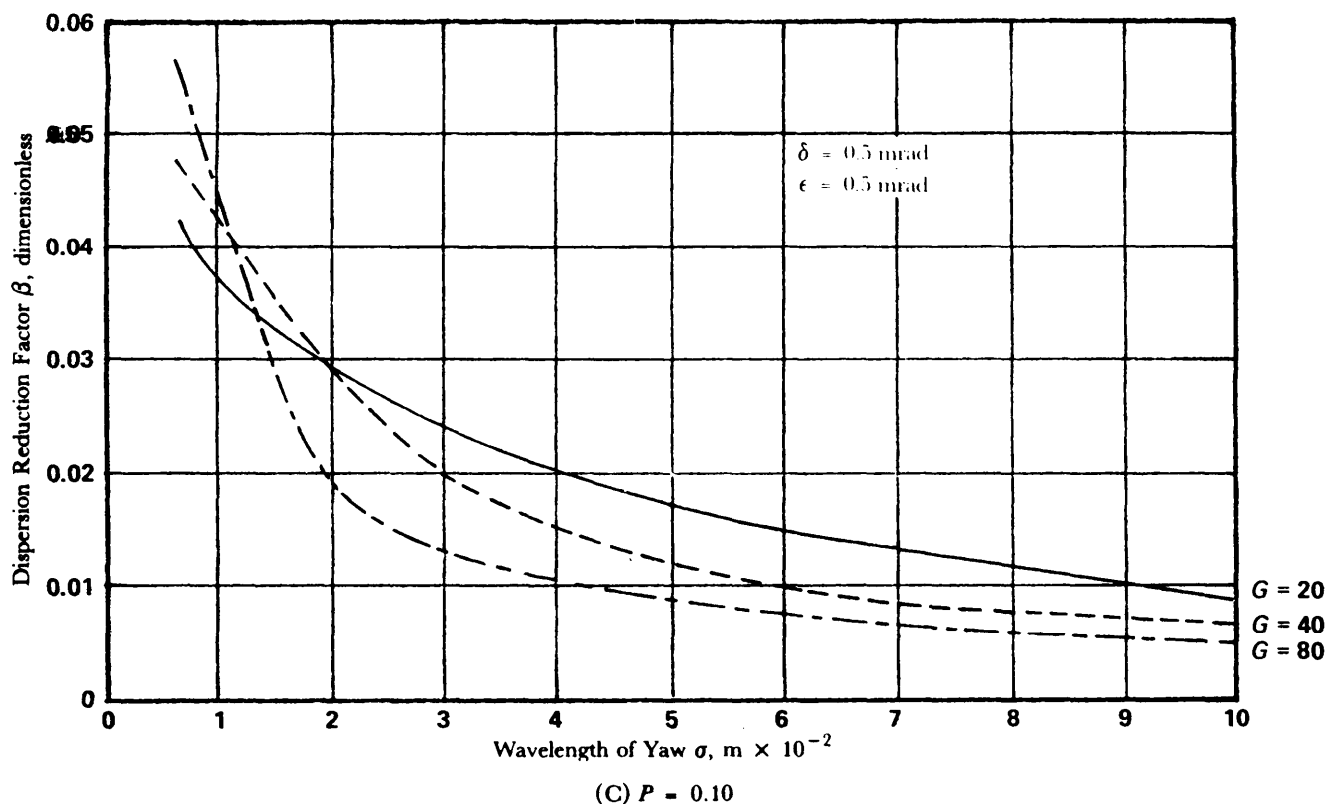
Figure 4-21. (cont'd)

4-4.2.4 Spin-Buck

The Spin-Buck concept is an attempt to eliminate the angular dispersion caused by thrust misalignment by reversing the spin direction of the rocket. By this reversal, the error accumulated prior to the reversal should be cancel led by the subsequent error (see Ref. 4). The motivation behind this concept can be better understood if we consider the case of a nonrotating rocket with a thrust misalignment. From Fig. 4-17, dispersion builds up rapidly during the first wavelength. If at some instant during this buildup the rocket were rotated 180 deg, the thrust misalignment would cause the accumulation of dispersion to reverse direction. With the proper choice of the rotation point, the resultant dispersion will be zero.

Since most of the angular dispersion occurs in a very small portion of the flight, it might be expected that the point at which the rotation occurs is very near the launch point. Fig. 4-22 shows how the distance for the instantaneous rotation varies with rocket acceleration level and wavelength of yaw.

From a practical standpoint, one shortcoming of this concept is the high sensitivity of the dispersion reduction factor to errors in the buck distance. Fig. 4-23 indicates that, for a rocket acceleration level G = 40, an error in the rotation or buck distance of approximately 10% changes the dispersion reduction factor ß from zero to 0.4.

The Spin-Buck concept is accomplished by firing two banks of spin rockets, one following the other and in opposing directions. The net result is similar to the idealized case just discussed. A small residual spin is allowed to reduce the effect of any error related to inaccuracies in the system. Field tests of the Spin-Buck concept indicate that a dispersion reduction factor of 0.1 is possible.

4-4.2.5 Very High Spin Rates

Previous paragraphs have presented information on rockets considered to have a slow spin; however, in this paragraph very high spin rates will be considered. When spin is used to reduce other sources of
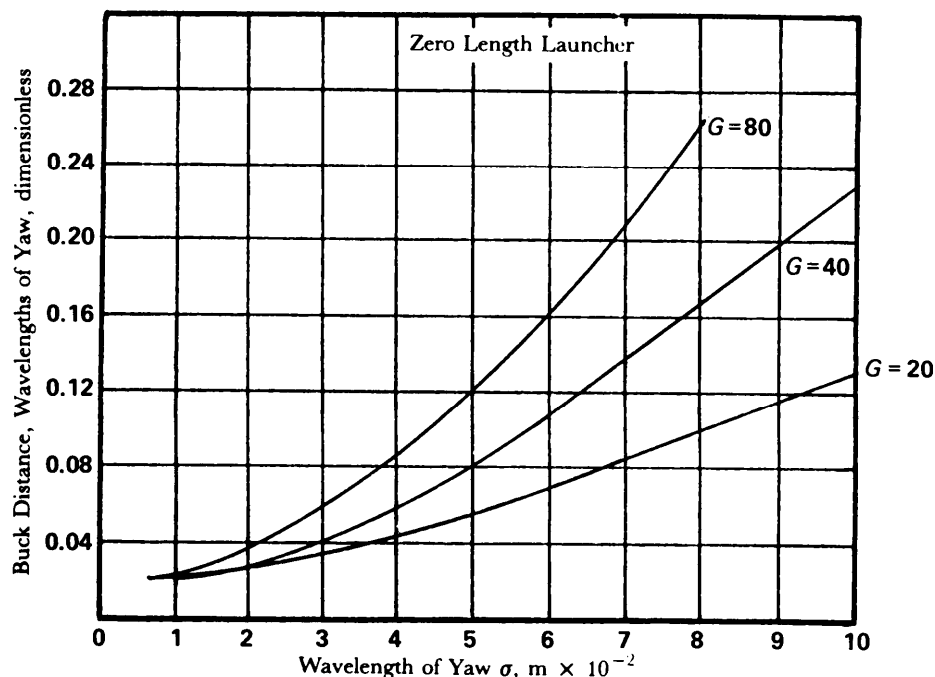
Figure 4-22. Effect of Wavelength of Yaw on Buck Distance for Zero Angular Dispersion
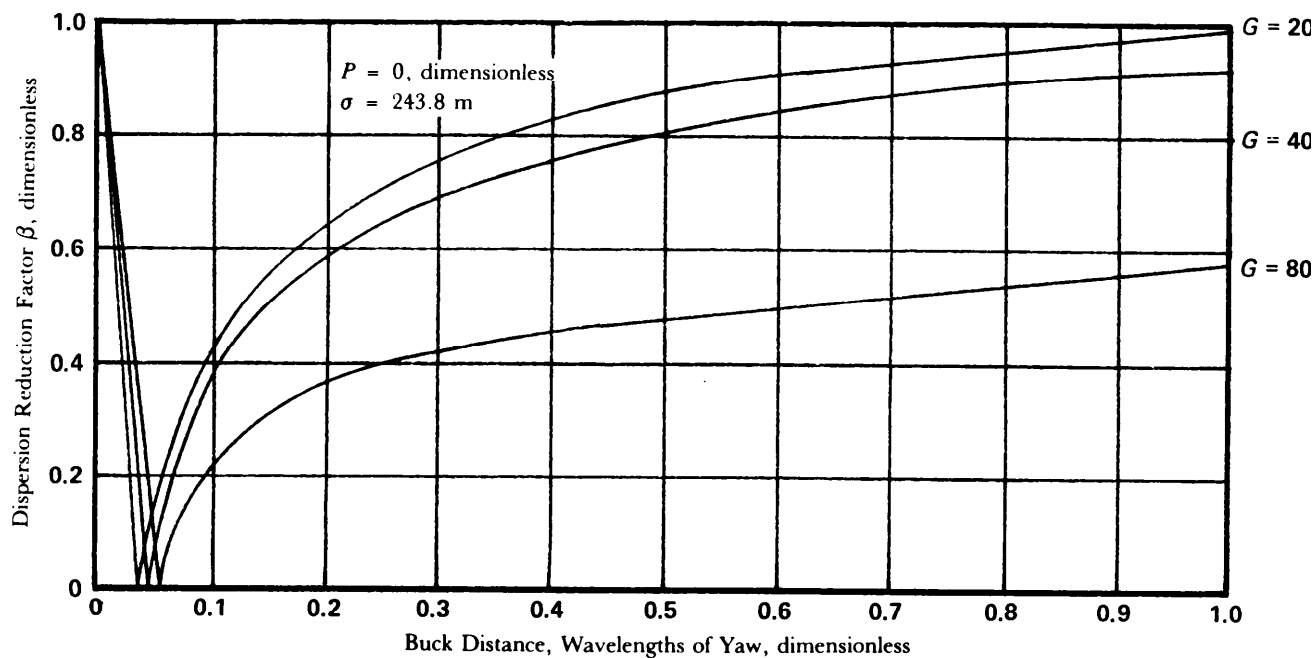
Figure 4-23.   Effect of Buck Distance on Dispersion Reduction

dispersion, error will be introduced due to dynamic imbalance. This effect can usually be kept small by careful design and manufacturing control so that the conflicting requirements can be satisfied without introducing a significant amount of dispersion. Spinning the rocket at very high rates increases the requirement to reduce dynamic imbalance. Further, the gyroscopic moments introduced by rapid spinning are no longer negligible. The stabilizing effects of the gyroscopic moments can be useful (Ref. 3)

4-39

to rockets with low stability, i.e., large ó. The gyroscopic effect will introduce a slow precession or drift in the trajectory, which can be treated as a bias error and accounted for in aiming.

Another effect that becomes increasingly important in rapidly spinning finned rockets is the magnus forces (Ref. 8). The magnus forces arise from nonlinear aerodynamic effects that produce trajectory curvature similar to that of the gyroscopic. effect. Roll resonance is a dynamic phenomenon that occurs when the rocket roll frequently is at or near the pitching frequency. Usual practice (Ref. 9) in rocket design for a spinning rocket is to operate above the roll resonance frequency and well below the significant magnus effect.

Finally, rocket and launcher interaction is further complicated by high spin rates. The forms transmitted to the launcher by rocket static and dynamic imbalance, and the possibility of resonance between launcher and rocket, are both increased. Rocket and launcher mot ion, and structural loading are further complicated by rapid spin rates through the higher structural frequencies when the rocket or launcher can no longer be considered a perfectly rigid system.

4-4.2.6 Spin Techniques

The preceding discussion showed that spin is highly effective in reducing boost-phase dispersions. Since dispersions during boost are a significant portion of free rocket total dispersion, a variety of techniques have been developed to produce early spin. Chapter 8 contains futher consideration associated with some of the spin techniques discussed in the paragraphs that follow.

4-4.2.6.1 Helical Rails

This method employs rails constructed in the form of a helix. The rocket is constrained by shoes to follow the helix in its departure from the launcher. Rocket acceleration level, and helix length and angle determine the spin rate at the end of the rail.

This is a relatively simple method for inducing spin; however, the disturbances to the launcher are relatively large and are caused by the reaction forces that the rail must impart to the rocket. Accordingly, the rails and launcher must be somewhat heavier than those employed with other spin methods to absorb the reaction forces without damage. Dynamic imbalance err-m-s are relatively unaffected by this spin technique.

4-4.2.6.2 Spin-on-Straight-Rail (SOSR)

Although the effects of dynamic imbalance produce undesirable results, prespinning a rocket on a rigid launcher before launch is sometimes beneficial. The benefits derived overshadow the ill effects of dynamic imbalance sufficiently to justify the inflexible launcher. Thus the rocket is provided with bearing systems in which it can rotate while on the launcher and can then be launched along a rail in the usual manner. This technique has been termed spin-on-straight-rail (SOSR). Although helical rails could be used, they may be undesirable because of length, weight, or other factors. Also the spin rate desired may not be attainable with any reasonable rail length and helix angle. However, in the SOSR system almost any desired spin rate can be achieved. The spinning method can be an integral part of either- the rocket or launcher. The spin mechanism, if it is a part of the rocket, may be a system of small rocket motors exhausting tangentially to the longitudinal axis. If the spin mechanism is a part of the launcher, it may be electrical, hydraulic, mechanical, or it may use whatever power source is most applicable. Power transmission to the rocket may be by belt, gears, or other appropriate means.

4-4.2.6.3 Spin Motors

As previously mentioned, small rocket motors may be mounted to produce opposing, tangential forces that cause the rocket to spin. This method, while simple, causes the spin motor cases to be carried as inert weight for the remainder of the trajectory. The cases may be ejected when burned out; however, this feature increases complexity and reduces reliability.

If multiple boost motors are employed, either the motors or nozzles may be tangentially canted to produce the desired spinning motion.

4-4.2.6.4 Jet Vanes

The boost motot exhaust gases may be used to impart spin by inserting vanes into the exhaust stream which are canted to the direction of exhaust flow. A similar method is to machine small grooves in the nozzle inner surface which also gives a tangential component to the exhaust flow.

Since solid rocket motor exhaust is highly erosive, nonsymmetric erosion of the jet vanes or fluted nozzle will cause additional thrust misalignment effects that are more pronounced in the jet-vane method.

4-4.2.6.5 Canted Fins

As in the jet-vane method, tangentially canting the rocket fins will produce rocket spin through aerodynamic effects. However, fins are not as effective as thrust in producing spin at the lower velocities that occur early in the launch and boost phases. Thus fins may not produce enough spin in the critical fraction of rocket wavelength after launch (see Fig. 4-17).

The spin profile for a rocket with canted, or misaligned, fins is typically a linear increase in the spin rate through maximum dynamic pressure, usually at burnout, followed by an exponential decay in spin rate to some steady value commensurate with the rocket velocity.

Fin cant is an effective method of selecting and maintaining spin during the coast phase of flight.

4-4.2.6.6 Spin Power Transmission

This launcher-induced spin method supplies power to spin the rocket before ignition. As mentioned in par. 4-4.2.6.2, power to spin the rocket may be applied by belts, gears, or other appropriate means. These methods require a relatively more complex launcher and an associated power generation system. With these methods the rocket must be mechanically isolated from the launcher in roll as it is in the SOSR and prespin automatic dynamic alignment (PADA) techniques.

4-4.2.6.7 Prespin Automatic Dynamic Alignment (PADA)

The PADA concept for dispersion reduction differs from those previously discussed in that it is not simply a method of spinning the rocket to reduce the effect of thrust misalignment. It is designed to reduce errors due to mallaunch, thrust misalignment, and dynamic imbalance.

Development of the PADA launcher evolved from the desire to launch a rocket with an initial spin rate. The problem of bulky launchers, which developed in past attempts to launch spinning rockets, was eliminated by mounting the launching shoes on rings attached to the rocket by bearings. The dynamic imbalance effect—which normally limits the maximum spin rate—is overcome by a spring suspension system. The system is designed so that the natural frequency of the transverse angular motion of the rocket on the launcher is consider-ably less than the rocket spin frequency. The result is that the rocket dynamic axis aligns itself with the spin axis. Theoretically (Ref. 10), PADA launchers can be constructed that will reduce the effect of dynamic imbalance by more than 90% and, possibly, by as much as 99%.

Disadvantages of this system are the increased complexity of such a launcher and the difficulty in aiming.

4-4.2.6.8 Autospin

This method uses a device in the rocket which spins the warhead in one direction while imparting spin of the opposite direction to the remainder of the rocket. This technique requires the warhead to be isolated in roll from the rest of the rocket through a bearing or other suitable means. A simple mechanical device, such as a preloaded spring, could be used to produce the required spin. The disadvantages of autospin are the limited spin rates achievable and the additional mass of the spin actuation device.

4-4.3 THE EFFECT OF ACCELERATION LEVEL

The acceleration level is one of the primary parameters which the rocket designer must consider. Chapter 3 provides information on the effect of the acceleration level on rocket performance. This

paragraph presents information on the effect of the acceleration level on accuracy. Rocket acceleration G' is directly proportional to the thrust of the rocket motor and inversely proportional to rocket mass, i.e.,

$$G' = F_T / m, \ \ m / s^2 \tag{4-25}$$

where

F_T = thrust, N

m = mass, kg.

Normalized acceleration G will be referred to as the acceleration level of the rocket. Since G is a function of thrust, its effect is only experienced during the launch and boost phases.

During launch, the rocket thrust disturbs the launcher; the magnitude of the disturbance depends on the thrust rise time and the launcher frequency response. The launcher, in turn, disturbs the rocket: this launcher/rocket inter-action creates a mallaunch. High-G rockets may or may not cause a greater mallaunch than low-G rockets, depending on the phasing of thrust. Another factor is that the high-G rocket remains on the launcher a shorter time.

Increasing the acceleration level of the rocket has an effect similar to that of increasing the launcher guidance length. That is, the rocket will exit the launcher with a higher velocity as G is increased, or a shorter launcher guidance length is required to exit with the same velocity. If the rocket exits the launcher into a steady crosswind, the disturbing moment due to the angle of attack will be reduced for a rocket with higher velocity. As the rocket velocity increases due to G, the steady state angle of attack is further reduced. Accordingly, a high-G rocket will be less sensitive to winds during the boost phase if compared to an identical situation with lower acceleration.

Higher acceleration levels will also impose greater structural load requirements on the rocket and launcher. Exhaust plume effects for high thrust (high-G) rockets may also induce violent, nonlinear effects that greatly disturb the aerodynamic flow and, consequently, rocket dispersion at burnout. In selecting G, the rocket designer must maintain an awareness of the preceding interactions and effects to avoid introducing further dispersion sources.

A further effect of thrust is the jet-damping effect. When a thrusting rocket is rotated about a lateral axis, a force is produced in the nozzle which opposes the rotation. Simply stated, the force is produced by the momentum of the exhaust gases resisting the change in direction due to rocket rotation. The magnitude of the force is proportional to the mass flow rate $\dot{m}$ and to the rocket lateral rotation rate $\dot{\theta}$. The jet damping force exerts a stabilizing moment proportional to the distance from the rocket CG to the motor nozzle. High thrust (high-G) rockets produce larger jet damping forces.

Although it is unusual in that it does not introduce spin of any kind, there is another useful dispersion reduction technique. The dispersion reduction is accomplished by changing the acceleration history of the rocket. This can be done with a throttleable rocket motor or with a combination of rocket motors. The example considered is a rocket with two levels of acceleration. The thrust level is assumed to change instantaneously at some point in flight (Ref. 11).

How the rocket acceleration history effects angular boost dispersion is not immediately obvious. Ref. 11 indicates that the dispersion due to various error sources, such as mallaunch and thrust misalignment, is affected differently by the change of acceleration. However, the following description, taken from Ref. 11, describes the phenomenon.

The angular dispersion γ_{TS} is found by integrating $\dot{\gamma}$ with flight time. It can be shown that $\dot{\gamma}$ is an oscillating function whose magnitude varies as the inverse of the square of rocket velocity. Therefore, the first half-cycle (when $\dot{\gamma}$ has one sign) has greater amplitude than the second half-cycle (when $\dot{\gamma}$ has the opposite sign). The result obtained when $\dot{\gamma}$ is integrated over the entire cycle is that the first half-cycle dominates the second. If the acceleration is decreased at some time before the second half-cycle begins, the contribution of the second half-cycle can be increased to offset the first half.

Although the variable acceleration technique suffers from the same sensitivity as the Spin-Buck technique, it is presented to show that there is a possibility for dispersion reduction without spin. Once the dispersion reduction factor β is known, it can be used in the equations of this chapter in an identical manner as the β's produced by spin.

Variable acceleration profiles can be accomplished by nozzle chokes or other mechanical means that would be relatively complicated and costly. Most free rockets are propelled by solid fuel motors; therefore, throttleable motor performance by variable fuel injection methods is not possible as it would be for liquid propelled rockets.

Changes in the acceleration level for solid propellant motors can be accomplished by casting separate propellant/oxidizer mixtures, one inside the other. For example, a high thrust propellant could be cast inside a lower thrust propellant. The physical size and shape of the first propellant would enable it to be consumed at the point of the required acceleration reduction, and the second propellant would be ignited by the first.

4-4.4 THE EFFECT OF AERODYNAMIC STABILITY

As was discussed and shown in previous paragraphs, rocket stability influences dispersions caused by thrust misalignment and winds. Consequently, this effect is limited to the boost and ballistic flight phases.

Rocket stability is alternately described by the yaw oscillation distance ó and the static margin l_s. When a rocket is placed at an incidence angle to the velocity vector, the aerodynamic flow produces a distribution of relative pressure over the total rocket surface. This pressure distribution produces a net force and moment on the vehicle. Static margin is the ratio of the aerodynamic moment to the force and has units of length. Static margin often is normalized to the diameter of a rocket, and the units commonly are referred to as calibers (cal). The relationship between ó and l_s was shown by Eq. 4-7. The more stable rocket has a larger static margin and a smaller yaw wavelength.

During boost a rocket with a large static margin would settle at a small, steady state angle of attack to balance the effect of thrust misalignment. A vehicle with a small static margin would settle at some proportionately larger angle to balance the moment due to the same thrust misalignment.

The effect of wind on a stable rocket causes the nose of the rocket to rotate in the direction from which the wind is blowing. The higher the stability, the farther and faster the rocket will rotate. During boost, the thrust, consequently, tends to drive the rocket upwind. During the ballistic phase, the aerodynamic drag tends to cause the rocket to drift with the wind. As previously stated, thrust misalignment and wind pose conflicting demands upon stability. Par. 4-4.2 introduced this conflict and the concept of an optimum a (Fig. 4-14) to minimize the dispersion caused by these two effects.

Fig. 4-24 illustrates the trim forces and moments for a rocket with thrust misalignment. The steady state trim angle of attack for this case is

$$\alpha_{ss} = \frac{2F_T \delta l_t}{C_{N\alpha} l_s \rho V_R^2 A_{ref}} \text{ , rad} \tag{4-26}$$

where

α_{ss} = steady state trim angle of attack with thrust misalignment, rad

V_R = rocket velocity relative to wind, m/s

The disturbing force due to wind is proportional to the wind velocity V_w and inversely proportional to the relative velocity V_R. Fig. 4-25 illustrates this transient effect. If the disturbance were a steady wind, the rocket would eventually drift inertially with the wind. When this occurs, the rocket would no longer experience the wind since its inertial velocity has a component identical to the wind velocity. Eventually, in a steady wind the angle of attack would return to zero.
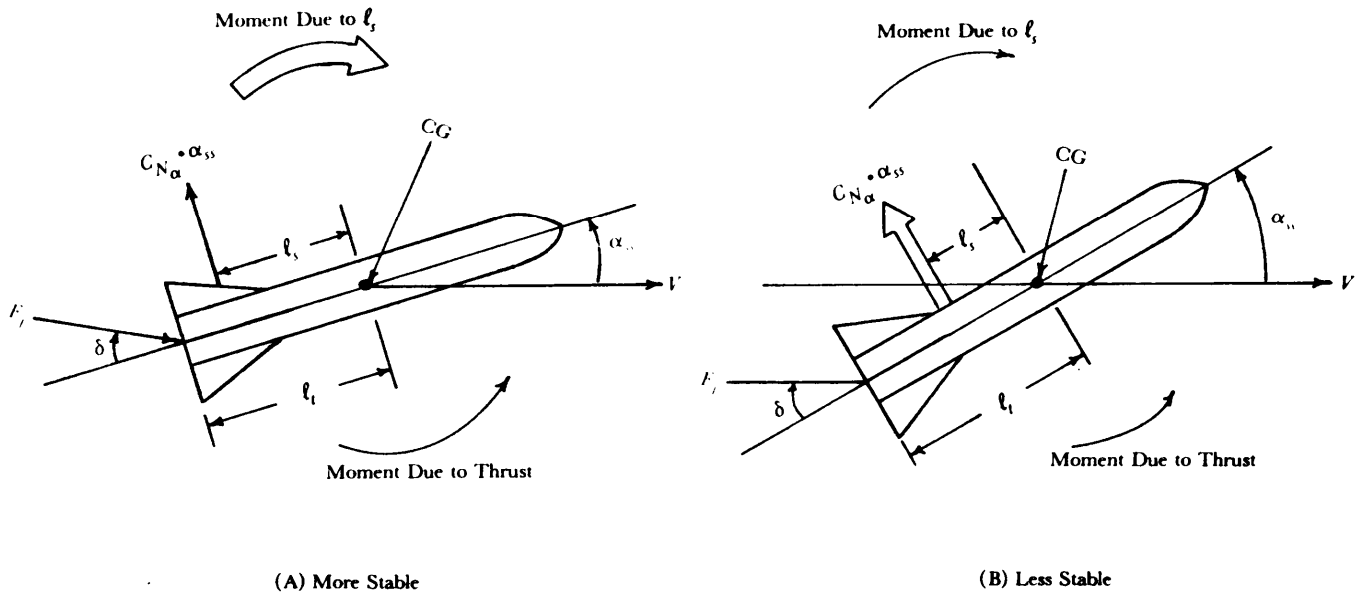
Figure 4-24.   Effect of Static Margin on A Rocket With Thrust Misalignment
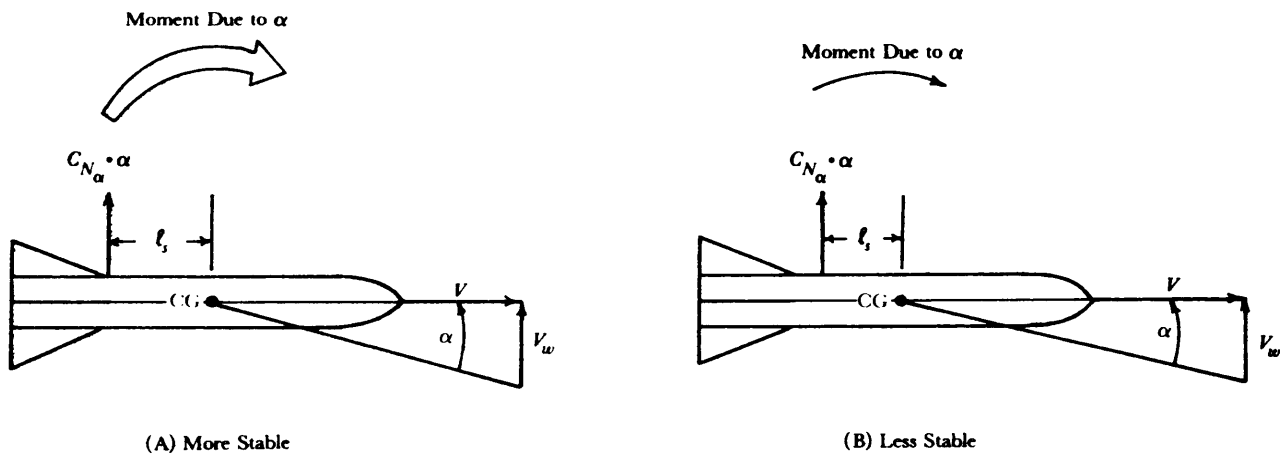
Figure 4-25.   Effect of Static Margin on Wind Disturbance

Because of variations among individual rockets, no two rockets will have exactly the same stability margin. Careful attention to the aerodynamic shape of the rocket components, especially the nose and fins, will minimize the sensitivity of stability-induced dispersions.

One method by which the effect of stability can be controlled is by changing the rocket stability during flight. Depending on the velocity regime, the external configuration could be designed to provide the most desirable level of stability during each flight phase.

Since spin greatly reduces dispersion caused by thrust misalignment without appreciably affecting stability, more emphasis can be placed on using stability tailoring to reduce wind dispersion. This is particularly true during the boost phase when folded fins are used. The reduction of wind dispersion by using folded fins is accomplished in the manner that follows. Chapter 5 states that a finless rocket is aerodynamically unstable. That is, it will turn away from a wind normal to its line of flight in contrast to the stable rocket that turns into a normal wind. Therefore, when the thrusting rocket with folded fins is launched, wind-induced error is accumulated in one direction. At some point in the boost phase

4-44

the fins are deployed, and the rocket will turn into the wind and accumulate error in the opposite direction. Judicious selection of the fin deployment time can cause the net dispersion from winds to be zero. Stability can be further tailored by variable deployment of the fins—either by partial deployment followed by full deployment or by full deployment followed by a partial retraction as the particular situation demands. Reduced stability through partial retraction or some other means is particularly useful during the ballistic phase when wind disturbances are a major source of dispersion.

4-4.5 THE EFFECT OF LAUNCHER GUIDANCE LENGTH

For most of the error sources described, relatively long launcher guidance has a beneficial effect. This is primarily because longer guidance lengths enable the rocket to leave the launcher at a higher velocity for the same acceleration level. At higher velocity, disturbances from winds will be decreased; higher velocity also increases aerodynamic effectiveness which aids in overcoming thrust misalignment. However, since launchers are not perfectly rigid, the effectiveness of long launchers on dispersion is a much more complex issue than is indicated. The interaction of a long flexible launcher and a rocket with thrust and mass imbalances could increase the mallaunch errors to intolerable levels. Operating mode, mobility requirements, and other factors also affect the determination of launcher length. Therefore, the rocket designer should carefully consider these points and maintain reasonable expectations when selecting a launcher guidance length for the rocket.

4-4.6 PRELAUNCH-PHASE DISPERSION REDUCTION

Methods of reducing aiming errors during the prelaunch phase are grouped into three categories, i.e.,

1. Those that provide better location and orientation for the launcher
2. Those that provide better location of the target
3. Those that provide better information about the error sources in the external environment.

Each category is discussed in the subparagraphs that follow.

4-4.6.1 Launcher Location and Orientation

For a relatively permanent launch site, it is possible to provide good information on several parameters that are vital to the success of a fire mission. First, the location of the launch site is usually well-surveyed and related to map grid coordinates. Next, the site is leveled to provide a reference for the QE angle, and the direction reference for true north is available for accurate azimuth orientation. However, operational considerations and local tactical conditions may not offer the advantages of a well-prepared site. Under these conditions, the rocket system designer must rely on equipment that can be transported with the launcher. There are many devices and techniques that could supply needed information on launcher location or orientation. Portable north-seeking and vertical sensors may be employed for angular reference; these can range from simple compass and spirit level devices to sophisticated inertial reference packages. Navigation satellites or ranging devices could be employed for map grid location.

Bias errors within the launcher itself can be discovered and reduced through testing. Manufacturing precision will cause some aiming error to be present through random accumulation of tolerances between the upper and lower carriages, but these can be controlled to some extent. However, operating in a battlefield environment tends to increase these tolerances through shock and vibration during off-road transport. Accordingly, the launcher must be designed to withstand the operational environment for which it is intended.

Another random aiming error is the launcher angular positioning error, i.e., how well the servomechanism drives the launcher to the commanded aim angles.

4-4.6.2 Target Location

Usually the location of the target is known to even less accuracy than the launcher. Observation of impact points by a forward observer can supply required corrections to the fire direction center.

Remotely piloted vehicles or other aircraft in the forward area may be employed in this role. Optical, infrared, and laser ranging and tracking devices can be employed to locate the target when the target is visible to the launcher or another surveyed location.

4-4.6.3 External Error Sources

Firing tables normally ae prepared to account for propellant temperature, rotation of the earth, and other fixed bias effects for a given rocket system. Errors of winds and atmospheric temperature and density can be reduced by frequent update of meteorological data. Ref. 12 describes a method for estimating the meteorological errors by a technique called dynamic aiming. Briefly, this technique tracks a rocket fired at the target. The burnout condition is measured, and a prediction of the position and velocity of the rocket is calculated for some point in the ballistic trajectory, e.g., summit altitude. The jactual rocket state at the summit is then measured ad compared to the predicted state, and any differences are ascribed to ballistic bias errors. The launcher is adjusted accordingly for the next rocket(s) fired shortly thereafter. This method reduces the bias effects of wind and ballistic density. Ref. 12 also shows that the total error approaches system precision 9random) errors for the dynamically aimed second through ninth rockers of a salve. The dispersion reduction factor ß for such a technique could be computed and ussed with the methods of this chapter for accuracy analyses.

Most of the methods mentioned increase the complexity and cost of the launcher, and they incur further penalties in crew workload and training.

4-4.7 LAUNCH-PHASE DISPERSION REDUCTION

Previous paragraphs defined the principal sources of dispersion to the translational velocity normal to the launcher axis and to the lateral rotational rates at rocket release. These mallaunch effects arise from the interaction of the launcher with the thrust misalignment, the static and dynamic imbalance, and the acceleration level of the rocket. Par. 4-3.3 described some of the conflicting requirements imposed on acceleration level G, launcher guidance length P, and yaw wavelength ó by these error sources. Longer launcher guidance lengths reduce rotational mallaunch error (again assuming a rigid launcher to estimate first-order effects). A properly designed nonrigid launcher can be beneficial in reducing launch and boost errors by responding out-of-phase with the dispersion-producing forces (see Chapter 8).

The study of launchers as passive control devices is required before active control measures can be applied effectively. A properly designed passive system will reduce the requirements imposed on an active launcher control scheme.

Careful selection of launch technique, close attention to launcher design, and control of rocket asymmetries are all beneficial to the reduction of launch-phase dispersion. Several launch techniques are described throughout this chapter with comments on the error sources that each seeks to eliminate. Further consideration of launcher complexity, design, and analysis is found in Chapter 8.

Ref. 13 describes an active launch control technique in which rocket attitude, angular rate, and velocity are determined by magnetic sensors while the rocket is in the launch tube. The motion of the rocket through the tube is controlled by cold gas jets acting normal to the tube axis. Since the magnetic sensor measures rocket motion relative to the tube, an inertia] motion sensor is required to measure tube motion. This inertial sensor provides information used in eliminating the launcher motion from the magnetically sensed motion of the rocket.

4-4.8 BOOST-PHASE DISPERSION REDUCTION

Previous paragraphs established that the principal sources of error during the boost phase are thrust misalignment, winds normal to the launcher axis, and speed change errors caused by motor per-formance.

Control of motor performance is accomplished through careful manufacturing technique, protection from mishandling, and thermal conditioning. Thermal conditioning attempts to control the tempera-

ture of the motor propellant, which reduces variation in performance by insuring that each rocket is ignited at the same temperature.

Spinning the rocket to reduce body-fixed error sources (such as thrust misalignment) while tailoring the stability margin to reduce sensitivity to winds is an effective combination of techniques for boost dispersion reduction. Spin may be achieved by any of the techniques previously described. Static margin may be controlled by the size, shape, and deployment of fins or by the size and shape of the rocket body elements (nose, tail, and midsection).

4-4.9 BALLISTIC-PHASE DISPERSION REDUCTION

Par. 4-3.5 demonstrated that ballistic phase errors can accrue in three general ways, namely,

1. Ballistic winds
2. Nonstandard atmospheric conditions
3. Variations in drag magnitude and direction.

Any free projectile eventually will drift with a steady ballistic wind. Therefore, the design of the rocket is only an indirect factor in reducing dispersions from this source. The stability of the rocket and its ballistic coefficient only determine the time it takes the rocket velocity to approach that of the wind. Chapter 3 showed that increasing the ballistic coefficient reduced the flight time of a rocket. Reduced flight time gives the disturbing wind a shorter period to cause dispersion. The same argument holds for nonstandard atmospheric conditions.

The most fruitful methods of reducing dispersion from these sources are by better determination of the nonstandard conditions and by measuring their effect upon the rocket. Once an estimate of the nonstandard ballistic effects is known, appropriate changes in the aiming of the rocket can be made.

Determination of the ballistic wind and atmosphere can be done through established meteorological methods-weather balloons of various types, sounding rockets, ground weather stations, and satellites. Dynamic aiming (par. 4-4.6.3) is one way to measure the effect of ballistic wind and atmosphere upon the rocket. The frequency of meteorological data updates would be one concern which dynamic aiming eliminates.

Many possibilities exist for reducing ballistic dispersion from drag. One group of methods seeks to reduce or cancel the drag force. In so doing, they eliminate induced forces normal to the trajectory when the rocket is laterally rotated by transient winds or other disturbances. A collapsible skirt that will produce a boattail effect after burnout is one method of configuration change to reduce drag.

Relatively long-burning propellant mixtures at low thrust levels will reduce the base drag. However, such methods are susceptible to thrust misalignment errors. Modulation of the drag force may be achieved by sensing the axial acceleration and by maintaining constant drag through thrust modulation or aerodynamic surface modulation.

Several effects exist that can cause the ballistic rocket to orient itself at some standoff angle away from the velocity vector; this rocket orientation causes an increase in drag from a component of the induced normal force. Spin, static and dynamic imbalance, pitch-yaw aerodynamic coupling, and a bent or misaligned fin can induce the rocket nose to rotate around the velocity vector in a coning motion. A small moment from aerodynamic damping will cause the rocket longitudinal axis to lag behind the velocity vector, and the rocket will rotate in pitch at the same rate as the velocity vector along the trajectory. The aerodynamic moment from damping will be balanced by the moment due to the normal force and incidence angle. The static aerodynamic forces, however, will not be in balance.

Unburned propellant, variations in density of the warhead and rocket structure, and manufacture tolerances will cause the burnout inert mass and frontal area of each rocket to be somewhat different. These conditions will cause variations in the rocket ballistic coefficient. Careful attention to manufacturing and assembly procedures can contain these errors within acceptable levels.

Dependent on type and intended use, the rocket warhead may be detonated at impact or it may be detonated at some time after launch, corresponding to an expected altitude in the target area. Variability in the action time of these types of fuses will cause dispersions in the warhead event. These variabilities usually are controllable in manufacture and assembly.

4-5 ACCURACY COMPUTATION
4-5.1 GENERAL

Pars. 4-2 through 4-4 have presented methods that can be used to determine the condition of the rocket at motor burnout. The dispersion at burnout associated with the prelaunch, launch, and boost phases has been given. With the burnout conditions as inputs, par. 4-5.5 will describe completely how to determine the dispersion of the rocket at the warhead event. In addition to the prelaunch, launch, and boost errors, the errors associated with the ballistic phase were introduced. The final results are the dispersions of the rocket—caused by error sources throughout the flight—at the warhead event. For the purpose of this handbook only those ballistic phase errors that have the greatest influence on the accuracy have been included. These errors are change in atmospheric density, change in the ballistic coefficient, and ballistic wind. Par. 4-5.5 presents a numerical example of the calculation of rocket dispersions at the warhead event when the magnitude of the error sources is known or can be estimated.

So far the methods described to determine rocket dispersion have assumed that the effects of the error sources, taken singularly or in combination, are linear and statistically independent. This assumption means (1) the dispersion due to an error source is directly proportional to the magnitude of the error and (2) changing the magnitude of one error source has no effect on the remaining error sources. In practice these assumptions do not severely affect the results. Therefore, the rocket designer must exercise good judgment in the selection and apportionment of error to the several sources identified to maintain the validity of the assumptions.

The approach taken to this point has been to assess the various error sources by flight phase. The advantages to this approach have been to

1. Allow the identification of error sources through analytic solution.
2. Identify the dominant error sources in each flight phase.
3. Enable the solution of the dispersion from error sources to be defined.

This method is particularly suitable during the early design phases of a rocket system. During these design phases, major system elements such as the launcher may not be designed in any great detail, and the rocket configuration may not be finalized.

A method for determining rocket error which involves considerably more effort is to record the impact points of rockets and to calculate the accuracy. The rockets may be those of a tightly controlled test program or they may be simulations of physically realizable rockets. The error sources would be carefully measured for each rocket prior to the testing program. The simulation-type effort would describe the error sources in terms of their statistical distribution, and a process for selecting a given error from the distribution could be used. The selection of all the error sources would then represent a physically realizable rocket selected from a population of such rockets. This method would enable the designer to include the effect of each round on all phases of flight, including launcher flexibility if a launcher model existed. Refs. 14 and 15 describe a procedure for an evaluation of accuracy through Monte Carlo simulation, a powerful technique for analyzing complex physical problems involving random processes. Refs. 16 through 18 have annotated bibliographies and discuss several topics related to the Monte Carlo method. There are several disadvantages associated with this type of accuracy assessment; foremost is that it is a relatively expensive technique. It is expensive because it irr~'elves either accurate measurement of rocket asymmetries and the actual firing of the rockets on a calibrated range or it involves computer costs for the simulation of many rocket trajectories. Another disadvantage is the difficulty of apportioning the resulting dispersion to the individual error sources (see Ref. 15). Since statistical techniques do not explain the reasons for correlations discovered within a population of impact points, the rocket designer must be aware of the possibility of specious correlation.

The remainder of par. 4-5 presents information on the simulation of rockets and the calculation of rocket accuracy. The 6-degree-of-freedom (DOF) equations of motion are introduced, and reduced DOF equations also are presented. Methods of calculating statistical parameters for rocket impacts are presented. These parameters are principally measures of the central tendency and measures of dispersion

for a rocket. Finally, a sample error budget and an example problem are presented to illustrate how the techniques of this chapter can be applied to estimate the accuracy of a given free rocket.

4-5.2 SIX-DEGREE-OF-FREEDOM EQUATIONS OF MOTION

The equations of motion for a rocket moving in space have received extensive treatment in the literature. Refs. 19, 20, and 21 present excellent developments of the equations required. Refs. 19 and 20 provide detailed and extensive development of the equations of motion, and Ref. 21 contains equations for a four-finned missile. Each equation provides a slightly different form for determining the Euler parameters relating the body-centered coordinate system to the inertial coordinate system. Also each contains a different treatment for the expansion of external force and moment terms.

The equations of motion are presented without development. For the equations presented the following effects are considered negligible:

1. Time rate of change of rocket moments of inertia
2. Forces and moments due to jet damping and rotating internal machinery
3. Velocity and acceleration of the center of gravity (CG) with respect to the body-centered coordinate system.

The third assumption requires the CG to be relatively slow-moving during the rocket burn phase and restricts the equations to inflexible bodies.

The inertial equations of motion are written for a translating and rotating coordinate system referred to as the (x, y, z)-body-centered system. The body-centered system has its origin at the rocket CG. The x-body-centered axis is directed along the rocket axis of symmetry, positive in the direction of the nose. The y- and z-body-centered axes form a right-handed orthogonal set and usually are oriented at the convenience of the user. For a 4-finned rocket the axes may be directed along two of the fins. Most rocket-dependent data—thrust, aerodynamics, and error parameters—are expressed in this system. The origin of the (X, Y, Z) inertial coordinate system usually is located at the launch point. The X-axis is usually directed in the intended direction of fire (range direction); the Y-axis is directed in the cross-range (deflection) direction; and the Z-axis forms a right-handed orthogonal set and is directed toward the center of the earth. The atmospheric, wind, and gravity models usually are expressed in the inertial coordinate system. Fig. 4-26 illustrates the two coordinate systems, and Fig. 4-27 shows the positive conventions for the equations of motion.

Table 4-1 presents the rotational equations of motion in matrix notation. Table 4-2 presents the translational equations in similar notation. Table 4-3 presents the Euler matrix relating the inertial and body coordinate systems, and the kinematic relationship between the Euler angle rates $(\dot{\phi}, \dot{\theta}, \dot{\psi})$ and the body-centered rates (p, q, r). The rotation sequence selected for the Euler matrix is not unique; there are many other sequences available (see Ref. 19). Ref. 21 presents a quaternion formulation of the inertial-to-body coordinate relationship which offers several advantages in the computer implementation of these equations.

The expansion of the rotational equations of Table 4-1 into three separate equations will produce terms involving pq and pr. These terms represent the significant gyroscopic terms for a rapidly spinning rocket and will produce coupling of the pitch and yaw motions even in the absence of cross products of inertia.

The principal external forces and moments required for free rockets arise from thrust, aerodynamics, gravity, and jet damping. Ref. 19 presents detailed developments for each of these terms. Refs. 19, 20, and 21 also demonstrate the diversity of the expansion of the aerodynamic forces and moments. In the interest of brevity only the most common of the aerodynamic terms have been included throughout this chapter.

4-5.3 REDUCED DEGREE-OF-FREEDOM EQUATIONS OF MOTION

There are several forms of the 6-DOF equations which are suitable for accuracy analysis. Each form usually seeks to simplify the equations by neglecting certain terms. Further simplification is performed in the expansion of the external forces and moments. One simplification commonly employed involves
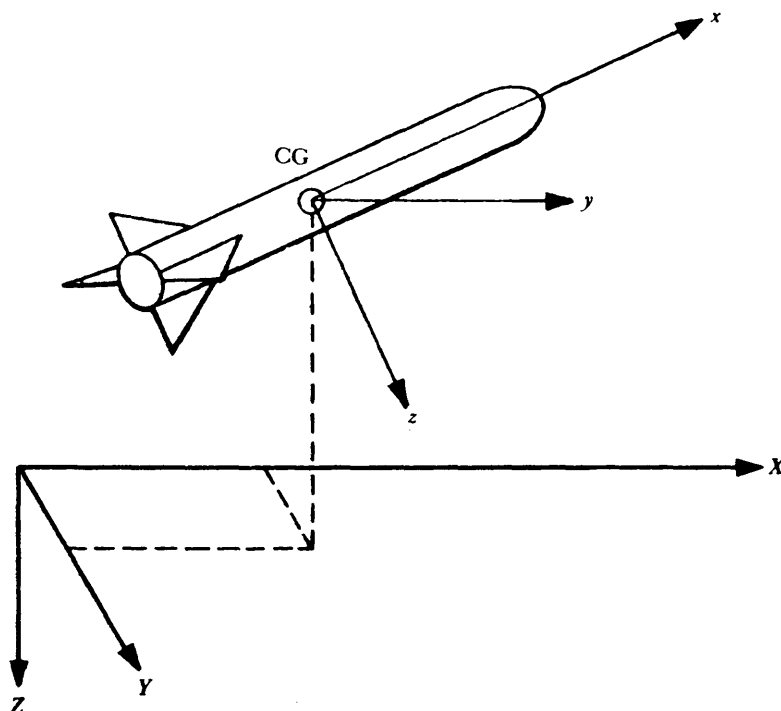
Figure 4-26. **The Inertial Coordinate System and Body-Centered Coordinate System for a Free Rocket**
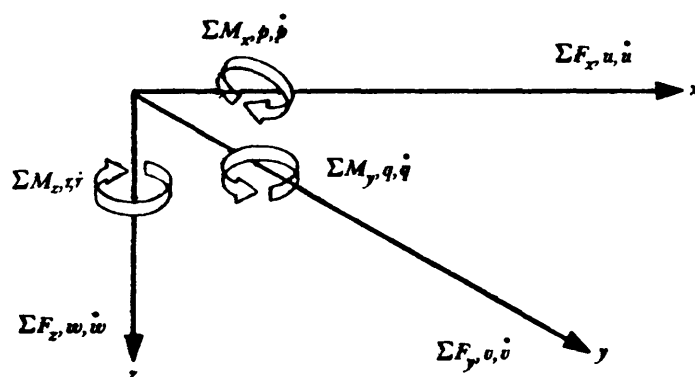
Figure 4-27. **Positive Sign Conventions of the Six-DOF-Equations of Motion**

the assumption that there is only one cross product of inertia (I_{xz}) of any consequence. The rotational equations of motion then become

$$\Sigma M_x = I_{xx}\dot{p} - I_{xz}(\dot{r} + pq) + (I_{zz} - I_{yy})qr, \text{ N} \cdot \text{m} \tag{4-27}$$

$$\Sigma M_y = I_{yy}\dot{q} + I_{xz}(p^2 - r^2) + (I_{xx} - I_{zz})rp, \text{ N} \cdot \text{m} \tag{4-28}$$

$$\Sigma M_z = I_{zz}\dot{r} - I_{xz}(\dot{p} - qr) + (I_{yy} - I_{xx})pq, \text{ N} \cdot \text{m} \tag{4-29}$$

where

$\Sigma M_x, \Sigma M_y, \Sigma M_z$ = external moments about the body-centered x-, y-, and z-axes, respective y, NŽm

I_{xx}, I_{yy}, I_{zz} = principal moments of inertia about the body-centered x-, y-, and z-axes, respectively, kgŽm²

TABLE 4-1. SIX-DEGREE-OF-FREEDOM ROTATIONAL EQUATIONS OF MOTION

$$\begin{bmatrix} \Sigma M_x \\ \Sigma M_y \\ \Sigma M_z \end{bmatrix} = [I] \begin{bmatrix} \dot{p} \\ \dot{q} \\ \dot{r} \end{bmatrix} + \begin{bmatrix} 0 & -r & q \\ r & 0 & -p \\ -q & p & 0 \end{bmatrix} [I] \begin{bmatrix} p \\ q \\ r \end{bmatrix}$$

where

$$[I] = \begin{bmatrix} I_{xx} & -I_{xy} & -I_{xz} \\ -I_{xy} & I_{yy} & -I_{yz} \\ -I_{xz} & -I_{yz} & I_{zz} \end{bmatrix}$$

$\Sigma M_x, \Sigma M_y, \Sigma M_z$ = summation of external moments (thrust, aerodynamic) about x-, y-, and z-body-centered axes, respectively, (N·m)

$\dot{p}, \dot{q}, \dot{r}$ = rotational accelerations of the rocket about x-, y-, and z-body-centered axes, respectively, rad/s²

p, q, r = rotational rates about the x-, y-, and z-body-centered axes, respectively, rad/s

I_{xx}, I_{yy}, I_{zz} = principal moments of inertia, kg·m²

I_{xz}, I_{xy}, I_{yz} = cross products of inertia, kg·m²

TABLE 4-2. SIX-DEGREE-OF-FREEDOM TRANSLATIONAL EQUATIONS OF MOTION

$$\begin{bmatrix} \Sigma F_x + F_{g_x} \\ \Sigma F_y + F_{g_y} \\ \Sigma F_z + F_{g_z} \end{bmatrix} = m \begin{bmatrix} \dot{u} \\ \dot{v} \\ \dot{w} \end{bmatrix} + \begin{bmatrix} 0 & -r & q \\ r & 0 & -p \\ -q & p & 0 \end{bmatrix} \begin{bmatrix} u \\ v \\ w \end{bmatrix}$$

where

$\Sigma F_x, \Sigma F_y, \Sigma F_z$ = summations of external forces (thrust, aerodynamic) along the x-, y-, and z-body-centered axes, respectively, N

$F_{g_x}, F_{g_y}, F_{g_z}$ = forces due to gravity along x-, y-, and z-body-centered axes respectively, N

$\dot{u}, \dot{v}, \dot{w}$ = translational acceleration along x-, y-, z-body-centered axes, respectively, m/s²

u, v, w = translational velocities along x-, y-, and z-body-centered axes, respectively, m/s

p, q, r = rotational rates about x-, y-, and z-body-centered axes, respectively, rad/s.

I_{xz} = cross product of inertia about the indicated axes, kg·m²

p = rotational rate of rocket about the body-centered x-axis, rad/s

$\dot{p}$ = time rate of change of p, rad/s²

q = rotational rate of rocket about body-centered y-axis, rad/s

$\dot{q}$ = time rate of change of q, rad/s²

r = rotational rate of rocket about body-centered z-axis, rad/s

$\dot{r}$ = time rate of change of r, rad/s².

Eqs. 4-27 and 4-29 are coupled, first-order nonlinear differential equations. By eliminating $\dot{r}$ from Eq. 4-27—$\dot{r}$ determined from Eq. 4-29—and by making use of the following notation:

$$K_1 = \frac{1}{I_{xx}} \left[\Sigma M_x - (I_{zz} - I_{yy}) qr \right], \text{rad/s}^2 \tag{4-30}$$

TABLE 4-3. EULER TRANSFORMATION RELATING THE INERTIAL COORDINATE SYSTEM AND BODY-CENTERED COORDINATE SYSTEM

	ROLL About x	PITCH About y	YAW About z	(3-2-1 Rotation Sequence)

$$\begin{bmatrix} x \\ y \\ z \end{bmatrix} = \begin{bmatrix} 1 & 0 & 0 \\ 0 & \sin\phi & \cos\phi \\ 0 & \cos\phi & -\sin\phi \end{bmatrix} \begin{bmatrix} \cos\theta & 0 & -\sin\theta \\ 0 & 1 & 0 \\ \sin\theta & 0 & \cos\theta \end{bmatrix} \begin{bmatrix} \cos\psi & \sin\psi & 0 \\ -\sin\psi & \cos\psi & 0 \\ 0 & 0 & 1 \end{bmatrix} \begin{bmatrix} X \\ Y \\ Z \end{bmatrix}$$

$$\begin{bmatrix} x \\ y \\ z \end{bmatrix} = \begin{bmatrix} \cos\theta\cos\psi & \cos\theta\sin\psi & -\sin\theta \\ \sin\phi\sin\theta\cos\psi - \sin\psi\cos\phi & \sin\phi\sin\theta\sin\psi + \cos\phi\cos\psi & \sin\phi\cos\theta \\ \cos\phi\sin\theta\cos\psi + \sin\phi\sin\psi & \cos\phi\sin\theta\sin\psi - \sin\phi\cos\psi & \cos\phi\cos\theta \end{bmatrix} \begin{bmatrix} X \\ Y \\ Z \end{bmatrix}$$

$$\begin{bmatrix} x \\ y \\ z \end{bmatrix} = [\Phi] \begin{bmatrix} X \\ Y \\ Z \end{bmatrix}$$

$$\begin{bmatrix} X \\ Y \\ Z \end{bmatrix} = [\Phi]^T \begin{bmatrix} x \\ y \\ z \end{bmatrix}$$

$$\dot{\theta} = q\cos\phi - r\sin\phi$$

$$\dot{\psi} = \frac{q\sin\phi + r\cos\phi}{\cos\theta}$$

$$\dot{\phi} = p + \left(\frac{q\sin\phi + r\cos\phi}{\cos\theta}\right)\sin\theta$$

where

x, y, z = body-centered coordinate system

X, Y, Z = inertial coordinate system

ϕ, θ, ψ = Euler roll, pitch, and yaw angles, respectively, rad

$\dot{\phi}, \dot{\theta}, \dot{\psi}$ = the time derivatives of $\phi, \theta,$ and ψ, respectively, rad/s

p, q, r = rotational rates about x-, y- and z-body-centered axes, respectively, rad/s.

$$K_2 = \frac{1}{I_{zz}}\left[\Sigma M_y - (I_{yy} - I_{xx})pq\right], \text{rad/s}^2 \tag{4-31}$$

$$I_x' = \frac{I_{xz}}{I_{xx}}, \text{dimensionless} \tag{4-32}$$

$$I_z' = \frac{I_{xz}}{I_{zz}}, \text{dimensionless.} \tag{4-33}$$

Eqs. 4-27 through 4-29 can be written

$$\dot{p} = \frac{K_1 + I_x'(K_2 - I_z'rq + pq)}{1 - I_x'I_z'}, \text{rad/s}^2 \tag{4-34}$$

$$\dot{q} \;=\; \frac{1}{I_{yy}} \left[\Sigma M_y - I_{xz}(p^2 - r^2) - (I_{xx} - I_{zz})rp \right], \text{rad/s}^2 \qquad \textbf{(4-35)}$$

$$\dot{r} \;=\; K_2 + I'_z \,(\dot{p} - rq)\;, \text{rad/s}^2. \qquad \textbf{(4-36)}$$

Note that $\dot{p}$ in Eq. 4-36 is actually Eq. 4-34. Although analog computer implementation of Eqs. 4-27 through 4-29 is straightforward, Eqs. 4-34 through 4-36 are more amenable to digital computer implementation. The dynamic imbalance angle ϵ in Eq. 4-20 is related to the inertias by

$$\tan(2\epsilon) \;=\; \frac{2I_{xz}}{I_{zz} - I_{xx}}, \; \text{dimensionless} \qquad \textbf{(4-37)}$$

where

ϵ = dynamic imbalance angle, rad.

The development of the presented reduced DOF equations is not complete nor is it extremely detailed. The major steps and assumptions are given with comments on application. Use of these equations without a thorough understanding of the effects of the assumptions could lead to serious misapplication of the equations or misinterpretation of results. Chapter II, Ref. 20, contains a clear, unambiguous development of reduced DOF equations.

There are two common sets of reduced DOF equations useful in the study of rocket accuracy. Both sets reduce the full 6-DOF to 3-DOF. The first set is derived by eliminating the rotational degrees of freedom by setting p, q, and r and their derivatives equal to zero. The remaining translational equations of Table 4-2 are shown in Table 4-4. These equations are called the 3-DOF or point-mass equations of motion. In this formulation the (u, v, w) notation is dropped, and the variables are expressed

TABLE 4-4.
POINT-MASS EQUATIONS OF MOTION

$$\dot{X} \;=\; \frac{F_{g_x}}{m} + \frac{\Sigma F_x}{m}$$

$$\dot{Y} \;=\; \frac{F_{g_y}}{m} + \frac{\Sigma F_y}{m}$$

$$\dot{Z} \;=\; \frac{F_{g_z}}{m} + \frac{\Sigma F_z}{m}$$

$$\theta = \text{Tan}^{-1}\,(-\dot{Z}/\dot{X})$$

$$\psi = \text{Tan}^{-1}\,(\dot{Y}/\sqrt{\dot{X}^2 + \dot{Z}^2})$$
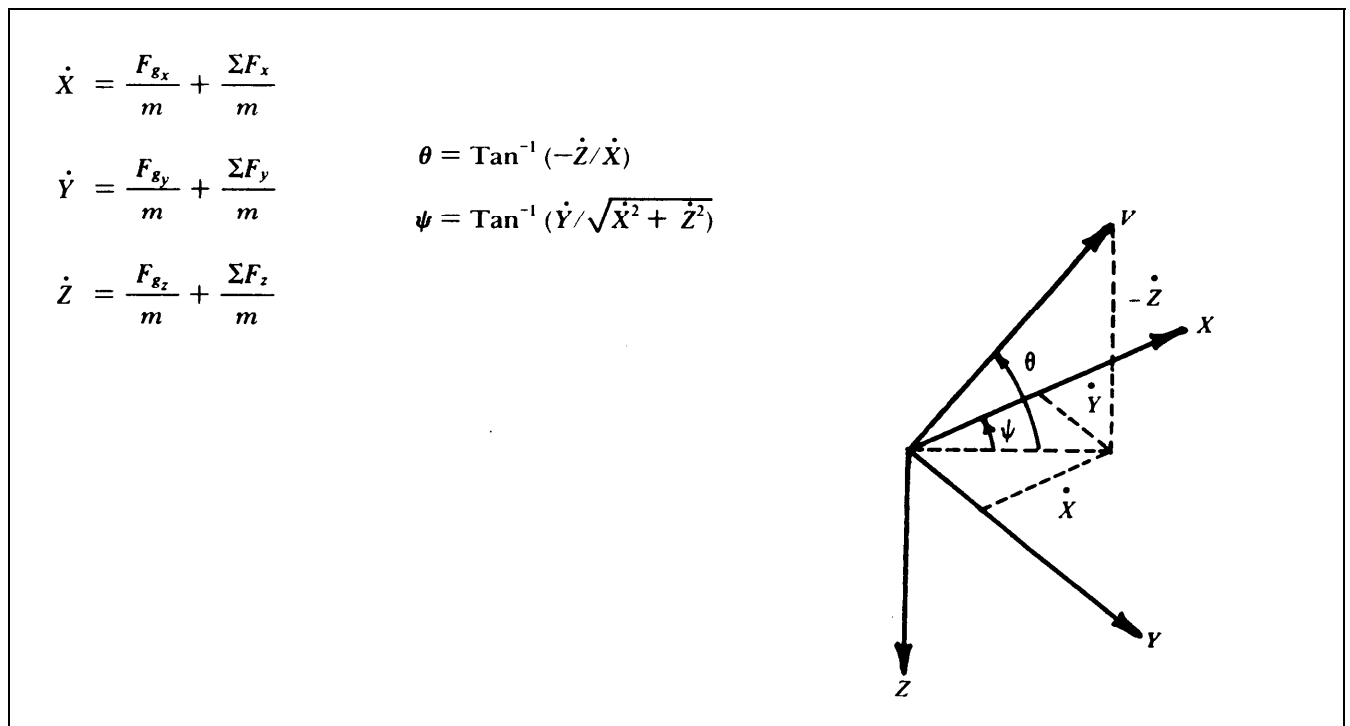
in terms of the inertial notation $(\dot{X}, \dot{Y}, \dot{Z})$ since the requirement for a separate body-coordinate system no longer exists. Also the flight path angle γ and pitch attitude angle θ become synonymous. Thrust, drag, and gravity normally are considered to be the only forces of importance in the expansion of external forces. Thrust and drag are assumed to act along the velocity vector. Al] forces acting on the body may then be related to the inertial coordinate system through the flight path angle θ and the heading ψ (see Table 4-4). These equations are the ones most often employed in performance analyses such as those of Chapter 3.

A second set of reduced DOF equations exists that is more useful in the study of free rocket accuracy. The set is derived by eliminating p, r, and v from the 6-DOF equations. The remaining equations are shown in Table 4-5. These equations are called the pitch plane equations of motion. They are useful in that they retain the range- and altitude-DOF and a lateral, rotational-DOF. This allows the relationships between speed, altitude, and the stability parameter ó to be studied. Eqs. 4-9 through 4-15 are a form of the pitch plane equations derived through a process of linearization and simplification. Equations derived by such a process are called linearized or small perturbation equations of motion. The derivation of the linearized equations is beyond the scope of this handbook, but the process contains the following simplifications (see Ref. 20, Chapter II):

1. The velocities and angles involved may be replaced by a steady component plus a small disturbance (perturbation) component.

2. The disturbances from the steady flight condition are assumed to be small enough so that the products and squares of the changes in velocities are negligible in comparison to the changes themselves. Also the disturbance angles are assumed to be small enough so that the sines of these angles may be set equal to the angles and the cosines set equal to one. Products of small perturbations are much less than the perturbations themselves and can be neglected. Also since the disturbances are small, the change in air density encountered by the rocket during any disturbance can be considered zero.

3. The gravity forces (F_{gx} and F_{gz}) are considered to be a constant external bias and are eliminated from the equations.

TABLE 4-5.
PITCH PLANE EQUATIONS OF MOTION

$$\dot{u} = \frac{\Sigma F_x + F_{gx}}{m} - qw \qquad \dot{X} = u\cos\theta + w\sin\theta$$

$$\dot{Z} = w\cos\theta - u\sin\theta$$

$$\dot{w} = \frac{\Sigma F_z + F_{gz}}{m} + qu \qquad \gamma = \theta - \alpha$$
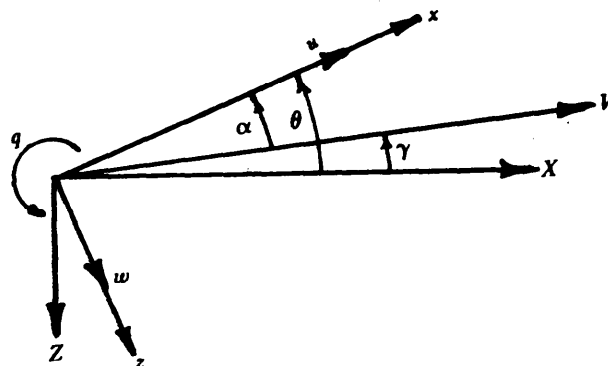
$$\dot{q} = \frac{\Sigma M_y}{I_{yy}} \qquad \dot{\theta} = q$$

By applying these simplifications, the equations of Table 4-5 become

$$\dot{u} = \frac{\Sigma F_x}{m} - qw \text{ , m/s}^2 \tag{4-38}$$

$$\dot{w} = \frac{\Sigma F_z}{m} + qu \text{ , m/s}^2 \tag{4-39}$$

$$\dot{q} = \frac{\Sigma M_y}{I_{yy}} \text{ , rad/s}^2 \tag{4-40}$$

$$\dot{X} = u, \text{ m/s (The term } w\theta \text{ is zero for a rigid launcher since the inertial axis is aligned with the launch axis.)} \tag{4-41}$$

$$\dot{Z} = w - u\theta, \text{m/s} \tag{4-42}$$

$$\dot{\theta} = q, \text{rad/s} \tag{4-43}$$

$$\alpha = w/u, \text{rad.} \tag{4-44}$$

These assumptions not only limit the applicability of Eqs. 4-38 through 4-44 to small perturbations, but they also reduce them to linear equations and yield a simplification of the mathematical methods necessary for the analysis of complicated motions. In the rigorous mathematical sense these equations are applicable only to infinitesimal disturbances; however, experience has shown that quite accurate results can be obtained by applying these equations to disturbances of finite, nonzero magnitude.

The external forces and moments (ΣF_x, ΣF_z, ΣM_y) used in Eqs. 4-9 through 4-11 involve thrust and thrust misalignment, aerodynamic drag, normal force, static margin, pitch damping, and aerodynamic misalignment. Further, the body-fixed forces and moments (thrust and aerodynamic misalignment) are modulated by the cosine of the roll angle ϕ. This allows the simulation of the effect of various spin programs on the pitch plane motion. The following equations express parts of Eqs. 4-9 through 4-11, which constitute the external forces and moments:

$$\Sigma F_x = F_T \cos\delta - \frac{\rho u^2}{2} (C_D A_{ref}), \text{ N} \tag{4-45}$$

$$\Sigma F_z = - \frac{\rho u^2}{2} \left(C_{N_\alpha} \alpha A_{ref} \right) + F_T \sin\delta \cos\phi \text{ , N} \tag{4-46}$$

$$\Sigma M_y = F_T (\sin\delta) \ell_t \cos\phi - \frac{\rho u^2}{2} (C_{N_\alpha} \alpha A_{ref} \ell_s)$$
$$+ \left(\frac{\rho u^2}{2} \right) \left[C_{m_q} \left(\frac{qd}{2u} \right) A_{ref} d \right] + \frac{\rho u^2}{2} (C_{N_\alpha} \delta_f A_{ref} \ell_s), \text{ N·m} \tag{4-47}$$

where

$\delta = $ thrust misalignment angle, mrad
$\delta_f = $ aerodynamic misalignment angle, mrad
$C_{N_\alpha} = $ aerodynamic normal force coefficient gradient, rad[-1].

The final form of Eqs. 4-9 through 4-11 is then obtained by the use of the following approximation and identities:

$$\frac{4\pi^2}{\sigma^2} = \frac{\rho A_{ref} \ell_s C_{N\alpha}}{2I_{yy}}, \ \mathrm{m}^{-2} \ (\text{from Eq. 4-7})$$

$$\cos\delta \approx 1 \text{ and } \sin\delta \approx \delta \text{ for small values of } \delta.$$

The term

$$\alpha = (w + w_z)/u, \text{ rad}$$

includes the effects of the external wind w_z in the equations of motion.

4-5.4 STATISTICAL METHODS

Up to this point, the chapter has been concerned with identifying the sources of error in a rocket system and determining the effect of each error source on the dispersion of the rocket at the warhead event. This paragraph considers the calculation of the parameters necessary to relate the dispersion due to error sources into expected distributions of rockets at the warhead event. Recall from par. 4-2.1 that bias errors are random errors affecting all the rockets in a group in the same manner and that precision errors are random errors affecting each rocket in a different manner. The topics of this paragraph relate to statistical estimation theory and include the estimation of parameters, confidence interval estimates, and probable error, for one- and two-dimensional distributions.

4-5.4.1 Measures of Central Tendency

The most common measure of central tendency is the arithmetic mean, or mean, of a set of n numbers. The mean of a population (the whole class about which conclusions are to be made) is denoted by μ. The mean of a finite set of numbers is denoted $\overline{x}$, which may also be taken to be an estimate of the population mean. The mean $\overline{x}$ of a set of n sample values x_i, is given by

$$\overline{x} = \frac{1}{n} \sum_{i=1}^{n} x_i . \tag{4-48}$$

4-5.4.2 Measures of Dispersion

The most common measures of dispersion for one-dimensional distribution are the variance, standard deviation, and probable error.

The variance σ^2 of a population is defined as the average of the squares of the distances from the population mean. If a sample of n values is drawn from a population, with mean μ, the variance σ^2 of the population is estimated by the equation

$$\sigma^2 = \frac{1}{n} \sum_{i=1}^{n} (x_i - \mu)^2 . \tag{4-49}$$

Generally, μ is not known, and an estimated mean $\overline{x}$ of the sample values must be used. If $\overline{x}$ is substituted for μ, σ^2 becomes a biased estimator of the variance. This bias can be corrected by using (n-1) rather than n in the denominator of Eq. 4-49. The unbiased estimator s^2 of the population variance then becomes

$$s^2 = \frac{1}{n-1} \sum_{i=1}^{n} (x_i - \overline{x})^2. \tag{4-50}$$

The standard deviation ó is the most important measure of dispersion. The standard deviation is the deviation from the mean value μ of a set of random values such that approximately 68% of the values are between (μ — ó) and (μ + ó), i.e., one standard deviation on either side of the mean. It is also a more understandable measure of dispersion than the variance because the standard deviation is the square root of the variance and, therefore, has the same dimensions as the variable. The standard deviation s is estimated from a sample of size n by the equation

$$s = \left[\frac{1}{n-1} \sum_{i=1}^{n} (x_i - \bar{x})^2 \right]^{1/2} \tag{4-51}$$

where s is the estimator of ó. Computation can be simplified by the algebraically equivalent form

$$s = \left\{ \frac{1}{n-1} \left[n\Sigma x_i^2 - (\Sigma x_i)^2 \right] \right\}^{1/2} . \tag{4-52}$$

The probable error (PE) is the deviation from the mean μ such that 50% of the observations are expected to lie between (μ — PE) and (μ + PE). It can be found, from a percentage of the normal distribution table, that the PE for a normal distribution is equal to 0.6745 times the standard deviation, u, i.e.

$$PE = 0.6745 \; ó. \tag{4-53}$$

To convert PE to the standard deviation ó, multiply by 1.483, i.e.,

$$ó = 1.483(PE).$$

The standard deviation is also a very important measure of dispersion for two-dimensional (bivariate) distributions. For a bivariate distribution (x and y), the standard deviation s can be estimated by using.

$$s = \left[\sum_{i=1}^{n} \frac{(x_i - \bar{x})^2 + (y_i - \bar{y})^2}{2(n-1)} \right]^{1/2} . \tag{4-54}$$

It is often desirable to establish an interval about the sample standard deviation or mean in which we can state, with a specified level of confidence α, that the true standard deviation or true mean lies. This is the confidence interval. The confidence interval for the standard deviation ó is (Ref. 14)

$$\left[\frac{(n-1) s^2}{\chi^2_{\alpha/2}} \right]^{1/2} \leq \sigma \leq \left[\frac{(n-1) s^2}{\chi^2_{1-(\alpha/2)}} \right]^{1/2} \tag{4-55}$$

where

s = computed estimate of the standard deviation.

$$\alpha = 1 - \text{(level of confidence)}. \tag{4-56}$$

The values for $\chi^2_{\alpha/2}$ and $\chi^2_{1-(\alpha/2)}$ are obtained from a chi-square distribution table, with (n – 1) degrees of freedom.

The confidence interval about the mean μ is computed by

$$\left[\bar{x} - \frac{st_{\alpha/2}}{n} \right] < \mu < \left[\bar{x} + \frac{st_{1-(\alpha/2)}}{n} \right] \tag{4-57}$$

4-57

where

$t_{\alpha/2}$ = Student's t value for (n – 1) degrees of freedom at the $\alpha/2$ percentile point
$t_{1-(\alpha/2)}$ = Student's t value for (n – 1) degrees of freedom at the $1 - (\alpha/2)$ percentile point.

Circular error probable (CEP) is the most widely used measure of dispersion for determining rocket accuracy for a two-dimensional distribution. The CEP is defined as the radius of a circle within which one-half of the values are expected to fall. The center of the circle is the mean of the values. The most popular equation used to compute the CEP is

$$CEP = K\sigma, \text{ m} \tag{4-58}$$

which can be estimated by

$$CEP = K \sum_{i=1}^{n} \left[\frac{(x_i - \bar{x})^2 + (y_i - \bar{y})^2}{2(n-1)} \right]^{1/2}, \text{ m} \tag{4-59}$$

where

K = 1.1774

and the expression for σ is substituted from Eq. 4-54.
This value of K is true only when x and y are independent, normally distributed, and have a common standard deviation u, i.e., $\sigma_y = \sigma_x = \sigma$.
For distributions without a common standard deviation, the distribution becomes elliptical, not circular. An approximation of the CEP for an elliptical distribution can be determined by the equation

$$CEP = 1.1774 \left(\frac{\sigma_x + \sigma_y}{2} \right), \text{ m} \tag{4-60}$$

where σ_x and σ_y are the standard deviations in the x- and y-directions, respectively. This approximation is correct to within 2.5% if the ratio σ_x / σ_y of the standard deviations is less than 7:1.
Fig. 4-28, in which the standard deviations in the x- (range) and y- (deflection) distances are averaged, provides more accurate CEP values over a range of σ_x / σ_y ratios for an elliptical distribution, i.e.,

$$CEP = K \left(\frac{\sigma_x + \sigma_y}{2} \right), \text{ m} \tag{4-61}$$

In Fig. 4-28, the smaller of the two standard deviations is divided by the larger. The ratio is then read on the horizontal axis and extended to the curve. The vertical value of this point on the curve is the value of **K** in Eq. 4-61.
Fig. 4-29 also provides more accurate CEP values for an elliptical distribution. In this case, however, the larger σ_{max} of the two standard deviations is used to determine CEP, i.e.,

$$CEP = K\sigma_{max}, \text{ m}. \tag{4-62}$$

In Fig. 4-29, the minimum value of the two standard deviations is divided by the maximum and the ratio is the vertical value on the curve. The horizontal value corresponding to this point on the curve is the value of K in Eq. 4-62.

4-5.4.3 Measures of Dispersion for Several Error Sources

The measures of dispersion previously discussed are used when the errors are from one source. For the total dispersion resulting from several independent dispersion sources, the root-sum-square (vector
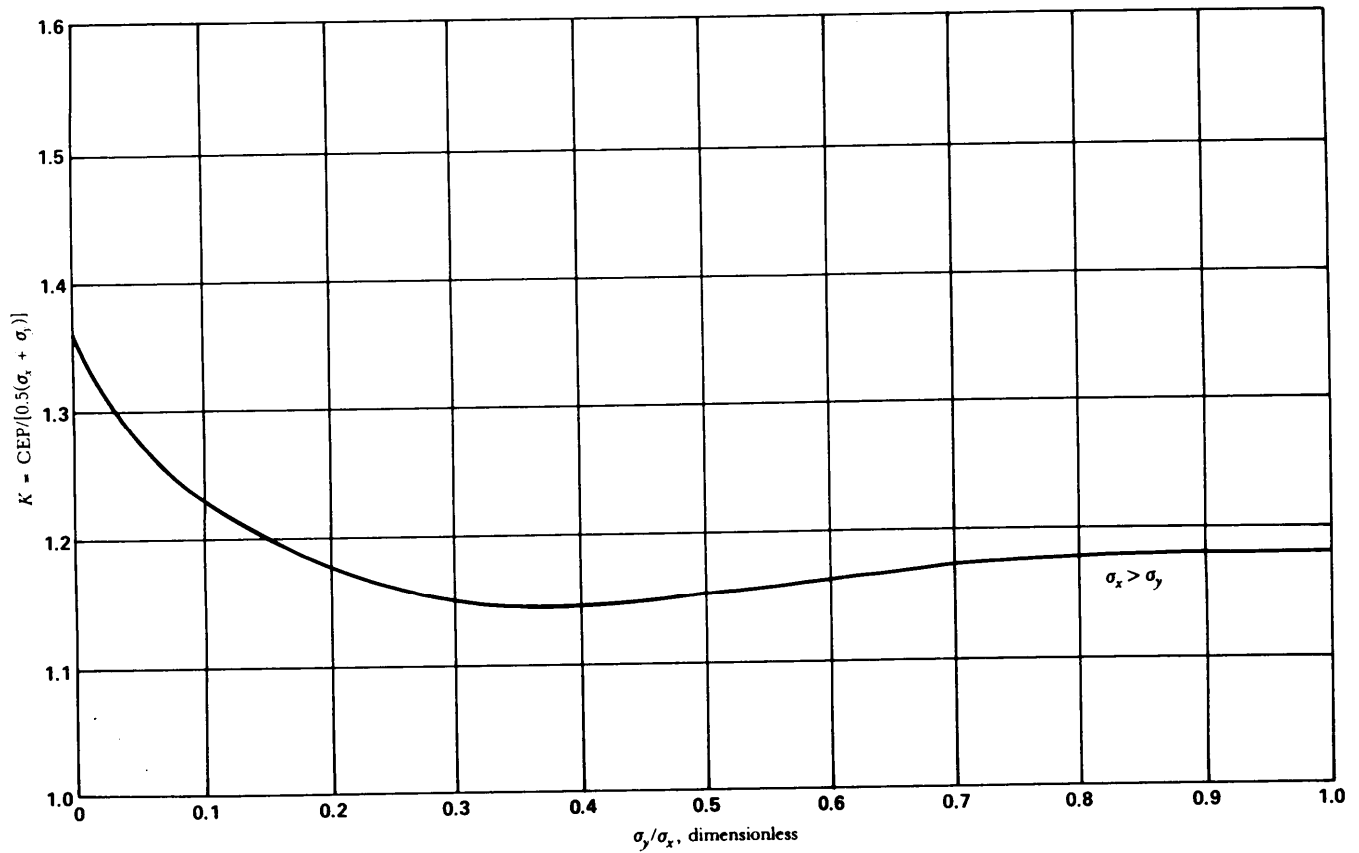
Figure 4-28. Ratio of CEP to σ_y/σ_x for Elliptical Distribution

sum) method is used. The total dispersion is determined by squaring the errors from each source and then summing the squares. The square root of this summation is the total error σ_{tot}. In equation form

$$\sigma_{tot} = (\sigma_1^2 + \sigma_2^2 + \cdots + \sigma_n^2)^{1/2}, \text{ m or mrad.}$$

For a two-dimensional distribution, the total error—$\sigma_{x_{tot}}$ and $\sigma_{y_{tot}}$—in each dimension must be determined and the average of the two taken to obtain the total error σ_{sys}, for the system i.e.,

$$\sigma_{x_{tot}} = (\sigma_{x1}^2 + \sigma_{x2}^2 + \cdots + \sigma_{xn}^2)^{1/2}, \text{ m} \tag{4-64}$$

$$\sigma_{y_{tot}} = (\sigma_{y1}^2 + \sigma_{y2}^2 + \cdots + \sigma_{yn}^2)^{1/2}, \text{ m} \tag{4-65}$$

$$\sigma_{sys} = \frac{\sigma_{x_{tot}} + \sigma_{y_{tot}}}{2}, \text{ m.} \tag{4-66}$$

The CEP is then found by the equation

$$\text{CEP} = 1.1774\sigma_{sys}, \text{ m} \tag{4-67}$$

for the condition that the ratio $\sigma_{x_{tot}}/\sigma_{y_{tot}} < 7{:}1$.

Figs. 4-28 and 4-29 can be used to estimate the CEP of an elliptical distribution.

The vector sum method is used extensively in the preliminary design phase of a rocket system. The CEP required in order for the missile system to meet its overall accuracy requirement is specified. The
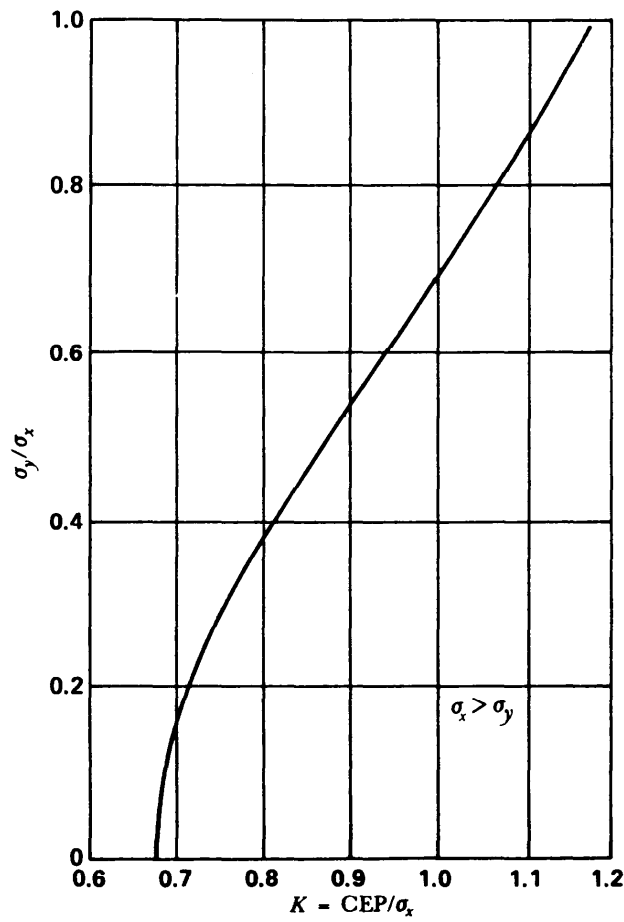
Figure 4-29. **Ratio of CEP to óx for Elliptical Distribution**

one-sigma errors of each of the independent error sources are found by testing each of the components that contribute errors. The effects of these one-sigma values on the range and deflection of the rocket at the impact point are found by simulation. These errors in range and deflection are then combined by the vector sum method to obtain the total error for the system. The CEP is computed and is compared with the required CEP. If this computed CEP does not meet the requirements, some or all of the components that contribute to the total error must be improved. In this manner, the best design of the rocket components can be determined.

4-5.4.4 Range and Deflection Probable Errors

From Eq. 4-53 the range error probable (REP) is defined by

$$REP = 0.6745 ó_{range}, \text{ m or mrad} \tag{4-68}$$

where

$$\sigma_{range} = \left(\sum_{i=1}^{n} \sigma_{R_i}^2 \right)^{1/2}, \text{ m or mrad} \tag{4-69}$$

$\sigma_{R_i}^2$ = variance due to individual error sources in range. Similarly, the deflection error probable (DEP) is

$$DEP = 0.6745 ó_D, \text{ m or mrad} \tag{4-70}$$

where

$$\sigma_D = \left(\sum_{i=1}^{n} \sigma_{D_i}^2 \right)^{1/2}, \text{ m or mrad} \tag{4-71}$$

$\sigma_{D_i}^2$ = variance due to individual error sources in deflection. The variations of REP, DEP, and CEP with range are shown in Figs. 4-30, 4-31, and 4-32, respectively, for a typical rocket with an impact fuze.

4-5.4.5 Probability of Hit

The probability of hitting a target depends on many factors such as

1. Target size, shape, and vulnerability
2. Warhead lethality
3. System reliability
4. Overall rocket system accuracy.

In terms of CEP, the probability P_{HIT} of hitting a target is given by the following expression:

$$P_{HIT} = 1 - \exp\left[-0.6926 \frac{r_t^2}{(CEP)^2} \right], \text{ dimensionless} \tag{4-72}$$

where

r_t = effective radius of the target, m.
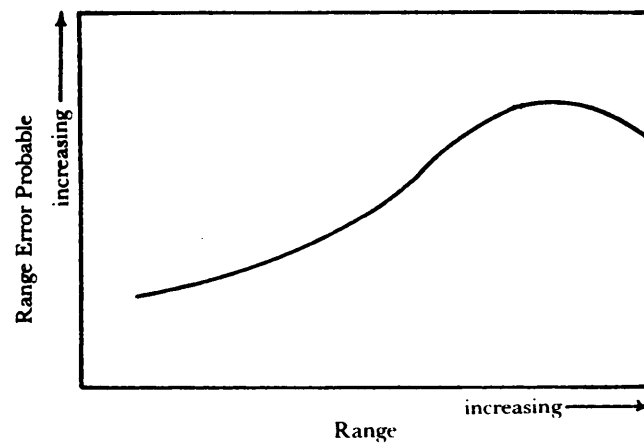
Figure 4-30.   Variation of Range Error Probable With Range-Impact Fuze
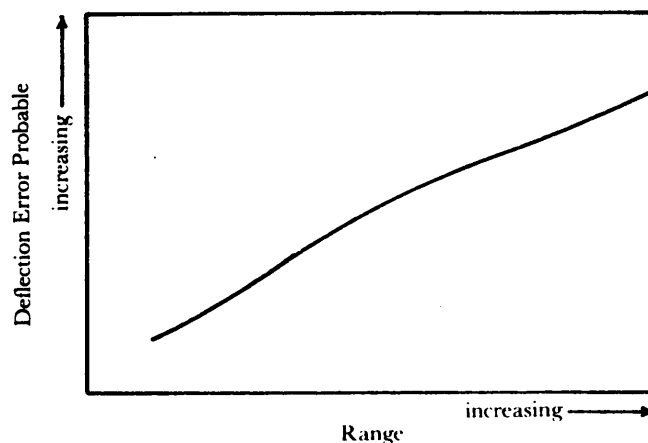
Figure 4-31.   Variation of Deflection Error Probable With Range-Impact Fuze

4-61
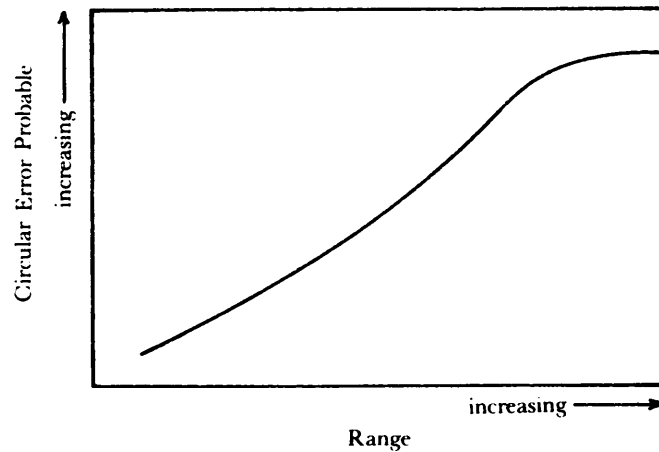
Figure 4-32.   Variation of CEP With Range-Impact Fuze

Eq. 4-72 assumes that the centers of the CEP and target coincide and that only one rocket is fired. Warhead lethality, and target size and shape are considerations in defining the effective target radius.

4-5.5 ERROR BUDGET AND SAMPLE CALCULATION
4-5.5.1 General
Free rocket accuracy calculation may be performed by simulating many rockets as described in par. 4-5.1, recording the rocket locations at the warhead event, and applying the statistical methods of par. 4-5.4. The Monte Carlo method suffers from several disadvantages for the design phases of rocket systems; the most important of which is that the relationship between the dispersions in rocket impacts and individual error sources becomes difficult to assess.

This paragraph presents a method for rapidly assessing the accuracy of free rockets by using

1. Information from previous paragraphs which give the dispersions due to individual error sources up to rocket burnout

2. New material defining dispersions encountered during the ballistic flight phase.

An example problem illustrates the method for calculating the dispersion at the warhead event caused by error sources throughout the flight.

For the purposes of this handbook only those ballistic-phase errors that have the greatest influence on the accuracy have been included, namely,

1. Errors in atmospheric density

2. Errors in the ballistic coefficient

3. Errors in ballistic wind.

The graphs in this paragraph show the changes in range and deflection for unit changes in the several rocket variables. The plotted data are the results of numerous digital computer calculations. The graphs are used by determining the nominal QE and range; these parameters, in turn, are used to establish the unit effects. The example calculations illustrate how the dispersion at the warhead event is calculated and is tabulated into an error budget used in the further calculation of PE components.

4-5.5.2 Example Problem
Given: An indirect-fire rocket with impact fuze and constant spin.

Ballistic coefficient: $B = 12,000$ kg/m^2

Maximum range: $R_{max} = 28.5$ km at optimum QE

Wavelength of yaw: $ó = 150$ m

Specific Impulse: $I_{SP} = 250$ s

Acceleration level: $G = 48$

MIL-HDBK-762(MI)

Quadrant elevation: QE = 4.5 deg (assumed optimum)
Dimensionless launcher length: P = 0
Spin rate: p = 10 rev/s
Booster mass ratio: r_b = 1.4
Assumed one-sigma values for the error sources are shown in Table 4-6.
Determine: The dispersions at the warhead event.

4-5.5.2.1 Prelaunch Errors

The given aiming error (Table 4-6) is 1 mrad in each plane, azimuth and elevation. The error in deflection from Eq. 4-1 **is**

$\Delta Y = \Delta \psi_0 R$
$\Delta Y = (1 \text{ mrad}) (28.5 \text{ km})$
$\Delta Y = 28.5 \text{ m.}$

TABLE 4-6. ERROR BUDGET AT WARHEAD EVENT FOR INDIRECT FIRE ROCKET WITH IMPACT FUZE

Source of Error	One-Sigma Magnitude	ΔR, m	ΔY, m	ΔR, mrad	ΔY, mrad
I. Prelaunch Errors					
A. All Sources	1 mrad	0	28.5	0	1
II. Launch Errors					
A. Translation	0.1 m/s	0	−24.7	0	−0.87
B. Rotation	15 mrad/s	0	81.2	0	2.85
C. Dynamic Imbalance	0.5 mrad	0	170	0	5.97
III. Boost Errors					
A. Wind	3.5 m/s	0	−698	0	−24.5
B. Thrust Misalignment	0.5 mrad	0	161	0	5.63
C. Total Impulse	1%	430	0	15.1	0
IV. Ballistic Errors					
A. Density	0.5%	222	0	7.79	0
B. Ballistic Wind	2.3 m/s	138	108	4.84	3.8
C. Ballistic Coefficient	0.75%	167	0	5.86	0

Note the use of range R as the normalizing factor for ΔY.. In the mathematically rigorous sense the error should be normalized to the trajectory path length (Ref. 1, p. 56). Since the purpose of this sample problem is the exploration of relative error effects on dispersion, the use of range is tolerated. For a ballistic coefficient B = 12,000 kg/m², a maximum range R_{max} = 28.5 km, and with the use of Fig. 4-33, the initial velocity required is determined to be 915 m/s. By use of Fig. 4-34(B) in conjunction with this information, the ratio of a percent change in range per change in departure angle is determined. In this example the range we are interested in is the maximum value; therefore, the ratio of range desired to maximum range is unity. As seen in Fig. 4-34(B), the partial derivative $\partial R / \partial \theta$ is zero at unity ratio; thus, an error in aim results in a negligible error in range at maximum range. This leads to the zeros in Table 4-6 for AR.
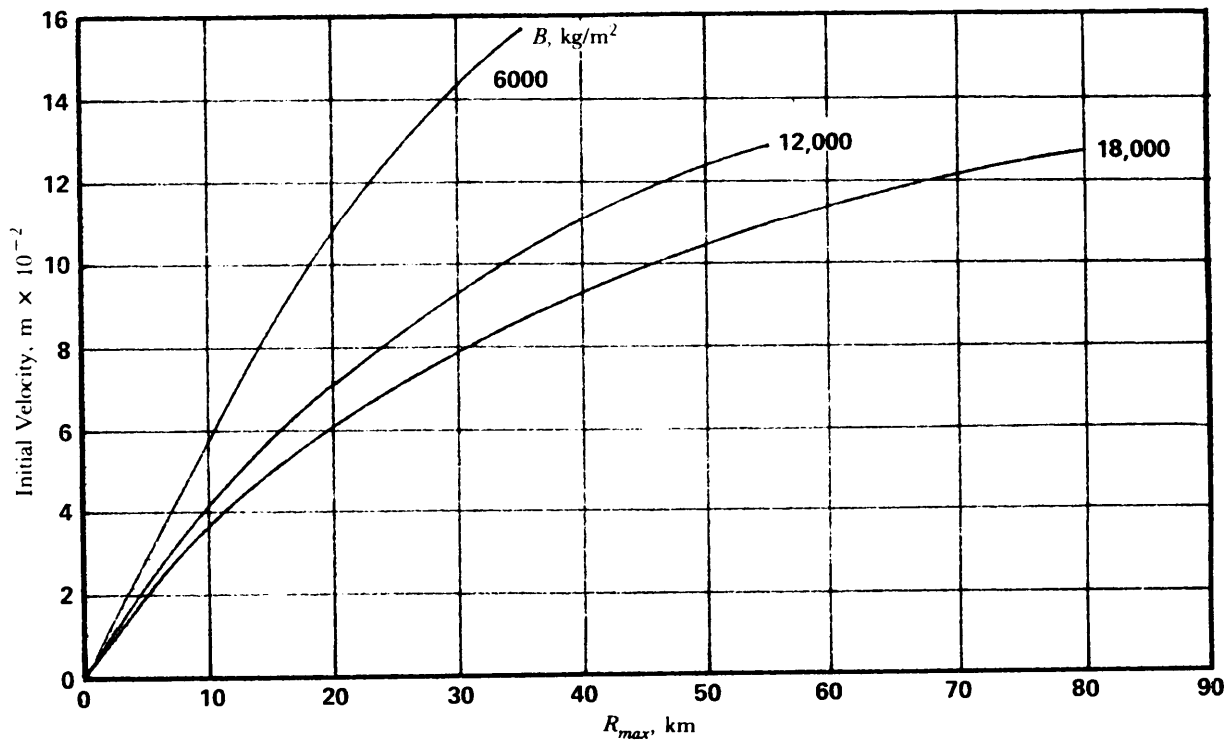
Figure 4-33. Initial Velocity vs Maximum Range

4-5.5.2.2 Launch Errors

Fig. 4-1 l(A) shows that for a translation error of 0.3 m/s, P = 0, ó = 150 m, and G = 48, a resultant angular dispersion γ_{TS} of — 2.6 mrad is obtained. The deflection error due to the assumed value of 0.1 m/s (Table 4-6) is

$$\Delta Y = \left(\frac{0.1 \text{ m/s}}{0.3 \text{ m/s}}\right)(-2.6 \text{ mrad}) = -0.867 \text{ mrad}$$

$$\Delta Y = (-0.867 \text{ mrad})(28.5 \text{ km})$$

$$\Delta Y = -24.7 \text{ m.}$$

The change in range clue to initial translational velocity is zero for the same reasons as given for the prelaunch aiming errors.

An initial rotational velocity of q = 100 mrad/s, P = 0, G = 48, and ó = 150 m produces an error γ_{TS} of 19 mrad from Fig. 4-10(A). For the assumed error value of 15 mrad/s (Table 4-6),

$$\gamma_{TS} = 19 \text{ mrad}\left(\frac{15 \text{ mrad/s}}{100 \text{ mrad/s}}\right)$$

$$\gamma_{TS} = 2.85 \text{ mrad.}$$

This assumes that the angular dispersion, as a function of G and ó, is affected linearly by rotation rate, so the deflection error is

$$\Delta Y = (2.85 \text{ mrad})(28.5 \text{ km})$$

MIL-HDBK-762(MI)

Curve	I_0, m/s	R_{max}, km
1	304.8	5.75
2	609.6	10.97
3	914.4	16.46
4	1219.2	23.12
5	1524.0	31.19

R/R_{max}, dimensionless

(A) B = 6000 kg/m^2

$\partial R/\partial\theta$, %/mrad
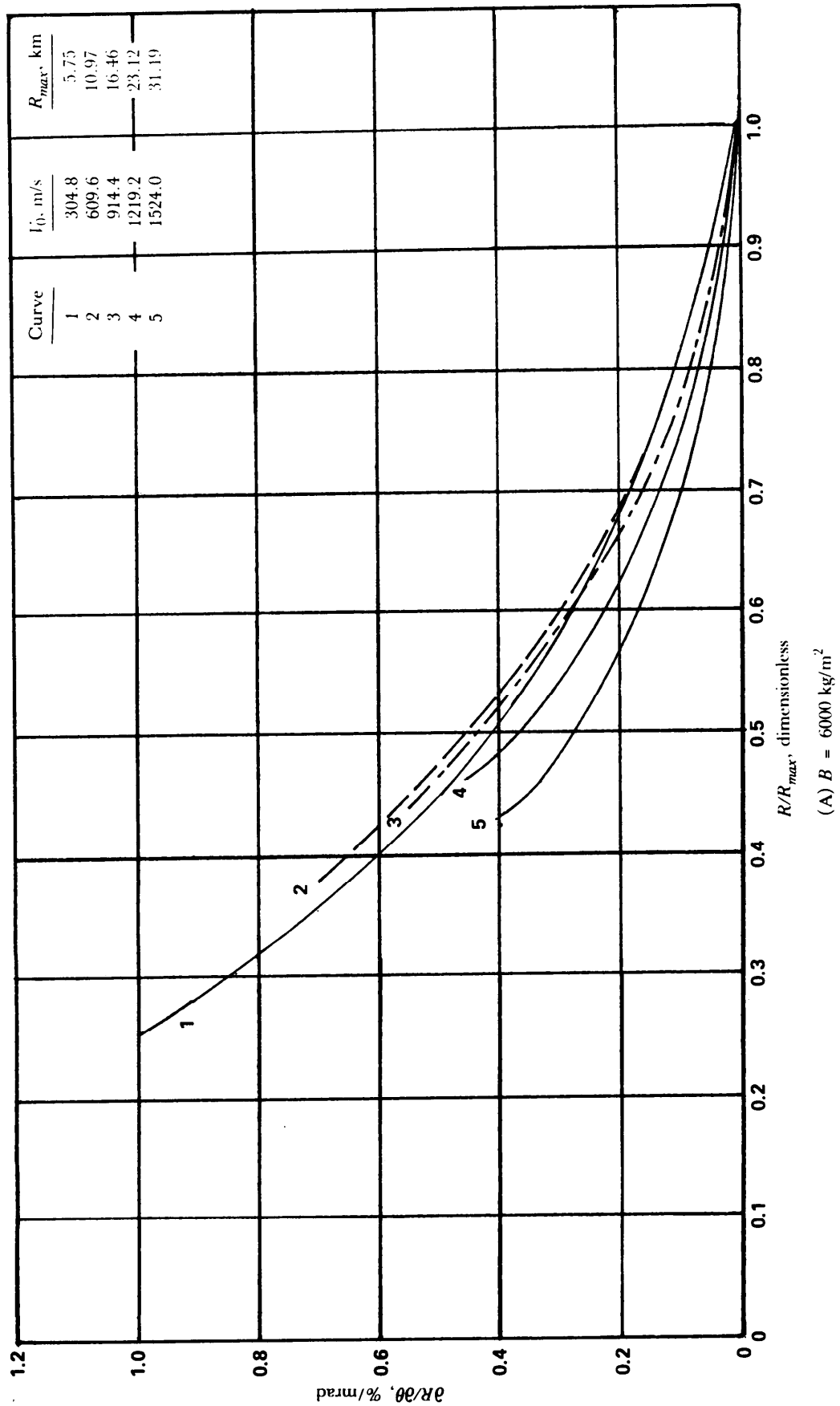
Figure 4-34.   Unit Effect, Range/Departure Angle vs R/R_{max} for Various B Values—Impact Fuze

Curve	V_0, m/s	R_{max}, km
1	304.8	7.08
2	609.6	16.39
3	914.4	28.46
4	1219.2	50.53

R/R_{max}, dimensionless

$\partial R/\partial \theta$, %/mrad

(B) B = 12,000 kg/m^2

Figure 4-34.   (cont'd)

Curve	I_0, m/s	R_{max}, km
1	304.8	7.70
2	609.6	19.90
3	914.4	39.07
4	1219.2	73.60

R/R_{max}, dimensionless

(C) $B = 18,000$ kg/m²
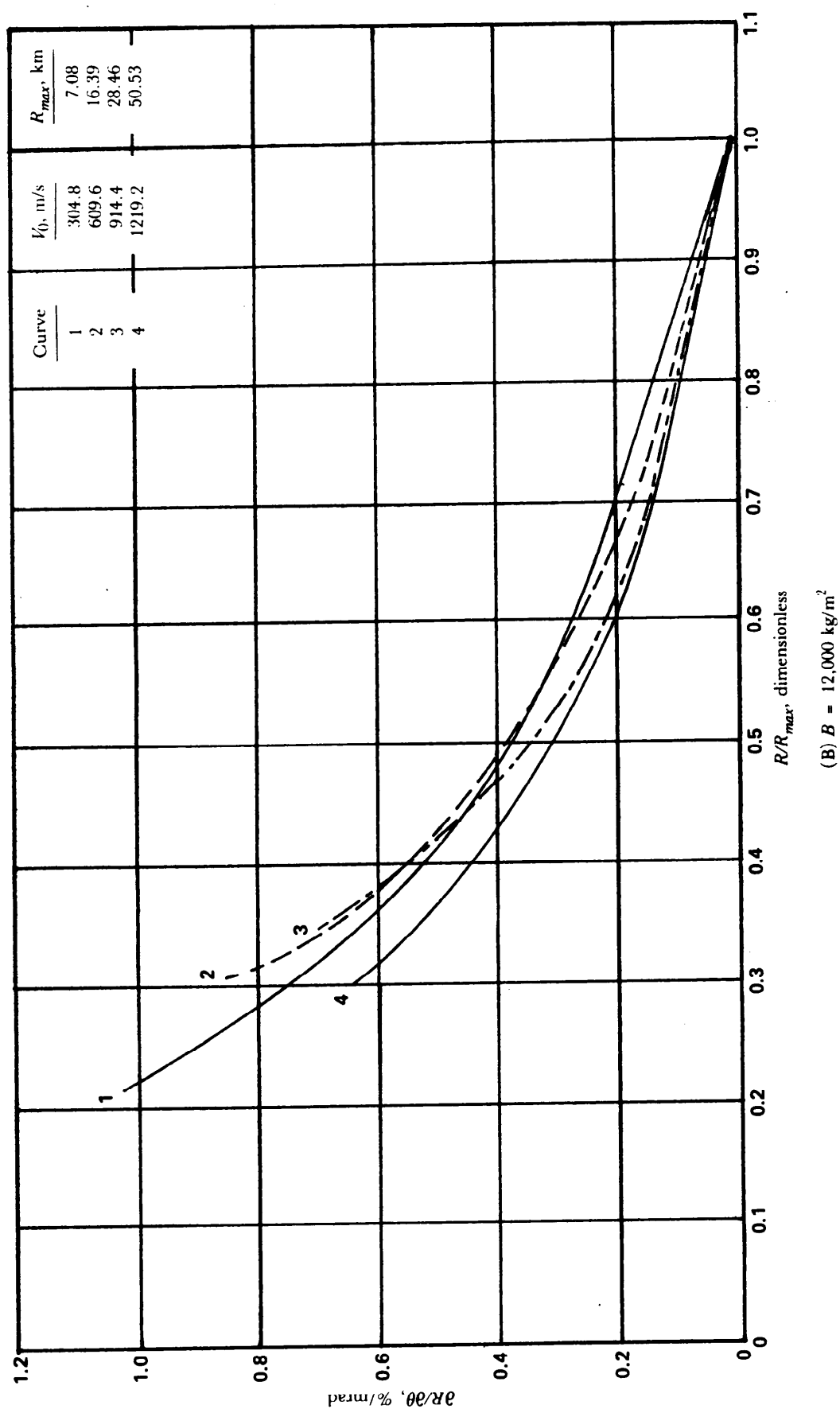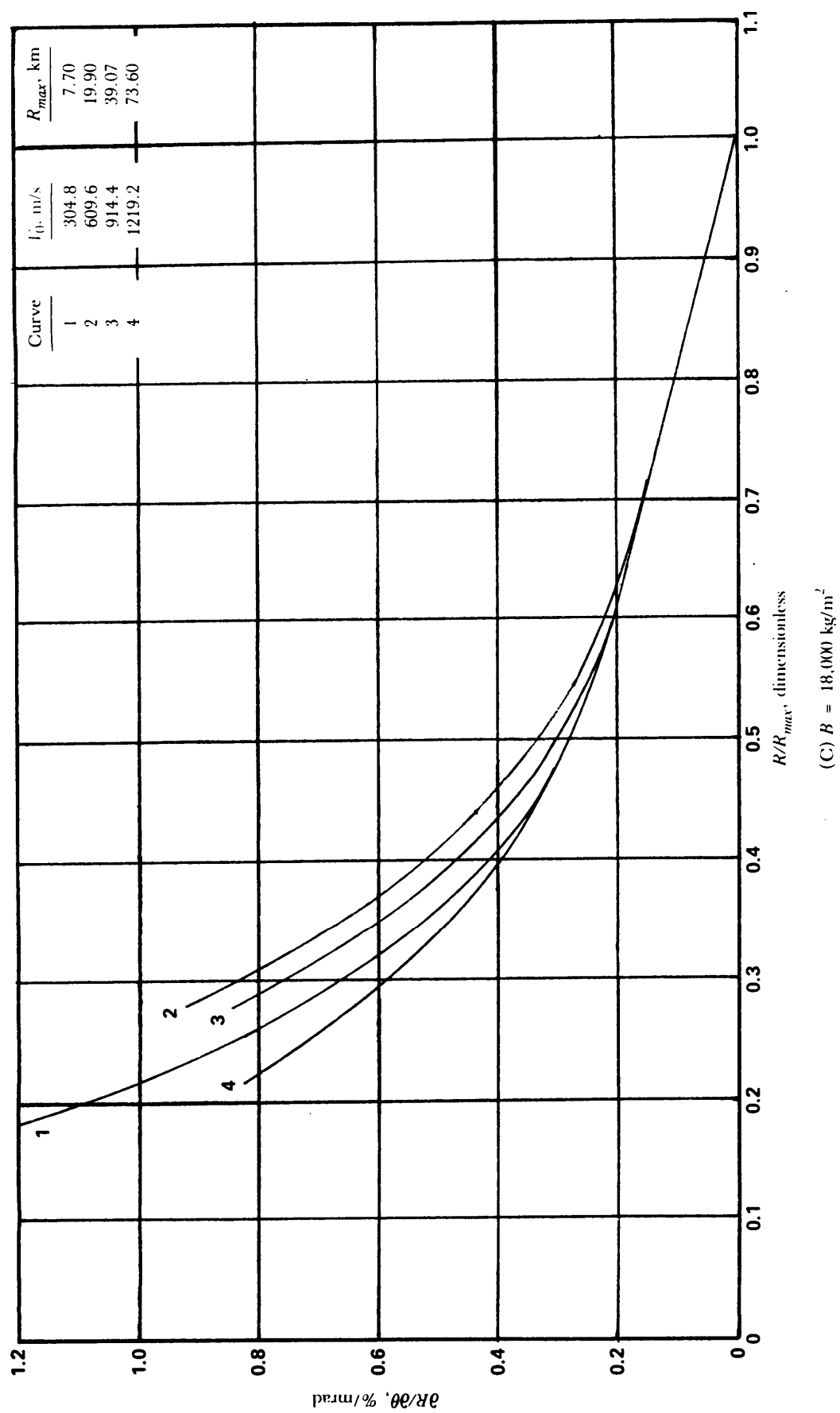
Figure 4-34.   (cont'd)

$$\Delta Y = 81.2 \text{ m}$$

and

$$\Delta R = 0.$$

For a dynamic imbalance error ϵ = 0.5 mrad (Table 4-6) and a spin rate p = 10 rev/s, the equivalent initial angular rate q_{equiv} due to dynamic imbalance is (from Eq. 4-20)

$$q_{equiv} = p\epsilon$$

$$q_{equiv} = \left(10\frac{\text{rev}}{\text{s}}\right)\left(2\pi \frac{\text{rad}}{\text{rev}}\right)(0.5 \text{ mrad})$$

$$q_{equiv} = 31.4 \text{ mrad/s.}$$

Since in Fig. 4-10(A) q = 100 mrad/s, following the procedure for translational rotation error results in

$$\gamma_{TS} = 19 \text{ mrad} \left(\frac{31.4 \text{ mrad/s}}{100 \text{ mrad/s}}\right)$$

$$\gamma_{TS} = 5.97 \text{ mrad}$$

$$\Delta Y = (5.97 \text{ mrad}) (28.5 \text{ km})$$

$$\Delta Y = 170 \text{ m}$$

and

$$\Delta R = 0.$$

4-5.5.2.3 Boost Errors

With a boost wind error of 3.5 m/s (Table 4-6), G = 48, ó = 150 m, and P = 0, Fig. 4-12(A) shows the angular dispersion γ_{TS} due to a 3-m/s wind is—21 mrad, therefore,

$$\gamma_{TS} = -21 \text{ mrad} \left(\frac{3.5 \text{ m/s}}{3 \text{ m/s}}\right)$$

$$\gamma_{TS} = -24.5 \text{ mrad}$$

$$\Delta Y = (-24.5 \text{ mrad}) (28.5 \text{ km})$$

$$\Delta Y = -698 \text{ m}$$

and

$$\Delta R = 0 .$$

Spinning the vehicle is an attempt to minimize dispersion from thrust misalignment error. Ref. 2 and Fig. 4-18 give the theoretical value for the dispersion reduction factor β as

$$\beta = \frac{1}{2n_\sigma} , \text{ dimensionless.} \tag{4-73}$$

Since V_0 from Fig. 4-33 was determined to be 915 m/s, the number of revolutions n_o made by the spinning rocket in the first wavelength of yaw ó is

MIL-HDBK-762(MI)

$$n_\sigma = \frac{p\sigma}{V_0}$$

(4-74)

$$n_\sigma = (10 \text{ rev/s}) \left(\frac{1}{915 \text{ m/s}}\right) (150 \text{ m})$$

$$n_\sigma = 1.6 \text{ rev}$$

$$\beta = \frac{1}{(2)\,(1.6)} \text{ (from Eq. 4-73)}$$

$$\beta = 0.313 .$$

From Fig. 4-13(A) the dispersion γ_{TS} from thrust misalignment δ = 0.5 mrad (Table 4-6) for P = 0, G = 48, and ó = 150m is

$$\gamma_{TS} = 18 \text{ mrad}$$

$$\Delta Y = \beta\gamma_{TS}R$$

$$\Delta Y = 0.313 \,(18 \text{ mrad})\,(28.5 \text{ km})$$

$$\Delta Y = 161 \text{ m}$$

and

$$\Delta R = 0 .$$

An alternate method of estimating the affect of thrust misalignment is by use of Fig. 4-19(A). The figure shows the dispersion reduction factor β for a zero-length launcher and constant spin. The values of β achieved for this figure were determined by using the optimum spin rate to minimize the dispersion from a 0.5-mrad thrust misalignment δ and from a 0.5-mrad dynamic imbalance ϵ. If it is assumed that comparable values of β may be achieved from any reasonable combination of $\delta, \epsilon,$ and optimum spin, this figure may be used directly. If Fig. 4-19(A) is used, the 0.5-mrad dynamic imbalance effect should be deleted since it will have been accounted for in the use of the figure.

If this procedure for thrust misalignment were used, then Fig. 4-19(A) gives

By following the described method

$$\gamma_{TS} = 18 \text{ mrad (from Fig. 4-13(A))}$$

$$\Delta Y = \beta\gamma_{TS}R$$

$$\Delta Y = 0.19 \,(18 \text{ mrad})\,(28.5 \text{ km})$$

$$\Delta Y = 97.5 \text{ m}$$

and

$$\Delta R = 0 \ .$$

    The dispersion caused by total impulse variation is obtained by first determining the sensitivity of boost velocity V_B to specific impulse I_{sp}. Eq. 3-19 gives the ideal velocity relationship as

$$\frac{\Delta V_B}{\Delta I_{sp}} = g_0 \ln r_b$$

or

$$\Delta V_B = \Delta I_{sp} g_0 \ln r_b, \ \mathrm{m/s} \qquad\qquad \textbf{(4-75)}$$

$$\Delta V_B = \Delta I_{sp} \ (9.8 \ \mathrm{m/s}^2) \ (\ln 1.4)$$

$$\Delta V_B = 3.3 \ \Delta I_{sp}, \ \mathrm{m/s}.$$

For the given $I_{sp} = 250$ s and an error of 1% (Table 4-6),

$$\Delta I_{sp} = (0.01) \ (250)$$

$$\Delta I_{sp} = 2.5 \ \mathrm{s} \ .$$

Therefore

$$\Delta V_B = (3.3 \ \mathrm{m/s}^2) \ (2.5 \ \mathrm{s})$$

$$\Delta V_B = 8.25 \ \mathrm{m/s} \ .$$

By using Fig. 4-35(B) for $V_0 = 915$ m/s and $R/R_{max} = 1$,

$$\frac{\partial R(\%)}{\partial V(\%)} = 1.67$$

and

$$\Delta V \ = \ \frac{8.25}{915} \ (100) = 0.902\%$$

$$\Delta R = 1.67 \ \Delta V$$

$$\Delta R = 1.67(0.902) = 1.51\%$$

$$\Delta R = 0.0151(28.5 \ \mathrm{km})$$

$$\Delta R = 430 \ \mathrm{m}$$

and

$$\Delta Y = 0.$$

Curve	V_0, m/s	R_{max}, km
1	304.8	5.75
2	609.6	10.97
3	914.4	16.46
4	1219.2	23.12
5	1524.0	31.19

R/R_{max}, dimensionless

(A) $B = 6000$ kg/m^2

$\partial R/\partial V$, %/%
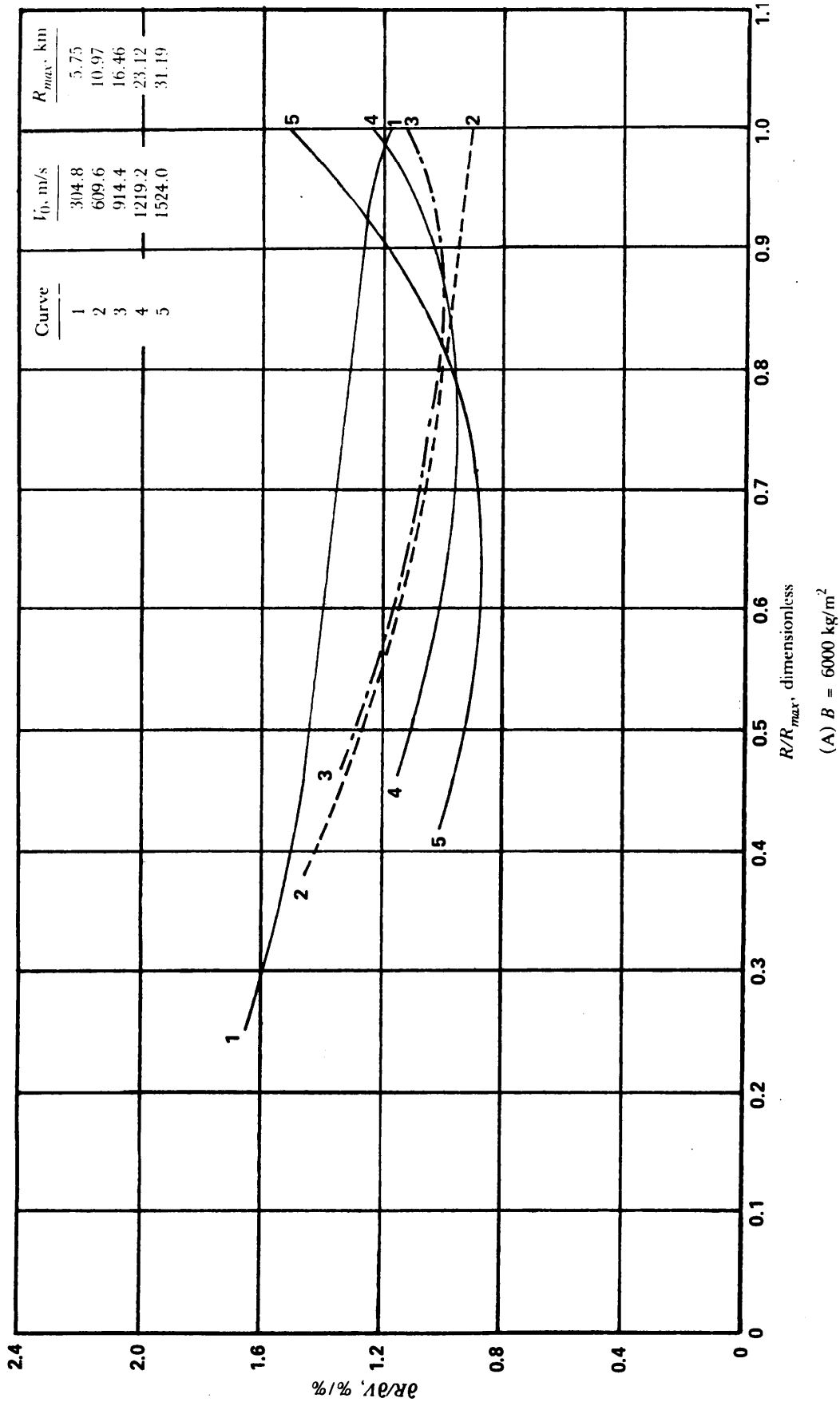
Figure 4-35. Unit Effect, Range/Velocity vs R/R_{max} for Various B Values—Impact Fuze

Curve	V_0, m/s	R_{max}, km
1	304.8	7.08
2	609.6	16.39
3	914.4	28.46
4	1219.2	50.53

R/R_{max}, dimensionless

(B) $B = 12,000$ kg/m^2

Figure 4-35.   (cont'd)

4-72

Curve	V_0, m/s	R_{max}, km
1	304.8	7.70
2	609.6	19.90
3	914.4	39.07
4	1219.2	73.60

R/R_{max}, dimensionless

(C) $B = 18,000$ kg/m^2

Figure 4-35. (cont'd)

4-73
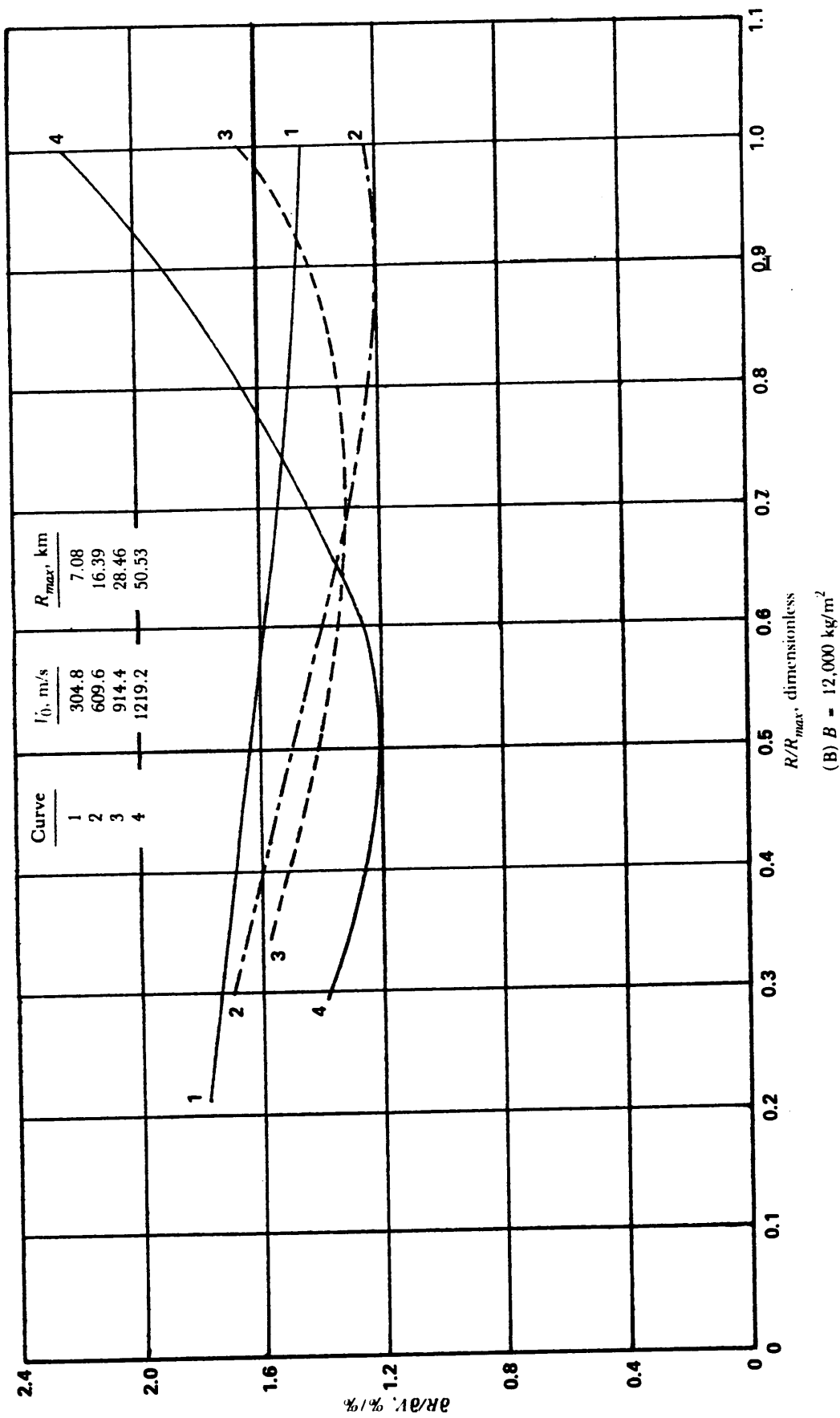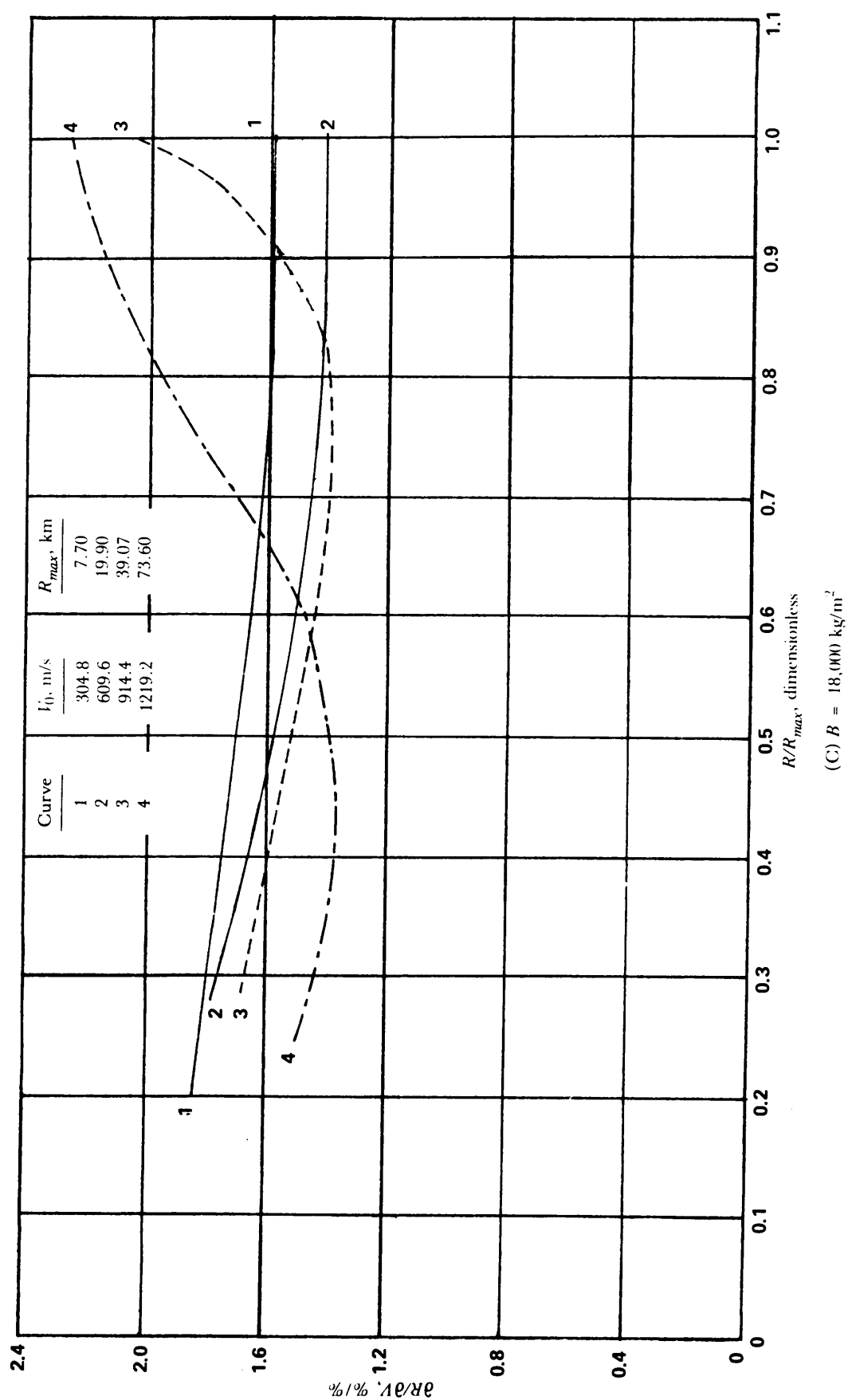
4-5.5.2.4 Ballistic Errors

The density error is 1% (Table 4-6). From Fig. 4-36(B) for $V_0 = 915$ m/s and $R/R_{max} = 1$,

$$\frac{\partial R(\%)}{\partial \rho(\%)} = 0.78$$

$$\Delta R = (1)(0.78)\% = 0.78\%$$

$$\Delta R = 0.0078 \, (28.5 \text{ km})$$

$$\Delta R = 222 \text{ m}$$

and

$$\Delta Y = 0 \ .$$

The ballistic wind error is 2.3 m/s (Table 4-6). For this example problem the error is assumed to exist in each plane, i.e., range and deflection.

From Fig. 4-37(B) for $V_0 = 915$ m/s and $R/R_{max} = 1$,

$$\frac{\partial R}{\partial V_w} = 0.21 \frac{\%}{\text{m/s}}$$

$$\Delta R = 0.21(2.3)\%$$

$$\Delta R = 0.483\%$$

$$\Delta R = 0.00483(28.5 \text{ km})$$

$$\Delta R = 138 \text{ m}.$$

From Fig. 4-38(B) for $V_0 = 915$ m/s and $R/R_{max} = 1$,

$$\frac{\partial Y}{\partial V_w} = 0.164 \frac{\%}{\text{m/s}}$$

$$\Delta Y = 0.164(2.3)\%$$

$$\Delta Y = 0.377\%$$

$$\Delta Y = 0.00377(28.5 \text{ km})$$

$$\Delta Y = 108 \text{ m}.$$

The ballistic coefficient error of 0.75% (Table 4-6) includes errors caused by drag and burnout mass variation. This error is treated as if it were an error in density.

(A) $B = 6000$ kg/m^2

Figure 4-36.   Unit Effect, Range/Density vs R/R_{max} for Various B Values—Impact Fuze

Curve	V_{f_0}, m/s	R_{max}, km
1	304.8	7.08
2	609.6	16.39
3	914.4	28.46
4	1219.2	50.53

R/R_{max}, dimensionless

(B) $B = 12,000$ kg/m²

Figure 4-36.   (cont'd)

Curve	V_0, m/s	R_{max}, km
1	304.8	7.70
2	609.6	19.90
3	914.4	39.07
4	1219.2	73.60

R/R_{max}, dimensionless

(C) B = 18,000 kg/m²

$\partial R/\partial c$, %/%

Figure 4-36. (cont'd)

Curve	I_0, m/s	R_{max}, km
1	304.8	5.75
2	609.6	10.97
3	914.4	16.46
4	1219.2	23.12
5	1524.0	31.19

R/R_{max}, dimensionless

(A) $B = 6000$ kg/m^2

$\partial R/\partial I_w$, %/m·s^{-1}
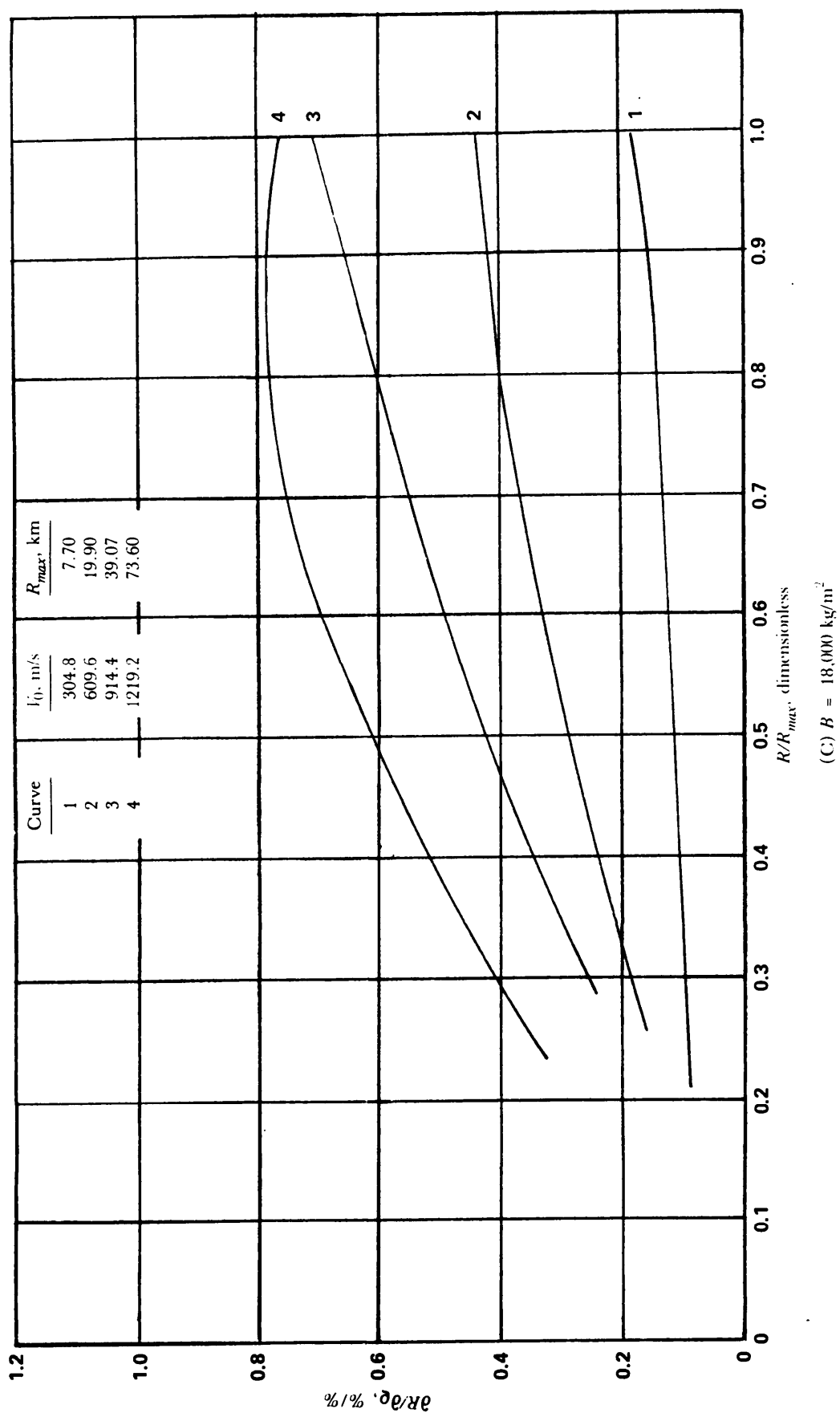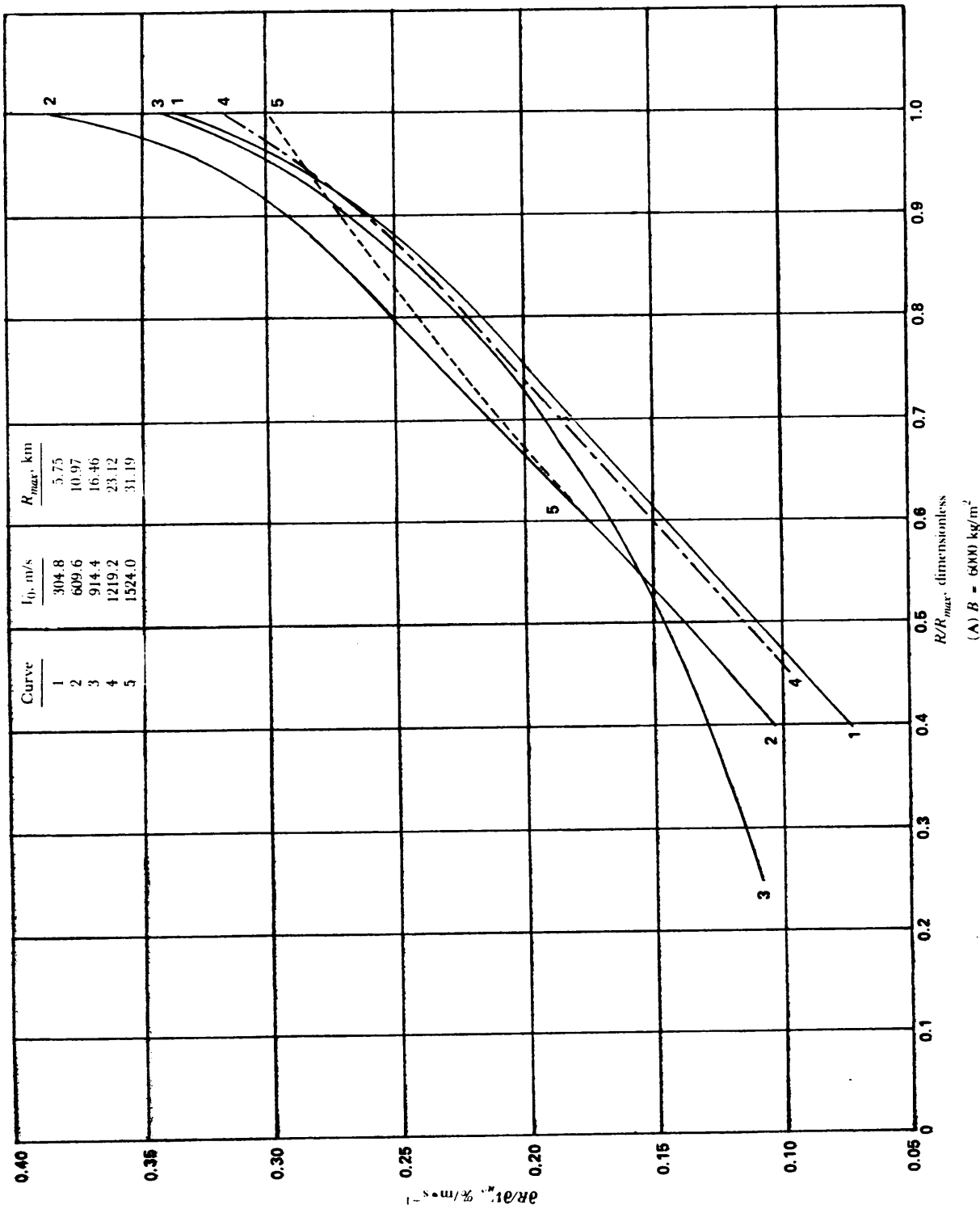
Figure 4-37. Unit Effect, Range/Wind vs R/R_{max} for Various B Values—Impact Fuze

(cont'd on next page)

Curve	v_0, m/s	R_{max}, km
1	304.8	7.08
2	609.6	16.39
3	914.4	28.46
4	1219.2	50.53

R/R_{max}, dimensionless

(B) $B = 12,000$ kg/m²

Figure 4-37. (cont'd)

Curve	V_0, m/s	R_{max}, km
1	304.8	7.70
2	609.6	19.90
3	914.4	39.07
4	1219.2	73.60

R/R_{max}, dimensionless

(C) $B = 18,000$ kg/m^2
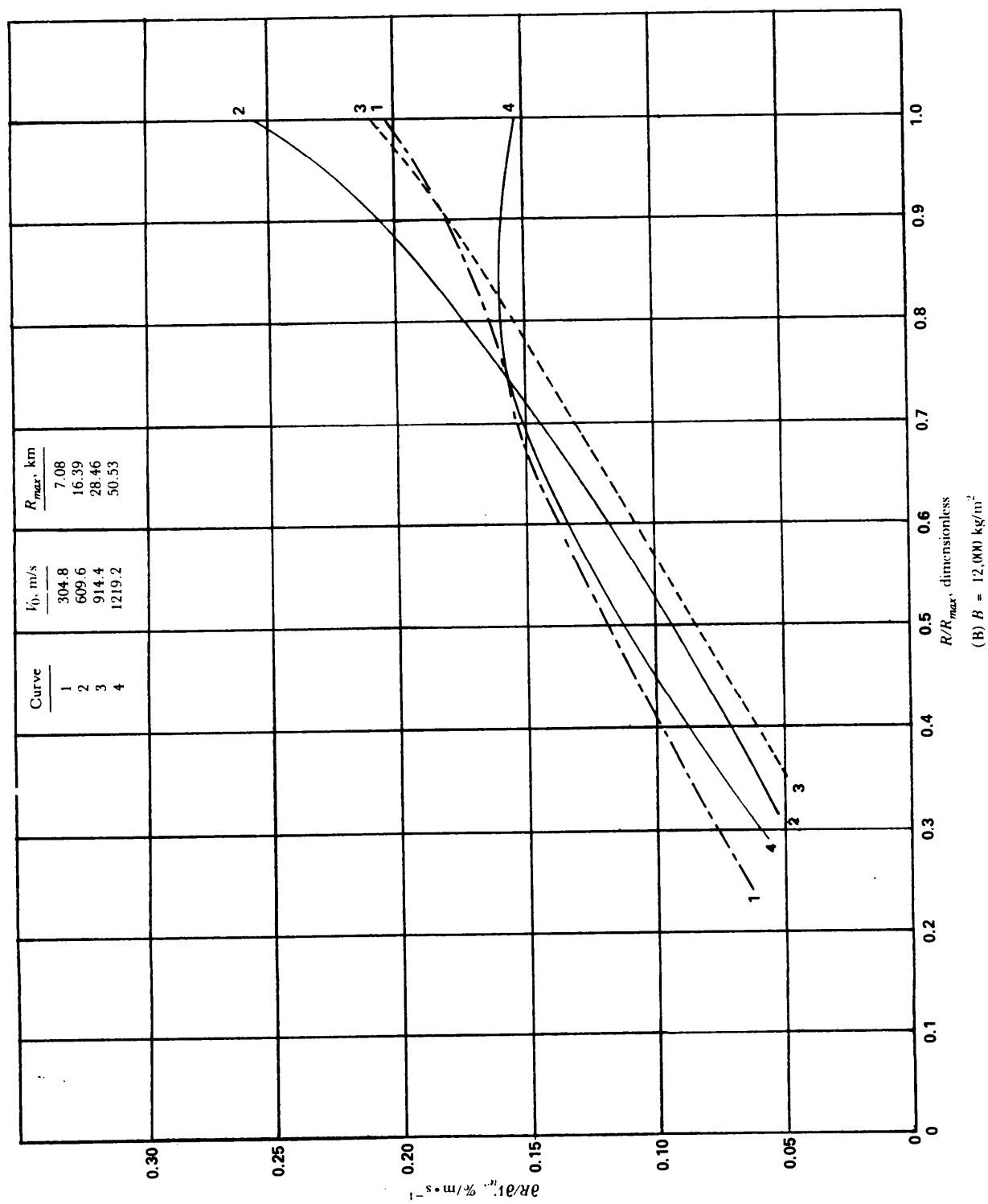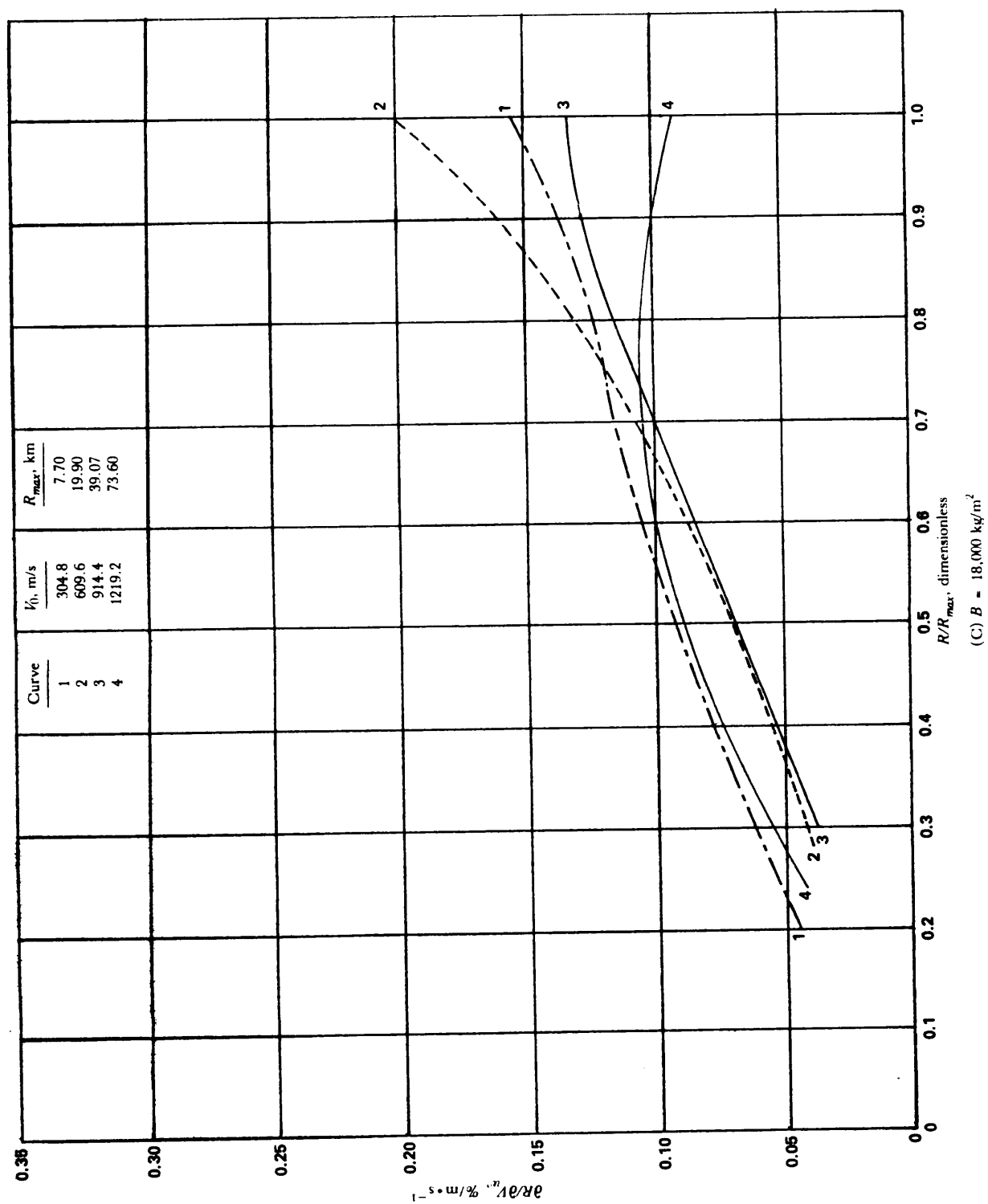
Figure 4-37. (cont'd)

MIL-HDBK-762(MI)

Curve	V_0, m/s	R_{max}, km
1	304.8	5.75
2	609.6	10.97
3	914.4	16.46
4	1219.2	23.12
5	1524.0	31.19

R/R_{max}, dimensionless

(A) $B = 6000 \text{ kg/m}^2$
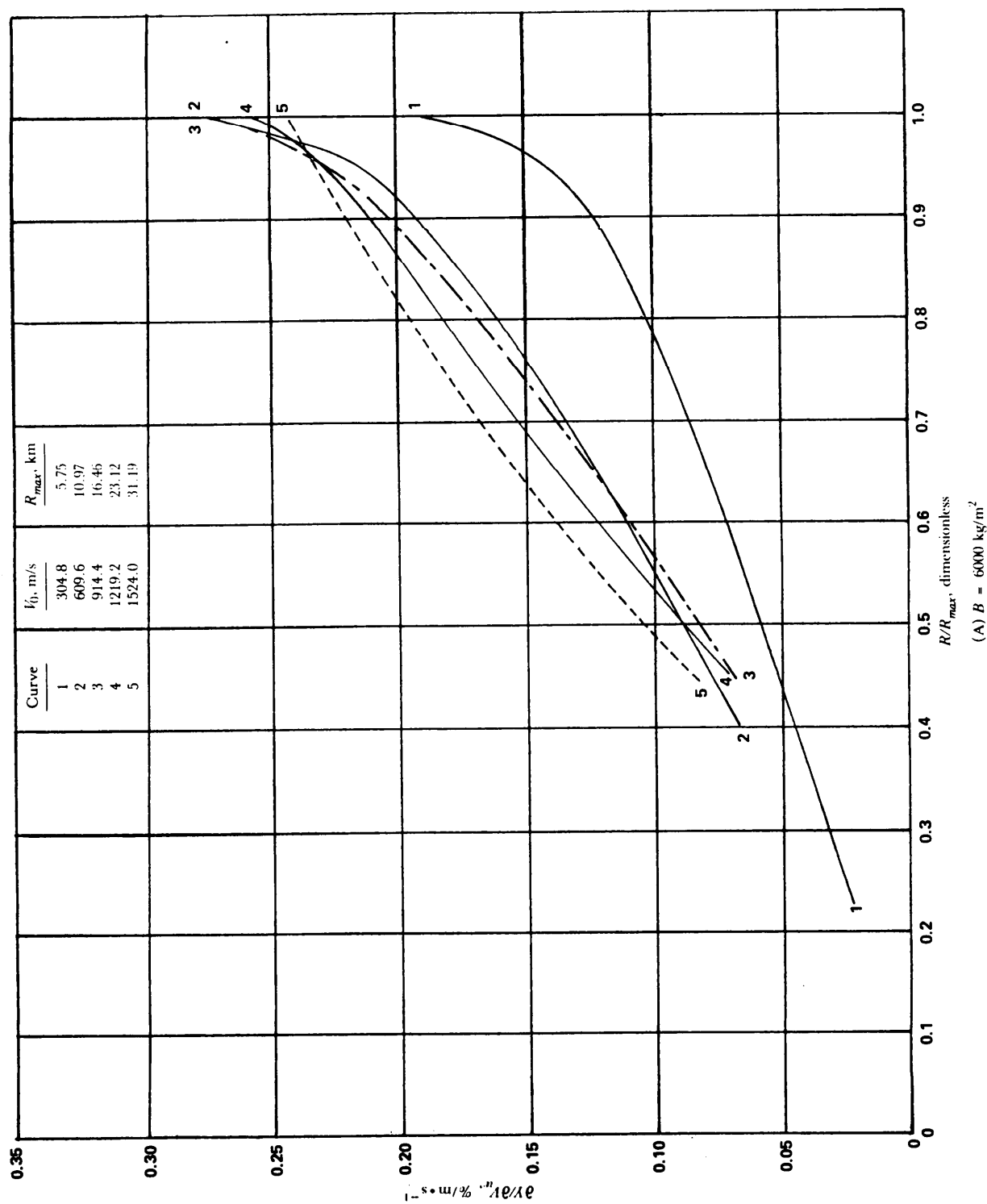
Figure 4-38. Unit Effect, Deflection/Wind vs R/R_{max} for Various B Values—Impact Fuze

(cont'd on next page)

4-81

Curve	V_0, m/s	R_{max}, km
1	304.8	7.08
2	609.6	16.39
3	914.4	28.46
4	1219.2	50.53

R/R_{max}, dimensionless

(B) $B = 12,000$ kg/m^2

$\partial y/\partial v$, %/m • s^{-1}
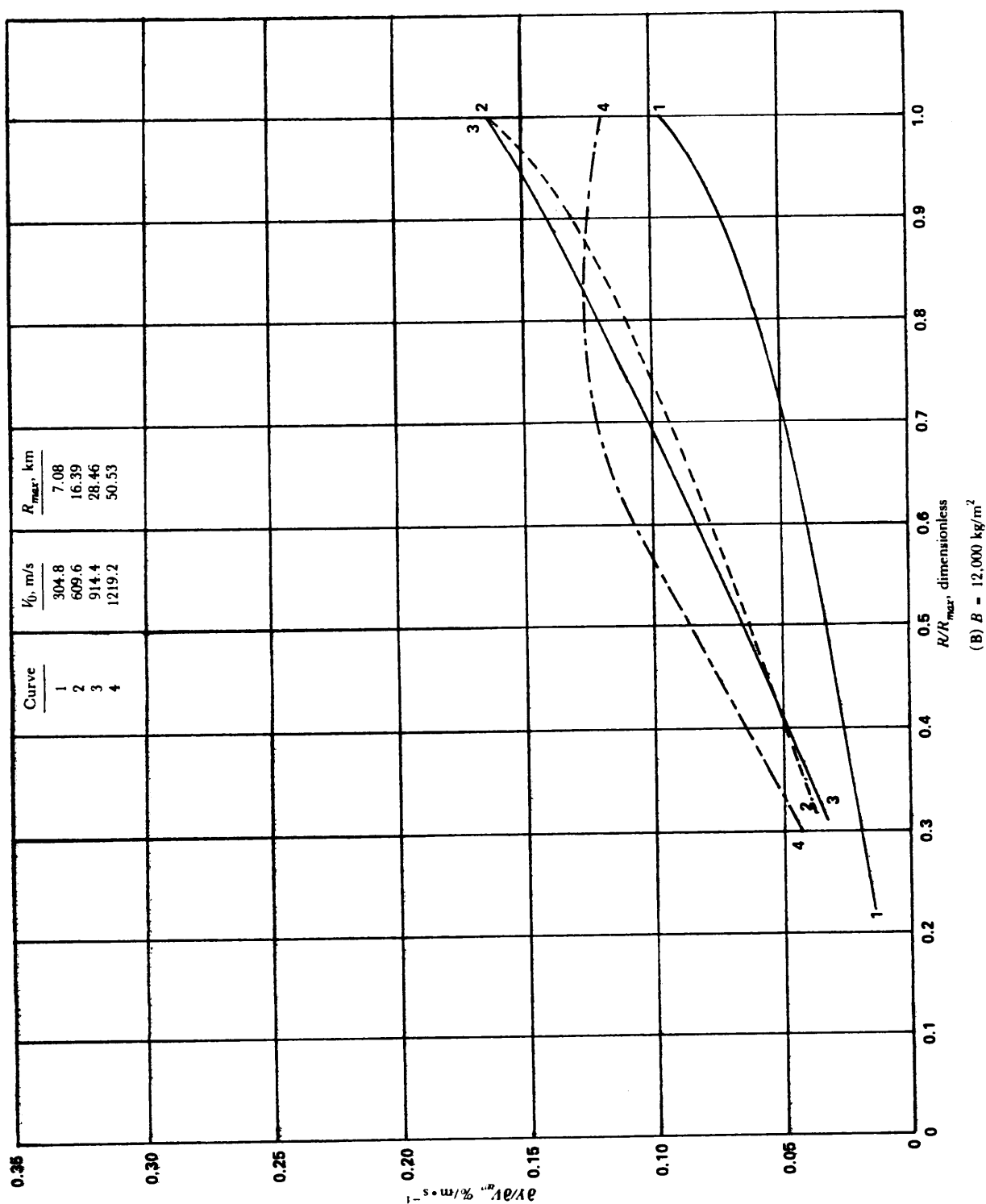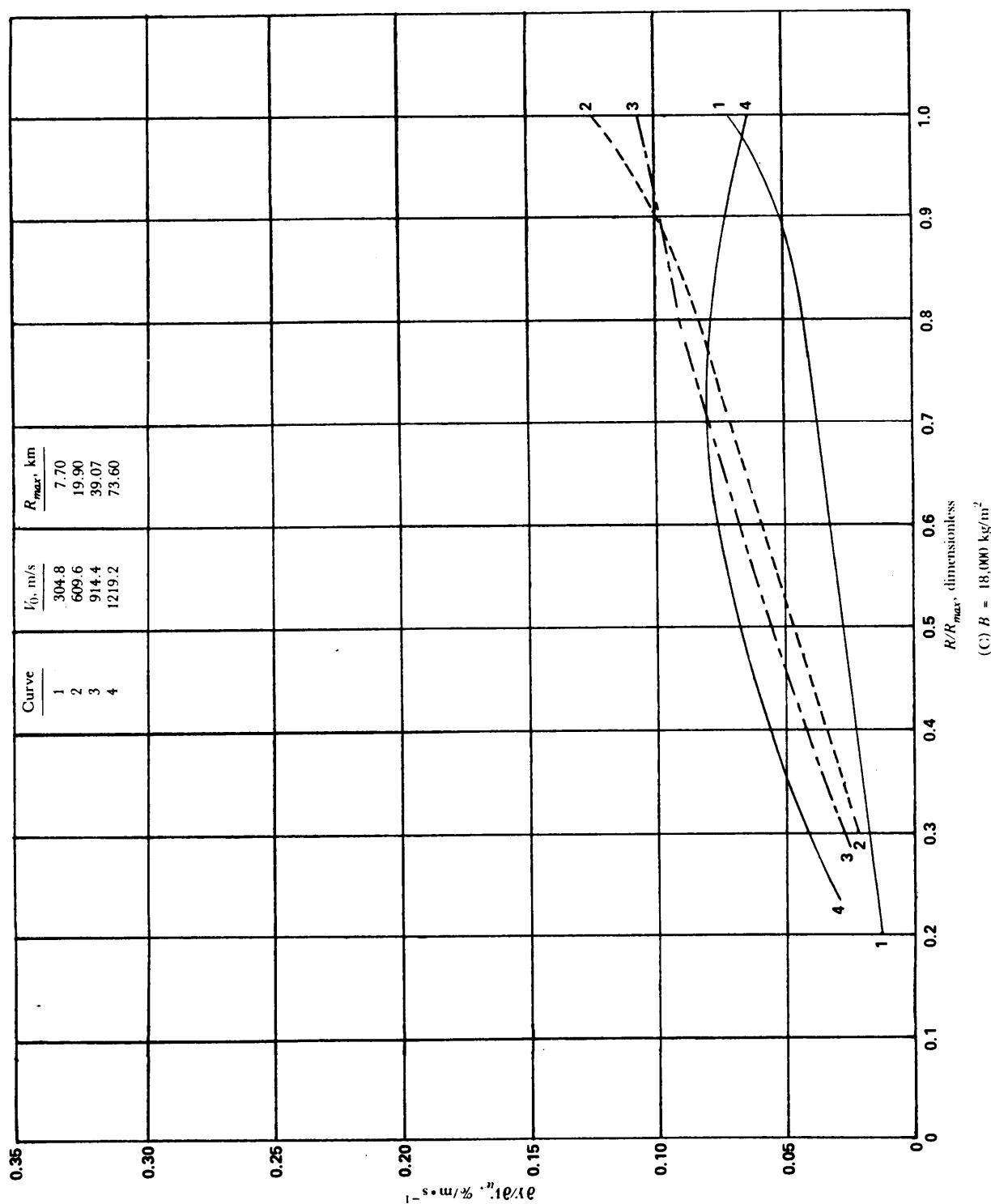
Figure 4-38. (cont'd)

MIL-HDBK-762(MI)

Curve	V_0, m/s	R_{max}, km
1	304.8	7.70
2	609.6	19.90
3	914.4	39.07
4	1219.2	73.60

R/R_{max}, dimensionless

(C) $B = 18,000$ kg/m^2

$\partial y/\partial t$, %/m·s^{-1}

Figure 4-38. (cont'd)

4-83

From Fig. 4-36(B) for $V_0 = 915$ m/s and $R/R_{max} = 1$,

$$\frac{\partial R}{\partial B} = 0.78$$

$$\Delta R = 0.75(0.78)\%$$

$$\Delta R = 0.585\%$$

$$\Delta R = 0.00585(28.5 \text{ km})$$

$$\Delta R = 167 \text{ m}$$

and

$$\Delta Y = 0 \ .$$

The results of these calculations have been tabulated and are shown in Table 4-6.

4-5.5.2.5 Additional Unit Effect Graphs

The example calculations just completed have all dealt with a rocket armed with an impact fuze. Figs. 4-39 and 4-40 give additional reference data for this type of rocket, and Figs. 4-41 through 4-51 give similar reference data for a rocket with a time fuze.

4-5.5.2.6 Example Range Error Probable (REP)

The one-sigma range dispersion values σ_{R_i} are listed in Table 4-6. Therefore, Eq. 4-69 yields a standard deviation in range $\sigma_{R_{tot}}$, of

$$\sigma_{R_{tot}} = [(15.1)^2 + (7.79)^2 + (4.84)^2 + (5.86)^2]^{1/2}$$

$$\sigma_{R_{tot}} = 18.6 \text{ mrad}.$$

Eq. 4-68 yields

$$\text{REP} = 0.6745 \ (18.6 \text{ mrad}) = 12.5 \text{ mrad}$$

$$\text{REP} = 12.5 \text{ mrad} (28.5 \text{ km}) = 356 \text{ m}.$$

4-5.5.27 Example Deflection Error Probable (DEP)

The one-sigma deflection dispersion values σ_{D_i} are listed in Table 4-6. Therefore Eq. 4-71 yields a total standard deviation in deflection $\sigma_{D_{tot}}$ of

$$\sigma_{D_{tot}} = \left[(1)^2 + (-0.87)^2 + (2.85)^2 + (5.97)^2 + (-24.5)^2 + (5.63)^2 + (3.8)^2\right]^{1/2}$$

$$\sigma_{D_{tot}} = 26.3 \text{ mrad}.$$

Eq. 4-70 yields

$$\text{DEP} = 0.6745 \ \sigma_{D_{tot}}$$

$$\text{DEP} = 0.6745 \ (26.3 \text{ mrad}) = 17.7 \text{ mrad}$$

$$\text{DEP} = (17.7 \text{ mrad}) \ (28.5 \text{ km}) = 504 \text{ m}.$$

MIL-HDBK-762(MI)

Curve	V_0, m/s	R_{max}, km
1	304.8	5.75
2	609.6	10.97
3	914.4	16.46
4	1219.2	23.12
5	1524.0	31.19

R/R_{max}, dimensionless

(A) $B = 6000$ kg/m²
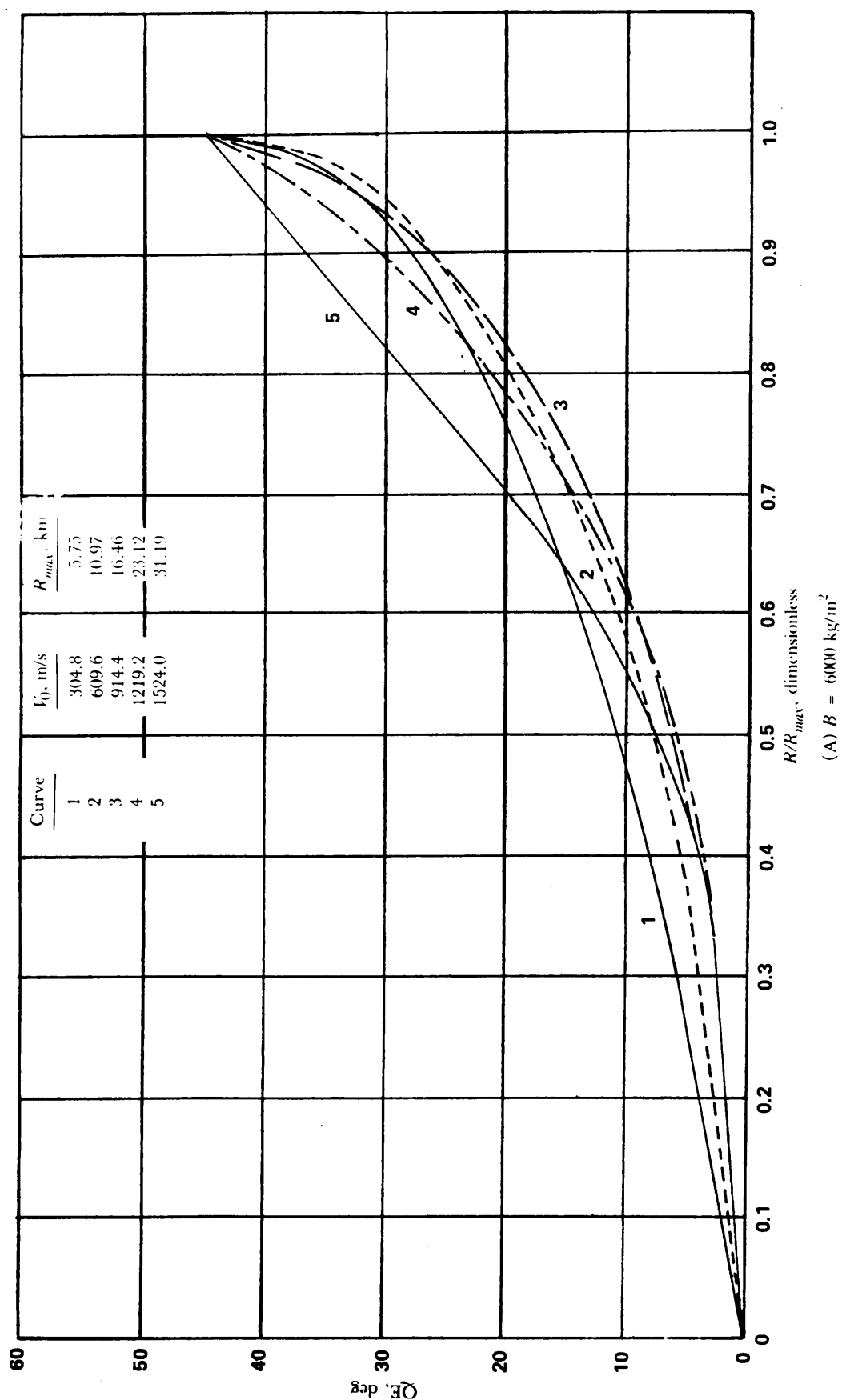
Figure 4-39. QE vs R/R_{max} for Various B Values—Impact Fuze

(cont'd on next page)

4-85

MIL-HDBK-762(MI)

Curve	V_0, m/s	R_{max}, km
1	304.8	7.08
2	609.6	16.39
3	914.4	28.46
4	1219.2	50.53

R/R_{max}, dimensionless

(B) $B = 12,000$ kg/m^2

Figure 4-39. (cont'd)

Curve	V_0, m/s	R_{max}, km
1	304.8	7.70
2	609.6	19.90
3	914.4	39.07
4	1219.2	73.60

R/R_{max}, dimensionless

(C) $B = 18,000 \text{ kg/m}^2$
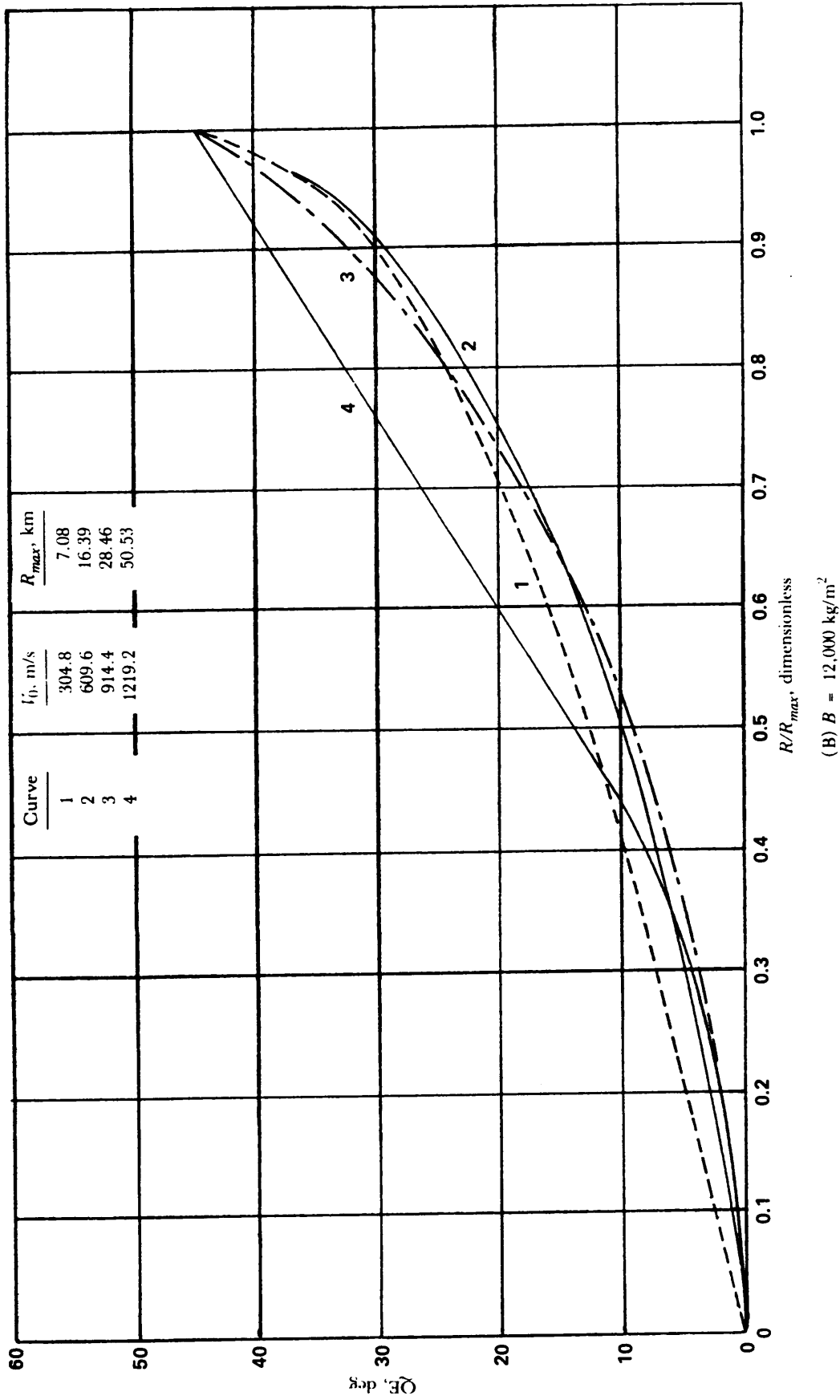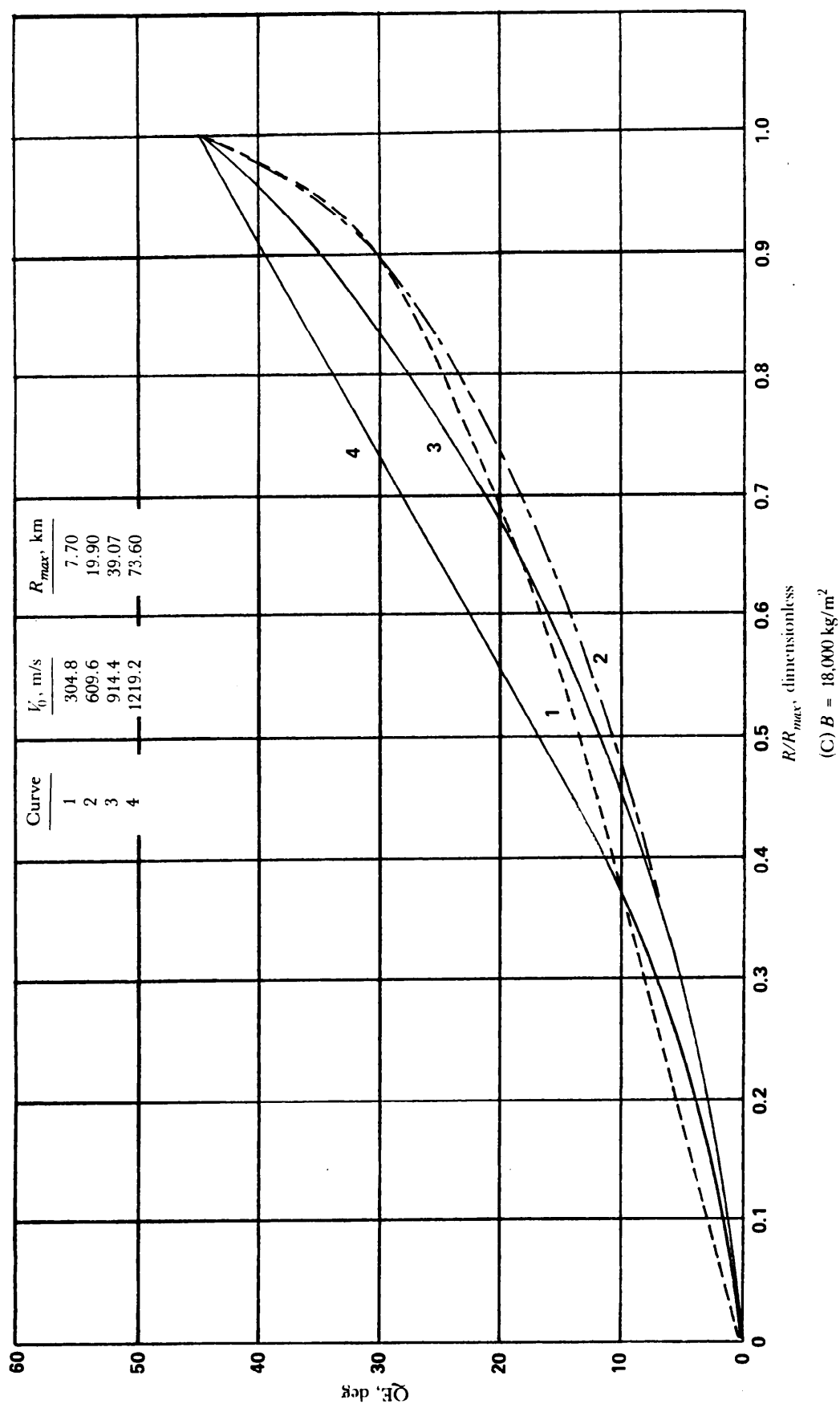
Figure 4-39.   (cont'd)

MIL-HDHK-762(MI)

Curve	V_0, m/s	R_{max}, km
1	304.8	5.75
2	609.6	10.97
3	914.4	16.46
4	1219.2	23.12
5	1524.0	31.19

R/R_{max}, dimensionless

(A) $B = 6000$ kg/m^2
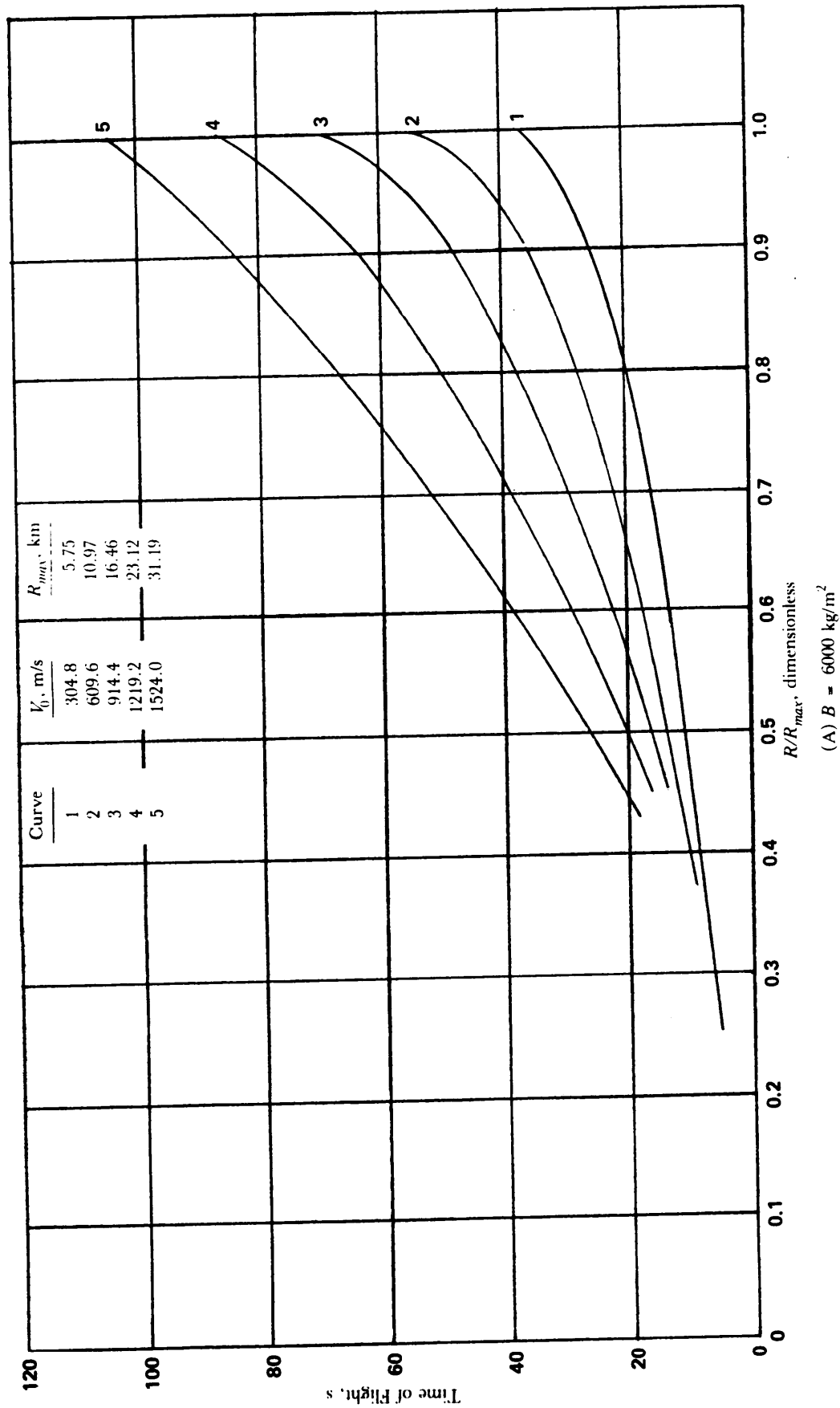
Figure 4-40.   Time of Flight vs R/R_{max} for Various B Values—Impact Fuze

MIL-HDBK-762(MI)

Curve	V_0, m/s	R_{max}, km
1	304.8	7.08
2	609.6	16.39
3	914.4	28.46
4	1219.2	50.53

R/R_{max}, dimensionless

(B) B = 12,000 kg/m²
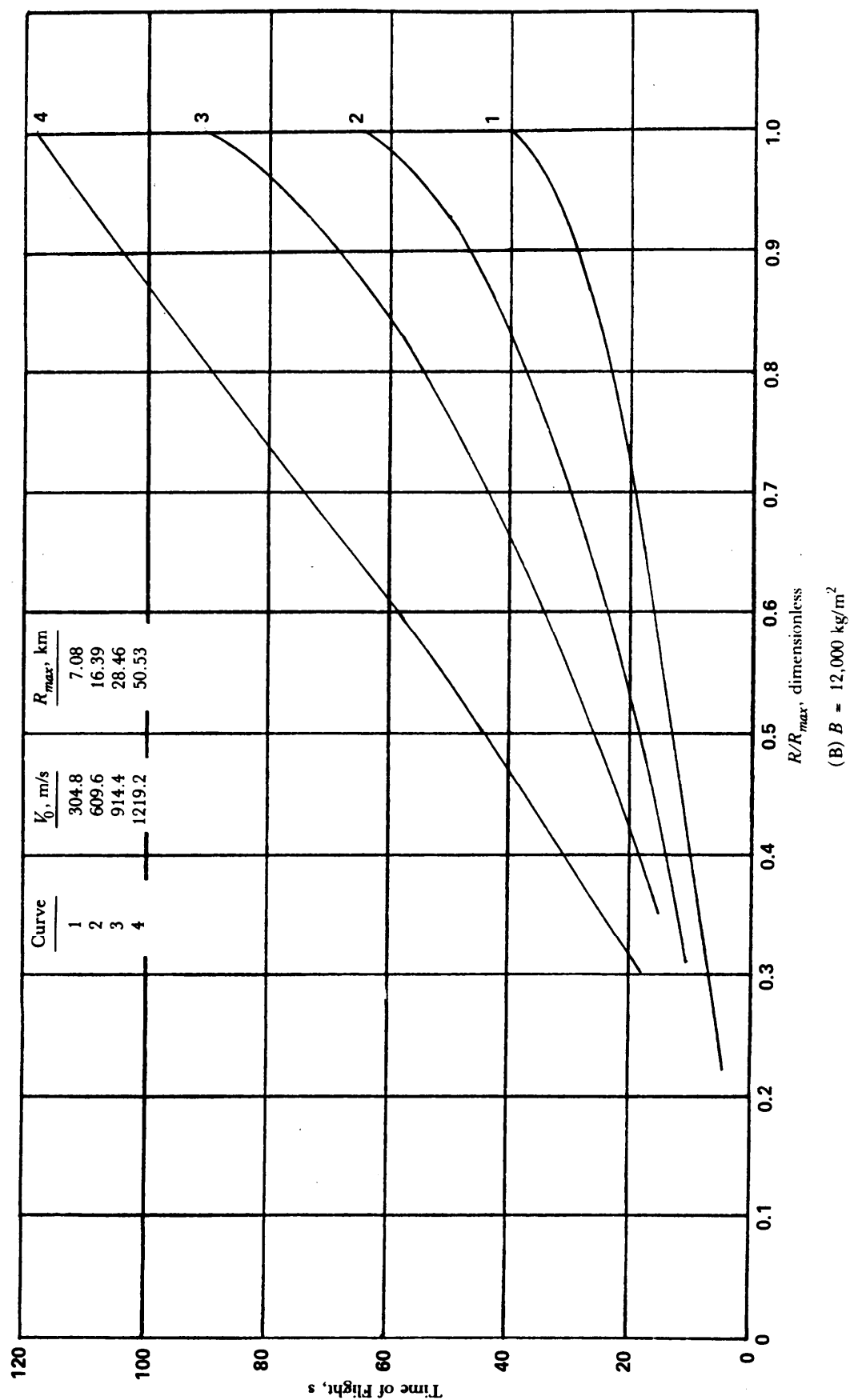
Figure 4-40. (cont'd)

(cont'd on next page)

4-89

Curve	V_0, m/s	R_{max}, km
1	304.8	7.70
2	609.6	19.90
3	914.4	39.07
4	1219.2	73.60

R/R_{max}, dimensionless

(C) B = 18,000 kg/m²

Time of Flight, s
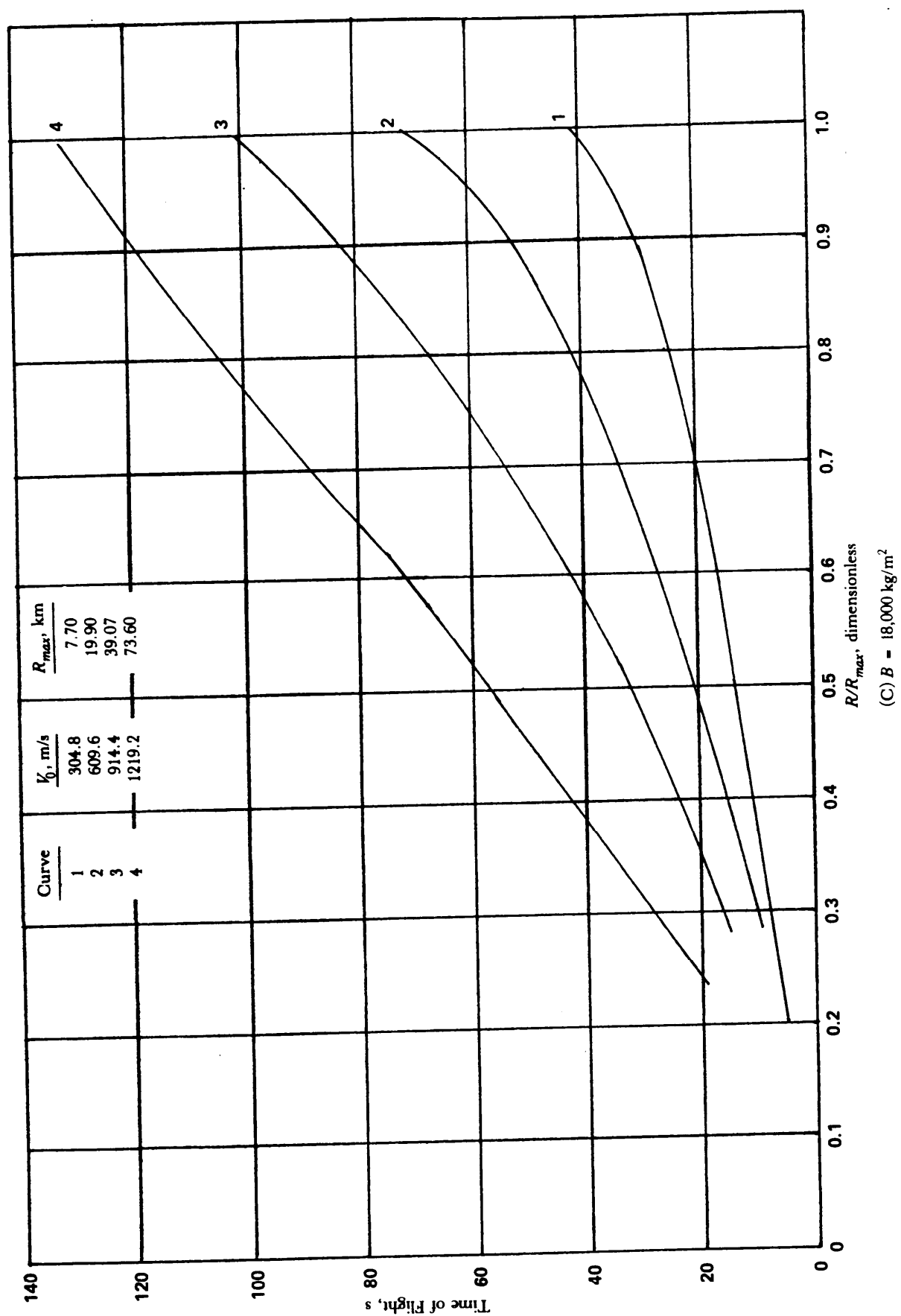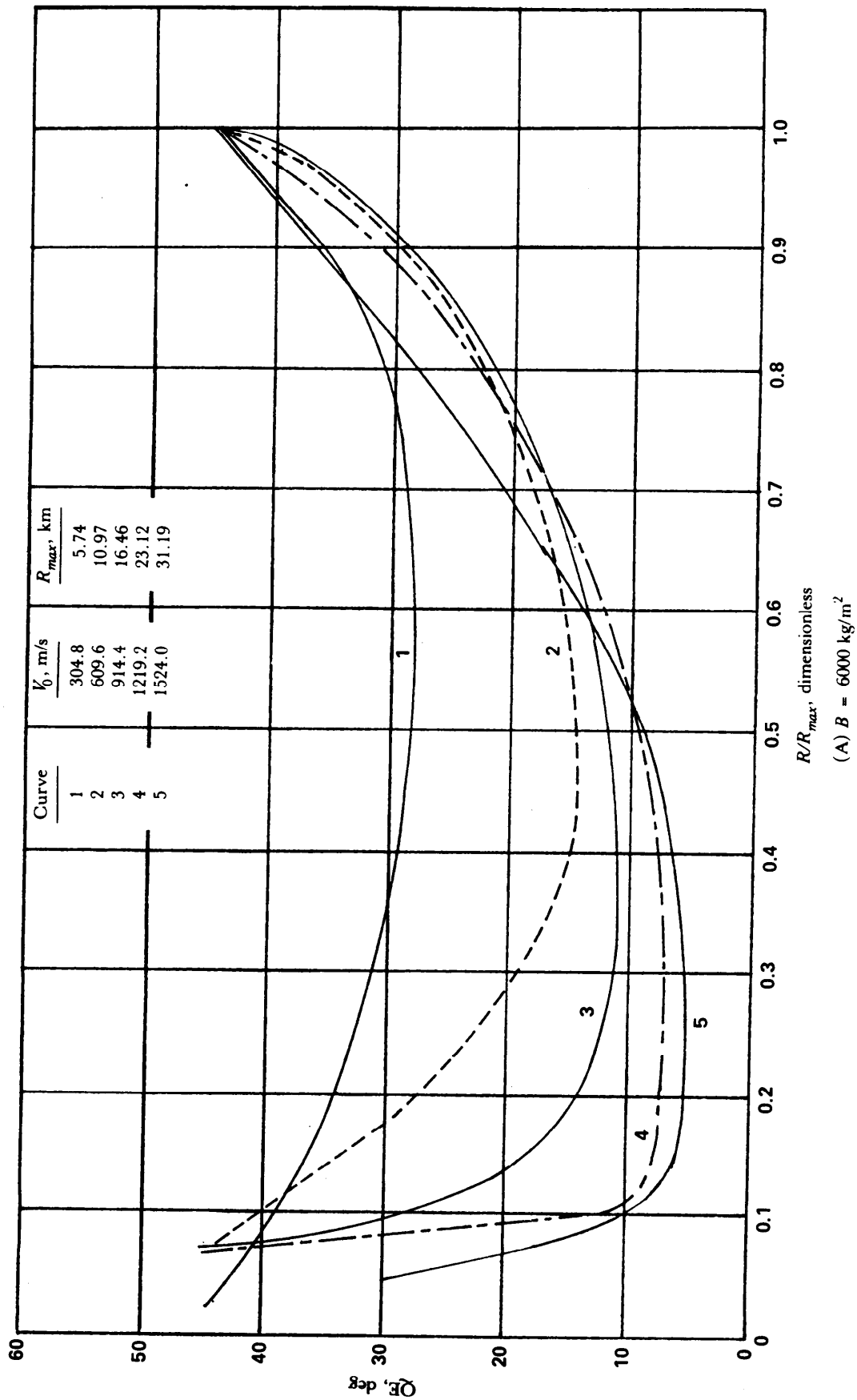
Figure 4-40. (cont'd)

Figure 4-41.   QE vs R/R_{max} for Various B Values—Time Fuze
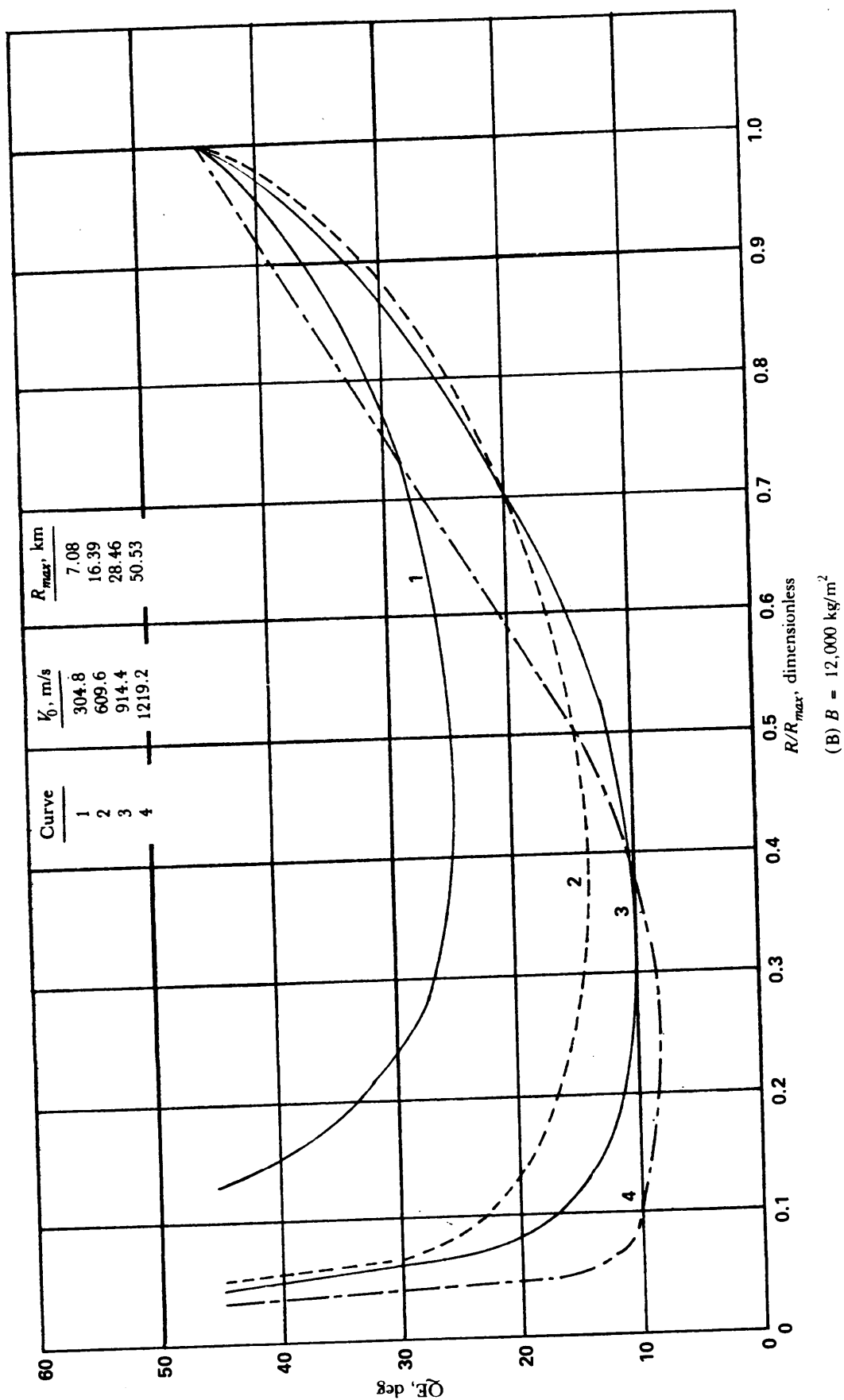
Curve	V_0, m/s	R_{max}, km
1	304.8	7.08
2	609.6	16.39
3	914.4	28.46
4	1219.2	50.53

R/R_{max}, dimensionless

(B) $B = 12,000$ kg/m^2

Figure 4-41. (cont'd)

QE, deg

Curve	V_0, m/s	R_{max}, km
1	304.8	7.70
2	609.6	19.90
3	914.4	39.07
4	1219.2	73.60

R/R_{max}, dimensionless

(C) B = 18,000 kg/m^2

Figure 4-41.   (cont'd)

(A) $B = 6000$ kg/m^2
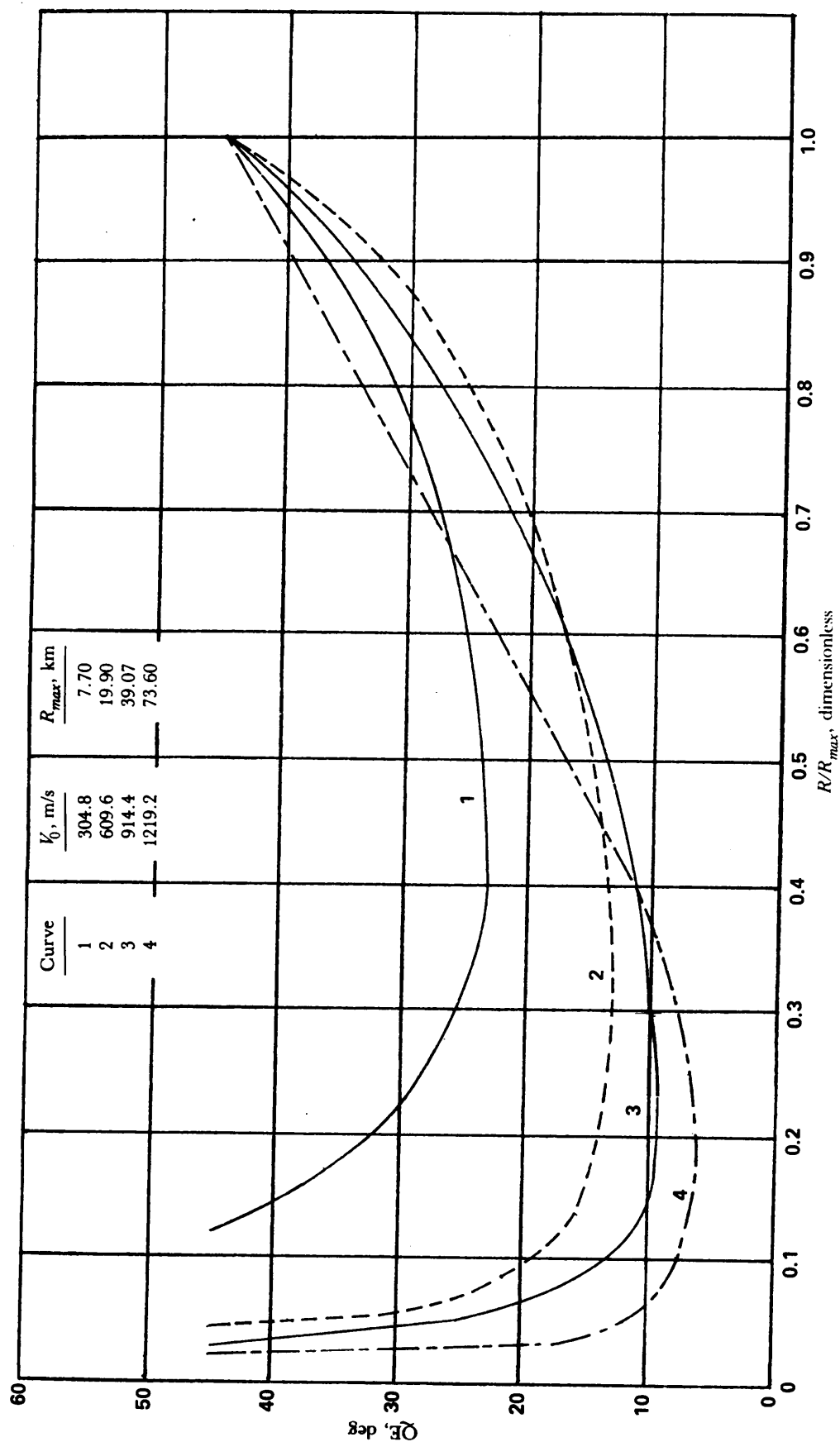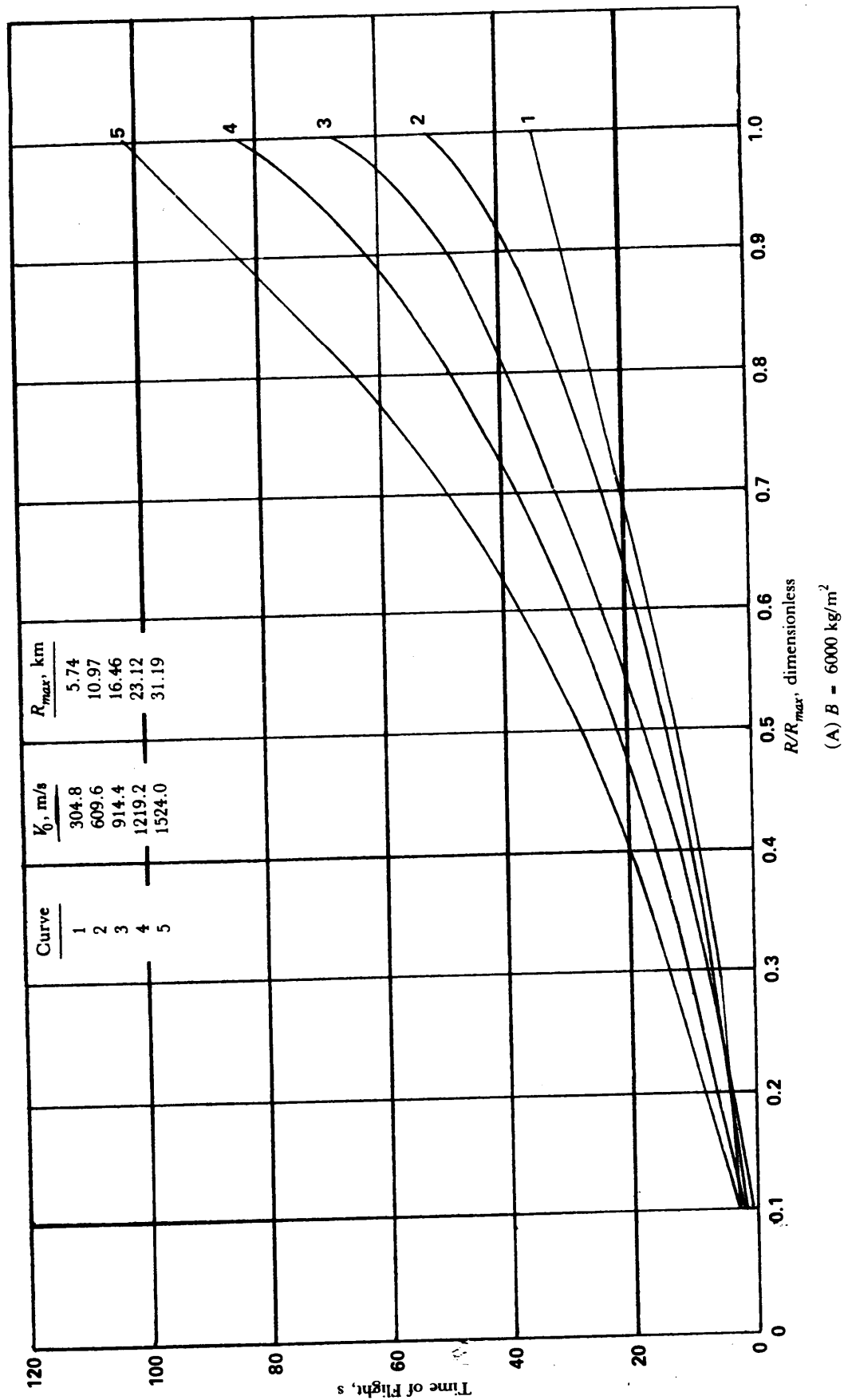
Figure 4-42.　Time of Flight vs R/R_{max} for Various B Values—Time Fuze

(cont'd on next page)

MIL-HDBK-762(MI)

Curve	V_0, m/s	R_{max}, km
1	304.8	7.08
2	609.6	16.39
3	914.4	28.46
4	1219.2	50.53

R/R_{max}, dimensionless

(B) $B = 12,000$ kg/m^2

Figure 4-42.   (cont'd)

Time of Flight, s

Curve	V_0, m/s	R_{max}, km
1	304.8	7.70
2	609.6	19.90
3	914.4	39.07
4	1219.2	73.60

R/R_{max}, dimensionless

(C) $B = 18,000 \ kg/m^2$

Figure 4-42. (cont'd)

Time of Flight, s

MIL-HDBK-762(MI)

Curve	V_0, m/s	R_{max}, km
1	304.8	5.74
2	609.6	10.97
3	914.4	16.46
4	1219.2	23.12
5	1524.0	31.19

R/R_{max}, dimensionless

(A) $B = 6000$ kg/m^2
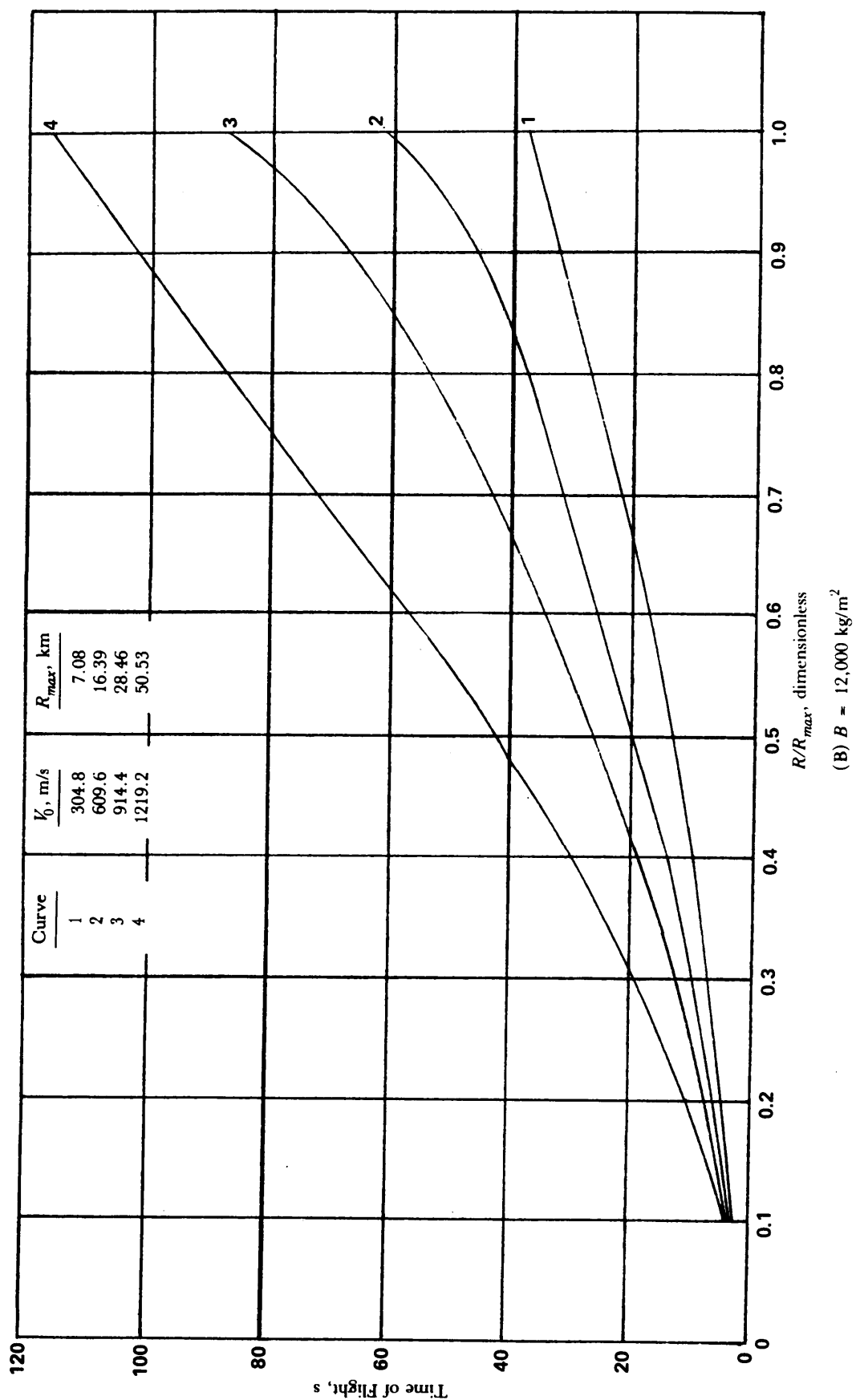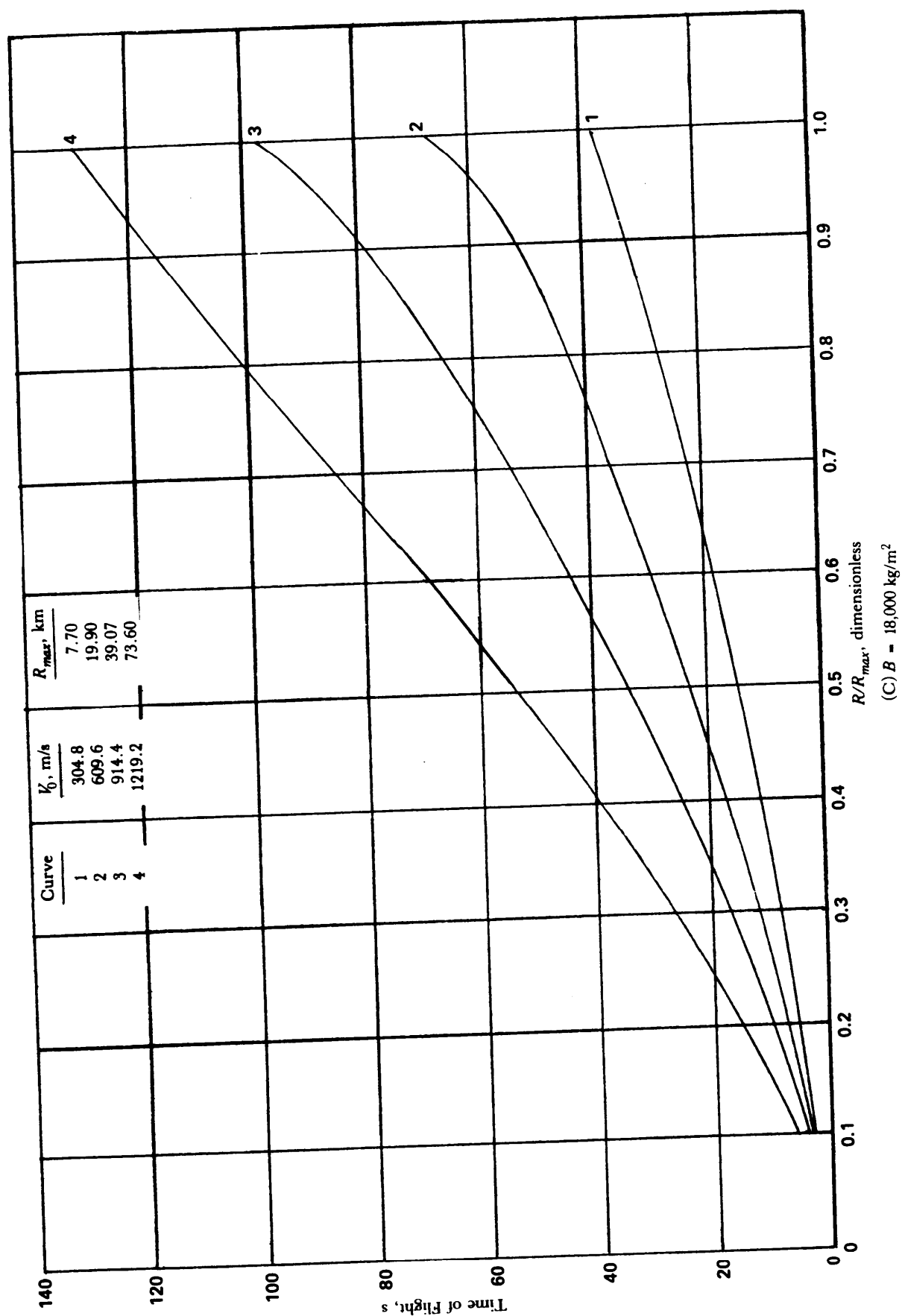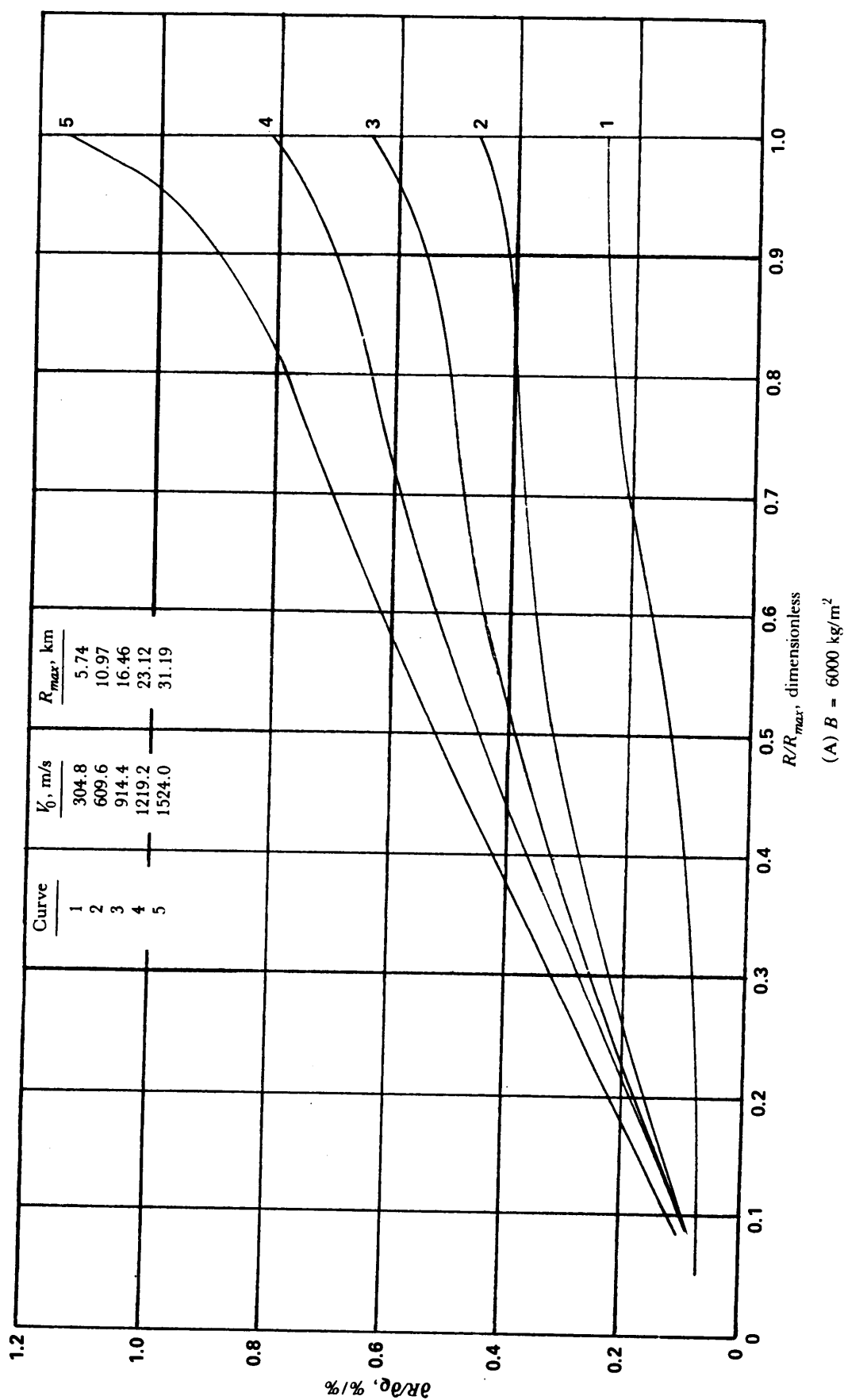
Figure 4-43. **Unit Effect, Range/Density vs R/R_{max} for Various B Values—Time Fuze**

(cont'd on next page)

Curve	V_0, m/s	R_{max}, km
1	304.8	7.08
2	609.6	16.39
3	914.4	28.46
4	1219.2	50.53

R/R_{max}, dimensionless

(B) B = 12,000 kg/m^2

Figure 4-43. (cont'd)

Curve	V_0, m/s	R_{max}, km
1	304.8	7.70
2	609.6	19.90
3	914.4	39.07
4	1219.2	73.60

R/R_{max}, dimensionless

(C) $B = 18{,}000$ kg/m^2

Figure 4-43.   (cont'd)

$\partial R/\partial_0$, %/%
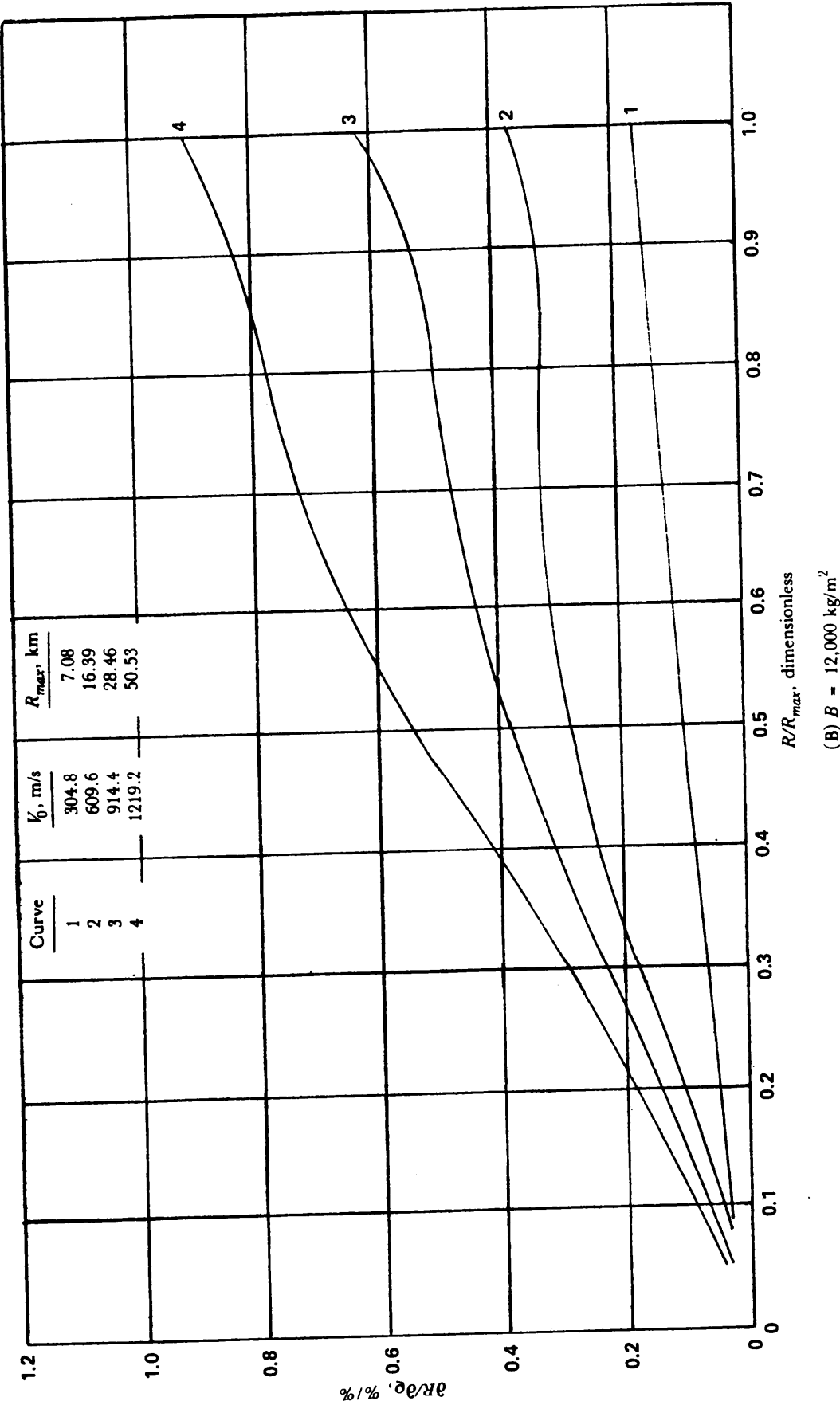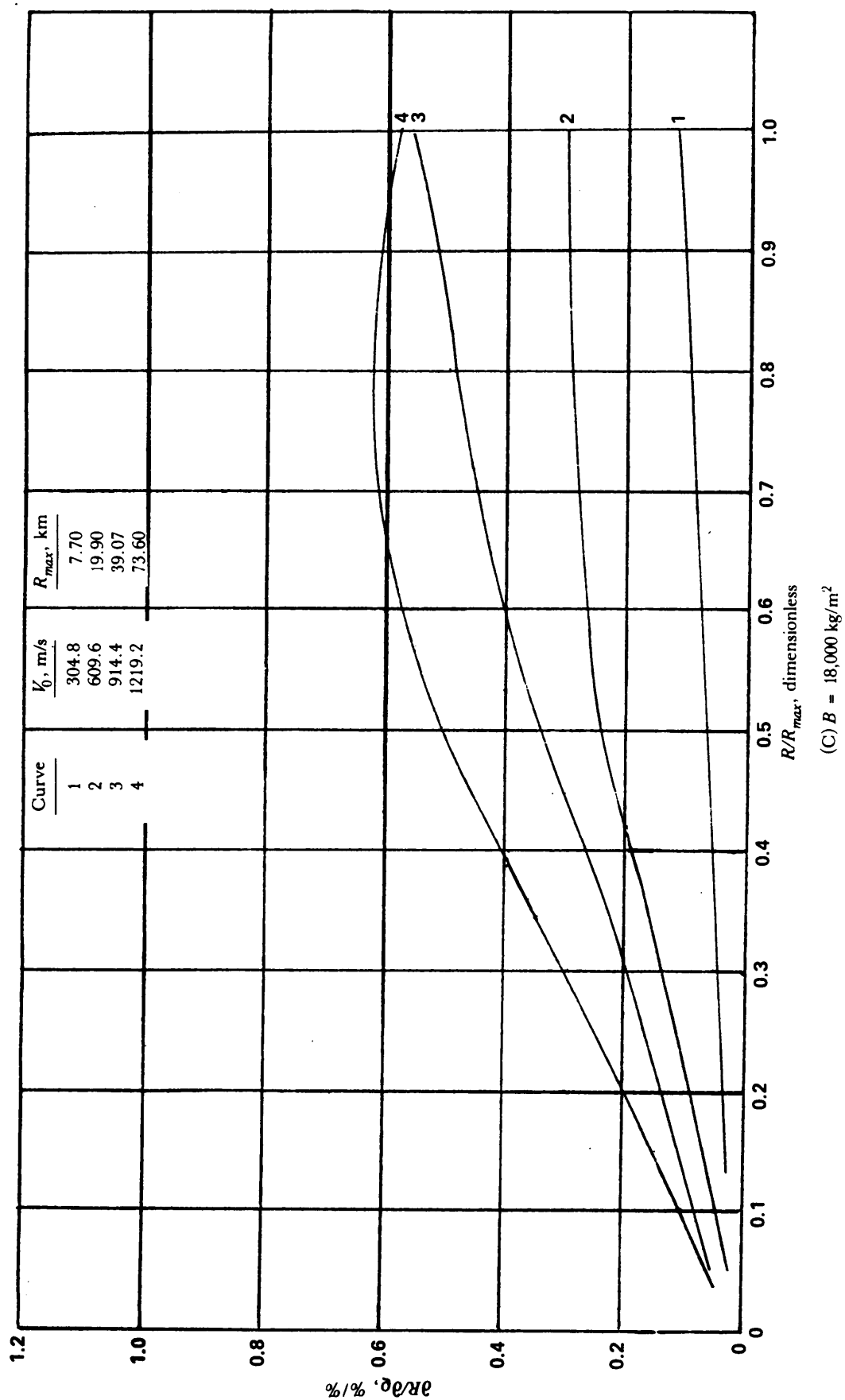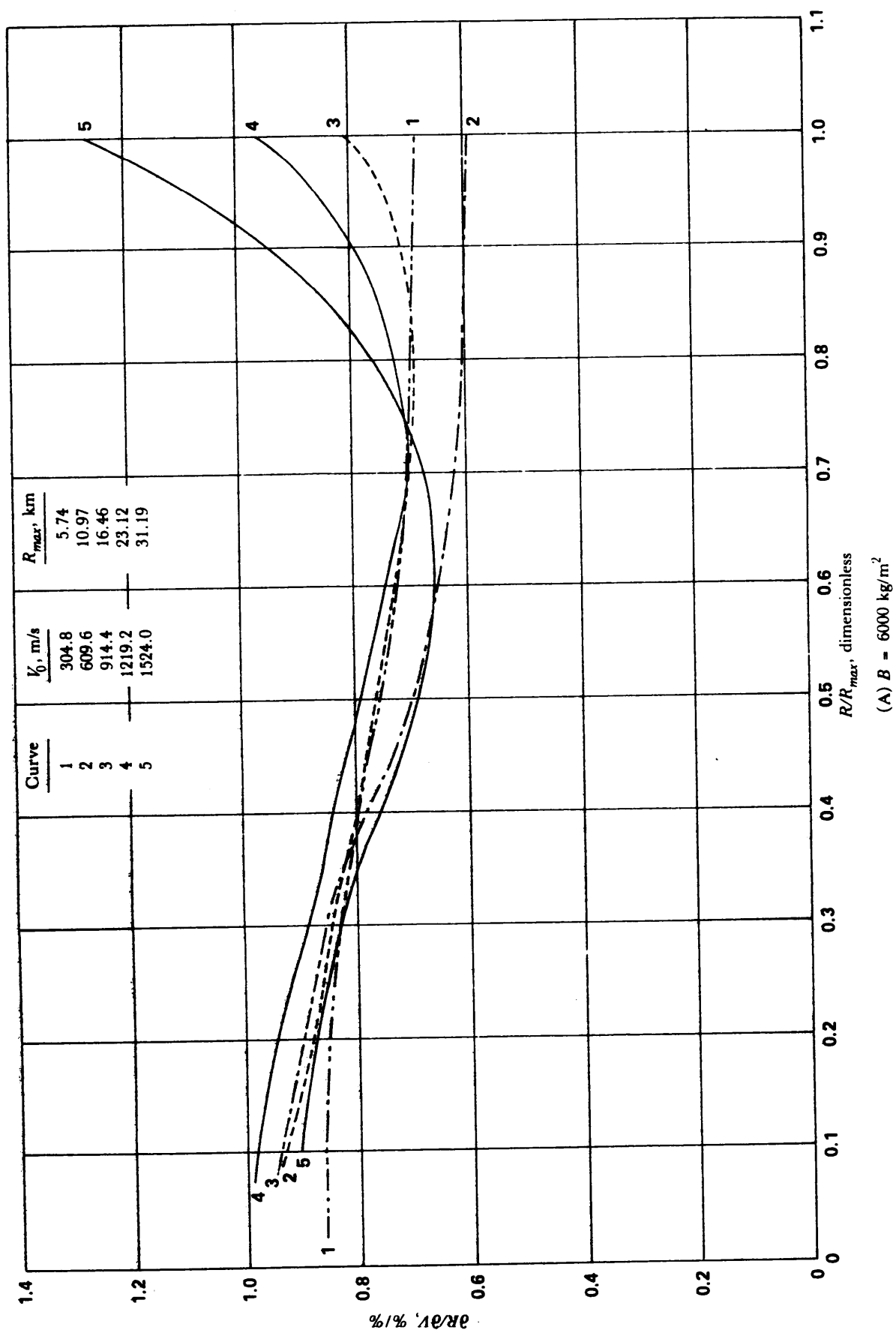
Figure 4-44. Unit Effect, Range/Velocity vs R/R_{max} for Various B Values—Time Fuze
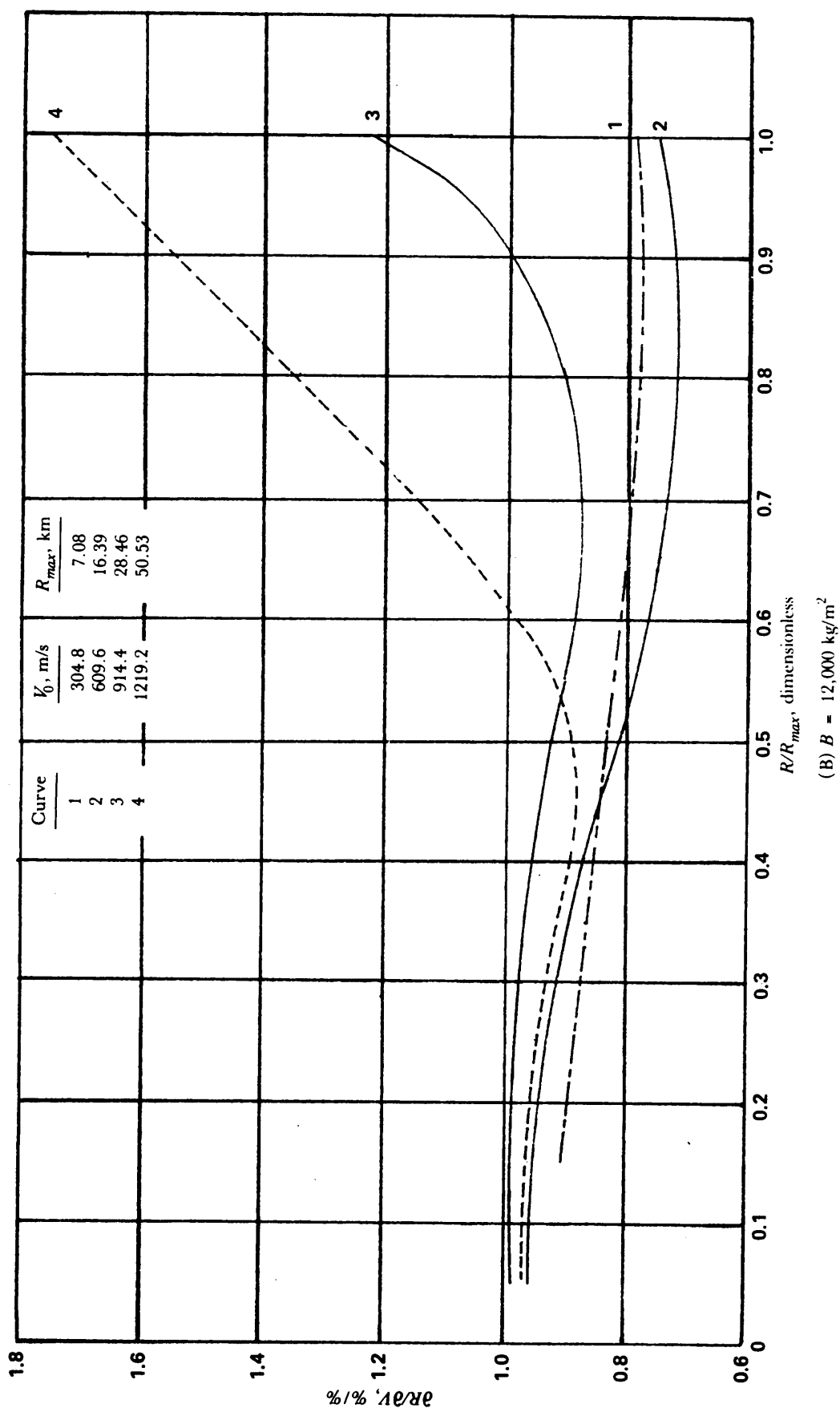
(cont'd on next page)

MIL-HDBK-762(MI)

Curve	V_0, m/s	R_{max}, km
1	304.8	7.08
2	609.6	16.39
3	914.4	28.46
4	1219.2	50.53

R/R_{max}, dimensionless

(B) $B = 12,000$ kg/m²

Figure 4-44.   (cont'd)

Curve	V_0, m/s	R_{max}, km
1	304.8	7.70
2	609.6	19.90
3	914.4	39.07
4	1219.2	73.60

R/R_{max}, dimensionless

(C) $B = 18,000$ kg/m^2

Figure 4-44.   (cont'd)

$\partial R/\partial v$, %/%

Curve	V_0, m/s	R_{max}, km
1	304.8	5.74
2	609.6	10.97
3	914.4	16.46
4	1219.2	23.12
5	1524.0	31.19

R/R_{max}, dimensionless

(A) B = 6000 kg/m²

$\partial R/\partial v_w$, %/m·s⁻¹
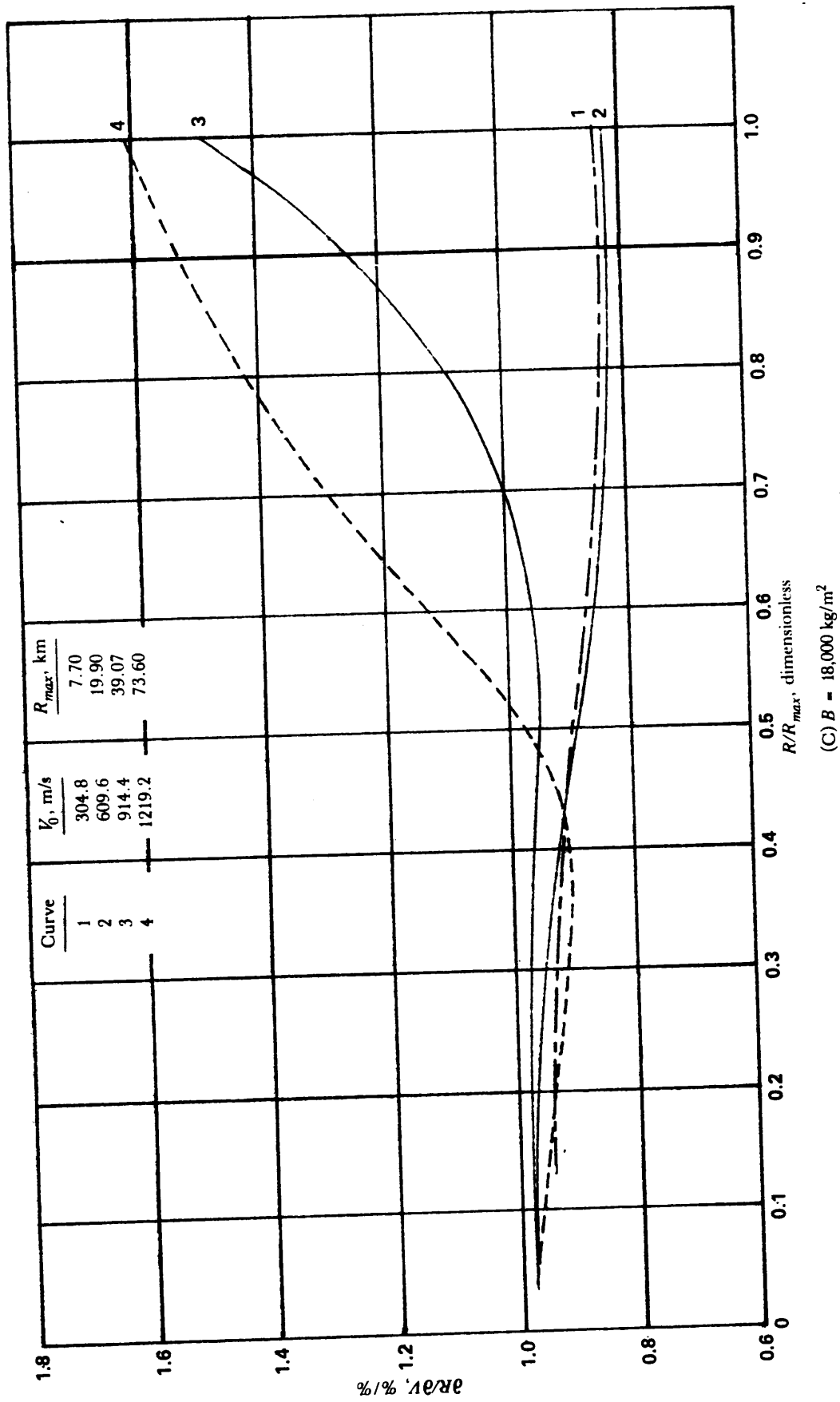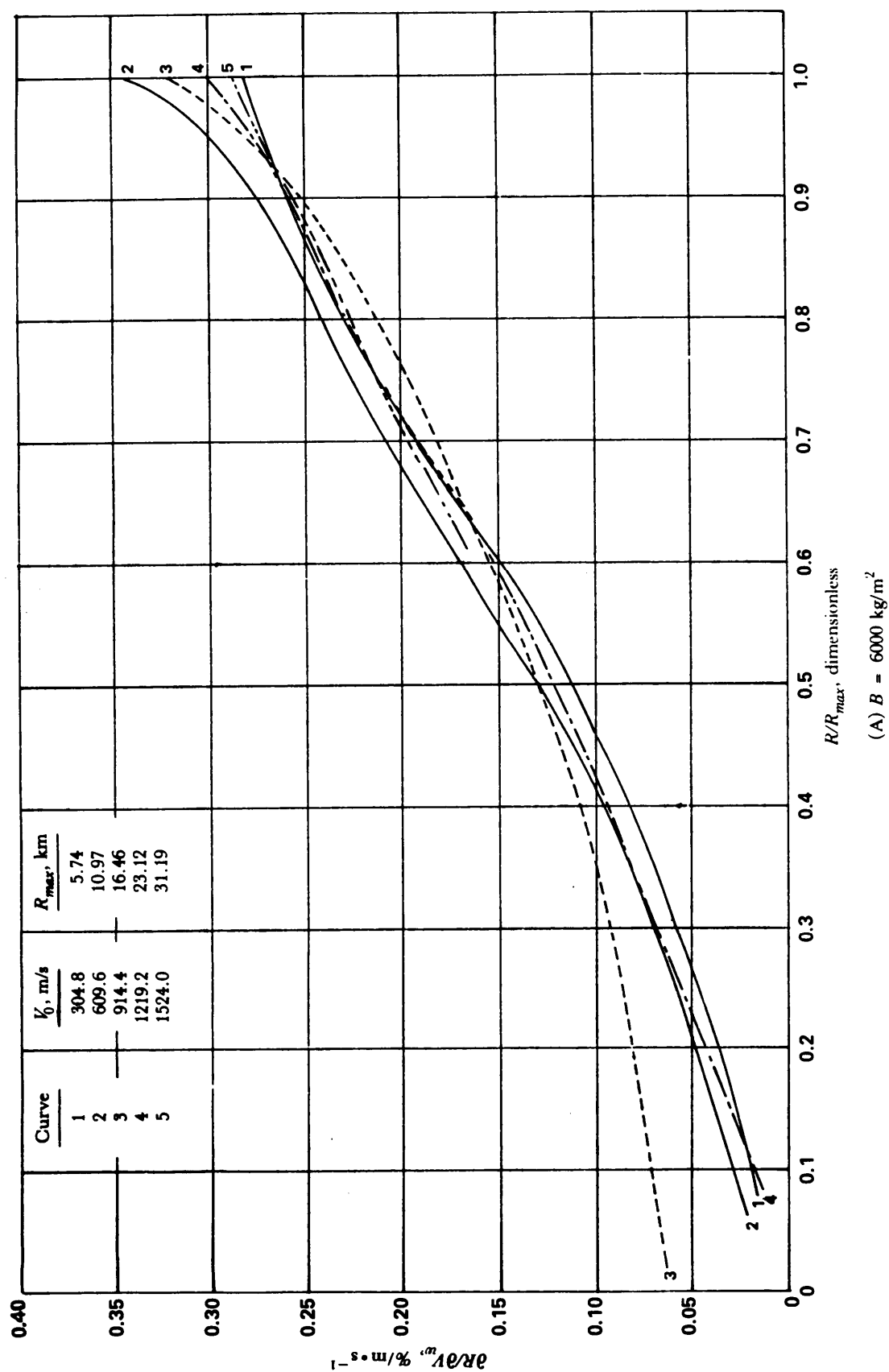
Figure 4-45.   Unit Effect, Range/Wind vs R/R_{max} for Various B Values—Time Fuze

MIL-HDBK-762(MI)

Curve	V_0, m/s	R_{max}, km
1	304.8	7.08
2	609.6	16.39
3	914.4	28.46
4	1219.2	50.53

R/R_{max}, dimensionless
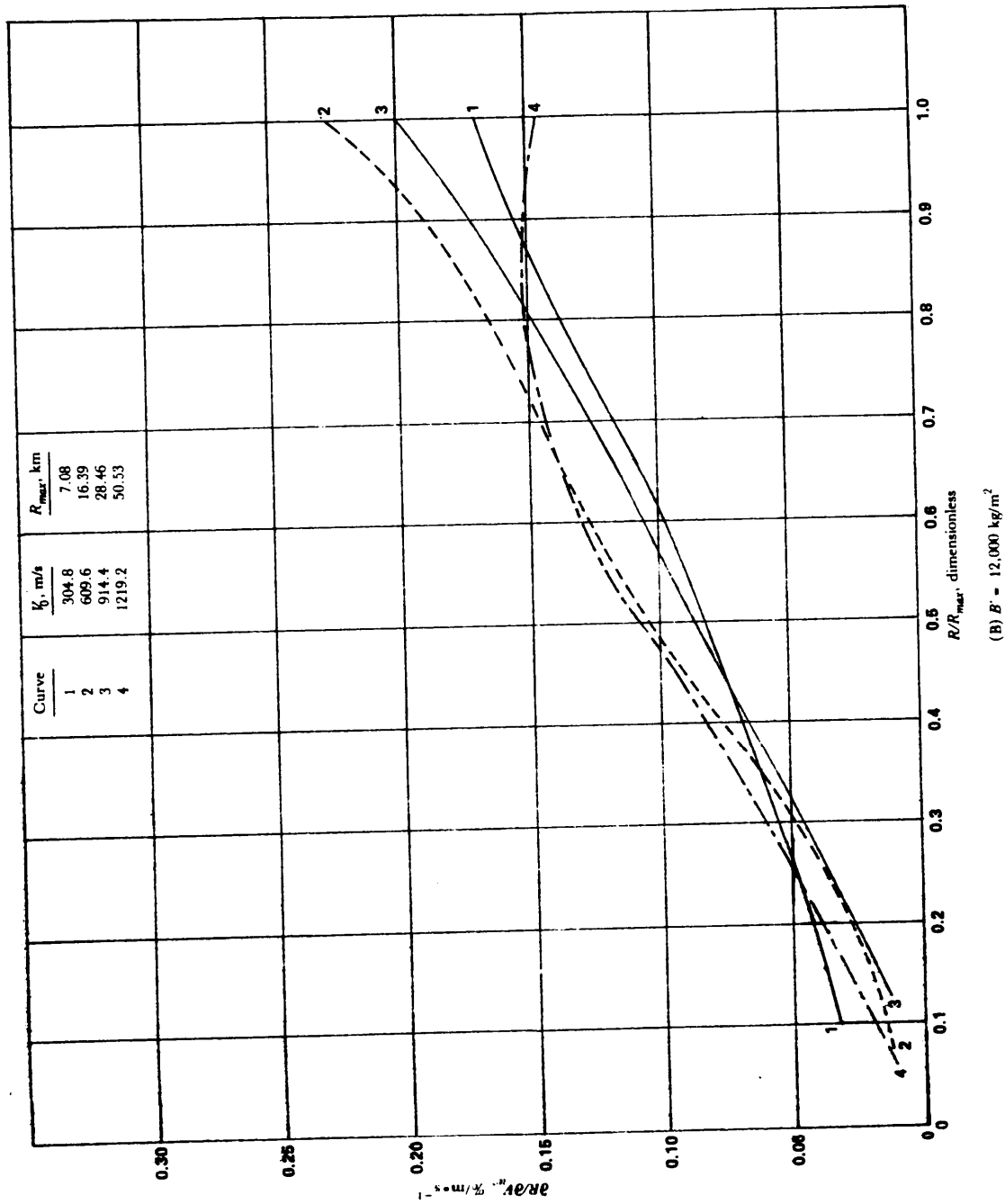
(B) $B' = 12,000$ kg/m^2

Figure 4-45.   (cont'd)

(cont'd on next page)

4-104

MIL-HDBK-762(MI)

Curve	V_0, m/s	R_{max}, km
1	304.8	7.70
2	609.6	19.90
3	914.4	39.07
4	1219.2	73.60

R/R_{max}, dimensionless

(C) $B = 18,000$ kg/m²

Figure 4-45.   (cont'd)

4-105

Curve	V_0, m/s	R_{max}, km
1	304.8	5.74
2	609.6	10.97
3	914.4	16.46
4	1219.2	23.12
5	1524.0	31.19

R/R_{max}, dimensionless

(A) $B = 6000$ kg/m^2
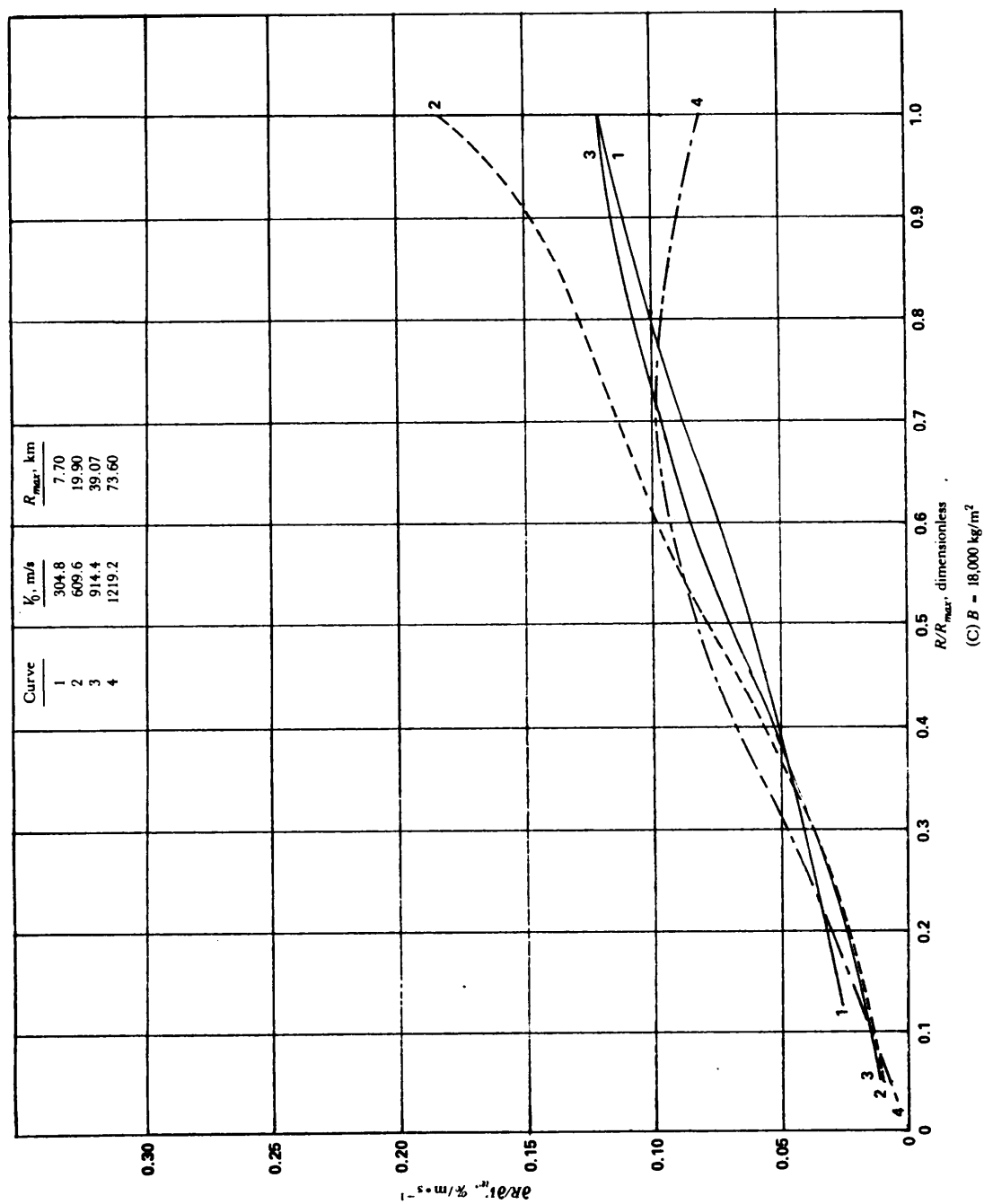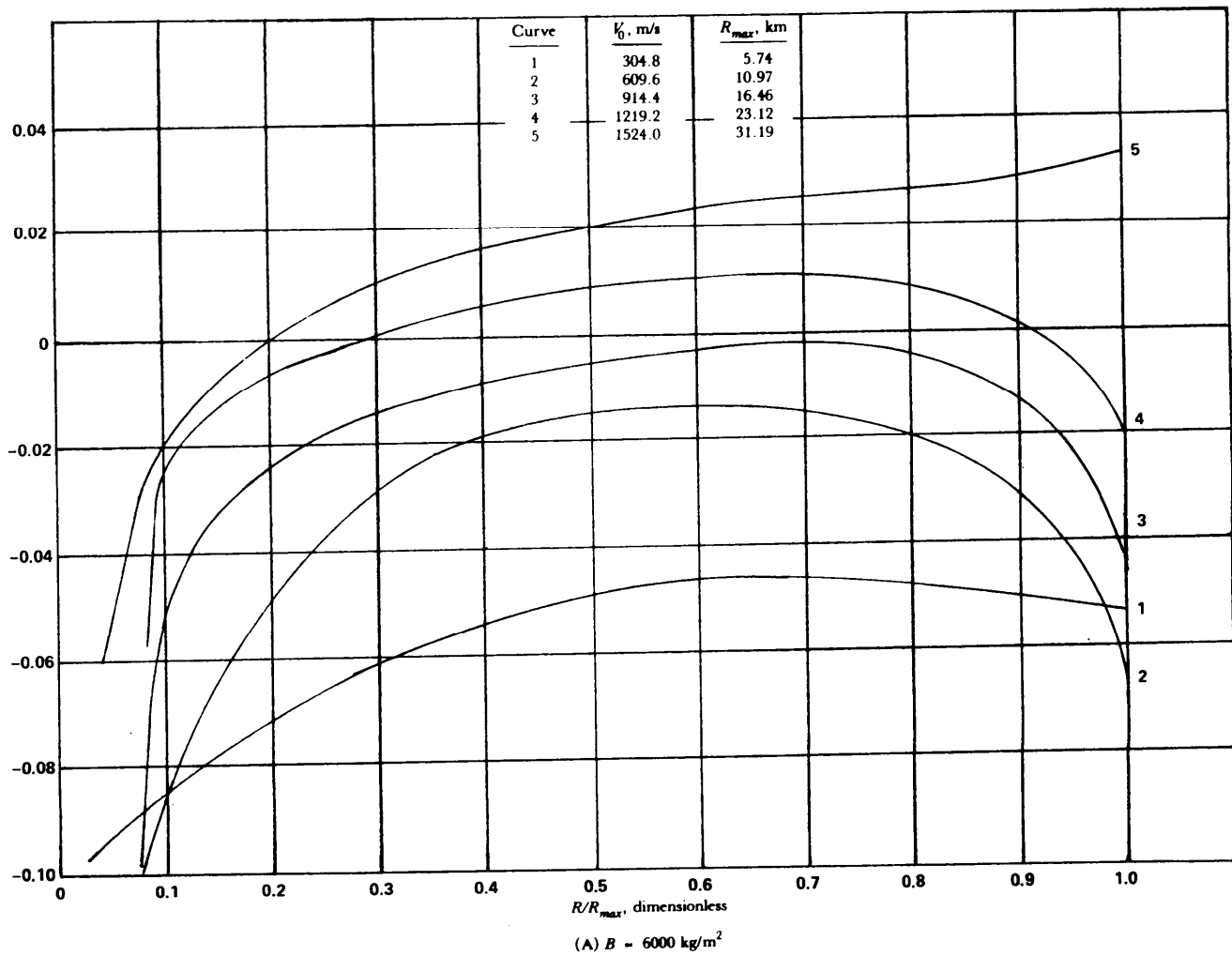
Figure 4-46. Unit Effect, Range/Departure Angle vs R/Rmax for Various B Values— Time Fuze

Curve	V_0, m/s	R_{max}, km
1	304.8	7.08
2	609.6	16.39
3	914.4	28.46
4	1219.2	50.53

(B) $B = 12,000$ kg/m^2

Figure 4-46. (cont'd)

Curve	V_0, m/s	R_{max}, km
1	304.8	7.70
2	609.6	19.90
3	914.4	39.07
4	1219.2	73.60

(C) $B = 18{,}000$ kg/m^2

Figure 4-46. (cont'd)

Curve	V_0, m/s	R_{max}, km
1	304.8	5.74
2	609.6	10.97
3	914.4	16.46
4	1219.2	23.12
5	1524.0	31.19

R/R_{max}, dimensionless

(A) $B = 6000$, kg/m^2

$\partial Z/\partial V_c$, %/m·s^{-1}
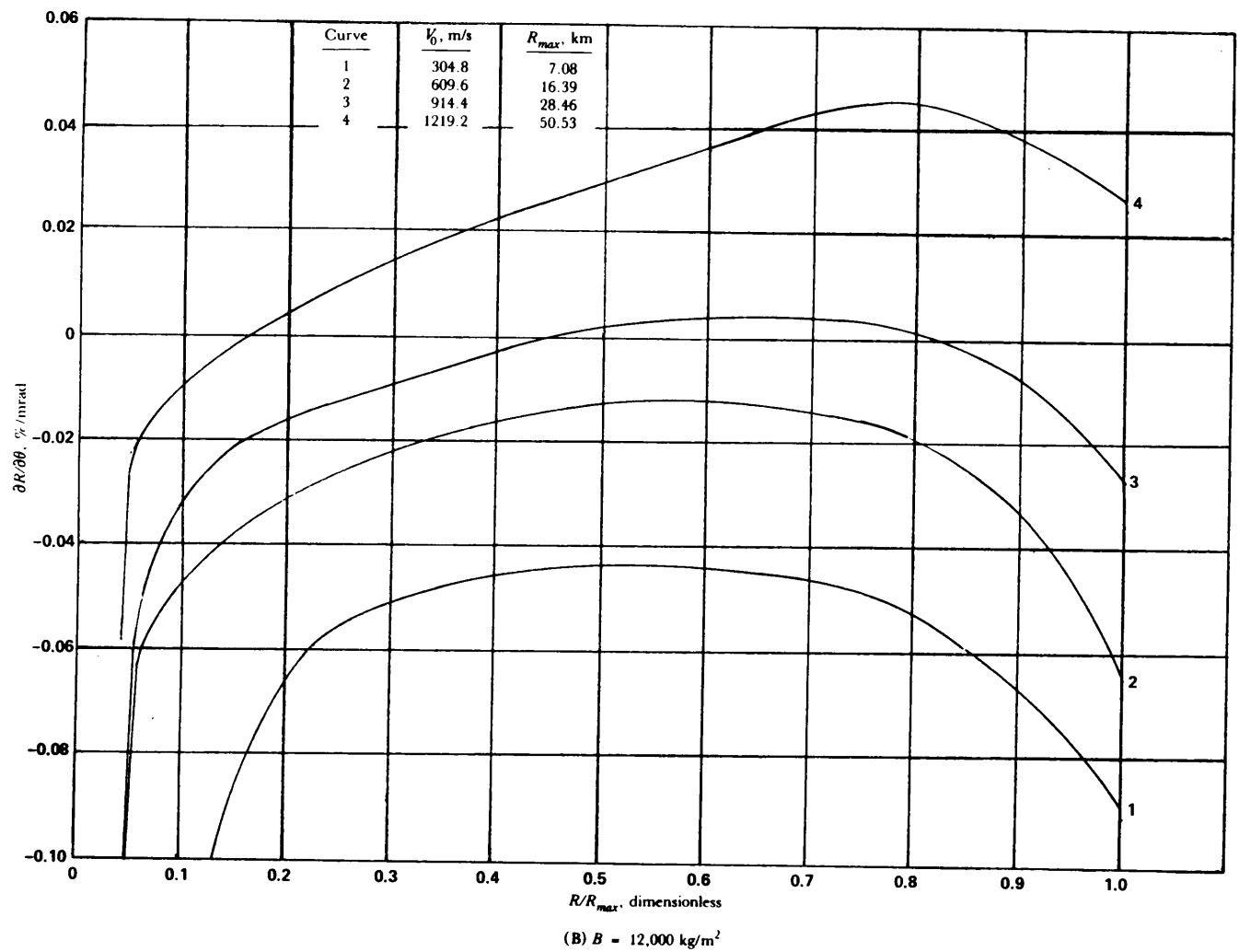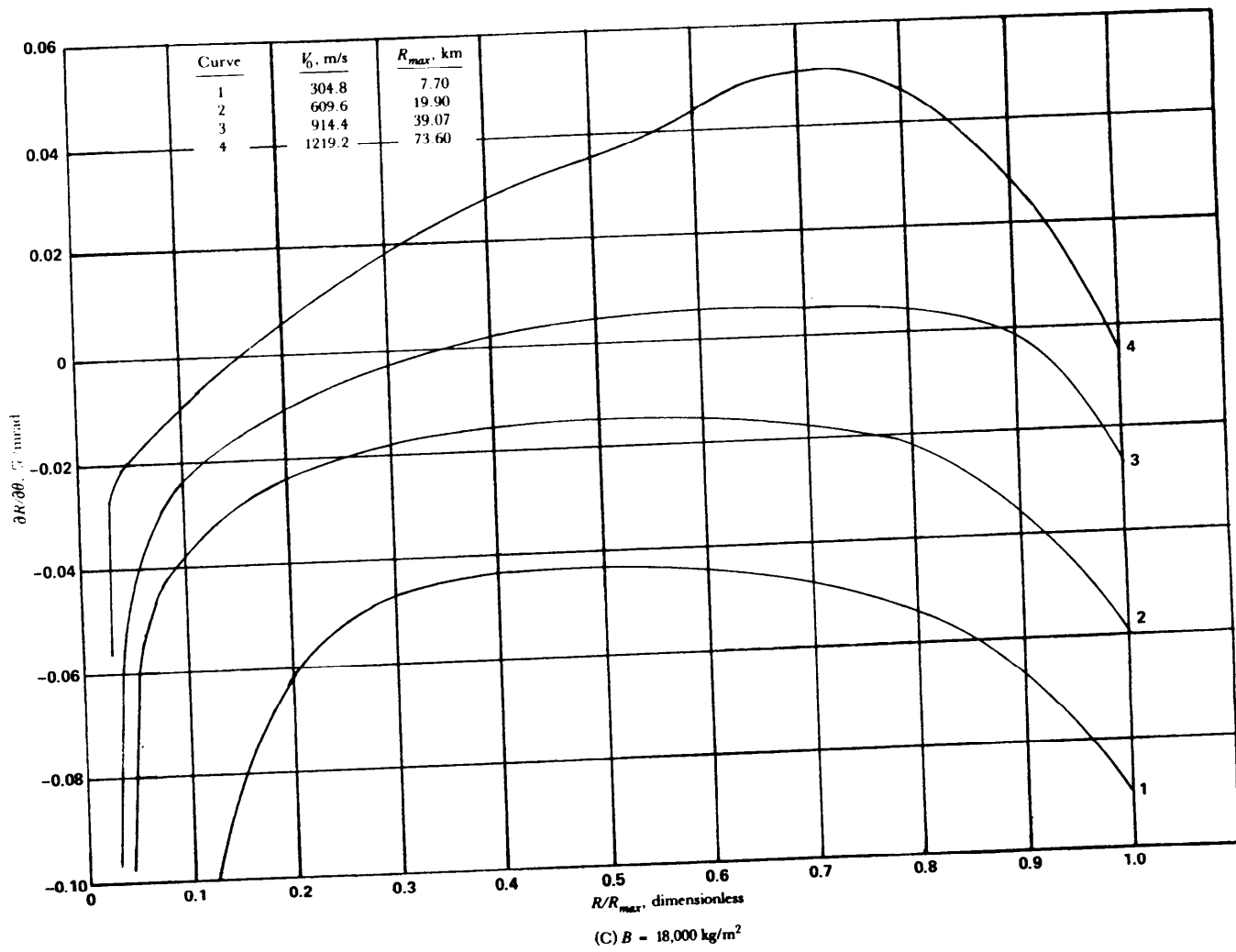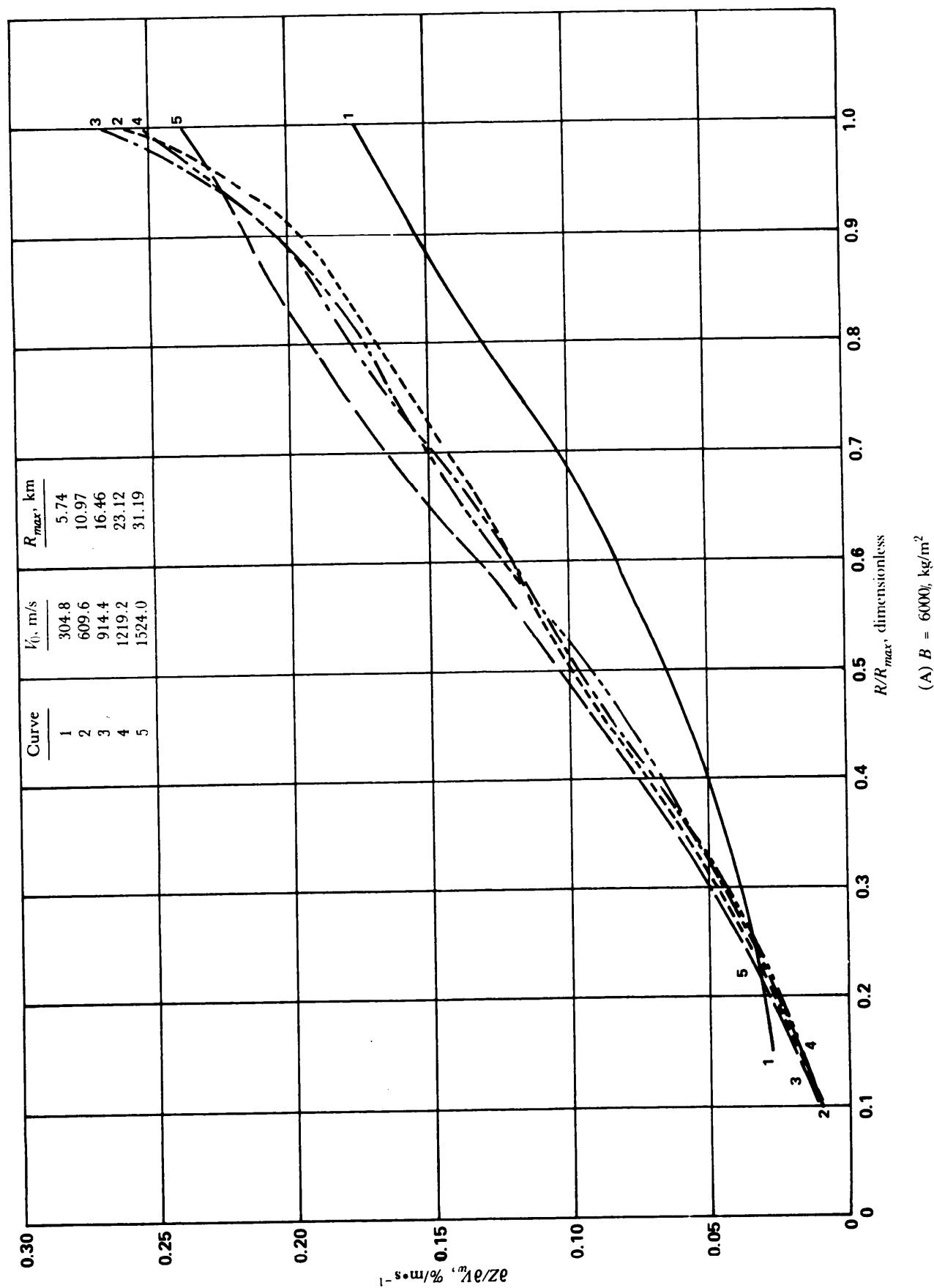
Figure 4-47. **Unit Effect, Deflection/Wind vs R/R_{max} for Various B Values—Time Fuze**

(cont'd on next page)

MIL-HDBK-762(MI)

Curve	V_0, m/s	R_{max}, km
1	304.8	7.08
2	609.6	16.39
3	914.4	28.46
4	1219.2	50.53

R/R_{max}, dimensionless

(B) $B = 12,000$ kg/m^2

Figure 4-47.   (cont'd)

$\partial z/\partial v_w$, %/m·s^{-1}

Curve	V_0, m/s	R_{max}, km
1	304.8	7.70
2	609.6	19.90
3	914.4	39.07
4	1219.2	73.60

R/R_{max}, dimensionless

(C) $B = 18{,}000$ kg/m^2

Figure 4-47. (cont'd)

$\partial z/\partial V_0$, %/m·s^{-1}

(A) $B = 6000$ kg/m^2

R/R_{max}, dimensionless

Curve	V_0, m/s	R_{max}, km
1	304.8	5.74
2	609.6	10.97
3	914.4	16.46
4	1219.2	23.12
5	1524.0	31.19
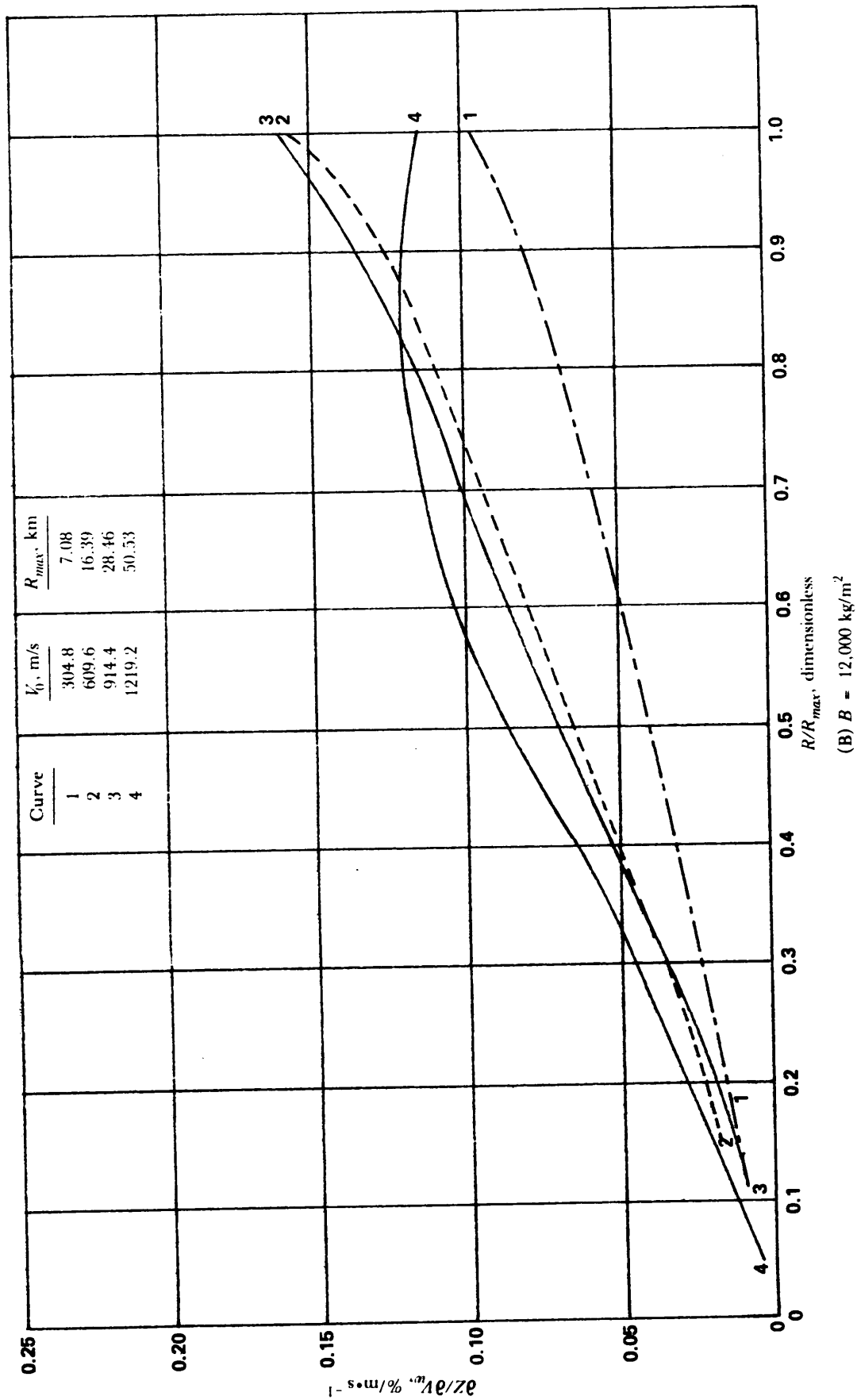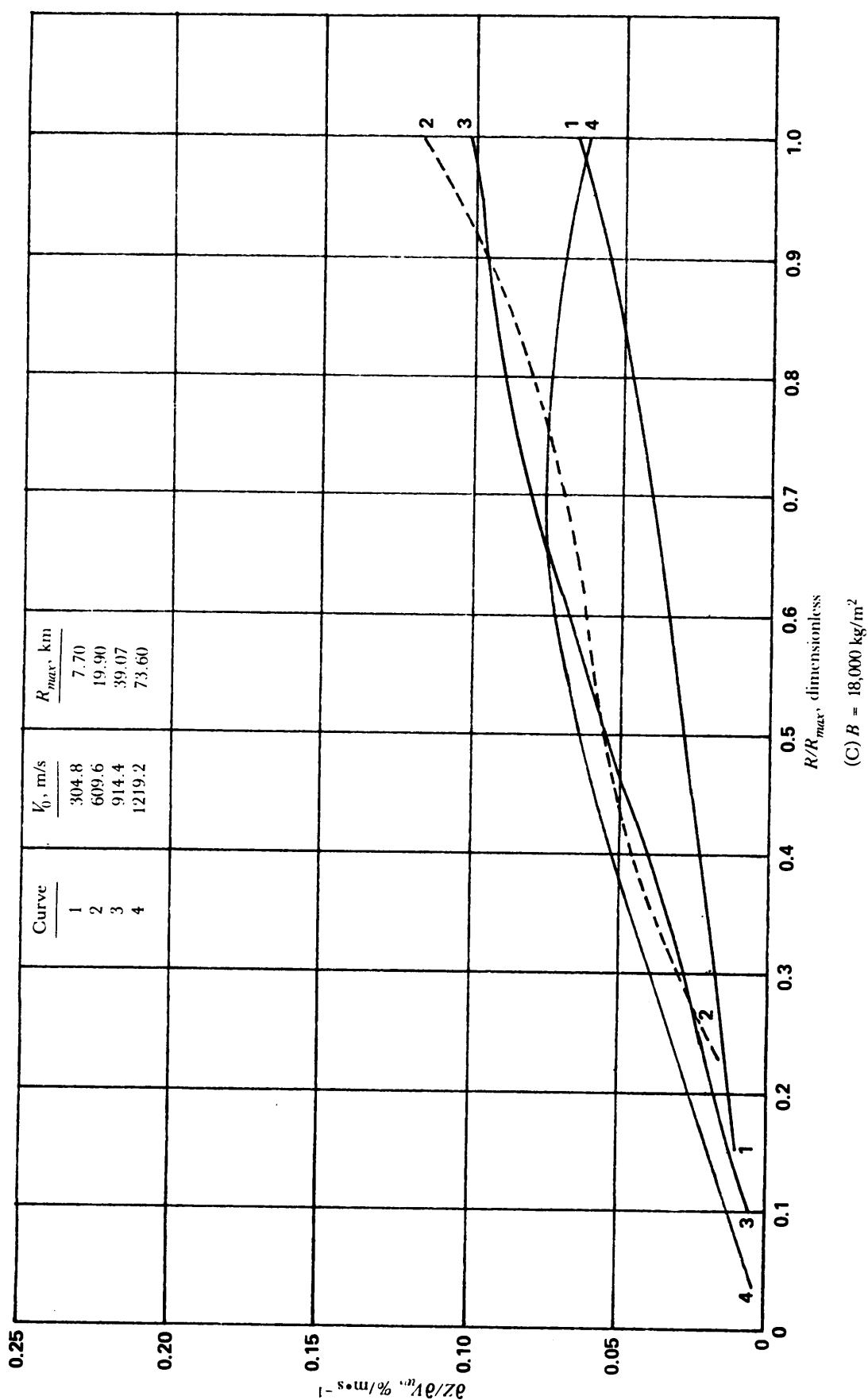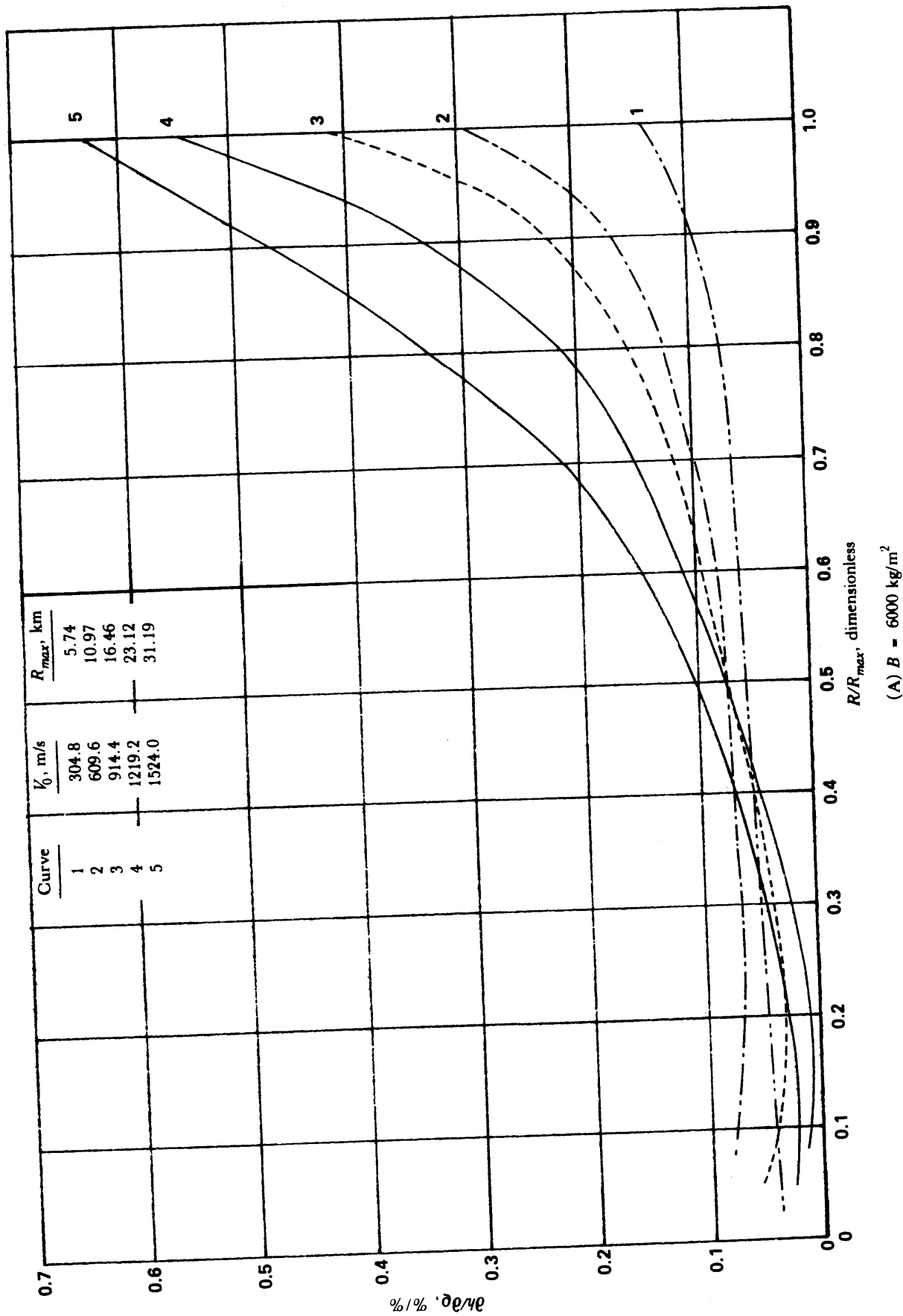
Figure 4-48. Unit Effect, Altitude/Density vs R/R_{max} for Various B Values—Time Fuze
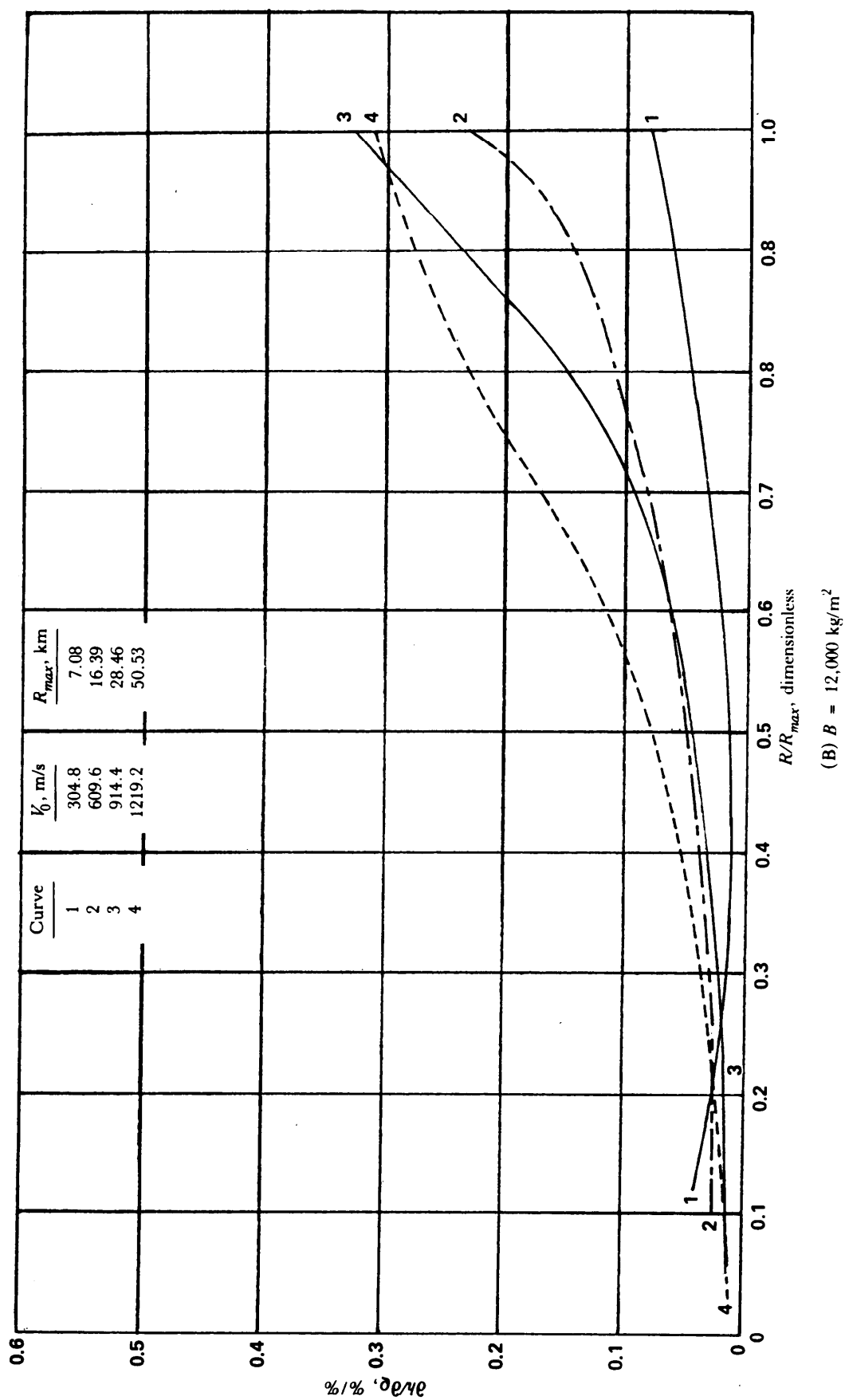
Curve	V_0, m/s	R_{max}, km
1	304.8	7.08
2	609.6	16.39
3	914.4	28.46
4	1219.2	50.53

R/R_{max}, dimensionless

$\partial h/\partial \varrho$, %/%

(B) $B = 12,000$ kg/m^2

Figure 4-48. (cont'd)

4-113

Curve	V_0, m/s	R_{max}, km
1	304.8	7.70
2	609.6	19.90
3	914.4	39.07
4	1219.2	73.60

R/R_{max}, dimensionless

(C) $B = 18,000$ kg/m^2

Figure 4-48. (cont'd)

Curve	V_0, m/s	R_{max}, km
1	304.8	5.74
2	609.6	10.97
3	914.4	16.46
4	1219.2	23.12
5	1524.0	31.19

(A) B = 6000 kg/m^2
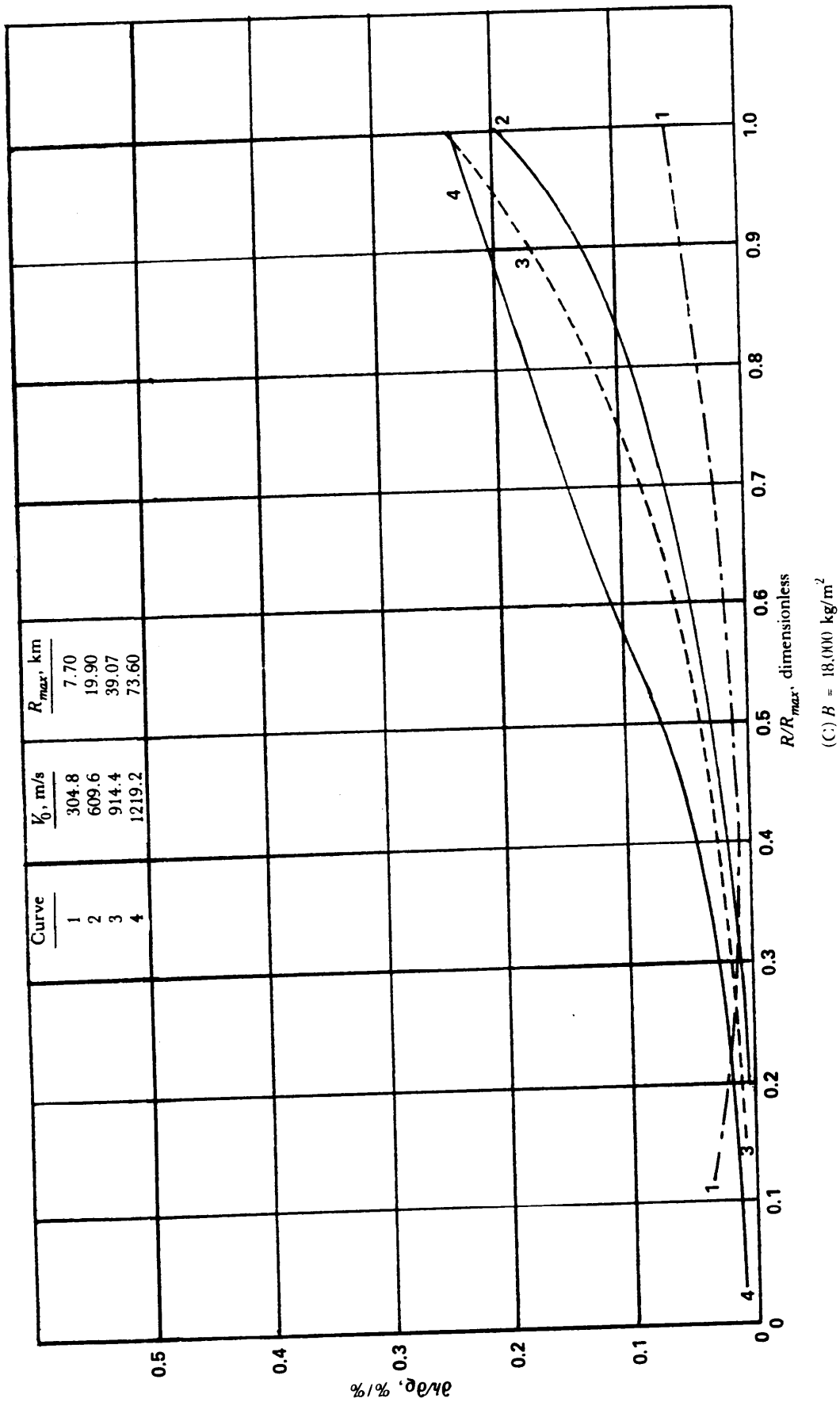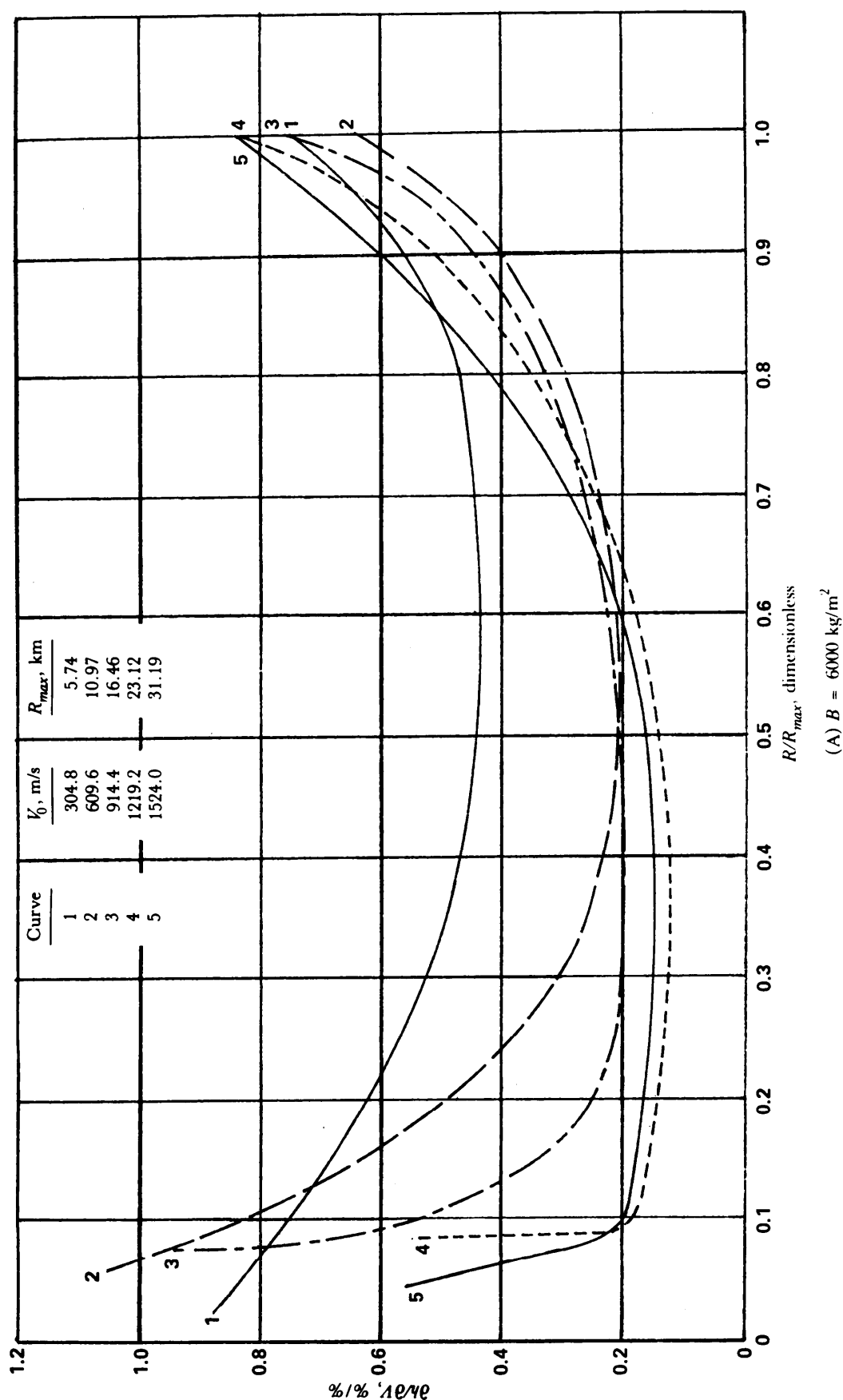
Figure 4-49. Unit Effect, Altitude/Velocity vs R/R_{max} for Various B Values—Time Fuze
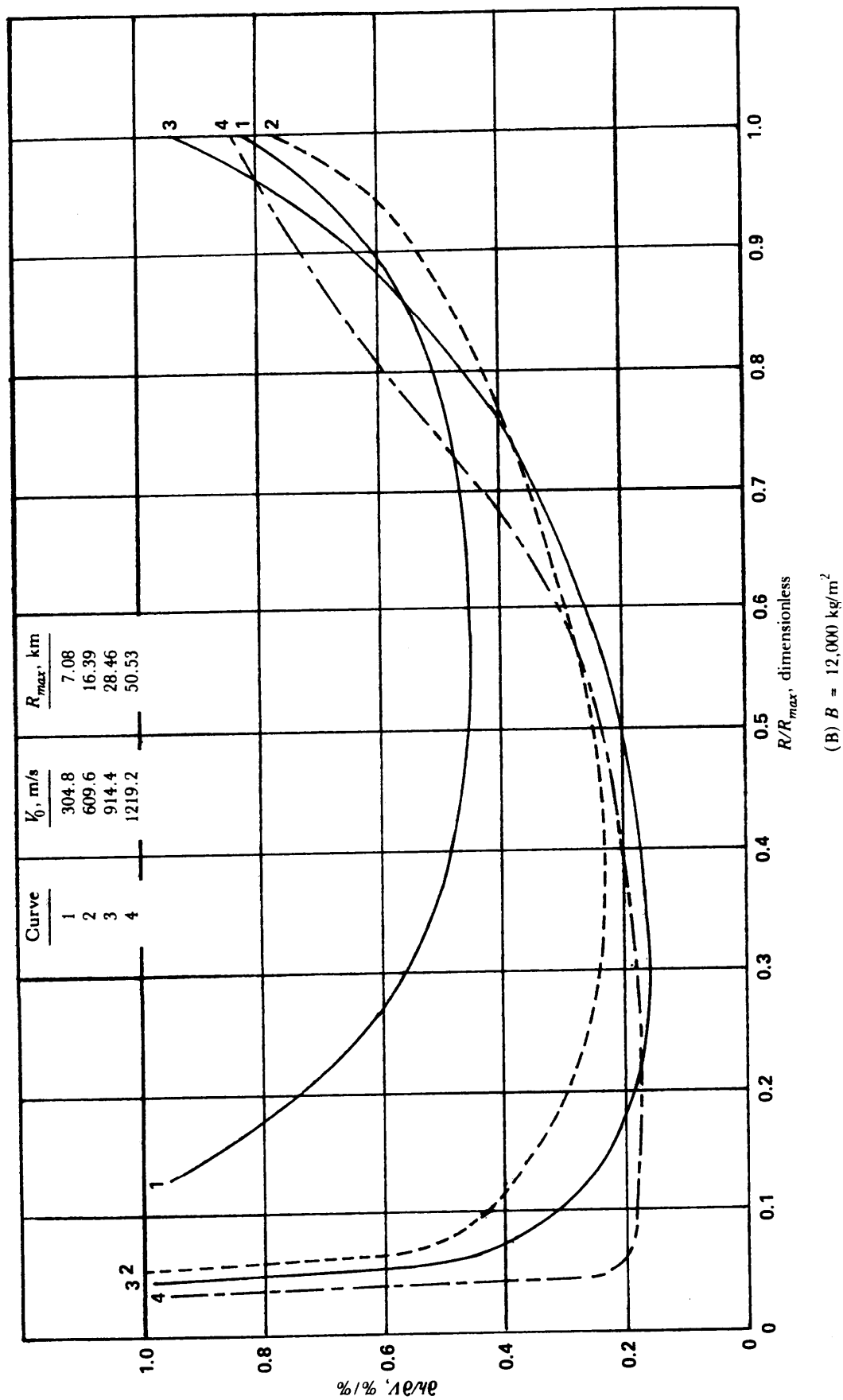
Curve	V_0, m/s	R_{max}, km
1	304.8	7.08
2	609.6	16.39
3	914.4	28.46
4	1219.2	50.53

(B) $B = 12,000$ kg/m^2

Figure 4-49.   (cont'd)

Curve	V_0, m/s	R_{max}, km
1	304.8	7.70
2	609.6	19.90
3	914.4	39.07
4	1219.2	73.60

R/R_{max}, dimensionless

(C) $B = 18,000$ kg/m^2

Figure 4-49. (cont'd)

Curve	V_0, m/s	R_{max}, km
1	304.8	5.74
2	609.6	10.97
3	914.4	16.46
4	1219.2	23.12
5	1524.0	31.19

(A) $B = 6000$ kg/m^2
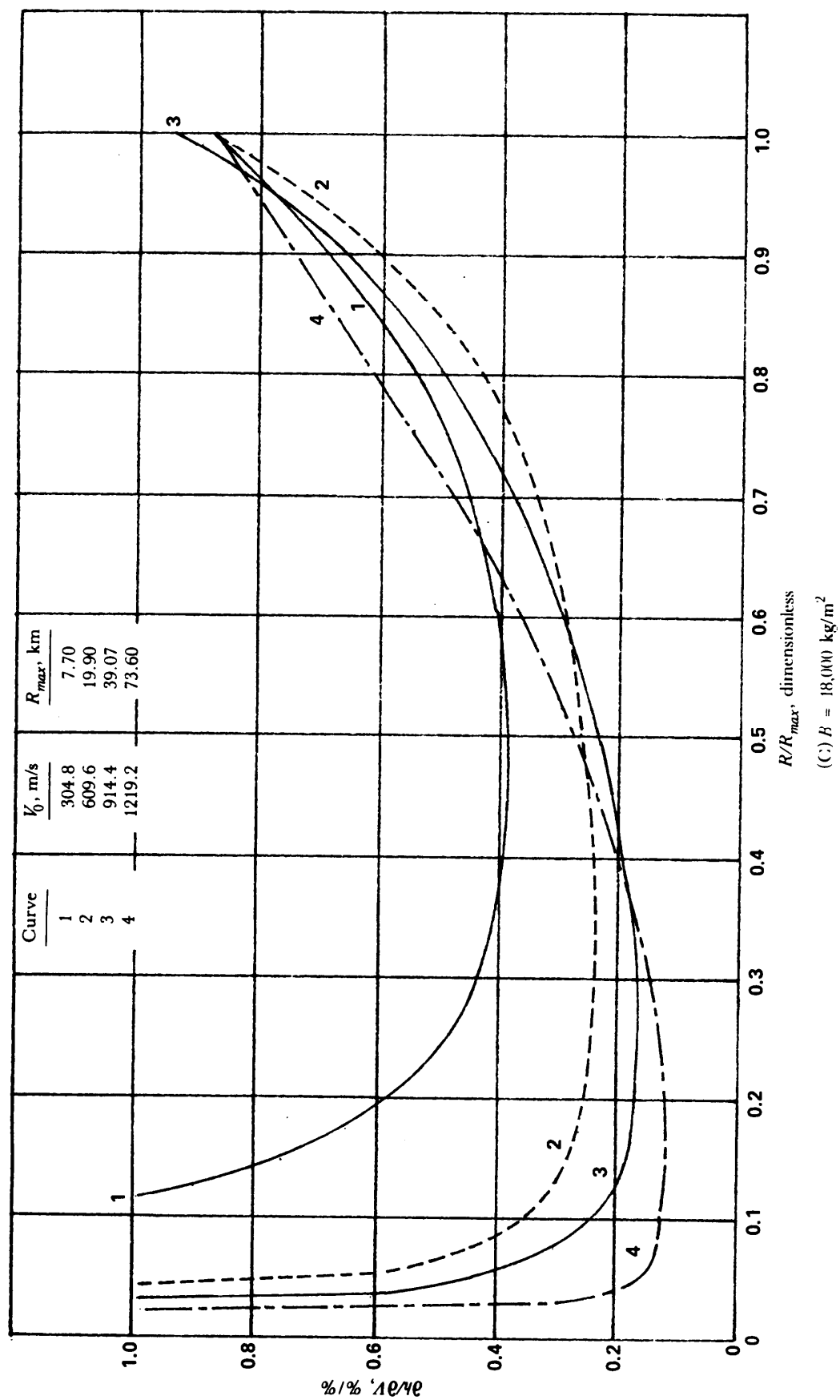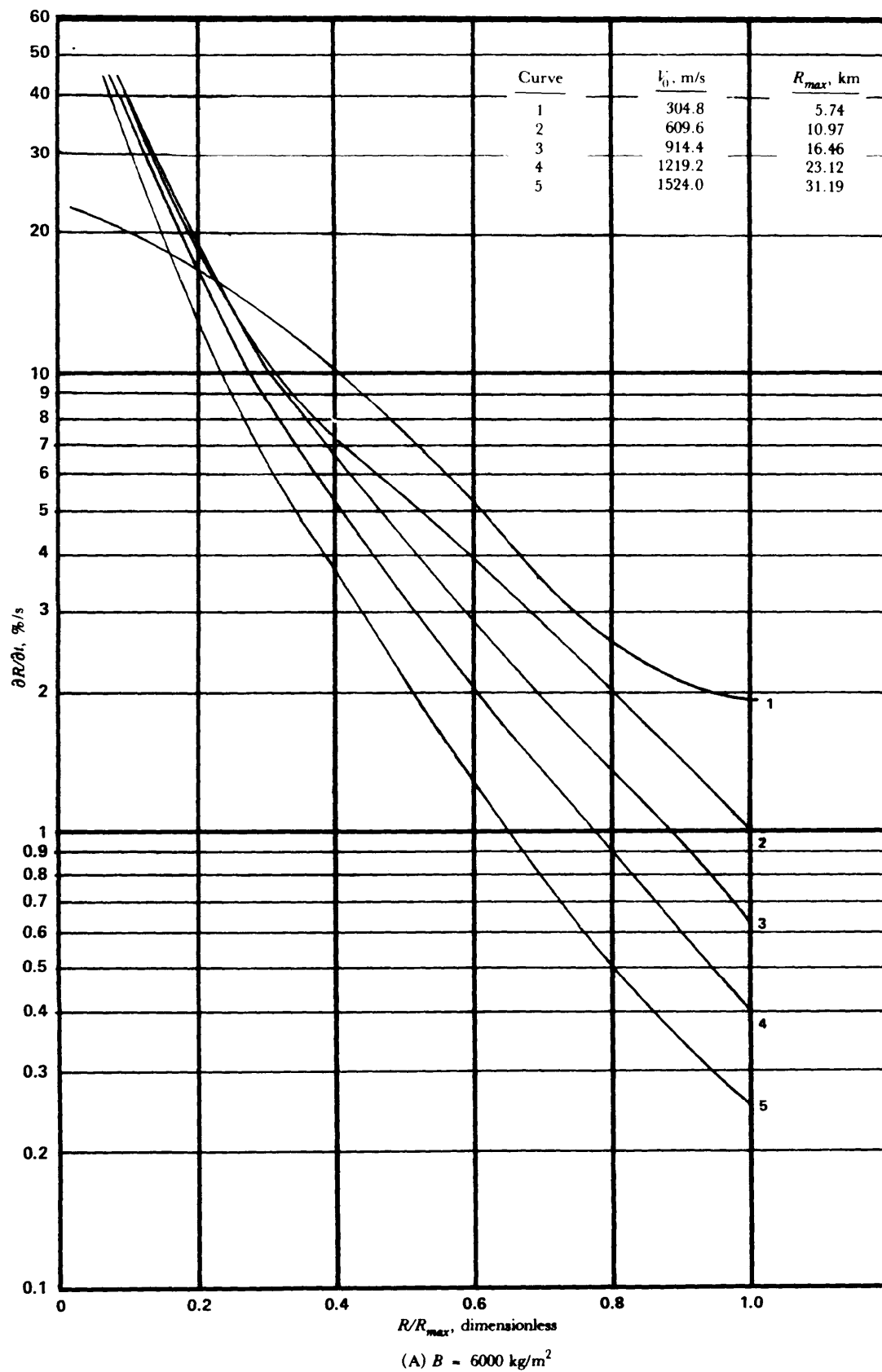
Figure 4-50. Unit Effect, Range/Time vs R/R$_{max}$ for Various B Values—Time Fuze
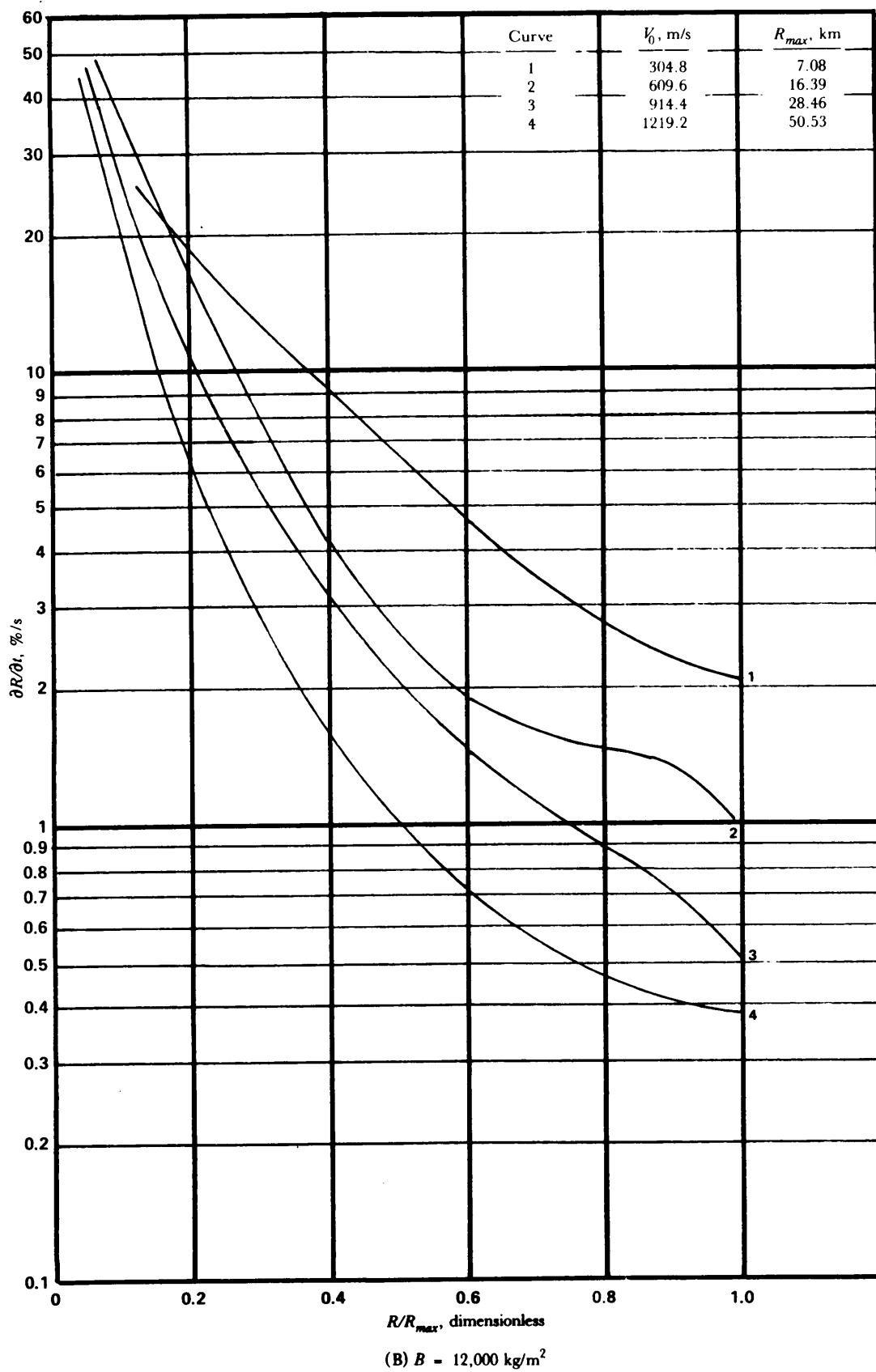
Curve	V_0, m/s	R_{max}, km
1	304.8	7.08
2	609.6	16.39
3	914.4	28.46
4	1219.2	50.53

(B) $B = 12,000$ kg/m^2

Figure 4-50. (cont'd)

Curve	I_0', m/s	R_{max}, km
1	304.8	7.70
2	609.6	19.90
3	914.4	39.07
4	1219.2	73.60

(C) $B = 18,000$ kg/m^2

Figure 4-50. (cont'd)

Curve	V_0, m/s	R_{max}, km
1	304.8	5.74
2	609.6	10.97
3	914.4	16.46
4	1219.2	23.12
5	1524.0	31.19

R/R_{max}, dimensionless

(A) $B = 6000 \text{ kg/m}^2$
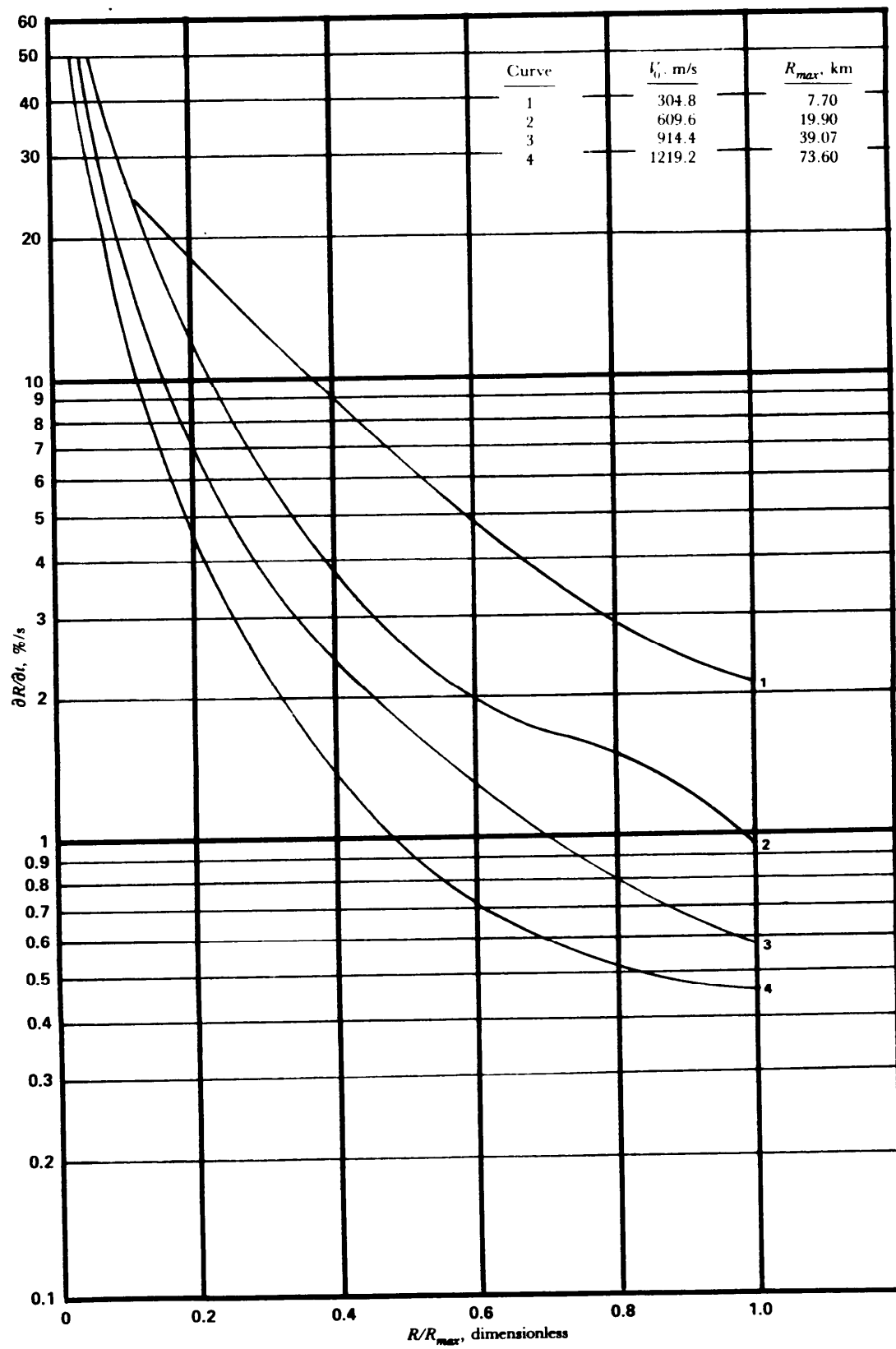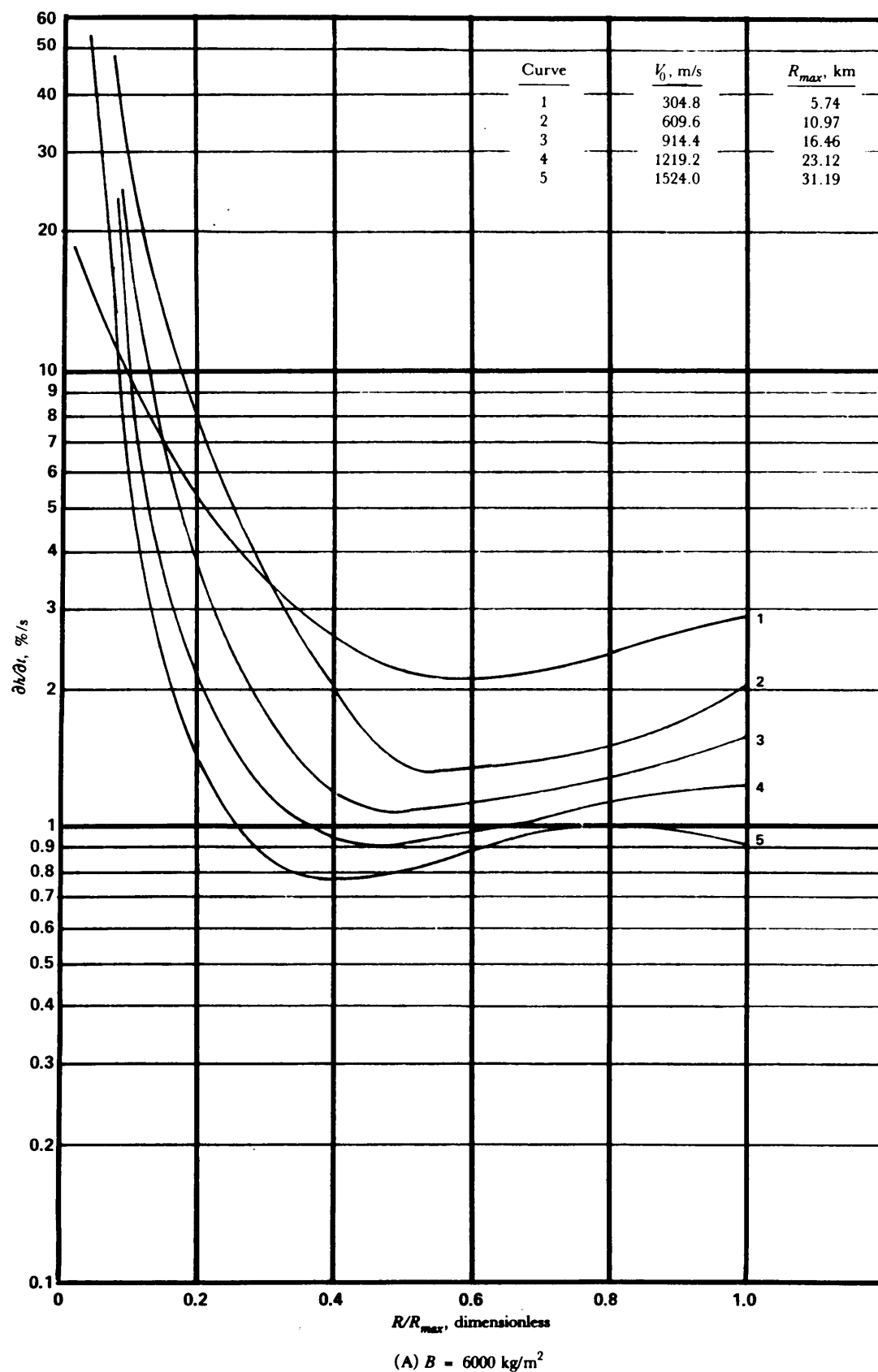
Figure 4-51. Unit Effect, Altitude/Time vs R/R_{max} for Various B Values—Time Fuze
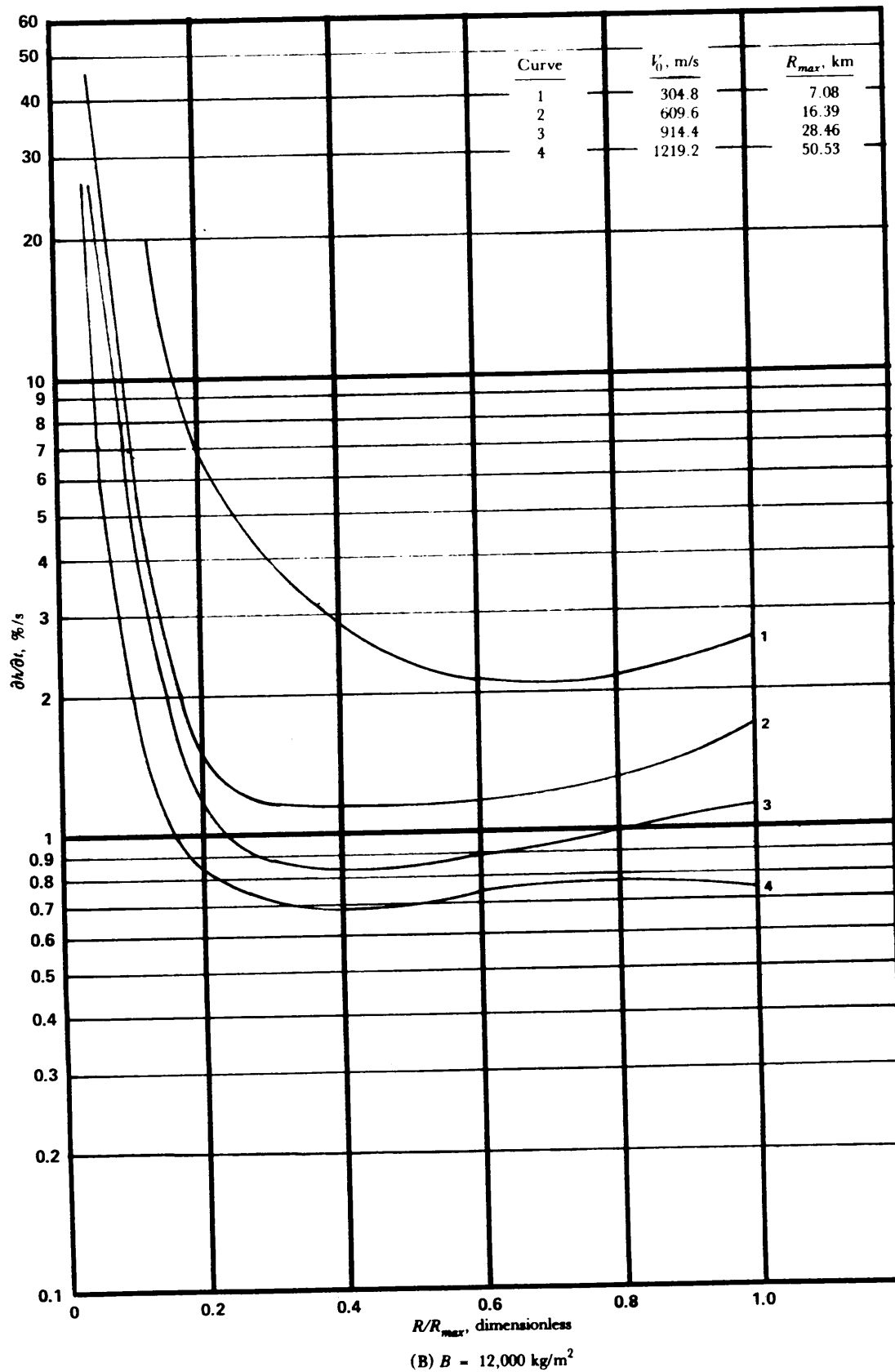
Curve	V_0, m/s	R_{max}, km
1	304.8	7.08
2	609.6	16.39
3	914.4	28.46
4	1219.2	50.53

(B) $B = 12,000$ kg/m²

Figure 4-51. (cont'd)

Curve	V_0, m/s	R_{max}, km
1	304.8	7.70
2	609.6	19.90
3	914.4	39.07
4	1219.2	73.60

(C) B = 18,000 kg/m^2
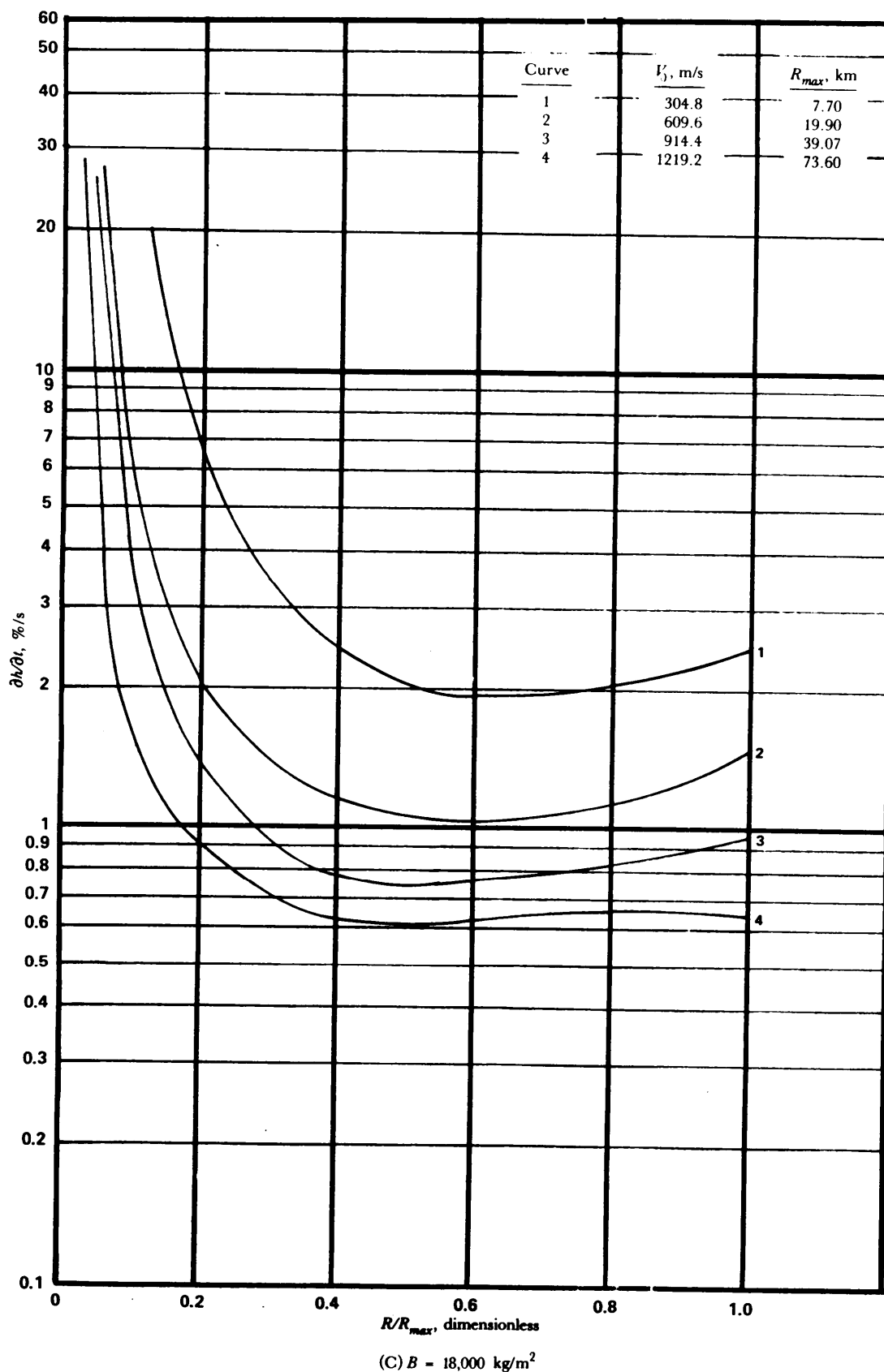
Figure 4-51. (cont'd)

4-5.5.2.8 Example Circular Error Probable (CEP)

First, from Eq. 4-66

$$\sigma_{sys} = \frac{18.6 + 26.3}{2} = 22.5 \text{ mrad}$$

$$\sigma_{sys} = (22.5 \text{ mrad}) (28.5 \text{ km}) = 641 \text{ m}.$$

From Eq. 4-67, since $\sigma_{R_{tot}} / \sigma_{D_{tot}} < 7$,

$$CEP = 1.1774 \ \sigma_{sys}$$

$$CEP = 1.1774 (22.5 \text{ mrad}) = 26.5 \text{ mrad}$$

or

$$CEP = 1.1774(641 \text{ m}) = 755 \text{ m}.$$

4-5.5.2.9 Example Probability of Hit

Assume that the example rocket with its warhead will be scored a hit if it impacts within an area defined by a circle with a 100-m radius. Therefore, by Eq. 4-72

$$P_{HIT} = 1 - \exp\left[-0.6926\frac{(100)^2}{(755)^2}\right]$$

$$P_{HIT} = 1 - 0.98792 = 0.01208.$$

The probability of hitting on or within the defined circle by firing one round of the example rocket is approximately 1.2%.

REFERENCES

1. J. B. Rosser *et al., Mathematical Theory of Rocket Flight,* McGraw-Hill Book Co., New York, NY, 1947.

2. L. Davis, Jr., *et al., Exterior Ballistics of Rockets,* D. Van Nostrand Co., Inc., New York, NY, 1958.

3. M. P. Stamps, *Reduction of Errors in a Free Rocket by High Spin Rates,* MICOM Report RD-TR-70-24, US Army Missile Command, Redstone Arsenal, AL, 1969.

4. M. W. Hunter *et al.,* "Some Recent Aerodynamic Techniques in Design of Fin-Stabilized Free-Flight Missiles for Minimum Dispersion", J. of the Aeronautical Sciences 23, 571-7 (June 1956).

5. R. R. Newton, *Spin Programs Which Cause the Dispersion Produced by Thrust Malalignment to Vanish,* Department of Physics Report PH-RR-19, The University of Tennessee, Knoxville, TN, January 1955.

6. R. E. Maerker and R. R. Newton, *Spin Programs Which Cause Dispersion Produced by Thrust, Malalignment to Vanish, Part II,* Department of Physics Report PH-RR-22, The University of Tennessee, Knoxville, TN, June 1955.

7. R. R. Newton, *Spin Programs Which Cause Dispersion Produced by Thrust Malalignment of Vanish, Part III,* Department of Physics Report Number 5164, Tulane University, New Orleans LA, August 1956.

8. A. S. Platou, "Magnus Characteristics of Finned and Nonfinned Projectiles", AIAA Journal 3, 83-90 (January 1965).

9. P. M. Brodie, "Roll-Resonance Effects on Controlled Rocket-Boosfed Projectiles", J. of Spacecraft and Rockets 6, 207-8 (February 1969).

10. W. C. McCorkle, *Recent Developments in High Accuracy Free Rocket Weapons Systems,* Report Number Miscellaneous 6, US Army Rocket and Guided Missile Agency, Redstone Arsenal, AL, April 1959.

11. R. R. Newton, *Effect of Variable Acceleration Upon the Dispersion of Fin-Stabilized Rockets,* Department of Physics Report PH-RR-10, University of Tennessee, Knoxville, TN, April 1953.

12. D. R. Combs, "Accuracy Improvement by a Dynamically Aimed Free Rocket", *Proceedings of the Third Annual Free Flight Rocket Workshop,* MIRADCOM Report T-SR-79-12, US Army Missile Command, Redstone Arsenal, AL, pp. 257-65, October 1978.

13. J. L. Batson, "Free Flight Rocket" Potpourri" *Proceedings of the Second Annual Free Flight Rocket Workshop, Volume 1,* MIRADCOM Report TF-TR-77-1, US Army Missile Command, Redstone Arsenal, AL, pp. 79, 87-9, August 1977.

14. W. W. Boyle and M. B. Mantler, *The Effects of Configuration Sensitivity on the Ballistics of Bombs—Part I, Aerodynamic Math Model and Tolerances,* NSI Report TN-230-1980, Northrop Services, Inc., Huntsville, AL, October 1978.

15. W. W. Boyle and M. B. Mantler, *The Effects of Configuration Sensitivity on the Ballistics of Bombs—Part II, Design Data,* NSI Report TN-230-1992, Northrop Services, Inc., Huntsville, AL, February 1980.

16. E. J. McGrath *et al., Techniques for Efficient Monte Carlo Simulation, Volume I, Selecting Probability Distributions,* SAI Report 72-59-LJ, Science Applications, Inc., LaJolla, CA, March 1973.

17. E. J. McGrath *et al., Techniques for Efficient Monte Carlo Simulation, Volume II, Random Number Generation for Selected Probability Distributions,* SAI Report 72-59-LJ, Science Applications, Inc., LaJolla, CA, March 1973.

18. E. J. McGrath *et al., Techniques for Efficient Monte Carlo Simulation, Volume III, Variance Reduction,* SAI Report 72-59-LJ, Science Applications, Inc., LaJolla, CA, March 1973.

19. R. C. Brown *et al., Six-Degree-of-Freedom Flight Path Study Generalized Computer Program,* AFFDL Report FDL-TDR-64-1, US Air Force Flight Dynamics Laboratory, Wright-Patterson AFB, OH, October 1964.

20. *Dynamics of the Airframe,* BU AER Report AD-61-4 II, Bureau of Aeronautics, Navy Department, Washington, DC, September 1952.

21. C. J. Cohen and D. Werner, A *Formulation of the Equations of Motion of a Four-Finned Missile,* NPG Report 1474, Exterior Ballistics Laboratory, US Naval Proving Ground, Dahlgren, VA, September 1956.

BIBLIOGRAPHY

S. S. Chin, Missile *Configuration Design,* McGraw-Hill Book Co., New York, NY, 1961.

R. R. Johnson, *Elementary Statistics,* Second Edition, Duxbury Press, North Scituate, MA, 1976.

M. G. Natrella, *Experimental Statistics,* Department of Commerce, NBS Handbook 91, National Bureau of Standards, Washington, DC, October 1966.

J. A. Lovingood, *A Technique for Including the Effects of Vehicle Parameter Variations in Wind Response Studies,* NASA Technical Memo X-53042, National Aeronautics and Space Administration, George C. Marshall Space Flight Center, AL, 1964.

C H A P T E R   5
A E R O D Y N A M I C S *

This chapter treats the aerodynamic aspects of free rocket design and provides a general introduction to applicable aerodynamic principles. Aerodynamic terms are defined, and aerodynamic characteristics of rocket components are discussed. Methods for determining total rocket aerodynamic characteristics from component aerodynamics are introduced. Experimental techniques for determining both component and total aerodynamics are discussed. Some information is presented on trade-off studies that should be made during preliminary aerodynamics design of free rockets. Sample calculations are included as a guide for use in performing trade-off studies.

5-0 LIST OF SYMBOLS

$dA =$ incremental cross-sectional area, m^2

$A_b =$ body base area, m^2

$A_{bt} =$ cross-sectional area of boattail, m^2

$A_{cyl} =$ body cross-sectional area, m^2

$A_{fl} =$ cross-sectional area of base of flare, m^2

$A_j =$ area of jet in nozzle exit plane, m^2

$A_M =$ model frontal area, m^2

$A_{ref} = \pi d^2/4,$ aerodynamic reference area, m^2

$A_T =$ aerodynamic test area, m^2

$A_{wet} =$ surface wetted area, m^2

$AR =$ b^2/S_F, fin aspect ratio, dimensionless

$'AR)_e = b_e^2/S_{F_e},$ exposed fin aspect ratio, dimensionless

$a_t = \beta \left(\dfrac{b_e/2}{c} \right)$, fin correlation parameter, dimensionless

$(a_t)_{rg} = \beta(B - 1)/(2C),$ for equivalent planar fins, the slope of line connecting tip leading edge to root trailing edge divided by slope of Mach line, dimensionless

$B =$ ringtail diameter in plane of trailing edge (see Fig. 5-60), m

$b =$ fin span, m

$b_e =$ exposed fin span, m

$C =$ longitudinal distance between leading edge and trailing edge (see Fig. 5-60), m

$=$ coefficient in Haack series, dimensionless (see Eq. 5-37)

$C_A = \dfrac{\text{axial force}}{q_\infty A_{ref}}$, axial force coefficient, dimensionless

$C_D = \dfrac{D}{q_\infty A_{ref}}$, drag coefficient, dimensionless

---

* All figures are located at the end of the chapter.

$$C_{D_b} = -C_{P_b} = \left(1 - \frac{p_b}{p_\infty}\right)\left(\frac{1}{0.7M_\infty^2}\right), \text{ base-drag coefficient, dimensionless}$$

$$(C_{D_b})_F = -(C_{P_b})_F\left(\frac{S_{F_b}}{A_{ref}}\right), \text{ fin base-drag coefficient, dimensionless}$$

$$C_{D_f} = C_f\left(\frac{A_{wet}}{A_{ref}}\right), \text{ skin-friction drag coefficient, dimensionless}$$

$C_{D_{fl}}$ = wave-drag coefficient of conical flare, dimensionless

C_{D_T} = total pressure drag coefficient, dimensionless

C_{D_w} = 3-dimensional wave-drag coefficient, dimensionless

C_{d_w} = 2-dimensional wave-drag coefficient, dimensionless

$$(C_{D_w})_{rg} = \frac{(\pi d_{rg})(c_{rg})(C_{d_w})}{A_{ref}}, \text{ ringtail wave-drag coefficient, dimensionless}$$

C_f = skin-friction coefficient, dimensionless

$$C_L = \frac{\text{lift force}}{q_\infty A_{ref}}, \text{ lift coefficient, dimensionless}$$

C_{L_α} = lift (normal) force gradient, rad^{-1} or deg^{-1}

$$C_l = \frac{\text{roll moment}}{q_\infty A_{ref} d}, \text{ roll moment coefficient, dimensionless}$$

$C_{l_p} = \partial C_l / \partial[pb/(2v)]$, roll damping moment coefficient gradient, rad^{-1} or deg^{-1}

$$C_{l_s} = \frac{\partial C_l}{\partial \delta}, \text{ roll moment effectiveness coefficient gradient, } \text{rad}^{-1} \text{ or } \text{deg}^{-1}$$

$$C_m = \frac{m}{q_\infty A_{ref} \ell}, \text{ aerodynamic pitching moment coefficient, dimensionless}$$

$C_{m_p} = \partial C_m / \partial(pdv/2)$ = magnus moment coefficient, rad^{-1} or deg^{-1}

$$C_{m_\alpha} = \frac{\partial C_m}{\partial \alpha}, \text{ aerodynamic pitching moment coefficient gradient at } \alpha = 0, \text{ rad}^{-1} \text{ or } \text{deg}^{-1}$$

$(C_{m_\alpha})_b$ = pitching moment coefficient gradient of body at $\alpha = 0$, deg^{-1} or rad^{-1}

$(C_{m_\alpha})_F$ = pitching moment coefficient gradient of fins at $\alpha = 0$, deg^{-1} or rad^{-1}

$(C_{m_\alpha})_T$ = total pitching moment coefficient gradient at $\alpha = 0$, deg^{-1} or rad^{-1}

$$\frac{C_{m_\alpha}}{C_{N_\alpha}} = \frac{X_{CG} - X_{cp}}{d}, \text{ stability margin, dimensionless}$$

$C_{m_{\dot\theta}} = \partial C_m / \partial(\dot\theta dv/2)$ = total pitch damping moment coefficient gradient, deg^{-1} or rad^{-1}

$$C_N = \frac{N}{q_\infty A_{ref}}, \text{ aerodynamic normal force coefficient, dimensionless}$$

$$C_{N_\alpha} = \frac{\partial C_N}{\partial \alpha}, \text{ aerodynamic normal force coefficient gradient at } \alpha = 0, \text{ rad}^{-1} \text{ or } \text{deg}^{-1}$$

$(C_{N_\alpha})_b$ = body aerodynamic normal force coefficient gradient, rad^{-1} or deg^{-1}

$(C_{N_\alpha})_{b(F)}$ = body normal force gradient in presence of a fin, rad^{-1} or deg^{-1}

$(C_{N_\alpha})_F$ = fin normal force coefficient gradient, rad^{-1} or deg^{-1}

$(C_{N_\alpha})_{F_e}$ = exposed fin normal force coefficient gradient, rad^{-1}

$(C_{N_\alpha})_{F(b)}$ = fin normal force gradient in presence of a body, rad^{-1} or deg^{-1}

$(\Delta C_{N_\alpha})_{fl}$ = incremental normal force coefficient gradient of a solid-flared afterbody in subsonic flow, rad^{-1}

$(C_{N_\alpha})_{rg}$ = ringtail normal force coefficient gradient, rad^{-1} or deg^{-1}

$(C_{N_\alpha})_T$ = total (sum of body and fins) normal force coefficient gradient, rad^{-1} or deg^{-1}

$\overline{(C_{N_\alpha})_T}$ = total effective normal force coefficient gradient, rad^{-1} or deg^{-1}

$C_n = \dfrac{\text{yawing moment}}{q_\infty A_{ref} d}$, yawing moment coefficient, dimensionless

C_{n_p} = magnus force coefficient, rad^{-1} or deg^{-1}

$C_p = \dfrac{p_{local} - p_\infty}{q_\infty}$, pressure coefficient, dimensionless

C_{P_b} = base-pressure coefficient, dimensionless

$(C_{P_b})_F$ = fin base-pressure coefficient, dimensionless

C'_{P_b} = local base-pressure coefficient, dimensionless

C_{P_c} = pressure coefficient of cone, dimensionless

C_{RT} = radial thrust coefficient, dimensionless

$C_T = \dfrac{T}{q_\infty A_{ref}}$, thrust coefficient, dimensionless

$C_y = \dfrac{\text{side force}}{q_\infty A_{ref}}$, side force coefficient, dimensionless

c = local fin chord length, m

$\bar{c}$ = mean aerodynamic chord length, m

c_r = root chord length, m

c_{r_e} = exposed root chord length, m

c_{rg} = ringtail projected root chord length, m

c_t = tip chord length, m

CG = center of gravity measured from nose unless otherwise stated, m or cal

cp = center of pressure measured from nose unless otherwise stated, m or cal

D = drag force, N

D_{rg} = ringtail drag, N

d = rocket or body diameter, m or cal

d_{ab} = afterbody maximum diameter, m or cal

d_b = rocket base diameter, m or cal

d_{bt} = boattail diameter, m

d_{cyl} = cylinder diameter, m

d_{fl} = flare maximum diameter, m

d_j = nozzle exit (jet) diameter, m

d_m = Me'plat diameter, cal

d_{rg} = ringtail diameter in plane of leading edge, m

E = longitudinal distance between ringtail trailing edge and plane of the body base (positive ahead of the base, see Fig. 5-61), m

F = ringtail strut diameter (see Fig. 5-60), m

$f_n = \ell_n/d$, nose fineness ratio (see Fig. 5-112), dimensionless

G = longitudinal distance from ringtail leading edge to projection of circular strut centerline on ringtail external surface (see Fig. 5-60)

g = spanwise gap between the rocket body and fin root chord, m

h = fin thickness at trailing edge (see Fig. 5-153), m

I = fin-fin interference parameter, dimensionless

I' = modified fin-fin interference parameter, dimensionless

$K_{F(b)}$ = fin-body interference factor, dimensionless

$K_{b(F)}$ = body-fin interference factor, dimensionless

$K_T = K_{F(b)} + K_{b(F)}$, total fin-body and body-fin interference factor, dimensionless

K' = parabola factor (see Eq. 5-36), dimensionless

$k_2 - k_1$ = Munk's apparent mass factor, dimensionless

$(k_\theta)_F$ = fin lift effectiveness parameter, dimensionless

L = characteristic length (see Eq. 5-41), m

ℓ = distance between adjacent fin root chords, m or cal

ℓ_{ab} = afterbody length, m or cal

ℓ_b = body length, m or cal

ℓ_{bt} = boattail length, m or cal

ℓ_{cyl} = cylinder length, m or cal

ℓ_{fl} = total flare length, m or cal

ℓ_{mid} = length of midsection (see Eq. 5-18), m or cal

ℓ_n = nose length, m or cal

ℓ_{ref} = reference length, m or cal

ℓ_T = total rocket length (nose, midsection, and afterbody), m or cal

ℓ_T/d = fineness ratio of total body or rocket, cal

ℓ' = distance between adjacent fin tip chords, m or cal

$M = v/v_s$, Mach number, dimensionless

M_j = jet-exit Mach number, dimensionless

M_1 = upstream Mach number, dimensionless

M_∞ = free-stream Mach number, dimensionless

M' = Mach number just forward of base (local) (see Fig. 5-139), dimensionless

m = pitching moment, N·m

$\dot{m}$ = mass flow, kg/s

N = normal force, N

n = number of fins

   = power factor (see Eq. 5-35), dimensionless

P = pressure, Pa

P_c = jet chamber pressure, Pa

p = rocket spin rate, rad/s

p_b = base pressure, Pa

p_b/p_∞ = ratio of base pressure to free-stream static pressure (commonly called base pressure ratio), dimensionless

$p_{b_{cyl}}$ = base pressure of cylindrical afterbody, Pa

$p_{b_{noncyl}}$ = base pressure of noncylindrical afterbody, Pa

p_j = jet pressure, Pa

p_{local} = local pressure, Pa

p_p = plateau pressure, Pa

p_{sep} = separation pressure, Pa

p_∞ = free-stream pressure, Pa

p' = pressure just forward of rocket base, Pa

$q_\infty = 0.5\rho_\infty v_\infty^2$, free-stream dynamic pressure, Pa

q' = local dynamic pressure (see Fig. 5-139), Pa

R = radius of a given ogive, m

$Re = vL/\nu$, Reynolds number, dimensionless

R_{mf} = jet-momentum flux ratio, dimensionless

R_T = radius of arc that defines surface of a tangent ogive (see Eq. 5-32 and Fig. 5-115), m

r = radial distance from rocket centerline or body radius, m

r_b = body radius at base of rocket (see Fig. 5-89), m

r' = radius/maximum radius ratio for forebody power series (see Eq. 5-35), dimensionless

S_{eff} = effective fin area, m^2

$\overline{S}_{eff}$ = average effective area projected in horizontal plane of all fins averaged over a roll cycle of $0 \leq \psi \leq \pi/n$, m^2

S_F = isolated fin planform area, m^2

S_{F_b} = base area of all fin panels, m^2

S_{F_e} = exposed fin planform area (two fin panels joined at root chord), m^2

S_{F_x} = fin planform area assuming hypothetical extension of fins through body (see Fig. 5-29), m^2

T = thrust, N

t = fin thickness, m

t/c = fin thickness to chord ratio, dimensionless

v = velocity, m/s

v_s = speed of sound in a flow medium, m/s

v_∞ = free-stream velocity, m/s

X = axial distance, measured from nose, m or cal

dX = incremental axial distance, m

X,Y,Z = inertial-coordinate system

X_b = axial distance forward of the rocket base (see Fig. 5-89), m

X_{CG} = axial distance from nose to CG, m or cal

X_{cp} = axial distance from nose to cp, m or cal

$(X_{cp})_b$ = axial distance from nose to body center of pressure, m or cal

$(X_{cp})_F$ = center of pressure of fin measured downstream of the fin leading edge at the root chord, m or cal

$[(X_{cp})_F]_{te}$ = fin center of pressure, percent of chord from trailing edge (see Fig. 5-78)

$(X_{cp})_{fl}$ = axial distance from cylinder-flare juncture to flare center of pressure, m

$(X_{cp})_T$ = axial distance from nose to center of pressure of total rocket, m or cal

$\dfrac{(X_{cp})_T}{d}$ = total stability margin, cal

X_j = distance of nozzle exit from base of rocket (see Fig. 5-149), m

x = ratio of distance from nose tip to total nose length (see Eq. 5-35), dimensionless

x,y,z = body-centered coordinate system with origin at center of gravity

x_b = axial distance from rocket center of gravity to body center of pressure, m

x_s,y_s,z_s = stability coordinate system

x_t = axial distance from rocket center of gravity to tail center of pressure, m

x_w,y_w,z_w = wind coordinate system

y = lateral distance from body centerline, m

y_r = distance from center of wind tunnel test section to the shock reflection boundary (see Fig. 5-163(A)), m

y' = lateral distance from body surface (see Eq. 2-27 and Fig. 5-75), m

α = angle of attack, rad or deg

α_{eff} = effective angle of attack, rad or deg

α_o = body angle of attack, rad or deg

$\bar{\alpha}_{eff}$ = average effective angle of all attack for all fins of a tail assembly averaged over a roll cycle $0 \le \psi \le \pi/n$ (n = number of fins) (see Eq. 5-25), rad or deg

$\beta = \sqrt{|M_\infty^2 - 1|}$, similarity parameter, dimensionless

γ_j = ratio of specific heats of rocket jet, dimensionless

γ_∞ = ratio of specific heats of free-stream flow, dimensionless

δ = fin cant angle (positive, clockwise viewed from base) (see Fig. 5-54), rad or deg

= ringtail internal expansion angle (see Fig. 5-133), rad or deg

ϵ = included angle of fin leading edge (see Figs. 5-28 and 5-34), rad or deg

θ = cone, flare or boattail half angle, rad or deg

= WAF opening angle (see Fig. 5-52), rad or deg

θ_c = nose cone half angle (see Fig. 5-163), rad or deg

θ_j = rocket nozzle half angle at exit, rad or deg

$\dot{\theta}$ = angular pitching velocity about center of gravity, rad/s

Λ = fin sweep angle, rad or deg

$\Lambda_{c/2}$ = fin sweep angle at midchord, rad or deg

Λ_{le} = leading edge sweep angle, rad or deg

Λ_{te} = trailing edge sweep angle, rad or deg

$\lambda = c_t/c_r$, fin taper ratio (see Fig. 5-34), dimensionless

$\lambda_e = c_t/c_{r_e}$, exposed fin taper ratio (see Fig. 5-68), dimensionless

μ = Mach angle, $\operatorname{Sin}^{-1}(1/M_\infty)$

ν = kinematic viscosity, m^2/s

ρ = atmospheric density, kg/m^3

ρ_∞ = free-stream atmospheric density, kg/m^3

σ = fin trailing edge sweep angle, rad or deg

ϕ = roll angle about longitudinal axis measured from horizontal (see Fig. 5-72, 5-73, and 5-75), rad or deg

ψ = angle or roll of tail assembly measured from vertical, rad or deg

ω = angle formed by line connecting the leading edge of root chord and trailing edge of tip chord and rocket body (see Fig. 5-28), rad or deg

5-1 INTRODUCTION

This chapter is a treatise on the aerodynamic design of free rockets, and it is slanted primarily toward the engineer in preliminary design. Both general and basic design criteria are considered. Included topics are static stability, aerodynamic drag, external configuration trade-offs, and airload distributions. Static stability in terms of aerodynamic normal force coefficient gradient C_{N_α} and aerodynamic pitching moment coefficient gradient C_{m_α}, and their relationships are discussed.

Free rockets usually are bodies of revolution and maybe comprised of nose sections, cylindrical sections, boattail afterbody sections, flare and split flare afterbody sections, oversized head sections, necked-down centerbody sections, and high fineness ratio body sections. Each of these rocket components is introduced, and, by way of example, several nose-body-tail combinations are discussed. These examples show possible applications and are useful in performing preliminary design. Fin types together with fin-fin and fin-body interference also are presented. Stability margin tailoring is discussed considering static margin variations resulting from aerodynamic design and vehicle center of gravity changes during flight. Factors affecting the static stability of complete configurations and a numerical example using total vehicle aerodynamic data are given.

The possible effects of the rocket exhaust plume on the rocket aerodynamic characteristics, nonlinear aerodynamics, high angles of attack, and certain facets of dynamic stability are introduced.

Drag coefficients for the various rocket body components with typical data trends and drag characteristics of complete configurations are presented and discussed. Also, a numerical calculation for the drag of a complete configuration is presented.

5-2 GENERAL DESIGN CONSIDERATIONS

The usual aerodynamic design goal is to select an external configuration that houses the payload and motor and provides stable flight with minimum drag through the desired altitude-velocity range. The preceding statement is a simplistic statement of design goals. The design process is quite often complicated by the requirement to achieve a specified accuracy in the presence of disturbances. Further, the requirement to be operable with an existing launcher also may place restrictions on the external configuration.

Fig. 5-1* illustrates the body, stability, and wind axes for a free rocket. The x-, y-, z-axes represent the body-centered coordinate system, and the origin is considered to pass through the center of gravity of the rocket. The x_s-, y_s-, z_s- axes represent the stability coordinate system. The stability axes and body axes can be considered identical for a free rocket in undisturbed flight if the effect of gravity is ignored. The wind coordinate system (x_w, y_w, z_w) is determined by the relative wind acting on the vehicle. Relative wind is the vector sum of the vehicle velocity vector and external winds.

For a rocket to possess flight stability, a restoring moment must be produced when the longitudinal axis of the missile is rotated from the flight direction, i.e., when an angle of attack exists. This flight stability is achieved in the case of an aerodynamically stabilized rocket b y selecting the external configuration such that the center of pressure of aerodynamic forces is located farther aft of the rocket nose tip than the center

---

* All figures are located at the end of the chapter.

of gravity. Since the aerodynamic forces are proportional to the angle of attack—the angle between the flight direction of the velocity vector and the longitudinal axis of the rocket-any deviation will produce a moment to restore the axis to its aligned condition. When the center of pressure is aft of the center- of gravity, the rocket is said to be statically stable.

The degree of aerodynamic stability, or the static margin requirement, varies with the desired accuracy of each rocket and its design approach. For example, a rocket designed for minimum dispersion during powered free flight requires a specific tailoring of the static margin over its Mach number regime; a high-accereration rocket that achieves most of its velocity prior to release from the launcher requires only that the stability margin remain within certain upper and lower bounds. The width of this stability band is governed primarily by the requirement to maintain a significant spread between the roll and pitch-yaw frequencies.

Although the static margin is of paramount importance to the accuracy of a free rocket during the powered high-acceleration phase, the aerodynamic drag or axial force is a prime factor affecting the accuracy and performance during the sustain and ballistic flight phases. For an unguided rocket, the angle of attack is nominally zero; therefore, the axial and drag forces are equal. The general goal is to keep the axial force coefficient as low as possible consistent with other design considerations such as body length, weight, and structural rigidity. Reduction of the axial force coefficient is more important generally for indirect fire, artillery-type rockets in which the sustain and ballistic flight times are much greater than that of the boost phase. Axial force reduction in this case can result in either a lighter or a smaller rocket for a specified maximum range or in an increased range for a fixed rocket size and weight. In addition, improved accuracy is achieved by reduced sensitivity to atmospheric variations during the ballistic flight because it is primarily through the aerodynamic axial force that nongravitational accelerations are transmitted to the rocket.

The external configuration of a free rocket can vary significantly, depending on the trade-off among aerodynamic requirements imposed by performance and accuracy considerations, launcher compatibility, and other system requirements. Some generalizations can be made, however, based on past designs. Typically, the external configuration of a rocket consists of a pointed body of revolution, housing a payload and propulsion units, with a stabilizing device attached to the aft section. A circular cross section is preferred because its symmetry about the longitudinal axis makes for simplicity both in manufacturing and in determining aerodynamic coefficients and mass inertia properties. Further, because of its load distribution characteristics, a circular cross section has structural advantages. Stability considerations often require that the rocket body, which is usually aerodynamically unstable, have stabilizing devices added to the aft end to provide the necessary aerodynamic restoring moment for stability. A more complete discussion of stabilizing devices is presented in par. 5-3.2. Thin-profile planar fins, spaced evenly around the circumference of the body, are used in many rocket designs as stabilizing devices. This type of fin usually will produce the maximum stabilizing moment with minimum weight and axial force. When the minimum overall diameter is a dominant design consideration, the ringtail and conical flare become of greater interest. A ringtail will produce, at both subsonic and supersonic velocities, approximately twice the restoring moment of cruciform planar fins with equal total span and chord. The price paid for this increased stability is increased drag. The drag penalty of the ringtail can be offset by a reduction in base drag for specific rockets having a fairly long sustainer burn time. At supersonic speeds the favorable interference between the ringtail and the jet plume serves to reduce the base drag. The conical flare is of interest for restricted-diameter rockets that experience high supersonic velocity. On the basis of projected planform area (for a discussion of planform area see par. 5-3.2.1.1) a conical flare will produce more than twice the normal force of cruciform fins at hypervelocity speeds. However, the axial force of a flare usually greatly exceeds that of fins providing an equal restoring moment.

Volumetrit efficiency in the packaging of the payload must be considered when designing the external configuration. Further, different payloads may require a particular geometric shape, thus placing specific requirements on the external configuration.

For some rockets it is advantageous to locate the main propulsive motor in the forward part of the vehicle. Forward propulsion units usually consist of pairs of horizontally opposed nozzles canted

approximately 5 to 20 deg out from the rocket longitudinal axis and with the thrust axis aligned with the rocket center of gravity. Normally, good design practices suggest locating the fins so that the jet plume does not impinge upon them; this minimizes interference by the plume wake. If the fins are totally immersed in the body-fixed plume, their effectiveness can be substantially changed from the free-stream characteristics. The plume and its effects can be minimized by interdigitating the fins with the exhaust nozzles. The forward jets will also cause an increase in fin pitch damping.

Wind-tunnel tests can be conducted to obtain an indication of jet plume effects on rocket stability. It is important to maintain the ratio of model thrust to wind-tunnel free-stream dynamic pressure and reference area with full-scale conditions. (Free-stream conditions exist if the presence of a model, rocket, aircraft, etc., does not disturb the flow of the stream.) At wind-tunnel velocities below 150 m/s the Reynolds number becomes an important correlation parameter.

It should be clear from the preceding discussion that a "best" aerodynamic configuration does not exist. The multitude of parameters affecting the configuration selection usually results in a choice being based on past design experience rather than on an optimization study. An optimization study can only be made after weighting factors are placed on the many parameters.

To estimate the aerodynamic stability characteristics for complete rocket configurations and to provide design guidance, it is necessary to know the aerodynamic coefficients of each major rocket component and the influence of these components on one another. Aerodynamic characteristics that are expressed in coefficient form are very convenient to use; this form facilitates the scaling of data. Force data can be converted to coefficient form by dividing the force data by the product of the free-stream dynamic pressure q_∞ and a reference area A_{ref}. Likewise, moment data can be converted to coefficient form by dividing the moment data by the product of the free-stream dynamic pressure q_∞ , a reference area A_{ref}, and a reference length ℓ_{ref}.

A word of caution is in order—there is no known recognized standard for reference area and reference length. For example, airplane designers often use the wing planform area—the shape or form of the wing, as seen from above, as in the plan view—as the reference area and the mean aerodynamic chord as the reference length. Rocket designers often use the area of the base of the rocket as the reference area and the diameter of the base as the reference length. Therefore, the designer must ascertain the reference area and the reference length that were used in the development of any data he might use in preliminary design.

The paragraphs that follow will discuss first the stability parameters for various rocket forebody shapes, fins, ringtails, conical flares, and boattails; and then they will discuss how these component aerodynamic coefficients are combined to arrive at values for the complete configuration. Where appropriate, simple analytical or semiempirical equations will be presented along with graphs to make aerodynamic estimates. No effort will be made to provide the theoretical basis or experimental substantiation for the data presented since numerous textbooks and reports exist which discuss these topics in great detail. Finally, a computational table will summarize sources and methods of obtaining design data, and it will provide a format and checklist for design computation.

5-3 STATIC STABILITY

A rocket is considered to be

1. Statically stable if a small disturbance from equilibrium sets up forces that tend to restore the rocket to equilibrium

2. Statically unstable if the forces tend to increase the effects of the disturbance.

Static stability can be illustrated with the use of Fig. 5-2. The point about which a rocket rotates when subjected to a disturbance is the center of gravity (CG). The point at which the resultant aerodynamic forces can be assumed to act is the center of pressure (cp). It should be noted that the cp and/or CG may not be on the longitudinal centerline of the rocket. If this occurs, an axial force component to stability must be considered. Par. 4-2.5 contains a detailed discussion of ballistic phase errors including effects of off-axis cp or CG. Simply stated, a rocket is statically stable when the cp is aft of the CG, both measured from the rocket tip.

The relationship of the forces and moments acting on a rocket can be expressed as

$$\text{(5-1)}$$

where

C_{m_α} = aerodynamic pitching moment coefficient gradient at a = 0, rad^{-1}
C_{N_α} = aerodynamic normal force coefficient gradient at a = 0, rad^{-1}
X_{CG} = axial distance from nose to CC, m or cal
X_{cp} = axial distance from nose to cp, m or cal
d = rocket diameter, m
α = angle of attack, rad or deg.

The degree of static stability is a function of the ratio of $C_{m_\alpha}/C_{N_\alpha}$. The algebraic sign of C_{m_α} indicates whether the rocket is statically stable (negative) or unstable (positive), and the magnitude of C_{m_α} is a measure of the degree of stability.

The stability margin is defined as

$$\frac{C_{m_\alpha}}{C_{N_\alpha}} = \frac{X_{CG} - X_{cp}}{d}, \text{dimensionless.} \qquad \text{(5-2)}$$

When d is the rocket diameter, the stability margin often is defined in calibers (cal). The expression X_{cp}/d is a normalized term that relates the center-of-pressure location and the diameter.

Each component of a rocket has aerodynamic forces and moments acting upon it. The summation of these forces and moments, together with interference effects, makes up the total aerodynamic forces acting upon the rocket. For preliminary estimates of static stability characteristics, the rocket can be divided into components consisting of the nose, body, and stabilizing device. The combination of the aerodynamic force and moment of each of these components with the estimate of the CG location will provide an estimate of static stability. When interference effects are considered, quite good estimates can be obtained. Later portions of this chapter provide additional useful information for making preliminary estimates.

5-3.1 BODIES OF REVOLUTION

This paragraph presents aerodynamic data for bodies of revolution. The bodies to be considered are nose-cylinder combinations, boattail after-bodies, oversized-head configurations, necked-down centerbodies, and high-fineness ratio nose-body, combinations. Each of these configurations is discussed in the subparagraphs that follow. Body shapes other than bodies of resolution can be used in rocket design; however, data for shapes other than bodies of revolution are not readily available in the literature. The use of unconventionally shaped rockets is usually restricted to special-purpose applications. Such special cases are beyond the scope of this handbook: therefore, the discussion here will be limited to symmetrical bodies of revolution.

In summary, the following general observations can be made concerning the aerodynamic characteristics of complete bodies of revolution:

1. The nose section contributes most of the normal force.

2. The nose can be rounded or blunted such that the ratio of the radius of the nose to the maximum radius of the body is 0.15 or less without any significant increase in drag.

3. The drag of a nose-body configuration depends primarily on nose shape and the amount of boattailing or flaring.

4. The presence of the jet greatly influences the base drag, especially during the sustain phase.

5-3.1.1 Nose-Cylinder Configurations

The nose or forebody of an aerodynamically stabilized free rocket usually consists of a pointed cone, an ogive, or a power series curve, followed by a cylindrical body section.

Nose sections vary from sharply pointed cones to relatively blunt hemispherical shapes. However, most rockets have a conical nose or an ogival shape. An ogive is similar to a cone except that the planform is formed by the arc of a circle instead of by a straight line. A tangent ogive is one whose base is tangent to the cylindrical midsection of the body of the rocket. A secant ogive is formed by a circular arc with the radius larger than that of a tangent ogive for a given nose length and with the center of radii aft of the perpendicular to the front face of the cylindrical midsection. Slender-body theory provides a satisfactory means of expressing the stability characteristics of nose-cylinder combinations in terms of the geometric parameters only, as given in Eq. 5-3,

$$\left(\frac{dC_N}{dX} \right)_b = \left(\frac{k_2 - k_1}{A_{ref}} \right) \left(\frac{dA}{dX} \right) \sin(2\alpha) \tag{5-3}$$

which, when integrated from $X = 0$ to $X = \ell_T$, gives

$$(C_{N_\alpha})_b = 2(k_2 - k_1) \left(\frac{A_b}{A_{ref}} \right), \text{rad}^{-1} \tag{5-4}$$

where

$\left(\dfrac{dC_N}{dX} \right)_b$ = derivative of C_N with respect to X for the body

$(C_{N_\alpha})_b$ = body aerodynamic normal force gradient at α = 0, rad^{-1} or deg^{-1}

$k_2 - k_1$ = Munk's apparent mass factor, dimensionless

ℓ_T = total rocket length (nose, midsection, and afterbody), m

dA = incremental cross-sectional area, m^2

dX = incremental axial distance, m

A_b = body base area, m^2

A_{ref} = reference area, m^2.

The factor $(k_2 - k_1)$ is the apparent mass factor as derived by Munk (Ref. 1). The values for ellipsoids of revolution presented in Fig. 5-3 represent a reasonable approximation for any axisymmetrical body of comparable total fineness ratio. The factor $(k_2 - k_1)$ usually is applied on the basis of total body length-to-diameter ratio. The center of pressure maybe assumed to act at the centroid of the nose projected area for the free-stream condition $M_\infty < 1$.

The fundamental assumptions of the theory are that all second-order partial derivatives of velocity can be neglected and that velocity perturbations along the body axis are small compared to the transverse values. The solution implies that adding cylinder length to the nose has no effect and that there is no compressibility effect due to varying the Mach number. However, experimental data and more refined theoretical solutions, too complex to discuss here, show these effects to be significant. The reader is referred to Refs. 2, 3, and 4 for further details of these solutions. During recent years, considerable experimental data have become available, and, wherever possible, it is strongly recommended that experimental data be used rather than theoretical solutions.

At supersonic Mach numbers, the normal force coefficient gradient and center-of-pressure estimates should be obtained, respectively, from Figs. 5-4 and 5-5 for tangent ogive-cylinder bodies and from Figs. 5-6 and 5-7 for cone-cylinder bodies. The curves were extracted from Ref. 5 and were constructed from

empirical data covering a Mach number range from $1.4 \leq M_\infty \leq 7.0$ and a nose-fineness ratio range from 3.0 $\leq \ell_n/d \leq 7.0$. Stated accuracies are ±10% for normal force coefficient and 0.5 cal for center of pressure. In these and related figures ℓ_n indicates nose length and ℓ_{ab} indicates after-body length.

An extensive experimental study of the effects of particular nose shapes and cylindrical lengths is prescmted in Ref. 6. Aerodynamic-stability parameters are determined at Mach numbers from $0.8 \leq M_\infty \leq$ 4..5 for tangent-ogive, conical, and power-series noses- all with a nose-fineness ratio $\ell_n/d = 4$ cal, combined with cylindrical after-body lengths of from $4 \leq \ell_{ab} \leq 11$ cal. The effect of changing the nose-fineness ratio from three to five for conical and tangent-ogive shapes was determined for a cylindrical afterbody length ℓ_{ab} of 6 cal. Since the over-all study covers body configurations of general interest to free rocket design, the pertinent results are presented in Figs. 5-8 through 5-13.

The data presented in Figs. 5-14, 5-15, and .5-16 from Ref. 7 are examples of the variety of data available. Fig. 5-14 presents normal force coefficient gradient and center-of-pressure data for 2-cal tangent ogive noses followed by an 8-cal and a 10-cal cylindrical afterbody. Fig. 5-1.5 presents the same type data for a 3-cal tangent ogive nose with 10-cal cylindrical afterbody. The significant difference between the 2-cal and 3-cal nose cylinder configurations is the more rearward center of pressure.

The effects of nose bluntness for three examples are illustrated in Fig. 5-16 (Ref. 7). Refs. 8,9, and 10 are also excellent data sources for nose bluntness effects.

The trend in free rocket design appears to be toward higher fineness ratios. Much data exist for rockets with total length-to-diameter ratios $12 \leq \ell_T/d \leq 14$, but the data are limited for higher fineness ratios. Fig.Text 5-26, par. 5-3.1.6, shows normal force coefficient gradient and center of pressure data for three bodies with fineness ratios of 18.45, 19.4, and 24.

There are also cases where a "spike-type" nose is required. Fig. 5-17 presents a normal force coefficient gradient and center-of-pressure data as a function of Mach number for the rocket in the sketch in Fig. .5-17.

5-3.1.2 Boattail Afterbody Sections

The primary purposes for using a boattail are to tailor the stability margin for minimum change throughout the Mach number range and to reduce base drag. A rocket can be boattailed if the rocket propulsive nozzle is smaller in diameter than the body cylinder diameter. For a positive angle of attack the local normal loading over a boattail is negative, which reduces the total normal force coefficient and shifts the center of pressure forward. Therefore, care must be exercised in trading off the advantages of reduced drag and the possible disadvantages of the forward movement of the center of pressure. In practice, the length of a boattail is generally limited to one or two calibers because of the geometry of the rocket motor and nozzle.

Slender-body theory predictions should be used for the subsonic Mach number range since results of systematic empirical investigations are not available. The slender-body theory predicts the aerodynamic normal force coefficient gradien C_{N_α} to be

$$C_{N_\alpha} = \frac{-2A_{bt}}{A_{ref}} \left[1 - \left(\frac{d_{bt}}{d} \right)^2 \right], \text{rad}^{-1} \tag{5-5}$$

where

A_{bt} = cross-sectional area of boattail, m²
d_{bt} = boattail diameter, m.

The center of pressure for the boattail normal force can be assumed to be located about 0.6 of the boattail length downstream of the rocket body-boattail juncture.

Slender-body theory states that body force characteristics are not functions of Mach number. Therefore, for the transonic regime, it is recommended that and differences between subsonic values and supersonic values be faired out smoothly in the transonic range. Boattail component data at transonic and supersonic Mach numbers can be obtained from Figs. 5-18 and 5-19 (Ref. 11).

It is recommended that boattails be designed with angles of less than 8 deg to avoid the effects of flow separation on the boattail.

5-3.1.3 Oversized-Head Configurations

Missile payload volume, interchangeable warhead types, and other design considerations may require that the nose section have a larger diameter than that of the cylindrical afterbody or stages. Slender-body theory can be used to estimate normal force and center of pressure through the subsonic-transonic Mach number regime. For the supersonic regime, methods provided in previous paragraphs can be used to calculate the nose-cylinder configuration and boattail characteristics, neglecting the aft-cylinder normal force contribution.

If a tapered boattail is not used to provide a transition section between the nose and cylinder or if the boattail angle exceeds 12 deg, then the normal force and center-of-pressure characteristics should be calculated assuming an effective 12-deg boattail angle.

Ref. 12 contains experimental data for a nose-cylinder configuration in combination with a family of afterbodies. This family includes cylindrical, boattail-cylindrical, and boattail afterbodies which vary both in diameter and length. Each configuration was tested with and without fins. Fig. 5-20 presents an example of normal force coefficient gradients C_{N_α}, axial force coefficients C_A at zero degree angle of attack, and pitching moment coefficient gradients C_{m_α} for three afterbody diameter to head diameter ratios. These data can be used for preliminary design estimates for rockets with oversized heads with afterbody diameter to head diameter ratios of approximately 0.5 to 0.8.

Figs. 5-21 and 5-22 show the effect of boattail length for two afterbody diameter to head diameter ratios, i.e., $d_{ab}/d = 0.55$ and $d_{ab}/d = 0.75$, where d_{ab} is the afterbody maximum diameter.

5-3.1.4 Necked-Down Centerbody

The influence of a necked-down centerbody can perhaps best be illustrated by comparing the aerodynamics of a necked-down body with the same body with the necked-down portion shrouded. Wind-tunnel tests were conducted on a typical rocket with a necked-down centerbody both with and without a shroud over the necked-down portion. The model—actually flight hardware with the motor modified to form an adapter for the force-moment balance system—is show n in Fig. 5-23. Dashed lines indicate the position of the shroud. Fig. 5-24 (Ref. 13) shows variation of the normal force coefficient gradient curve, variation of center of pressure, and variation of axial force both with and without the shroud over the necked-down portion of the rocket body versus Mach number. The base drag has been subtracted from the axial force data shown in Fig. 5-24. Ref. 13 contains data for four necked-down centerbodies with a family of fins both in the folded and unfolded modes. From these and similar data, estimates can be made for the preliminary design of necked-down centerbody rockets.

5-3.1.5 High-Fineness Ratio Body Data

The trend in free rocket design is toward higher total fineness ratio l_T/d bodies. There are distinct disadvantages and advantages to high l_T/d configurations which the rocket designer should consider. The disadvantages are that the higher the l_T/d, the more susceptible the rocket is to the effects of body misalignments, bending is more likely to occur, and the effects of dynamic unbalance are magnified. Further, these effects are additive.

High-fineness ratio l_T/d bodies have the advantages of high longitudinal moment of inertia and longitudinal pitch damping which tend to reduce oscillations during the boost phase. Further, high l_T/d bodies permit the fins to be located forward of the base, thereby alleviating the plume effects on the fins. Also high l_T/d bodies have high ballistic factors during the coast phase, which results in better performance and accuracy.

Data trends for several bodies of revolution with total fineness ratio l_T/d varying from 8 to 24 are presented in Figs. 5-25 and 5-26 (Refs. 6, 14, 15, and 16). The variation of the center of pressure for bodies of different fineness ratios is shown in Fig. 5-25. For example, at a Mach number of 0.8, note that the 8-cal body has a center of pressure of about 3 cal aft of the nose tip, and the 15-cal body has a center of pressure of about 4.6 cal aft of the nose tip. Keep in mind that the nose contributes most of the normal force. Fig. 5-26 presents additional experimental normal force coefficient gradients and center of pressure for three bodies

having total fineness ratios l_T/d of 188.45, 19.4, and 24.0. The data presented in Fig. 5-26 were taken from Refs. 14, 15, and 16.

5-3.2 STABILIZING DEVICES

Stabilizing devices that have been used to some degree include planar fins, wraparound fins (WAF), ringtails, and flares. Each device is discussed in the paragraphs that follow.

The various fin types used to stabilize free rockets include coplanar (two fins in the same plane) in multiples of two with four, six, eight, etc. , arrangements. Also included are WAF both tangentially—and perpendicularly —mounted triform and ringtail (ring) fins. Fig. 5-27 presents fin types in the most common arrangements along with other stabilizing devices. Fig. 5-28 presents nomenclature of typical rocket components.

Thin profile coplanar fins, spaced evenly around the circumference of the rocket body, are generally used for free rockets. This type of fin configuration has the advantage of producing the maximum stabilizing moment with minimum weight and minimum axial force penalties. A further advantage is simplicity of design and thus relatively low cost. When space is limited, designs other than coplanar fins may be more suitable. For example, WAF can be stowed inside a limited diameter launch tube and, upon leaving the tube, open to provide their full projected planform fin area, and. accordingly, produce as much normal force as a cruciform arrangement. Induced roll is a characteristic of WAF and may prove to be a disadvantage. This same phenomenon also occurs with tangentially folded fins. Another disadvantage associated with tangentially folded fins is that the wing-body carryover (see par. 5-3.4.2) is lower than the wing-body carryover of a cruciform fin arrangement.

Tangent fins can be swept back and provide a more rearward center of pressure and thus a longer moment arm. Further, tangentially folded fins, like other folded fins, can have a high aspect ratio that is particularly suitable for use on transonic to low supersonic free rockets.

Projected fin area is the most important factor to be considered in fin design. Triform fin arrangements can provide adequate projected fin area with one less fin than a cruciform design and, therefore, may cost less and weigh less. Also triform fins may be more suitable than cruciform fins on certain rail launchers.

When maximum overall diameter is a dominant design consideration, ringtails can be employed. A ringtail will produce, at both subsonic and supersonic velocities, approximately twice the restoring moment of an unfolded cruciform planar fin arrangement with equal total span and chord. Ringtails, however, are high drag devices. The drag penalty of the ringtail can be offset by a reduction in base drag for specific rockets having a fairly long sustainer burn time. At supersonic speeds the favorable interference between the ringtail and the jet plume serves to reduce the base drag.

Flare-type afterbodies are also useful as stabilizing devices where overall diameter is a design consideration. These devices, which include both solid and split flares, are advantageous for tube launched, high acceleration, high supersonic speed rockets. From the previous discussion it is apparent that the choice of the type of stabilizing device must be based on the amount of stability required, specific application of the rocket, and the various design constraints.

5-3.2.1 Fins

5-3.2.1.1 Coplanar Fins

The determination of stability characteristics for various fin configurations—such as WAF, tangent fins, and multiple fins—generally is based on a cruciform configuration in which two equally loaded coplanar fins are positioned in the horizontal plane. For estimation purposes, changing the roll orientation of the cruciform configuration does not alter its stability characteristics. The coplanar fins-two fins in the same plane-consist of two exposed fins, or fin panels (see Fig. 5-29). A hypothetical wing joined by the two fin panels at their root chord. C_{r_e} determines the geometry and flow parameters affecting normal force and center of pressure. In other words, this hypothetical wing is used to determine governing geometric parameters such as aspect ratio AR, taper ratio A, and sweepback angle A. The fin reference area A_{ref} is also based on this hypothetical wing configuration. (The conversion of fin reference

MIL-HDBK-762(MI)

area to configuration reference area is discussed in par. 5-3.4.1.) Fin stability values based on this hypothetical wing are then obtained from finite wing theory or from isolated wing experimental results. These values are then used for the two coplanar wings in conjunction with the rocket body to determine stabilizing effectiveness (see par. 5-3.4).

Generally, two joined fin panels are used as the reference fin configuration throughout this handbook and in the sample calculation (see par. 5-3.4.5). There are two exceptions, however, in the handbook to using two joined fin panels as the reference fin. The first exception is in par. 5-3.4.3 in which fin-fin interference is discussed. The second exception is in the discussion of roll effectiveness in par. 5-3.2.1.3 (Fig. 5-53) and roll damping in par. 5-4.2 (Fig. 5-103).

Theoretical studies have shown the fin aspect ratio AR to be the dominant geometric factor governing the lifting characteristics of unswept wings or fins. The normal force coefficient gradient varies from $\pi(AR)/2$ for a very low aspect ratio (approaching zero), to 2π for an aspect ratio approaching infinity. For subsonic Mach numbers, a simple correlation based on lifting-line theory (Ref. 17) gives

$$\text{(5-6)}$$

assuming that the section lift coefficient equals 2π and where

AR = fin aspect ratio, dimensionless
$\beta = \sqrt{|M_\infty^2 - 1|}$, dimensionless
M_∞ = free-stream Mach number, dimensionless
$\Lambda_{c/2}$ = fin sweep angle at midchord position, deg.

A variation of Eq. 5-6, plotted in Fig. 5-30, is valid for thin unswept or swept fins of any aspect ratio and for $M_\infty \le 0.6$. However, for low aspect ratio fins that are of primary interest to rocket designers, valid results can be expected up to Mach numbers approaching unity. Subsonically, the fin center of pressure may be assumed at 25% of the mean aerodynamic chord $\bar{c}$ measured rearward from the leading edge. *

The complex nature of transonic flow has precluded reasonably simple mathematical solutions for the flow field about fins, except in the case of thin fins with very low aspect ratios. The linearized slender-wing theory predicts that

$$\text{(5-7)}$$

Using transonic similarity laws and experimental data (Ref. 18), McDevitt obtained the correlations shown in Figs. 5-31 and 5-32 for rectangular planform fins.

Linearized flow theory has been found to be an accurate means of predicting supersonic stability characteristics of thin-profile fins. Thickness effects are important, primarily when the Mach line—a line representing a Mach wave or a Mach cone, the cone-shaped shock wave generated by a sharp, pointed body such as a rocket while flying faster than the speed of sound—emanating from the leading edge of the root chord, lies close to the rocket body. Figs. 5-33 and 5-34 present linear theory normal force gradient curves versus Mach number for rectangular and delta fins, respective y. These curves were developed by deJong (Ref. 19). Ref. 20 presents charts, based on linearized theory, to estimate normal force coefficient gradient and center of pressure for swept leading-edge fins of arbitrary planform. Figs 5-35 and 5-36, respectively, are duplications of the generalized graphs from Ref. 20 for normal force coefficient gradient and center of

---

* Mean aerodynamic cord $\bar{c}$ is the average chord which, when multiplied by the average section moment coefficient, dynamic pressure, and fin area, gives the moment for the entire fin.

pressure of various fin taper ratios λ.. Fig. 5-36 provides reasonable estimates of center of pressure for the subsonic, transonic, and supersonic regions for fin planforms other than rectangular.

The supersonic normal force coefficient gradient and center of pressure of rectangular planform fins as derived by linearized theory (Ref. 21) are presented in Fig. 5-37. These data are valid for $\beta(AR) \geq 0.5$.

A general presentation of linearized supersonic wing theory and aerodynamic estimation charts can be found in Ref. 22; the reader is referred to this work for fin planforms not covered by the graphs in this handbook.

Using three-dimensional linearized theory, Gafarian and Phillips developed normal force and center-of-pressure data for a family of fins or wings (Ref. 23). These data are shown in Figs. 5-38 and 5-39 and apply to fins with no trailing edge sweep and with planforms ranging from rectangular to clipped delta to pure delta. These data are useful in determining the influence of taper ratio.

Pettis (Ref. 24) showed that a straight line fairing lot values of the fin correlation parameter a_t, $0 \leq a_t \leq 0..5$, matched experimental data more closely than linear theory. This is illustrated in Fig. 5-40.

Ref. 25 discusses the results of a wind-tunnel investimation to determine the aerodynamic characteristics of a series of triangular and clipped triangular fins (wings). Fig. .5-41 shows the fin geometry of the models that were tested. Figs. 5-42 and 5-43 show the effects of fin taper ratio λ, Mach number M_∞ and thickness ratio t/c on C_{N_α} and X_{cp}, respectively. Refer to Ref. 25 for further details.

Very small aspect ratio fins, sometimes called strakes, sometimes can be used to achieve adequate static stability for tube-launched or other limited diameter rockets. Increasing the chord length is one method of increasing planform area—the major factor affecting lift at supersonic Mach numbers. However, increasing the fin chord forward results in a forward shift of the fin center of pressure, and there is a maximum chord length beyond which no further stability is gained. When this condition is reached, there may not be adequate stability; thus methods other than increasing chord length-such as multiple fins, WAF, or folding fins—must be employed.

The aerodynamic characteristics of each rocket component must be referenced to the same common reference area as the missile body aerodynamics.

The aerodynamic characteristics of fins must be referenced to the same reference area as the missile body aerodynamics. Relationships for converting fin data, which are referenced to fin planform area, to body reference are covered in par. 5-3.4.1.

5-3.2.1.2 Wraparound Fins and Tangent Fins

Both WAF and tangential fins appear suitable as stabilizing devices for tube-launched free rockets. Both types of fins have approximately the same stabilizing efficiency as coplanar fins with the same planform. Both WAF and tangential fins have induced roll moment variation with Mach number which is affected by a number of parameters. The technology is much more advanced for the WAF due to an intense research program carried on between 1971 and 1976. This research is summarized in Ref. 26.

The stabilizing effectiveness of both WAF and tangential fins is compared with flat (coplanar) fins in Fig. .5-44 taken from Ref. 27. Shown is the center of pressure of the various fins in combination with a typical rocket body $(\ell/d = 9.06)$ Except for the reduction in the transonic peak, the $(X_{cp})_F$ location-the location of the center of pressure of the fin measured downstream of the fin leading at the root chord—for the tangential fins and WAF compared favorably with the coplanar fins.

The normal force coefficient gradient and center of pressure for WAF and flat (coplanar) fins in combination with a 10-cal body are shown in Fig. 5-45 (Ref. 26). There is good agreement among the various fin types throughout the Mach number range.

Both WAF and tangential fins have self--induced roll moments at zero angle of attack. In general, a change in algebraic sign occurs for roll moment at transonic speeds. For the WAF, the self-induced force is toward the center of cut curvature of the WAF (outward from the rocket body) at subsonic speeds and away from the (enter of curvature at supersonic speeds with the crossover occurring at $M_\infty = 1$ (Refs. 28 and 29). For the tangential fins. The subsonic roll force is in the direction of the cuspformed by the fin and the body with a roll reversal for supersonic speeds. There are various changes in geometry which can affect roll moment characteristics. For example, Fig. 5-46, Ref. 27. illustrates the change in the roll moment coefficient C_l when the leading edge sweep angle varies from 0 deg to—5 deg. The effect of sweepback angle

and roll position on C_ℓ for high aspect ratio tangential fins is shown in Fig. 5-47 (Ref. 30). This figure shows the roll moment at two Mach numbers. For more complete information, including data for other Mach numbers, see Refs. 26, 29, and 30.

Fig. 5-48 (Ref. 26) shows the effect of Reynolds number on the roll moment characteristics of WAF. For the step-down body (step-down more realistically simulates flight hardware hinge recesses), there is a double crossover in the direction of self-induced roll forces. If there is a step-up at the body base for the step-down body, the roll moment has the same characteristics as that for WAF with a smooth body. The effect of fin geometry and fin-body gap is shown in Figs. 5-49 and 5-50 (Ref. 26) for $\alpha = 0$ and $t/c_{r_e} = 3\%$—t is the fin thickness, and C_{r_e} is the root chord length.

The effect of WAF closing angle on stabilizing effectiveness is shown in Fig. 5-51 (Ref. 26); the effect of WAF opening angle on rolling moment is shown in Fig. 5-52 (Ref. 26).

5-3.2.1.3 Fin Roll Effectiveness

It is desirable sometimes to impart an aerodynamic roll torque to give the desired roll rate during flight. Roll torque usually is accomplished by differentially deflecting (or canting) opposing fin panels. Shown in Fig. 5-53 is the roll moment-effectiveness coefficient developed from slender-wing theory by Adams and Dugan (Ref. 31). The effectiveness coefficient is the roll moment coefficient C_ℓ, normalized by aspect ratio AR, and is based on wing (fin) planform area. Both the aspect ratio and area include the hypothetical extension of the fins through the body. Shown in Fig. 5-54 is the roll moment coefficient C_ℓ for WAF at various cant angles δ (Ref. 26). The roll moment coefficient for this figure is based on body cross-sectional area.

5-3.2.2 Flare-Type Afterbody

For tube-launched rockets there is often a requirement that the diameter of aerodynamic stabilizing surfaces be not more than the inside diameter of the launching tube during launch phase. Conical nose-cylinder configurations with flare-type afterbodies satisfy this requirement. Further, flare-type afterbodies have some advantages over other stabilizing devices that are suitable for a tube-launched, high acceleration, supersonic rocket. As noted earlier in par. 5-2, solid flares are more effective than fins as stabilizing devices at high supersonic Mach numbers. Also a solid flare is an effective device for inhibiting the onset of the adverse effects of an underexpanded rocket plume of static stability.

The slender-body prediction for the incremental normal force coefficient gradient of a solid-flared afterbody in subsonic flow is

$$(\Delta C_{N\alpha})_{fl} = 2 \left(\frac{A_{fl}}{A_{ref}} \right) \left[1 - \left(\frac{d}{d_{fl}} \right)^2 \right], \text{rad}^{-1} \tag{5-8}$$

and the center of pressure, expressed in terms of flare length, of the normal force increment is

$$\left[\frac{(X_{cp})_{fl}}{\ell_{fl}} \right]_{fl} = \frac{2 - \dfrac{d}{d_{fl}} \left(\dfrac{d}{d_{fl}} + 1 \right)}{3 \left[1 - \left(\dfrac{d}{d_{fl}} \right) \right]^2}, \text{dimensionless} \tag{5-9}$$

where

$(\Delta C_{N\alpha})_{fl}$ = incremental normal force coefficient gradient of a solid-flared afterbody in subsonic flow, rad^{-1}

$[(X_{cp})_{fl}/\ell_{fl}]_{fl}$ = center of pressure of normal force increment of a solid-flared afterbody in subsonic flow, expressed in terms of flare length, dimensionless

A_{fl} = cross-sectional area of base of flare, m^2

$(X_{cp})_{fl}$ = axial distance from cylinder-flare juncture to flare center of pressure, m

ℓ_{fl} = total flare length, m

d_{fl} = flare maximum diameter, m.

The most important geometric parameter is the ratio of forebody cylinder diameter to base diameter. Flare angle and Mach number do not influence the flare normal force within the limitations of the slender-body assumptions. To a limited degree, the experimental data of Ref. 12 verify this trend at transonic Mach numbers and for flare angles of less than 8 deg.

The actual normal force contribution of flared after-bodies is shown by other theories (Refs. 13 and 14) and by experimental results to be influenced by flow conditions for-ward of the flare as well as by flare angle and length. Also, large flare angles—greater than about 10 deg—are known to cause flow separation at the cylinder-frustum juncture, which alters considerably the local normal force loading in this region. Precise estimates of the flared-afterbody stability contribution must consider the complete upstream flow field, including boundary layer characteristics.

For preliminary design estimates, however, the incremental normal force coefficient gradients presented in Figs. 5-55 through 5-59 are considered adequate. These data were computed from linearized potential flow theory and correlate fairly well with the experimental data presented in Ref. 15.

For values of $d_{fl}/d > 1.5$, the location of the center of pressure of the incremental normal force, as predicted by slender-body theory, varies from approximately 50% to 66% of the flare length aft of the flare leading edge. The use of 60% for flare geometric variations within the parameters of the investigations described in Refs. 12 and 15 is, therefore, consistent with the overall experimental accuracy. The combination of data in Figs. 5-55 through 5-59 with cone-cylinder or ogive-cylinder forebody data derived from par. 5-3.1.1 should provide overall normal force coefficient gradients within ±10% and center-of-pressure locations within ±0.5 cal.

The preceding discussion was restricted to solid flares. An alternative to solid flares is a split-petal flare that can be folded into a cylindrical shape while in the launch tube and expanded into a split flare upon leaving the launcher. Split flares can meet launcher restraints and may satisfy aerodynamic requirements as well.

There are two primary geometric differences between the split flares and solid flares, and the effects of these differences are qualitatively easy but quantitatively difficult to predict. First, the split flares have less surface area than solid flares of the same length and diameter. Intuitively, the effect of this difference would be reduced stabilizing effectiveness for the split flare but not a reduction equal to the surface area ratio because of petal-to-petal interference. Second, the split flare probably would not inhibit the onset of afterbody flow separation due to an under-expanded jet plume as well as the geometrically similar solid flare because of the high base pressure feeding up through the splits in the afterbody. However, as a practical matter, the effectiveness of split flares and solid flares should not be compared on a similar external geometric *or* surface area basis. Whereas the solid flare is fixed by the diameter of the launch tube, the opening angle of the split petal is not restricted. Because of the three-dimensional nature of the flow about the split petals, it is difficult to separate the flow on the face of the petals: therefore, they are effective up to ramp angles of 20 to 30 deg, especially at supersonic speeds.

Ref. 16 contains basic longitudinal stability coefficients for a 3-cal tangent ogive nose, a cylindrical afterbody, two solid-flare after-bodies, and foul split-flare afterbodies. These experimental data were obtained for Mach numbers of 0.70, 1.05, 1.2.5, and 1.10. Some effects of rocket plumes are included. The data in Ref. 16 can be used for preliminary design estimates for nose-cylinder configurations that use split petal flares for longitudinal stability.

5-3.3 RINGTAILS

As noted in par. 5-3.2, coplanar fins are used unless them is a special case requiring a ringtail. A convenient way of presenting the comparison between ringtails and planar fins is by the use of the parameter $(a_i)_{rg}$, the ratio of the gradient of the line connecting the equivalent planar fin leading edge tip

and root trailing edge to the Mach line gradient. Fig. 5-60 shows ringtail geometry for nine different configurations. The variation with a_t of ringtail ΔC_{N_α} to planar fin ΔC_{N_α} ratio (which includes fin-body interference) is shown in Fig. 5-61. The minimum values of the normal force ratio occur at approximately the same value of $(a_t)_{rg} = \beta(B - 1)/(2C)$ for the various configurations.

The strong similarity in the variation of normal force ratio with $(a_t)_{rg}$ for such a wide variation in geometry and Mach number suggests that supersonic linearized planar wing theory may be useful in the analysis of ringtail aerodynamics. Generally, the most forward ring position has the lowest value of the ringtail normal force coefficient gradient (C_{N_α}), except for Mach numbers greater than those for which the Mach line does not impinge upon the body surface. This is illustrated in Fig. 5-62.

Fig. 5-63 shows the effects of chord, leading-edge ringtail diameter, and longitudinal position of the ringtail on $(C_{N_\alpha})_{rg}$. It is obvious that additional lift, i.e., a larger $(C_{N_\alpha})_{rg}$, is obtainable with ringtails by increasing either the chord or diameter.

Data for a family of longitudinal strut-supported ringtails (Fig. 5-64) are shown in Fig. 5-65. A more complete treatment of ringtail aerodynamics is contained in Refs. 32 and 33.

5-3.4 STATIC STABILITY OF COMPLETE CONFIGURATIONS

5-3.4.1 General

In the preceding paragraphs consideration has been given to the prediction of force and moment characteristics of individual free rocket components. When the force and moment characteristics of the complete configuration are computed, two major factors must be considered:

1. The data for the individual components maybe summed for the total only if a consistent set of data is used.

2. Certain interference effects must be taken into account when the components are joined to form the complete configuration.

The first factor concerns equatability between the force and moment coefficients—i.e., the force coefficients must be reduced on a common reference area, and the moment coefficients must be reduced on a common reference area and length as well as a common reference point.

To explain further, the aerodynamic normal force coefficient gradient C_{N_α} for small values of α is defined as

$$C_{N_\alpha} = \frac{N}{q_\infty A_{ref}}, \text{ rad}^{-1} \tag{5-10}$$

where

$N = \text{normal force, N}$

$q_\infty = 0.5\rho_\infty v_\infty^2, \text{ free-stream dynamic pressure, Pa}$

$v_\infty = \text{free-stream velocity , m/s.}$

Thus the unit of measure for C_{N_α} simplifies to units per radian for α measured in radians (representing a gradient). C_{N_α} is sometimes presented in units per degree, which can be converted to radian measure by

$$\left(\frac{C_{N_\alpha}}{\text{deg}}\right)\left(57.3 \frac{\text{deg}}{\text{rad}}\right) = C_{N_\alpha}, \text{ rad}^{-1}. \tag{5-11}$$

Either radian or degree units may be used; however, the units for all coefficients must be consistent. To illustrate, assume we have obtained the following data:

1. Body aerodynamic normal force coefficient gradient

$(C_{N_\alpha})_b = 2.0/\text{rad}$ with A_{ref} equal to body cylindrical cross-sectional area A_{cyl}.

2. Fin normal force coefficient gradient

$(C_{N_\alpha})_F = 0.06\backslash\text{deg}$ with A_{ref} equal to exposed fin planform area S_{F_e}.

First, convert $(C_{N\alpha})_F$ to radian measure, i.e.,

Next, select a common reference area—usually the body cylindrical cross-sectional area is selected—as $A_{ref} = A_{cyl}$.
Therefore,

$(C_{N\alpha})_b = 2.0/\text{rad}$ (based on body cylindrical cross-sectional area)

$(C_{N\alpha})_b = 2.0/\text{rad} \left(\dfrac{A_{cyl}}{A_{ref}} \right)$ (based on common area A_{ref})

$(C_{N\alpha})_F = 3.44/\text{rad}$ (based on exposed fin planform area S_{F_e}) since $A_{ref} = A_{cyl}$

$(C_{N\alpha})_F = 3.44 \left(\dfrac{S_{F_e}}{A_{ref}} \right)$ (based on common area A_{ref}).

(Note that for the generally used cruciform fin configuration, S_{F_e}, consists of the two joined exposed fin panels in the horizontal plane.)

The total (sum of body and fin) normal force coefficient gradient $(C_{N\alpha})_T$ is then expressed as

$$(C_{N\alpha})_T = (C_{N\alpha})_b + (C_{N\alpha})_F$$

$$= 2.0 + 3.44 \left(\frac{S_{F_e}}{A_{ref}} \right), \text{ rad}^{-1} \tag{5-12}$$

and the reference area for the total coefficient. $(C_{N\alpha})_T$ is A_{ref}.

The aerodynamic pitching moment coefficient gradient $C_{m\alpha}$ is defined as follows for small values of α:

$$C_{m\alpha} = C_{N\alpha} \left(\frac{X_{cp}}{\ell_{ref}} \right) = \frac{m}{q_\infty A_{ref} \ell_{ref} \alpha}, \text{ rad}^{-1} \tag{5-13}$$

where

$m = $ pitching moment, NŽm
$X_{cp} = $ axial distance from reference point to center of pressure, m
$\alpha = $ angle of attack, rad.

As previously explained, radian or degree measures may be used. A comparison of the expressions for $C_{m\alpha}$ and $C_{N\alpha}$ indicates that, in addition to a common area reference, the moment coefficient must be reduced on a common reference length and a common reference point.

To illustrate, assume we have obtained the following data concerning the configuration shown in the following sketch:
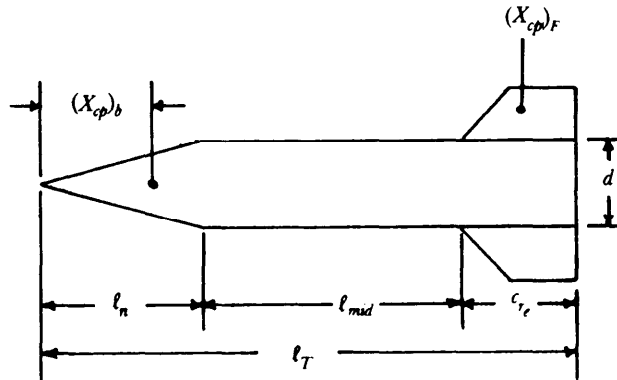
$$(C_{N\alpha})_b = 2.0/\text{rad}, \left(\text{ based on } \frac{\pi d^2}{4} \right)$$

$$(X_{cp})_b = \left(\frac{2}{3} \right) \ell_n, \text{ m}$$

$$(C_{N\alpha})_F = 3.0/\text{rad}, \left(\text{ based on } \frac{\pi d^2}{4} \right)$$

$$\frac{(X_{cp})_F}{c_{r_e}} = 0.5 \text{ (in root chord lengths)}.$$

First, a reference length ℓ_{ref} and a reference point must be selected—usually the body diameter and nose of the body, respectively, are selected. Then, when

$$A_{ref} = \frac{\pi d^2}{4}, \ell_{ref} = d, \text{ and reference point = nose tip,}$$

from Eq. 5-13

$$(C_{m\alpha})_b = 2\left[\left(\frac{2\ell_n}{3} \right) \left(\frac{1}{d} \right) \right], \text{rad}^{-1}. \tag{5-14}$$

When

$$A_{ref} = \frac{\pi d^2}{4}, \ell_{ref} = \quad \text{ and reference point = junction of fin root chord and body surface,}$$

from Eq. 5-13

$$(C_{m\alpha})_F = (C_{N\alpha})_F \left(\frac{X_{cp}}{c_{r_e}} \right)_F, \text{rad}^{-1}. \tag{5-15}$$

However, if the ℓ_{ref} and reference point are changed, i.e., $\ell_{ref} = d$ and reference point = nose tip, then from Eq. 5-15 and sketch

$$(C_{m\alpha})_F = \frac{3.0\left\{ \ell_n + \ell_{mid} + \left[\frac{(X_{cp})_F}{c_{r_e}} \right] c_{r_e} \right\}}{d}, \text{rad}^{-1}. \tag{5-16}$$

Now, since both moment coefficients have a common reference area $A_{ref} = \pi d^2/4$, reference length $\ell_{ref} = d$, and reference point = nose tip, we can write $(C_{m\alpha})_T$ as

$$(C_{m\alpha})_T = (C_{m\alpha})_b + (C_{m\alpha})_F, \text{rad}^{-1} \tag{5-17}$$

or we can write, substituting from Eqs. 5-14 and 5-16,

$$(C_{m\alpha})_T = 2.0 \left(\frac{2}{3} \right) \left(\frac{\ell_n}{d} \right) + 3.0 \left\{ \frac{\ell_n + \ell_{mid} + \left[\frac{(X_{cp})_F}{C_{r_e}} \right] C_{r_e}}{d} \right\}, \text{rad}^{-1}. \tag{5-18}$$

The total center of pressure $(X_{cp})_T$ may be found as

$$(X_{cp})_T = d \left(\frac{C_{m\alpha}}{C_{N\alpha}} \right)_T, \text{m} \tag{5-19}$$

measured rearward from the nose tip or by rearranging Eq. 5-19 the total center of pressure expressed in body diameters (or calibers) is

$$\left(\frac{X_{cp}}{d} \right)_T = \left(\frac{C_{m\alpha}}{C_{N\alpha}} \right)_T, \text{dimensionless} \tag{5-20}$$

measured rearward from the nose tip.

The foregoing has treated the procedures that can be used to assure that component data are referenced to the same base and are thus consistent. It is also necessary when designing a rocket to use a realistic center of gravity, i.e., the point about which a free rocket rotates when subjected to a disturbance. A convenient reference point is the nose tip of a rocket, and the center of gravity an dth ecenter of pressure can be referenced to this point. Further, the normal force of nose cylinder configurations is positive, and since the nose is the major contributor, the center of pressure is forward of the center of gravity. Thus the body has a destabilizing moment that must be offset by the stabilizing effects of the tail. The static margin as discussed in par. 5-3 is expressed (Eq. 5-1) as

$$C_{m\alpha} = \left(\frac{X_{CG} - X_{cp}}{d} \right) C_{N\alpha}, \text{rad}^{-1}.$$

A rocket is statically stable if the algebraic sign of $C_{m\alpha}$ is negative; therefore, the center of pressure must be aft of the center of gravity and the algebraic sign of $C_{N\alpha}$ must be ositive. Fig. 5-2 clearly illustrates this.

The second major factor to be considered concerns the fin-body and fin-fin interference effects which are discussed in pars. 5-3.4.2 and 5-3.4.3, respectively.

5-3.4.2 Fin-Body Interference

When fins are attached to a body of revolution, interference effects increase the normal force over that of isolated fins. This interference effect is particularly important for low aspect ratio fins in which the fin span is approximately equal to the body diameter.

The presence of a cylindrical afterbody induces an increased local angle of attack along the fin span. If the nose effects are neglected, a reasonably accurate prediction of the upwash distribution in the horizontal plane is given by Beskin (Ref. 34) as

$$\frac{\alpha}{\alpha_o} = 1 + \left(\frac{r}{y} \right)^2, \text{dimensionless} \tag{5-21}$$

where

α = angle of attack, rad
α_o = body angle of attack, rad
r = body radius, m
y = lateral distance from body centerline, m.

If we use the approach of Ref. 35 based on slender-body theory, the ratio of the fin normal force gradient $(C_{N_\alpha})_{F(b)}$ in the presence of a body to the fin normal force gradient $(C_{N_\alpha})_F$ of an isolated fin is

$$K_{F(b)} = \frac{(C_{N_\alpha})_{F(b)}}{(C_{N_\alpha})_F}, \text{ dimensionless}$$

$$= \frac{\frac{2}{\pi}}{\left(1 - \frac{d}{b}\right)^2} \left\langle \left(1 + \frac{d^4}{b^4}\right) \left\{ \frac{1}{2} \operatorname{Tan}^{-1}\left[\frac{1}{2}\left(\frac{b}{r} - \frac{d}{b}\right)\right] + \frac{\pi}{4} \right\} \right.$$

$$\left. - \frac{d^2}{b^2}\left[\left(\frac{b}{d} - \frac{d}{b}\right) + 2\operatorname{Tan}^{-1}\left(\frac{d}{b}\right)\right] \right\rangle, \text{ dimensionless} \qquad (5\text{-}22)$$

where
$K_{F(b)}$ = fin-body interference factor, dimensionless
d = body diameter (rocket diameter), m
b = fin span, m (Total span includes body; see insert Fig. 5-69(A)).

The primary parameter is seen to be the ratio of fin span b to body radius r. Although a more precise analysis would show dependence on Mach number, fin planform, and location of the fin on the body, the slender-body result will give adequate preliminary design estimates of the ratio $K_{F(b)}$. Fig. 5-66 presents $K_{F(b)}$ as a function of d/b.

Additional normal force is produced on the cylindrical body adjacent to the fins by carryover to the body of lifting pressure distribution on the fins. Subsonically, the method for determining this carryover by slender-body theory is

$$K_{b(F)} = \frac{(C_{N_\alpha})_{b(F)}}{(C_{N_\alpha})_F} = \left(1 + \frac{d}{b}\right)^2 - K_{F(b)}, \text{ dimensionless} \qquad (5\text{-}23)$$

where
$(C_{N_\alpha})_{b(F)}$ = body normal force gradient in presence of a fin, rad^{-1} or deg^{-1}
$K_{b(F)}$ = body-fin interference factor, dimensionless

for values of $M_\infty \leq 1$. Fig. 5-66 presents $K_{b(F)}$ as a function of d/b.

Contrary to the case for subsonic Mach numbers, fin planform and Mach number are important parameters in determining the supersonic fin carryover normal force to the body. The ratio of carryover normal force to the isolated-fin normal force $K_{b(F)}$ is determined adequately by the method of Ref. 35. This method, based on slender-body theory, integrates the carryover pressure distribution over the region defined by the Mach cones—the cone-shaped shock wave generated by a sharp-pointed body, as at the nose of a high speed aircraft or missile—emanating from the root-chord leading edge and trailing edge as shown in Fig. 5-67 (Ref. 35).

If the fin trailing edge is located flush with the body base, as is the case in many rocket designs, the body area influenced by fin carryover pressures is restricted to that defined by the Mach cone from the root-chord leading edge and the body base. Values of the ratio $K_{b(F)}$ are presented in Fig. 5-68 for configurations with no afterbody and with an afterbody. The curves of Fig. 5-68 represent more refined estimates than those presented in Fig. 5-66.

A second method of estimating total fin-body interference for all Mach numbers and unswept fins ($0 < \beta(AR) < \infty$) was developed by Morikawa (Refs. 36 and 37). This method gives the total interference K_T as

$$K_T = K_{F(b)} + K_{b(F)}, \text{ dimensionless} \qquad (5\text{-}24)$$

only when the trailing edge of the fin is unswept and flush with the base. Fig. 5-69 presents the total interference $K_T = C_{N\alpha}/(C_{N\alpha})_F$ (ratio of fin $C_{N\alpha}$ with interference to basic "isolated" fin), as a function of fin to body geometry, Mach number, and taper ratios from $0 \leq a_t/m \leq 1$. (a_t and m are defined in Fig. 5-69.) This method generally is easier to use when compared to that previously presented and gives preferred data if the configuration being analyzed meets the stated restrictions.

Fig. 5-70 (Ref. 38) presents a convenient way of estimating the normal force curve gradient plus the fin-body interference effects for fin-bed}' combinations with the trailing edge unswept and flush with the rocket base for various values of aspect ratio and exposed fin semispan. The data can be used for estimates from $M_\infty = 0$ up to transonic speeds by using the Prandtl-Glauret compressibility factor which indicates that $C_{N\alpha}$ varies approximately inversely as $\sqrt{|1 - M_\infty^2|}$. Fig. 5-28 presents pertinent geometric information to be used with Figs. 5-70 and 5-71.

Ref. 38 also contains center-of-pressure data for a family of fin-body combinations for various values of aspect ratios and exposed semi span. Fig. 5-71 presents these data for exposed fin taper ratios of 0, 0.25, 0.50, 0.75, and 1.0.

The influence of roll angle ϕ on fin-body interference was investigated by Pettis (Ref. 24). A small decrease in $C_{N\alpha}$, approximately 6%, was observed for the 4-fin configuration rolled 45 deg from the initial position (Fig. 5-72). However, the 8-fin configuration data exhibit essentially no change with roll (Fig. 5-73). It can be assumed that the influence of roll angle on fin-body interference can be neglected for preliminary design purposes.

Fin-body interference for WAF fins is the same as that for flat cruciform fins (Ref. 29). Further, the estimation of the fin-body interference for tangential fins should be treated similarly. Fig. 5-44 presents a comparison of the stabilizing effectiveness of WAF with flat (coplanar) fins and tangential fins with flat (coplanar) fins. The stability margin for tangential and WAF compares favorably with that for coplanar fins except for the reduction in the transonic peak region.

5-3.4.3 Fin-Fin Interference

Cruciform fins—four fins equally spaced around the body circumference-are the most common means of stabilizing free flight rockets. In most cases, this configuration provides the highest ratio of restoring moment to axial force. The data previously presented will permit the prediction of force and moment characteristics of this configuration. However some designs may require more than four fins to obtain the necessary restoring moment. This could be particularly true for a configuration that was span limited, with a center of gravity located farther aft than normal. The information that follows will permit reasonably accurate estimates for certain multifinned configurations or plan forms and also will serve as a guide in estimating the force and moment characteristics of other planforms.

The slender-body theory predicts that, at subsonic speeds, the ratios of the normal force coefficient gradients for six and eight fins (equally spaced around the body circumference) to the gradient for twin fins (four fins, 2 equally loaded) are 1.37 and 1.62, respectively. Thus for speeds from subsonic up to sonic, the following relations are expected to apply:

$$\frac{(C_{N\alpha})_{6\text{-fins}}}{(C_{N\alpha})_{4\text{-fins}}} = 1.37$$

and

$$\frac{(C_{N\alpha})_{8\text{-fins}}}{(C_{N\alpha})_{4\text{-fins}}} = 1.62$$

where $(C_{N\alpha})_{4-\text{fins}}$ can be determined from methods previously presented, and the center of pressure may be assumed at 25% of the mean aerodynamic chord length $\bar{c}$ measured from the fin leading edge.

At supersonic speeds, shock waves from the leading edge can be expected to impinge on adjacent surfaces and cause considerable fin-fin interference. Wind-tunnel tests (Ref. 39) on a series of clipped-delta planforms were conducted, and a correlation parameter I was determined by

$$I = \frac{c_{r_e}}{\beta d \sin(\pi/n)}, \text{ dimensionless} \tag{5-25}$$

where

c_{r_e} = exposed root chord length, m
$\beta = \sqrt{M_\infty^2 - 1}$, dimensionless
d = body diameter, m
n = number of fins, dimensionless.

The parameter I is shown as the abscissa in Fig. 5-74. The ordinate represents the value of $C_{N\alpha}$ based on a dimensionless expression

$$\frac{\bar{\alpha}_{eff} \bar{S}_{eff}}{\alpha S_{F_e}}$$

which is a function of the number of fins n in accordance with the following table of values:

No. of Fins n	$\bar{\alpha}_{eff} \bar{S}_{eff}/(\alpha S_{F_e})$
4	1.63
6	2.43
8	3.24

where

$\bar{\alpha}_{eff}$ = average effective angle of attack for all fins of a tail assembly averaged over a roll cycle $0 \leq \psi \leq \pi/n$, rad or deg
α = angle of attack, rad or deg
$\bar{S}_{eff}$ = average effective area projected in a horizontal plane of all fins in a tail assembly averaged over a roll cycle $0 \leq \psi \leq \pi/n$, m^2
S_{F_e} = exposed fin planform area (two fins joined at root chord) of all fins in a tail assembly, m^2
ψ = roll angle of tail assembly measured from the vertical, rad or deg.

The effective normal force coefficient gradient $\overline{(C_{N\alpha})_T}$ can be obtained by adjusting for the average effective angle of attack $\bar{\alpha}_{eff}$ and the average effective fin area $\bar{S}_{eff}$, i.e.,

$$\overline{(C_{N\alpha})_T} = (C_{N\alpha})_T \left(\frac{A_{ref}}{S_{F_e}}\right)\left(\frac{\alpha}{\bar{\alpha}_{eff}}\right)\left(\frac{S_{F_e}}{\bar{S}_{eff}}\right)$$

$$= (C_{N\alpha})_T \left(\frac{\pi}{4}\right)\left(\frac{d^2}{S_{F_e}}\right)\left(\frac{S_{F_e}}{\bar{\alpha}_{eff} \bar{S}_{eff}}\right), \text{ rad}^{-1}. \tag{5-26}$$

Thus, data for a multifinned configuration may be obtained by computing the parameter I by Eq. 5-25, entering Fig. 5-74 at this value of I, and reading $(C_{N\alpha})_F$ for the appropriate Mach number. Then,

multiplying the value of $(C_{N\alpha})$ by the appropriate value of $\alpha_{eff}S_{eff}/(\alpha S_{ref})$ (dependent on number of fins) yields the total fin contribution based on a reference area A_{ref} equal to the exposed planform area of one fin panel.

Pettis, Ref. 24, modified the fin-fin interference parameter I of Ref. 39. An examination of the geometry in Fig. 5-75, relative to the interference parameter $I = y/\ell$, indicates that I is not a function of span since ℓ is the distance between the adjacent root chords. Pettis took the value of ℓ—labeled ℓ'—as the distance between the adjacent tip chords. The modified fin-fin interference parameter- 1', with the new length ℓ', is defined as

$$I' = \frac{y'}{\ell'} = \frac{c_{r_e}}{\beta(d + b_e)\sin(\pi/n)}, \text{ dimensionless} \qquad (5\text{-}27)$$

where
$y' =$ lateral distance from body surface, m
$\ell' =$ distance between adjacent fin tip chords, m
$b_e =$ exposed fin span, m
$c_{r_e} =$ exposed root chord, m
$n =$ number of fins.

The correlation results are shown in Fig. 5-76 which presents $\beta\overline{(C_{N\alpha})_T}$ versus I'. The $\overline{(C_{N\alpha})_T}$ data were obtained in wind-tunnel tests using a model with a 4-cal tangent ogive nose with an 8-cal cylindrical afterbody and a family of low aspect ratio rectangular fins. Fig. 5-77 depicts the geometric characteristics of the fins. An apparent correlation with span exists which may or may not hold for much larger or smaller span/diameter ratios.

Fig. 5-78 is a faired center of pressure versus interference parameter I for the data presented in Ref. 24. Notice that the center-of-pressure data are presented as the percentage of chord measured from the trailing edge, thus labeled $[(X_{cp})F]_{te}$.

When the value of I is less than unity, the Mach cone emanating from the leading edge of one fin does not impinge on adjacent fins. Therefore, the ratio of the multifin normal force coefficient gradient to the twin-fin gradient (four fins, two equally loaded) is a function of the number of fins only and can be written as

$$\frac{(C_{N\alpha})_{6\text{-fins}}}{(C_{N\alpha})_{4\text{-fins}}} = 1.50, \text{ for } I < 1$$

and

$$\frac{(C_{N\alpha})_{8\text{-fins}}}{(C_{N\alpha})_{4\text{-fins}}} = 2.00, \text{ for } I < 1$$

and the 4-fin data may be computed by methods previously presented.

The preceding discussion concerned 2-, 4-, 6-, or 8-fin bodies. However, as noted in par. 5-3.2, triform fin arrangements may prove useful for some purposes; therefore, fin-fin interference should be considered. If we assume Eq. 5-26 is applicable for triform configurations, interference effects will be less than that for four or more fins. Also, when triform fins are unsymmetrical in the pitch plane, there are induced side forces. These forces are not due to fin-fin interference; they are caused by local flow conditions.

5-3.4.4 Stability Tailoring

The accuracy of unguided or free rocket can be improved by flying with an optimum static stability margin. For most trajectories it is undesirable to have a large stability margin early in the trajectory. A

crosswind, or wind component normal to the desired flight path, results in an effective angle of attack of the rocket with the relative wind and causes a statically stable rocket to "weather vane" or turn into the resultant wind so that it is driven upwind of the target during the boost stage. Fig. 4-5 illustrates this effect. On the other hand, during the ballistic phase, a statically stable rocket subjected to a crosswind will "weather vane" but will drift downwind of the target. This effect is illustrated in Fig. 4-8.

The more stable the rocket, the greater the aerodynamic moment caused by the crosswind and the quicker the rocket aligns with the resultant wind. For a given crosswind, the resultant angle of attack is greater early in flight while the forward velocity is still relatively low. From this point of view, it is desirable to keep the static stability margin small, especially during the subsonic and transonic portions of the flight. Unfortunately, the typical fin-stabilized rocket inherently has a maximum peak in stability margin near $M_\infty = 1$. The ability to reduce or to eliminate this transonic stability increase is highly desirable and is an important requirement in stability margin management.

Most of the transonic stability increase is due to the fins used to stabilize the vehicle. The stability of a fin-stabilized rocket is a function of the fin normal force and center of pressure. Generally, the best planform for accomplishing a reduction in the transonic stability margin is the low aspect ratio rectangular planform. The lower the aspect ratio, the lower is the transonic rise in normal force. Figs. 5-31 and 5-32 clearly illustrate this.

There are occasions in rocket design, however, when the lower aspect ratio cannot be tolerated at the extremes of the flight Mach number regime. For these cases, higher aspect ratio fins may be required than are desirable at transonic speeds. When trade-offs between fin aspect ratio and fin area give unsatisfactory transonic static margin, other methods of reducing the transonic fin lift maybe desirable. One method of doing this is to use more than four multiple fins (Ref. 24). The use of multiple fins, however, may be precluded by the increase of cost and structural complexity, and multiple fins may cause undesirable weight penalties. See par. 5-3.4.3 for a more complete discussion on multiple fins.

Another method of decreasing the fin lift is to allow bleeding between the fin root chord and the body surface through fin-body gaps and thereby to allow equalization of fin-body interaction pressure. Dahlke and Pettis (Ref. 40) conducted a thorough investigation of the effects of fin-body gaps on the normal force effectiveness of several fin planforms at Mach numbers of $0.8 \leq M_\infty \leq 5.0$. It was determined that fin effectiveness is reduced significantly by adding streamwise gaps between the fin and body of rocket configurations. The largest reduction of fin effectiveness occurs at the transonic and low supersonic Mach numbers, which tend to flatten the (C_{N_α}) versus Mach number variation. Further, small gaps cause a large reduction in fin effectiveness; larger gaps cause a lower rate of change in effectiveness reduction. Fig. 5-79 (Ref. 41) illustrates these effects for one fin-body configuration with four different fin-body gaps. Additional fin effectiveness data for other rectangular and delta planforms are contained in Refs. 40 and 41.

The static margin for rockets with high thrust/high acceleration may be dominated by the effects of rocket-motor-plume-induced boundary layer separation. This phenomenon may well be one of the most useful tools for stability tailoring. Fig. 5-80 (Ref. 42) shows stability characteristics for a typical rocket with and without plume effects. Note that the center of pressure moves forward by more than four calibers during the all-important power-on transonic regime; however, X_{cp}/d is fairly constant in the transonic region of coast. An in-depth discussion of plume effects on aerodynamic characteristics is presented in par. 5-3.5.2.

Forward surfaces—canards, fixed wings, or fins—located just downstream of the center of gravity can be used as downwash generators and thus can be an effective device in tailoring stability. Fig. 5-81 (Ref. 43) shows the variation of center of pressure versus Mach number and illustrates that the transonic peak can be reduced. Adding downwash generators will increase the total normal force, which may be undesirable. However, if the pitching moment can be reduced during the critical transonic portion of flight, then downwash generators may be acceptable devices to use for stability tailoring.

Other devices useful in static margin management are end-plated fins and double-delta planforms (see Fig. 5-27).

5-3.4.5 Sample Calculation Sheet

Since the trend for artillery-type free rockets is toward high total fineness ratio ℓ_T/d configurations, a 24-cal body having a 3-cal nose was selected for the sample calculation. A review of several preliminary design studies at the US Army Missile Command indicated that realistic values of center of gravity would be as follows:

    1. Initial CG = 11.33d aft of nose
    2. Burnout CG = 9.58d aft of nose.

Low aspect ratio cruciform (4) fins of rectangular planform with trailing edges flush with the base were selected to conform with stability tailoring criteria (par. 5-3.4.4). Additional fin area maybe required if the stability tailoring devices mentioned in par. .5-3.4.4 are used. At end of boost (burnout) free-stream Mach number of 3.5 was assumed. It was also assumed that boost acceleration was not high enough to result in rocket plume effects on stability (see par. 5-3.5).

As a general rule, experimental data should be used for body-alone aerodynamic coefficients where available. Analytical methods are not available for the transonic range and do not appear to account correctly for afterbody length at all Mach numbers. For the sample calculation, transonic body data were obtained from Fig. 5-26. Supersonic data were guided by data from Fig. 5-15 and extrapolations of the correlations of Figs. 5-4 and 5-5. Estimated coefficients for the sample body are shown in Fig. 5-82. Also shown for comparison are values obtained using the second-order shock expansion method (see Ref. 44).

Since a rectangular fin with trailing edge flush with the body base was selected, information from Refs. 18 and 23 was convenient to use for transonic and supersonic speeds (see Figs. 5-31,5-32,5-38, and 5-39). An interference factor for subsonic and transonic speeds was obtained from Ref. 35 (see Fig. 5-66). Low subsonic speed fin data that include interference effects were obtained from Ref. 38 (see Figs. 5-70(E) and 5-7 l(E). A straight-line fairing was used for the supersonic fin normal force where ≤ 0.5 as suggested in Ref. 24 (see Fig. 5-40).

All configuration dimensions are shown in body diameters (calibers) for convenience. A fin chord of c = 2 cal was selected. Exposed fin span be was varied until a static margin of about one caliber was obtained with an exposed fin semispan of $b_e/2 = 0.32$ cal. Afterbody geometry and design data are presented in Fig. 5-83. The total configuration and final estimates of aerodynamic coefficients are shown in Fig. 5-84. The sample calculations are shown in Tables 5-1 and 5-2.

5-3.5 ROCKET PLUME INTERACTION

The trend toward short burning time, high acceleration free rockets introduces an additional dimension to free rocket design. The resulting highly underexpanded jet plume has an effect on the flow characteristics on the rocket just ahead of the base. In this region either flow separation or a change in the flow field causes a loss in local normal force slope which can adversely affect the Longitudinal stability and cause a serious reduction in fin roll effectiveness.

On the positive side, plume interference acts to reduce the large, stable transonic pitching moment associated with free rocket configurations. This plume effect gives the free rocket designer an opportunity to tailor the static stability margin variation with Mach number in a manner that can significantly reduce wind sensitivity during boost (see discussion in par. 5-3.4.4).

5-3.5.1 Definition of Problem

A better understanding of jet plume effects on rocket stability may be obtained by being aware of the characteristics of base pressure p_b. Base pressure is the pressure present in the separated flow region behind rearward-facing steps, blunt bodies, or the blunt trailing edge of tu'o-dimensions] wings. As the flow passes the base, it contracts and tends to mix with the dead air and, acting like a suction pump, reduces the pressure at the base. When a central jet is added to the rocket base, the base flow is more complicated, and the base pressure is influenced by many factors.

Generally, the effect of the central jet at low levels of thrust is to reduce base pressure below the jet-off value and then to increase p_b as thrust is increased. As the thrust increases to a level where p_b becomes positive, the flow on the body immediately ahead of the base is affected. .

The ratio p_b/p_∞—commonly referred to as base pressure ratio—of base pressure p_b to free-stream static pressure p_∞ is, therefore, a good indicator and predictor of the presence of adverse plume effects on free

MIL-HDBK-762(MI)

TABLE 5-1
FIN SELECTION AND CALCULATION OF SUPERSONIC STABILITY COEFFICIENTS*

① Mach No. M_∞	② β	③ $b_e/2$	④ λ	⑤ a_t	⑥ S_{F_e}/A_{ref}
3.5	3.354	0.40	0.556	0.671	2.037
3.5	3.354	0.35	0.588	0.587	1.783
3.5	3.354	0.30	0.625	0.503	1.528
3.5	3.354	0.32	0.610	0.537	1.630
3.0	2.828	0.32	0.610	0.452	1.630
2.5	2.291	0.32	0.610	0.367	1.630
2.0	1.732	0.32	0.610	0.277	1.630
1.5	1.118	0.32	0.610	0.179	1.630

Column notes (bottom):

① Arbitrarily selected, dimensionless

② $\beta = \sqrt{M_\infty^2 - 1}$, dimensionless

③ trial values and selected values of $b_e/2$, cal

④ $\lambda = \dfrac{d/2}{b_e/2 + d/2}$, $\dfrac{0.5}{③ + 0.5}$ dimensionless

⑤ $a_t = \beta \left(\dfrac{b_e/2}{c_e} \right)$, $\dfrac{②\cdot③}{2.0}$, dimensionless

⑥ S_{F_e}/A_{ref}, dimensionless

*Supporting body and fin data are shown on Fig. 5-83

(cont'd on next page)

MIL-HDBK-762(MI)

TABLE 5-1 (cont'd)

① Mach No. M_∞	⑦ $(C_{N_\alpha})_b$	⑧ $(X_{cp})_b$	⑨ $(C_{m_\alpha})_b$	⑩ K_T
3.5	3.75	3.35	12.56	1.92
3.5	3.75	3.35	12.56	2.04
3.5	3.75	3.35	12.56	2.11
3.5	3.75	3.35	12.56	2.08
3.0	3.65	3.15	11.50	2.19
2.5	3.45	3.10	10.70	2.32
2.0	3.30	3.50	11.55	2.48
1.5	3.15	4.25	13.39	2.57

$(C_{N\alpha})_b$, see Fig. 5-82(A), rad^{-1}

$(X_{cp})_b$, see Fig. 5-82(B), calibers from nose (since $d = 1$ cal)

$(C_{m\alpha})_b = $ ⑦ $\cdot$ ⑧ , rad^{-1} about nose

K_T, see Fig. 5-69(A), dimensionless (Note: $\lambda = d/b_t$, i.e., ④ , and corresponding value of a_t are read from ⑤)

(cont'd on next page)

TABLE 5-1 (cont'd)

① Mach No. M_∞	⑪ $\beta(C_{N_\alpha})_F$	⑫ $(C_{N_\alpha})_F$	⑬ $(X_{cp}/c_{r_e})_F$	⑭ $\dfrac{(X_{cp})_F}{d}$
3.5	2.52	0.751	0.40	22.80
3.5	2.32	0.692	0.38	22.76
3.5	2.00	0.596	0.33	22.66
3.5	2.14	0.638	0.35	22.70
3.0	1.83	0.647	0.29	22.58
2.5	1.50	0.655	0.20	22.40
2.0	1.12	0.647	0.07	22.14
1.5	0.73	0.653	0.00	22.00

$\beta(C_{N_\alpha})_F$, see Fig. 5-38 $(a_t/m = 0)$ and 5-40 based on fin planform area, rad^{-1}

$(C_{N_\alpha})_F = $ ⑪ / ② , rad^{-1}

$(X_{cp}/c_{r_e})_f$, see Fig. 5-39, fraction of c_{r_e} from leading edge, dimensionless

$\dfrac{(X_{cp})_F}{d} = 24 - c_{r_e} + c_{r_e} \cdot$ ⑬
$= 22 + 2 \cdot$ ⑬ , cal from nose

TABLE 5-1 (cont'd)

① Mach No. M_∞	⑮ $(C_{N_\alpha})_F$	⑯ $(C_{N_\alpha})_T$	⑰ $(C_{m_\alpha})_F$	⑱ $(X_{cp})_T$
3.5	2.937	6.687	66.96	11.89
3.5	2.517	6.267	57.29	11.15
3.5	1.922	5.672	43.55	9.89
3.5	2.163	5.913	49.10	10.43
3.0	2.310	5.960	52.16	10.68
2.5	2.477	5.927	55.48	11.17
2.0	2.615	5.915	57.90	11.74
1.5	2.735	5.885	60.17	12.50

$$(C_{N_\alpha})_F = (C_{N_\alpha})_F K_T \left(\frac{S_{F_e}}{A_{ref}} \right) = ⑫ \cdot ⑩ \cdot ⑥ \text{, rad}^{-1} \text{ based on } A_{ref}$$

$$(C_{N_\alpha})_T = ⑮ + ⑦ \text{, rad}^{-1}$$

$$(C_{m_\alpha})_F \text{ about nose} = ⑮ \cdot ⑭ \text{, rad}^{-1}$$

$$(X_{cp})_T \text{ from nose} = \frac{⑰ + ⑨}{⑯} \text{, cal}$$

TABLE 5-2

CALCULATION OF SUBSONIC AND TRANSONIC STABILITY COEFFICIENTS*

① Mach No. M_∞	② $(C_{N_\alpha})_b$	③ $(X_{cp})_b$	④ $(C_{m_\alpha})_b$	⑤ $\dfrac{M_\infty^2 - 1}{(t/c)^{2/3}}$	⑥ $(AR)_e(t/c)^{1/3}$
0.2	3.60	8.05	28.98	−13.03	0.087
0.75	2.96	6.25	18.50	− 5.94	0.087
0.90	3.15	6.55	20.63	− 2.58	0.087
0.95	3.25	6.70	21.78	− 1.32	0.087
1.00	3.28	6.80	22.30	0.00	0.087
1.04	3.27	6.78	22.17	1.11	0.087

| Arbitrarily selected, dimensionless | $(C_{N_\alpha})_b$, see Fig. 5-82(A), rad⁻¹ | $(X_{cp}/d)_b$, see Fig. 5-82(B) (Note: d = 1 cal), cal | $(C_{m_\alpha})_b$ = ② · ③ rad⁻¹ about nose | $\dfrac{M_\infty^2 - 1}{(t/c)^{2/3}}$, t/c = 0.02, dimensionless | $(AR)_e(t/c)^{1/3}$ = (0.32)(0.272), dimensionless |

---

*Supporting body and fin data are shown on Fig. 5-83

TABLE 5-2 (cont'd)

① Mach No. M_∞	⑦ $(C_{N\alpha})_F \left(\dfrac{t}{c}\right)^{1/3}$	⑧ $(C_{N\alpha})_F$	⑨ $d/(b_e + d)$	⑩ K_T	⑪ $2r/b_e$
0.2	—	—	0.61	—	1.56
0.75	0.0026	0.549	0.61	2.58	1.56
0.90	0.0026	0.549	0.61	2.58	1.56
0.95	0.0027	0.570	0.61	2.58	1.56
1.00	0.0028	0.591	0.61	2.58	1.56
1.04	0.0032	0.676	0.61	2.58	1.56

$(C_{N\alpha})_F \left(\dfrac{t}{c}\right)^{1/3}$, see Fig. 5-31, deg^{-1}

$(C_{N\alpha})_F = [57.3 \cdot ⑦]/(t/c)^{1/3}$, rad^{-1}

$d/(b_e + d) = $ body diameter/total span, dimensionless (since $b_e = 0.64d$)

$K_T = K_{(b)F} + K_{(F)b}$, see Fig. 5-66, dimensionless

$2r/b_e = $ body diameter/fin exposed span, dimensionless

(cont'd on next page)

MIL-HDBK-762(MI)

TABLE 5-2 (cont'd)

① Mach No. M_∞	⑫ $(C_{N\alpha})_F$	⑬ $K_T(C_{N\alpha})_F$	⑭ $(C_{N\alpha})_F$	⑮ $(C_{N\alpha})_T$	⑯ X_{cp}/c_{r_e}
0.20	1.63	—	2.657	6.257	0.092
0.75	—	1.416	2.308	5.268	0.039
0.90	—	1.416	2.308	5.458	0.030
0.95	—	1.471	2.398	5.648	0.020
1.00	—	1.525	2.486	5.766	0.026
1.04	—	1.744	2.843	6.113	0.034

$(C_{N\alpha})_F$, see Fig. 5-70(E), (includes interference), rad^{-1}

$K_T(C_{N\alpha})_F = ⑩ \cdot ⑧$, based on fin area, rad^{-1}

$(C_{N\alpha})_F$, based on $A_{ref} = ⑥ \cdot [$ ⑫ or ⑬ $]$, rad^{-1} (Note: ⑥ is from Table 5-1)

$(C_{N\alpha})_T = (C_{N\alpha})_b + (C_{N\alpha})_F = ② + ⑭$, rad^{-1}

x_{cp}/c_{r_e}, see Fig. 5-32 or Fig. 5-71(E), fraction of c_{r_e} from leading edge

MIL-HDBK-762(MI)

TABLE 5-2 (cont'd)

① Mach No. M_∞	⑰ X_{cp}	⑱ $(C_{m_\alpha})_F$	⑲ $(C_{m_\alpha})_T$	⑳ $(X_{cp})_T$
0.2	22.18	58.93	87.91	14.05
0.75	22.08	50.96	69.46	13.19
0.90	22.06	50.91	71.54	13.11
0.95	22.04	52.85	74.63	13.21
1.00	22.05	54.82	77.12	13.37
1.04	22.07	62.75	84.92	13.89

$X_{cp} = 22.0 + 2.0$ ⑯ , cal from nose

$(C_{m_\alpha})_F$ about nose = ⑰ · ⑭ , rad^{-1}

$(C_{m_\alpha})_T$ about nose = ⑱ + ④ , rad^{-1}

$(x_{cp})_T$ from nose = ⑲ / ⑮ , cal

5-36

rockets. The thrust coefficient C_T is a convenient parameter for relating thrust to the flight environment of the free rocket and is also used as a parameter for correlating base pressure characteristics. The thrust coefficient C_T is given by*

$$C_T = \frac{T}{q_\infty A_{ref}}, \text{dimensionless} \qquad\qquad \textbf{(5-28)}$$

where

$\quad\quad T = \text{thrust, N}$
$\quad\quad q_\infty = \text{free-stream dynamic pressure, Pa}$
$\quad\quad A_{ref} = \text{aerodynamic reference area, m}^2.$

(The relationship of p_b/p_∞ with C_T at lower levels of thrust is discussed in detail in par. 5-5.3.2.) Shown in Fig. 5-85 is the variation of p_b/p_∞ with C_T for high thrust levels. Part of this figure is taken from Fig. 5-150 in which at sustain thrust levels, free-stream Mach number M_∞, jet exit half angle θ_j, and nozzle exit to base diameter ratio d_j/d_b, (d_j = nozzle exit (jet) diameter, d_b = rocket base diameter) have little effect on p_b/p_∞ (other than that accounted for by C_T).

For the high thrust data shown in Fig. 5-85, base pressure p_b follows a similar trend but is affected by M_∞ (for example, note where p_b/p_∞ (is near 1.0). With increasing values of thrust coefficient C_T, base pressures for each value of M_∞ break from the general trend and tend to approach a plateau pressure ratio. The plateau pressure ratio is given approximately by

$$p_p/p_\infty \approx 1 + \frac{M_\infty}{2}, \text{dimensionless} \qquad\qquad \textbf{(5-29)}$$

where

$\quad\quad p_p = \text{plateau pressure, Pa.}$

Base pressure at this level is also affected by d_j/d_b, θ_j, and jet-exit Mach number M_j. As will be discussed in par. 5-5.3.2, there is also an effect of afterbody geometry (boattails or flares). These data are from Ref. 45 in which four nozzles having different internal geometry were designed to produce the same plume shape when tested at a particular jet pressure ratio. Base pressures for the four nozzles tend to merge into a single line when plotted as a function of C_T. Examples of the variations of p_b/p_∞ with C_T for the four nozzles for free-stream Mach numbers of 1.0 and 2.0 are shown in Figs. 5-86 and 5-87, respectively.

Typical variations in afterbody surface pressure distributions at zero lift with thrust are shown in Fig. 5-88 for a free-stream Mach number of 0.9 (Ref. 46) and in Fig. 5-89 for a free-stream Mach number of 2.5 (Ref. 47). In general, the plume can affect the rocket afterbody over a large area at subsonic speeds with the affected area reduced considerably as Mach numbers increase to supersonic values. However, the effect on local loading is much greater at the higher Mach numbers. An overall view of jet plume effects is given in Fig. 5-90. Here, the variation with C_T and M_∞ is shown for the static pressure of a single orifice located 0.225 cal ahead of the base (Ref. 48). Although data presented are for a single orifice location, the variation of p/p_∞ with C_T also represents pressure distributions at various Mach numbers. Burt (Ref. 49) has shown that when various plume effect simulators are tested at different longitudinal locations aft of the base, the pressure distributions translate (move along the body) longitudinally with the plume simulator. Therefore, the base of a cylindrical afterbody could be assumed to be located at any position along the abscissa of Fig. 5-90 to obtain an idea of the pressure distribution at a particular C_T and M_∞.. Although no loading distributions are shown, the level of surface pressures at zero angle of attack gives an indication of the severity in changes in local loading due to plume effects. An example of plume effects on the loading distribution on a cylindrical afterbody at small angles of attack is available in Ref. 50.

---

* This definition of C_T is not the same definition of thrust coefficient as used in propulsion systems.

5-3.5.2 Effects on Aerodynamic Characteristics

Generally, there is a slight effect on rocket aerodynamic characteristics when p_b/p_∞ rises above unity. A significant effect occurs when p_b/p_∞ approaches the separation pressure. Zukowski (Ref. 51) has analyzed data for Mach numbers from approximately one to six to obtain the pressure rise across the separation region as a function of Mach number just upstream of the separation point. This correlation is given by

$$p_{sep}/p_\infty = 1 + 0.365 M_1, \text{ dimensionless} \tag{5-30}$$

where

p_{sep} = separation pressure, Pa
M_1 = upstream Mach number, dimensionless.

The variation of separation pressure ratios is shown for the supersonic base pressures in Fig. 5-85.

The free rocket designer should be aware of the possibility of adverse jet plume effects. A check of this possibility can be made by determining the value of C_T for the proposed rocket and using data such as that shown in Figs. 5-85 and 5-89 (Ref. 48). A boattailed afterbody will increase the likelihood of plume effects, whereas a flared afterbody will decrease the possibility. Plume effects can be delayed to higher levels of thrust by reducing the plume diameter near the base. This reduction can be accomplished by reducing d_j/d_b, reducing θ_j, increasing M_j, or by using a nozzle design with nearly uniform flow at the exit.

An example of jet plume effects on rocket stability characteristics is shown in Fig. 5-91 (Ref. 52). As the simulated thrust level is increased, the gradient C_{N_α} at zero angle of attack becomes negative and the configuration has a positive (unstable) slope of C_{m_α}. Since the variation of C_N with angle of attack mirrors the pitching moment characteristics, it is convenient to restrict further discussion to normal force characteristics. In this case various body lengths and moment centers may be considered. The measure of thrust level in Fig. 5-91 is given by the radial thrust coefficient C_{RT}. This parameter is similar to C_T and is used with a normal jet effect simulator (described in par. 5-7). The radial thrust coefficient C_{RT} is given by

$$C_{RT} = \frac{\text{radial thrust}}{q_\infty A_{ref}}, \text{ dimensionless.} \tag{5-31}$$

The normal jet simulator is useful for simulating plume effects with a sting-mounted model. The radial thrust required for the normal jet simulator is on the order of 10% of the thrust required by an axial plume to simulate the same level of plume effect. As indicated in Fig. 5-92 (Ref. 45), this ratio varies with free-stream Mach number and nozzle geometry. A value of 10% is adequate for preliminary design and for planning wind-tunnel tests.

For very high acceleration boost rockets it is unlikely that plume effects on aerodynamics can be avoided. However, by proper location and sizing of the fins, it is possible to stabilize the rocket at supersonic speed and also to reduce or eliminate the large, stable peak in pitching moment which occurs at transonic speeds. In this manner the rocket sensitivity to wind during boost is reduced (see par. 5-3.4.4). Shown in Fig. 5-93 (Ref. 53) are the plume effects on the normal force characteristics of each of the four fin panels at three longitudinal locations on the rocket afterbody. It is apparent that the horizontal fins (C_{N_2} or C_{N_4}) in the aft position (Position 1) have a negative normal force slope at zero angle of attack, whereas the normal force for the horizontal fins in Position 3 (fin trailing edge 0.5 diameter ahead of base) appears to be unaffected by the plume. With fins located in the forward position there will still be a significant effect of the plume on the rocket afterbody (that portion of the body aft of the fins) up to moderately high supersonic Mach numbers.

Also shown in Fig. 5-93 are the normal force characteristics C_{N_1} or C_{N_3} of the vertical fins, which should be representative of the configuration side forces. (Some of the earlier tests of plume effects indicated large side forces.) It appears that side forces are small except for angles of attack of ±3 deg or larger for the aft fins. The side forces near zero angle of attack are probably more a result of airstream and model misalignments

than from plume effects. Side forces and yawing moments due to plume effects do not seem to be present in the most recent investigations in which wind-tunnel to model cross-sectional area ratio is large and in which the plume simulator support system is fairly symmetric.

Shown in Figs. 5-94 and 5-95 (Ref. 54) are plume effects on the normal force gradient of components and the total configuration of a model with the fin trailing edge 1.5 body diameters ahead of the base. The normal force gradient of the body (Fig. 5-94) decreases with increasing plume effects and becomes negative at a moderately low value of C_{RT}. When C_{N_α} of the body is zero, the nose C_{N_α} remains the same as with no plume effect; therefore, the afterbody has an equal negative C_{N_α} with the center of loading near the base. Also shown in Fig. 5-94 are the plume effects on C_{N_α} of the fin-body combination. The plume effects on one fin panel are shown in Fig. 5-95. The forward location of the fin delays the adverse effects of the plume or fin normal force to a much higher value of C_{RT} than is apparent for the body alone and the total configuration (see Fig. 5-95). The plume effects on a fin panel are shown for lower values of M_∞ in Fig. 5-96. At subsonic speeds the loss in fin normal force with increasing C_{RT} is more gradual than the loss at high speeds.

The value of C_{RT} is primarily an inverse function of the free-stream Mach number squared. If it were assumed that rocket thrust and altitude were constant and that a value of C_{RT} of 16 correctly simulated the jet plume effects at a Mach number of unity, the variations of C_{RT} with M_∞ would be as follow:

M_∞	C_{RT}
0.2	640
0.4	256
1.0	16
1.25	10.2
1.5	7.1
1.7	5.5
2	4
2.3	3

Assume this variation of C_{RT} with M_∞ (and refer back to Figs. 5-94 to 5-96); an accelerating rocket would regain most of its fin effectiveness as its velocity increases from $M_\infty = 1.5$ to $M_\infty = 1.7$ (C_{RT} decreases from 7.1 to 5.5). However, the body-alone C_{N_α} (Fig. 5-94) is still affected by the plume at the highest test velocity ($M_\infty = 2.0$).

The split flair is another device that has proven effective in stabilizing free rockets in a very high thrust environment. This device is especially attractive as a stabilizer for short-range, hypervelocity free rockets that are tube launched. The split flare consists of a number of petals that fold to form a cylindrical shape having the same diameter as the rocket motor while the rocket is in the launch tube. The petals deploy to a split-flare configuration upon exit from the launcher. Shown in Fig. 5-97 (Ref. 55) is a comparison of the stability characteristic of split-flare configurations with cylindrical and solid flare afterbodies at various levels of simulated plume effects.

5-3.5.3 Plume Simulation

There are various devices (see Refs, 5-49, 56, and 57) that can be used to simulate jet plume effects on free rocket aerodynamics. The type of simulator to be used in a wind-tunnel test depends upon the type of information required and the stage of development of the vehicle of interest. If the rocket is in an advanced state of development for which flight base pressures have been measured at the Mach number of interest, the simplest simulator that will match the base pressure ratio should suffice. For a preliminary design in which the plume characteristics are in doubt, it is best to use a simulator with air or other cold gases so that the plume effects can be simulated over a large thrust range.

Some of the simpler simulators for use on sting-mounted models are cones, discs, and solid plumes. This type of simulator usually is valid for only one thrust level. However, the disc can be moved longitudinally to simulate a change in p_b/p_∞.

Another type of simulator is a hybrid between a solid plume and an axial jet. In this case an annular-air jet surrounds a partial diameter solid plume. A small change in plume effects can be simulated with a change in jet flow rate.

Some of the early simulations of rocket plume effects were done by NASA (see, for example, Ref. 58). These tests usually simulated high altitudes at high Mach numbers. An annular nozzle surrounding the support sting was used as the plume simulator. A low mass flow air supply was required for these tests because of the low free-stream static pressure.

Most of the plume effect investigations done by the US Army Missile Command used two types of air (or nitrogen) supplied simulators. The first type of plume simulator consisted of a strut-mounted model with air supplied through the strut to an axial nozzle. This type of model usually is tested at zero or small angles of attack to obtain static pressure measurements on the base and afterbody surface. These measurements give the "pressure distributions and an indication of afterbody loading caused by the jet plume. By changing the model afterbody, the effects of nozzle and afterbody geometry may be investigated. By replacing the nozzle afterbody with an attachment device, this type of model also can be used to determine the characteristics of various solid and gaseous sting-mounted plume simulators. (The desired simulator can then be used in tests for a particular plume problem.) An advantage of the axial plume simulator is that a wide range of thrust levels— including levels where the base is aspirated—and various free-stream Mach numbers may be tested without shutting down the wind tunnel. Another advantage is that gas dynamic similarity parameters, e.g., C_T, may be used to relate test condition to rocket flight condition.

Disadvantages of the axial jet plume simulator include the high mass flow requires to simulate large plumes. This rate of flow requires a very high pressure air supply and a support strut of a reasonable size to accommodate the high axial loads and the air supply. There are also flow interference effects emanating from the strut-bed) juncture and other interference effects due to shock and expansion waves reflecting from the model nose or emanating from the strut-tunnel wall juncture.

Most of the plume effects stability characteristics presented in par. 5-3.5.2 were obtained using a normal jet plume simulator with a sting-supported model. This simulator consists of a number of small, normal jets issuing radially from a common air chamber surrounding the support sting. (A more detailed description of the normal jet simulator is given in par. 5-7, "Aerodynamic Testing".) The normal jet simulator tends to match the radial component of momentum of the plume exiting from an axial nozzle. For this reason, only about 10% of the mass flow of the axial plume is required for the same plume effect on aerodynamics. The lower mass flow also permits a larger diameter model. Because the simulator is aft and separated from the model, there is no unintended interference to the flow field or interference with model balances. As with the axial gas plume simulator, a range of thrust levels and Mach numbers maybe tested without shutting down the wind tunnel. Also, a dynamic similarity parameter C_{RT} exists which tends to relate wind-tunnel to flight conditions.

The primary advantage of the normal jet simulator is that the aerodynamic characteristics of complete configurations can be obtained over a large range of simulated thrust levels. For example, Burt and Deep (Ref. 55) used a normal jet simulator to obtain aerodynamic design information on a rocket with a split flare stabilizer. The plume characteristics of the actual rocket were only approximately known, and the effectiveness of the stabilizer in a rocket plume environment was almost totally unknown. However, by testing over a wide range of C_{RT}, they were able to bracket the necessary information. A successful high acceleration, hypervelocity rocket demonstration program was conducted using this design information.

A disadvantage of the normal jet simulator is its inability to simulate the transition from aspirating base flow to where the plume affects the flow on the model surface. Also, if the wind-tunnel test section cross-sectional area is not large enough with respect to the plume size, choking or breaking down of the free-stream flow can occur.

5-3.6 NONLINEAR AERODYNAMICS

Nonlinear aerodynamics occur due to induced high angles of attack at low speeds. Sources of high angles of attack include launching in high crosswinds, launching from a moving vehicle or aircraft, and launching from a low forward speed or hovering helicopter.

The initial slopes of the normal force and pitching moment coefficients versus angle of attack are usually used for free rocket analysis. However, nonlinearity at high angles of attack can occur as illustrated in Fig. 5-98 (Ref. 42). This nonlinearity can prove to be quite important, especially for rockets designed to

have a small static margin. For example, the initial slope of the normal force coefficient curve in Fig. 5-98 is about 0.06 while the slope at an angle of attack of 10 deg is about 0.13. The use of the initial slope rather than the slope at 10 deg would cause a significant error in estimating accuracy. Fig. 5-98 shows normal force coefficient C_N for $M_\infty = 0.4$. The curve for $M_\infty = 0.0$ is included for interpolation purposes. The error that is most affected by nonlinear aerodynamics is the crosswind because it produces a larger angle of attack than either mallaunch or thrust misalignment. Fig. 5-99 (Ref. 42) presents path-angle error as a function of crosswind speed for a specific rocket with nonlinear aerodynamics. This curve was developed using available data for $0 \leq M_\infty \leq 1.2$, which is apparently the most sensitive area of Mach number. Linear coefficients were used for $M_\infty > 1$.

Another significant problem in free rocket design results from that the fact the effects of high thrust cause the basic aerodynamic coefficients of a rocket to be nonlinear along with a significant change in slope with angle attack. Fig. 5-91 (Ref. 52) shows the plume effects on stability coefficients at a free-stream Mach number of 1.0 for an ogive-cylinder body with fins.

5-4 DYNAMIC STABILITY

The motion of a free rocket in flight is determined by rocket launcher interaction at launch, propulsive forces, gravity forces, inertial characteristics of the rocket, and aerodynamic forces. In preliminary design an unguided rocket can be considered as a free body with six degrees of freedom, i.e., translational and rotational motions about the X-, Y-, and Z-inertial-coordinate system axes. The preceding paragraphs have treated the static stability characteristics of free rockets which, if known in sufficient detail, are adequate for preliminary design purposes. However, it is advisable to consider the dynamic aspects of stability also.

In many cases of finned rockets, it has become necessary to spin the rocket during flight to overcome manufacturing asymmetries of the fins and other rocket components. Therefore, it is necessary that the designer consider the aerodynamic loads and coefficients resulting from rocket rotation.

Hence, the damping characteristics, both in roll and in pitch, should be considered. The pitch damping moment is that moment which arises from the pitching velocity and which tends to reduce oscillations in pitch. Likewise, roll damping tends to reduce roll about the longitudinal axis. Further, the magnus moment is the result of the interaction of the transverse force generated by the rocket rotating about its longitudinal axis and the component of the wind acting perpendicularly to that axis. This is discussed in more detail in par. 5-4.3.1.

A complete dynamic stability analysis will not be covered in this handbook. It is recommended that Refs. 59, 60, and 61 be used as a guide to perform dynamic stability analyses of free rockets.

5-4.1 LONGITUDINAL DYNAMIC STABILITY

The dynamic stability, including longitudinal dynamic stability, of guided rockets with canards is thoroughly treated in Ref. 61, which is recommended as a basic resource tool for free rocket design. For purposes of this handbook on free rockets, the component method is appropriate. Both the body and the fins, along with body-fin and fin-body interference, contribute to the total damping. Thus the total pitch damping moment coefficient gradient $C_{m_{\dot{\theta}}}$ can be approximated by a modified version of Chin's (Ref. 66) equation for complete model damping.

$$C_{m_{\dot{\theta}}} \approx - \left\{ 2(C_{N_\alpha})_b \left(\frac{x_b}{d} \right)_b^2 + 2\,(C_{N_\alpha})_F \left[K_{F(b)} + K_{b(F)} \right] \left(\frac{S_{F_e}}{A_{ref}} \right) \left(\frac{x_t}{d} \right)_F^2 \right\} , \; \text{rad}^{-1} \qquad (5\text{-}32)$$

where

      x_b = axial distance from rocket center of gravity to body center of pressure, m

      x_t = axial distance from rocket center of gravity to tail center of pressure, m.

Note that the terms to the right of the equal sign in Eq. 5-32 are static stability terms for the rocket nose-body and the fins modified by interference factors. Thus if the rocket component force gradients are

known, it is relatively easy to calculate the pitch damping characteristics of a free rocket. Fig. 5-100 (Ref. 42) presents a comparison of pitch damping coefficient estimate to experiment.

It was noted in par. .5-2 that it is sometimes advantageous to locate the main propulsion motor in the forward part of the rocket vehicle. This could result in the fin lift being altered by the proximity to the jet plumes. Fig. 5-101 depicts a general free-flight rocket configuration that was used to conduct a study to determine the effect of forward-located rocket nozzles on dynamic pitch damping of a free rocket. The wind-tunnel data consisted of main- and fin-balance data and flow field surveys for both thrusting and nonthrusting condition. Fig. 5-102 shows a comparison of the total pitch damping moment coefficient gradient $C_{m_{\dot\theta}}$ for thrusting and nonthrusting conditions. The figure shows that, for the configuration tested, there is little effect on damping at the lower Mach numbers and an increase in jet plume influence on damping with increasing Mach number.

The component method is one of several available. Another method, developed by Ericson and Reding (Ref. 62), using quasisteady analyses for application to guided missiles may be used to determine the dynamic stability characteristics of free rockets.

Par. 5-3.6 discussed the effects of nonlinear aerodynamics on accuracy estimation. Because pitch damping is a function of C_{N_α} which may not be linear with angle of attack, the use of initial slope of the C_N versus a curve may lead to errors in estimating pitch damping and thus accuracy estimation. Fig. 5-98 clearly illustrates that C_N is nonlinear with angle of attack for the rocket in question. Therefore, errors will exist if the damping coefficients are determined using initial slope only.

5-4.2 ROLL DYNAMICS

Spin, which is often used to reduce effects of thrust malalignment and manufacturing asymmetries, can lead to a condition of pitch-roll resonance. Pitch-roll resonance occurs when the pitch natural frequency is equal to the roll frequency. This condition must be avoided because it results in magnification of the steady state trim yaw-causing nonrepeatable drag during coast and, therefore, results in random errors in range accuracy estimation. Although pitch-roll resonance can yield large trim angles, the probability of a steady-state roll rate exactly equal to that of the pitching rate is quite small. Trim refers to the condition of flight in which the overall aerodynamic moment about the center of glavity is zero so that the rocket will neither increase nor decrease its angle of attack. Trim angle, therefore, is the rocket angle of attack at which trim exists. However, when the frequencies are the same and remain so, roll lock-in occurs. When frequencies diverge, roll break-out occurs. When the roll damping moment coefficient gradient C_{l_p} equals roll moment effectiveness coefficient gradient C_{l_s}, then roll equilibrium exists, i.e., $-C_{l_\delta} = -C_{l_p}$.

Free rockets are often spun during launch, and it is often necessary that they continue "to spin throughout the flight. Roll torque is usually accomplished by differentially deflecting (or canting) oppossing fin panels (see Fig. 5-103 (Ref. 31.)) In Fig. 5- 103, the ordinate is the coefficient of roll-moment effectiveness, normalized by the aspect ratio AR. The abscissa d/b is the body diametet d divided by the fin span b including the fin hypothetical extension through the body. Fig. 5-103 gives the roll moment effectiveness coefficient gradient for cruciform wing-body (fin-body) combinations with both the deflected and undeflected surfaces as well as their algebraic sum, i.e., the total roll-moment effectiveness for the total configuration. Fig. 5-53 also gives the roll moment ellectiveness coefficient gradient for a slender planar fin-body combination with different incidence of the fin surfaces.

It can be seen from Figs. 5-53 and 5-103 that although the roll moment supplied by the loading of the deflected surfaces of the cruciform fin-body combinations is larger than for the planar fin-body combination, the counter roll moment incluced on the unreflected surfaces reduces the total roll moment of the cruciform fin-body combination to approximately 75% of that for the planar fin-body combination.

See par. .5-3.2 for a discussion of self-induced roll characteristics of various fin types.

A spinning or rolling finned body experiences a roll moment due to rolling. Fig. 5-104 presents the coefficient of damping C_{l_p} normalized by the aspect ratio AR as a function of body-diameter maximum-span ratio d/b. The area used in defining both the aspect ratio and the moment coefficient is the area of the horizontal surfaces of the cruciform fin, including its hypothetical extension through the body. Methods for calculation of roll damping can be found in Ref. 31.

5-4.3 SIDE FORCES AND MOMENTS

5-4.3.1 Magnus Forces

A rocket flying at an angle of attack is subjected to a component of the free-stream flow normal to the longitudinal axis of the rocket. Thus a crossflow with a velocity of $v \sin \alpha$ occurs. Further, if the rocket is rotating about its longitudinal axis, a circulation is developed around the rocket, and hence a transverse force is generated that is normal to the plane containing the longitudinal axis and the total velocity vector of the rocket. This effect is known as the magnus effect.

The magnus force is a small force relative to the total normal force. Figs. 5-105 through 5-108 developed by Platou (Ref. 63) show a comparison of magnus force and magnus moment coefficients for both finned and nonfinned rockets. A comparison of Fig. 5-105 with Fig. 5-108 gives an indication of the effects of Mach number and Reynolds number. However, Platou states that the data used to develop these curves are not sufficiently accurate to show variations due to Reynolds number, Mach number, and configuration differences. Even so, Platou did reach the following conclusions:

1. The wake created by the body of a spinning finned-body configuration interferes with the lift force on the rotating fins in a manner that results in a side force.

2. The side force on the fins of a configuration that is not in free spin is opposite in direction to the body magnus force; thus the resulting side force can be in either direction or zero.

3. The side force on the fins of a configuration that is in free spin will be in the same direction as the body magnus force at low angles of attack. At higher angles of attack, the magnus force will decrease toward zero.

4. The body magnus force and the fin side force usually do not have the same centers of pressure. Therefore, a moment exists, which is independent of the center of gravity, and is equal to the lesser of the two forces multiplied by the disturbance between them. This moment, plus the moment due to the unbalanced force, can move the center of pressure outside of the projectile length.

5. The side forces and moments on a slowly spinning finned projectile can be as large as those existing on a rapidly spinning nonfinned projectile.

5-4.3.2 Other Side Forces

Side forces on free rockets are not limited to those resulting from the magnus effect. It was noted in par. 5-3.6 that induced high angles of attack result from high crosswinds. Perhaps one of the worst conditions of launch for a free rocket occurs when launching from a low forward speed or hovering helicopter. The downwash of the helicopter creates high "crosswind" conditions at a critical time in the trajectory of a free rocket.

Additional sources of side forces include the effect of vortex shedding at high angles of attack. Fins that are canted to impart spin to the rocket also create a condition of side force. Fig. 5-109 (from Ref. 64) shows the variation of side force coefficient C_y and yawing moment coefficient C_n as a function of angle of attack for various fin cant angles at three Mach numbers and three Reynolds numbers.

5-5 DRAG COEFFICIENT

The estimation of drag for free rockets can be limited to zero-lift condition since the rocket follows a ballistic path. Thus zero-lift drag is equal to the axial force experienced by the rocket opposite to the direction of flight. The designer of free rockets, however, must recognize that the assumption of zero-lift conditions may be too restrictive for some specific cases. The total zero-lift drag for slender configurations, typical of free rockets, is equal to the sum of the wave drag produced by pressure forces normal to all surfaces except the base, plus the skin-friction drag produced by forces tangential to the surfaces, plus the base drag produced by pressure forces acting normal to the base. There can be wave drag due to lift; however, since zero-lift flight has been assumed here, wave drag due to lift will not be discussed.

The drag of free rockets with power-on can be quite different from the drag with power-off. The development of power-on versus power-off drag coefficients as a function of Mach numbers is required for point mass performance computer simulation. Power-on drag and power-off drag are discussed in some detail in pars. 5-5.3.1 and 5-5.3.2.

The drag coefficient CD is given by

$$C_D = \frac{D}{q_\infty A_{ref}} \text{ , dimensionless}$$ (5-33)

where
$D = $ drag force, N.

The total zero-lift drag is determined by combining wave drag and the skin-friction drag for each component of the rocket. In addition to theoretical techniques, drag can be determined from wind-tunnel tests. The usual procedure is to measure the drag of the entire rocket by the use of strain gage balances. Remember that the drag and the axial force are the same at zero angle of attack. For practical purposes this is also true for small angles of attack.

The base drag, i.e., drag on the base of the rocket, and the nose or forebody drag can be determined as follows. The base pressure is measured using static pressure probes. This base pressure is then algebraically subtracted from the free-stream pressure. The result is then multiplied by the base area to yield the base drag. The base drag is subtracted from the total drag, and the result is the forebody or nose drag. If the rocket is equipped with some type of stabilizing device—such as fins, flare, or ringtail—the drag of these components must be considered. The usual method for measuring component drag is to conduct wind-tunnel tests on the rocket both with and without stabilizing devices. The difference between the body-alone drag and the body -with-stabilizing-device drag is the stabilizing-device drag.

It is also possible to measure the fin or other component drag directly by having a drag balance for the fin or component. Drag on various nose configurations can also be determined by measurement of static pressures along one meridian of the forebody for symmetrical bodies at zero angle of attack. Again, as in determining base drag, the static pressure is subtracted from the free-stream pressure. The result is then multiplied by surface area to yield the pressure or wave drag.

5-5.1 WAVE DRAG

Wave drag is present on the rocket nose, the afterbody, and the fins or other stabilizing surfaces. Since wave drag is produced by pressures normal to the surface, no wave-drag component is present on cylindrical sections at zero angle of attack. If the nose or forebody of a rocket is followed by a midbody section with a diameter that is different from (he nose, then there will be midbody wave drag.

The wave drag of bodies of revolution rises sharply when the rocket approaches the speed of sound. It is usual to define the Mach number at which the drag starts to increase rapidly as the drag divergence or critical Mach number. A fundamental discussion of the transonic aerodynamic characteristics of bodies is beyond the scope of the handbook; however, Chapter XVI, Ref. 65, contains an extensive discussion. For this handbook, suffice it to say that the wave-drag coefficient rises sharply through the transonic region and then decreases with increasing Mach number.

In addition to an increase in drag at transonic Mach numbers, the center of pressure can move appreciably, thus affecting stability. Therefore, care must be exercised to consider this facet of drag during rocket design.

5-5.1.1 Forebody Wave Drag

A general discussion of forebody wave-drag estimating procedures and of general types of rocket components that produce wave drag is presented in the paragraphs that follow.

5-5.1.1.1 Nose

The nose shapes of free rockets are slender except for special applications such as noses that house payloads, e.g., shaped charges. Spherical blunting of the nose with a radius equal 0.1 to 0.2 times the maximum body diameter avoids a sharp point for manufacturing and safety reasons and reduces drag if the nose length is constant.

Nose wave drag is influenced primarily by fineness ratio, now shape, and Mach number. The general trend of nose wave-drag characteristics is shown in Figs. 5-110 and .5-111 (Ref. 66). The fineness ratio fn of each nose shown in Fig. 5-111 is 3, and the total fineness ratio ℓ_T/d of each rocket configuration, 56 through 63, is 12. For most slender nose shapes, the coefficient is zero below a Mach number of about **0.8** and 0.9, rises sharply through the transonic region, and decreases with increasing supersonic Mach number. The coefficient decreases with increasing nose fineness ratio. However, in practical design, nose fineness ratios are limited by rocket total length requirements, weight requirements, and increasing friction drag.

For preliminary design estimates, the family of nose shapes-of-interest for free rockets is bounded by cones and ogives. A secant ogive, formed by a circular arc with twice the radius of a tangent ogive, yields minimum wave drag for low supersonic Mach numbers (Ref. 67); wave-drag characteristics of this nose shape are presented in Fig. 5-112. For higher Mach numbers, a secant ogive with 2.5 to 3 times the radius of a tangent ogive is optimum. However, when optimizing overall configuration nose shape, factors other than drag must be considered, e.g., packaging of payloads.

The transonic wave-drag coefficient of general ogives is presented in Fig. 5-113. Unfortunately, there is no apparent, reliable correlation of the transonic wave drag for cones. It is suggested that estimates be guided by Figs. 5-110 and 5-111 and other experimental data such as Refs. 66 and 68.

Values of supersonic wave drag for cones and general ogives presented in Fig. 5-114 area more detailed extension of the values presented in Figs. 5-110 and 5-111.

The preceding discussion of forebody wave drag and wave-drag prediction procedures included both theoretical and experimental data. It is strongly recommended that, whenever possible, experimental data rather than theoretical data be used for design estimates.

As noted in previous paragraphs, forebodies may have a variety of shapes—cones, ogives, and, in special cases, flat-faced cylinders. The following are the equations for the tangent series, the power series, the parabolic series, and the Haack series (Ref. 69):

   1. Tangent Series:

$$\frac{R_T}{d} = \left(\frac{\ell_n}{d}\right)^2 + \frac{1}{4}, \text{ dimensionless} \tag{5-34}$$

where

   R_T = radius of arc that defines surface of a tangent ogive, m. (See Fig. 5-1 15).

   2. Power Series:

$$r' = x^n, \text{ dimensionless} \tag{5-35}$$

where

   r' = radius/maximum radius ratio, dimensionless
   x = distance from nose/total nose length ℓ_n ratio, dimensionless, for $0 \leq x \leq 1$, where $n = 1$ for a cone and n = 1/2 for a parabola with the vertex at x = O.

   3. Parabolic Series:

$$r' = \frac{2x - K'x^2}{2 - K'}, \text{ dimensionless} \tag{5-36}$$

where

   K' = parabola factor, dimensionless, for $0 \leq x \leq 1$, where $K' = 0$ for a cone, $K' = 1$ for a parabola, $K' = 0.75$ for a 3/4 parabola, and $K' = 0.5$ for a 1/2 parabola.

5-45

4. Haack Series:

$$r' = \frac{1}{\sqrt{\pi}} \sqrt{\phi - \frac{1}{2} \sin(2\phi) + C\sin^3\phi}, \text{ dimensionless, for } 0 \le x \le 1, \qquad \text{(5-37)}$$

where

$\phi = \mathrm{Cos}^{-1}(1 - 2x)$, $C = 0$ for the Von Karman nose shape or the L-D Haack nose, $C = 1/3$ for the L-V Haack nose.

The L-D signifies given length and diameter, and L-V signifies a given length and volume. The letters L-D and L-V refer to boundary conditions for which drag was minimized. Profiles of the power series, parabolic series, the tangent series, and the Von Karman and Haack series for ogive and cones are presented in Fig. 5-116.

A complete discussion on the development of nose shapes is presented in Ref. 69. There is no best nose; rather each of the shapes shown in Fig. 5-116 has its best application from a drag standpoint at certain ranges of Mach numbers. Therefore, the selection of nose shape involves trade-off decisions for a specific application. The least drag configuration is usually selected; however, some missions may require a certain payload volume that dictates a particular shape. The volumetric efficiency of nose shapes varies.

A discussion is presented in par. 5-5 which explains how forebody drag and base drag can be obtained by wind-tunnel testing. Nose skin-friction drag can be similarly obtained. Skin-friction drag can be obtained by one of several methods. Refs. 70 and 71 describe techniques for determining skin-friction drag in wind tunnels. Accordingly, techniques exist for obtaining skin-friction drag for the nose and forebody. Forebody drag consists of both wave drag and skin-friction drag; therefore, by subtracting the skin-friction drag from the total forebody drag, the forebody wave drag can be determined.

In the analysis of nose drag it is sometimes helpful to consider the effects of shape and fineness ratio separately. Fig. 5-110 (Ref. 66) shows the variation at a Mach number of $M_\infty = 1.4$ of the nose wave drag with nose fineness ratio. The lower curve represents near minimum nose pressure drags. At lower values of nose fineness ratio, the minimum drag curve was constructed by fairing through the flat-face value and hemispheric values. Since the calculations and experimental data agree well for noses having a fineness ratio of 3, as shown in Fig. 5-110, confidence may be placed in the values shown. Second-order calculations are also shown in Fig. 5-110 for a parabolic nose. Taylor-Maccoll cone values are also shown for comparison.

Although nose fineness ratio is shown to be a powerful parameter, the effects of nose shape can also be important. This is illustrated in Fig. 5-111. As can be seen from this figure, there is no minimum drag shape for the entire Mach number range, but several do well over the entire range. Refs. 72, 73, and 74 present drag data of many shapes not shown in this handbook. Also, Ref. 66 contains a comprehensive collection of zero-lift drag data on bodies of revolution obtained from free-flight tests.

Fig. 5-117 presents a comparison of the wave drag of cones, tangent ogives, and various secant ogives (Ref. 67).

The installation of fuzes or various types of instrumentation in the nose of free rockets often necessitates the blunting of the nose. Fortunately, as noted earlier, there is little or no drag increase for a slight blunting of an ogival nose. In fact, there is a decrease in drag for Me'plat (the flat nose formed by truncation of the ogival portion of the rocket or projectile} diameters up to 0.2 cal with an optimum of 0.15 cal. The blunting of a conical nose yields similar results, with the optimum again for a Me'plat diameter of 0.15 cal.

Fig. 5-118 presents percentage difference in ΔC_D drag for several configurations or types. The data shown are for noses that have been blunted by opening up the nose contour, maintaining a constant head length. Types 1 and 2 are truncated ogives. Type 5 is a truncated cone followed by a truncated ogive to form the complete nose. The data presented here are from Ref. 75. Additional data on blunted noses are contained in Refs. 76, 77, 78, and 79.

Spike noses afford a solution to some design requirements and are included here as a special case. The curves presented in Fig. .5-119 are faired values obtained from free-flight testing of three special nose configurations. Fig. 5-119(A) gives a description of the models; Fig. 5-119(B) presents the drag coefficient as a function of Mach number (Ref. 66).

5-5.1.1.2 Midbody Wave Drag

Most rocket configurations have a midsection that is cylindrical. This shape is advantageous from the standpoints of drag, ease of manufacturing, and load-carrying capablity. The zero-lift drag of a cylindrical body is caused by viscous forces only (skin friction). There can be wave dragon the midbody if the surface is wavy or if there are protuberances. This phenomenon is discussed in par. 5-5.5, "Protuberances". The wave drag due to sections that decrease in cross-sectional areas with length is presented in par. 5-5.1.2, "Boattail Sections". Likewise, discussions of sections that increase in cross-sectional area with length will be presented in par. 5-5.1.3, "Flare".

5-5.1.2 Boattail Sections

The purpose of the boattail is to decrease the drag of a body that has a squared off base. This squared off base has local pressure on its surface much less than the free-stream pressure and, therefore, produces a large drag force. When the exit diameter of the rocket nozzle is smaller than the body-cylinder diameter, the afterbody maybe tapered to form a boattail to reduce the base area and thus reduce the base drag. However, for a given boattail length, decreasing the base diameter increases the boat tail wave drag. Therefore, an optimum configuration can be strongly influenced by the boattail design. This is clearly illustrated in Fig. 5-120 (Ref. 80) which shows the variation in the total zero-lift drag of a 10.5-cal body having a 3.0-cal tangent-ogive nose, a 6.0-cal cylindrical afterbody, and a 1.5-cal conical boattail with various base diameters. In subsonic flow, decreasing the base diameter continues to decrease the total drag. In transonic and supersonic flows, however, decreasing the base diameter to a ratio of $d_{bt}/d = 0.4$ or lower results in an increase in the total drag. In supersonic flow, as the Mach number increases, the influence of the base drag decreases rapidly and thus allows larger base diameters to achieve a minimum drag boattail design.

Fig. 5-121 presents theoretical subsonic and transonic boattail wave drag for various boattail angles and diameter ratios (Ref. 81). Figs. 5-120 and 5-121 show that subsonic drag is relatively unimportant when compared to transonic and low supersonic drag.

The supersonic wave drag of conical and parabolic boattails is presented in Figs. 5-122 and 5-123, respectively. No analytical method or suitable parametric experimental data exist for the accurate prediction of boattail wave drag at subsonic and transonic speeds. If experimental data for a particular configuration cannot be found, it is suggested that supersonic data be extrapolated to peak value at a Mach number range of $1.0 \leq M_\infty \leq 1.2$, with a sharp reduction to a lower value at subsonic speeds.

The lift of a boattail is in the negative direction, and although the usual boattail is relatively very short and thus decreases the lift very little, it does have a strong destabilizing effect—i.e., the boattail tends to move the overall body center of pressure forward quite markedly. This means that a larger stabilizing device is required to stabilize the rocket. Thus the increase in drag of the larger stabilizing device may negate the saving in drag realized by the boattail.

Accurate determination of boattail drag is rather difficult because of the dependence on the geometry of the fore and aft portions of the body and the real fluid effects. However, for preliminary design analysis, results from the correlation of both theoretical and experimental data should be used when available.

5-5.1.3 Flare

Pars. 5-2 and 5-3.1.3 presented some of the advantages and disadvantages of both solid and split-petal flares. It was noted earlier that on the basis of projected planform area, a conical flare will produce more than twice the normal force of cruciform fins at hypervelocity speeds. However, the axial force of a flare greatly exceeds that of fins providing equal restoring moment. Therefore, the use of flare and split-flare afterbodies as stabilizing devices is restricted to special applications. Examples of these are tube-launched, high acceleration, supersonic rockets, and limited or maximum diameter rockets.

Solid flares are mom effective as aerodynamic stabilizing devices than split flares of the same base diameter and length. However, in some cases a split-petal flare can provide adequate static stability with less drag penalty than a solid flare. Extensive investigation of various stabilizing devices, including flares and split flares, have been carried out at Redstone Arsenal. Refs. 82, 83, 84, and 85 are examples of these. Another good source of information concerning stabilizing devices is the work by Elwell (Ref. 86).

5-5.1.3.1 Conical Frustum

The wave-drag characteristics of conical frustum (flare) and split-flare rocket sections were discussed in pars. .5-2,5 -3, and 5-,5.1.3. Parametric experimental data and several theoretical methods, which agree well with experimental results, are available for estimating flare wave drag. Care should be exercised in the use of experimental data for large flare angles since flow separation at the cylinder-flare juncture may be more pronounced in some tests in which the Reynolds numbers are lower than would be expected in actual flight. The wave-drag coefficient determined experimentally (Ref. 82) for a series of flares is presented in Figs. 5-124(A) through 5-124 (1) as a function of Mach number.

Likewise, Fig. 5-125 presents additional supersonic conical wave-drag coefficient data using the supersonic similarity parameter ß (Ref. 20). The drag coefficient data are presented as a function of flare diameter ratio d/d_{fl}.

Conical-frustum wave drag can be estimated by using cone data (Ref. 87). The pressure coefficient C_{P_c} of a cone in supersonic flow with the shock wave attached is equal to the wave-drag coefficient since the pressure coefficient over the surface of a cone is constant. Although the pressure coefficient over a conical flare is not constant, it can be assumed constant for preliminary design purposes. (The angle of attack should be limited to or less than the cone-frustum half angle, and Mach numbers should range from low supersonic to infinity (Ref. 87). Pressure coefficients as a function of cone semivertex angle for a Mach number range of $1.0.5 \leq M_\infty \leq \infty$ are given in Ref. 88.

By the use of the cone pressure coefficient, the wave-drag coefficient $C_{D_{fl}}$ of a conical flare can be determined from

$$C_{D_{fl}} = C_{P_c} \left[\left(\frac{d_{fl}}{d} \right)^2 - 1 \right], \text{dimensionless} \tag{5-38}$$

where

C_{P_c} = pressure coefficient of cone, dimensionless
d = diameter of base of cone or diameter of cylindrical body forward of flare, m
d_{fl} = flare maximum diameter, m.

See Fig. 5-126 for an interpretation of the terms of Eq. 5-38.

5-5.1.3.2 Split Flare

The split flare appears to be an excellent stabilizing device for hypervelocity, tube-launched rockets. Shown in Fig. 5-127 is a comparison of drag or flared, split flare, and a split flare with a shroud covering the gaps over the forward half. The transonic values are from Refs. 15, 85, and 89 and include the total drag minus the nose drag for each configuration. (The base drag of the cylindrical portion of the base is not included.) It appears that the solid flare has the highest supersonic drag and the split flare has the lowest supersonic drag; this suggests a correlation of device drag based on either surface or effective base area. The peaking of the drag of the two split-flare configurations at a low Mach number suggests the effect of two-dimensional base drag (see par. 5-.5.3.2, especially Fig. 5-152). Supersonic data are shown for clarity and were obtained from Ref. 89.

5-5.1.4 Fin Wave Drag

The wave drag of fins is small compared to the total rocket drag. The drag is influenced strongly by the thickness-to-chord ratio, sectional shape, and sweep angle. Figs. 5-128(A) through 5-128(H) present the

theoretical wave-drag coefficient, based on fin planform area **SF,** at zero-lift for various sectional shapes and planforms. The discontinuities in the curves will not exist in practice, and the values at transonic speeds are not precise. The wave drag for wedge-type sectional shapes not shown in Figs. 5-128(D) through 5-128(H) may be evaluated as follows:

1. In Fig. 5-129 locate the wave-drag coefficient for a symmetrical double-wedge section having the same thickness and planform geometry as the sectional shape-of-interest.

2. Multiply the value so obtained by the factor for the particular shape from Fig. 5-129. This product will be the desired wave-drag coefficient.

The transonic wave-drag coefficient of rectangular and delta planform fins is shown in Figs. 5-130 and 5-131, respectively. The wave drag for other planforms will be between the values on Figs. 5-130 and 5-131 for fins with the same sectional shape, thickness-to-chord ratio, and aspect ratio.

5-5.1.5 Ringtail Wave Drag

The ringtail wave-drag coefficient based on an artillery reference area, e.g., A_{ref}, can be obtained by multiplying the two-dimensional drag coefficient for a specific airfoil section by the product of the ringtail circumference times the chord length (or "rolled out" planform area), i.e.,

$$(C_{D_w})_{rg} = \frac{(\pi d_{rg})(c_{rg}) C_{d_w}}{A_{ref}}, \text{ dimensionless} \tag{5-39}$$

where

$\quad (C_{D_w})_{rg} = $ ringtail wave-drag coefficient, dimensionless

$\quad C_{d_w} = $ 2-dimensional wave-drag coefficient, dimensionless

$\quad d_{rg} = $ ringtail diameter in the plane of leading edge, m

$\quad c_{rg} = $ ringtail projected root chord length, m.

The section wave drag can be obtained by shock expansion or other methods (Refs. 18 and 44). The shock expansion method is sufficiently accurate if the expansion wave from the ring edge does not impinge on the inner surface of the ring after reflection from the body. Experiments have shown that for a Mach number range of $1.5 \leq M_\infty \leq 4.0$ only the smaller diameter rings at their forward positions and at the lower free-stream Mach numbers violate this condition (Ref. 90). However, estimates should still be acceptable for these conditions.

At supersonic speeds, the two-dimensional wave-drag coefficients for particular sectional shapes maybe obtained from Fig. 5-129. At transonic speeds, the two-dimensional drag coefficient for a symmetrical double-wedge profile may be obtained from Fig. 5-132. For other profiles, the transonic drag coefficient should be modified by the factors given in Fig. 5-129.

When ringtails are used as stabilizing surfaces for free rockets, various geometric parameters—including support strut geometry—have an influence on ringtail drag. Shown in Fig. 5-133 is the effect of ringtail internal expansion angle δ_i and ring longitudinal position on ringtail drag (Ref. 90).

5-5.2 FRICTION DRAG

Skin-friction drag depends primarily on Reynolds number, Mach number, and wall temperature. The skin-friction drag coefficient C_{D_f} for a rocket component can be estimated by using

$$C_{D_f} \approx C_f \left(\frac{A_{wet}}{A_{ref}} \right), \text{ dimensionless} \tag{5-40}$$

where

$\quad C_f = $ skin-friction coefficient, dimensionless

$\quad A_{wet} = $ surface wetted area, m^2.

(Note: Surface wetted area is the surface of a rocket which is in contact with the flow medium.)

The friction drag-coefficient must be determined for both the rocket body and stabilizing device.

The skin-friction coefficient C_f for Hat plates, based on wetted areas, can be read directly from Fig. 5-134 for a given Mach number and Reynolds number. If the Mach number, altitude regime, and physical characteristics for the rocket being designnrd are known, it is only necessary to determine the Reynolds number to use Fig. 5-134. Eq. 5-41 can be used to calculate the Reynolds number Re, i.e.,

$$Re = \frac{vL}{\nu}, \text{ dimensionless} \tag{5-41}$$

where

v = velocity, m/s

L = characteristic length, a convenient reference length of a given configuration such as overall length of a rocket, the maximum diameter or radius of a body of revolution, or a chord or a span of a lifting surface, m

ν = kinematic viscosity, m^2/s.

An alternate method for determining Reynolds number involves the use of Fig. 5-135. This figure shows Reynolds number per meter versus Mach number, wth altitude as an independent variable. Since graphical interpolation is required, the accuracy of the determined Reynolds number may be question-able. However, the accuracy is probably satisfactory for preliminary design use.

The Reynolds number having been determined for the given rocket component being designed, it is now possible to read the skin-friction coefficient C_f from Fig. 5-134 and to use Eq. 5-40 to calculate the friction drag coefficient. The flat-plate coefficient should be used for fins and ringtail surfaces. Correlation of experimental data has shown that the skin-friction coefficient for bodies of revolution is about 15% higher than the flat-plate value (Refs. 91 and 92). Therefore, for preliminary design purposes, the values obtained from Fig. 5-134 should be multiplied by 1.15 when the surface is a body of revolution.

The use of Reynolds number based on the length from the rocket nose to the base of the rocket or trailing edge of the fins or ringtails is usually accurate enough for most free rockets. An alternate method uses the local Reynolds number at various longitudinal locations to determine the local skin-friction coefficient. The local skin-friction coefficient, weighted by the local surface area, is then integrated to give the skin-friction coefficient.

5-5.3 BASE DRAG

Base drag is the result of pressure forces due to airflow separation from rearward-facing steps such as body bases and fin trailing edges. The drag is affected by the geometry of the rearward-facing step and by the properties of the airstream approaching the step, including boundary layer conditions. A rocket exhaust complicates the base flow phenomenon by adding a second stream with different properties, boundary layer conditions, and approach geometry. The mixing of and interaction between the air and rocket exhaust streams produce a complex fluid mechanics problem.

General curves and empirical relationships will be presented to allow a rapid estimation of the base drag of a quality suitable for preliminary estimates. No attempt will be made to discuss in detail the effects of various parameters on base drag. Insufficient experimental data exist, throughout the range of parameters to allow use of design graphs.

The base pressure p_b at the rocket base has a variation with rocket thrust similar to the variation shown in Fig. 5-136 (Ref. 93). Of primary interest to the designer of free rockets is the jet-off or burnout base pressure. Also of interest from the drag standpoint are the regions of base bleed and power-on. Base bleed occurs when residual burning continues after rocket burnout, causing a random reduction in base drag and an increase in range during the rocket coast phase. The power-on region (rocket jet plume on) is of interest for the relatively few rocket designs having a sustainer phase. During sustainer burning, it is

possible for base drag to amount to as much as one-half of the total drag. During the boost phase, base pressure is much higher and affects only the small base-annular area surrounding the nozzle exit. The base drag during boost is so small, when compared to thrust, that it has negligible effect on the rocket performance.

As shown in Fig. 5-137 the entire base, including the cavity formed by the nozzle and motor, senses jet-off base pressure. (p_b is assumed to be constant throughout the separated region and downstream to the closure of the wake.) The area used to determine jet-off base drag is the projected area of the base, nozzle, and the head end of the motor case. In the jet-on case, p_b is restricted to the separated region formed by the jet and the external stream and is sensed only by the area of the annulus. This annular area is the area used to determine jet-on base drag.

5-5.3.1 Body-of-Revolution Base Drag, Rocket Jet Plume-Off

The boundary layer approaching the base of the free rocket is generally turbulent. Although wide variations in base pressure occur with Reynolds number for laminar boundary layers, the effect with turbulent boundary layers is small (see Fig. 5-138, Ref. 94). The supersonic base-pressure coefficient C_{pb}—negative of the base drag coefficient, based on the area seen by the base pressure—is well defined from numerous flight and wind-tunnel tests. These data have been correlated by Love in Ref. 95. Shown in Fig. 5-139 (Ref. 96) is the variation of a base-pressure coefficient $C_{p'b}$ with the local Mach number M' just before the base. For a free rocket with a cylindrical afterbody, the local Mach number and local pressure should equal the free-stream values; thus the curve could be used directly by substituting free-stream Mach number M_∞ for M'. The use of local values of both pressure and Mach number in Fig. 5-139 tends to correlate base pressure for bodies with various shapes and total fineness ratios. The solid line in Fig. 5-139 is Love's correlation of experiments (Ref. 95). Additional base-pressure data (with turbulent boundary layer) are presented in Fig. 5-140 which shows the effect of Reynolds number and free-stream Mach number (Ref. 97). (Generally speaking, with M_∞ and model length constant, the Reynolds number will be proportional to p_∞.) The effect of Reynolds number is small for supersonic velocities, and the data agree well with Love's correlation. The large variation in data at subsonic and transonic speeds probably is due to the difficulty of measuring the small pressure difference between the base and free-stream pressures. The variation of base-pressure coefficients at free-stream Mach numbers below about 1.2 is not very well defined. However, a good preliminary estimate can be obtained by averaging the $p_\infty = 1$ atmosphere experimental values in Fig. 5-140.

Base pressures on boattail afterbodies appear to correlate as a function of base-to-cylindrical area ratio for supersonic speeds. Shown in Fig. 5-141 (Ref. 98) is the ratio of cylindrical to boattail base pressure versus area ratio for various conical boattails at free-stream Mach numbers of 2.5, 3.0, and 3.5. The same base pressure ratio is shown for various conical flares in Fig. 5-142 (Ref. 99) at Mach numbers of 1.65 and 2.21. The line faired through the flare data does not have the same gradient as the line representing the boattail data (boattail data from Fig. 5-141). Jet-on data appear to correlate with a single straight line for both flares and boattails (see Fig. 5-148(C)).

Base pressures for boattails and flares do not appear to correlate at subsonic and transonic speeds. Shown in Fig. 5-143 (Ref. 100) is the comparison of base-pressure coefficients of various boattails and flares with a cylindrical afterbody.

The base drag coefficient C_{D_b} is related to base pressure ratio p_b/p_∞ and base-pressure coefficient C_{P_b} in the following manner:

$$C_{D_b} = -C_{P_b} = \left(1 - \frac{p_b}{p_\infty}\right)\left(\frac{1}{0.7\, M_\infty^2}\right), \text{dimensionless} \tag{5-42}$$

where

C_{D_b} = base drag coefficient, dimensionless
C_{P_b} = base-pressure coefficient, dimensionless

5-51

p_b = base pressure, Pa

p_∞ = free-stream static pressure, Pa.

In the preliminary design of free rockets, base drag is obtained from various experimental sources as presented previously in this chapter. If a wind-tunnel test is made of the proposed design by using a sting-mounted model, measured base pressures cannot be used in calculating base drag. The presence of the sting alters the wake flow which has an effect on base pressure. The measured base pressure is used only to determine the drag of the exposed base of the model so that it can be subtracted from the total measured drag to obtain forebody drag. It is standard procedure at some wind-tunnel facilities to use the measured base pressure to determine a base drag coefficient for the total base.

The use of a boattail is effective in reducing the total coast drag of the rocket. Generally, boattailing is accomplished by using the space between the aft end of the motor and the nozzle exit. Therefore, both the length and diameter of the boattail are limited in practice. Since friction drag on the afterbody changes only slightly with changes in geometry, the total pressure drag gives a good indication of the effect of boattails on drag. Shown in Fig. 5-144 are the variation of wave drag C_{D_w}, base drag C_{D_b}, and tots] pressure drag C_{D_T} coefficients with base-diameter-to-cylinder-diameter ratio d_b/d_{cyl}. It appears that little drag reduction can be obtained by reducing d_b/d_{cyl} much below 0.7. Data for the figure were obtained from Ref. 98 which also indicated that conical boattails give lower drag than other boatlail shapes such as ogives.

Another type of configuration used to stabilize rockets launched from a tube is the split-petal stabilizer. The split petals fold to a cylindrical shape when in the launcher and deploy to a flare-like shape upon exit from the tube. The split petal is a very effective aerodynamic stabilizer for high-acceleration rockets.

The measured base pressure for several split-petal configurations is shown in Fig. 5-145 and is compared to Love's (Ref. 95) compilation of cylindrical data. Compared are the 15-deg split petal (shown), an 18-deg split petal, and the 1.5-deg split petal with a shroud filling the gaps for the forward half of the stabilizer. Although these data were obtained with a sting-supported model, they should give an indication of the base-pressure characteristics. Solid flare base pressure was available for only one Mach number, but it appears that there is little change among the various configurations.

5-5.3.2 Body-of-Revolution Base Drag, Rocket Jet Plume-On

A typical example of the base pressure, with the effects of the rocket jet considered, is shown in Fig. 5-146 (Ref. 101). Examination of the figure reveals several important facts concerning free rocket design. During boost, when the jet exit diameter d, usually approaches the base diameter d, base drag is relatively unimportant. The combination of high chamber pressure, high base pressure, and small base-annular area results in a low base drag or even a base thrust. For sustainer operation, the jet-exit-diameter-to-base-diameter ratio d_j/d and jet-pressure-to-free-stream-pressure ratio p_j/p_∞ are usually low—resulting in low values of p_j/p_∞ and therefore, high values of base drag —amounting to as much as 50% to 70% of the total drag. Mass added to the base region as a result of residual burning serves to increase the pressure ratio in the base region, resulting in base pressures considerably higher than would be predicted for the jet-off case. This phenomenon is shown by the peak in the base-pressure ratio p_b/p_∞ at low jet pressure to free stream pressure ratios p_j/p_∞. This decrease in base drag due to residual burning effects may lead to errors in range prediction if not considered.

Jet-on base pressure is affected by many factors. Factors of primary importance include free-stream pressure and free-stream Mach number, afterbody shape, nozzle geometry, and thrust level. The region of interest for free rocket sustained flight is from the minimum base-pressure ratio shown in Fig. 5-146 up to moderate levels of thrust, i.e. , thrust value ratios up to double of triple the value at minimum p_b/p_∞. In this region, Brazzel (Ref. 102) has developed a technique that correlates base-pressure ratio p_b/p_∞ with either jet-momentum flux ratio R_{mf} or thrust coefficient C_T, i.e.,

$$R_{mf} = \frac{(\dot{m}v)_j}{(\dot{m}v)_\infty} = \frac{\gamma_j p_j A_j M_j^2}{\gamma_\infty p_\infty A_{ref} M_\infty^2} \text{ , dimensionless} \tag{5-43}$$

where

$(\dot{m}v)_j$ = jet-momentum flux, N

$(\dot{m}v)_\infty$ = free-stream momentum flux, N

p_j = jet pressure, Pa

A_j = area of jet in nozzle exit plane, m^2

M_j = jet exit Mach number, dimensionless

γ_j = ratio of specific heats of rocket jet, dimensionless

γ_∞ = ratio of specific heats of free-stream flow, dimensionless

and

$$C_T = \frac{T}{q_\infty A_{ref}} = \left(\frac{2A_j}{A_{ref}}\right)\left[\frac{\gamma_j p_j M_j^2 + (p_j - p_\infty)}{\gamma_\infty p_\infty M_\infty^2}\right], \text{ dimensionless.} \qquad (5\text{-}44)$$

where

T = thrust, N.

The jet-momentum flux $(\dot{m}v)_j$ is the predominant term in Eq. 5-45:

$$T = (\dot{m}v)_j + A_j(p_j - p_\infty), \text{ N} \qquad (5\text{-}45)$$

therefore,

$$T \approx (\dot{m}v)_j, \text{ N.}$$

Also the free-stream momentum flux is

$$(\dot{m}v)_\infty = 2q_\infty A_{ref}, \text{ N.} \qquad (5\text{-}46)$$

Therefore—by substituting Eqs. 5-44 and 5-46 into Eq. 5-43 and using the expression for C_T from Eq. 5-46—in aerodynamics terminology, we observe that R_{mf} is nearly proportional to C_T, i.e.,

$$R_{mf} \approx \frac{T}{2q_\infty A_{ref}} \approx \frac{C_T}{2}, \text{ dimensionless.} \qquad (5\text{-}47)$$

For a single jet with a cylindrical afterbody, this technique appears to be successful in correlating all parameters except jet-exit Mach number M_j. (For the higher thrust levels discussed in par. 5-3.5, both jet-diameter-to-base-diameter ratio d_j/d_b and nozzle exit angle θ_j have a significant effect on base pressure.) Shown in Fig. 5-147 is a correlation of base-pressure ratios from Fig. 5-146 with R_{mf}.

The effect of the jet on base pressures at thrust levels (or jet pressure ratios) above where minimum base pressure occurs indicates that a proportionality exists between the base-pressure ratio on the base of a cylindrical afterbody and the base-pressure ratios on noncylindrical afterbodies. Shown in Fig. 5-148, for example, is the comparison of base-pressure characteristics between various boattails and a cylindrical afterbody. It is apparent that the ratio between cylindrical base pressure and boattail base pressure is almost constant with p_j/p_∞ and also that base diameter (or base area) is the governing parameter rather than boattail angle. The same trends are also apparent from the experimental results of Refs. 103, 104, and 105 for boattailed bodies and Ref. 103 for flared bodies. Shown in Fig. 5-118(C) is the variation of the proportionality factor with base-area-to-cylindrical-body-area ratio for various boattails and flares. Other factors that exhibit this proportionality are M_j and nozzle longitudinal position X_j/d. (The effect of X_j/d on incremental base-pressure ratio $\Delta(p_b/p_\infty)$ is shown in Fig. 5-149.) (X_j = distance of nozzle exit from base of rocket.)

By use of the correlation of base-pressure ratio p_b/p_∞ with R_{mf} and the proportionality characteristics of base pressure, an empirical technique was developed for estimating power-on base drag (see Ref. 93). This technique allows the simultaneous consideration of all of the significant parameters affecting single jet base drag, but it is considered beyond the scope of this handbook.

Shown in Fig. .5-150 is a variation of base-pressure ratio with C_T for a cylindrical after-body with an air-supplied nozzle having an exit half angle $\theta_j = 20$ deg and a jet-exit Mach number $M_j = 2.7$. The exit plane of the nozzle is flush with the base. Fig. 5-150, Ref. 106, results from the additional correlation of data at transonic and subsonic speeds (Ref. 45). Examination of Fig. 5-150 will give a good overall picture of the characteristic.s of plume effects on base pressure. The base-pressure ratios of interest for determining sustain phase base drag are also the heavy line beginning at a minimum value for each free-stream Mach number M_∞ and running along this line for about one-half the distance between minimum base-pressure ratio and where base-pressure ratio is equal to unity.

An example of the base-pressure characteristics for $M_\infty = 1$ is denoted by the arrows in Fig. 5-150. Starting at (1), which represents plume-off base pressure, the base-pressure ratio decreases with increasing C_T until a minimum value is reached at (2). The base-pressure ratio then increases along a line common for all free-stream Mach numbers to (3) where the jet plume begins to affect rocket stability (discussed in par. 5-3). With further increase in C_T, base pressure reaches a plateau pressure (1) for each value of free-stream Mach number M_∞. For $M_\infty = 1$, the region of interest is from (2) along the heavy line up to a base-pressure ratio of about 0.7, i.e., $0.4 + (1.0 - 0.4)/2 = 0.7$.

For afterbodies other than a cylinder, base pressure can be corrected by using the proportionality factor pb_{cyl}/pb_{noncyl} of Fig. 5-148(C) where pb_{cyl} is the base pressure of a cylindrical afterbody and pb_{noncyl} is the base pressure of a noncylindrical afterbody. For example, a boattailed afterbody will cause an increase in the base-pressure ratio, and a flare will cause a decrease in the base-pressure ratio.

In a similar manner the effect of longitudinal extension of the nozzle on base pressure can be corrected by using Figs. .5-149 (A) and 5-149(B).

There is also an effect of M, which is not accounted for in Fig. .5-150. The exit Mach number for most free rockets will range between approximately $2.5 \leq M_j \leq 2.9$, so there should only be a small correction from the value of 2.7 in the figure. A decrease in M, will increase the base-pressure ratio, and an increase in M, will decrease the base-pressure ratio. The change should be about 5% for each 0.1 change in M_j.

For boost-level thrusts there is also an effect of nozzle-diameter-to-base-diameter ratio, nozzle-exit angle, and free-stream Mach number (see par. 5-3.5). Other effects not discussed are the difference in the ratio γ of specific heats between the actual rocket and the air nozzle, and the temperature differences for the actual rocket especially when afterburning occurs. Afterburning does not appear to recur on the low to moderate thrust solid propellant rockets at low altitudes where base drag is a problem (see Ref. 107).

The effect of multiple jets on base pressure depends upon the arrangement of the nozzles. Generally, the impingement between two jet plumes results in an increase in base pressure in the affected area. The investigation of Ref. 108 indicates a fairly even distribution of pressure over the base of one-, two-, and four-nozzle configurations. The base-pressure ratios for the single- and six-nozzle configurations are shown in Fig. 5-1.51 compared to the data of Fig. 5-150.

For the determination of the base drag coefficient during rocket motor burning. base pressure acts on the area of the base minus the area of the nozzle exit (See Fig. 5-137). Generally, base pressure is nearly uniform over the base. However, for some multiple nozzle configurations, pressure will vary significantly over the base. In this case a mean value of base pressure must be determined.

The base drag coefficient C_{D_b} is determined as follows:

$$C_{D_b} = \left(1 - \frac{p_b}{p_\infty} \right)\left(\frac{A_b - A_j}{A_{ref}} \right)\left(\frac{1}{0.7\, M_\infty^2} \right), \text{dimensionless} \tag{5-48}$$

where

$\quad A_j =$ area of jet in nozzle exit plane, m^2

$\quad A_b =$ area of body base, m^2.

5-5.3.3 Fin-Base Drag

The boundary layer approaching the base of fins and other stabilizing surfaces is generally turbulent. The effects of profile shape on the base-pressure coefficient at supersonic speeds with a turbulent boundary layer are small. Shown in Fig. 5-152 (Ref. 109) are data representing flight results for a wide range of Reynolds numbers and Mach numbers. The drag-brakes-closed data compare very well with Korst's theory (Ref. 110) which assumes a very thin boundary layer. It is suggested that Korst's theory be used for supersonic fin base-drag. Further insight may be gained by perusing Nash's analysis of two-dimensional turbulent base flow including the effect of the approaching boundary layer (Ref. 111).

At transonic and subsonic speeds, the ratio h/c of trailing-edge fin thickness h to fin chord length c is significant; Fig. 5-153 should be used as a guide for estimating the base pressures.

The fin base-drag coefficient is determined by

$$(C_{D_b})_F = - (C_{p_b})_F \left(\frac{S_{F_b}}{A_{ref}} \right), \text{ dimensionless} \tag{5-49}$$

where

$(C_{D_b})_F$ = fin base-drag coefficient, dimensionless
$(C_{p_b})_F$ = fin base-pressure coefficient, dimensionless
S_{F_b} = base area of all fin panels, m^2.

5-5.4 DRAG CHARACTERISTICS OF COMPLETE CONFIGURATIONS

The drag of free rocket components usually can be added directly to obtain total drag because of the slenderness of the rocket. One exception is the interference effect of fins or other stabilizers on the base drag. The various drag components must be related to the same reference area before they are combined. The drag coefficient C_D is defined (see Eq. 5-33) as

$$C_D = \frac{D}{q_\infty A_{ref}}, \text{ dimensionless}$$

where

q_∞ = free-stream dynamic pressure, a function of rocket velocity and atmospheric pressure, Pa
D = drag force, N.

Skin-friction drag is based on surface (or wetted) area A_{wet} of all of the fins and is a function of Mach number and altitude. Skin-friction drag is related to A_{ref} as follows:

$$C_D(\text{based on } A_{ref})_f = \frac{C_f(A_{wet})}{A_{ref}}, \text{ dimensionless} \tag{5-50}$$

where

C_{D_f} = skin-friction drag coefficient, dimensionless
C_f = skin-friction coefficient, dimensionless.

The body and fin skin-friction drags are calculated separately because of a difference in Reynolds number. As previously mentioned, body skin-friction is multiplied by 1.15 to correct for the flat-plate value. For cruciform fins, for example, it is necessary to use the surface on both sides of all four fin panels in computing wetted area.

Pressure drag (wave and base) coefficients are generally functions of the cross-sectional area of the component affected.

5-55

The body wave-drag coefficient usually is based on body cross-sectional area, so no change in reference area is necessary. The fin wave-drag coefficient normally is based on the exposed planform area of the fins and the fin base-drag coefficient is based on body base area (in case of a cylindrical afterbody, base area equals reference area). The body base-drag coefficient during operation of the jet is effective only on the base annular area (base area less nozzle exit area) (see Fig. 5-137).

In summing up the total drag coefficient, the drag coefficient of each component is referenced to a common reference area (usually the rocket cross-sectional area) as shown in Eq. .5-.51, i.e.,

$$C_D(\text{based on } A_{ref}) = \frac{C_{D_{\text{component (component reference area)}}}}{A_{ref}}, \text{ dimensionless.} \qquad \textbf{(5-51)}$$

5-5.4.1 Interference Effect—Fin on Base

The presence of fins on rockets affects the external flow characteristics and usually results in increased base drag. The most important parameters appear to be fin thickness, fin longitudinal position, number of fins, and free-stream Mach number. Experimental data on the effects of fins are sparse if all important parameters are considered. It is suggested that the empirical relation developed in Ref. 112 be used in estimating the change in base-drag coefficient due to the fins. This relationship is

$$\Delta(C_{d_b})_F = \frac{t}{c}\ (0.825 - 0.05M_\infty)\ \frac{n}{M_\infty^2}, \text{ dimensionless} \qquad \textbf{(5-52)}$$

where

$\quad t$ = fin thickness, m
$\quad c$ = fin chord, length, m
$\quad n$ = number of fins.

This relation is limited to the case where the fin trailing edge is flush with the base. Predicted values using the relationship of Eq. 5-52 appear to be high at approximately $M_\infty < 1.5$.

As previously mentioned, ringtail configurations can have a favorable effect on base drag. Shown in Fig. 5-154 are the interference effects of a ringtail on jet-off and sustain level base pressure ratios p_b/p_∞. The data are typical of results obtained on several configurations in an investigation reported in Ref. 113. Although a significant decrease in base drag can be obtained, an increase in configuration drag is usually the result.

5-5.4.2 Sample Drag Calculation

The same configuration used for the stability calculation (Fig. 5-83) is used for the sample drag calculation. The fin and base configuration is shown in more detail in Fig. 5-155 along with parameters necessary for determining various drag components.

The method of obtaining drag coefficients is shown in Table 5-4. Table 5-3 provides data for use in Table 5-4. (Note that in some cases it is necessary to extrapolate in order to make estimates.) A breakdown of the calculated drag components is shown in Fig. 5-156.

5-5.5 PROTUBERANCES

The influence of protuberances on rocket aerodynamics is not considered during preliminary design. However, the designer should be aware that protuberances and other irregularities will be present on the final vehicle. Proper design of protuberances is necessary to minimize the increase in drag and reduce the likelihood of possible effects on stability characteristics.

Generally included under the subject of protuberances are manufacturing irregularities, gaps and misalignments, launch lugs, roll torque lugs, recesses and other cavities, and electrical conduits. Also

TABLE 5-3
VARIATION OF REYNOLDS NUMBER AND DYNAMIC PRESSURE WITH ALTITUDE
(Ref. 130)

Altitude, m	Re per meter at $M_\infty = 1$, m^{-1}	$\frac{q_\infty}{M_\infty^2}$, kPa
0	23.296×10^6	70.928
500	22.269×10^6	66.823
1000	21.276×10^6	62.913
1500	20.317×10^6	59.192
2000	19.393×10^6	55.651
2500	18.499×10^6	52.284
3000	17.639×10^6	49.085
3500	16.809×10^6	46.046
4000	16.010×10^6	43.162
4500	15.239×10^6	40.426
5000	14.497×10^6	37.834

included are protuberances such as nuts, bolts, screws, rivets, and joints. The type of surface finish required for minimum friction drag is also considered under this heading.

The primary factor influencing protuberance drag is boundary layer thickness. Where a choice exists, it is better to locate holes or external protuberances as far aft on the rocket as possible where the boundary layer is relatively thick. A detailed description of the effect of protuberances on missile drag is given in Ref. 114.

5-6 AIRLOAD DISTRIBUTIONS

The longitudinal distribution of the aerodynamic loading on the free rocket is important to the structural designer. At the small angles of attack usually encountered by the free rocket, normal loading is concentrated in the vicinity of the nose and the stabilizing surfaces. At higher angles of attack, the normal force is distributed along the length of the body.

The distribution of the local normal force coefficient gradient for a tangent ogive with cylindrical afterbody at $M_\infty = 2$ is shown in Fig. 5-157 (Ref. 115). The distribution given by slender-body theory represents the loading at subsonic speeds and is restricted to the nose section. At supersonic speeds there is a carryover of nose force to the cylinder. Also shown in Fig. 5-157 is the loading at various angles of attack α.

Normal force coefficient gradient load distributions determined by the second-order shock expansion method (Ref. 44) are presented in Fig. 5-158 for cone-cylinder, cone-cylinder-boattail, and cone-cylinder-flare configurations at $M_\infty = 2$. Since the pressure over the surface of the cone is constant, a triangular distribution exists over the cone. Although the second-order shock expansion method does not give a negative loading as shown by the theoretical and experimental curves in Fig. 5-157, it gives a fairly accurate distribution of loading over nose cylinders at $M_\infty \geq 2$.

The distribution of the local axial force coefficient C_A on a cone at $M_\infty = 0.95$ is shown in Fig. 5-159 (Ref. 116). This distribution is derived from the pressure distribution of Fig. 5-160. The axial force distributions of the flare and boattail configurations of Fig. 5-158 are shown in Fig. 5-161.

The loading over the fins and the adjoining body is difficult to generalize. The distribution depends upon the fin geometry, free-stream Mach number, and whether or not an afterbody is present. The total forces due to the fins and fin-body interference maybe determined by the methods cited in pars. 5-3.2 and 5-3.4.2.

For an analysis of the fin structural loading, a spanwise elliptic distribution may be assumed. The chordwise loading distribution over the fin must be considered at several spanwise stations and is dependent upon fin geometry and M_∞.

TABLE 5-4
DRAG CALCULATION SHEETS*

① Mach No. M_∞	② Altitude	③ Re per meter at $M_\infty = 1$	④ Re per meter	⑤ Re based on body length
0.5	60	23.17×10^6	11.59×10^6	44.5×10^6
0.7	115	23.06×10^6	16.14×10^6	62.0×10^6
0.9	170	22.95×10^6	20.66×10^6	79.3×10^6
0.95	190	22.91×10^6	21.76×10^6	83.6×10^6
1.0	205	22.87×10^6	22.87×10^6	87.8×10^6
1.1	240	22.80×10^6	25.08×10^6	96.3×10^6
1.2	280	22.72×10^6	27.26×10^6	104.7×10^6
1.6	480	22.31×10^6	35.70×10^6	137.1×10^6
2.0	715	21.83×10^6	43.66×10^6	167.7×10^6
2.4	990	21.26×10^6	51.02×10^6	195.9×10^6
2.8	1310	20.68×10^6	57.90×10^6	222.3×10^6
3.2	1700	19.95×10^6	63.84×10^6	245.1×10^6

| ① Arbitrarily selected | ② Flight altitude at corresponding Mach number, m | ③ From Table 5-3, m⁻¹, (Function of ②) | ④ ③·①, m⁻¹ | ⑤ 3.84·④, dimensionless, abscissa entry for Fig. 5-134 (Body length = 3.84 m given in Fig. 5-155) |

*Supporting body and fin data are shown on Fig. 5-155

TABLE 5-4 (cont'd)

① Mach No. M_∞	⑥ Re based on Fin Chord	⑦ Body Skin-Friction Coefficient $(C_f)_b$	⑧ Body Skin-Friction Drag Coefficient $(C_{D_f})_b$	⑨ Fin Skin-Friction Drag Coefficient $(C_f)_b$
0.5	3.7×10^6	0.0022	0.233	0.0030
0.7	5.2×10^6	0.0021	0.223	0.0029
0.9	6.6×10^6	0.0020	0.212	0.0028
0.95	7.0×10^6	0.0020	0.212	0.0027
1.0	7.3×10^6	0.0020	0.212	0.0027
1.1	8.0×10^6	0.0019	0.201	0.0026
1.2	8.7×10^6	0.0019	0.201	0.0025
1.6	11.4×10^6	0.0017	0.180	0.0023
2.0	14.0×10^6	0.0015	0.159	0.0021
2.4	16.3×10^6	0.0013	0.138	0.0018
2.8	18.5×10^6	0.0012	0.127	0.0016
3.2	20.4×10^6	0.0011	0.117	0.0014

⑥ $0.32 \cdot$ ④, dimensionless, abscissa entry for Fig. 5-134 (fin chord length = 0.32 m given in Fig. 5-155)

⑦ From Fig. 5-134 and Re from ⑤, Ref. area = A_{wet}, dimensionless

⑧ $(C_{D_f})_b = 1.15 \cdot$ ⑦ $\cdot 92.15$, dimensionless, Ref. area = A_{ref}. $((A_{wet}/A_{ref})_b = 92.15$ given in Fig. 5-155. The factor 1.15 results from discussion in par. 5-52.)

⑨ From Fig. 5-134 and Re from ⑥, Ref. area = A_{wet}, dimensionless

TABLE 5-4 (cont'd)

① Mach No. M_∞	⑩ Fin Skin-Friction Drag Coefficient $(C_{D_f})_F$	⑪ Total Skin-Friction Drag Coefficient $(C_{D_f})T$	⑫ $(M_\infty^2 - 1)(l_n/d)^2$	⑬ $C_{D_w}(l_n/d)^2$
0.5	0.020	0.253	—	—
0.7	0.019	0.242	—	—
0.9	0.018	0.230	−1.71	0.06
0.95	0.018	0.230	−0.88	0.10
1.0	0.018	0.230	0	0.47
1.1	0.017	0.218	1.89	0.98
1.2	0.016	0.217	3.96	1.05
1.6	0.015	0.195	—	—
2.0	0.014	0.173	—	—
2.4	0.012	0.150	—	—
2.8	0.010	0.137	—	—
3.2	0.009	0.126	—	—

$(C_{D_f})_F = ⑨ \cdot 6.52$, dimensionless, Ref. area $= A_{ref}$. $((A_{wet}/A_{ref})_F = 6.52$ given in Fig. 5-155.)

$(C_{D_f})_T = ⑧ + ⑩$, dimensionless

Abscissa entry for Fig. 5-113, dimensionless $(l_m/d = 3.0$ given in Fig. 5-155)

From Fig. 5-113 and ⑫, dimensionless

TABLE 5-4 (cont'd)

① Mach No. M_∞	⑭ Nose Wave-Drag Coefficient $(C_{D_w})_n$	⑮ $M_\infty/(\ell_n/d)$	⑯ $(M_\infty^2)(C_{D_w})_n$	⑰ Nose Wave-Drag Coefficient $(C_{D_w})_n$	⑱ $\sqrt{M_\infty^2 - 1}$
0.5	—	—	—	—	—
0.7	—	—	—	—	—
0.9	0.007	—	—	—	—
0.95	0.011	—	—	—	—
1.0	0.052	—	—	—	—
1.1	0.109	—	—	—	—
1.2	0.117	—	—	—	0.663
1.6	—	0.533	0.28	0.109	1.249
2.0	—	0.667	0.38	0.095	1.732
2.4	—	0.800	0.51	0.089	2.182
2.8	—	0.933	0.67	0.085	2.615
3.2	—	1.067	0.85	0.083	3.040

Transonic nose $(C_{D_w})_n$, ⑬$/(\ell_n/d)^2$, dimensionless, Ref. area $= A_{ref}$ ($\ell_n/d = 3$ given in Fig. 5-155)

Abscissa entry for Fig. 5-114, dimensionless ($\ell_n/d = 3$ given in Fig. 5-155)

From Fig. 5-114 and ⑮, dimensionless

Supersonic $(C_{D_w})_n = $ ⑯$/M_\infty^2$, dimensionless, Ref. area $= A_{ref}$

TABLE 5-4 (cont'd)

① Mach No. M_∞	⑲ $(AR)_e\sqrt{M_\infty^2 - 1}$	⑳ $\dfrac{(C_{D_w})_F}{(AR)_e \left(\dfrac{t}{c}\right)^2}$	㉑ Fin Wave-Drag, Coefficient $(C_{D_w})_F$	㉒ $\dfrac{M_\infty^2 - 1}{(t/c)^{2/3}}$
0.5	—	—	—	—
0.7	—	—	—	—
0.9	—	—	—	—
0.95	—	—	—	−1.32
1.0	—	—	—	0.00
1.1	—	—	—	2.85
1.2	0.212	12.0	0.003	—
1.6	0.400	8.3	0.002	—
2.0	0.554	6.7	0.001	—
2.4	0.698	5.7	0.001	—
2.8	0.837	4.9	0.001	—
3.2	0.973	4.2	0.001	—

⑲ $0.32 \cdot$ ⑱ , dimensionless
Abscissa entry for Fig. 5-128(H).
(Exposed fin aspect ratio $AR_e = 0.32$ given in Fig. 5-155)

⑳ From Fig. 5-128(H) and ⑲ , dimensionless

㉑ $(C_{D_w})_F =$ ⑳ $\cdot (AR)_e \left(\dfrac{t}{c}\right)^2 \left(\dfrac{S_{F_e}}{A_{ref}}\right)$, dimensionless

$=$ ⑳ $\cdot (0.000128)\,(1.36)$

Ref. area $= A_{ref} = A_{ref}((AR)_e(t/c)^2 = 0.000128$ and $S_{F_e}/A_{ref} = 1.36$ given in Fig. 5-155)

㉒ Abscissa entry for Fig. 5-130, dimensionless

TABLE 5-4 (cont'd)

① Mach No. M_∞	㉓ $(AR)_e \left(\dfrac{t}{c}\right)^{1/3}$	㉔ $\dfrac{(C_{D_w})_F}{\left(\dfrac{t}{c}\right)^{5/3}}$	㉕ Fin Wave-Drag Coefficient $(C_{D_w})_F$	㉖ Fin Base-Drag Coefficient $(C_{P_b})_F$	㉗ Base-Drag Coefficient C_{D_b}
0.5	—	—	—	−0.35	−0.35
0.7	—	—	—	−0.35	−0.35
0.9	—	—	—	−0.35	−0.35
0.95	0.087	0.0	0.0000	−0.40	−0.40
1.0	0.087	0.2	0.0005	−0.65	−0.65
1.1	0.087	0.3	0.0007	-0.65	−0.65
1.2	—	—	—	−0.50	−0.50
1.6	—	—	—	−0.3 i	-0.31
2.0	—	—	—	-0.23	−0.23
2.4	—	—	—	−0.18	−O. 18
2.8	—	—	—	−0.15	-0.15
3.2	—	—	—	-0.12	-0.12

Given in Fig. 5-155, dimensionless

From Fig. 5-130, ㉒, and ㉓, dimensionless

$(C_{D_w})_F = $ ㉔ $\cdot \left(\dfrac{t}{c}\right)^{5/3} \left(\dfrac{S_{F_e}}{A_{ref}}\right)$

$= $ ㉔ $\cdot (0.00147) (1.63)$, dimensionless

Ref. area $= A_{ref} ((t/c)^{5/3} = 0.00147$ and $S_{F_e}/A_{ref} = 1.63$ given in Fig. 5-155.)

Fin base pressure coefficient from Figs. 5-152 and 5-153, dimensionless

$(C_{D_b})_F = -$ ㉖, Ref. area
$= $ fin base area

MIL-HDBK-762(MI)

TABLE 5-4 (cont'd)

① Mach No. M_∞	㉘ $(C_{D_b})_F$	㉙ Total Fin Wave-Drag Coefficient $(C_{D_w})_F + (C_{D_b})_F$	㉚ Jet-Off Body Base- Pressure Coefficient $(C_{p_b})_b$	㉛ Jet-Off Base-Drag Coefficient C_{D_b}
0..5	0.023	0.023	−0. 170	0.170
0.7	0.023	0.023	−0. 163	0.163
0.9	0.023	0.023	−0. 156	0.156
0.95	0.026	0.026	−0. 163	0.163
1.0	0.042	0.043	−0.183	0.183
1.1	0.042	0.043	−0.215	0.215
1.2	0.033	0.036	−0. 194	0.194
1.6	0.020	0.022	−0. 168	0.168
2.0	0.015	0.016	−0.147	0.147
2.4	0.012	0.013	−0. 124	0.124
2.8	0.010	0.011	−0. 106	0.106
3.2	0.008	0.009	−0.089	0.089

㉗ · 0.0652, dimensionless
Ref. area $= A_{ref_F}$ ((fin base-area)/A_{ref} = 0.0652 given in Fig. 5-155.)

㉘ + (㉑ or ㉕), dimensionless

From Fig. 5-140, dimensionless, $p_\infty = 1$ atm (transonic experiment)
(Note that $(C_{p_b})_b$ values read from Fig. 5-140 are negative.)

$C_{D_b} = -$ ㉚, dimensionless
Ref area $= A_{ref}$

(cont'd on next page)

5-64

MIL-HDBK-762(MI)

TABLE 5-4 (cont'd)

① Mach No. M_∞	㉜ q_∞/M_∞^2	㉝ Dynamic Pressure q_∞	㉞ Thrust T	㉟ Thrust Coefficient C_T
0.5	70.4	17.6	13.5	38.35
0.7	70.0	34.3	13.5	19.68
0.9	69.5	56.3	13.5	11.99
0.95	69.4	62.7	13.5	10.77
1.0	69.2	69.2	13.5	9.75
1.1	69.0	83.5	13.5	8.08
1.2	68.6	98.8	13.5	6.83
1.6	67.0	171.5	13.5	3.94
2.0	65.1	260.4	13.5	2.59
2.4	63.0	362.9	13.5	1.86
2.8	60.6	475.1	13.5	1.42
3.2	57.8	591.9	13.5	1.14

Interpolated value from Table 5-3 and ②

$q_\infty = ㉜ \cdot ①^2$, kPa

Assumed constant, kN

$C_T = ㉞/(㉝ \cdot A_{ref})$, dimensionless, ($A_{ref} = 0.02$ m² given in Fig. 5-155)

MIL-HDBK-762(MI)

TABLE 5-4 (cont'd)

① Mach No. M_∞	㊱ Base-Pressure Ratio p_b/p_∞	㊲ Jet-On Base-Pressure Coefficient C_{P_b}	㊳ Jet-On Base-Drag Coefficient C_{D_b}	㊴ Total Jet-On Drag Coefficient $(C_D)_{T\text{(jet on)}}$	㊵ Total Jet-Off Drag Coefficient $(C_D)_{T\text{(jet off)}}$
0.5	1.005	0.029	−0.010	0.266	0.446
0.7	1.005	0.029	−0.010	0.255	0.428
0.9	0.975	−0.044	0.016	0.276	0.416
0.95	0.930	−0.111	0.040	0.307	0.430
1.0	0.880	−0.171	0.062	0.387	0.508
1.1	0.810	−0.224	0.081	0.451	0.585
1.2	0.750	−0.248	0.089	0.459	0.564
1.6	0.590	−0.229	0.082	0.408	0.494
2.0	0.490	−O. 182	0.066	0.350	0.431
2.4	0.425	−0.143	0.051	0.303	0.376
2.8	0.380	−0.113	0.041	0.274	0.339
3.2	0.345	−0.091	0.033	0.251	0.307

From Fig. 5-150
Base-Pressure Coefficient, dimensionless
(Function of ㉟ and ①)

$(p_b/p_\infty - 1)/[\left(\dfrac{\gamma}{2}\right) M_\infty^2] = (㊱ - 1)/(0.7 \cdot ①^2)$, dimensionless

($\gamma = 1.4$ given in Fig. 5-155)

$-(㊲)$(annular area/A_{ref}) $= -㊲ \cdot 0.36$, dimensionless
(Annular area/$A_{ref} = 0.36$ given in Fig. 5-155.)

$(C_D)_{T\text{(jet on)}} = ⑪ + (⑭ \text{ or } ⑰) + ㉙ + ㊳$, dimensionless

$(C_D)_{T\text{(jet off)}} = ⑪ + (⑭ \text{ or } ⑰) + ㉙ + ㉛$, dimensionless

For a critical structural analysis on the missile body, a distributed load is used for the nose loads, and the fin loads are replaced by a concentrated load. The longitudinal center of pressure of the fin loads maybe determined from par. 5-3.2. The forces on the fin in the presence of the fin-body interference factor $K_{F(b)}$ and the forces on the body in the presence of the body-fin interference factor $K_{b(F)}$ are given in par. 5-3.4.2. It is recommended that the center of pressure of the body upwash $K_{F(b)}$ on fin loading be assumed to be the same as the fin alone (see Ref. 35). The center of pressure acting on the body due to the fin, i.e., due to $K_{b(F)}$ is discussed in detail in Ref. 35. For low aspect ratio fins with no afterbody, the fin-alone location is recommended for preliminary design use. With an afterbody present the center of pressure due to $K_{b(F)}$ will shift rearward with increasing supersonic Mach numbers (see Fig. 5-67).

5-7 AERODYNAMIC TESTING

5-7.1 GENERAL

The aerodynamic performance of rockets can be evaluated by theoretical estimates, free-flight testing, rocket-sled testing, aeroballistic range testing, and wind-tunnel testing. Each of these evaluation tools has distinct advantages and limitations.

Theoretical estimates, due to lack of refinement, often fail to provide adequate quantitative aerodynamic data. Free-flight testing has the advantage that tests are conducted in the actual flight environment. However, since the test vehicle is usually destroyed, the cost associated with free-flight testing is a severe limitation. Further, recent advances in electronic technology have resulted in telemetry packages that allow a satisfactory rate of data collection. Also, parameter identification techniques that have been used extensively for obtaining aerodynamic coefficients from aircraft flight tests have only recently been applied to rockets (Ref. 117). An Extended Kalman Filter—a linear system in which the mean squared error between the desired output and the actual output is minimized when the input is a random signal generated by white noise—can be used to process flight test (tracking and telemetry) data to estimate the rocket aerodynamic coefficients. This procedure is being applied by using a computer program that has an Extended Kalman Filter Algorithm and a 6-DOF simulation that includes a wind-tunnel-based aerodynamic model. The 6-DOF simulation is forced to match the accelerations, rates, positions, etc., that are measured during the flight test. In doing this, the filter estimates perturbation terms to the aerodynamic model which will allow the match between flight test and simulation to occur. The aerodynamic perturbation terms are then statistically combined from several flights and used to update the aerodynamic model in the 6-DOF simulation. The successful use of this technique requires a carefully planned flight test and considerable insight into aerodynamics and flight testing.

Rocket-sled testing, like free-flight testing, has the advantage of subjecting the test article to near actual flight environments. Further, data collection is simpler, and the quantity of data is not so restricted as in free-flight testing. Also rocket-sled testing is usually nondestructive; however, test articles may have to withstand high acceleration forces and vibrations which can adversely affect the data being obtained. Therefore, the use of rocket-sled tests to obtain aerodynamic data usually is restricted to special cases.

Wind-tunnel testing, however, allows more precise control of test conditions. A wide range of model geometry and flow conditions may be investigated in a complete wind-tunnel program. An indication of the wind tunnels available in the U.S. is given in Refs. 118 through 123. The uniqueness of the available tunnels dictates the necessity for matching particular tunnel characteristics to the particular test requirements. Tunnel operating capabilities and size are foremost among the considerations in selecting a test facility. However, availability, accessory equipment, and cost of test time are important considerations. Since wind-tunnel testing is the most extensive technique employed, it will be discussed in detail in par. 5-7.2.

5-7.2 WIND TUNNELS

5-7.2.1 Classification

Wind tunnels normally are classified according to their operating speed range as follows:

Tunnel Classification	Mach Number Range
Subsonic	Less than 0.7
Transonic	0.7 to 1.2
Supersonic	1.2 to 5.0
Hypersonic	Greater than 5.0.

Due to inherent problems associated with operating at different speed (or Mach number) ranges, wind-tunnel facility personnel usually elect to operate their facilities only within the range of their classification Mach numbers. Since a large portion of the rockets considered in this handbook operate over a wide range of the Mach number spectrum, complete testing will usually require more than one facility. The upper limit, M_∞ 5, for supersonic tunnels has been set from considerations of operating procedures and not from abrupt changes in flight characteristics. When air is expanded to a Mach number of approximately five and above, the attendant large change in the temperature results in liquefaction of the air. To prevent this, heaters of large capacity or a medium other than air maybe used to maintain temperatures above the liquefaction point.

5-7.2.2 Capabilities and Limitations

The Reynolds number capability of a wind tunnel is an important consideration. Matching full-size-rocket Reynolds number on a scale model usually is not possible. However, it is important that the transition to turbulent boundary layer occurs on the forward part of the rocket. In situations in which very small models are tested, forward transition of the boundary layer is accomplished by the use of the proper roughness or grit on the model nose. For some rockets the drag of protuberances or other surface irregularities may be considered to be critical. The effect of plumes such as spin jets or the propulsive jet on the aerodynamic characteristics may also be important. In these cases it maybe desirable to conduct tests in a large wind tunnel having a specially high Reynolds number capability. Although ground level Reynolds numbers for large rockets will not be matched, the information obtained should be sufficient for the required aerodynamic estimates.

The capability for matching flight environment temperature in a wind tunnel is only important in the study of high velocities such as may be produced by reentry trajectories. Flight environment temperatures are not significant on the classes of rocket considered in this handbook.

It is desirable to test the full-size rocket in order to have the maximum degree of confidence in the data. Generally, however, this is not practical, and a scaled down test model must be fabricated and tested. Model size decisions must be based on the characteristics to be investigated, the instrumentation located in the model interior, the model support capabilities, and the size of available test facilities. The model scale must be large enough so that the component parts normally exposed to free-stream flow on the full-size article will not be submerged in the boundary layer of the test model. It is desirable that the selected scale provide a boundary layer of the same character which will exist on the full-size article. To maintain a desirable scale and duplicate boundary layer conditions, the boundary layer often must be controlled by artificial means. There are practical limits to the duplication of small details of the full-size rocket. Duplication of details such as surface condition, small protuberances, screw heads, and small gaps in the scale model usually serves only to increase the fabrication cost and affects the data to such a small extent that measuring accuracies do not reveal their presence. The tolerances used in manufacturing the full-size rocket should be considered in development of the test model. The data presented in Fig. 5-162 show a comparison of the test results obtained from a full-size model and an 8% scale model of a typical artillery rocket; it can be seen that the agreement is excellent.

The amount of instrumentation that must be located inside the model often determines the minimum scale that can be used. Also, the scale of the model often is determined by the ability of the support to withstand the loads imposed on it.

The dimensions of the wind-tunnel test section must be large enough so that the model does not significantly alter the velocity of the airstream and so that disturbances imparted to the airstream do not

reflect from the tunnel boundaries to the model. Further, to obtain the largest aerodynamic forces and Reynolds number, it is desirable to design a model for the maximum size possible. However, there are certain aerodynamic limitations on model size which require attention.

One of these limits is that of the reflected bow shock impinging on the model. Permissible model length for a wind tunnel can be estimated with the experimental shock wave coordinates, reflection angles, and effective test section heights. Fig. 5-163 presents information abut two wind tunnels at the Arnold Engineering Development Center which can be used to estimate allowable model size. For example, assume that it is desired to run some tests in Tunnel A at M_∞ = 2.0. Further assume a cone half angle $\theta_c = 10$ deg and $l/d = 10$. In the fourth column of the table in Fig. 5-163(A) under $M_\infty = 2$ and opposite an $l/d = 10$, read yr/d = 6.10. Continue in the same column opposite 40X40, and ready, = 19.35 in. Now d can be calculated to be 3.172 in. This is the maximum diameter of the model, along with the other model characteristics that were assumed, which can be tested in Tunnel A.

It is not possible to quote maximum allowable model dimensions that will avoid all difficulties since the difficulties are dependent on the overall configuration, the position of the model in the tunnel, the operating conditions, and the precision of test measurements. Theoretical means of defining the relationship between model maximum size and test section size are not precise. Design decisions must be based on experimental investigations and an intimate knowledge of the test facility. The curves in Fig. 5-163(B) relate the ratio of the model frontal area A_M to the aerodynamic test area A_T, model nose half angle θ_c, and Mach number M_∞. This figure clearly illustrates that the model nose half angle must be kept as low as feasible so that the AM/AT ratio can be kept within acceptable limits. Fig. 5-163(C) shows the difference in test section area at two stations along the test chamber.

Fig. 5-163 presented data about two wind tunnels and the manner in which information can suitably be used for preliminary test planning. However, it must be clearly understood that although some planning of a very general nature maybe done by using Fig. 5-163, planning a test in any facility requires a thorough knowledge of the facility to be used.

A survey of the descriptive literature on several transonic tunnels indicates that the model maximum cross-sectional area should be less than 2% of the test cross-sectional area. This ratio may be slightly increased if the model is not to be tested at large angles of attack. The allowable model cross-sectional area in subsonic tunnels is less restrictive and may be as high as 10% of the test cross-sectional area. The maximum model length in subsonic tunnels is determined by the length of the test section containing the desired flow properties.

The necessity of supporting the model in the airstream prevents exact duplication of flow patterns over the base of the model. The normal means of supporting the model is a horizontal sting that extends from the interior of the model through the base and is cantilevered from a vertical support member downstream. Unlike flight conditions, the sting promotes wake stabilization and creates disturbances that might propagate into the base region. To reduce these effects, the sting should be as small as structural considerations will allow, and abrupt increases in the lateral dimensions should be avoided to provide a relatively straight member over a considerable length. A rule of thumb often applied is that the flow disturbances created by abrupt changes in the support system may be propagated upstream through the support boundary layer and model wake for a distance five times greater than the lateral dimensions of the disrupting portion.

Design decisions on the materials and fabrication of a model must be based on the anticipated loads, severity of vibrations, and structural temperature gradients. The majority of test facilities requires that model construction provide a factor of safety of at least four, based on maximum anticipated loads that in supersonic tunnels often occur during the establishment of flow in the test section. At $M_\infty = 5.0$ the stagnation temperature at some points on the model is approximately six times greater than the static temperature at other points.

The high cost of tunnel test time requires that model changes, necessary during the test, be made in a minimum of time. The expense of designing and fabricating a quick-change capability in a model can usually be justified by the savings realized through increased use of tunnel time.

5-7.2.3 Instrumentation

Balances, fitted in the interior of the test mode], resolve the net aerodynamic forces and moments acting on the model into the components shown in Fig. 5-164. The measuring elements of these balances are electrical strain gages with an accuracy of approximately 0.25% to 0.5% of the maximum rated load. To obtain the greatest accuracy, a balance should be selected with a maximum load rating corresponding closely to the predicted test loads—especially if small changes in the total loads are to be measured. Balances can be compensated to operate in temperature as high as 350 to 400 K. When models are being tested in hypersonic tunnels, water cooling is quite often used.

In addition to determining the forces and moments acting on a free rocket, it is sometimes necessary to know how the loads are distributed. Detailed knowledge of the flow over a model may be obtained by measuring surface pressure with pressure transducers. If the density of pressure orifices is adequate, then upon integrating the pressure over the rocket surface, the load distribution is known. Measuring devices should be located in or very near the test model, and the orifices and connecting lines should be large enough to prevent lengthy time delays in sensing pressure changes. The maximum number of pressure orifices that are feasible should be used. Of course, there are practical considerations such as maximum internal volume of the model, instrumentation availability, and response characteristics. For quite some time, mechanically driven scanivalves have been used as a "switching" device which handles up to 48 pressure readings. This device makes it possible to use one transducer instead of 48 and thus makes it possible, spacewise, to have more pressure readings. Electronic scanivalves are becoming available which are much smaller than mechanically driven scanivalves. Further, response time is much less with electronic scanivalves; thus many more pressure readings per unit time are possible.

There may be a need to measure model surface temperature. Unfortunately, the state of the art is not good, and the designer should use temperature measurements with reservation. Temperature measurement can be made directly with thermocouples that should be selected for the expected temperature range and the compatibility with tunnel readout instrumentation.

Flow visualization techniques are useful in making qualitative evaluations of the flow over a model. Subsonic flow patterns may be determined by observing tufts attached to the surface of the model. A mixture of linseed oil and artist paint can be used to visualize transonic and supersonic flow. Such paint-oil flow tests have an advantage over tufts because photographs of flow patterns can be studied after a given test run is completed. Paint-oil flow tests require complete cleaning of the model after each run and are thus time-consuming. Areas where the flow exhibits unusual turbulence or separates from the model surface may be identified by coating the surface with a volatile substance and observing evaporation rates. At supersonic velocities, the compression and expansion waves emanating from the model surfaces are characterized by marked changes in density which may be identified by shadowgraphs, schlierens, or interferometers.

5-7.2.4 Conduct of Tests

Because a free rocket in flight is completely free from geometrical constraint, travels at high speed, and responds to disturbances with motions involving many degrees of freedom, it is inherently prone to dynamic instability. Therefore, it is necessary to determine the dynamic characteristics of a free rocket early in the design stage. Although both analytical and experimental methods are available, it is recommended that experimental information be used where possible.

A straightforward approach to the problem is to construct a dynamically scaled model of the rocket and to test it in a wind tunnel under conditions of dynamic similarity. If the total system, i.e., rocket and environment, is properly scaled and interference effects made negligible or corrected for, the data obtained from the wind-tunnel tests are directly applicable, after proper analyses, to the full-scale prototype.

The coefficient of damping in pitch $C_{m_{\dot{\theta}}}$ may be determined from static aerodynamic coefficients obtained in wind-tunnel tests by using Eq. 5-33. Additional damping coefficients may be obtained by several dynamic test techniques. Refs. 124, 12.5, and 126 are suitable sources anti may be used as a guide for general planning for dynamic tests. For specific planning, descriptive literature issued by each facility is the best source of information.

Some general requirements for dynamic test mounting systems should be noted. First, the system should provide a soft support such that the natural frequencies associated with the mount are well below the frequencies of the free-flight rigid body and elastic modes of interest. A soft support implies that the model should be given freedom to respond with large amplitude motions. A second requirement is that moving masses associated with the mount are negligible relative to the total mass of the test article. Also, aerodynamic interference associated with a mount structure exposed to the airstream should be low, especially if the system is to be operated at high subsonic or transonic Mach numbers. Another very important requirement is that the system have both static and dynamic stability under all operating conditions.

The mounting system requirements described apply to all dynamic tests. There are, however, some special requirements related to roll dynamics testing. Roll testing may be conducted to determine roll damping and roll effectiveness coefficients. In either case, the bearing that allow the model to roll freely must be as frictionless as possible. Since frictionless bearings do not exist, friction tare must be considered; otherwise, the resulting data will be misleading.

The investigation of the influence of a propulsion system on the aerodynamic characteristics of a rocket requires a facility with the capability of propulsion testing or propulsion jet simulation. Operation of a rocket propulsion system in a tunnel creates potential fire and explosion hazards and requires a means for removing the combustion products from the tunnel airstream. Accordingly, tests of active rockets in a wind tunnel are complicated and expensive. The test time for each firing is a matter of seconds or fractions of a second while the setup time for the next firing may take 4 to 8 h. Special instrumentation and data acquisition equipment also are required. It is best if wind-tunnel tests with active rockets are a part of a long-term research project rather than part of a free rocket design study.

The effects of rocket plumes, especially those of highly underexpanded jets, are discussed in pars. 5-3.5, 5-3..5.1, and 5-3.5.2. The effect of rocket plumes on the rocket aerodynamics is especially important, and it is often necessary to conduct wind-tunnel tests to determine aerodynamic parameters under the influence of the jet plume.

It is simpler to simulate the rocket plume effects with air or other cold gases rather than fire an active rocket. Plume effects should be examined for both base-drag characteristics and stability characteristics. Base drag is important for a free rocket if it has a sustain phase or if it is boost-only but has residual burning. With a sustainer, the low base pressures induced by the plume can cause the base drag to amount to as much as 50% of the total drag. For investigation of base drag, a strut-supported model is used. Air is supplied through the strut to a settling chamber and then to the nozzle. Base drag is obtained by integrating pressure measurements over the base area. The support strut should be as thin as possible to minimize interference with the body yet be able to withstand the thrust force from the jet. A high pressure air supply is necessary to obtain an adequate mass flow rate. The wind tunnel should be large enough so that the jet plume is kept within the test shock rhombus. The strut should be swept-back so that the shock emanating from the juncture of the strut and the floor does not interfere with the simulated jet plume. Shock impingement on the model and the plume cannot be avoided for some transonic Mach numbers.

The plume shape is varied by changing chamber pressure. Although it is desirable to match exact flight conditions, it is not possible since the flight base pressure is not known. It is better to test at a series of chamber pressures so that the proper plume size is bracketed. Some kind of gas dynamics similarity parameter such as C_T (see Eq. 5-44) is desirable so that the model and the wind-tunnel environment can be matched to the actual rocket and its flight environment.

It is not possible to simulate exactly the actual rocket exhaust with air (or other cold gases) primarily because of the inability to account for the effect of temperature and afterburning (combustion of unburned propellant gases in the wake). However, some degree of sophistication in simulation of rocket plume effects can be accomplished by using the modeling procedure described in Ref. 127. A nozzle can be designed which corrects for the difference in specific heat ratios by decreasing the model plume Mach number and yet maintains similar plume shapes. This model nozzle will not match the rocket nozzle but will consist of a smaller exit angle and have a lower exit Mach number.

To investigate the effects of the jet plume on the stability characteristics of the complete rocket configuration, it is necessary to use a sting-mounted model. (In some cases, strut mounted models are used for plume investigations with measurements made on the model aft portion only.) Usually rocket stability is affected when the jet plume is large enough to increase the base pressure and the rocket afterbody pressure significantly above the free-stream value. Any technique that gives the desired base pressure—such as a forward forcing step, disc, cone, or solid plume shape—will give an indication of the plume effects on rocket stability characteristics. However, since base pressure is not precisely known prior to the tests, it is necessary to test sever-al sizes of the chosen simulator. It is difficult to interpolate correctly between the different sizes, especially if the base pressure is near the plateau pressure.

A more realistic and efficient technique for simulating the jet effects on rocket stability is the use of a normal jet simulator (see Fig. 5-165). The normal jet simulator consists of a number of normal sonic jets arranged circumferentially around a common air chamber that fits around the model sting usually one-half to one caliber aft of the model base. Normal jet simulators previously tested had 12 or 24 jets, and the total exit area amounted to between 4% and 6% of the model base area (Refs. 128 and 129). The change in the simulated plume is accomplished by a change in chamber pressure. A parameter, similar to the thrust coefficient C_T used for the axial jet, is the radial thrust coefficient C_{RT} which is the sum of the thrust of all the normal jets normalized by free-stream dynamic pressure and reference area (see Eq. 5-31). The normal jet simulator uses about 10% of the mass flow required to simulate an axial jet (see Fig. 5-92).

A recommended source of information in planning wind-tunnel tests is the descriptive literature issued by each test facility. This literature provides detailed information for all problem areas covered in the foregoing discussion.

R E F E R E N C E S

I. M. M. Munk, *The Aerodynamic Forces on Airship Hulls,* NACA TR 184, National Advisory Committee for Aeronautics, Washington, DC, 1924.

2. M. D. Van Dyke, *Practical Calculation of Second-Order Supersonic Flow Post Nonlifting Bodies of Revolution,* NACA TN2744, National Advisory Committee for Aeronautics, Washington, DC 1952.

3. M. Van Dyke, "First- and Second-Order Theory of Supersonic Flow Past Bodies of Revolution", Journal of the Aeronautical Sciences 18, 161-78 (March 1951).

4. H. S. Tsien, "Supersonic Flow Over an Inclined Body of Revolution", Journal of the Aeronautical Sciences 18, 480-3 (October 1938).

5. *Aerodynamics,* Royal Aeronautical Society, London, England, Data Sheets 1 (1960).

6. D. J. Spring, *The Effect of Nose Shape and After-body Length on Normal Force and Neutral Point Location of Axisymmetrical Bodies at Mach Numbers of 0.8 to 4.5,* Report RF-TR-64-13, US Army Missile Command, Redstone Arsenal, AL, 1964.

7. C. B. Butler, E. S. Sears, and S. G. Pallas, *Aerodynamic Characteristics of 2-, 3-, and 4-Caliber Tangent-Ogive Cylinders With Nose Bluffness Ratios of 0.00, 0.25, 0.50, and 0.75 at Mach Numbers from 0.6 to 4.0,* Report AFATL-TR-77-8, US Air Force Armament Laboratory (AFATL), Air Force Systems Command, Eglin Air Force Base, FL, January 1977.

8. R. A. Taylor and J. B. McDevitt, *Pressure Distributions at Transonic Speeds for Parabolic-Arc Bodies of Revolution Having Fineness Ratios of 10, 12, and 14,* NACA TN 4234, National Advisory Committee for Aeronautics, Washington, DC, 1958.

9. J. B. McDevitt and R. A. Taylor, *Force and Pressure Measurements at Transonic Speeds for Several Bodies Having Elliptical Cross Sections,* NACA TN 4362, National Advisory Committee for Aeronautics, Washington, DC, 1958.

10. J. B. McDevitt and R. A. Taylor, *Pressure Distributions at Transonic Speeds for Slender Bodies Having Various Axial Locations of Maximum Diameter,* NACA TN 4280, National Advisory Committee for Aeronautics, Washington, DC, 1958.

11. W. D. Washington and W. Pettis, Jr., *Boattail Effects on Static Stability at Small Angles of Attack,* Report RD-TM-68-5, US Army Missile Command, Redstone Arsenal, AL, July 1965.

12. W. A. Corlett and C. S. Richardson, *Effect of First-Stage Geometry on Aerodynamic Characteristics in Pitch on Two-Stage Rocket Vehicles from Mach 1.57 to 2.86,* NASA TN D-2709, National Aeronautics and Space Administration, Washington, DC, 1965.

13. J. C. Craft, *Summary of SMAWT Aerodynamics,* Technical Report RD-73-13, US Army Missile Command, Redstone Arsenal, AL, 1973.

14. J. H. Henderson, C. W. Dahlke, and G. Batiuk, *An Experimental Investigation Using Normal Jet Simulator to Determine Plume Effects on a Long Slender Rocket Configuration at Mach Numbers from 0.2 to 1.5,* Report TR-TD-77-2, US Army Missile Command, Redstone Arsenal, AL, 1977.

15. A. A. Hesbeth, *Documentation of a Wind Tunnel Test to Investigate the Aerodynamic Characteristics of the SPIKE Rocket With a Simulated Jet Plume at Mach Numbers from 0.6 to 1.3,* AEDC-TSR-78-V17, Arnold Air Force Station, TN, January 1979.

16. D. J. Spring, *Development Tests for the Medium Assault Weapon Study (MAW),* unpublished data, US Army Missile Command, Redstone Arsenal, AL, 1965.

17. J. G. Lowry and E. C. Polhamus, *A Method for Predicting Lift Increments Due to Flap Deflection at Low Angles of Attack in Incompressible Flow,* NACA TN 3911, National Advisory Committee for Aeronautics, Washington, DC, 1957.

18. J. B. McDevitt, *A Correlation by Means of Transonic Similarity Rules of Experimentally Determined Characteristics of a Series of Symmetrical and Cambered Wings of Rectangular Planform,* NACA TR 1253, National Advisory Committee for Aeronautics, Washington, DC, 1956.

19. C. DeJonge, *The Effect of Low Aspect Ratio Rectangular and Delta Cruciform Fins on the Stability* of *Bodies of Revolution With Tangent Ogives at Small Angles of Attack Through a Mach Number Range of O to 3.5,* Report RF-TR-62-1, Revised, US Army Ordnance Missile Command, Redstone Arsenal, AL, 1962.

20. D. E. Hoak, M. W. Carlson, and R. D. Finck, "USAF Stability and Control Datcom", *USAF Stability and Control Methods,* McDonnell Douglas Corporation, Douglas Aircraft Division for Flight Control Division, US Air Force Flight Dynamics Laboratory, Wright-Patterson Air Force Base, OH, 1960.

21. P. A. Lagerstrom and M. E. Graham, *Low Aspect Ratio Rectangular- Wings in Supersonic Flow,* Report No. SM 13110, Douglas Aircraft Company, Santa Monica, CA, 1947.

22. E. Lapin, *Charts for the Comparison of Lift and Drag of Finite Wings at Supersonic Speeds,* Report No. SM 13480, Douglas Aircraft Company, Santa Monica, CA, 1949.

23. A. V. Gafarian and W. L. Phillips, *The Supersonic Lift and Centers of Pressure of Rectangular and Clipped-Delta Fins in Combination With Long Cylindrical Bodies—Comparison Between Theory and Experiment,* NOTS TM-966, US Naval Ordnance Test Station, Inyokern China Lake, CA, 1953.

24. W. Pettis, *Aerodynamic Characteristics of Multiple Fins of Rectangular Planform on a Body of Revolution at Mach Numbers of 1.48 to 2.22,* Report RD-TM-67-5, US Army Missile Command, Redstone Arsenal, AL, 1967.

25. H. F. Emerson, *Wind Travel Investigation of the Effect of Clipping the Tips of Triangular Wings of Different Thickness, Camber, and Aspect Ratio-Transonic Pump Method,* NACA TN 3671, National Advisory Committee for Aeronautics, Washington, DC, 1956.

26. C. W. Dahlke, *The Aerodynamic Characteristics of Wraparound Fins at Mach Numbers of 0.3 to 3.0,* Technical Report RD-77-4, US Army Missile Command, Redstone Arsenal, AL, 1976.

27. J. C. Craft, H. L. Greene, and D. V. Rubin, *Wind-Tunnel Tests of Curved and Tangential Fins for Advanced LAW: Analysis Report,* Report RD-TR-70-1, US Army Missile Command, Redstone Arsenal, AL, 1970.

28. H. A. Featherstone, *The Aerodynamic Characteristics of Curved Tail Fin,* Report No. ERR-PO-019, Convair Division of General Dynamics Corporation, Pomona, CA, 1960.

29. C. W. Dahlke, *Aerodynamics of Wraparound Fins, A Survey of the Literature,* Report RD-TR-71-7, US Army Missile Command, Redstone Arsenal, AL, 1971.

30. I-I. J. Gauzza, *Static Stability Test of Tangent and Wraparound Fin Configurations at Supersonic Speeds,* NAVORD Report 3743, US Naval Ordnance Laboratory, White Oak, MD, 1956.

31. J. G. Adams and D. Dugan, *Theoretical Damping in Roll and Roiling Moment Due to Differential Wing Incidence for Slender Cruciform Wings and Wing-Body Combinations,* NACA Report 1088, National Advisory Committee for Aeronautics, Washington, DC, 1952.

32. C. E. Brazzel, J. H. Henderson, and J. C. Craft, *Longitudinal Stability Characteristics of a Series of Ringtail-Body Combinations at Mach Numbers of 0.8.—4.5,* Report RD-TR-65-7, US Army Missile Command, Redstone Arsenal, AL, 1970.

33. C. Wayne Dahlke, *Aerodynamics of Longitudinally Supported Ringtail Configurations,* Report RD-TM-71-6, US Army Missile Command, Redstone Arsenal, AL, 1971.

34. L. Beskin, *Determination of Upwash Around a Body of Revolution at Supersonic Velocities,* Report No. CM-251, Applied Physics Laboratory, Johns Hopkins University, Baltimore, MD, 1946.

35. W. C. Pitts, J. N. Nielsen, and G. E. Kaattari, *Lift and Center of Pressure of Wing-Body-Tail Combinations at Subsonic, Transonic, and Supersonic Speeds,* NACA TR-1307, National Advisory Committee for Aeronautics, Washington, DC, 1957.

36. G. Morikawa, "Supersonic Wing Body Lift", Journal of the Aeronautical Sciences 18, No. 4,217-28 (April 1951).

37. G. Morikawa, *The Wing-Body Problem for Linearized Supersonic Flow,* Progress Report No. 4-116, Jet Propulsion Laboratory, California Institute of Technology, Pasadena, CA, 1949.

38. H. N. Stone, *Calculation of Aerodynamic Characteristics of Low Aspect Ratio Wing-Body Combinations at Subsonic Speeds,* CAL AF-743-A-5, Cornell Aeronautical Laboratory, Inc., Buffalo, NY, 1952.

39. J. L. Potter, N. M. Shapiro, and W. D. Murphree, *An Interference Factor for Multifinned Tail Assemblies in Supersonic Flow,* Report 2R12F, US Army Ordnance Missile Laboratories, Redstone Arsenal, AL, 1956.

40. C. W. Dahlke and W. Pettis, *Normal Force Effectiveness of Several Fin Planforms With Streamwise Gaps at Mach Numbers of 0.8 to 5.0,* Report RD-TR-70-8, US Army Missile Command, Redstone Arsenal, AL, 1970.

41. W. Pettis, Jr., *Effects on Normal Force of Streamwise Gaps Between the Body and Fins of a Missile Configuration.* Thesis for Master of Science, Aerospace Engineering, University of Alabama, University, AL, 1971.

42. D. B. Brown, *et al., Free-Flight Rocket Technology Program Aeroballistic Directorate FY 75 Activity Report,* Report TR-RD-76-12, US Army Missile Command, Redstone Arsenal, AL, 1975.

43. B. W. Douglas, *et al., Free-Flight Rocket Technology Program Aeroballistics Directorate FY 74 Activity Report,* Report TR-RD-75-3, US Army Missile Command, Redstone Arsenal, AL, 1974.

44. C. A. Syvertson and D. H. Dennis, *A Second-Order Shock-Expansion Method Applicable to Bodies of Revolution Near Zero Lift,* NACA TR-1328, National Advisory Committee for Aeronautics, Washington, DC, 1957.

45. J. H. Henderson, *An investigation for Modeling Jet Plume Effects on Missile Aerodynamics,* Report No. RD-CR-82-25, New Technology, Inc., Huntsville, AL, 1982.

46. J. H. Henderson, *Results of Transonic Wind-Tunnel Investigations to Determine the Effects of Nozzle Geometry and Jet Plume on the Aerodynamics of a Body of Revolution,* Technical Report RD-TR-72-17, US Army Missile Command, Redstone Arsenal, AL, November 1972.

47. J. C. Craft and C. E. Brazzel, *An Experimental Investigation of Base Pressure on a Body of Revolution at High Thrust Levels and Free-Stream Mach Numbers of l.5 and 2.87,* Report No. RD-TM-70-6, US Army Missile Command, Redstone Arsenal, AL, July 1970.

48. R. A. Deep, J. H. Henderson, and C. E. Brazzel, *Thrust Effects on Missile Aerodynamics,* Report No. RD-TR-71-9, US Army Missile Command, Redstone Arsenal, AL, May 1971.

49. J. R. Burt, Jr., *An Investigation of Several Devices in Simulating Rocket Plume at Free-Stream Mach Numbers of 0.9 to 1.2,* Report RD-TR-71-22, US Army Missile Command, Redstone Arsenal, AL, September 1971.

50. J. R. Burt, Jr., *An Experimental Investigation* of *the Effects of Rocket Plume Simulators on the Radial and Longitudinal Pressure Distributions of a Sting-Mounted Body of Revolution at Transonic Mach Numbers,* Report TR-RD-72-21, US Army Missile Command, Redstone Arsenal, AL, July 1973.

51. E. E. Zukowski, "Turbulent Boundary-Layer Separation in Front of a Forward-Facing Step", Journal of the American Institute of Aeronautics and Astronautics 5, No. 10,1746-53 (October 1967).

52. C. Wayne Dahlke, *An Investigation of Flow and Stability Characteristics For a Body of Revolution With Fins and Flare in Presence of Plume-Induced Separation at Mach Numbers 0.7 to 1.4,* Report TR-RD-77-11, US Army Missile Command, Redstone Arsenal, AL, May 1977.

53. J. H. Henderson, *Transonic Wind-Tunnel Investigation of Thrust Effects on the Longitudinal Stability Characteristics* of *Several Body-Fin Configurations (Sting-Mounted Model With Normal Jet Plume Simulator),* Report TR-RD-75-14, US Army Missile Command, Redstone Arsenal, AL, December 1974.

54. J. H. Henderson, *Investigation of Jet Plume Effects on the Longitudinal Stability Characteristics* of *a Body of Revolution With Various Fin Configurations at Mach Numbers from 0.2 to 2.3 (Normal Jet Plume Simulator),* Report TR-RD-76-22, US Army Missile Command, Redstone Arsenal, AL, February 1976.

55. J. R. Burt, Jr., and R. A. Deep, *Aerodynamic Effectiveness of Split Flare Stabilizers,* AIAA Preprint, 79-0093, 17th Aerospace Sciences Meeting, New Orleans, LA, 15-17 January 1979.

56. J. R. Burt, Jr., *An Experimental Investigation of the Effect of Several Rocket Plume Simulators on the Pressure Distribution* of a *Body* of *Revolution at Free-Stream Mach Numbers of 0.9 to 1.2,* Report RD-TR-70-23, US Army Missile Command, Redstone Arsenal, AL, November 1970.

57. J. H. Burt, J. H. Henderson, and W. Pettis, Jr., *The Effects of Three Rocket Plume Simulators on the Aerodynamic Characteristics of Several Missile Configurations,* Report RD-TR-70-20, US Army Missile Command, Redstone Arsenal, AL, October 1970.

58. W. F. Henson and R. J. McGhee, *Effects of Jet Pluming on the Static Stability of Five Rockets at Models at Mach Numbers 4, 5, and 6 and Static Pressure Up to 26,000 Feet,* NASA TN-D 4064, National Aeronautics and Space Administration, Langley Station, Hampton, VA, 1962.

59. C. H. Murphy, *Symmetric Missile Dynamic Instabilities—A Review,* ARBRL-TR-02228, US Army Armament Research and Development Command, US Army Ballistic Research Laboratories, Aberdeen Proving Ground, MD, 1980.

60. C. H. Murphy, *Free-Flight Motion of Symmetric Missiles,* BRL Report 1216, US Army Ballistic Research Laboratories, Aberdeen Proving Ground, MD, 1963.

61. S. S. Chin, *Missile Configuration Design,* McGraw-Hill Book Company, Inc., New York, NY, 1961, pp. 130-53.

62. Lars-Eric Ericson and J. Peter Reding, *Report on Saturn I—Apollo Unsteady Aerodynamics,* LMSC-A650215, Lockheed Missiles and Space Company, Sunnyvale, CA, 1964.

63. A. S. Platou, *The Magnus Force on a Finned Body,* BRL Report No. 1193, US Army Ballistic Research Laboratories, Aberdeen Proving Ground, MD, 1963.

64. J. C. Uselton and J. B. Carman, "A Study of the Magnus Effects on a Sounding Rocket at Supersonic Speeds", Journal of Spacecraft 8, No. 1, 28-33 (January 1971).

65. Sighard F. Hoerner, *Fluid—Dynamic Drag,* Midland Parks, NJ, 1958, pp. 16-4 through 16-13, 16-21 through 16-27.

66. W. E. Stoney, Jr., *Collection of Zero-Lift Drag Data on Bodies of Revolution from Free-Flight Investigations,* NASA TR-R-100, National Aeronautics and Space Administration, Washington, DC, 1952.

67. *Handbook of Supersonic Aerodynamics,* Section 8, "Bodies of Revolution", Report 1488 (Volume 3), Bureau of Naval Weapons, Department of the Navy, Washington, DC, October 1961.

68. Aerodynamics Facilities Section Staff, *Aerodynamic Characteristics of Spherically Blunted Cones at Mach Numbers from 0.5 to 5.0,* MTP-AERO-61-38, Marshall Space Flight Center, Huntsville, AL, 1961.

69. W. E. Stoney, Jr., *Transonic Drag Measurements of Eight Body-Nose Shapes,* NACA RM L53K17, National Advisory Committee for Aeronautics, Washington, DC, 1954.

70. D. W. Sinclair, *Skin-Friction Measurements at Subsonic and Transonic Mach Numbers With Embedded-Wire Gages,* AEDC-TR-80-29, Arnold Engineering Development Center, Arnold Air Force Station, TN, 1981.

71. V. S. Murthy and W. C. Rose, *Buried Wire Gage for Wall Shear Stress Measurements,* AIAA 10th Aerodynamic Testing Conference, San Diego, CA, 19-21 April 1978.

72. S. C. Sommer and J. A. Stark, *The Effect of Bluntness on the Drag of Spherical-Tipped Truncated Cones of Fineness Ratio 3 at Mach Numbers 1.2 to 7.4,* NACA RM A52B13, National Advisory Committee for Aeronautics, Washington, DC, 1952.

73. E. D. Perkins and L. H. Jorgensen, *Investigation of the Drag of Various Axially Symmetric Nose Shapes of Fineness Ratio 3 for Mach Numbers from 1.24 to 3.67,* NACA RM A52H28, National Advisory Committee for Aeronautics, Washington, DC, 1952.

74. A. J. Eggers, M. M. Resnikoff, and D. H. Dennis, *Bodies of Revolution Having Minimum Drag at High Supersonic Airspeeds,* NACA Report 1306, National Advisory Committee for Aeronautics, Washington, DC, 1957.

75. E. R. Dickinson, *Some Aerodynamic Effects of Blunting a Projectile Nose,* BRL MR 1596, US Army Ballistic Research Laboratories, Aberdeen Proving Ground, MD, 1964.

76. E. J. Roschke, *The Effect* of Nose *Truncation on the Aerodynamic Properties of 9-Caliber Long, Army-Navy Spinner Rocket Models Near Sonic Velocity,* BRL-TN 902, US Army Ballistic Research Laboratories, Aberdeen Proving Ground, MD, 1955.

77. A. C. Charters and H. Stein, *The Drag* of *Projectiles With Truncated Cone Headshapes,* BRL-R624, US Army Ballistic Research Laboratories, Aberdeen Proving Ground, MD, 1952.

78. C. H. Murphy and L. E. Schmidt, *The Effect of Length on the Aerodynamic Characteristics of Bodies* of *Revolution in Supersonic Flight,* BRL-R876, US Army Ballistic Research Laboratories, Aberdeen Proving Ground, MD, 1953.

79. L. E. Schmidt and C. H. Murphy, *The Aerodynamic Properties of the 7-Caliber Army-Navy Spinner Rocket in Transonic Flight,* BRL-MR775, US Army Ballistic Research Laboratories, Aberdeen Proving Ground, MD, 1954.

80. L. Mason, L. Devan, F. G. Moore, and D. McMillian, *Aerodynamic Design Manual for Tactical Weapons,* NSWC TR 81-156, Naval Surface Weapons Center, Dahlgren, VA, 1981.

81. J. M. Cubbage, *Jet Effects on the Drag of Conical Afterbodies for Mach Numbers of 0.6 to 1.23,* NACA RML57C21, National Advisory Committee for Aeronautics, Washington, DC, 1957.

82. D. J. Spring, *The Static Stability Characteristics of Several Cone-Cylinder Flare-Cylinder Configurations at Mach Numbers* of *0.4 to 4.5,* Report RF-TR-63-14, US Army Missile Command, Redstone Arsenal, AL, 1963.

83. J. H. Henderson, *Normal Force, Pitching Moment, and Center of Pressure of Eighty Cone-Cylinder-Frustum Bodies of Revolution at Mach Numbers of 1.50 to 4.04,* Report Number 6R 3F, US Army Ordnance Missile Laboratories, Redstone Arsenal, AL, 1956.

84. R. A. Deep and J. H. Henderson, *Study of Aerodynamic Characteristics of Cone-Cylinder-Conical Frustum Bodies by Linearized Theory of Supersonic Flow,* Report 6R2P, US Army Ordnance Missile Laboratories, Redstone Arsenal, AL, June 1955.

85. J. R. Burt, Jr., *An Investigation of the Aerodynamic Stabilizing Effectiveness of Several Split Flare Afterbody Configurations in the Presence of an Underexpanded Jet Plume at Transonic Mach Numbers,* Technical Report T-78-31, US Army Missile Research and Development Command, Redstone Arsenal, AL, 1978.

86. R. E. Elwell, *A Study of Various Stabilizing After-bodies on a Body of Revolution in the Presence of a Simulated Rocket Plume at Transonic Mach Numbers,* AEDC-DR-77-80, Arnold Engineering Development Center, Arnold Air Force Station, TN, September 1977.

87. R. W. Truitt, *Hypersonic Aerodynamics,* The Ronald Press Company, New York, NY, 1959.

88. Ames Research Staff, *Equations, Tables, and Charts for Compressible Flow,* NACA Report 1135, National Advisory Committee for Aeronautics, Washington, DC, 1953.

89. D. H. Fikes, *Static Force Tests of the Army SPIKE and Free-Flight Demonstration Rocket Missile Configurations With Jet Plume Simulation at Mach Numbers 1.75 to 4.50,* AEDC-TSR-78-V17, Arnold Air Force Station, TN, July 1978.

90. "P. R. Connolly, *The Zero-Lift Foredrag and Body Base Drag Coefficients of a Series of Ringtail-Strut-Body Configurations at Mach Numbers* from *0.80 to 4.50,* Report RD-TR-65-8, US Army Missile Command, Redstone Arsenal, AL, 1965.

91. R. W. Truitt, *Fundamentals of Aerodynamic Heating,* The Ronald Press Company, New York, NY, 1960.

92. D. B. Lee and M. A. Faget, *Charts Adapted from Van Driest's Turbulent Flat Plate Theory for Determining Values of Turbulent Aerodynamic Friction and Heat Transfer Coefficient,* NACA TN 3811, National Advisory Committee for Aeronautics, Washington, DC, 1956.

93. Charles E. Brazzel and James H. Henderson, "An Empirical Technique for Estimating Power-On Base Drag of Bodies of Revolution With a Single Jet Exhaust", *The Fluid Dynamic Aspects of Ballistics,* NATO—AGARD CP No. 10, Paris, France, September 1966, pp. 241-61.

94. D. R. Chapman, An *Analysis of Base Pressure at Supersonic Velocities and Comparison With Experiments,* NACA TR 1051 (Supersedes NACA TN 2137), National Advisory Committee for Aeronautics, Washington, DC, 1951.

95. E. S. Love, Base *Pressure at Supersonic Speeds on Two-Dimensional Airfoils and on Bodies of Revolution With and Without Fins Having Turbulent Boundary Layers,* NACA TN 3819, National Advisory Committee for Aeronautics, Washington, DC, 1957.

96. A. Seiff, *et al., Aerodynamic Characteristics of Bodies at Supersonic Speeds,* NACA RM A51J25, National Advisory Committee for Aeronautics, Washington, DC, 1951.

97. C. E. Brazzel, *A Kinetic Energy Concept for Establishing Power-Off Base Pressure,* Report RD-TN-68-8, US Army Missile Command, Redstone Arsenal, AL, 1968.

98. D. V. Rubin, C. E. Brazzel, and J. H. Henderson, *The Effects of Jet Plume and Boattail Geometry on Base and Afterbody Pressures of a Body of Revolution at Mach Numbers of 2.0 to 3.5,* Report RD-TR-70-5, US Army Missile Command, Redstone Arsenal, AL, 1970.

99. J. H. Henderson, *Jet Effects on Base Pressures of Cylindrical and Flared Afterbodies at Free-Stream Mach Numbers of 1.65, 1.82, and 2.21,* ARGMA TR-1G3R, US Army Ordnance Missile Command, Redstone Arsenal, AL, 1960.

100. D. Rubin, *A Transonic Investigation of Jet Plume Effects on Base and Afterbody Pressures of Boattail and Flare Bodies of Revolution,* Report RD-TR-70-10, US Army Missile Command, Redstone Arsenal, AL, 1970.

101. J. Reid and R. C. Hastings, *The Effect of a Central Jet on the Base Pressure of a Cylindrical Afterbody in a Supersonic Stream,* RAE Report Aero 2621, Royal Aircraft Establishment, Farnborough, England, December 1959.

102. Charles E. Brazzel, *The Effects of Base Bleed and Sustainer Rocket Nozzle Diameter and Location on the Base Drag of a Body of Revolution With Concentric Boost and Sustainer Rocket Nozzles,* Report RF-TR-53-23, US Army Missile Command, Redstone Arsenal, AL, July 1963.

103. James M. Cubbage, Jr., *Jet Effects on Base and Afterbody Pressures of a Cylindrical Afterbody at Transonic Speeds,* NACA Report RML56C21, National Advisory Committee for Aeronautics, Langley Field, VA, May 1956.

104. E. M. Cortright and A. H. Schroeder, *Investigation at Mach Number 1.91 of Side and Base Pressure Distributions Over Conical Boattails Without and With Jet Flow Issuing from the Base,* NACA Report RME51F26, Lewis Flight Propulsion Laboratory, Cleveland, OH, September 1961.

105. L. E. Baughman and F. D. Kochendorfer, *Jet Effects on Base Pressure of Conical Afterbodies at Mach Numbers of 1.91 and 3.12,* NACA Report RME57E06, Lewis Flight Propulsion Laboratory, Cleveland, OH, August 1957.

106. C. E. Brazzel, *Estimated Power-On Base Drag for a Rocket-Assisted Projectile, (USAMC)* Report RD-TM-70-7, US Army Missile Command, Redstone Arsenal, AL, July 1970.

107. B. J. Walker and A. L. Addy, *Preliminary Investigation of the Effect of Afterburning on Base Pressure,* Report RD-TM-71-6, US Army Missile Command, Redstone Arsenal, AL, December 1971.

108. N. Charczenko and C. Hayes, *Jet Effects at Supersonic Speeds on Base and Afterbody Pressures on a Missile Model Having Single and Multiple Jets,* NASA Technical Note D-2046, Langley Research Center, Hampton, VA, 1963.

109. S. A. Geocke, *Comparison of Wind-Tunnel and Flight-Measured Base Pressures from the Sharp Leading-Edge Upper Vertical Fin of the X-15 Airplane for Turbulent Flow at Mach Numbers from 1.5 to 5.0,* NASA TN-D-6348, Flight Research Center, Edwards, CA, May 1971.

110. H. H. Korst, *Compressible Two-Dimensional Jet Mixing at Constant Pressure,* ME-TN-392-1, University of Illinois, Office of Scientific Research TN-54-82, April 1954, (Reproduced as Office of Technical Services Collection, Pub. No. 132044, Dept. of Commerce).

111. J. H. Nash, *An Analysis of Two-Dimensional Turbulent Base Flow, Including the Effect of the Approaching Boundary Layer,* Reports and Memoranda No. 3344, Aeronautical Research Council Ministry of Aviation, Aeronautical Research Council, Her Majesty's Stationary Office, London, England, 1963.

112. E. E. Honeywell, *Compilation of Power-Off Base Drag Data and Empirical Methods for Predicting Power-Off Base Drag,* Report No. TM-334-337, Convair Division, General Dynamics Corporation, Pomona, CA, 1959.

113. D. V. Rubin, *Tabulated Data for Secondary Flow Field and Nozzle Geometry Interactions on Base Drag,* Report RD-TN-66-2, US Army Missile Command, Redstone Arsenal, AL, February 1966.

114. Egon Schuett, *Lance Missile System Methods for the Evaluation of the Drag Contributions Attributed to Protuberances and Aerodynamic Tolerances,* Report No. 7-531 10/4R-R91, Ling Temco Vought Corp., Michigan Division, Warren, MI, February 1964.

115. E. W. Perkins, *Comparison* of *Experimental and Theoretical Normal Force Distributions (Including Reynolds Number Effects) on an Ogive-Cylinder Body at Mach Number 1.98,* NACA TM 3716, National Advisory Committee for Aeronautics, Washington, DC, 1956.

116. H. B. Reese, *Results of an Experimental Investigation to Determine the Aerodynamic Loadings on Three Saturn Payload Shapes,* Chrysler TN-AE-64-16 (ADDENDUM), Chrysler Corporation Space Division, New Orleans, LA, 10 November 1964.

117. J. E. Kain, C. M. Brown, Jr., and J. G. Lee, *Missile Aerodynamic Parameter and Structure Identification from Flight Test Data,* Report AFATL TR-77-129, The Analytic Science Company, Reading, MA, November 1977.

118. *National Wind-Tunnel Summary,* NASA-DOD-Summary, July 1961, Panel of the Aeronautics and Astronautics Coordination Board, Department of Defense and National Aeronautics and Space Administration, Washington, DC, 1961.

119. *Test Facilities Handbook,* Eleventh Edition, Arnold Engineering and Development Center, Arnold Air Force Station, TN, June 1979.

120. D. D. Baals and W. R. Corliss, *Wind Tunnels of NASA,* NASA SP-440, National Aeronautics and Space Administration, Washington, DC, 1981.

121. *High Reynolds Number Research-1980,* NASA Conference 2183, 8-9 December 1980, National Aeronautics and Space Administration, Washington, DC, 1981.

122. J. C. McMullen, *Wind Tunnel Testing Facilities at the Ballistic Research Laboratories,* Report BRL-MR-1292, US Army Ballistic Research Laboratories, Aberdeen Proving Ground, MD, 1960.

123. R. H. Curtin, Editor, *Technical Facilities Catalog,* Volumes I, II, and III, NASA NHB 8800.5A, National Aeronautics and Space Administration, Washington, DC, October 1974.

124. Lee Arnold, *Dynamic Measurements in Wind Tunnels,* AGARDograph II, Advisory Group for Aeronautical Research and Development, North Atlantic Treaty Organization, AD-09253 1, August 1955.

125. R. H. Prislin, *Free-Flight and Free-Oscillation Techniques for Wind-Tunnel Dynamic-Stability Testing,* JPL-TR-32-878, Jet Propulsion Laboratory, Pasadena, CA, March 1966.

126. *Proceedings of Symposium on Aeroelastic and Dynamic Modeling Technology,* RTD-TDR-63-4197, Research and Technology Division, Wright-Patterson Air Force Base, OH, March 1964.

127. H. H. Korst, *Approximate Determination* of *Jet Contours* Near *the Exit of Axially Symmetrical Nozzles and Basis for Plume Modeling,* Report TR-RD-72-14, US Army Missile Command, Redstone Arsenal, AL, 1972.

128. J. R. Burt, *An Investigation of the Aerodynamic Stabilizing Effectiveness of Several Split Flare Afterbody Configurations in the Presence of an Underexpanded Jet Plume at Transonic Mach Numbers,* Technical Report T-78-31, US Army Missile Research and Development Command, Redstone Arsenal, AL, 1978.

129. James H. Henderson, *An Investigation of Jet Plume Effects on the Stability Characteristics of a Body of Revolution in Conjunction With Fins of Various Geometry and Longitudinal Positions at*

Transonic Speeds (Sting-Mounted Model With Normal Jet Plume Simulator), Report TR-RD-75-37, US Army Missile Command, Redstone Arsenal, AL, 1975.

130. *US Standard Atmosphere,* Government Printing Office, December 1962.

Note:
1. Positive values of forces, moments, and angles are indicated by arrows.
2. Origins of wind and stability axes have been displaced from center of gravity for clarity.

C_A = axial force coefficient
C_L = lift coefficient
C_ℓ = roll moment coefficient
C_m = aerodynamic pitching moment coefficient
C_N = aerodynamic normal force coefficient
C_n = yawing moment coefficient
C_y = side-force coefficient
x, y, z = body-centered coordinate system
x_s, y_s, z_s = stability coordinate system
x_w, y_w, z_w = wind coordinate system

Figure 5-1. Rocket Axes—Showing Direction and Sense of Forces, Moments, and Angular Quantities
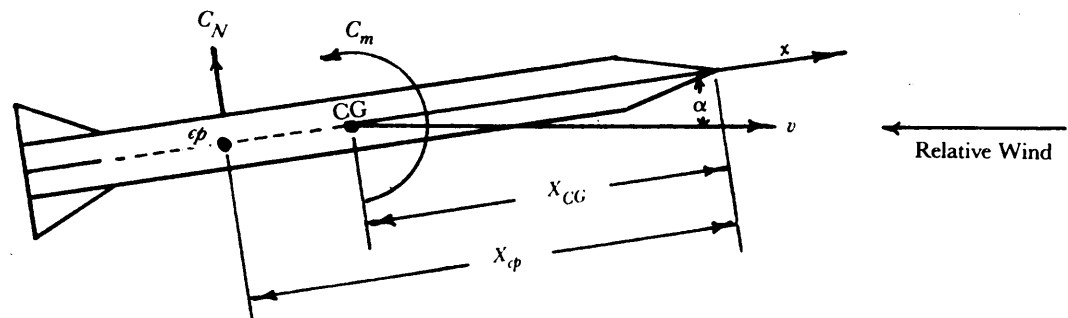
Figure 5-2. C_N, C_m and α Relationships
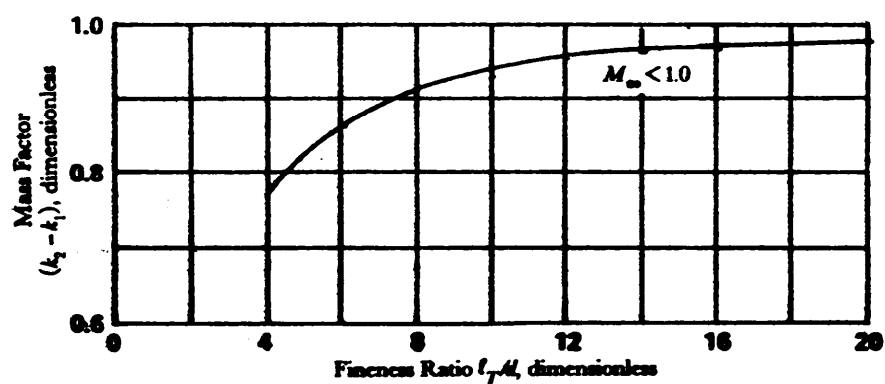
Figure 5-3. (k_2-k_1) vs Total Fineness Ratio l_T/d (Ref. 1)
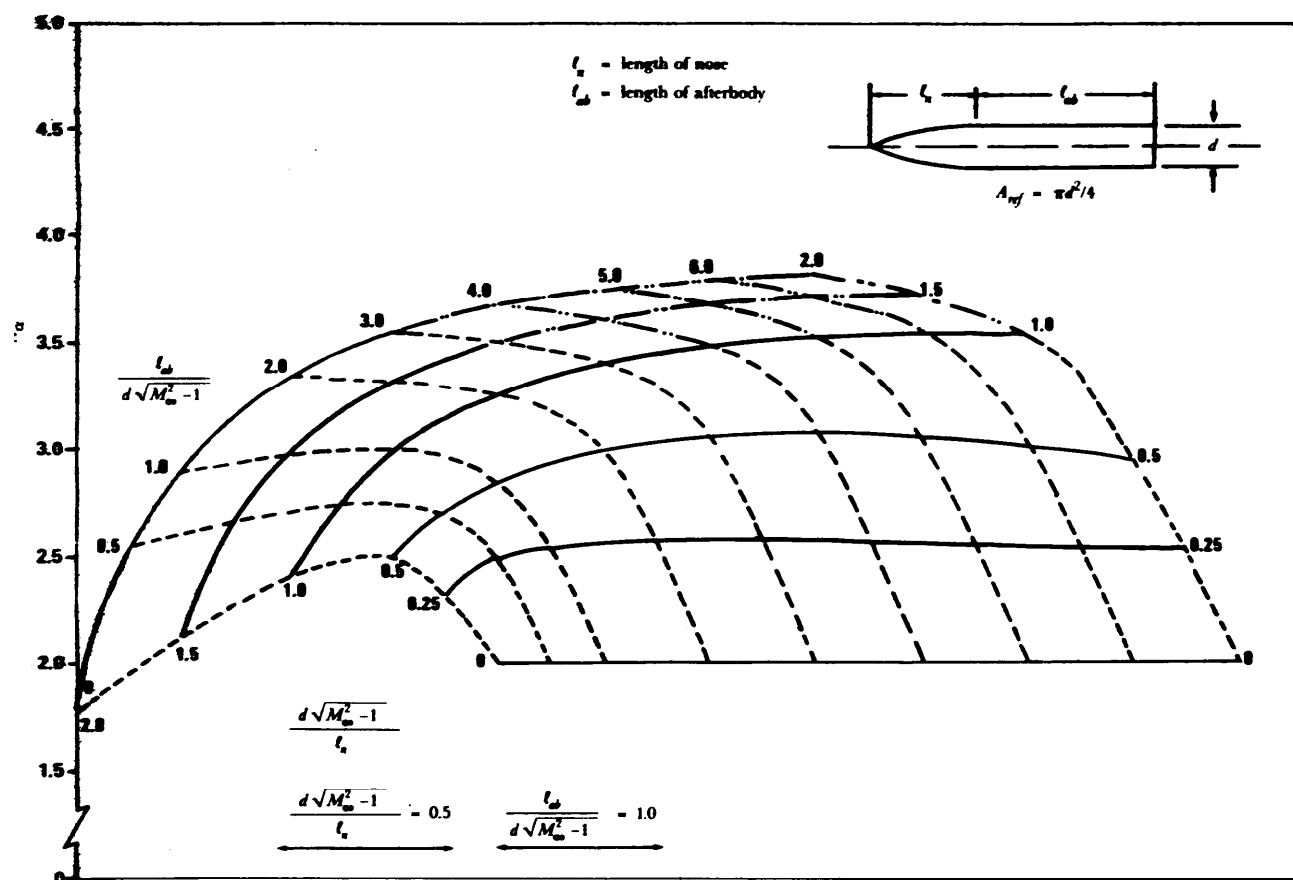
Figure 5-4. Normal Force Coefficient Gradient for Tangent Ogive-Cylinder Configurations
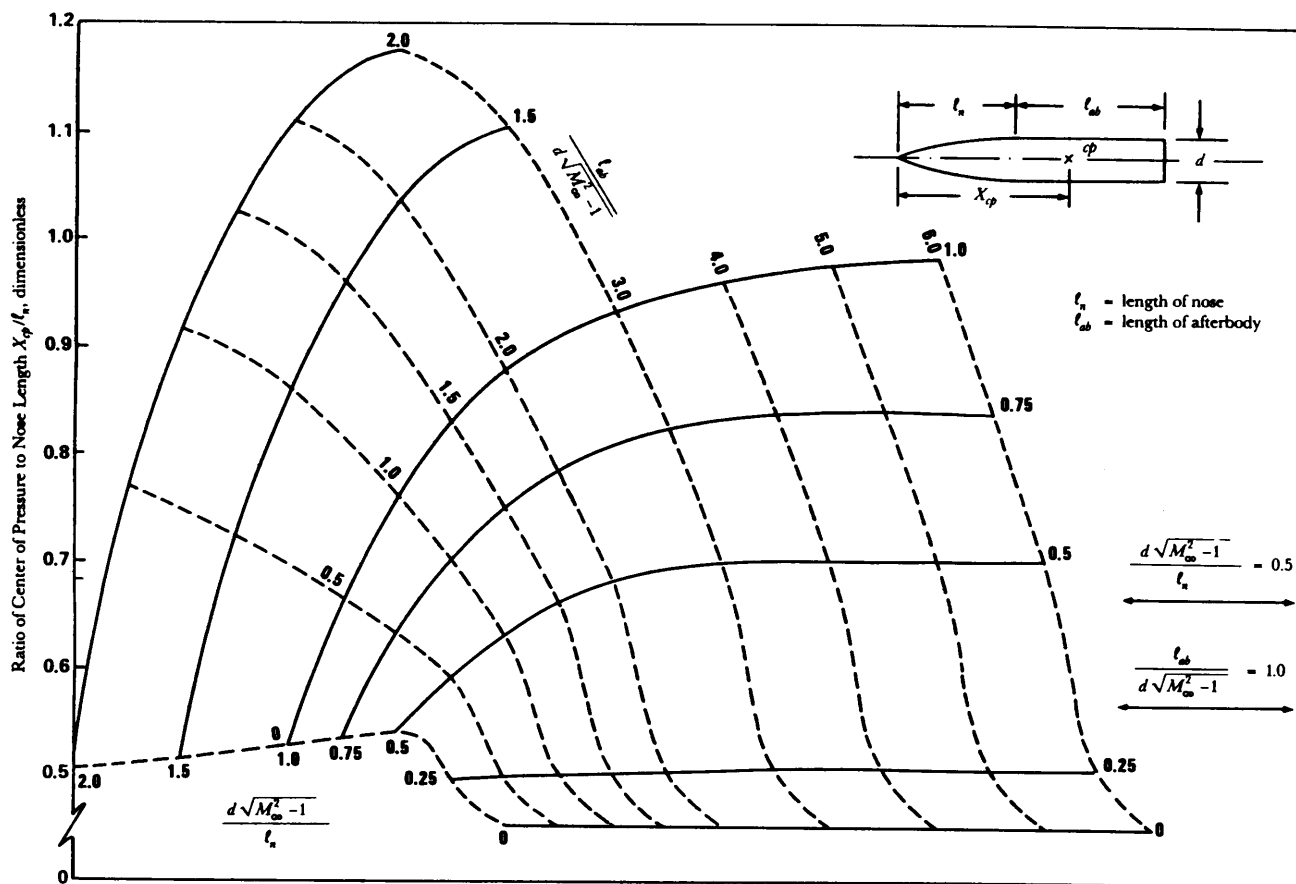
Figure 5-5. Center of Pressure for Tangent Ogive-Cylinder Configurations (Ref. 5)
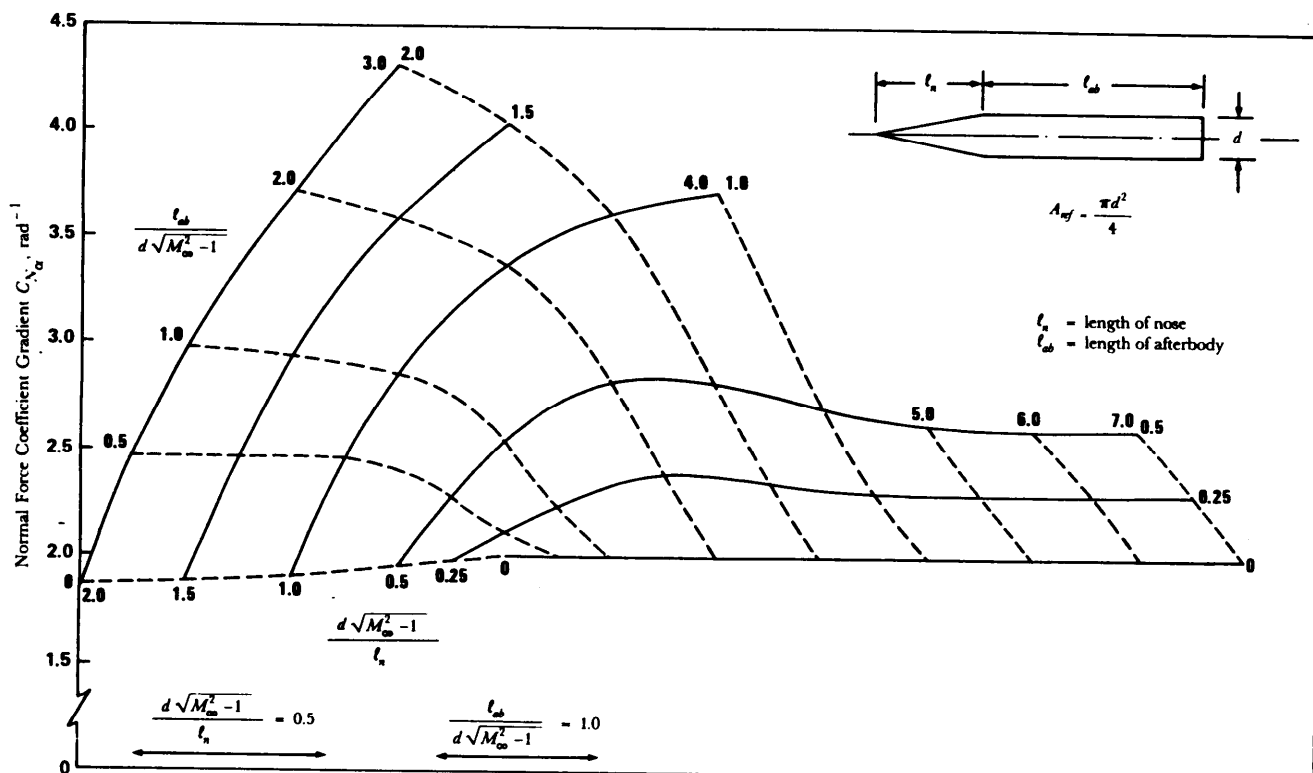
Figure 5-6. Normal Force Coefficient Gradient for Cone-Cylinder Configurations (Ref. 5)
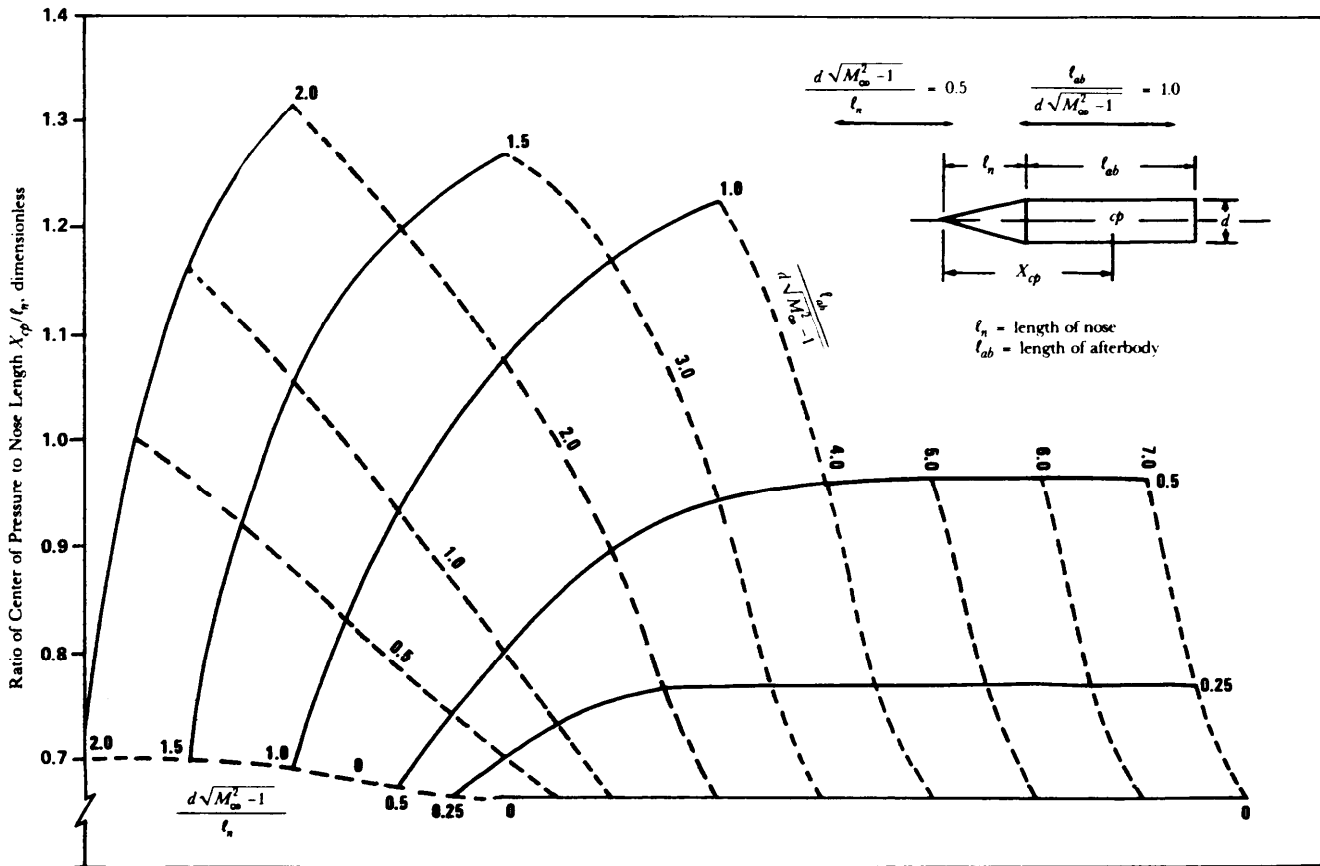
Figure 5-7. Center of Pressure for Cone-Cylinder Configurations (Ref. 5)
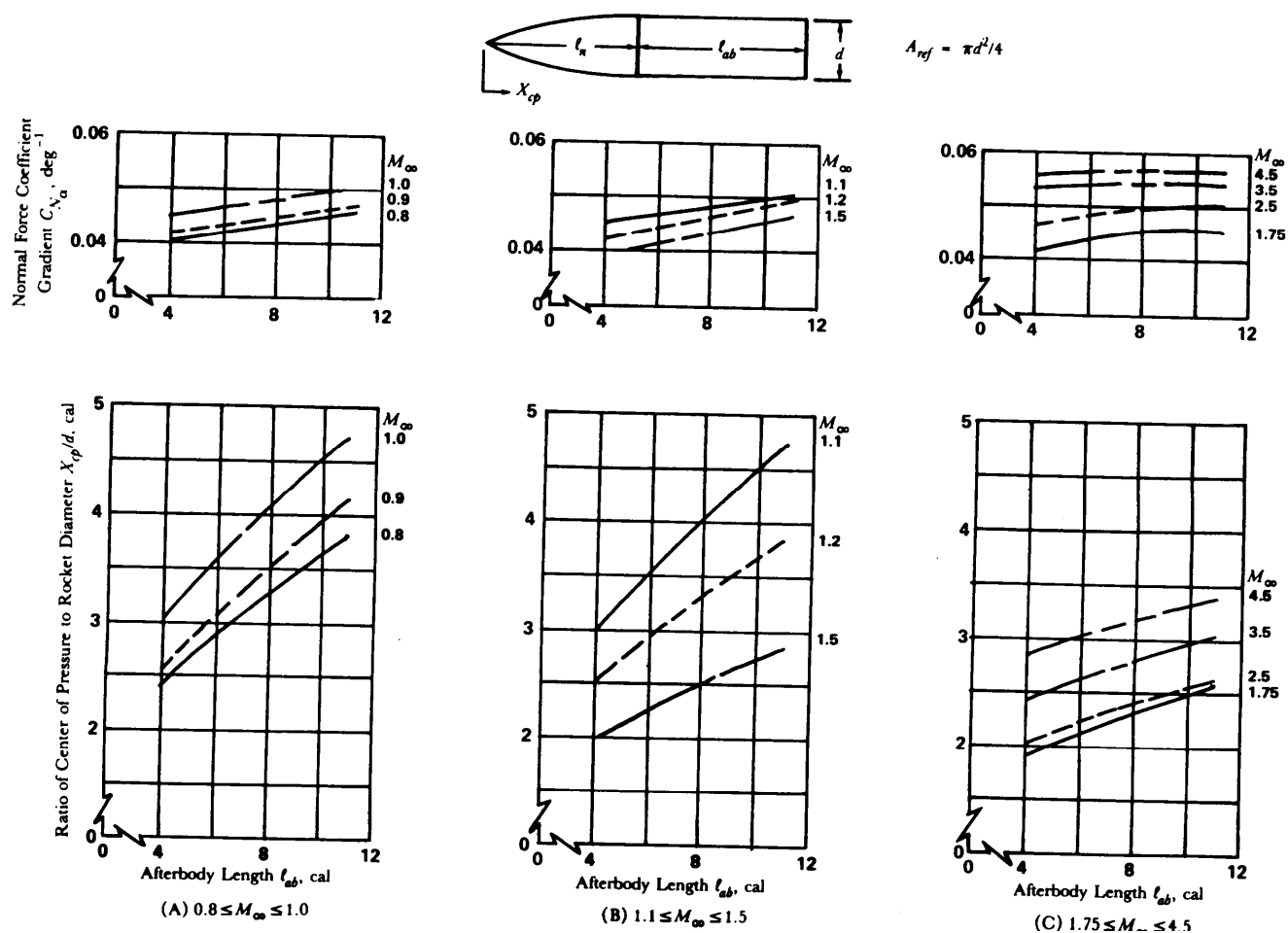
Figure 5-8. Normal Force Coefficient Gradient and Center of Pressure-4-cal Tangent Ogive With Varying Afterbody Lengths (Ref. 6)

Figure 5-9. Normal Force Coefficient Gradient and Center of Pressure—7.125-deg Cone With Varying Afterbody Lengths (Ref. 6)

Figure 5-10. Normal Force Coefficient Gradient and Center of Pressure—1/2-Power Nose With Varying Afterbody Lengths (Ref. 6)

MIL-HDBK-762(MI)
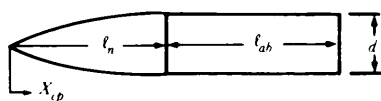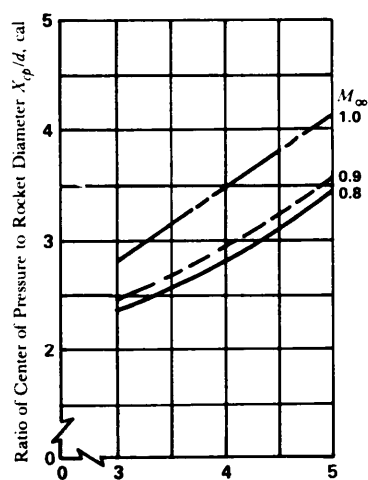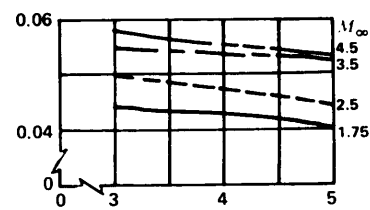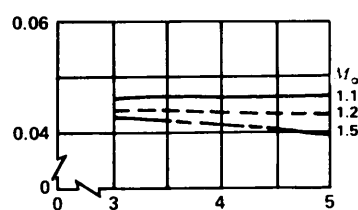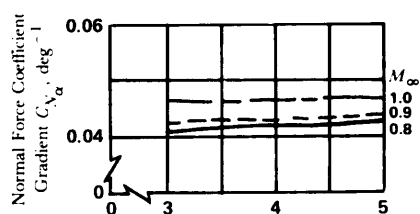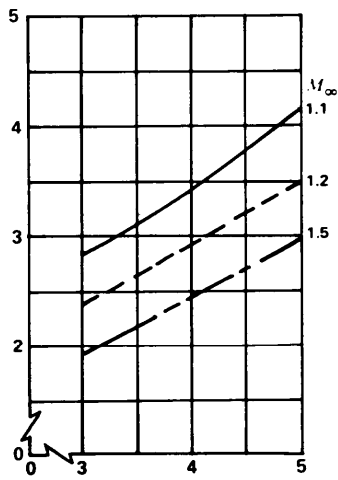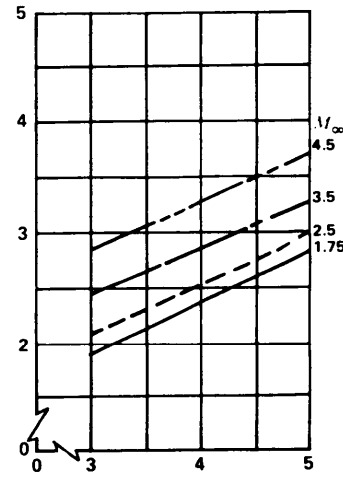
Figure 5-11. Normal Force Coefficient Gradient and Center of Pressure—Varying Tangent Ogive Nose Lengths With Constant Afterbody Length of 6 cal (Ref. 6)
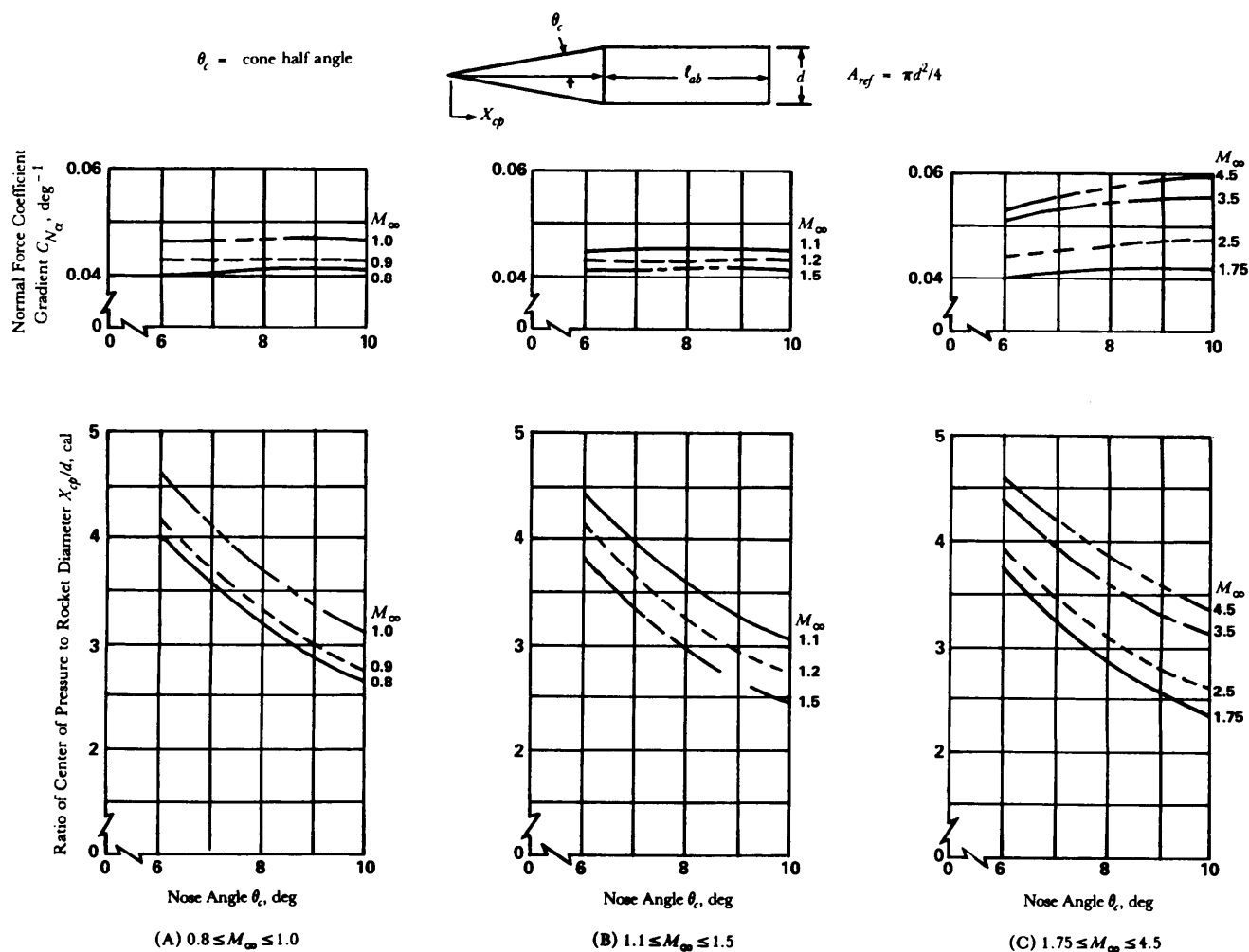
Figure 5-12. Normal Force Coefficient Gradient and Center of Pressure-Varying Conical Nose Angle With Constant Afterbody Length of 6 cal (Ref. 6)

Figure 5-13. Normal Force Coefficient Gradient and Center of Pressure—Varying n-Power Nose Shape With Constant Afterbody Length of 6 cal (Ref. 6)

MIL-HDBK-762(MI)
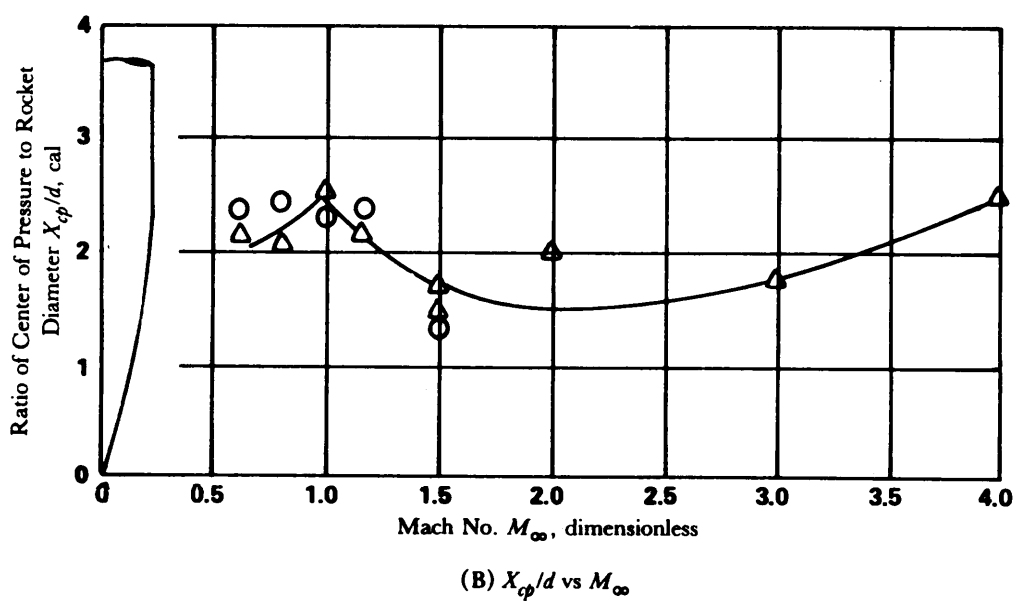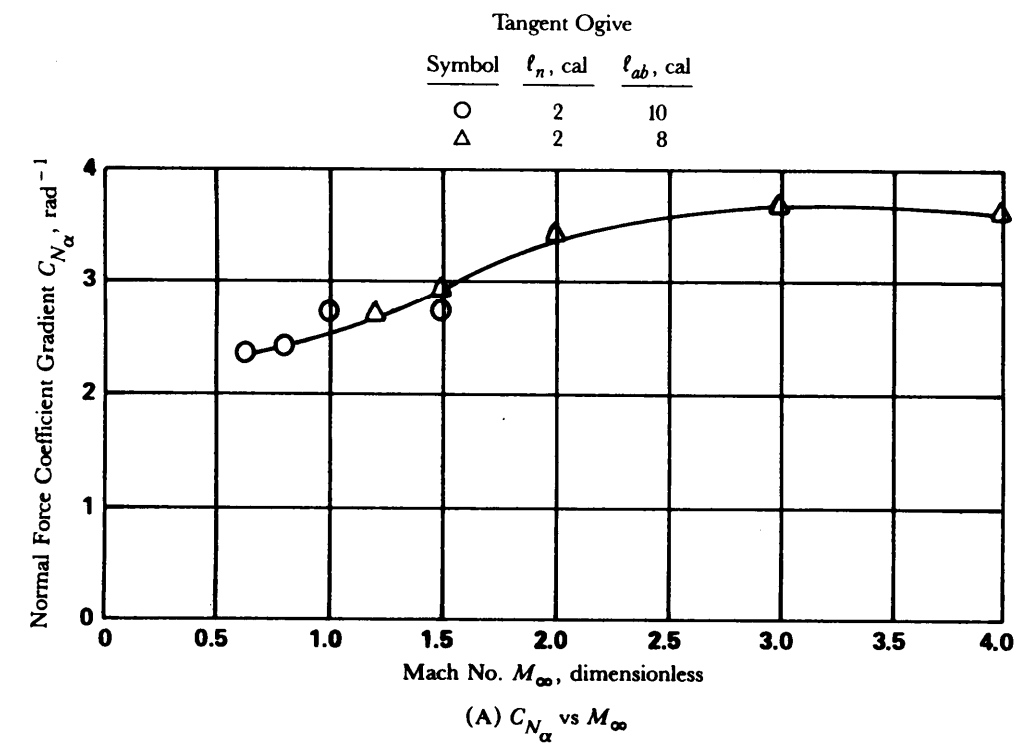
Figure 5-14. Variation of Normal Force Coefficient Gradient and Center of Pressure vs Mach for 2-cal Ogive Cylinders (Ref. 7)

Symbol	ℓ_n, cal	ℓ_{ab}, cal
O	3	10

(A) C_{N_α} vs M_∞

(B) X_{cp}/d vs M_∞
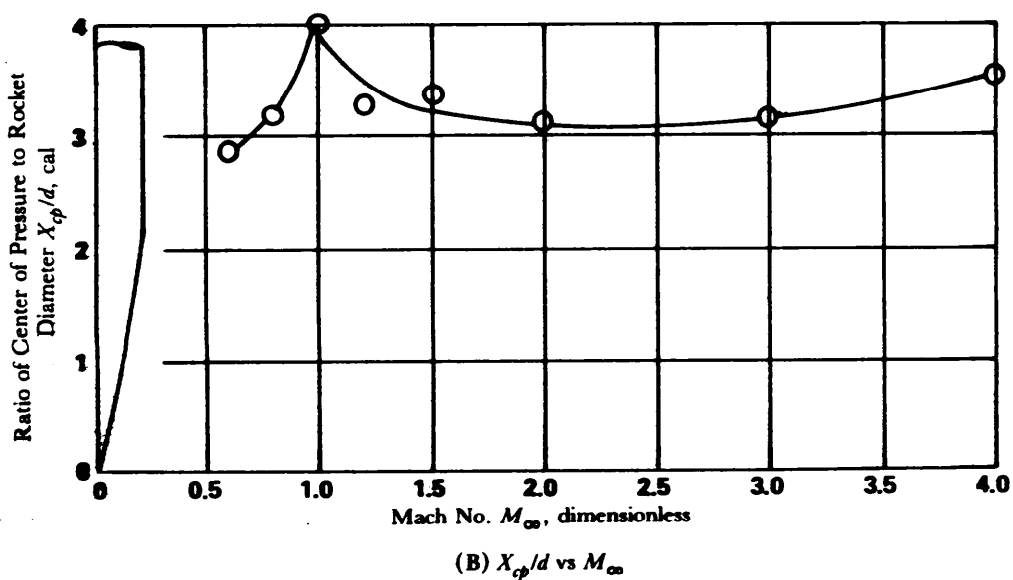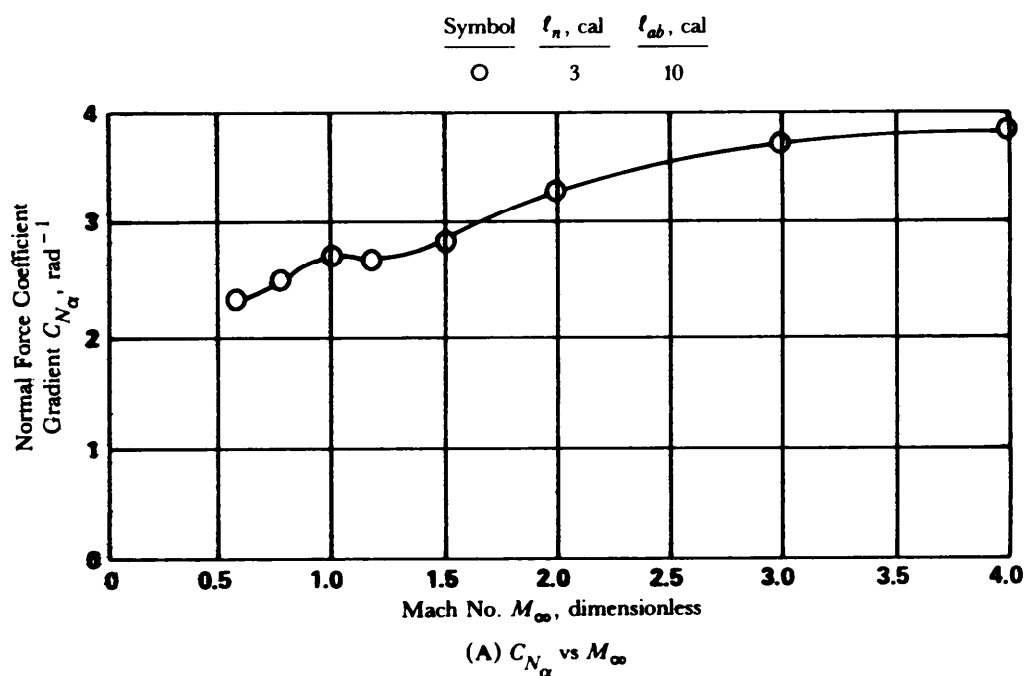
Figure 5-15. Variation of Normal Force Curve Gradient and Center of Pressure vs Mach Number for 3-cal Ogive Cylinders (Ref. 7)

(A) C_{N_α} vs M_∞
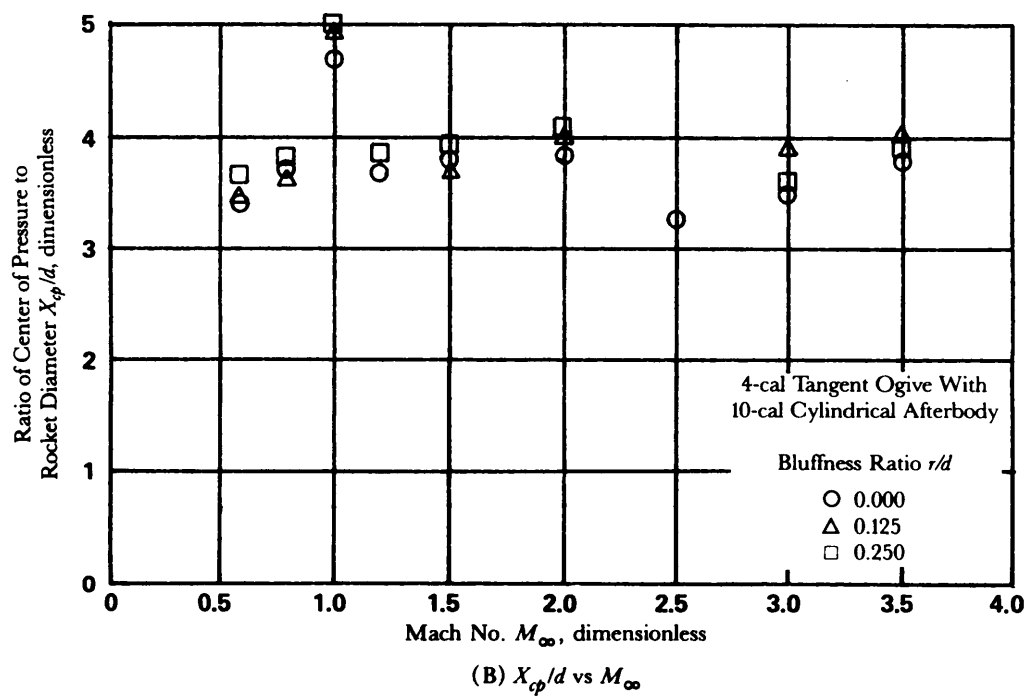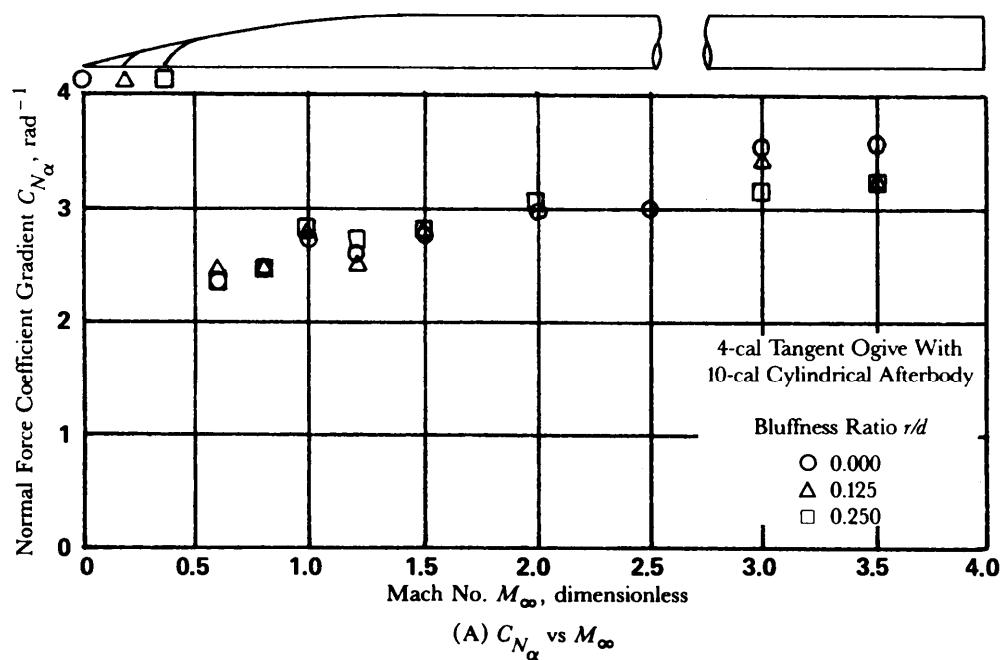
(B) X_{cp}/d vs M_∞

Figure 5-16. Effect of Nose Blunting of a 4-cal Ogive on Normal Force Coefficient Gradient and Center of Pressure (Ref. 7)

(A) C_{N_α} vs M_∞
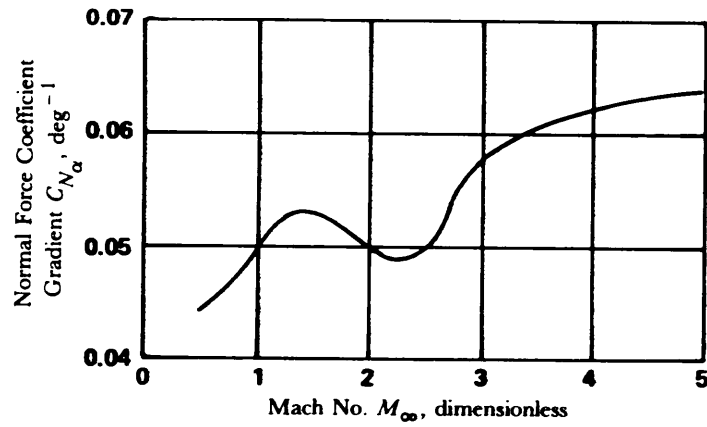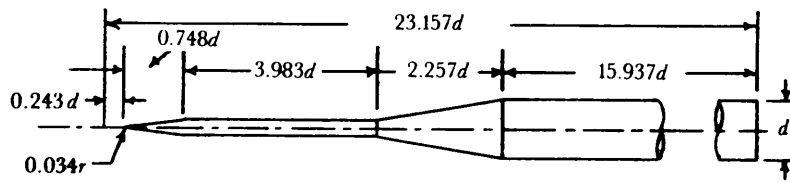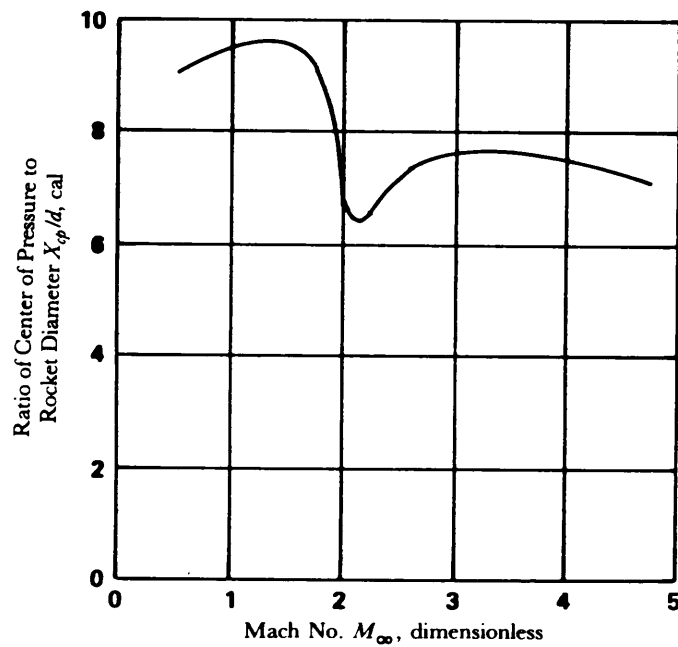
(B) X_{cp}/d vs M_∞

Figure 5-17. Some Aerodynamic Characteristics of a Spike-Nosed Rocket
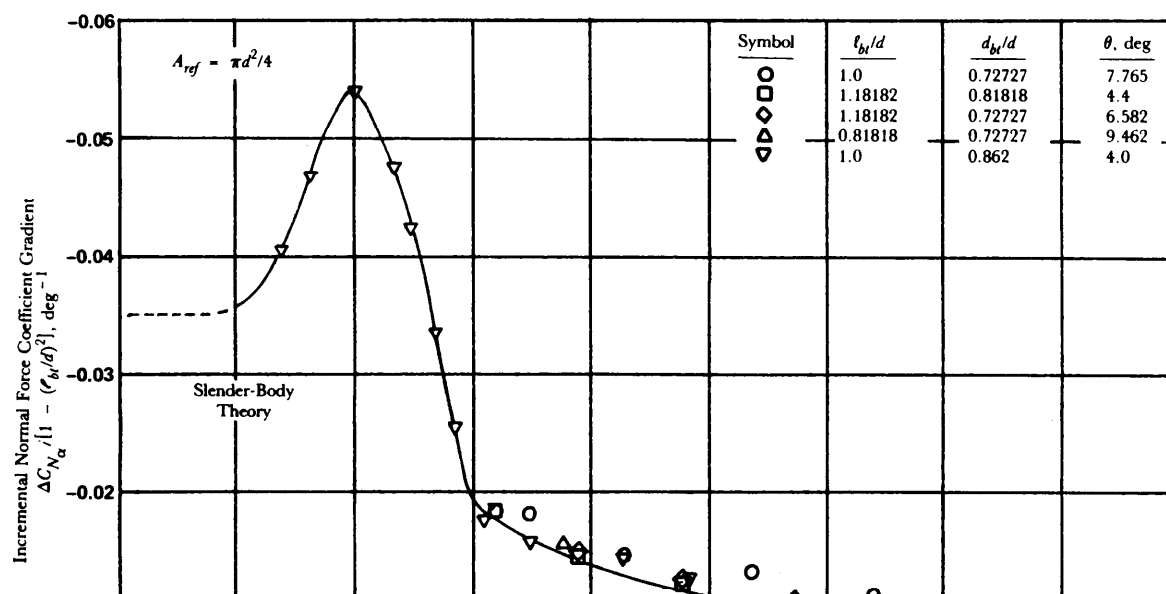
Figure 5-18. Boattail Normal Force Correlation Coefficient (Ref. 11)
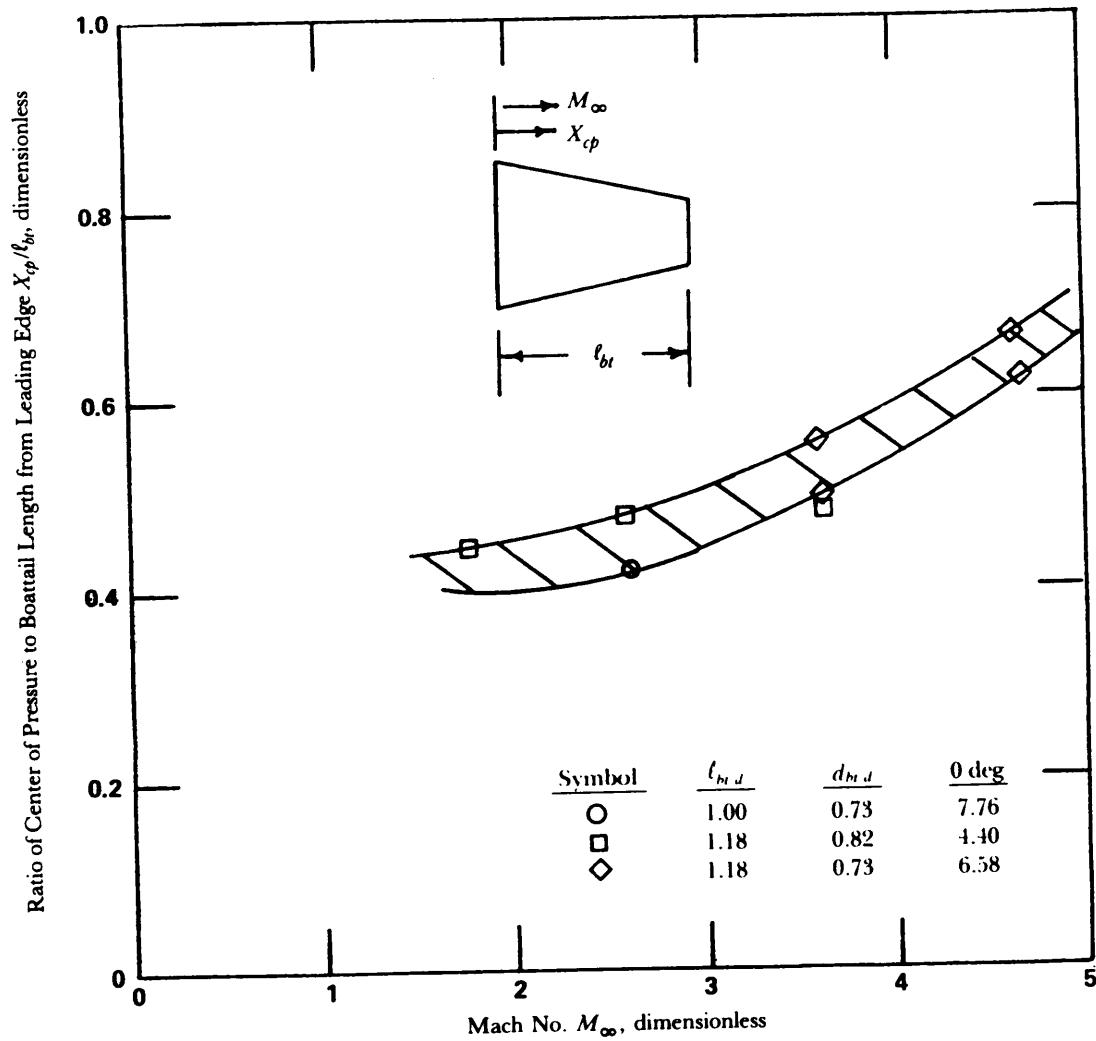
Figure 5-19. Ratio of Boattail Center of Pressure to Boattail Length (Ref. 11)

(A) C_{m_α} vs M_∞

(B) C_A vs M_∞

(C) C_{N_α} vs M_∞
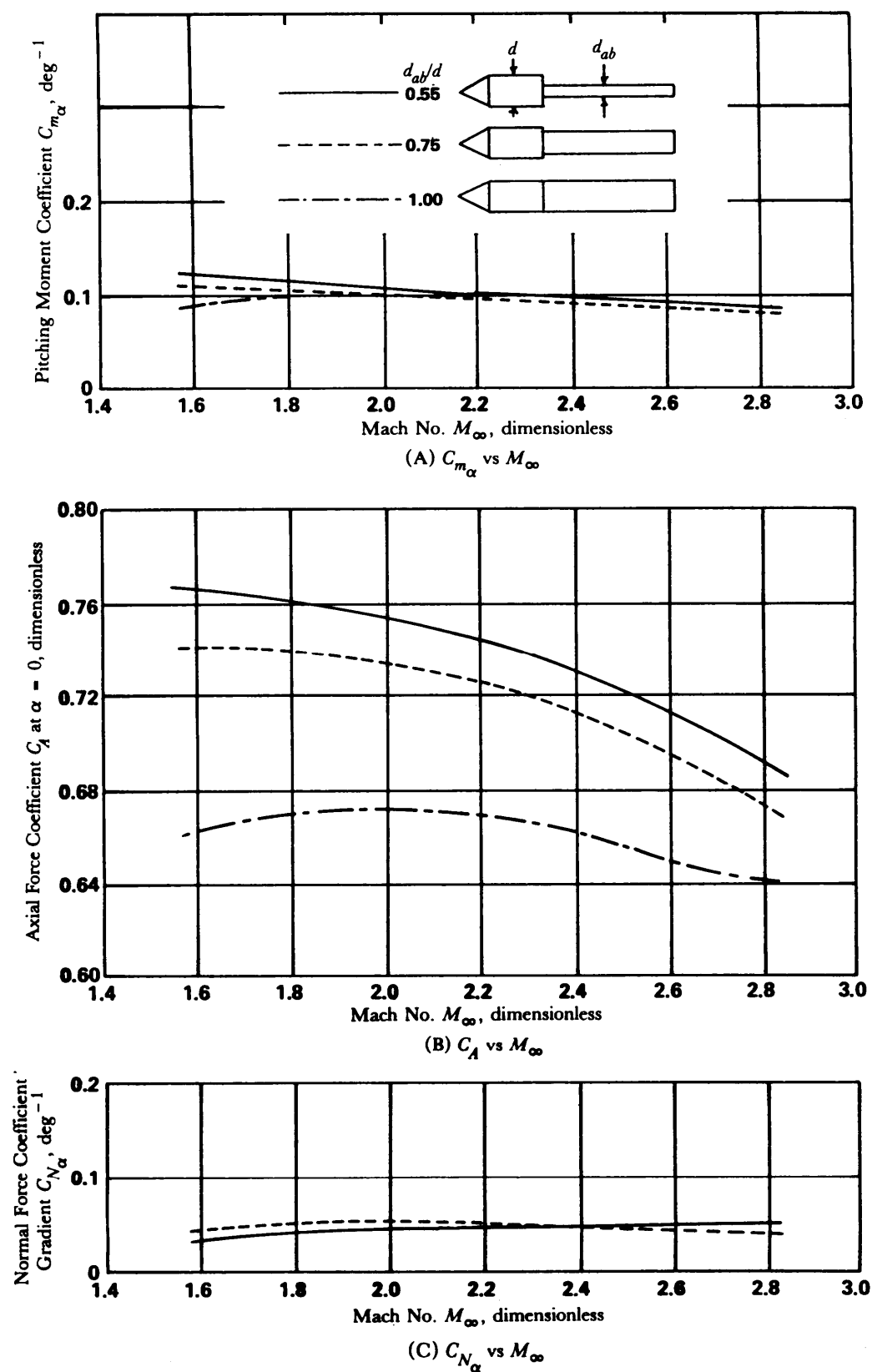
Figure 5-20. Effect of Afterbody Diameter to Head Diameter Tatio on Aerodynamic Parameters (Ref. 12)
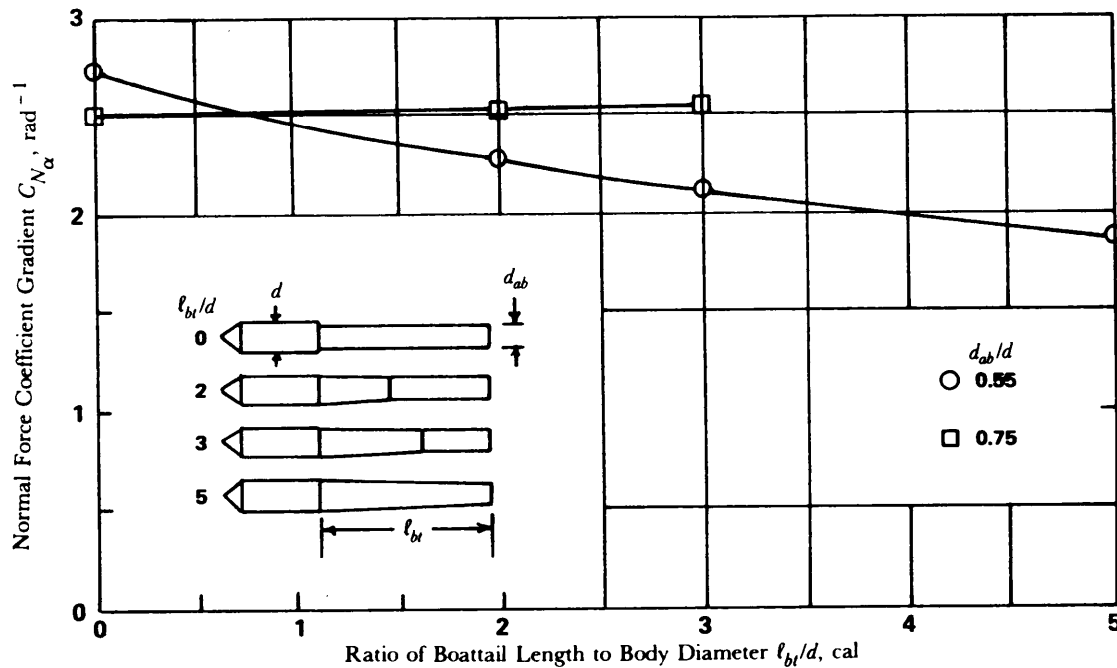
Figure 5-21. Normal Force Coefficient Gradient vs Boattail Length to Afterbody Diameter Ratio at M_∞ = 2.2 (Ref. 12)
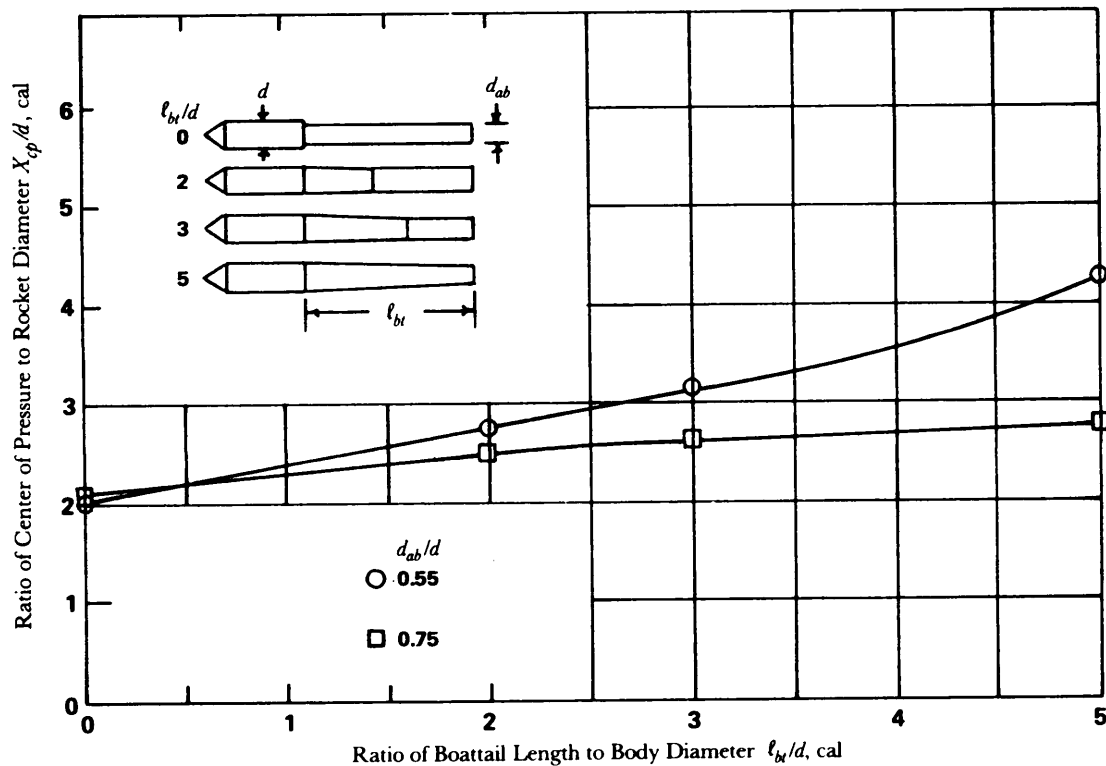
Figure 5-22. Center of Pressure vs Boattail Length to Afterbody Diameter Ratio at M_∞ = 2.2 (Ref. 12)

(Dashed lines indicate shroud position.)
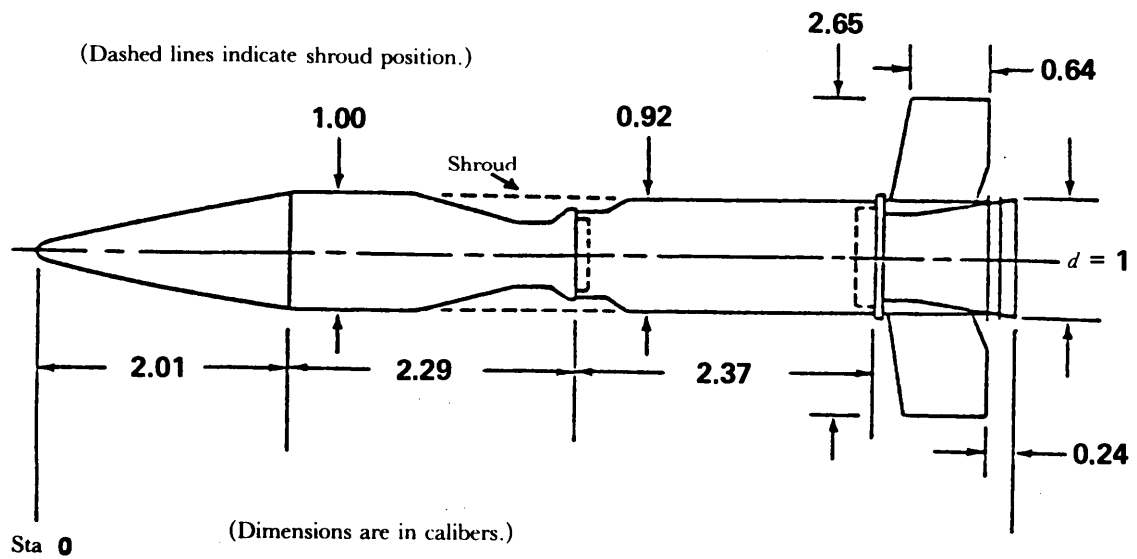
Figure 5-23 Rocket With Necked-Down Center Body (Ref. 13)
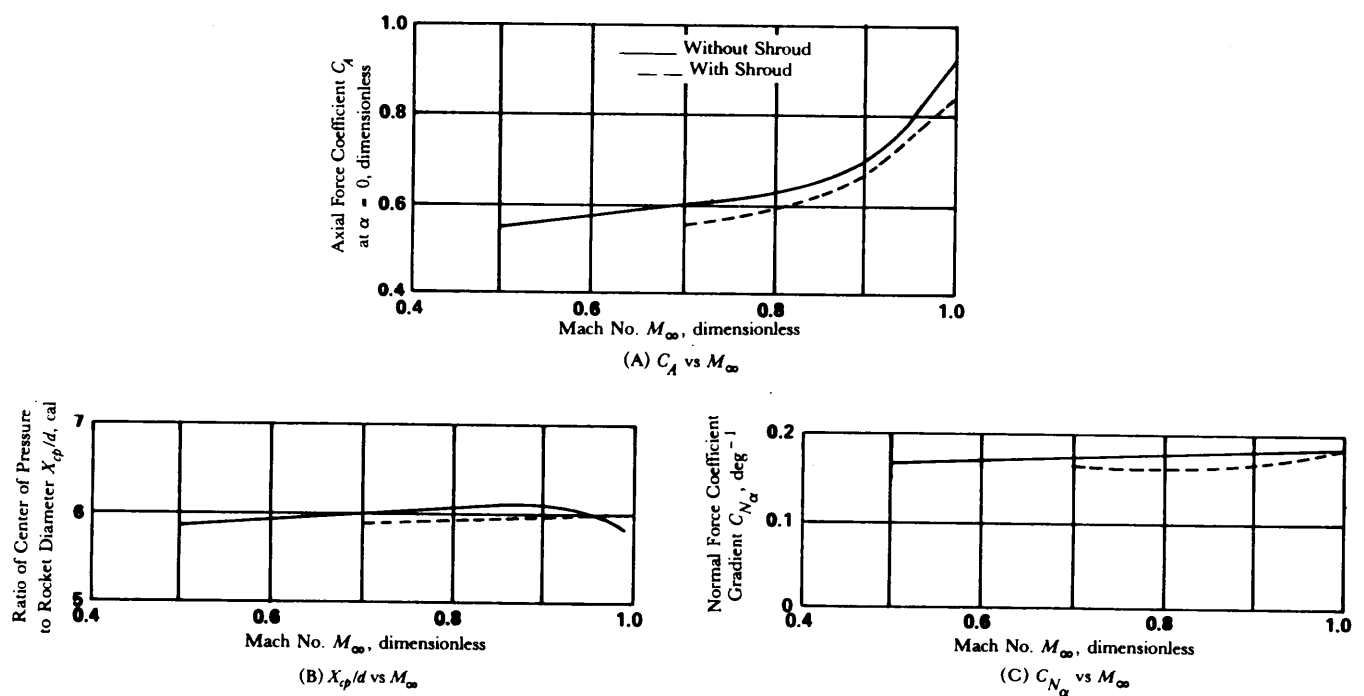
Figure 5-24. Aerodynamic Characteristics of Necked-Down Center Body With and Without Shroud (Ref. 13)
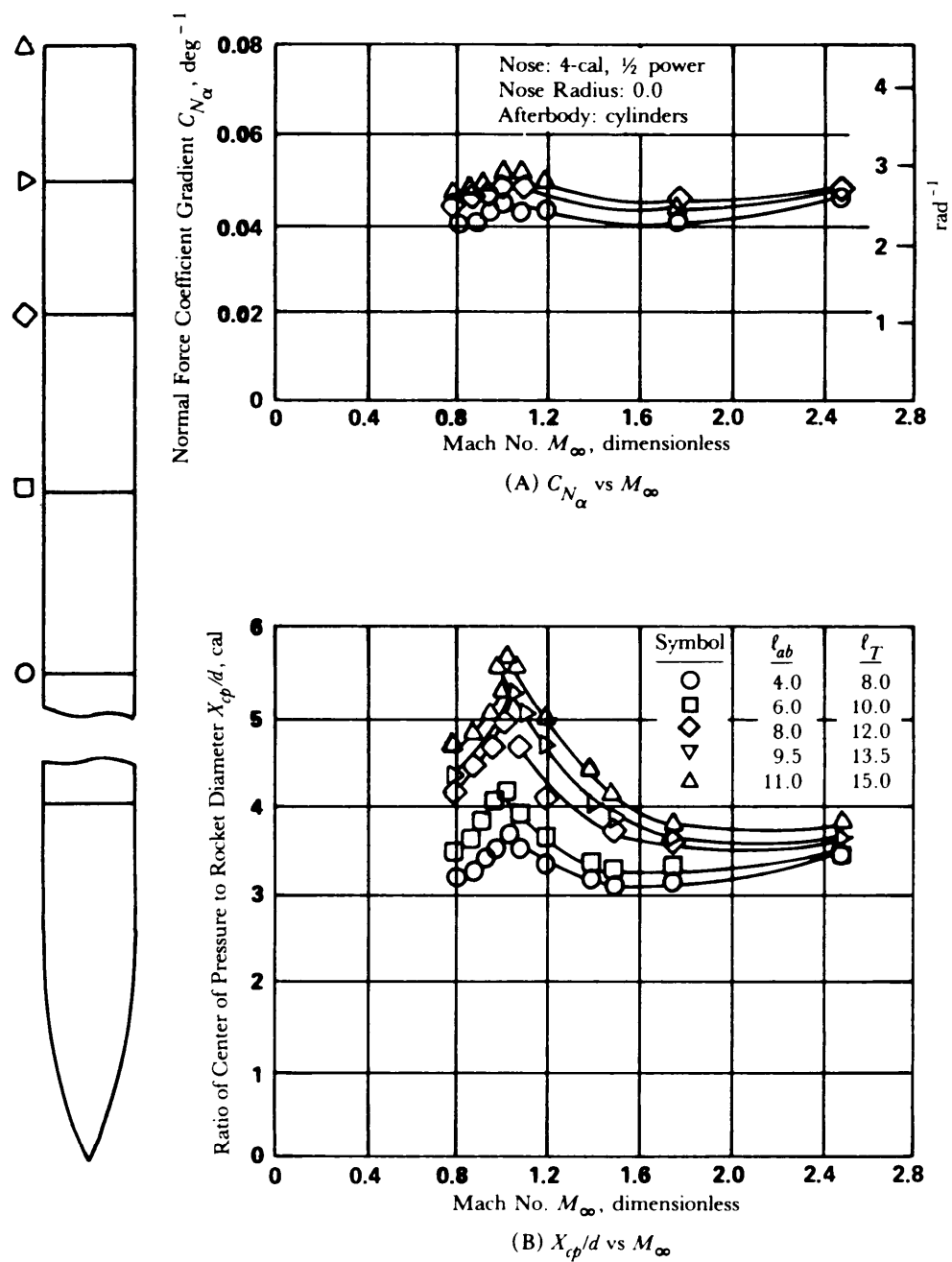
Figure 5-25. Normal Force Coefficient Gradient and Center of Pressure Over Rocket Diameter Ratio vs Mach Number for Family of Nose-Cylinder Configurations—4-cal Nose (Ref. 6)
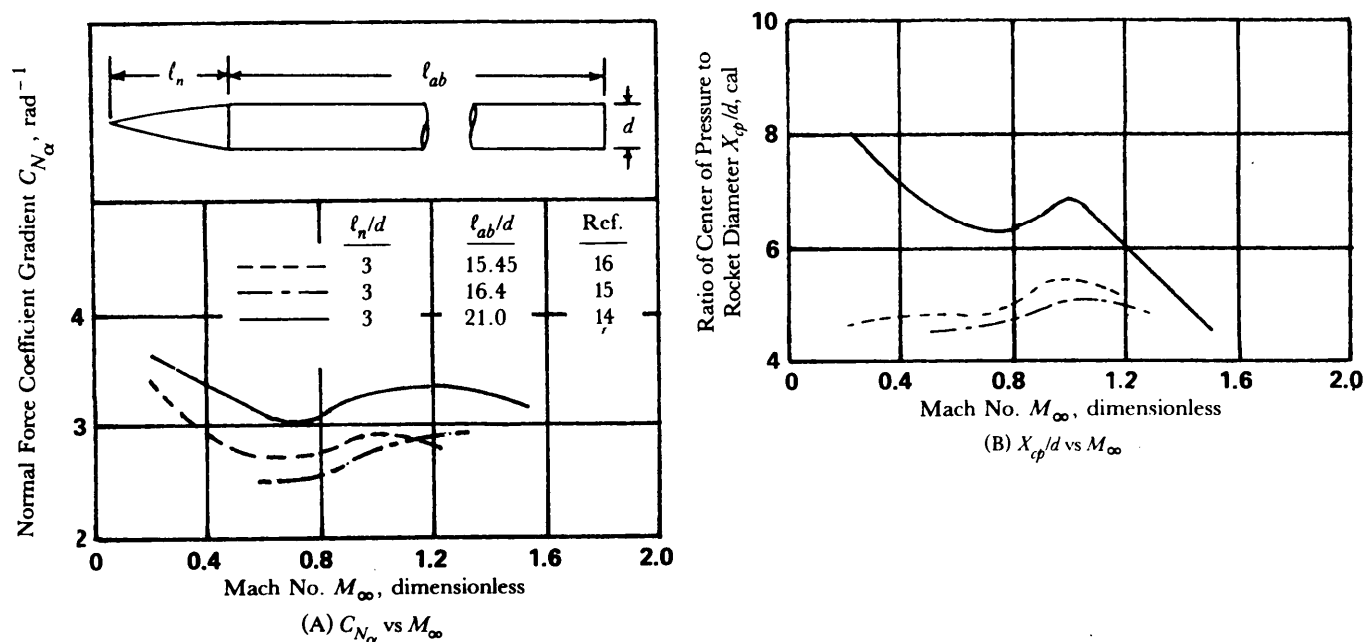
Figure 5-26. Normal Force Coefficient Gradient and Center of Pressure Over Rocket Diameter vs Mach Number for Family of Nose Cylinder Configurations—3-cal Tangent Ogive Nose (Refs. 14, 15, 16)
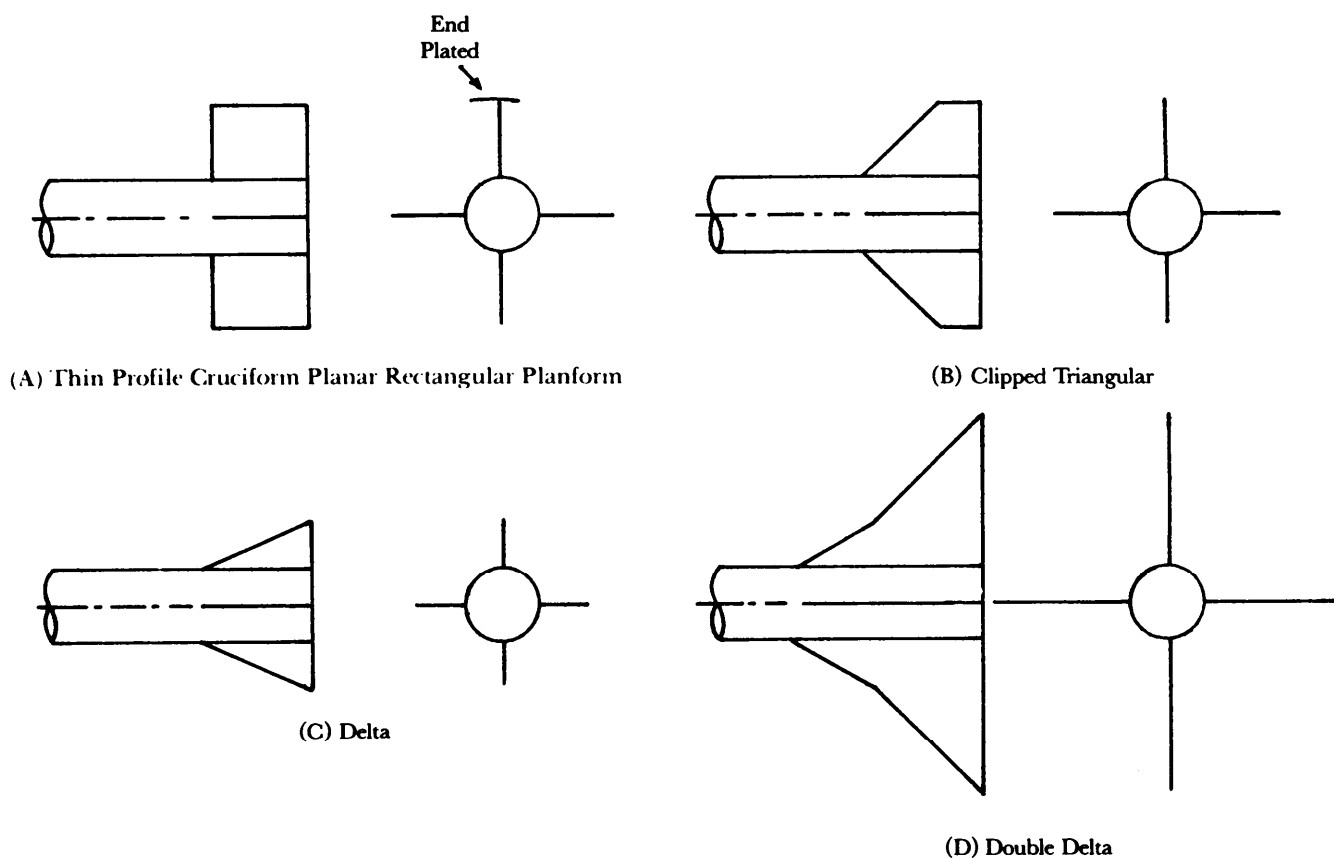
Figure 5-27. Typical Free Rocket Stabilizing Devices

Fully
Open

Partially
Open

Fully
Closed
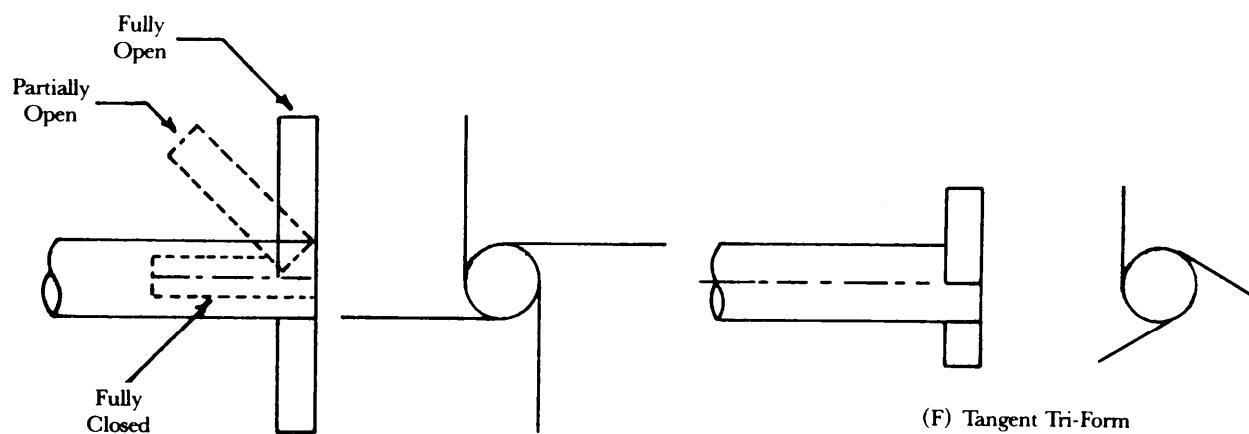
(E) Tangentially Folding

(F) Tangent Tri-Form

(G) Conical Flare—Solid

(Petals 5 and 6 are
omitted for clarity.)
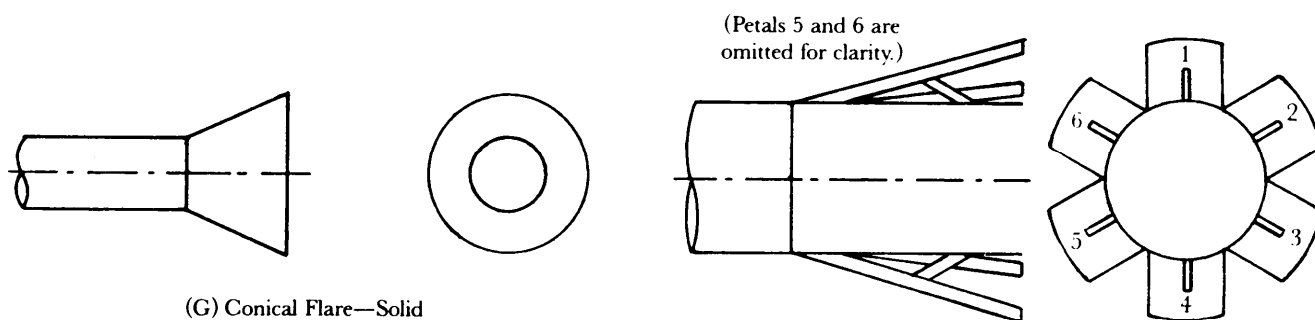
(H) Conical Flare—Split Petal

Support
Post

Cutaway
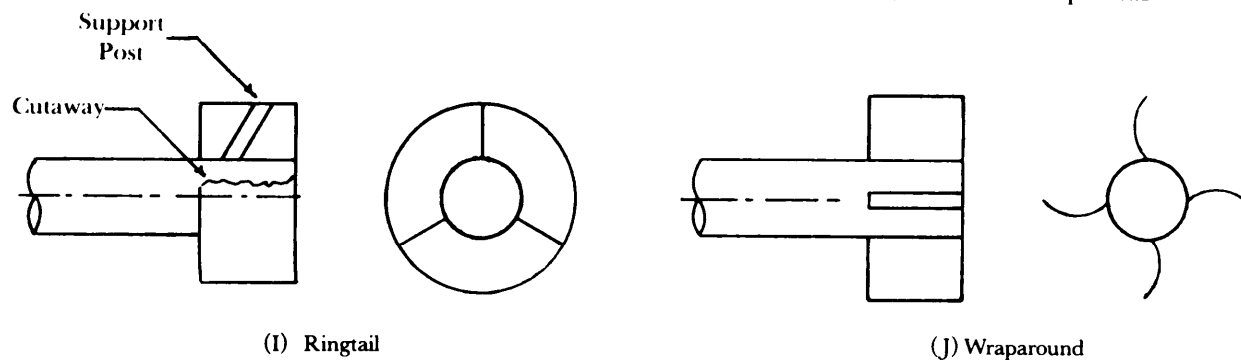
(I) Ringtail

(J) Wraparound

Figure 5-27. (cont'd)
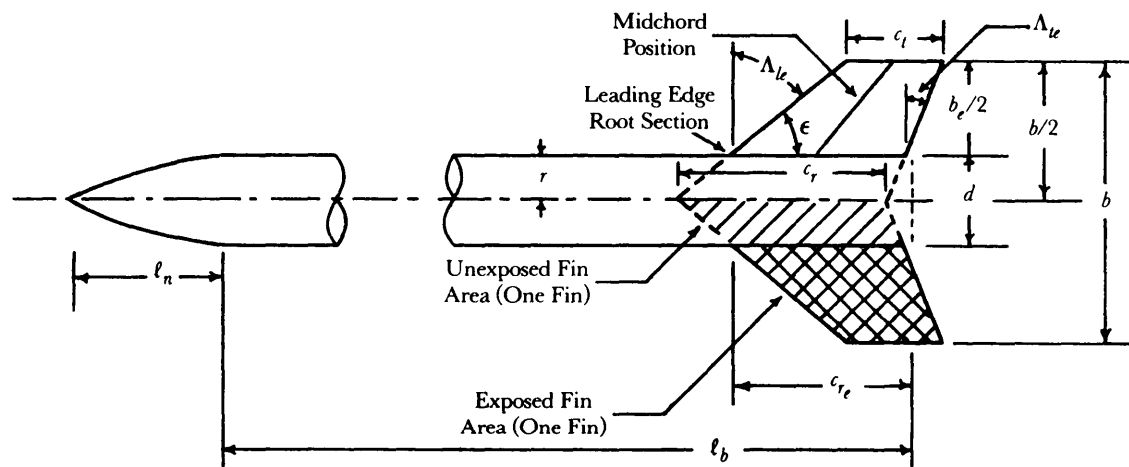
b = span or total span, m

$b/2$ = semispan, m

$b_e/2$ = exposed semispan, m

c_r = root chord length of hypothetical extension of fin, m

c_{r_e} = exposed root chord length, m

c_t = tip chord length, m

d = rocket diameter, m

ℓ_b = body length, m or cal

ℓ_n = nose length, m or cal

ϵ = included angle of fin leading edge, rad

Λ_{le} = leading edge sweep angle, rad

Λ_{te} = trailing edge sweep angle, rad

Figure 5-28.   Nomenclature of Some Typical Rocket Components

In this configuration the term "exposed" is applicable—i.e., the notation is $(AR)_e$, $b_e/2$, c_{r_e}, λ_e, S_{F_e}, etc.

In this configuration of two joined fin panels, the notation is AR, b, c_r, S_F, etc.

(A) Fin-Body Configuration

(B) Isolated Wing Formed by Joining Two Panels at c_r

(C) Extension of Fin Panels Into Body
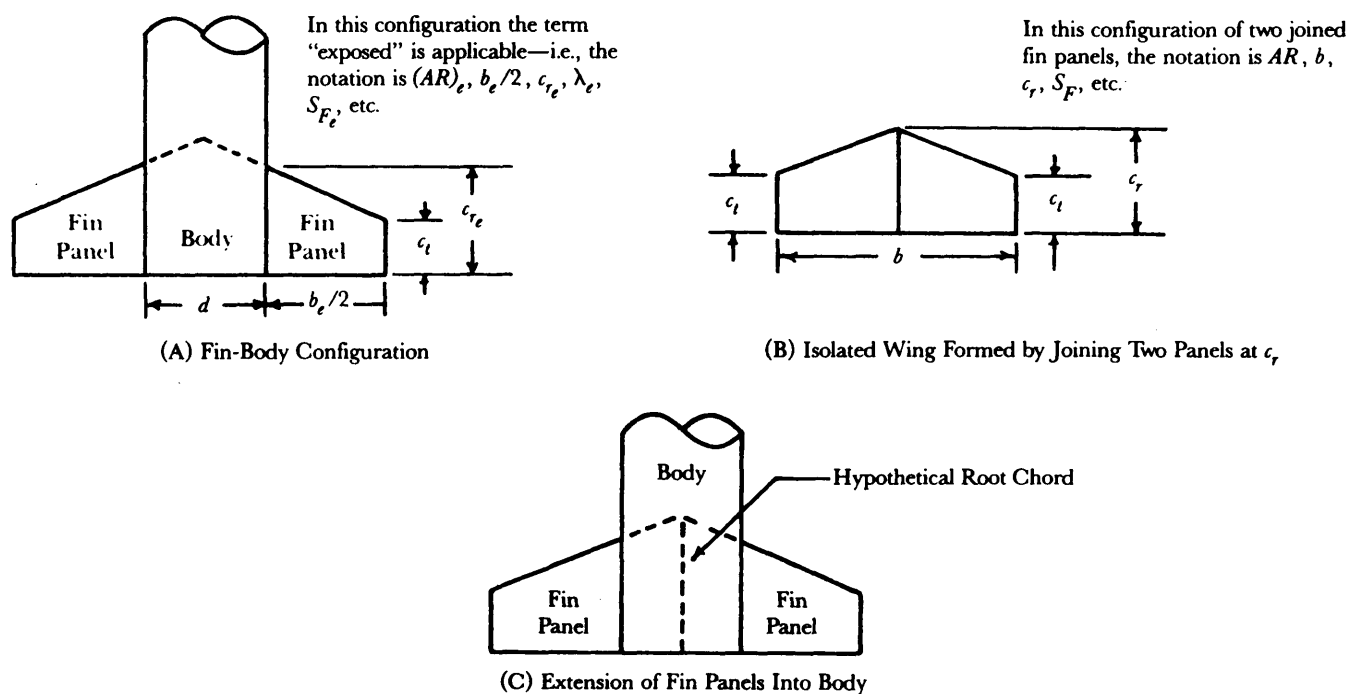
Figure 5-29. Illustration of Exposed Fin-Body and Isolated Wing Geometry, and Accompanying Notation

5-103
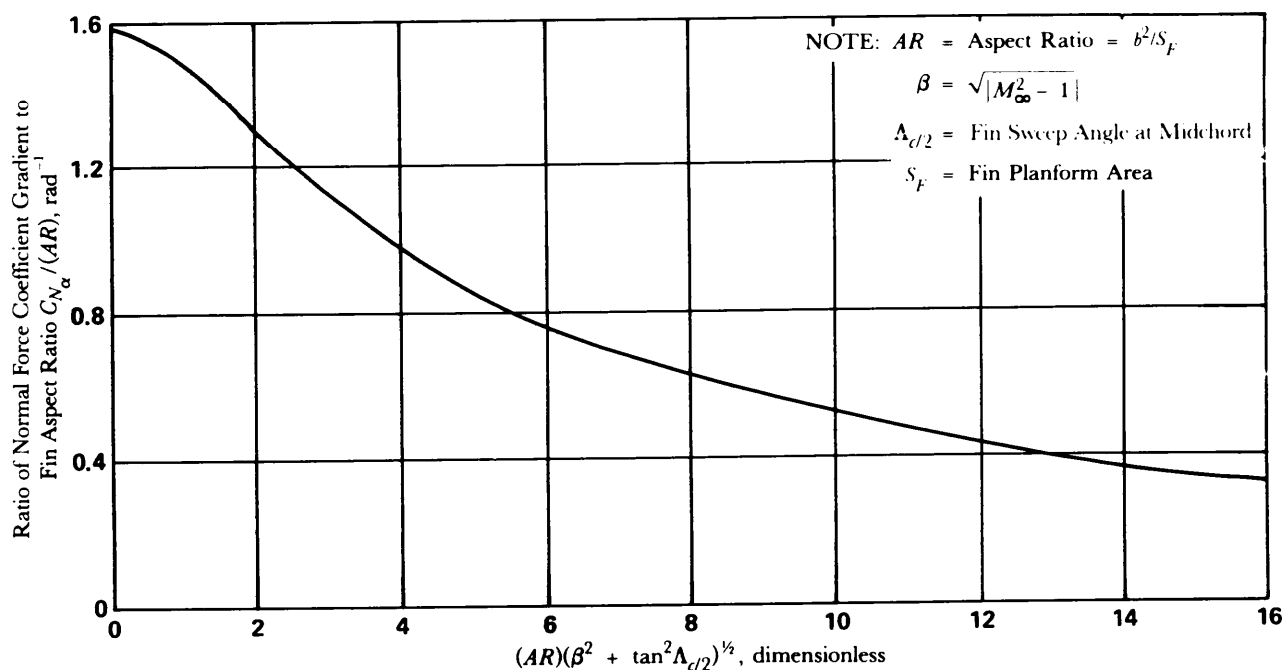
Figure 5-30. Subsonic Fin Normal Force Coefficient Gradient (Adapted from Ref. 22)
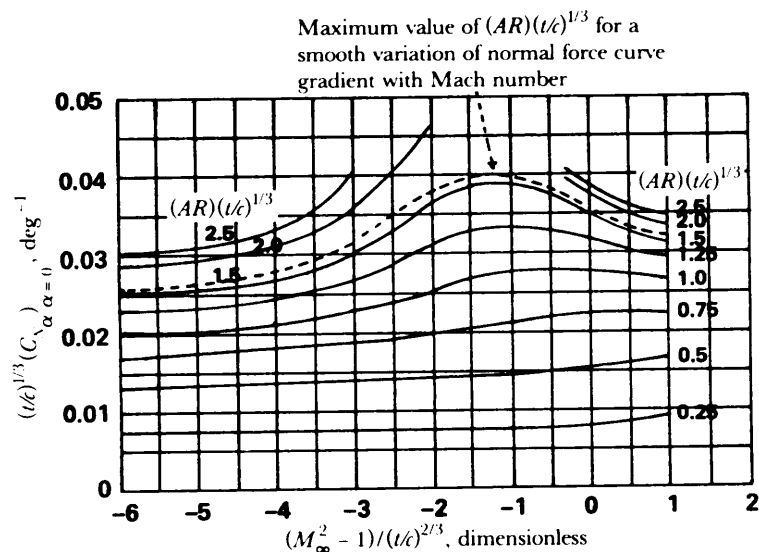
Figure 5-31. Summary Curves of the Generalized Normal Force Gradient for Rectangular Fins at Transonic Speeds (Ref. 23)
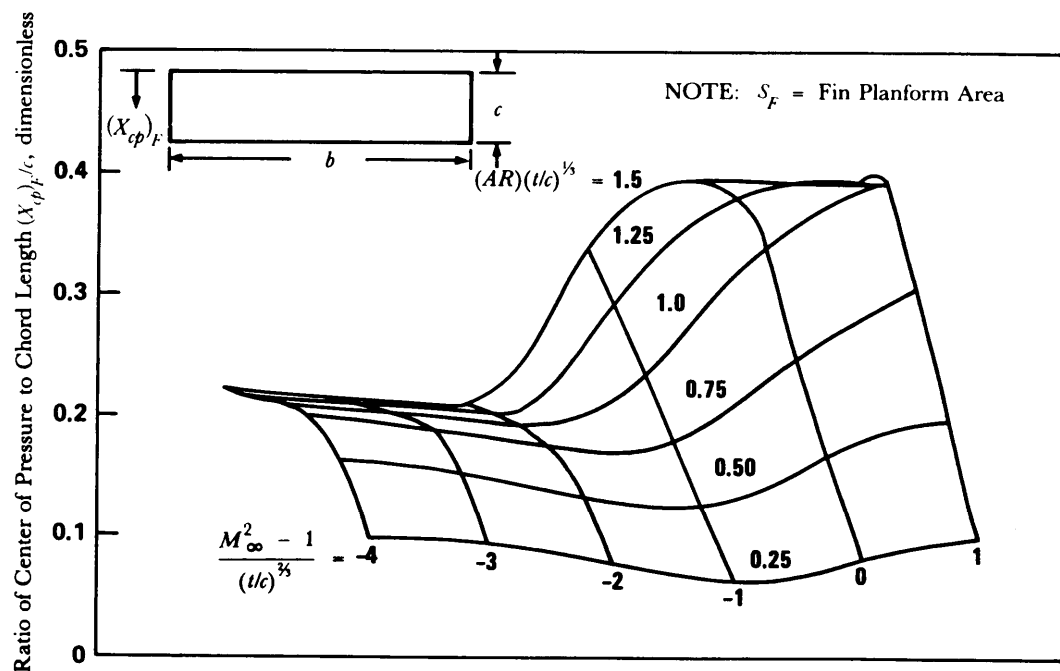
Figure 5-32.   Center of Pressure for Rectangular Fins at Transonic Speeds (Ref. 18)
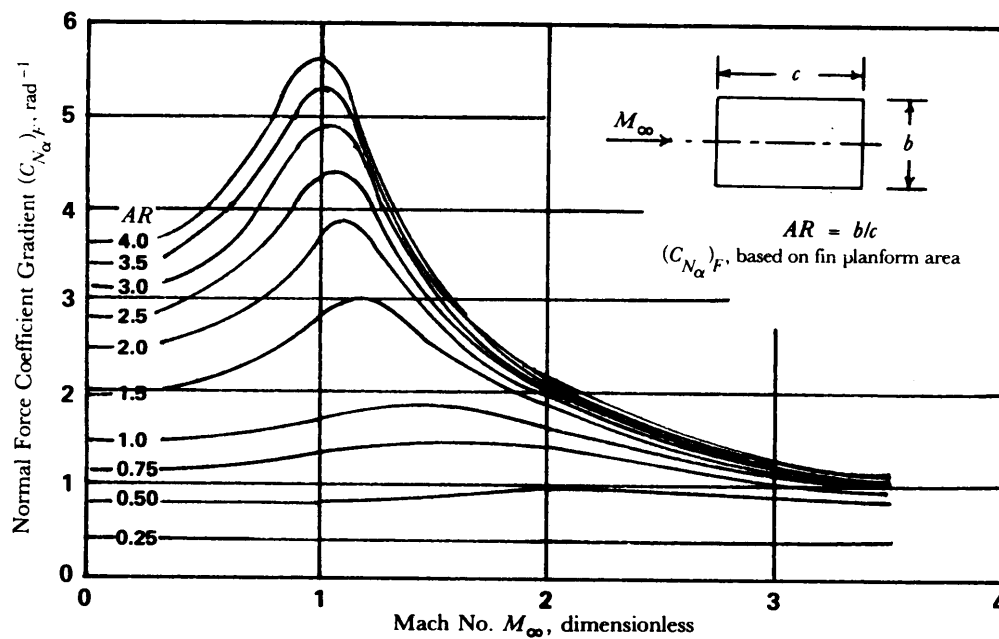
Figure 5-33. Linear Theory Normal Force Gradient of Rectangular Fins vs Mach Number (Ref. 19)
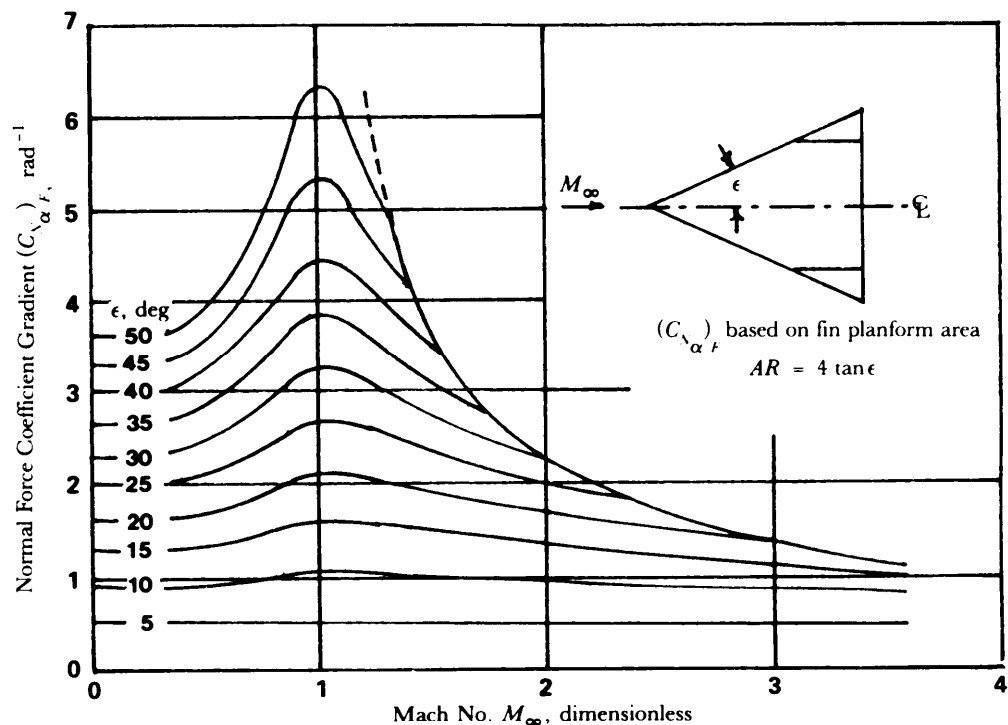
Figure 5-34. Linear Theory Normal Force Gradient of Delta Fins vs Mach Number (Ref. 19)

(A) $\lambda = 0$
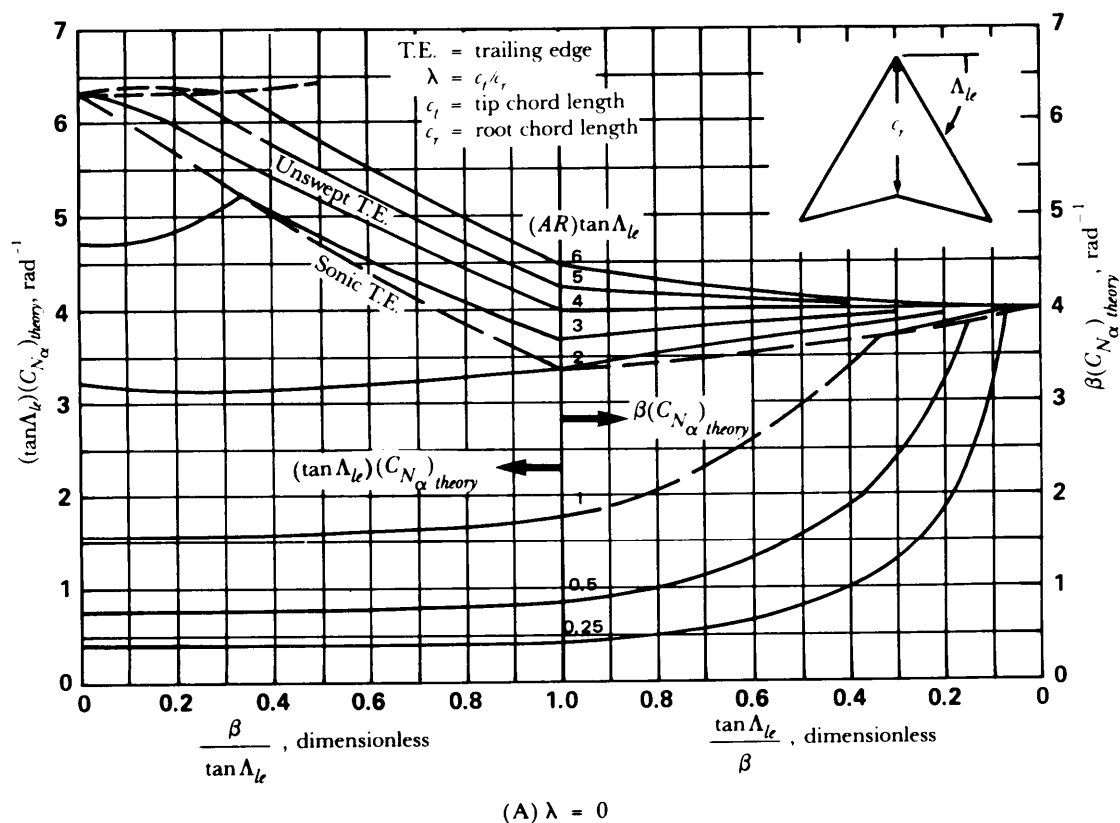
Figure 5-35.   Fin Normal Force Coefficient Gradient at Supersonic Mach Numbers for Various Fin Taper Ratios (Ref. 20)

MIL-HDBK-762(MI)

(B) λ = 0.25

Figure 5-35. (cont'd)
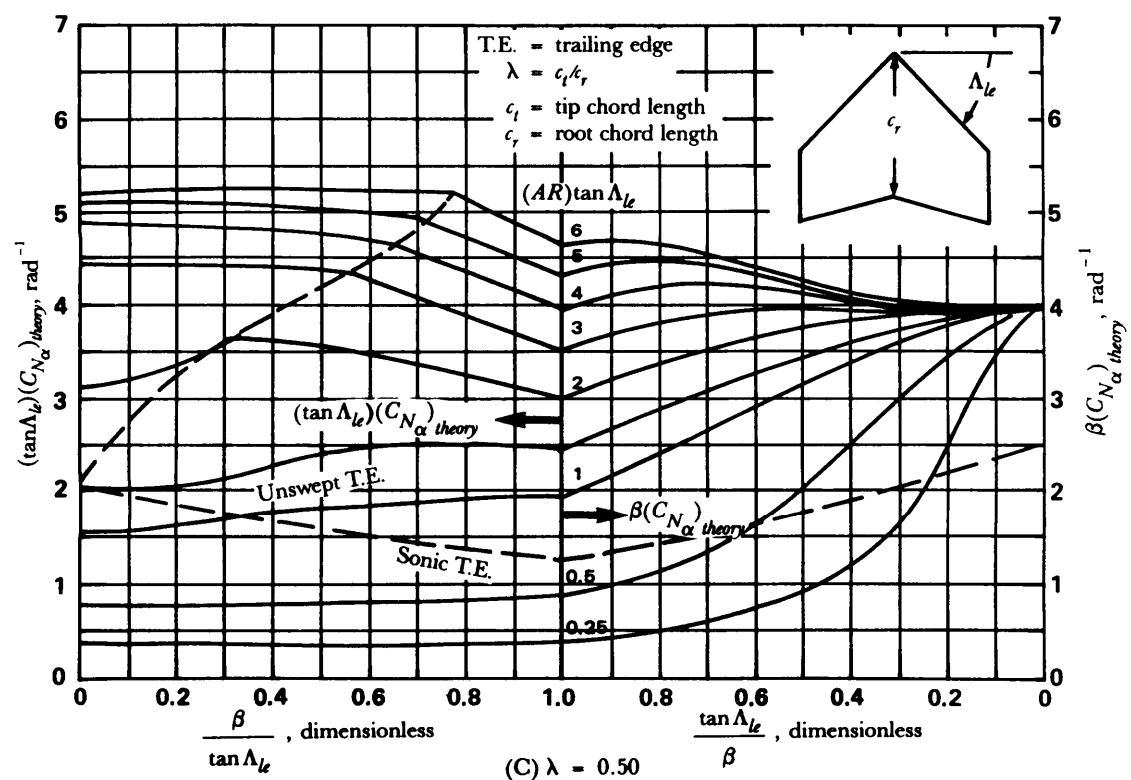
(C) λ = 0.50

Figure 5-35. (cont'd)

(cont'd on next page)

(D) λ = 1.0

Figure 5-35. (cont'd)

(A) λ = 0
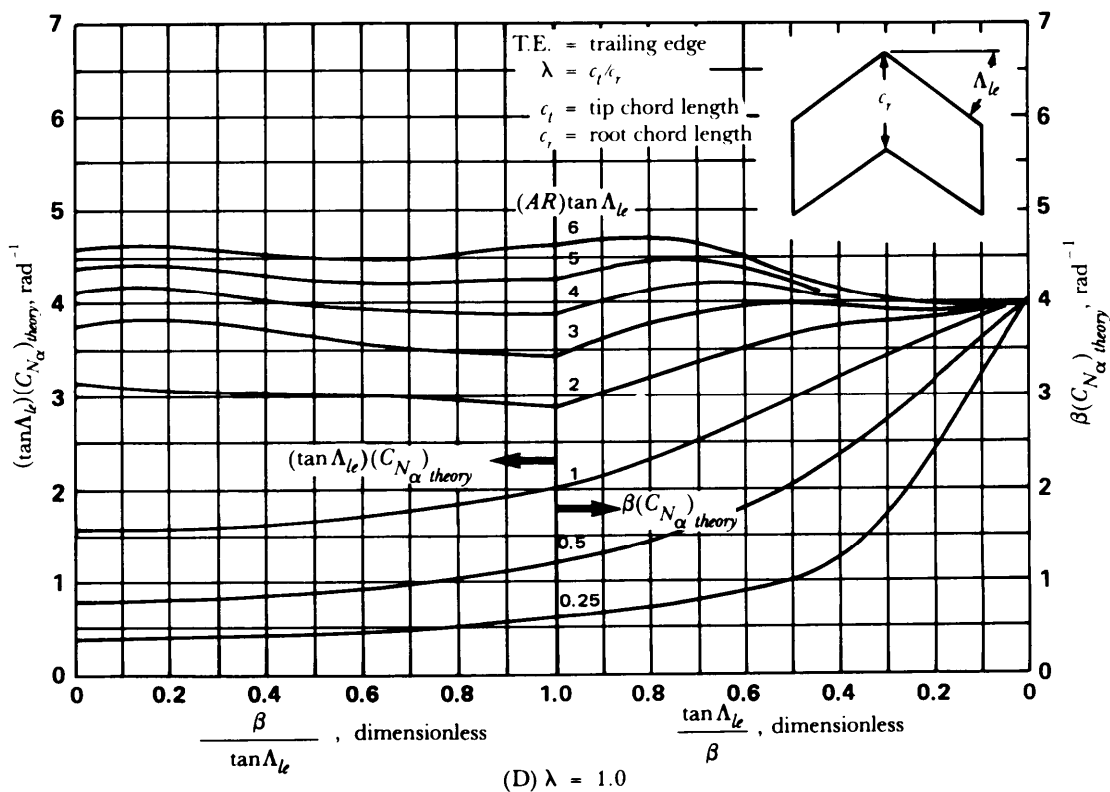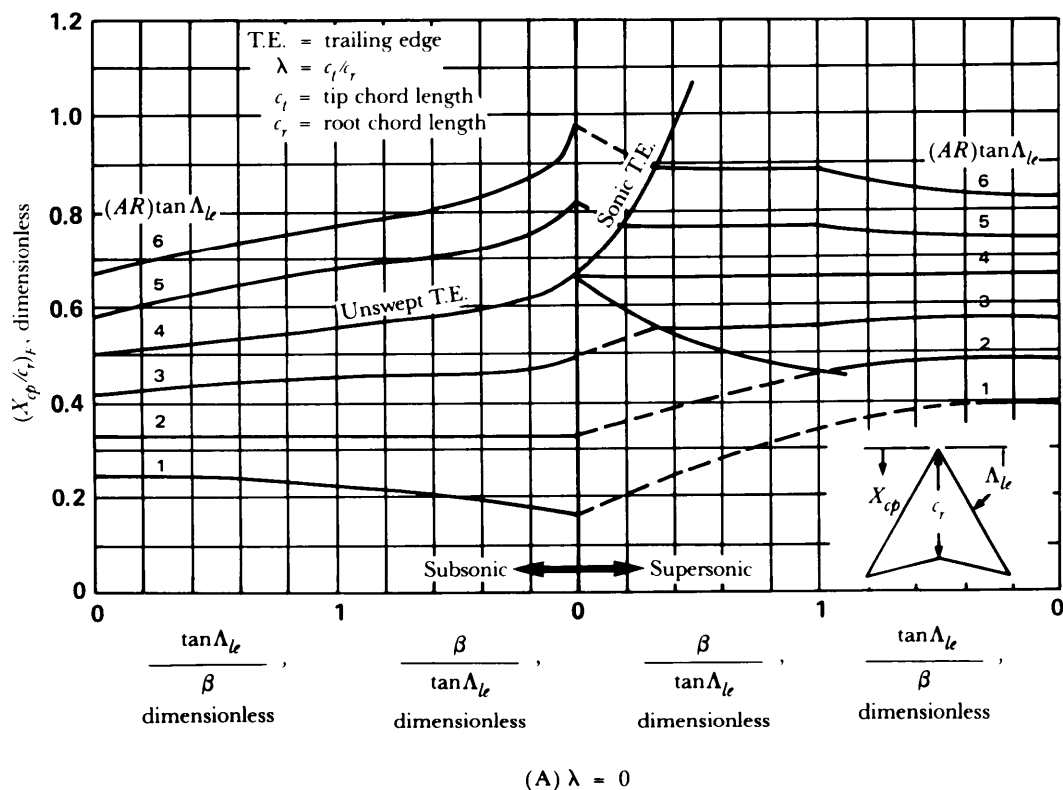
Figure 5-36. Ratio of Fin Center of Pressure to Fin Root Chord Length for Various Fin Taper Ratios (Ref. 20)

(cont'd on next page)

(B) $\lambda = 0.25$

Figure 5-36. (cont'd)

(C) $\lambda = 0.50$

Figure 5-36. (cont'd)

(D) $\lambda = 1.0$
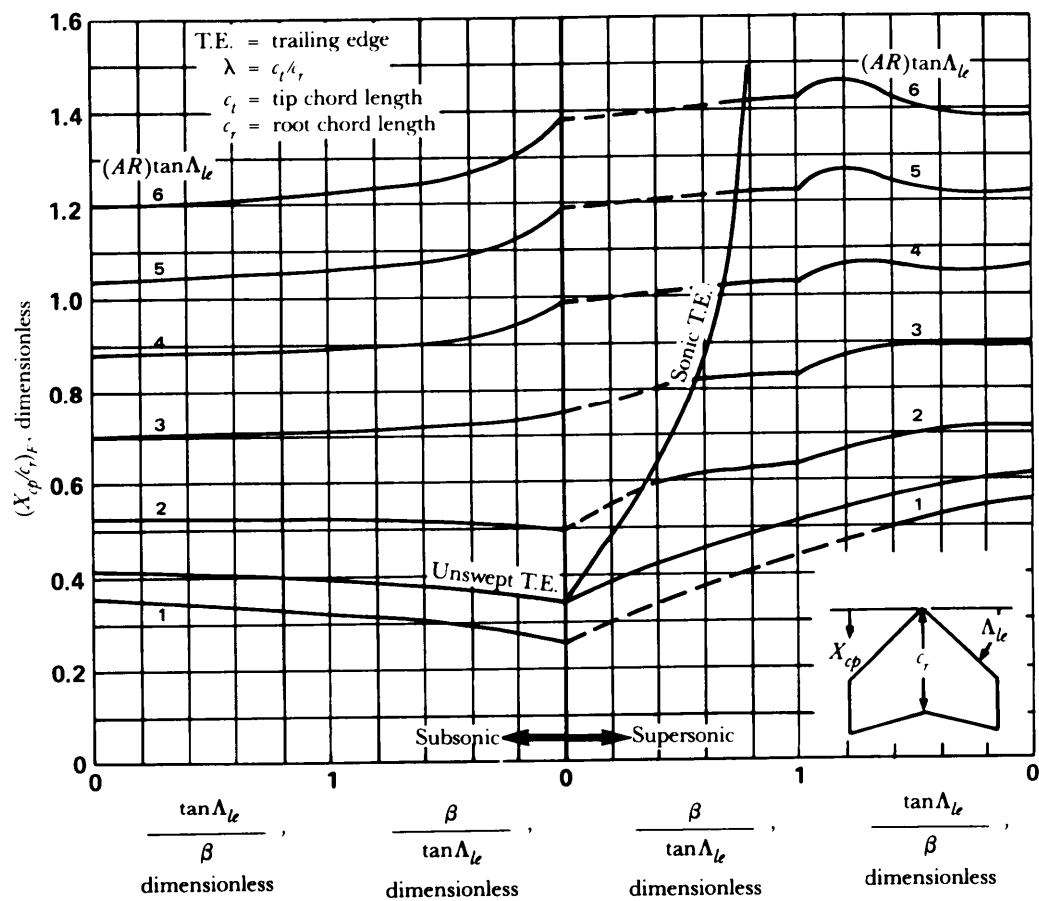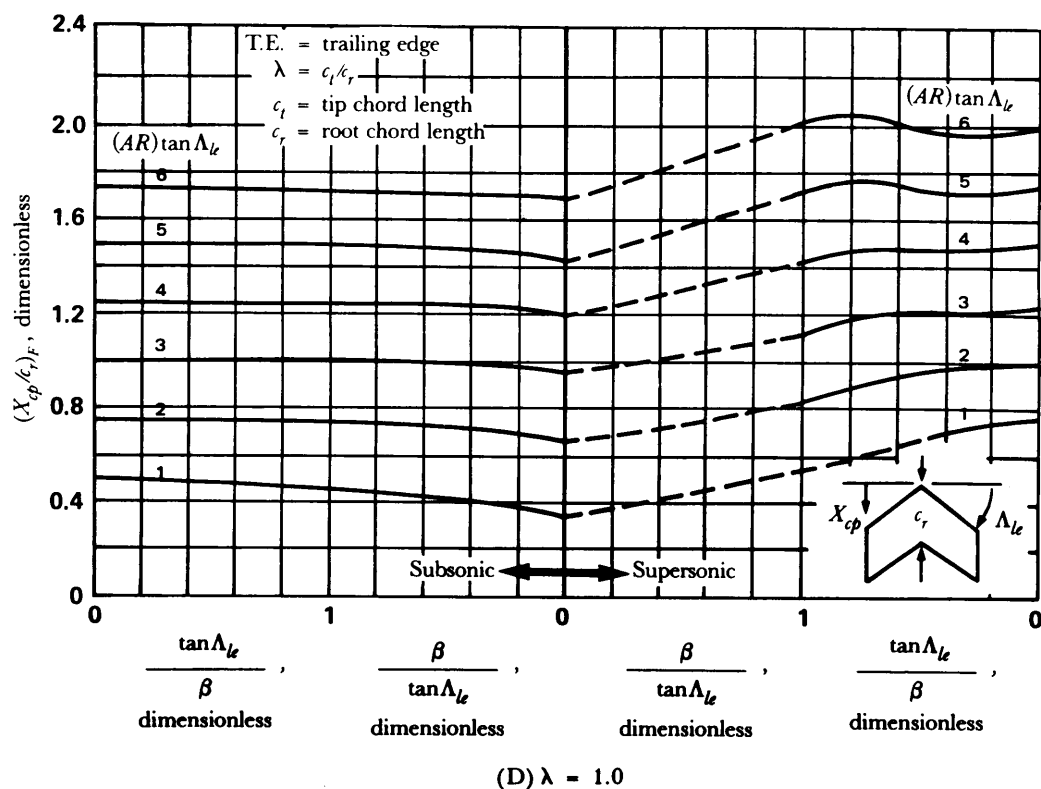
Figure 5-36. (cont'd)
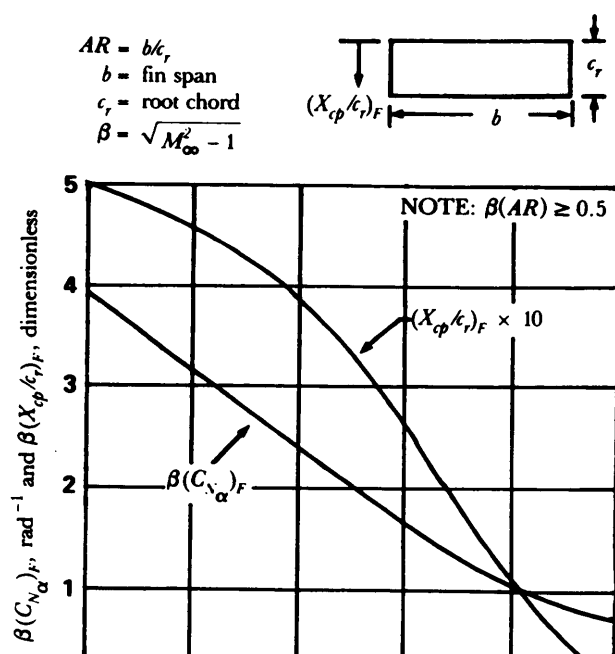
Figure 5-37. Normal Force Coefficient Gradient and Center of Pressure for Rectangular Fins (Ref. 21)
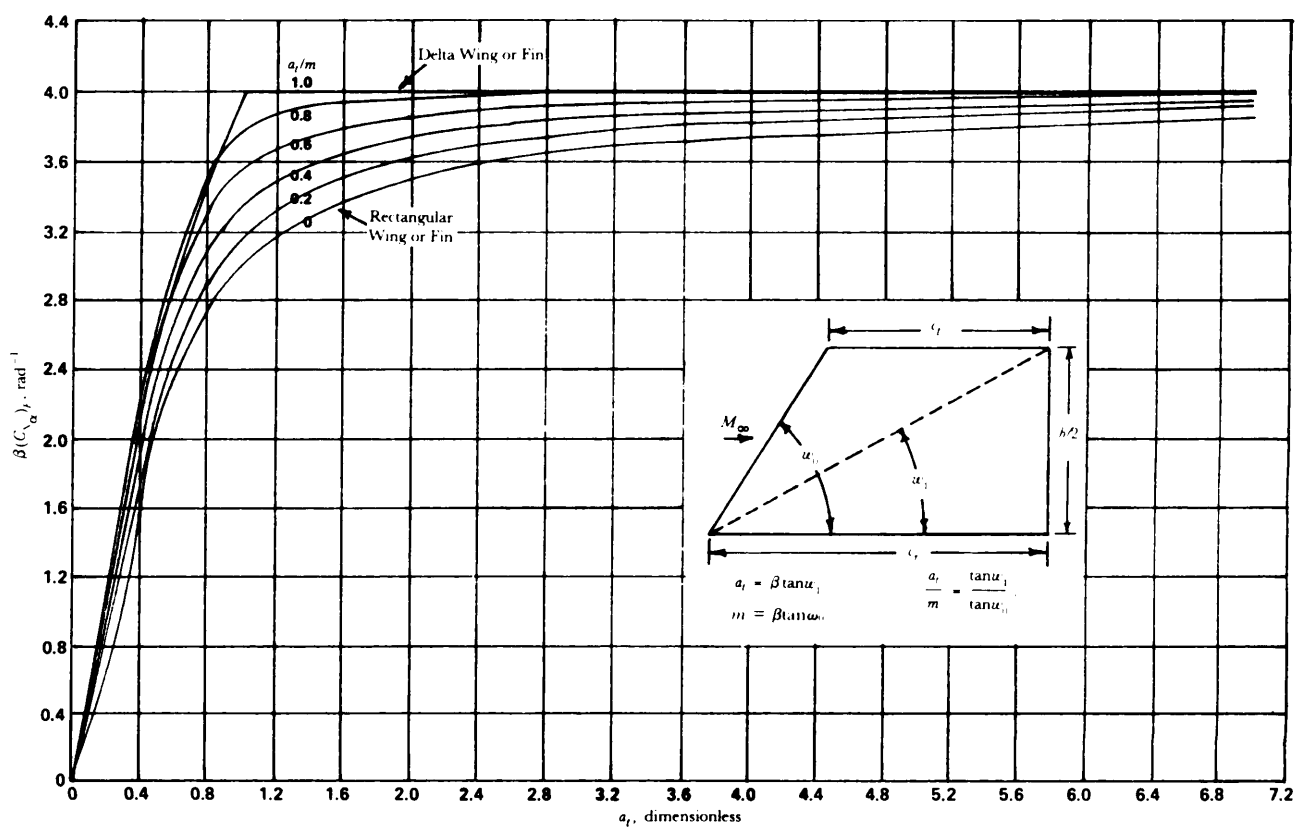
Figure 5-38. $\beta(C_{N\alpha})$ vs a_t (Ref. 23)
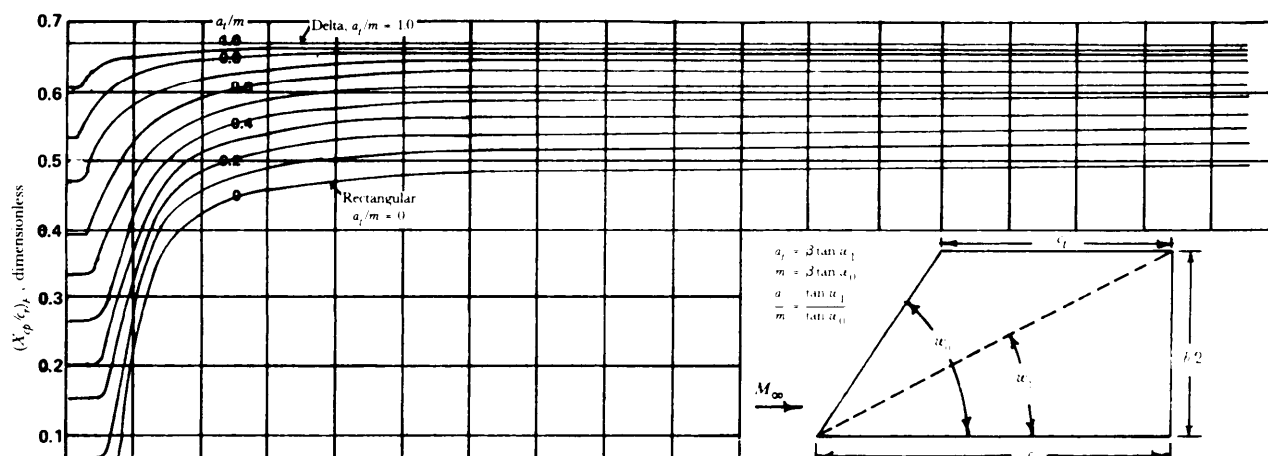
Figure 5-39. $(X_{cp}/C_r)_F$ vs a_t (Ref. 23)
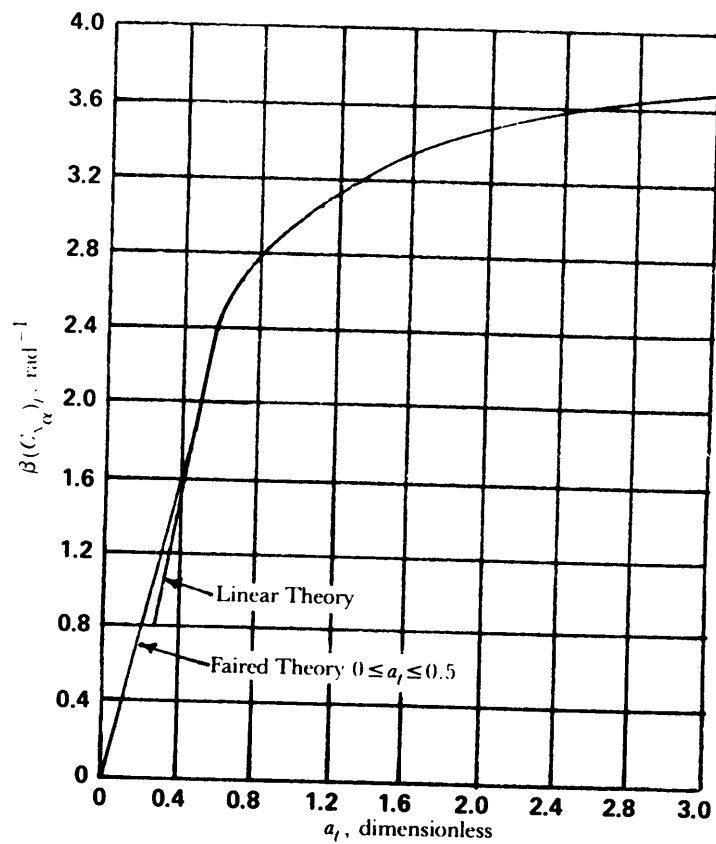
Figure 5-40. $\beta(C_{N\alpha})_f$ a_t: **Theory and Faked Curves for Rectangular Fins (Ref. 24)**
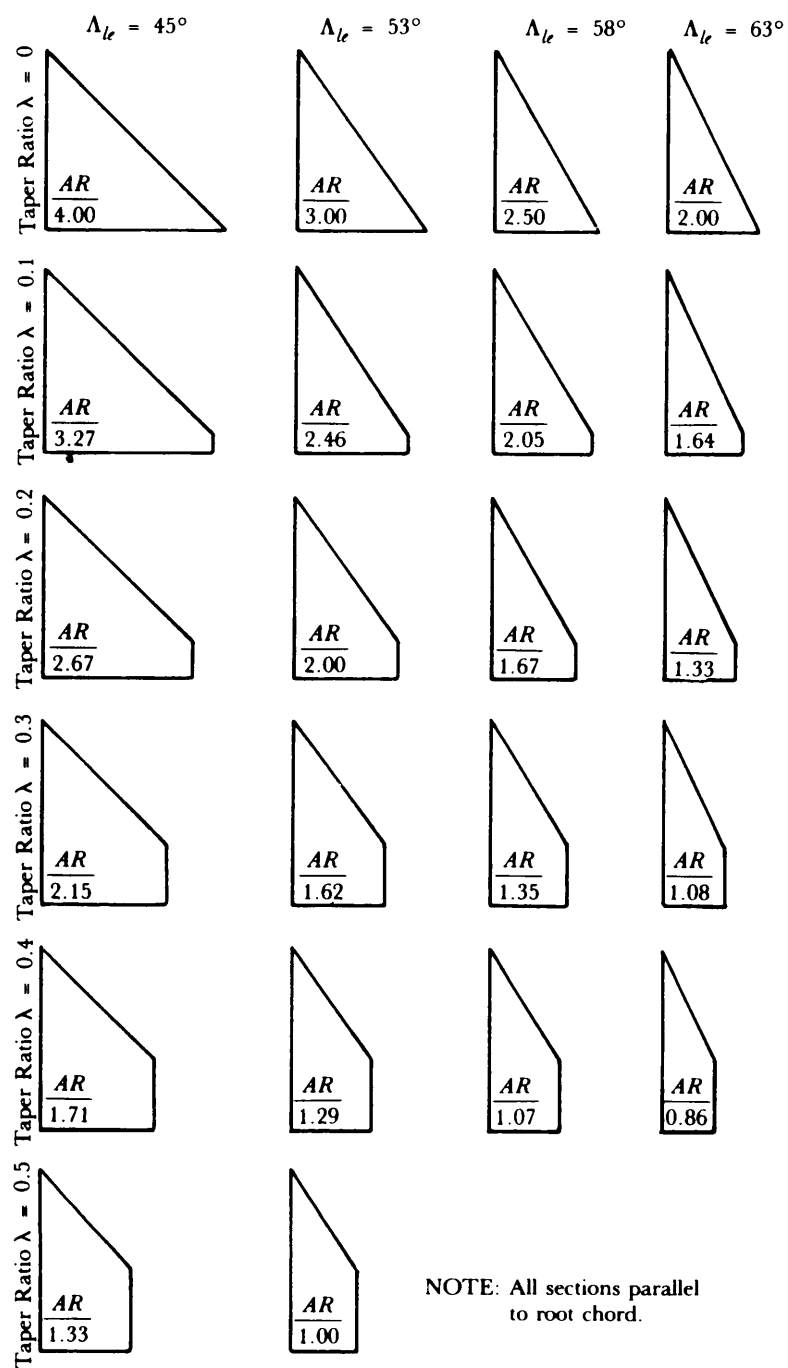
Figure 5-41. Fin Geometry (Ref. 25)
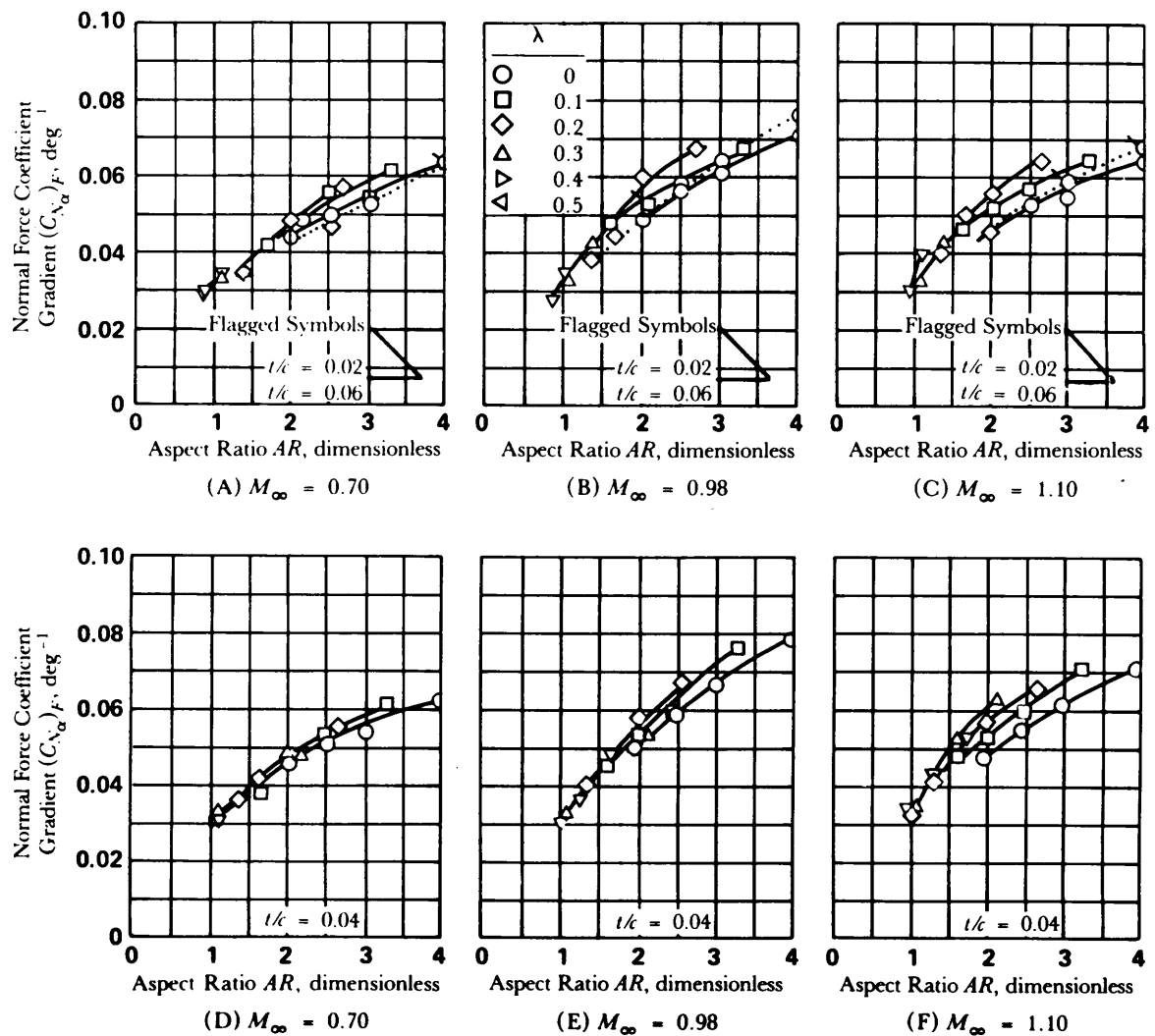
Figure 5-42. **Variation of Normal Force Coefficient Gradient With Aspect Ratio (Ref. 25)**
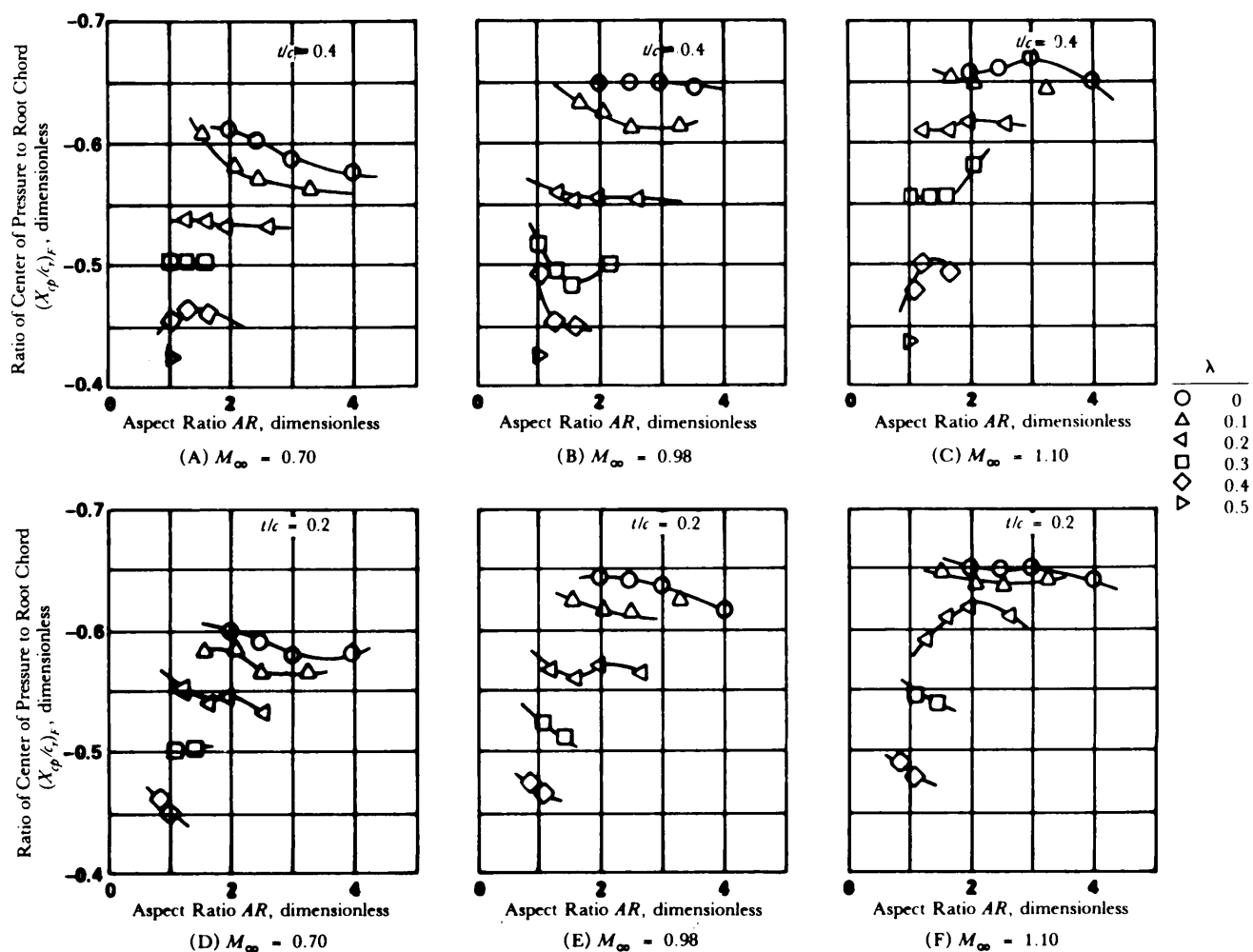
Figure 5-43. Center of Pressure for Clipped-Delta Wings for Various Aspect and Thickness Ratios (Center of pressure is measured from the leading edge of the root chord.) (Ref. 25)

(A) Tangential Fins
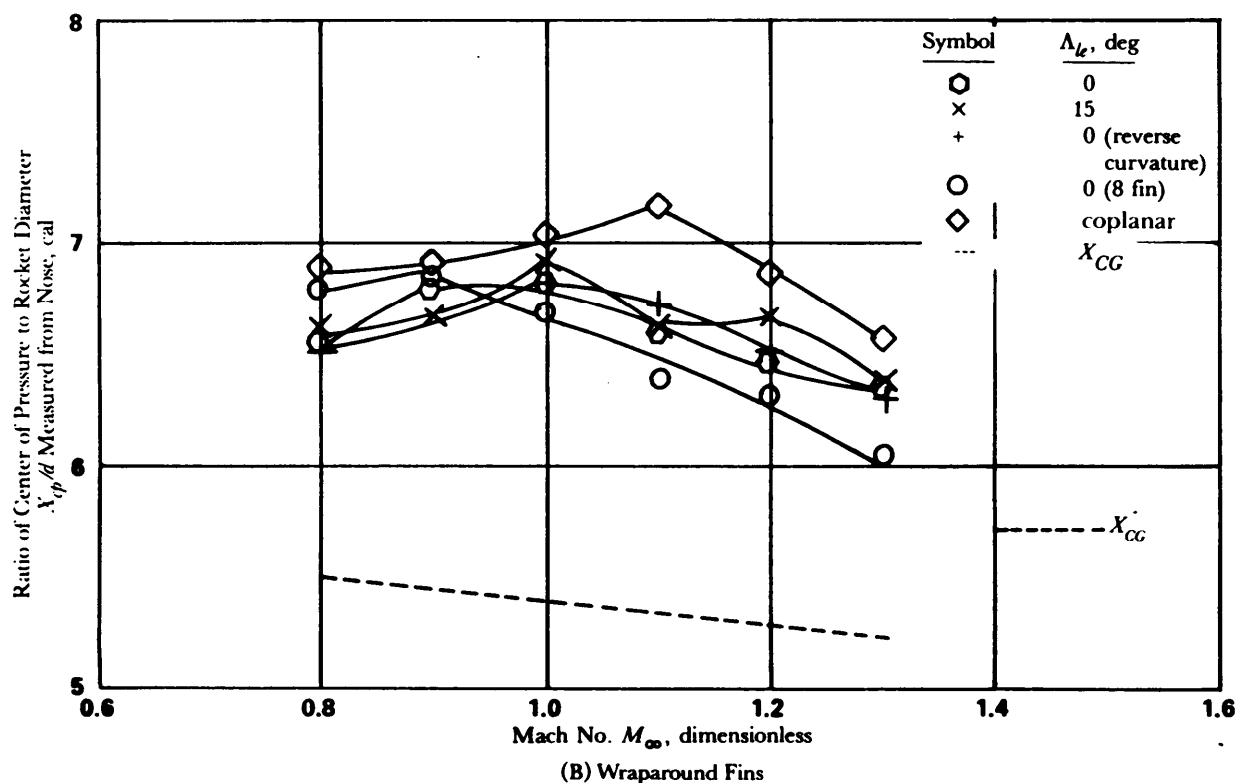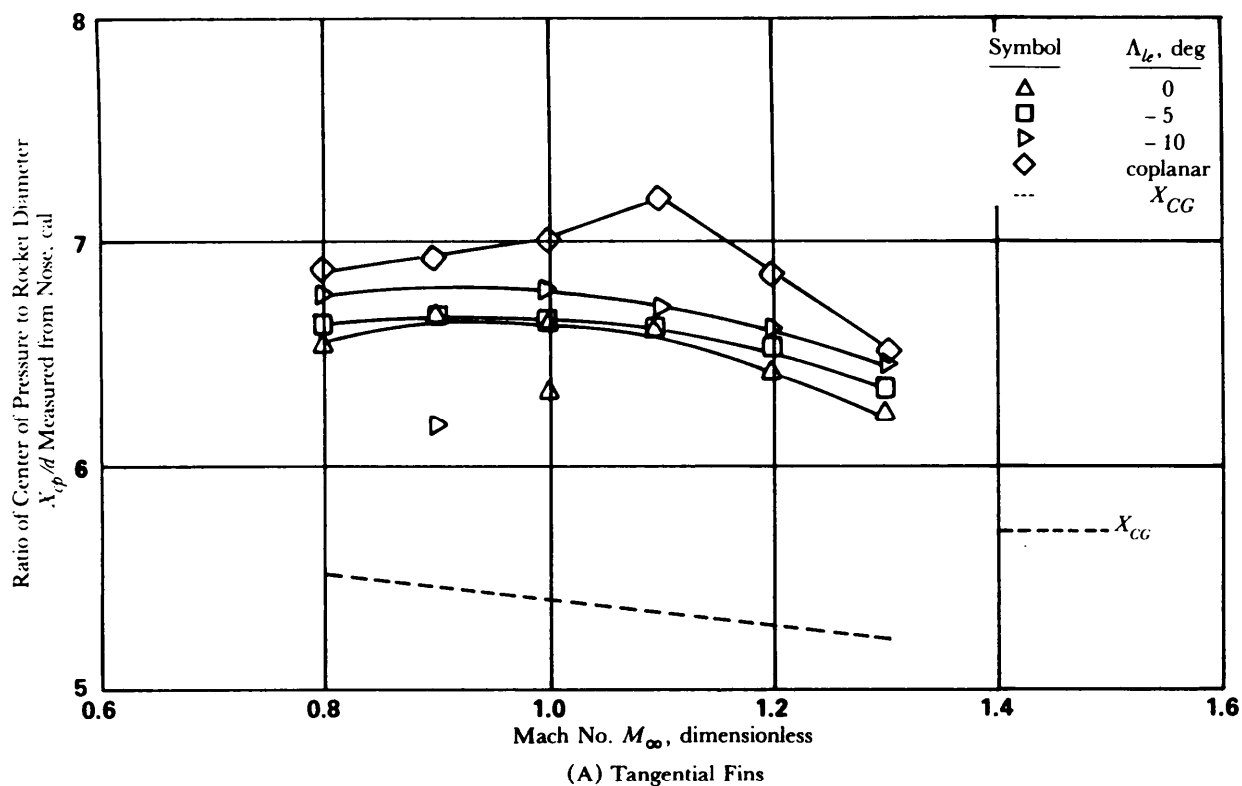

(B) Wraparound Fins

Figure 5-44. Stabilizing Effectiveness of Tangential Fins and WAF (Ref. 27)
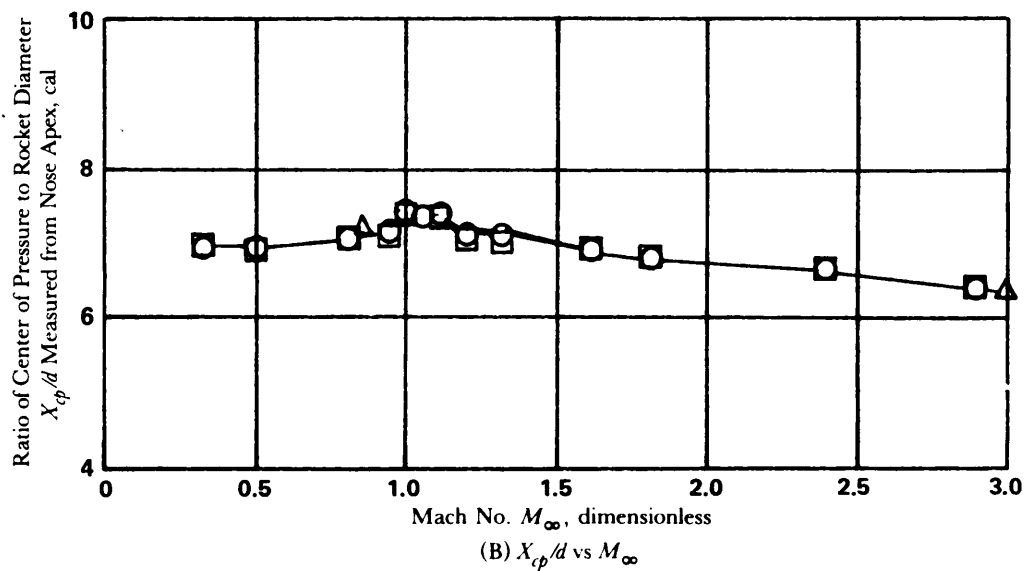
(A) C_{N_α} vs M_∞

(B) X_{cp}/d vs M_∞
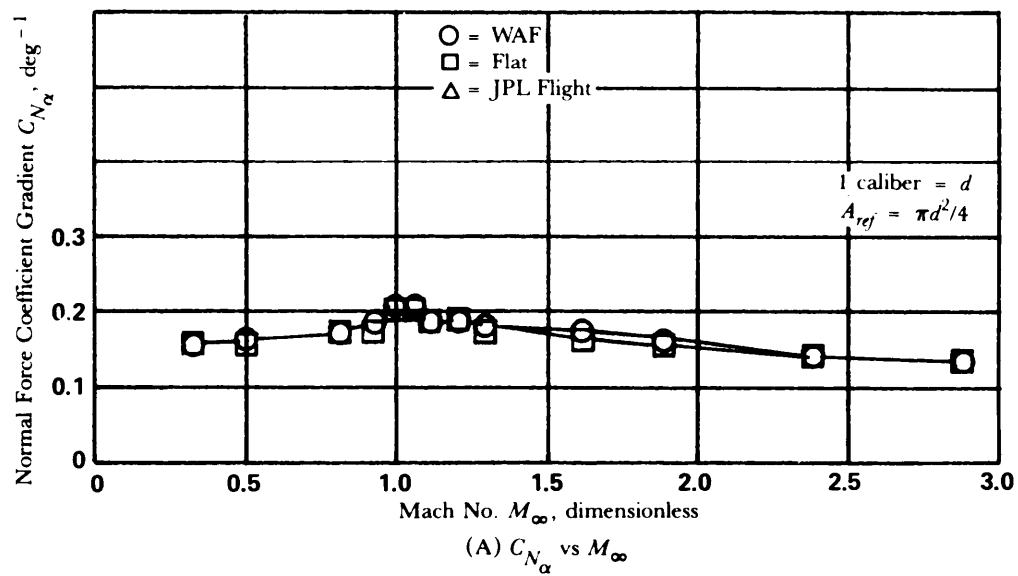
Figure 5-45. Comparison of Flat and WAF Static Stability Derivatives for a Typical (Ref. 26)
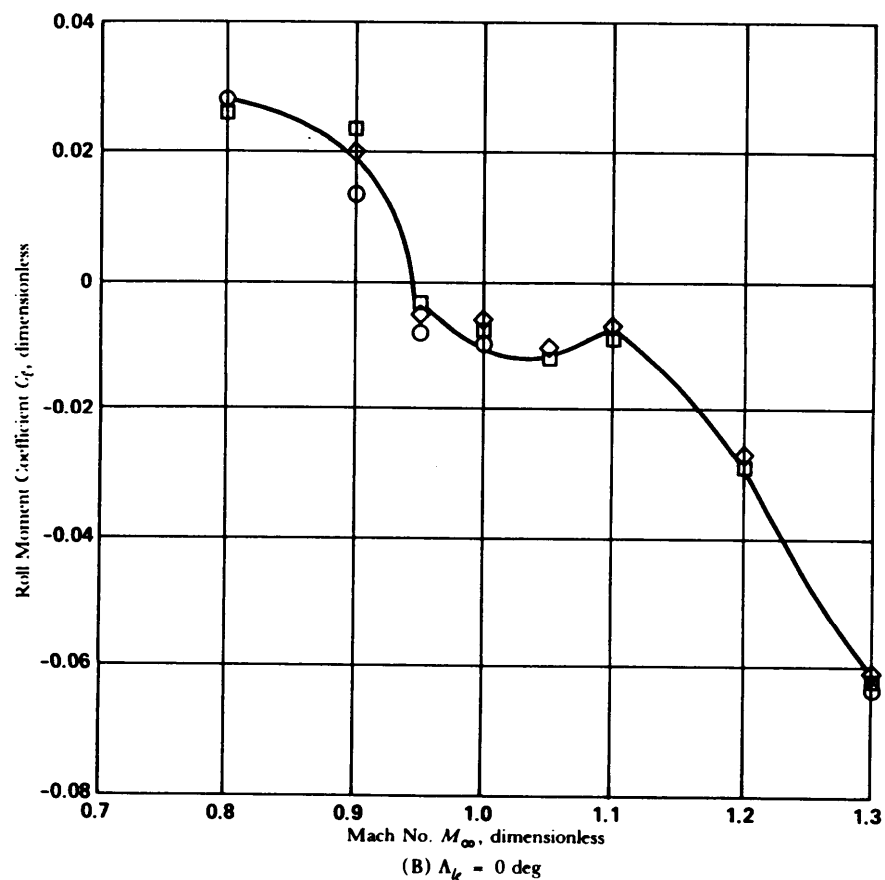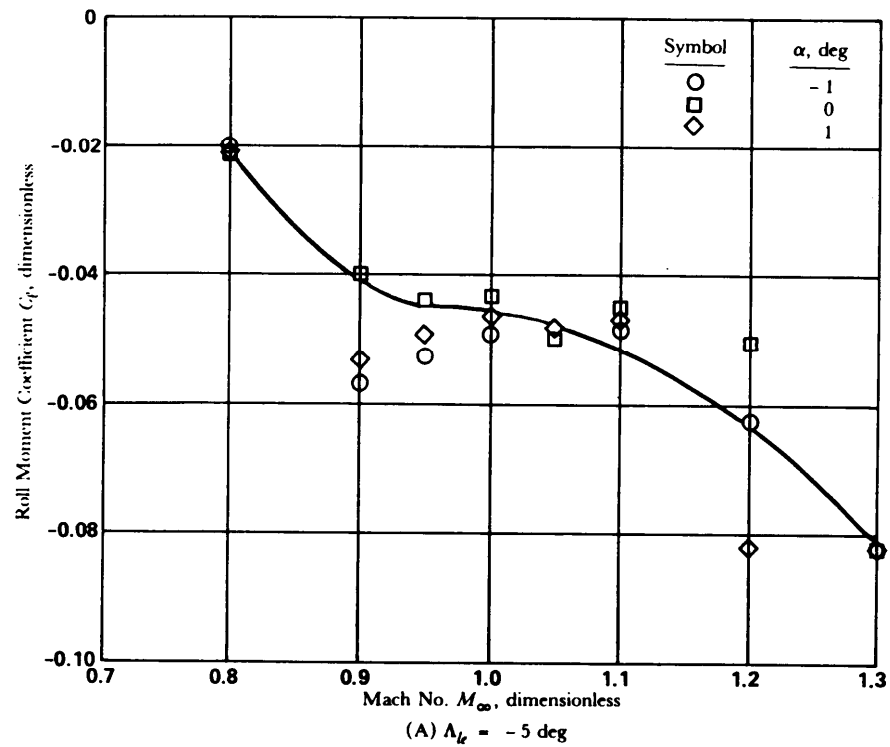
Figure 5-46.   Variation of Roll Moment Coefficient With Mach Number for Tangent Fins Having 0-deg and –5-deg Sweepback (Ref. 27)
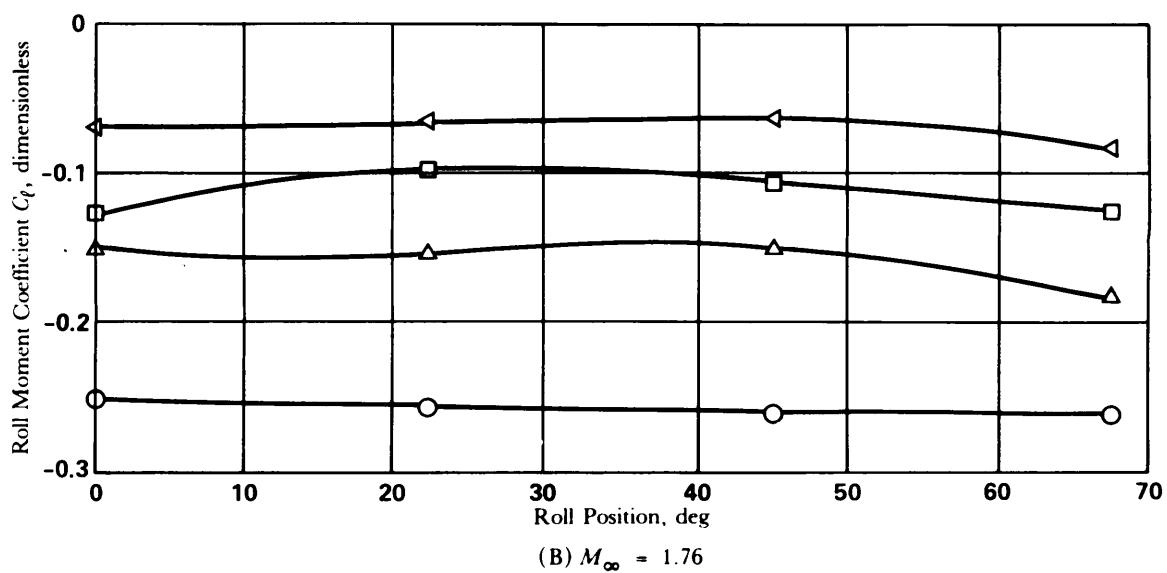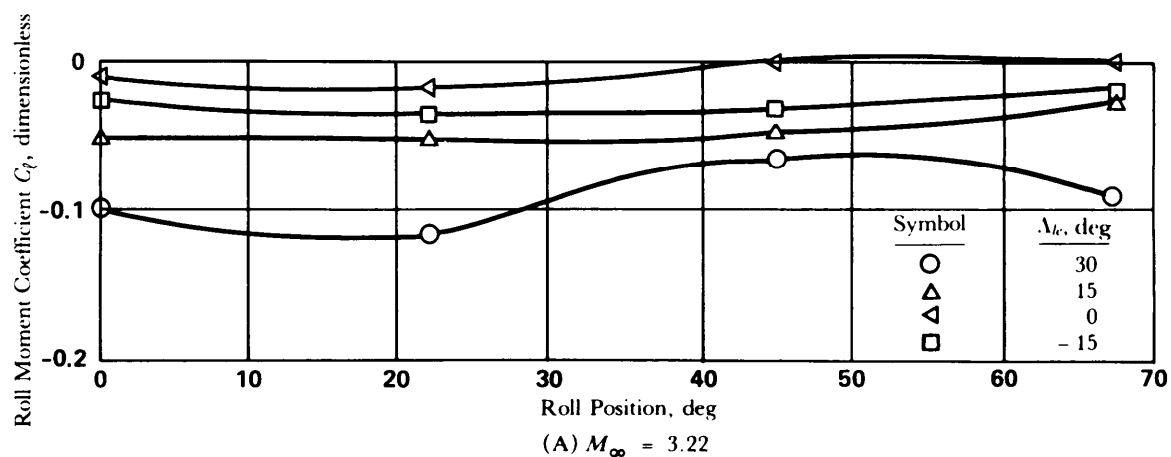
Figure 5-47.   Effect of Sweepback Angle and Roll Position on Roll Moment Coefficient on High Aspect Ratio Tangent Fins (Ref. 30)

MIL-HDBK-762(MI)
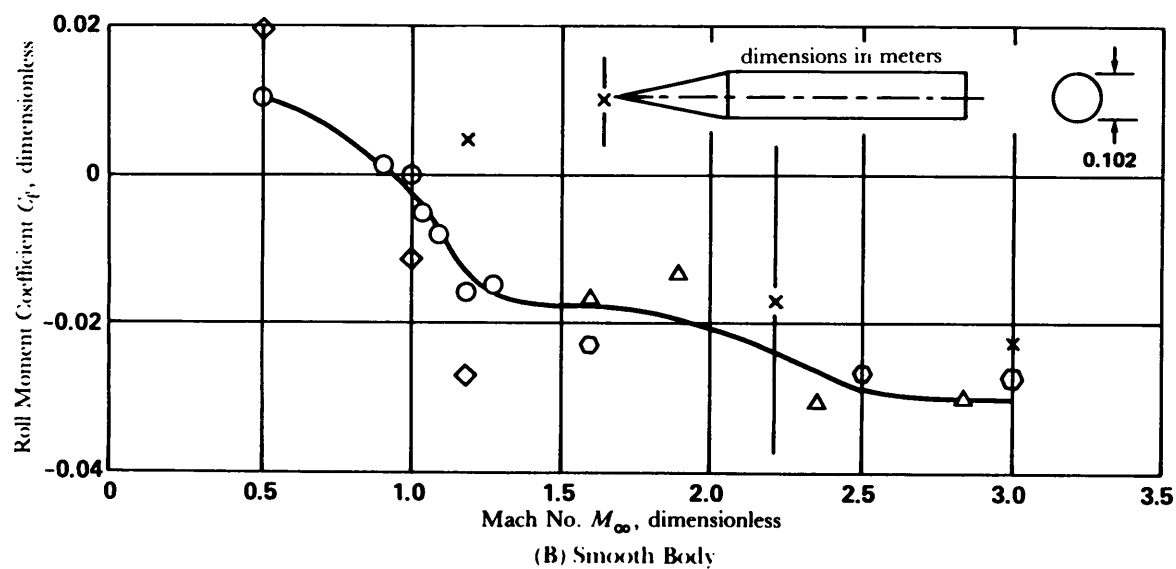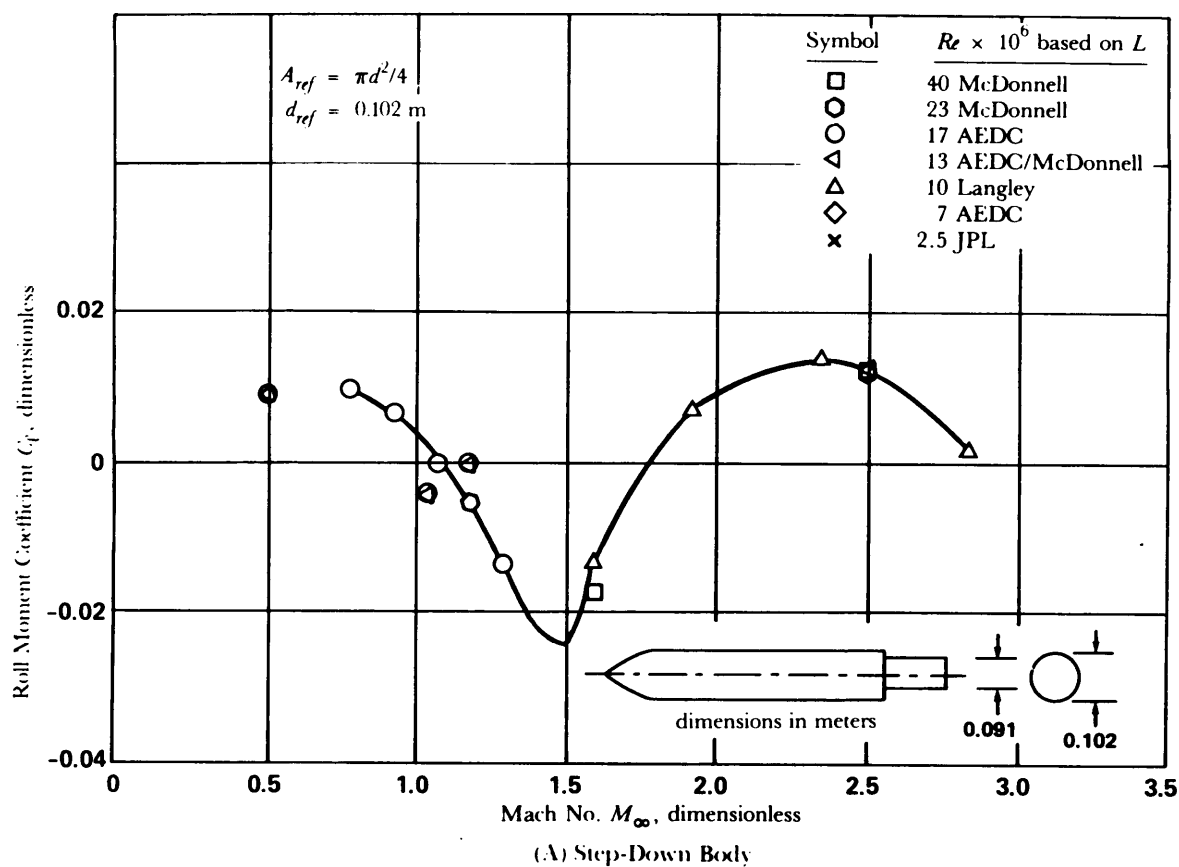
Figure 5-48. WAF Roll Moment Coefficients at Zero Angle of Attack (Ref. 26)

Symbol	$(AR)_e$	c_{r_e}/d
O	0.75	1.75
△	1.33	1.00
□	2.66	0.50
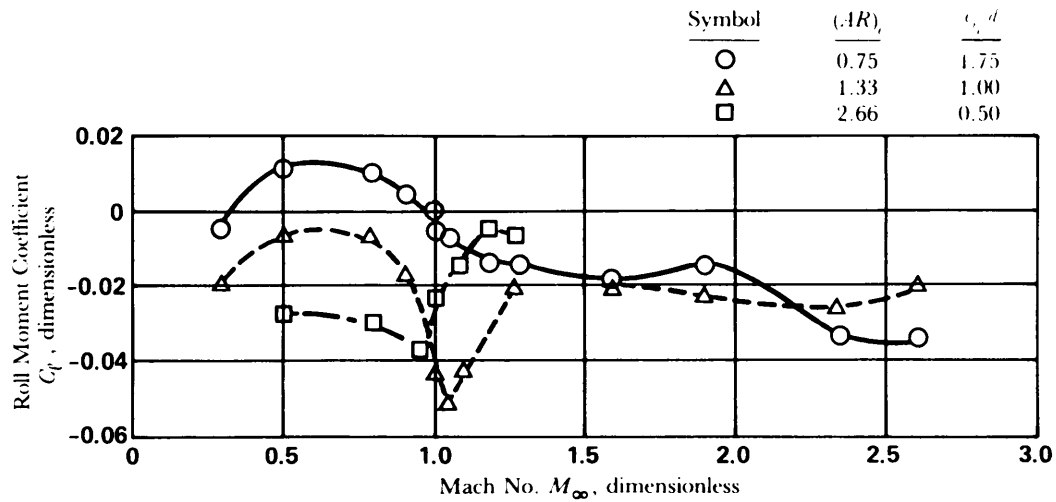
Figure 5-49. WAF Roll Moment Coefficient vs Mach Number, $\alpha = 0$, $t/c_{r_e} = 3\%$ (Ref. 26)

(A) Tip Chord Modification

(B) Root Chord — Body Surface Gap
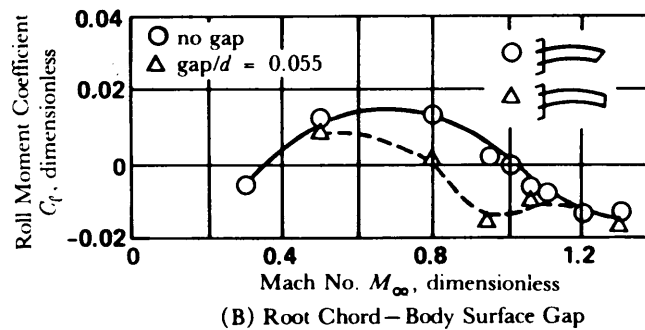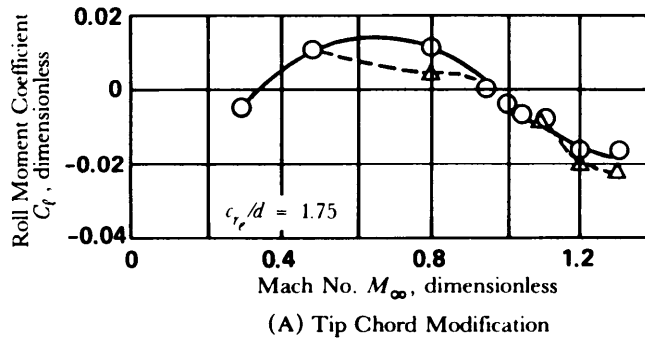
Figure 5-50. Effect of Modifying WAF Root and Tip Chord Cross Section on Roll Moment, $\alpha = 0$, $t/c_{r_e} = 3\%$ (Ref. 26)
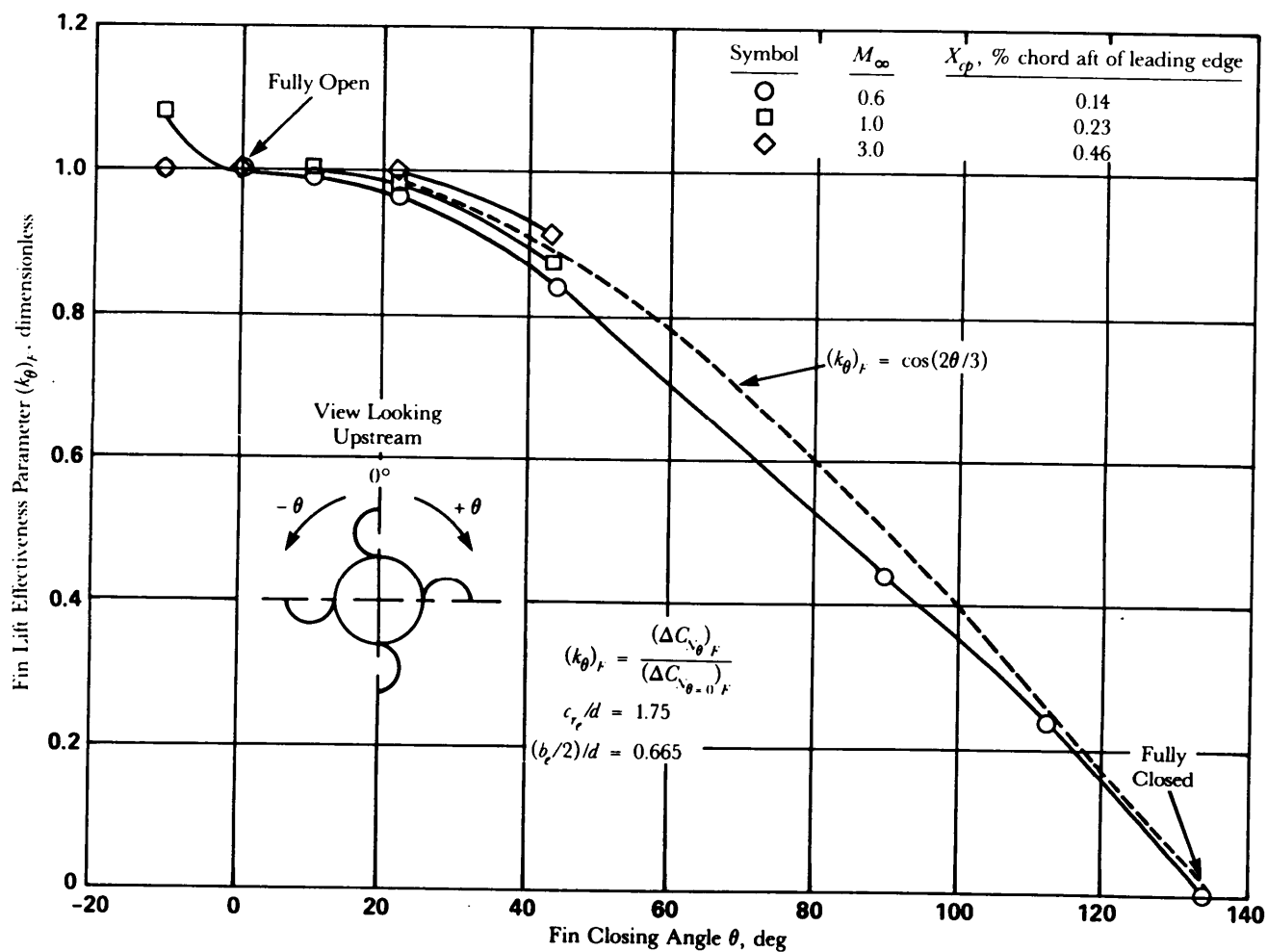
Figure 5-51. Ratio of WAF Lift Effectiveness at Closing Angles (Ref. 26)
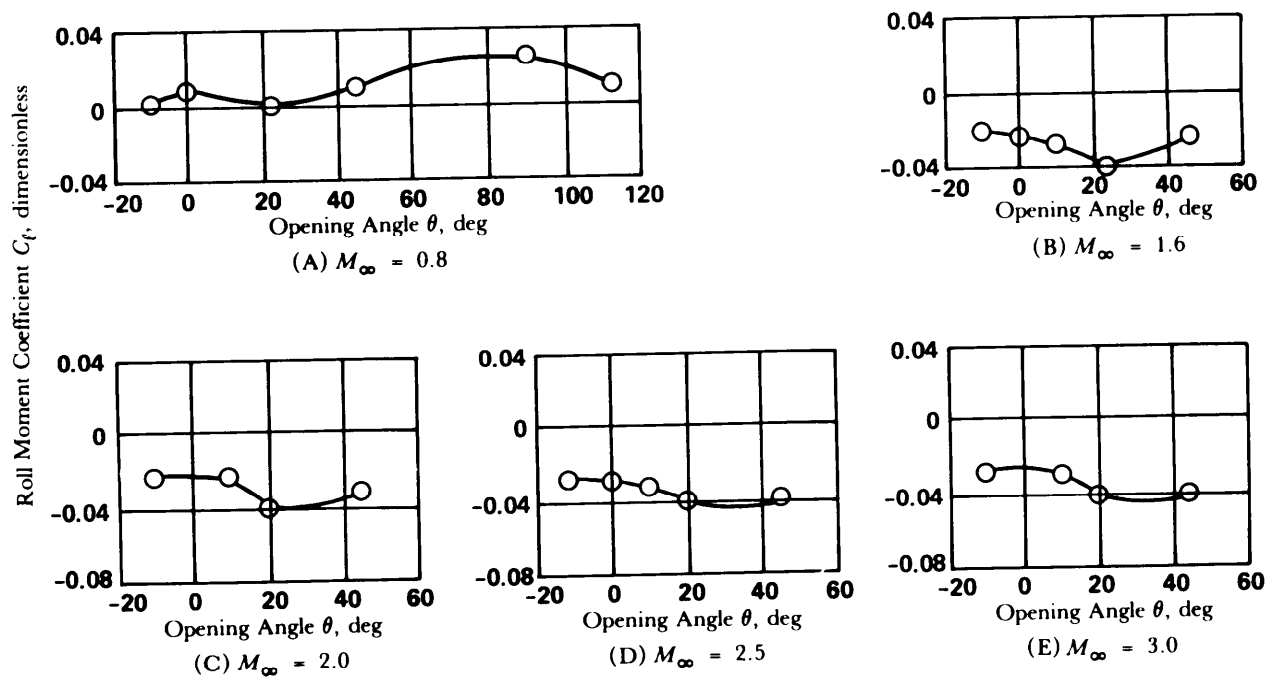
Figure 5-52. Effects of Opening Angle θ, WAF Roll Moment at Zero Angle of Attack $c_{r_e}/d = 1.75$, $b_e/(2d) = 0.665$ (Ref. 26)
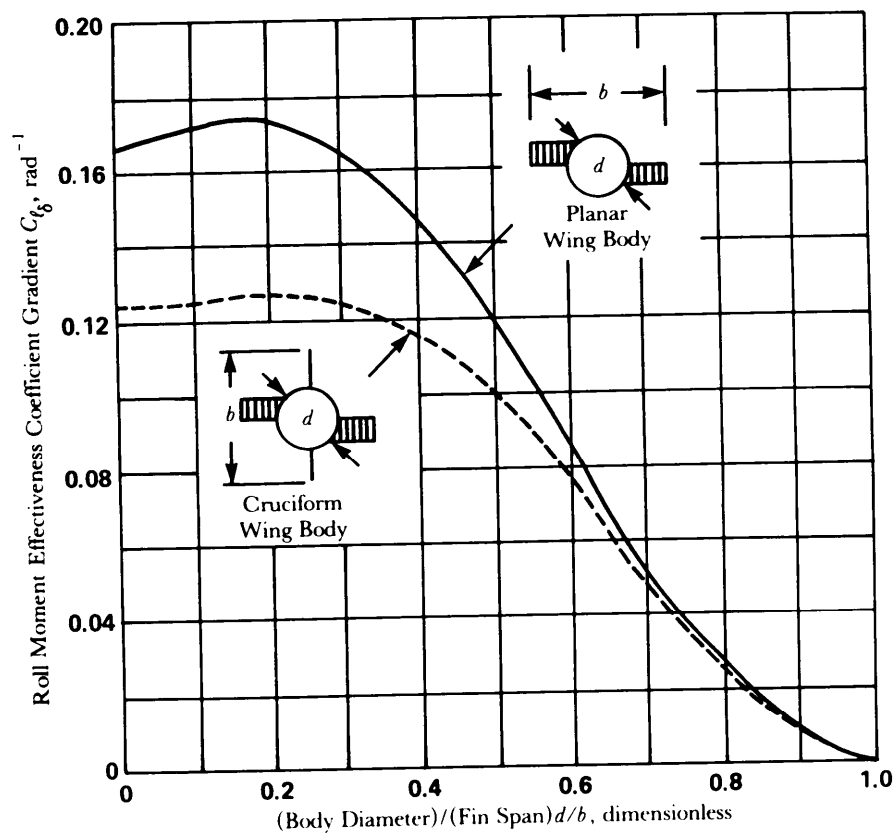
Figure 5-53. Roll Moment Effectiveness Coefficient Gradient for Cruciform and Planar Wing-Body Combinations With Differential Incidence of the Horizontal Surfaces (Ref. 31)
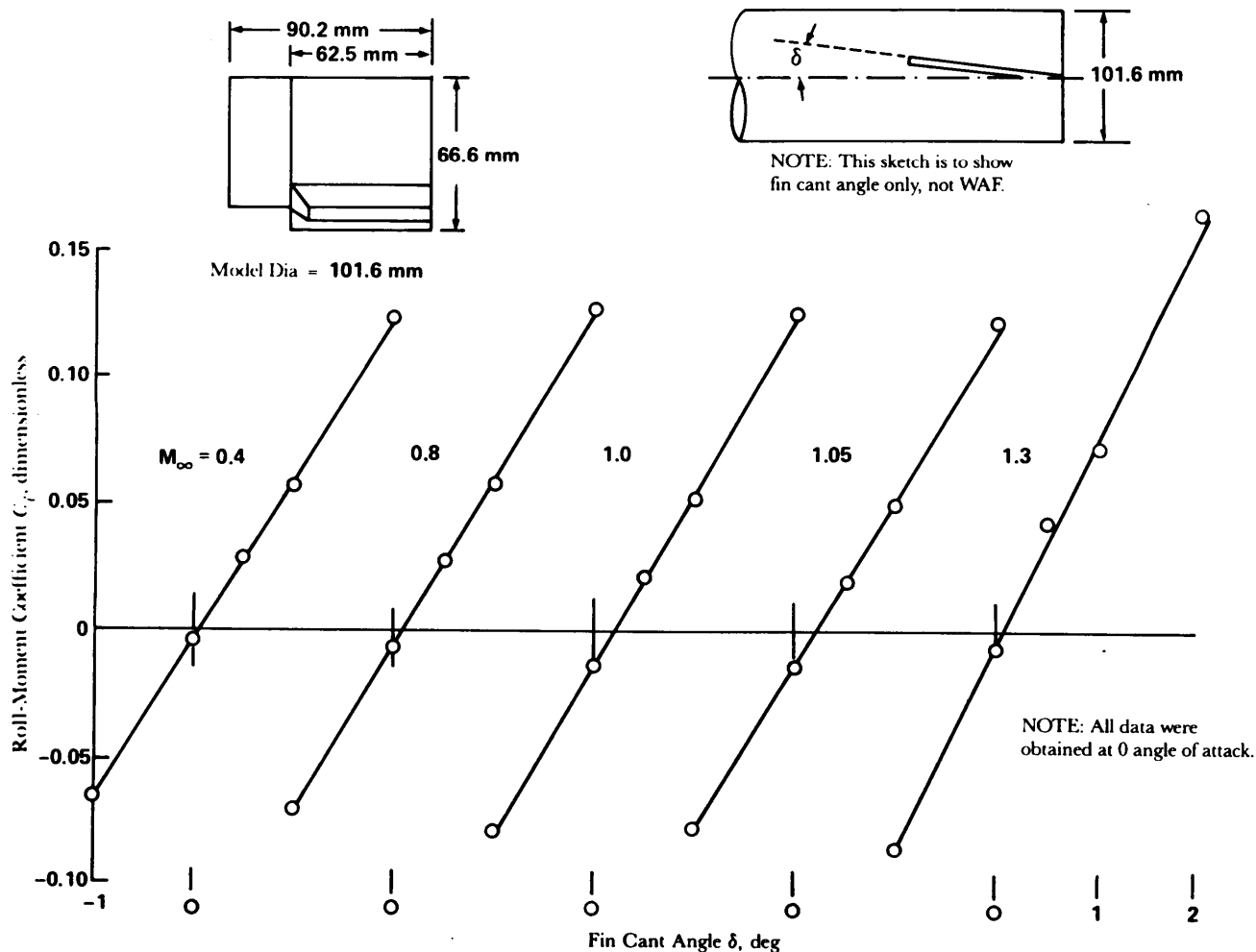
Figure 5-54. WAF Roll-Moment Coefficient With Varying Fin Cant Angles (Ref. 26)
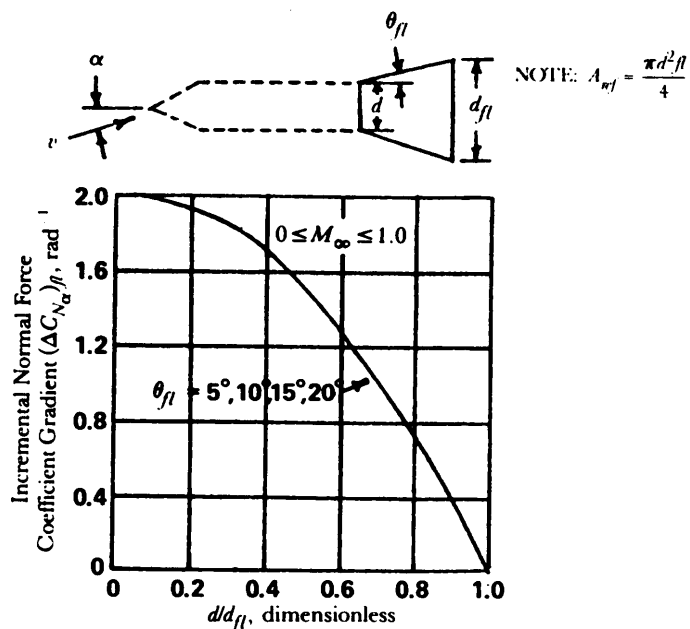
Figure 5-55. Incremental Normal Force Coefficient Gradient for a Flare

NOTE: $A_{ref} = \dfrac{\pi d^2_{fl}}{4}$

(A) $M_\infty = 1.5$ (B) $M_\infty = 2.0$
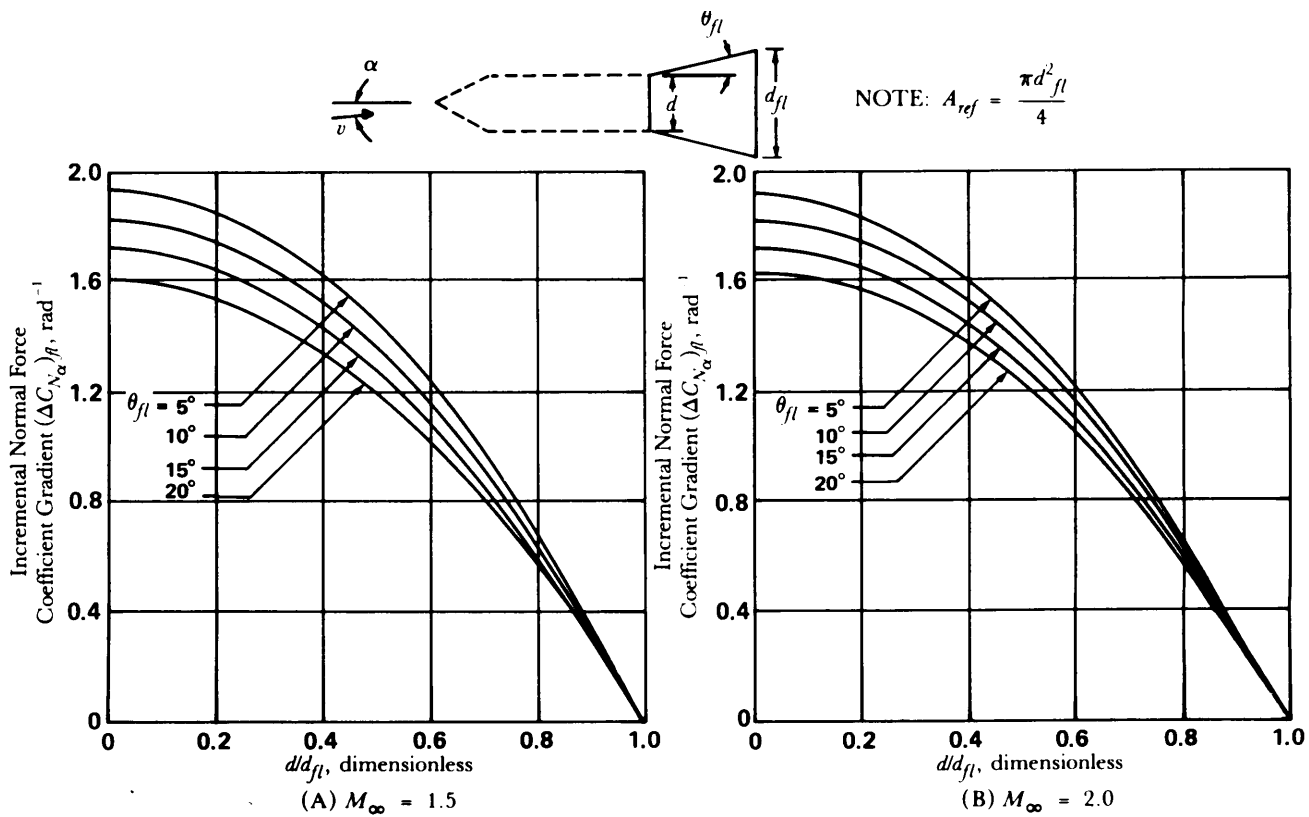
Figure 5-56.   Incremental Normal Force Coefficient Gradient for a Flared Afterbody for $M_\infty = 1.5$ and $M_\infty = 2.0$

NOTE: $A_{ref} = \dfrac{\pi d^2_{fl}}{4}$
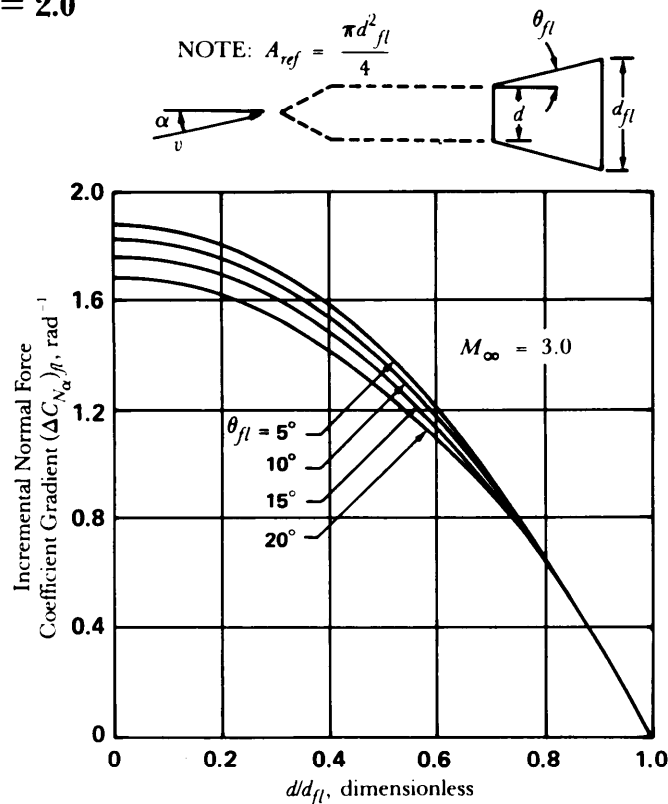
Figure 5-57.   Incremental Normal Force Coefficient Gradient for a Flared Afterbody for $M_\infty = 3.0$

5-126
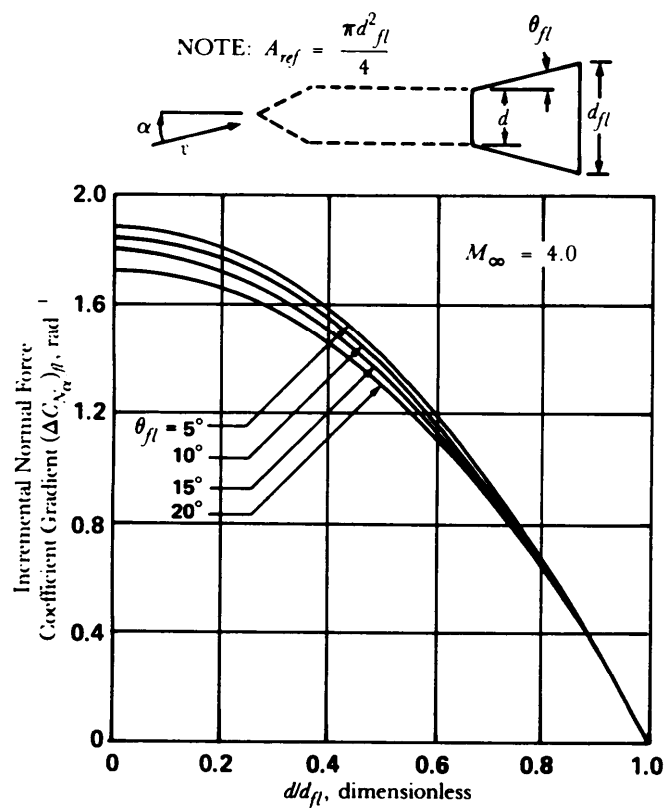
Figure 5-58. Incremental Normal Force Coefficient Gradient for a Flared Afterbody for $M_\infty = 4.0$
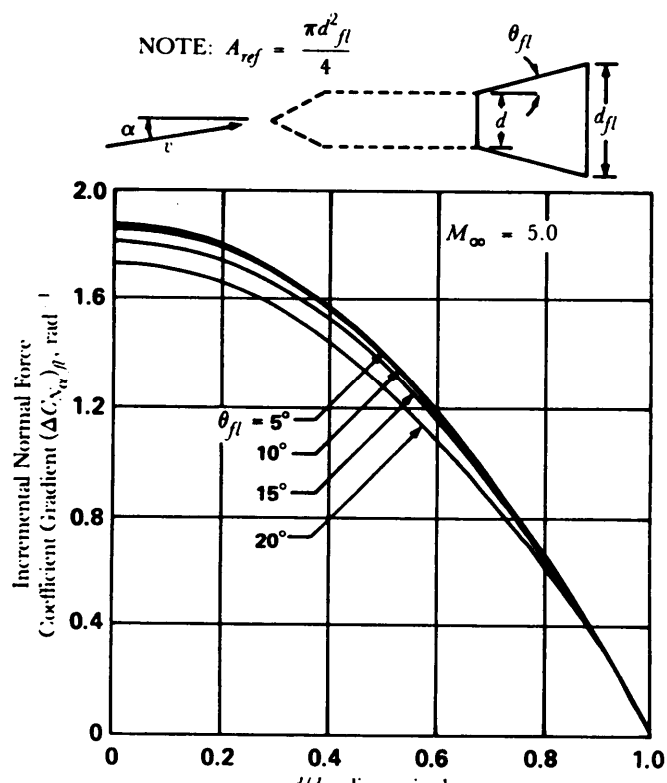
Figure 5-59. Incremental Normal Force Coefficient Gradient for a Flared Afterbody for $M_\infty = 5.0$
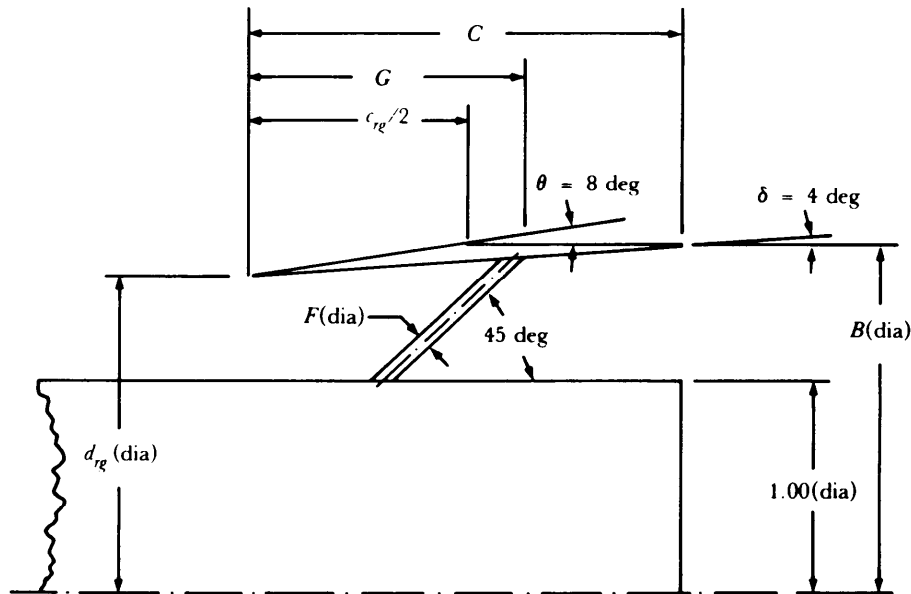
θ = angle between outer surface of ringtail
at leading edge and model longitudinal axis

Ringtail	d_{rg}	B	C	F	G^*
T1	1.500	1.605	0.750	0.046	0.375
T2	1.500	1.657	1.125	0.052	0.563
T3	2.000	2.210	1.500	0.080	0.750
T4	2.000	2.140	1.000	0.070	0.500
T5	2.000	2.080	0.600	0.060	0.300
T10	2.500	2.675	1.250	0.092	0.625
T11	2.500	2.605	0.750	0.080	0.375
T12	1.250	1.425	1.250	0.048	0.782
T13	1.250	1.381	0.937	0.048	0.623

*See List of Symbols for definitions of d_{rg}, B, C, F, c_{rg}, and δ.

Figure 5-60. Ringtail Geometry, δ = 4-deg Angle (Ref. 26)
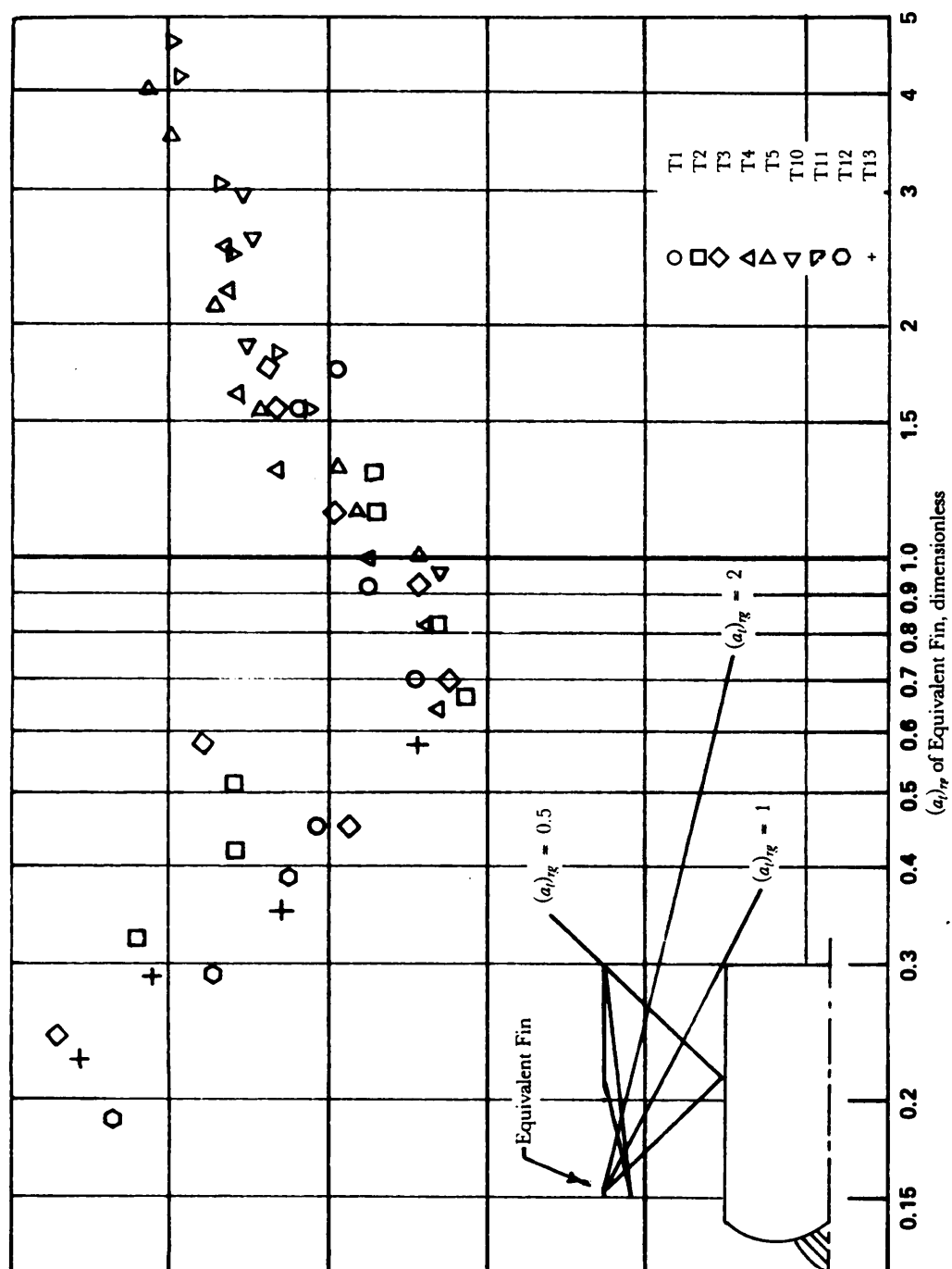
Figure 5-61. Ratio of Ringtail to Equivalent Planar Fin Normal Force Coefficent Gradient (Ref. 32)

(A) T12, $d_{rg} = 1.125$, $C = 1.25$

(B) T13, $d_{rg} = 1.25$, $C = 0.937$

(C) T1, $d_{rg} = 1.5$, $C = 0.75$

(D) T2, $d_{rg} = 1.5$, $C = 1.125$
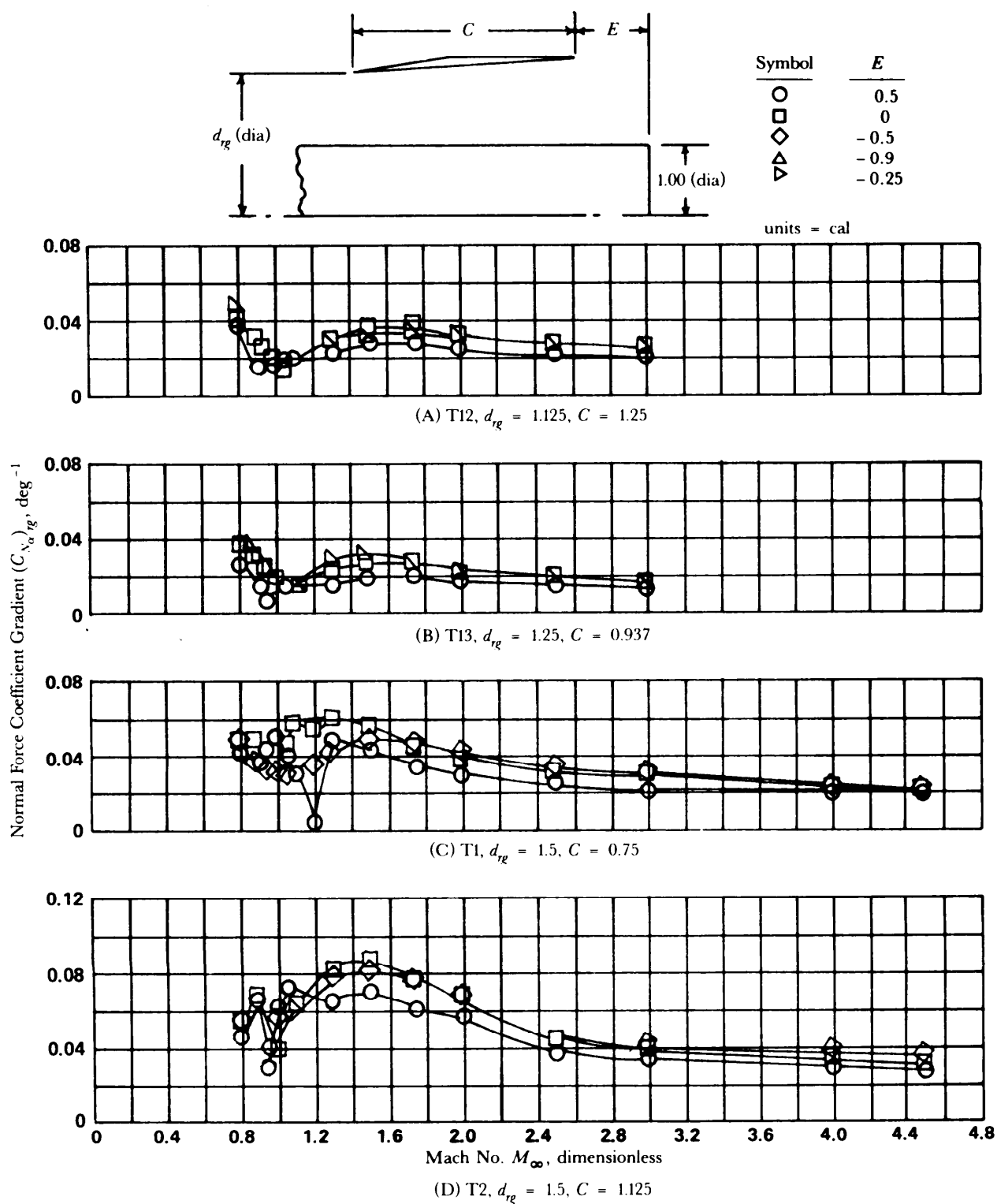
(NOTE: See Fig. 5-60 for complete dimensions of T1, T2, T12, and T13.)

Figure 5-62. Effect of Ringtail Geometry and Longitudinal Position on the Variation of $(C_{N\alpha})_{rg}$ With Mach Number, 4-deg Internal Expansion Angle (Ref. 32)

Figure 5-63. Effects of Chord, Diameter, and Longitudinal Position on $(C_{N\alpha})_{rg}$ on Ring-tails, 4-deg Internal Expansion Angle (Ref. 32)

MIL-HDBK-762(MI)

(A) Configuration 1

Dimensions are in millimeters.

(B) Configuration 2

(C) Configuration 3

(D) Configuration 4
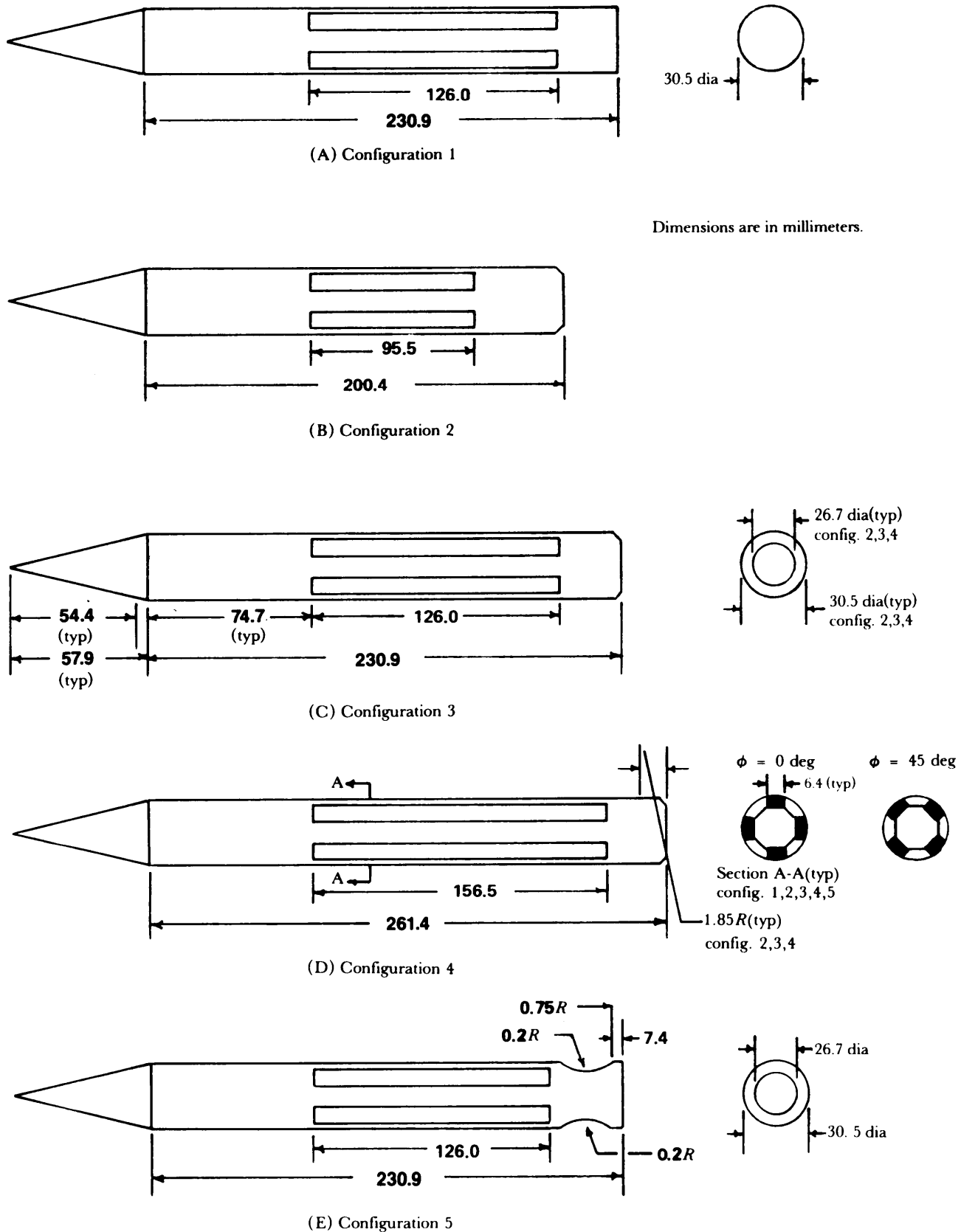
(E) Configuration 5

Figure 5-64. Five Typical Configurations of Longitudinal Strut-Supported Ringtails (Ref. 33)
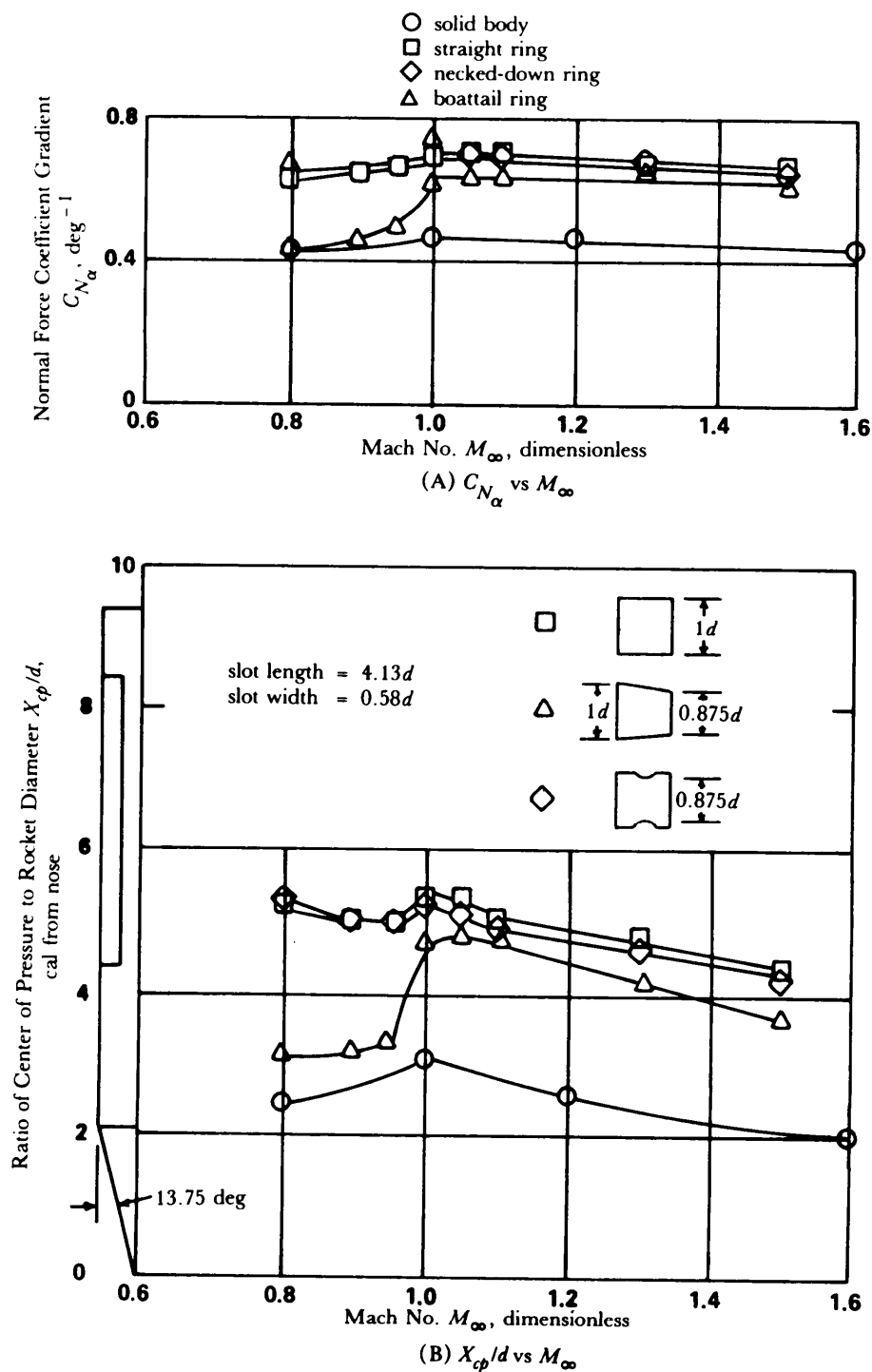
Figure 5-65. Aerodynamic Stability Coefficients for Various Longitudinally Supported Ring Shapes Compared to Solid Body (Ref. 33)
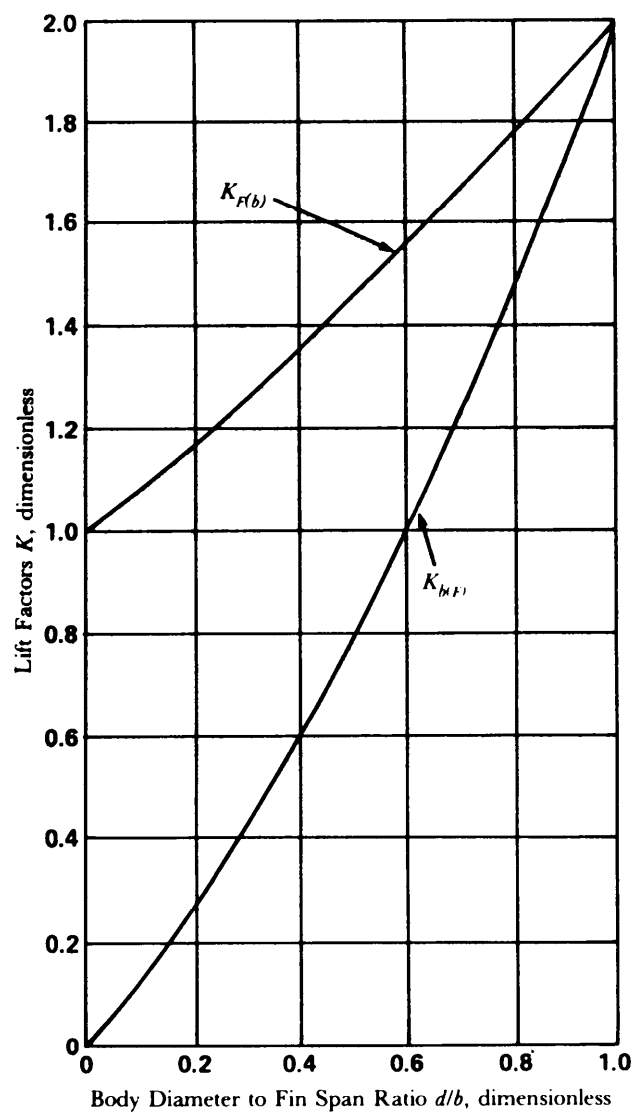
Figure 5-66. Values of Lift Ratios Based on Slender Body Theory (Adapted from Ref. 35)
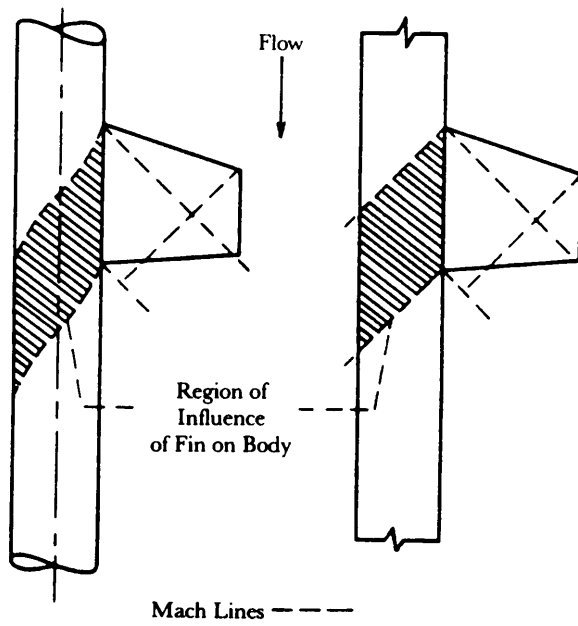
(A) Nonplanar Model　　　　**(B) Planar Model**

Figure 5-67.　Interference Effect of Fin on Body (Ref. 35)

(A) With Afterbody

(B) Without Afterbody
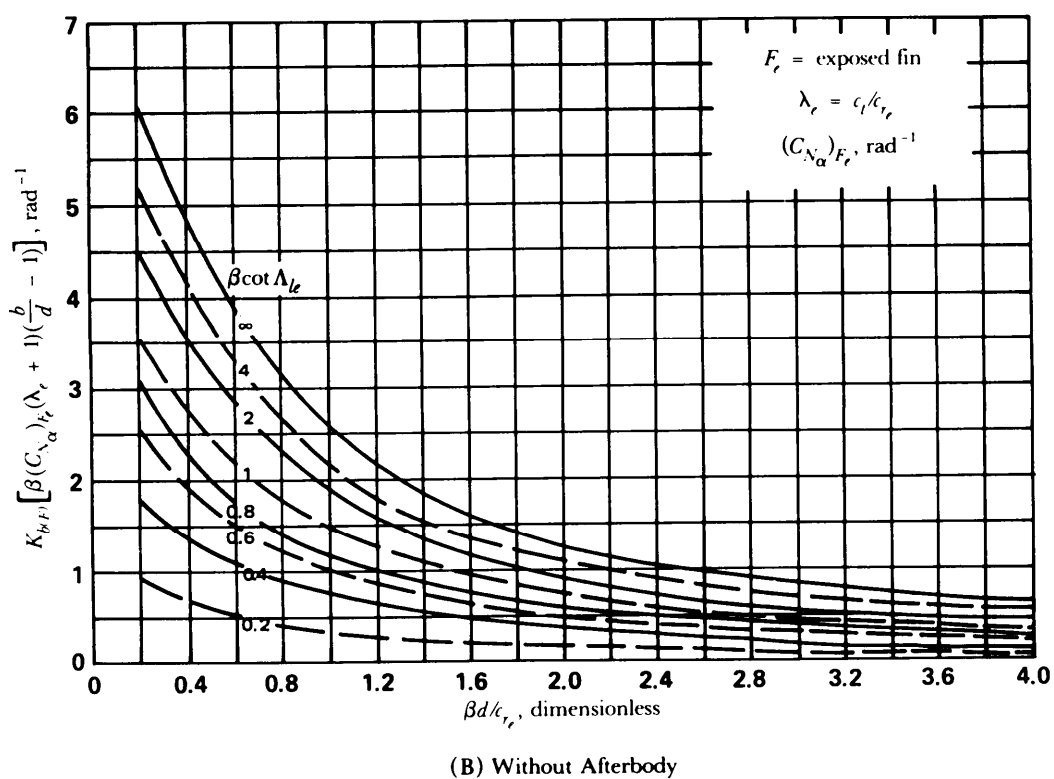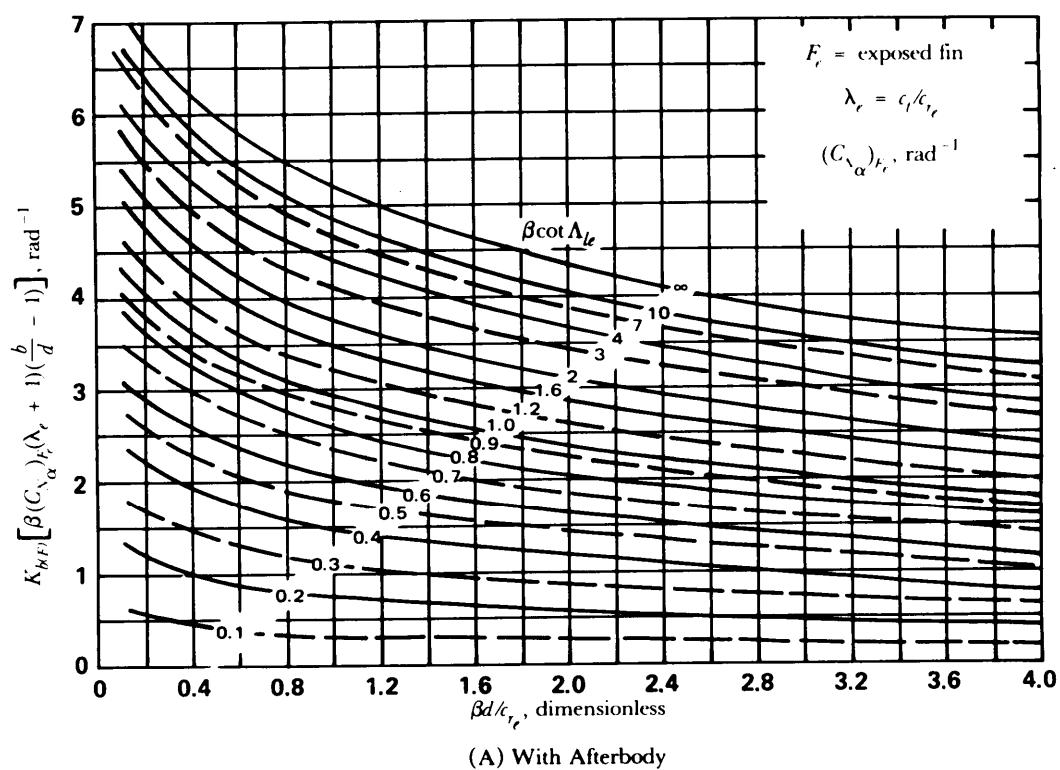
Figure 5-68.   Lift Factors—Influence of Fin on Body (Adapted from Ref. 35)

(A) $a_l/m = 0$ (Rectangular Fin)

(B) $a_l/m = 0.2$ (Clipped Delta Fin)
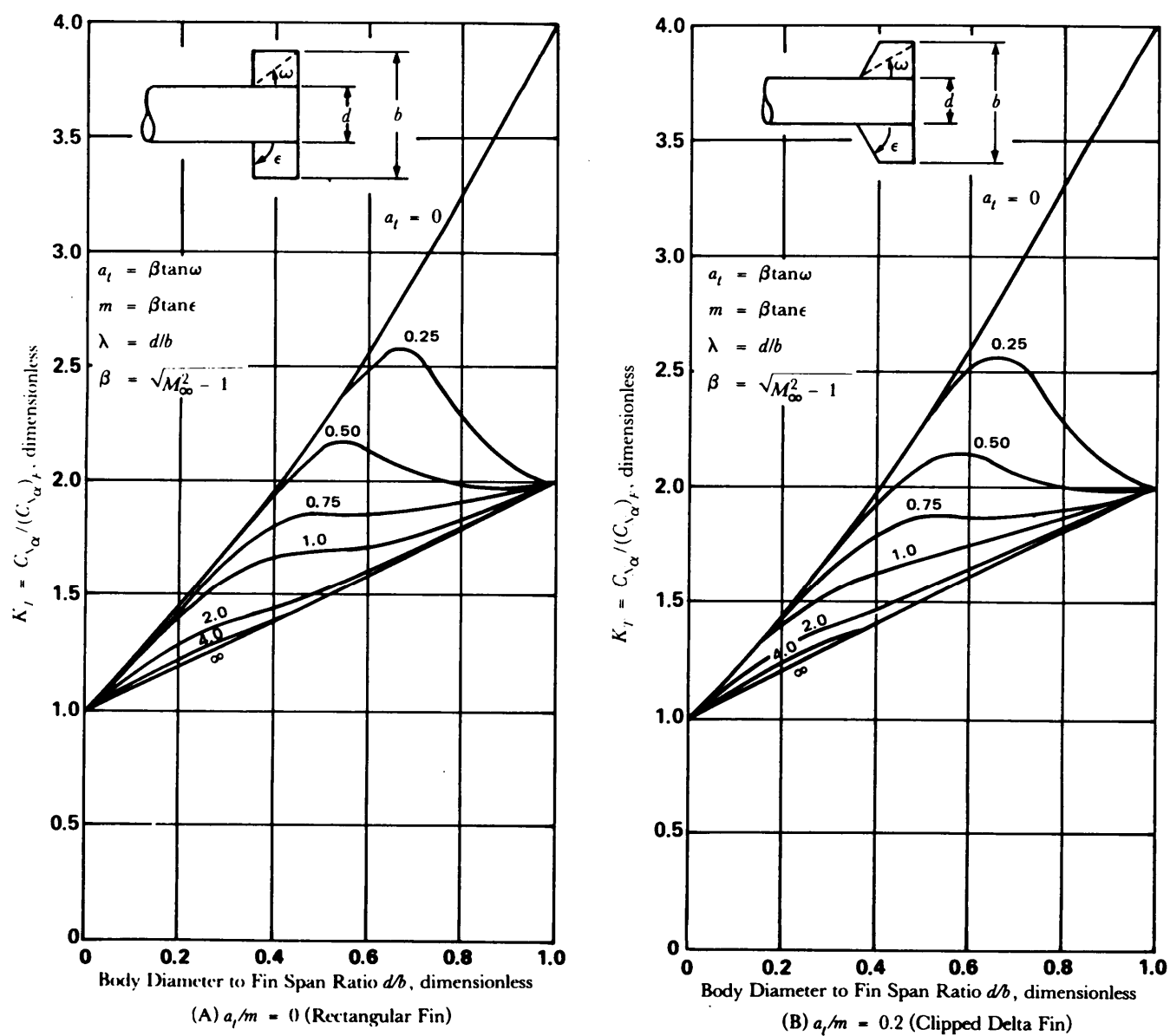
Figure 5-69.   Total Fin-Body Interference Factor for Various a_l/m Ratios

(C) $a_t/m = 0.4$ (Clipped Delta Fin)

(D) $a_t/m = 0.6$ (Clipped Delta Fin)
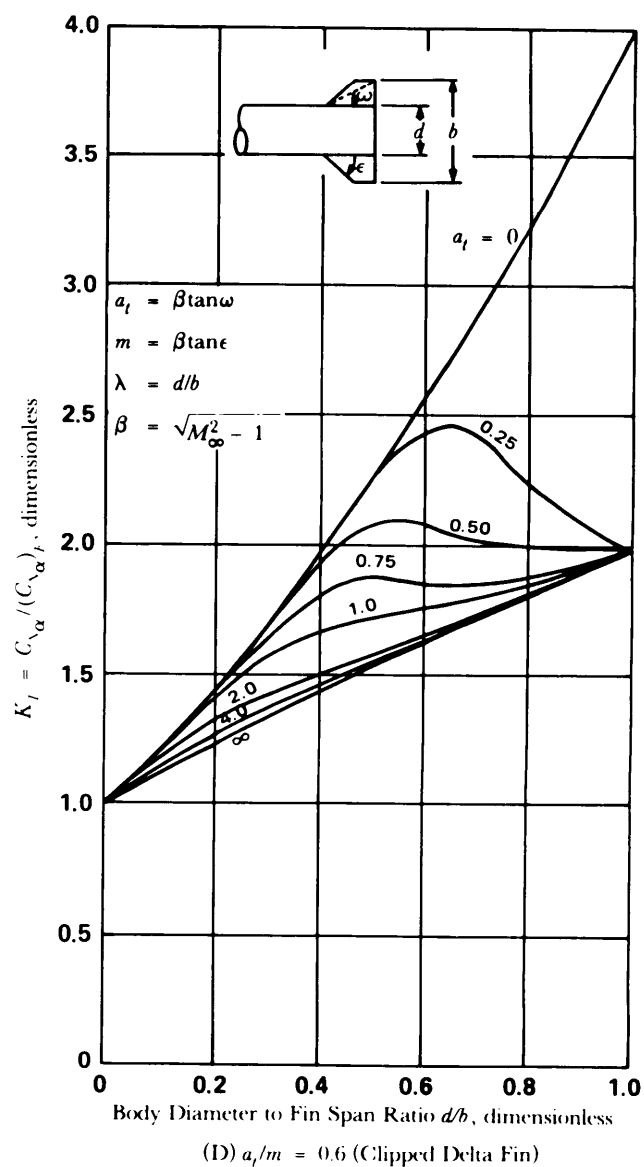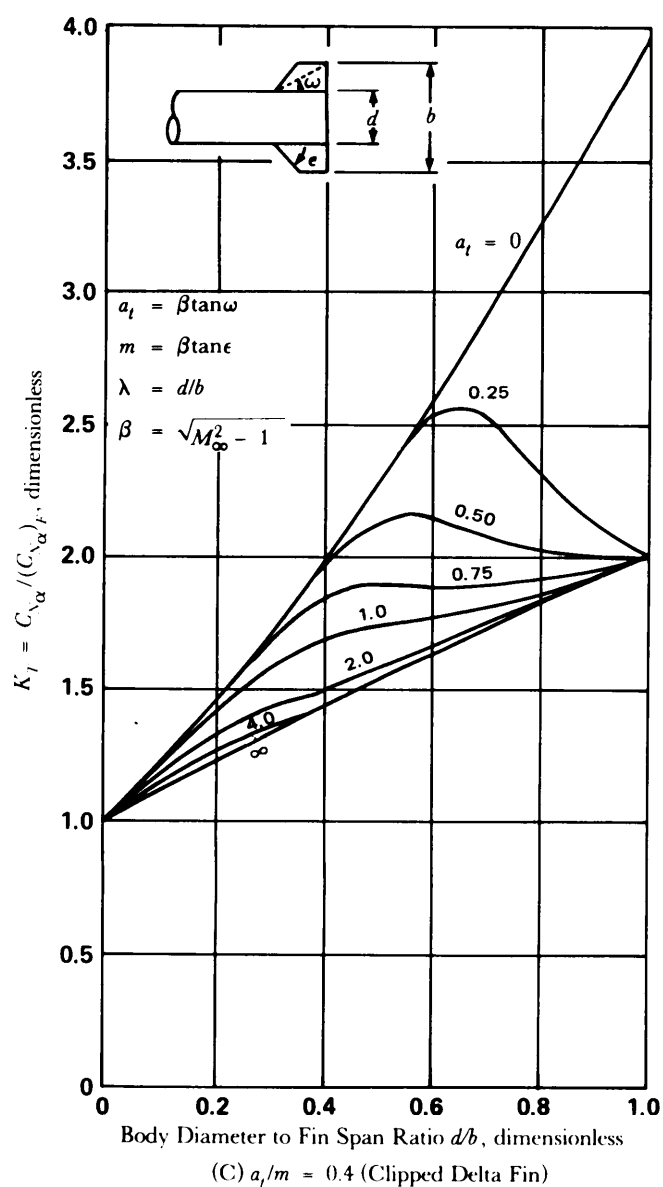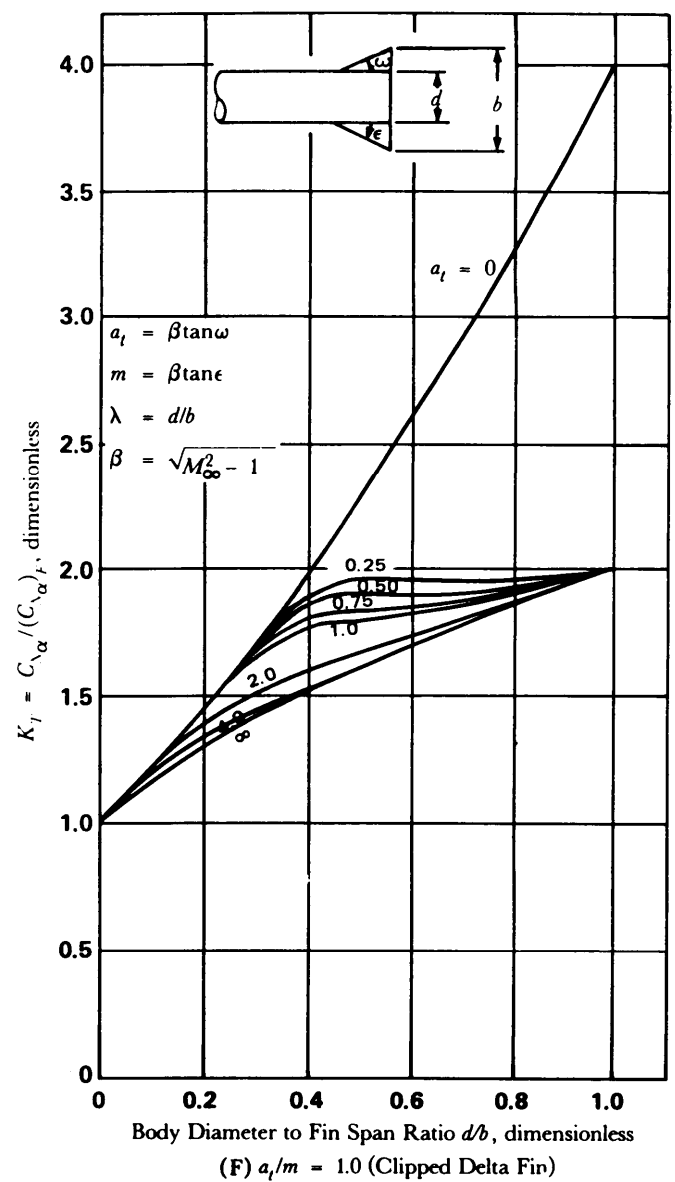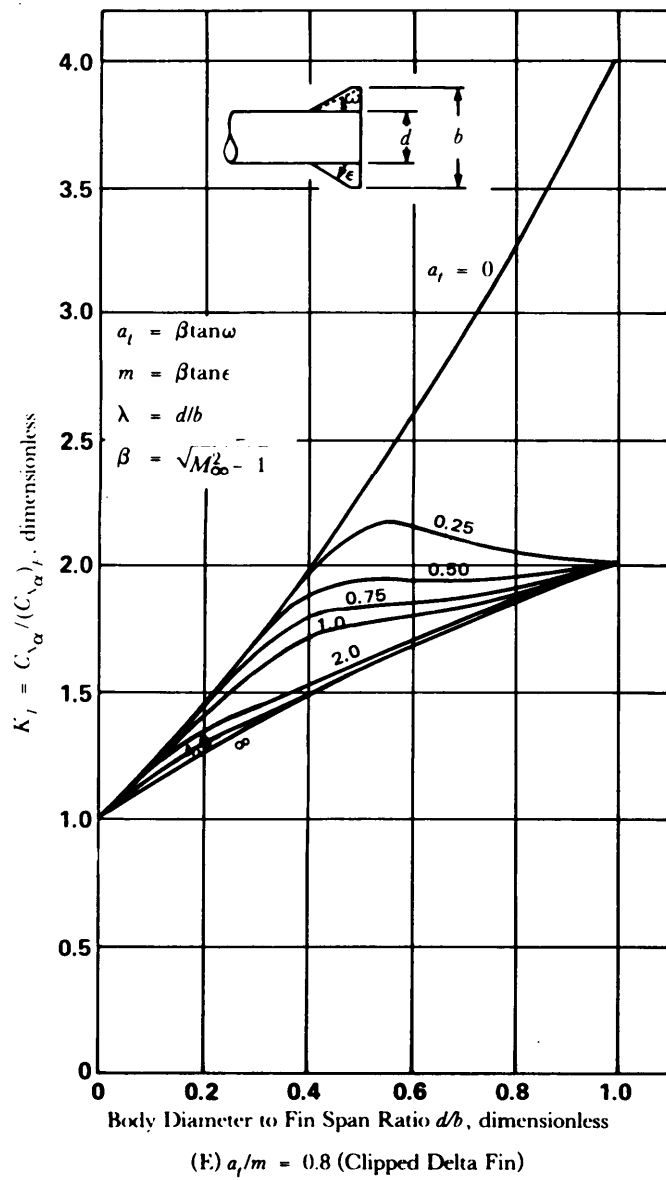
Figure 5-69. (cont'd)

Figure 5-69. (cont'd)
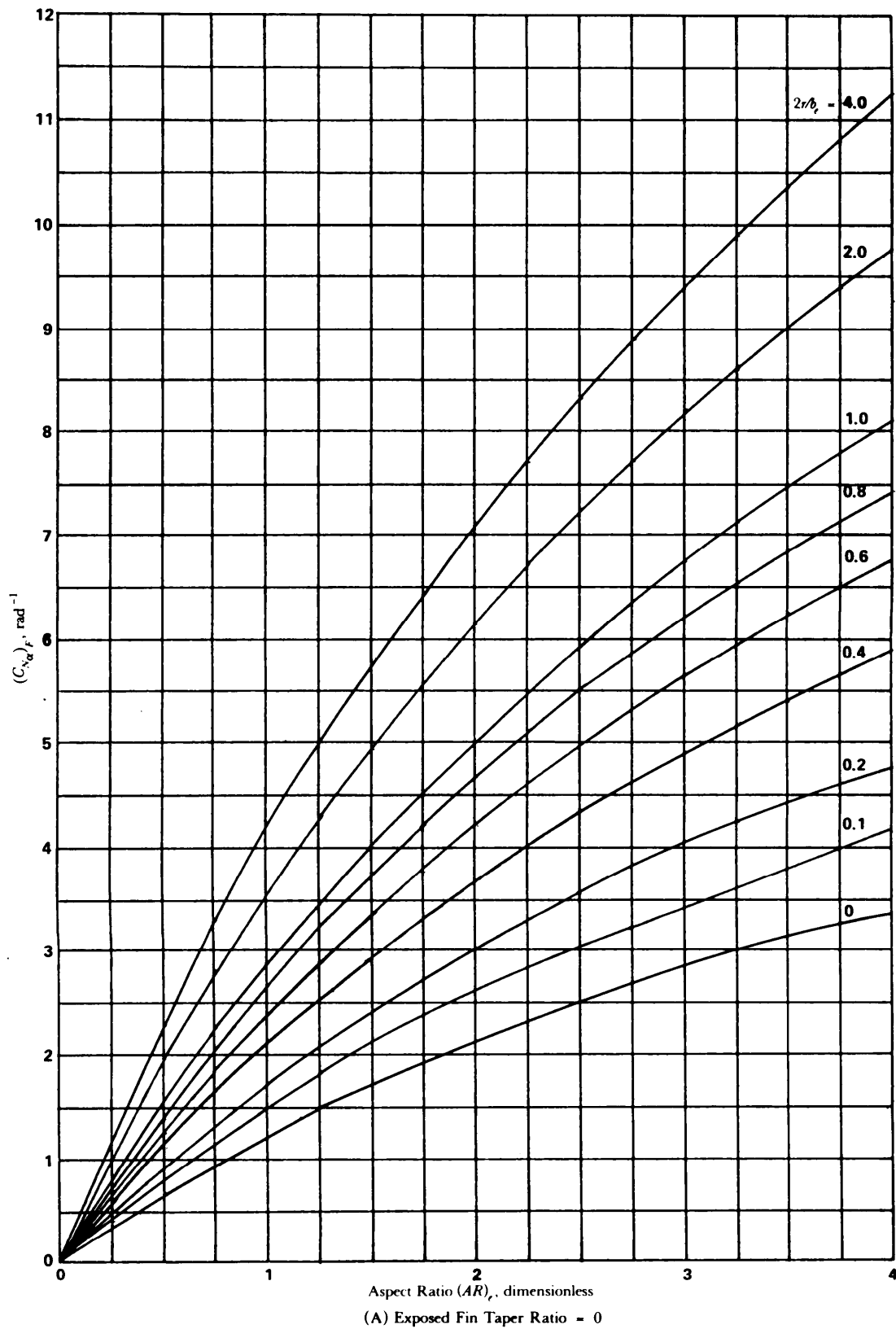
Figure 5-70. Normal Force of Fin-Body Combinations for Various Values of (AR), and $2r/b_e$ (Ref. 38)
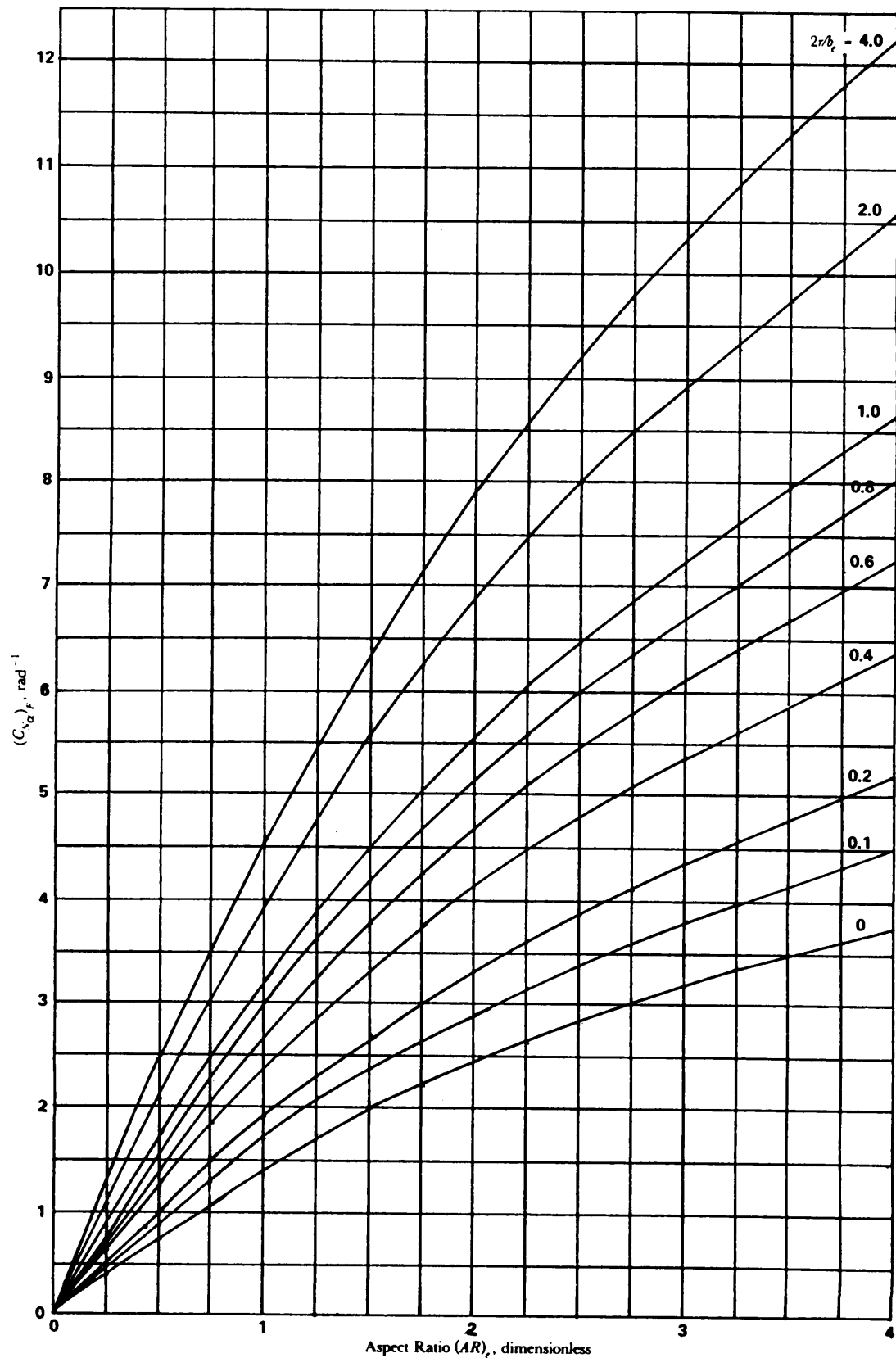
(B) Exposed Fin Taper Ratio = 0.25

Figure 5-70. (cont'd)

(C) Exposed Fin Taper Ratio = 0.50
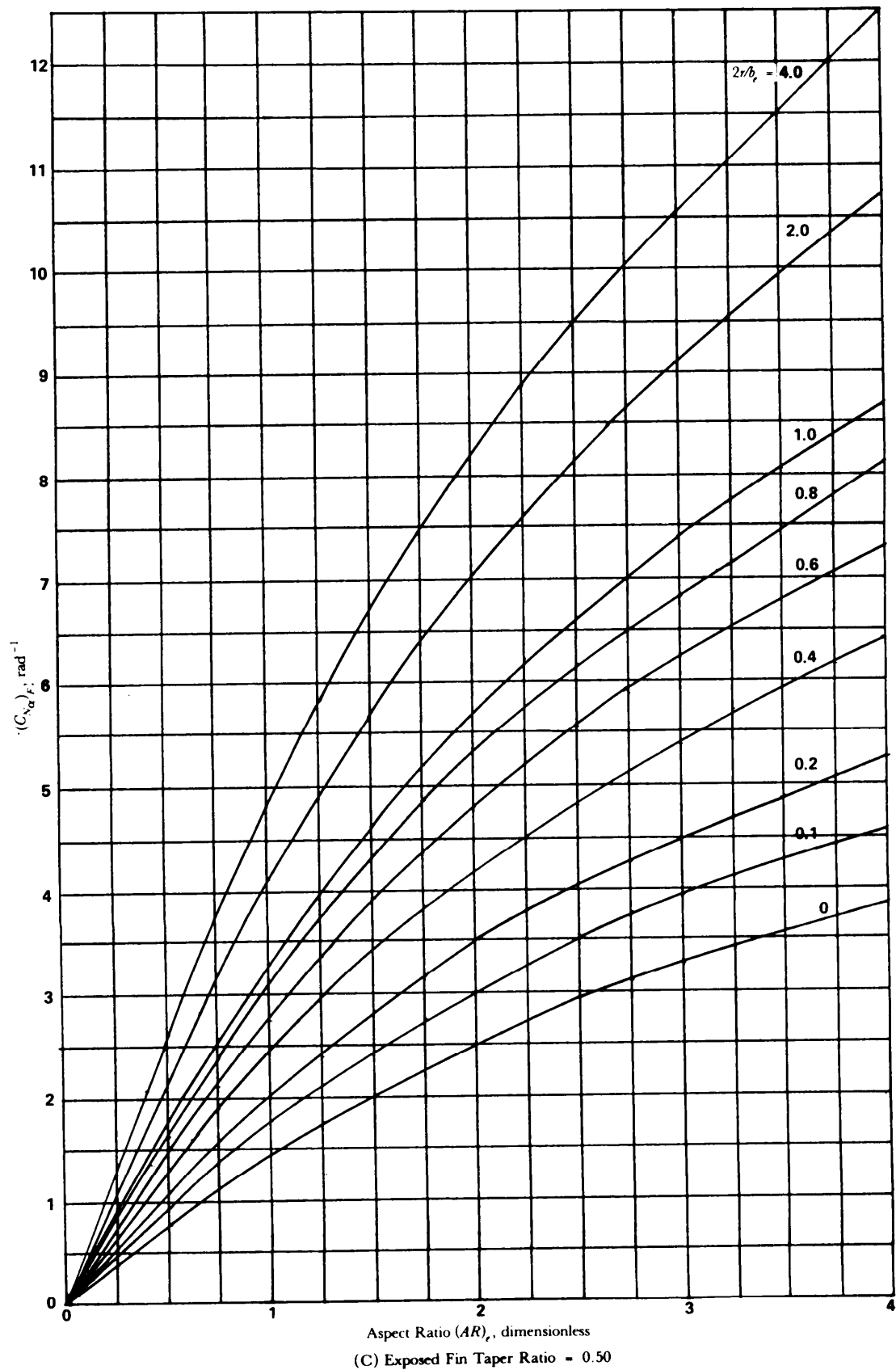
Figure 5-70. (cont'd)

MIL-HDBK-762(MI)

(D) Exposed Fin Taper Ratio = 0.75

Figure 5-70. (cont'd)

(E) Exposed Fin Taper Ratio = 1.00
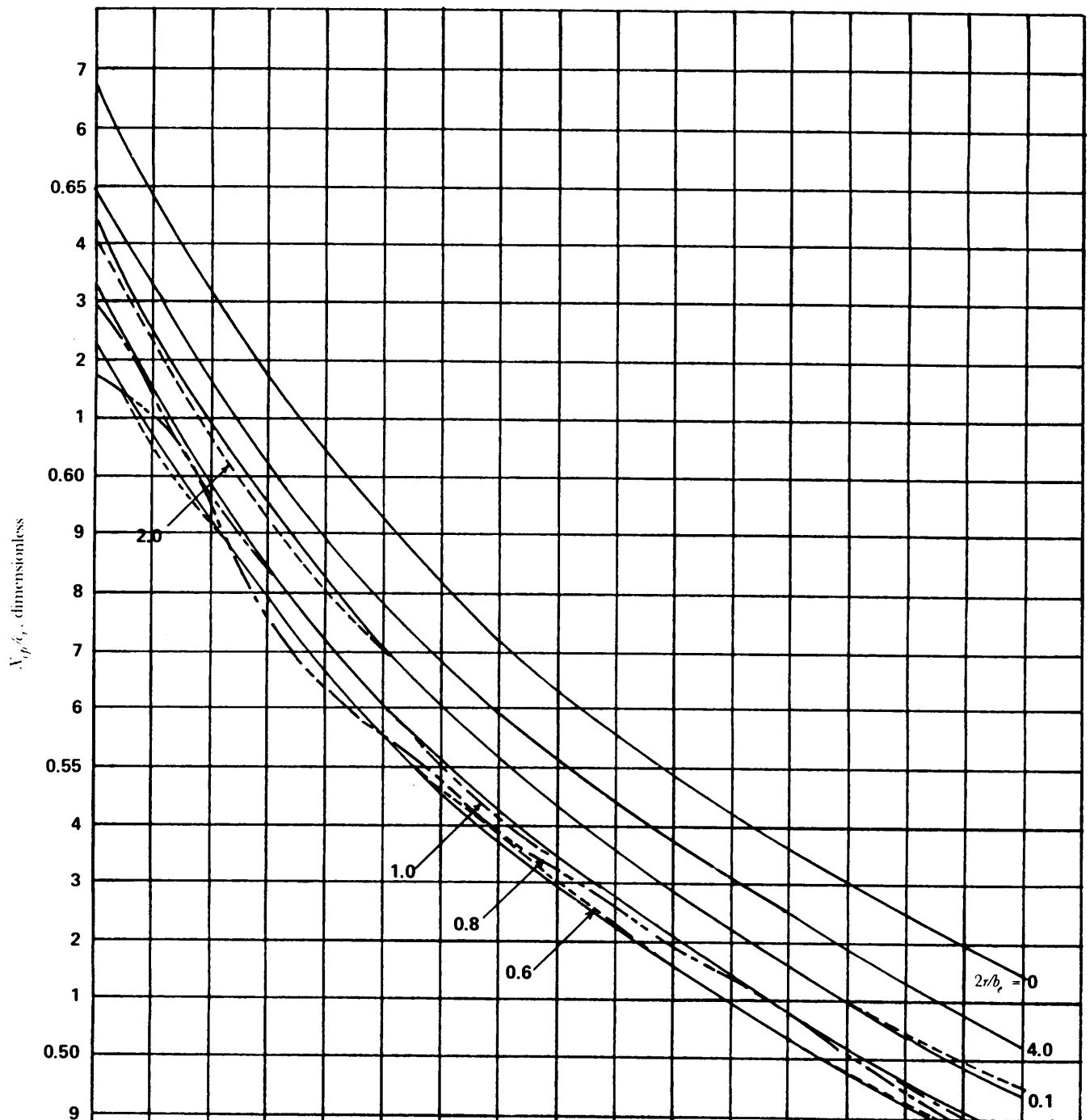
Figure 5-70. (cont'd)

Figure 5-71. Center of Pressure for Fins With Fin-Body Interference for Various Values of (AR)ₑ and 2r/bₑ (Ref. 38)

(cent'd on next page)
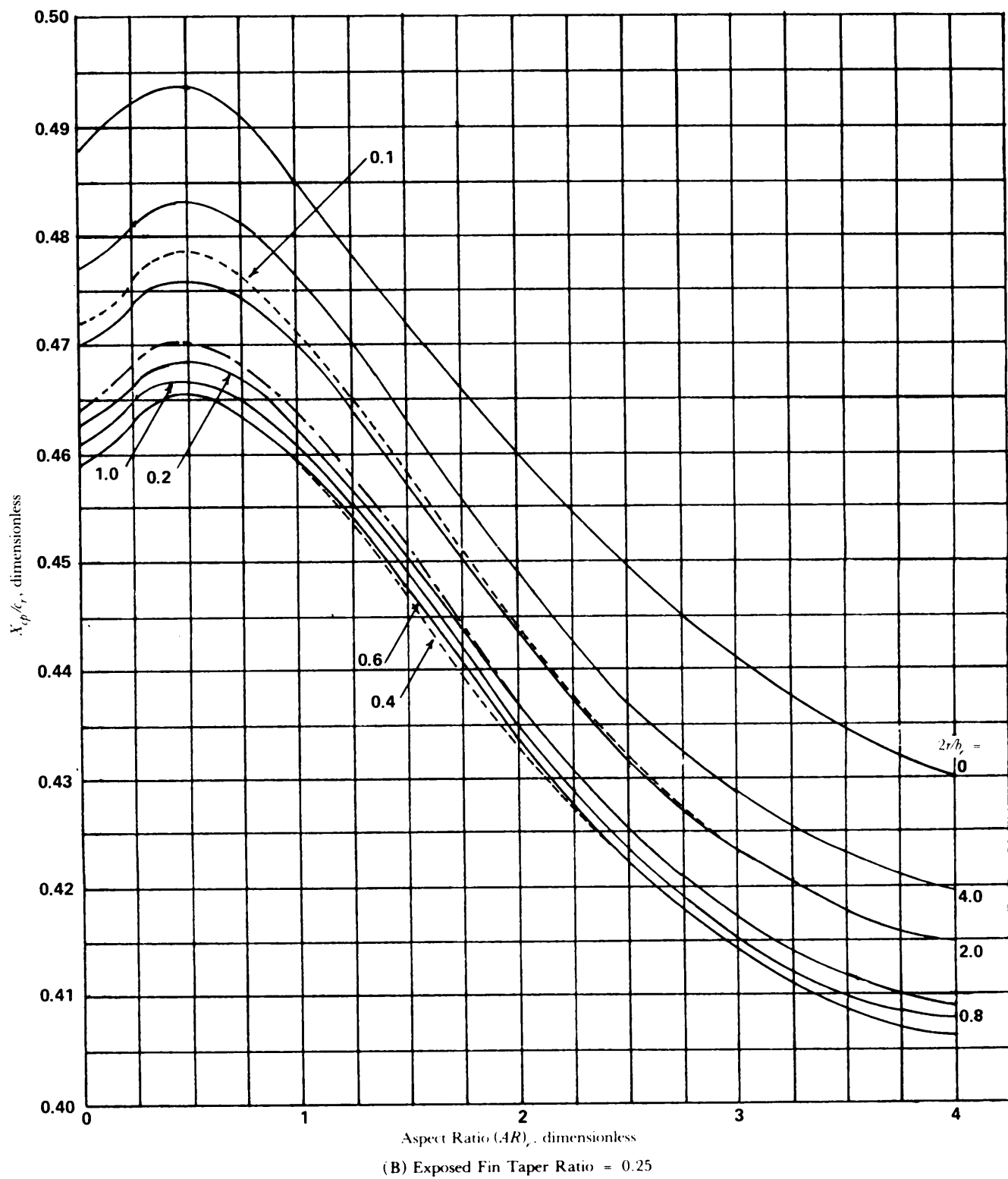
(B) Exposed Fin Taper Ratio = 0.25
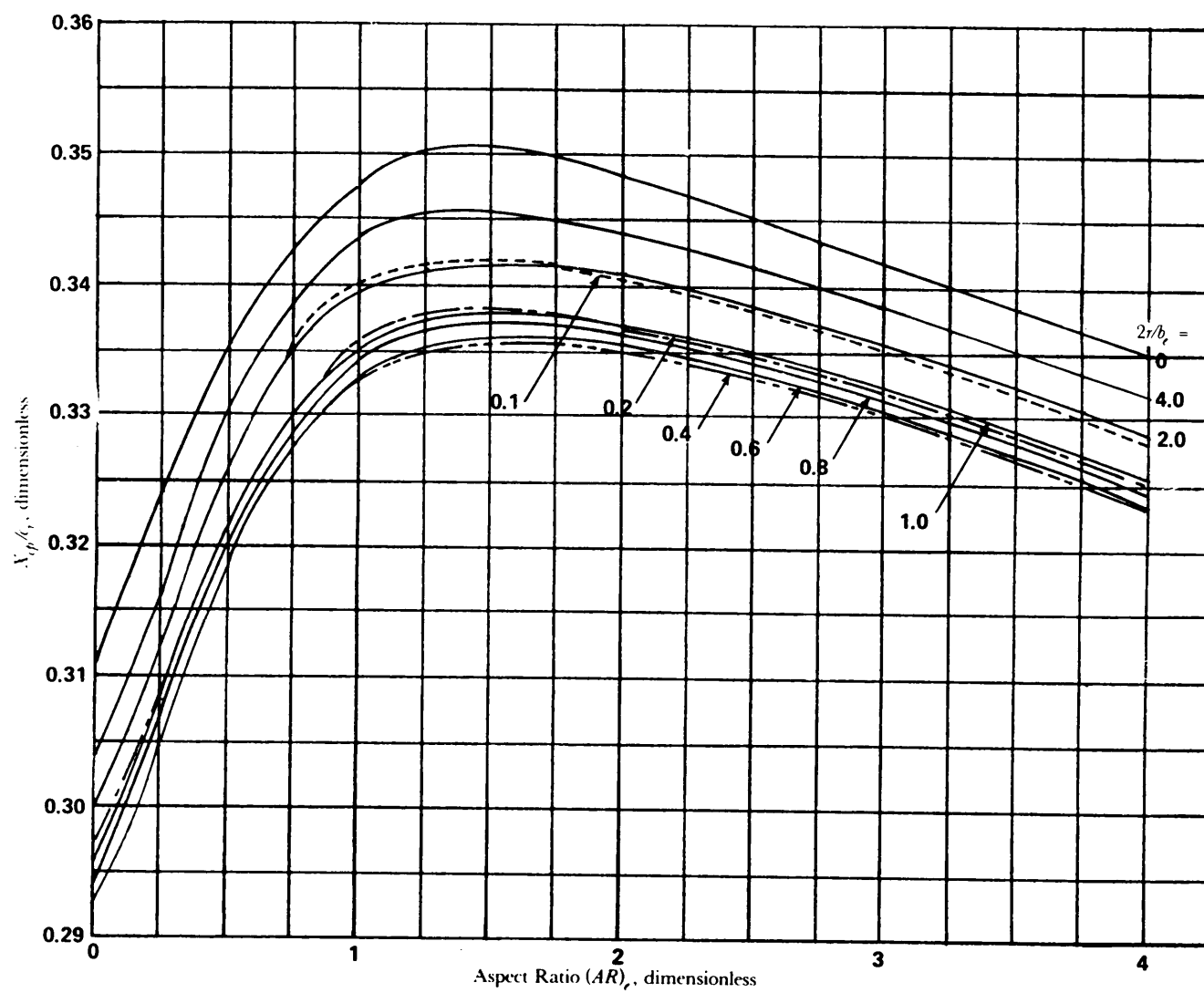
Figure 5-71. (cont'd)

(C) Exposed Fin Taper Ratio = 0.50

Figure 5-71. (cont'd)
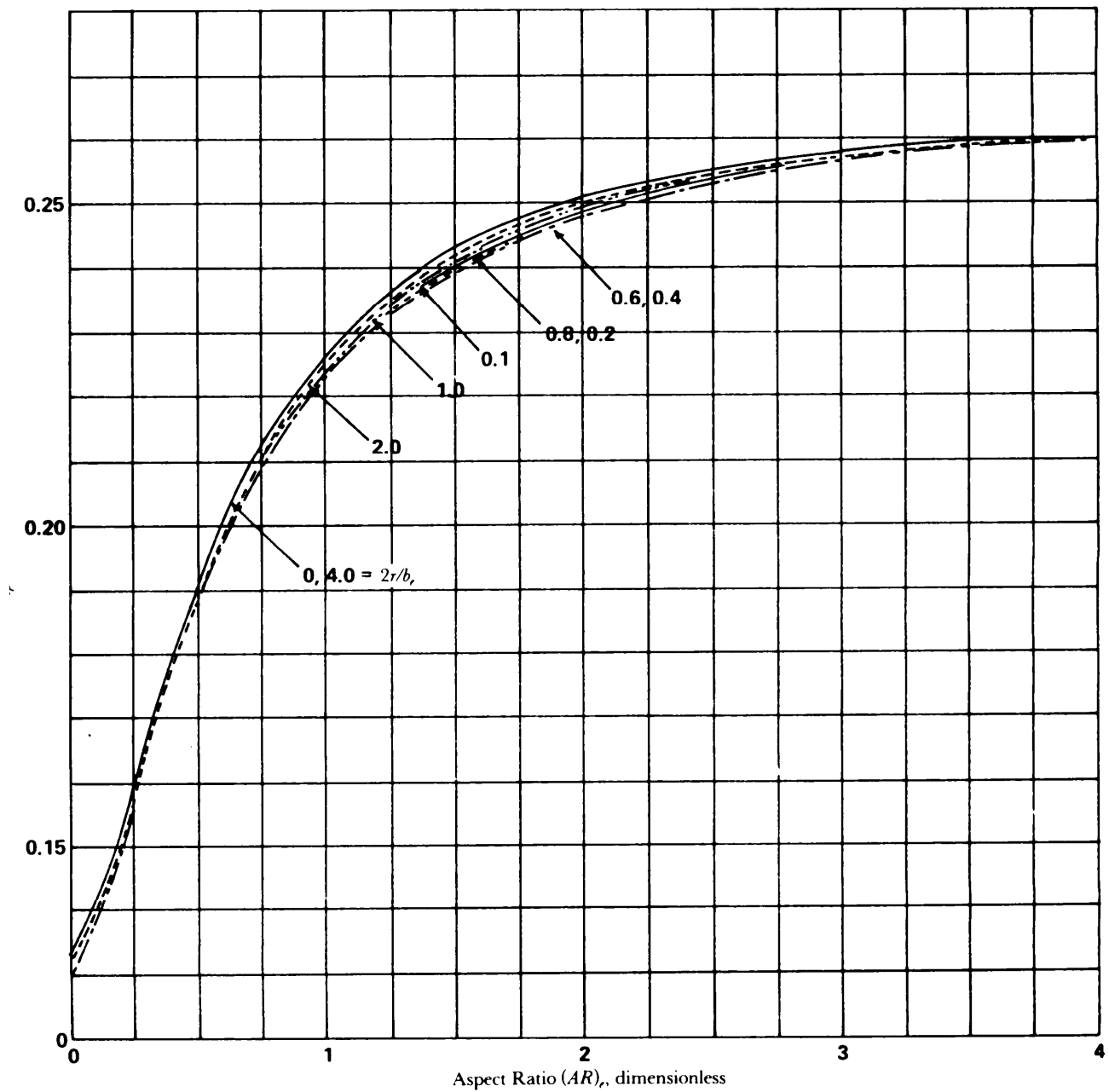
(D) Exposed Fin Taper Ratio = 0.75

Figure 5-71. (cont'd)
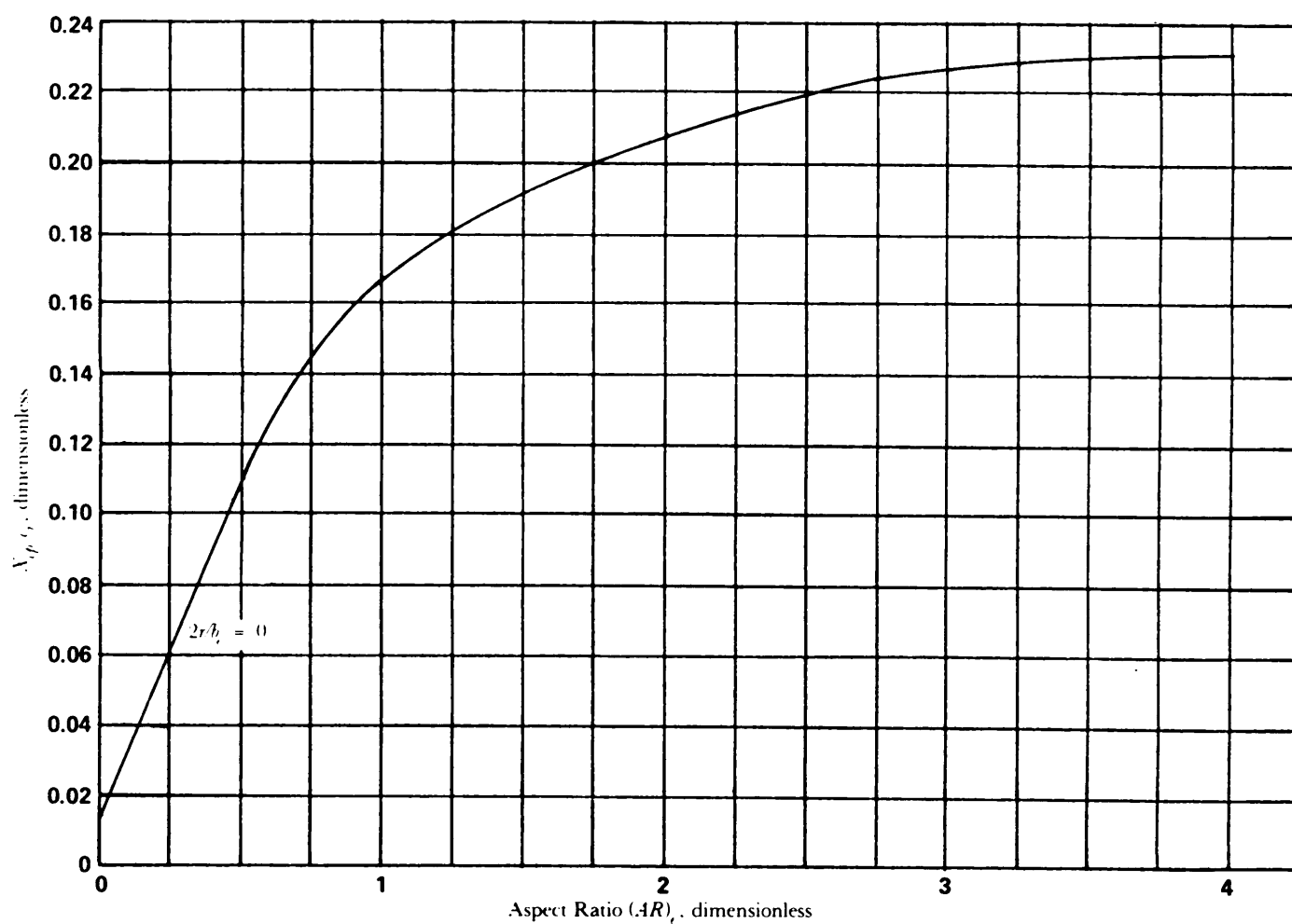
(E) Exposed Fin Taper Ratio = 1.00

Figure 5-71. (cont'd)
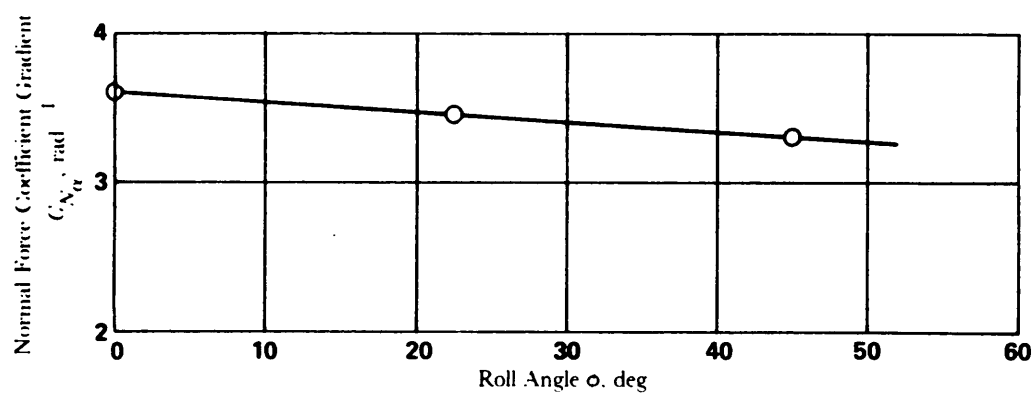
Figure 5-72. Effect of Roll Angle on Cruciform Fins at $M_\infty = 1.48$ **(Ref. 24)**
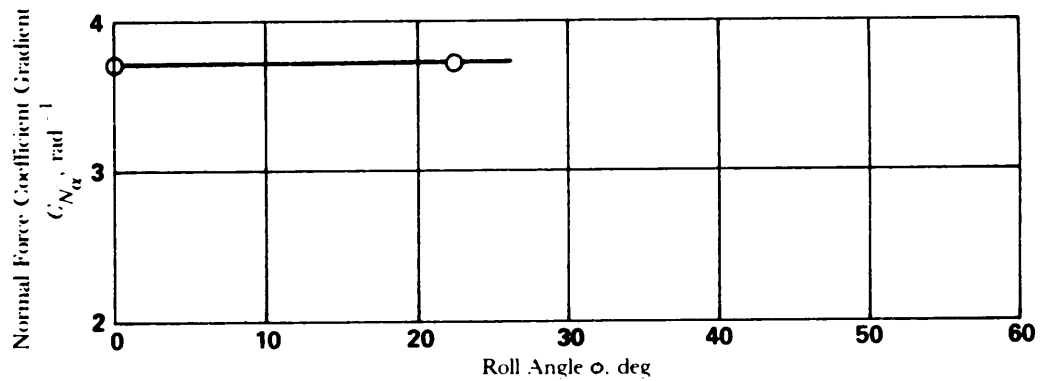
Figure 5-73.   Effect of Roll Angle on 8-Fin Configuration at $M_\infty = 1.48$ (Ref. 24)
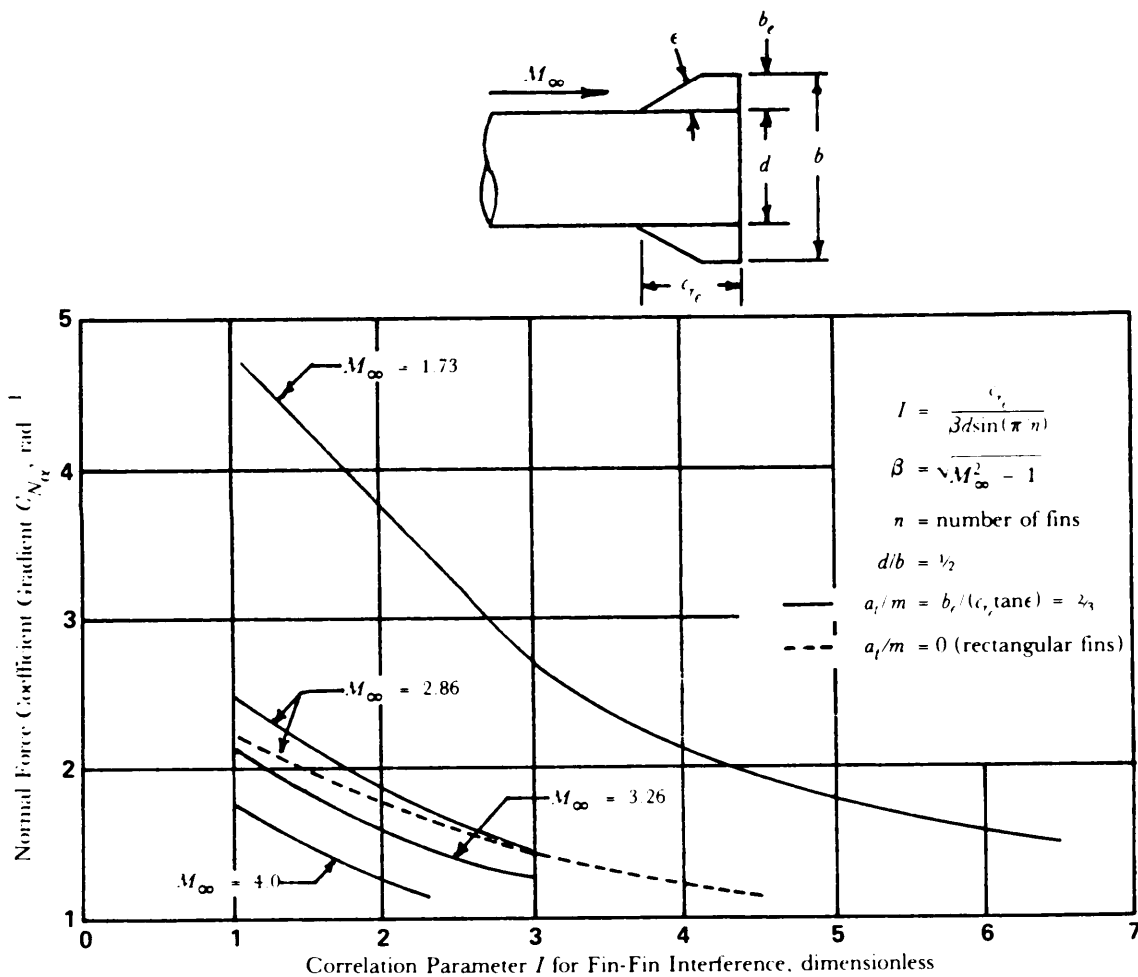
Figure 5-74.   Normal Force Coefficient of Multiple Fins at Various Supersonic Speeds (Adapted from Ref. 39)

$$\mu = \sin^{-1}(1/M_\infty), \text{ Mach angle, deg}$$

$$I = \frac{y}{\ell} = \frac{c_{r_f}}{\beta d \sin(\pi/n)} \quad \text{(Ref. 39)}$$

$$I' = \frac{y'}{\ell'} = \frac{c_{r_f}}{\beta(d + b_f)\sin(\pi/n)} \quad \text{(Ref. 24)}$$

(A) (B) (C)
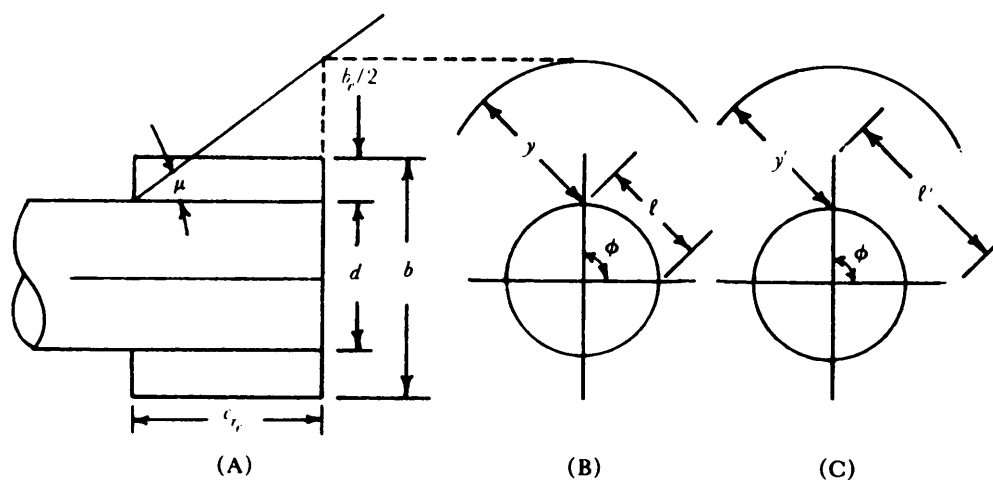
Figure 5-75. Interference Parameters Z and Z', and Fin Geometry (Ref. 24)

$$I' = c_{r_f}/[\beta(d + b_f)\sin(\pi/n)], \text{ dimensionless}$$
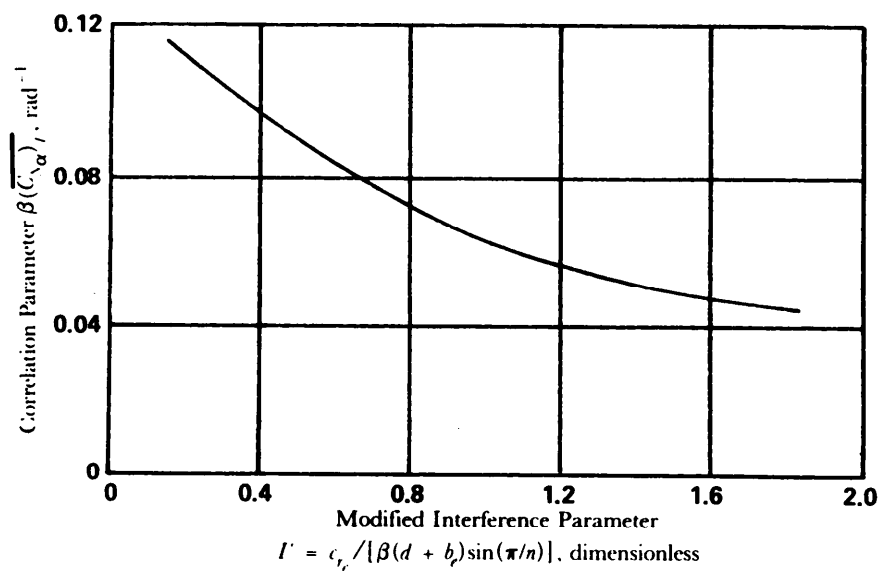
Figure 5-76. Correlation of Data with I' for Various Aspect Ratios (Ref. 24)

5-151

Config. No.	$b_\ell/2$, mm	c_{r_ℓ}, mm	No. Fins
0000	0.00	0.00	0
F800	8.89	35.56	4
MF1	8.89	35.56	8
MF2	8.89	25.40	8
MF3	8.89	19.23	8
MF4	6.35	19.23	8
MF5	8.89	15.24	8
MF6	8.89	13.74	8
MF7	6.35	13.74	8
MF8	8.89	8.26	8
MF9	6.35	8.26	8
MF10	6.35	35.56	4
MF11	8.89	25.40	4
MF12	6.35	25.40	4
MF13	8.89	15.24	4
MF14	6.35	15.24	4
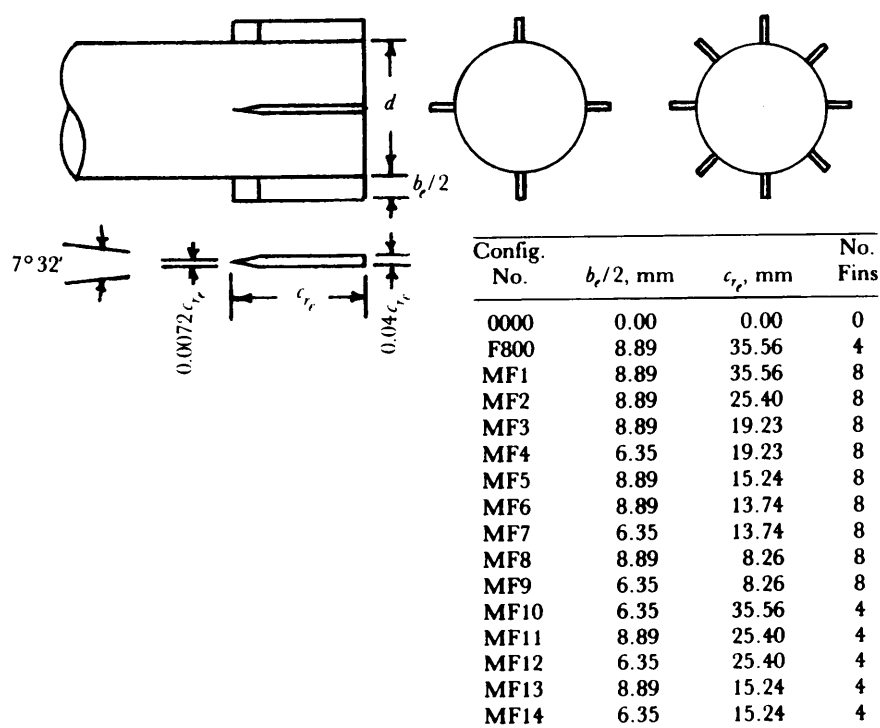
Figure 5-77. Multiple Fin Model Geometry (Ref. 24)
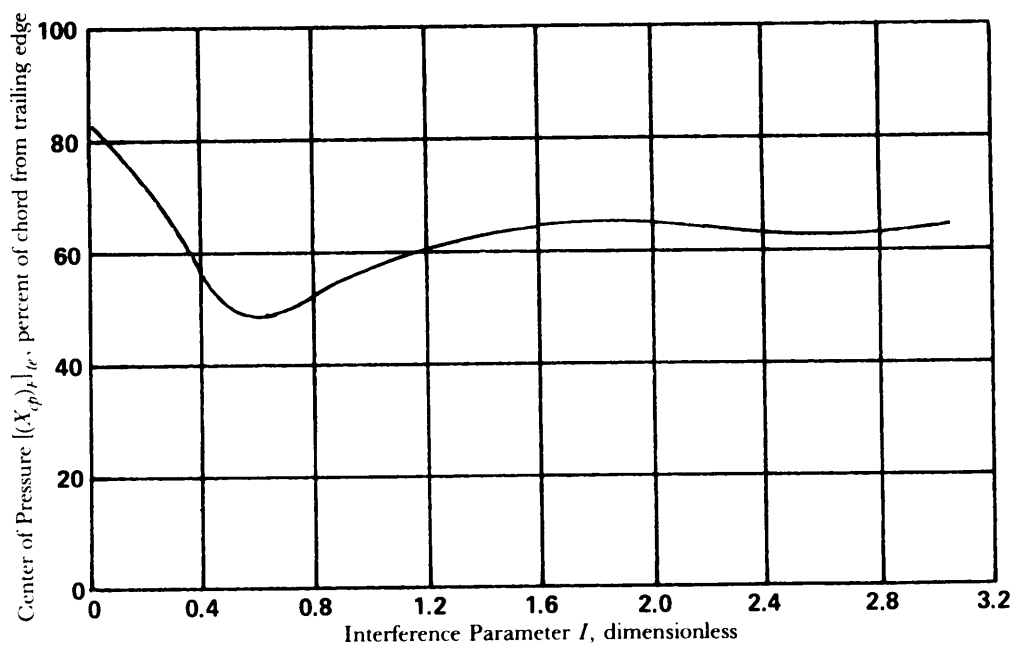
Figure 5-78. Faired Center of Pressure vs Interference Parameter I (Ref. 24)
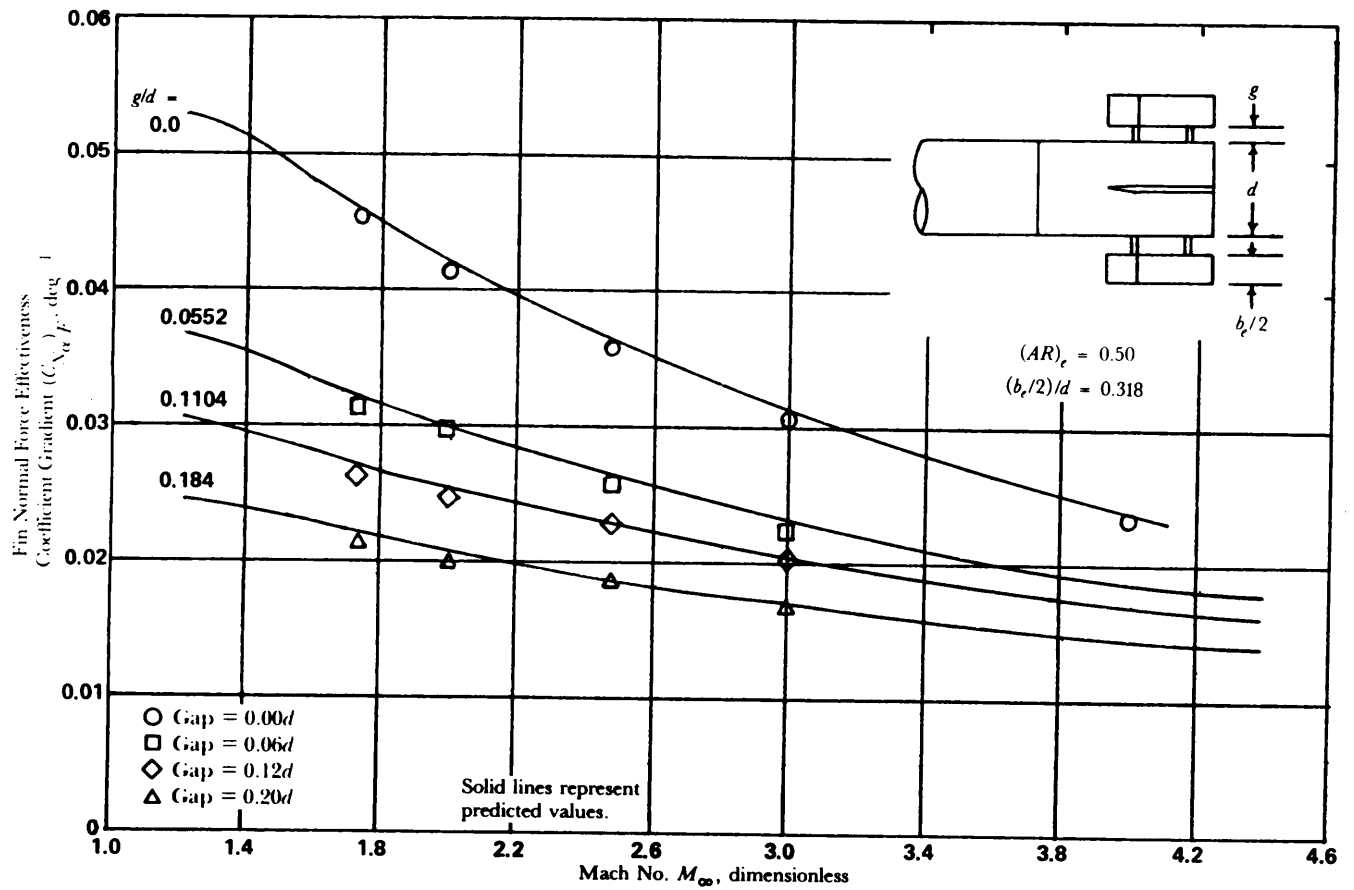
Figure 5-79. Fin Effectiveness With Gaps as a Function of Mach Number (Ref. 41)

(A) X_{cp}/d vs M_∞

(B) C_{N_α} vs M_∞
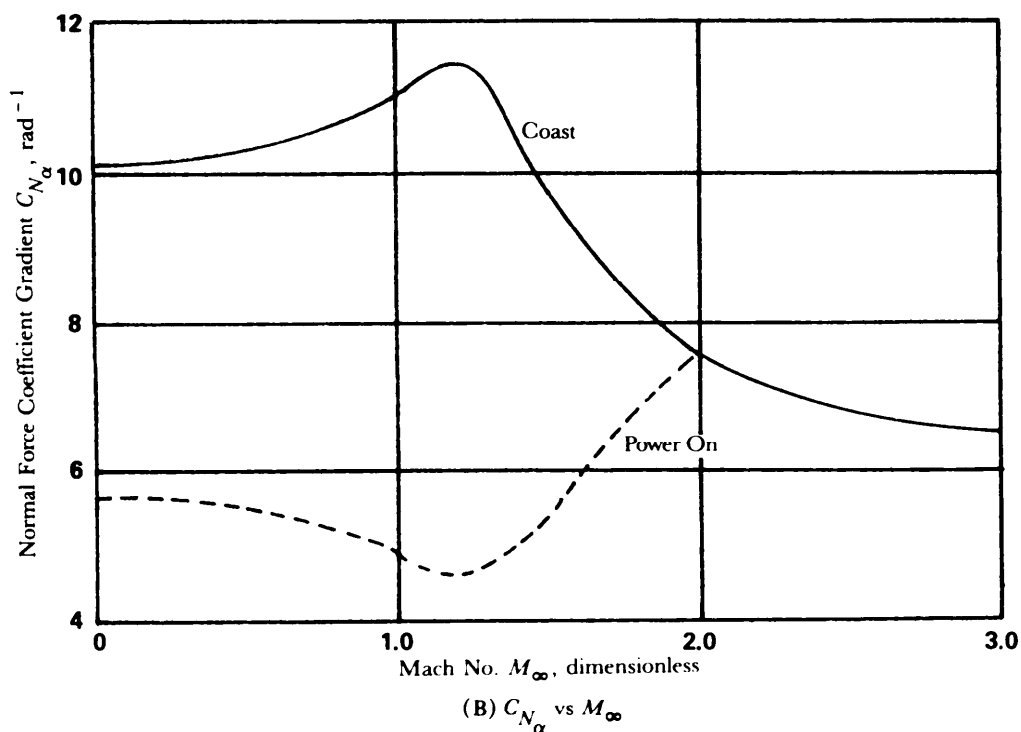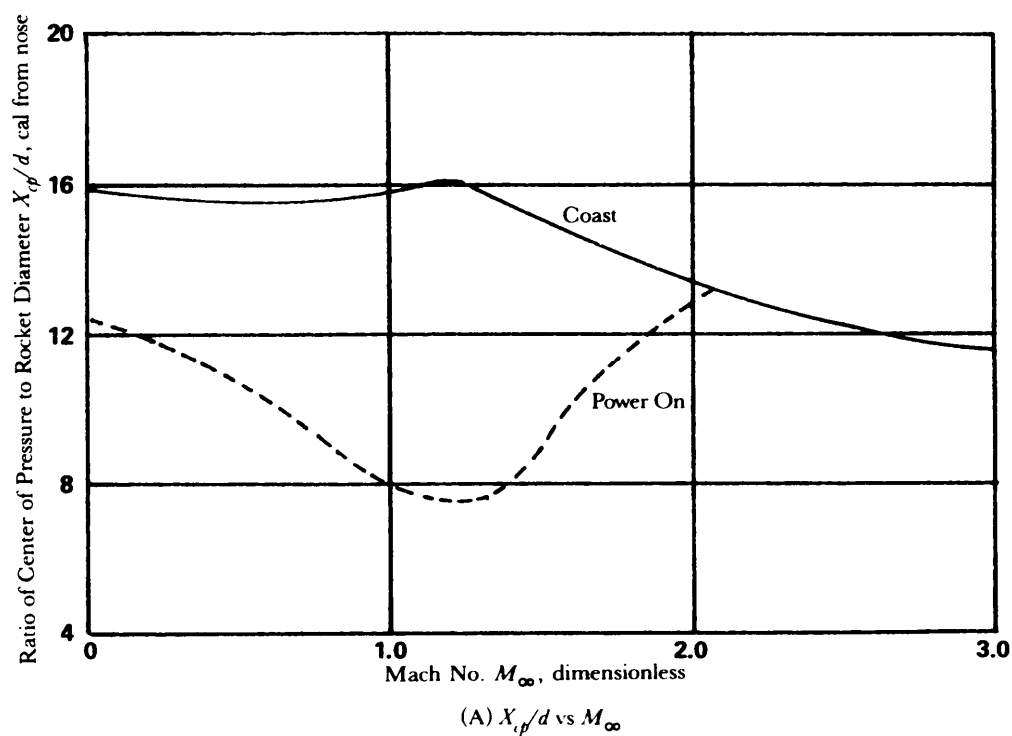
Figure 5-80. Normal Force Coefficient Gradient and Ratio of Center of Pressure to Rocket Diameter vs Mach Number of a Typical Rocket With and Without Thrust (Ref. 42)

MIL-HDBK-762(MI)
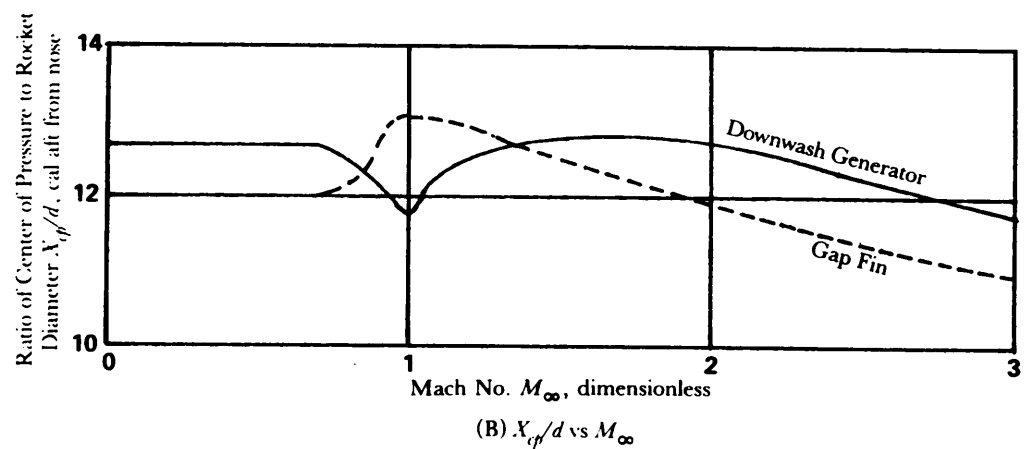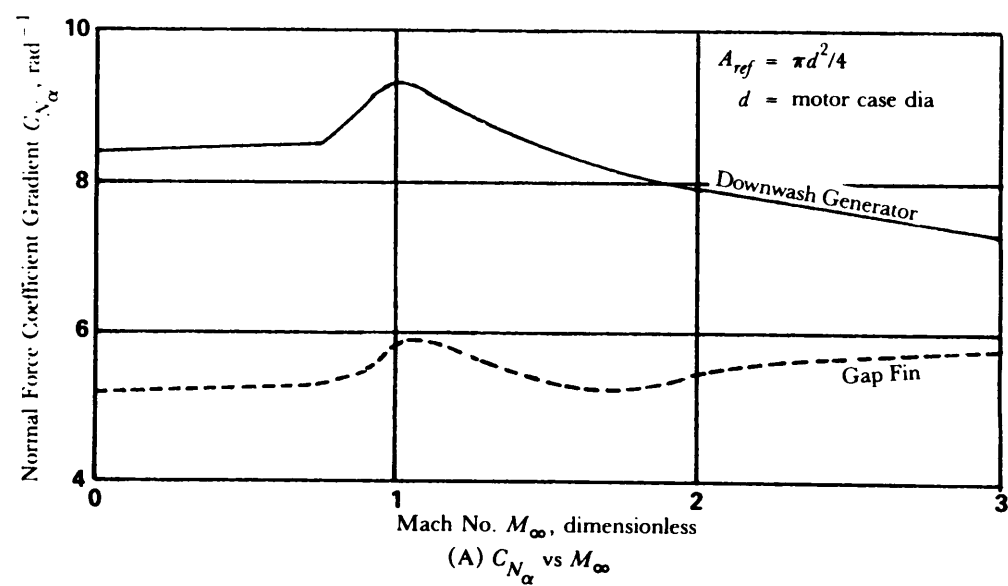
Figure 5-81. Effect of Downwash Generators and Fin-Body Gaps on Static Stability (Ref. 43)

(A) $(C_{N_\alpha})_b$ vs M_∞

(B) $(X_{cp}/d)_b$ vs M_∞
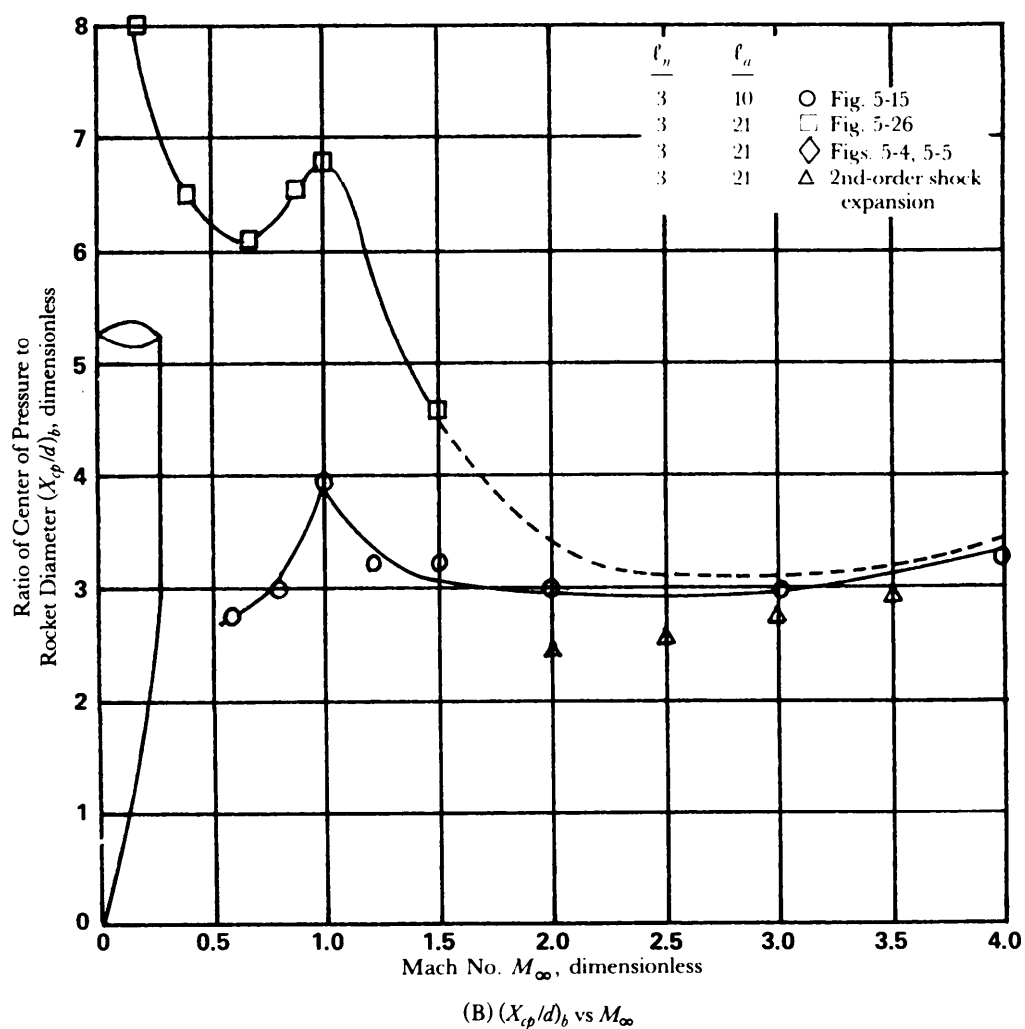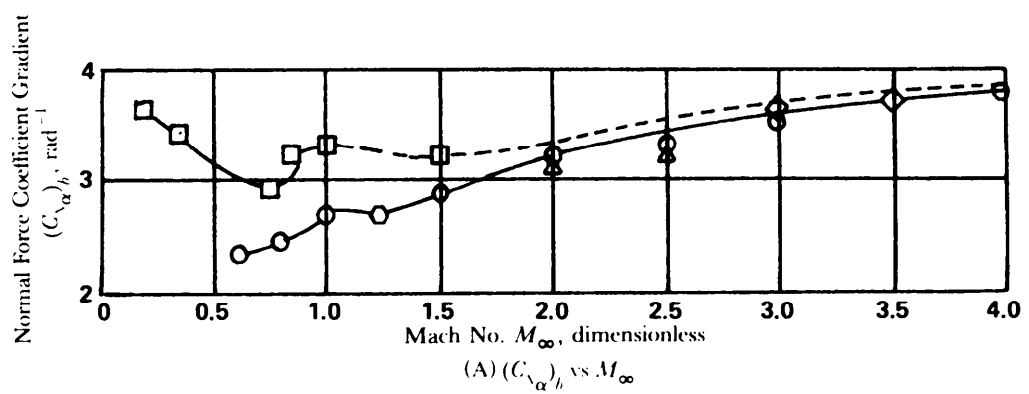
Figure 5-82. Body Data—Sample Calculation

(All dimensions in calibers)

$b/2 = 0.32d$

BODY DATA

$$d = 1 \text{ cal}$$
$$\ell_n = 3.0 \text{ (tangent ogive) cal}$$
$$\ell_{ab} = 21.0 \text{ cal}$$
$$\ell_T = \ell_n + \ell_{ab} = 24.0 \text{ cal}$$
$$CG_{gross} = 11.33 \text{ cal from nose}$$
$$CG_{burnout} = 9.58 \text{ cal from nose}$$

FIN DATA

Fins are designed to provide about 1 cal static margin at maximum $M_\infty = 3.5$. Fins are rectangular planform.

$$c = c_e = c_{r_e} = 2.0 \text{ cal}$$

$$t = 0.04 \text{ cal}$$

$$(AR)_e = \frac{b_e^2}{S_{F_e}} = \frac{b_e^2}{(2)(c_{r_e})(b_e/2)} = \frac{b_e}{c_{r_e}} = \frac{2(0.32d)}{2d} = 0.32$$

$$\lambda = \frac{d}{2(b_e/2) + d} = \frac{1}{b_e + 1} \quad \text{(since } d = 1 \text{ cal)}$$

$$\frac{r}{b_e/2} = \frac{2r}{b_e} = \frac{d}{b_e} = \frac{1}{b_e} \quad \text{(since } d = 1 \text{ cal)}$$

$$b/c = t/c = \frac{0.04}{2} = 0.02 \quad \text{(since fin profile is flat)}$$

$$\frac{S_{F_e}}{A_{ref}} = \frac{c_{r_e}(b_e/2)(2)}{\pi d^2 /4} = \frac{4b_e c_{r_e}}{\pi} \quad \text{(since } d = 1 \text{ cal)}$$

(S_{F_e} is fin planform area in one plane.)

$$a_t = \frac{\beta(b_e/2)}{c_{r_e}} = \frac{\beta(b_e/2)}{2} \quad \text{(since from figure } c = 2d \text{ and } d = 1 \text{ cal)}$$

$$(AR)_e(t/c)^{1/3} = (AR)_e(0.02)^{1/3} = 0.271 (AR)_e$$

$$\Lambda_{1/2} = 0 \quad \text{(no midchord line sweep)}$$

$$(AR)_e(t/c)^2 = (AR)_e(0.02)^2 = 0.0004 (AR)_e$$

$$(t/c)^{5/3} = (0.02)^{5/3} = 0.00147$$

Figure 5-83. Fin-Afterbody Configuration and Design Parameters for Sample Stability Calculation

MIL-HDBK-762(MI)

(A) C_{N_α} vs M_∞

(B) X_{CG}/d and X_{cp}/d vs M_∞
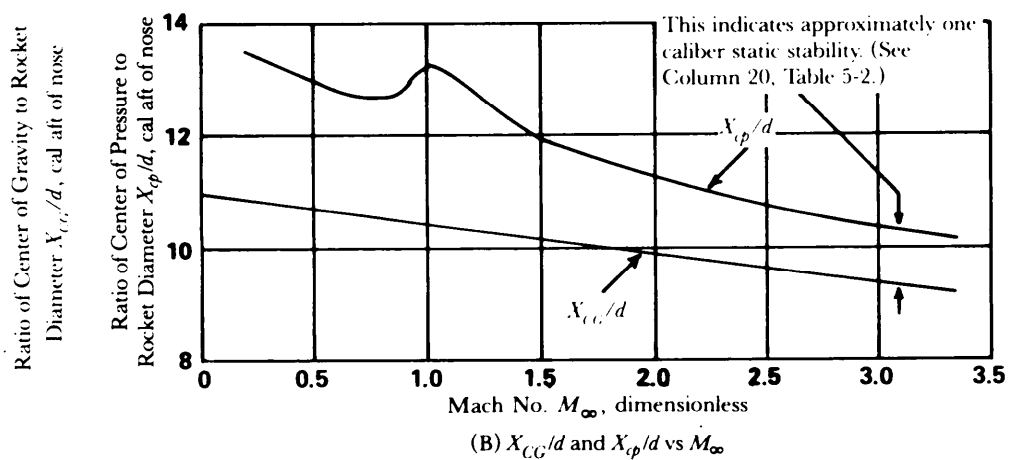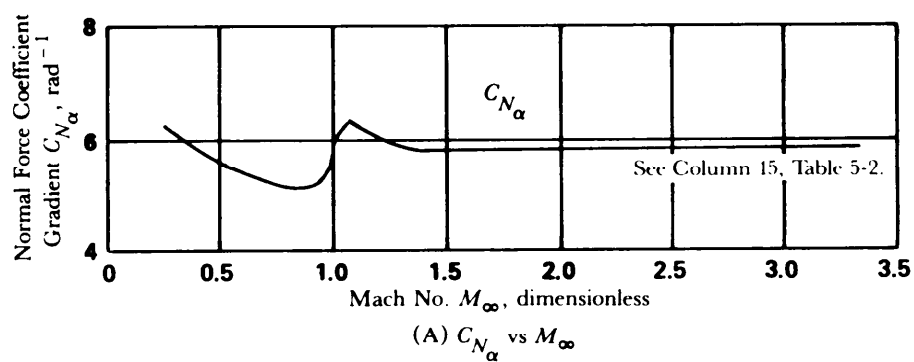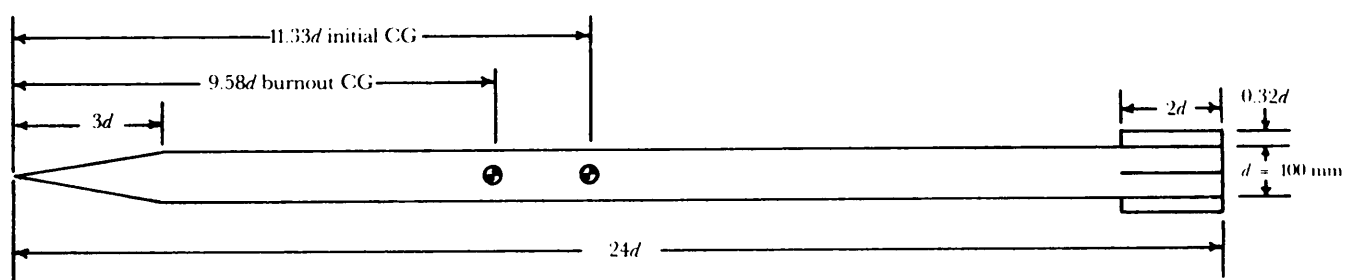
Figure 5-84.   Configuration and Aerodynamic Coefficients—Sample Calculation
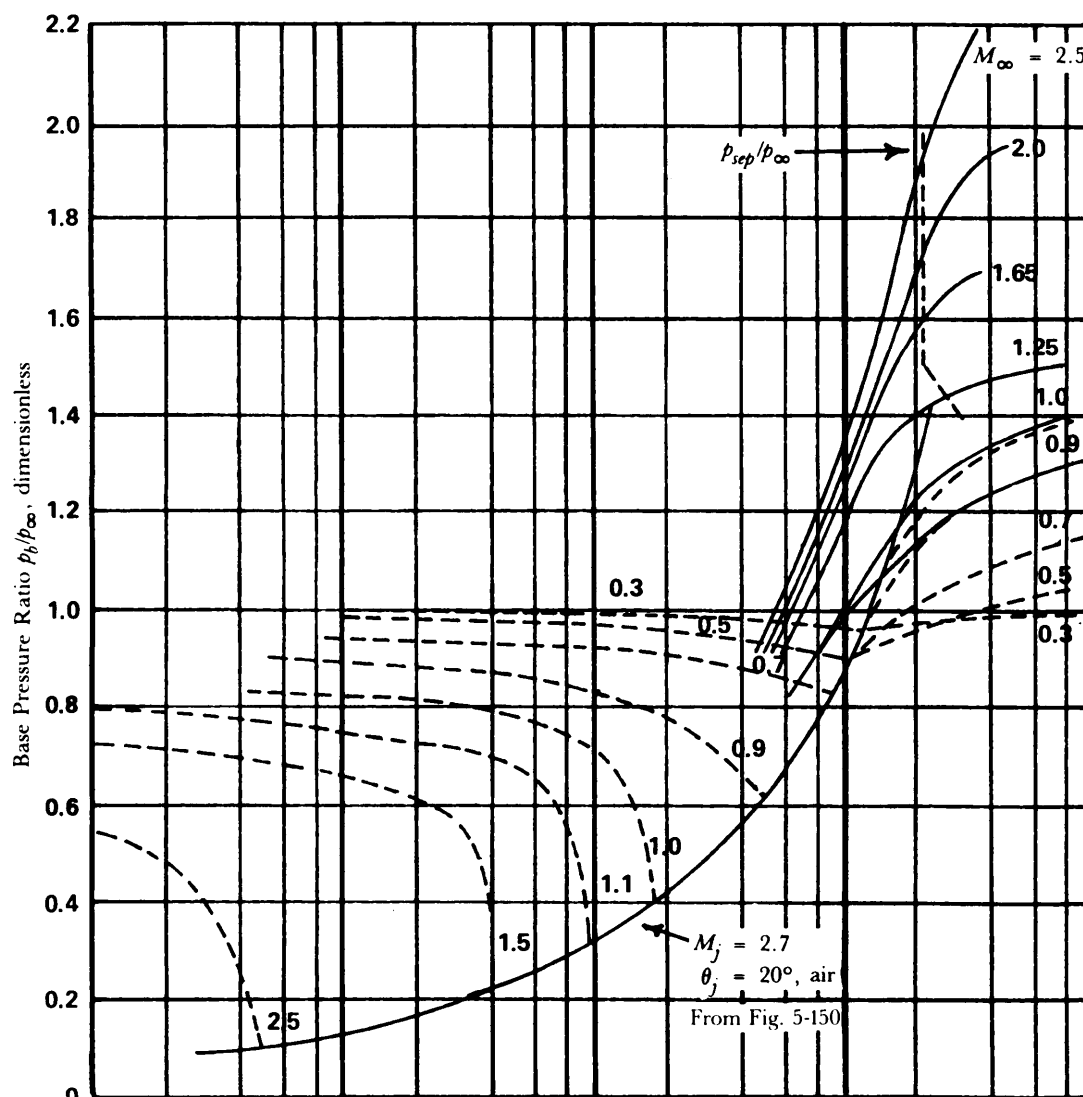
Figure 5-85. Variation of p_b/p_∞ With C_T for Variour Values of M_∞ (Cylindrical Afterbody $d_j/d_p = 0.8$, Air Nozzles Having Similar Plume Shapes)(Adapted from Refs. 45 and 106).
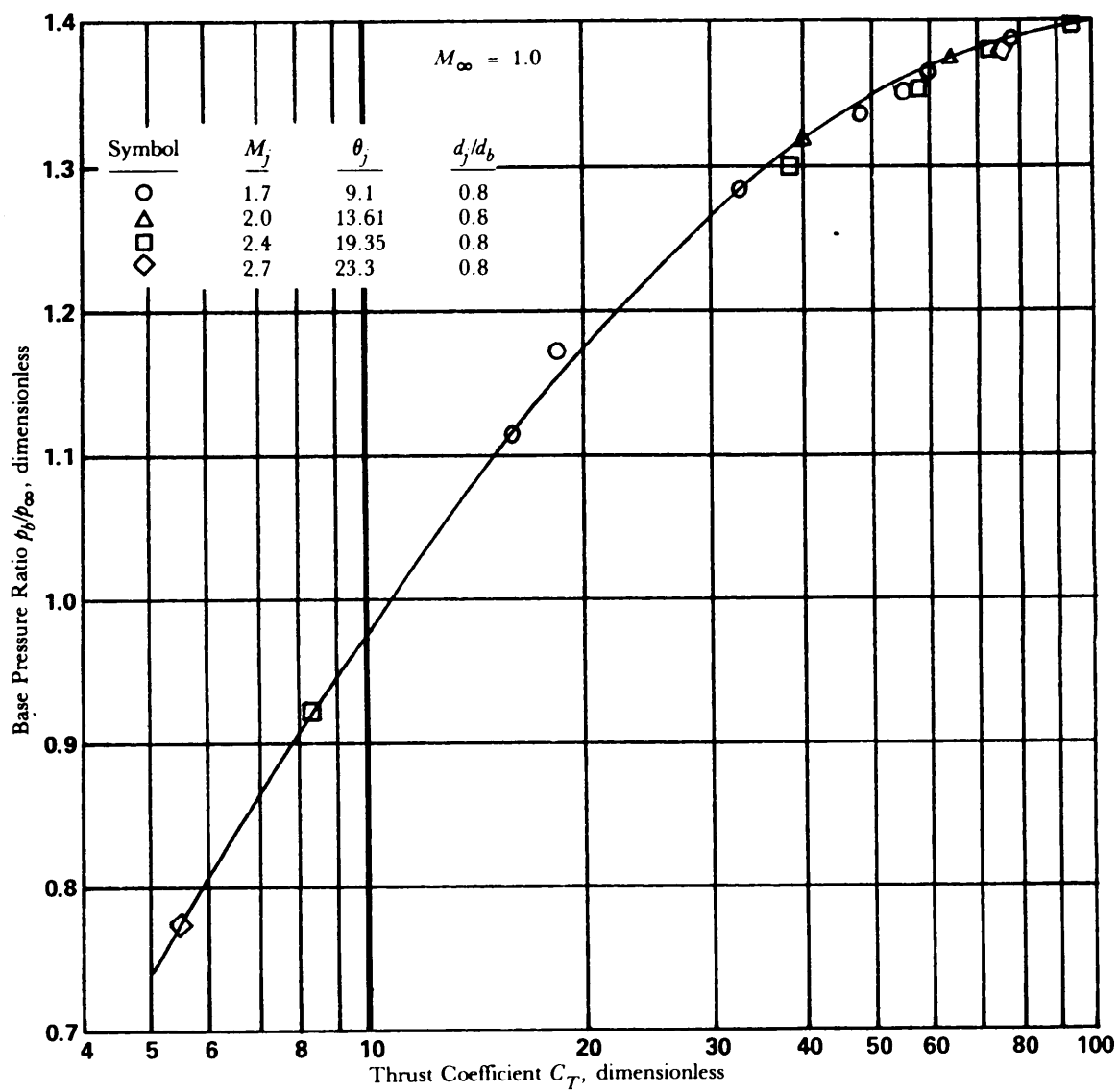
Figure 5-86. Variation of Base Pressure With C_T for Various Nozzles at M_∞ = 1 (Ref. 45)
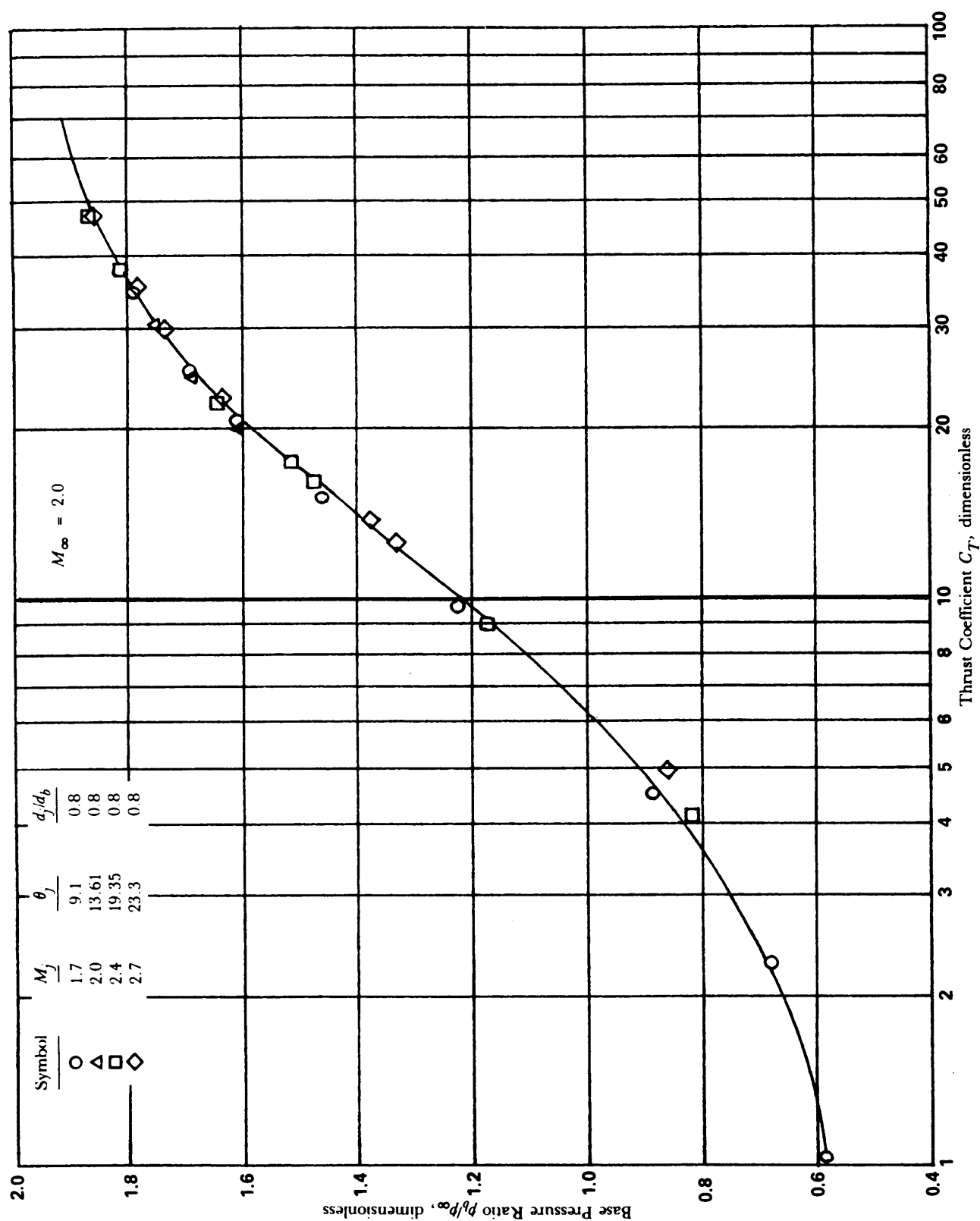
Figure 5-87.   Variation of Base Pressure With C_T for Various Nozzles at $M_\infty = 2.0$ (Rd. 45)
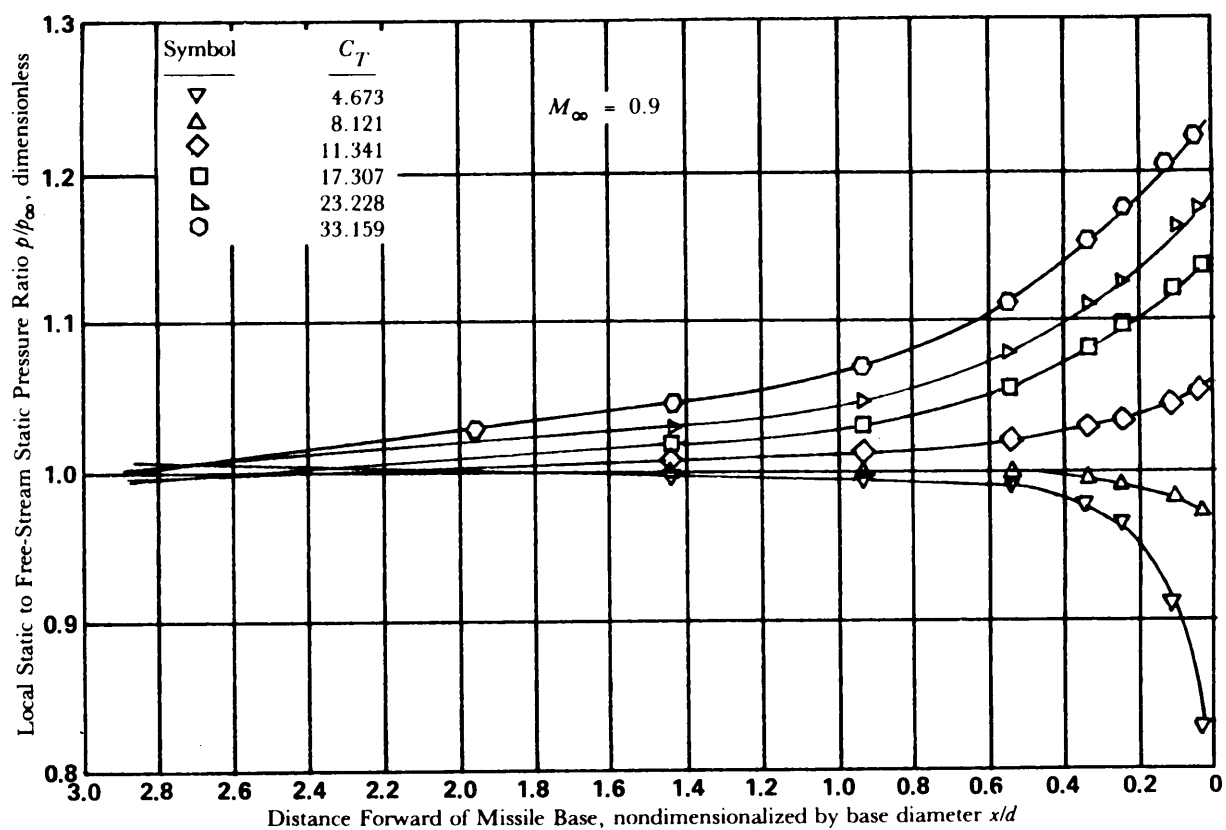
Figure 5-88. **Effect of Thrust on Body Surface Pressure Distribution on Cylindrical Afterbody at $M_\infty = 0.9$ ($M_j = 2.7$, $\theta_j = 20$ deg, $d_j/d_b = 0.95$)** (Ref. 46)
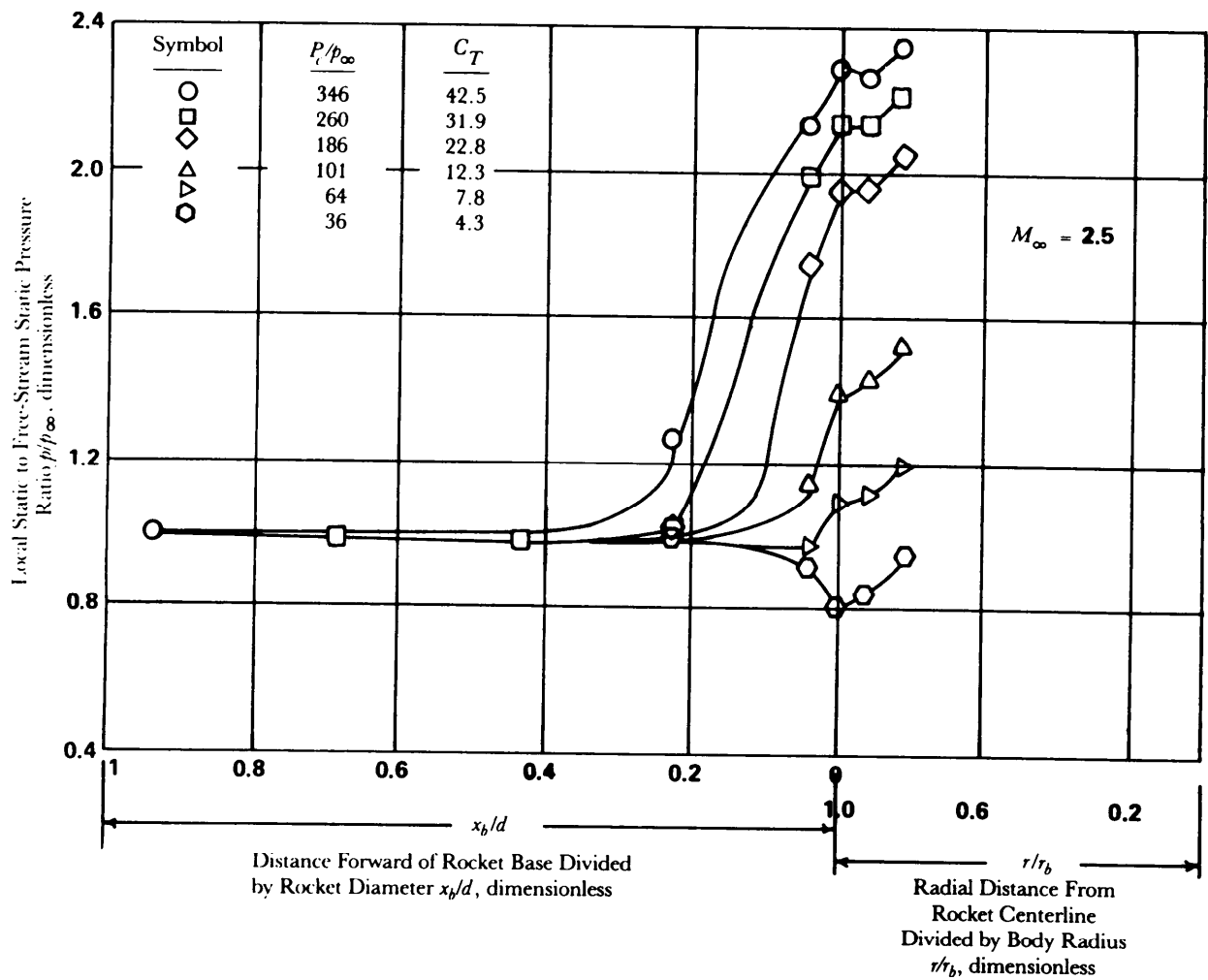
Figure 5-89. **Effect of Thrust on Base and Body Surface Pressure Distribution on Cylindrical Afterbody** at $M_\infty = 2.5$ ($M_j = 2.0$, $\theta_j = 10$ deg, $d_j/d_b = 0.8$) (Ref. 47)
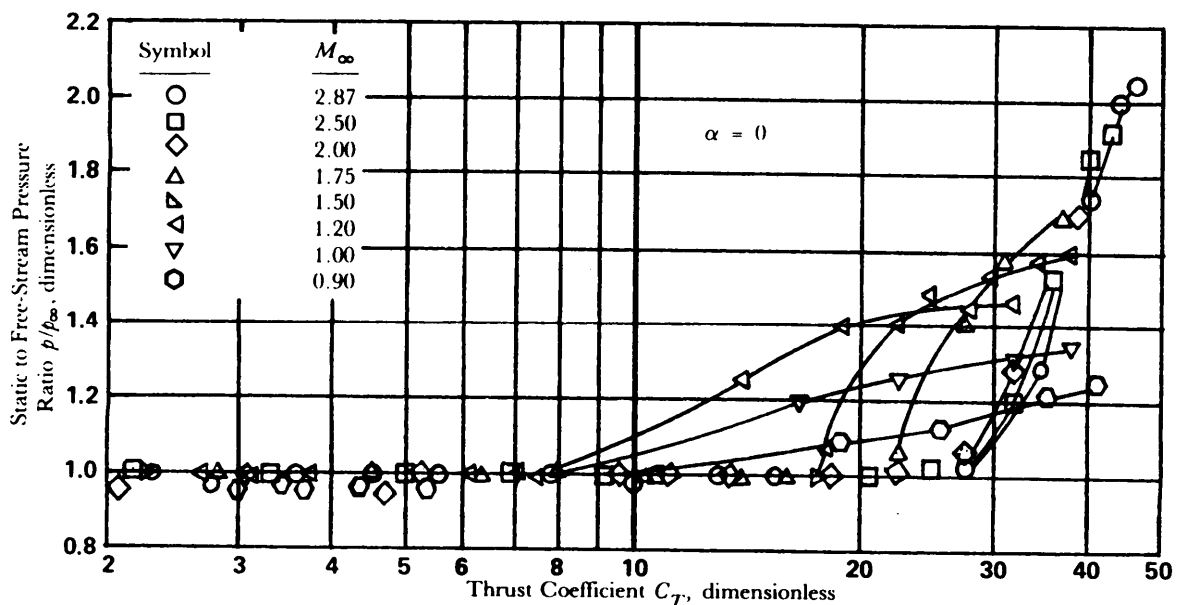
Figure 5-90. Effect of Thrust on Body Pressure X/d = 0.225, Cylindrical Sonic Nozzle $d_j/d_b = 0.45$) (Ref. 48)
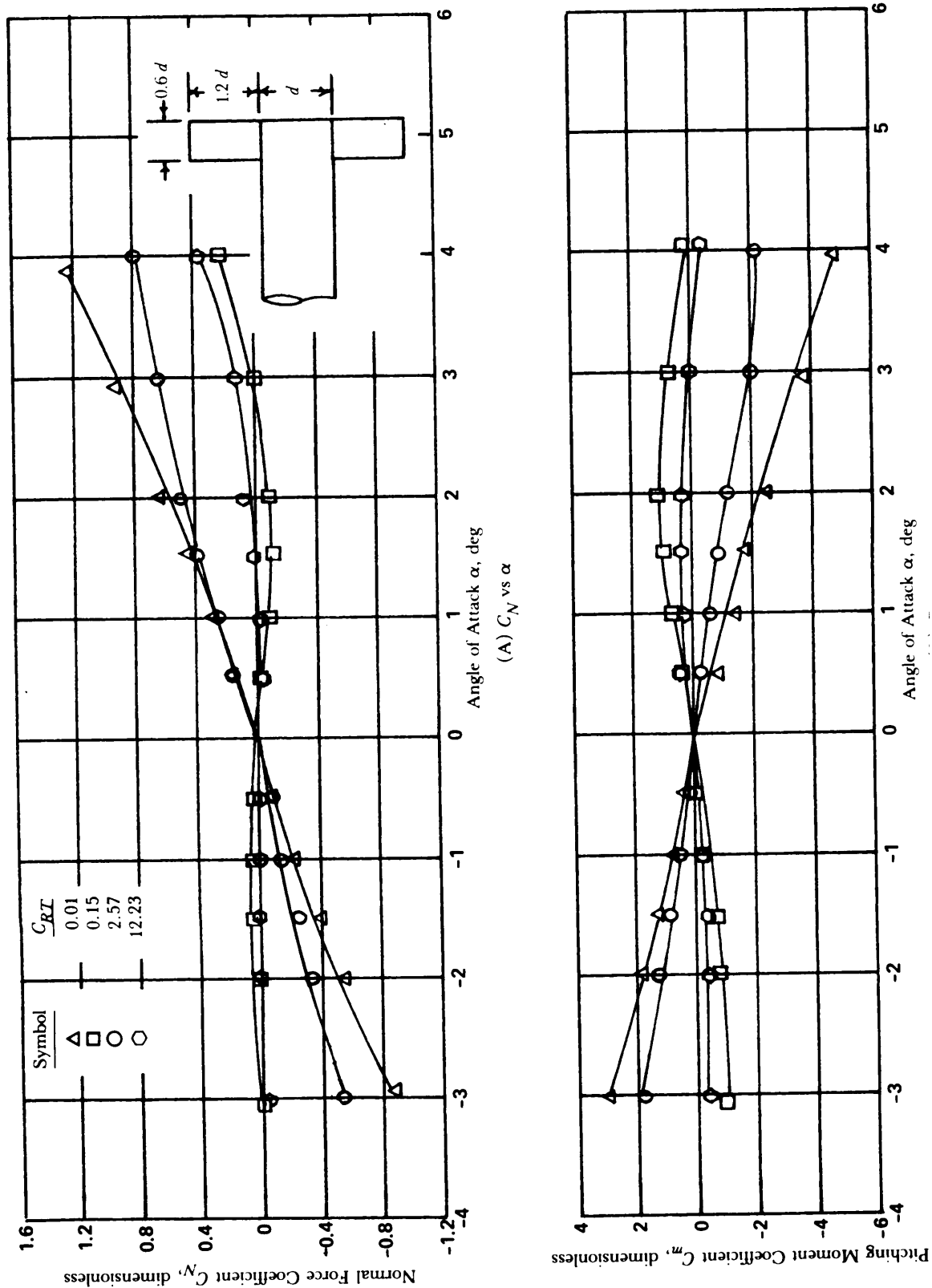
Figure 5-91. Plume Effects on Configuration Stability Characteristics at M_∞ = 1.0 (Ogive-Cylinder Body l/d = 10.2, Moment Center 5.1d Aft of Nose) (Ref. 52)
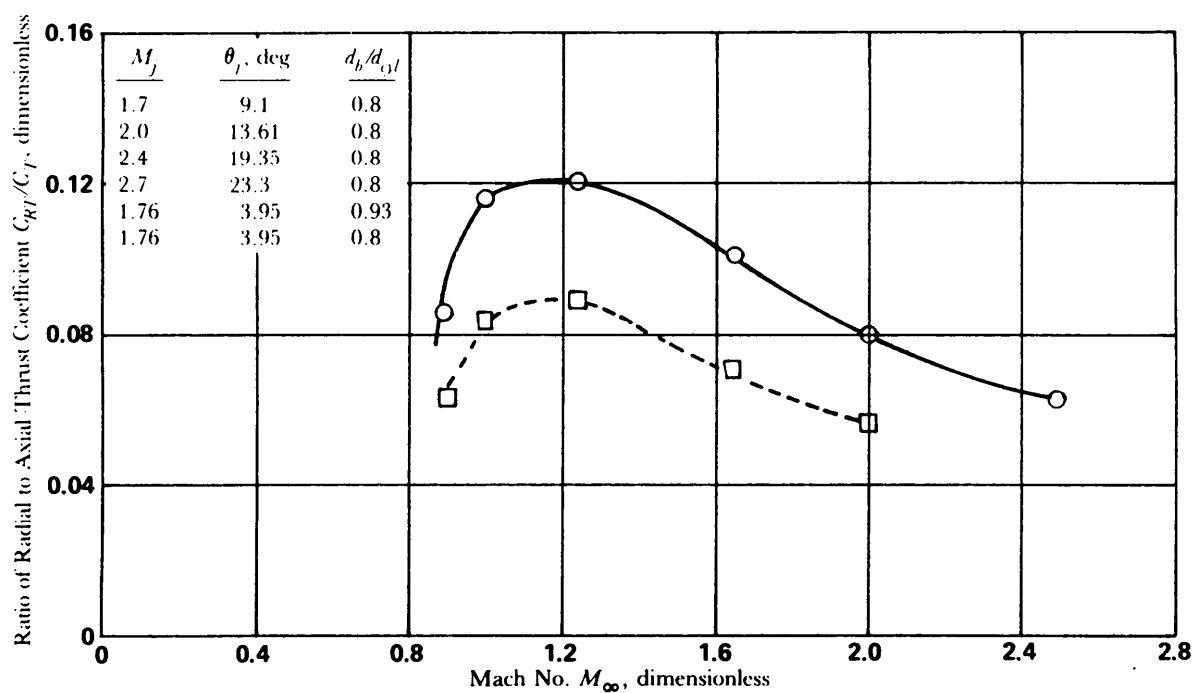
Figure 5-92.   Ratio of Radial Thrust to Axial Thrust Required for Same Plume Effect (Ref. 45)

MIL-HDBK-762(MI)
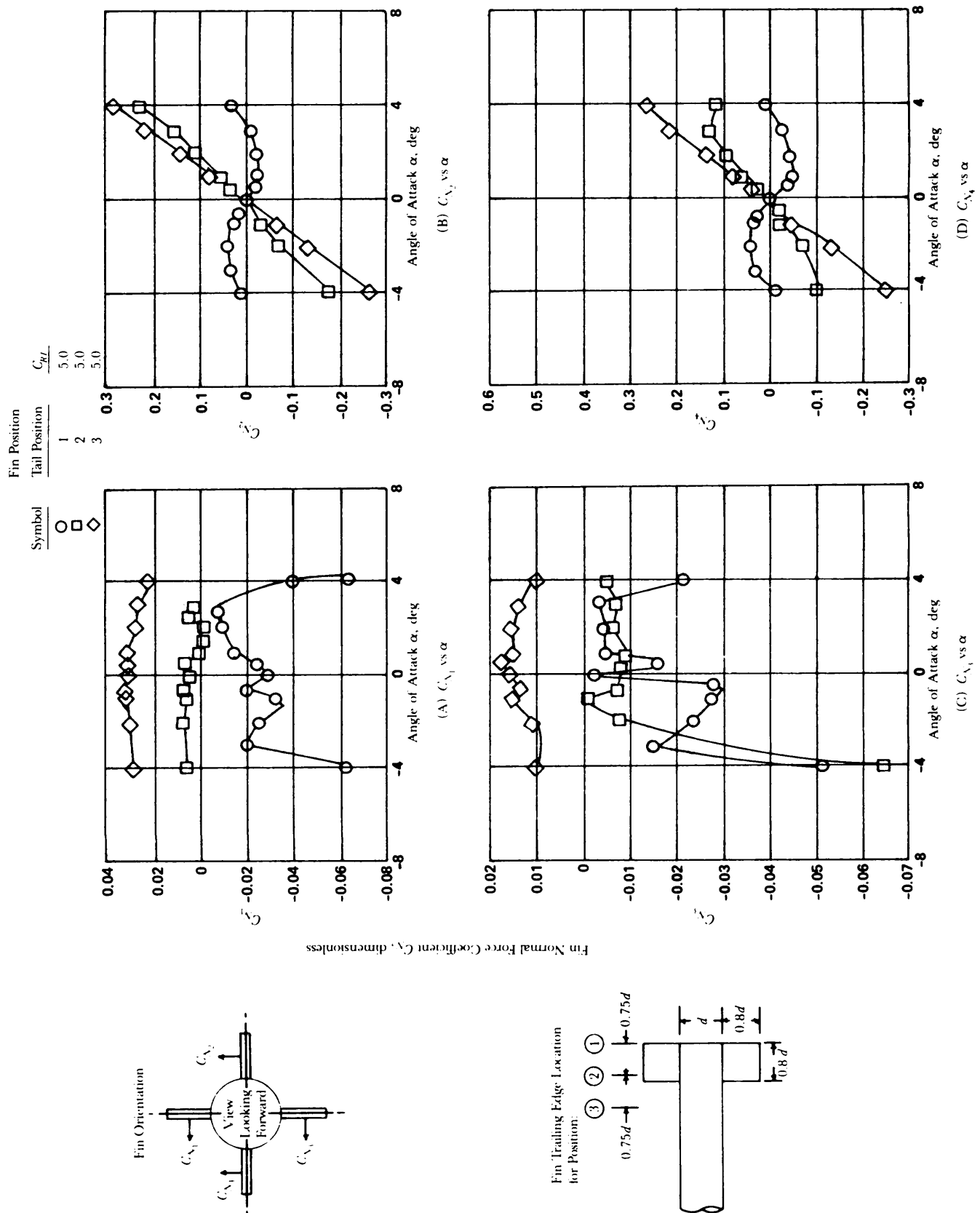
Figure 5-93. Effect of Plume on Normal Force Characteristics of Fins Located at Three Different Longitudinal Positions Along Body at M_∞ = 1.25 (Ref. 53)
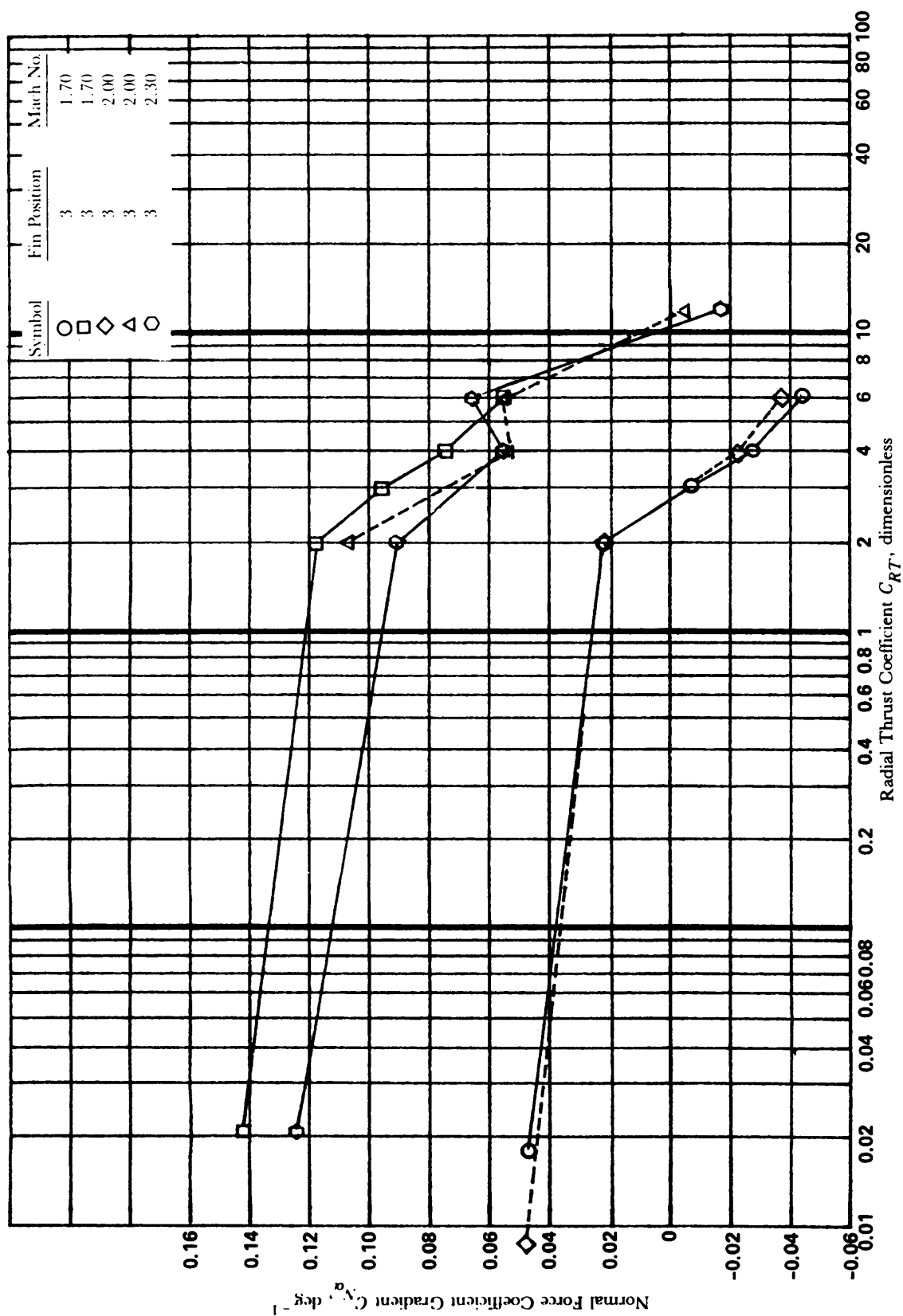
Figure 5-94. Effect of Radial Thrust Coefficient on Longitudinal Derivatives (Ref. 54)
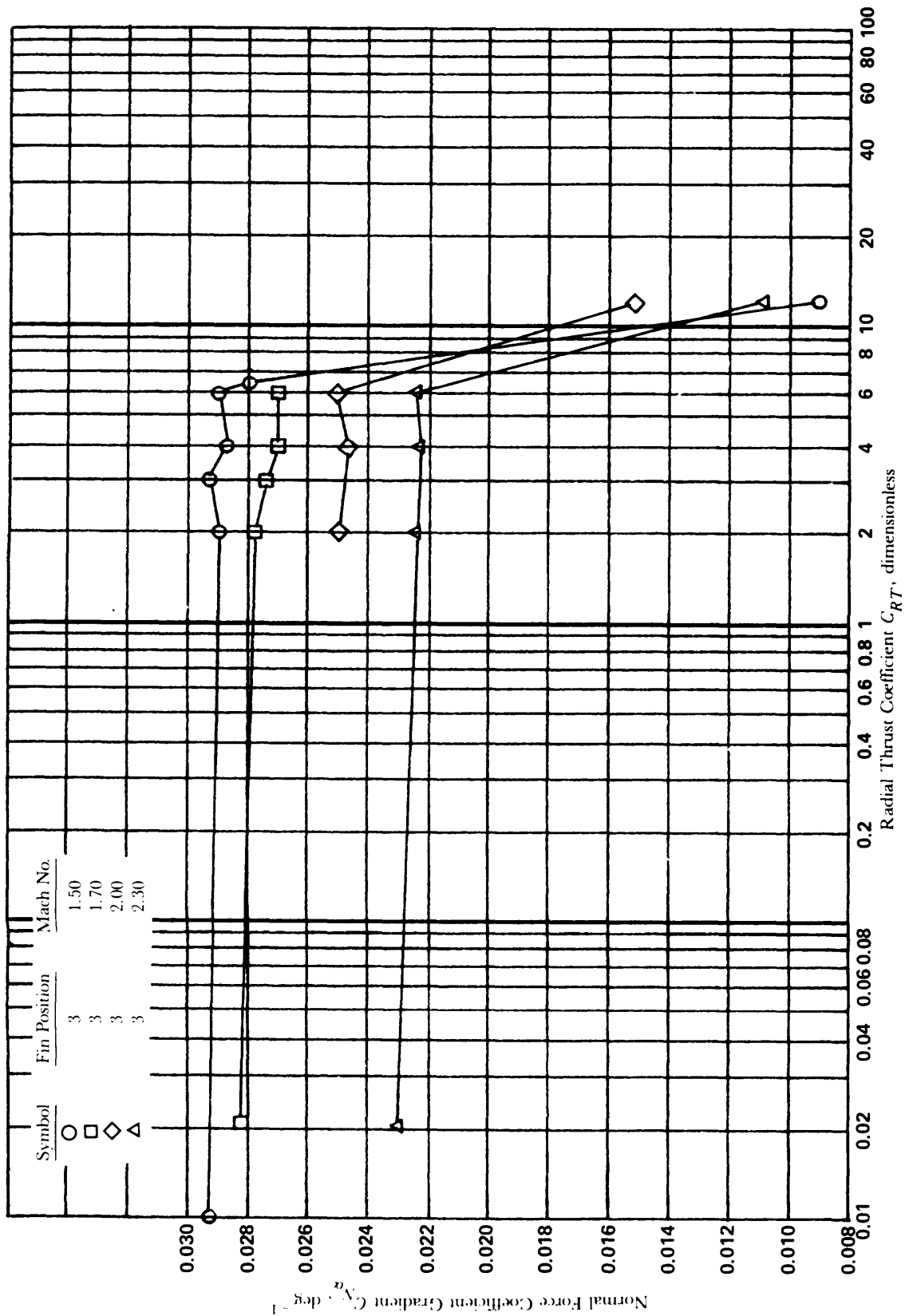
Figure 5-95. Effect on Fin Number 2 Normal Force Characteristics in Forward Position ($M_\infty = $ 1.5, 1.7, 2.0, and 2.3) (Ref. 54)
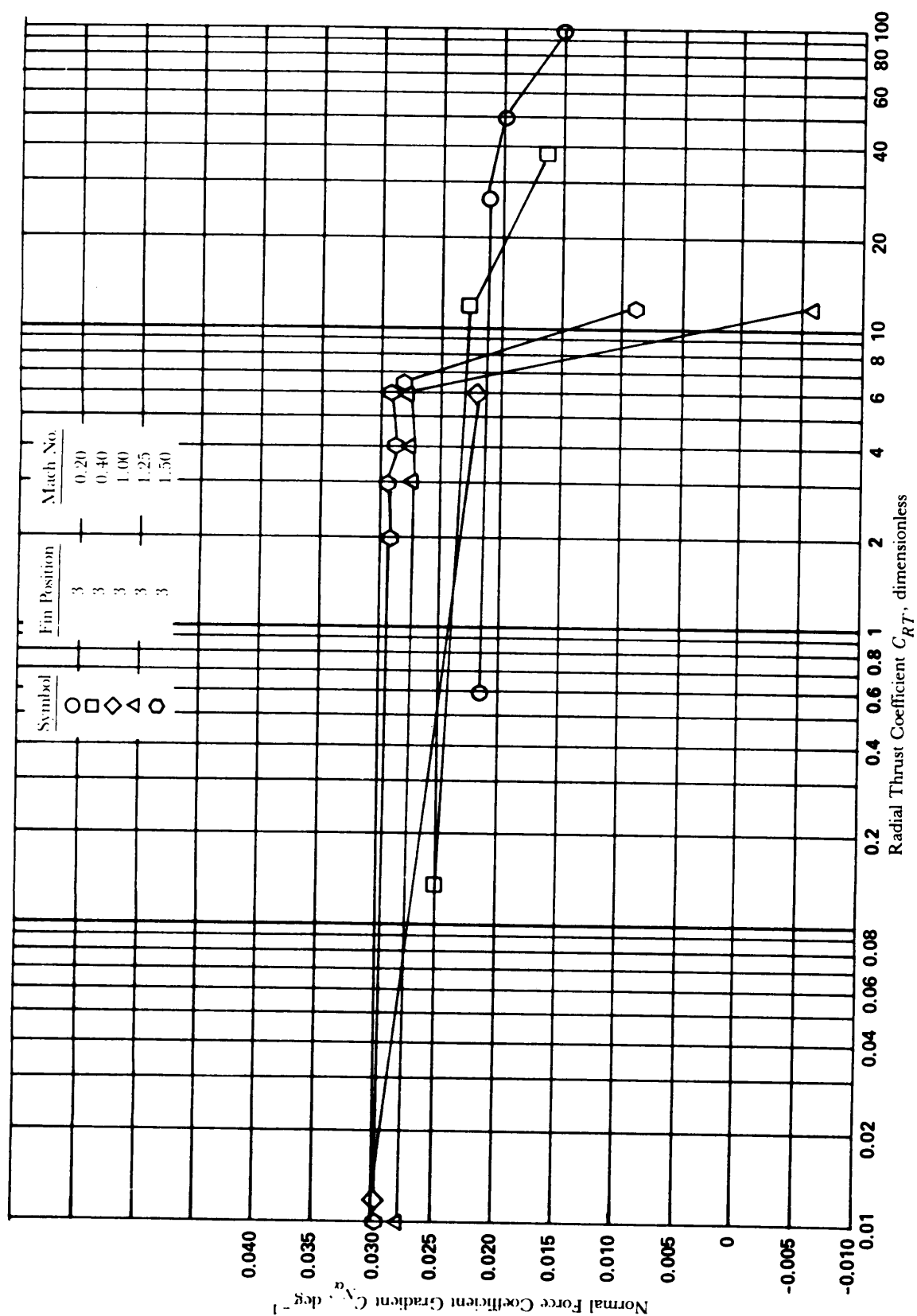
Figure 5-96. Thrust Effects on Horizontal Fin Panel Normal Force Characteristics—Fin in Forward Position (M_∞ = 0.2, 0.4, 1.0, 1.25 and 1.5) (Ref. 54)
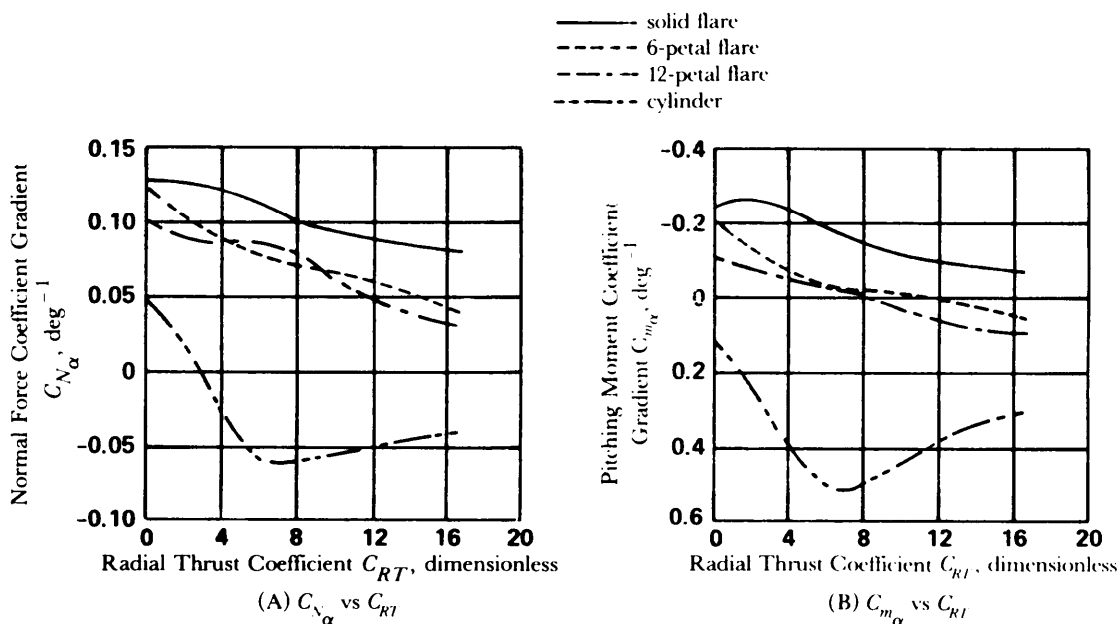
Figure 5-97. Plume Effects of Afterbody Static Stability $(M_\infty = 1.05)$ (Ref. 55)
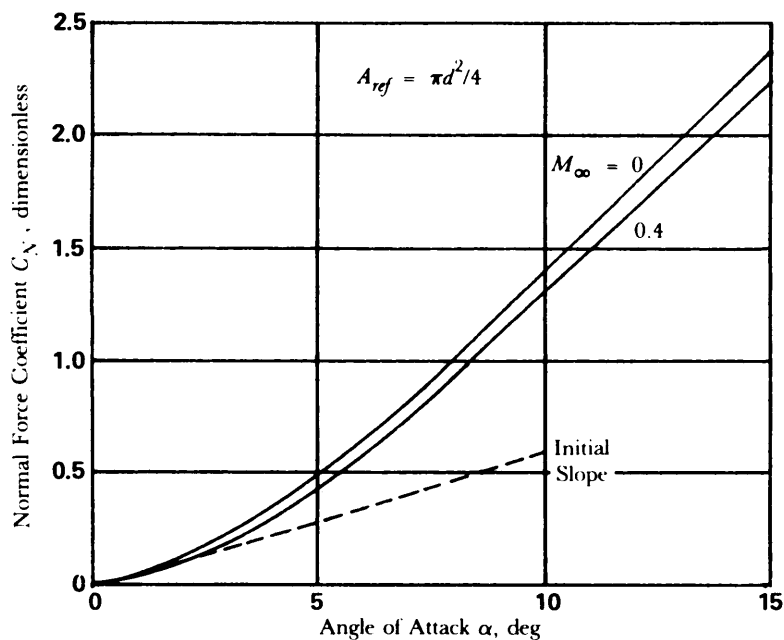
Figure 5-98. Normal Force Coefficient vs Angle of Attack (Ref. 42)
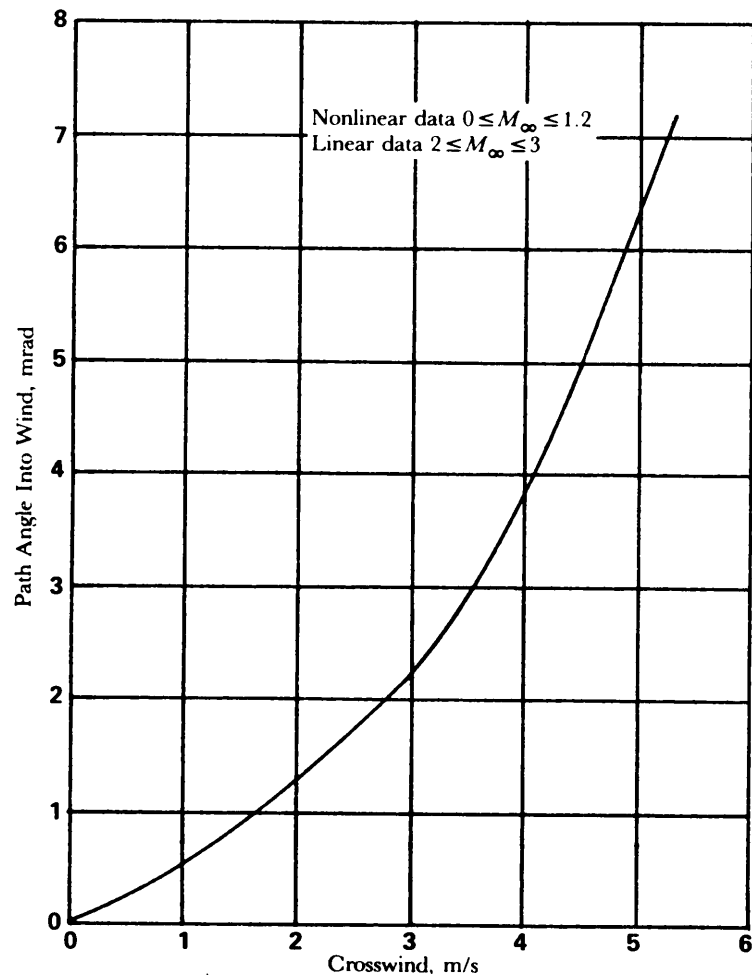
5-99. Crosswind in Nonlinear Aerodynamic Environment (Ref. 42)
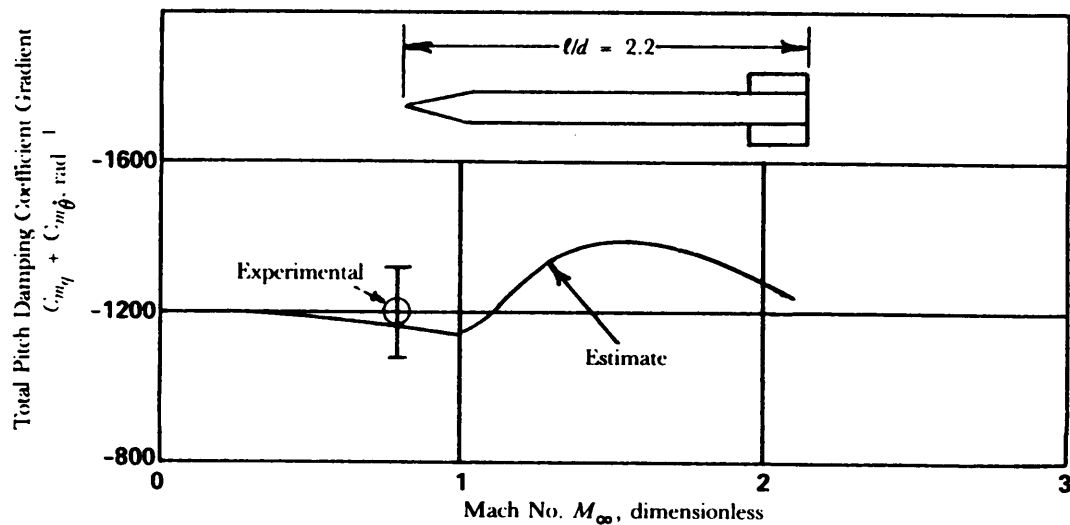
Figure 5-100. Comparison of Pitch Damping Coefficient Estimate to Experiment (Ref. 42)
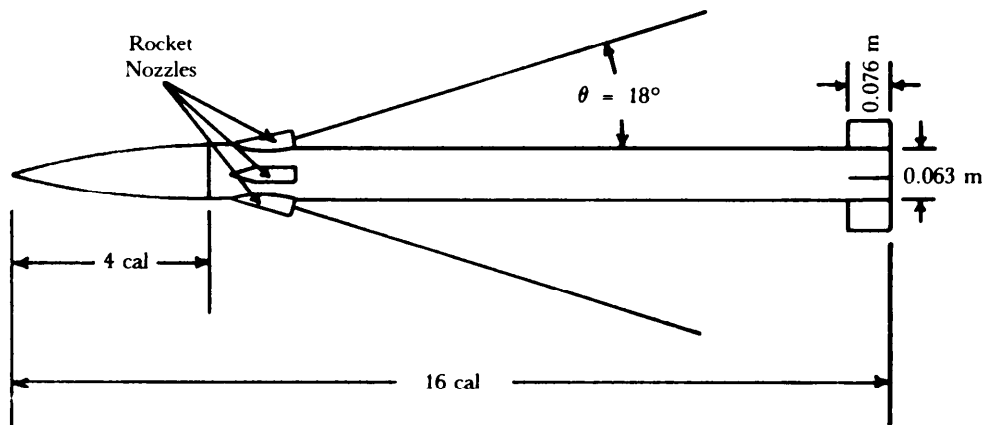
Figure 5-101.   General Army Free Flight Rocket Configuration (Ref. 42)
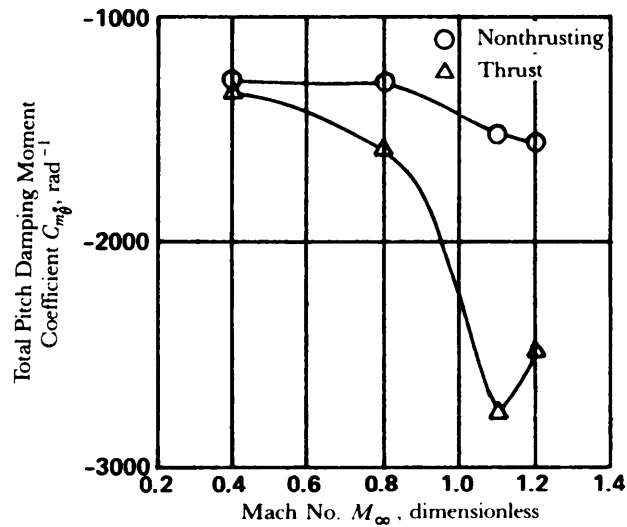
Figure 5-102. Thrust Effects on Total Pitch Damping Coefficient (Ref. 42)
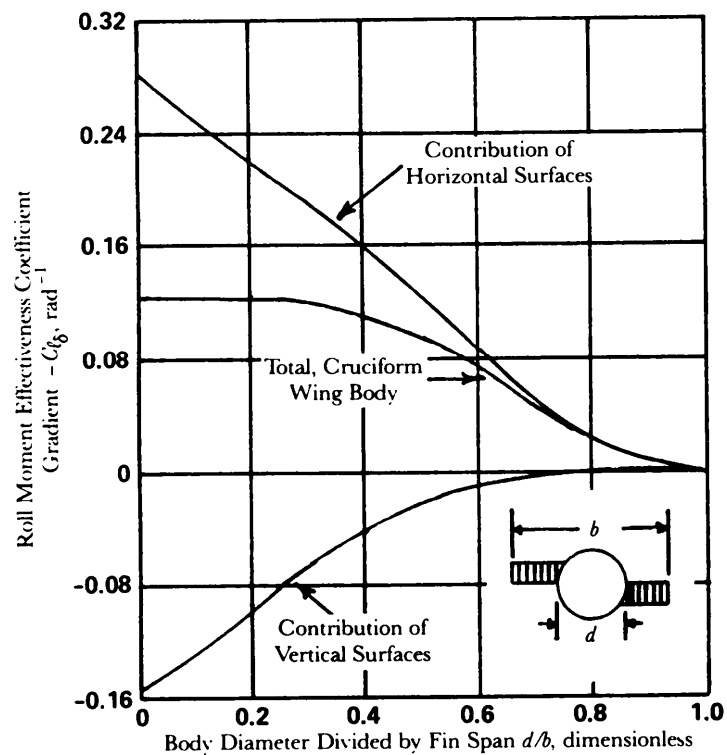
Figure 5-103. **Coefficient of Roll Moment Effectiveness for Cruciform and Planar Wing-Body Combinations With Differential Incidence of Horizontal Surfaces (Ref. 31)**
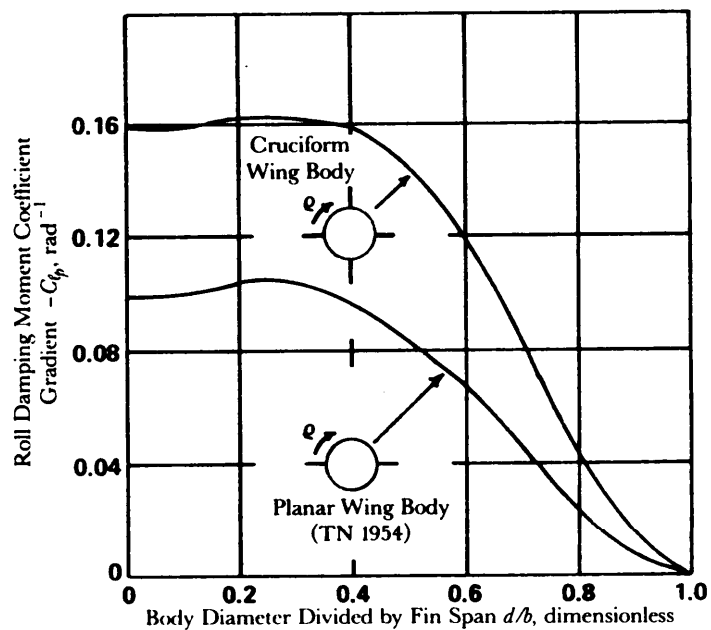
Figure 5-104. **Coefficient of Damping in Roll for Cruciform and Planar Wing-Body Combinations (Ref. 31)**
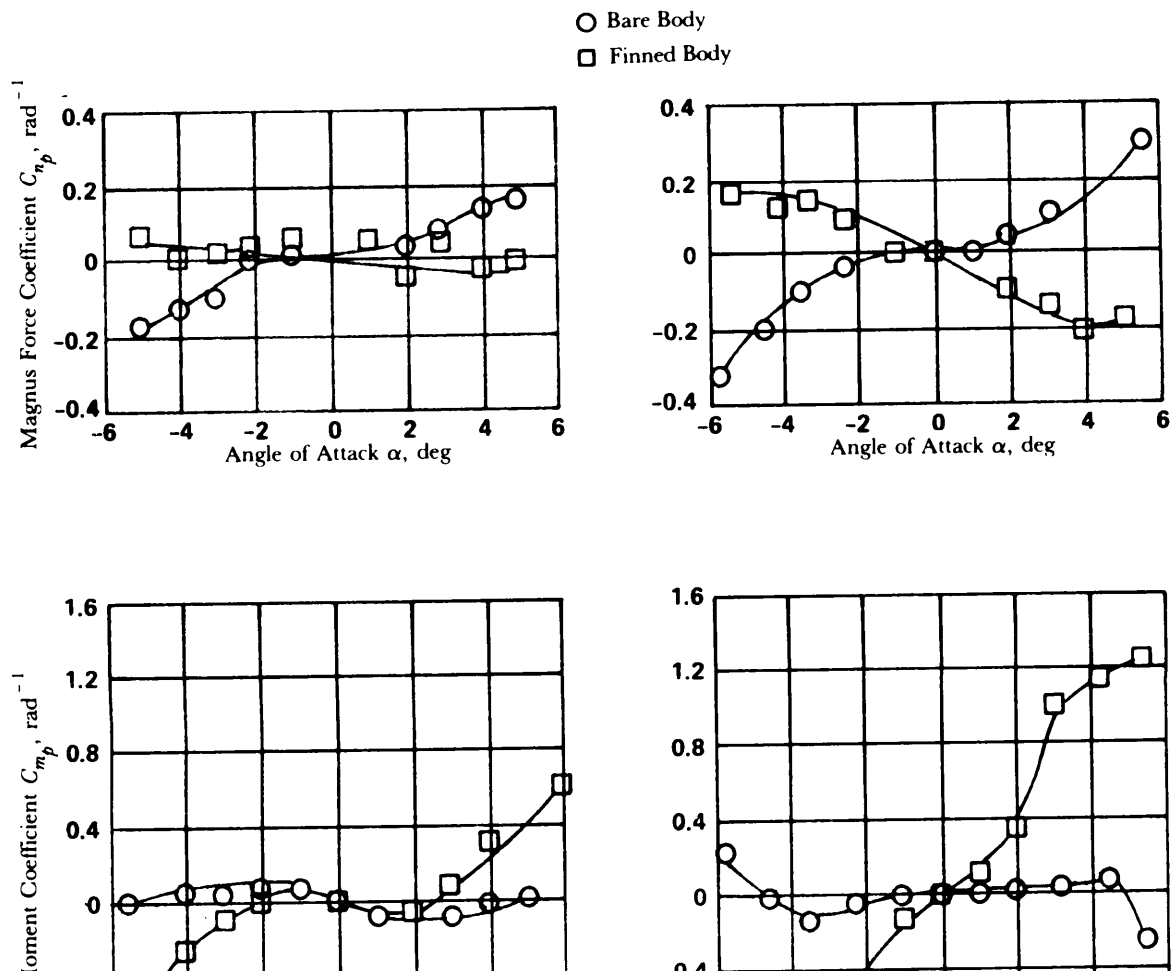
Figure 5-105. Magnus Characteristics fo Finned and Nonfinned Rockets at $M_\infty = 1.75$, $Re = 0.71 \times 10^6$ (Ref. 63)

○ Bare Body
□ Finned Body

(A) Spike Nose

(B) Cone Nose
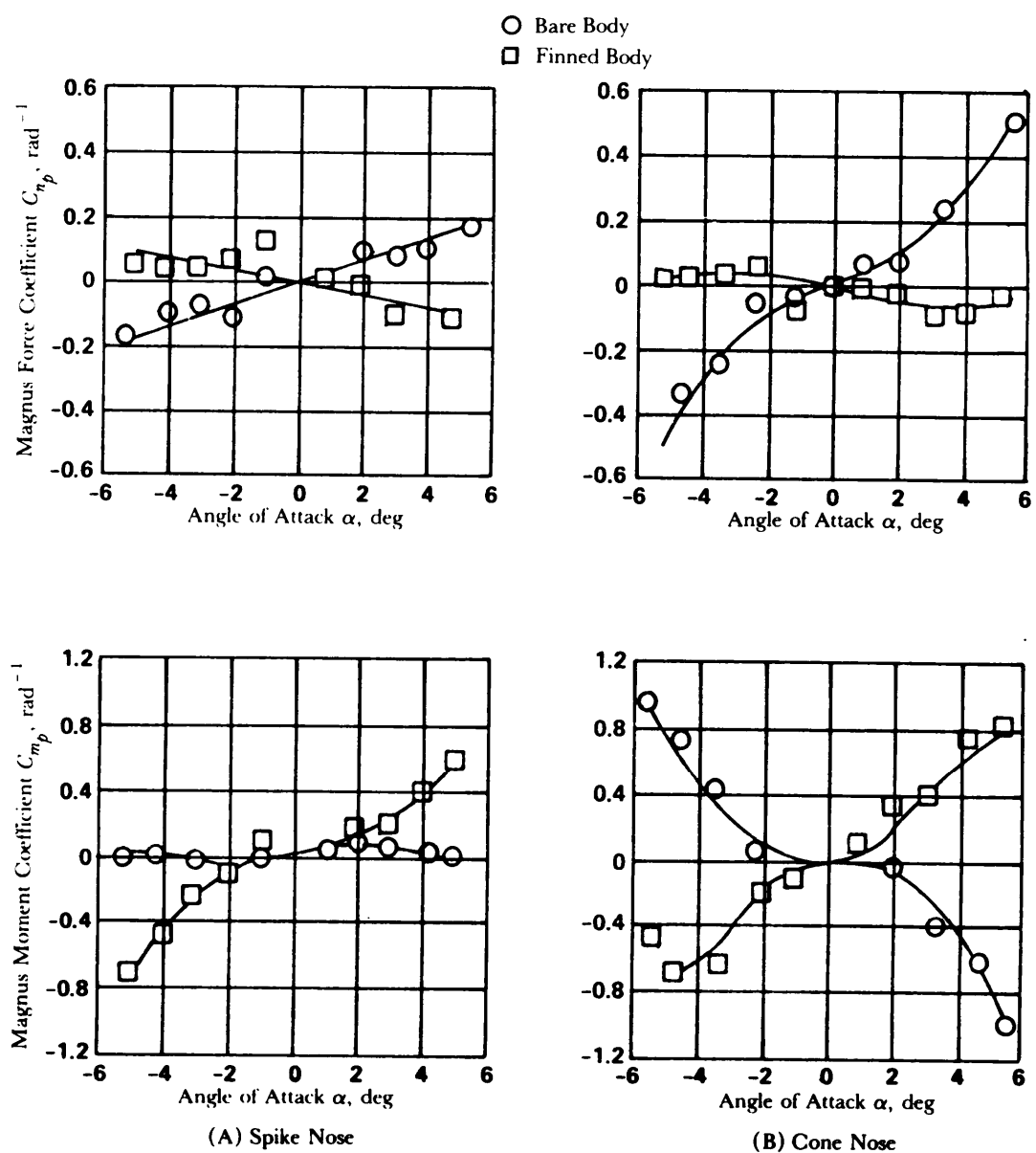
Figure 5-106. Magnus Characteristics of Finned and Nonfinned Rockets at $M_\infty = 2.0$, Re $= 0.65$ X 10^6 (Ref. 63)
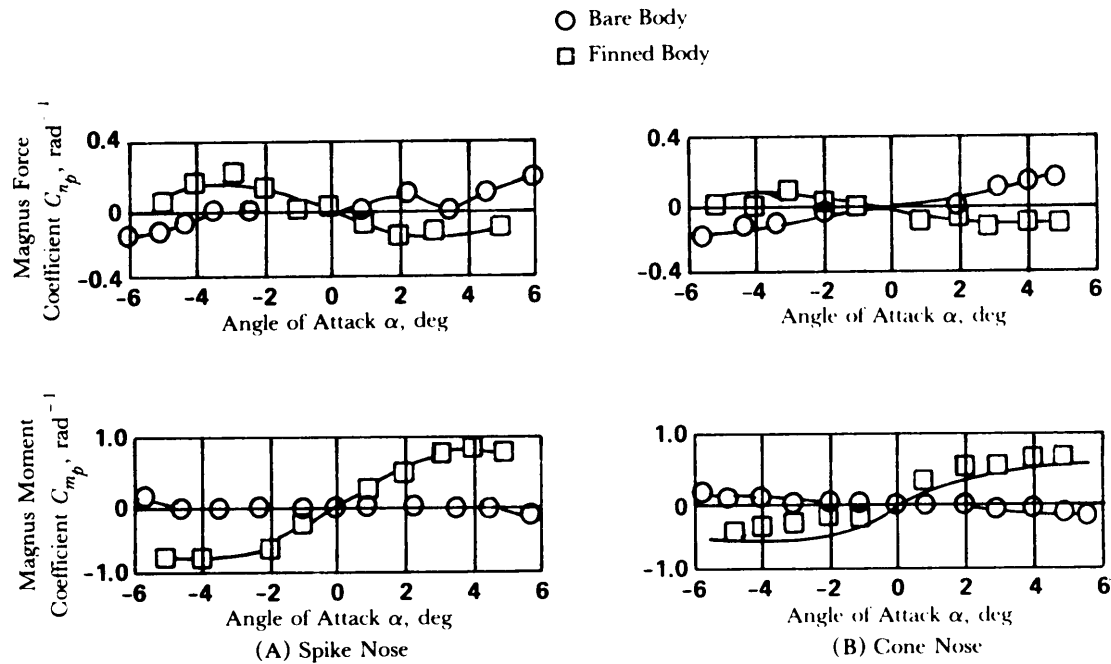
Figure 5-107. **Magnus Characteristics of Finned and Nonfinned Rockets at** $M_\infty = 3.02$, Re = 0.65 X 10⁶(Ref. 63)
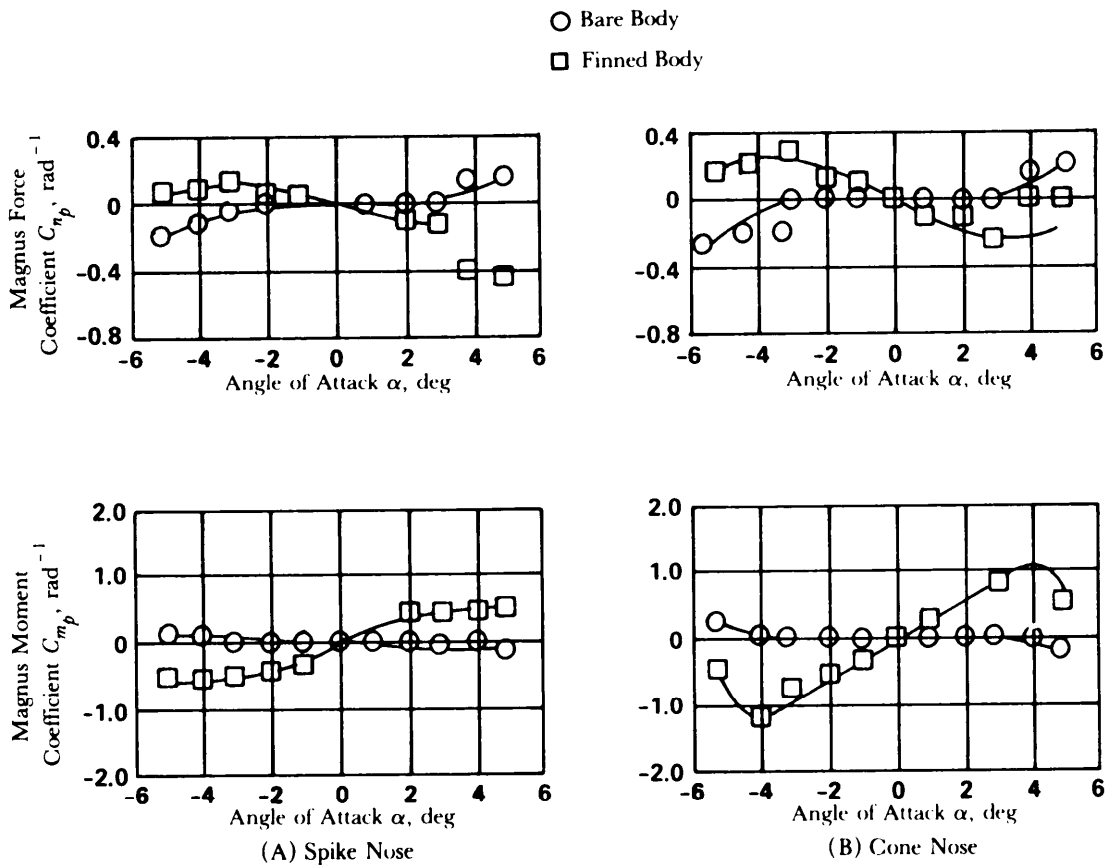
Figure 5-108. **Magnus Characteristics of Finned and Nonfinned Rockets at Text** $M_\infty = 3.02$, Re = 0.65 X 10⁶(Ref. 63)

Symbol	Cant Angle δ, deg
○	0
△	−1
□	−2
◇	+2

(A) $M_\infty = 2.99$, $Re = 15.4 \times 10^6$

(B) $M_\infty = 4.01$, $Re = 10.0 \times 10^6$

(C) $M_\infty = 5.04$, $Re = 11.9 \times 10^6$

NOTE: Re is based on model length of 1.2639 m.
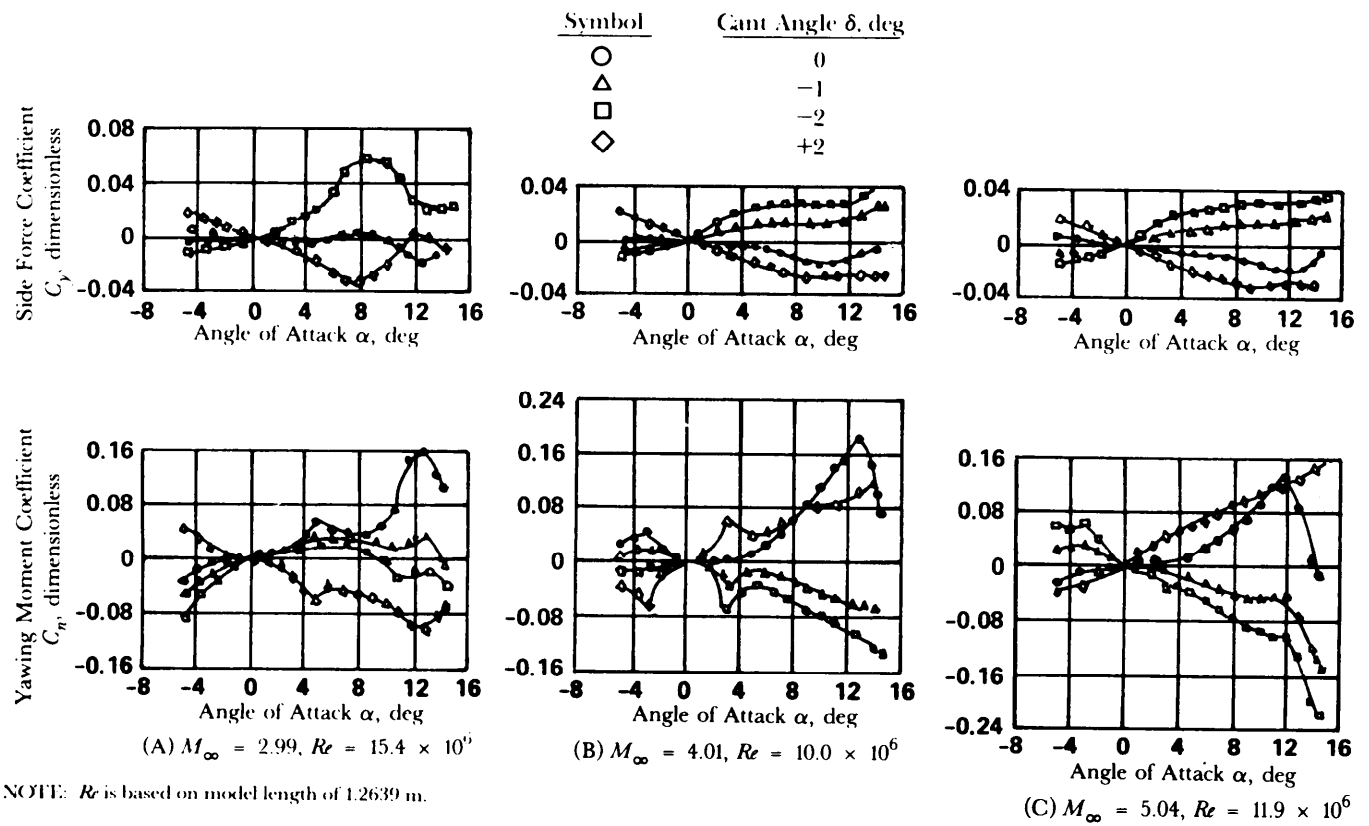
Figure 5-109. Variations of Side Force Coefficient and Yawing Moment Coefficient With Angle of Attack and Fin Cant Angle (Ref. 64)
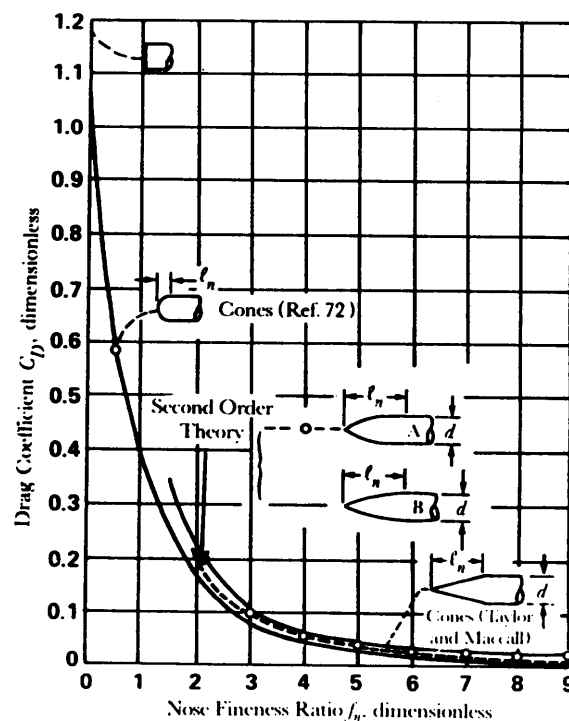
Figure 5-110. Drag Coefficients Due to Pressures on Noses at $M_\infty = 1.4$ (Ref. 66)

5-177

NOTE: ℓ_1/d = 12 for Configurations 56 through 63
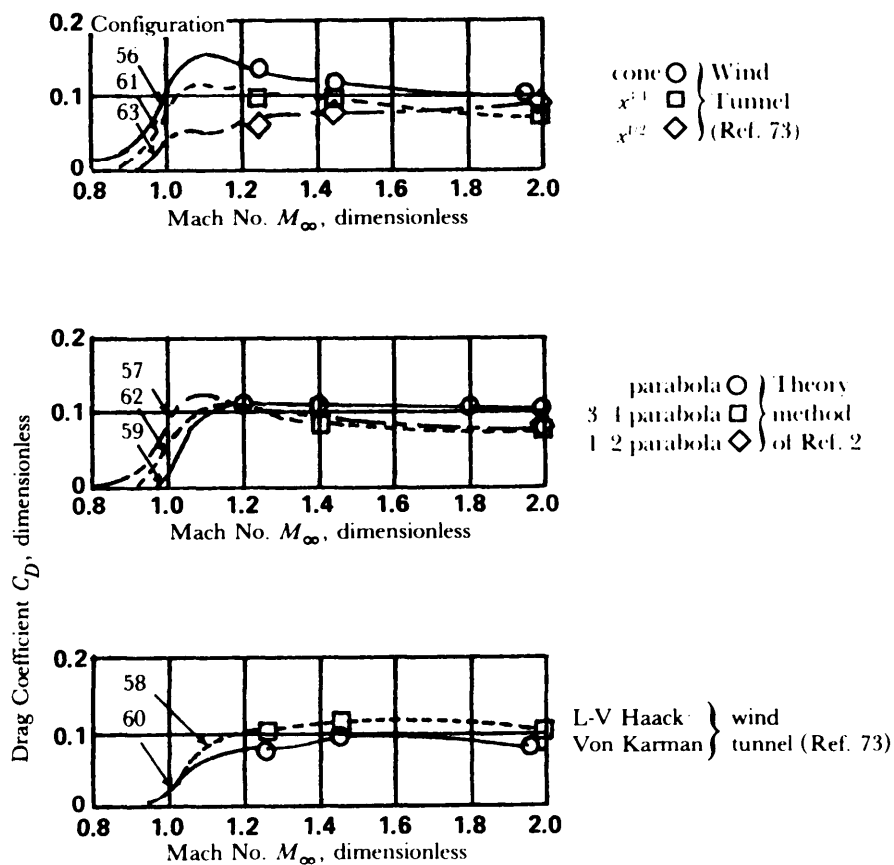
(A) Nose Pressure Drag of Flight Models Compared
With Wind-Tunnel Results and Theory
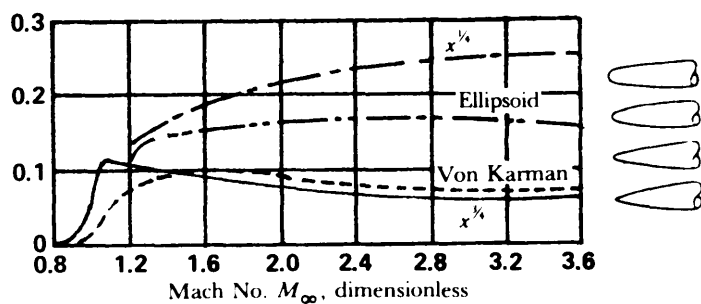
(B) Nose Pressure Drag From Ref. 73 Showing
General Effects of Nose Shape on Drag

Figure 5-111.   Pressure Drag of Noses of Fineness Ratio 3, Total Fineness Ratio $\ell_T/d = 12$ (Ref. 66)

MIL-HDBK-762(MI)
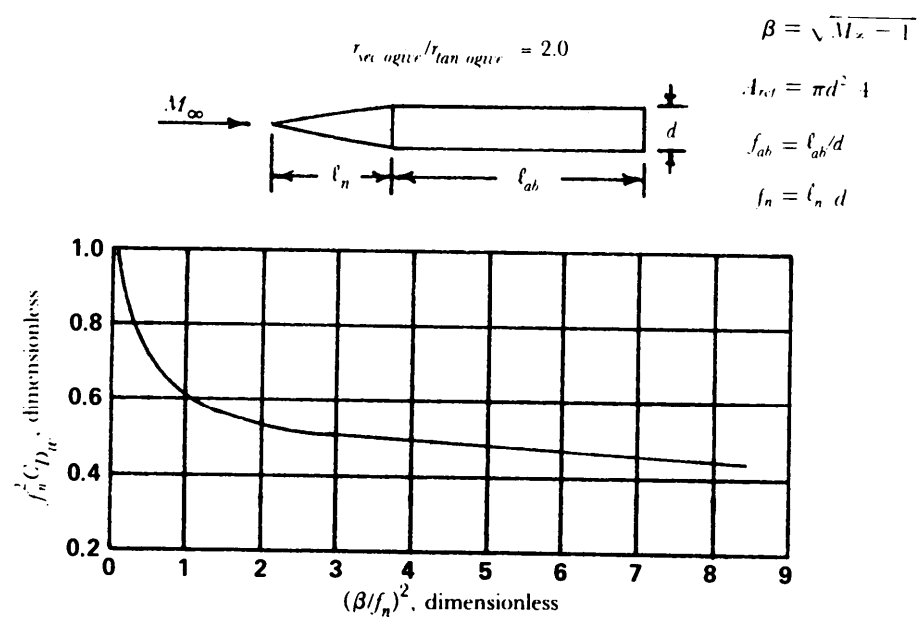
Figure 5-112. Wave-Drag Coefficient of Optimum Secant Ogive Cylinder at Transonic Speed (Ref. 67)
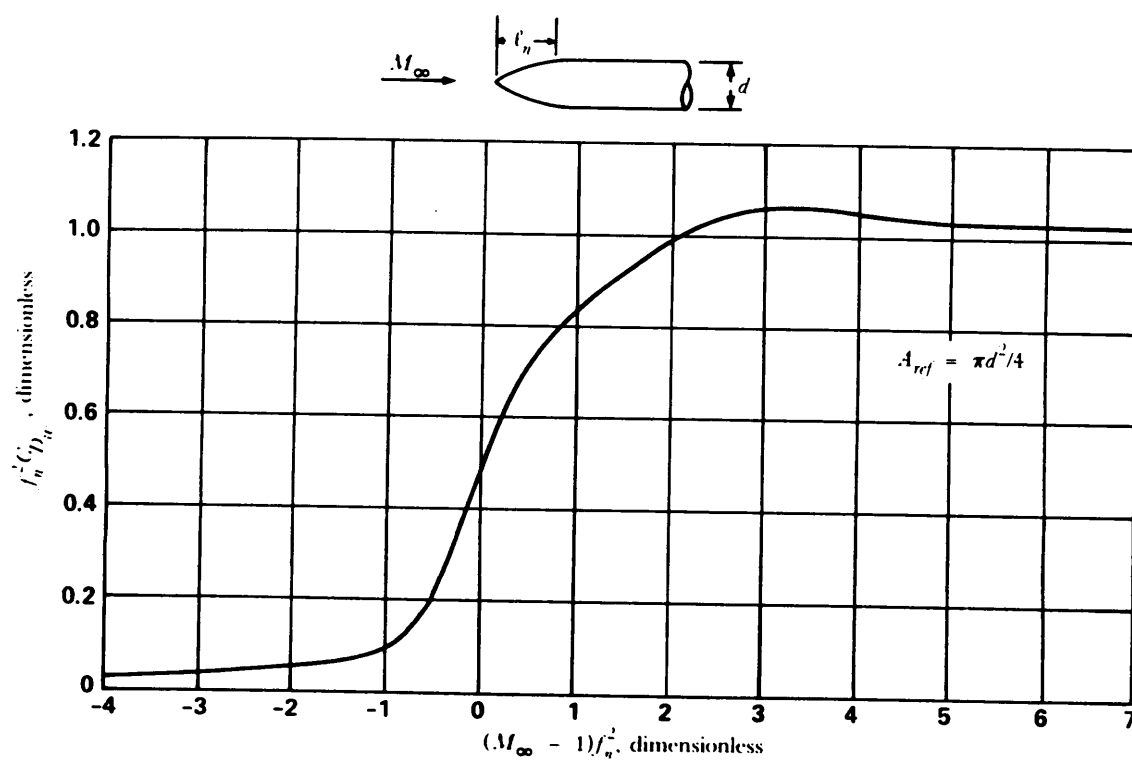
Figure 5-113. Wave-Drag Coefficient of Slender Ogives at Transonic Speeds (Ref. 67)
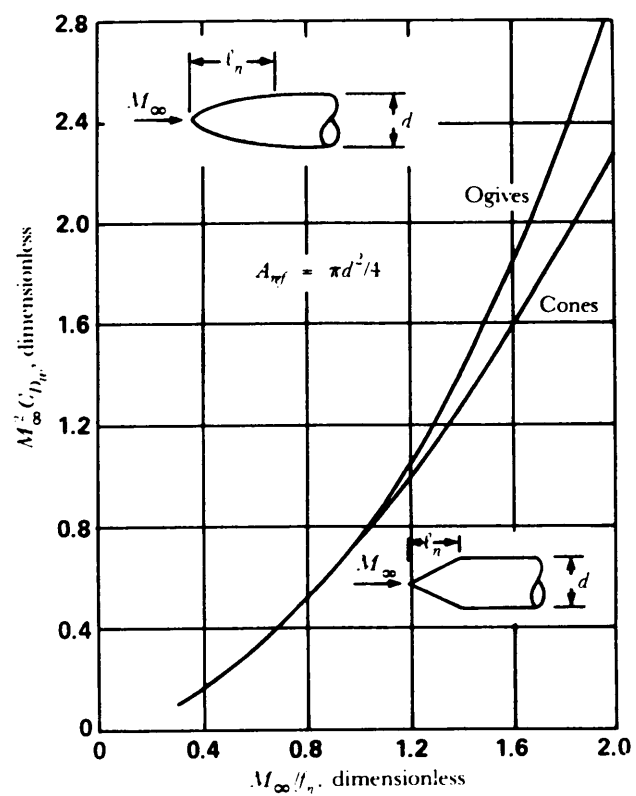
Figure 5-114.　Wave-Drag Coefficient of Cones and Ogives at Supersonic Speeds

d = rocket or base of nose diameter
R = radius of a given ogive
R_1 = radius of a tangent ogive
r = radial distance from rocket centerline
X = axial distance measured from nose
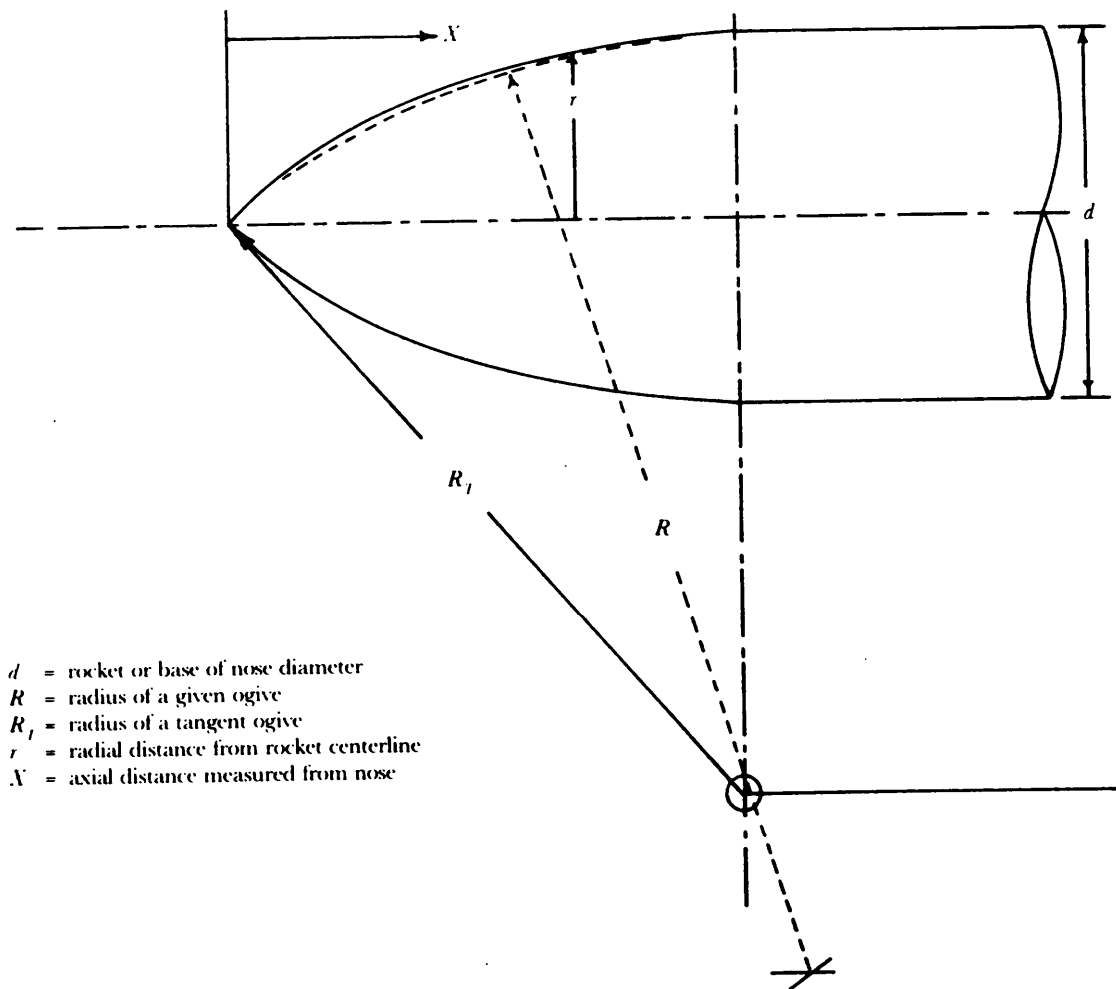
Figure 5-115. Sketch Depicting Development of Tangent Ogive (2 cal in this case) and "Given" Ogive
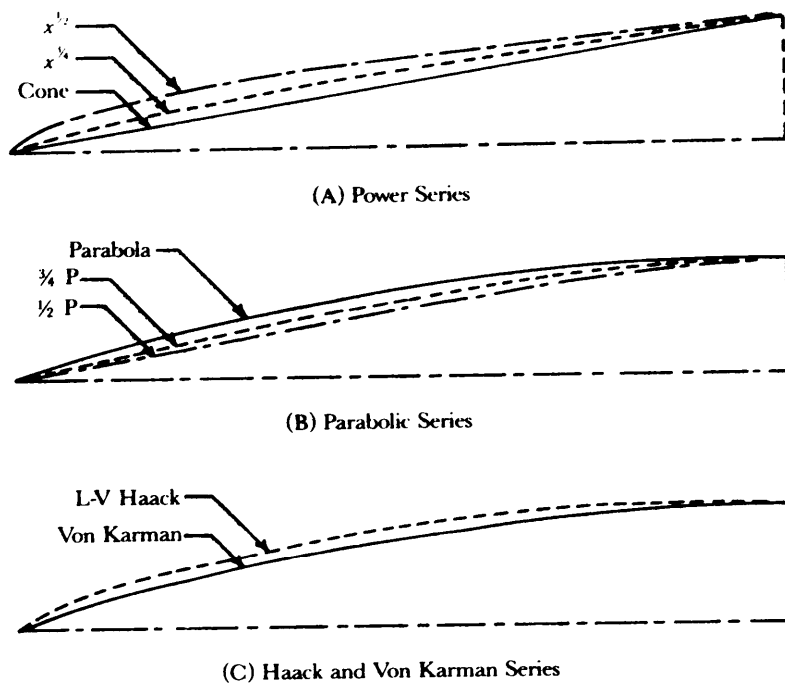
Figure 5-116. Profiles of Nose Shapes (Ref. 69)
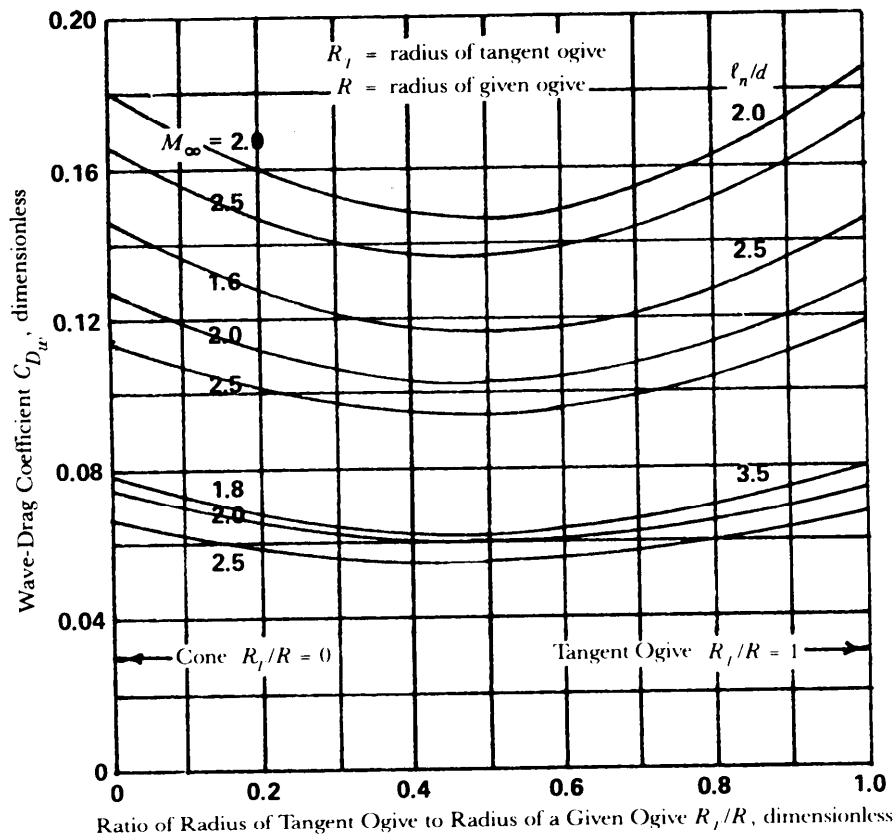
Figure 5-117. Wave Drag of Secant Ogives in Terms of Ogive Radius for Several Mach Numbers and Nose Fineness Ratios (Ref. 67)
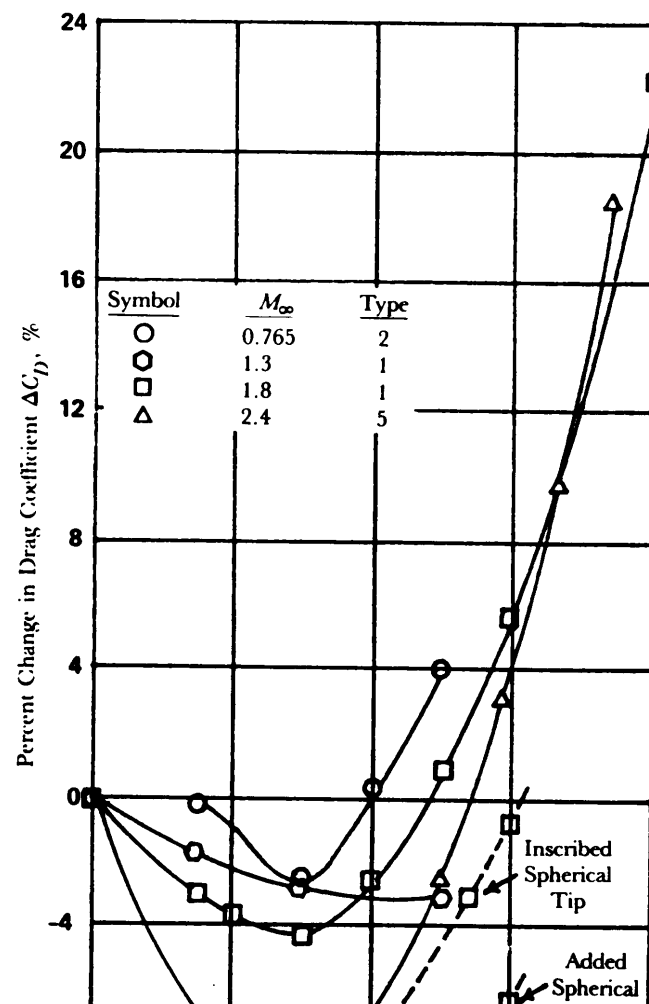
Figure 5-118.   Percent Change in Drag Coefficient vs Me'plat Diameter (Flat unless otherwise indicated) (Ref. 75)

(All dimensions in Nose Diameters)
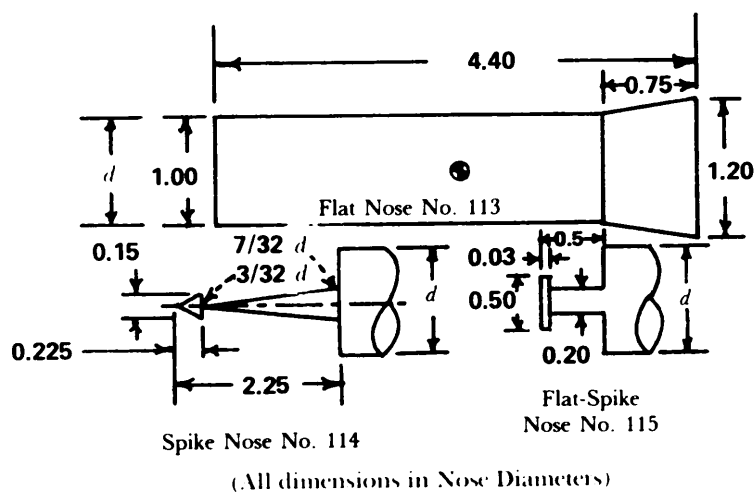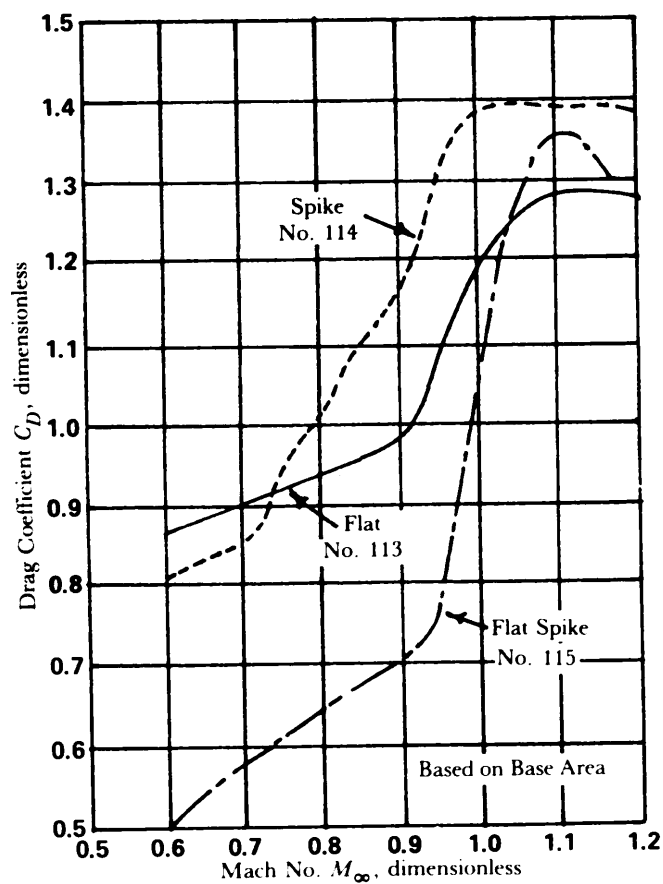
(A) Configurations

(B) Drag Data

Figure 5-119. Zero Lift Drag on Three Special Nose Configurations
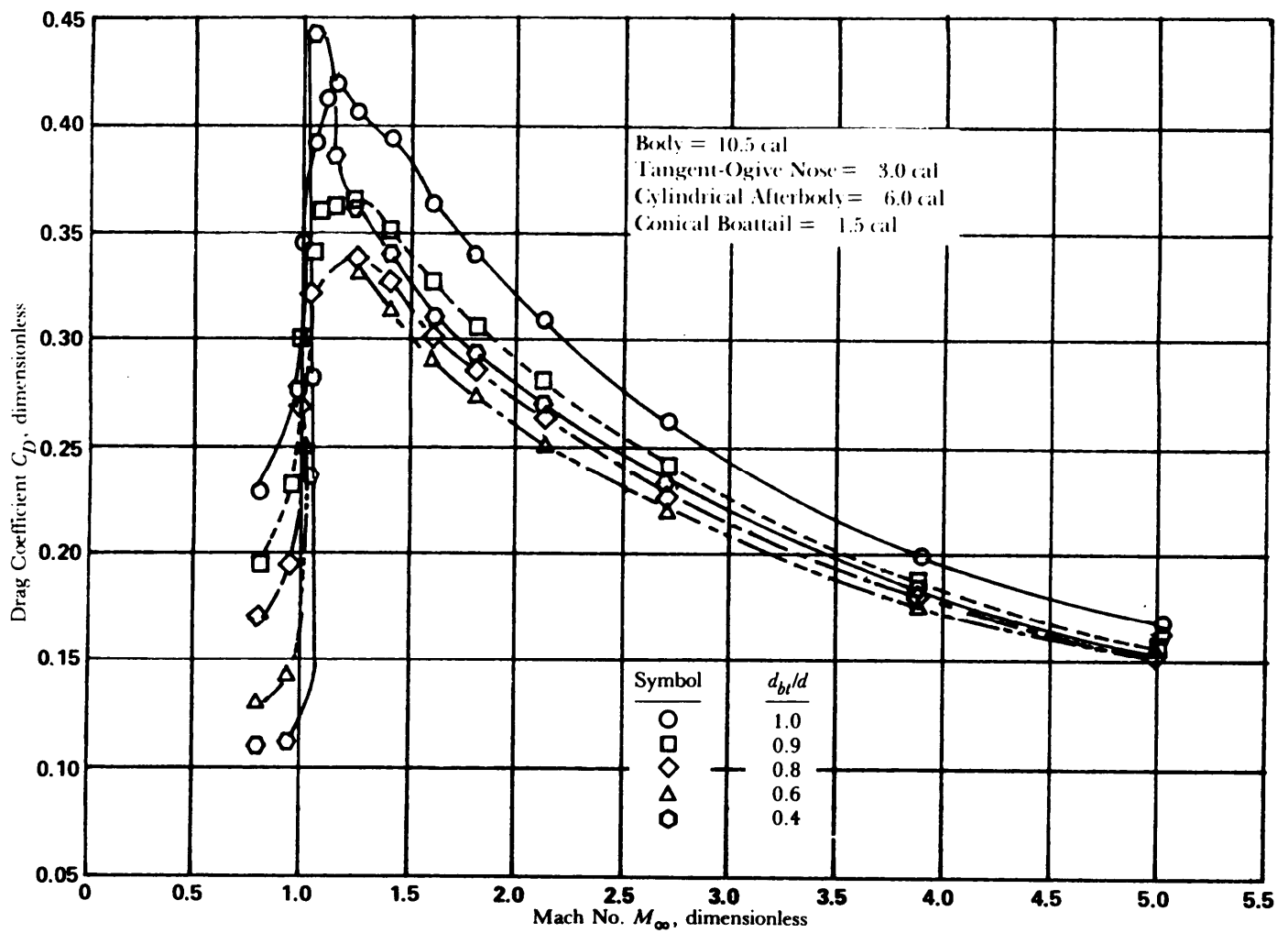
Figure 5-120. **Variance of Boattail Base Diameter on Total Drag vs M_∞ for Complete Body Configuration (Ref. 80)**
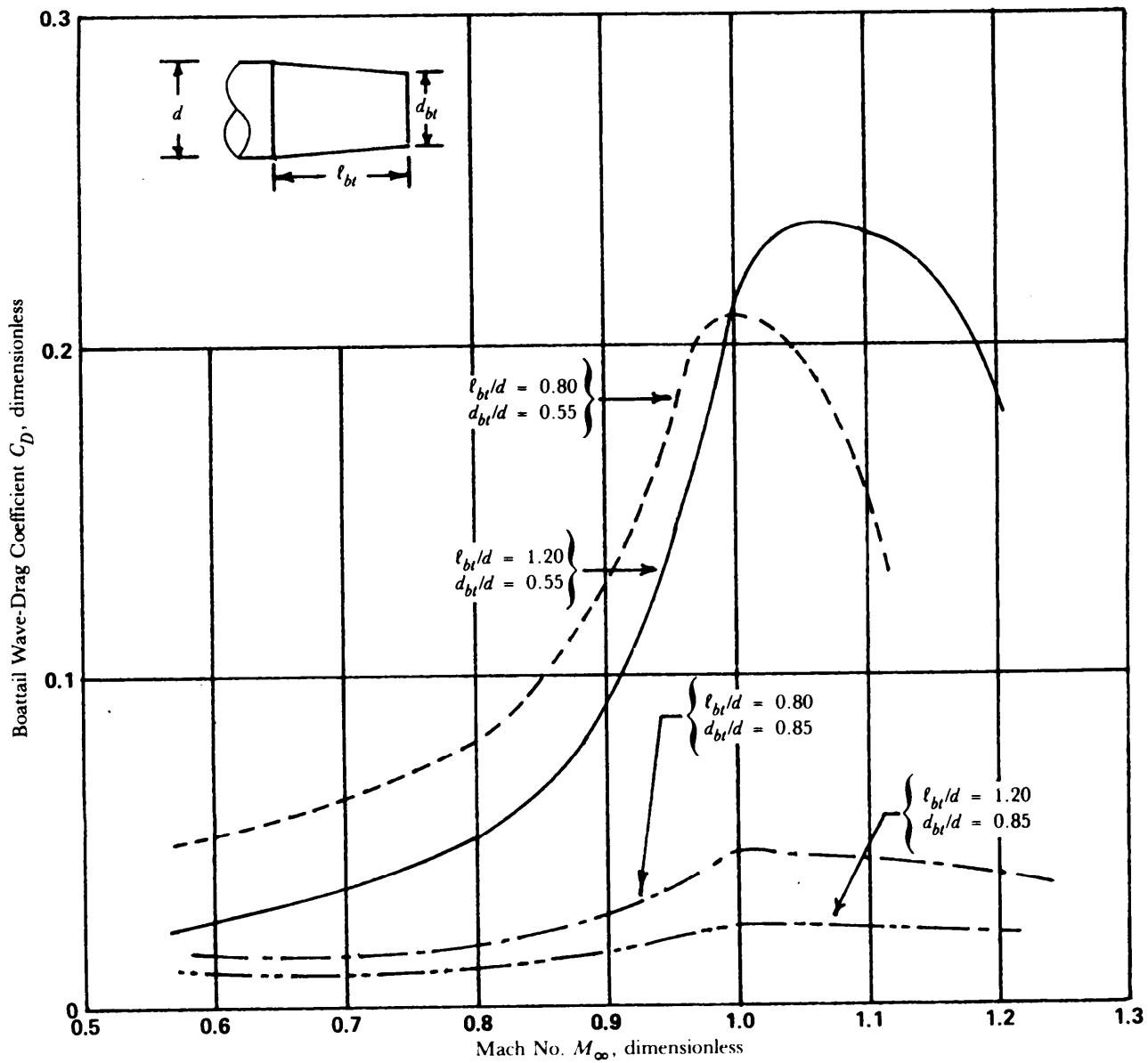
Figure 5-121. Subsonic/Transonic Boattail Wave Drag vs Mach Number for Various Length-to-Diameter Ratios (Ref. 81)
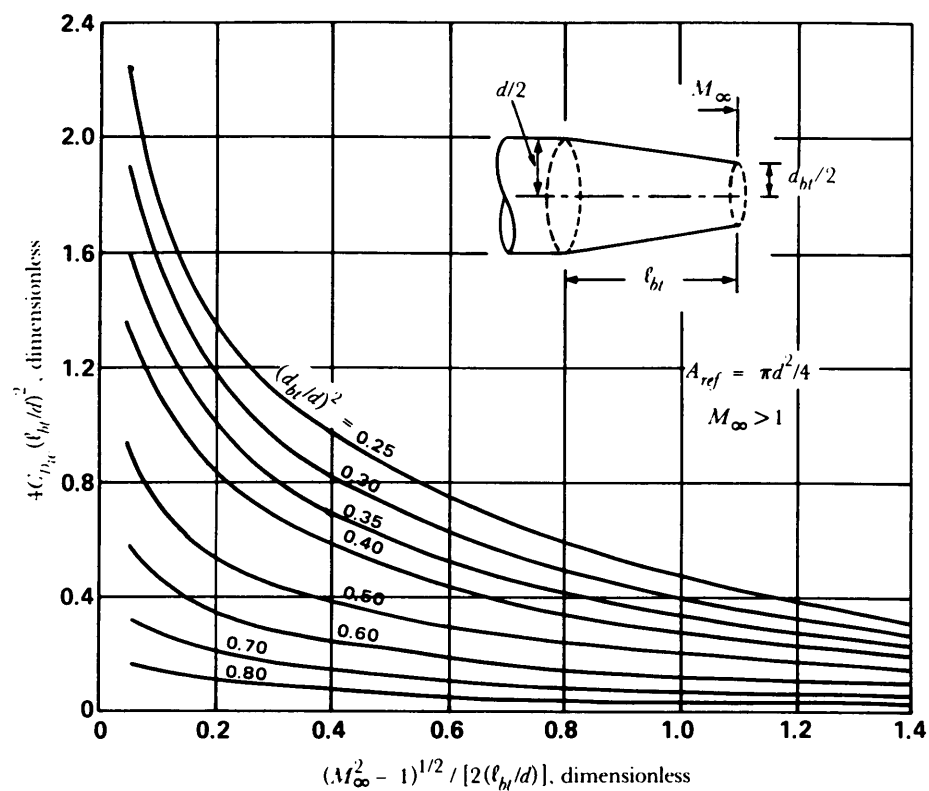
Figure 5-122.   Wave-Drag Coefficient of Conical Boattails at Supersonic Speeds
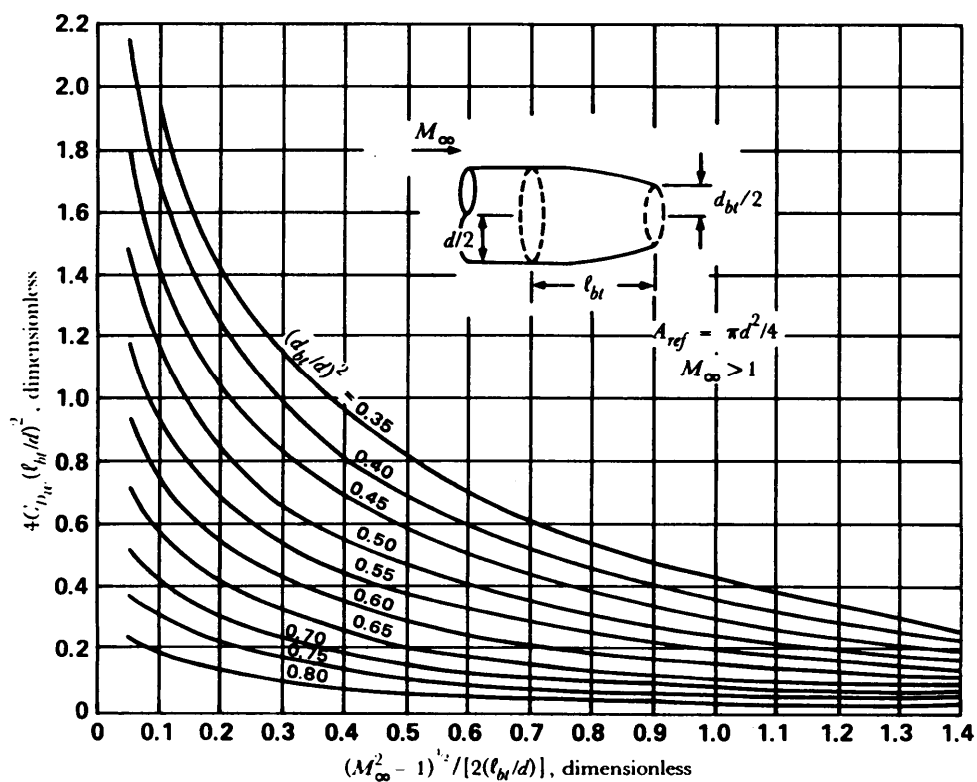
Figure 5-123.   Wave-Drag Coefficient of Parabolic Boattails at Supersonic Speeds
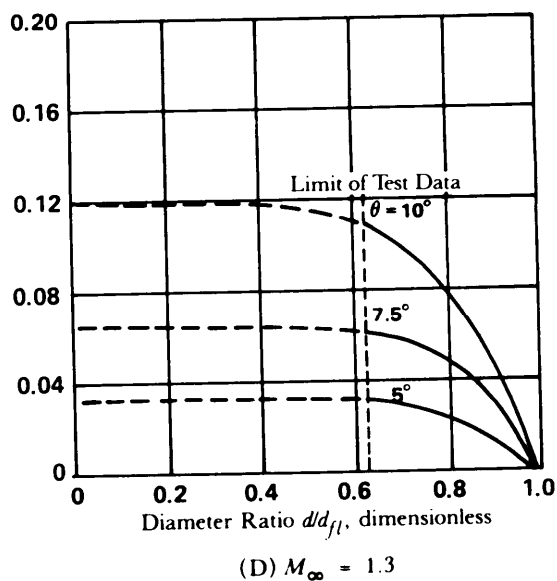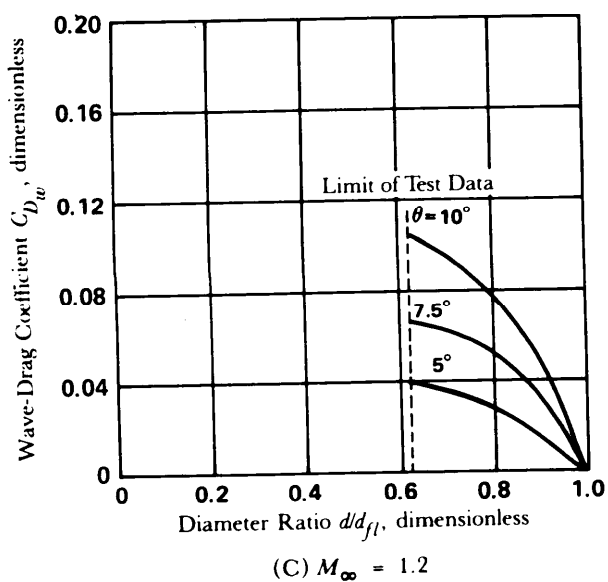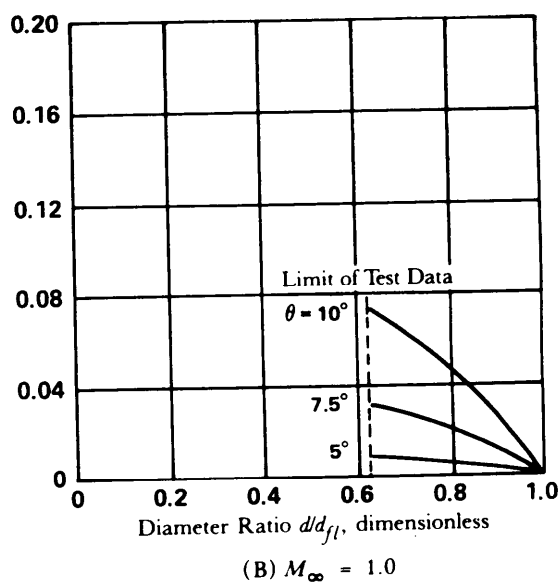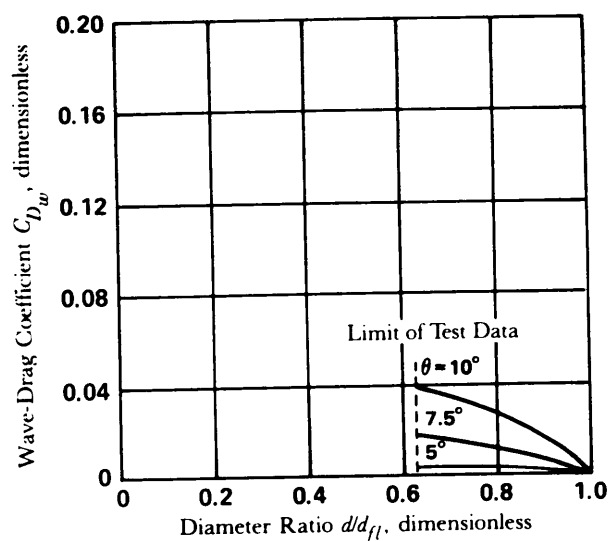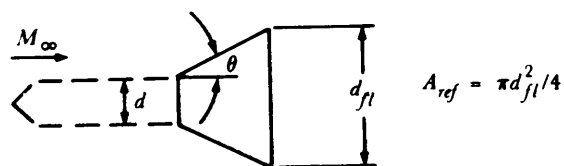
Figure 5-124. Wave-Drag Coefficient of Conical Flare at Various Mach Numbers (Ref. 82)
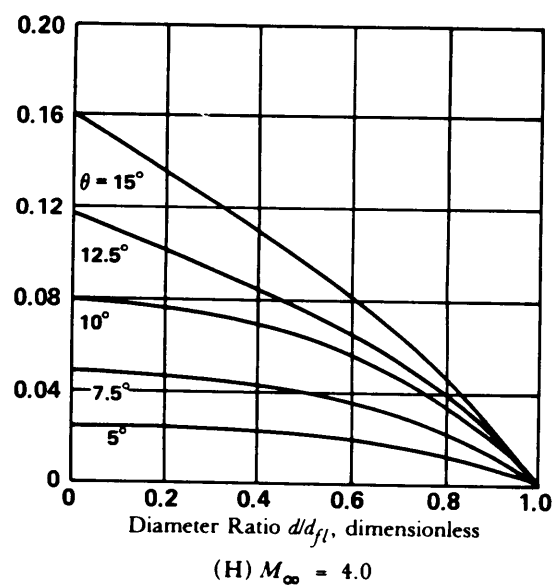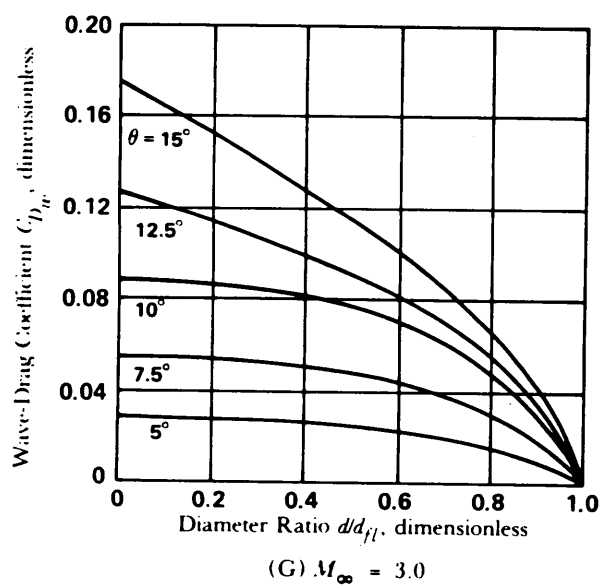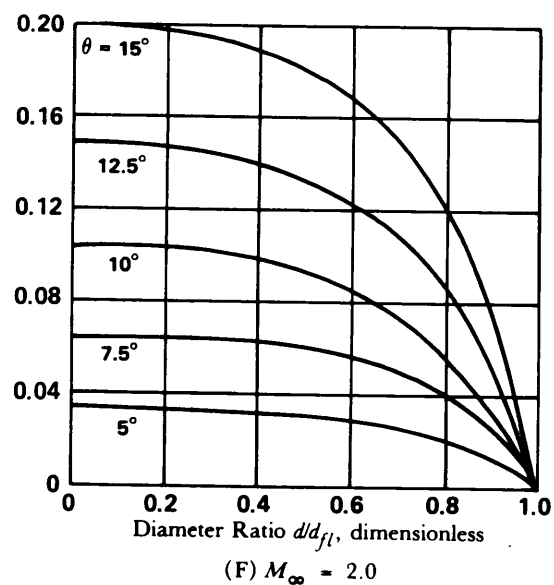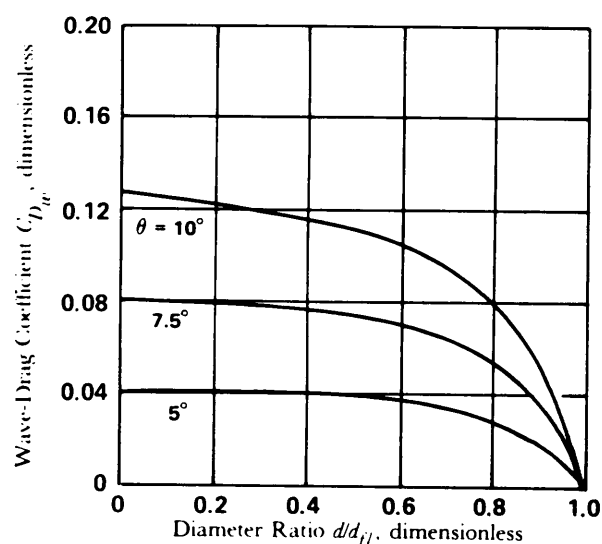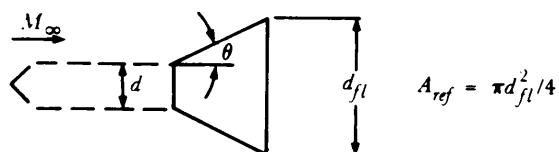
Figure 5-124. (cont'd)

(I) $M_\infty = 5.0$
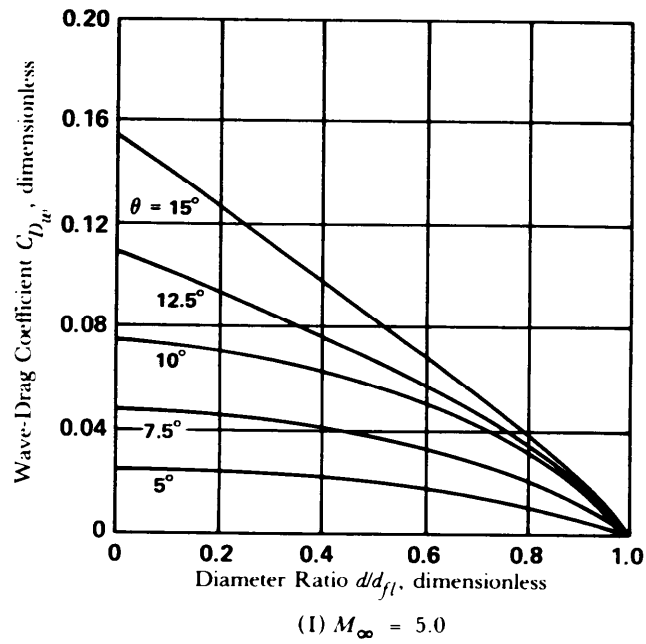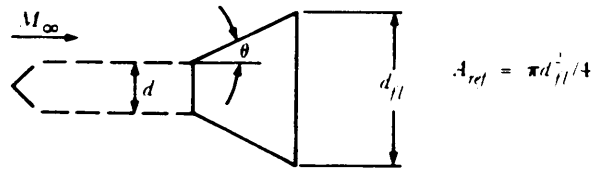
Figure 5-124. (cont'd)
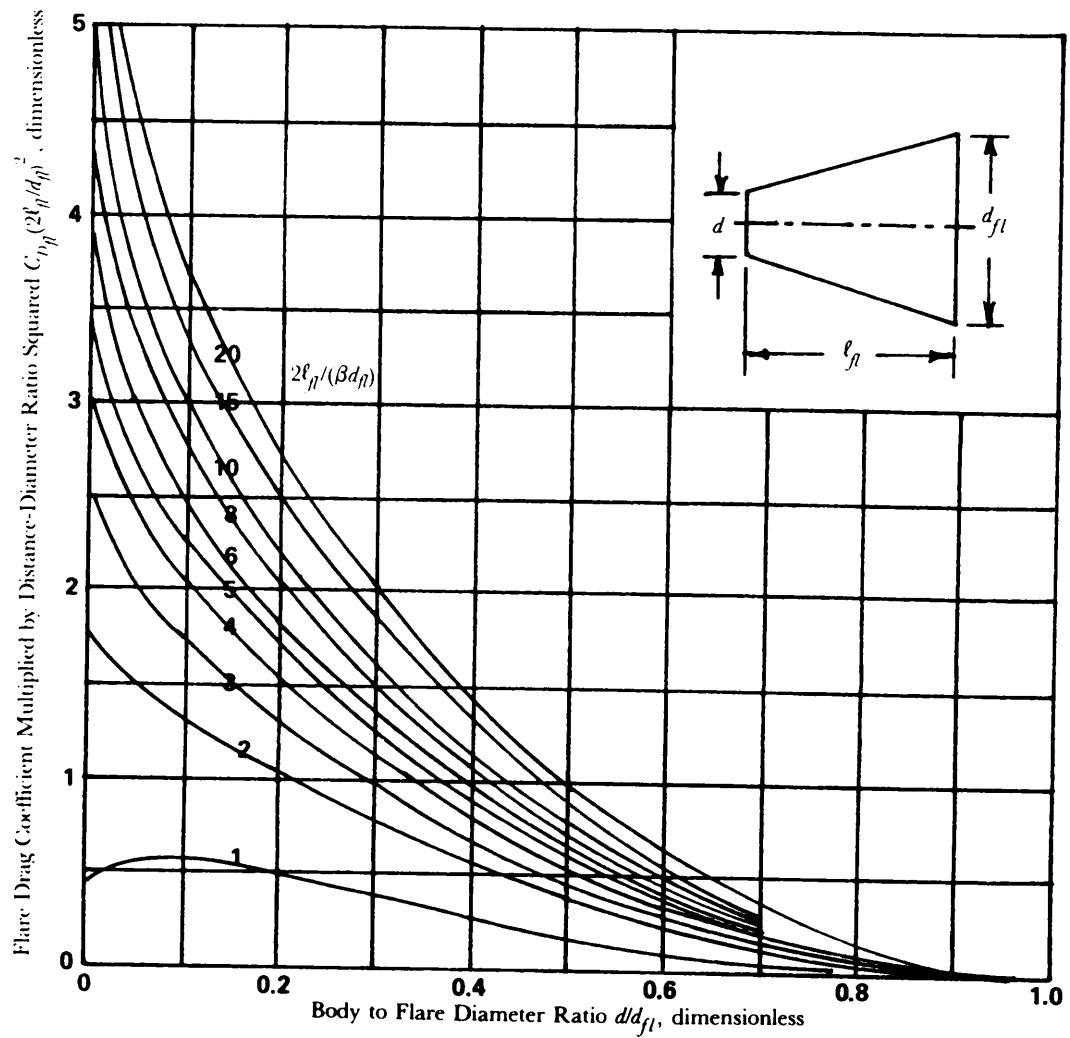
Figure Drag of Slender Conical Afterbodies or Forebodies (Ref. 25)
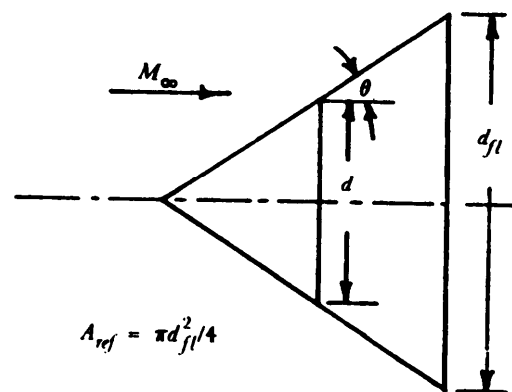
Figure 5-126. Sketch Showing Diameters to be Used in Eq. 5-39.
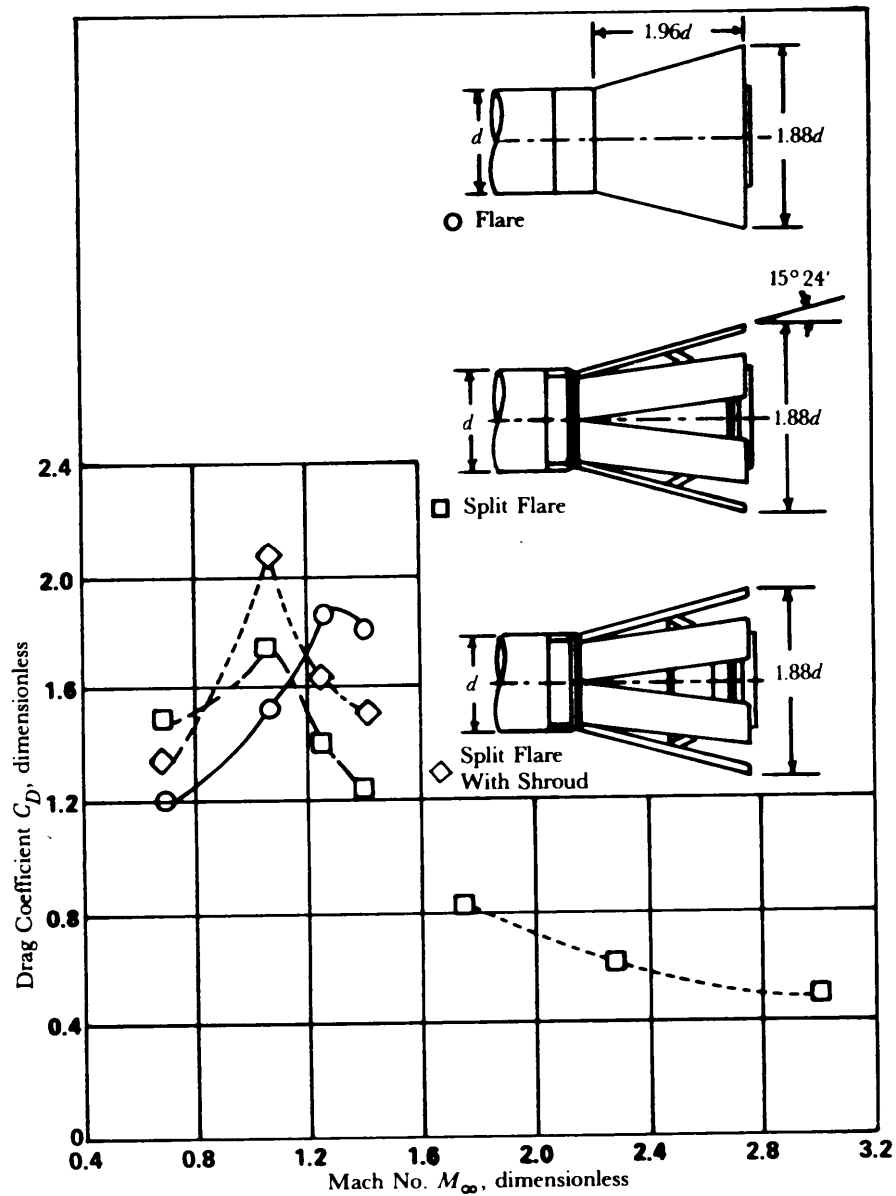
Figure 5-127. Comparison of Drag of Flare, Split Flare, and Split Flare With Shroud (Ref. 15, 85, and 89)
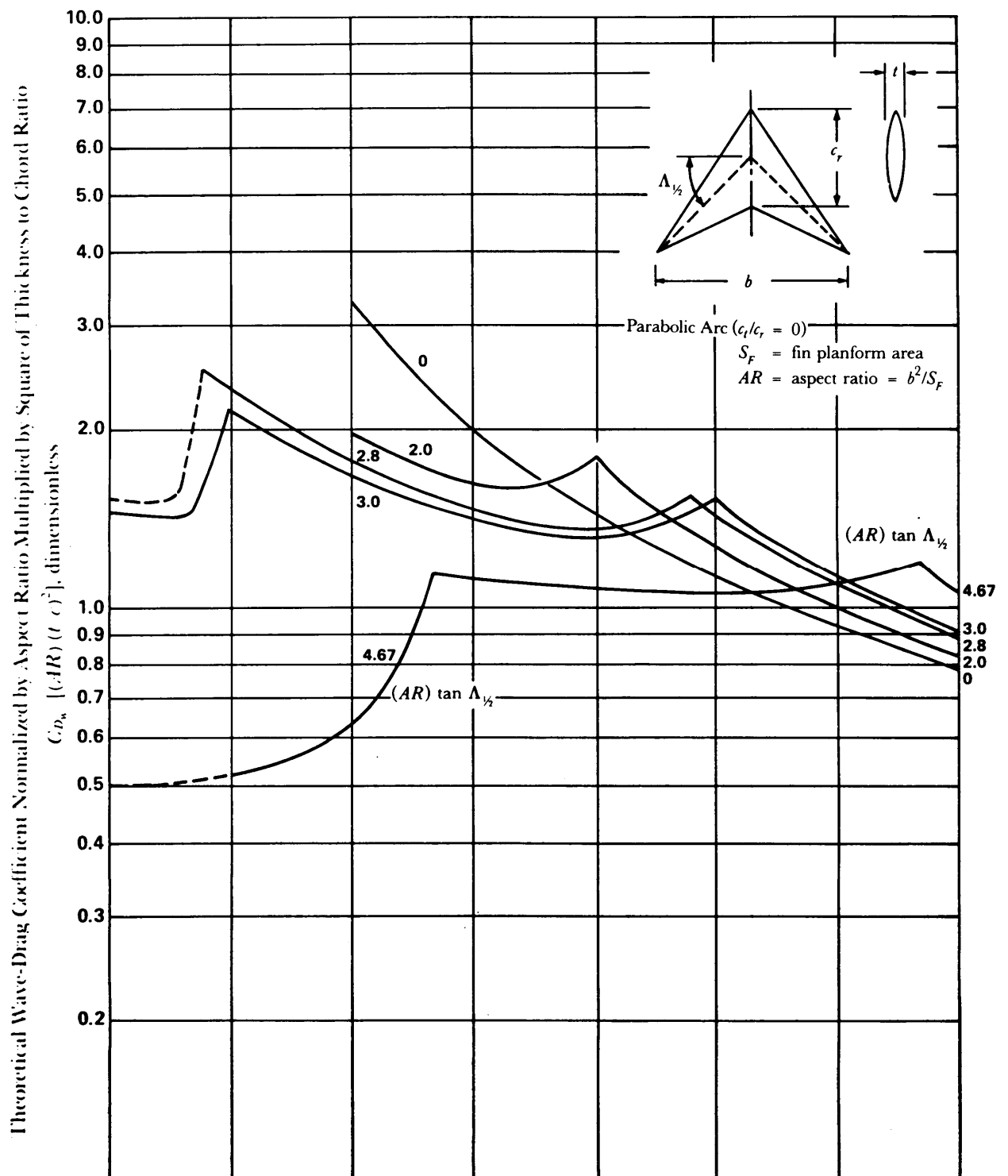
Figure 5-128. Wave-Drag Coefficient of Fins at Supersonic Speeds for Parabolic Arc and Double-Wedge Shapes for Various c_t/c_r Ratios
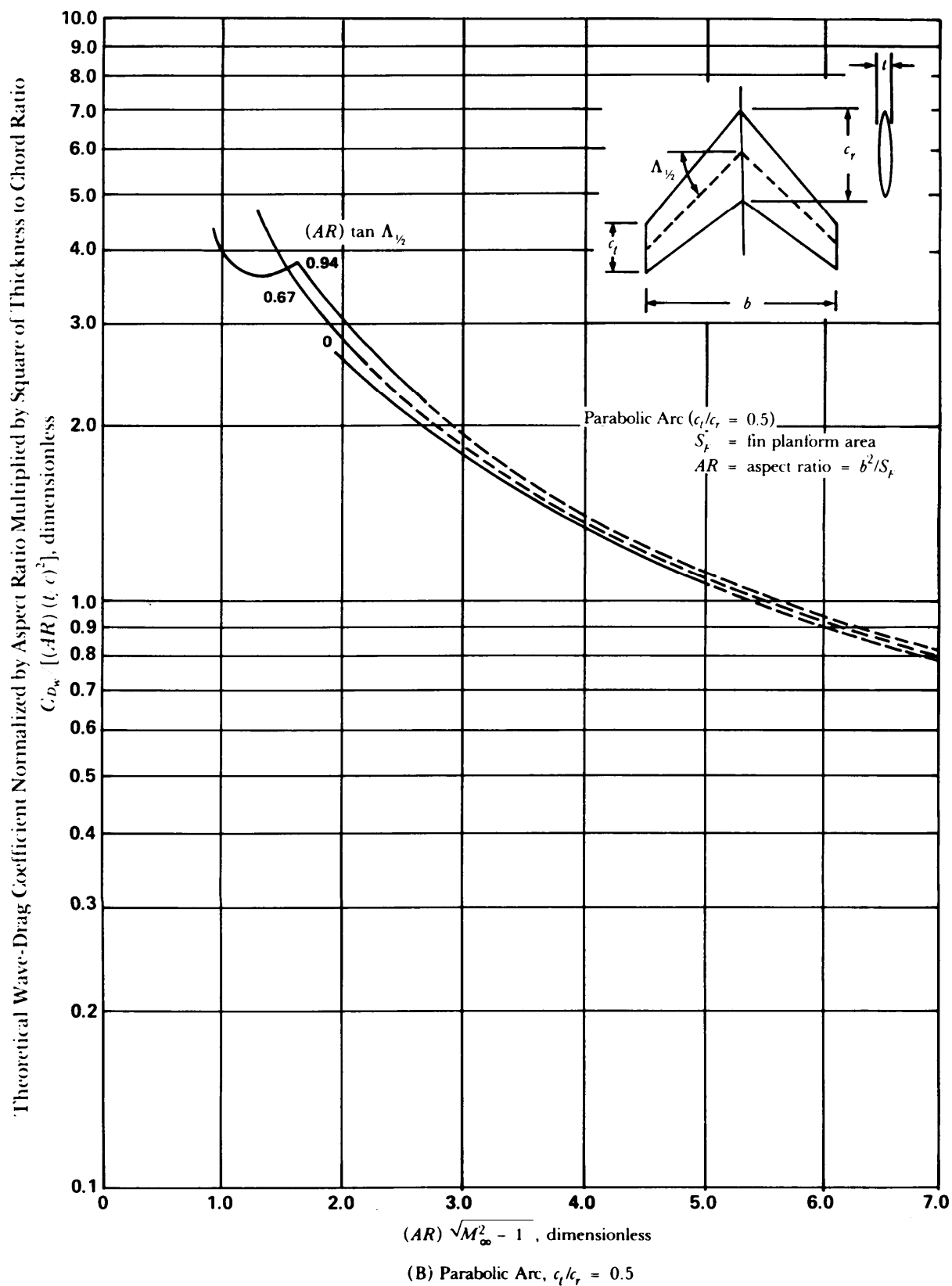
(B) Parabolic Arc, $c_t/c_r = 0.5$

Figure 5-128. (cont'd)

Figure 5-128. (cont'd)

Figure 5-128. (cont'd)

Figure 5-128. (cont'd)

(E) Double Wedge, c_t/c_r = 1.0, max t at $0.3c_r$
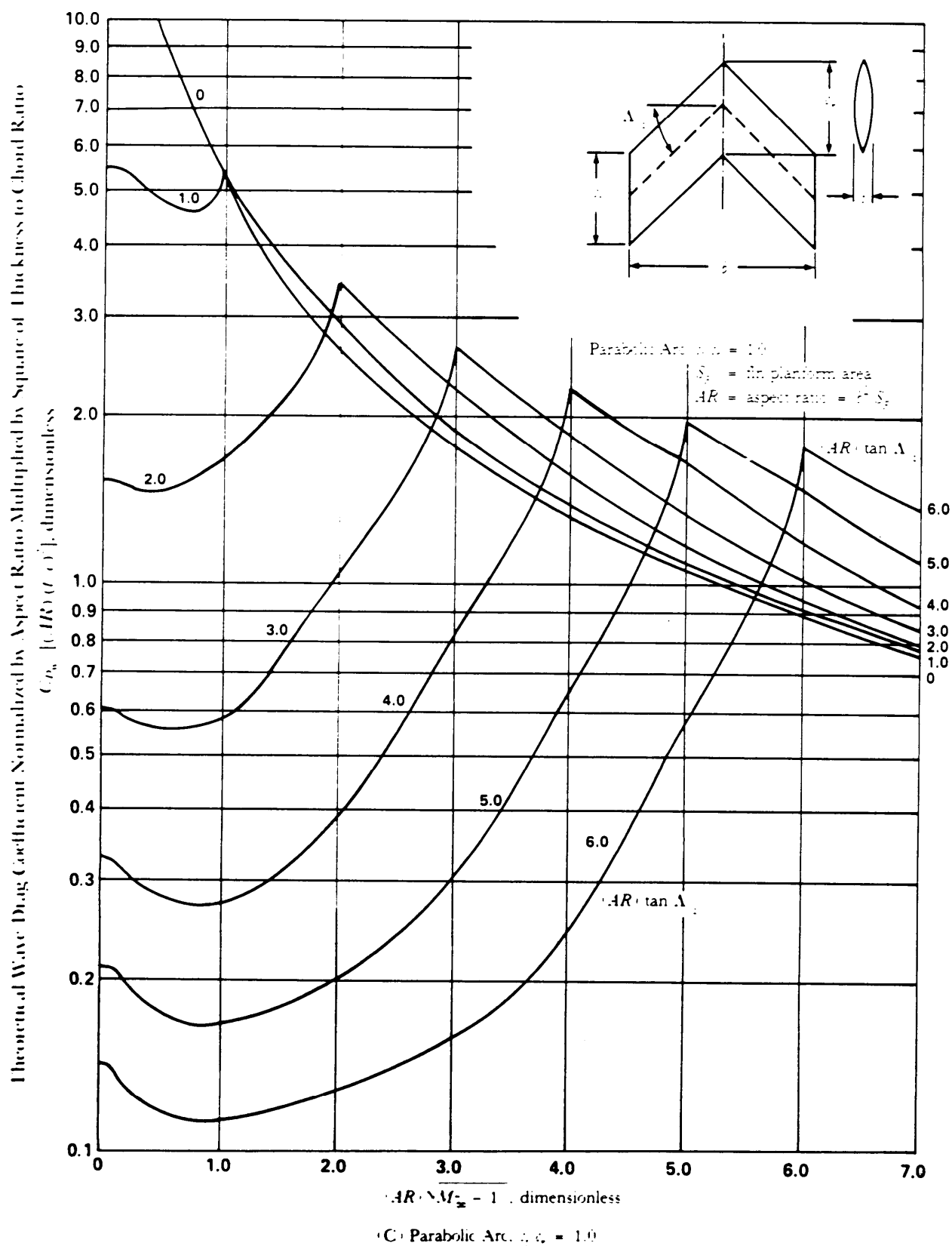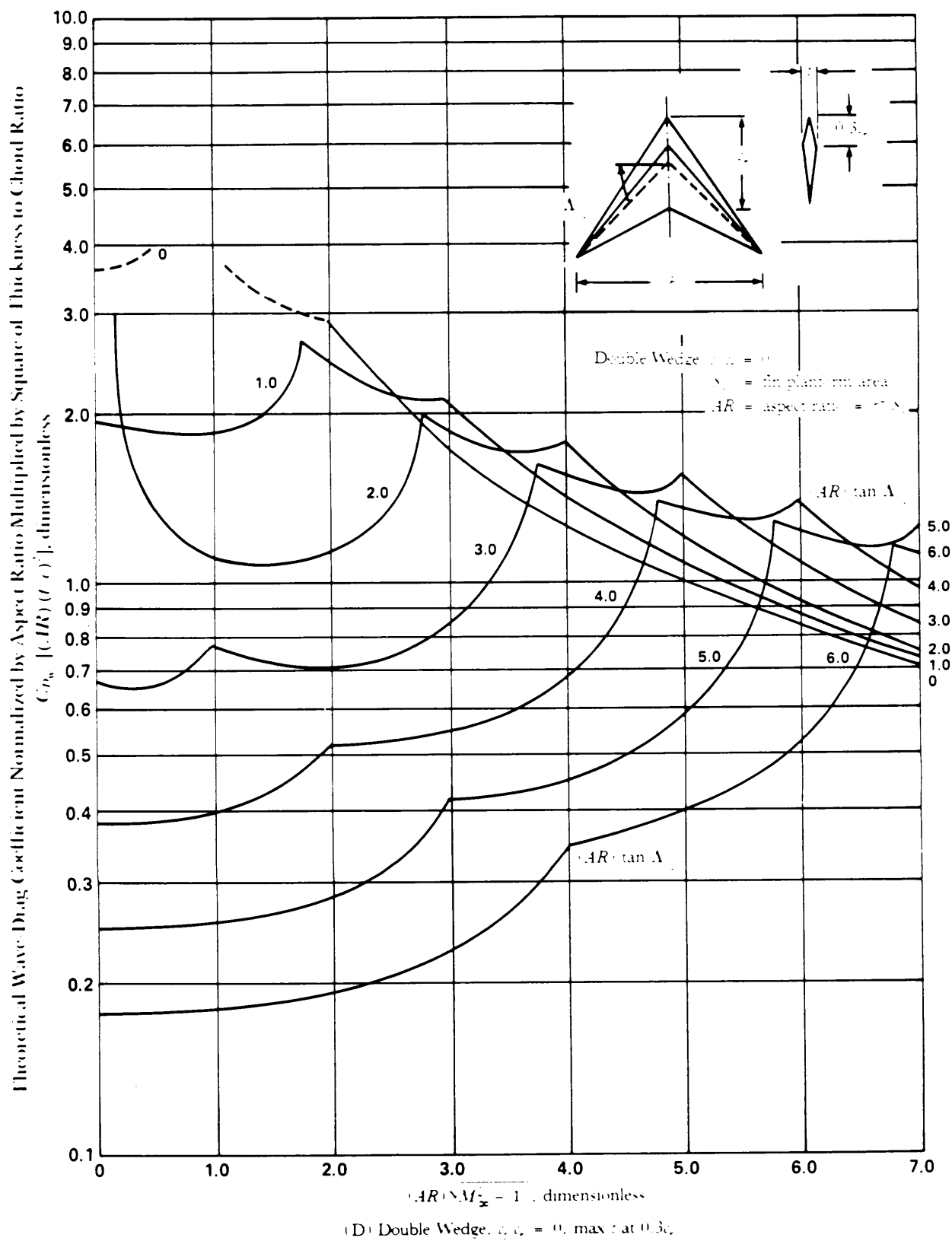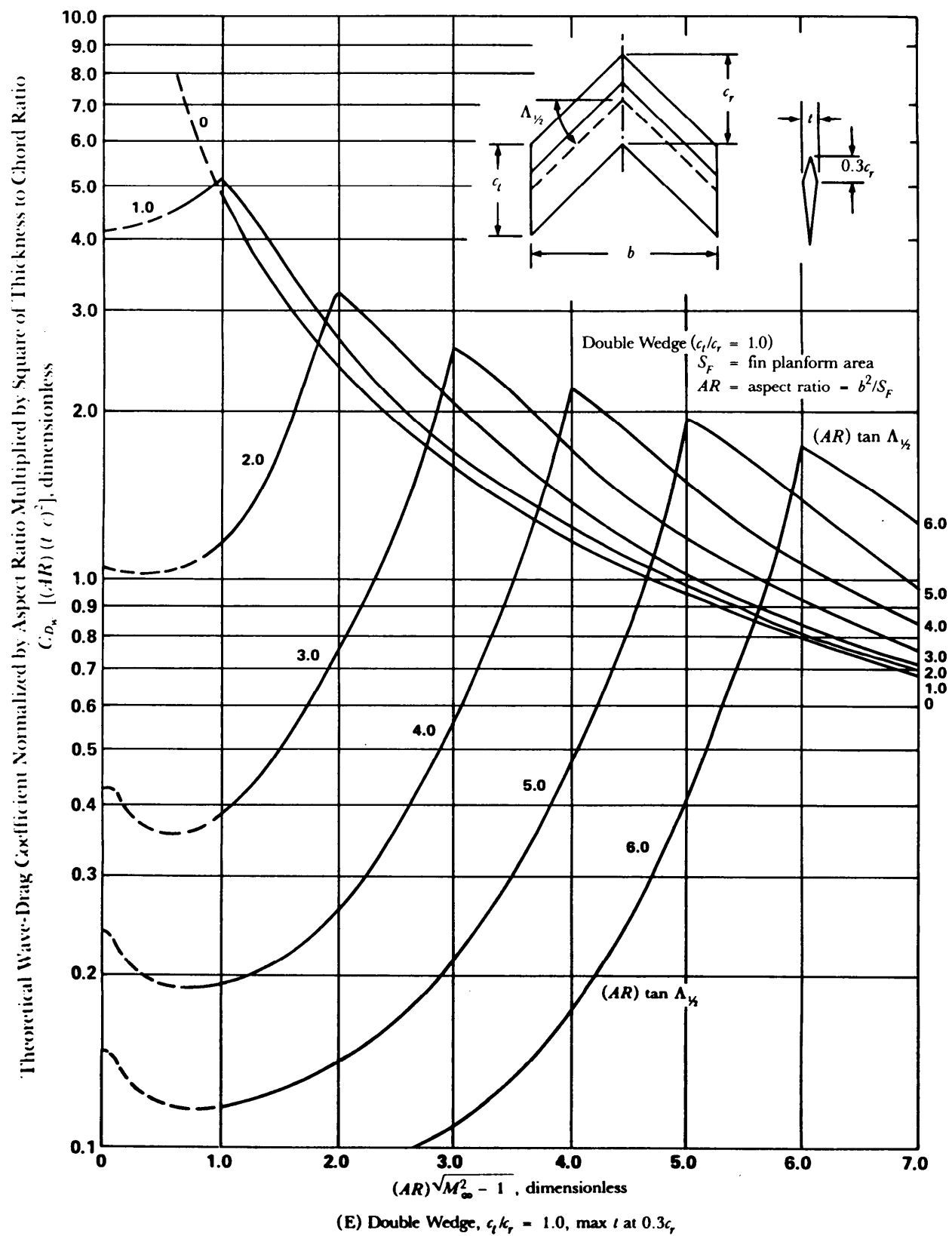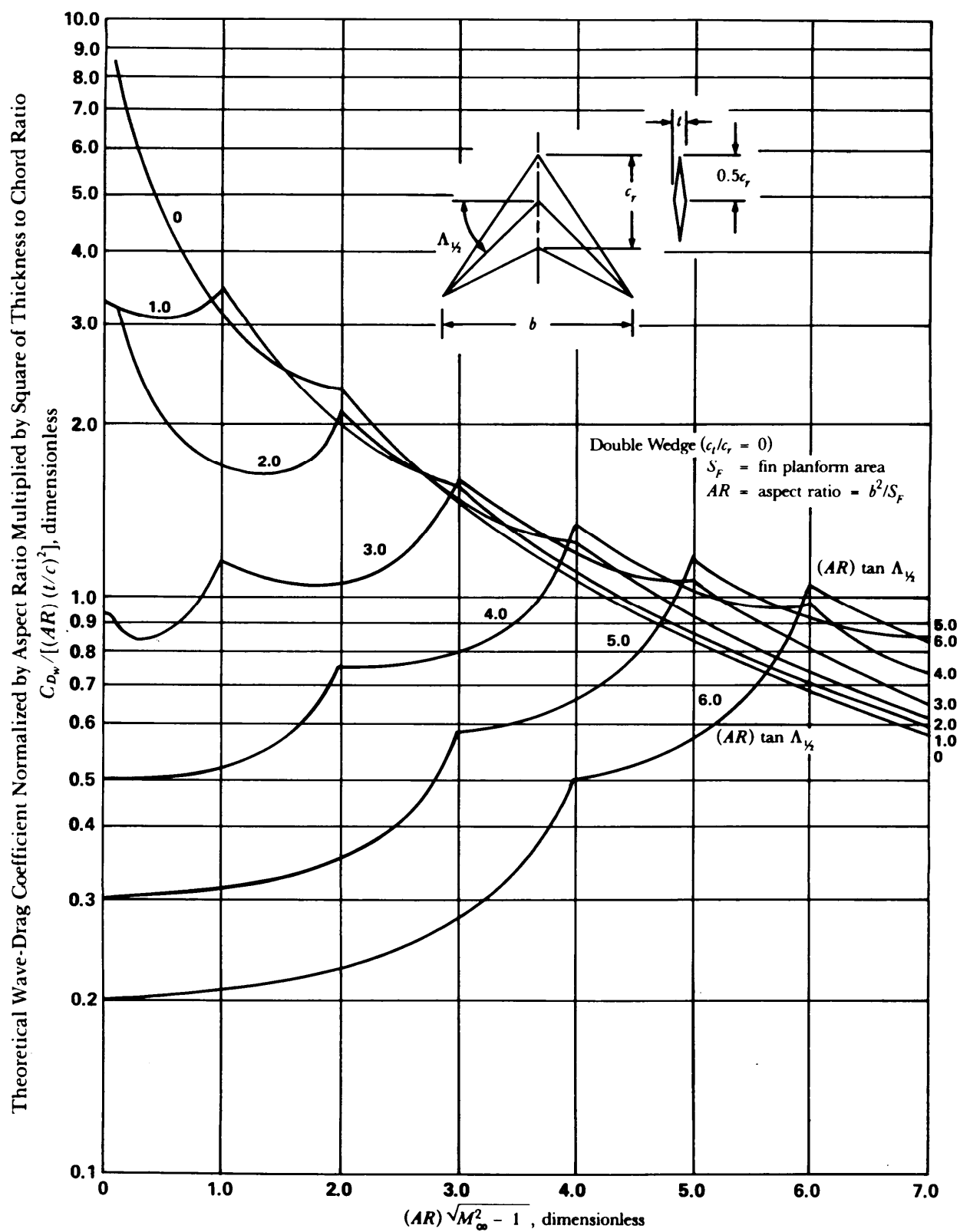
(F) Double Wedge, $c_t/c_r = 0$, max t at $0.5c_r$

Figure 5-128. (cont'd)

(G) Double Wedge, $c_t/c_r = 0.5$, max t at $0.5c_r$

Figure 5-128. (cont'd)

(H) Double Wedge, c_t/c_r = 1.0, max t at $0.5c_r$
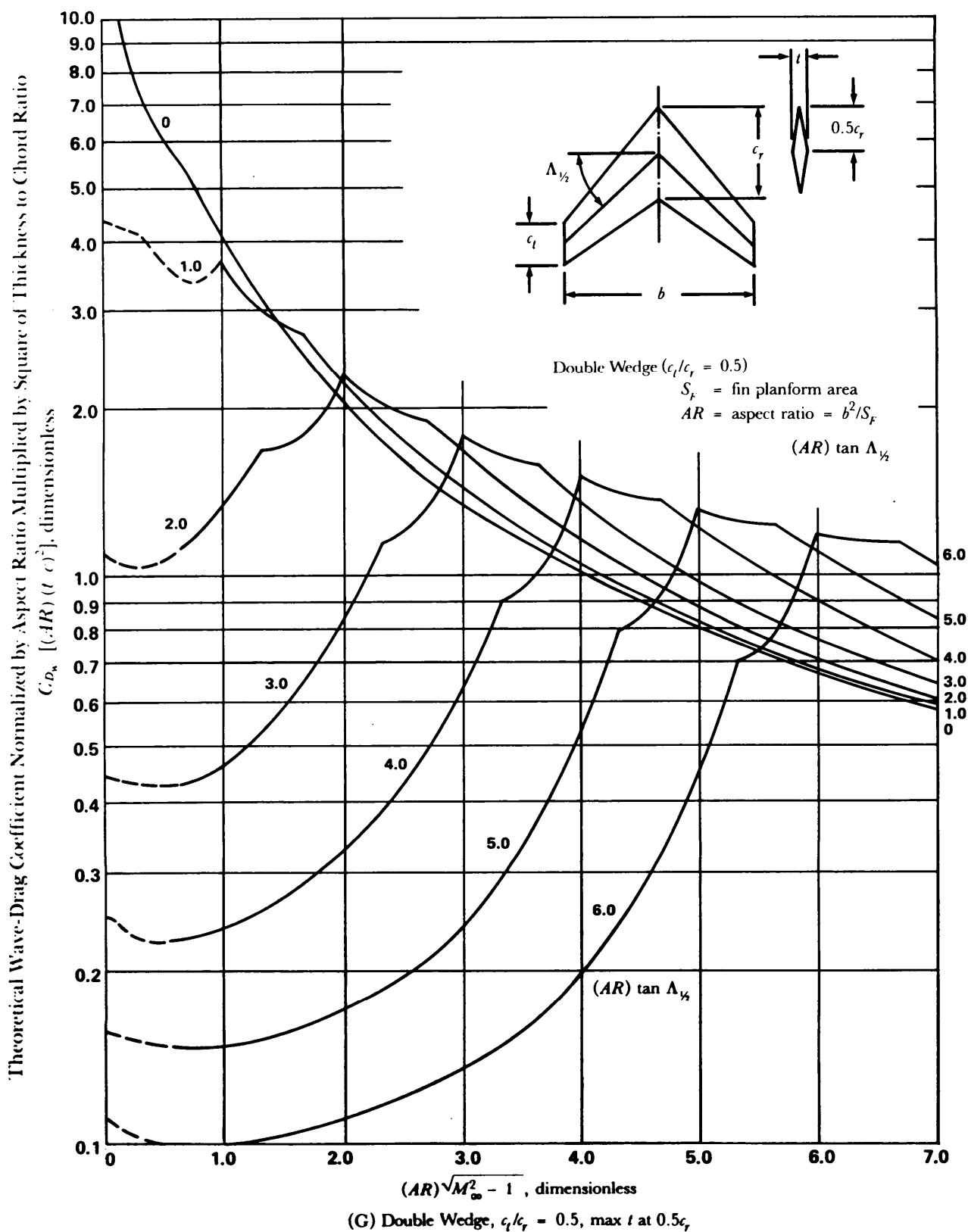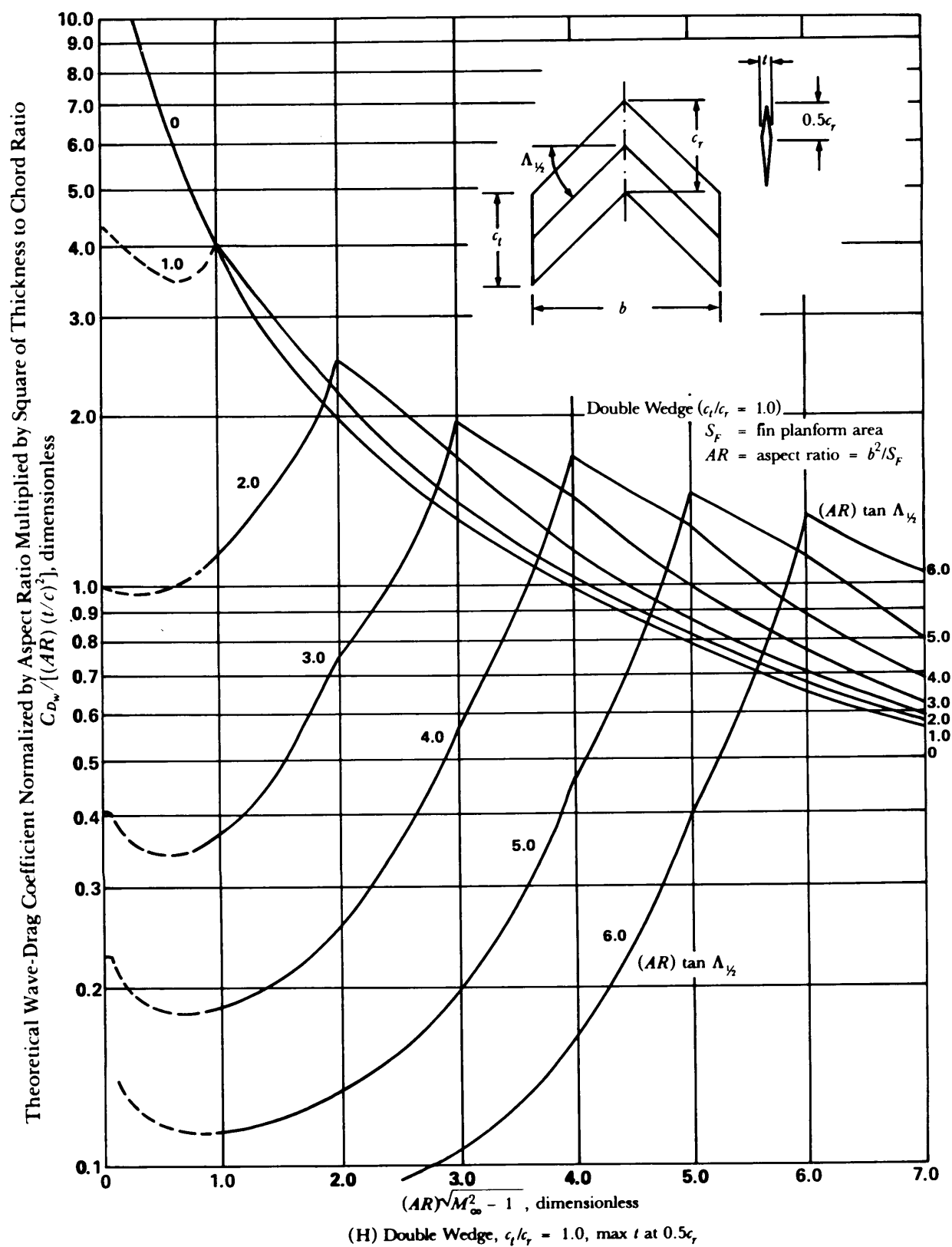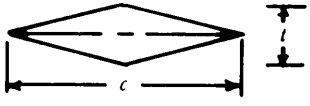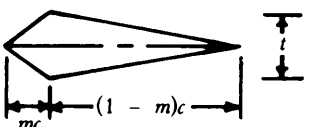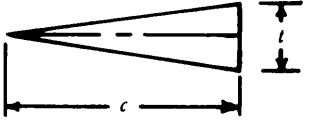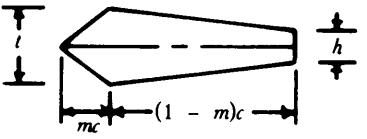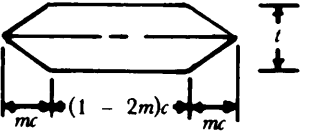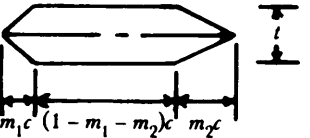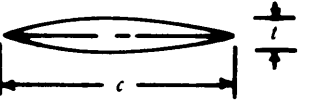
Figure 5-128. (cont'd)

Type	Profile	Two-Dimensional Drag Coefficient Based on Planform Area	Factor
Symmetrical Double Wedge		$\dfrac{4}{\beta}\left(\dfrac{t}{c}\right)^2$	1
Double Wedge		$\dfrac{1}{\beta} \cdot \left(\dfrac{t}{c}\right)^2 \cdot \dfrac{1}{m(1-m)}$	$\dfrac{1}{4m(1-m)}$
Single Wedge		$\dfrac{1}{\beta} \cdot \left(\dfrac{t}{c}\right)^2$	$\dfrac{1}{4}$
Cropped Double Wedge		$\dfrac{1}{\beta}\left[\left(\dfrac{t}{c}\right)^2 \cdot \dfrac{1}{m} + \dfrac{(t-h)^2}{c^2(1-m)}\right]$	$\dfrac{1}{4}\left[\dfrac{1}{m} + \dfrac{\left(1-\dfrac{h}{t}\right)^2}{1-m}\right]$
Symmetrical Parallel Double Wedge		$\dfrac{2}{\beta}\left(\dfrac{t}{c}\right)^2 \cdot \dfrac{1}{m}$	$\dfrac{1}{2m}$
Parallel Double Wedge		$\dfrac{1}{\beta} \cdot \left(\dfrac{t}{c}\right)^2 \left[\dfrac{1}{m_1} + \dfrac{1}{m_2}\right]$	$\dfrac{1}{4}\left[\dfrac{1}{m_1} + \dfrac{1}{m_2}\right]$
Symmetrical Biconvex (Circular or Parabolic Arcs)		$\dfrac{4}{\beta} \cdot \dfrac{4}{3} \cdot \left(\dfrac{t}{c}\right)^2$	$\dfrac{4}{3}$

$$\beta = \sqrt{M_\infty^2 - 1}$$

Figure 5-129.   Wave-Drag Coefficient of Fins of Various Sectional Shapes
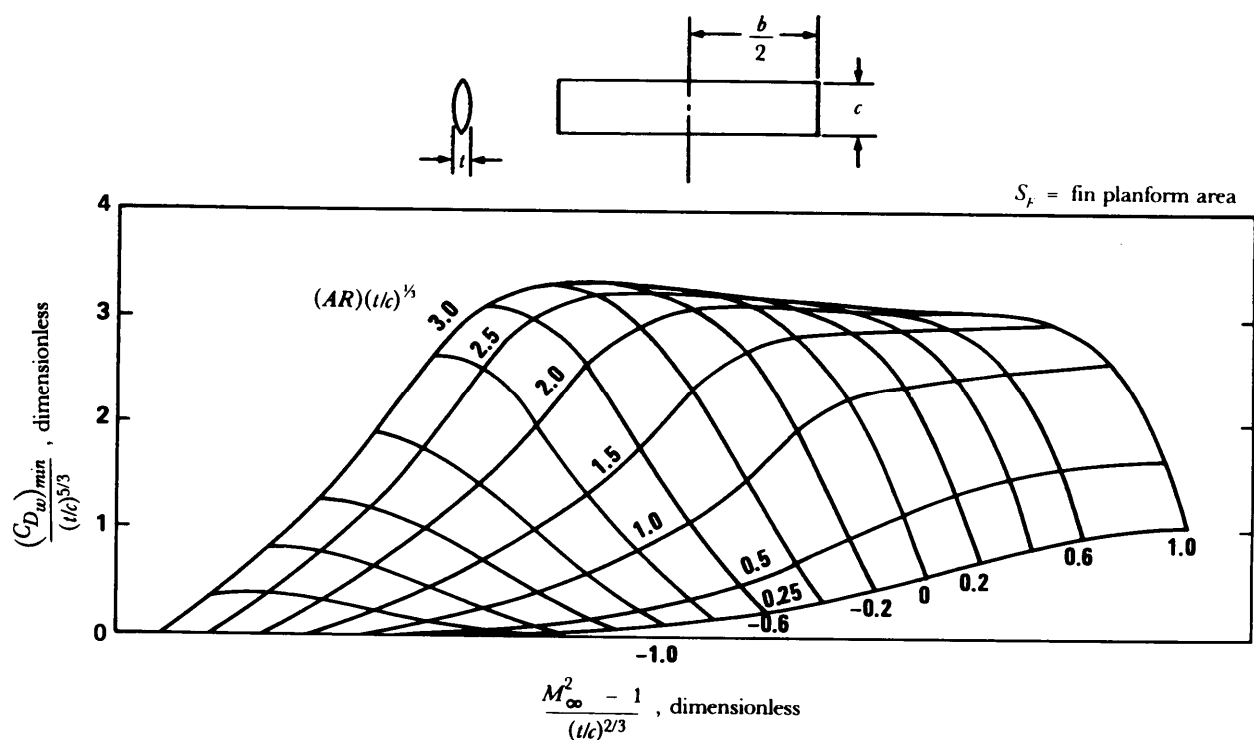
Figure 5-130. Wave-Drag Coefficient of Rectangular Fins at Subsonic and Transonic Speeds (Ref. 18)
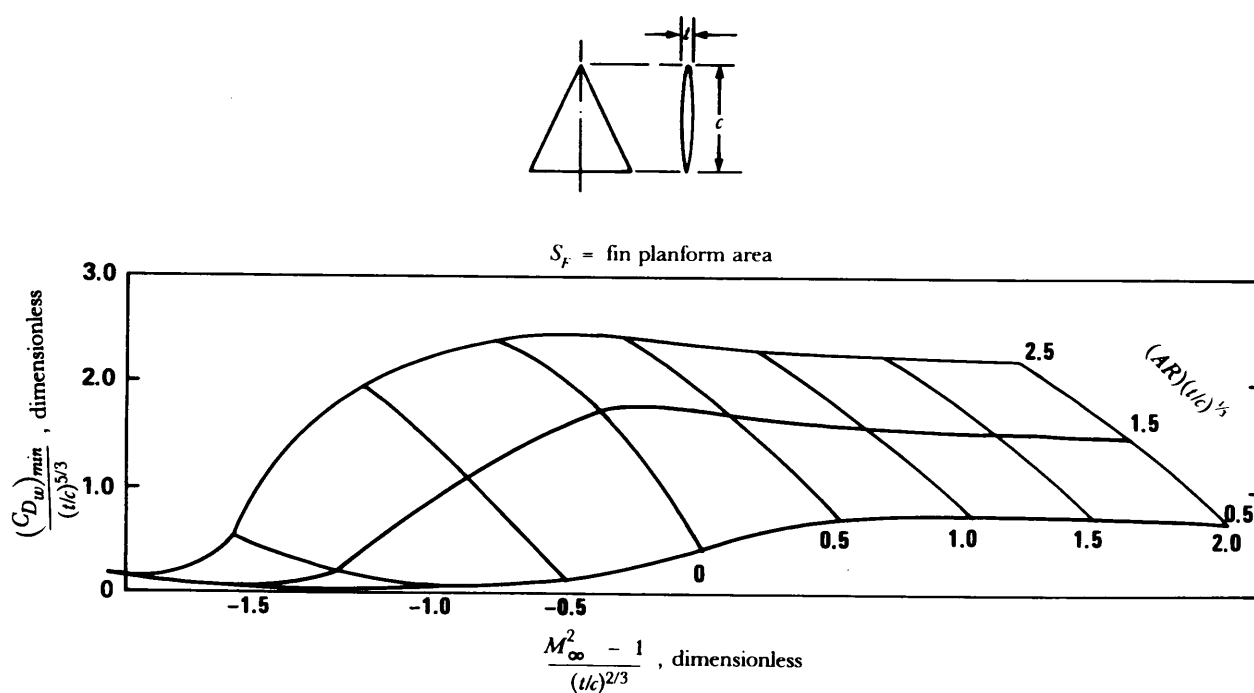
Figure 5-131. Wave-Drag Coefficient of Delta Fins at Subsonic and Transonic Speeds
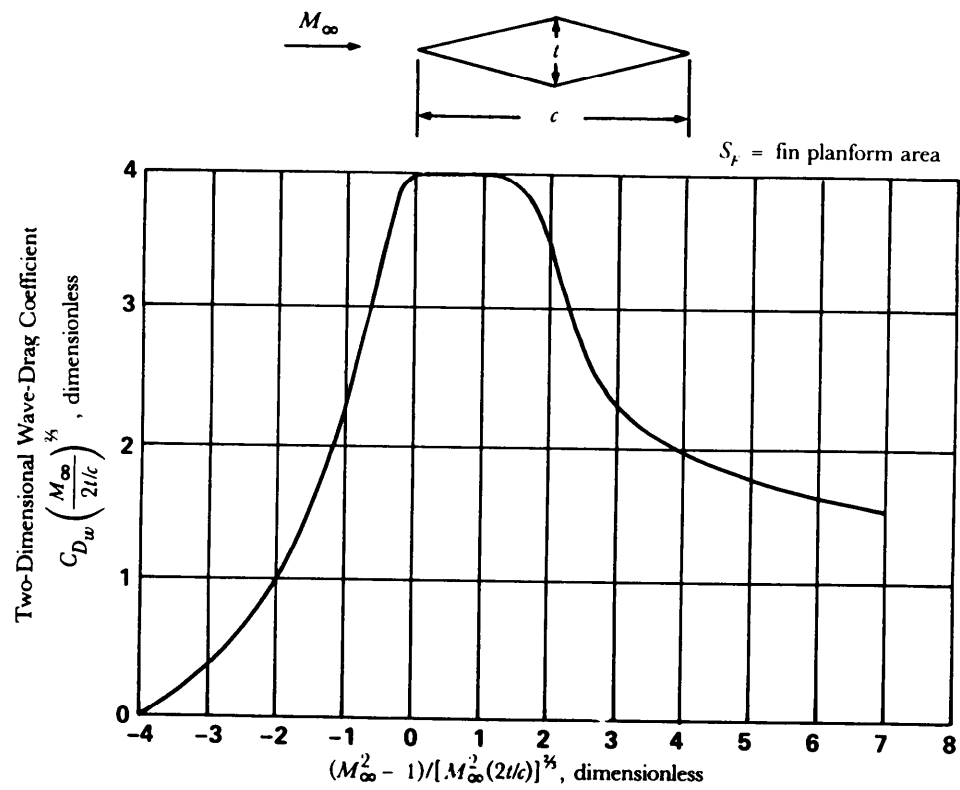
Figure 5-132. Wave-Drag Coefficient of a Double-Wedge Fin at Transonic Speeds

(A) Internal Expansion Angle δ = 0 deg

(B) Internal Expansion Angle δ = 6 deg
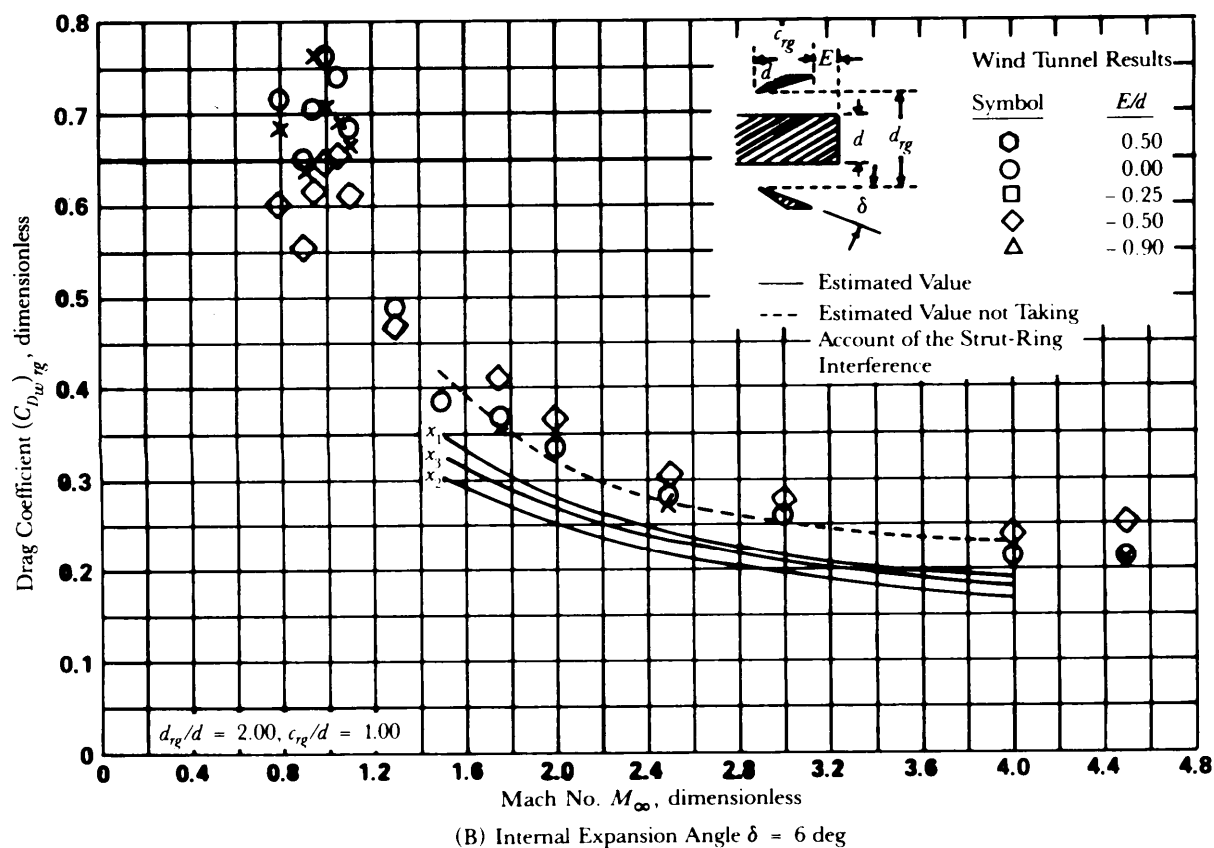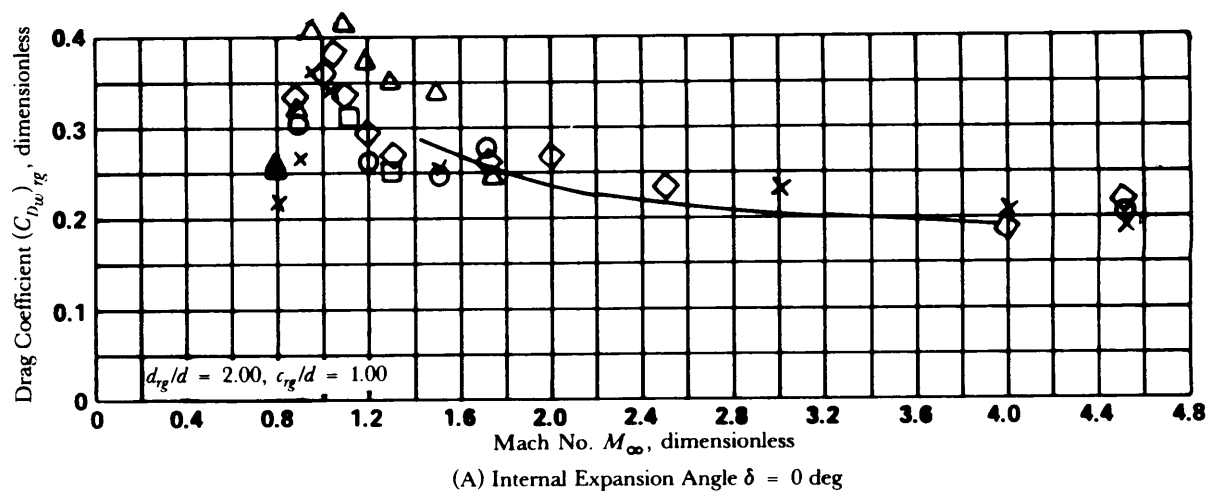
Figure 5-133. Effect of Internal Expansion Angle δ and Longitudinal Positioning E/d on Ringtail Drag (Ref. 90)
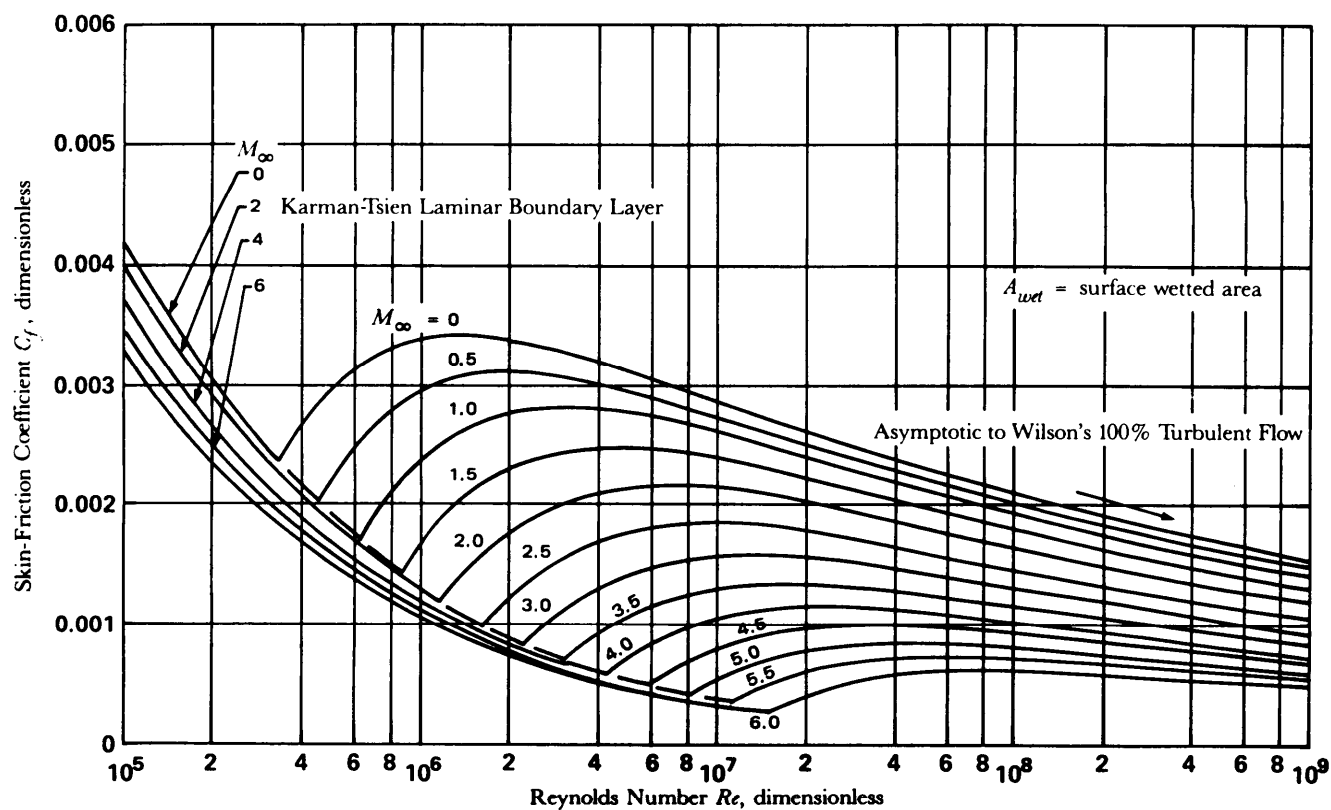
Figure 5-134. Flat Plate Average Skin-Friction Coefficient
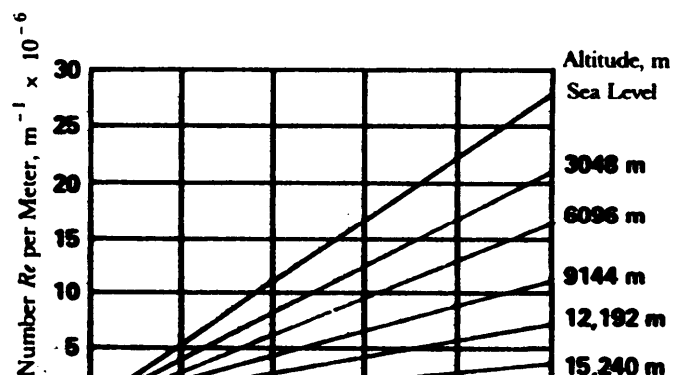
Figure 5-135. Reynolds Number as a Function of Flight Mach Number and Altitude
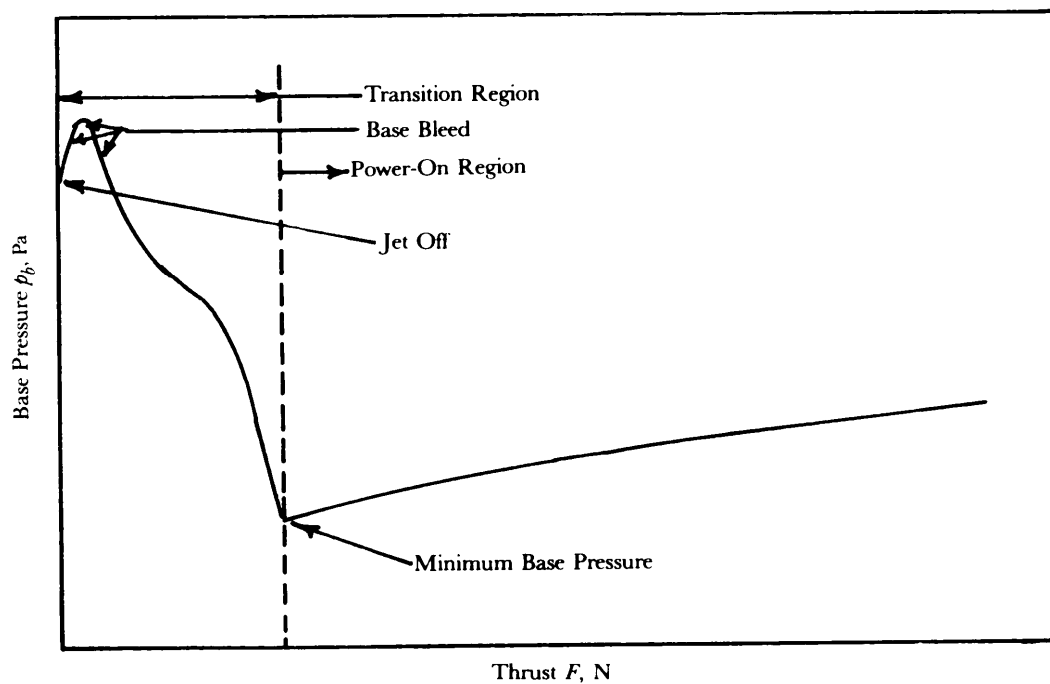
Figure 5-136. Typical Variation of Base Pressure With Thrust (Ref. 93)

(A) Jet Off

(B) Jet On
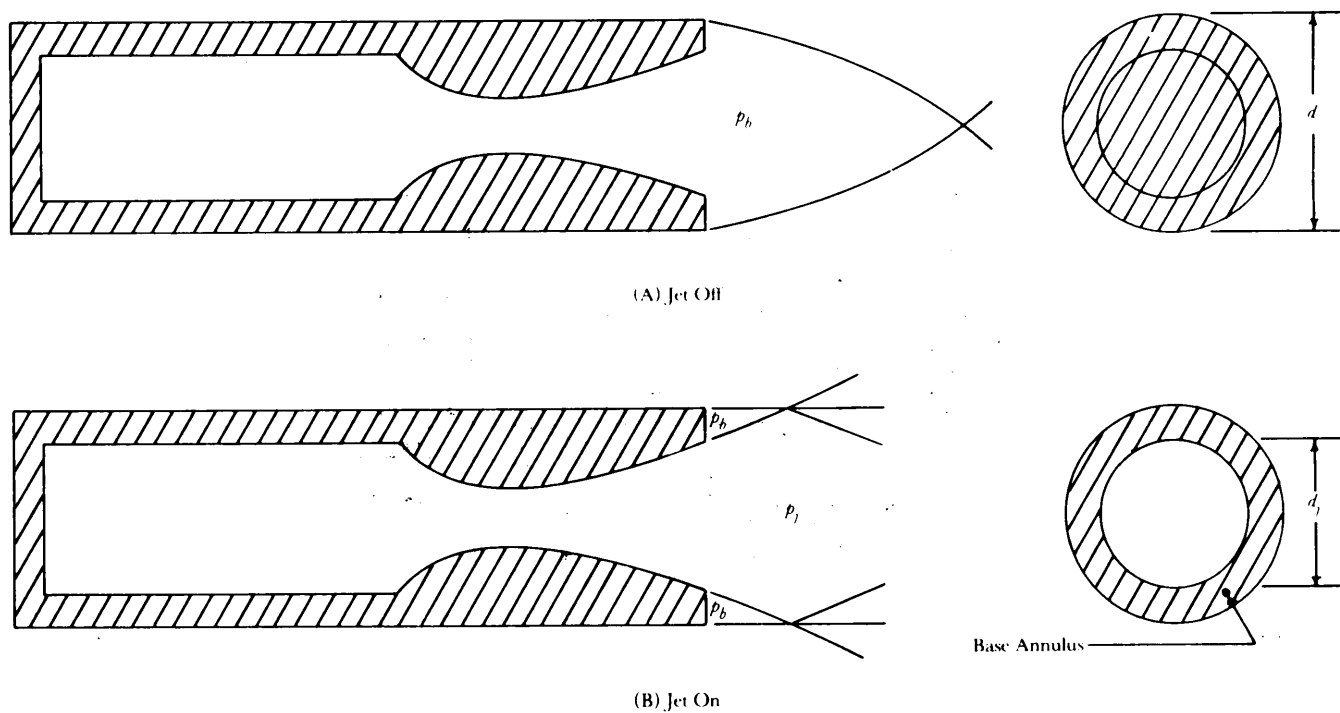
Figure 5-137. Base Flow Geometry
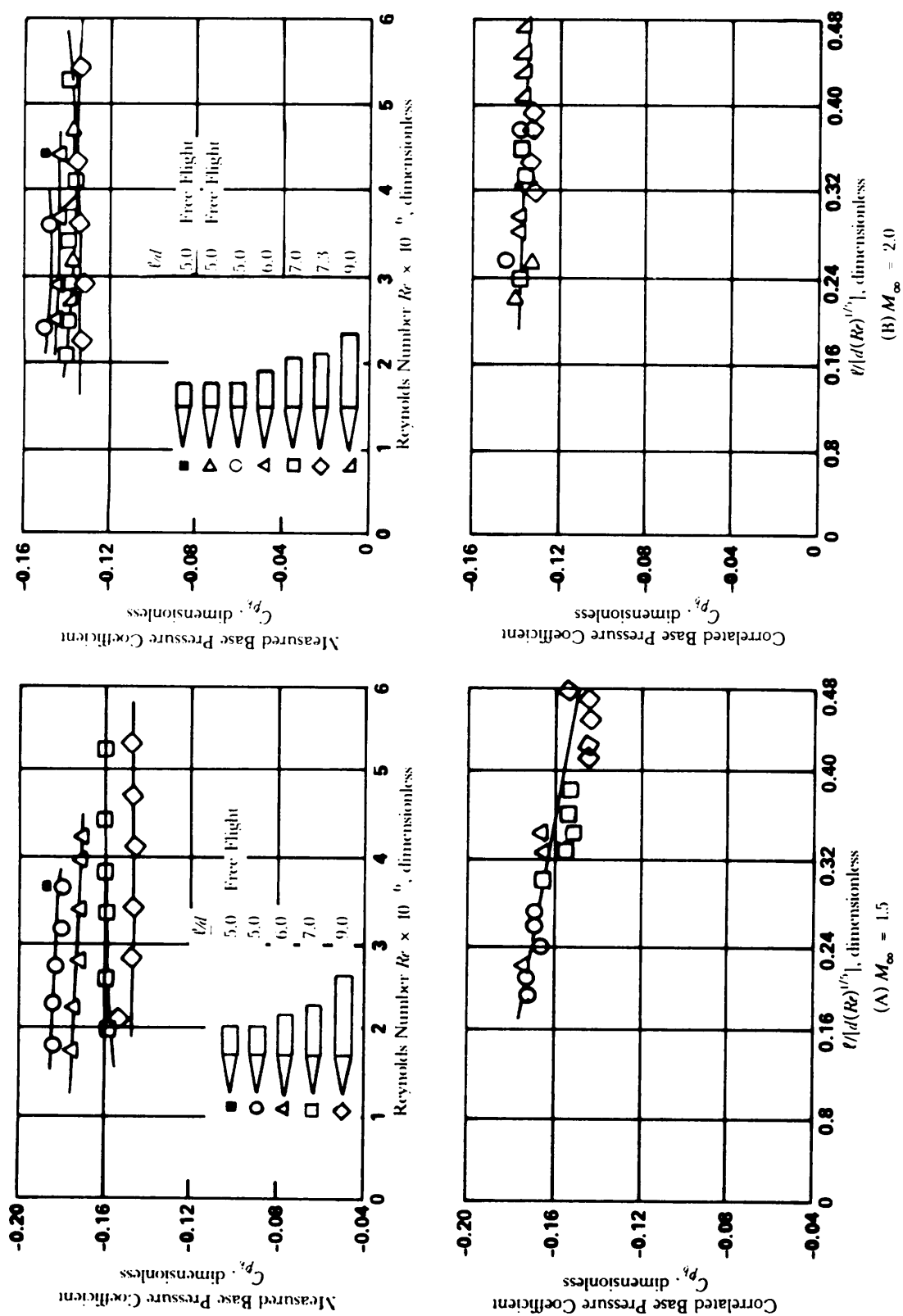
Figure 5-138. Measured and Correlated Base Pressure for Several Configurations. $M_x = 1.5$ and 2.0, Turbulent Boundary Layer (Ref. 94)
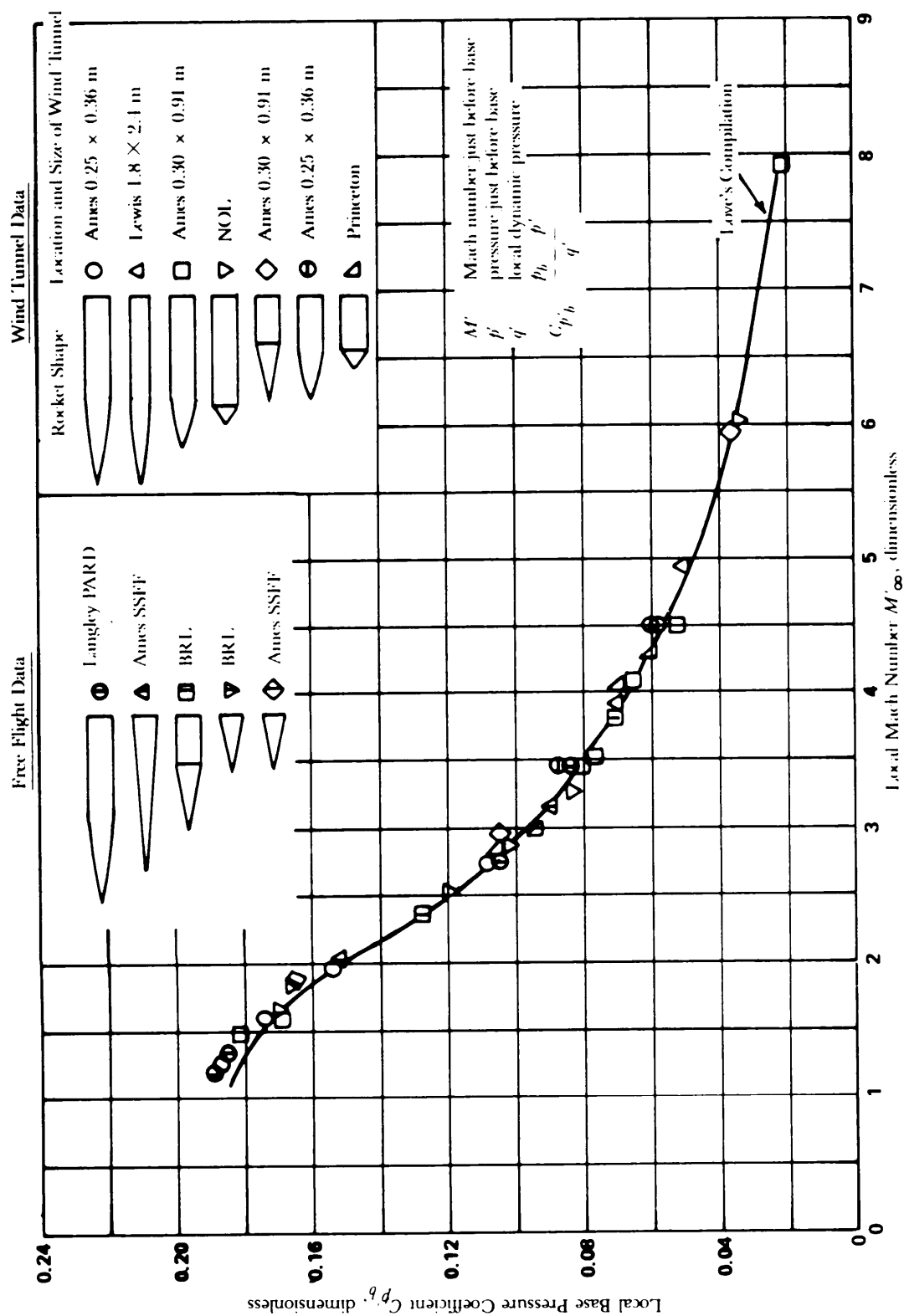
Figure 5-139. Base Pressure Coefficient for Finless Bodies of Revolution in Terms of Local Pressure and Local Mach Number Ahead of Base, $\alpha = 0$ deg (Ref. 96)
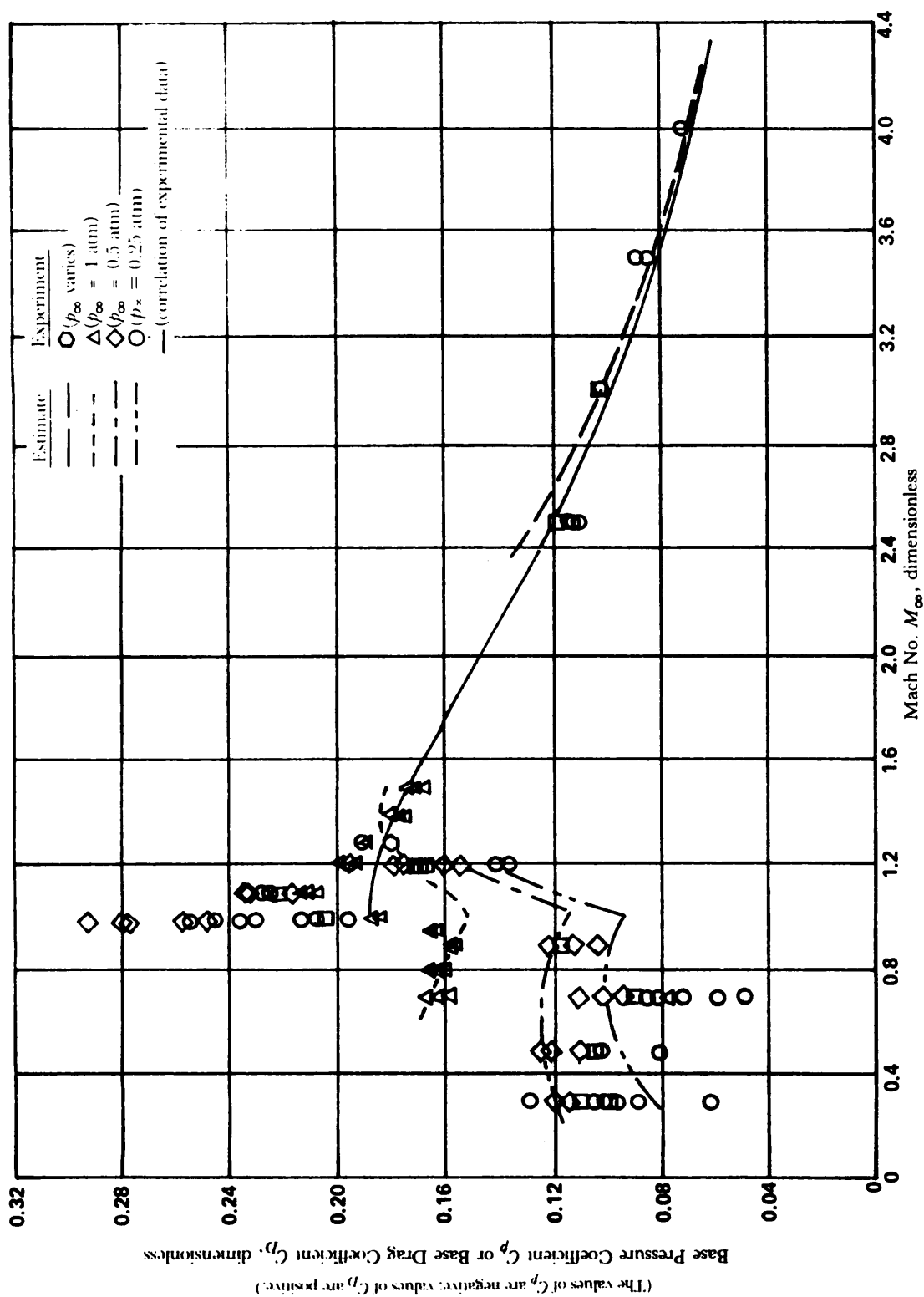
Figure 5-140. Effects of Mach Number and Reynolds Number on Base Pressure (Ref. 97)
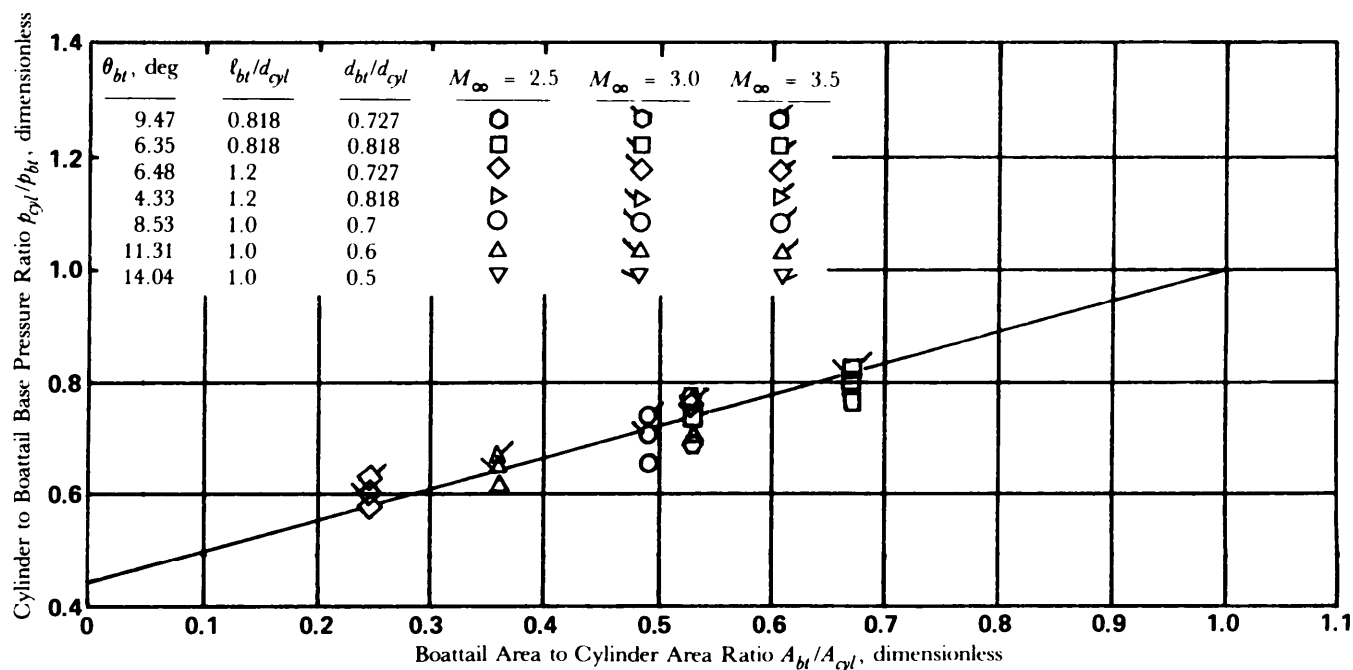
Figure 5-141. Cylinder to Boattail Base Pressure Ratio as a Function of Base Area Ratio (Power-Off) (Ref. 98)
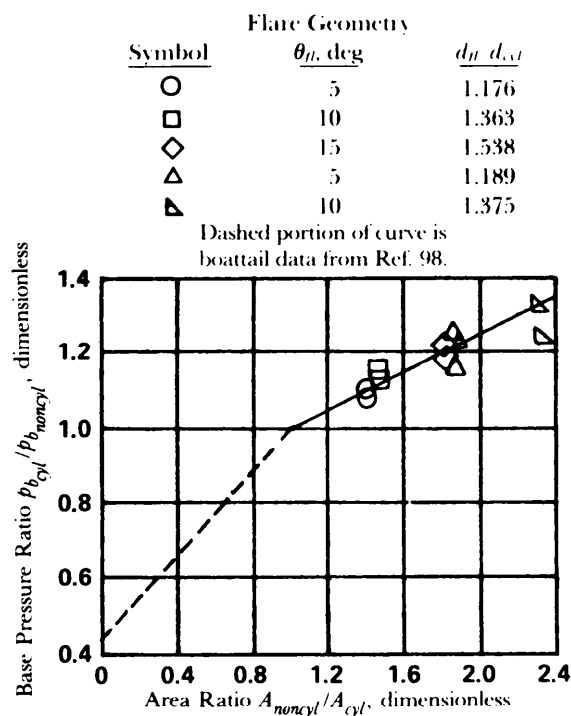
Figure 5-142. Effect of Boattailed and Flared Afterbodies on Jet-Off Pressures (Flare data were obtained at free-stream Mach numbers of 1.65 and 2.21.) (Ref. 99)
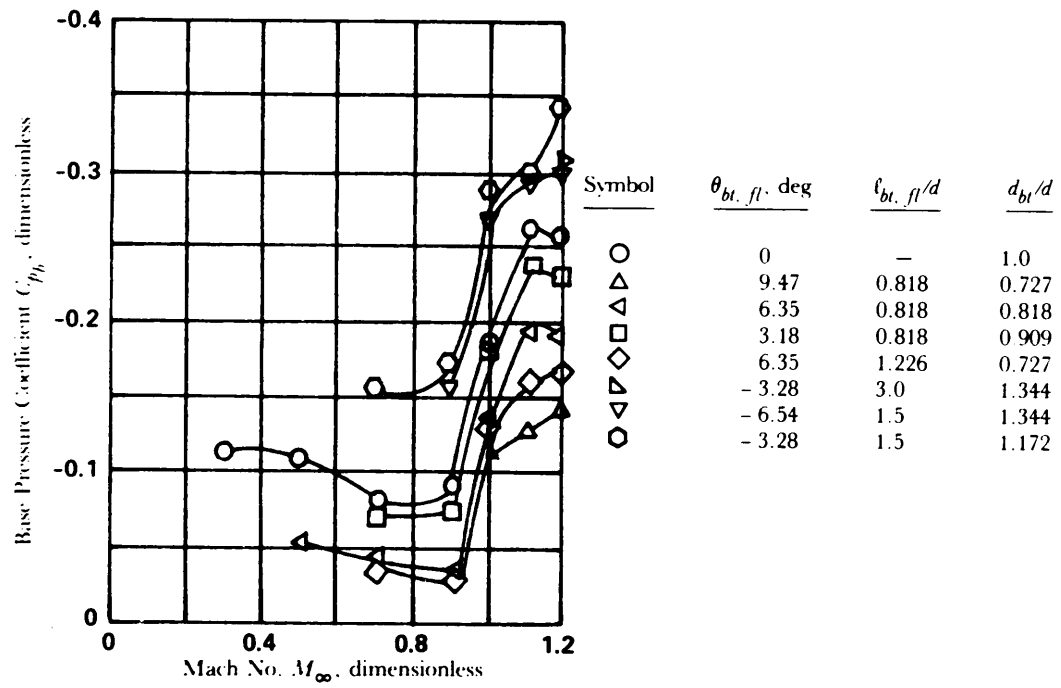
Figure 5-143. Plume-Off Boattail and Flare Base Pressure Coefficients (Ref. 100)

MIL-HDBK-762(MI)
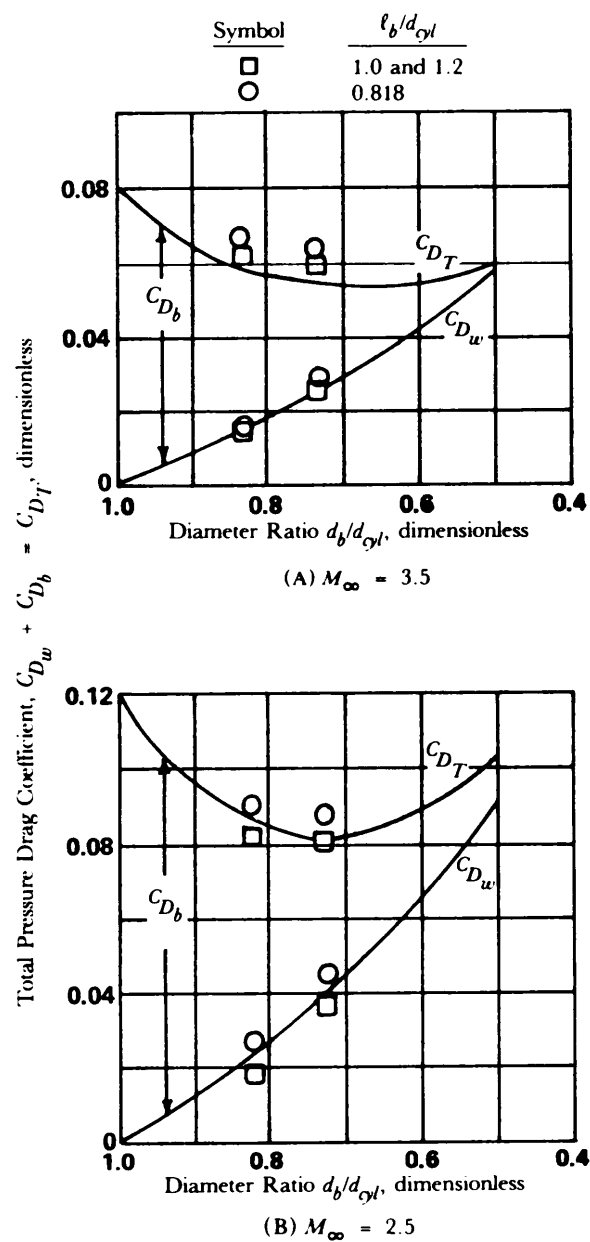
Figure 5-144. Variation of Conical Boattail Wave and Base Drag With Base Diameter to Cylinder Diameter Ratio (Ref. 98)
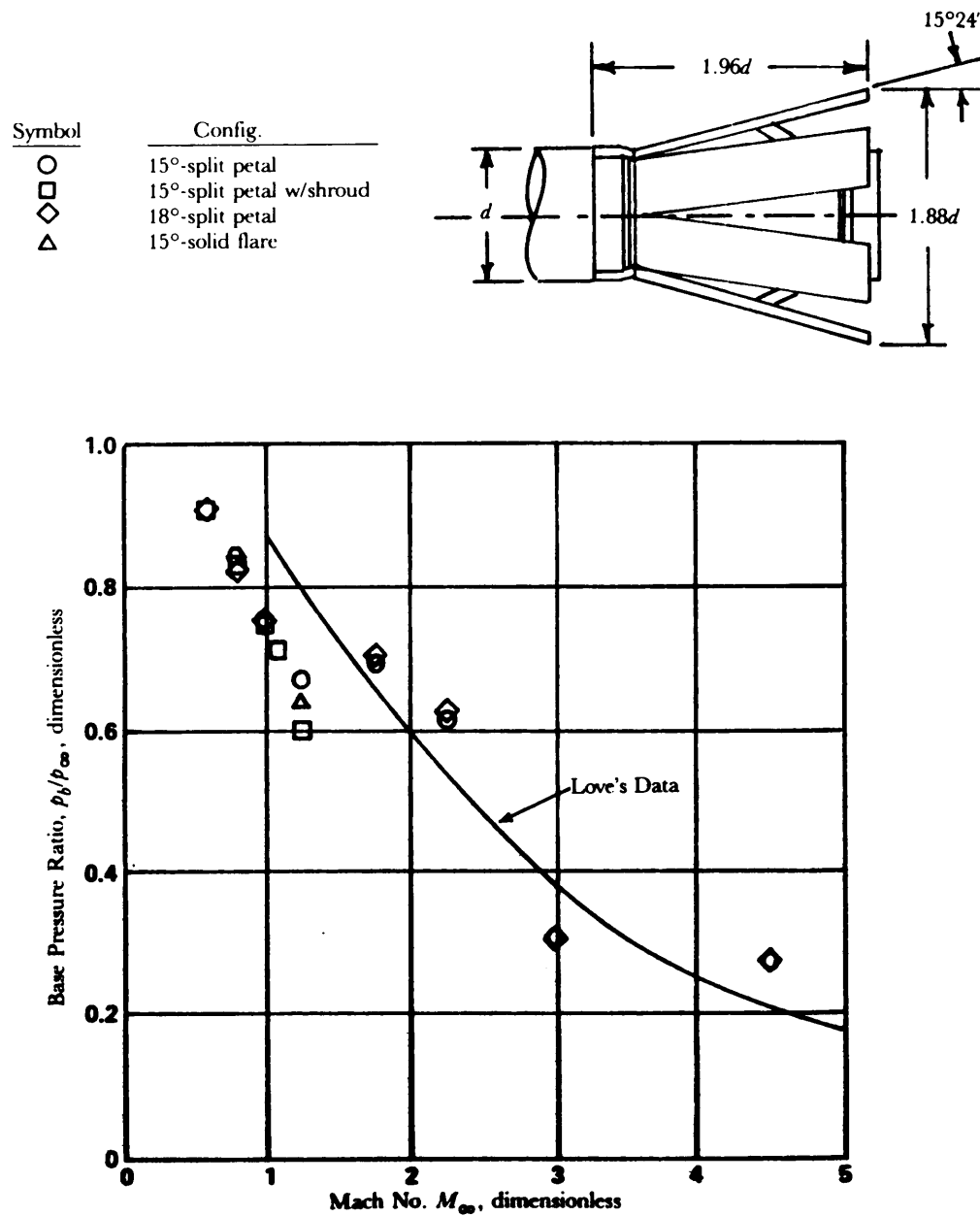
Figure 5-145.   Base Pressure for Various Split Petal Configurations (Jet-Off) (Refs. 15, 85, 89)
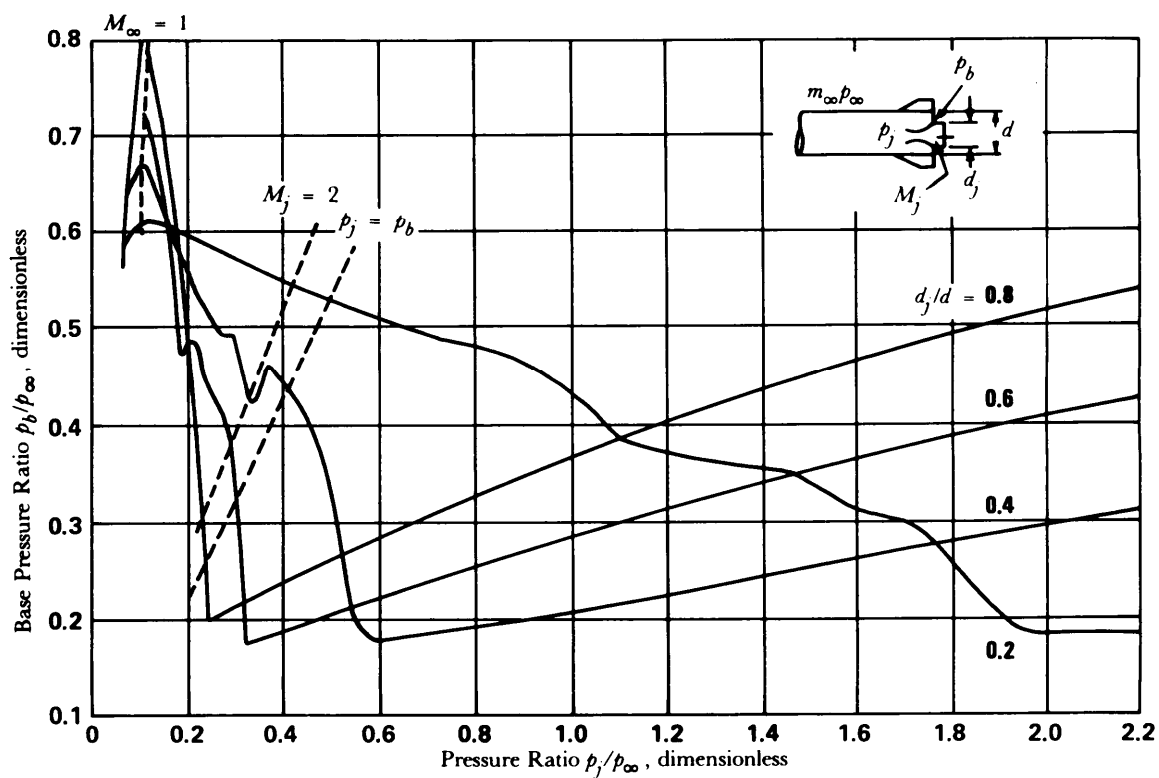
Figure 5-146. Effect of Rocket Jet Plume on Base Pressure at $M_\infty = 2.0$ (Ref. 101)
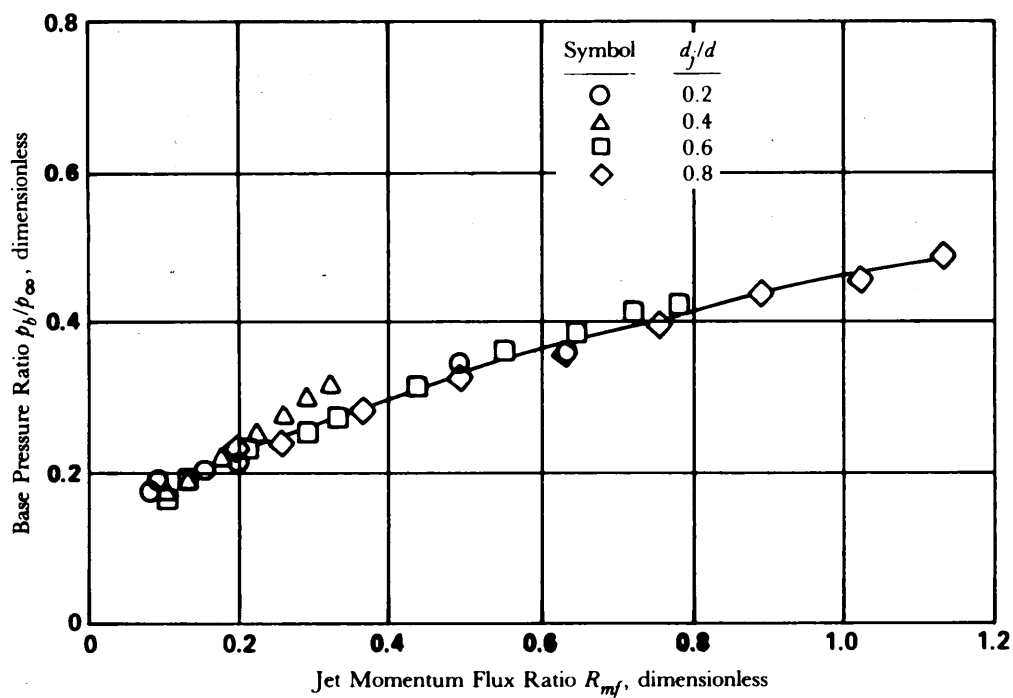
Figure 5-147. Base Pressure Variation With Jet Momentum Flux Ratio (Ref. 93)
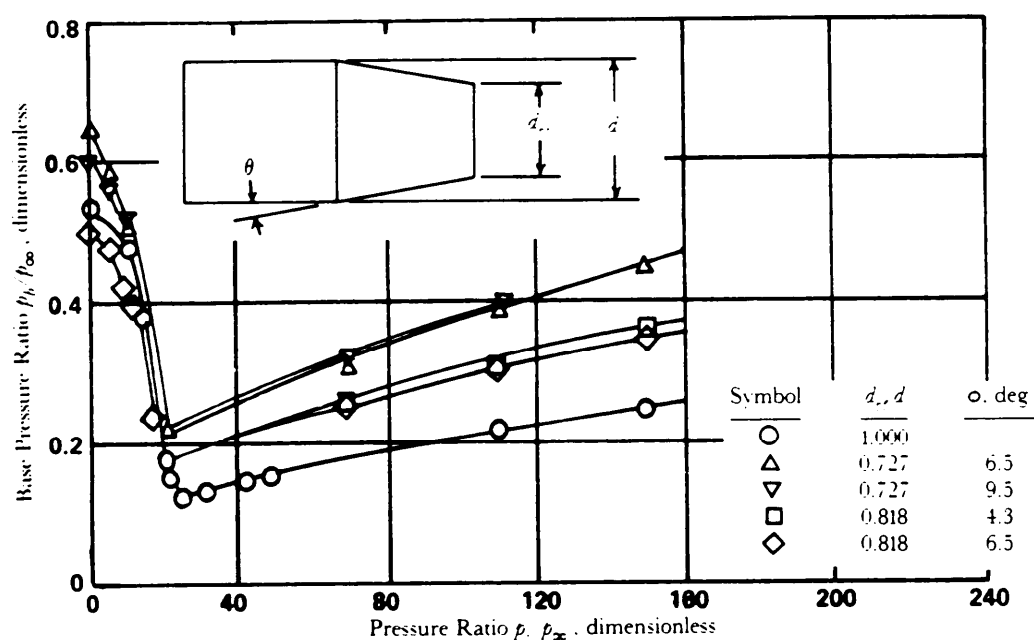
(A) Variation of Base Pressure With Jet Total Pressure Ratio for Various Afterbodies (M_∞ = 2.5)
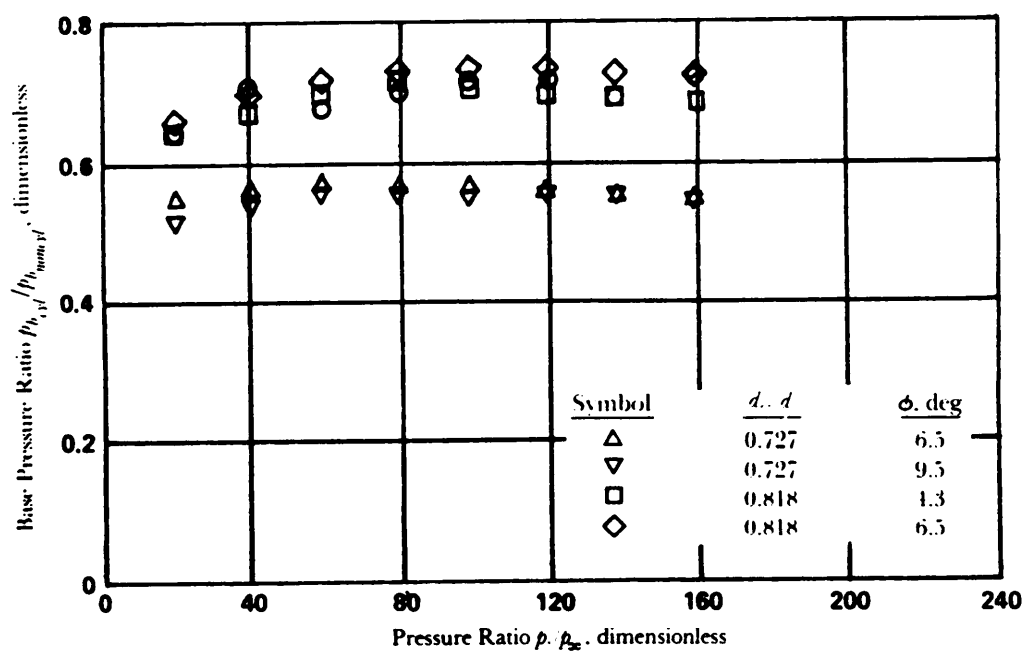
(B) Proportionality Factor as a Function of Jet Total Pressure Ratio (M_∞ = 2.5)

Figure 5-148. **Effect of Conical Afterbody Geometry on Base Pressure Ratio (Ref. 93)**
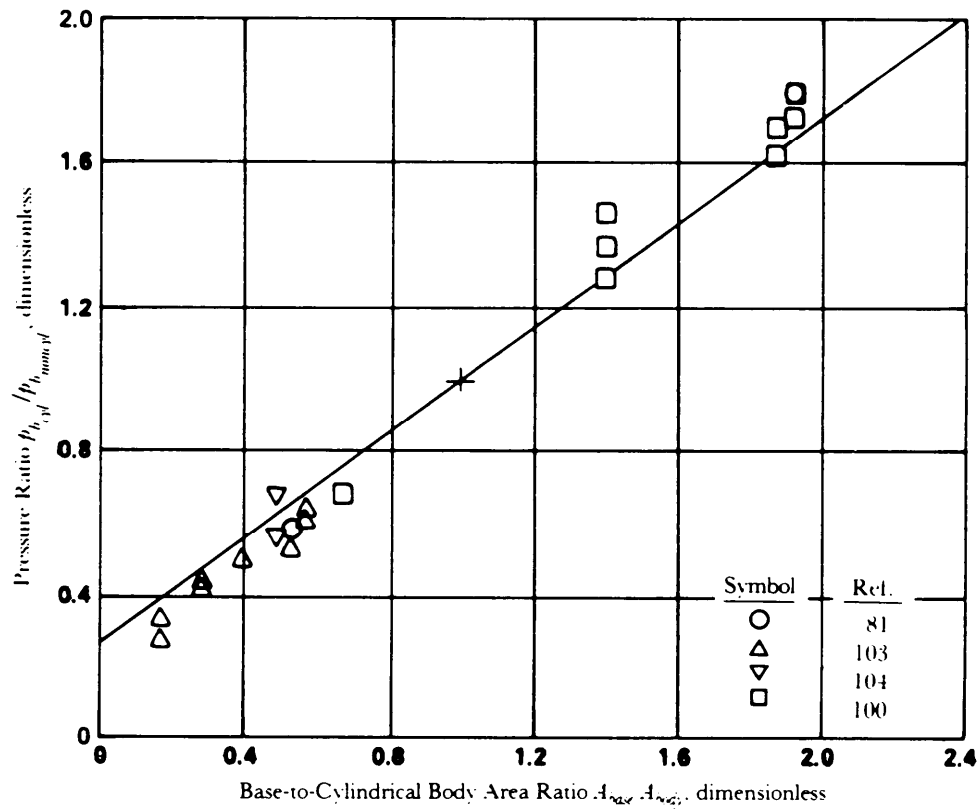
(C) Proportionality Factor as a Function of Base Area Ratio for Flare and Boattailed
Afterbodies

Figure 5-148. (cont'd)
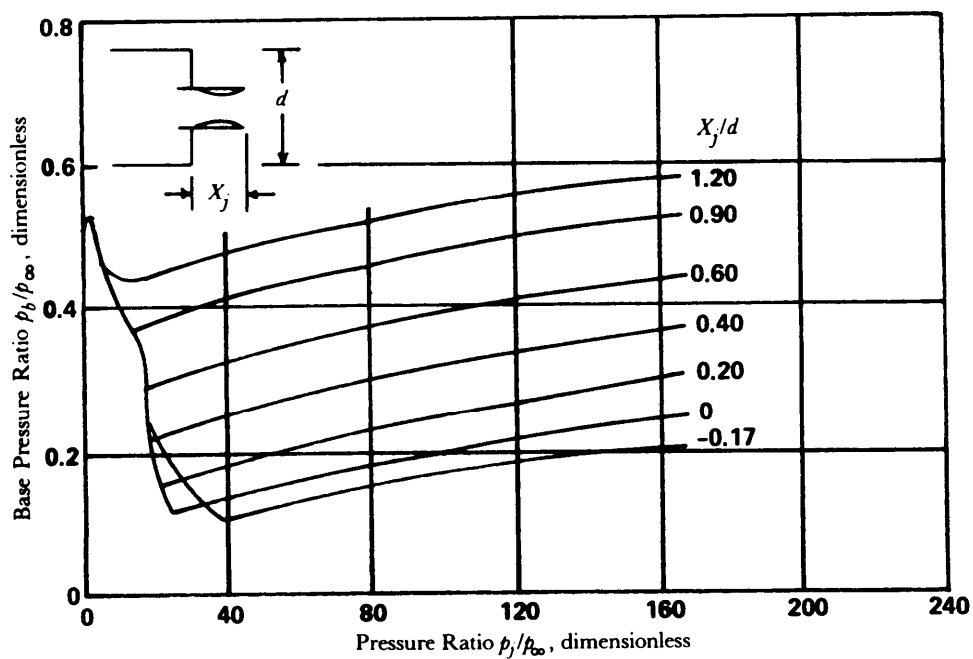
(A) Base Pressure Ratio as a Function of Jet Pressure Ratio $(M_\infty = 2.5)$
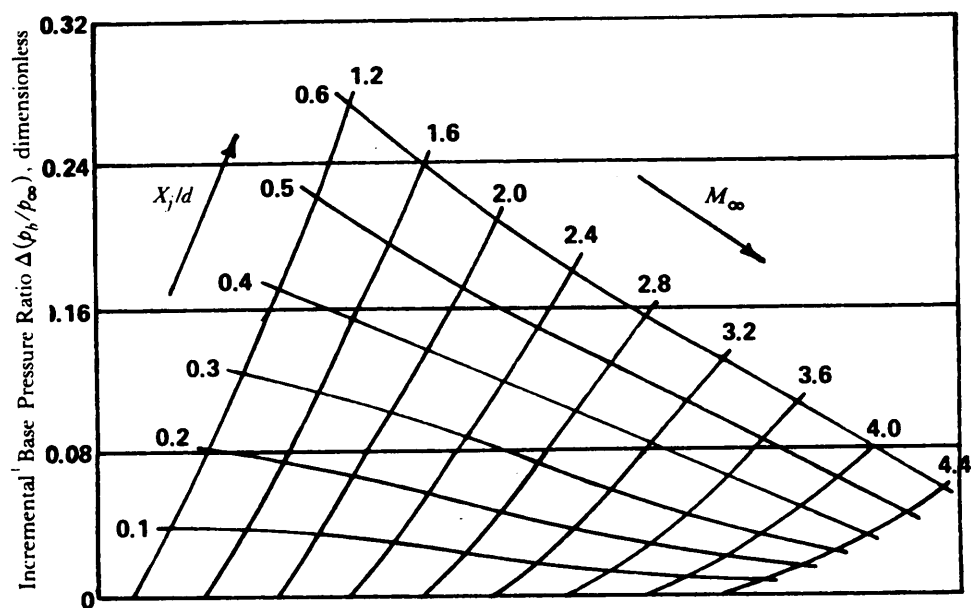
(B) Incremental Effects of Nozzle Position as a Function of Mach Number

Figure 5-149. Effects of Nozzle Position on Base Pressure (Ref. 93)
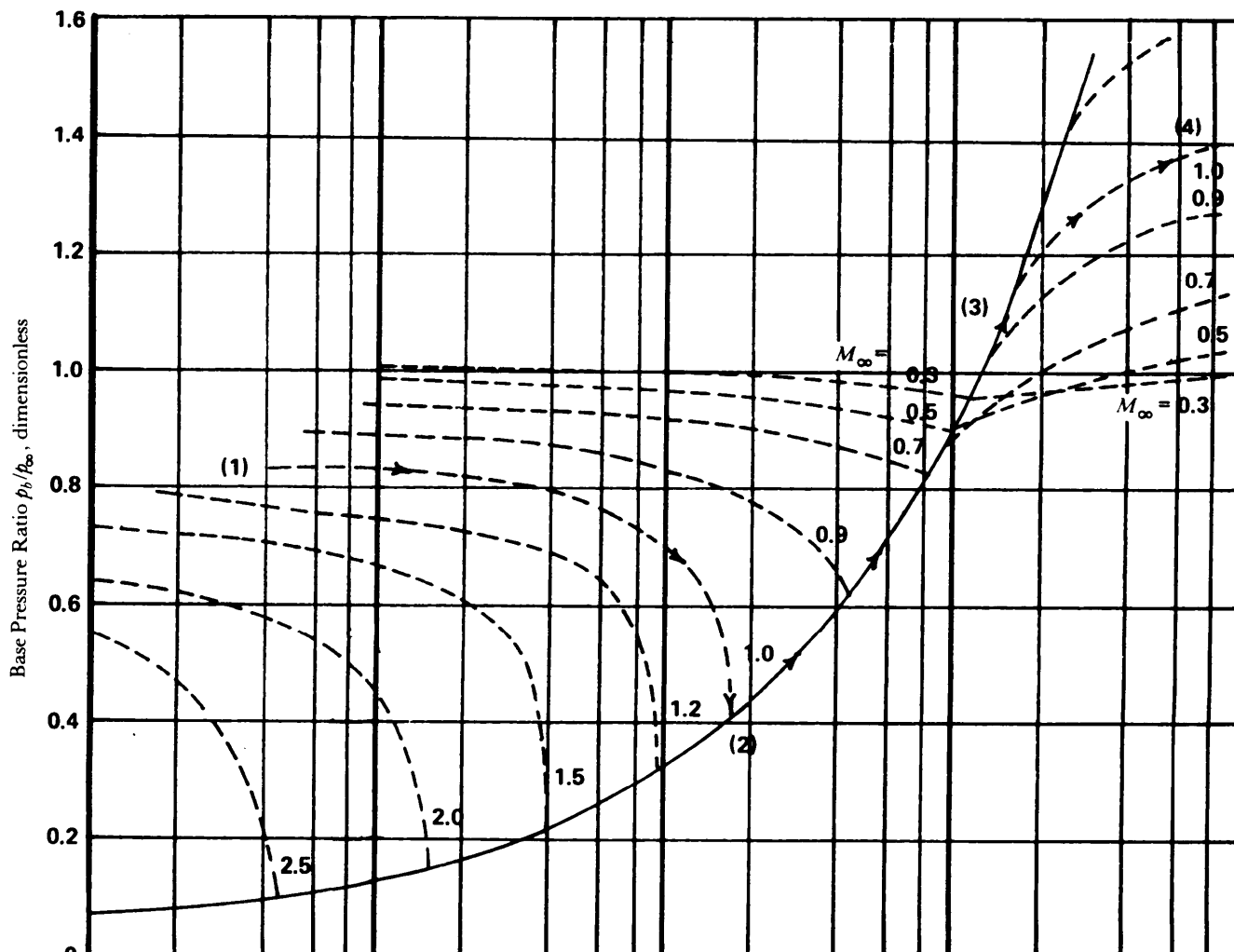
Variation With Thrust for Cylindrical Afterbody With Nozzle Flush With Base ($M_i = 2.7$, $\theta_i = 20$ **deg**) (Ref. 106)
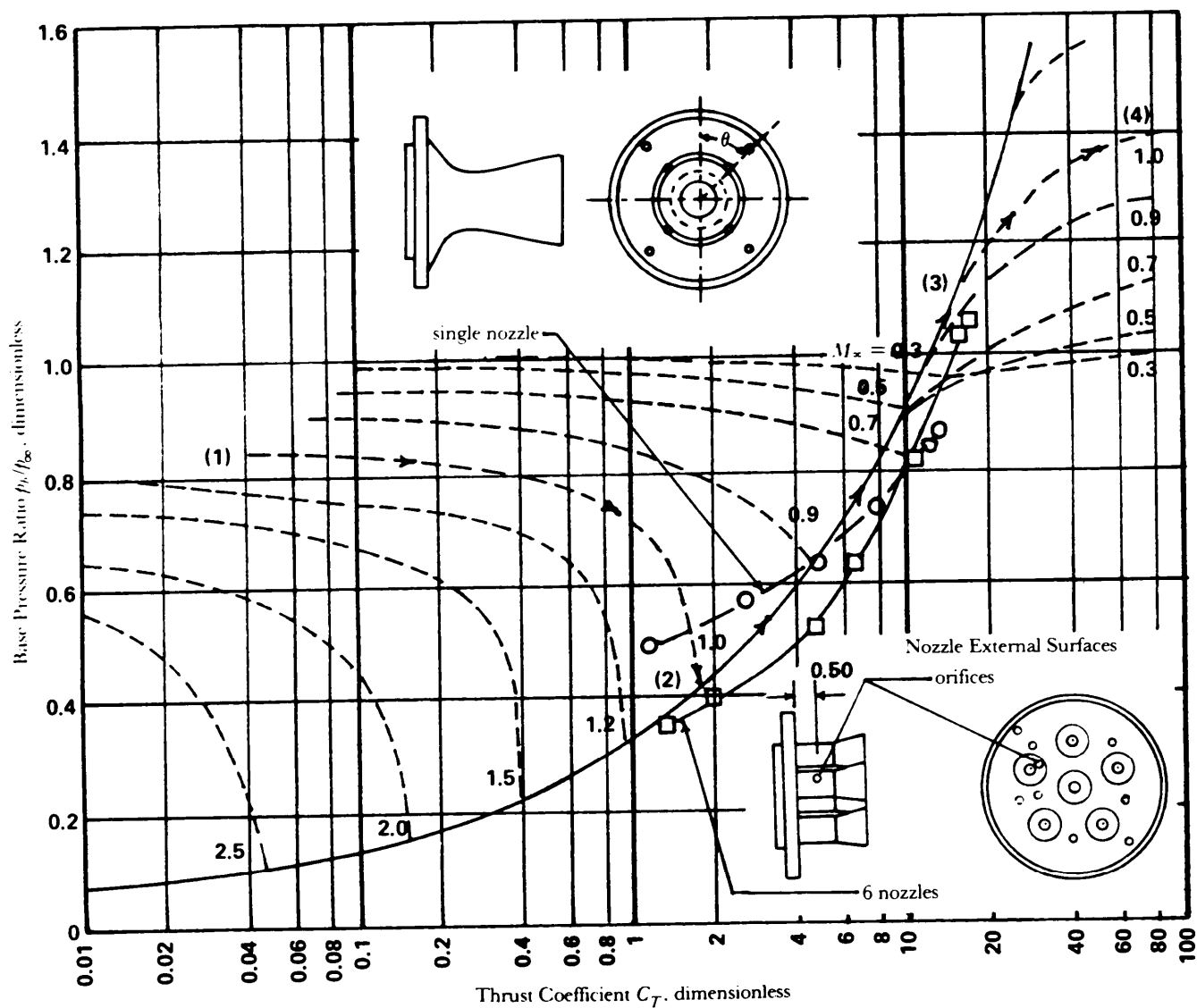
Figure 5-151. Effect of Multiple Nozzles on Base Prewssure (mx = 2.3)(Ref. 108)Text
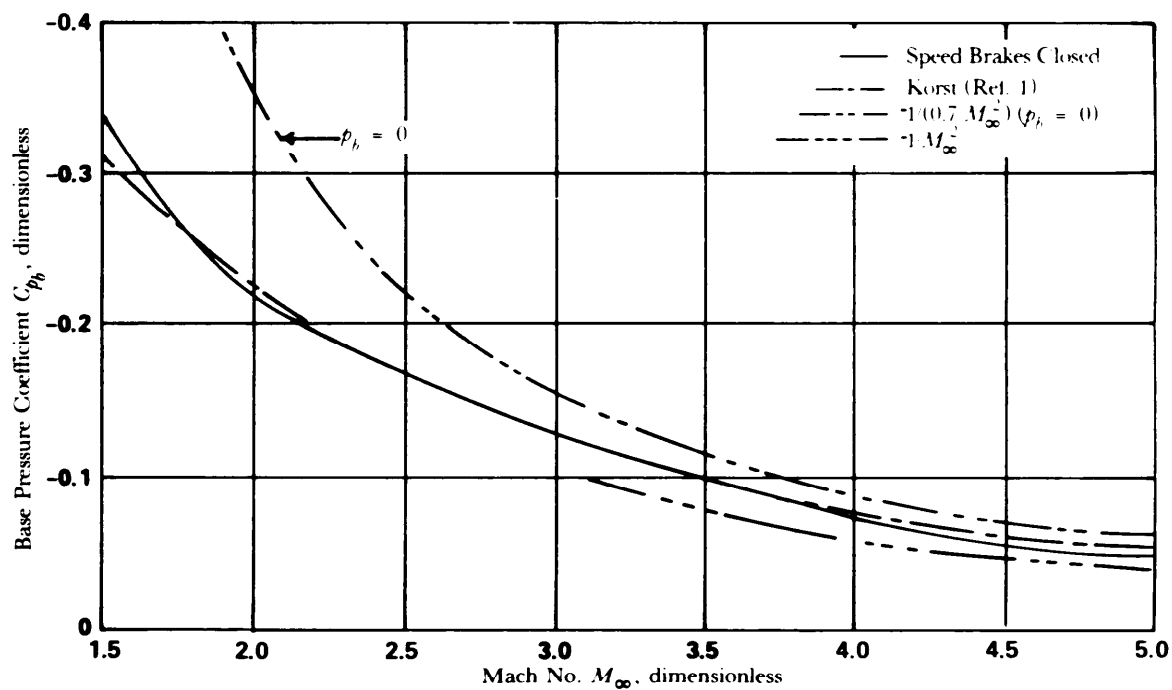
Figure 5-152. Comparison of Two-Dimensional Base Pressures From Upper Vertical Fin of X-15 Airplane With Theory (Ref. 109)
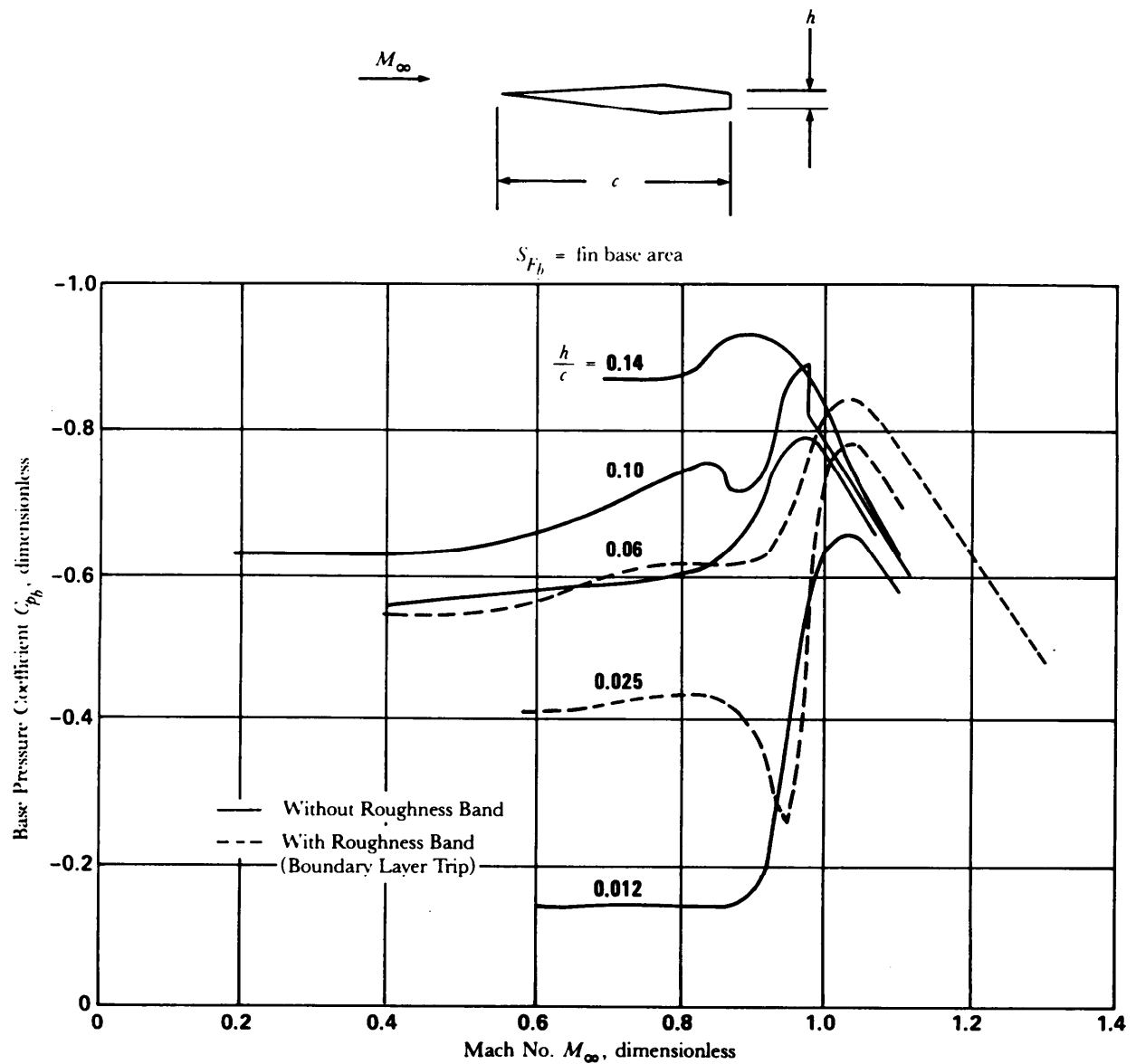
Figure 5-153. Base Pressure Coefficient of Fins at Transonic Speeds
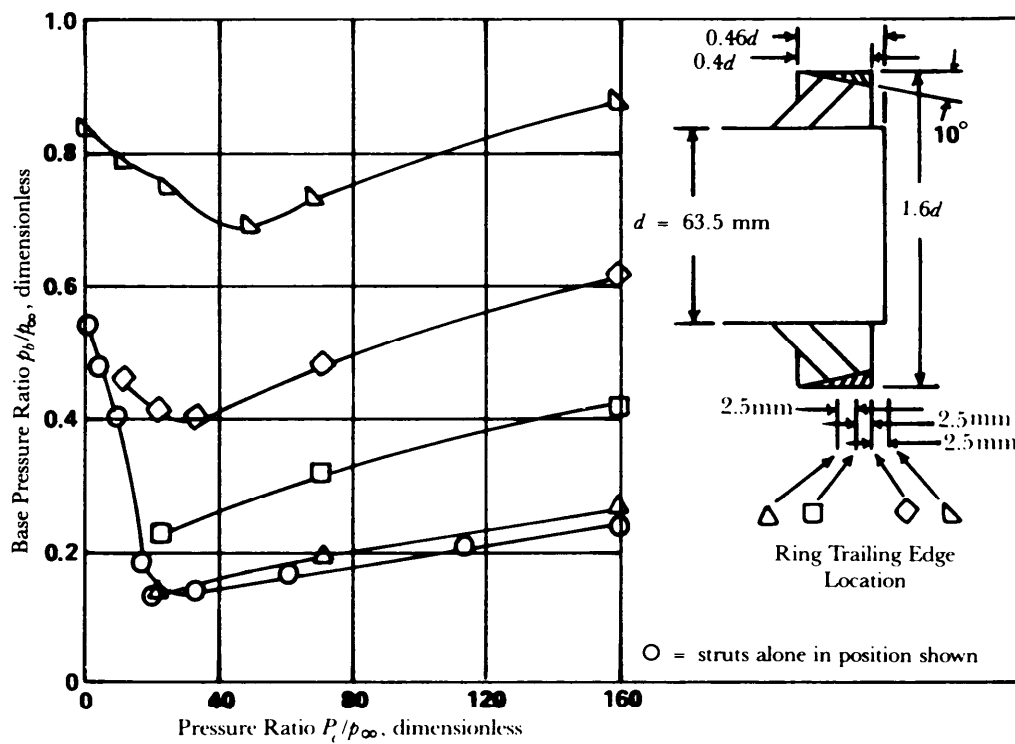
Figure 5-154. Effect of Ringtail Longitudinal Location on Base Pressure Characteristics of Body Revolution Having a d_j/d = 0.2 Jet Ratio (M_∞ = 2.5) (Adapted from Ref. 113)
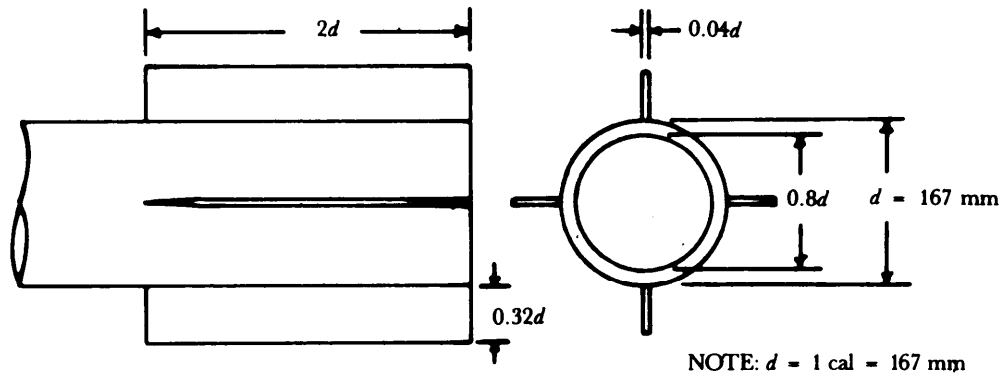
FIN GEOMETRY AND FIN DRAG PARAMETERS

fin exposed semispan $b_e/2 = 0.32d$

fin chord length $c = 2d = 0.32$ m

fin thickness $t = 0.04d$

$\gamma = 1.4$

fin $t/c = \dfrac{0.04d}{2d} = 0.02$

$\dfrac{\text{fin base area}}{A_{ref}} = \dfrac{(4)(0.04d)(0.32d)}{\pi d^2/4} = 0.0652$

exposed aspect ratio $(AR)_e = \dfrac{b_e^2}{S_{F_e}} = \dfrac{(2b_e/2)^2}{(2d)(2)(0.32d)} = \dfrac{[(2)(0.32d)]^2}{(4d)(0.32d)} = 0.32$

$\dfrac{\text{exposed fin planform area } S_{F_e}}{A_{ref}} = \dfrac{\text{area of 2 joined fin exposed panels}}{\text{reference area}} = \dfrac{(2)(0.32d)(2d)}{\pi d^2/4} = 1.63$

$\dfrac{\text{fin wetted area}}{A_{ref}} = \dfrac{(8)(2d)(0.32d)}{\pi d^2/4} = 6.52$ (The factor 8 represents both sides of four fins.)

$(AR)_e(t/c)^2 = (0.32)(0.02)^2 = 0.000128$

$(t/c)^{2/3} = (0.02)^{2/3} = 0.0737$

$(t/c)^{5/3} = (0.02)^{5/3} = 0.00147$

$(t/c)^{1/3} = (0.02)^{1/3} = 0.271$

$(AR)_e(t/c)^{1/3} = (0.32)(0.271) = 0.0867$

BODY GEOMETRY AND BODY DRAG PARAMETERS

$\ell_n = \dfrac{\ell_n}{d} = 3.0$ cal

$\ell_{cyl} = \dfrac{\ell_{cyl}}{d} = 21.0$ cal

Figure 5-155. Configuration and Design Parameters for Sample Drag Calculation

$$\ell_T = \ell_n + \ell_{cyl} = 3.0 + 21.0 = 24.0 \text{ cal}$$

$$\left(\frac{A_{wet}}{A_{ref}}\right)_b = \left(\frac{A_{wet}}{A_{ref}}\right)_n + \left(\frac{A_{wet}}{A_{ref}}\right)_{cyl}$$

$$\left(\frac{A_{wet}}{A_{ref}}\right)_{cyl} = \frac{\pi d \ell_{cyl}}{\pi d^2/4} = \frac{\pi d(21d)}{\pi d^2/4} = 84.0$$

$(A_{wet})_n$, for a 3-cal tangent ogive

$$(A_{wet})_n = 2\pi \left\{ \frac{\ell}{2} \left[\sqrt{R^2 - \ell^2} + \frac{R^2}{2} \operatorname{Sin}^{-1}\left(\frac{\ell}{R}\right) - \ell\left(R - \frac{d}{2}\right) \right] \right\}$$

where

$$R = \frac{d}{4} + \frac{\ell^2}{d^2} \quad \text{(ogive radius)}$$

and for $\ell/d = 3$, $R = 9.25$

$$A_{wet} = 2.011\pi d^2$$

$$\left(\frac{A_{wet}}{A_{ref}}\right)_n = \frac{2.011\pi d^2}{\pi d^2/4} = 8.04$$

$$\left(\frac{A_{wet}}{A_{ref}}\right)_b = 84.0 + 8.04 = 92.04$$

$d_j/d_b = 0.8$, $d_b = d$

$$\frac{\text{annular area}}{A_{ref}} = \frac{\pi/4\,[d^2 - (d_j/d)^2]}{\pi d^2/4} = \frac{d^2 - (0.8d)^2}{d^2} = 0.36$$

body length $\ell_b = 24\,(0.16 \text{ m}) = 3.84 \text{ m}$

$$A_{ref} = \frac{\pi(0.16)^2}{4} = 0.020 \text{ m}^2$$

Figure 5-155. (cont'd)
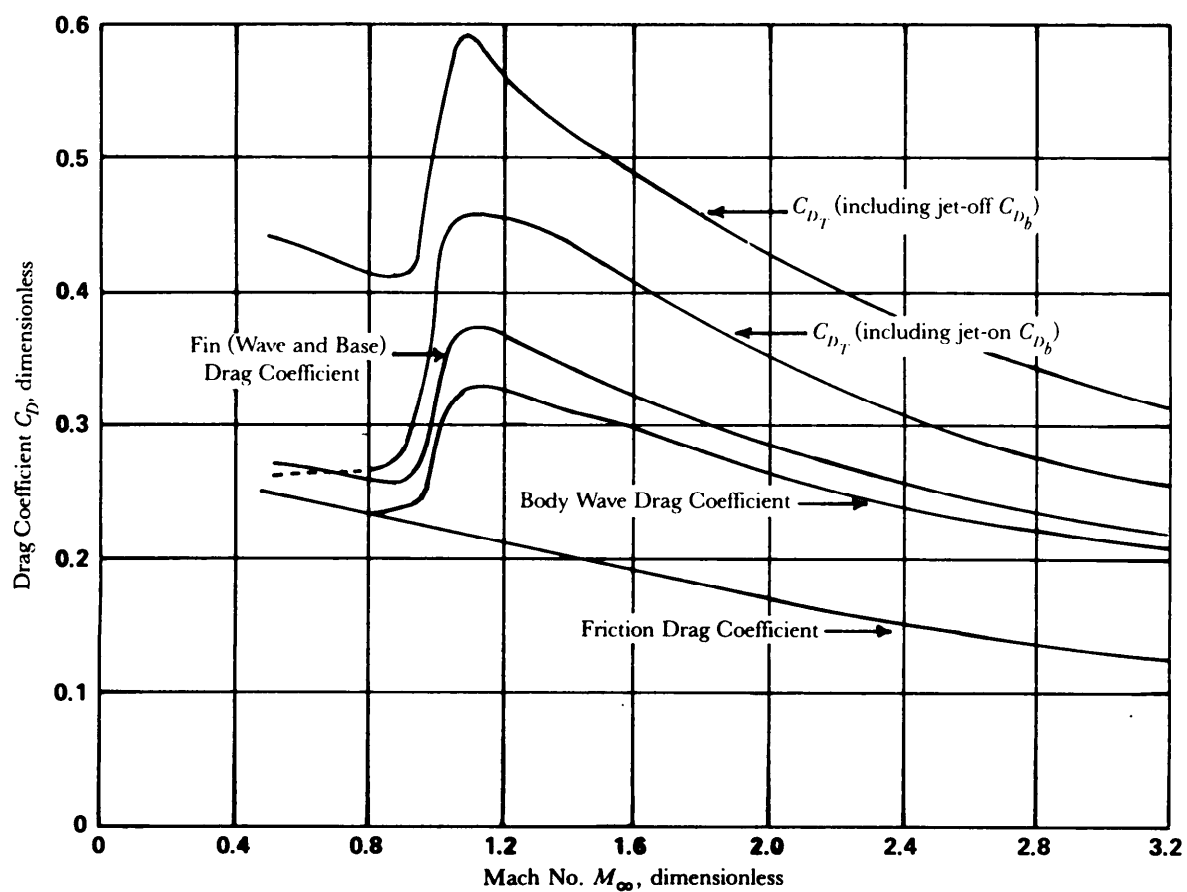
Figure 5-156. Sample Total and Component Drag Coefficients vs Mach Number
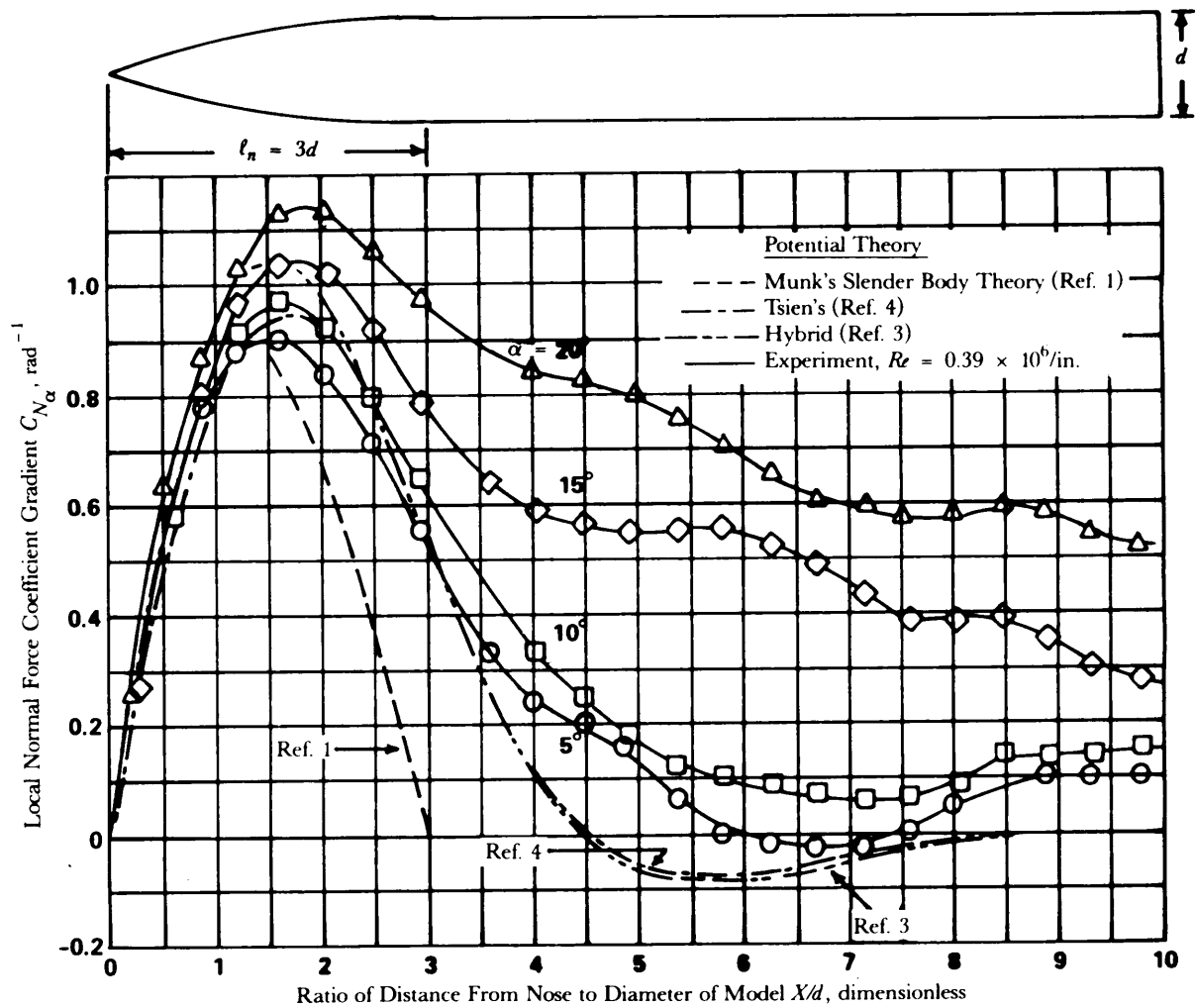
Figure 5-157. Local Normal Force Coefficient Gradient Ratio Distribution for Tangent Ogive With Cylindrical Afterbody at M_∞ = 2.0 (Ref. 115)
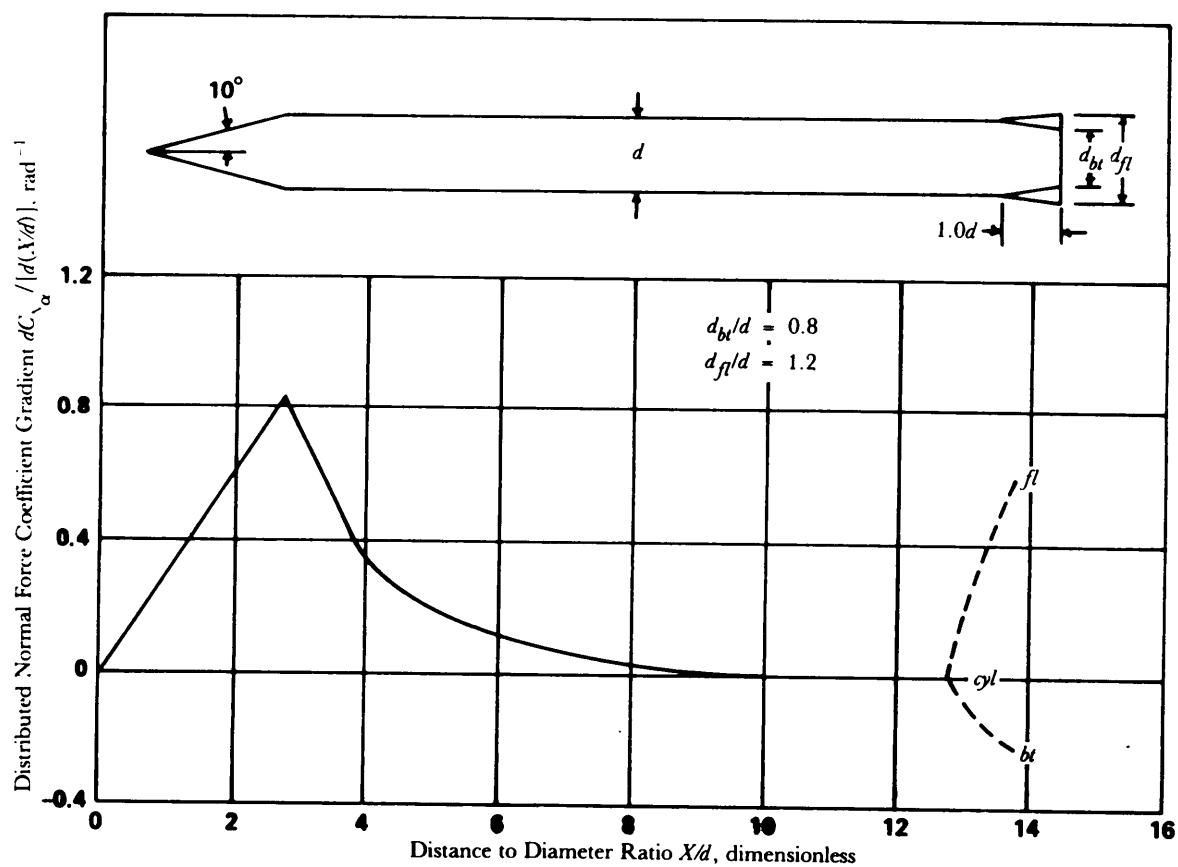
Figure 5-158. Distributed Normal Force Coefficient Gradient on Cone-Cylinder, Cone-Cylinder-Boattail, and Cone-Cylinder-Flare Configurations at $M_\infty = 2.0$
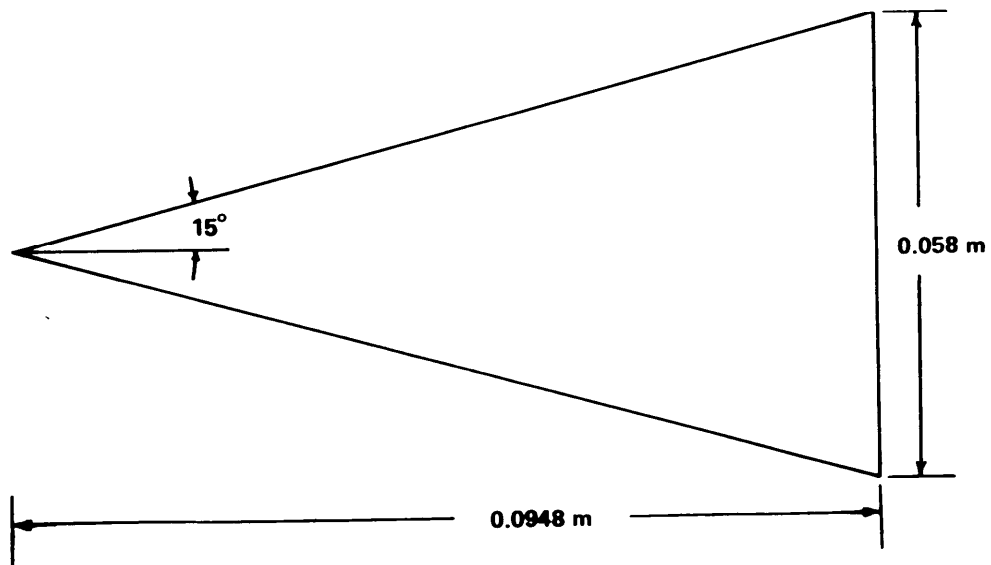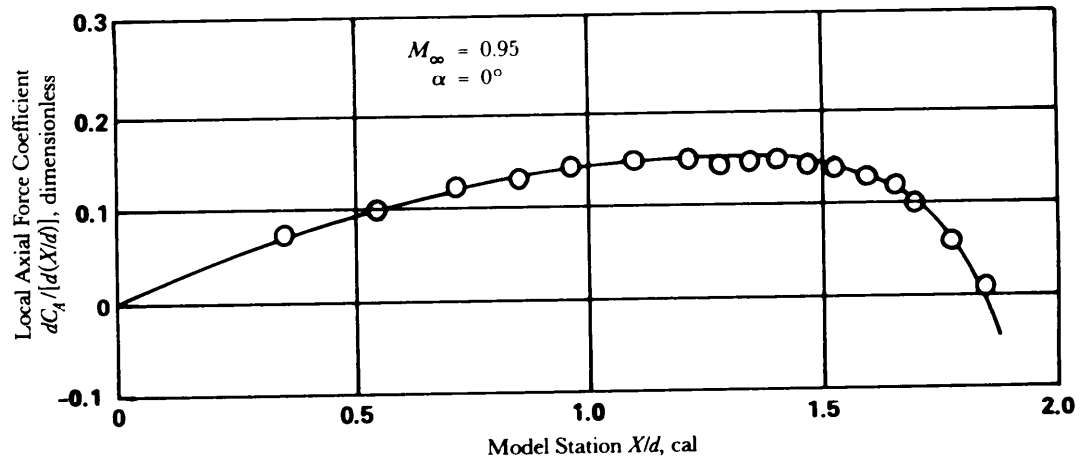
Figure 5-159. Distribution of Local Axial Force Coefficients (Ref. 116)
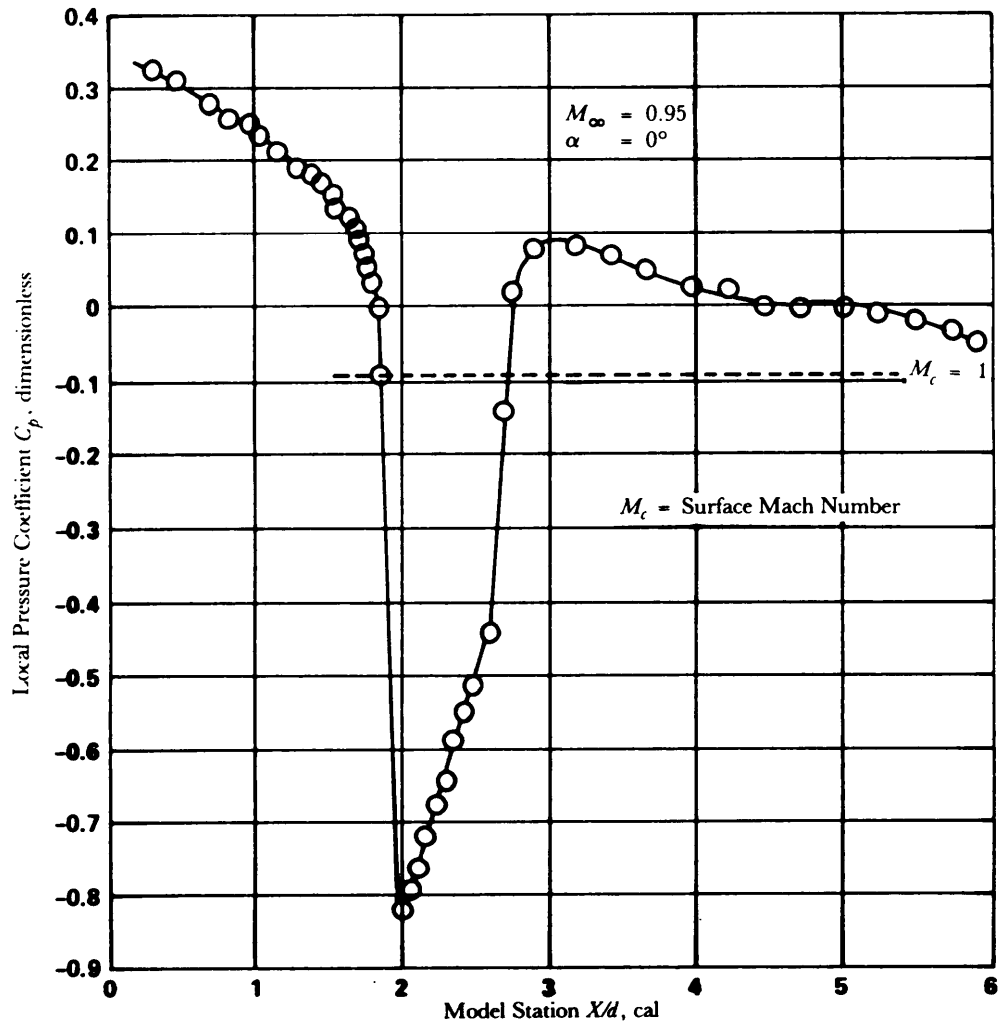
Figure 5-160.   Distribution of Local Pressure Coefficients (Ref. 116)
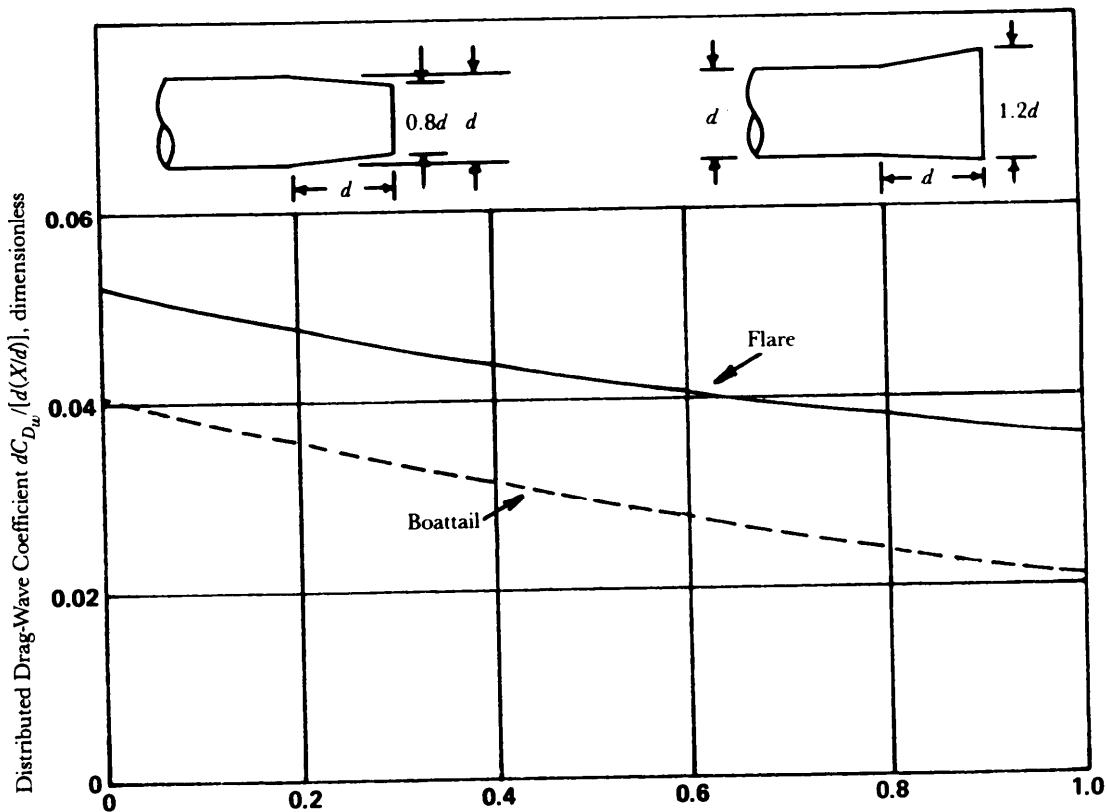
Figure 5-161. **Axial Force Distributions on Conical Flare and Boattail Following a Cylinder** $M_\infty = 2.0$
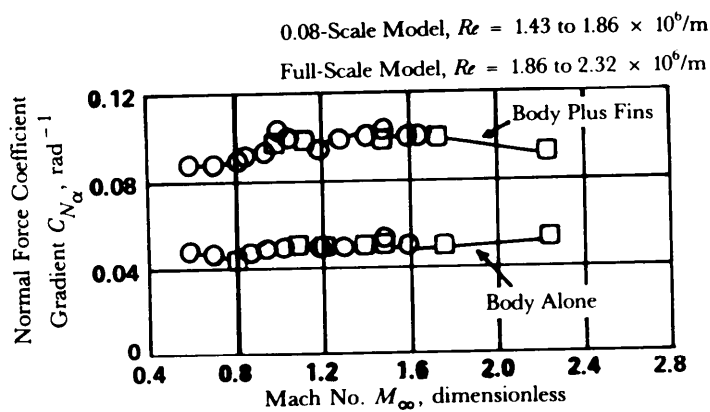
Figure 5-162. **Comparison of Test Results on Full-Size and Scale Model Artillery Rocket**

(A) Shock Wave Coordinates

θ_i, deg	t/d	Mach Number						
		1.5	2.0	2.5	3.0	4.0	5.0	6.0
10	2	y_r/d = 1.90	1.20	0.95	0.80	0.65	0.60	0.55
	4	3.80	2.40	1.90	1.30	1.15	1.00	
	6	5.60	3.65	2.80	2.50	2.00	1.70	1.50
	8	7.50	4.90	3.80	3.30	2.60	2.30	2.13
	10	9.40	6.10	4.70	4.15	3.30	2.90	2.63
20	2	2.30	1.60	1.35	1.20	1.00	1.00	0.95
	4	4.45	3.20	2.60	2.30	1.90	1.70	1.55
	6	6.50	4.65	3.65	3.10	2.55	2.30	2.15
	8	8.60	5.95	4.65	4.00	3.25	2.85	2.65
	10	10.70	7.20	5.60	4.90	3.95	3.40	3.10
Hemi	2	3.75	2.65	2.20	2.00	1.70	1.65	1.60
	4	5.95	4.10	3.35	3.00	2.75	2.30	2.20
	6	8.00	5.37	4.45	3.90	3.20	2.95	2.80
	8	10.05	6.70	5.40	4.70	3.90	3.60	3.10
	10		7.95	6.35	5.60	4.65	4.20	3.90
θ_r, deg		18	32.5	25.5	21.5	16	13	11
Tunnel								
(A) 40×40	y, in.	19.35	19.35	19.30	19.20	18.80	18.20	17.10
(B) 12×12	y, in.	5.87	5.87	5.86	5.81	5.79	5.71	

Diagram (A): Reflection Boundary, (y_r/d), θ_r, y/d, dimensionless, $d/2$, θ_i, X/d, dimensionless.

(A) Shock Wave Coordinates

Figure (B) labels: A_M = Model Frontal Area; A_T = Aerodynamic Test Section Area; M_∞ = 6.0, 5.0, 4.5, 4.0, 3.5, 3.0, 2.5, 2.0, 1.5. Axes: A_M/A_T, dimensionless (0 to 0.5); Model Nose Half Angle θ_i, deg (90-45, 40, 35, 30, 25, 20, 15).

(B) Model Blockage Data

Figure (C) labels: A = Approximate Test Section Area = 1600 in.^{2}; A_T = Aerodynamic Test Section Area. Axis A/A_T, dimensionless (1.00 to 1.48); Mach No. M_∞, dimensionless (1 to 6). Tunnel Section (-30); Tunnel Station (0).

(C) Effective Cross-Sectional Area of Test Section for Wind Tunnel A, AEDC

Figure 5-163.   Relationship Between Maximum Allowable Model Dimensions and Test Section Dimension in Tunnel A and 12X12-in. Tunnel at Von Karman Gas Dynamics Facility at Arnold Engineering Center (Ref. 119)
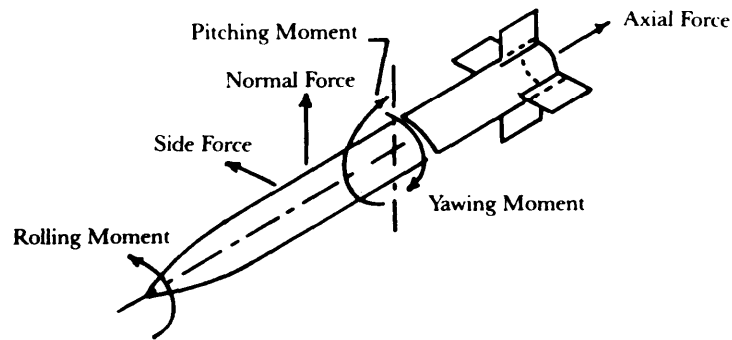
Figure 5-164. Aerodynamic Force Components

NOTE: A_j = 24 × 0.000008205 = 0.000197 m²

A_j/A_b = 0.060

All dimensions in meters

Two rows of 12 equally spaced (30 deg) 0.00318 dia orifices. Rows are staggered 15 deg.
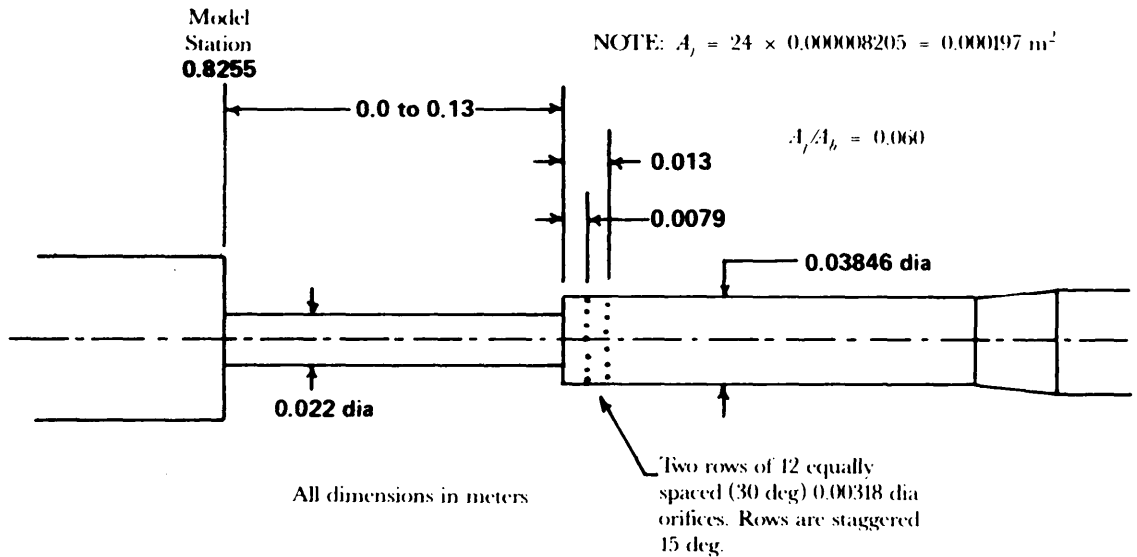
Figure 5-165. Typical Normal Jet Plume Simulator (Ref. 56)

MIL-HDBK-762(MI)

C H A P T E R   6
P R O P U L S I O N

This chapter provides the reader with a general understanding of rocket propulsion principles and applications for aerodynamically stabilized free rockets. The main emphasis is on solid propellant motors with some discussion of liquid Propellant systems. The types of propellant, motor case and nozzle designs, and methods of calculating Performance are discussed. Information is included on the trade-off studies that must be Performed during Preliminary design of a rocket motor application to a missile system. Satisfactory Performance of a given propulsion system is determined by the laws of mechanics and thermodynamics plus the proper application and behavior of propellant combinations and structural materials. Tests that are conducted to establish propellant and structural integrity, ballistic Performance, and quality assurance are discussed.

6-0 LIST OF SYMBOLS

A = area, m^2

A_b = burning surface area, m^2

$\quad$ = asymmetric grain base area, m^2

A_c = chamber cross-sectional area, m^2

A_e = nozzle exit area, m^2

A_p = port area, m^2

A_r = regression coefficient, m^3/J

A_t = nozzle throat area, m^2

A_x = cross-sectional area at point x, m^2

A_ϵ = eroded throat area, m^2

A^* = area at unity Mach number, m^2

a = empirical constant in burning rate equations

b = empirical constant in burning rate equations

C_F = thrust coefficient, dimensionless

$\overline{C}_F$ = average thrust coefficient, dimensionless

c = effective exhaust velocity, m/s

c_p = specific heat at constant pressure, J/ kg·K

$\overline{c}_p$ = average specific heat at constant pressure, J/ kg·K

c_v = specific heat at constant volume, J/ kg·K

c^* = characteristic exhaust velocity, m/s

$\overline{c}^*$ = average characteristic exhaust velocity, m/s

D = aerodynamic drag, N

d = diameter, m

F = thrust, N

F_i = ideal thrust, N

F_r = reference thrust value, N

6-1

f = scale factor, dimensionless

g = acceleration due to gravity, m/s^2

g_0 = 9.80665 m/s^2, reference acceleration due to gravity

$\overline{H}$ = average port-to-throat ratio, dimensionless

h = static specific enthalpy, J/kg

h_c = stagnation specific enthalpy in combustion chamber, J/kg

h_e = specific enthalpy at nozzle exit, J/kg

I = impulse, N·s

I_s = specific impulse based on mass units, N·s/kg

I'_s = specific impulse parameter, dimensionless

$\overline{I}_s$ = average specific impulse, N·s/kg

I_{sp} = specific impulse based on weight units, s

j = running index with k, dimensionless

K = ratio of burning surface area to nozzle throat area based on port average pressure, dimensionless

k = number of species or constituents, dimensionless

   = propellant erosion constant, dimensionless

ℓ = truncated nozzle length, m

ℓ_c = combustion chamber length, m

ℓ_n = nozzle cone length, m

M = u/u^* = Mach number, dimensionless

M_e = nozzle exit Mach number, dimensionless

M_p = Mach number at port, dimensionless

M_x = Mach number at point x, dimensionless

M' = molecular weight, kg/mole

M'_j = molecular weight of constituent j, kg/mole

$\overline{M'}$ = average molecular weight, kg/mole

m = mass of rocket, kg

m_i = initial mass of rocket, kg

m_m = motor mass, kg

m_p = propellant mass consumed, kg

$\dot{m}$ = propellant mass-flow rate, kg/s

$\dot{m}_g$ = mass-flow rate of gas, kg/s

$\dot{m}_p$ = mass-flow rate of propellant consumed, kg/s

$\dot{m}^*$ = mass-flow rate that produces a Mach number of unity in the constant cross-sectional area channel, kg/s

MR = $m_i/(m_i - \dot{m}t_b)$ = rocket mass ratio, dimensionless

n = burning rate equation pressure exponent, dimensionless

   = number of moles

n_j = number of moles of constituent j

---

[1]All pressures in this chapter are absolute, i.e., gage plus local (ambient) atmospheric pressures, unless otherwise indicated.

n_m = number of moles in mixture

p = static pressure [1], Pa

p_a = ambient pressure, Pa

p_c = combustion chamber pressure, Pa

p_e = nozzle-exit pressure, Pa

p_r = reference pressure, Pa

p_t = nozzle throat pressure, Pa

p_x = static pressure at point x, Pa

p^* = static pressure at unity Mach number, Pa

$q = \rho u^2/2$ = dynamic pressure, Pa

q_e = dynamic pressure of nozzle exhaust gas, Pa

$\overline{q}_B$ = average Bartz heat flux, J/s·m^2

$R = 8.31434 \times 10^3$, J/kmole·K, universal gas constant

r = radius corresponding to regression point, m

r_p = port radius, m

r_t = nozzle throat radius, m

r' = effective bend radius of curvature, m

r^* = radius at unity Mach number, m

$\dot{r}$ = burning rate or regression rate of propellant, m/s, cm/s, or mm/s

$\dot{r}_r$ = reference burning rate, m/s

$\dot{r}_0$ = propellant burning rate without erosive gas flow, m/s

$\overline{\dot{r}}$ = average insulation regression rate, m/s

T = absolute temperature, K

T_c = combustion chamber temperature, K

T_e = temperature of exhaust gas, K

T_t = nozzle throat temperature, K

T^* = critical temperature (at unity Mach number), K

t = time variable, s

t_b = propellant burning time, s

u = local isentropic velocity, m/s

u_c = local port velocity, m/s

u_e = nozzle-exit gas velocity, m/s

u_{ex} = axial component of gas exit velocity, m/s

u_i = ideal velocity, m/s

u_{max} = maximum velocity, m/s

u_t = nozzle throat velocity, m/s

u^* = critical velocity (velocity of sound), m/s

$\ddot{u}$ = rocket acceleration, m/s^2

V = volume, m^3

V_c = combustion chamber volume, m^3

v = specific volume, m^3/kg

Z = expansion factor, dimensionless

α = nozzle cone divergence half angle, deg

β = cant angle, rad

$\gamma = c_p/c_v$ = ratio of specific heats, dimensionless

ϵ = erosive-rate ratio, dimensionless

ζ = propellant mass fraction, dimensionless

Θ = flight path angle with horizontal plane, deg

θ = wall angle, deg

λ = nozzle angle correction factor, dimensionless

Π_F = temperature sensitivity coefficient of reference thrust F_r, K^{-1}

Π_p = temperature sensitivity coefficient of reference pressure p_r, K^{-1}

$\Pi_{\dot{r}}$ = temperature sensitivity coefficient of reference burning rate $\dot{r}_r$, K^{-1}

ρ = density, kg/m^3

ρ_c = density of chamber gases, kg/m^3

ρ_e = density of nozzle exhaust gas, kg/m^3

ρ_P = density of propellant, kg/m^3

τ = propellant web thickness, m

v = specific internal energy, J/kg

Φ = average entrance angle, deg

ϕ = nozzle velocity coefficient, dimensionless

Ψ = combustion chamber-pressure parameter, Pa

ω = propellant volume correction factor, dimensionless

6-1 INTRODUCTION

The rocket propulsion system is defined to include all classes of propulsive devices that carry within themselves the total reactive mass to be expelled. The rocket motor, or engine, is a form of jet propulsion and is a means of locomotion derived by the reaction to momentum of the ejected matter-. The duct, or air-breathing propulsion system, differs from the rocket in that it carries only the fuel on board; the oxidizer is obtained from the surrounding atmosphere.

Rocket propulsion systems are generally grouped into two major classes: liquid propellant engines and solid propellant motors. The liquid system, as the name implies, uses a liquid propellant that may involve separate tanks for the fuel and the oxidizing agent or a monopropellant flowing through a catalyst bed for decomposition. The liquids are pressurized and injected into the rocket combustion chamber where combustion takes place. In the solid system the propellant is a solid mixture of the oxidizing agent and the fuel formed directly in or inserted into the combustion chamber. There is also a hybrid class of rocket in which various combinations of liquids and solids are used.

There are advantages and disadvantages of each of the major classes of rockets. The solid rocket motor is relatively simple, easily handled, easily stored, and highly reliable. It is capable of a high propulsive thrust and has a rapid initial thrust buildup. The liquid system involves complicated plumbing and pressurization systems and may require handling and loading hazardous liquids at the launch site. However, the liquid system has greater flexibility in the control of the thrust-time relationship. Higher-energy propellants such as liquid oxygen and liquid hydrogen are available in their liquid state.

The selection of either the solid or the liquid system will be based on the mission to be accomplished. Due to the normal advantages of solid propulsion in aerodynamically stabilized free flight rockets, this handbook discusses only the solid propellant motor and its principles of operation and applications. The intent of this chapter is to provide the reader with an understanding of rocket propulsion and the interrelationships with other technical disciplines.

6-2 G E N E R A L

This paragraph provides a general description of the methods used in calculating rocket motor performance quantities. Several parameters used to describe rocket motor performance are presented. The equation for the thrust of a rocket may be derived by a detailed integration of the forces acting over the internal and external surfaces of the motor. The results of this process are expressed in the following thrust equation:

$$F = \dot{m}u_e + (p_e - p_a)A_e, \text{ N} \tag{6-1}$$

where

F = thrust, N
$\dot{m}$ = propellant mass-flow rate, kg/s
u_e = nozzle-exit gas velocity, m/s
p_e = nozzle-exit absolute pressure †, Pa
p_a = ambient absolute pressure †, Pa
A_e = nozzle exit area, m².

The first term of Eq. 6-1 is the momentum thrust, and the second term is the pressure thrust. Optimum thrust can be obtained when the exhaust pressure equals the local ambient pressure, i.e., when the flow is ideally expanded in the nozzle.

A useful performance indicator is the impulse I, often referred to as the total impulse. The impulse is the integral of the thrust over the burning, or action time, of the propellant. This is expressed mathematically as

$$I = \int_0^{t_b} F\,dt, \text{ N·s} \tag{6-2}$$

where

I = impulse, N·s
t = time variable, s
t_b = propellant burning time, s.

As an example, if the average thrust over the period of burning is known, the impulse is simply the product of the average thrust and burning or action time.

Another important performance indicator is the specific impulse. It is a function of many variables and is generally quoted for standard sea level conditions and/or vacuum conditions. Specific impulse is a measure of the efficiency of the system including the propellant, interior ballistics, and the nozzle design. It is defined as the thrust that can be obtained from a rocket motor that has a propellant mass-flow rate of unity. This definition is expressed as

$$I_s = \frac{F}{\dot{m}}, \text{ N·s/kg} \tag{6-3}$$

where

I_s = specific impulse based on mass units, NŽs/kg.

Because of tradition, Chapters 3 and 4 of this handbook use specific impulse based on a weight flow rate rather than mass flow rate. This specific impulse is expressed in the following equation:

$$I_{sp} = \frac{F}{\dot{m}g_0}, \text{ s} \tag{6-4}$$

where

I_{sp} = specific impulse based on weight units, s
g_0 = 9.80665 m/s², reference acceleration due to gravity.

† All pressures are absolute, i.e., gage plus local (ambient) pressure.

It is important that the concepts of mass, weight, and gravity be distinguished in the application of these equations. Since weight changes with altitude and gravitational fields, mass units are preferred in the modern references on rocketry. Therefore, specific impulse as used in this chapter will carry the units of force per unit mass-flow rate.

The effective exhaust velocity c has been defined in the literature (Ref. 1) as a performance parameter and is equivalent to the specific impulse I_s, i.e.,

$$c = \frac{F}{\dot{m}}, \text{ m/s or N·s/kg} \tag{6-5}$$

or, by substitution of the expression for F from Eq. 6-1,

$$c = u_e + \frac{(p_e - p_a)A_e}{\dot{m}}, \text{ m/s.} \tag{6-6}$$

When $p_e = P_a$, the effective exhaust velocity c is equal to the average actual exhaust velocity u_e of the combustion gases. Rearrangement of the terms of Eq. 6-5 yields

$$F = c\dot{m}, \text{ N} \tag{6-7}$$

which is equivalent to Eq. 6-1 for $p_e = P_a$.

The characteristic exhaust velocity c^* is a performance parameter that defines the relationship of the combustion product gas properties in the combustion chamber, i.e.,

$$c^* = \frac{p_c A_t}{\dot{m}}, \text{ m/s} \tag{6-8}$$

where
   P_c = combustion chamber absolute pressure, Pa
   A_t = nozzle throat area, m^2.

The thrust coefficient C_F is defined as

$$C_F = F/(A_t p_c), \text{ dimensionless.} \tag{6-9}$$

Combining Eqs. 6-8 and 6-9, the equation for the thrust of the rocket can be written as

$$F = \dot{m}c^*C_F, \text{ N.} \tag{6-10}$$

In Eq. 6-10, c^* and C_F characterize the performances of the combustion chamber and the nozzle, respectively.

6-2.1 THE REACTION PRINCIPLE

Methods for propelling a body in either a fluid medium or in space are basically an application of Newton's reaction principle (Ref. 2). The reaction principle states that forces always occur in equal and opposite pairs—i.e., to every action (force) there is an equal, but oppositely directed, reaction (force). Examples of the reaction principle maybe observed at any time that a person or object moves. Examples of the application of the reaction principle to propulsion problems are rowing a boat, swimming in a pool. the screw for propelling a ship, the propeller for moving an airplane, and the rocket for propulsion.

In each of the propulsion examples, the application of the reaction principle involves increasing the momentum of a flowing mass of fluid in one direction so that the reaction to the action force causes a thrust for propelling the body. The thrust is the result of increasing the momentum of a flowing fluid in the direction opposite to that desired for the body.

6-2.2 ESSENTIAL FEATURES OF CHEMICAL ROCKETS

Solid-propellant rockets have been used in a variety of applications in short duration boost motors, in military missile systems, and in aerospace launch vehicles where longer action times have been achieved. The basic rocket motor consists of an igniter, a propellant charge, insulation, a liner, a case, and a nozzle. The motor case includes a forward skirt and dome, a cylindrical section, and an aft skirt and dome. Insulation usually is required at selected locations in the motor such as the head end, the aft dome, and in the nozzle. Across section of a typical case bonded, unrestricted burning rocket motor is shown in Fig. 6-1.
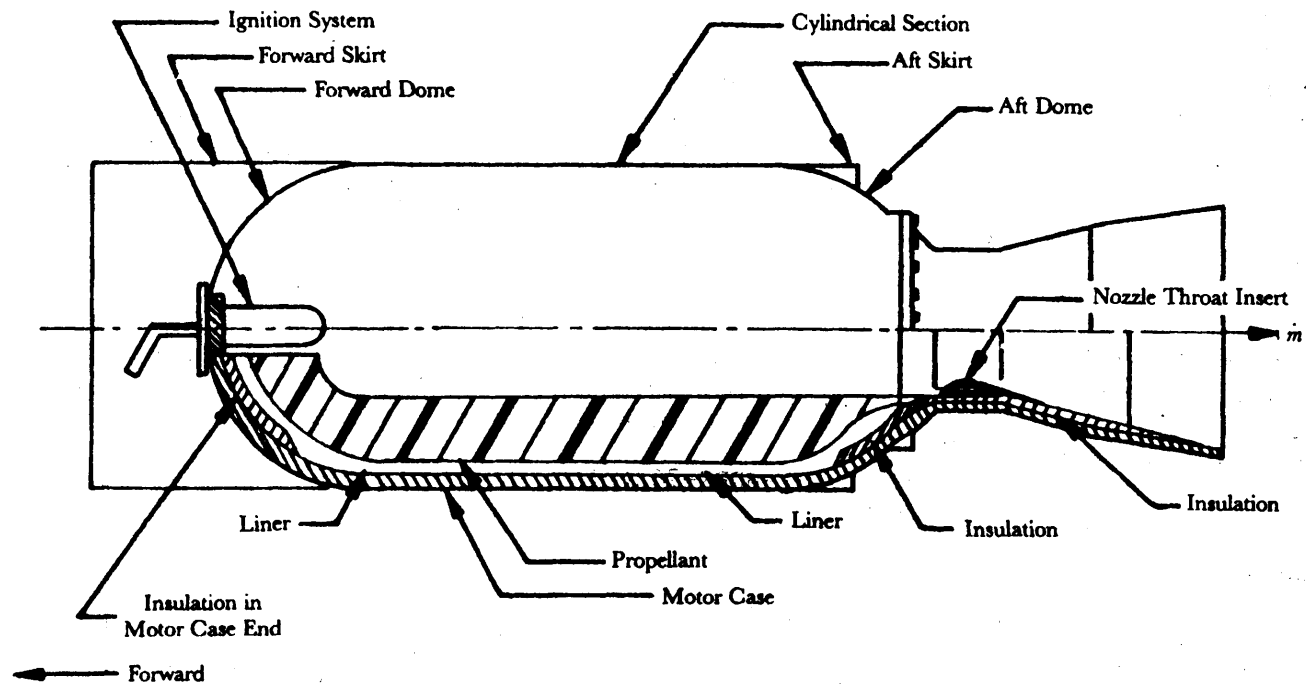
Figure 6-1. Case Bonded Solid Propellant Rocket Motor

6-3 PROPELLANT TYPES

The working substance of a rocket is its propellant which, during the burning process, undergoes chemical and thermodynamic changes. The propellant is either in the form of a solid or one or more liquids. In either case a fuel and an oxidizing agent must be present.

6-3.1 LIQUID PROPELLANTS

Liquid propellant rockets usually use two or more propellant components. In some cases a liquid monopropellant may be used.

Liquid bipropellant rocket engines commonly are used in large missile systems. A liquid fuel and a liquid oxidizer are carried in separate propellant tanks. They are pressurized, injected into the combustion chamber, and ignited to produce high-pressure gases that provide the reaction force through an exhaust nozzle.

A liquid monopropellant contains the oxidizing agent and the fuel in a single substance. It may be a mixture of compounds such as hydrogen peroxide and alcohol or it may be a homogeneous chemical agent such as nitromethane. Monopropellants must be stable at ordinary environmental conditions and decompose when heated in the presence of a catalyst under pressurized conditions to yield the combustion gases.

6-3.2 SOLID PROPELLANTS

A solid propellant is a chemical or mixture chemicals in a plastic or rubber form which produces high-pressure gases when it burns. These high-pressure gases' when exhausted from a combustion

chamber provide a reactive force for rocket propulsion. Atypical solid propellant may include two or more of the following functional ingredients: oxidizer, fuel, additives, and inhibiters. Solid propellants at-e formulated to include all the materials necessary for reaction. The solid block of propellant is called the grain and is formed in or inserted into the combustion chamber.

For military applications solid propellant rockets are usually preferred over liquid propellant systems, especially for applications in aerodynamically stabilized free rockets. One of the main capabilities of the liquid systems—control of thrust during flight-is seldom required in aerodynamically stabilized free rockets. The advantages of the solid propellant rocket are its simplicity, mobility, reliability, ease of storage, and ease of launching. The solid propulsion system has no moving parts such as valves, pressurization systems, and controls. It is simple and easy to use and requires little servicing.

Three general types of processed solid propellant are double-base, composite, and composite double-base propellants. The composite propellant is a heterogeneous mixture of oxidizing crystals in an organic rubber or plastic-like fuel binder. The double-base propellant, sometimes called homogeneous propellant, is a propellant in which the fuel and oxidant are contained in the same molecule (Ref. 3). The composite double-base propellant consists of a combination of the chemical compounds of the other two types of propellants. Each type of propellant is discussed further in the paragraphs that follow.

6-3.2.1. Double-Base Propellants

Double-base propellants, of which there are several kinds, in general are colloidal monopropellant mixtures comprising three principal ingredients: a polymer, an oxidizer-plasticizer, and a fuel plasticizer (Refs. 4 and 5). The polymer is the binder which acts as a suspension medium for the fuel and oxidizer in the double-base propellant. The oxidizer and fuel are chemically linked in the same molecule, and energy is released when the mixture burns.

The most widely used double-base polymer is nitrocellulose or cellulose hexanitrate (NC) (Ref. 4). It is an amorphous material which ignites at about 160° to 170°C. Since it is underoxidized, it can also be regarded as a fuel.

The oxidizer-plasticizer must be physically compatible with the polymer. A widely used double-base oxidizer-plasticizer is nitroglycerin or glycerol trinitrate (NG), a high-energy explosive in the form of an oily liquid that explodes at 260°C. Another double-base propellant was developed that replaces NG with diethylene glycol dinitrate (Ref. 5). This material is safer to handle than NG and is a better gelatinizing agent for NC. The optimum stoichiometric mixture from energy considerations of these two compounds should contain about 8.6 parts of NG to 1 part of NC. However, to obtain reasonable physical and storage characteristics of the solid colloid, the amount of NG must be limited to approximately 25% (Ref. 3). This under oxidization results in the tactical double-base propellants attaining energy levels far less than the optimum available.

The fuel-plasticizer must be physically compatible with the polymer. The fuel-type plasticizers are frequently some form of plastic. Some propellants tend to deteriorate or thermally degrade in storage at high temperature, and stabilizer additives are added to suppress the thermal degradation process.

Small quantities of other additives are usually included to promote smooth burning, improve mechanical proper-ties, and tailor performance characteristics.

6-3.2.2 Composite Propellants

Modern composite propellants have three principal ingredients: a fuel, which is an organic polymer, called the binder; a finely powdered inorganic oxidizer (generally ammonium perchlorate (AP)); and additives (Ref. 6), The additives are for the purpose of catalyzing the combustion process, increasing density, increasing specific impulse, improving physical properties, and increasing storage life. The fuel-binder acts as a suspension medium for the oxidizer and a metallic fuel additive if an additive is used. The fuel-binder can be any combustible material with reasonable strength and adhesion to the oxidizer particles. Various rubbers and plastics have been used over the years as the fuel-binder. The present preferred binder for tactical solid motors is a hydroxy terminated polybutadiene (HTPB) rubber. Binders used in composite propellants are primarily the elastomeric monomers. Binders receiving the most

development effort and application are listed in Table 6-1. All of the binders listed have been used in making castable propellants. For a detailed discussion of the binders for composite propellants, see Ref. 7.

TABLE 6-1
BINDERS FOR COMPOSITE PROPELLANTS

Polysulfides
Polyurethane
Butadiene Acrylic Acid Copolymers (PBAA)
Polyvinyl Chloride
Car-boxy Terminated Polybutadiene (CTPB)
Hydroxy Terminated Polybutadiene (HTPB)

The oxidizers used in composite propellants are the chlorates, perchlorates, and inorganic nitrates. Table 6-2 lists some of the inorganic oxidizers which might be considered for use in solid propellants. Variables that must be considered in selecting an oxidizer are the amount of available oxygen, heat of formation of the oxidizer, molecular weight of the exhaust gases, oxidizer density, hygroscopicity, and toxicity and corrosive properties of the exhaust products. The total amount of oxygen in the oxidizer cannot be made available to support the combustion of the fuel; some of this oxygen reacts chemically with other elements and is exhausted as by-products of the combustion.

TABLE 6-2
INORGANIC OXIDIZERS FOR
COMPOSITE PROPELLANTS

Oxidizer	Chemical Symbol	Molecular Weight	Density p, g/cm^3
Ammonium Nitrate	NH_4NO_3	80.05	1.73
Ammonium Per-chlorate	NH_4ClO_4	117.49	1.95
Sodium Nitrate	$NaNO_3$	84.99	2.26
Potassium Per-chlorate	$KClO_4$	138.55	2.52
Sodium Perchlorate	$NaClO_4$	122.55	2.48
Potassium Nitrate	KNO_3	101.10	2.109
Lithium Perchlorate	$LiClO_4$	106.40	2.428
Lithium Nitrate	$LiNO_3$	68.90	2.38
Nitronium Perchlorate	NO_2ClO_4	145.50	2.21

Most solid propellants have ingredients that are hydroscopic; consequently, it is necessary to consider the effects of moisture on these materials. Ammonium perchlorate (AP) and potassium perchlorate (KP) are useful in situations in which the propellant is exposed to moisture since these perchlorates are only slightly soluble in water.

Transition metal oxide (TMO) catalysts such as Fe_2O_3, CuO, MnO_2, and $CuCr_2O_4$, form a very popular group of catalysts for burning rate modification of composite solid propellants (Ref. 8). It is known that these oxides affect the decomposition characteristics of polymers and oxidizers such as AP and KP. These burning rate modifiers give composite propellants a wide range of burning rates and must be considered in the propellant selection.

The energy content of a solid propellant can be increased by including certain light metals such as finely powdered aluminum in the propellant formulation. The addition of aluminum increases the combustion temperature and thereby the specific impulse. In addition, it increases the propellant loading density and is effective in suppressing high frequency combustion pressure oscillations.

6-3.2.3 Composite Double-Base Propellants

Composite modified double-base propellants contain both homogeneous (double-base) propellants and heterogeneous mixtures (composite propellants). In these propellants, solid oxidizers such as ammonium salts or nitramines are held together in a matrix of nitrocellulose-nitroglycerin. Since nitrocellulose and nitroglycerin are both explosives, processing and handling of double-base and composite double-base propellants involves hazards; consequently, special precautionary measures are required.

6-4 BASIC PERFORMANCE PARAMETERS

The basic performance parameters for a solid rocket motor include thrust, characteristic exhaust velocity, specific impulse, propellant burning rate, flame temperature, action time, and the ideal velocity of the rocket.

6-4.1 INTERNAL BALLISTICS

Internal ballistics is the science that treats the motion of the propellant gas in the motor combustion chamber and nozzle. Internal ballistics includes a study of both the propellant design and the nozzle design. The motion of the combustion products depends on ballistic parameters that are essentially thermochemical properties of propellant gases, such as specific impulse and characteristic velocity, and on the design of the propellant grain and the nozzle (Ref. 7).

6-4.1.1 Propellant Burn Rate

Control of the propellant burn rate is one method for shaping the thrust-time history for a rocket motor. The choice of a propellant burn rate can be a trade-off between achieving the desired thrust-time history and assuring reproducibility and stability of specific impulse. Propellant burn rate and the parameters and variables within the propulsion system which affect the burn rate are discussed in this paragraph.

The velocity at which the solid propellant is consumed during operation is called the burning rate. Burning progresses in a direction normal to the exposed burning surface at a rate that is a function of propellant composition, ambient grain temperature, combustion pressure, and a few minor influences such as a high acceleration environment and propellant grain configuration. The burning rate can also be affected by the flow of high velocity gases parallel to the burning surface. This parallel flow of gases is called erosive burning. Usually the erosion is the greatest near the nozzle end of the motor where the gas velocity is high.

Burn rate catalysts can modify the propellant burn rate. Copper chromate, $Cu_2Cr_2O_4$, and iron oxide, Fe_2O_3, are most effective among the TMO catalysts on composite propellants using perchlorate oxidizers (Ref. 8). For example, in some formulations, the addition of 0..5'% copper chromate doubles the burning rate. These TMO catalysts also may affect the gas phase, the subsurface condensed phase, and the surface condensed phase separately or all of them simultaneously. Therefore, the propellant burn rate depends upon many variables but mainly on pressure, initial grain temperature, effect of oxidizer partcle size, and presence of additives.

For a given propellant combination the burning rate may be approximated by an empirical relation in which the influence of the performance parameters is usually small compared to the influence of the chamber pressure and the initial grain temperature. Most of the proposed relationships or composite models are based on the gas conditions and treat the burning surface as being planar, dry, and homogeneous. In actual practice the surface has been found to contain a molten layer and to be rough. The models do not explain the effect of particle size distribution, binder characteristics, surface temperature, catalyst, condensed-phase heat release, or sensitivity of burning rate to temperature, but they are formulated to predict the trend of the burning rate as a function of pressure. Several empirical relationships that are used to relate burn rate to pressure are given in Eqs. 6-11 through 6-13. The motor manufacturer uses the model that best describes the burn rate test data for the specific propellant and motor configuration.

$$\dot{r} = b p_c^n, \text{ m/s} \tag{6-11}$$

$$\dot{r} = a + bp_c^n, \text{ m/s} \tag{6-12}$$

$$\frac{1}{\dot{r}} = \frac{a}{p_c} + \frac{b}{p_c^{1/3}}, \text{ s/m} \tag{6-13}$$

where

$\dot{r}$ = propellant burning rate, m/s

$a, b,$ and n = empirical constants.

The empirical constants are adapted to provide a mathematical approximation of the test results, and they take on the units that are appropriate to balance the equation dimensionally. The constants have values that depend on the gas phase reaction rates, diffusion rates, temperature, and pressure. In Eq. 6-11 for example, the value of n for most propellants is between 0.35 and 0.9. For homogeneous (double-base) propellants, n is approximately 0.7; for heterogeneous (composite) propellants, n is approximately 0.4; and for mesa propellants, n is approximately zero.

6-4.1.2 Thermodynamic Considerations

Rocket engine performance parameters are dependent on the thermodynamic states of the propulsive gas created in the rocket by the combustion of fuel with an oxidizer. Certain thermodynamic considerations are often referred to as stagnation conditions since they are especially applicable to the combustion chamber. The stagnation condition (of pressure, temperature, enthalpy, etc.) is defined as the condition in a fluid flow field where the velocity of the fluid is brought to rest reversibly and adiabatically, i.e., isentropically. A static condition is one that can be measured by means of a probe moving with the fluid. This is to say that the static pressure, for example, is the gage pressure as unaffected by the fluid flow, and the stagnation pressure is a total pressure where the velocity is reduced to zero isentropically. The static temperatures of the gases entering the exhaust nozzle will range from 2778 K to approximately 3600 K and are well above the critical temperature of the individual gas components forming the combustion gas mixture. The combustion pressures— 1.7 to 20.7 MPa—are low compared to the corresponding critical pressures. It is reasonable to assume that the combustion gas mixture produced in the rocket motor behaves as an ideal gas and that there are no interactions among phases. The equation of state for such a mixture is

$$pv = nRT/M', \text{ J/kg} \tag{6-14}$$

or

$$p = \rho RT/M', \text{ Pa} \tag{6-15}$$

where

p = absolute static pressure, Pa

v = specific volume, m³/kg

n = number of moles

R = universal gas constant = 8.31434×10^3 J/kmole·K

T = absolute temperature, K

ρ = density, kg/m³

M' = molecular weight, kg/mole.

Eqs. 6-14 and 6-15 are assumed to be correct even when small amounts of condensed species (up to several percent by weight) are present. The condensed species occupy a negligible volume and exert a negligible pressure compared to the gaseous species. The variables v and n define the specific volume of the gas and the number of moles of the gas, respectively. The symbol **p** refers to the density of the mixture including condensed species.

The average molecular weight $\overline{M}'$ of the gas mixture, is defined as the sum of the individual masses of each constituent present divided by the sum of the number of moles of each. This relationship is expressed as

$$\overline{M}' = \sum_{j=1}^{k} \frac{n_j M_j'}{n_m}, \text{ kg/mole} \tag{6-16}$$

where

$\overline{M}'$ = average molecular weight, kg/mole
n_j = number of moles of constituent j
M_j' = molecular weight of constituent j, kg/mole
n_m = number of moles in mixture
k = number of constituents.

6-4.1.3 Continuity Equation

For steady flow the law of conservation of mass, the continuity equation, is represented by

$$\dot{m} = \rho A_b \dot{r}, \text{ kg/s} \tag{6-17}$$

w-here

A_b = burning surface area, m².
Eq. 6-17 assumes that the burning of a solid propellant is one-dimensional, normal to the burning surface, and neutral. For steady state in the combustion chamber, the mass-flow rate of propellant consumed $\dot{m}_p$ must equal the mass-flow rate of gas $\dot{m}_g$ expended from the nozzle.

For transient internal ballistics, Eq. 6-17 should be replaced by

$$\dot{m} = \int_0^t \left[\rho A_b \left(\frac{\partial \dot{r}}{\partial t} \right) + \rho \dot{r} \left(\frac{\partial A_b}{\partial t} \right) + A_b \dot{r} \left(\frac{\partial \rho}{\partial t} \right) \right] dt, \text{ kg/s}. \tag{6-18}$$

Eq. 6-18 includes terms that account for the chamber pressurization rate—$\dot{r} = f(p)$, $\rho = f(p)$—and a non-constant burn surface.

6-4.1.4 Propellant Temperature Effects

A solid propellant will not ignite until its surface temperature is above an ignition temperature, and the surface must be maintained above the ignition temperature until the required activation energy for self-sustaining combustion has been absorbed. In addition to the temperature requirement, the igniter must produce enough gas to raise the chamber pressure to the lower deflagration limit.

The ballistic sensitivity of a given propellant, with respect to the bulk temperature of the propellant grain, is expressed as the change of a particular parameter per unit change of the temperature of the grain. Temperature sensitivity coefficients II; are defined for chamber pressure, burning rate, and thrust, respectively, for a constant burning surface area ratio $K = A_b/A_t$, the ratio of burning surface area A_b to nozzle throat area A_t (Refs. 4 and 5) as follows:

$$\Pi_p = \frac{\partial \ln p_c}{\partial T} = \left(\frac{1}{p_c} \right) \left(\frac{\partial p_c}{\partial T} \right), \text{ K}^{-1} \tag{6-19}$$

$$\Pi_{\dot{r}} = \frac{\partial \ln \dot{r}}{\partial T} = \left(\frac{1}{\dot{r}} \right) \left(\frac{\partial \dot{r}}{\partial T} \right), \text{ K}^{-1} \tag{6-20}$$

$$\Pi_F = \frac{\partial \ln F}{\partial T} = \left(\frac{1}{F}\right)\left(\frac{\partial F}{\partial T}\right), \; K^{-1}. \tag{6-21}$$

Eqs. 6-19 through 6-21 can also be expressed as follows:

$$\frac{p_r}{p_c} = \exp(\Pi_p \Delta T), \text{ dimensionless} \tag{6-22}$$

$$\frac{\dot{r}_r}{\dot{r}} = \exp(\Pi_{\dot{r}} \Delta T), \text{ dimensionless} \tag{6-23}$$

$$\frac{F_r}{F} = \exp(\Pi_F \Delta T), \text{ dimensionless} \tag{6-24}$$

where

Π_p = temperature sensitivity coefficient of reference pressure p_r, K^{-1}
$\Pi_{\dot{r}}$ = temperature sensitivity coefficient of reference burning rate $\dot{r}_r$, K^{-1}
Π_F = temperature sensitivity coefficent of reference thrust F_r, K^{-1}.

Fig. 6-2 gives an example of the effect of initial propellant temperature on measured pressure and thrust. Temperature can also affect the physical characteristics of the propellant. A propellant may become brittle and crack-prone at low temperatures (–40°C) and become nonrigid at high temperatures (60°C). Some additives are available that suppress the effects of storage temperatures on propellant performance.

6-4.2 NOZZLE

The primary function of the nozzle is to expand the hot propellant gases from the high pressure in the combustion chamber to or near the external ambient pressure, thereby converting thermal energy into directed kinetic energy or thrust. The theoretical thermodynamic relations provide methods for the calculations of rocket motor performance and design parameters. The flow of combustion gases as they are expanded through the nozzle is assumed to be isentropic flow (adiabatic and reversible) based on an average nozzle specific heat ratio or from a knowledge of the chemical equilibrium composition of the reactant products. Mass flow calculations for both converging and converging-diverging nozzles are discussed in Ref. 5.

The maximum thrust from a motor is obtained when the combustion gases are expanded to the ambient atmospheric pressure. Since rockets usually operate at varying altitudes and the atmospheric pressure varies with altitude, the selected design expansion ratio of the nozzle is usually a compromise between the thrust and the nozzle expansion ratio, length, and weight.

6-4.2.1 Nozzle Design Factors

The design of a propulsive nozzle involves consideration of a variety of conditions and parameters. These include the environment in which the nozzle is to operate; the propellant to be used; thrust requirement; the flow rate; and certain parameters to be optimized such as weight, length, exit diameter, and cost. The nozzles of solid propellant motors are usually uncooled and are subjected to severe conditions with relatively high heat-transfer rates and mechanical erosion. Nozzle configuration design involves analyses of aerodynamic, thermal, structural, fabrication, and operational considerations which are significant factors that relate directly to rocket performance. Often it is not feasible from economic and weight considerations to expand ideally the combustion products in the nozzle. The design consists of trade-offs and optimization of pertinent parameters which are tailored to the operational requirements.

The cost of the nozzle is related to the materials used in its construction and to the complexities of the manufacturing process. Construction materials used in nozzles must be selected to satisfy thermal and
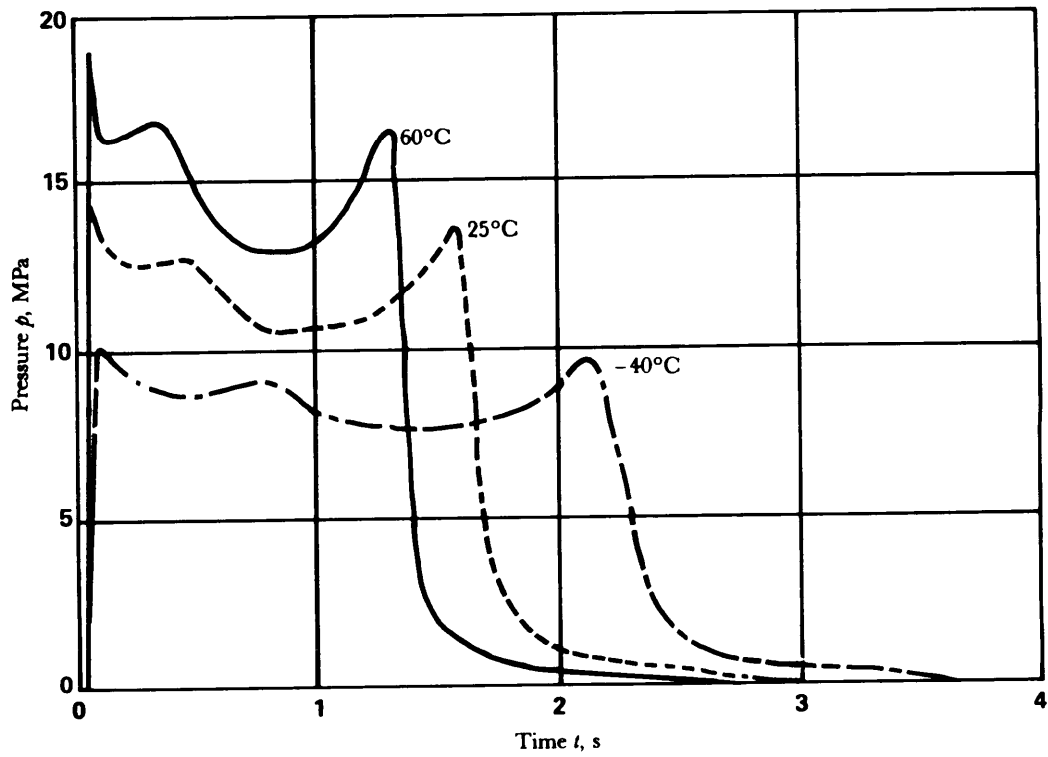
(A) Effect of Temperature on Pressure
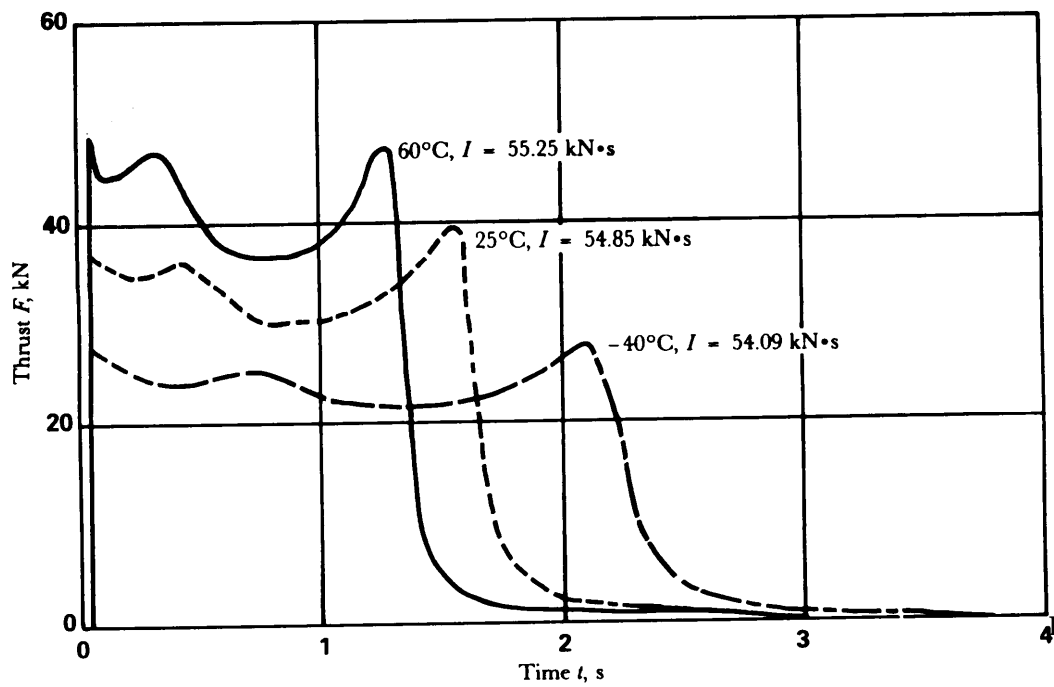
(B) Effect of Temperature on Thrust

Figure 6-2. Motor Performance and Temperature Effect

loading conditions. The pressures encountered in the nozzle cause radial, axial, and hoop loads which are compounded by the very steep thermal gradients that are experienced. For applications where the temperature is relatively low and the duration short, simple steel nozzles are adequate. For longer durations, high temperatures, and corrosive propellants, inserts of special materials—tungsten, various carbides, molybdenum, or graphite- must be added to the throat section. These materials are brittle and difficult to use, and they increase the cost appreciablely. Ablative materials may be used; however, this usually. results in an enlarged throat that affects the design characteristics of the nozzle.

Nozzle-throat materials should be selected that have the most reproducible erosion characteristics. The relative rankings based on the ratio of standard deviation of the final eroded throat area A_E to the initial nozzle-throat area A_t are given in Table 6-3.

TABLE 6-3
NOZZLE MATERIAL EROSION CHARACTERISTICS

Material	$A_\epsilon\ A_t, \%$
Tungsten (2% Molybdenum)	0.06
ATJ Graphite	**0.11**
Glass Phenolic	0.16
Silica Wrapped Tape	0.23
G-90 Grapite	0.26
CS Graphite	0.31
Carhitex 700	0.36

The best material is tungsten with an erosion rate so low that variability is not a factor. A close second is ATJ graphite which is superior to the more expensive grade G-90. The ATJ graphite was determined to be the best nozzle-throat material based on a cost-effectiveness analysis.

Accurate alignment of the nozzle axis with the rocket center of gravity is especially important in aerodynamically stabilized free rockets in order to minimize flight errors. Careful selection of materials is necessary to minimize erosive effects (par. 6-4.2.4) that may result in malalignment of the thrust vector.

Design requirements and design factors must be carefully selected and defined with considerations for ease of manufacture and cost. Nozzles maybe designed for an ideal expansion ratio and then truncated to a shorter length to facilitate manufacture and reduce cost (par. 6-4.2.3). A weight saving and a cost saving may be attained at the expense of a small loss in thrust or performance. Other design considerations are discussed in pars. 6--4.2.2 and 6-5.5.

6-4.2.2 Thermodynamic Relations

Thermodynamic and gas dynamic theory provides the basic process relationships required in analyzing the combustion and gas expansion within the nozzle. The nozzle of a rocket may be of a converging or converging-diverging configuration. Fig. 6-3 illustrates schematically the manner in which the flow area varies for these two general classes of nozzles.

The ideal flow relationship is applicable for converging nozzles and converging-diverging (de Laval) nozzles. The converging nozzle (Fig. 6-3(A)) is suitable for applications in which lower thrusts are acceptable and length is a premium. A cent'erging nozzle is capable of developing 65 to 75% of the available total thrust.

The thermodynamic relations are presented in equation form and are based on the analytical treatment of flow of a compressible fluid through a nozzle, assuming steady, one-dimensional, isentropic flow (ideal nozzle flow). Thermodynamic properties that are significant in this analysis are the specific heats at constant pressure C_p and constant volume C_v, respectively; the ratio of specific heats $y = c_p/c_v$; and enthalpy. The specific enthalpy h (heat content per unit mass) is defined as the sum of the specific internal energy. v and the product p_v of the absolute pressure p and the specific volume v, i.e.,
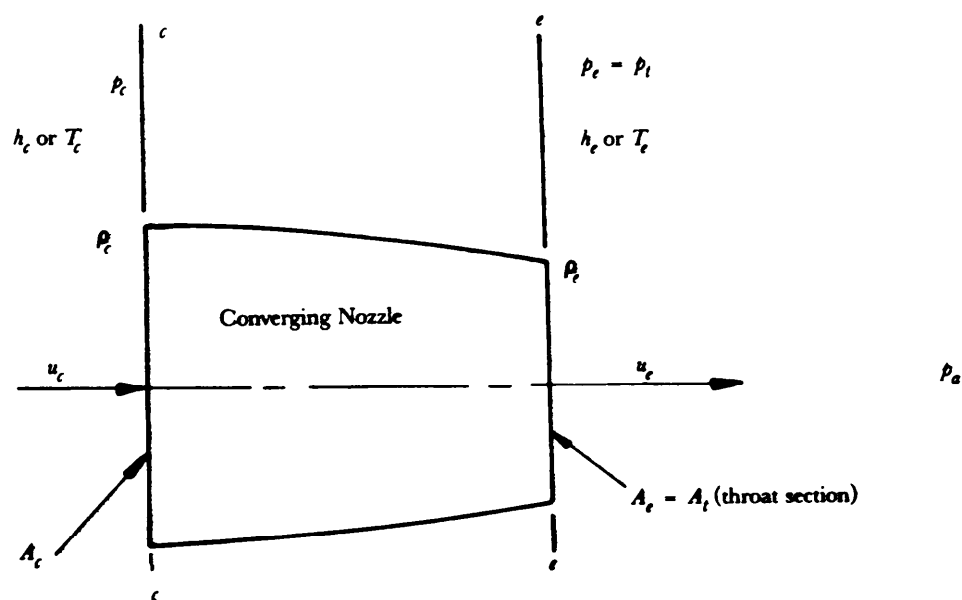
(A) Ideal Nozzle Flow in a Converging Nozzle
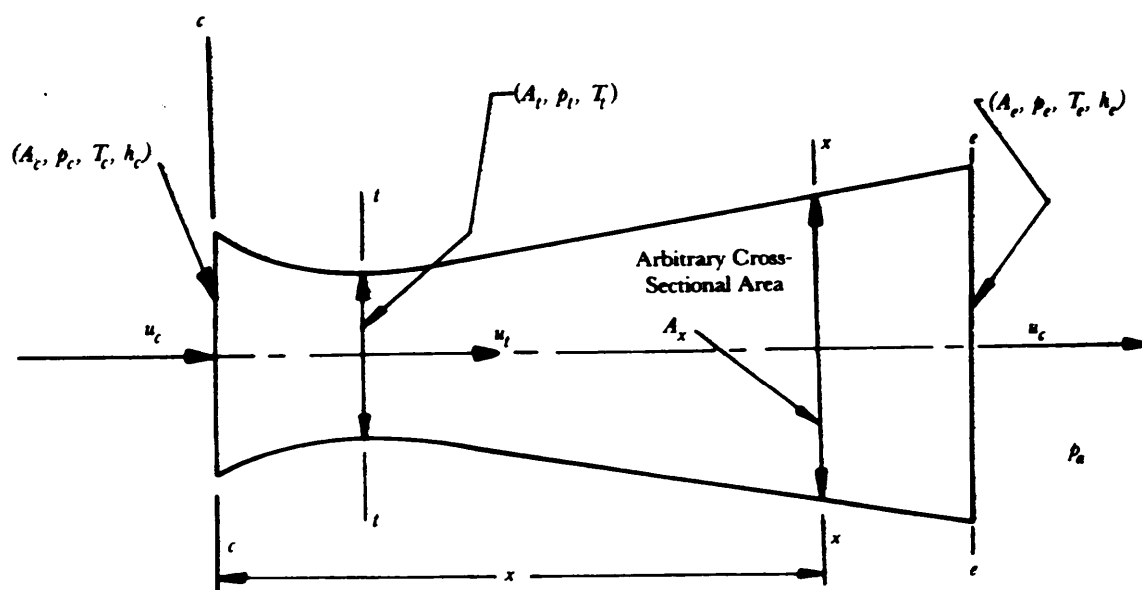
(B) Ideal Nozzle Flow in a Converging-Diverging or de Laval Nozzle

Figure 6-3. Two Basic Types of Nozzles Employed in Rocket Motors (Ref. 5)

$$h = v + pv, \text{ J kg} \tag{6-25}$$

where
$\qquad h$ = static specific enthalpy, J kg
$\qquad v$ = specific internal energy, J kg.

The important thermodynamic states of a propulsive gas as it accelerates from the combustion chamber through the rocket nozzle are illustrated by Fig. 6-3. If it is assumed that the velocity in the combustion chamber is negligible, the local isentropic velocity u at each position through the nozzle maybe calculated by

$$u = \sqrt{2(h_c - h)}, \text{ m/s} \tag{6-26}$$

or

$$u = \sqrt{2\overline{c_p}T_c Z}, \text{ m/s} \tag{6-27}$$

$$Z = 1 - \left(\frac{p}{p_c}\right)^{(\gamma-1)\,\gamma}, \text{ dimensionless} \tag{6-28}$$

where

h_c = stagnation specific enthalpy in combustion chamber, J/kg
$\overline{c_p}$ = average specific heat at constant pressure, J/kg·K
T_c = combustion chamber temperature, K
γ = ratio of specific heat c_p/c_v, dimensionless
Z = expansion factor, dimensionless.

Several reference velocities can be calculated for an ideal nozzle. By setting the static enthalpy in Eq. 6-26 to zero (expansion to absolute zero pressure), the maximum velocity u_{max} is given by

$$u_{max} = \sqrt{2h_c} = \sqrt{2c_p T_c} = \sqrt{\left(\frac{2\gamma}{\gamma - 1}\right)\frac{RT_c}{M'}}, \text{ m/s} \tag{6-29}$$

in which the ideal gas relationship $c_p = \gamma R/[(\gamma - 1)M']$ is substituted,

where

C_p = specific heat at constant pressure, J/kgŽK.

Another useful reference velocity is the critical nozzle throat velocity u* which occurs at the velocity of sound. The asterisk is used to denote critical conditions which are defined as those occurring at unity Mach number.

$$u^* = \sqrt{\gamma R T^*/M'} \tag{6-30}$$

where

T^* = critical temperature, K
u^* = critical velocity, m/s.

Eq. 6-27 can be restructured using the definitions for u_{max} and u* as follows:

$$u = u_{max}\sqrt{Z} = u^* \sqrt{\left(\frac{\gamma + 1}{\gamma - 1}\right)Z}, \text{ m/s}. \tag{6-31}$$

The temperature, pressure, and density relations for the simplified isentropic flow approach for nozzle flow are defined by Eqs. 6-32, 6-33, and 6-34, respectively,

$$\frac{T_c}{T} = 1 + \left(\frac{\gamma - 1}{2}\right)M^2, \text{ dimensionless} \tag{6-32}$$

$$\frac{p_c}{p} = \left[1 + \left(\frac{\gamma - 1}{2}\right)M^2\right]^{\gamma/(\gamma-1)}, \text{ dimensionless} \tag{6-33}$$

$$\frac{\rho_c}{\rho} = \left[1 + \left(\frac{\gamma - 1}{2}\right)M^2\right]^{1/(\gamma-1)}, \text{ dimensionless} \tag{6-34}$$

where

T_c = combustion chamber temperature, K
T = absolute static temperature, K
p = absolute static pressure, Pa
ρ_c = density of chamber gases, kg/m^3
ρ = static density, kg/m^3
M = Mach number, dimensionless.

The static values of temperature, pressure, and density pertain to a specific axial location in the chamber or nozzle where M is evaluated.

The required area ratio A_x/A_t for expanding an ideal gas isentropically from the stagnation conditions p_c and T_c to the static pressure p_x at the cross-sectional area A_x for critical nozzle flow as is illustrated in Fig. 6-4 is provided by Eq. 6-35, i.e.,
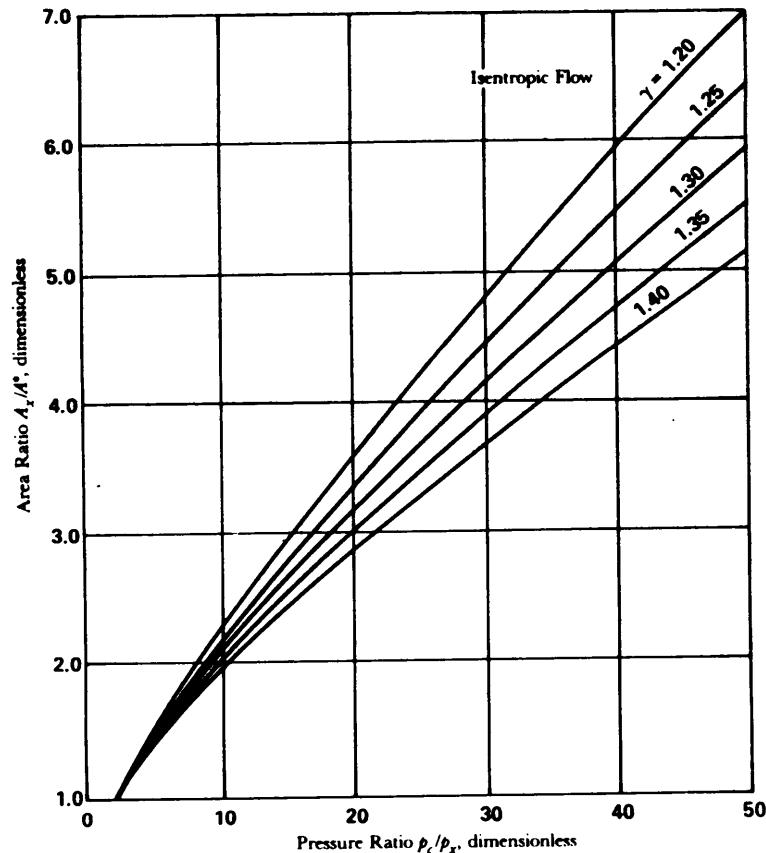
Figure 6-4. Area Ratio A_x/A^* for Complete Expansion as a Function of the Nozzle Pressure Ratio p_c/p_x for Different Values of $\gamma = c_p/c_v$ (Ref. 5)

$$\frac{A_x}{A_t} = \frac{A_x}{A^*} = \frac{\left(\frac{2}{\gamma+1}\right)^{1(\gamma-1)}\sqrt{\frac{\gamma-1}{\gamma+1}}}{\left(\frac{p_x}{p_c}\right)^{1/\gamma}\sqrt{1-\left(\frac{p_x}{p_c}\right)^{(\gamma-1)/\gamma}}}, \text{ dimensionless.} \tag{6-35}$$

This equation can also be presented with A_x/A_t as a function of M_x as follows:

$$\frac{A_x}{A_t} = \frac{A_x}{A^*} = \frac{1}{M_x}\left\{\left(\frac{2}{\gamma+1}\right)\left[1+\left(\frac{\gamma-1}{2}\right)M_x^2\right]\right\}^{(\gamma+1)/[2(\gamma-1)]}, \text{ dimensionless} \tag{6-36}$$

where

A_x = cross-sectional area at point x, m^2
A^* = area at unity Mach number, m^2
p_x = absolute pressure at point x, Pa
M_x = Mach number at point x, dimensionless.

In the conventional de Laval nozzle, unity Mach number occurs at the throat of the nozzle and A^* is the throat area A_t. A converging-diverging nozzle sample problem for ideal gas flow of air is presented on page 4-16, Ref. 5.

The exit Mach number in a converging-diverging nozzle can be subsonic or supersonic, depending on the ratio of chamber pressure to back pressure. A converging-diverging nozzle that has an isentropic mass flow rate less than critical will have subsonic flow throughout the nozzle. The small range of exit pressures which can be attained with a subsonic isentropic flow are indicated by Fig. 6-5. When a nozzle has the critical mass flow rate $\dot{m}^*$, only two exit pressures satisfy the requirement for isentropic flow. These are identified as "isentropic diffusion" and "isentropic expansion to supersonic velocities" in Fig. 6-5.

A converging-diverging nozzle having a fixed area ratio A_e/A^* and fixed inlet conditions provides complete expansion of the flowing gas when the exit pressure equals the back pressure. When the nozzle exit pressure is greater or less than the back pressure, the nozzle is classified as being underexpanded or overexpanded, respectively.

6-4.2.3 Surface Contours

The nozzles most often employed in rocket motors are converging and converging-diverging (de Laval nozzle). The shape of the subsonic or converging portion of a nozzle is not critical; however, the shape of the supersonic or diverging portion of the de Laval nozzle is very important. Improper shaping of the diverging portion may result in shock formations and, therefore, performance loss. Simple, conical divergent sections usually provide shock-free performance when they are expanded to the appropriate exit pressure. Divergence half angles between 12 and 18 deg usually provide the best performance (Ref. 1). For a given area ratio, smaller angles result in excessive nozzle lengths and corresponding] y large friction losses. Large angles cause radial flow (nonaxiality) losses and possible flow separation from the walls. The thrust of an ideal rocket of nozzle cone divergence half angle a is reduced by a nozzle angle correction factor A due to the nonaxialily of the exhaust products, i.e.,

$$u_{ex} = \lambda u_e, \text{ m/s} \tag{6-37}$$

$$\lambda = \frac{1+\cos\alpha}{2}, \text{ dimensionless} \tag{6-38}$$

where

u_{ex} = axial component of nozzle-exit gas velocity u_e, m/s
α = nozzle cone divergence half angle, deg
λ = nozzle angle correction factor, dimensionless.
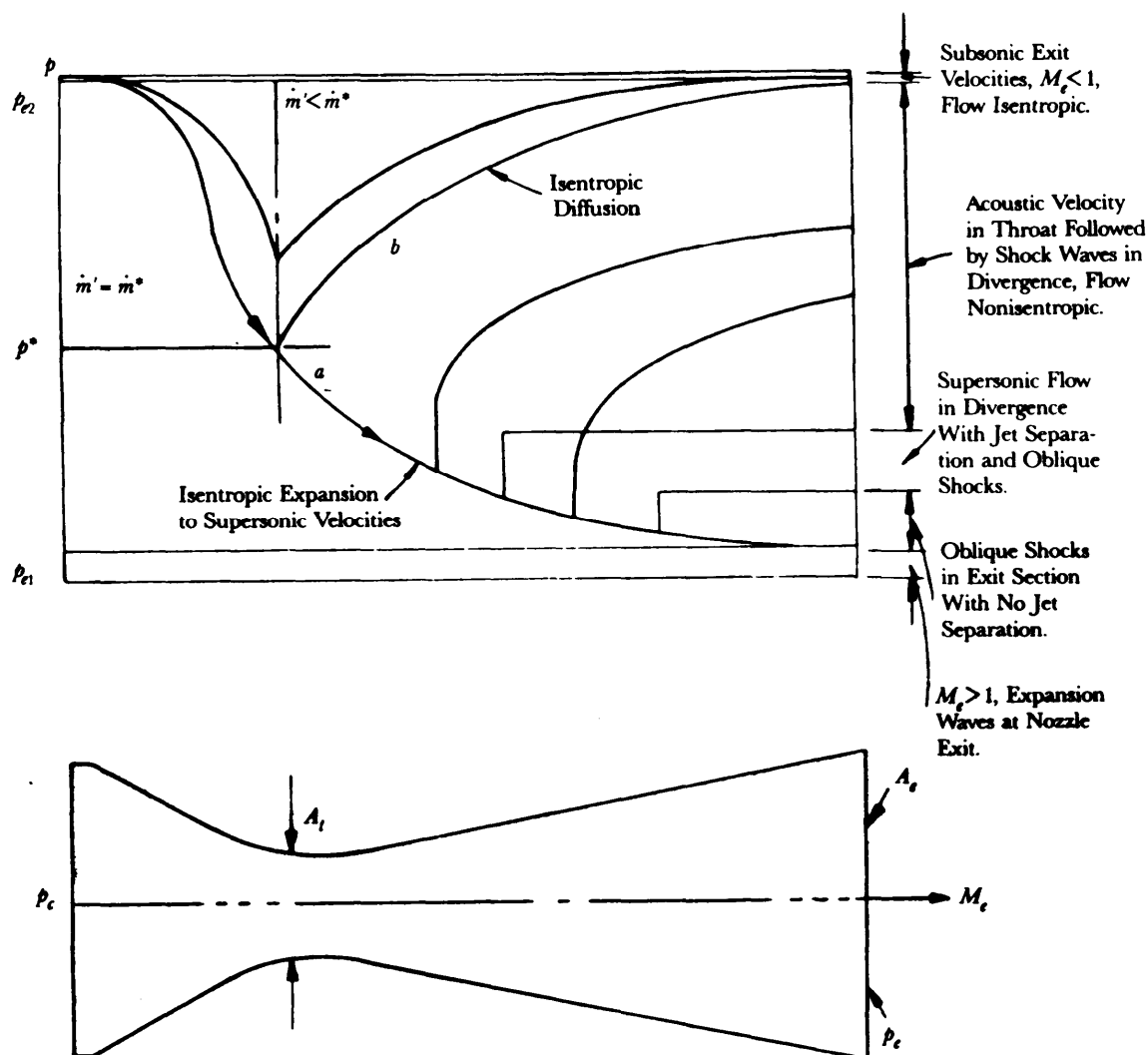
Figure 6-5. Pressure Distributions in a Converging-Diverging Nozzle Under Different Operating Conditions (Ref. 5)

Experimental verification of this correction for radial flow thrust loss is shown by Fig. 6-6 (Ref. 9). The figure provides a comparison of actual ideal thrust (axial component) for a series of conical nozzles. The expected performance (Eq. 6-38) is reduced here arbitrarily 0.5% to account for boundary layer losses.

The radial flow loss can be eliminated if the nozzle is suitably contoured to give a uniformly axial exhaust velocity. The design of a suitable nozzle contour to produce such a flow employs an analytical procedure called the method of characteristics (MOC). Discussion of nozzle design using the MOC is found in Ref. 10, Chapter 13, and in Ref. 11.

An optimized contour of a divergent nozzle has the approximate shape of a parabola (or bell). Consideration of the pressure forces on the exhaust end of the nozzle suggests that part of the nozzle might be removed with a saving in weight, which would more than compensate for the loss of thrust.

Nozzle design optimization methods are formulated to determine a nozzle shape that provides maximum performance for a given propellant flow, including possible truncation of the nozzle. Chapter 13, Ref. 10, and Ref. 12 provide data on the results of calculations for a family of perfect nozzles designed for various area ratios A_e / A_t and then truncated at various length ratios ℓ / r_t where r_t is the radius of the nozzle throat and ℓ is the truncated nozzle length.
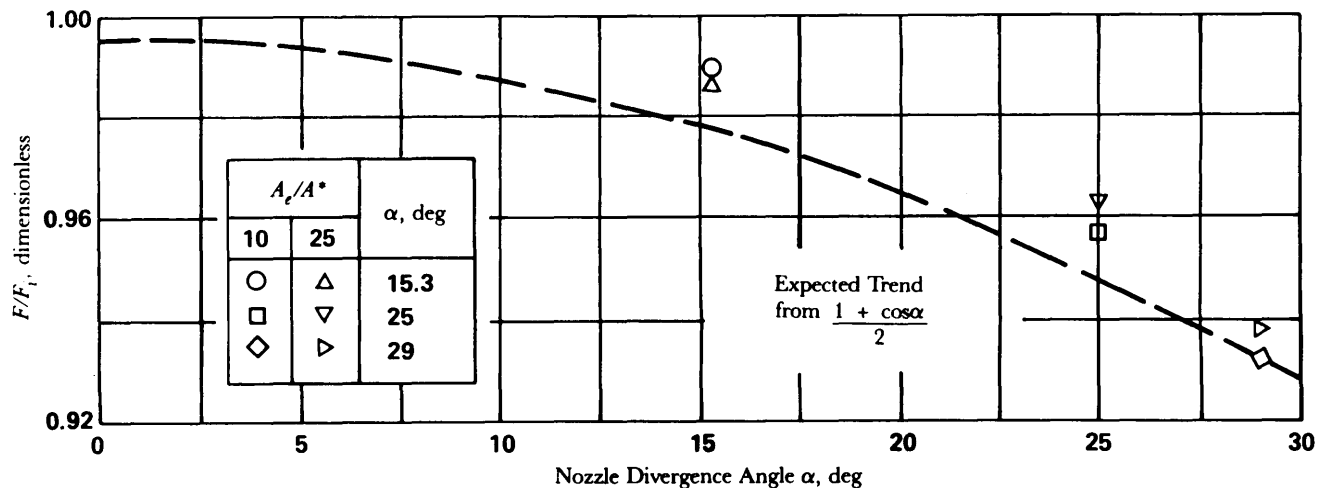
Figure 6-6. Design Thrust Ratio as Function of Nozzle Divergence Angle (Ref. 9)

In an attempt to offset the thrust loss associated with overexpansion and for other considerations, nozzle shapes other than conventional internal-flow configurations have been developed. Plug and expansion-deflection nozzles are shown schematically in Fig. 6-7. Flow from the combustion chamber passes through an annular throat in both configurations. For the plug nozzle the flow expands around a corner at the throat to ambient pressure on one side and along a central body or plug on the other. Expansion-deflection nozzles achieve the same result in an inverse geometry, i.e., with the solid boundary surrounding the free-jet boundary.
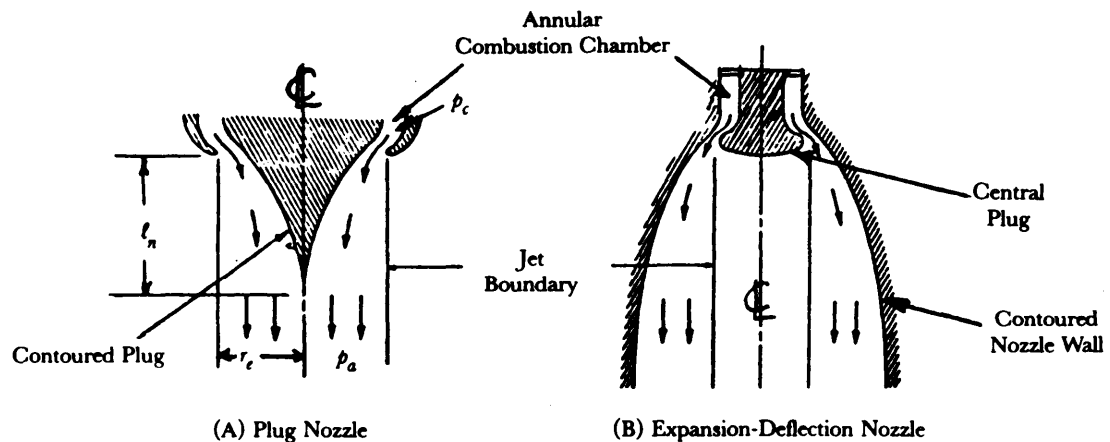
Figure 6-7. Schematic Cross Sections of Plug and Expansion-Deflection Nozzles (Ref. 5)

In both configurations the presence of a free-jet boundary to the expansion process lends a kind of self-adjustment to back-pressure variations. The flow expands around the corner to the actual ambient pressure, and thus overexpansion is essentially avoided. Fig. 6-8 illustrates the improved performance of a plug nozzle over a conventional nozzle at higher back pressures (Refs. 13 and 14). In this figure the thrust coefficient C_F is plotted versus the ratio of chamber pressure PC to ambient pressure p_a.

The main advantage of these configurations-plug and expansion-deflection—is that both types are substantially shorter than comparable internal-flow nozzles. Fig. 6-9 presents comparisons of the required lengths of various nozzles to produce 99.5% of the vacuum thrust coefficient of an ideal nozzle of the same area ratio where r* and A* are the nozzle throat radius and area, respectively, at Mach 1. The combustion chamber of an expansion-deflection nozzle design is similar to that for a conventional rocket. The main difficulties associated with these configurations are the processes of adequately supporting and cooling
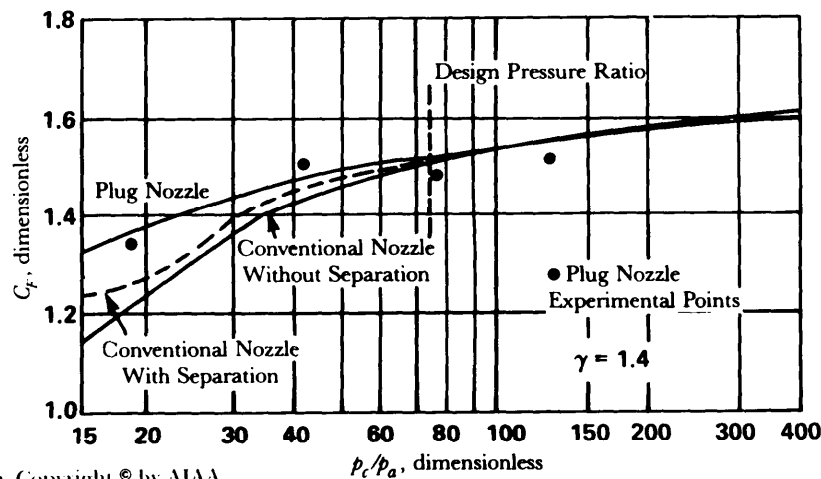
Figure 6-8. Off-Design Thrust Coefficients of Conventional and Plug Nozzles (Ref. 13)

the central plug. At the present time expansion-deflection nozzles have not displaced conventional nozzles, but for very high-thrust engines their size advantage is impressive.
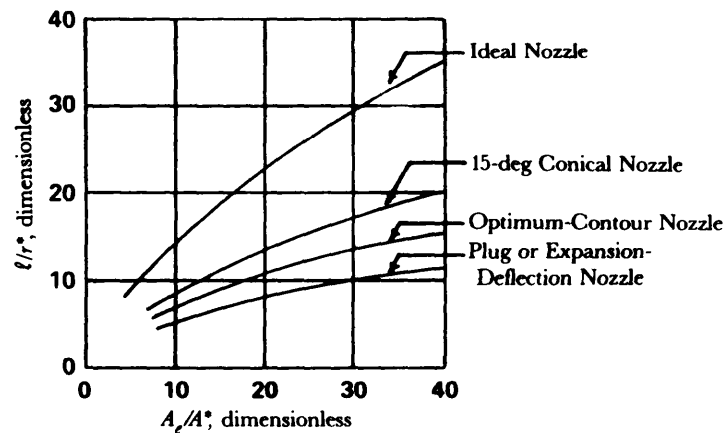
Figure 6-9. Comparison of Lengths of Various Types of Nozzles for γ = 1.23 (Ref. 14)

6-4.2.4 Nozzle Erosion

Failures due to erosion or deterioration of nozzle and solid-motor aft-closure surface materials result from surface oxidation or chemical reaction, thermal-stress cracking, erosion from melting, and physical removal caused by local shear forces. Materials used in areas subject to erosion must be carefully selected with consideration of the combustion environment and the operational and other requirements (see Table 6-3). Refs. 15 through 18 provide computer programs for performing nozzle flow and erosion calculations. These programs vary from simplified to complex analyses of thermochemistry, ablation, chemical reactions, heat conduction, etc.

The erosion rate of aft-closure insulation was empirically analyzed (Ref. 19) by correlating the aver-age ablation rate with a number of variables. The main correlating parameter was a heat flux based on the simplified Bartz heat transfer coefficient for two-dimensional effects multiplied by an arnplification factor. The factor contained terms related to port area to throat area ratio, local wall angle, grain geometry, and nozzle cant angle. The final insulation regression rate correlation equation applicable to the aft-end regions of conventional motor designs is

$$\bar{\dot{r}} = A_r \bar{q}_B \left(\frac{1 + \cos\Phi}{2}\right)^{0.9} \left[1 + 0.12\,\bar{H} + 4.0\sin\theta + 472(A_b/A_p)M_p^2 + 1.48(\ell_c/r_p)(r/r')^{0.5}\beta\right], \text{m/s}$$

(6-39)

where

$\bar{\dot{r}}$ = average insulation regression rate, m/s

A_r = regression coefficient, m^3/J

$\bar{q}_B$ = average Bartz heat flux, J/s·m^2

$\bar{H}$ = average port area to throat area ratio, dimensionless

A_b = asymmetric grain base area, m^2

A_p = port area, m^2

M_p = Mach number at port, dimensionless

ℓ_c = combustion chamber length, m

r_p = port radius, m

r = radius corresponding to regression point, m

r' = effective bend radius of curvature, m

β = cant angle, rad

θ = wall angle, deg

Φ = average entrance angle, deg.

Eq. 6-39 shows the importance of port area to throat area ratio $\bar{H}$, entrance angle Φ, local wall angle θ, grain design length ℓ_c, length to radius ratio ℓ_c/r_p, and cant angle β. Even more notably, Eq. 6-39 shows which parameters are important in designing scale test motors.

6-4.2.5 Jet Plume Effects

The exhaust gases form into an expanding plume as they leave the nozzle and enter the atmospheric environment. The size and shape of the plume depends to a great extent on the pressure change at the exit plane. The jet pressure ratio is a factor in the character of the plume and its effect on the rocket, and it is defined as the ratio of the nozzle exit pressure (jet-exit pressure) to the free-stream static pressure (ambient pressure). The nozzle exit pressure as used here is total pressure and includes not only the static (gage) pressure but also the dynamic pressure which is defined in Eq. 6-40:

$$q_e = \frac{1}{2}\left(\rho_e u_e^2\right), \text{Pa}$$

(6-40)

where

q_e = dynamic pressure of nozzle exhaust gas, Pa

ρ_e = density of nozzle exhaust gases, kg/m^3

u_e = velocity nozzle-exit gas, m/s.

The nozzle exhaust gases normally are underexpanded as they exit the divergent cone of the nozzle, and, as the rocket transverses its altitude range during flight, the jet-pressure ratio increases and the plume and its effects become larger as the ambient pressure diminishes. The highly underexpanded jet plume then affects the aerodynamic flow characteristics acting on the rocket forward of its base. The interaction of the plume with the surrounding flow field tends to cause air flow separation over the vehicle which renders a destabilizing influence on the aerodynamic surfaces of the rocket. This boundary layer separation results in localized conditions where the dynamic pressure decreases. Uncertain and irregular effects on the normal force coefficient occur, and the pitching-moment coefficient varies irregularly with jet-pressure ratio, angle of attack. and Mach number.

Plume effects are also discussed in par. 6-5.6. The effects of jet pluming are treated in greater detail in Chapter 5, "Aerodynamics", pars. 5-3.5 and 5-5.3.

6-4.2.6 Scarf Nozzle

The scarf nozzle, also called a skewed nozzle, is one of which the exit plane of the nozzle is canted or positioned at some angle other than 90 deg with the nozzle centerline. The result of this skewed effect is that the thrust vector is divided into an axial force component and a normal force component. A scarf nozzle may be applied in a rocket to satisfy stability requirements or some other requirement unique to the flight or mission of the rocket.

The normal force characteristics of a scarf nozzle are functions of the skew angle and the jet-pressure ratio. The skew angle is the angle that the nozzle exit plane makes with a normal plane. Wind-tunnel tests have shown that increasing the skew angle steadily increases the normal force to a maximum value that depends upon the jet pressure ratio (Ref. 20). Ref. 20 provides data on normal and axial force characteristics as functions of the jet pressure ratio for skew angles of 30 deg, 4.5 deg, 60 deg, and 75 deg.

6-4.3 MOTOR CASE

6-4.3.1 General

The rocket motor case, or thrust chamber, of a solid-propellant rocket is essentially a high pressure vessel containing the entire solid mass of the propellant, or grain. In addition to designing for the internal pressure, imposed loads can produce various combinations of bending, torsional, and axial stresses. These stresses can be steady-state or dynamic, the latter caused by accelerations over a very wide frequency regime. The deflections are those that are associated with the loads and their manner of application; for aerodynamic and aeroelastic reasons, these deflections must be kept within the elastic range of the material. Since dynamic loads are involved, the problems of resonant vibration conditions are always present, and certain resonant frequencies must be avoided to prevent undesirable vibration mode coupling.

US Army Missile Command investigations (Ref. 21) of errors associated with free flight rocket motors have identified the importance of rocket motor case variabilities (ovality, bow, and overall dimensional reproducibility). Strip-laminated cases provide excellent roundness and straightness characteristics and close dimensional control (Ref. 22). The structural integrity of the strip-laminated case was verified by environmental, hydroburst, and hydroproof testing.

Exit nozzles of the fixed or variable area types used on rocket motors are subjected to drag and pressure loads which produce motor case tensile stresses. Thermal stresses also may be very large, and it is important that appropriate consideration be given to space allowances or expansion and thermal loading of the structure. The motor case influence on nozzle deflection may also be critical to both the structural and performance characteristics.

During steady-state burning, temperatures between 260° and 816°C for different parts of an air-cooled case may be encountered. External pressures present a structural stability problem that is not amenable to very precise analysis inasmuch as the components usually contain a great many discontinuities.

6-4.3.2 Minimization of Weight

Weight saving is an important factor in rocket performance, and minimization of weight is a significant aspect of design. Factors that should be considered in motor-case design are discussed in the paragraphs that follow.

The motor case must be designed for the maximum expected operational pressure (MEOP); this directly influences the weight. The motor performance normally is determined on the basis of the aver-age chamber pressure. Since the case weight is influenced by the maximum anticipated pressure, the ideal situation would be for the average and ideal pressures to be equal. This condition is usually not attainable; therefore, a design optimization process should be applied to bring the value of maximum pressure as near to that of the average pressure as practicable for the purpose of minimizing the case weight.

The weight may be reduced by the careful selection of materials. The material strength-to-density ratio should be kept as low as possible.

The structural configuration has an influence on the case weight. Certain materials (composites) lend themselves to an integral configuration approach. The forward and rear ends of the motor may be

constructed integrally with the cylindrical portion of the case, thus eliminating heavy attachment hardware. Weight-saving advantages of the integral configuration may require a trade-off analysis with cost where twisting nonintegral hardware is readily available.

6-4.4 IDEAL VELOCITY EQUATION

The ideal velocity of a missile system is a measure of the motor performance in a given application. A simplified equation of motion for a rocket in a coordinate direction parallel to the rocket axis is as follows:

$$m\dot{u} = F - mg\sin\Theta - D, \text{ N} \tag{6-41}$$

or

$$\dot{u} + \frac{F}{m} - g\sin\Theta - \frac{D}{m}, \text{ m/s}^2 \tag{6-42}$$

where
$\dot{u}$ = rocket acceleration, m/s^2
m = mass of rocket, $f(t)$, kg
g = acceleration due to gravity = f(altitude), m/s^2
Θ = flight path angle with horizontal plane, deg
D = aerodynamic drag, N.

The ideal velocity is defined as the integral of the first term of Eq. 6-42, i.e., zero gravity and zero drag, over the burning time with the following substitutions:

$$F = c\dot{m} = I_s\dot{m}, \text{ N} \tag{6-5}$$

$$m = m_i - \dot{m}t, \text{ kg} \tag{6-43}$$

where

m_i = initial mass of rocket, kg
t = action time, s.

The ideal velocity u_i is determined as follows:

$$u_i = \int_0^{t_b} \frac{c\dot{m}dt}{m_i - \dot{m}t} = c\ln(MR) = I_s\ln(MR), \text{ m/s} \tag{6-44}$$

where
MR = mass ratio = $m_i/(m_i - m_p)$, dimensionless
m_p = $\dot{m}t_b$ = propellant mass consumed, kg
t_b = propellant burn time, s.

6-4.5 THRUST MALALIGNMENT

The rocket motor performance is dependent on the direction or alignment of the thrust vector. It is important that the rocket performance be predictable and repeatable if an aerodynamically stabilized free rocket is to be accurate and effective; therefore, thrust malalignment must be reduced to an abolsute minimum.

Thrust malalignment occurs when the thrust vector does not pass through the rocket center of mass and results in a turning moment. The turning moment results in variations that contribute to range and azimuth errors. Thrust malalignment is a dominant error source in aerodynamically stabilized free rockets

for short ranges as well as for long ranges. The dispersion due to thrust malalignment maybe minimized to some extent in spinning rockets.

6-4.5.1 Structure Geometry and Alignment

The sources of thrust geometric malalignment fall into two categories-the manufacturing sources that are basically geometric in nature and arise from the tolerance stack and the post-manufacture sources that arise from asymmetric loads and temperature distributions. Two techniques have been identified (Ref. 23) for minimizing thrust malalignment. The first technique is to accept the errors and use an adjustable nozzle to align the thrust vector; the second technique is to develop manufacturing techniques that minimize thrust malalignment. A properly designed adjustable nozzle will allow the geometric nozzle vector to be aligned precisely with the mass center of the assembled rocket round.

The four geometric manufacturing sources of thrust malalignment listed by Ref. 23 are (1) asymmetries or lack of concentricity of the nozzle contour in the nozzle itself, (2) nonalignment at the joint of the motor case and nozzle where either an angular deviation or an offset of the nozzle axis can occur, (3) a lack of straightness of the motor case, and (4) the failure of the rocket mass center to be on the geometric axis to which the alignment tolerances are referenced. The Ref. 23 study investigated methods of eliminating sources 1 and 3.

A lack of straightness of the motor case may be created by the action of chamber pressure, thrust, and acceleration on (1) any asymmetries present in the motor case nozzle structure, (2) wall thickness varia-tions, and (3) bowing created by nonuniform heating. Motor case bow is one of the major asymmetries. The best straightness tolerance (0.96 mrad) was calculated for both the shear forming and the expanding processes: Wall thickness variations induce severe penalties in bow on the rocket case when the motor case is designed for minimum thickness. This problem can be overcome by designing the case for considerably more strength than required by the operating conditions. The largest source of thermal bow is due to nonuniform heating from solar radiation in storage. Proper use of insulation between the shipping container and the rocket will minimize thermal bowing.

6-4.5.2 Propellant Grain and Mass Flow Asymmetries

The chief sources of grain asymmetries are described by Fig. 6-10. Two kinds of asymmetry, i.e., motor case ovality and bow, occur in motor cases and affect the inner chamber wall boundary. Ovality and bow are defined schematically by Fig. 6-10.

Ovality and bow tolerances representative of the various motor case forming processes are summarized in Ref. 23. The best tolerances are achieved either with shear forming, the process by which the case is formed over a rigid mandrel, or in those instances in which an expanding operation is used subsequent to forming.

Mandrel malalignment is also defined in Fig. 6-10. Tolerances on mandrel malalignment are difficult to generalize because they are the result of tolerance stacking of casting fixture components. Analytically (Ref. 23) it was determined that a configured design has less impulse variation than a nonconfigured design for all the malalignment conditions studied. The reason for this lies in the sliver formation process. The circular part of the shell design is theoretically sliver-less, but any asymmetry leads to the formation of a large sliver. Of those studied, the shell was the most sensitive (progressive geometry); the configured grain is only moderately sensitive (neutral geometry); and the slot is the least sensitive (regressive geometry). Mandrel malalignment was the largest contributor to asymmetric grain sources of impulse variation.

Nonuniform chamber combustion conditions, asymmetric entrance or throat conditions, and misalign-ment of the supersonic nozzle contour all lead to gas axial misalignment. The result is a failure of the thrust vector to coincide with the nozzle geometric axis. Theoretical work has shown that the magnitude of the produced turning moments depends primarily on the geometrical shape of the supersonic portion of the nozzle. By adjusting the geometry, it is possible to reduce these turning moments to zero (Ref. 24).

Ovality: Defined as the difference between the major and minor diameters of an equivalent ellipse.
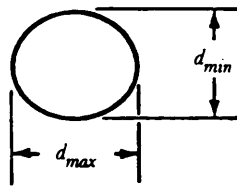
(A) Ovality

Bow: Defined as the amount of departure from a straight line over a fixed length.
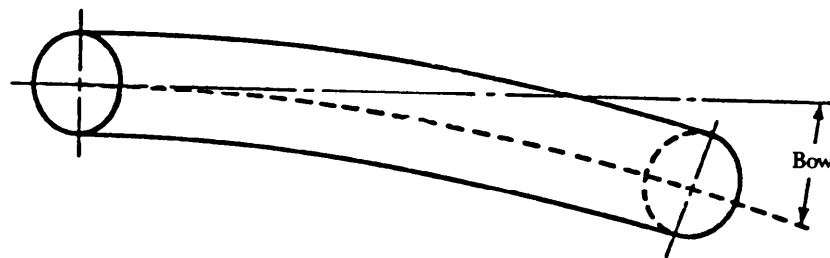
(B) Bow

Mandrel Misalignment: Defined as the amount of offset between the mandrel centerline and the motor case centerline.
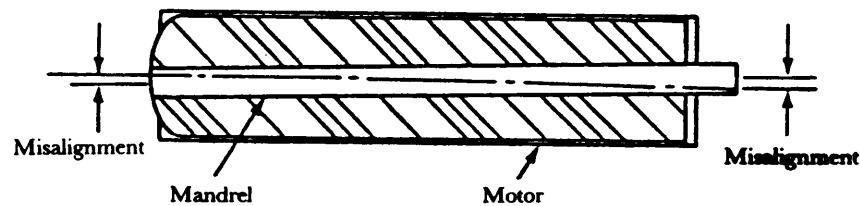
(C) Mandrel Misalignment

Figure 6-10.   Grain Asymmetries Considered

6-4.5.3 Test Environment

Thrust-vector alignment merits attention during firing test preparations and in the conduct of the test. Instrumented measurements are made to verify the performance of the motor and include thrust, pressure, temperature, vibration, propellant burn rates, etc. The test fixture and the instrumentation should be properly positioned and calibrated to verify the alignment of the thrust vector, and care must be taken that the rocket not be malaligned due to the testing environment. Thrust measurements should be determined in both axial and normal components. The resultant thrust vector should coincide as near as practicable with the rocket longitudinal axis.

Testing at different grain temperatures involves heating or cooling the motor, and a uniform temperature of the grain is desired for accurate alignment measurements. Uneven temperature in the propellant grain due possibly to improper heating of the motor or uneven exposure to the sun can lead to false alignment measurements.

False alignment measurements can occur due to the introduction of inadvertent constraints due to improper installations of equipment, bearing friction, instrument connections, etc. The placement of temperature measurement thermocouples on the interior walls disturbs the heat flux and temperature distribution in the junction of the thermocouple.

The testing operation itself often involves a hostile environment for instrumentation that is essential to proper measurements. Instruments, including pickups and transducers, which are subjected to hostile conditions, are subject to failure or giving false readings.

Nozzle erosion (par. 6-4.2.4) can effect alignment during a test firing or in an operational flight. Analysis of test results should include an evaluation of the nozzle erosion characteristics.

6-5 DESIGN CONSIDERATIONS

This paragraph gives the preliminary design engineer sufficient information in the area of motor sizing, combustion considerations, motor case performance, propellant selection, nozzle throat selection, and plume considerations to perform preliminary design trade-off studies for design of a solid rocket motor. The plume considerations include aerodynamics, radiation signature, and impulsive noise (Ref. 25).

6-5.1 MOTOR SIZING

The rocket motor is sized in terms of estimated performance, weight, and envelope dimensions. Motor sizing is an iterative process in which the internal ballistic, aerodynamic, thermodynamic, structural, and fabrication considerations are manipulated within the constraints and requirements to produce a preliminary design configuration (see Fig. 6-11). Careful consideration must be given to each design requirement and each constraint to reach the optimum design for each application. Motor design requirement and constraint parameters are discussed in Refs. 26 and 27.

The major motor design iterations involve the active participation of the designers and the analysts. The common practice is for the designer to use quick sizing techniques including design curves, computer programs, and engineering judgment to lay out the internal and external aerodynamic contours. He then adds pertinent structure, propellant, insulation, liners, and nozzle to the contour. The ballistician, fluid dynamicist, thermodynamicist, and structural analysts then apply more refined techniques to identify questionable areas. The designer uses this information to reconfigure the design, changing materials and moving interfaces as needed, and issues an updated drawing. The analysts then analyze the revised configuration, often with techniques more sophisticated then those thosed previously, and make further recommendations. Fabrication specialists are consulted at this point for suggestions as to cost reduction, elimination of potentially troublesome areas, etc. The incorporation of these suggestions and recommendations usually completes the design process.

One first-iteration approach is that outlined in Ref. 1 in which the designer is provided thrust and burn duration as requirements. A propellant is then selected based on the theoretical ideal relationships for calculating specific impulse, burning rate, and ratio of burn area to nozzle throat area or to select a standard propellant with available experimental properties. The theoretical specific impulse I_s for a rocket is expressed in the following equation for low velocity chamber gases (Ref. 10, pp. 335 and 485):

$$I_s = \sqrt{\left(\frac{2\gamma}{\gamma - 1}\right)\frac{RT_c}{M'}\left[1 - \left(\frac{p_e}{p_c}\right)^{(\gamma-1)/\gamma}\right]}, \text{N·s/kg.} \tag{6-45}$$

A modification of this relationship defines a reduced specific impulse parameter I'_s as a function of the pressure ratio as

$$I'_s = \frac{I_s}{\lambda\phi\left(\frac{RT_c}{M'}\right)^{1/2}} = \left(\frac{2\gamma}{\gamma - 1}\right)^{1/2}\left[1 - \left(\frac{p_e}{p_c}\right)^{(\gamma-1)/\gamma}\right]^{1/2}, \text{dimensionless} \tag{6-46}$$
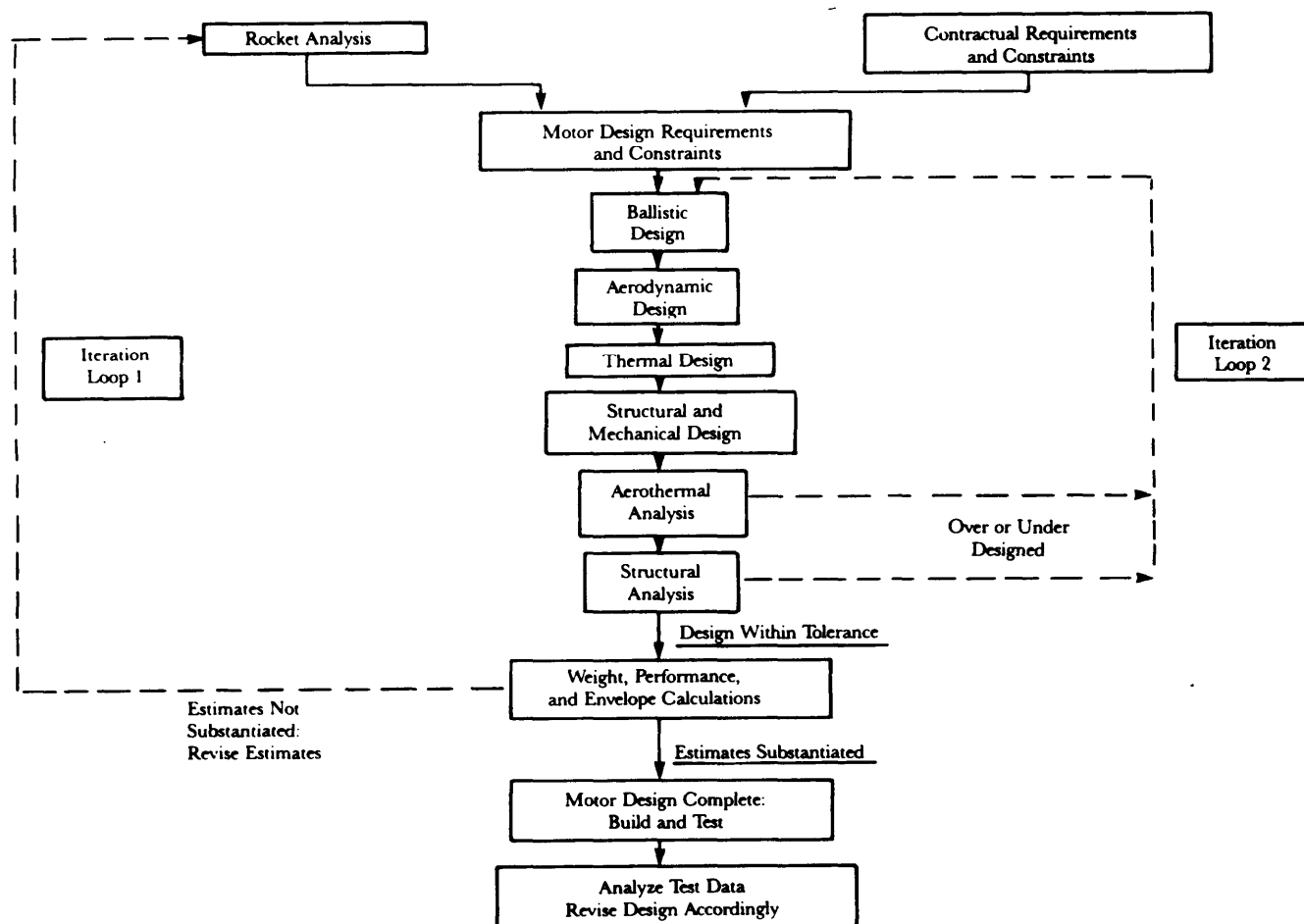
Figure 6-11.   Flow Chart of Motor Design Sequence Showing Major Iteration Loops (Ref. 26)

where

λ = nozzle angle correction factor, dimensionless

ϕ = nozzle velocity coefficient, dimensionless.

Fig. 6-12 provides a theoretical plot of the reduced specific impulse parameter I'_s versus normalized chamber pressure p_c/p_e. Empirical propellant burn rate relationships based on gas theory are provided by Eqs. 6-11 through 6-13. Theoretical values for the area ratio may be obtained from Fig. 6-4. Measured propellant data are provided by Fig. 6-13. These figures indicate specific impulse $I_s = c$, burning rate $\dot{r}$, and area ratio $K = A_b/A_t$ as a function of chamber pressure p_c.

The average chamber pressure p_c, used for this analysis, is chosen to be no lower than 689 kPa above the lower combustion pressure limit and no higher than the expected average pressure trace for the selected propellant. The specific impulse, burn rate, and area ratio can be obtained once the combustion chamber pressure p_c is established. This allows calculation of the required propellant mass m_p as follows:

$$m_p = \frac{Ft_b}{I_s} , \text{kg.} \tag{6-47}$$

The required web thickness, burning surface area, nozzle throat area, and chamber volume are calculated using the following relationships:
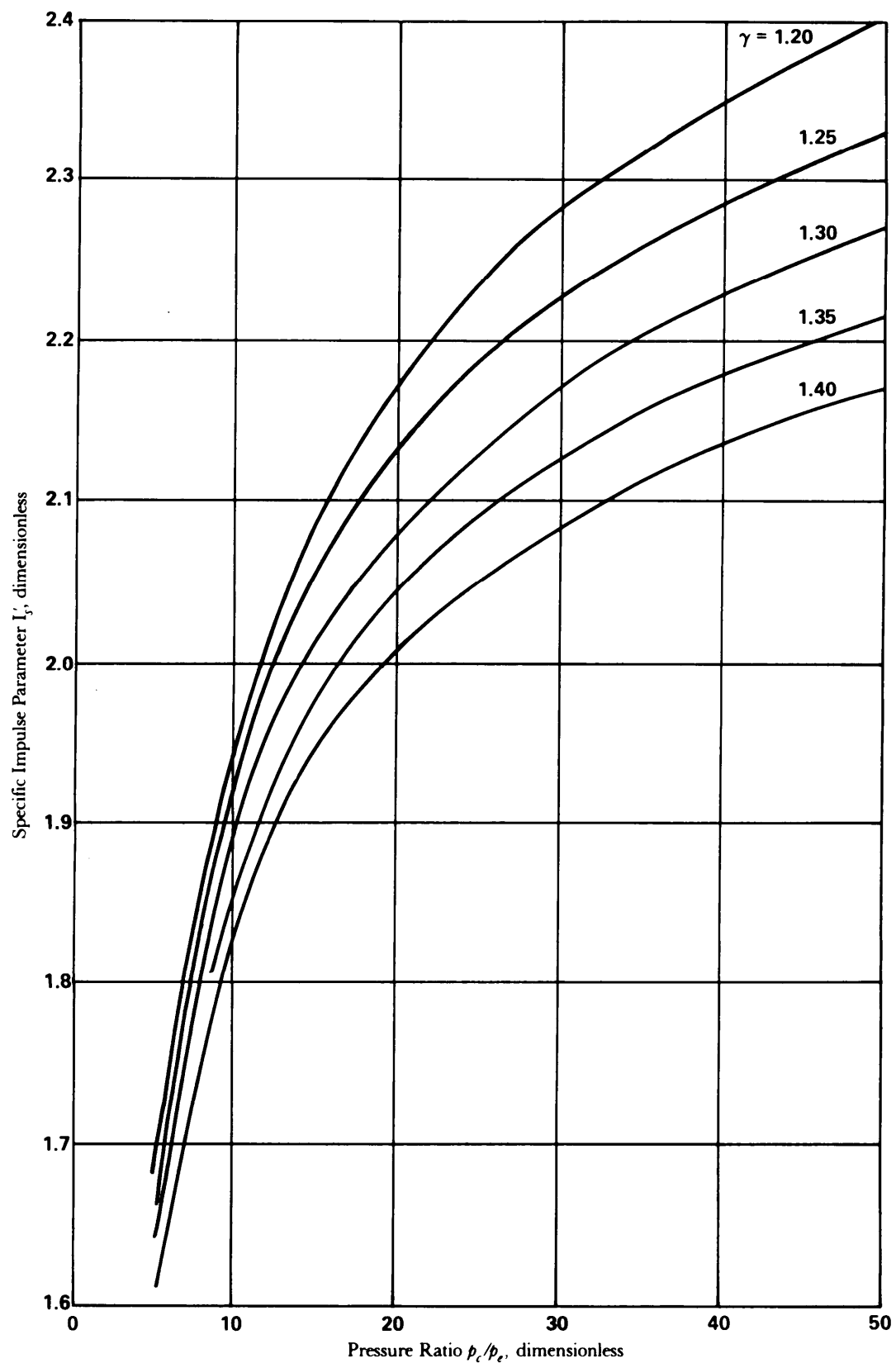
Figure 6-12. Specific Impulse Parameter as a Function of Pressure Ratio for Different Specific Heat Ratios
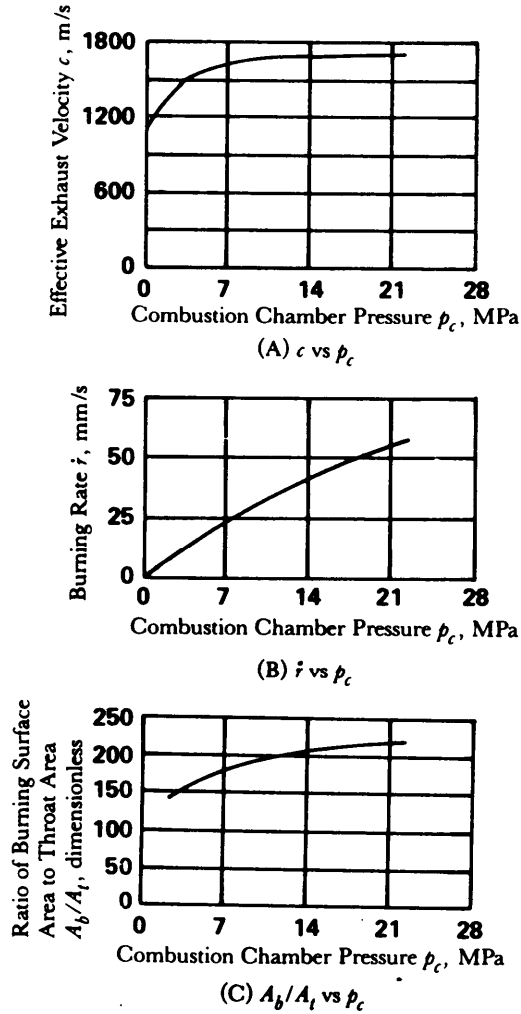
Figure 6-13.   Typical Characteristic Curves for a Solid Propellant (Ref. 1)

$$\tau = \dot{r}t_b, \text{ m} \tag{6-48}$$

$$A_b = \frac{m_p}{\tau\rho_p} , \text{ m}^2 \tag{6-49}$$

$$A_t = \frac{A_b}{A_b/A_t} = \frac{A_b}{K} , \text{ m}^2 \tag{6-50}$$

$$V_c = \tau A_b\omega, \text{ m}^3 \tag{6-51}$$

where

τ = propellant web thickness, m
A_b = burning surface area, m^2
A_t = nozzle throat area, m^2
ρ_p = propellant density, kg/m^3
$K = A_b/A_t$, dimensionless
V_c = combustion chamber volume, m^3
ω = propellant volume correction factor, dimensionless.

The propellant volume correction factor w may vary from 1.2 to 6.0 for unrestricted burning units. Eqs. 6-47 through 6-51 provide basic relationships for the parameters necessary to predict the motor internal ballistics.

6-5.2 COMBUSTION CONSIDERATIONS

Both experimental and theoretical techniques are employed in the analysis of the combustion mechanisms of solid propellants. Conditions that must be considered are ignition requirements, pressure-temperature environment for steady state combustion, performance requirements, stagnation conditions, burning rate, erosive burning, and combustion instability. Detailed design information on the theoretical and experimental aspects of combustion, including correlations and measured data, is given in Ref. 27, Chapters 5-10.

Burning characteristics for a given propellant vary with variations in the combustion chamber conditions. Chamber pressure is the principal design parameter that affects the combustion of the propellant grain. Other factors are temperature, port dimensions, propellant characteristics, etc. The chamber pressure directly influences burning rate, combustion gas properties, erosive burning, mass flow rate, and thrust. At very low chamber pressures the combustion becomes unsteady or may cease altogether. The low pressure at which this condition occurs is called the combustion limit for a particular propellant. There is no practical upper pressure limit.

The gas laws for isentropic flow generally apply in the determination of thermodynamic conditions in a rocket motor. Terms in these equations usually relate to stagnation conditions in the combustion chamber. This condition—derived from Eq. 6-26—can be expressed in the following equation for stagnation specific enthalpy:

$$h_c = h + \frac{u^2}{2}, \text{ J/kg}$$

where

h_c = chamber stagnation specific enthalpy, J/kg

h = static specific enthalpy at a point near stagnation condition, J/kg

u = velocity of gas at point corresponding to h, m/s.

The stagnation pressure is practically equal to the static pressure at the head end of the chamber due to the low flow velocity at the point. The static pressure decreases and the velocity increases as the distance from the chamber head increases. The magnitude of these changes is a function of the ratio of the open port area to the throat area. All states along the chamber port lie in a line of constant entropy and have the same stagnation temperature. The state of zero velocity is called the isentropic stagnation state.

The burning of the propellant grain is initiated by an igniter, usually of the pyrotechnic or the pyrogen type, that is located in the combustion chamber. The ignition system (igniter plus nozzle closure) must provide sufficient surface heating for ignition and provide a chamber pressure high enough to sustain steady combustion. It is necessary to achieve ignition over a relatively large surface area to assure proper recession of the burning face.

Burning rate and erosive burning were discussed in par. 6-4.1.1. Figs. 6-14(A), (B), and (C) present composite propellant burning rate versus pressure for several values of local port velocity for propellant compositions A, B, and C (Ref. 27). These figures show a burning rate sensitivity to pressure as the gas velocity in the central port increases. The erosive burning effect must be considered in the preliminary design of a solid propellant rocket.

Rocket motors are sometimes subject to combustion instabilities in the form of pressure oscillations within the chamber. Such instabilities may change burning rate, erosive burning characteristics, heat transfer rates to the grain or to the hardware, or chamber pressures. Engine failure may result due to increased pressure or increased wall heat transfer. Corrective measures usually involve expensive experimental studies. Instabilities have been reduced by the placing of an irregular rod of nonburning material
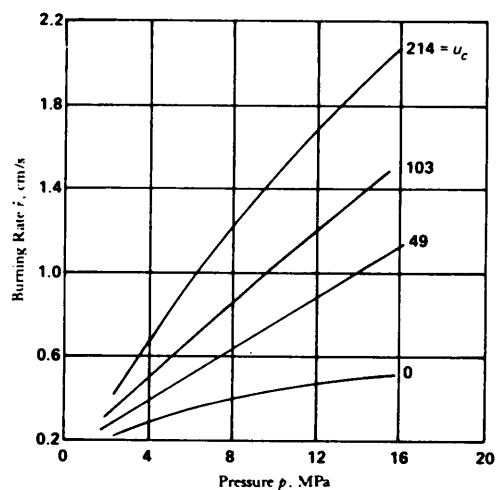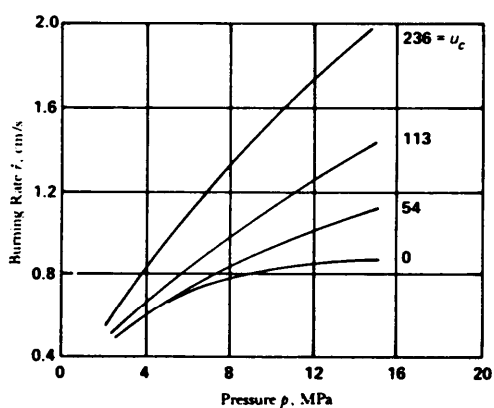
(A) Propellant A

(B) Propellant B
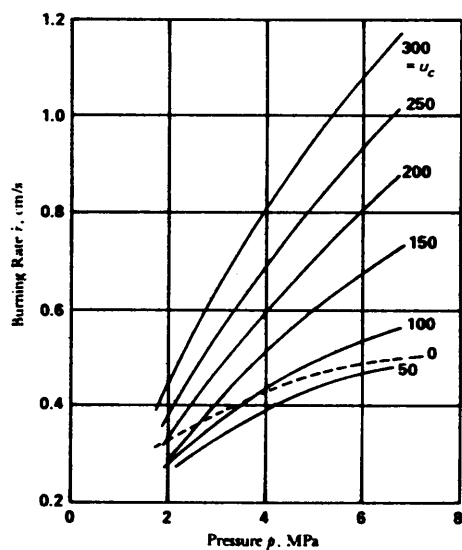
(C) Propellant C

Figure 6-14.   Influence of Pressure and Gas Flow Velocity of Burning Rate

within the burning volume. Radial holes drilled at intervals in the propellant grain have also been found to reduce instabilities.

6-5.3 MOTOR CASE PERFORMANCE

The motor case, or combustion chamber, is designed to contain the propellant grain and has to withstand pressure, starting surges, and often severe heating. The design must allow for uneven pressure distributions, pressure surges, etc. The physical properties of the stress-carrying members vary, depending on the internal pressure of the chamber and the temperature experienced by the wall or other components. As the temperature of the load-carrying member increases, its ability to carry load diminishes. The most important parameter is the design pressure, referred to as the maximum expected operational pressure (MEOP). As a first guess, the MEOP may be estimated to be 110% of the maximum measured pressure or 120% of average measured pressure. In both cases, the pressures should be obtained from the maximum propellant grain temperature tests.

A typical motor case consists of a cylindrical wall section, a forward closure or dome, an aft closure, a forward skirt, and an aft skirt. The forward closure is usually hemispherical or elliptical in shape. The aft closure contains a nozzle attachment flange with a nozzle flange pressure seal. The motor case design involves trade-offs among overall missile performance, compatibility with other systems and components, and cost. Weight is a very important performance parameter (par. 6-4.3.1). Therefore, attention to design details is required to obtain greater structural efficiencies through the use of high-strength materials. The propellant mass fraction ζ (Eq. 6-88) is a useful performance parameter, i.e., a measure of the design loading efficiency. It may be defined as the ratio of the loaded propellant mass to the total motor mass. Solid propellant motor mass fractions vary from about 0.3 to 0.96. Due to the sensitivity of performance to mass or weight, the motor case should be optimized for the minimum inert weight.

6-5.3.1 Material Selection

The motor case is exposed to extreme thermal, corrosive, and dynamic conditions, and it is usually pressure critical. The most efficient materials that satisfy the structural loading conditions at the critical operating environment should be selected. The case must have the capability to withstand the internal pressure, vibration, and thermal cycling and to resist buckling, fracturing, fatigue, cracking, and corrosion.

The material selection should consider aerodynamic heating (boundary layer and local heating at appendages), internal heating from burning of the propellant, and radiant and conductive heating during handling, assembly, test, and checkout. Thermal conductivity, thermal diffusivity, and the thermal coefficients of expansion must be taken into account when applications involve thermal stress and thermal fatigue.

The structural materials used most frequently for rocket motors are metals and composite materials (Ref. 26). The metals include steel, aluminum, and titanium. occasionally, relatively high operating temperatures dictate the use of tungsten, molybdenum, columbium, or a Haynes alloy. The composite materials consist of some type of fibrous roving, tape, or cloth bonded together in a phenolic or epoxy resin system. The elastic and strength properties of these composite materials vary widely with respect to type and orientation of the reinforcement system and the binder system used.

Some lightweight designs use honeycomb materials in the areas where elastic stability is a problem. Both metal and fiberglass are used for the facings, and the core material is usually aluminum or fiberglass.

The aluminum, steel, and composite materials are used as cases, compliance rings, attachment flanges, and brackets. Molybdenum and columbium generally are used in the structure of the nozzle load-carrying members because of the structural material strength requirements at elevated temperature.

High-modulus composite materials are used for motor structures in which weight and/or stiffness requirements dictate their use. Materials available include Kevlar 49 epoxy, graphite epoxy, boron epoxy, glass epoxy, phenolics, and PRD-49. The VIPER and PERSHING II are two recent rocket systems that use composite material for a motor case.

In most motor designs, epoxy adhesive is used for-both adhesive and sealant functions. Epoxy adhesives that cure at room temperature are most common; however, adhesives that cure at elevated temperatures are used for some applications, pw-titularly if the adhesive must function in the design at an elevated temperature. Curing at an elevated temperature may result in gaps caused by thermal expansion differences between the adhesive and the components to be bonded.

The internal motor case insulation, used in the forward and aft closures of most motor cases, protects the case structure from heat and erosion while the motor is operating and limits the maximum temperature in areas where other components are attached. Internal motor insulation is needed wherever the motor case is not protected by the propellant and where the propellant is thin as shown by Fig. 6-1.

The insulating materials commonly used on the inside of motor cases are the ablative materials. They have relatively low thermal conductivities and partially decompose to form gases or vapors when exposed to very high temperature. This process absorbs heat caused by the endothermic reactions involved, and the ablative gases shield the insulation material from the combustion gases. Insulation materials may be rigid, flexible, or semiflexible, and their application depends on the system requirements.

6-5.3.2 Safety Factor

Safety factors or margins in a specific motor case design will reflect the design philosophy of the overall system. Safety factors are influenced by (1) the amount of analytical effort budgeted in the design and analysis phase; (2) the degree of characterization available for the elastic, thermal, and erosional properties of materials being used; (3) the similarity of the basic design to previous successful designs with respect to materials and geometry; and (4) the end use of the rocket. Since performance requirements require a lightweight motor case that will function safely and reliably, the safety factor must be selected to be as low as practicable and yet be consistent with the operating reliability requirements.

6-5.4 PROPELLANT SELECTION

A propellant is a composition of matter, stable at room temperature, which, when ignited, evolves gas continuously at high temperatures without dependence on the atmosphere for the combustion process. It must hold its shape over an extended temperature range and must withstand the stresses imposed on it during handling, storage, ignition, and firing in a rocket. The selection of a solid propellant depends on its application and the mission that must be accomplished.

The oxidizer should have a high oxygen content and high density, produce a large number of moles of gas, have a low heat of formation, be nonhygroscopic, have low cost, and in some cases be smoke free. Fuel binders and fuels are selected for their ability to be oxidized and are responsible for the mechanical properties and processing characteristics of the solid propellant. The fuel binder should be resistant to interaction with the oxidizer to obviate degradation of the propellant during aging and storage.

The factors to be considered in judging the merit of a solid propellant for a given application are specific impulse, density of propellant, hygroscopicity, controllable linear burning rate, coefficient of thermal expansion, thermal conductivity, chemical stability, toxicity, shock sensitivity, explosive hazard, smoke in exhaust, attenuation of electromagnetic signals, availability of raw materials, fabrication and process control, and cost. All of these factors are discussed in Ref. 5.

6-5.4.1 Thermochemical Considerations

Thermochemical considerations may be evaluated for conditions in the combustion chamber and for conditions in the nozzle. Chamber conditions include the combustion temperature, the composition of the reaction products, and the mean molecular weight and the specific heats of the gases. This information is useful in the determination of heat transfer, nozzle conditions, and other chamber criteria. Evaluation of the nozzle conditions include motor parameters (specific impulse and characteristic exhaust velocity) and combustion product conditions (composition, molecular weight, temperature, specific heats, etc.).

The kinetic energy of the exhaust gases of the rocket motor is derived from the thermochemical energy of the combustion of the propellants. The chemical reaction is exothermic and involves the evolution of large quantities of gases. The combustion is associated with changes of identity of the chemicals involved.

A high heating capability is a desirable property of propellants to give a high specific impulse. The combustion energy released is the sum of changes in chemical energy due [o the electronic processes and the change in thermal energy due to the motion of atoms and molecules. This energy is called the heat of reaction or the heat of formation. The content of thermal energy in the propellant is the enthalpy h (par. 6-4.2.1), and the change in enthalpy Δh is given by

$$\Delta h = \int_{T_1}^{T_2} c_p dT, \text{ J/kg.} \tag{6-52}$$

A high heat of combustion per unit volume of propellant is an important consideration in propellant selection which makes possible a smaller rocket size. The bulk specific gravity should be large to minimize the volume requirements for the propellant. This can be accomplished by the addition of solid particles such as aluminum. There may be a need for some compromise between specific impulse and propellant density since solid particles do not transfer heat rapidly, are unable to expand, and can cause erosion of the nozzle.

6-5.4.2 Burn Rate

Propellant burning rate can be characterized theoretically in terms of combustion pressure and ambient grain temperature and can be expressed by the empirical Eqs. 6-11 through 6-13 (par. 6-4.1.1). The actual burning process is a complex function of the chemical composition, the method of propellant preparation, the action or burning time, the shape of the grain, and the gas velocity adjacent to the grain. Since this process is complex and is not well understood, the burning rate is often determined empirically based on measured test data.

High-velocity gas parallel to the grain surface has an erosive effect and is referred to as erosive burning. Erosion is characterized by an increase in burning rate and is expressed in terms of an erosive rate coefficient ϵ as defined by

$$\epsilon = \dot{r}/\dot{r}_0, \text{ dimensionless} \tag{6-53}$$

where

$\dot{r}$ = burning rate with erosion, m/s

$\dot{r}_0$ = burning rate of the same propellant without erosive gas flow, m/s.

The erosive rate is a function of the gas velocity or the mass-flow rate. This function can be expressed as the empirical relation (Ref. 1)

$$\epsilon = 1 + k\dot{m}/\dot{m}^*, \text{ dimensionless} \tag{6-54}$$

where

k = propellant erosion burning constant, dimensionless

$\dot{m}^*$ = mass-flow rate that produces a Mach number of 1 in the constant cross-sectional area channel, kg/s.

The erosion constant k varies inversely with the burning rate $\dot{r}_0$.. Typical values are shown in Fig. 6-15. Eq. 6-55 gives an example of the burning rate; when Robert's law (Eq. 6-11) is corrected for erosion, i.e.,

$$\dot{r} = \epsilon b p^n, \text{ m/s} \tag{6-55}$$

where

n,b = empirical constants.
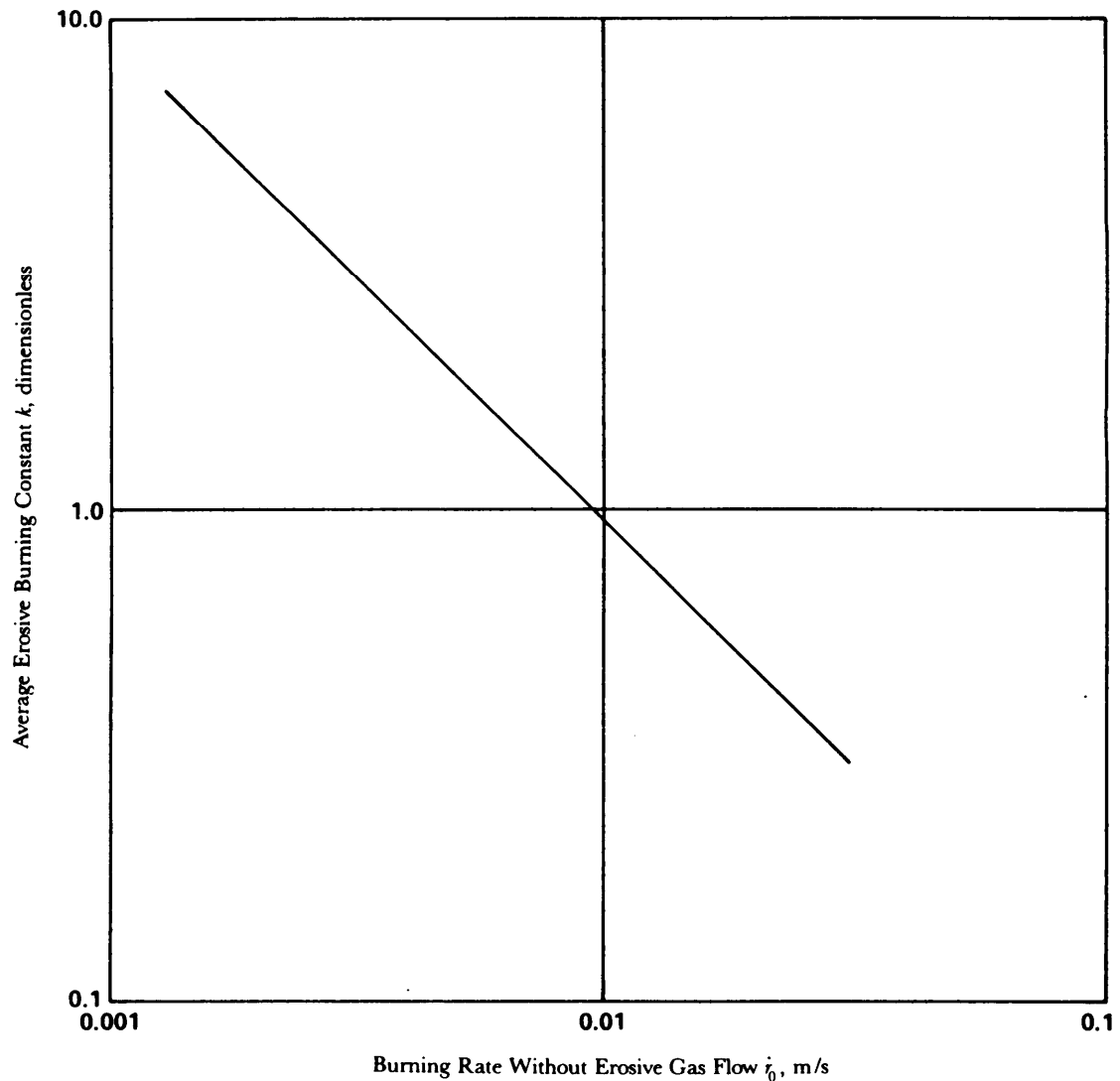
Figure 6-15. Typical Variation of Erosive Constant With Burning Rate

For most restricted burning propellants, n has values between 0.4 and 0.85 and is essentially independent of the initial grain temperature. The constant b has values between 0.05 and 0.002 and varies with initial grain temperature. A state-of-the-art comparison of industrial burning rate models is provided by Ref. 28 for composite propellants.

Since the burning rate depends upon the composition of the propellant, the burning rate can be controlled very efficiently within limits by a proper choice of catalysts and oxidizer particle size.

In addition to chemical means, there exists physical means for controlling the burning rate. Addition of suitably shaped heat conducting materials to the propellant is an effective way to obtain an increased burning rate that is needed for achieving a specified regression rate or burning rate history. The most widely used technique consists of introducing metal wires into the grain during the casting process. Silver threads a few hundredths of a micron in diameter are the most efficient.

One can also exploit erosive phenomena by designing the grain with slits through which the hot gases flow in patterns that increase the erosive effect. Typical burning rates for a few applications are given in Table 6-4.

TABLE 6-4
TYPICAL PROPELLANT BURNING RATES

Application	Burning Rate $\dot{r}$ mm/s
Booster	25.4-254
Sustainer-Motor	5.08-25.4
Separation	25.4-254
Spin-Motor	2.5.4-254
Space Applications	1.27-127
Gas Generator	0.254-5.08

6-5.4.3 Signature

Rocket exhaust signatures (Ref. 25) are created by smoke particles and infrared radiation in the rocket plume that may be visible to an enemy or contain exhaust products that interfere with communications. The radiation signature of a rocket is greater if metal particles are added to the propellant. Normally, metallic additives are not used in propellants in which signature is important. One of the following crystalline high explosives, HMX (cyclotetramethylene tetranitramine) and RDX (cyclotrimethylene trinitramine), may be included in smokeless (nonmetal) propellant formulations to achieve improved performance characteristics. Relatively high percentages, e.g., 45%, may be used in double-base propellants, and small percentages are used in composite and composite double-base propellants to ensure efficient combustion, increase the burning rate, and improve specific impulse (Ref. 1).

Smokeless propellants comprise a separate area of study and new information is being developed. Ref. 29 provides information on this subject.

6-5.4.4 Mechanical Properties

Solid propellant grains are viscoelastic materials. Many structural problems for propellant grains can be solved with sufficient accuracy by using methods lying within the domain of infinitesimal liner elasticity. However, there are problems associated with grain slump, reinforced grains, grain flow (creep), and with finite deformations which require viscoelastic concepts for analysis. Many of the numerical techniques for the stress analysis of grains of complex geometries now employ viscoelastic equations when accurate stress analyses are required. Both double-base and composite propellant grains exhibit significant time-dependent mechanical properties and, therefore, must be considered as viscoelastic materials.

Structural analyses are performed to determine whether deformations and stresses are within safe working limits. Stress analysis should be made for a variety of the more severe conditions-such as sudden application of internal pressures and high surface temperatures during motor ignition, high axial accelerations during rocket flight, and long-time oscillations during transportation or storage of the grain—that the motor is expected to experience.

A viscoelastic stress analysis is presented in Ref. 27 for infinitely long, hollow, tubular grains with circular ports. The phenomenological theory of linear viscodasticity is dealt with by representing the viscoelastic properties in terms of Boltzmann's superposition principle. This method does not provide solutions for the more complex geometries; however, it is a relatively accurate and simple analysis. The effects of the external motor case, motor spin, ablation (or burning) of the internal surface of the grain, nonisothermal temperature distributions, axial acceleration, and wire reinforcement of the grain are all discussed.

Analyses of the star grain can also be approached by finite-element methods (Refs. 30 and 31), photoelastic experiments (Refs. 32, 33, and 34), or the conformal mapping technique (Refs. 35 and 36).

Solid propellant grain deterioration can result in motor failure through the formation of fissures in the propellant, which rapidly increase the burning area and result in a sudden increase in combustion pressure. The increased pressure can rupture the motor case. The safe tensile loading region for a

propellant can be determined from measured stress-strain data Aging and the environmental history have a deteriorative effect on the stress-strain properties of a propellant. An analysis of stress versus strain under aging conditions should be made to determine the influence of aging on the structural integrity.

A high density propellant may be desired. High density of the propellant permits the use of a small chamber volume and therefore a small chamber weight.

6-5.4.5 Combustion Stability

The combustion pressure of a burning solid propellant may increase almost instantaneously to a value several times the equilibrium value when an inherently unstable resonant cavity is excited. The pressure increase usually occurs with internal grain configurations. and there is little evidence of its occurrence with external-burning configurations. Combustion instability appears to be more prevalent with the higher performance propellants. The phenomenon of combustion instability is difficult to analyze, but new analytic tools are under development. Combustion instability is also discussed in par. 6-5.2.

6-5.5 NOZZLE THROAT SELECTION

A nozzle throat cannot be selected or designed independently of the rest of the motor. Because of this interrelationship, nozzle throat design is an iterative process in which internal ballistic, aerodynamic. thermodynamic, structural, and fabrication considerations are iterated to provide a design that meets the requirements and constraints. The nozzle design iterative process is included in the motor sizing (par. 6-.5.1 discussions related to Fig. 6-11.

Aerodynamic structural, and fabrication considerations are included under general considerations. The internal ballistics are discussed in terms of propellant grain. burn rate. and throat area interaction in 6-.5..5.2. Thermodynamic considerations are included in par. 6-5.5.3.

6-5.5.1 General Considerations

The scope of this paragraph will be limited to discussions regarding the design of the de Laval nozzle since it is the one most often used, and the design of the convergent portion of this nozzle applies to subsonic and sonic nozzles.

Basic nozzle nomendature for both a submerged and external de Laval nozzle is presented by Fig. 6-16 (Ref. 26). The external nozzle is entirely external to the combustion chamber. The nozzle entry,m throat, and part on all of the exit section are cantilevered into the combustion chamber for the submerged nozzle configuration.

Analysis of the nozzle is comprised of both aerothermal and structural analyses. Aerothermal analysis encompasses definition of combustion-product thermodynamic properties and composition, transport properties determination, aerodynamic analyses, heat transfer analyses, and material response analyses Par 7-7. "Structures", provides a detailed description of the aerothermal analysis.

6-5-5.1.1 Gas Dynamics

A major design consideration consists of configuring the nozzle surfaces exposed to the exhaust gases in a manner such that the conversion of thermal energy to kinetic energy is a practical maximum consistent with other design constraints. In general terms. maximum practical energy is extracted by maintaining a smoothly accelel-sting flow through the nozzle. Design philosophy for nozzles is included in Refs. 26, 27, 37, 38, and 39.

Gas dynamic analysis of rocket nozzles involves calculations of the inviscid flow properties. These properties are then used to calculate the viscous flow field from which the convective heat transfer coefficient is determined. These properties are also needed to calculate the nozzle thrust coefficient and the aerodynamic loads. The velocity flow regimes through nozzles are subsonic, transonic, and supersonic. The subsonic flow can be analyzed by using the finite-difference technique of Ref. 40: the transonic flow field can be analyzed using the techniques of Ref. 41. Supersonic flow can be analyzed by the method of characterisics (Refs. 42 and 43) or the axisymmetric two-phase gas performance program (Ref. 44). For

nonequilibrium flow field analysis. the Ref. 45 computer program is available. The programs of Refs. 44 and 45 require specification of the propellant. relaxation rates, and nozzle geometry.

6-5.5.1.2 Structural Considerations

The structural and mechanical design phase consists of configuring the basic srtuctural framework to support the insulators and liners and carry the nozzle loads. The nozzle structure is configured to meet the most critical design requirements.

The basic structure of both external and submerged nozzles (Fig. 6-16) is subjected to internal pressure loads, thermal loads, and flight loads. The internal pressure load is divided into an axial ejection (blowout) load and an opposing axial thrust load. The flight loads include aerodynamic loads, inertial loads, and vibration loads. In addition to these loads, the submerged structure of a submerged nozzle is subjected to chamber pressure loads.

Several methods-bolted joint. threaded attachment, snap ring, key joint, and lockwire joint—for attaching the nozzle to the chamber are in common use. Each of these joints has advantages and disadvantages (Ref. 27).

Flow ➡
Thermal Liner
Throat
Insulator
Structure
Exit
Entrance
Combustion Chamber

(A) External Nozzle

Flow ➡
Thermal Liner
Throat
Entrance
Structure
Exit
Reentry
Combustion Chamber

(B) Submerged Nozzle
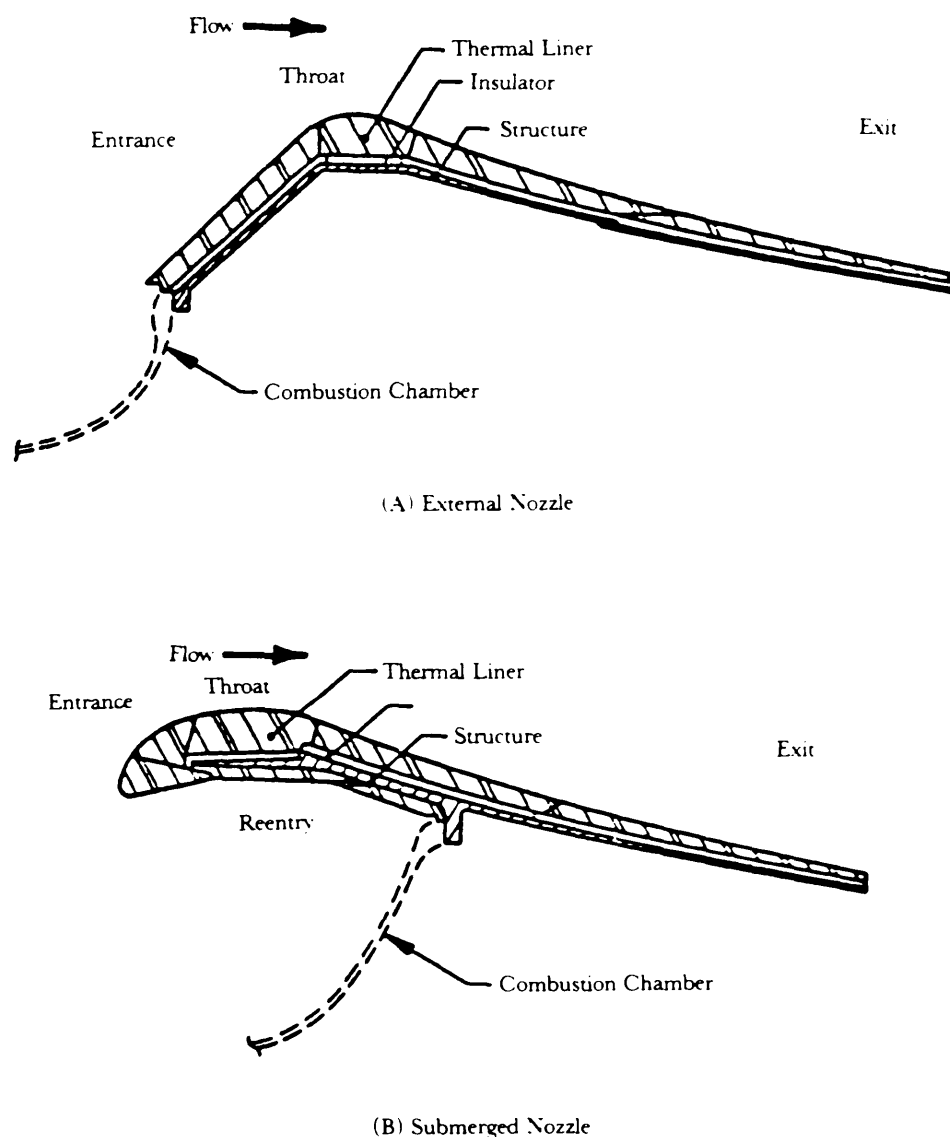
Figure 6-16.   Illustration of Basic Nozzle Configurations and Nozzle Nomenclature (Ref. 26)

Structural analyses of the nozzle encompass prediction of stress distribution, calculation of structural deflection, and prediction of thermal-mechanical effects. Detailed analyses of nozzle structure are accomplished almost universally with computerized finite-element methods for shell structures. Descriptions of the programs for finite-element analysis are included in Chapter 7.

6-5.5.1.3 Fabrication Considerations

A major fabrication consideration is the ability to maintain geometric alignment of the motor case and nozzle when exposed to internal pressure and external loads in order to minimize the malalignment effects (Chapter 3) of the resultant thrust vector. Fabrication processes for ablative materials are dependent on the types of materials to be processed, the desired physical properties, and the fiber orientation characteristics of the end-item. Bias tape is used for those components that require that the tape edge has the preferred orientation with respect to the nozzle exhaust gases and that can be wrapped at angles from 0 deg to 90 deg with the centerline. Bias tape wrapped parts are cured in hydroclaves, autoclaves, and presses. Straight tape is used where high strength and low thermal conductivity is a requirement. Molded components are used as insulators, entrance area components, and exit cones of the lower performance nozzles. Lay-ups are used in areas where interply shear load capability cannot be obtained by other means of manufacture. Ablative materials are applied in high performance nozzles. An illustration of thermal protection materials used in a nozzle is given in Figs. 6-16 and 6-17.

Item	Material	Function
1	Graphite/phenolic tape	Entrance thermal liner
2	Asbestos/phenolic tape	Entrance insulation
3	Polycrystalline graphite	Throat insert
4	Silica/phenolic tape	Throat insulation
5	Graphite/phenolic tape	Exit thermal liner
6	Asbestos/phenolic tape	Exit insulation
7	Steel	Attach structure
8	Glass-cloth/epoxy laminations	Entrance, throat, and exit structure

Figure 6-17.   Nozzle for PERSHING First Stage (Ref. 26)

Metal manufacturing processes are dependent on the size of the component, material type, tolerances, configuration, surface finish, and heat treatment requirements. Metal manufacturing processes for nozzles include forging, welding, and spinning. Fabrication techniques are discussed in more detail in Ref. 39.

6-5.5.2 Propellant Grain/Burn Rate/Throat Area Interaction

The burning rate of the propellant can be shown to be related to the equilibrium chamber pressure by considering mass flow through the nozzle and the mass of gas generated at the propellant burning surface The nozzle throat mass-flow rate is obtained from the expression for characteristic velocity, Eq 6-8. The rate $\dot{m}$ of gas generation at the burning surface is given by Eq. 6-17. Setting the flow rate from these two equations equal to each other yields the following expression for burning rate $\dot{r}$:

$$\dot{r} = \frac{p_c A_t}{c^* \rho_p A_b} = \frac{p_c}{c^* \rho_p K}, \text{ m/s} \tag{6-56}$$

$$K = \frac{A_b}{A_t}, \text{dimensionless} \tag{6-57}$$

$$c^* = \sqrt{\frac{1}{\gamma}\left(\frac{\gamma + 1}{2}\right)^{(\gamma+1)/(\gamma-1)} \frac{R T_c}{M'}}, \text{ m/s.} \tag{6-58}$$

The substitution of Robert's law for the burning rate, Eq. 6-11, into Eq. 6-56 gives the following expression for stagnation chamber pressure p_c:

$$p_c = (b\rho_p c^*)^{1/(1-n)} K^{1/(1-n)}, \text{ Pa.} \tag{6-59}$$

The introduction of the symbol ψ for the first term of Eq. 6-59 yields

$$p_c = \psi K^{1/(1-n)}, \text{ Pa} \tag{6-60}$$

where

ψ = combustion chamber-pressure parameter constant, Pa.

The relationship between p_c and K (Eq. 6-59) is one of the most useful parameters for solid propellant calculations since ψ is basically a propellant property and K is a design parameter that is under some control by the designer.

6-5.5.3 Thermodynamic Considerations

Fig. 6-17 illustrates the thermal protection system for a nozzle. The objective of the thermal-design phase is to maintain a reasonable nozzle aerodynamic design and to limit the temperature of the structure to acceptable levels. A thermal liner forms the nozzle aerodynamic contour, the surface of which is exposed to the exhaust-product flow. An insulator is a material placed behind a liner to serve as a thermal barrier to protect the structural member from excessive temperature. A single material thickness often serves as both liner and insulator. A throat insert is a special erosion-resistant liner placed in the throat area.

In practice, the throat insert and other liners usually are designed first, followed by the insulators. Liner and throat-insert materials usually are selected for erosion resistance, and insulator material is selected for low thermal diffusivity. The materials suitable for liners are, in general, considerably more expensive than those suitable for insulators; so liner use generally is minimized. The use of throat inserts usually is limited to the throat region because of the high cost of inert materials and the special support and retention provisions required for use.

Six groups of materials have been evaluated as nozzle throat inserts, namely, reinforced plastics, polycrystalline graphite, pyrolytic graphite and pyrolytic graphite codeposited with silicon carbide, refractory metals, carbon or carbon composites, and ceramics. The first four materials are in common usage, and the carbon or carbon composites (also called fibrous graphites or prepyrolyzed composites) are

in advanced development. The ceramics presently have poor thermal shock characteristics; currently, they are not considered usable by nozzle designers for solid rocket application. Typical properties of materials **used** as throat inserts are provided in Ref. 26.

6-5.6 PLUME CONSIDERATIONS

The rocket motor and nozzle designer must consider adverse jet plume effects during launch, during transonic acceleration, and during all of the boosted flight. Jet plume effects are also discussed in par. 6-4.2.5.

6-5.6.1 Aerodynamic Effects

Plume effects can penalize the rocket aerodynamics during launch due to blowback (backflow) and flow field residue from a previous firing. Plume residue from earlier firings can cause nonsymmetric loading on subsequent rocket firings for multi launch tube launchers. This effect can be eliminated by allowing sufficient time between firings for the plume gases to disperse. Blowback past the rocket and launcher guidance mechanisms can result in nonsymmetrical loading on the rocket (Ref. 46). When an underexpanded plume impinges on a constriction in a launcher, a system of shocks is created which can result in a transonic plume backflow through the front of the launcher. This backflow may create a "tip-off" condition if the rocket exhaust encounters a flow restriction (choked flow). par 8-3.4.1, "Launcher Considerations", presents information with illustrations of this effect.

Dispersions are caused by rocket plume-induced flow separation (Refs. 47 and 48). Separation of the flow over the aft portion of the body can result from the interaction of the expanding rocket exhaust gases will the external flow field about the rocket. This results in erratic transient aerodynamic forces and moments on the rocket which can differ greatly from those during jet-off flight condition. The severity of this problem depends on the exit conditions of the flow from the nozzle and the free-stream Mach number. Generally, the higher the thrust, the more severe the problem. A problem is more likely to occur at transonic speeds. It can be controlled by nozzle shaping (to reduce the radial flow velocity at the exit plane) and by reducing the thrust. The adverse effects of the plume on the fins can be alleviated by moving the trailing edge of the fins a minimum of 1.5 calibers forward of the nozzle exit plane.

Fre rocket technology program studies have indicated that it is desirable to have a slightly unstable condition during the transonic boost region as a means of reducing dispersions due to wind. This stability effect is explained in par. 4-4.4, "Accuracy". The fin location may be moved forward in the plume-induced flow-separation region to a point at which this stability characteristic is created and the fins still retain most of their stabilizing effect. The extent of the plume-induced flow-separation region on the rocket body determines the desired location of the fins.

Nonsymmetric loading results when scarf nozzles (par. 6-4.2.6) are employed in a missile. A scarf nozzle is one in which the exit plane of the nozzle is beveled or slanted away from the normal plane of the motor. The expansion of the exhaust gases, therefore, is not symmetric, and the resulting nozzle-exit velocity vector is diverted in a nonaxisymmetric direction. The plume effects of the scarf nozzle should be evaluated with consideration for their application and location.

6-5.6.2 Thermodynamic Effects

Jet plume analyses for a free flight rocket are mainly of two types– restricted plume expansion during launch and unrestricted plume expansion during free flight.

An analysis for an underexpanded jet exhausting from a conical nozzle into a cylindrical tube launcher has been performed in Ref. 49. The analytical results were compared to test results. Computer programs have been developed by using a method of characteristics for steady, axisymmetric, rotational flow, and the base flow model (Refs. 50, 51, and 52).

The profile for an unrestricted plume can be calculated by using a small hand calculator and the equation defined by Ref. 53. The entire structure for an unrestricted plume can be calculated using the methods published in Ref. 54. The Level I techniques of Ref. .54 are hand calculation procedures; the Level III techniques are computer program methods.

6-6 SCALING

6-6.1 GENERAL

The gas dynamic relationships of this chapter identify propulsion parameters that become essential factors in the design or evaluation of solid propellant rocket motors. The parameters are generally interrelated such that when one is changed others are affected. No general rule exists for the design of a solid propellant motor because of the number and complexity of the design parameters. As a conceptual design approach, the design engineer may apply scaling factors. At best, the use of scaling factors provides approximate design information, and the user should be aware that certain risks are involved. The scale factors to be employed depend upon the design or performance requirements that have been established for which data are to be generated, and, generally, certain additional assumptions must be made. Scaled data can be useful as a basis for further engineering analyses.

6-6.2 SCALING FACTORS

The performance characteristics available for one or more basic motors can be modified by scaling factors to approximate data for a similar motor having different performance and operating characteristics. The following relations apply when dimensions are varied from the basic motor dimensions by the same scale factor f:

$$F_{scaled} = f^2 F_{basic} \text{ , N} \tag{6-61}$$

$$\left(\frac{F}{m_m}\right)_{scaled} = \frac{1}{f}\left(\frac{F}{m_m}\right)_{basic} \text{ , N/kg or m/s}^2 \tag{6-62}$$

$$I_{scaled} = f^3 I_{basic}, \text{ N·s} \tag{6-63}$$

and

$$(t_b)_{scaled} = f(t_b)_{basic}, \text{ s} \tag{6-64}$$

where

m_m = mass of motor, kg
f = scale factor, dimensionless.

In evaluating the rocket motor mass m_m, it is assumed that the same materials and structural criteria are applied to both the basic and scaled motors.

When only the length of the grain (with restricted ends) is varied from the basic by the scale factor-j and when the nozzle flow areas are adjusted to maintain the same chamber pressure as in the basic motor,

$$F_{scaled} = f F_{basic}, \text{ N} \tag{6-65}$$

$$(A_t)_{scaled} = f(A_t)_{basic}, \text{ m}^2 \tag{6-66}$$

$$(A_e)_{scaled} = f(A_e)_{basic}, \text{ m}^2 \tag{6-67}$$

and

$$(m_m)_{scaled} = f(m_m)_{basic}, \text{ kg.} \tag{6-68}$$

If it is desirable to change the nozzle throat area by using inserts while maintaining the same exhaust area as the basic nozzle, i.e.,

$$(A_e)_{scaled} = (A_e)_{basic} \ , \ \mathrm{m}^2, \tag{6-69}$$

then

$$F_{scaled} = f \left[\frac{(C_F)_{scaled}}{(C_F)_{basic}} \right] F_{basic}, \ \mathrm{N} \tag{6-70}$$

$$(I_s)_{scaled} = \left[\frac{(C_F)_{scaled}}{(C_F)_{basic}} \right] (I_s)_{basic}, \ \mathrm{N \cdot s/kg} \tag{6-71}$$

and

$$I_{scaled} = \left[\frac{(C_F)_{scaled}}{(C_F)_{basic}} \right] I_{basic}, \ \mathrm{N \cdot s}. \tag{6-72}$$

The thrust coefficients C_F in Eqs. 6-70 through 6-72 maybe be estimated by substituting basic or scaled values as appropriate in Eq. 6-9 as follows:

$$\mathbf{C}_F = F \ / \ (A_t p_c), \ \mathrm{dimensionless}.$$

It is usually reasonable to assume for the purpose of scaling that the grain erosion is not altered significantly.

The motor thrust level may be changed by scaling the nozzle throat area by the factor f so that

$$F_{scaled} = f^{-n/(1-n)} \left[\frac{(C_F)_{scaled}}{(C_F)_{basic}} \right] F_{basic}, \ \mathrm{N} \tag{6-73}$$

$$(p_c)_{scaled} = f^{-1/(1-n)} \ (p_c)_{basic}, \ \mathrm{N/m}^2 \tag{6-74}$$

$$\dot{r}_{scaled} = f^{-n/(1-n)} \ \dot{r}_{basic}, \ \mathrm{m/s} \tag{6-75}$$

$$(t_b)_{scaled} = f^{-n/(1-n)} \ (t_b)_{basic}, \ \mathrm{s} \tag{6-76}$$

$$I_{scaled} = \left[\frac{(C_F)_{scaled}}{(C_F)_{basic}} \right] I_{basic}, \ \mathrm{N \cdot s} \tag{6-77}$$

$$(I_s)_{scaled} = \left[\frac{(C_F)_{scaled}}{(C_F)_{basic}} \right] (I_s)_{basic}, \ \mathrm{N \cdot s/kg} \tag{6-78}$$

where

n = exponent in burning rate equation (Eq. 6-11).

If the grain erosion effects are significantly altered, or if the chamber pressure during burning is not constant, this technique is not applicable. Also the given technique requires an iterative solution because the thrust coefficient is a function of the nozzle thrust area and combustion chamber pressure.

The impulse may be changed by scaling the nozzle exhaust flow area, thus changing the expansion ratio so that

$$F_{scaled} = \left[\frac{(C_F)_{scaled}}{(C_F)_{basic}} \right] F_{basic}, \text{ N} \tag{6-79}$$

$$(I_s)_{scaled} = \left[\frac{(C_F)_{scaled}}{(C_F)_{basic}} \right] (I_s)_{basic}, \text{ N·s/kg} \tag{6-80}$$

$$I_{scaled} = \left[\frac{(C_F)_{scaled}}{(C_F)_{basic}} \right] (I)_{basic}, \text{ N·s.} \tag{6-81}$$

When the propellant composition is changed and when it is desirable to maintain the same chamber pressure as the basic motor by changing the nozzle configuration,

$$(A_t)_{scaled} = \left(\frac{\psi_{scaled}}{p_c} \right)^{1-n_{scaled}} \left(\frac{p_c}{\psi_{basic}} \right)^{1-n_{basic}} (A_t)_{basic}, \text{ m}^2 \tag{6-82}$$

$$(A_e)_{scaled} = \left[\frac{(A_t)_{scaled}}{(A_t)_{basic}} \right] (A_e)_{basic}, \text{ m}^2 \tag{6-83}$$

$$F_{scaled} = \left[\frac{(A_t)_{scaled}}{(A_t)_{basic}} \right] F_{basic}, \text{ N} \tag{6-84}$$

$$(t_b)_{scaled} = \cdot \left(\frac{b_{basic}}{b_{scaled}} \right) \left[p_c^{(n_{basic}-n_{scaled})} \right] (t_b)_{basic}, \text{ s.} \tag{6-85}$$

The chamber-pressure parameter ψ maybe estimated by substituting basic or scaled values as appropriate in the following equation as determined from Eqs. 6-59 and 6-60:

$$\psi = (b\rho_p c^*)^{1/(1-n)}, \text{ Pa.} \tag{6-86}$$

The empirical constants b and n are those in Saint-Robert's law for burning rate, Eq. 6-11. The value of b depends upon propellant temperature, propellant composition, and the chamber-pressure range. The value of the pressure exponent constant n depends upon the propellant composition and the pressure range. The scaled values of b and n should be consistent with the chamber pressure, propellant composition, and temperature of the scaled motor and normally are obtained from a motor manufacturer. The characteristic exhaust velocity c* for the scaled motor can be estimated by substituting basic or scaled values as appropriate in Eq. 6-8 as follows:

$$c^* = p_c A_t/\dot{m}, \text{ m/s.}$$

The scaled value of mass-flow rate may be determined from Eq. 6-87 as follows:

$$\dot{m}_{scaled} = f \left[\frac{F_{scaled}}{(I_s)_{scaled}} \right], \text{ kg/s.} \tag{6-87}$$

The scaling Eqs. 6-82 through 6-87 are applicable provided the erosion characteristic: are not altered significantly and the chamber pressure does not vary significantly during burning.

6-6.3 DISCUSSION

Some component designs are influenced primarily by the mass of the propellant; others are influenced primarily by the thrust level. The proportionality, or scaling factors, depend upon a multitude of technological design aspects of the rocket and its propulsion system. The propellant mass fraction ζ and the mass ratio MR are useful quantities to measure propulsion efficiency and performance. The propellant mass fraction ζ is defined as the ratio of the propellant mass to the loaded-motor mass as follows:

$$\zeta = m_p/m_m, \text{ dimensionless} \tag{6-88}$$

where

    m_p = propellant mass, kg
    m_m = initial mass of loaded rocket motor, kg.

Tlhe propellant mass fraction is useful as a scaling parameter for estimating the mass of the motor for a given propellant load, i.e.,

$$m_m = m_p/\zeta, \text{ kg.} \tag{6-89}$$

The rocket mass ratio MR is defined, Eq. 6-90, as the ratio of the total rocket mass to the burnout mass. The rocket mass includes motor, payload, aerodynamic surface attachment hardware, etc.

$$MR = m_i/(m_i - m_p), \text{ dimensionless} \tag{6-90}$$

where

    m_i = initial rocket mass, kg
    m_p = propellant mass consumed, kg.

The effect of the mass ratio on the rocket velocity is a major one. This is borne out by the ideal velocity Eq. 6-44 which is the maximum velocity that can be obtained in a gravitationless vacuum, i.e.,

$$u_i = I_s \ln (MR), \text{ m/s.}$$

The ideal velocity u_i varies directly with variations in the specific impulse I_s, (effective exhaust velocity c):

$$(u_i)_{scaled} = \left[\frac{(I_s)_{scaled}}{(I_s)_{basic}}\right] (u_i)_{basic}, \text{ m/s.} \tag{6-91}$$

The ideal velocity varies exponentially with variations in mass ratio, i.e.,

$$(u_i)_{scaled} = \left\{\frac{[\ln(MR)]_{scaled}}{[\ln(MR)]_{basic}}\right\} (u_i)_{basic}, \text{ m/s.} \tag{6-92}$$

The influence of the rocket mass on rocket performance is very significant. Eq. 6-90 can be rearranged into the form of the scaling equations:

$$m_i = (MR)(m_i - m_p), \text{ kg}$$

or

$$m_p = \left[\frac{(MR - 1)}{MR}\right] m_i, \text{ kg.}$$

When changes in the basic motor require more than one of the techniques described, the scaling should be performed in steps. One scaling technique should be completed, and all scaled characteristics computed. This new information then is used to complete the next scaling technique, etc.

Scaling is not an exact science, and, when possible, scaled results should be verified by engineering analyses and/or tests. Care must be exercised in scaling motors in which erosion is significant. Erosion characteristics may not scale well even when the ratio of grain internal-flow area to nozzle-throat area is preserved in the scaling.

6-7 TESTING

Testing of a rocket motor consists of mechanical, propellant grain integrity, quality assurance, and ballistic tests. Tests are performed on raw material, processed-propellant samples, and selected components and motors as appropriate to verify propulsion and structural characteristics.

6-7.1 STRUCTURAL INTEGRITY TESTS

The structural integrity tests consist of an instrumented hydrostatic proof test that maybe followed by a burst test. The motor chamber must withstand proof pressures—maximum expected operating pressure condition at 60°C—without yielding. For a burst test the chamber is pressurized until it fails. The chamber must show a margin of safety at failure based on burst pressure of 1.5 times the MEOP. In addition to the proof and burst pressure tests, tensile and metallurgical tests are performed to characterize the motor case material properties and to determine the effect of machining on the raw material. Axial and hoop oriented microtensile specimens are taken from material for each chamber to be tested. Standard tensile specimens are taken in the axial orientation for correlation purposes, and metallurgical specimens are taken from the hydroburst chambers. Material properties—yield strength, ultimate strength, strain, etc.—are determined from the standard and microtensile specimens taken from worked and nonworked bars. These data are correlated with results of theoretical finite element analysis for the chamber case. Structural testing is discussed further in par. 7-8.

6-7.2 PROPELLANT GRAIN INTEGRITY TESTS

Solid propellant grains are both viscous and elastic (viscoelastic). Propellant tests involve the determination or verification of both the mechanical properties and propulsion characteristics with consideration of environmental conditions. Ref. 55 provides information and requirements for testing solid propellant.

6-7.2.1 Mechanical Properties

Mechanical requirements that are determined by propellant tests include tensile, compressive, and shear strengths; stress-strain data; adhesive qualities; modulus of elasticity; and elongation (strain). Testing should provide data related to grain deformation and grain failure, and determine the ultimate strength and the point of rupture or failure. These requirements apply for storage conditions and for thrusting in test or in flight. The axial pressure distribution due to viscous shear from the gas flow and vehicle acceleration tends to move the propellant toward the nozzle. For a given configuration and propellant, a critical Young's modulus exists below which bulging and pressure rise continue until the chamber bursts.

Stress-strain characteristics are determined by testing samples of propellant (raw material, polymer, or processed propellant) under designated tensile, compressive, and shear loads. Stress-strain data to be established include elastic modulus, elastic limit, ultimate strength, and point of rupture. Stress-strain properties are highly dependent on both the temperature and the strain rate of the propellant. Low strain rates are usually characteristic of thermal strains during curing and storage; high strain rates occur during ignition conditions. Therefore, testing should be made for various temperature and strain-rate conditions.

Stress relaxation tests are conducted on processed propellant and on certain constituents. A nominal stress is applied over a period of time during which a measure of the relaxation is made.

A slump test involves determining the downward drift or slump of a propellant sample due to its own weight. The weight and other forces due to acceleration, etc., can cause bulging of propellant near the nozzle which may result in reduced port area, and thus accentuate pressure and viscous forces.

Stress-strain data for a propellant grain are sometimes determined by a nondestructive indentation test. A testing device is used to apply given strain rates to the surface of the propellant by means of a compressive pad or indentor. Deformations and stress are measured, and certain mechanical properties of the propellant can be determined that approximate the stress-strain curve of a standards specimen test.

The propellant density is determined in accordance with methods 510.1.1 or T510.3 of MIL-STD-286 (Ref. 58). The test for determination of density usually involves weighing a test specimen of known volume and determining the density as the ratio of the mass to the volume of the propellant sample. Method T510.3 specifies a sample mass of approximately 25 g, and the volume is to be determined with an air pycnometer.

6-7.2.2 Thermal Properties

The propellant should be tested to assure that the grain will meet storage and operational requirements. The physical properties and combustion characteristics (burning rate) should be predictable and not affected appreciably over a wide range of storage and operating temperatures. The temperature sensitivity of a propellant grain is usually relatively low.

Thermal properties of the propellant are determined by the application of heat to propellant samples. Two significant properties that are determined by thermal tests are the coefficient of thermal expansion and the thermal conductivity, i.e.,

1. The coefficient of thermal expansion is the unit strain that is produced by a unit temperature change. The test involves the application of heat uniformly to a propellant test specimen (bar or rod) and recording the dimensional change with the corresponding temperature and temperature change (Ref. 56).

2. Thermal conductivity (Ref. 56) is the time rate of heat flow under steady conditions, through a unit area, per unit temperature gradient in the direction perpendicular to the area. The guarded hot plate test covers the determination of the steady state thermal transmission properties of propellant specimens using a guarded hot plate. This test is described in Ref. 57.

6-7.2.3 Performance Characteristics

Propellant-test firings are made during propellant development programs and also after manufacture of the complete full-scale rocket. In the motor-test approach to propellant performance determination, a statistical analysis of test data acquired in many motor firings is used to obtain the best estimates of the propellant performance parameters. The raw test data consist of measured parameters and test recordings. Measured parameters are the mass of the propellant burned (obtained by subtracting the weight after the firing from the weight prior to firing) and the cross-sectional area A_t of the nozzle throat which, in the case of ablating nozzles, varies with time. The test recordings contain the histories of the thrust and the chamber pressure over the burning or action time of the propellant. Test recordings show a pressure-time curve that increases to a peak followed by a decrease to a near level condition and ends with a gradual tailoff. Mean values can be defined rather accurate] y from these curves. For example, the mean characteristic velocity $\overline{c^*}$ is

$$\overline{c^*} = \frac{\left[\int_0^{t_b} p_c(t)dt\right] A_t}{m_p}, \text{ m/s} \tag{6-93}$$

where

$p_c(t)$ = chamber pressure as a function of time, Pa
$\int_0^{t_b} p_c(t)dt$ = area under the pressure-time curve, N·s/m²
m_p = mass of propellant consumed, kg.

The propellant consumed is equivalent to the mass difference in the motor before and after firing. A mean thrust coefficient $\overline{C_F}$ can be written in a similar way, i.e.,

$$\bar{C}_F = \frac{\int_0^{t_b} F(t)dt}{\left[\int_0^{t_b} p_c(t)dt\right] A_t} \text{ , dimensionless} \tag{6-94}$$

where

$F(t)$ = thrust as a function of time, N.

The corresponding mean specific impulse $\bar{I}_s$ is

$$\bar{I}_s = \frac{\int_0^{t_b} F(t)dt}{m_p} = \frac{I}{m_p} \text{ , N·s/kg.} \tag{6-95}$$

These definitions are unambiguous, and for each firing it is easy to determine $\bar{c}^*$, $\bar{C}_F$, and $\bar{I}_s$ accurately and to compare their values with theory.

Experimental determination of propellant performance by means of conventional motor testing must be based on a large number of firings. Statistical analyses of the performance should be made by obtaining mean values and standard deviations for a large number of parameters such as pressure, thrust, characteristic velocity, mass flow rate, thrust coefficient, and specific impulse.

Chapter 3, Ref. 27, describes a method for measurement of the gas velocity in the motor being fired. It is desirable to study and determine the relationship of the gas velocity with the erosion effects.

6-7.3 TEST FOR NEW PROPELLANT FORMULATION

A mode of testing for new propellant formulations involves the use of small propellant rod grain samples called strands. The liner burning rate may be evaluated by the use of such strands. The process involves a determination of the time intervals between the burning out of fine wires imbedded at predetermined locations of the strands. The burning of strands provides data on combustion characteristics such as burning rate, oscillations, thermal explosions, and chuffing. The strand burner is also useful in the correlation of burning rate characteristics with the burning rate laws, par 6-4.1.1.

6-7.4 QUALITY ASSURANCE TESTING

Solid propellant rocket motors undergo testing to assure acceptable reliability and quality of the system and its components with consideration for manufacture, storage, environment, test, and flight operations. Methods of testing include both destructive and nondestructive tests. Greater emphasis is placed on nondestructive tests because the integrity of the system is preserved.

6-7.4.1 Nondestructive Testing

Nondestructive test methods consist of numerous well-defined techniques that may, in turn, vary in effectiveness depending on the magnitude of parameters such as energy level, frequency of interrogating energies, sensing methods, and data presentation. Radiography, ultrasonics, and microwaves are the principal methods used to test propellant grain, insulation, composite materials, binder materials, etc.

Radiography is well established as a method of nondestructively detecting flaws in materials and structures. A radiographic image is obtained as a picture of the intensity distribution of X rays that have passed through the material. The material attenuates the radiation according to mass, type, and size of the defects present, and the intensity of the radiation varies with the flaw distribution.

Ultrasonic waves are vibrational waves of higher frequency than the hearing range of the human ear. Ultrasonic flaw detection usually is accomplished with frequencies in the order of 10^6 to 10^7 Hz. Frequencies up to 5×10^7 Hz are used in material property int'estimations. Various techniques using ultrasonic methods are employed to detect discrete flaws in materials or to detect changes in material properties which may result from aging or environmental conditions.

Microwaves occur in that portion of the electromagnetic spectrum between radio waves and infrared radiation. Their frequencies range from 300 MHz to 300 GHz. Microwaves interact with materials on a molecular level, can penetrate most nonmetallic materials. and are reflected or scattered from internal surfaces to detect flaws or discontinuities.

These techniques are employed to discover cracks, voids. delamination of laminated materials, and contaminants in composite materials, graphites, elastomers. and metals.

6-7.4.2 Destructive Testing

Certain critical components are subject to tests that damage or destroy the component. Selective or statistical sampling techniques used for such tests. These tests include tests for tensile and compressive strength, modulus or elasticity, and hardness. For plastic composite materials, tests are conducted for density, volatile content, resin content, acetone-soluble content, and interlaminar strength. Quality assurance aspects for rocket metal cases are discussed in Ref. 59.

6.7.5 ENVIRONMENTAL TESTING

Environmental tests include salt spray, humidity, accelerated aging. and temperature cycling. These tests are described in detail in military standards (Ref. 60).

REFERENCES

1. George P. Suttton. *Rocket Propulsion Elements.* 3rd Edition. John Wiley & Sons. Inc.. New York, NY 1963. pp. 30, 62, 310-86.
2. M. J. Zucrow . *Aircraft and Missile Propulsion-Vol. I.* John Wiley & Sons. Inc.. New York. NY. 1958. pp. 337-77.
3. R. B. Kruse. *Modern Materials— Solid Propelants. Vol. 6.* Academic Press. New York. NY. 1968. pp. 69-179.
4. *M.* J. Zucrow . *Aircraft and Missile Propulsion- V0l. II.* John Wiley & Sons. Inc.. New York. NY, 1958, pp. 419-590.
5. AMCP 706-285. Engineering Design Handbook. *Elements of Aircraft and Missile Propulsion,* July 1969. pp. 4-10 to 4-40. 7-1 to 7-11, 8-13.
6. K. Kishore. "Comprehensive View of the Combustion Models of Composite Solid Propellants". AIAA Journal 17. 1216 (November 1979).
7. AMCP 706-175. Engineering Design Handbook. *Explosives Series. Solid Propellants, Part One,* September 1964. pp. 3-11, 89-111.
8. K. Kishore and M. R. Sunitha. "Effect of Transition Metal Oxides on Decomposition and Deflagration of Composite Solid Propellant Systems: A Survey" AIAA Journal 17, 1118 (October 1979).
9. C. E. Campbell and J. M. Farley. *Performance of Several Conical Convergent-Divergent Rocket-Type Exhaust Nozzles.* NASA TN-D467. Lewis Research Center. Cleveland. OH. September 1960.
10. P. G. Hill and C. R. Peterson. *Mechanics and Thermodynamics of Propulsion,* Addison-Wesley Publishing Company. Inc.. Reading. MA. 1965. pp. 355.398-407.485.
11. M. J. Zucrow and J. D. Hoffman, *Gas Dynamics-Vol.* 2, John Wiley & Sons, Inc.. New York, NY. 1977. pp. 143-69, 230-45.
12. J. H. Ahlberg. *et al..* "Truncated Perfect Nozzles in Optimum Nozzle Design.". Journal American Rocket Society 31, 614-20 (May 1961).
13. K. Berman. "The Plug Nozzle: A New Approach to Engine Design". Astronautics 5.22-4 (April 1960).
14. G. V. R. Rao. "'Recent Developments in Rocket Nozzle Configurations". Journal American Rocket Society 31. 1488-94 (November 1961).
15. D. R. Bartz. "A Simple Equation for Rapid Estimation of Rocket Nozzle Convective Heat Transfer Coefficients". Jet Propulsionl 27. 49-51 (January 1957).

16. Harry Tong. *Aerothern Graphic Surface Kinetics Computer Program, Vol I–Program Description and Sample Problem,* Aerothermal Report UM-72-25 (AFRPL-TR-72-23). Acurex Corp..Aerotherm Div.. Mountain View.CA.January 1972.

17. M. R. Wool. *User's Manual–Aerotherm Equilibrium Surface Thermochemistry Computer Program, Version3–Program Description and Sample Problem, Aerotherm Report* UM-70-13 (AFRPL-TR-70-93).Acurex Corp..Aerotherm Div..Mountain View.CA.April 1970.

18. H. Tong. *et al..Nonequilibrium Chemistry Boundary Layer Integral Matrix Procedure.* Aerotherm Report UM-73-67 (NASA-CR-134039).Acurex Cort..Aerotherm Div..Mountain View. CA. 1973

19. E. Stompfl and E. M. Landsbaum. "Solid Motor Aft Closure Insulation Erosion". Journal of Spacecraft 12, 599-607 (October 1975)

20. D. J. Carter, Jr.. and A. R. Vick. *Experimental Investigations of Axial and Normal Force Characteristics of Skewed Nozzles.* NACA-TN-4336. Langley-Aeronautical Laboratory, Langley Field. VA. September 1958.

21. A. R. Maykut, "Propulsion Technology for Free-Flight Rockets"(U). CPIA Publication 260.Vol. III Part II.Johns Hopkins University.Baltimore.MD.January 1975.pp. 583-603.(THIS DOCUMENT IS CLASSIFIED CONFIDENTIAL.)

22. J. M. Viles and S. P. D. Smith. *Strip Laminate Free Flight Motor Demonstration.* Proceedings of the Third Annual Free Flight Rocket Workshop.Rocket No. T-SR-79-12.US Army Missile Research and Development command.Redstone Arsenal.Al.10-12 October 1976.

23. A. R. Maykut. *Technology for Improving Solid Rocket Motor Reproducibility.* TR-RK-77-2.US Army Missile Command.Redstone Arsenal.AL.1 October 1978

24. H. M. Darwell and G. F. P. Trubridge."Design of Rocket Nozzles to Reduce Gas Misalignment". Journal of Spacecraft 5. 36-41 (January 1968)

25. J. H. Arszman. *Impulsive Noise of Propulsion Systems—Sources.Analysis.Systems.* TR-RK-82-7.US Army Missile Command.Redstone Arsenal.AL.July 1983

26. R. A. Ellis and R. B. Keller, Jr.. *NASA Space Vehicle Design Criteria Chemical Propulsion.Solid Rocket Motor Nozzle.* NASA SP-8115.Lewis Research Center. Cleveland. OH. June 1975

27. F. A. Williams. *et al..Fundamental Aspects of Solid Propellant Rockets.* AGARDograph Number 116. The Advisory Group for Aerospace Research and Development. NATO. Published by Technivision Servises. Slough. England. October 1969.

28. N. S. Cohen. "review of Composite Propellant Burn Rate Modeling".AIAA Journal 18. 277-93 (March 1980)

29. D. R. Dreitzler. *et al..Climatic Performance of Smokeless Propellants.* Technical Report T-78-54. US Army Missile Research and Development Command. Redstone Arsenal. AL. May 1978.

30. J. H. Argyris and S. Kelsey. *Recent Advances in Matrix Methods of Structural Analysis.* The Macmillan Co.. New York NY. 1964. pp. 87-114.

31. J. H. Argyris. *Modern Fuselag Analysis and the Elastic Aircraft.* Butterworths. Inc.. Washington. DC. 1963. pp. 25-32. 93-100.

32. M. L. Williams. *et al..Fundamental Studies Relating to Systems Analysis of Solid Propellants.* Report No. SM61-5. Graduate Aeronautical Laboratories. California Institute of Technology. Pasadena. CA February 1961.

33. M. E. Fourney and R. R. Parmerter. Stress Concentrations for Internally Perforated Star Grains. Bureau of Naval Weapons. NAVWEPS Report 7758. US Naval Ordnance Test Station. China Lake. CA. December 1961.

34. M. E. Fourney and R. R. Parmerter. "Photoelastic Design Data for Pressure Stresses in Slotted Rocket Grains". AIAA Journal 1. 697 (1963)

35. C. H. Parr. *The Application of Numerical Methods to the Solution of Structural Integrity Problems of Solid Propellant Rockets.* Rohm and Haas Corp.. Huntsville. AL. January 1967.

36. *H. B.* Wilson Jr., "Stressing Owing to Internal Pressure in Solid Propellant Rocket Grains", Journal American Rocket Society, 309 (1961).

37. L. J. Jacques, *General Principles for the Aerodynamic Design of Solid Rocket Nozzles,* AIAA Paper No. 75-1338, AIAA SAE Propulsion Conference, Anaheim, CA, 29 September to 1 October 1975.

38. L. Lemoine, *Solid Rocket Nozzle Thermostructural Behavior,* AIAA Paper No. 75-1339, AIAA\SAE Propulsion Conference, Anaheim, CA, 29 September to 1 October 1975.

39. M. J. Fischer, *Nozzle Materials and Manufacturing Processes,* AIAA Paper No. 72-1191, AIAA/SAE 8th Joint Propusion Specialist Conference, New Orleans, LA, 29 November to 1 December 1972.

40. C. H. Wright and R. K. Lund, *Internal Aerodynamics of Solid Rocket Motors,* Paper presented at the 62nd National Meeting, American Institute of Chemical Engineers, Salt Lake City, UT, 21-24 May 1967.

41. D. F. Hopkins and D. E. Hill, "Effects of Small Radius of Curvature on Transonic Flow in Axisymmetric Nozzles", AIAA Journal 4, 1337-43 (August 1966).

42. R. J. Prozan, *Development of a Method of Characteristics Solution for Supersonic Flow of an Ideal Frozen or Equilibrium Reacting Gas,* Report LMSC/HREC A782535-A, Lockheed Missiles and Space Co., Huntsville, AL, April 1966.

43. Ascher H. Shapiro, *The Dynamics and Thermodynamics of Compressible Fluid Flow, Vol. I,* The Ronald Press Company, New York, NY, 1953, pp. 462-523.

44. J. R. Kliegel and G. R. Nickerson, *Axisymmetric Two Phase Perfect Gas Performance Program, Vol. I, Engineering and Programming Description,* Report MSC-1174, Systems Group, TRW, Inc., Rodondo, CA, April 1967.

45. J. R. Kliegel, *et al., One-Demensional Two-Phase Reacting Gas Non-equilibrium Performance Program, Vol. I, Engineering and Programming Description,* Report MSC-1178, Systems Group, TRW, Inc., Rodondo, CA, August 1967.

46. R. R. Morris and J. J. Bertin, *Experimental Study of an Underexpanded, Supersonic Nozzle Exhausting Into an Expansive Launch Tube,* Aerospace Engineering Report 77001, University of Texas at Austin, Austin, TX, January 1977.

47. G. Batiuk, A *Bibliography of Plume Effects Investigations Conducted by the Army Missile Command, Report No.* RD-TR-76-16, US Army Missile Command, Redstone Arsenal, AL, December 1975.

48. W. C. McCorkle and J. A. Lilly, *An Adjusted Fire Technique* for a *Highly Accurate Free-Flight Rocket Artillery System,* Report No. RD-TR-74-13, US Army Missile Command, Redstone Arsenal, AL, 25 June 1971.

49. J. L. Batson, *Rocket Exhaust Flow in Tube Launchers,* Report No. RL-76-12, US Army Missile Command, Redstone Arsenal, AL, 19 January 1976.

50. H. H. Korst, *et al., Research on Transonic and Supersonic Flow of a Real Fluid at Abrupt Increases in Cross Section.* ME Technical Report 392-5, University of Illinois, Urbana, IL, December 1959.

51. A. L. Addy, *Detailed Analyses for the Base-Pressure Programs* (TSABPP-1,2), Report No. RD-TN-69-7, US Army Missile Command, Redstone Arsenal, AL, August 1969.

52. A. L. Addy. *Analysis of the Axisymmetric Base Pressure and Base Temperature Problem with Supersonic Interacting Freestream Nozzle Flow Based on the Flow Model of Korst et al.,* Report No. TD-TR-69-11, US Army Missile Command, Redstone Arsenal, AL, February 1970.

53. J. Batson, *Proceedings of the Second Annual Free Flight Rocket Workshop, Vol. I,* TF-TR-77-1, US Army Missile Research and Development Command, Redstone Arsenal, AL, 2-4 August 1977, pp. 72-85.

54. *JANNAF Handbook, Rocket Exhaust Plume Technology, Chapter 2, Fluid Dynamic Flow Models,* CPIA Publications 263, Johns Hopkins University, Baltimore, MD, May 1975.

55. MIL-STD-2100(OS), *Propellant, Solid, Characterization of,* 30 March 1979.

56. CPIA Publication No. 21, *Solid Propulsion Mechanical Behavior Manual,* Chemical propulsion Information Agency, Johns Hopkins University, Baltimore, MD.

57. ANSI/ASTM C-177, *Standard Test Method for Steady-State Thermal Transmission Properties by Means of the Guarded Hot Plate,* Annual ASTM Standards Part 35, 1976.

58. MIL-STD-286, *Propellants, Solid: Sampling, Examination, and Testing,* 1 September 1980.

59. W. G. Ramroth, *Solid Rocket Motor Metal Cases, NASA Space Vehicle Design Criteria Monograph,* NASA Sp-8025, NASA, Office of Advanced Research Technology, Washington, DC, April 1970.

60. MIL-STD-810, *Environmental Test Methods,* 19 July 1983.

MIL-HDBK-762(MI)

CHAPTER 7
STRUCTURES

This chapter deals with the structural design considerations of free flight rocket components-providing a general description of the components and containing specific structural design in-formation, Considerations are given to both externally and internally applied loads. These loads may be either static, dynamic, or thermal. Design information includes mass estimation, internal load generation, stress analysis techniques, material selection, dynamic analysis, and thermal protection systems. A general discussion of aeroelasticity, combustion instability, and other related topics are also included to provide guidance in the development of a reliable free flight rocket.

7-0 LIST OF SYMBOLS

A = area, m^2

A_{cs} = cross-sectional area of airfoil, m^2

A_{equiv} = equivalent two-flange plate area, m^2

$A_{ref} = \pi d^2$ 4, rocket reference area, m^2

A_S = surface area, m^2

A_s = effective cross-sectional shear area at fin root, m^2

A_{xx} = area of transverse plane on which motor (internal) pressure acts, m^2

$ACMF$ = aft closure and nozzle mass factor, dimensionless

a = rocket acceleration along longitudinal axis, m/s^2

a_N = rocket normal acceleration, m s^2

a_{N_i} = normal acceleration at station i, m s^2

$a_{N_{CG}}$ = normal acceleration at CG location, m s^2

$a_{N_{max}}$ = maximum normal acceleration at fins, m/s^2

a_{N_x} = total normal acceleration at station x, m/s^2

a_T = temperature shift factor, dimensionless

$\hat{a} = l - \hat{b}$ (see Eqs. 7-85 and 7-86), m

BF = biaxial improvement factor, dimensionless

b_e = exposed fin span, m

$\hat{b}$ = distance from beam end to applied load, m

C_A = aerodynamic axial force coefficient, dimensionless

C_H = Stanton No., convective heat transfer, dimensionless

C_M = Stanton No., mass transfer, dimensionless

$C_{N_\alpha} = (\partial F_N / \partial \alpha) 1 (q A_{ref})$, aerodynamic normal force gradient coefficient, rad^{-1}

C_T = strength correction factor for temperature, dimensionless

C_1 = empirical constant used to determine a_T, dimensionless

C_2 = empirical constant used to determine a_T, dimensionless

c = specific heat of insulation, kJ kg·K

= caliber, dimensionless

c_p = specific heat of gas at constant pressure, kJ kg·K

c_r = fin root chord, m

c_t = fin tip chord, m

D = characteristic length, m

d = rocket diameter (reference length), m

= warhead diameter, mm

d_{mc} = diameter of motor case, m

E = modulus of elasticity (Young's Modulus), Pa

E_e = equilibrium modulus, Pa

E_g = glassy modulus, Pa

E_{mc} = modulus of elasticity (Young's Modulus) of motor case, Pa

E_p = modulus of elasticity (Young's Modulus) of propellant, Pa

EI = beam bending stiffness, N·m^2

F_A = axial force, N

= sum of axial components of aerodynamic force, N

F_{Aj} = axial force at station j, N

F_{A_x} = axial force on rocket forward of plane x-x, N

$F_{A_{xx}}$ = axial load on rocket at plane x-x, N

F_g = mg_0, gravitational force of components, N

F_{gbody} = gravitational force of body section, N

F_{gfin} = gravitational force of fin section, N

F_{gnose} = gravitational force of nose section, N

F_{g-w} = shape/emissivity factor for radiation gas to wall or particles to wall, dimensionless

F_h = hoop load per unit length, N m

F_m = axial meridional load, N

$F_{N_{fin}}$ = fin normal force, N

F_{N_i} = normal force at location i, N

$F_{N_{total}}$ = total air load, N

F_s = shearing force, N

F_{s_j} = shear load at station j, N

F_{st} = flange shear load, N

F_T = rocket motor thrust, N

f_n = ℓ_N/d, fineness ratio, dimensionless

$FCMF$ = forward closure mass factor, dimensionless

FS = factor of safety, dimensionless

$(FS)_u$ = factor of safety based on ultimate stress criterion, dimensionless

$(FS)_y$ = factor of safety based on yield stress criterion, dimensionless

$G = E\ [2(1 + \nu)]$, shear modulus, Pa

$g_0 = $ reference acceleration due to gravity, m s^2

$H = $ altitude, km

$h = $ distance between centroids of equivalent two-flange beam, m

$= $ convective heat transfer coefficient, W m^2·K

$h_1, h_2 = $ lengths of shear-carrying members, m

$h_{equiv} = $ fin root equivalent beam height, m

$\hat{h} = $ enthalpy-based heat transfer coefficient, kg m^2·s

$I = $ area moment of inertia, m^4

$I_c = $ mass moment of inertia about axis c-c, kg·m^2

$I_g = $ mass moment of inertia about axis g-g, kg·m^2

$\bar{I} = $ mass moment of inertia referenced to a CG, kg·m^2

$\bar{I}_{CG} = $ mass moment of inertia about rocket CG, kg·m^2

$\bar{I}_o = $ mass moment of inertia about CG, kg·m^2

$\bar{I}_{oi} = $ mass moment of inertia of mass i about CG of m_i, kg·m^2

$\bar{I}_{ox}, \bar{I}_{oy}, \bar{I}_{oz} = $ principal mass moments of inertia, kg·m^2

$\bar{I}_{rocket} = $ mass moment of inertia of section referenced to rocket CG, kg·m^2

$\bar{I}_{section} = $ mass moment of inertia of section about section CG, kg·m^2

$I_{sp} = $ specific impulse, N·s kg

$I_{xx} = $ mass moment of inertia about x-x axis, kg·m^2

$i_R = $ recovery enthalpy, J kg

$i_w = $ wall enthalpy, J kg

$= $ air enthalpy at wall condition, J kg

$K_b = E\ [3(1 - \nu)]$, bulk modulus, Pa

$K_s = $ fin shear correction factor, dimensionless

$k = $ parameter used in defining nose shapes, dimensionless

$= $ thermal conductivity, W m·K

$\ell = $ length, m

$(\ell\ m)_{mc} = $ fineness ratio of motor case, dimensionless

$\ell_c = $ location of the projection of the center of an ogival generating radius r_s along the rocket centerline, m

$\ell_{cyl} = $ length of cylindrical section of payload section, m

$\ell_{mc} = $ length of cylindrical section of motor case, m

$\ell_N = $ nose length, m

$M = $ bending moment, N·m

$M_{fin} = $ bending moment at fin root, N·m

$M_i = $ local bending moment at station i, N·m

$M_j = $ bending moment at station j, N·m

$MS = $ margin of safety, dimensionless

$(MS)_y = $ margin of safety based on yield stress criterion, dimensionless

$(MS)_u = $ margin of safety based on ultimate stress criterion, dimensionless

M_{total} = total bending moment, N·m

M_∞ = free-stream Mach number, dimensionless

m = mass, kg

m_{ac+n} = mass of aft closure and nozzle, kg

m_{bo} = mass of rocket at burnout, kg

m_{fc} = mass of forward closure, kg

m_{fins} = total mass of fins, kg

m_I = inert motor mass, kg

m_i = mass of "lumped" mass i, kg

m_{in+b} = mass of insulation and propellant binder, kg

m_{mc} = mass of cylindrical segment of motor case, kg

m_{other} = mass of igniter and other hardware associated with motor case, kg

m_p = propellant mass, kg

m_{pi} = variable propellant mass, kg

m_{pld} = payload mass, kg

m_{total} = total mass of rocket, kg

m_x = mass of rocket forward of plane x-x, kg

m_0 = rocket gross mass at ignition, kg

n = number of segments, dimensionless

= number of elements in a series, dimensionless

P_H = probability of hit, dimensionless

P_K = probability of kill, dimensionless

$P_{K\,H}$ = probability of kill given a hit, dimensionless

P_{MEOP} = maximum expected operating pressure, Pa

P_{nozzle} = pressure at nozzle station of interest, Pa

PMF = $m_p/(m_I + m_p)$, propellant mass fraction of rocket, dimensionless

Pr = $\mu c_p/k$, Prandtl number, dimensionless

p = chamber absolute pressure, Pa

= motor internal pressure, Pa

= internal pressure at nozzle station, Pa

q = $0.5\rho_{atmos}V^2$, dynamic pressure, Pa

q_{aero} = heat flux due to aerodynamic heating, W m²

q_{conv} = convective heat flux, W m²

q_{hw} = hot wall heat flux, W m²

q_{max} = maximum dynamic pressure, Pa

$q_{net\,rad}$ = net radiation exchange among particles, gas, and wall, W m²

q_{tot} = total heat flux, W m²

Re = $Dv\rho\,\mu$, Reynolds number, dimensionless

r = radius, m

Δr = radial displacement of cylindrical displacement of motor case, m

r_b = propellant bore radius, m

r_e = insulation regression (erosion rate), m/s

r_i = inner (bore) radius of propellant, m

= inside radius of nozzle, m

r_{ir} = r_i/r, dimensionless parameter

r_{mc} = average radius of motor case, m

r_n = normalized local transverse nose radius at station x, dimensionless

r_o = outer radius of propellant, m

= outside radius of nozzle, m

r_{oi} = r_o/r_i, dimensionless parameter

r_{or} = r_o/r, dimensionless parameter

r_s = radius of circular arc, i.e., secant ogive generating radius, m

r_t = tangent ogive meridian generating radius, m

ST = Stanton number, convection heat transfer, dimensionless

T = temperature, K

= insulation temperature as a function of time and space, K

T_{actual} = temperature of body, K

T_{cure} = curing temperature, K

T_g = gas temperature, K

T_{ref} = reference temperature usually taken as 298 K

T_w = wall (motor case) temperature, K

ΔT = temperature difference, deg K

ΔT_{eff} = effective temperature difference, deg K

ΔT_V = temperature change based on propellant volumetric shrinkage during cure, deg K

t = thickness, m

= time, s and min

= flight time, s

t_b = motor burn time, s

t_{mc} = thickness of motor case, m

t_{min} = minimum motor case thickness away from discontinuities, m

u = linear displacement, m

V = volume, m^3

V_{cyl} = volume of cylindrical shell, m^3

V_{LE} = propellant volumetric loading efficiency, dimensionless

V_{nose} = volume of nose fairing, m^3

V_{reg} = payload volume required, m^3

VSR = propellant volumetric shrinkage ratio during cure, m^3/m^3

v = velocity, m/s

WE = weld efficiency, dimensionless

X_{CG} = location of center of gravity along rocket axis, m

x = distance of regressing surface into insulation, m

= distance aft of nose vertex (body station), m

x_{cp} = distance to center of pressure measured from x_{ref}, m

x_i = station i, m

= distance of mass m_i from origin, m

x_j = station j, m

x_n = x/ℓ_N, normalized distance aft of nose vertex (body station), dimensionless

x_{ref} = any convenient station about which bending moment may be calculated, m

Y_{CG} = distance to center of gravity of mass measured normal to axis of rocket, m

y = transverse displacement, m

$y_{dynamic}$ = peak displacement due to a periodic load, m

y_i = displacement at station i due to a unit force, m/N

y_{ij} = displacement at mass point i due to a unit load at mass point j, m/N

y_{static} = deflection of structure due to static application of peak of periodic load, m

y_x = beam displacement at station x, m/N

α = angle of attack, rad

= linear coefficient of thermal expansion, m/m·K

= thermal diffusivity, m²/s

α_{mc} = linear coefficient of expansion for motor case, m/m·K

α_p = linear coefficient of thermal expansion for propellant, m/m·K

β = rotational displacement, rad

$\bar{\gamma}$ = effective gas-specific heat ratio, dimensionless

ϵ = strain, m/m

ϵ_b = propellant mechanical bore strain, m/m

ϵ_e = propellant endurance strain, m/m

ϵ_h = hoop strain, m/m

ϵ_{mech} = mechanical strain, m/m

ϵ_r = radial strain, m/m

ϵ_{total} = total strain, m/m

ζ = structural damping ratio, dimensionless

θ = angle between rocket longitudinal axis and local vertical, rad

$\ddot{\theta}$ = pitch angular acceleration, rad/s²

μ = dynamic viscosity of gas, N·s/m²

ν = Poisson's ratio, dimensionless

Ξ = $\text{Cos}^{-1}(1 - 2x_n)$, parameter used in defining the Haack series of nose shapes, dimensionless

ρ = mass density, kg/m³ or kg/mm³

= insulation density, kg/m³

ρ_{mc} = density of motor case, kg/m³

ρ_p = average propellant density, kg/m³

σ = stress or strength, Pa

= Stefan-Boltzmann constant, 5.67×10^{-3} W/m²·K⁴

σ_{allow} = allowable stress, Pa

$\sigma_{allow,u}$ = ultimate allowable stress, Pa

$\sigma_{allow,y}$ = yield allowable stress, Pa

σ_{crit} = critical compressive stress for a long elastic cylinder, Pa

σ_{des} = calculated stress at design loads, Pa

σ_h = hoop stress, Pa

σ_m = combined meridional stress, Pa

σ_r = radial stress, Pa

σ_s = strength at room temperature (298 K), Pa

= allowable average shear stress, Pa

σ_t = allowable tensile strength, Pa

$\sigma_{u,eff}$ = effective ultimate strength, Pa

$\sigma_{y,eff}$ = effective yield strength, Pa

Ω = parameter used in calculating propellant stress, dimensionless

Ω_p = parameter used in calculating nozzle stress, dimensionless

Ω_t = parameter used in calculating nozzle stress, dimensionless

$\widetilde{\Omega}$ = factor used in beam frequency calculations to account for end constraints, dimensionless

ω_e = excitation frequency, rad/s

ω_n = undamped natural frequency, rad/s

7-1 GENERAL

Recent advancements in materials and manufacturing techniques have led to improved rocket performacne. Contributions also have been made by the advent of advanced computer technology introducing the use of numerical analysis techniques into the design cycle. These advancements now provide the designer with the capability to consider a multitude of configurations to arrive at a near optimum design for a specific set of design constraints.

The designer of a free flight rocket, however, requires knowledge of classical analysis techniques to determine the feasibility of a new system. Considerations must be given to the determination of internal loads induced by the environments, and the effects of internal and external heating also must be addressed. The bulk of this chapter deals with these aspects of the design. The use of the computer, however, is encouraged since intensive efforts are being directed by the aerospace industry toward automated design procedures.

The structural design of a rocket is influenced by the interaction of all the applied loads and the response of the structure. An optimum design can only be achieved through an iterative process. A typical analysis-design cycle is shown in Fig. 7-1.

The execution of the design cycle requires knowledge in many disciplines. Complex topics such as the interrelationship of combustion and structural responses should, however, not be a limiting factor during the preliminary design phase. Acceptability of the conceived design can only be verified through detailed analysis and controlled tests.

The airframe of a typical rocket is comprised of the motor case, the supporting load-carrying structure, and the payload associated structure. The airframe is subjected to a variety of loads from several sources. Airframe load environments include handling and transportation, flight, aerodynamic, thermal, vibration and shock, and buffeting. All load environments must be considered in the assessment of the rocket airframe structure. Airframe loads are generally translated into shear, axial, and bending loads that identify which loading environment is critical at selected locations on the rocket airframe. This allows an assessment of the critical loading environment and allows trade-off studies of the variation in rocket operational factors versus loading environment and structural concepts.
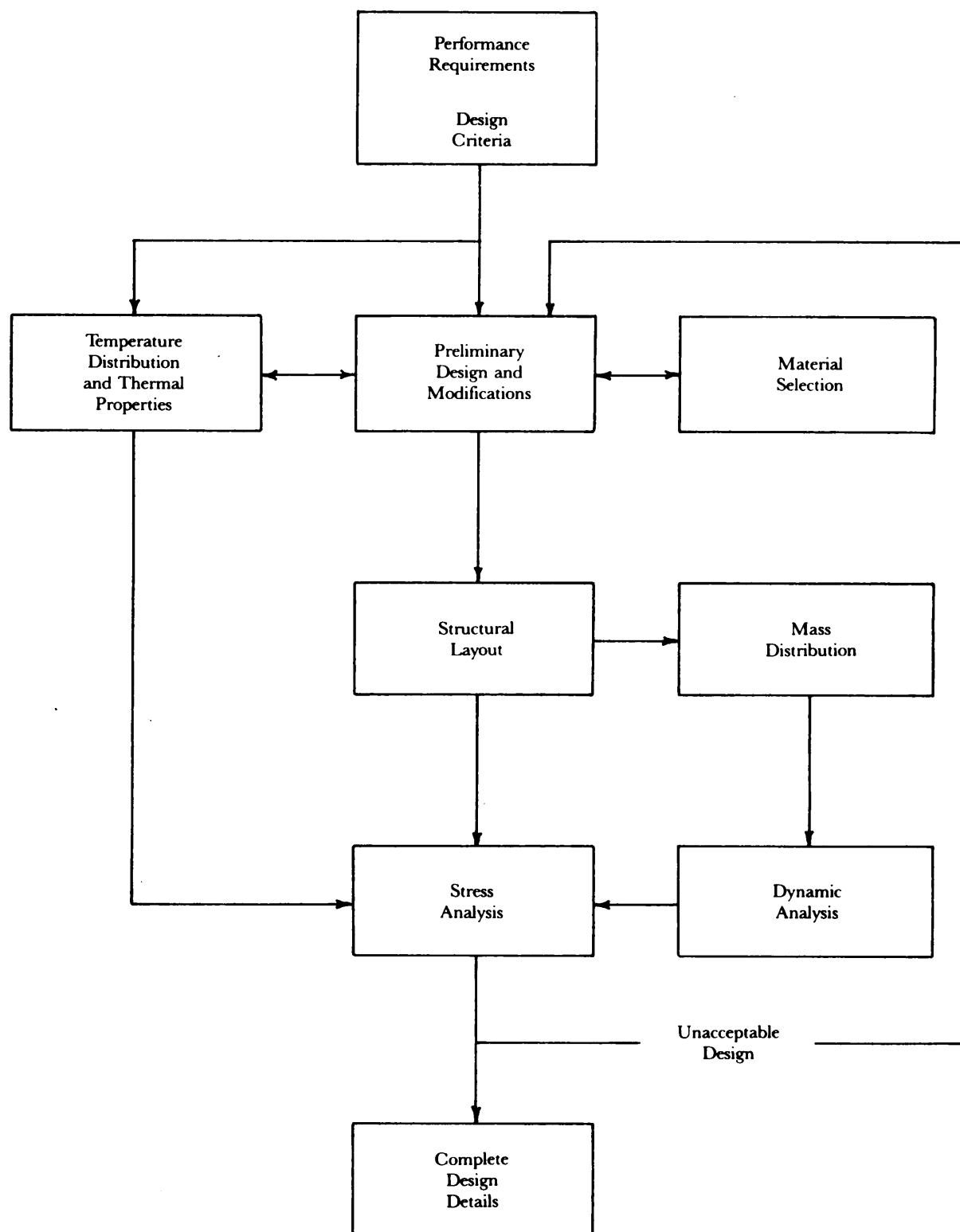
Figure 7-1. Analysis Cycle for Free Flight Rockets

The primary structural design of the airframe can include monocoque (unstiffened) shells, semi-monocoque shells (stiffened with stringers, frames, or corrugation), and trusses and frames. The structural design must be capable of withstanding the tensile loads, and general and local compressive loads. Material properties alone are generally sufficient to evaluate the tensile loading capacity of structural members. Compressive shell loading, however, requires design charts or complex analysis techniques to evaluate failure due to structural instability.

7-2 MASS AND BALANCE

The mass and balance characteristics of a rocket are important elements in the overall evaluation of the structural characteristics. The determination of the loads on a given structural component involves the mass, the mass distribution, the center of gravity (CG) location, and the inertia of the total configuration.

These characteristics vary with time during the motor burn phase of a rocket. A 20-km range rocket might have a mass variation during burn of 40%, a CG variation of 15% of the rocket length, and inertia variation of 30%. The paragraphs that follow present methods for estimating the mass and balance characteristics of a rocket along with their variations during motor operation.

7-2.1 MASS AND CENTER-OF-GRAVITY ESTIMATION

The mass of rocket components or sections can be estimated if equivalent homogeneous mass densities are available and if the volume can be defined. The mass of sections of this nature can be estimated by multiplying the section volume by the average mass density. Average densities of major rocket components are presented in par. 7-4.2.6, "Mass and Size Estimating Relationships".

The mass of a rocket varies with time during motor operation because of the loss of propellant mass. Total mass during the propellant burning phase can be estimated by determining the mass prior to motor ignition and subtracting the product of propellant burning time and average mass flow rate.

The material volume of thin-skinned monocoque shells can be approximated by multiplying the shell surface area by the skin thickness. Equations for evaluating the volume of typical rocket components are presented in Table 7-1.

The surface area and volume of certain nose shapes are not so easily determined. Nose shapes can be divided into three classes or families—the Power Series, the Parabolic Series, and the Sears-Haack Series —and are defined as follows:

1. The Power Series is defined by (see Fig. 7-2(A))

$$r_n = x_n^k, \text{ dimensionless} \tag{7-1}$$

where

r_n = normalized transverse nose radius at station x, dimensionless
$x_n = x/\ell_N$, normalized distance aft of nose vertex, dimensionless
k = parameter defining nose shape, dimensionless
x = distance aft of nose vertex (body station), m
ℓ_N = nose length, m.

Three nose shapes of the Power Series family investigated in Ref. 1 are

Nose Shapes	k
Cone	1
3/4 Power Nose	3/4
1/2 Power Nose	1/2 (parabola with vertex at $x = 0$).

2. The Parabolic Series shape is defined by

$$r_n = \frac{2x_n - kx_n^2}{2 - k}, \text{ dimensionless} \tag{7-2}$$

TABLE 7-1. MASS PROPERTIES OF SIMPLE GEOMETRIC SHAPES
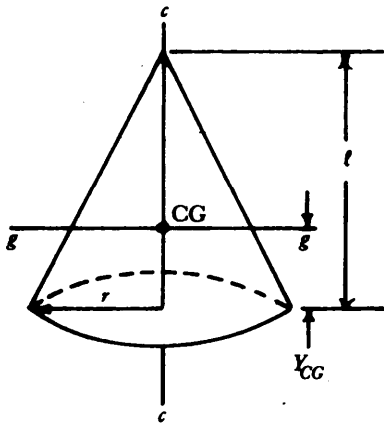
CONE

Surface
  Area $= \pi r (r^2 + \ell^2)^{0.5}$

Volume $= (\pi r^2 \ell)/3$

$Y_{CG} = \ell/4$

$\bar{I}_g = \dfrac{3m}{20}[r^2 + (\ell/2)^2]$

$\bar{I}_c = \dfrac{3mr^2}{10}$
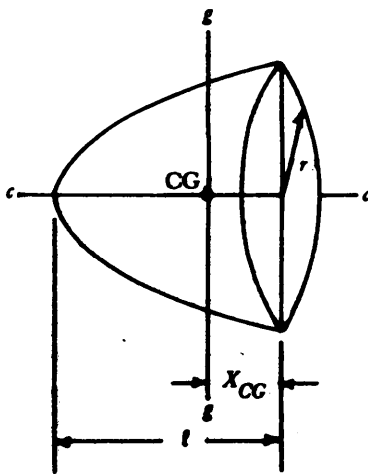
PARABALOID OF REVOLUTION

Surface
Area $= \dfrac{4\pi r}{3\ell^2}\left[\left(\dfrac{r^2}{4} + \ell^2\right)^{1.5} - (r/2)^3\right]$

Volume $= (\pi \ell r^2)/2$

$X_{CG} = \ell/3$

$\bar{I}_g = \dfrac{m}{18}(3r^2 + \ell^2)$

$\bar{I}_c = mr^2/3$
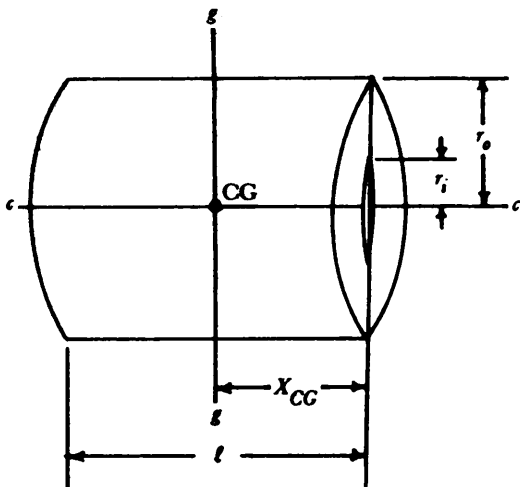
ANNULAR CYLINDER

Surface
  Area $= 2\pi r_o \ell$
(outside)

Volume $= (r_o^2 - r_i^2)\pi\ell$

$X_{CG} = \ell/2$

$\bar{I}_g = \dfrac{m}{12}(3r_o^2 + 3r_i^2 + \ell^2)$

$\bar{I}_c = \dfrac{m}{2}(r_o^2 + r_i^2)$

TABLE 7-1. (cont'd)

FIN
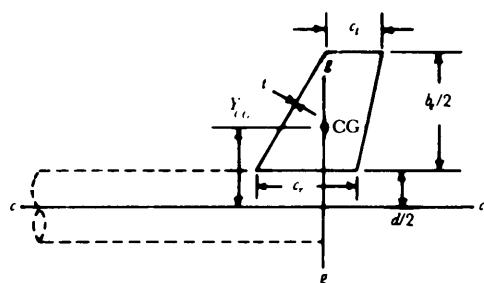
$$\text{Surface Area} = \text{Treat as sum of simple shapes.}$$

$$Y_{CG} = \left(\frac{b_e}{6}\right)\left(\frac{c_r + 2c_t}{c_r + c_t}\right) + \frac{d}{2}$$

X_{CG} is at centroid of area.

$$\text{Volume} = \frac{b_e l}{4}(c_r + c_t)$$

$$\bar{I}_g \approx 0 \text{ (compared to pitch inertia)}$$

$$\bar{I}_c = \frac{m}{4}\left[d^2 + \left(\frac{b_e^2}{6}\right)\left(\frac{c_r + 3c_t}{c_r + c_t}\right)\right]$$
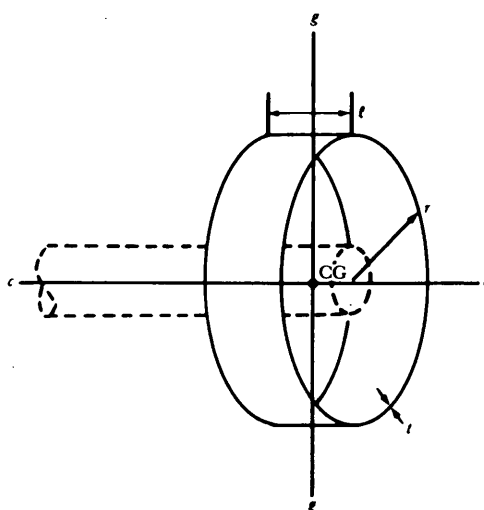
RINGTAIL

$$\text{Surface Area} \approx 2\pi r l$$

CG is area sectional centroid projected onto c-c.

$$\text{Volume} = 2\pi r A_{cs}$$

$$\bar{I}_g \approx 0$$

$$\bar{I}_c \approx mr^2$$

A_{cs} is cross-sectional area of airfoil.

where

r_n = normalized local transverse nose radius at station x, dimensionless.

Three popular series of the parabolic family are

Nose Shapes	k
1/2 Power Parabolic Nose	1/2
3/4 Power Parabolic Nose	3/4
Parabolic Nose	1 (circular arc).

When $k = 0$, Eq. 7-2 reduces to a cone.

The circular are nose shape gives rise to a series of noses called secant ogives or ogives. Ogives are completely defined by two parameters: (1) the radius r_s of the circular arc, i.e., secant ogive generating radius and (2) the location ℓ_c of the projection of the center of the circle of radius r_s along the rocket centerline.

A tangent ogive is one in which the circular arc of the ogive becomes tangent to the cylinder as illustrated in Fig. 7-2(B). This figure also shows the location of the center of the circular arc for a secant ogive which forms a corner or discontinuity at the juncture to a cylinder. That is, a tangent ogive has a center of

(A) Radial Nose Coordinates

(B) Ogive Meridional Generating Radii
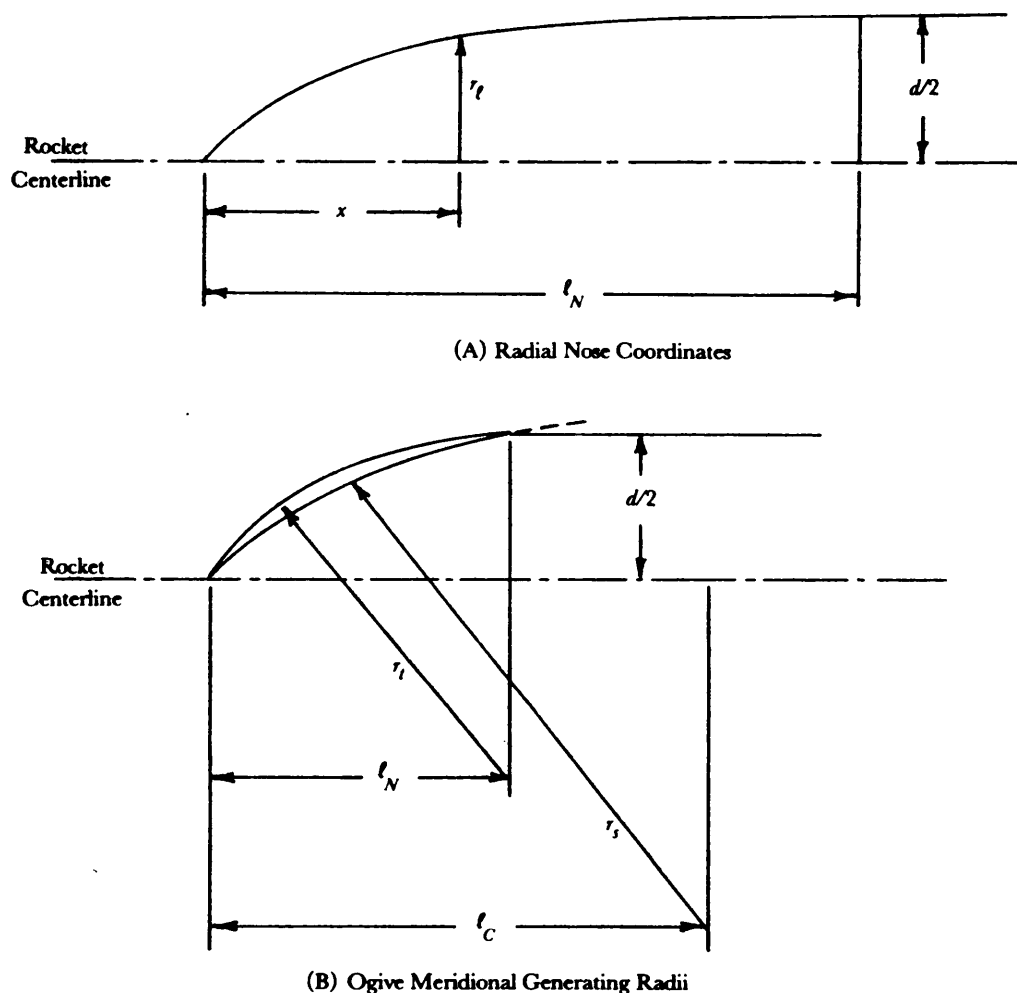
Figure 7-2. Illustration of Symbols Used in Nose Shape Defining Equations

curvature on a line perpendicular to the longitudinal axis directly below the tangent point, whereas the secant ogive has its center of curvature below and aft of this line.

The term ℓ_N/d is called the nose fineness ratio. The radius of curvature of an ogival surface usually is defined in calibers (cal), which is the radius of the arc divided by the diameter of the base. Hence a "3-cal ogive" has a radius of curvature that is 3 times the diameter of the base. The caliber and the center of arc locations describe the shape and the length-to-diameter ratio of an ogival shape.

For a tangent ogive, the relation between caliber c and length-to-diameter ratio ℓ_N/d is

$$\frac{\ell_N}{d} = \sqrt{c - 0.25}, \text{ dimensionless.} \tag{7-3}$$

Ogives have the advantage, without increasing drag, of providing larger apex angles and greater nose volumes than cones of the same fineness ratio. The drag of a tangent ogive is slightly larger than that of the inscribed cone, and a secant ogive has less drag than either. A minimum drag secant ogive has a contour radius that is twice the tangent ogive radius.

3. The Sears-Haack Series shape is defined by

$$r_n = \frac{1}{\sqrt{\pi}} \sqrt{\Xi - \frac{1}{2} \sin(2\Xi) + k(\sin\Xi)^3}, \text{ dimensionless} \tag{7-4}$$

where

$$\Xi = \text{Cos}^{-1}(1 - 2x_n), \text{ dimensionless} \tag{7-5}$$

r_n = normalized local transverse radius of station x, dimensionless.

Two popular shapes of the Sears-Haack Series are

Nose Shapes	k
L-D (Von Karman)	0
L-V	1/3.

L-V designates the boundary condition of length and volume used in an analysis to determine the minimum drag shape, and L-D denotes length and diameter. The Von Karman nose shape has the most volume of any of the shapes described.

The Von Karman nose shape has a low transonic drag coefficient that is only slightly higher than the minimum drag secant ogive. It has an 8% larger volume than the minimum drag secant ogive, giving the Von Karman the most efficient volume per unit nose drag.

The normalized shape of the meridian of each of these noses is presented in Table 7-2. The volume of several nose shapes may be determined from Fig. 7-3. The volume of various secant ogives is presented in Fig. 7-4 as the ratio of the nose volume to the volume of a cone with the same fineness ratio. The volume of the equivalent cone can be obtained from Fig. 7-3, or it can be calculated by using the equation in Table 7-1. The secant ogive configurations are identified in terms of the ratio r_t/r_s of the tangent ogive meridian generating radius r_t to the secant ogive meridian generating radius r_s. The minimum drag secant ogive has a generating radius ratio of $r_t/r_s = 0.5$. The volume ratio versus nose fineness ratio f_n is presented in Fig. 7-5 for the Von Karman, the tangent ogive, and the minimum drag secant ogive.

The surface area of various nose shapes may be determined from Fig. 7-6. The surface area ratio versus the meridian generating radius ratio for the family of secant ogives is presented in Fig. 7-7. The cone surface area can be obtained by using the equation in Table 7-1. The surface area ratio versus fineness ratio is presented in Fig. 7-8 for selected ogives.

The location of the CG of typical rocket sections is presented in Table 7-1. The CG of an ogive-shaped mass may be determined from Fig. 7-9. For convenience, the location of the CG of each section should be referenced to a common reference point. The location of the CG of the complete rocket configuration can be estimated by summing moments of the mass of each section about a rocket reference point and dividing by the total mass.

Applications of Table 7-1, Fig. 7-6, and Fig. 7-9 to two shell types are illustrated in Example 7-1.

EXAMPLE 7-1:

Determine the masses and CG locations of two thin-walled payload fairings in which planforms are described by the tangent ogive and the cone. Parameters basic to both geometric types are

$d = 100$ mm, base diameter

$\ell_N = 300$ mm, length of fairing

$t = 2.54$ mm, thickness of fairing

$\rho = 2.768 \times 10^{-6}$ kg/mm³, density of material.

MIL-HDBK-762(MI)

TABLE 7-2. NORMALIZED COORDINATES OF SEVERAL NOSE SHAPES

| Nose Station | Power Series | | Parabolic Series | | | Sears-Haack Series | | Minimum Drag Secant Ogive $(r_t/r_s = 0.5)$ |
	½-Power Nose $(k = \frac{1}{2})$	¾-Power Nose $(k = \frac{3}{4})$	"½-Power" Parabolic $(k = \frac{1}{2})$	"¾-Power" Parabolic $(k = \frac{3}{4})$	†Parabolic Nose $(k = 1)$	L-D Sears-Haack (Von Karman) $(k = 0)$	L-V Sears-Haack $(k = \frac{1}{3})$	
x_n	r_n	r_n	r_n	r_n	r_n	r_n	r_n	r_n
0	0	0	0	0	0	0	0	0
0.05	0.2236	0.1057	0.0658	0.0785	0.0975	0.1367	0.1658	0.0745
0.10	0.3172	0.1778	0.1300	0.1540	0.1900	0.2281	0.2738	0.1463
0.15	0.3873	0.2410	0.1925	0.2265	0.2750	0.3067	0.3643	0.2154
0.20	0.4472	0.2991	0.2533	0.2960	0.3600	0.3773	0.4435	0.2820
0.25	0.5000	0.3536	0.3125	0.3625	0.4375	0.4422	0.5142	0.3459
0.30	0.5477	0.4054	0.3700	0.4260	0.5100	0.5022	0.5779	0.4072
0.35	0.5916	0.4550	0.4258	0.4865	0.5775	0.5585	0.6356	0.4660
0.40	0.6325	0.5030	0.4800	0.5440	0.6400	0.6112	0.6880	0.5222
0.45	0.6708	0.5494	0.5325	0.5985	0.6975	0.6606	0.7355	0.5758
0.50	0.7071	0.5946	0.5833	0.6500	0.7500	0.7071	0.7785	0.6269
0.55	0.7416	0.6387	0.6325	0.6985	0.7975	0.7507	0.8174	0.6755
0.60	0.7746	0.6817	0.6800	0.7440	0.8400	0.7915	0.8522	0.7215
0.65	0.8062	0.7239	0.7258	0.7865	0.8775	0.8295	0.8833	0.7652
0.70	0.8367	0.7653	0.7700	0.8260	0.9100	0.8647	0.9107	0.8061
0.75	0.8660	0.8059	0.8125	0.8625	0.9375	0.8969	0.9346	0.8446
0.80	0.8944	0.8459	0.8533	0.8960	0.9600	0.9261	0.9550	0.8806
0.85	0.9220	0.8853	0.8925	0.9265	0.9775	0.9518	0.9719	0.9142
0.90	0.9487	0.9240	0.9300	0.9540	0.9900	0.9736	0.9853	0.9452
0.95	0.9747	0.9622	0.9658	0.9785	0.9975	0.9906	0.9950	0.9739
1.00	1.0000	1.0000	1.0000	1.0000	1.0000	1.0000	1.0000	1.0000

†More commonly known as the "tangent ogive" nose shape with $r_t = l_N$.

Solution:

Compute fineness ratio f_n:

$l_N/d = 300/100 = 3$

and, using this parameter, refer to appropriate figures or Table 7-1 to determine mass and CG location.

Tangent Ogive   Cone

Ratio of Surface Area A_S to Square of Base Diameter d

$A_S/d^2 = 6.375$, from Fig. 7-6 $A_S/d^2 = 4.75$, from Fig. 7-6

Surface Area

$A_S = 6.375(100)^2$ $A_S = 4.75(100)^2$
$\quad = 63,750 \text{ mm}^2$ $\quad = 47,500 \text{ mm}^2$

(Also calculable from equation in Table 7-1)
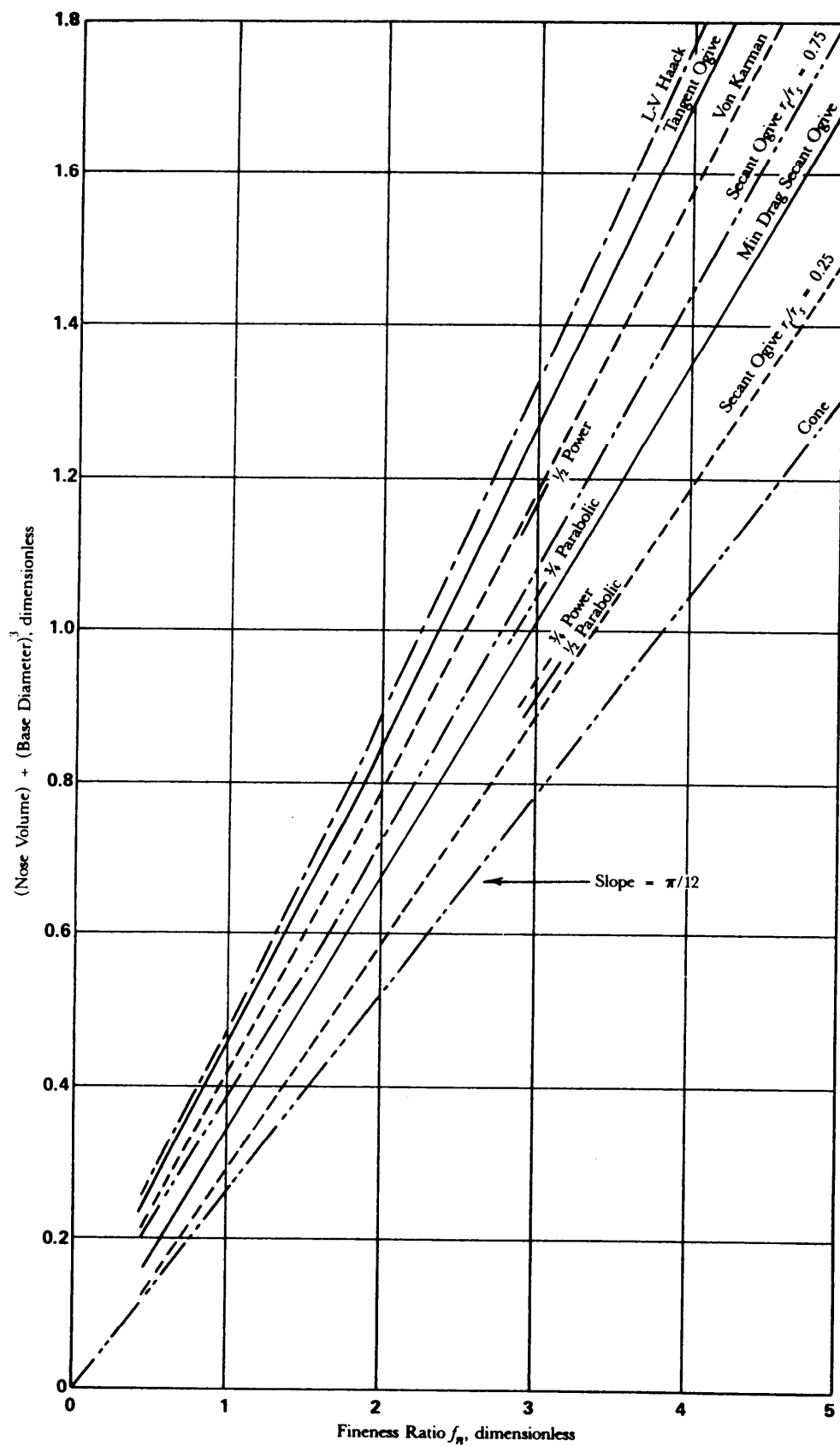
Figure 7-3. Volume of Nose Shapes
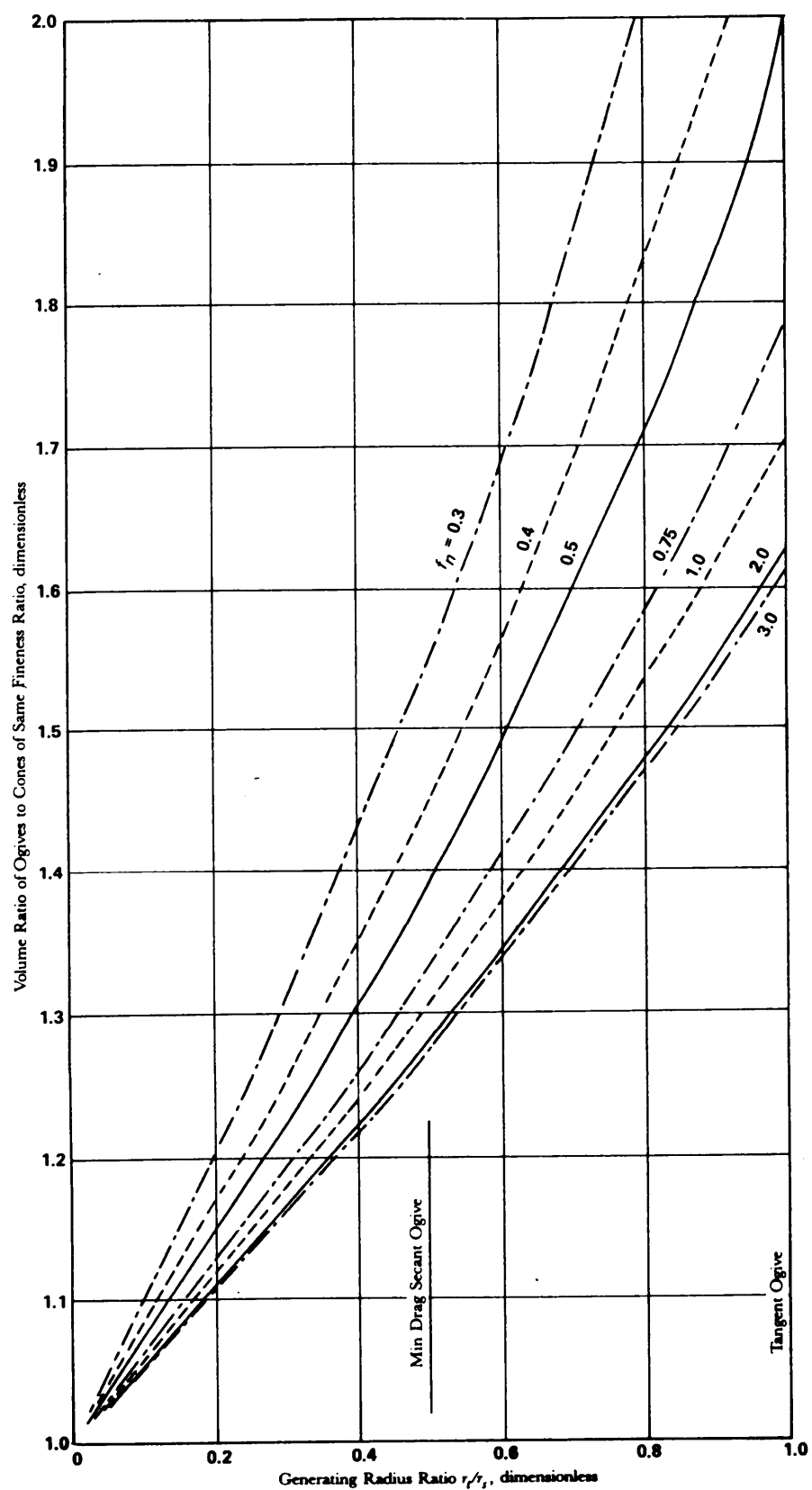
Figure 7-4. Ratio of Secant Ogive Volumes to Cone Volume
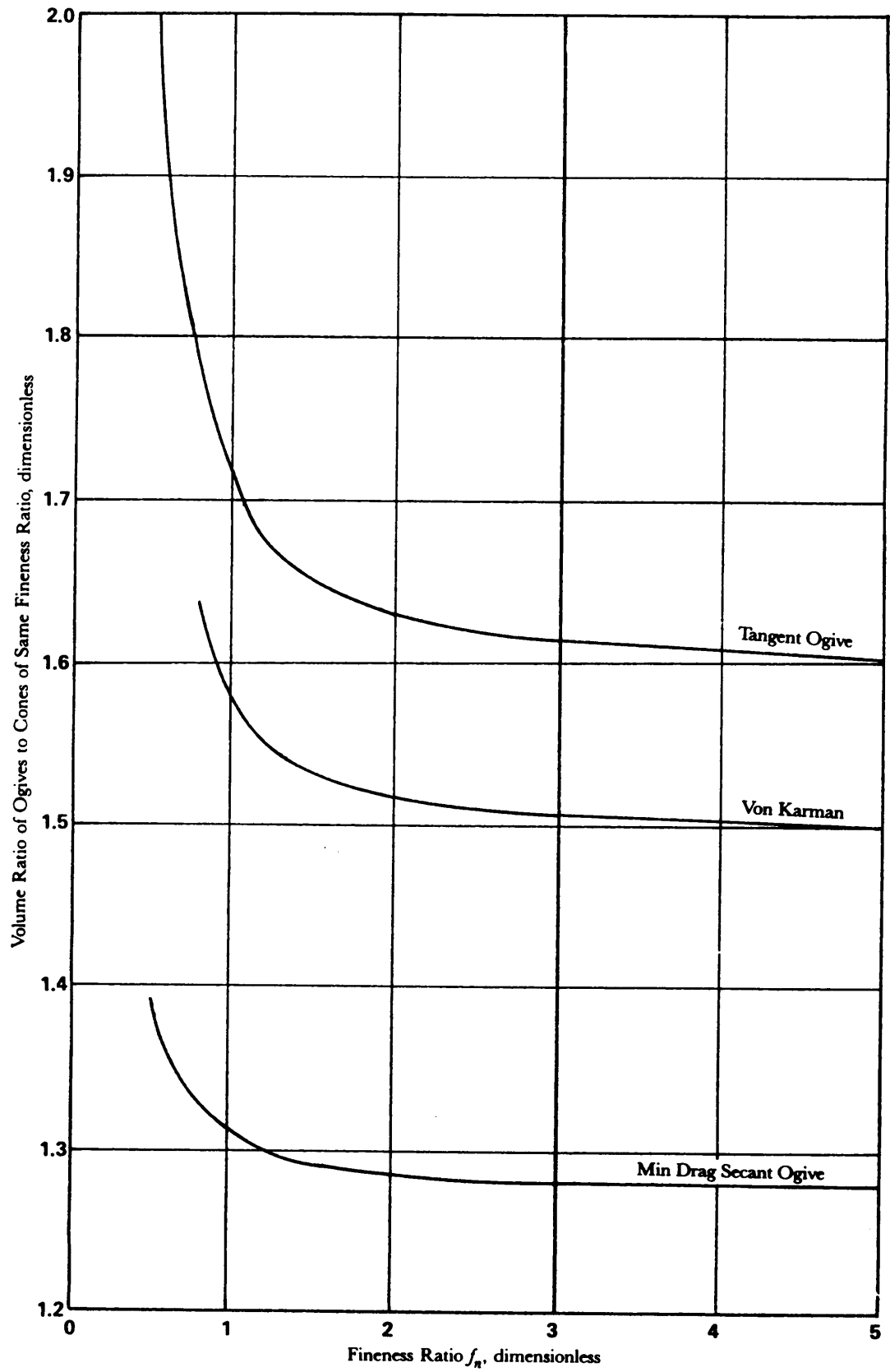
Figure 7-5. Ratio of Ogival Volumes to Cone Volume
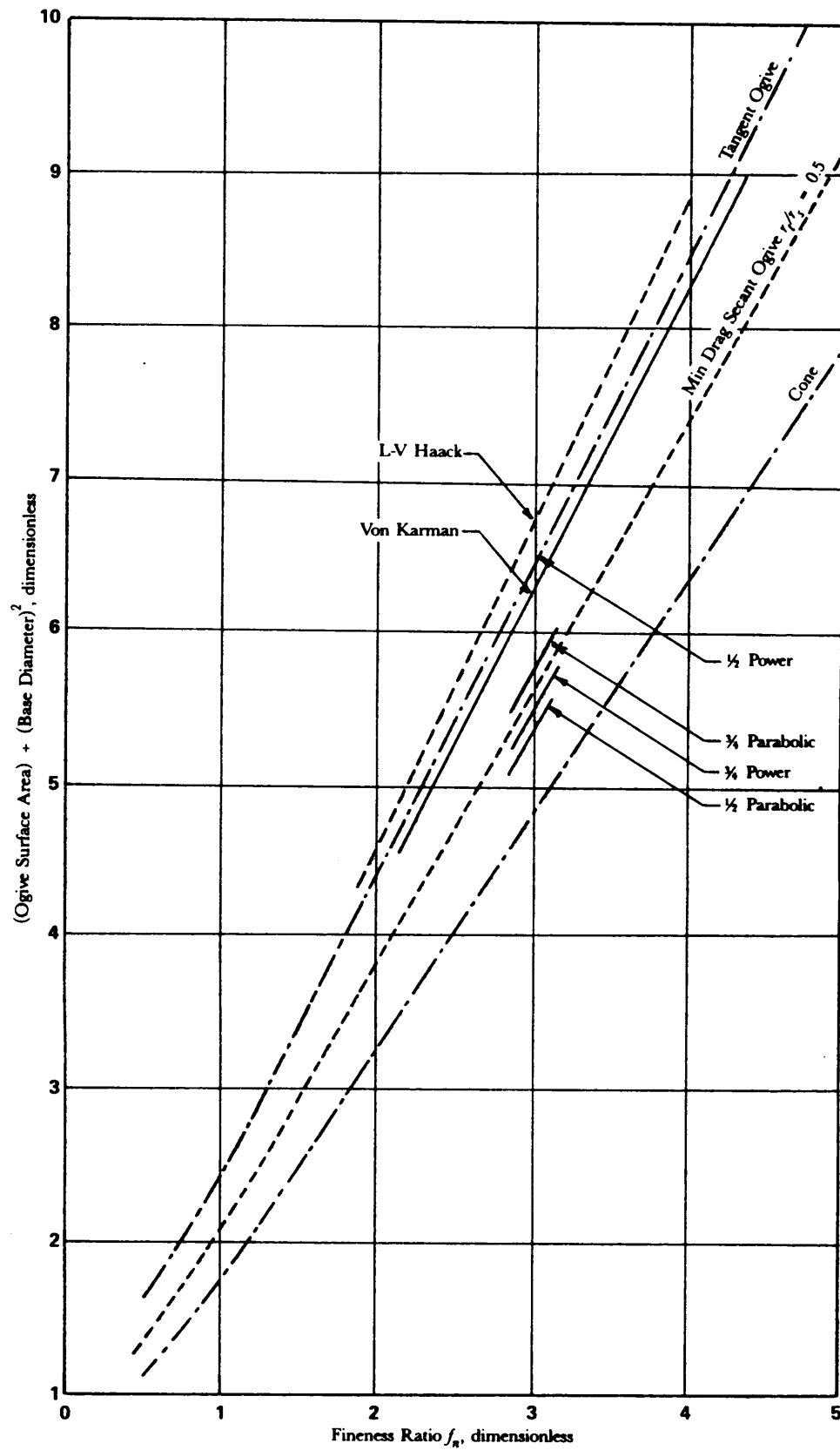
Figure 7-6. Surface Area of Nose Shapes
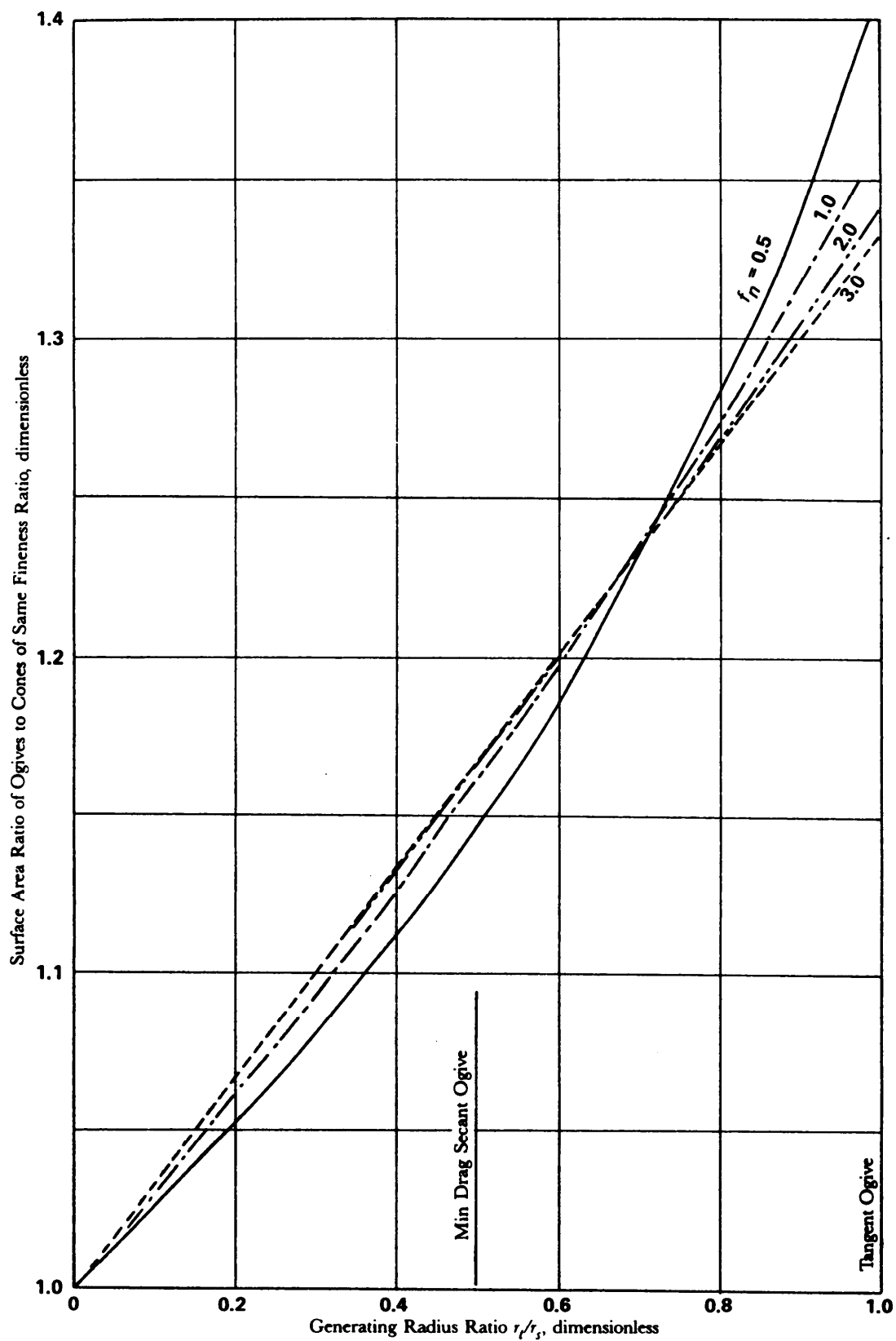
Figure 7-7. Ratio of Secant Ogive Surface Areas to Cone Area
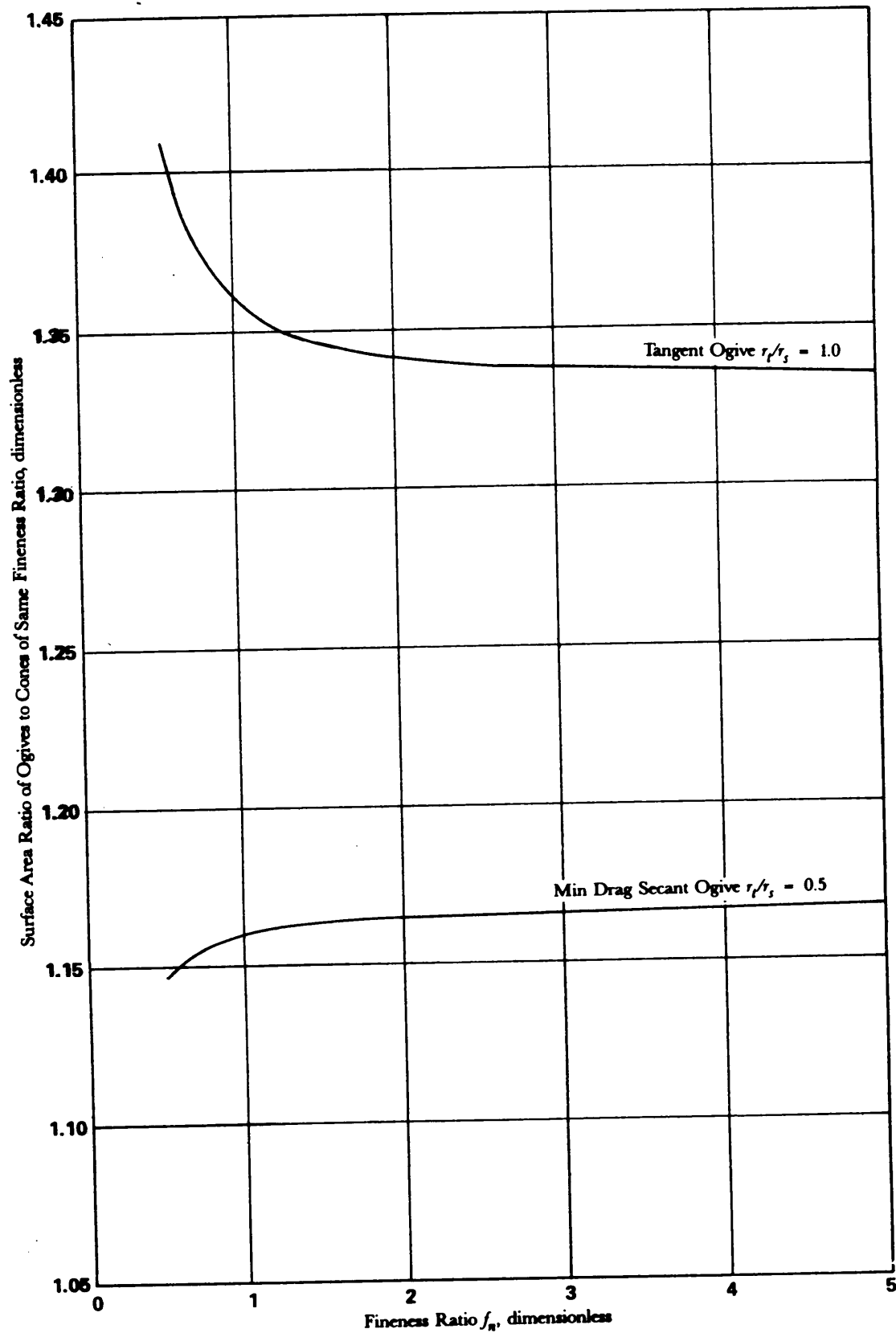
Figure 7-8. Ratio of Ogival Surface Areas to Cone Area
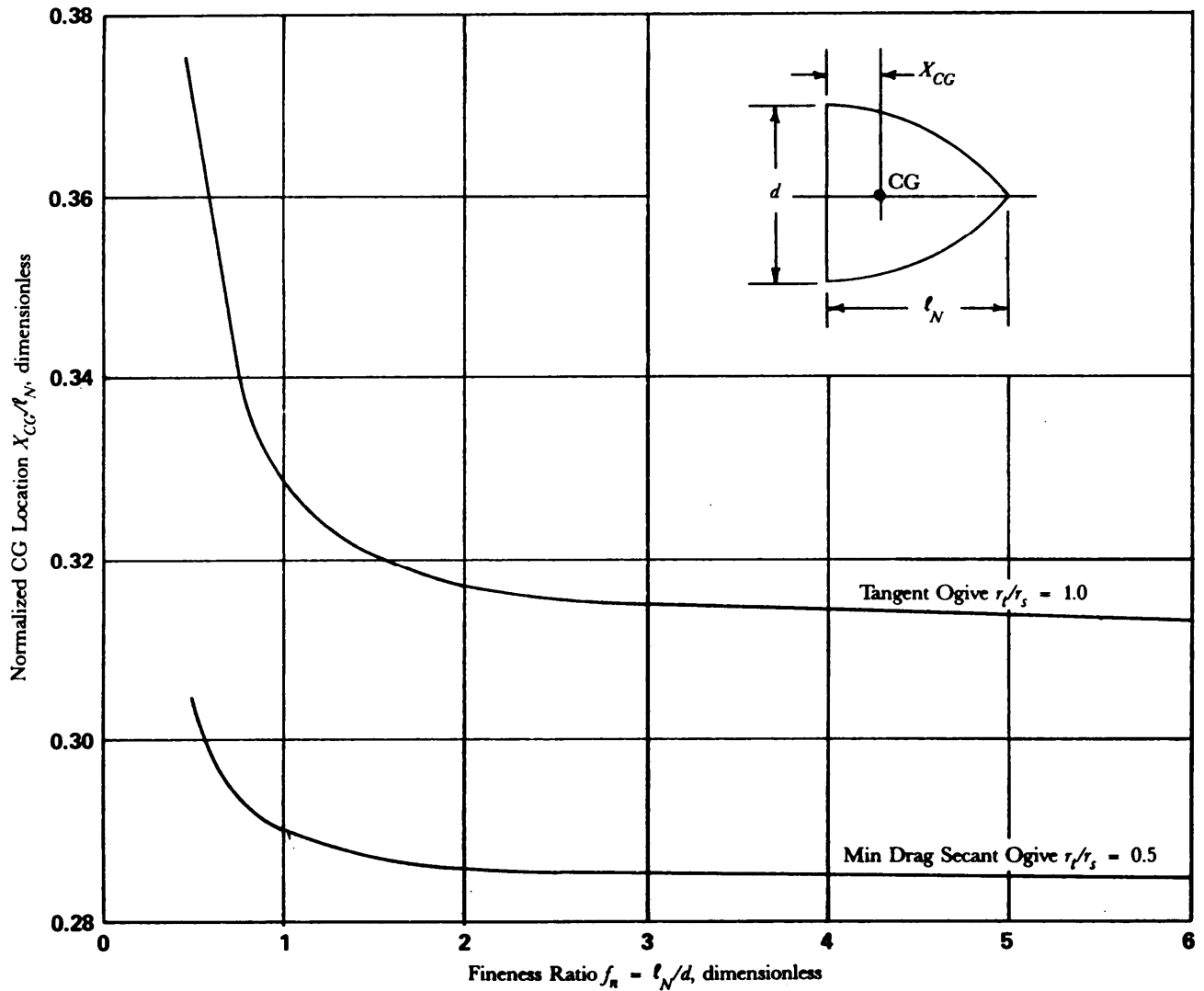
Figure 7-9. CG Location **of Ogival Shapes**

Tangent Ogive	Cone

Volume of Fairing

$V = A_s t$
$\quad = 63{,}750\,(2.54)$
$\quad = 161{,}925 \text{ mm}^3$

$V = A_s t$
$\quad = 47{,}500\,(2.54)$
$\quad = 120{,}650 \text{ mm}^3$

Mass

$m = V\rho$
$\quad = 161{,}925\,(2.768 \times 10^{-6})$
$\quad = 0.4482 \text{ kg}$

$m = V\rho$
$\quad = 120{,}650\,(2.768 \times 10^{-6})$
$\quad = 0.3340 \text{ kg}$

CG Location From Base

$X_{CG}/\ell_N = 0.315$, from Fig. 7-9
$\quad X_{CG} = 0.315\,(300)$
$\quad\quad = 94.5 \text{ mm}$

$X_{CG} = \ell_N/4$, from Table 7-1
$\quad = 300/4$
$\quad = 75 \text{ mm.}$

7-2.2 TRANSVERSE MOMENT OF INERTIA

The rocket transverse moment of inertia is the mass moment of inertia of the complete configuration referenced to the CG about a transverse axis. The transverse moment of inertia varies from rmotor ignition to burnout as the rocket mass and CG location change. The determination of the transverse moment of inertia during motor operation can be a difficult and time-consuming process for complex propellant grain configurations. Preliminary values can be obtained by estimating the transverse moment of inertia for the fully loaded rocket and the rocket at burnout and by assuming a linear variation with burn time or a bilinear variation for a boost-sustain burn mode. Estimates of the transverse moments of inertia can be made by dividing the rocket into sections of homogeneous materials and easily defined geometries.

The transverse moment of inertia of the complete configuration can then be determined by calculating the moments of inertia of individual sections and then transferring the section moments of inertia to the rocket CG location. The section moments of inertia can be evaluated with respect to an axis through the section CG using the equations presented in Table 7-1. The normalized transverse moment of inertia of various ogival configurations about the nose CG is presented in Fig. 7-10. The section moments of inertia can be transferred to the rocket CG by using the Parallel Axis Theorem, i.e.,

$$\overline{I}_{rocket} = \overline{I}_{section} + m\ell^2, \text{ kg·m}^2 \tag{7-6}$$

where

$\overline{I}_{rocket}$ = mass moment of inertia of section referenced to rocket CG, kg·m^2
$\overline{I}_{section}$ = mass moment of inertia of section about section CG, kg·m^2
m = mass of section with moment to be transferred, kg
ℓ = distance from CG of section to CG of rocket, m.

The moments of inertia of rocket sections that are partially hollow or are made up of composite materials can be estimated by assuming that the total moment of inertia is equal to the algebraic sum of the parts. Thus, the total moment of inertia of a cone with a cylindrical hole can be approximated by the moment of inertia of the solid cone less the moment of inertia of the "solid" cylindrical cavity.

7-2.3 ROLL MOMENT OF INERTIA

The roll moment of inertia is the mass moment of inertia of the complete rocket configuration about the longitudinal axis of symmetry. The roll moment of inertia of a rocket also varies as the propellant mass is consumed. Preliminary estimates of the roll inertia can be made by dividing the rocket into simple sections of homogeneous materials in the same manner as was used to determine the transverse moment of inertia. The normalized roll moment of inertia of the complete configuration is the algebraic sum of the individual section moments of inertia. The moment of inertia of a typical rocket section can be determined by using the equations in Table 7-1. The roll moment of inertia for an ogive shape can be estimated from Fig. 7-11, and the equation for the roll moment of inertia of a cone can be found in Table 7-1. The moments of inertia of sections that are partially hollow or are made up of composite materials may be evaluated as outlined in par. 7-2.2 by the algebraic summation of the moments of inertia by parts.

7-3 LOADS

The term "applied loads" refers to the maximum loads anticipated on the rocket during its service life. The rocket should be capable of supporting the applied loads without suffering detrimental, permanent deformations. Ultimate or design loads are equal to the applied loads multiplied by a factor of safety FS.

The preliminary design of a rocket must satisfy the requirements of the various environments that may be experienced during its operational life. The environments include storage, transportation and handling, launch, and flight. If the payload consists of submunitions, then payload dispersal loads also must be considered. Additional load requirements may be imposed on the warhead from impact
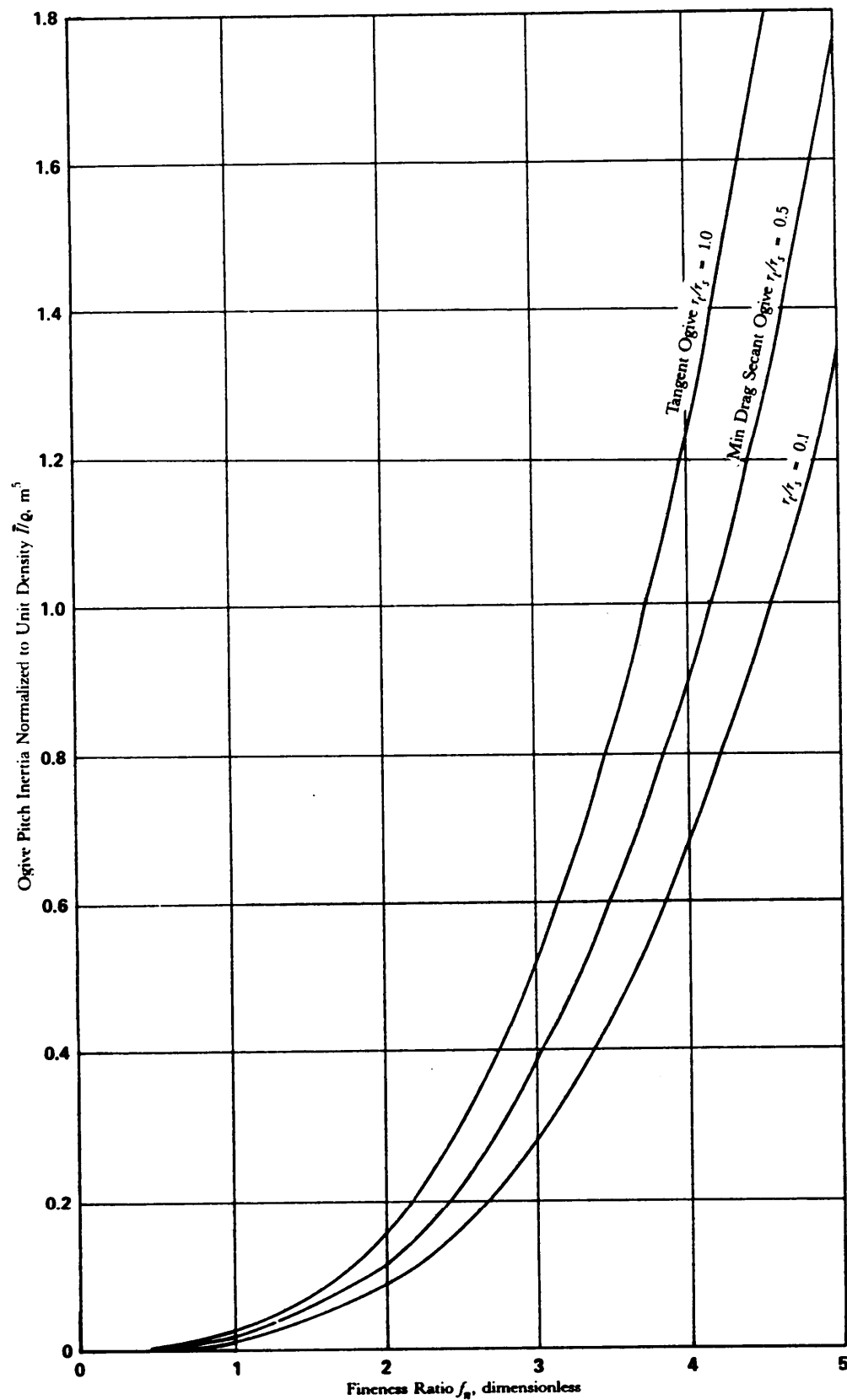
Figure 7-10. Secant Ogive Pitch Inertia vs Fineness Ratio
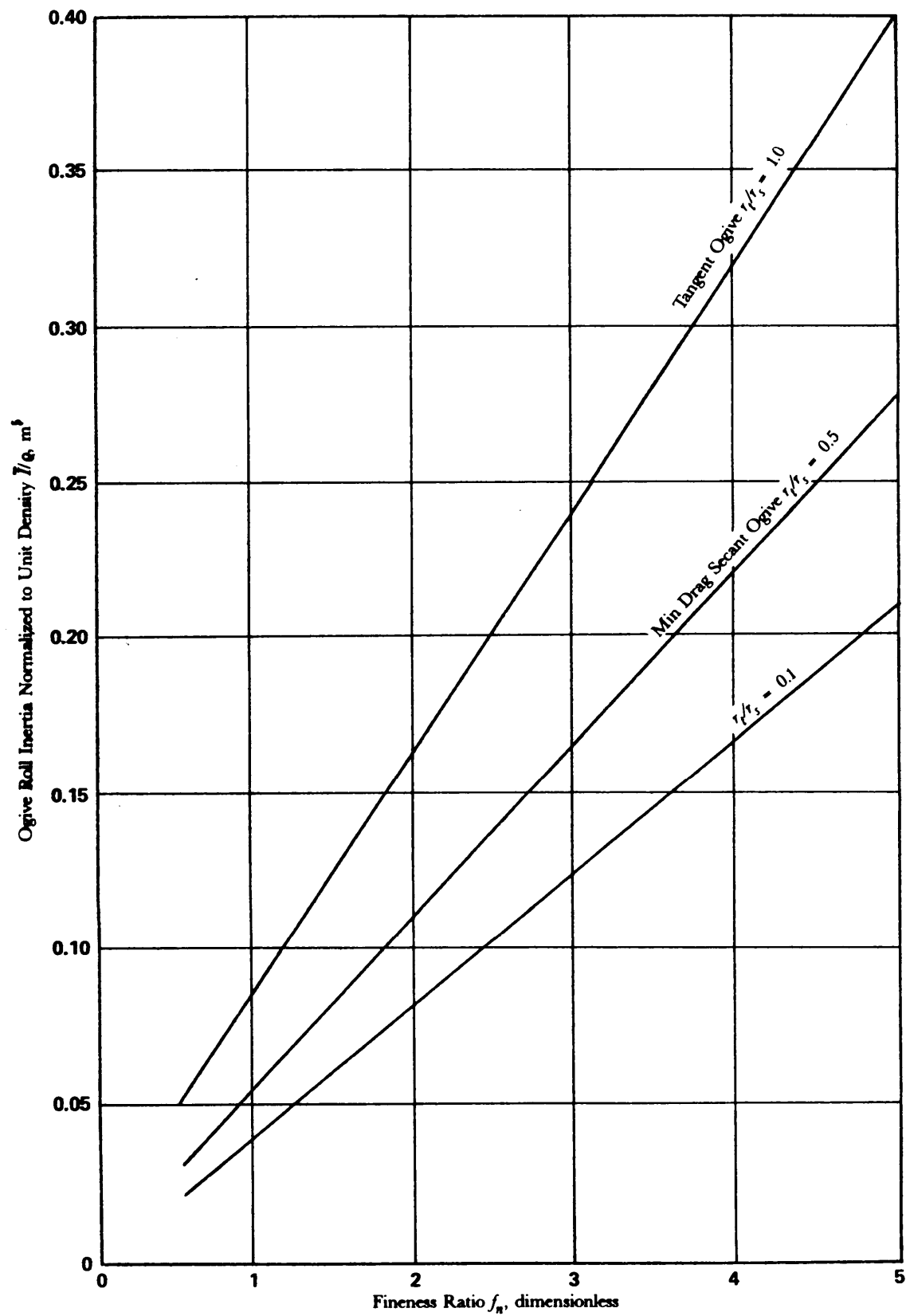
Figure 7-11. Secant Ogive Roll Inertia vs Fineness Ratio

considerations. The load conditions described in the paragraphs that follow address only transportation and handling, launch, and flight loads.

7-3.1 TRANSPORTATION AND HANDLING LOADS

During transportation and handling, the rocket will be subjected to vibration, shock, temperature changes, and moisture. Transportation and handling loads may have to be considered for both the total rocket and individual components. Rocket components can be designed to be transported in separate containers for assembly in the field. The container may be designed to be a combination container and launcher. Container launchers are discussed in Chapter 8.

Various packaging techniques are available for shipment (Ref. 2). The loads during shipment by truck, ship, railway, or airplane have been specified in a number of reports (Refs. 3 through 5). Ref. 6 discusses the design of containers for rockets.

The variations caused by the human factors involved in handling make the problem of specifying loads very difficult. In general, realistic field conditions are simulated by drop tests. The heights used for these tests vary from 1.0 m for 9-kg articles to 0.3 m for articles whose mass is more than 45 kg.

The field carrier vehicle for the rocket must also be considered. If the rocket is an indirect fire weapon, it could be carried by a tracked vehicle or a truck. Rockets launched from aircraft maybe subjected to aircraft maneuver loads and severe vibrations.

The field carrier vehicle load environments should be determined from manufacturer's or the (government's performance specifications for the particular vehicle involved. Military specifications are generally available to define the environmental conditions for the design of a particular class of rockets. The specifications should be consulted when evaluating design loads.

7-3.2 LAUNCH LOADS

Launching a rocket produces significant loads that must be assessed in the development of the total load environment. Launch loads are principally a function of motor chamber pressure, rocket acceleration level, and the interaction of the rocket and launcher during initial guidance.

The rocket inter-acts with the launcher through launch shoes, bore riders, or other mechanical interfaces. Thrust misalignment, mass unbalances, and the type and location of the mechanical interfaces can combine to produce significant bending of the rocket during launch. The dynamic interaction between the flexible rocket and the flexible launcher is a complex problem and few generalized results are available for use in the preliminary design phase. Some approximate analysis techniques, however, are available in Ref. 7.

Transient loads may be significant during motor ignition and at the release of the mechanical interfaces. Chapter 8 presents several rocket/launcher interfaces and discusses rocket bending effects in more detail.

7-3.3 FLIGHT LOADS

During flight, the rocket is subjected to loads from motor thrust, aerodynamic lift, aerodynamic drag, inertia of rocket components, gravity, and internal pressures. These loads are reacted by the rocket structure as axial load, shear load, and beam bending moment.

The axial load is made up of forces from the motor thrust, aerodynamic drag, inertia of the rocket mass in the axial direction, gravitational force component acting along the axis of the body, and internal pressures. Fig. 7-12 shows a descriptive free-body diagram of the axial forces acting on a rocket in powered flight. In accelerated flight, equilibrium requires that

$$am - F_T + F_A + mg_0 \cos\theta = 0, \text{ N} \tag{7-7}$$

where

a = rocket acceleration along longitudinal axis, m/s^2

F_T = rocket motor thrust, N

(A) Axial Loads   (B) Principal Forces on Rocket Section
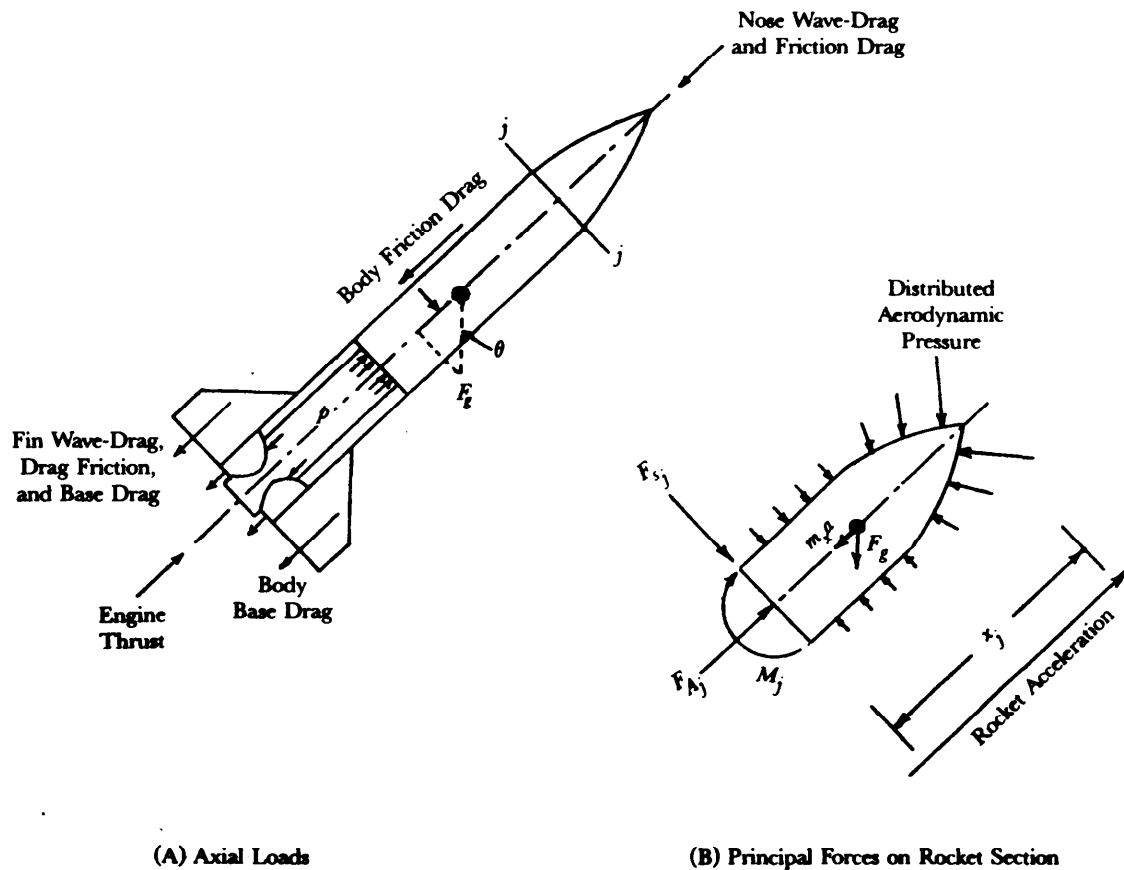
Figure 7-12. Axial Loads on Free Flight Rocket

F_A = sum of axial components of aerodynamic forces, N
g_0 = acceleration due to gravity, m/s^2
θ = angle between rocket longitudinal axis and local vertical, rad.

Likewise, the axial load $F_{A_{xx}}$ at any plane x-x is found by

$$F_{A_{xx}} = am_x + F_{A_x} + m_x g_0 \cos\theta - pA_{xx}, \text{ N} \qquad (7\text{-}8)$$

where
$F_{A_{xx}}$ = axial load on rocket at plane x-x, N
m_x = rocket mass forward of plane x-x, kg
F_{A_x} = axial force on rocket forward of plane x-x, N
p = motor internal gage pressure, Pa
A_{xx} = area of the plane perpendicular to the longitudinal axis on which the motor (internal) pressure acts, m^2.

The axial force coefficients on the rocket sections can be evaluated by the methods of Chapter 5. The axial force F_A can then be determined as follows:

$$F_A = C_A q A_{ref}, \text{ N} \qquad (7\text{-}9)$$

where

C_A = aerodynamic axial force coefficient, dimensionless
q = dynamic pressure, Pa
A_{ref} = rocket reference area, m^2.

The normal force coefficient gradient of rocket sections can be evaluated as indicated in par. 5-3. The normal force FN can be determined as follows:

$$F_N = C_{N_\alpha} \alpha q \, A_{ref}, \text{ N} \qquad (7\text{-}10)$$

where

F_N = normal force, N
α = angle of attack, rad
C_{N_α} = aerodynamic normal force coefficient gradient, rad^{-1}.

The bending moment M at any section of the rocket is equal to the algebraic sum of the moments of the folces. A schematic of the moments and forms acting at rocket station x_j is shown in Fig. 7-12(B).

The circumferential load in the combustion chamber cylinder walls, as shown in Fig. 7-13, is caused by the internal pressure acting on all exposed surfaces along the cylinder. The circumferential (hoop) load per unit length is

$$F_h = p r_{mc}, \text{ N/m} \qquad (7\text{-}11)$$

where

F_h = hoop load per unit length, N/m
r_{mc} = average radius of the motor case, m.

The bending moment at rocket station x_j results from the combined action of aerodynamic lift and inertial forces acting in a direction perpendicular to the body axis at some distance away from station x_j.
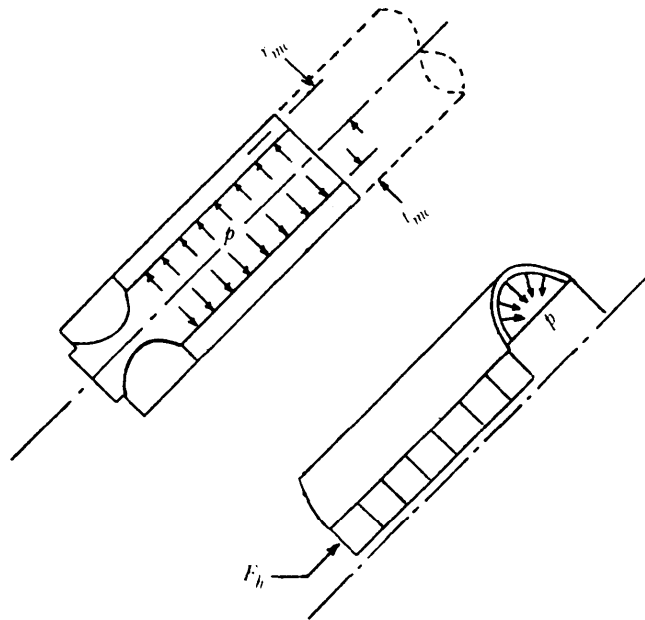
Figure 7-13. Circumferential Loads on Motor Case

For preliminary design purposes, the mass of the rocket sections can be considered to be concentrated at the CG of the sections. The lift forces of the sections can be considered to be concentrated at the center of Pressure (CP) of the sections. Bending moment may also be introduced by the axial load as a result of motor thrust misalignment and structural eccentricity.

Fig. 7-14 shows the bending loads acting on a rocket in flight. The total inertial load is equal to the mass of the section, multiplied by the acceleration acting in the direction perpendicular to the longitudinal axis. The total bending moment M, is

$$M_j = \sum_{i=1}^{n} F_{N_i}(x_j - x_i) + \sum_{i=1}^{n} M_i, \text{ N·m} \qquad (7\text{-}12)$$

where

M_j = total bending moment acting at station j, N·m

F_{N_i} = normal force at station i, N

n = number of segments, dimensionless

x_i = station i, m

x_j = station j, m

M_i = local bending moment at station i, N·m.

Figure 7-14. Concentrated Loads on Free Flight Rockets
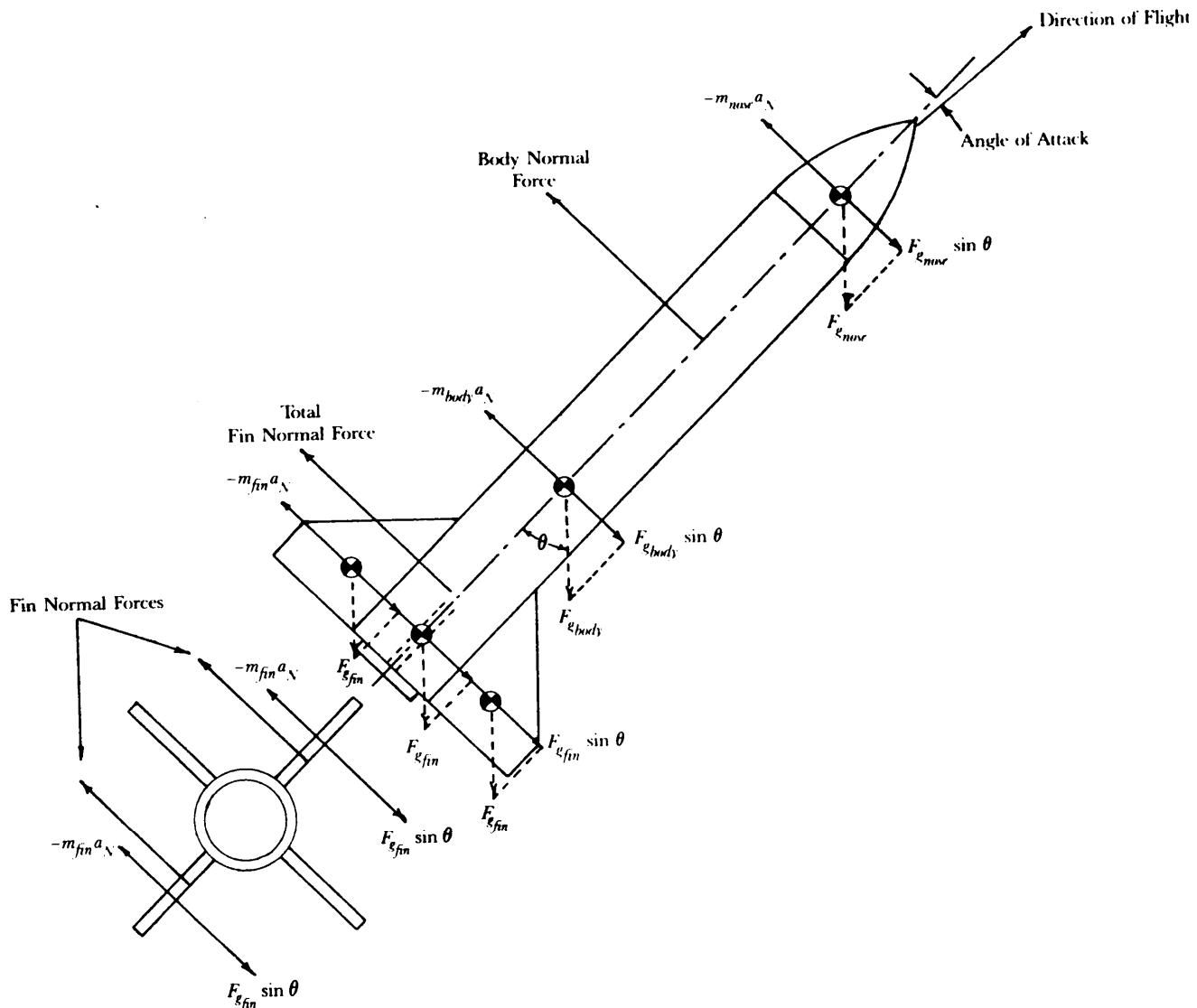
7-4 STRUCTURAL DESIGN ANALYSIS

7-4.1 CONCEPTUAL DESIGN

The conceptual design of a rocket structure requires input from various other groups. Guidelines from these groups are required to satisfy mission requirements of the rocket. A typical rocket application would require the following information: rocket size and shape; mass goal; range requirements; payload and other fixed hardware definition; cost goal; quantity; safety factors; load environments imposed by storage at temperature extremes, handling and transportation, launch, flight, and impact; and other specified characteristics.

The conceptual phase of rocket design requires that the best compromise be achieved in meeting design objectives. For example, low cost may be achieved with some sacrifice in performance. It is, therefore, desirable to preassign penalties for each constraint to aid in the selection process. Evaluation of the various concepts should be made on as equal a basis as possible. Structural analysis for each concept should be carried out to the same degree of completeness as other analyses. Stress analysis equations to support this design phase may be found in several common sources (Refs. 8 through 17). Final selection among leading candidates may then require additional structural analyses.

7-4.2 PRELIMINARY DESIGN

7-4.2.1 Structural Components

Preliminary design of the rocket is facilitated by analyzing individual components—i.e., motor case, nozzle, payload, etc. Preliminary load calculations are performed by using characteristics from components and sections in a manner similar to that indicated in Figs. 7-12 through 7-14. Structural analyses may then be performed to establish the basic structural dimensions of each component. This step will lead to a better definition of the applied loads and permit further refinements of the designs.

The design of efficient structural components sometimes requires complex geometric shapes. It may not be feasible to define the stress state of this class of structures with simple equations. The design engineer should, therefore, consult with the structural analysis group for assistance in approximating the stresses on such components.

The paragraphs that follow provide the basic equations and graphs to be used in the preliminary design of some common rocket component geometries.

7-4.2.1.1 Motor Case

The motor case experiences external loads due to aerodynamic forces and inertial forces due to accelerations. These forces are generally available in the form of axial, shear, and bending moment diagrams. These diagrams are discussed in more detail in pars. 7-4.2.2.4 through 7-4.2.2.6. The flight environment may also produce aerodynamic heating that should be considered. Nearly uniform or uniformly varying temperature distributions in similar materials generally produce negligible thermal stresses. Thermal stresses can result, however, even at uniform temperatures with dissimilar materials. Elevated temperatures generally result in reduced material strength and stiffness. Thermal protection from motor combustion generally is required because of the severe environment.

Internal loads, in the form of motor pressures, usually are of short duration in solid propellant motors. The motor pressure, however, usually determines the critical pressure vessel dimensions. Strength requirements to support the high internal motor pressure usually result in shell thicknesses that exceed the stiffness requirements for shell stability. A preliminary estimate for the motor case thickness can be calcuated by

$$t_{min} = \frac{p_{MEOP} r_{mc}(FS)}{\sigma_s(BF)(C_T)} \text{ , m} \tag{7-13}$$

where

t_{min} = minimum motor case thickness away from discontinuities, m

p_{MEOP} = maximum expected operating pressure, Pa

FS = factor of safety, (see par. 7-4.2.5), dimensionless

$= \begin{cases} \text{yield} \\ \text{ultimate} \end{cases}$

σ_s = strength at room (298 K) temperature, Pa

$= \begin{cases} \text{yield strength} \\ \text{tensile strength} \end{cases}$

BF = biaxial improvement factor, dimensionless

C_T = strength correction factor for temperature, dimensionless.

Structural instability of the motor case during motor operation usually is precluded as a result of the tensile stresses produced by the internal pressure. The unpressurized forward skirt experiences compressive axial stress during this phase of operation and should be evaluated for instability by using the procedure discussed in par. 7-4.2.3.4. An extensive treatment of structural stability is found in Ref. 8.

A simple check can be made for the unpressurized motor case using the equation

$$\sigma_{crit} = \frac{E}{\sqrt{3(1 - \nu^2)}} \left(\frac{t_{min}}{r_{mc}} \right), \text{ Pa} \tag{7-14}$$

where

σ_{crit} = critical compressive stress for a long elastic cylinder, Pa

ν = Poisson's Ratio, dimensionless

E = modulus of elasticity, Pa.

The value should be compared to the calculated compressive stress under design loads.

Shipping and handling loads should also be considered in motor case design. Strap-down loads can produce beam bending and\or local hoop loads in excess of flight-induced loads.

Bending moment diagrams should include the effects of bending caused by nonaxisymmetric inertial loads. In certain applications, misalignment of structural components may induce severe local bending loads.

Solid propellant rocket motors require igniters to initiate motor operation. Igniters sometimes are mounted on the forward closure, which requires access through the closure. This penetration produces a highly stressed local region unless reinforced. A general rule is to reinforce the cutout with material equal in volume to that removed. Forward closures can be either flat or contoured. Flat closures are structurally inefficient but may be desirable for certain applications. Contoured closures can be of either tensile or compressive type, depending on the application.

Equations to compute stresses and thicknesses for these closures can be found in Ref. 9. The compression closure should be analyzed for both stress and stability failure modes. Local stress risers due to structural discontinuities should be minimized by eliminating abrupt changes in geometry where possible.

Optimum closure design requires considerable analytical effort. In the preliminary design phase, the use of the following rules of thumb is recommended:

1. Flat plate. Determine thickness in accordance with plate equations.

2. Contoured (tensile). Closure thickness away from discontinuities should be equal to the thickness of the cylindrical case wall.

3. Contoured (compressive). Closure thickness away from discontinuities should be a minimum of 1.5 times the thickness of the cylindrical case wall.

These recommendations, obviously, do not cover all the shapes, joint configurations, and materials of combinations possible in closure design. It is generally desirable that the weakest link in a rocket motor be the (cylindrical case wall and, therefore, closures are usually conservatively designed.

7-4.2.1.2 Nozzle

A typical nozzle design cross section is presented in Fig. **7-15.** The nozzle consists of the main structure, an insulator, and a thermal liner. The main structure carries the nozzle loads and transmits the loads to the motor case or aft closure. The insulator is a material placed between the nozzle structure and the thermal liner to protect the structure from excessive temperatures. The thermal liner forms the inner contour of the nozzle. An insert of a special erosion-resistant material may be placed in the throat region of a nozzle to limit the increase in throat area resulting from erosion.
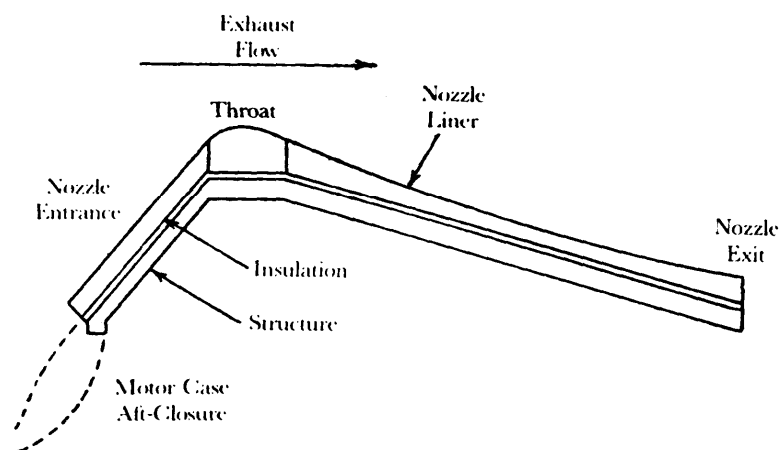
Figure 7-15. Nozzle Structural Configuration

The primary load on a nozzle is the pressure along the inner surface of the nozzle. This pressure varies from nearly 100% motor pressure along the entrance region to approximately 58% at the throat and decreases to nearly ambient pressure at the exit plane. A modified isentropic flow generally is assumed in describing the behavior of the exhaust gasses through the nozzle.

Survival of the nozzle requires that the main structure support the low strength thermal liner. Structural failure of the thermal liner is one of the primary causes of nozzle failure. The nozzle-to-aft closure joint is another critical region. The joint must be designed to withstand the nozzle blow-off load, which can be estimated by multiplying the motor chamber pressure by the upstream projected area of the joint. The relieving action of pressure acting on the exit cone can be ignored for the preliminary design in the interest of conservatism.

Initial thickness of the thermal liner and insulator should be determined from the thermal protection required by the primary support structure. The type of analysis to assess adequately the insulator depends on the heat transfer properties of the components and the critical combination of temperature and load. Initial geometry and initial uniform temperature can be assumed in analyzing the highly effective insulators. This approximation is possible because the heated layer is generally thin and soft, and does not introduce significant thermal loads. However, highly conductive materials such as carbon and tungsten require careful thermal stress analysis. Preliminary estimates of the stress state under pressure and thermal loads can be computed by applying the methods in par. 7-4.2.3.6.

Pressure acting on the inner surface of the exit cone produces hoop tension and meridional compression. Hoop stresses can be calculated by using elementary shell equations. The meridional

compressive load, varying along the length of the exit cone, is zero at the exit plane and maximum just aft of the throat. Meridional stress is computed from the load at a given station divided by the effective cross-sectional area at that station.

The compressive axial force also produces shear stress in the conical section. The plane of shear can be visualized by considering the cone to be composed of short cylinders of varying diameters that tend to nest under the axial loading. This failure mode is generally not critical for isotropic materials. Special designs such as tape-wrapped composites, however, may be susceptible to interlamina shear failure.

The nozzle may also have to withstand aerodynamic loads, inertia] loads, vibratory loads, and external heating loads. These loads are usually neglected during the preliminary design unless they are unusually large.

7-4.2.1.3 Propellant

There are several ways in which solid propellants are applied in rocket motors. There is a class of motors whose propellants are considered to be "stress-free" by design. Another popular motor design uses propellants that are bonded to the motor case. This latter type of construction does produce stress in the grain (propellant as cast) and requires demonstrable structural integrity.

The design of a solid propellant rocket motor grain is determined primarily by the mission requirements and the ingenuity of the interior ballistics group. Several solid propellant grain geometries are shown in Fig. 7-16.
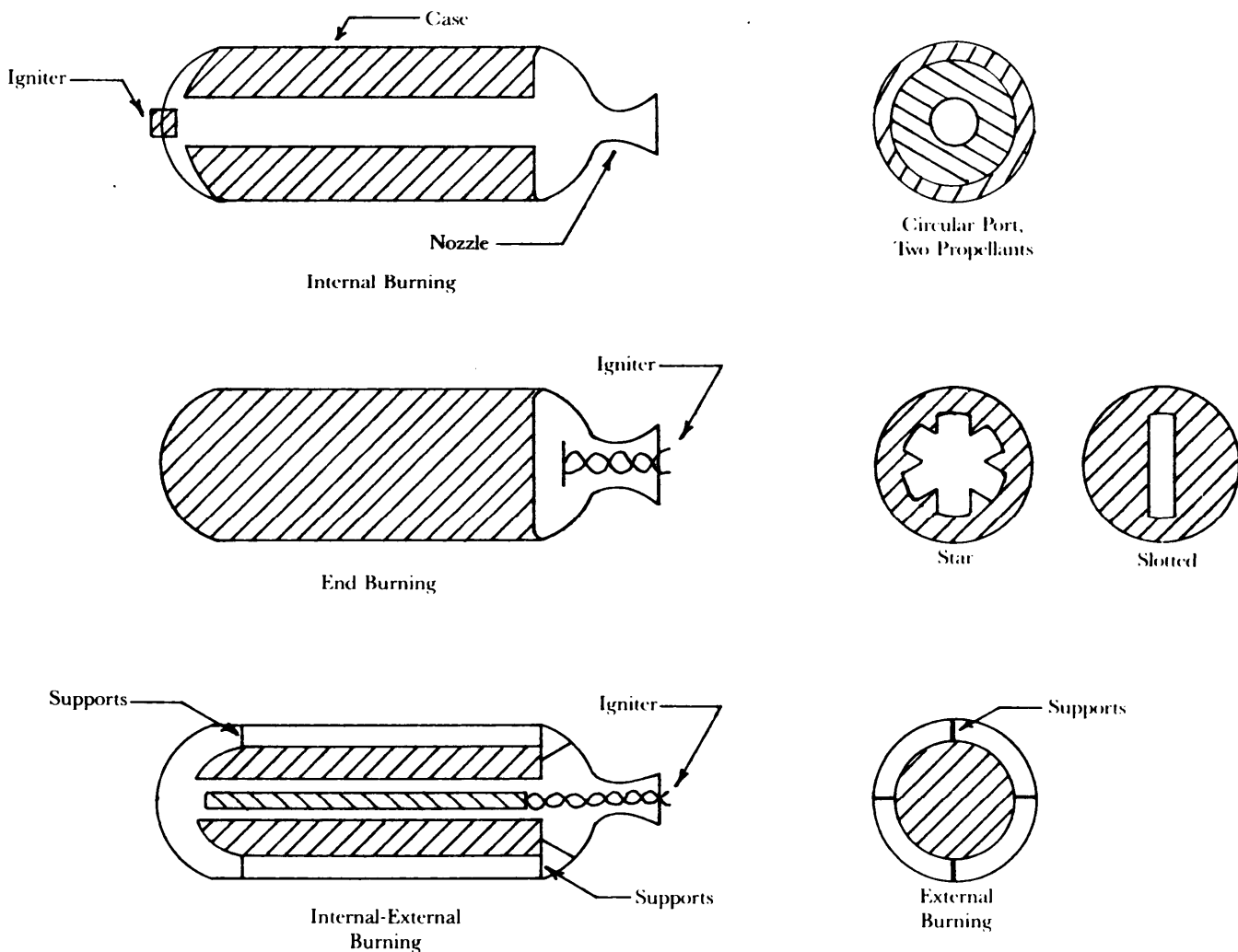
Figure 7-16. Representative Solid Propellant Grain Geometries

Physical properties of the propellants are generally not available at the early stages of the design. The preliminary analysis, therefore, provides only a qualitative assessment of the grain design and simplifying assumptions are fully justified.

Several failure modes of case-bonded grains are described in par. 7-4.2.3.6. Most of the local failure modes can be avoided by improved manufacturing techniques or changes in the local geometry. Basic dimensions, which generally govern the motor performance, can be analyzed approximately with design data sheets and engineering equations. Extensive numerical analyses are not warranted in view of the approximation regarding the uncertainties in material characteristics, preliminary geometry, and the expense of computer analysis.

The rocket can also fail due to combustion instability. Instability is characterized by a rapid growth of pressure fluctuation which may be dynamically coupled to the structure or it may be related only to the cavity of the combustion chamber and the intrinsic stability parameters of the propellant.

The coupling of the structure with the combustion process is a complex subject and is beyond the scope of this chapter. Instability of the combustion process is also a complex subject, however, procedures are available to give guidance in remedial actions if unacceptable pressure fluctuations are detected.

Case/grain geometry determines the acoustic structure of the cavity. Influential geometric parameters include the number and location of slots in the propellant, the cavity dimensions, the distribution of burn area, and the degree of nozzle submergence. Instability may appear at any web fraction or even at several web fractions in the course of a firing. No special significance may be assigned to either ignition or depressurization transients as triggering mechanisms in a linear stability context, nor can it be said that a transverse mode (tangential or radial) is intrinsically more severe than a longitudinal mode since high amplitude pressure fluctuations and large shifts in mean pressure have been observed in each instance. The occurrence depends upon the balance of acoustic energy gains and losses at any given time. Within any mode category, the first, lowest frequency, mode is usually (but not always) dominant with higher modes becoming relatively less intense. It is generally conceded that high ℓ/d motors and localized regions of large burn surfaces tend to encourage longitudinal modes, whereas axisymmetric geometries tend to encourage tangential modes.

The Air Force Rocket Propulsion Laboratory (AFRPL), Edwards Air Force Base, CA, Standard Stability Prediction Codes are generally employed to calculate the acoustic modes and stability margins. These codes continue to be used as a guide for propellant grain modification to enhance motor stability. Both the axial code and the multidimensional code evaluate individual gain and loss factors to determine the linear stability of the system.

Cooldown or storage at low temperature is generally the prime consideration in grain design. Motors surviving this condition usually survive ignition loading. Some notable exceptions occur when the propellant is unusually soft and unable to maintain its geometry under nonuniform pressure distribution during the ignition transient and/or under high axial accelerations. Propellants with equilibrium modulus greater than 700 kPa are generally acceptable for conventional applications.

Structural integrity at low temperature can be assessed by infinitesimal linear elasticity theory for preliminary design purposes. The motor is assumed to be in equilibrium in both temperature and stress. Case-bonded grains experience thermal stresses and strains even at equilibrium temperatures because of the differences in linear and bulk coefficients of thermal expansion between the propellant and motor case. The critical strain that produces failure is called the mechanical strain and is defined as

$$\epsilon_{mech} = \epsilon_{total} - \alpha \Delta T, \text{ m/m} \tag{7-15}$$

where

ϵ_{mech} = mechanical strain, m/m
ϵ_{total} = total strain, m/m
α = linear coefficient of thermal expansion, m/m·K
ΔT = temperature difference, deg K.

The total strain at a point is the measurable strain at that point. Total strain measured for a free specimen would be equal to the free thermal strain and, therefore, the specimen would be stress free. The difference between the total strain and the free thermal strain is the strain associated with the stress in the part.

The preliminary design analysis of some common geometries is discussed in Ref. 10. Discussed in this reference are

1. Aerodynamic Heating
2. Dynamic Loads
3. Vibration
4. Accelerations
5. Pressurization
6. Shock
7. Temperature.

Thermal strain in a circular port (CP) grain, bonded to a thin-walled cylindrical case, can be computed by assuming that the longitudinal strains of (longitudinal) fibers are equal (denoted as plain strain). For an incompressible material, the mechanical bore strain ϵ_b is given by

$$\epsilon_b = -1.5\ \alpha_p \Delta T \left\{ \left[\frac{1 - 0.867\left(\frac{\alpha_{mc}}{\alpha_p}\right)}{\Omega} \right]\left(\frac{r_o}{r_i}\right)^2 - 1 \right\} - \alpha_p \Delta T,\ \text{m/m} \qquad (7\text{-}16)$$

where

ϵ_b = mechanical bore strain, propellant strain in circumferential direction, m/s

$$\Omega = 1 + \frac{\left[\left(\frac{r_o}{r_i}\right)^2 - 1\right] 0.91 r_o E_p}{1.5 t E_{mc}},\ \text{dimensionless parameter}$$

r_i = inner (bore) radius of propellant, m (see Fig. 7-33)
r_o = outer radius of propellant, m (see Fig. 7-33)
E_{mc} = Young's modulus of motor case, Pa
E_p = Young's modulus of propellant, Pa
t = motor case thickness, m (see Fig. 7-33)
α_{mc} = linear coefficient of thermal expansion for motor case, m/m·K
α_p = linear coefficient of thermal expansion for propellant, m/m·K
ΔT = temperature difference (actual temperature − cure temperature), deg K.

Propellants may also experianec shinkage during cure. This effect may be simulated by computing an effective temperature difference. The relationship is given as

$$\Delta T_V = (VSR)/(3\alpha_p),\ \text{deg K} \qquad (7\text{-}17)$$

where

ΔT_V = temperature change based on volumetric shrinkage during cure, deg K
VSR = propellant volumetric cure shrinkage ratio, m³/m³.

If the cure shrinkage is known, the effective temperature difference, ΔT_{eff} can be taken as

$$\Delta T_{eff} = \Delta T - \Delta T_V,\ \text{deg K.} \qquad (7\text{-}18)$$

Example 7-2 illustrates the method for calculating mechanical bore strain ϵ_b.

EXAMPLE 7-2:

Determine the mechanical bore strain ϵ_b for a long CP grain with the given information:

$$r_i = 25.4 \text{ mm}$$
$$r_o = 76.2 \text{ mm}$$
$$t = 2.54 \text{ mm}$$
$$E_{mc} = 2.068 \times 10^8 \text{ kPa}$$
$$E_p = 6.895 \times 10^2 \text{ kPa}$$
$$\alpha_{mc} = 1.134 \times 10^{-5} \text{ m/m·K (steel case)}$$
$$\alpha_p = 9.9 \times 10^{-5} \text{ mm/mm·K (typical for double-base propellants)}$$
$$T_{actual} = 280 \text{ K}$$
$$T_{cure} = 336 \text{ K}$$
$$VSR = 0.005 \text{ mm}^3/\text{mm}^3$$

Solution:

From Eq. 7-18:

$$\Delta T_{eff} = (280 - 336) - 0.005/[3(9.9 \times 10^{-5})]$$
$$= -72.8 \text{ deg K.}$$

From Eq. 7-16:

$$\Omega = 1 + \frac{\left[\left(\frac{76.2}{25.4}\right)^2 - 1\right](0.91)(76.2)(6.895 \times 10^2)}{(1.5)(2.54)(2.068 \times 10^8)} = 1.0005$$

and, therefore,

$$\epsilon_b = -(1.5)(9.9 \times 10^{-5})(-72.8)\left\{\left[\frac{1 - (0.867)\frac{(1.134 \times 10^{-5})}{(9.9 \times 10^{-5})}}{1.0005}\right]\left(\frac{76.2}{25.4}\right)^2 - 1\right\}$$
$$- (9.9 \times 10^{-5})(-72.8)$$
$$= 8.40 \times 10^{-2} \text{ m/m.}$$

The assumption of plane strain applies to high length-to-diameter grains. A correction factor can be applied to the calculated strain (Ref. 10, Figs. 12 and 13) to account for the reduction in bore strain for low length-to-diameter grains.

The adequacy of the design can then be assessed by computing the margin of safety (MS). The MS should be equal to or greater than zero when computed by Eq. 7-19

$$MS = \frac{\epsilon_e}{\epsilon_b(FS)} - 1, \text{ dimensionless} \tag{7-19}$$

where

ϵ_e = propellant strain endurance, m/m

ϵ_b = computed mechanical bore strain, m/m

7-4.2.1.4 Payload

An illustration of a typical paiload structural arrangement is presented in Fig. 7-17. The payload structure consists of a now fairing, a warhead, and a payload-to-motor case attachment structure. The payload nose fairing generally consists of a thin metal shell that is formed over a forward ring. The nose fairing for a shaped charge warhead is generally a thin metal shell with an inner structure that also functions as an impact fuze. The warhead structure may consist of a hollow, cylindrical shell for containment of a shaped charge (Ref. 11). The aft portion of the warhead generally contains a threaded boss that is used to attach the warhead to the motor case.
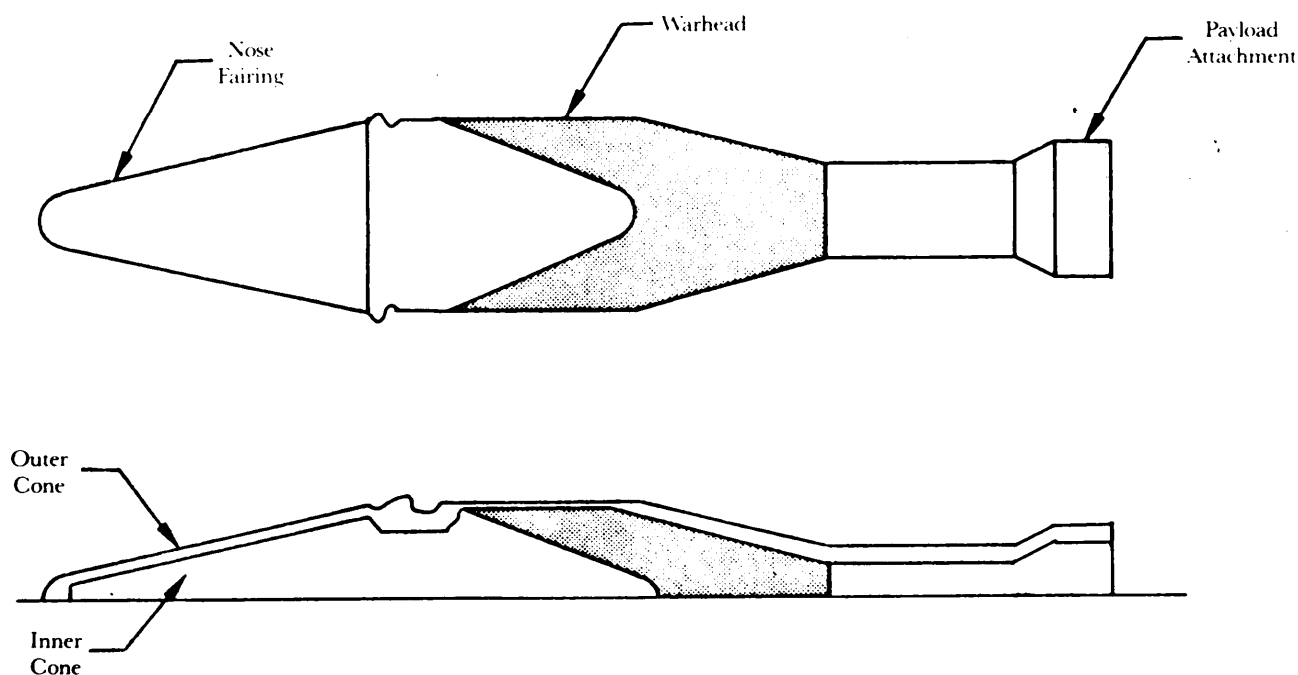
Figure 7-17. Payload Structure Configuration

The payload and its supporting structure typically experience maximum loads during motor operation. Payloads on rockets that are spun experience tangential loads during spin-up and radial loads from the rotational velocity.

Structural requirements to support the payload during boost generally exceed the strength required to resist shear and bending loads during flight. However, induced shear and bending loads during shipping and handling should also be considered.

Submunition-type payloads also experience severe side loads during boost and dispensing. Nesting techniques generally are employed to increase packaging efficiency and to reduce side loads.

7-4.2.1.5 Payload Nose Fairing

The payload nose fairing is generally a shell-type structure, as shown in Fig. 7-18, that contains the payload and transmits the aerodynamic and payload loads to the motor case. The payload nose fairing generally develops a substantial aerodynamic and inertial load due to its position on the rocket and its shape. Nose fairings are generally analyzed as thin-walled shell sections such as cylinders and conical frustums. Ref. 8 presents extensive analysis and design charts for monocoque and stiffened shells. Shell stability under pure axial compression, bending, tension, shear, and external pressure loads is treated along with stability under combined loading.
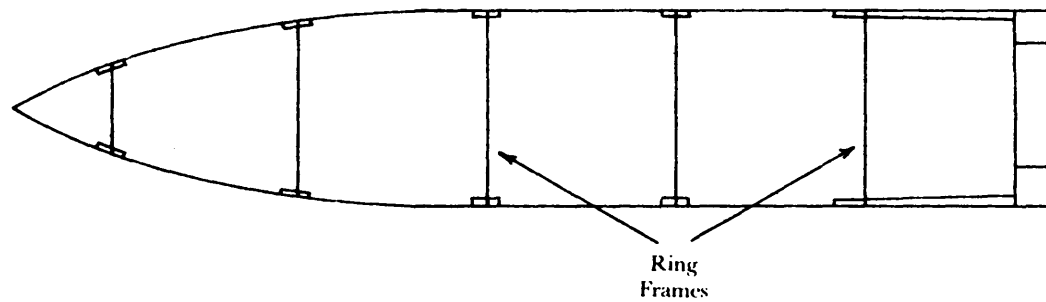
Figure 7-18. Payload Nose Fairing

7-4.2.1.6 Fins

The structural design of fins involves analysis of the structure, material, allowable temperature, flutter, and aeroelastic effects. Fin structural design concepts can vary greatly, even when considering the same environments. Examples of the variations in fin structural configurations are shown in Fig. 7-19. Fin structural concepts include honeycomb, rib and stringer, thick skin, and stiffened skin design concepts. Comparisons of several structural concepts are presented in Table 7-3.
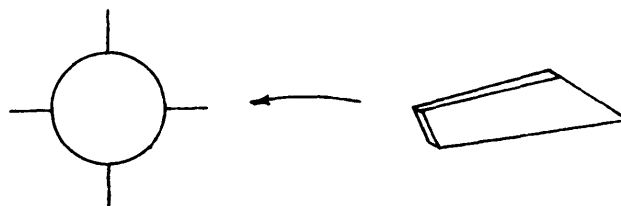
(A) Fixed Fin

(B) Deployable Curved Fin
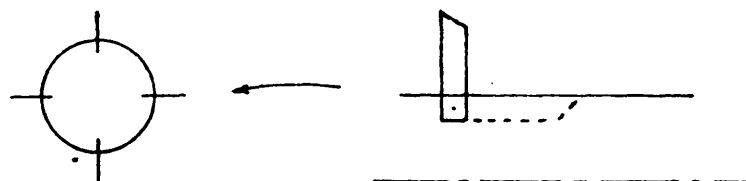
(C) Deployable Switch-Blade Fin

Figure 7-19. Thin-Plate Fin Concepts

TABLE7-3. FIN STRUCTURAL CONCEPT COMPARISONS

Design Concept	Maintenance Free For 5 Years	Number of Parts	Relative Cost	Problem Areas
Honeycomb	No	High	Intermediate	Metat Bonding Outgassing and Life
Rib & Stringer	Yes	High	High	Number of Assembly Operations
Thick Skin	Yes	High	Low	Bending of Leading Edge
Integrally Stiffened Skin	Yes	Low	High	Accurate Machining Required
Forged Skin	Yes	Low	High	Precision Forging
Beaded Doubler	Yes	Intermediate	Low	Panel Buckle
Thin Plate	Yes	Low	Low	Limited Surface

The wing structural design concepts are variations of two extremes. The honeycomb design, which has a very stiff skin, uses the skin shell to transmit the load to the main spar. The conventional rib and stringer concept has a thin skin, which has little stiffness, and is used to transmit the airload to internal ribs and stringers. Other concepts, which trade skin stiffness for internal rib and stringer stiffness, are essentially variations of these two. Panel flutter must be evaluated when the skin stiffness is reduced. Components with reduced stiffness require consideration of aeroelasticity effects. Aeroelasticity analysis is the analysis of the deflected shape of the structure under flight loads and the analysis of the change in loads due to the deflections. The aerodynamicist must evaluate the fin shape under design load conditions to determine the design loads for the deflected shape. Additional details of the analysis technique are presented in pars. 7-4.2.2 and 7-6.

Attachment hardware requirements of the fins to the rocket structure depend upon the fin type and application. Movable fins require a hinged connection and generally attach to a fitting in the rocket structure. Fixed fins can be supported over their entire length by rail attachments or integrally formed rails. Deployable fins are generally hinged and are mechanically locked in the deployed position.

7-4.2.2 Preliminary Load Estimation

The type of structural loading determines the type of analysis that is necessary to evaluate the stress state. Generally, there are four types of loading conditions-short-term static loading, long-term static loading, repeated loading, and dynamic loading. A discussion of each type of loading follows:

1. Short-Term Static Loading. This is the condition under which the structure is loaded gradually so that inertial loads are negligible. Testing of a structure under a short-term load condition is conducted by gradually increasing the load until the desired load is achieved. The duration of the test may be several minutes. In service, the load is increased progressively up to a maximum value and then is reduced, and the load is not repeated in order to avoid fatigue considerations. Flight aerodynamic load conditions are generally considered short-term static loading conditions.

2. Long-Term Static Loading. This is a loading condition in which material and flow characteristics become important. Storage at high or low temperature is an example of long-term static loading.

3. Repeated Loading. This is a loading condition under which the structure experiences stress variations over its lifetime. The frequency of load application may be high as in a vibratory environment or relatively low as in the case of thermal cycling.

4. Dynamic Loads. These are usually short-duration loads that occur, for example, during the motor ignition transient and during handling. A discussion of dynamic load environments maybe found in Ref. 12.

As previously stated, loads on a rocket are imposed during flight, transportation and handling, launch, storage, etc. Each load condition has to be examined to determine the critical design loads. A combined load diagram will help identify the critical environment for the various portions of the rocket. A typical superposed shear diagram is shown in Fig. 7-20.
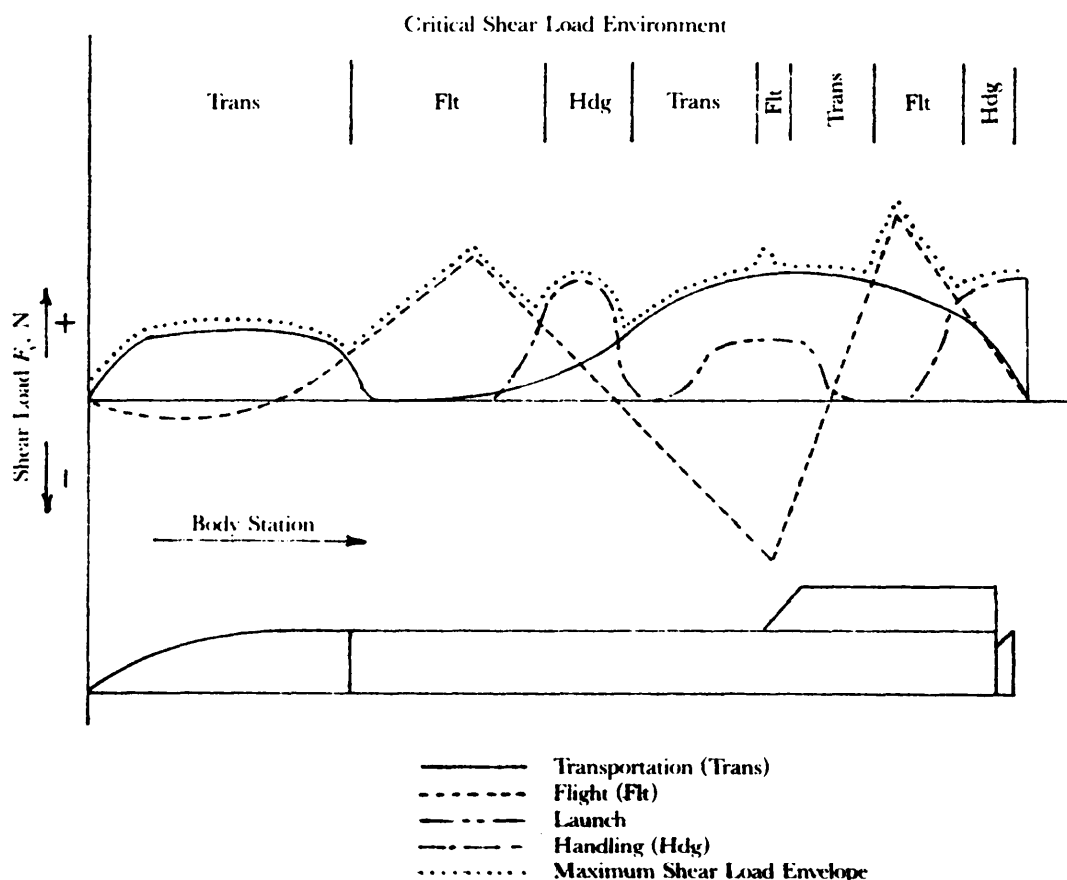
Figure 7-20. Superposed Shear Diagram

7-4.2.2.1 Mass Distribution

The accuracy of the loading diagrams improves with the definition of the distribution of the external and internal loads. During the preliminary design phase, loads must be based on estimates of the mass of components of the rocket because detailed mass distributions are not known. Estimates may be made by approximating the distribution of the known component mass over the length of the component. The mass distribution of a typical rocket can be approximated as shown in Fig. 7-21 by the solid line. The actual mass distribution of the rocket may be similar to that indicated by the dashed line.

7-4.2.2.2 Moment of Inertia

Any solid-such as a cube, sphere, or ellipsoid—may have its moment of inertia determined by direct integration. The integration must be extended over the entire volume of the body. An irregular composite body has to be divided into elementary bodies whose moments of inertia are calculable. The term
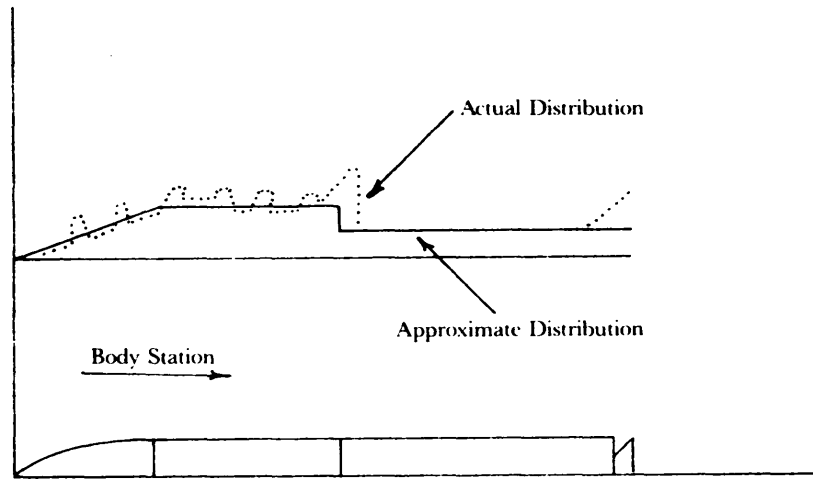
Figure 7-21. Methods of Mass Distribution Approximation

"moments of inertia" infers a given reference axis or point. The chosen designated axis may be any axis conveniently located. Ordinarily, the moments of inertia of a solid are calculated with respect to its CG axes. Fig. 7-22 and Eq. 7-20 define the mass moments of inertia with respect to the three coordinate axes. Definitions of the principal mass moments of inertia* are

$$\bar{I}_{ox} = \int (y^2 + z^2)dm = \int r_1^2 dm, \text{ kg·m}^2$$
$$\bar{I}_{oy} = \int (x^2 + z^2)dm = \int r_2^2 dm, \text{ kg·m}^2 \qquad (7\text{-}20)$$
$$\bar{I}_{oz} = \int (x^2 + y^2)dm = \int r_3^2 dm, \text{ kg·m}^2$$

where

$\bar{I}_{ox}, \bar{I}_{oy}, \bar{I}_{oz}$ = mass moment of inertia about principal x-, y-, and z-axes, respective] y, kgŽm².

A useful equation to determine the moment of inertia with respect to any parallel axis is given by the Parallel Axis Theorem, i.e.,

$$I_{xx} = \bar{I}_o + m\ell^2, \text{ kg·m}^2 \qquad (7\text{-}21)$$

where
I_{xx} = mass moment of inertia about x-x axis, kg·m²
ℓ = distance between x-x axis and a parallel axis through CG, m
$\bar{I}_o$ = mass moment of inertia about CG, i.e., $\bar{I}_{ox}, \bar{I}_{oy}, \bar{I}_{oz}$, kg·m².

The moment of inertia of a rocket can be estimated by approximating the rocket by a series of "lumped" masses as shown in Fig. 7-23 and by applying Eqs. 7-20 and 7-21. The mass moment of inertia $\bar{I}_{CG}$ about the rocket CG can be expressed as

$$\bar{I}_{CG} = \sum_{i=1}^{n}(m_i x_i^2 + \bar{I}_{oi}) - X_{CG}^2 \sum_{i=1}^{n} m_i, \text{ kg·m}^2 \qquad (7\text{-}22)$$

---

*In everp plane area, a given point being taken as the origin, there is at least one pair of rectangular axes in the plane of the area about which the moment of inertia is a maximum, and a minimum about the other. These moments of inertia are referred to as the principal moments, of inertia and the axes about which they are taken are referred to as the principal axes of inertia. Axes of symmetry of an area are always principal axes inertia.
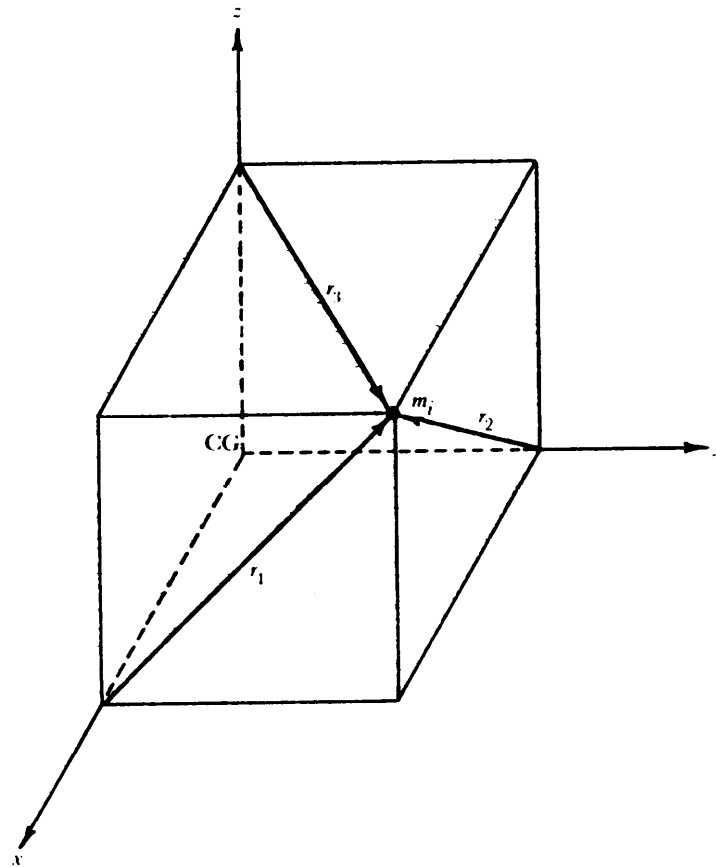
Figure 7-22. Coordinates for Moment-of-Inertia Calculations
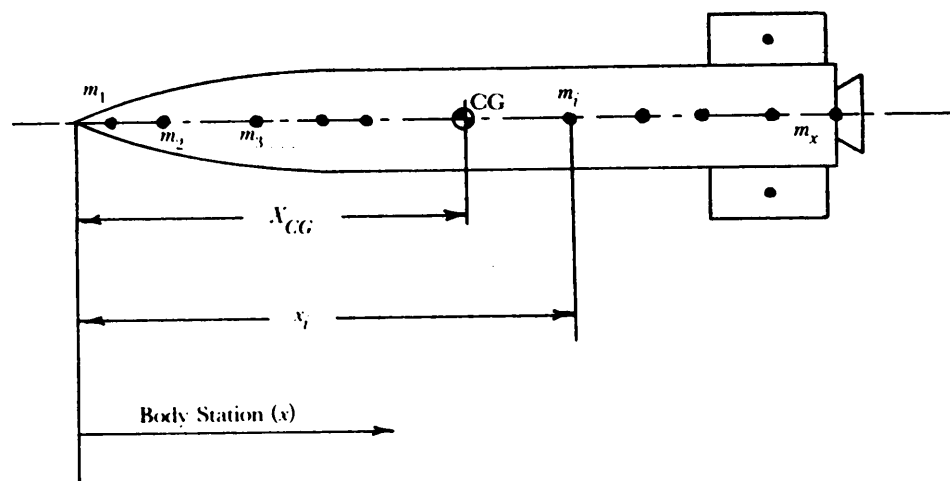
Figure 7-23. Lumped Mass Model of a Typical Rocket

MIL-HDBK-762(MI)

$$a_{N_{CG}} = \frac{1}{m} \sum_{i=1}^{n} (F_{N_i} - mg_0\sin\theta), \text{ m/s}^2 \tag{7-29}$$

$$\ddot{\theta} = \frac{1}{\bar{I}_{CG}} \sum_{i=1}^{n} [F_{N_i}(X_{CG} - x_i) + M_i], \text{ rad/s}^2 \tag{7-30}$$

where

$\ddot{\theta} =$ pitch angular acceleration, rad/s^2

$m = \Sigma m_i$, kg.

The total normal acceleration a_{N_x} at any station x is the sum of the $a_{N_{CG}}$ component plus a component from the pitch acceleration $\ddot{\theta}$, as shown in Fig. 7-24, i.e.,

$$a_{N_x} = \frac{F_{N_{total}}}{m} - g_0\sin\theta + \ddot{\theta}(X_{CG} - x_i), \text{ m/s}^2. \tag{7-31}$$
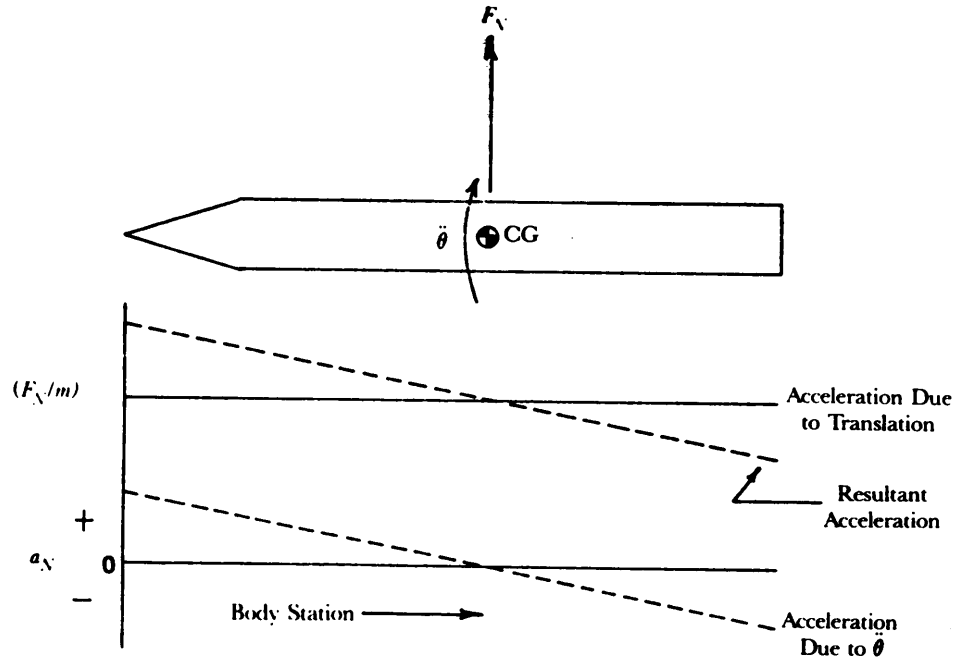
Figure 7-24. Components of Total Normal Acceleration

The net aerodynamic axial force F_A is by Eq. 7-9

$$F_A = C_A q A_{ref}, \text{ N}. \tag{7-32}$$

The axial acceleration a in powered flight is then by Eq. 7-7

$$a = \frac{F_T - F_A - mg_0\cos\theta}{m}, \text{ m/s}^2. \tag{7-33}$$

These equations may be used to evaluate the rocket shear loads, bending moments, and axial loads at any slation j as indicated in Fig. 7-12.

The total shear load F_{s_j} at station j is the summation of the external aerodynamic normal loads minus the inertial be expressed as

$$F_{s_j} = \sum_{i=1}^{j} F_{N_i} - \sum_{i=1}^{j} m_i a_{N_i}, \text{ N} \tag{7-34}$$

where

a_{N_i} = normal acceleration at station i, m/s^2.

Equilibrium requires that the total bending moment M_j at station j be equal to the summation of the local bending moments, plus moments $F_{N_j} x$ due to the normal loads acting at a distance x, minus the inertial loads due to angular acceleration (the last term in Eq. 7-35), i.e.,

$$M_j = \sum_{i=1}^{j} M_i + \sum_{i=1}^{j} F_{N_i}(x_j - x_i) - \sum_{i=1}^{j} m_i a_{N_i}(x_j - x_i), \text{ N·m.} \tag{7-35}$$

The axial load at any station is the sum of all axial and inertial loads forward of that station. For solid propellant motors, the axial load produced by the chamber pressure is included in the calculation. The axial load F_{A_j} at station j is

$$F_{A_j} = \sum_{i=1}^{n} F_{A_i} + a \sum_{i=1}^{j} (m_i + m_{pi}), \text{ N.} \tag{7-36}$$

The procedure for determining inertial forces for a load and mass distribution is illustrated in Example 7-3.

EXAMPLE 7-3:

Determine the inertial forces for the load and mass distribution shown in Fig. 7-25(A). Consider the moment of inertia of each mass about its CG as negligible for the purposes of this example. Table 7-4 gives the required mass properties. The solution follows:

From Eq. 7-28

$$X_{CG} = \frac{\Sigma m_i x_i}{\Sigma m_i} = \frac{10.7}{23} = 0.4652 \text{ m.}$$

From Eq. 7-22

$$\overline{I}_{CG} = \Sigma m_i x_i^2 + \Sigma \overline{I}_{oi} - x_{CG}^2 \Sigma m_i$$
$$= 5.93 + 0 - (0.4652)^2(23) = 0.9525 \text{ kg·m}^2 \text{ (since } \Sigma \overline{I}_{oi} = 0 \text{ based on given data).}$$

From Eq. 7-29 assuming vertical flight ($\theta = 0$ deg and, therefore, $\sin\theta = 0$)

$$a_N = \frac{\Sigma F_{N_i}}{\Sigma m_i} = \frac{950}{23} = 41.30 \text{ m/s}^2.$$

From Eq. 7-30 ($\Sigma M_i = 0$ since all masses are along the centerline and thus produce no local bending moments)

$$\ddot{\theta} = \frac{\Sigma F_{N_i}(X_{CG} - x_i)}{\overline{I}_{CG}} = \frac{366.94}{0.9525} = 385.24 \text{ rad/s}^2.$$
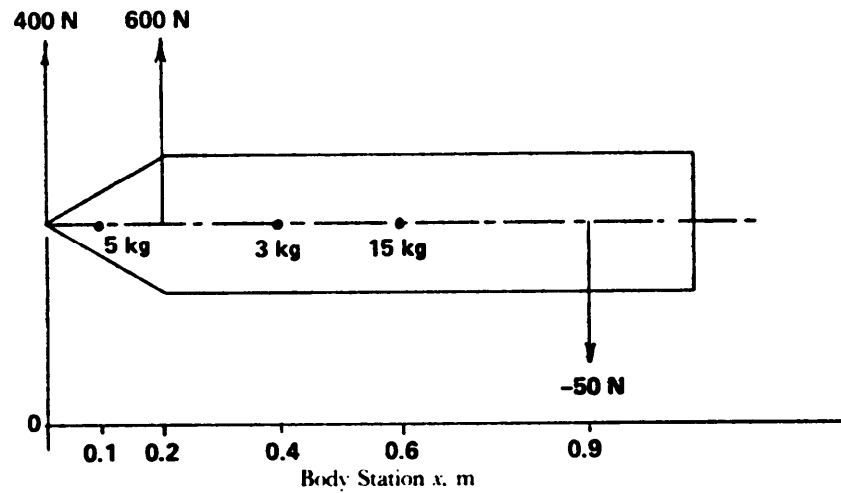
(A) Loads and Lumped Mass Model for Inertial Load
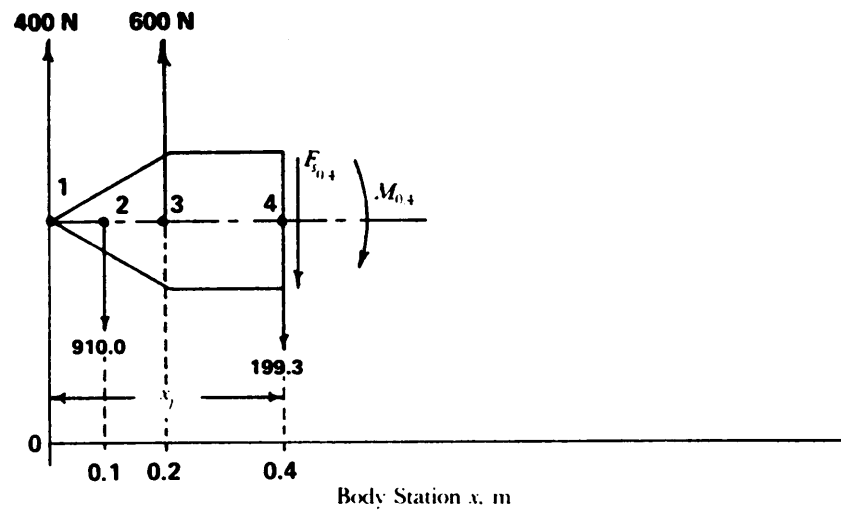
(B) Free-Body Diagram for Cut at Body Station 0.4 m

Figure 7-25. Example Problem to Illustrate Shears and Bending Moments on a Typical Rocket

TABLE 7-4. EXAMPLE 7-3 PROPERTY TABLE

x_i, m	F_{N_i}, N	m_i, kg	$F_{N_i}x_i$, N·m	m_ix_i, kg·m	$m_ix_i^2$, kg·m^2
0	400		0		
0.1		5		0.5	0.05
0.2	600		120		
0.4		3		1.2	0.48
0.6		15		9.0	5.40
0.9	−50		−45		
Totals	950	23	75	10.7	5.93

The accelerations at mass points, from Eq. 7-31, with $\sin\theta = 0$ are

$$
\begin{aligned}
a_{N_1} &= a_N + \ddot{\theta}\,(X_{CG} - x_1) \\
&= 41.30 + 385.24\,(0.4652 - 0.1) = 181.99 \text{ m/s}^2 \\
a_{N_2} &= 41.30 + 385.24\,(0.4652 - 0.4) = 66.42 \text{ m/s}^2 \\
a_{N_3} &= 41.30 + 385.24\,(0.4652 - 0.6) = -10.63 \text{ m/s}^2.
\end{aligned}
$$

The inertial forces at the mass points are

$$
\begin{aligned}
m_1 a_{N_1} &= 5(181.99) = 910.0 \text{ N} \\
m_2 a_{N_2} &= 3(66.42) = 199.3 \text{ N} \\
m_3 a_{N_3} &= 15(-10.63) = -159.5 \text{ N}.
\end{aligned}
$$

The sum of the inertial forces is 949.8 N as compared to 9.50 N from Table 7-1, which shows good agreement.

7-4.2.2.4 Shear Diagram

In general, elementary procedures applied in developing shear diagrams for beams also apply to rocket configurations. The rocket in flight can be assumed to be in dynamic equilibrium because the external forces are balanced by body forces. All loads acting normal to the longitudinal axis of the rocket are considered in developing the shear diagram.

A shear diagram for the example in par. 7-4.2.2.3 will be constructed to illustrate the procedure. A tabulation of loads is recommended to simplify the numerical calculations. Once the loads are defined, shear can be computed using Eq. 7-34. For example, the shear at station $x = 0.4$ m in the example in par. 7-4.2.2.3 was calculated by using Eq. 7-34 and Table 7-5 as follows:

$$
\begin{aligned}
F_{S_4} &= \sum_{i=1}^{4} F_{N_i} - \sum_{i=1}^{4} m_i a_{N_i} \\
&= F_{N_1} + F_{N_3} - m_2 a_{N_2} - m_4 a_{N_4} \\
&= 400 + 600 - 910.0 - 199.3 = -109.3 \text{ N}.
\end{aligned}
$$

The free body is shown on Fig. 7-25(B). The entire result is summarized in Table 7-.5 and the shear diagram shown in Fig. 7-26.

TABLE 7-5. EXAMPLE 7-3 SHEAR TABLE

X_i, m	F_{N_i}, N	$m_i a_{N_i}$, N	F_s, N
0	400		**400**
0.1		910.0	—510.0
0.2	600		90.0
0.4		199.3	−109.3
0.6		-159.5	50.2
0.9	−50		0.2
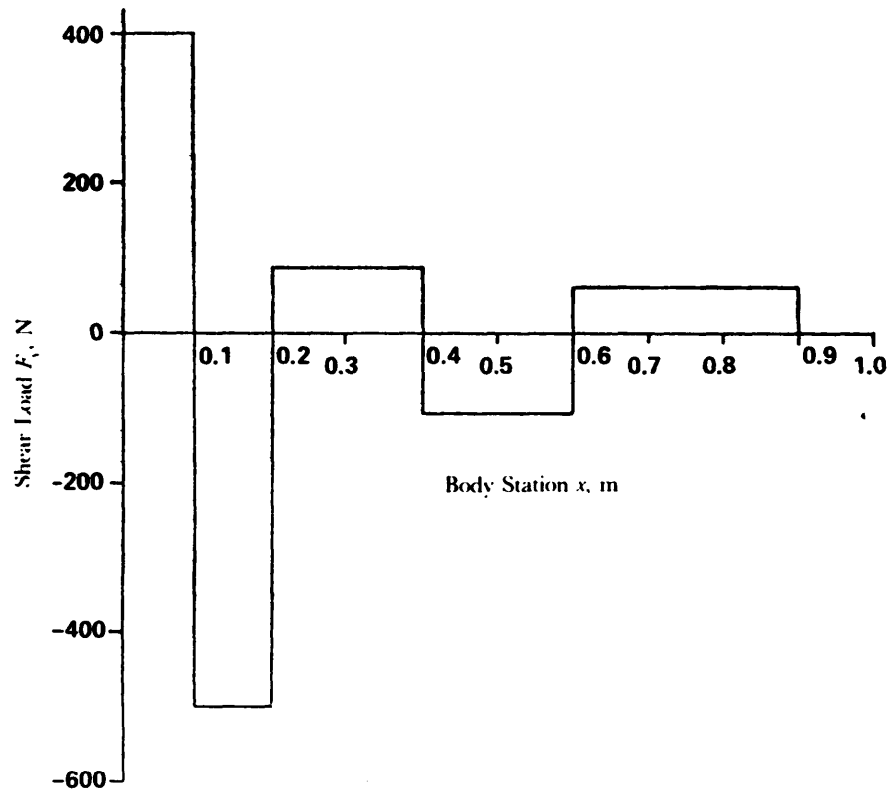
Figure 7-26. Shear Load Diagram for Inertial Load Sample Problem

7-4.2.2.5 Bending Moment Diagram

Bending moments on a rocket are the result of external loads and body forces. The bending moment at and station x, may be computed with Eq. 7-35 or, in general, may be determined by integration. The different in bending moment between two stations $x = x_j$ and $x = X_j$-l maybe expressed as an integral of the shearing forces F_s by

$$M_j - M_{j-1} = \int_{x_{j-1}}^{x_j} F_s dx \tag{7-37a}$$

where

$F_s =$ may be a continuous function of x.

For a lumped mass system with discrete nodes (points), Eq. 7-37a can be expressed as

$$M_j = M_{j-1} + F_{s_{j-1}}(x_j - x_{j-1}), \ \text{N·m.} \tag{7-37b}$$

For example, the bending moment at station $x = 0.4$ m in the example in par. 7-4.2.2.3 was calculated using Eq. 7-35 and Table 7-5 as follows (again the $\Sigma M_i = 0$):

$$M_j = \sum_{i=1}^{j} F_{N_i}(x_j - x_i) + \sum_{i=1}^{j} M_i - \sum_{i=1}^{j} m_i a_{N_i}(x_j - x_i)$$

$$M_4 = 400(0.4) + 600(0.2) + 0 - 910(0.4 - 0.1) = 7 \ \text{N·m.}$$

This bending moment is shown on the free body in Fig. 7-25(B).

Bending moments for the example problem were calculated by using Table 7-5 and Eq. 7-37b. The results are tabulated in Table 7-6. The associated bending moment diagram is shown in Fig. 7-27.

TABLE 7-6. EXAMPLE 7-3 BENDING MOMENTS TABLE

x_i, m	0	0.1	0.2	0.4	0.6	0.9
F_s, N	400	−509.9	90.1	109.2	50.2	0.2
M_j, N•m	0	40.0	−11.0	7.0	−14.8	0.2
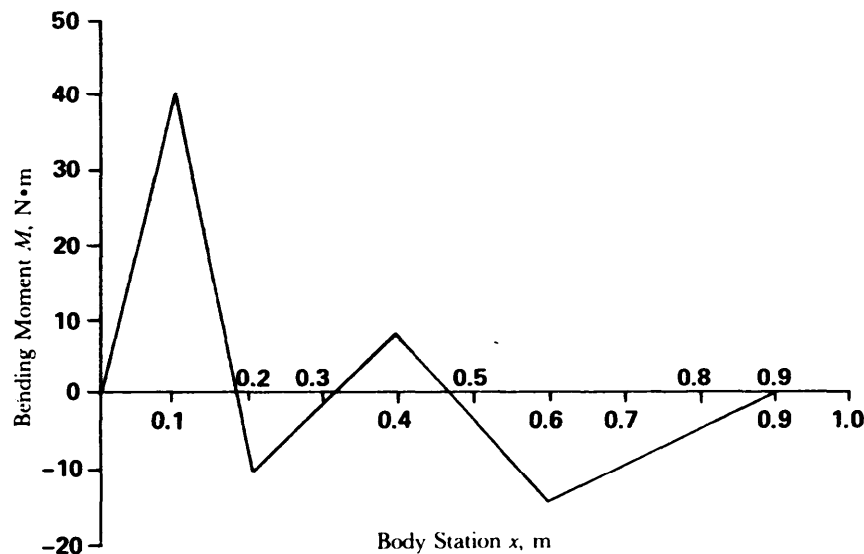
Figure 7-27. Bending Moment Diagram for Inertial Load Sample Problem

7-4.2.2.6 Axial Load Diagram

The axial load diagram is a plot of the actual load along the length of the rocket. Actual loads are the result of external, internal, and inertial forces. These loads apply primarily to the rocket outer shell and do not represent axial loads experienced by the individual components such as the nozzle.

The primary source of axial loads is the thrust of the motor. Thrust force in a rocket is produced by the net action of motor pressure acting on the inner surfaces of the motor and nozzle. The axial force at any station in a rocket motor is equal to the integral of the varying pressure acting on the entire area aft of the station in question plus the sum of masses aft of that station multiplied by the axial acceleration of the rocket. In preliminary} design, it is generally appropriate to ignore body forces in the motor case design unless the axial acceleration is unusually high, i.e., greater than $100g_0$.

A typical axial load diagram is shown in Fig. 7-28.

7-4.2.3 Stress

Numerical analysis techniques such as the finite element and finite difference methods are useful in preliminary design in which elementary equations, tables, and graphs may have proven to be inadequate. Elementary techniques, however, are necessary for initial sizing and serve as a means of gaging numerical analysis results of complex geometries with approximate solutions.

The subparagraphs that follow provide the basic analysis techniques used in the stress analysis of rocket components. Also discussed are the critical regions of a rocket motor and their possible failure modes.
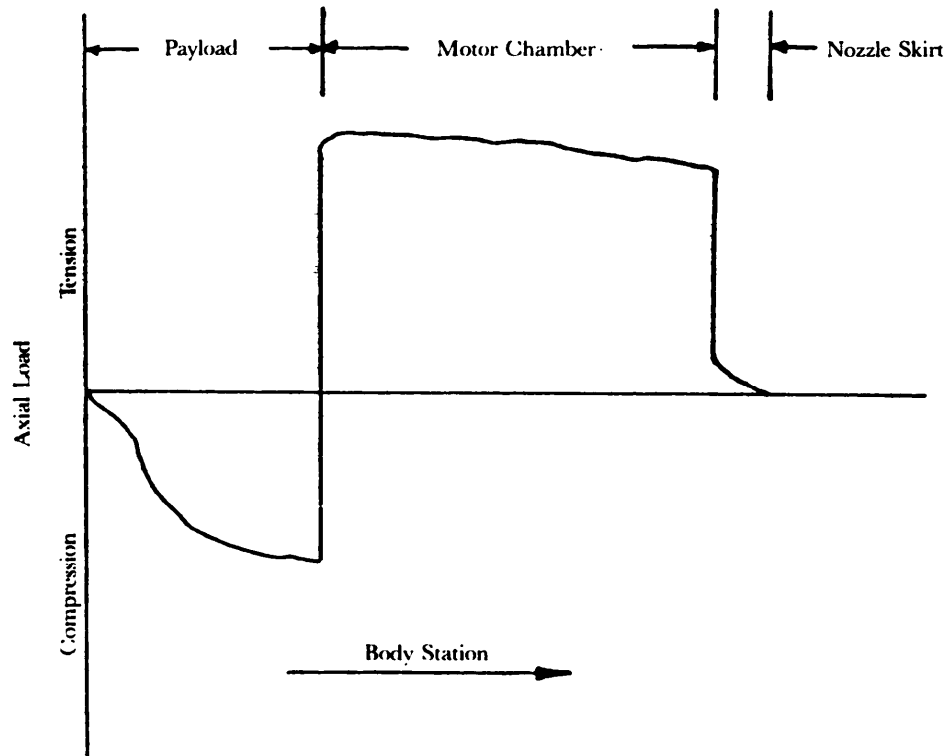
Figure 7-28. Typical Axial Load Diagram During Powered Flight

7-4.2.3.1 Motor Chamber

The motor chamber is usually a thin-walled cylinder with a head-end closure and a nozzle at the aft end. There are of course other configurations such as the spherical and the nozzleless motors.

The stress state in a conventional cylindrical motor case is similar to that of a closed cylinder under pressure, i.e., the hoop stress is approximately twice that experienced in the meridional direction. The hoop stress σ_h, away from discontinuities of the geometry such as those indicated in Figs. 7-29 and 7-32, can be expressed as

$$\sigma_h = \frac{p r_{mc}}{t_{mc}}, \text{ Pa} \tag{7-38}$$

where
$\quad p$ = motor (chamber) pressure, Pa
$\quad r_{mc}$ = mean radius of motor case, m
$\quad t_{mc}$ = thickness of motor case, m.

Uniform meridional stress in the motor case results from the total axial force acting on the afterbody of the motor. This force includes the effect of the chamber pressure acting on the surface of the aft closure, the integral of the pressure distribution along the nozzle bore, and the body (inertial) forces due to axial acceleration. Absolute pressures are generally used in the calculation of the axial force. The contribution of the inertial loads is generally negligible except for unusually high acceleration rockets. Bending due to external loads also produces meridional stress in the motor case. The combined meridional stress σ_m due to the axial force and bending moment can be expressed as
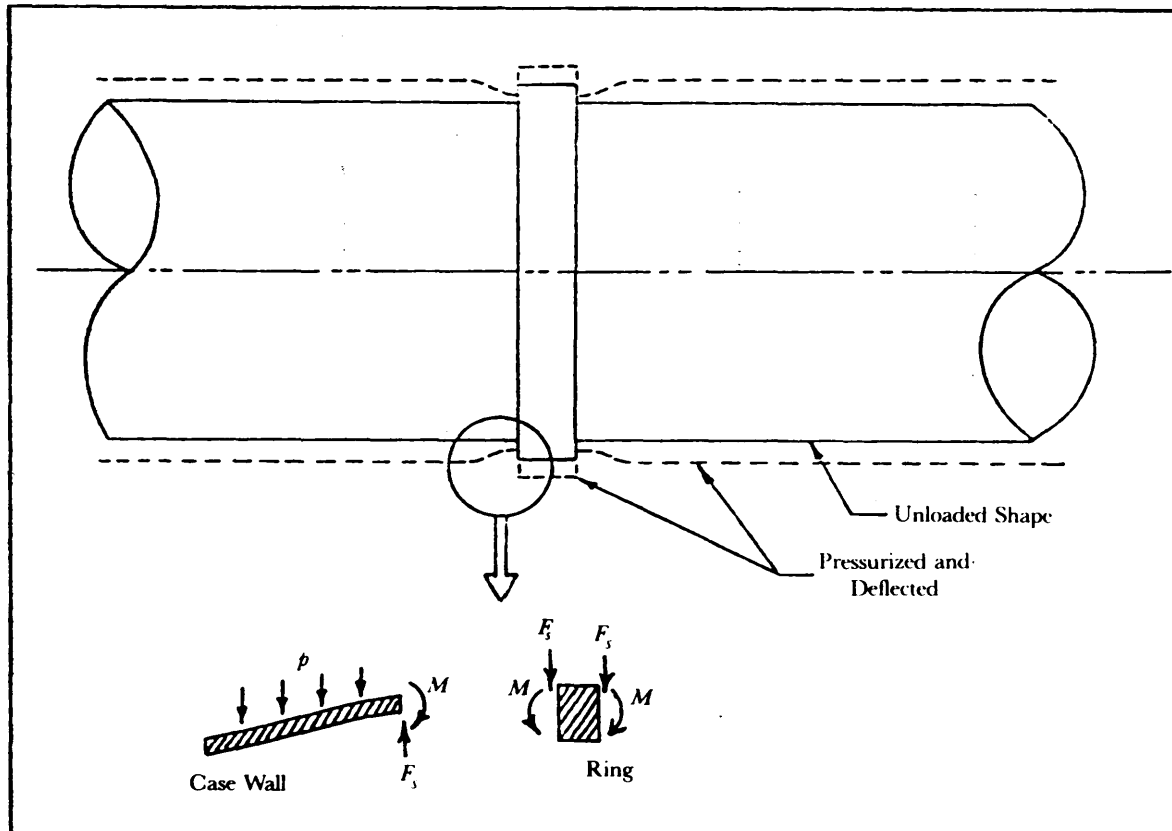
Figure 7-29. Motor Case Discontinuity Stress

$$\sigma_m = \frac{F_m}{2\pi r_{mc} t_{mc}} \pm \frac{M}{\pi r_{mc}^2 t_{mc}}, \text{Pa} \qquad (7\text{-}39)$$

where

F_m = axial meridional load, N

M = bending moment, N·m.

Radial displacement Δr of the cylindrical portion of the motor case can be computed from the hoop and meridional stresses by .

$$\Delta r = \frac{r_{mc}}{E}(\sigma_h - \nu\sigma_m), \text{m.} \qquad (7\text{-}40)$$

Discontinuities in shell geometries produce local stresses that may significantly affect the motor design. Reinforcements also can produce effects that may be detrimental as indicated in Fig. 7-29. In general, severe changes in geometry produce severe discontinuity stresses. Common and unavoidable discontinuities occur in the transitions from cylindrical shell-to-end closures.

Local shear forces and bending moments along the circumference are the result of geometric discontinuities. The resulting stresses are called discontinuity stresses and are superposed upon the membrane stresses. For thin shells, the discontinuity stresses become negligible a short distance away from the discontinuity. Equations such as those found in Ref. 9 can be used to determine the magnitudes of the stresses at and adjacent to the discontinuity.

Examples of the technique to determine the local edge (shear and membrane) forces and bending moment are given in Ref. 9. Basically, the unknown edge forces and moments are given in terms of radial displacement and rotations so that they can be determined by requiring compatibility (radial displacement and slope) at the discontinuity.

The capacity of a motor case to resist failure due to discontinuity stresses depends on the ductility of the material. Motor cases made from ductile materials (elongation greater than 7%) seldom fail as a result of the peak surface stress. A pressurized low carbon steel motor case with an integral head-end closure, for example, usually experiences hoop failure in the cylindrical wall at some distance away from the slell-to-closure discontinuity. A motor case made from high-strength, low-ductility material (elongation less than 1%) is susceptible to failure as a result of stresses produced at the discontinuities. The maximum tensile stress or tensile strain theory affords a satisfactory failure criterion for brittle materials. Failure of ductile materials are adequately determined by the maximum shear or maximum distortion energy theory (Ref. 13). The applicability of any failure theory, however, is dependent on the characteristics of the slecific material.

Experiments conducted on cylindrical specimens indicate improvement of the load-carrying capabilities of certain materials (low carbon steels) in the biaxial stress state. This improvement affects both the yield and ultimate capability of the material. These improvements are called the biaxial improvement factors BF and can be applied as follows:

$$\left.\begin{aligned} \sigma_{y,eff} &= \sigma_y(BF)_y, \text{ Pa} \\ \sigma_{u,eff} &= \sigma_u(BF)_u, \text{ Pa} \end{aligned}\right\} \tag{7-41}$$

where

$\sigma_{y,eff}$ = effective yield strength, Pa

$\sigma_{u,eff}$ = effective ultimate strength, Pa.

These effective yield and ultimate strengths are then compared with the maximum expected stress. Biaxial factors generally range between 1.0 and 1.2. Specific values can be found in Ref. 14.

The use of high-strength metals in the design of rocket motor cases has increased the importance of fracture mechanics. Fracture mechanics analysis considers that the case wall will be fabricated with a minute flaw and that certain relations can be formulated to be used to evaluate the conditions under which the flaw grows. An overview of the design considerations in rocket motor cases, considering the fracture mechanics of metallic and filament-wound motor cases, is presented in Ref. 15.

Under certain conditions, a rocket motor case will be subjected to environments that cause a nonuniform temperature distribution. A condition of this nature will develop a nonuniform strain distribution and the motor case may bow. An example of circumferential strain distribution is presented in Fig. 7-30(A), and the resultant bow of the motor case from the nonuniform circumferential strain is presented in Fig. 7-30(B). The radius of curvature of the bow is a function of the strain at both the top and bottom of the case. The bow of the motor case is detrimental to the accuracy of the rocket. Approximate methods for estimating the bow are presented in Ref. 16.

Filament-wound motor cases are made from one or more types of high tensile strength fibers. The fiber filaments are wound by using netting analysis in which the wrap angles are determined by the size of the polar openings and the shape of the end closures. The art of designing a filament-wound motor case is beyond the scope of this handbook. Detailed design information is usually proprietary data with the leading manufacturer-s of filament-wound motor cases. However, preliminary design may be accomplished with the netting equations contained in Ref. 17.

An example of a filament-wound motor case is shown in Fig. 7-31. The wrap angle indicated on Fig. 7-31 is dependent on the hoop-to-meridional load ratio and may also be influenced by bending stiffness requirements.
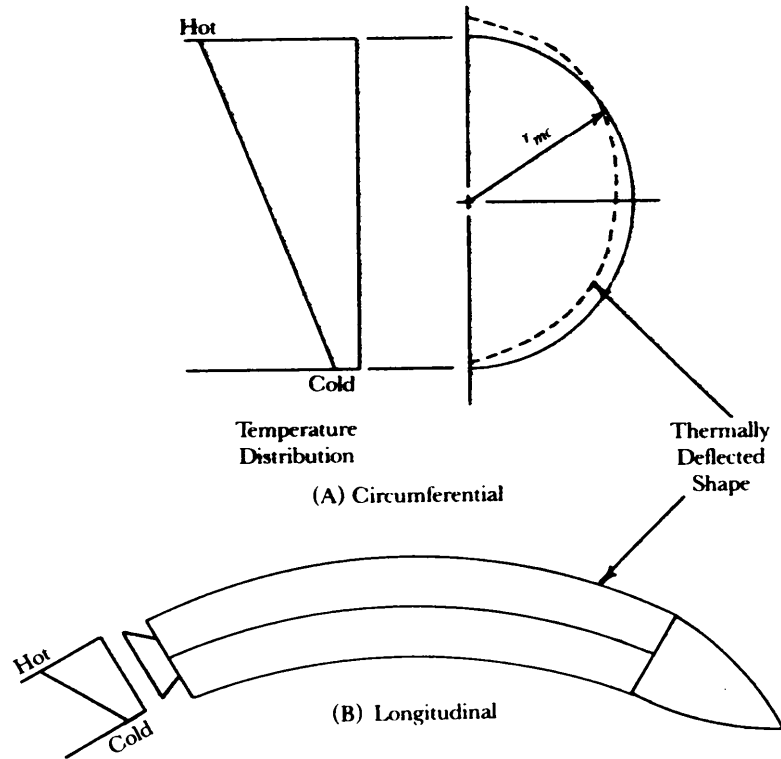
Figure 7-30. Motor Case Thermally Induced Strain
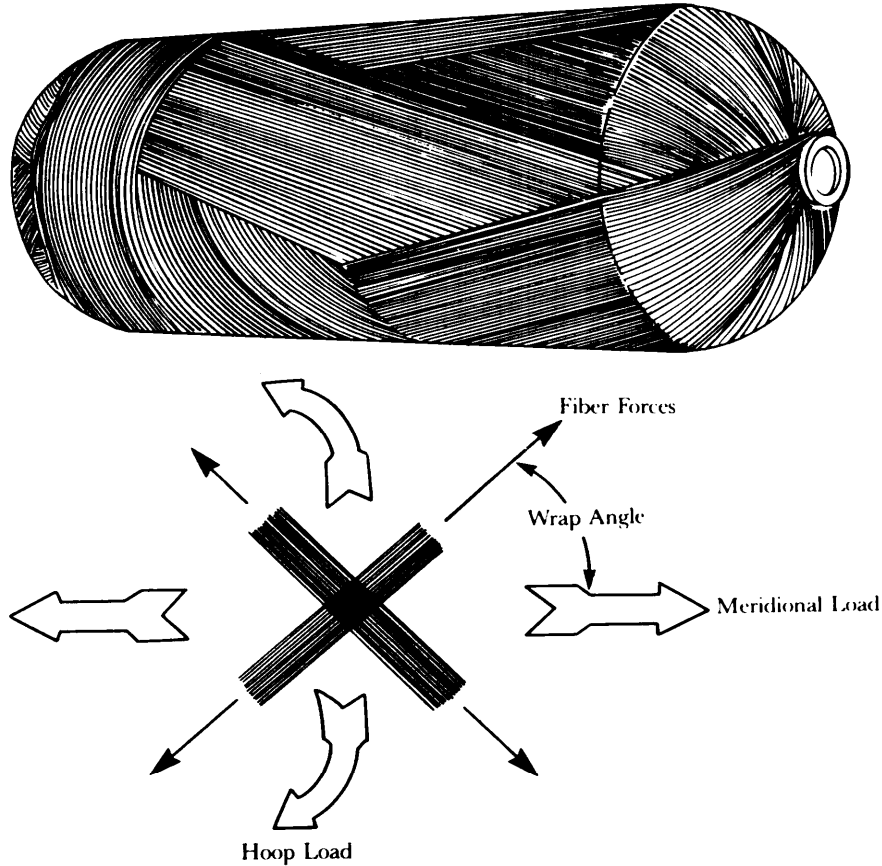
Figure 7-31. Filament Wound Motor Case

7-4.2.3.2 End Closure

End closure in rocket motors may be made integral to the cylindrical case wall or may be attached by mechanical means. The closures may be contoured domes or flat plates. Contoured domes may be either concave or convex.

Stress analysis of flat closures can be conducted with equations found in Ref. 9. The use of these equations in establishing the thickness of the closure generally results in an overdesigned component because the equations are based on linear theory. The use of these equations should, however, suffice for the preliminary design of flat closures.

Equations for the analysis of contoured closures are also available in Ref. 9. Concave closures are generally made integral with the cylinder wall. The structure at the juncture of the closure and the cylinder generally resembles a Y and, therefore, is called a Y-ring. An example of a typical Y-ring is shown in Fig. 7-32(/1).

Stress analysis of a Y-ring is performed by modeling the joint as a series of shell elements as shown on Fig. 7-32(B). The analysis of the idealized model requires the solution of a system of simultaneous equations for the unknown displacements and edge forces. The procedure can be very tedious and is not recommended when computer analysis is possible. Finite element computer programs are routinely used for such problems. Finite element models are discussed in par. 7-4.3.2.2.
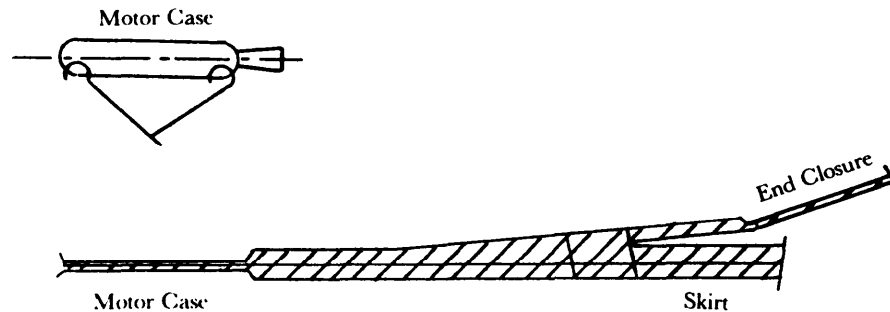
(A) Typical Y-Ring Structure
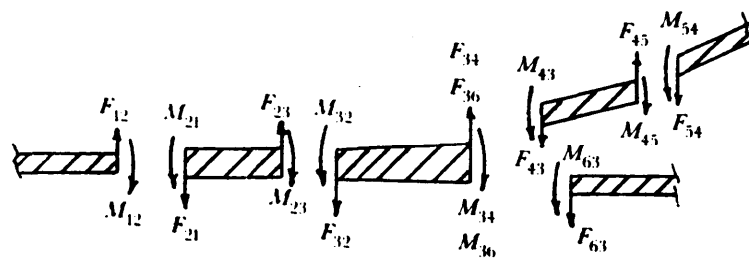
(B) Idealized Y-Ring Shell Elements

Figure 7-32. Modeling Y-Ring Structure by Shell Elements

7-4.2.3.3 Nozzle

Requirements for efficient low-mass nozzles have led to complex nozzle designs. These designs generally consist of several material types, each selected to perform a particular function in the nozzle. The result is a highly indeterminate structure composed of a combination of anisotropic and isotropic materials. Final stress analysis of such nozzles requires highly developed numerical analysis techniques. Considerations of

nonlinear behavior may be required for the accurate assessment of the structural integrity of these components. Fortunately, all nozzles are not very complex and can be adequately analyzed with elementary equations for preliminary design purposes.

Motor pressure is generally the critical loading condition for the nozzle. A modified isentropic flow usually is assumed in determining the varying pressure along the nozzle internal surface.

The internal configuration of a nozzle is dictated by the ballistic requirements of the rocket, and the external configuration usually is varied to satisfy the structural requirements. Throat diameter, exit plane diameter, and exit cone half angle generally are determined by the interior ballistics group.

Stress analysis of exit cones and blast tubes of single-layer, homogeneous materials may be approximated using elementary equations. The hoop stress σ_h at any nozzle station may be determined by the thick-walled cylinder equation

$$\sigma_h = P_{nozzle} \left(\frac{r_o^2 + r_i^2}{r_o^2 - r_i^2} \right), \text{Pa} \tag{7-42}$$

where

P_{nozzle} = pressure at nozzle station of interest (external pressure is assumed to be zero), Pa
r_0 = outside radius of nozzle at station of interest, m
r_i = inside radius of nozzle at same station, m.

Stability analysis should be performed for thin-shelled exit cones under the action of exhaust gas pressure in the nozzle which produces compressive load in the axial direction. Compressive buckling strength can be estimated from the methods of Ref. 8, Chapter C8.

For multilayer nozzle designs (see Fig. 7-15), equations are available which model the nozzle in two layers, i.e., a thick-wall inner cylinder and a thin outer shell. The equations allow the estimation of radial and hoop stress and strain due to internal pressure and temperature gradient. The equation assumes the condition of plane strain, i.e., the strain along the cylinder axis is assumed to be zero.

The stress equations for applied internal pressure are

$$\sigma_r = \frac{p}{r_{oi}^2 - 1} \left[(1 - r_{or}^2) - \frac{2(1 - \nu_i)}{\Omega_p} (r_{oi}^2 - r_{or}^2) \right], \text{Pa} \tag{7-43}$$

$$\sigma_h = \frac{p}{r_{oi}^2 - 1} \left[(1 + r_{or}^2) - \frac{2(1 - \nu_i)}{\Omega_p} (r_{oi}^2 + r_{or}^2) \right], \text{Pa.} \tag{7-44}$$

The total strain equations are

$$\epsilon_r = \frac{(1 - \nu_i) p}{(r_{oi}^2 - 1) E_i} \left\{ (1 - 2\nu_i - r_{or}^2) + \frac{2(1 - \nu_i)}{\Omega_p} \right.$$

$$\times \left. [(1 - 2\nu_i) r_{oi}^2 - r_{or}^2] \right\}, \text{m/m} \tag{7-45}$$

$$\epsilon_h = \frac{(1 + \nu_i) p}{(r_{oi}^2 - 1) E_i} \left\{ (1 - 2\nu_i + r_{or}^2) - \frac{2(1 - \nu_i)}{\Omega_p} \right.$$

$$\times \left. [(1 - 2\nu_i) r_{oi}^2 + r_{or}^2] \right\}, \text{m/m} \tag{7-46}$$

$$\Omega_p = 1 + (1 - 2\nu_i)r_{oi}^2 + \left(\frac{r_o}{t}\right)\left(\frac{E_i}{E_o}\right)\left(\frac{1 - \nu_o^2}{1 + \nu_i}\right), \text{ dimensionless} \qquad (7\text{-}47)$$

$$r_{oi} = r_o/r_i, \text{ dimensionless} \qquad (7\text{-}48)$$

$$r_{or} = r_o/r, \text{ dimensionless} \qquad (7\text{-}49)$$

where

σ_r = stress in radial direction, Pa

σ_h = hoop stress, Pa

ϵ_r = strain in radial direction, m/m

ϵ_h = hoop strain, m/m

E = Young's modulus, Pa

ν = Poisson's ratio, dimensionless

p = internal pressure at nozzle station under consideration (external pressure is assumed to be zero), Pa

t = thickness of outer layer, m

r_o = outer radius of inner layer, m

r_i = inner radius of inner layer, m

r = radius of point within inner layer where stress and strain are being estimated, m.

Fig. 7-33 illustrates the basic nomenclature.
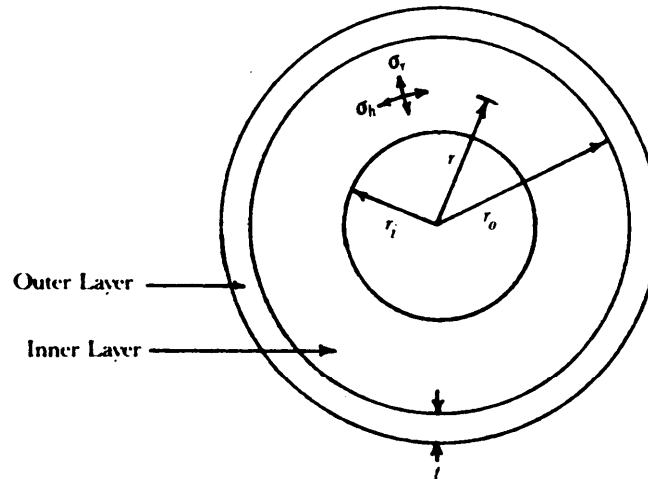
Figure 7-33. Geometry of Plane-Strain Analysis Model

The stress equations for thermal stress are

$$-E_i\alpha_i\Delta T r_{oi}^2(1 - r_{ir}^2)\left[\frac{1 - \dfrac{\alpha_o(1 + \nu_o)}{\alpha_i(1 + \nu_i)}}{\Omega_T}\right], \text{ Pa} \qquad (7\text{-}50)$$

$$\sigma_h = -E_i\alpha_i\Delta T r_{oi}^2(1 + r_{ir}^2)\left[\dfrac{1 - \dfrac{\alpha_o(1 + \nu_o)}{\alpha_i(1 + \nu_i)}}{\Omega_T}\right], \text{Pa.} \tag{7-51}$$

The total strain is

$$\epsilon_r = -(1 + \nu_i)\alpha_i\Delta T\left\{(1 - 2\nu_i - r_{ir}^2 r_{oi}^2)\left[\dfrac{1 - \dfrac{\alpha_o(1 + \nu_o)}{\alpha_i(1 + \nu_i)}}{\Omega_T}\right] + 1\right\}, \text{m/m} \tag{7-52}$$

$$\epsilon_h = -(1 + \nu_i)\alpha_i\Delta T\left\{(1 - 2\nu_i + r_{ir}^2 r_{oi}^2)\left[\dfrac{1 - \dfrac{\alpha_o(1 + \nu_o)}{\alpha_i(1 + \nu_i)}}{\Omega_T}\right] - 1\right\}, \text{m/m} \tag{7-53}$$

$$\Omega_T = (1 - 2\nu_i)r_{oi}^2 + 1 + \left(\dfrac{r_o}{t}\right)\left(\dfrac{E_o}{E_i}\right)(r_{oi}^2 - 1)\left(\dfrac{1 - \nu_o^2}{1 + \nu_i}\right), \text{dimensionless} \tag{7-54}$$

$$r_{ir} = r_i/r, \text{dimensionless} \tag{7-55}$$

where

α = linear coefficient of thermal expansion, m/m·K

ΔT = temperature change (design temperature minus stress-free temperature) from motor ignition to operating temperature at the radius and station of interest, deg K

and the subscripts i and o associated with the previously defined basic symbols refer to inner and outer respectively.

7-4.2.3.4 Payload

The structural function of a payload structure is highly dependent upon the mission requirements. For example, the warhead may serve as the airframe of the forebody of the rocket or the warhead may be attached locally to a shroud that serves as the airframe. Regardless of the application, structural analysis of the payload structure must include the air-loads-shear, moment, and axial force—and the loads associated with accelerations from handling, transportation, and elastic response.

Thin shells, which serve primarily as fairings, experience the aerodynamic forces. These forces generally produce compressive loads, requiring that a stability analysis be performed to prevent collapse even at relatively low levels of stress. As stated in par. 7-4.2.1.5, these payload fairings may be designed by the methods of Ref. 8.

7-4.2.3.5 Fin

Rocket fin configurations vary widely. In general, fins used on smaller rockets are of simple construction, i.e., mainly thin plates for which stress analysis equations are available (Refs. 8 and 9).

Large rockets may require a more complex fin construction to minimize weight. Such fins can be of honeycomb construction or of sheet-stringer construction.

It is not possible to provide the analytical procedure within the scope of this chapter for the design of the many types of fins. The discussion that follows, therefore, has been limited to a delta fin shape with thin skin, stringer, and rib construction.

The lift force applied at the center of pressure of the finis shown in Fig. 7-34. Stress analysis of the delta wing construction is presented in Ref. 18. The procedure follows.

The maximum shear load F_s at the fin root is

$$F_s = F_{N_{fin}} - a_{N_{max}} (m_{total} - m_{fin}), \text{ N} \tag{7-56}$$

where

$a_{N_{max}}$ = maximum normal acceleration at fins, m/s^2
m_{total} = total mass of rocket, kg
m_{fin} = total mass of fins, kg
$F_{N_{fin}}$ = fin normal force, N.
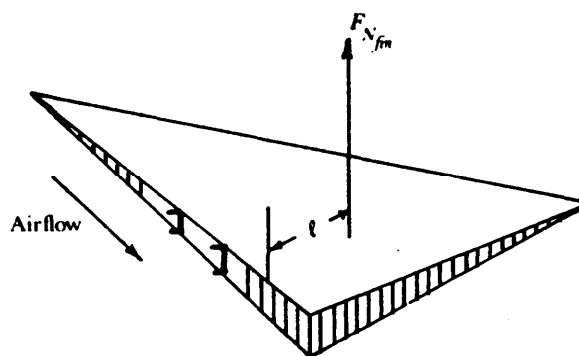
Figure 7-34. Fin and Airload

The effective cross-sectional area A_s of the shear material at the root is determined by

$$A_s = \frac{F_{N_{fin}}}{\sigma_s} \text{ , m}^2 \tag{7-57}$$

where

σ_s = allowable average shear stress, Pa.

However, σ_s is a function of the type of construction, i.e., truss, thin-web, etc. By taking construction type into account and the effects of the depth of the shear member, a more realistic cross section and root shear stress is

$$\sigma_s = \frac{F_{N_{fin}}}{A_s - K_s h^2} \text{ , Pa}$$

where

σ_s = allowable average stress on portion of fin root area that corresponds to direct loading, Pa
h = depth of fin root shear member, m
K_s = correction factor for construction type, dimensionless (typically 0.00025 for sheet-stringer-web construction).

NOTE: It is imperative to include the safety factor (par. 7-4.2.5) as a load multiplier or alternatively as a factor in reduding the material capability to a working (allowable) stress level.

If it is assumed that all the shear is carried equally by two main shear members as shown in Fig. 7-3.5, the shear stress σ_s at the wing root is

$$\sigma_s = \cfrac{0.5 F_{N_{fin}}}{A_s - \left[\cfrac{K_s(h_1 + h_2)^2}{4h}\right]^2} \text{ , Pa} \tag{7-59}$$

where
   h_1 and h_2 = lengths of shear carrying members, m.
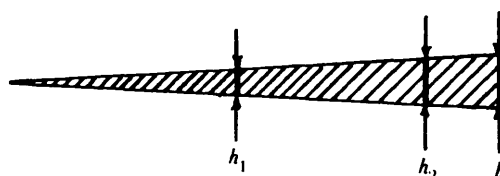
Figure 7-35. Fin Shear Carrying Members

Thus the allowable stress in the shear members is equal to the shear load divided by the sum of the shear area and an average shear depth squared.

The net bending moment of the fin at the root is resisted by the couple as shown in Fig. 7-36. The estimated flange shear load F_{st} is

$$F_{st} = \cfrac{M_{fin}}{h_{equiv}} \text{ , N} \tag{7-60}$$

where
   M_{fin} = net bending moment at fin root, N·m
   h_{equiv} = distance between centroids of equivalent two-flange beam, m.
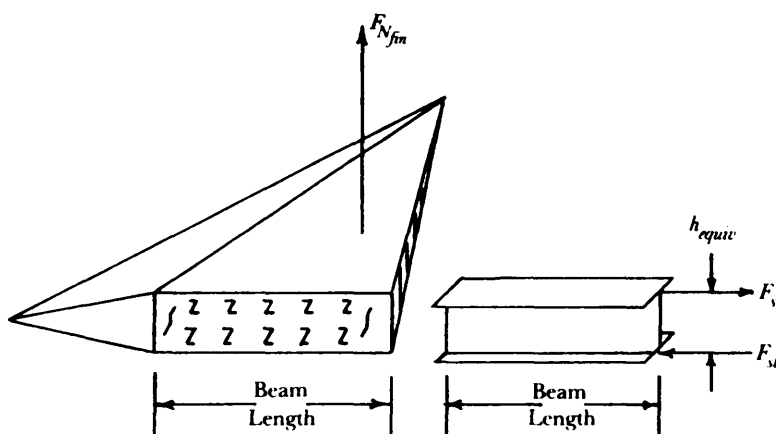
Figure 7-36. Equivalent Two-Flange Beam Fin

The load F_{st} in the top and bottom flanges at the root of the equivalent two-flange beam for a uniform airload FN_{fin} on a delta wing is

$$F_{st} = \frac{F_{N_{fin}}}{3k_e h^2} \ , \ \text{N}$$

(7-61)

and the stress σ_t is

$$\sigma_t = \frac{F_{st}}{A_{equiv}} \ , \ \text{Pa}$$

(7-62)

where
A_{equiv} = equivalent two-flange plate area, m^2
σ_t = allowable tensile stress in flange, Pa.

7-4.2.3.6 Propellant Grain

Sol id propellants in rocket motors maybe supported by case bonding, end-bonded cartridges, stress-free liners, etc. Of particular interest are the case-bonded grains since this method of support is inherently stress producing.

Critical load conditions for case-bonded grains include

1. Storage at Low Temperature. Low temperature produces tensile stress and strains in the propellant grain due to the differential contraction between the propellant and motor case. The coefficient of thermal expansion for a propellant is generally ten times greater than that for steel.

2. Storage at Elevated Temperature. High-temperature exposure over a prolonged period is generally detrimental to the physical properties of the propellant.

3. Ignition at Low Temperature. Low temperature generally reduces the ultimate strain capability of the propellant at the high strain rates experienced during ignition.

4. Ignition at High Temperature. The reduced stiffness (effective modulus) of the propellant at high temperature may result in unacceptable distortions in a nonuniform pressure field or in a high-acceleration environment.

5. Handling and Transportation. Handling and transportation requirements produce stress from shock and vibratory loads. Shock loads may produce high bondline stresses at grain terminations. Solid propellants are generally good vibration dampers, and structural integrity under this environment is usually confirmed by testing.

The viscoelastic behavior of a solid propellant grain is simulated by use of an equivalent elastic modulus. The equivalent modulus is determined from a relaxation modulus curve for the propellant with the appropriate temperature and load time. A typical relaxation modulus curve is presented in par. 7-4.2.4.

Detailed stress analyses of solid propellant grains are conducted with finite element models that can account for the complex geometries. Long circular port (CP) grain configurations act as thick-walled cylinders and can be analyzed for thermal and pressure loads by use of Eqs. 7-43 through 7-55. Preliminary stress analysis equations for slotted grains are given in Refs. 10 and 19.

7-4.2.4 Materials

The selection of structural materials for rocket motors is one of the more complex tasks facing a motor designer. It involves the simultaneous consideration of fabrication techniques, intended mission, environmental effects during the service life, compatibility of materials, cost, manufacturing plan, minimum mass, stiffness requirements, etc.

It is not the intent of this handbook to provide the designer with a complete description of materials used in rocket design. However, the paragraphs that follow provide some general information on physical

properties, manufacturing techniques, and cost considerations. Tables of physical properties of commonly used materials are also provided.

7-4.2.4.1 Structural Materials

A wide variety of materials are used in rocket construction. They range from the homogeneous metals such as steel, aluminum, and titanium to the nonhomogeneous materials such as fiber-reinforced plastics, metallic laminates, and paper-reinforced plastics.

Medium-alloy steels—such as the AISI 4100-series steels that are alloyed with chromium and molybdenum— are the primary materials used for solid rocket motors. These steels provide tensile strengths that range from 620 MPa in the normalized condition to about 1240 MPa in the heat-treated condition. The particular alloy should be selected on the basis of the required strength level, thickness of the finished part, and the desired fabrication technique. AISI 4340 steel and steels related to it—such as D6AC and 300-M steels—were developed to produce even higher tensile strengths (1380 MPa and above). Also capable of operating at this level are the hot-worked die steels such as the H-11 and Potomac M. The AISI 4340-type steels are less difficult to fabricate and result in more reliable motor cases. However, extreme caution must be exercised to maintain adequate ductility in order to reduce notch sensitivity of these highly hardened alloy steels. Another class of steels— called maraged because they maintain their tough hard martensitic structure during aging at elevated temperature- may be used at yield strengths of 1380 to 2070 MPa, but they are not as notch sensitive as the high-strength steels described previously. Maraged steels have the advantages of good forming and forging characteristics of the annealed alloy, heat treatment at low temperature (727 to 783 K) with ambient-air cooling, good dimensional stability during the heat treatment, and heat treatment without the necessity of controlled atmosphere.

Titanium alloys are used in rocket motor cases primarily because their strength-to-density ratio is higher than that for steels. Titanium is reasonably formable and weldable, presents no severe fabrication problems, and is capable of yield strengths from 1100 to 1240 MPa. Titanium is not susceptible to corrosion, but certain compounds under some conditions can produce stress corrosion in titanium alloys.

Aluminum alloys are very useful for small motors, e.g., up to 2.50 or 300 mm in diameter, when large numbers are to be manufactured, primarily because of the ease of forming the alloy to almost final dimension. Another application has been to employ mill-run extruded tubing directly for the cylindrical section of the motor case. The low density of aluminum can be important in mass-limited systems, but the low strengths (from 240 to 480 MPa) cause the strength-to-density ratio to be lower than that of steels. Aluminum cannot be used if aerodynamic heating is a design factor because of the rapid deterioration of strength with increased temperature. Furthermore, stress corrosion is of particular concern and must be carefully evaluated when an aluminum alloy is used as a structural material.

Glass fiber embedded in a resin matrix (sometimes called "composite'" or "plastic") is beginning to be commonly used for rocket structures. Continuous filaments of glass are coated with a suitable resin in one of two ways. In one approach, the filaments are preimpregnated with the resin, partially cured, then wound back on a spool. The case is then manufactured by winding the coated filaments over a removable form or mandrel. The mandrel rotates about its longitudinal axis while a filament guide mechanism traverses the length of the case. After all the preimpregnated filaments have been wrapped on the mandrel, the assembly is placed in an oven to cure at elevated temperature. In the second approach, resin is applied to the filaments just prior to winding onto the mandrel. The remainder of the manufacturing cycle is the same as with the preimpregnated filament.

Glass fiber cases offer the unique advantage of orienting the direction of the filaments in accordance with the varying stress requirements. The mapping pattern can be adjusted to account for different load requirements in different applications. Resins are selected on the basis of design environmental conditions. Although the hoop ultimate tensile strength of a glass-resin composite may be only 1380 MPa at best, its low density of 2 g/cm^3 results in a strength-to-density ratio that is significantly better than the best steel. The tensile modulus of a composite with the best glass is 55,200 MPa, but again the low density produces a stiffness-to-density ratio equal to that of the best steel. If moderate tensile strength and low

stiffness are acceptable for a given application, glass fiber composite cases are very attractive. Another disadvantage that must be addressed is the susceptibility of the composite to local damage. Metallic cases can usually accommodate some amount of local damage depending on the notch sensitivity of the particular material. The glass fiber composite case has relatively little tolerance to local damage. Glass fiber composite cases also have a fairly low service temperature (420 K for S-glass). Other fibers such as Kevlar® and graphite are used to obtain high-performance motor cases.

Paper impregnated with epoxy resin (paper phenolics) can be obtained either as flat laminated sheets or as tubes formed on a mandrel. Both are widely used as commercial products and thus are attractive for case materials because of their relatively low cost. Design strength is extremely low (140 MPa); accordingly, volume-limited rocket motors probably cannot employ this material because of the extremely thick components required to withstand the operating pressure. A cylinder made from flat sheet stock is bonded or fastened with pins inside one end of a tube to form the forward closure. A nozzle of suitable material is similarly fastened in the aft end.

Strip (wrap) laminate or wound metal cases are made by winding thin strips (50 to 75 mm wide) in a spiral pattern on a cylindrical mandrel. Several layers are applied with overlapping joints until the required thickness is obtained. Adhesive applied to the metal during wrapping binds the layers together. The ends of the tube are then bonded to metal rings that are shaped to transfer the shell loads gradually to the stiffening rings. Closures and nozzle are then secured to these rings with conventional attachments such as retaining rings or radial pins. The primary advantage of such a construction technique is that ultrhigh-strength steels with relatively high stiffness (and brittleness) can be formed into a tube by using thin (0.80 mm) strips for each layer. Extremely close tolerances can be held because the wrapping mandrel controls the dimensions. Capability to withstand cyclic environmental conditions of temperature (290 to 3.50 K) and relative humidity (60 to 90%) has been demonstrated. High-temperature resins are available for applications in which aerodynamic heating is a factor. However, resins cannot operate at temperatures as high as steess can.

7-4.2.4.2 Physical Properties of Structural Materials

Generally, structural material is initially selected as being the most efficient material on the basis of mass, cost, and mass-per--unit cost, which will satisfy the overall critical loading condition at the critical operating temperature when the constraints of fracture mechanics are considered. Critical loading can be either internal pressure or aerodynamic pressure, depending on the vehicle location and the local structure. Thus the designer must consider tensile strength, compressive strength, and stiffness requirements.

Failure of the rocket structure can be either ductile or brittle in nature. Premature brittle failures can occur at stress levels considerably below the design service stress, even with materials that demonstrate adequate elongation. These fractures may result, for example, from environmental conditions that lead to stress-corrosion cracking at low sustained stress levels. Also local embrittlements and residual stresses may be inherent to the manufacturing process. Linear elastic fracture mechanics generally can be used to screen materials unsuitable for the intended application. The required information—including material selection, allowable working stress, fabrication methods, and inspection and testing—can be found in Refs. 20 through 24. The major point to be made here is that considerations of elastic behavior may not be sufficient to avoid structural failure.

Most ductile metals have compressive stress-strain relationships very similar to those for tensile stress. Compressive failure occurs when there is buckling, crippling, shearing, bearing, splitting, or crumbling. The maximum stress sustained by the materials is called the compressive strength.

Composite materials exhibit the same elastic behavior as homogeneous materials, except that there is little or no plastic behavior. Instead, the material strength listed is an ultimate value based on failure of the test article.

Properties of metallic structural materials at room temperature (298 K) are given in Table 7-7 for some common alloys, and several steels are compared in Table 7-8. Refs. 25 through 28 are commonly accepted

MIL-HDBK-762(MI)

TABLE 7-7. PROPERTIES OF METALLIC STRUCTURAL MATERIALS AT ROOM TEMPERATURE

Material	Design Yield Strength, MPa	Modulus of Elasticity, GPa	Density, kg/m³
HY Steel:			
HY-80	551.6	203.4	7890
HY-130/150	896.3—1034.2	203.4	7890
Low Alloy Steel:			
4130	1034.2—1241.1	199.9	7830
4335V	1241.1—1379.0	199.9	7830
D6aC	1241.1—1654.7	199.9	7830
Maraging Steel:			
Grade 200	1379.0	189.6	8000
Grade 250	1654.7	189.6	8000
Grade 300	1930.5	189.6	8000
HP Steel:			
9 Ni-4 Co-0.250	1241.1—1516.8	196.5	7750
9 Ni-4 Co-0.450	1792.6—2068.4	196.5	7750
Titanium:			
Ti-6Al-4V	1034.2	110.3	4620
Aluminum Alloys:			
2000 Series	241.3—448.2	71.0	2770
5000 Series	206.8—275.8	71.0	2770
6000 Series	255.1—324.1	71.0	2770
7000 Series	413.7—468.8	71.0	2770

sources of data for metals. These documents also provide the designer with general information on heat treatment requirements and the influence of various environments on the material properties. Resin reinforced with glass filaments, strip laminates, and paper phenolic properties are given in Table 7-9. A comparison of material properties is presented in Table 7-10.

7-4.2.4.3 Manufacturing Techniques

Metallic motor cases are manufactured by forming two or more sections produced by rolling, forging, drawings, and spin forming. The sections are joined together by welding-arc, gas, and inertia-or by mechanical means such as rivets, threads, bolts, or pins. Small cases can be formed out of a single piece of metal with subsequent machining to provide attachment points.

One of the more common manufacturing techniques consists of t-oiling a sheet of steel into a tube and welding it along its entire length. If the case is longer than a single sheet, several of the welded tubes are joined together by girth welds. If the circumference of the case is too large for a single sheet, several sheets may be longitudinally welded together after they are rolled into cylindrical segments. Once the proper cylindrical length is obtained, the tubes are girth welded to forward and aft closures formed by forging or drawing. The entire assembly is then heat treated.

Spin forming is a method of manufacturing often used to form cases from the high-strength, brittle steels. It is especially suited for materials that are not easily welded such as the highly alloyed materials. An initially large ring of steel is placed on a mandrel and rotated while large rollers, moving back and forth, press the steel ring into a thin, long tube. The girth welds used to attach the tube to end closures are

TABLE 7-8. COMPARISON OF SOME AEROSPACE STEELS AT ROOM TEMPERATURE

Medium Alloy Steels				
Tensile Properties	AISI and SAE Designation			
	4130	4135	4140	4340
Ultimate Stress, MPa	1310	1276	1241	1448
Yield Stress, MPa	1206	1172	1138	1379
Ultimate Elongation, %	12.0	12.0	12.0	10.0

Tool Steels				
Tensile Properties	Commercial Designation			
	D6aC	300-M	X-200	H-11
Ultimate Strength, MPa	1482	1551	1482	1655
Yield Strength, MPa	1379	1379	1310	1379
Ultimate Elongation, %	8.0	8.0	8.0	6.0

Maraging Steels		
Tensile Properties	18Ni(250)	18Ni(300)
Yield Strength, MPa	1758	1999
Elongation, %	13.0	11.5

TABLE 7-9. PROPERTIES OF COMPOSITE MATERIALS AT ROOM TEMPERATURE

Material	Modulus E, MPa	Composite Tensile Strength, kPa	Composite Density, kg/m^3	Fiber Ultimate Strength, MPa
S2-Glass Epoxy	51.0	3240	1965	4.58
E-Glass Epoxy	42.7	2413	2020	3.45
Crepe Craft Paper Phenolic Tape	6.2	59	1330	—
Strip Laminates		(Ultimate)		
Stainless Steel	207000	2000	7830	—
Martinsite	207000	1517	7830	—

generally subjected to only half the stress experienced by a longitudinal weld; accordingly, they do not require nearly the same physical properties.

Submerged are and tungsten arc welded by inert gas are the more widely used welding techniques. The submerged arc method is used primarily to join heavy welded sections for which large deposits of filler wire are necessary. Thin-walled, high-strength motor cases are more easily welded by using the tungsten

**TABLE 7-10. TYPICAL COMPOSITE
MATERIAL TENSILE PROPERTIES,
COMPARED WITH METALS
AT ROOM TEMPERATURE**

Material	Composite Density, kg/m^3	Composite Tensile Strength, MPa	Composite Tensile Modulus, GPa
E-Glass/Epoxy	2020	3240	51
S-Glass/Epoxy	1965	2413	42.7
Steel	7830	1500	200
Aluminum	2770	460	71
Titanium	4620	1030	110.3

arc process since there is less chance of atmospheric contamination than with the submerged arc technique.

Other welding techniques are also widely used. Laser welding employs a high-energy laser beam to form a joint that has a very narrow fusion and heat-affected zone. Major advantages of the laser technique are that it requires no vacuum or X-ray shielding and can employ a split beam for making two welds simultaneously. The major disadvantage is the high initial equipment cost, making the laser technique more applicable for- high-volume production. Electron beam welding also produces small heat-affected zones. It can be performed in three different modes—i.e. , in-vacuum, partial vacuum, and out-of-vacuum. Inertia welding is accomplished when a spinning part is forced against a stationary part and the resultant heat from the friction forges the two together. This technique, along with the laser and the electron beams, is particularly suited for high-volume, semiautomated assembly lines and can be accomplished with workers who are not trained welders.

Aluminum cases can be extruded or drawn either to nearly final dimensions or as tubes into which closures are fastened by one of several acceptable techniques. Steels up through the AISI 4130 series can be purchased as tubing to be used as the cylindrical portion of motor cases. However, there is a particular wall thickness below which the forming process cannot be used. So unless the motor design requires the available thickness, either the outside and/or inside surfaces must be machined.

7-4.2.4.4 Mass-Per-Cost Factors

It is extremely difficult, if not impossible, to make any general statements about mass and cost relationships for a rocket motor because every application requires its own unique blend of material, thickness, joining technique, etc. For a given material, the cost-per-unit mass increases as the strength level increases. Therefore, since for a given operating pressure the required thickness decreases, there is some offset to the cost increase.

Fig. 7-37 shows the variation of case cost with cylindrical wall thickness for a particular application. Shown on the figure also are ultimate tensile strengths for the materials. Within a given material class, higher strength means higher cost. However, if the question of mass versus cost is studied from a system viewpoint, it can be said that often higher strength can be obtained at lower cost by changing to a different class of material. This point is illustrated in Table 7-11 by comparing the total motor mass and cost for five systems that deliver the same performance by use of materials shown in Fig. 7-37.

MIL-HDBK-762(MI)
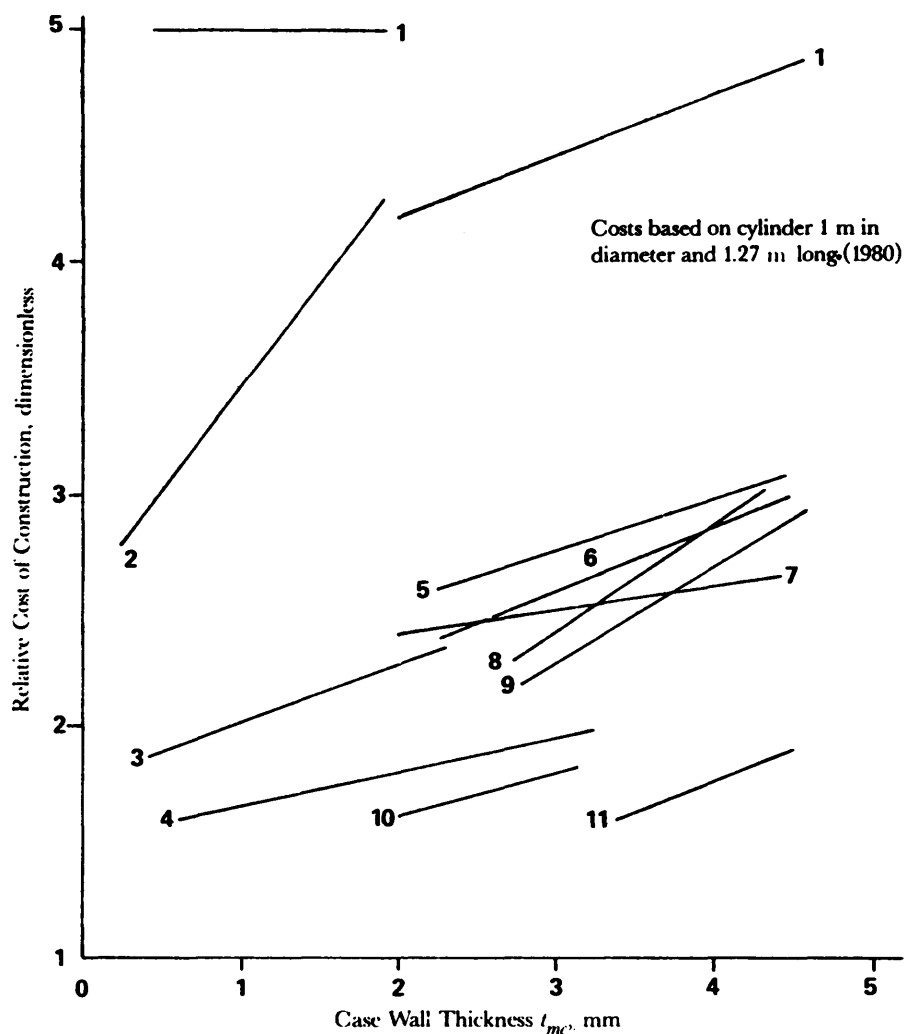
Figure 7-37. Relative Motor Case Cost vs Case Thickness

TABLE 7-11. EFFECT OF CASE MATERIAL SELECTION ON MOTOR MASS AND COST

Material	Relative Mass	Relative Cost
Aluminum (7075-T6 Extrusion)	1.0625	1.0780
Aluminum (2014-T6 Tubing)	1.0903	1.0355
Glass Fiber (E-Glass)	1.0	1.0
Stainless Steel (Strip Laminate)	1.0903	1.0071
Steel (AISI 1035)	1.3194	0.9929

7-4.2.4.5 Propellants

Propellants exhibit considerable variations in physical characteristics. The viscoelastic characteristics are influenced by the loading conditions. Furthermore, propellants may be chemically affected by the adjacent materials.

For a given analysis, the required physical characteristics depend on the assumptions made to facilitate the analysis. In general, the propellant is treated as elastic in the analyses of long-term storage at uniform temperature, acceleration, and ignition pressurization.

These types of analyses require some knowledge of the mechanical behavior of propellants. The paragraphs that follow discuss parameters required in the performance of elastic analysis.

Elastic analysis requires that representative values be defined for the tensile modulus E or shear modulus G and Poisson's ratio v or bulk modulus K_b. The relationship between these parameters is

$$K_b = \frac{E}{3(1 - 2\nu)}, \text{ Pa.} \tag{7-63}$$

A Poisson's ratio of 0.50 m/m generally is assumed unless K_b is known. Alternatively, Poisson's ratio may be computed by assuming the value of K_b to be 7×10^6 kPa.

The modulus is chosen to be consistent with the anticipated loading rate and temperature as determined from a relaxation modulus curve. A typical relaxation modulus curve is given by Fig. 7-38. The lower asymptotic value in this curve is called the equilibrium modulus E_e. Some propellants never achieve a state of equilibrium, and the value for E_e is estimated from samples that are strained for two weeks or more. The "glassy" modulus E_g is representative of the brittle behavior of propellants at very low temperatures or at very high loading rates. The glassy modulus represents the upper limit of the modulus.

The determination of an effective modulus proceeds as follows. The time t over which the strain is induced is determined. This may vary from a few milliseconds, during motor ignition in going from ambient to operating pressure, to several months for analysis of creep during storage. An operating temperature T is also specified. A temperature-time shift factor $\log a_T$ is then calculated by

$$\log a_T = \frac{C_1(T - T_{ref})}{C_2 + (T - T_{ref})}, \text{ dimensionles} \tag{7-64}$$

where
$\quad C_1$ and $C_2 =$ measured constants usually supplied by propellant manufacturer
$\quad\quad T =$ test temperature, K
$\quad\quad T_{ref} =$ reference temperature usually taken as 298 K.
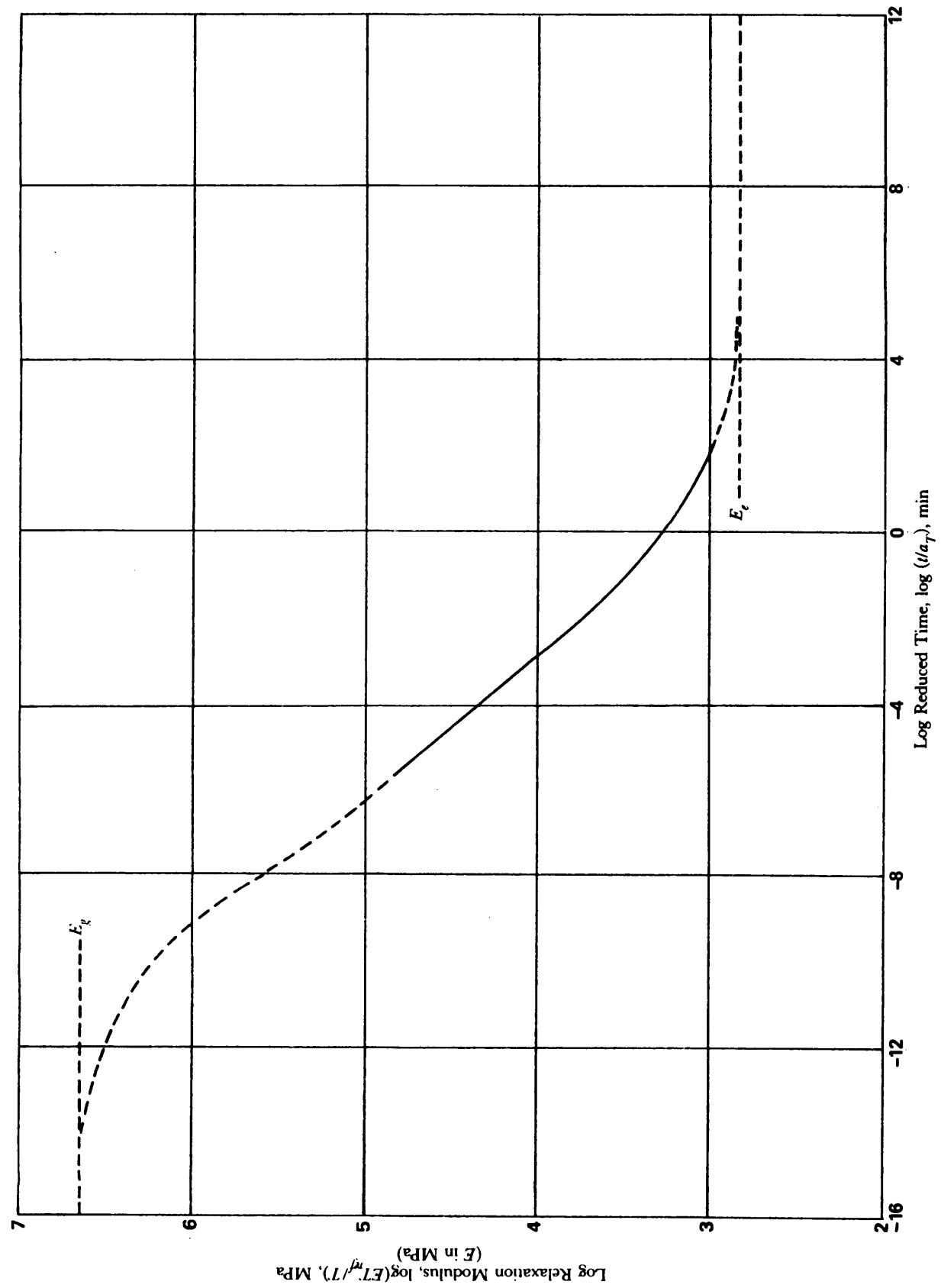
Figure 7-38. Relaxation Modulus Spectrum for a Typical Double-Base Propellant

The shift factor is described in Ref. 29. In general, the shift factor was conceived to adjust test data from uniaxial tensile test specimens so that measurements of the time- and temperature-dependent modulus conducted at various temperatures and rates could be superposed into a "master" relaxation modulus curve as shown in Fig. 7-38.

By use of the predetermined load action time t, in minutes, the parameter called reduced time $\log(t/a_T)$ is determined. A graph, such as Fig. 7-38, for the particular propellant is entered at this value of the abscissa and the value of $\log(ET_{ref}/'T)$ is determined from the ordinate, and thus the effective modulus E is determined. Poisson's ratio is then computed by using Eq. 7-63 with the known or assumed bulk modulus. The analysis then proceeds by treating the propellant as being isotropic and elastic.

There are several criteria for the prediction of structural failure of solid propellants. Some are based on stress (cumulative damage), others are based on strain and ultimate strain at a given strain rate, and still others are based on the combination of stress and strain.

In general, when displacements in a grain are limited by the displacements of the case, the propellant is strain critical. Grain displacements that are limited by its stiffness are generally stress critical. Cyclic loading generally is treated as stress critical, and the cumulative damage theory is commonly used. The primary disadvantage, because of the difficulty in determining the correct modulus, of the stress criterion is in computing the true stress.

Strain endurance is the limit of prolonged strain of the propellant and is determined from tensile tests of specimens over a two-week period. These tests generally involve several standard uniaxial tensile test specimens. Strain endurance of biaxial test specimens generally indicates insensitivity to biaxial stresses. However, exceptions to this must not be overlooked.

A complete assessment of the propellant grain should be conducted with the aid of the stress analysis group. In particular, a structurally adequate grain design cannot be achieved without consideration of bond stresses, fracture, and the viscoelastic characteristics of the propellant (Ref. 30). The paragraphs that follow discuss a few topics that may be useful to the beginning designer.

Propellants are usually cured at elevated temperatures (335 to 34.5 K). During cure, the polymerization process generally is accompanied by a volume shrinkage that is proportional to the binder volume present. Because of this shrinkage, the stress/strain free temperature generally would be higher than the cure temperature. The typical range for volumetric shrinkage is given in Table 7-12.

High humidity generally degrades the mechanical and chemical proper-ties of most solid propellants. The effect of humidity, however, has been observed to be reversible to some extent.

Aging during long-term storage also affects the mechanical and {heroical properties of most propellants. High temperature, as a rule, accelerates aging. Unlike the effects of humidity, aging is generally irreversible.

7-4.2.5 Safety Factors

Safety factors FS are applied to account for unforeseen variations in loads and in stress-producing environments. Safety factors may be applied to either the stresses induced by the limit loads or they may be

**TABLE 7-12. SELECTED THERMAL AND PHYSICAL PROPERTIES
OF TYPICAL PROPELLANTS**

Property	Typical Range
Mass density	$1.716—1.772 \times 10^3$ kg/m^3
Linear coefficient of expansion	$2.22—5.58 \times 10^{-5}$ m/m·K
Volumetric shrinkage during cure	$0.002—0.006$ m^3/m^3
Thermal conductivity	$15.32—18.16$ W/m·K
Specific heat	$1.046—1.340$ kJ/kg·K

applied to the limit loads initially in the performance of linear analysis. Stability or nonlinear analyses require that stress and strain be computed for the design loads. Design loads are the limit load multiplied by FS.

FS requirements in the structural design of rockets depend upon the projected use of the rocket. For example, higher safety factors usually are applied when crew safety is a consideration. Some typical FS values are given in Table 7-13.

TABLE 7-13. SAFETY FACTORS FOR ROCKET COMPONENTS

Component	Factor of Safety	
	Ultimate	Yield
Pressure Vessel:		
Motor Operation	1.40	1.10
All Other Loads	1.25	1.00
Propellant Grain:		
Storage	1.50	N/A*
Motor Operation	1.25	N/A
All Other Loads	1.25	N/A
All Other Components	1.25	1.00

*N/A = not applicable

An additional safety factor is generally used at connections because of local stress concentrations and structural (manufacturing) variations. This "fitting" factor is usually specified as 1.15 for rocket applicationss

The margin of safety MS is defined as the ratio of allowable stress σ_{allow} to the design stress σ_{des} and is expressed as

$$MS = \frac{\sigma_{allow}}{\sigma_{des}} - 1, \text{ dimensionless} \tag{7-65}$$

where

σ_{allow} = allowable stress representing ultimate or yield stress of material, including effects of temperature. It may also represent the limiting stress in compression (buckling), Pa

σ_{des} = calculated stress at design loads, Pa. (Design loads are the limit (maximum expected) load multiplied by the appropriate safety factors.)

Margins of safety $(MS)_y$ and $(MS)_u$ usually are calculated for both the yield and ultimate strengths, respectively, as follows:

$$(MS)_y = \frac{\sigma_{allow, y}}{\sigma(FS)_y} - 1, \text{ dimensionless,} \tag{7-66}$$

$$(MS)_u = \frac{\sigma_{allow, u}}{\sigma(FS)_u} - 1, \text{ dimensionless,} \tag{7-67}$$

where

$(MS)_y$ = margin of safety based on yield stress criterion, dimensionless

$(MS)_u$ = margin of safety based on ultimate stress criterion, dimensionless

$\sigma_{allow,u}$ = ultimate allowable stress, Pa

$\sigma_{allow,y}$ = yield allowable stress, Pa

σ = stress at limit load, Pa

$(FS)_y$ = factor of safety based on yield stress criterion, dimensionless

$(FS)_u$ = factor of safety based on ultimate stress criterion, dimensionless.

7-4.2.6 Mass and Size Estimating Relationships

Mass and size estimating relationships are used in preliminary design to provide estimates of the parameters needed in the analysis of rocket performance, aerodynamic characteristics, and accuracy. The mass of the rocket is divided into the components described in Chapter 3—namely, payload mass m_{pld} and motor mass of the rocket, which is composed of inert mass of the motor m_I and propellant mass m_p of the motor. Certain combinations of these parameters are used in Chapter 3 in the discussion on performance, namely,

$$m_{bo} = m_0 - m_p = m_{pld} + m_I, \text{ kg} \tag{7-68}$$

$$PMF = \frac{m_p}{m_I + m_p}, \text{ dimensionless} \tag{7-69}$$

$$I_{sp} = \frac{F_t t_b}{m_p}, \text{ N·s/kg} \tag{7-70}$$

where

m_0 = rocket gross mass at ignition, kg

m_{bo} = burnout mass of the rocket, kg

m_p = propellant mass, kg

PMF = propellant mass fraction of the rocket, dimensionless

I_{sp} = specific impulse, N·s/kg

F_T = motor thrust, N

t_b = motor burn time, s.

Propellant mass m_p is determined from the performance analysis given in Chapter 3. The paragraphs that follow discuss the mass and size relationships and system considerations for the inert rocket components and payload.

Data from the example problem of Chapter 3 will be used in the discussion to illustrate further sizing relationships. From Chapter 3, a 400-kg payload is to be delivered 30 km by indirect fire. The assumed payload shape is a tangent ogive ($\ell_N/d = 3$) with a cylindrical extension, if required. The assumed payload density is 2768 kg/m^3.

7-4.2.6.1 Payload

The payload of a rocket is the useful load carried by the rocket and consists of the warhead or an instrument package. Performance analyses presented in Chapter 3 consider the payload as the total mass of the rocket forward of the motor. Thus the payload includes the payload fairing, motor attachment structure, warhead safe/arming devices, and warhead.

Warhead effectiveness analyses are divided into separate parts of target kill probability given a hit $P_K/_H$ and target hit probability PH. The overall kill probability P_K for a given mission is a function of these two parameters, i.e.,

$$P_K = f(P_{K/H}, P_H), \text{dimensionless.} \tag{7-71}$$

$P_{K,H}$ includes such factors as warhead impact velocity, impact angles, fragment masses, and fragment distribution. P_H considers the approach angle of the warhead, miss distance, and overall rocket accuracy as discussed in Chapter 4. The source of $\mathbf{P_{K/H}}$ **is** based on vulnerability knowledge of a given target or target componets to a given warhead type. $P_{K/H}$ data are determined from experiments and are available in the Joint Munitions Effectiveness Manual (JMEM) (Ref. 11). Typical JMEM kill probability data for a certain shaped-charge warhead are presented in Fig. 7-39. These types of data are used to determine the required payload diameter. An additional method to size the payload is based on the average warhead density. Thus, if the payload mass is given, estimates of the payload volume can be determined from mass divided by density.

For the example considered in Chapter 3, the payload volume is assumed to be

$$\text{payload volume} = \frac{400 \text{ kg}}{2768 \text{ kg/m}^3} = 0.1445 \text{ m}^3.$$
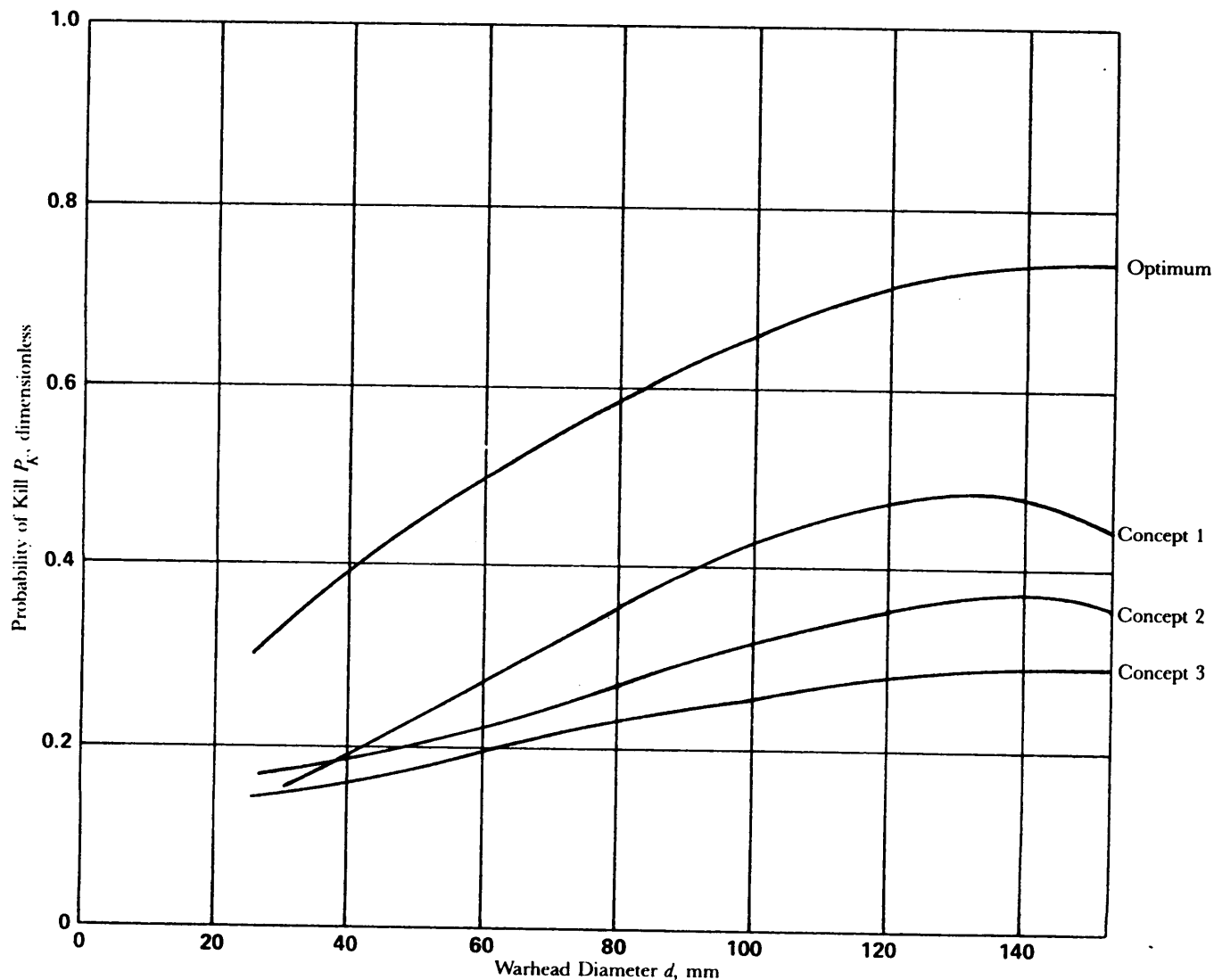
Figure 7-39. Probability of Kill vs Warhead Diameter

7-4.2.6.2 Propellant Mass Estimation

The propellant mass required to provide some specified performance parameter, e.g., total impulse or burnout velocity, is determined through the analyses described in Chapters 3 and 6.

7-4.2.6.3 Motor Sizing

The example that follows shows how preliminary rocket diameter and length estimates may be made, using payload mass m_{pld} and propellant mass m_p estimates from Chapter 3, based on parametric. relationships and representative experience.

The major components of the rocket motor are propellant, binder and insulation, cylindrical fast, forward closure, aft closure, and nozzle. Fins are considered part of the inert mass of the motor for performance considerations. In Chapter 3, relationships are presented for estimating the propellant mass that requires estimates of the mass fraction of the rocket motor propellant PMF. It is noted in Eq. 7-69 that PMF depends on the propellant mass m_p; thus estimates of PMF and m_p have to be determined by an iteration process involving the size of the motor.

The size of the rocket motor case can be estimated for various motor lengths and diameters by using a dimensionless average propellant volumetric loading efficiency V_{LE} that depends on the propellant grain burning surface area and port area. Fig. 7-40 presents an interesting comparison of typical rocket initial
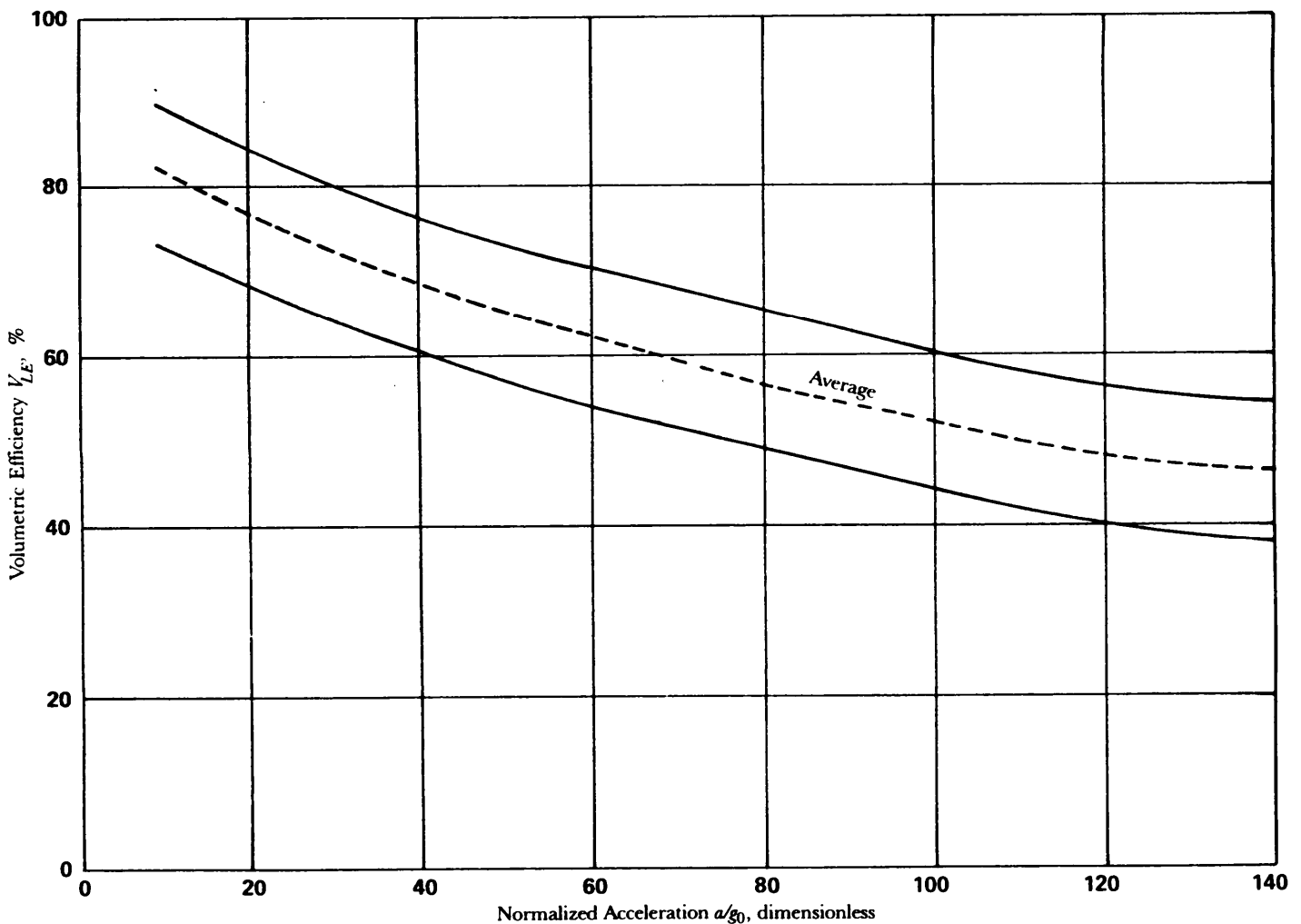
Figure 7-40. Propellant Volumetric Loading Efficiency

accelerations as a function of V_{LE}. Average values of V_{LE} are noted by the dashed line; older motors, by the lower solid line; and newer motor concepts, by the higher solid line.

Eq. 7-72 shows the relationship among propellant mass m_p, motor case length ℓ, rocket diameter d, average propellant density p_p, and V_{LE}. The diameter d_{mc} of the motor case can be estimated by

$$d_{mc} \approx \left[\frac{4m_p}{(\ell/d)_{mc}\pi \rho_p V_{LE}} \right]^{1/3}, \text{ m.} \qquad (7\text{-}72)$$

In Eq. 7-72, V_{LE} is expressed as a decimal, and $(\ell/d)_{mc}$ is referred to as the fineness ratio of the motor case.

Fig. 7-41 is a nomogragh calculated from the relationships defined by Eq. 7-72 and is typical of nomography that could be made for the range of values of interest in a particular design. The figure was developed with a V_{LE} of 60% and a p_p of 1720 kg/m³.

Example 3-1, Chapter 3, initially showed that a propellant mass of 110.9 kg would be required to deliver the 400-kg payload a distance of 30 km in a vacuum. Fig. 7-41 indicates that a propellant mass $m_p = 110.9$ kg would require a 0.2032-m diameter case for a motor case ℓ/d of 17; a 0.3048-m diameter case would require a motor case ℓ/d of 5; and a 0.4064-m diameter case would require a motor case ℓ/d of 2. By combining these motor sizes with the payload volume requirement of 0.1445 m³, the ℓ/d requirements of the payload size given in Table 7-14 result in the three rocket configurations shown in Fig. 7-42: Use the 0.2032-m diameter rocket as an example for a fineness ratio $\ell_N/d = 3$ and a tangent ogive. The volume of the tangent ogive is determined from Fig. 7-3 by reading "nose vol $\div$ d³ = 1.263". The nose volume V_{nose} can then be determined by

$$V_{nose} = 1.263(0.2032)^3 = 0.0106 \text{ m}^3.$$

Then the required volume V_{cyl} of the cylindrical segment of the payload can be determined by

$$V_{cyl} = V_{req} - V_{nose} = 0.1445 - 0.0106 = 0.1339 \text{ m}^3.$$

Cylindrical length ℓ_{cyl} can be calculated by

$$\ell_{cyl} = \frac{4V_{cyl}}{\pi d^2} = \frac{4(0.1339)}{3.1416 (0.2032)^2} = 4.129 \text{ m.}$$

Since the example is for a d = 0.2032 m and a given $\ell_N/d = 3$, $\ell_N = 3(0.2032) = 0.61$ m. The total payload length is equal to the length of the ogive plus the length of the cylinder, i.e., 0.61 + 4.129 = 4.739 m. Therefore, the overall payload ℓ/d for this example is 4.739/0.2032 = 23.3. The ℓ/d for the rocket is approximately 40 (see Fig. 7-42)—the case $\ell/d = 17$ plus the payload $\ell/d = 23.3$.

The overall results of the three rocket configurations are shown in Fig. 7-42. It is evident that the 0.2032-m diameter rocket is very long, and the 0.4064-m diameter rocket is very short. The smaller diameter rocket would have less drag losses but could have bending problems and other undesirable characteristics (see par. 5-3.1.6). The short rocket would have almost 80'% more drag than the 0.3048-m diameter rocket since the drag increases as the diameter squared. The 0.3048-m diameter rocket offers a reasonable ℓ/d. The 0.3048-m diameter rocket is selected to continue this illustrative example and for further use in the example problem of Chapter 3. As shown in Chapter 3, the propellant mass increased to 182.7 kg after the drag losses were considered. This resulted in an increase in motor ℓ/d from 5 to 8, the diameter being held constant at 0.3048 m. This increase in length is also shown in Fig. 7-42.

7-4.2.6.4 Motor Inert Masses

The inert masses of the rocket motor are estimated by using the rocket motor preliminary sizing data and the operating characteristics of the rocket motor. The estimating relationships are developed for the

MIL-HDBK-762(MI)
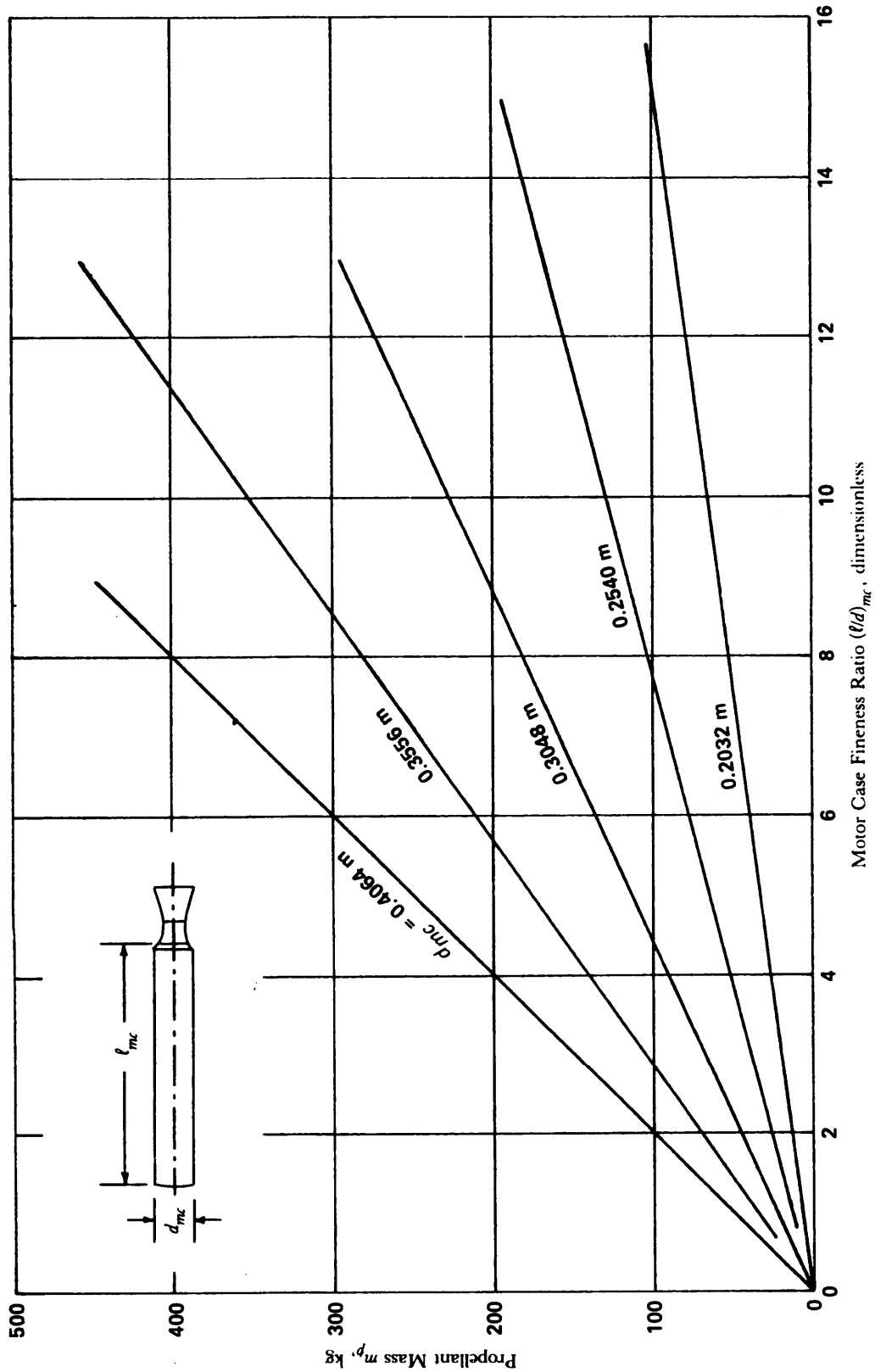
Figure 7-41. Propellant Mass vs Motor Case Fineness Ratio

TABLE 7-14. SAMPLE PROBLEM PAYLOAD VOLUME SUMMARY

Rocket Diameter, m	Tangent Ogive Volume, m³ l_N $d = 3$ (Fig. 7-3)	Req'd Cylindrical Volume, m³ (0.1445 m³ req'd ogive volume)	Cylindrical Length Req'd, m	Payload Length Req'd, m	Payload l d, dimensionless
0.2032	0.0106	0.1339	4.129	4.739	23.3
0.3048	0.0357	0.1088	1.491	2.405	7.9
0.4064	0.0848	0.0597	0.460	1.679	4.1
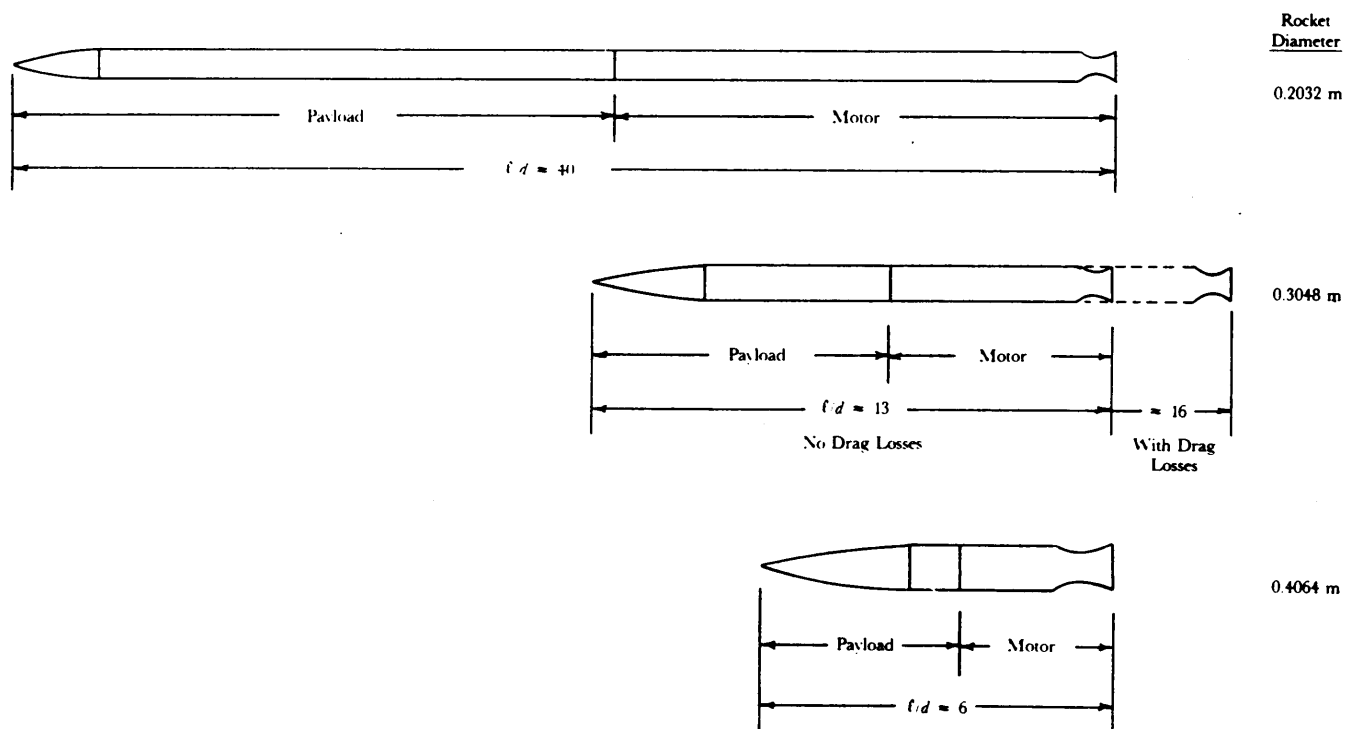
Figure 7-42. Rocket Sizing Trade-Off Summary

cylindrical portion of teh case by using the operating pressure of the motor and material characteristics of the motor case. Masses of other portions of the motor are evaluated as a percentage of the case mass. Motor case wall thickness t_{mc} is calculated by using the case wall hoop stress equation. Eq. 7-38.

If $(FS)_u (FS)_y$ is greater than $\acute{o}_u$, $\acute{o}_y$, then the case is sized by the ultimate criterion: otherwise it is sized by the yield criterion. For a design governed by the ultimate criterion, case thickness t_{mc}. **is** determined by

$$t_{mc} = \frac{P_{MEOP} (FS)_u r_{mc}}{\sigma_u (WE)} , \text{ m} \tag{7-73}$$

where

r_{mc} = motor case mean radius, m

P_{MEOP} = maximum expected operating pressure, Pa

$(FS)_u$ = safety factor based on ultimate stress criterion, dimensionless

WE = weld efficiency, dimensionless.

The mass m_{mc} of the cylindrical portion of the case is thus

$$m_{mc} = \pi \rho_{mc} d_{mc} \ell_{mc} t_{mc}, \text{ kg}$$ (7-74)

where

m_{mc} = mass of cylindrical section of motor case, kg
ℓ_{mc} = length of cylindrical section of motor case, m
ρ_{mc} = density of motor case material, kg m^3.

The forward closure mass m_{fc} is approximated by using the following equation:

$$m_{fc} = (FCMF)m_{mc}, \text{ kg}$$ (7-75)

where

FCMF = forward closure mass factor, dimensionless.

The FCMF varies from 0.41 for conventional metal cases to approximately 0.2 for filament-wound and paper phenolic cases.

The aft closure and nozzle mass factor ACMF varies from 0.75 to 1.0 depending on the design, with the lower value associated with more modern nozzle concepts that employ low-density materials for structural support. The aft closure and nozzle design mass m_{ac+n} is found from

$$m_{ac+n} = (ACMF)m_{mc}, \text{ kg}.$$ (7-76)

The propellant binder and insulation mass m_{in+b} is approximately 15% of the case mass, i.e.,

$$m_{in+b} \approx 0.15 m_{mc}, \text{ kg}.$$ (7-77)

The igniter and other hardware mass m_{other}, associated with the motor is approximately 20% of the case mass, i.e.,

$$m_{other} \approx 0.20 m_{mc}, \text{ kg}.$$ (7-78)

The total inert motor mass m_I is then

$$m_I = m_c + m_{fc} + m_{ac+n} + m_{in+b} + m_{other}, \text{ kg}.$$ (7-79)

The mass of fins and attachment hardware can be estimated from mass-per-unit-area considerations. For fixed fins with a fin aspect ratio less than 1.0, the mass unit area $(m\ A)_{fixed\ fin}$

$$\left(\frac{m}{A}\right)_{fixed\ fin} \approx \frac{q_{max}}{250g_0}, \text{ kg m}^2$$ (7-80)

where

q_{max} = maximum dynamic pressure, Pa.

A hinged fin will have a higher mass unit area $(m\ A)_{hinged\ fin}$

$$\left(\frac{m}{A}\right)_{hinged\ fin} \approx \frac{q_{max}}{100g_0}, \text{kg/m}^2. \tag{7-81}$$

The total fin mass m_{fins} is, therefore,

$$m_{fins} \approx [(m/A)_{one\ fin}\ A_{one\ fin}]\ (\text{number of fins}), \text{kg}. \tag{7-82}$$

The motor PMF is then

$$PMF = \frac{m_p}{m_{mc} + m_{fins} + m_p}, \text{dimensionless}. \tag{7-83}$$

7-4.2.6.5 System Considerations

Operational requirements should be considered in the mass and sizing analysis. Operational requirements may impose constraints on the mass, length, and diameter of a rocket. The constraints may be due to existing transport vehicle carry weight, launch vehicle carry weight, standard military container length, etc. An additional consideration that increases the complexity of the sizing and mass-estimating relations is the influence of production costs on the propulsion system. A lower cost propulsion system generally results in a decrease in system performance which can increase the size and mass of the system to the level where an impact on the payload warhead mass occurs. Complex system level mass-and sizing-estimating relationships for a particular rocket system are generally developed during the design process to allow parametric trade-offs to be made. Rocket system sizing studies involving the propulsion system performance, cost, accuracy, weapons effectiveness, and impact of operational constraints are contained in Ref. 31.

7-4.3 STRUCTURAL MODELING FOR SYSTEM ANALYSIS

7-4.3.1 Load Representation

Rocket structures experience both local and distributed loads which may be long duration, short duration, or time varying.

Long-duration loads, which are applied slowly, can be treated as static loads. Response to these loads can be addressed by developing shear, bending, and axial load diagrams as indicated in pars. 7-4.2.2.4 through 7-4.2.2.6.

Short-duration loads that are suddenly applied can be treated as shock loads. The evaluation of shock loads requires that the dynamic characteristics of the rocket be known. Dynamic amplification factors can then be determined, and an equivalent static load analysis can be performed to determine the internal loads in the rocket.

Dynamic response to periodic loads can be estimated by use of a magnification factor. The magnification factor is applied to the load and treated as an equivalent static loading. Loads that vary randomly (stochastic), except for the very simplest form, generally are best represented by numerical analysis. Representation of the dynamic load would then depend on the analysis type and structural model.

7-4.3.2 Structural Models

7-4.3.2.1 Lumped Parameter Models

The description of dynamic properties of any system must include a discussion of the concept of degrees of freedom (DOF). In general, a body will have six DOF, i.e., three translational and three rotational. A continuous elastic body requires three DOF for each point and, therefore, has an infinite number of DOF.

An alternative is to represent the continuous system by a discrete model consisting of a finite number of "lumped" masses and hence by a finite number of degrees of freedom as indicated in Fig. 7-43. Numerical analysis methods can then be applied to determine the dynamic properties of the discrete system. Sufficient accuracy generally is achieved for rockets that are simulated in this manner.

Initial estimates of the dynamic characteristics of the rocket may be estimated by the use of only a few lumped masses. A rocket maybe represented by as few as a single lumped mass located at the rocket CG and supported appropriately at one or both ends.
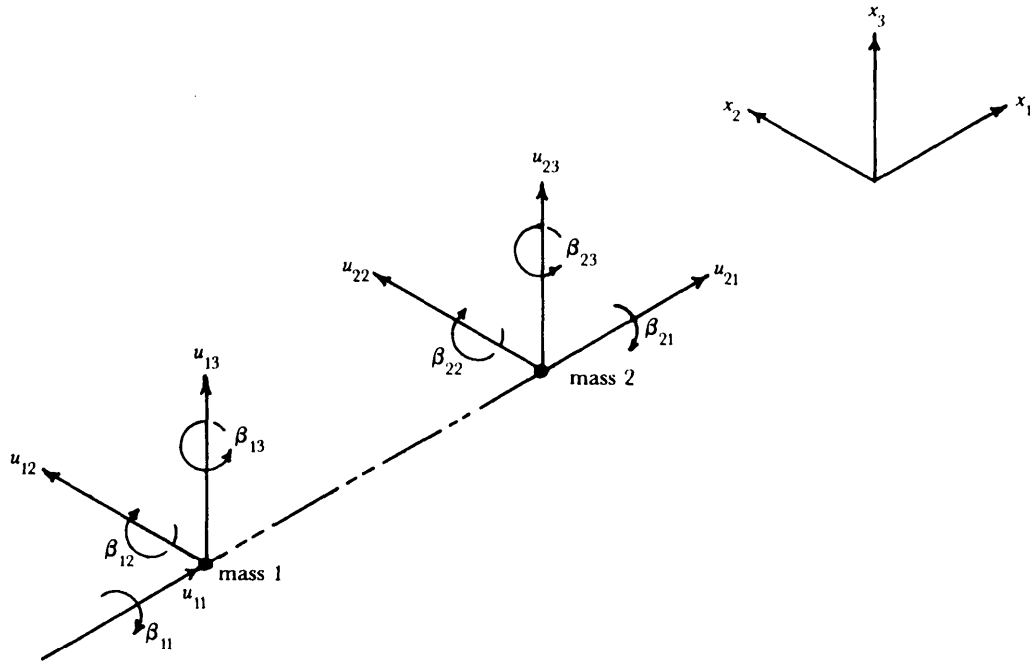
Figure 7-43. Degrees of Freedom in Local Coordinate System

A popular method of analyzing beam-type structures by the lumped mass method is discussed in Ref. 32. The method is an extension of Rayleigh's method of beam vibration and is based on approximating the dynamic deflection curve by the static deflection curve.

If the rocket is represented by a series of lumped masses m_1, m_2, m_3, . . . , and the static unit load mass deflections are y_1, y_2, y_3, . . . , then the fundamental frequency w_n can be expressed as

$$\omega_n = \sqrt{\dfrac{g_0 \sum\limits_{i=1}^{n} m_i y_i}{\sum\limits_{i=1}^{n} m_i y_i^2}}, \text{rad/s} \tag{7-84}$$

where

ω_n = fundamental undamped natural frequency, rad/s

m_i = mass at station i, kg

y_i = displacement at station i due to a unit force, m/N.

The fundamental lateral mode frequency for the two-mass model, shown in Fig. 7-44, is determined to illustrate the procedure. Fig. 7-45 depicts a simply supported beam loaded by a unit load.

The displacement of a beam at point i due to a load at point j can be found by various methods. Some common techniques are the moment-area method, dummy load method, etc. For illustrative purposes,
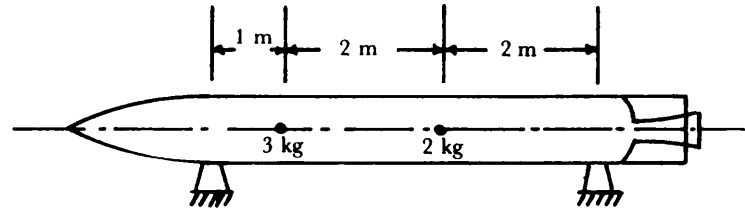
Figure 7-44. Two-Mass Rocket Model
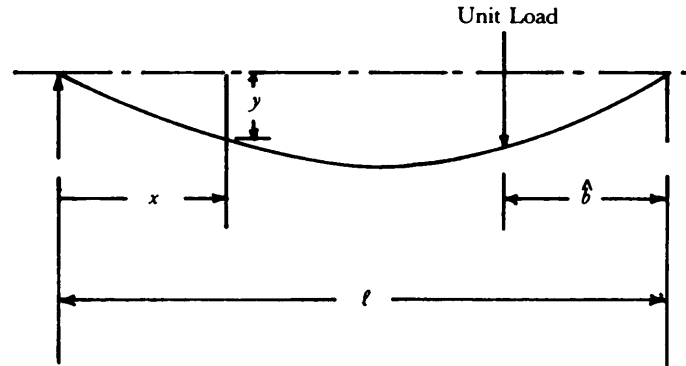
Figure 7-45. Beam Displacement Model

equations developed for continuous uniform beams are used. A beam, shown in Fig. 7-45, displaced a distance y at any point x due to a concentrated unit load applied a distance b from the end can be determined from

$$y_x = \frac{\hat{b}x}{(6EI)\ell}(\ell^2 - x^2 - \hat{b}^2), \text{ m/N, for } x \leq \hat{a} \tag{7-85}$$

$$y_x = \frac{\hat{b}}{(6EI)\ell}\left[\frac{\ell}{\hat{b}}(x-\hat{a})^3 + (\ell^2 - \hat{b}^2)x - x^3\right], \text{ m/N, for } x > \hat{a} \tag{7-86}$$

where
$\hat{a} = \ell - \hat{b}$, m
EI = bending stiffness, i.e., elastic modulus E multiplied by area moment of inertia I about neutral axis, N·m^2
y_x = beam displacement at station x, m/N
ℓ = beam length, m.

The displacement y may also be defined as follows:
  y_{ij} = displacement at mass point i due to a unit load at mass point j, m/N.
   Example 7-4 illustrates this application of the theory and notation described in this subparagraph.

EXAMPLE 7-4:
   Determine the fundamental lateral mode frequency for the two-mass model shown in Fig. 7-44—a simply supported rocket loaded only by its own mass.

The displacement components (see Fig. 7-4)—applying Eq. 7-84 and the definition of y_{ij}—become
For y_{11}: $b = 4, \ell = 5, x = 1$:

$$y_{11} = \frac{4(1)}{(6EI)5} (5^2 - 1^2 - 4^2) = \frac{1.0667}{EI}, \text{ m/N.}$$

For y_{12}: $\hat{b} = 2, \ell = 5, x = 1$:

$$y_{12} = \frac{2(1)}{(6EI)5} (5^2 - 1^2 - 2^2) = \frac{1.3333}{EI}, \text{ m/N.}$$

For y_{21}: $\hat{b} = 1, \ell = 5, x = 2$:

$$y_{21} = \frac{1(2)}{(6EI)5} (5^2 - 2^2 - 1^2) = \frac{1.3333}{EI}, \text{ m/N.}$$

The result $y_{21} = y_{12}$ illustrates the reciprocal theorem of Maxwell.
For y_{22}: $\hat{b} = 3, \ell = 5, x = 2$:

$$y_{22} = \frac{3(2)}{(6EI)5} (5^2 - 2^2 - 3^2) = \frac{2.40}{EI}, \text{ m/N.}$$

The displacements y_1 and y_2 at the mass points can then be computed by

$$y_1 = g_0(m_1 y_{11} + m_2 y_{12}) = \frac{g_0}{EI}[3(1.0667) + 2(1.3333)] = 5.8667 \frac{g_0}{EI}, \text{ m}$$

$$y_2 = g_0(m_1 y_{21} + m_2 y_{22}) = \frac{g_0}{EI} [3(1.3333) + 2(2.4)] = 8.7999 \frac{g_0}{EI}, \text{ m.}$$

From Eq. 7-84 the fundamental natural frequency w_n for the two-mass rocket model where EI $= 2.16 \times 10^5$ N Ž m² is

$$\omega_n = \sqrt{\frac{g_0(m_1 y_1 + m_2 y_2)}{m_1 y_1^2 + m_2 y_2^2}}, \text{ rad/s}$$

$$\omega_n = \sqrt{\frac{3(5.8667) + 2(8.7999) (2.16 \times 10^5)}{3(5.8667)^2 + 2(8.7999)^2}}, \text{ rad/s}$$

$$\omega_n = 172 \text{ rad/s.}$$

It is generally useful to estimate the natural frequency of the rocket by use of equations developed for uniform beams. Natural frequencies w_n of beams with various support conditions can be estimated by (see Ref. 33)

$$\omega_n = 2\pi\widetilde{\Omega} \sqrt{\frac{EI}{m\ell^3}}, \text{ rad/s} \tag{7-87}$$

where
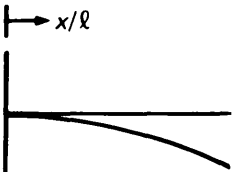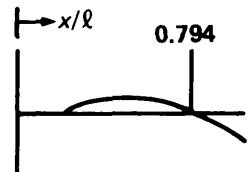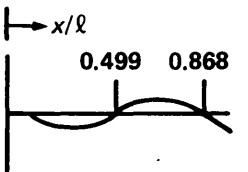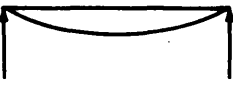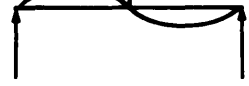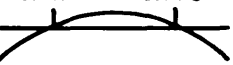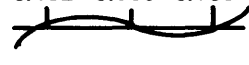
$\widetilde{\Omega}$ = constant from Table 7-15, dimensionless

EI = bending stiffness, i.e., elastic modulus E multiplied by beam area moment of inertia I about neutral axis, N·m^2

m = total mass, kg

ℓ = total length, m.

TABLE 7-15. FREQUENCY CONSTANTS AND NODE LOCATIONS OF UNIFORM BEAMS

Type of Supports	1st Mode	2nd Mode	3rd Mode
Cantilevered	$\widetilde{\Omega}$ = 0.560	0.794 $\widetilde{\Omega}$ = 3.51	0.499 0.868 $\widetilde{\Omega}$ = 9.82
Simply Supported at Ends	$\widetilde{\Omega}$ = 1.57	0.500 $\widetilde{\Omega}$ = 6.28	0.333 0.667 $\widetilde{\Omega}$ = 14.1
Free—Free	0.224 0.776 $\widetilde{\Omega}$ = 3.56	0.132 0.500 0.868 $\widetilde{\Omega}$ = 9.82	0.094 0.906 0.356 0.644 $\widetilde{\Omega}$ = 19.2

Assumptions: (1) $\partial m / \partial(x/\ell)$ = constant

(2) $\partial EI / \partial(x/\ell)$ = constant

The fundamental frequency of the two-mass rocket model shown in Fig. 7-44 can be approximated by assuming the following values for the indicated parameters:

$m = 3 + 2 = 5$ kg

$\ell = 5$ m

$EI = 2.16 \times 10^5$ N·m^2

$\widetilde{\Omega} = 1.57$ from Table 7-15 for a simply supported beam.

The frequency for the simply supported beam is by Eq. 7-87

$$\omega_n = 2\pi(1.57)\sqrt{\frac{2.16 \times 10^5}{5(5)^3}} = 183 \text{ rad/s}$$

which compares favorably with the 172 rad/s computed using the lumped mass procedure. A more detailed lumped mass model would have resulted in even closer agreement.

The effect of simulating distributed mass by a concentrated mass is discussed in Ref. 34. In general, distributed mass can be approximated at the CG of segments during the initial design stage. The significance of distributed mass effects can be reduced by increasing the number of mass points.

7-4.3.2.2 Finite Element Models

Theee are several general-purpse finite element (FE) computer programs suitable for the structural analysis of rocket components. A discussion of several programs may be found in Ref. 35. The analyst should investigate these and other available programs and select that program which is most suitable for each application.

Several of these programs are applicable for static as well as dynamic load analysis. It is generally more efficient to use a program based on shell elements in analyzing a shell structure. Complex geometrics requiring three-dimensional models can be very time-consuming and costly to execute. Simplifying assumptions to reduce the complexity of a model should be made whenever possible. Partitioning the structure into substructures generally reduces the computational effort.

Finite element methods are especially suitable for rocket geometries because of their generally axisymmetric configurations. Two-dimensional plane strain (stress) analysis models may be applicable to certain nonaxisymmetric cross sections.

The most important step in finite element analysis is the formulation of the actual continuous structure into a mathematically equivalent discrete-element model. Models used for stress analyses are usually not suitable for dynamic analysis because of the large number of DOF (unknowns) necessary to determine the peak (generally critical) stress of the structure. Dynamic analysis deals generally with the overall behavior and requires less definition of local effects and, therefore, requires fewer DOF. Furthermore, the determination of eigenvalues (natural frequencies) is generally a more complex procedure than that required to determine displacements (unknowns in a stress problem) in a stiffness formulation. Hence, it is generally not cost-effective to use the same geometric model for both analysis types.

Considerations of material and geometric nonlinearities generally pose a significant challenge to the structural analyst. The cost of executing a nonlinear analysis may be ten or more times that of a linear analysis of the same model. An experienced analyst should be consulted to effect a solution in all but the simplest geometry.

A typical FE analysis requires that the analyst proceed in the following general manner:

    1. Define the problem:
        a. Geometry
        b. Loads, load factor
        c. Dynamic analysis
        d. Static analysis
        e. Stability analysis
        f. Temperature
        g. Materials
        h. Support boundary conditions.
    2. Develop structural model:
        a. Determine element types
        b. Assemble elements.

3. Apply boundary conditions:
   a. Loads
   b. Supports.
4. Execute program:
   a. Static
   b. Dynamic
   c. Stability.
5. Process output:
   a. Tabulated
   b. Plots (stress and strain contours, displacements).
6. Assess output:
   a. Check convergence
   b. Check results with approximate solutions
   c. Determine margins of safety.
7. Report results.

Finite element programs are particularly useful for analyzing complex structures that are intractable by classical methods. A rocket nozzle, for example, maybe constructed of several interacting materials which result in a highly indeterminate structure. An FE model of such a nozzle is shown in Fig. 7-46.

The outlines of the materials before and after load application are shown in Fig. 7-47. Also shown in Fig. 7-47 are the applied boundary conditions that simulate the pressure variations—isentropic flow was
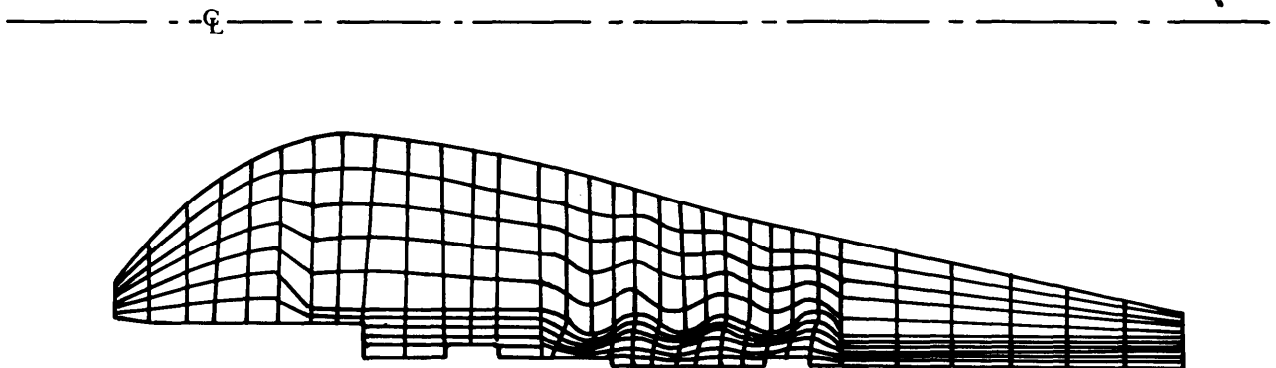
Figure 7-46. Finite Element Model of a Typical Nozzle
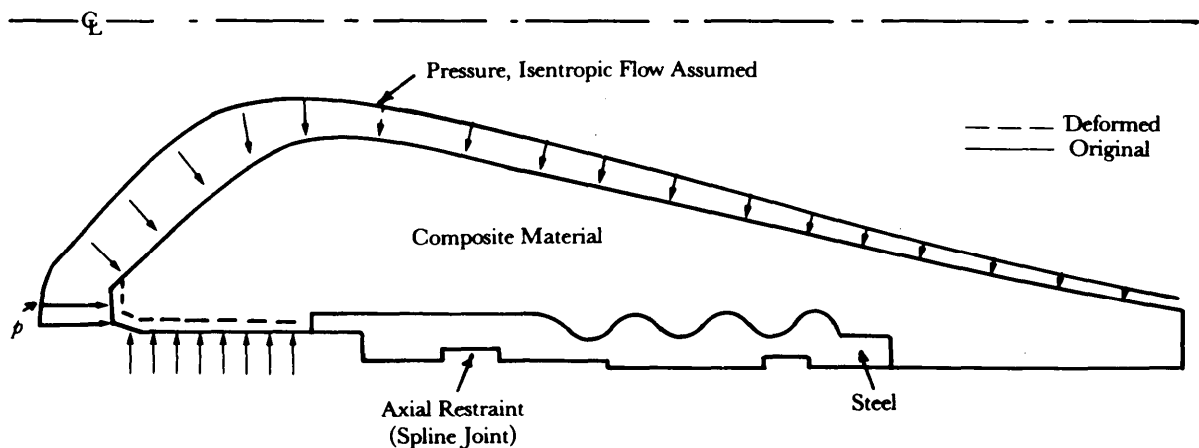
Figure 7-47. Magnified (50X) Deformed Outline

assumed-through the nozzle. A spline joint connecting the nozzle to the motor case was simulated by prescribing zero axial displacement at the splint groove. Radial interaction of the motor case with the nozzle was ignored in this example.

Most FE programs have extensive postprocessing capabilities. Plots of stress contours fall be particularly useful in optimization studies. For example, principal stress contours shown in Figs. 7-18 through 7-51 can be used to identify lightly stressed regions which may be relieved by slight geometric modifications. The critical stress indicated in Fig. 7-51 may be relieved by a simple relief groove.

FE analysis is also useful in the analysis of propellant grains because of the complex geometrics generally associated with case-bonded grains. Thermal stress, acceleration loading, and ignition conditions are simulated easily by programs used throughout the solid rocket industry.

7-5 DYNAMIC ANALYSIS

Static analysis assumes that the loaded structure is in static equilibrium. Dynamic analysis is concerned with structural response to transient or cyclic loads and is applicable to aeroelasticity and impact loads (shock).

A rocket is subjected to a variety of dynamic loads during its lifetime. It may experience periodic loads from motor operation, acoustic environments, and transportation. It may also experience shock loads as a result of the motor ignition transient and transportation handling. Dynamic loads may also be induced by spin.

Rockets propelled by solid propellant motors are generally sufficiently stiff so that linear analysis can be applied to the rocket body. However, body panels on the rocket and fins may respond nonlinearly.

Dynamic analyses may be performed using any of the several computer programs available. A discussion of these codes may be found in Ref. 35.

Dynamic response to cyclic loads can be approximated by the use of the magnification factor. The magnitude of magnification is dependent on the ratio w_e/w_n of the excitation frequently w_e to the natural frequency w_n of the rocket. It is also dependent on the structural damping ratio ζ.

The application of the magnification factor is as follows:

$$y_{dynamic} = y_{static} \left\{ \frac{1}{\left[1 - \left(\frac{\omega_e}{\omega_n}\right)^2\right]^2 + \left[2\zeta\left(\frac{\omega_e}{\omega_n}\right)\right]^2} \right\}, \text{m} \qquad \text{(7-88)}$$

where

$y_{dynamic}$ = peak deflection due to a periodic load, m

y_{static} = deflection of structure to static application of peak of period

ω_e = frequency of the excitation load, rad/s

ζ = structural damping ratio, dimensionless.

The term in brackets in Eq. 7-88 is called the magnification factor and is dimensionless.

Damping ratios for typical rockets range between 0.01 and 0.30, depending upon the method of construction, material properties, and other factors.

Dynamic amplification to a step excitation may be analyzed in a similar manner. The method and magnification factors for several step loadings are given in Ref. 36.

Dynamic amplification to a pulse input may also be analyzed in a similar manner. The effects of a rectangular, half-cycle sine, and versed sine-shaped pulses are also given in Ref. 36.

7-6 AEROELASTICITY

Aeroelasticity is the study of the interaction between aerodynamic forces and elastic deformation. A major problem in rocket design is the flutter of fin structure when small disturbances result in violent

MIL-HDBK-762(MI)
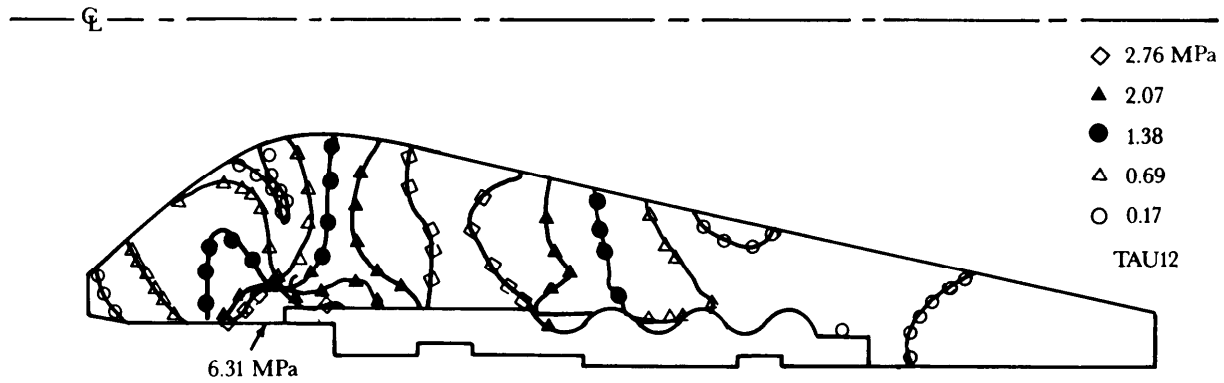
Figure 7-48. Maximum Shear Stress Contours

Figure 7-49. Hoop Stress Contours

Figure 7-50. Maximum Principal Stress Contours
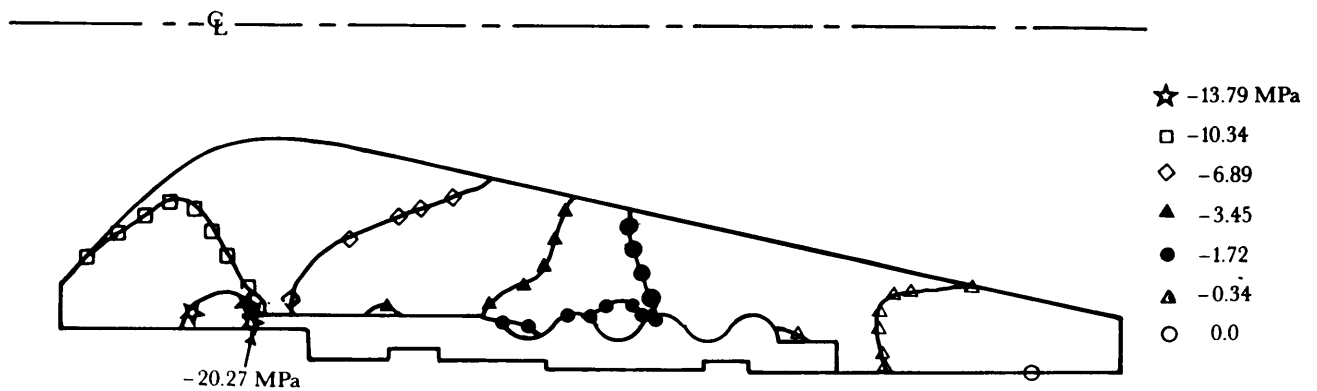
Figure 7-51. Minimum Principal Stress Contours

7-85

oscillations. Flutter is the unstable coupling of two or more structural vibration modes under the influence of aerodynamic exciting forces. There are two types of aeroelasticity instability—dynamic aerostatic instability considers (he interaction of aerodynamic, elastic, and inertia forces; and steady state or static instability considers the case of oscillation with zero frequency, generally neglecting inertial forces.
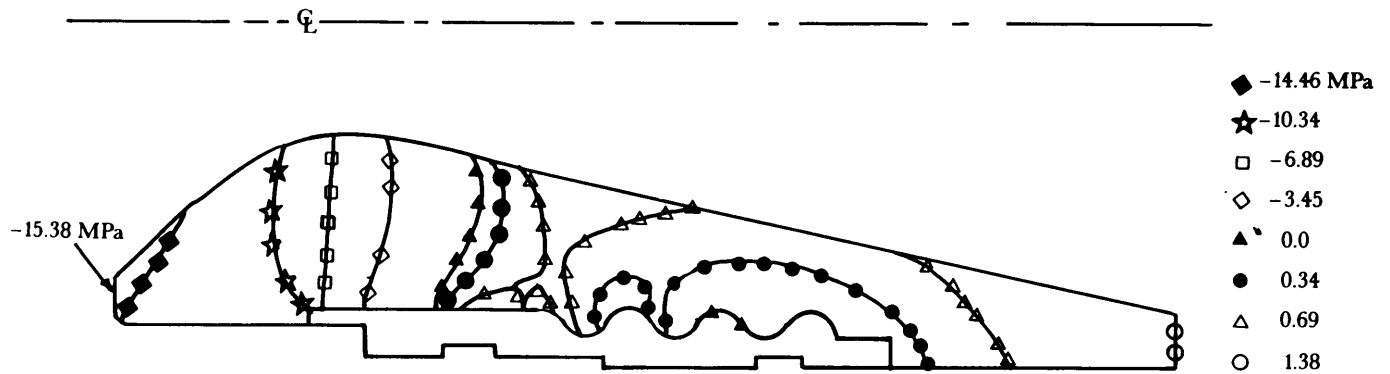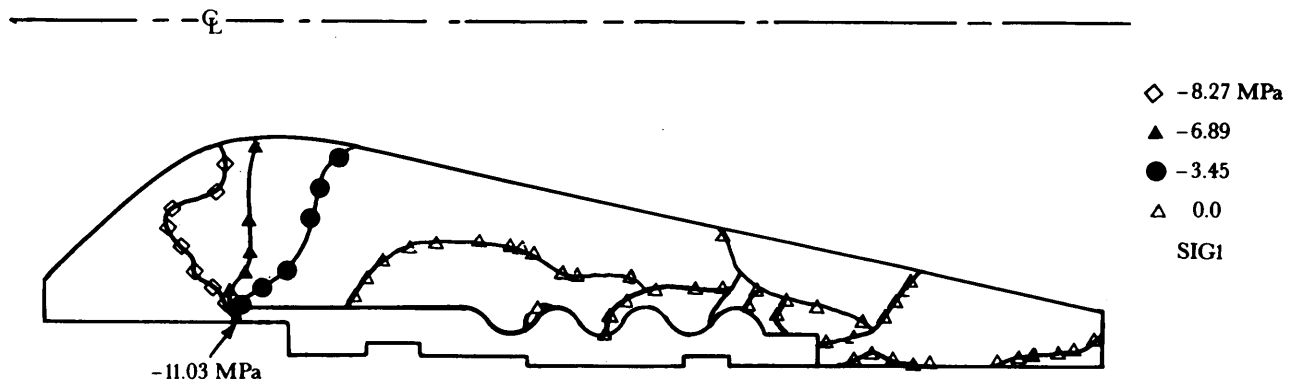
Since aeroelasticity is a rather extensive subject, it is recommended that the designer analyst refer to one of the many textbooks on the subject (Refs. 37 through 46).

Analysis of aeroelastic systems generally requires the use of computer programs. A summary of important features of a few aeroelastic analysis programs is given in Ref. 3.5.

7-7 HEAT TRANSFER

7-7.1 INTRODUCTION

This paragraph describes the roles of heat transfer analysis, particularly as they apply to design of thermal protection systems for free flight rockets. A thermal protection system is any system that results in holding a primary load-carrying structure within a specified temperature range in an environment that otherwise would cause a higher temperature.

Free flight rockets will typically employ a sacrificial (ablative) insulation as its thermal protection system because this approach is usually the most efficient means of protecting the structure. Although emphasis in this paragraph is clearly on thermal (and erosion) considerations in insulation design, the reader should not overlook the fact that rocket motor insulation selection (internal case and nozzle) will also depend on mechanical property, stress and strain, bonding, cost, availability, reliability, and manufacturing considerations which may ultimately have greater influence over the design than the "optimum thermal consideration".

Generally, heat transfer characteristics in a free flight rocket are similar to other tactical solid propellant rocket motors, but there are some design considerations that become more important in a free flight rocket. For example, a free flight rocket system should consist of a simple design conceived for low cost and high production. The rocket contains little (if any) critical on-board, temperature-limited instrumention. Frequently, heat transfer characteristics of the rocket motor plume will also be a significant design consideration for the launch 'eject system (tube) and for adjacent motors of a multiple launch capability free flight rocket system. Even though the selected design of a free flight rocket should be simplistic in order to achieve the necessary reliability and cost-effectiveness, this does not imply that proper attention should not be given to thermal considerations during the design phase.

Par. 7-7 first describes the role of heat transfer analysis in design of free flight rockets. Next, the physical situation and heating environment present in the motor are delineated. Mechanisms of thermal protection are then discussed, followed by thermal design considerations and constraints. The sequential approach taken in conducting heat transfer analysis is outlined, and typical free flight rocket insulation materials for the case and nozzle are described. Next, several analytical thermal analysis programs currently employed in thermal design of rocket motors are referenced, and the input parameters are delineated. Lastly, a sample thermal design problem involving aerodynamic heating of the motor case wall is presented.

7-7.2 THE ROLE OF HEAT TRANSFER ANALYSIS

A heat transfer analysis is not an end in itself; rather, it is a tool to use in determining the severity of a thermal environment and to aid in the design of thermal protection systems. In the analysis and design of a free flight rocket, heat-transfer-related considerations are employed to evaluate the following aspects of rocket motor design:

1. Insulation required on the interior of the combustion chamber (head end, (cylindrical section, and aft case)

2. Insulation required on the igniter

3. Insulation design of the nozzle (entrance, throat, and expansion section). For some designs, a combined thermal stress analysis is required

4. Significance of external (aerodynamic) heating to case wall and particularly to fins and protuberances

5. Effects of dump storage temperature cycling on rocket performance and aging

6. Effects of plume heating (radiation and flow impingement) on launcher and adjacent missiles

7. Influence of manufacturing defects and anomalies on motor performance and case integrity

8. Significance of thermal effects on static test and flight failures—if they occur

9. Magnitude of heat losses occurring in combustion chambers and nozzles. This is necessary to scale heavy wall test data and component test data to flight conditions.

7-7.3 PHYSICAL SITUATION

7-7.3.1 General

Although numerous scenarios must be considered to evaluate the various thermal design environments previously identified in the role of heat transfer analyses, Fig. 7-52 illustrates a typical in-flight design condition. In this figure the combined effects on motor case heating from internal and external (aerodynamic) heating are shown. Each effect is a very time-dependent function.

Miny areas of the motor case are protected from internal heating by the presence of propellant attached to the case wall for portions of the motor burn operation. During this interval, case wall heating results only from external sources. After the propellant has been consumed over parts of the case wall, the case wall is exposed to both internal and external heating. For these locations, case internal insulation is required.

In some situations (hypervelocity missiles) aerodynamic heating can also be of significance to the case heating scenario and, in extreme situations, external insulation will be required. For some designs that require spin stabilization, heat transfer can be locally enhanced from the spin effects. For example, internal heating to the head end can be augmented by vortex flows created by spin conditions. Local spots of high heat flux and erosion can also be created at the case wall under submerged nozzles and slots in the prpellant grain of a free flight rocket.

In regions of high heating rate (convection, nozzle, etc.), the energy equation frequently is dominated by insulation erosion processes. On the other hand, in regions of lesser heating (head end of combustion chamber) the energy transfer process is controlled by insulation char formation and attendant heat conduction into the substrate materials. This heat conduction process is highly transient and cannot be readily scaled in the time domain.

Heating conditions for all the design scenarios involve convection, conduction, and radiation modes of heat exchange with the dominant feature being transient heat conduction. Typically, heat is transferred across a thermal boundary layer to a sacrificial wall insulation that regresses proportionally to the heating rate (eroding insulation). Thus a time-dependent convective boundary condition with mass addition from the eroding insulation develops. Heat conduction occurs from the combustion gases through the ablating material to the virgin insulation and ultimately to the case structural components (see Fig. 7-53). This process involves heat conduction through a multilayered stack of charring insulation and several virgin insulation materials, all of which quite likely have temperature-dependent thermal properties.

7-7.3.2 External Heating

Aerodynamic heating to the rocket skin must be considered, particularly by hypervelocity free flight rockets. A detailed discussion of equations employed under this condition is beyond the scope of this overview. The reader is referred to discussions of external convective flows in Appendix C, computer programs B-2.7 and B-2.8 in Appendix B, and in Refs. 47 and 48 of this chapter. Further discussions of aerodynamic heating are included in a sample problem presented in par 7-7.9.

7-7.3.3 Internal Heating (Case and Nozzle)

The greatest sources of heating to be designed for in a free flight rocket occur in the rocket motor combustion chamber and nozzle. The length-distribution is depicted in Figs. 7-.54 and 7-55 for internal

Solid Rocket Motor

q_{aero}

q_{rad} (exhaust plume)

$q_{rad} + q_{conv}$

Regressing Propellant Surface
Protects Case Wall

r

Liner (bonding material)

Case Insulation (internal)

Motor Case Wall

q_{aero}

(A) Before Motor Case Wall Is Exposed to Internal Heating (q_{aero} only)

$q_{rad} + q_{conv}$

Erosion of Insulation

r_e

(Propellant and liner have
been consumed.)

q_{aero}

(B) After Motor Case Wall Is Exposed to Internal Heating
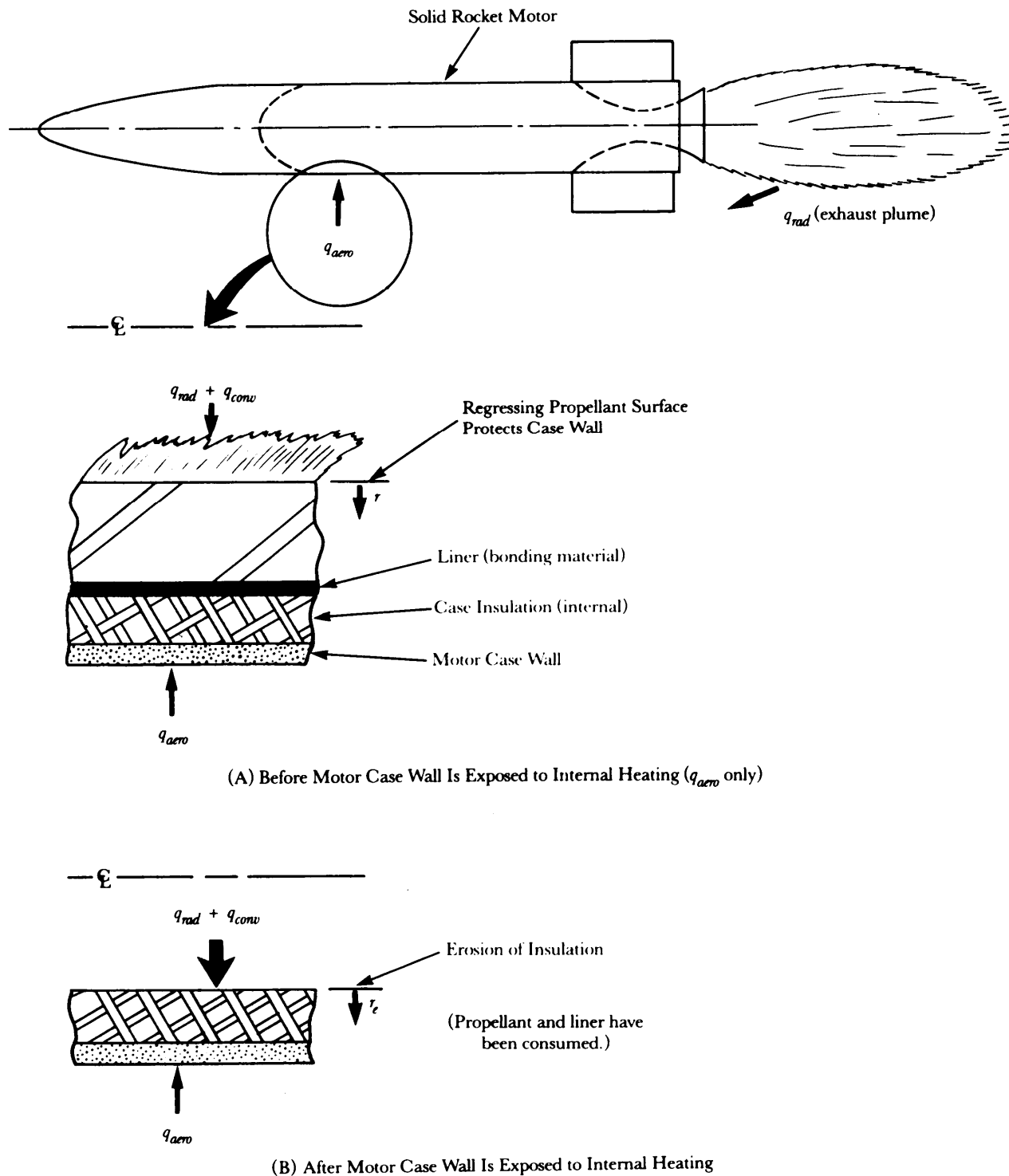
Figure 7-52. Typical Motor Case Wall Heating Before and After Propellant Is Consumed Adjacent to Case Wall
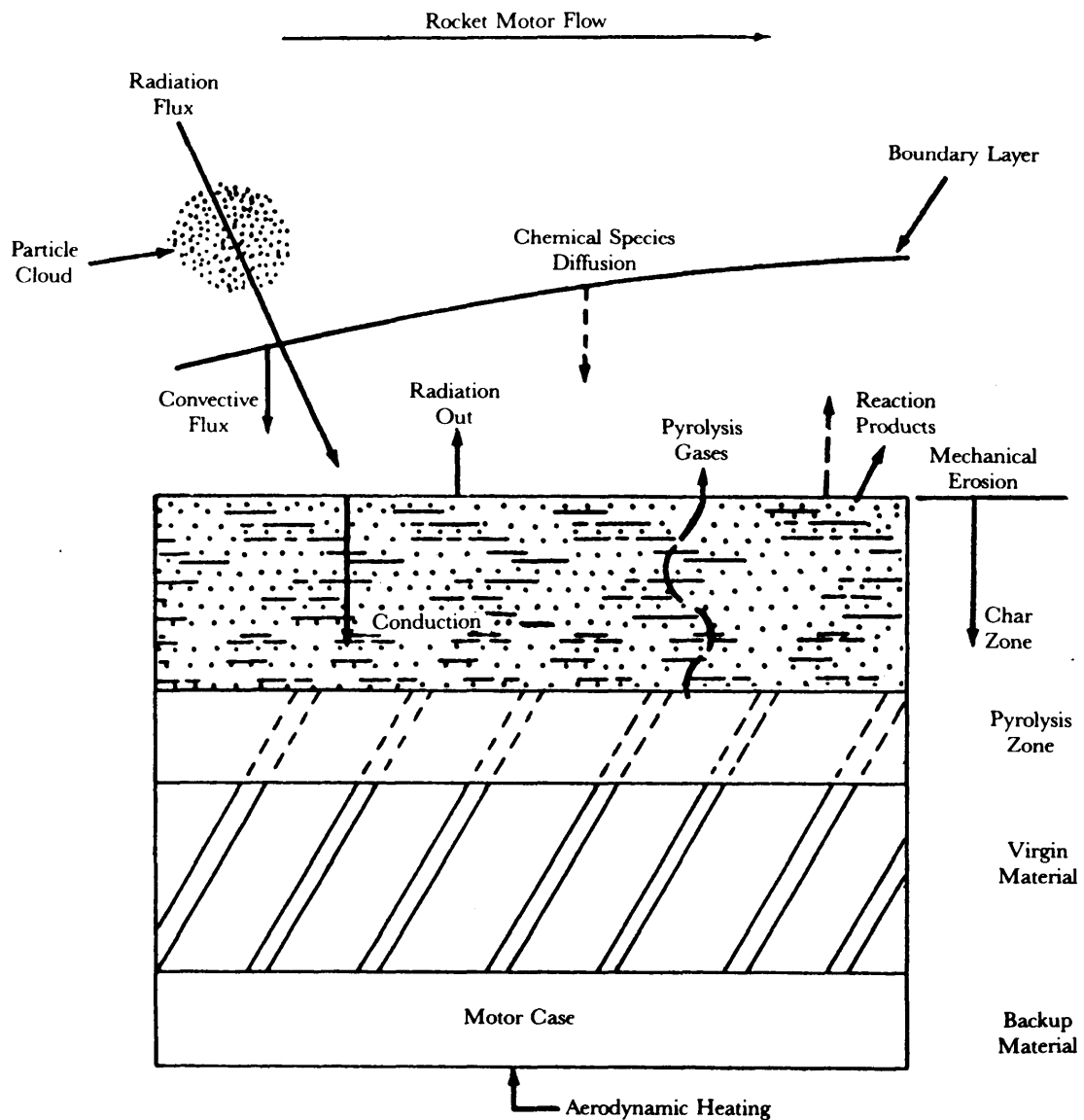
Figure 7-53. Physical Situation for Sacrificial Ablative Insulation

case and nozzle heating. Note that as gas velocities increase down the motor port toward the nozzle, the wall heat flux increases and becomes a maximum at the nozzle throat. Radiation remains relatively constant throughout the combustion chamber and then decreases as the local static temperature decreases in the nozzle.

Calculations for convective heat transfer coefficient of the nozzle flow are discussed in detail in Ref. 49 in which the integral boundary layer approach is employed. Ref. 50 discusses a simplified equation by Bartz based on pipe flow correlations to calculate the nozzle heat transfer coefficient. (This reference has wide acceptance in the thermal design community.) Further discussions of procedures for calculating convective heat transfer coefficients can be found in fundamental heat transfer textbooks such as Refs. 51 through 54. In essence, convective heating at a given location is determined primarily by motor pressure, gas enthalpy (flame temperature), and gas velocity.

The simplified Bartz turbulent flow correlation of Ref. 50 is shown in Eq. 7-89 in dimensionless form expressed as a Stanton Number ST or by the symbol C_H as shown in [he analysis program discussed in Appendix B-2.12.
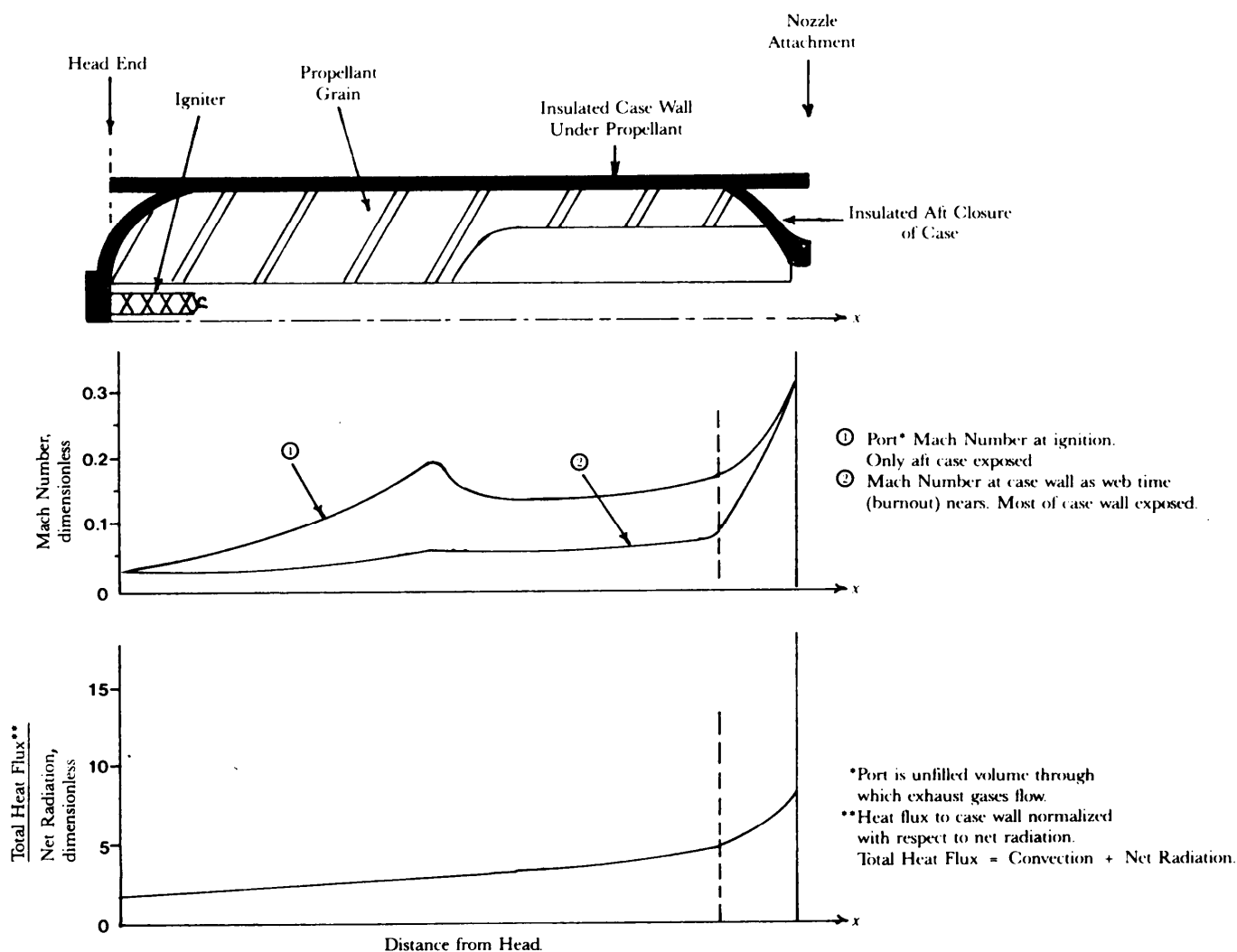
Figure 7-54. Motor Case Internal Heat Enviroment

$$ST = C_H = \frac{h}{R_e P_r} = \frac{hD}{kc_p\rho v} = \frac{\hat{h}}{\rho v} \text{ , dimensionless} \tag{7-89}$$

$$\frac{\hat{h}}{\rho v} = 0.026 \, R_e^{-0.2} P_r^{-0.4} \text{ , dimensionless} \tag{7-90}$$

where

h = convective heat transfer coefficient, $W/m^2 \cdot K$

c_p = gas specific heat at constant pressure, $kJ/kg \cdot K$

$\hat{h}$ = enthalpy-based heat transfer coefficient, $kg/m^2 \cdot s$

$Re = Dv\rho/\mu$, Reynolds number, dimensionless

D = characteristic length dimension, m

ρ = gas density, kg/m^3

v = gas velocity, m/s
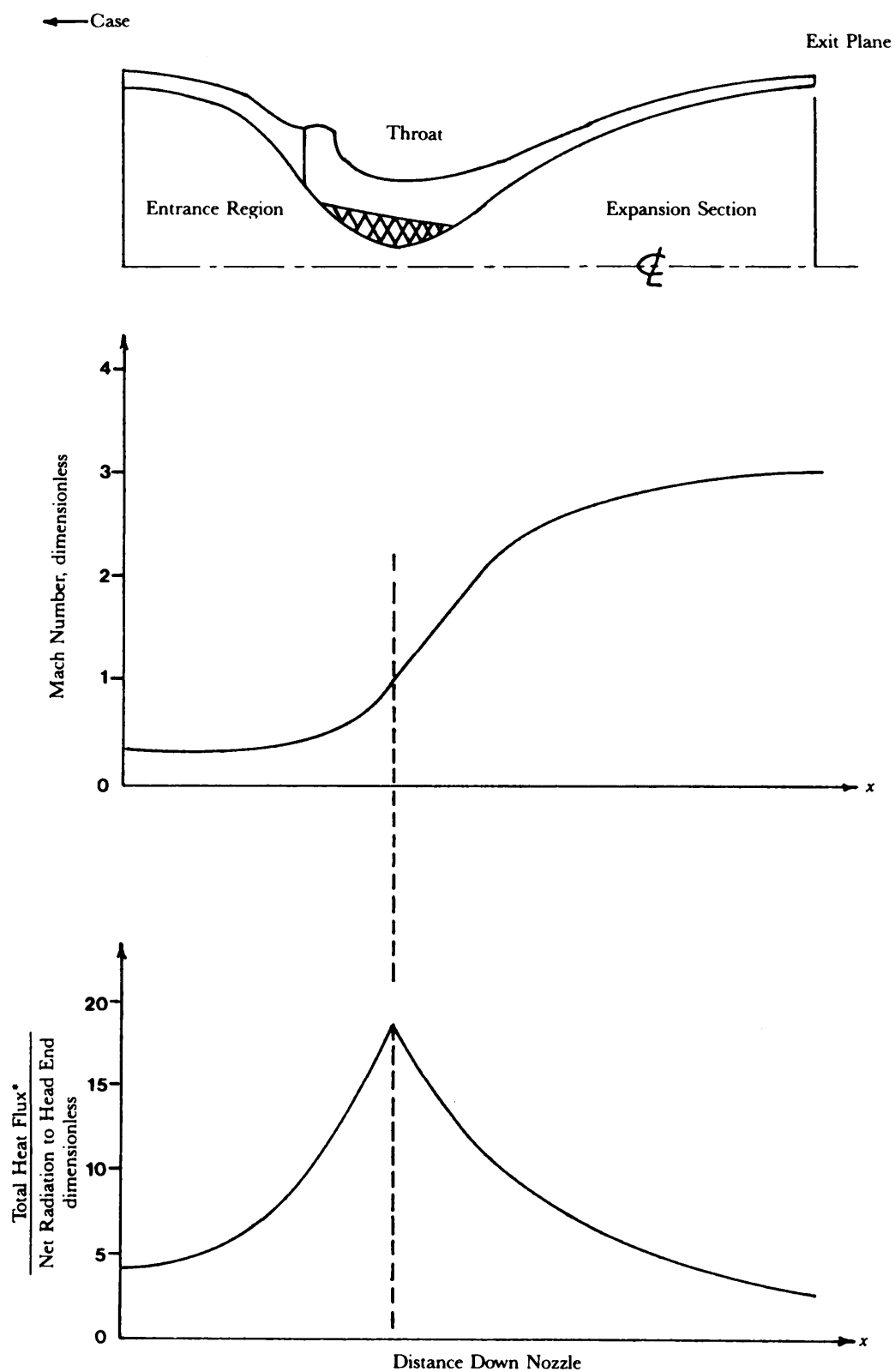
*Total Heat Flux = Convection + Net Radiation to Head End

Figure 7-55. Nozzle Internal Heating

$Pr = \mu c_p / k$, Prandtl number, dimensionless
μ = gas dynamic viscosity, kg/m·s
k = gas thermal conductivity, J/s·m·k.

The convective heat flux is then calculated from the following expression involving heat transfer coefficient and enthalpy:

$$q_{conv} = \hat{h}(i_R - i_w), \text{W/m}^2 \qquad (7\text{-}91)$$

where
q_{conv} = convective heat flux, W/m^2
$i_R = c_p T_g$ recovery enthalpy, J/kg
$i_w = c_p T_w$, wall enthalpy, J/kg
T_g = temperature of gas, K
T_w = temperature of wall, K.

The primary source of radiation heat transfer in a rocket motor is from particulate in the combustion gases. Classic radiation theory is employed to simulate radiation exchange between the combustion products and the case wall. By far, the most influential parameter in radiation is temperature because a fourth power relationship exists.

Ref. 55 covers thermal radiation heat transfer. In addition, commonly used textbooks such as Refs. 48, 51,52, and 53 can be consulted. The propellant characteristics-flame temperature and weight fraction of condensables—are the controlling parameters, followed by emissivities of the particles and the wall emissivity/absorptivity/view factor.

A commonly used equation for calculating the net radiation flux to the internal insulation for insulation design purposes is

$$q_{net \; rad} = F_{g-w} \, \sigma (T_g^4 - T_w^4), \text{W/m}^2 \qquad (7\text{-}92)$$

where
$q_{net \; rad}$ = net radiation exchange among particles, gas, and wall, W/m^2
F_{g-w} = form factor between gas/particle stream and the wall; it is the shape factor (frequently 1) multiplied by the emissivity factor (primarily controlled by particulates in the flow), dimensionless
σ = Stefan-Boltzmann constant, 5.67×10^{-8} W/m^2·K^4
T_g = gas/particle temperature, K
T_w = insulation surface (wall) temperature, K.

The total heat flux q_{tot} to an insulation is the sum of convection and net radiation as

$$q_{tot} = q_{conv} + q_{net \; rad}, \text{W/m}^2. \qquad (7\text{-}93)$$

The value of q_{tot} is applied as a boundary condition to a heat conduction model to calculate internal temperatures within a case insulation.

Transient heat conduction is well covered in Refs. 56 and .57. Simplified solutions in graphical form have been developed by Schneider (Ref. .58). The major problem with the classic conduction solutions is that it is extremely difficult to obtain a general solution to the regressing-boundary transient heat conduction scenario for variable boundary conditions of both convection and radiation. Consequently, numerical techniques involving finite differences and finite elements have been employed to solve most heat transfer problems associated with the design of solid rocket motors.

A solution to this transient heat conduction problem essentially involves integration of the following energy equation expressed in differential form for a regressing boundary (eroding insulation surface):

$$\overset{\text{I}}{\rho c \left(\frac{\partial T}{\partial t} \right)} = \overset{\text{II}}{k \left(\frac{\partial^2 T}{\partial x^2} \right)} + \overset{\text{III}}{\rho c r_e \left(\frac{\partial T}{\partial x} \right)} \tag{7-94}$$

where

ρ = insulation density, kg/m^3
c = insulation specific heat, kJ/kg·K
t = time, s
T = insulation temperature as a function of time and space, K
k = insulation thermal conductivity, W/m·K
r_e = regression rate (erosion) of insulation, m/s
x = distance from regressing surface into insulation, m.

The thermal properties vary with temperature, and the various terms in Eq. 7-94 have the following physical relationships:

I. Time late of energy accumulation. This term can be related to the temperature rise at a particular point.

II. Energy transfer by thermal conduction in the solid.

III. Rate of energy convection due to motion of the surface (if a moving coordinate system is used).

7-7.3.4 Exhaust Plume Heating

Another thermal discipline required for the design and analysis of free flight rockets is the ability to calculate exhaust plume heating. This discipline overlaps supersonic flow field analysis techniques. From a thermal standpoint the major parameters of interest are plume radiation and supersonic plume impingement heating.

The severity of plume radiation to a given point of concern is primarily controlled by the geometric view factor between the plume cloud and the point, the propellant gas and particle cloud temperature, and the particle content of the exhaust gases. (Highly aluminized propellants are most severe.)

Exhaust plume heating to a surface is primarily controlled by the local impingement angle of the particles and gas with the surface, the local pressure, and the local Mach number. Ref. 59, a JANNAF handbook, contains excellent discussions of the plume heating problem as well as other information on rocket exhaust plunes. The computer programs identified in Appendix B as B-2.11 (SPF) and B-2.l4 (BLIMPK) are also recommended sources of information for conducting plume heating calculations.

7-7.3.5 Propellant Effects

Propellant gas properties have a significant influence on the severity of heating to the case and nozzle walls. Depending on the trade-off between plume signature (minimum smoke) and motor performance, the propellant type in a free flight rocket motor can vary from a highly aluminized formulation for maximum performance to a nonaluminized, energetic binder system consisting of nitramines (RDX, HMX) or double-based (nitroglycerine, nitrocellulose) propellant for minimizing primary and secondary smoke emissions. For example, a highly aluminized (up to 23%) HTPB* propellant has a flame temperature of up to 3.560 K and a condensed-phase mass fraction of up to 34%. These characteristics create quite severe levels of radiative heating and particle impingement effects on the case wall. In contrast, the more benign minimum smoke propellant (nitramine or double-base) with its lower molecular weight, no

particulates, and 2000 to 2450 K flame temperatures, produces much lower levels of radiation and particle impingement.

As an intermediate intensity thermal environment, the reduced smoke. HTPB-composite propellants contain no aluminum but may have significant amounts of oxidizer. These propellants have a much lower flame temperature (2890 K) than the aluminized version and less than 1% condensed-phase particulate. However, the oxidation potential (chemical erosion) of the propellant gases, particularly with hydrocarbon insulations and liners. is high and frequently offsets the effect of lower flame temperature and mass fraction of particulates.

Calculations for propellant gas properties-flame temperature, molecular weight, specific heat. specific heat ratio, gas viscosity, etc. —are usually obtained from equilibrium thermochemical calculation programs such as the one presented by Svehla and McBride and referenced in par B-2.10. Appendix B.

7-7.3.6 Heating Interval

Significant)" different heating conditions occur between the pressurized interval (motor operation) and the coast-to-target interval when stored heat soaks out into the structure. The motor case is highly stressed during the pressurized interval and must be kept cool. However, during the coast-to-target stage, only flight bending loads apply; therefore, the structural members can tolerate some heating. The amount depends on the case material. Designs optimized for cost and performance may result in either a steel (of various strength levels), an aluminum, or a composite case. Accordingly, insulation design must be compatible with various case materials **as** well as a range of propellant types.

7-7.4 MECHANISMS OF THERMAL PROTECTION

The primary mechanism of thermal protection for internal insulation in a free flight rocket is ablation of a sacrificial material as shown in Fig. 7-53. As the material is exposed to high-temperature combustion gases, it decomposes into pyrolysis gases that leave the surface and feed into the boundary layer, creating some degree of transpirational cooling.

A char layer is left behind on the surface of the heated insulation. This char layer protects the virgin insulation, but the layer is swept away at an erosion rate that depends on a balance between the shear forces (Reynolds number) of flow across the surface of the char and the resistance of the char surface to this shear force. Char layer resistance to shear forces is very closely related to the integrity of the insulation filler material at char temperatures of up to 2800 K. Fiberous materials as fillers provide the greatest erosion resistance if the fibers can withstand the elevated temperatures without losing strength.

Thermal penetration below the char layer is primarily controlled by thermal properties-conductivity k, density p, and specific heat c—of the insulation. The entire process is transient so the thermal diffusivity k (pc) or a is the controlling thermal property of the material.

The most desirable thermal characteristics of an insulation would be to have filler materials that provide high erosion resistance to the char layer yet maintain the virgin insulation with a low thermal diffusivity to minimize thermal penetration. This type of material would provide the most protection with the least thickness.

7-7.5 MATERIALS

Although a variety of materials are employed as rocket motor insulations, the materials generally can be categorized by their ability to withstand certain heating environments and exposure times. For a given propellant selection, the heating environment is controlled primarily by motor pressure and local gas velocity, whereas exposure time is determined by grain design and motor burn time. With the exception of a few locations (such as the aft case), gas velocities are relatively low. in the motor case interior. The low velocities rapidly increase to high velocities in the nozzle. Accordingly, rocket motor insulating materials can be categorized roughly as case insulations and nozzle insulations. For purposes of describing a "typical" free flight rocket, the characteristics of several roctet motor insulations are discussed. However, the choice of materials presented is by no means all-inclusive; the selection of insulation material is a very empirical process.

7-7.5.1 Case Insulations

Rocket motor cases are coated with a "liner" whose primary function is to bond the propellant to the case wall. This liner also serves as a case insulation under conditions in which heating rates are low and exposure times are short. A heat transfer analysis must be conducted for exposed portions of the liner to confirm that thermal penetration to the case wall is not excessive. Typically, the liner will be composed of a polymer having the same characteristics as the propellant but will be filled with fine particulate such as carbon black. The material has relatively low thermal conductivity and little erosion resistance.

In regions of the motor where slots in the propellant grain burn through to the case wall before motor web time* (for pressure trace-shape control), gas velocities can be high and more erosion-resistant insulation materials must be employed. Frequently, a high elongation material such as a rubber will be filled with fibers rather than particles to increase erosion resistance over the basic liner material that may be used elsewhere.

Thermal property characteristics of typical rocket motor case insulations (and liners) that can be applied at the head end, cylindrical section, and propellant slots are shown in Table 7-16.

7-7.5.2 Nozzle Insulations

The aft case and nozzle entrance region are grouped together for discussion purposes. In this entrance region, gas velocities rapidly accelerate from a Mach number of around 0.10 in the propellant grain section along the case wall to a Mach number of 1.0 in the throat. Furthermore, this converging flow has a wall impingement component that can become very significant on heat transfer and erosion in the nozzle

*Motor web time is the time at which major portions of the burning surgace reach the case wall. After this time the burning surface area rapidly decreases.

TABLE 7-16. TYPICAL INSULATION THERMAL PROPERTIES (ROOM TEMPERATURE VALUES)

Location General Specific	Insulation Material	Density ρ, kg/m^3	Thermal Conductivity k, W/m·K	Specific Heat c, kJ/kg·K	Function
Case Heat End, Cylindrical Section	Carbon-filled polymer (liner)	1370.	0.23	1.44	Bond propellant to case. Provide insulation for low gas velocity regions.
Case—Under Propellant Slots (Aft Case)	Asbestos fiber-filled rubber	1360.	0.21	1.37	Case insulation to protect case after propellant burns out in higher gas velocity regions.
Nozzle Entrance and Nozzle Expansion Section	Glass Phenolic* Carbon Phenolic* Cellulose Phenolic* Silica Phenolic*	1922. 1500. 1370. 1550.	0.42 0.82 0.26 0.35	1.00 1.00 1.72 1.26	Insulate aft closure and nozzle entrance.
Nozzle Throat	Monolithic Graphite or Carbon Carbon Carbon Phenolic** Silica Phenolic**	1730. 1730. 1500. 1550.	75.0 0.85 0.31	1.05 1.00 1.26	Minimize throat erosion. Erodes more than carbon/carbon. High, but reproducible throat erosion, oxidation resistant.
Nozzle Expansion Section	Glass Phenolic* Silica Phenolic** Cellulose Phenolic*	1922. 1650. 1370.	0.42 0.31 0.26	1.00 1.26 1.72	Insulate exit cone and maybe provide structural member. ·

*Molding compound
**Tape wrapped

entrance region. Consequently, a more erosion-resistant material is needed in the aft case/nozzle entrance. At this point hard insulations are used to provide greater shear strength in the char layer.

Entrance region insulations frequenty consist of a fiber-filled phenolic, which, if erosion resistance is adequate, will be fabricated from a molding compound for cost reasons. For a free flight rocket application, the design guideline (or constraint) is usually to select the least expensive insulation that will provide the necessary erosion resistance and performance reliability) for the heating environment and exposure time at the location of concern. In fact, this guideline applies throughout the nozzle including the entrance, throat, and expansion sections.

The throat section is most critical structurally and thermally because heating rates and pressures as well as the axial gradients of these parameters are greatest at this point.

Selection of throat materials requires an interaction with the interior ballistics specialists to decide whether the motor design is to be based on a relatively constant throat area or an eroding (increasing with time) throat-area concept. Once the throat erosion approach has been established, an appropriate throat insert material can be selected. An economical, relatively low erosion rate throat material choice is a monolithic graphite or a carbon/carbon (more expensive) insert. If these materials are used, they must be backed up with an appropriate, lower conductivity insulation to prevent heat penetration to the nozzle structural members during motor operation. Thermal and stress analyses are mandatory for this design approach.

If an "eroding throat" concept is employed in the design, a carbon phenolic or silica phenolic throat insert can be used. For this design approach the most important aspect of an analysis becomes the prediction of throat erosion.

Selection of insulation materials for the exit cone will also depend on the throat insert because transition to the exit cone material must be compatible with the flow and erosion characteristics of the insert material. Otherwise, a supersonic flow downstep will be created at the material interface, resulting in performance losses and locally enhanced heating in the expansion section insulation. Typical thermal properties for nozzle insert and expansion sections are shown in Table 7-16. It should be noted that these thermal properties are highly temperature dependent. Generally, the thermal conductivity and specific heat of the phenolics increase with temperature while those of graphites and carbon/carbons decrease at elevated temperatures. All values shown in Table 7-16 are for room temperature conditions.

7-7.6 DESIGN REQUIREMENTS AND CONSTRAINTS

The first step in the analysis and design of a thermal protection system is to establish clearly the insulation design requirements and constraints for the entire missile. For a free flight rocket, as well as most rocket motors, the major insulation design requirement will be related to the maximum allowable temperature at which structural integrity of the missile system can be maintained. Structural integrity also implies that the insulation system should remain intact under all combinations of operating conditions. This means that appropriate bond interfaces between adjacent materials and components should maintain their integrity.

Maximum allowable temperatures may be further subdivided into time-dependent limits that apply to motor operation when internal pressure loads and possible flight-bending loads are on the case and to the postpropulsive coast-to-target stage when only flight-bending loads apply.

Allowable case and nozzle structural member temperatures will depend on the materials used and the stress levels experienced by the materials. A typical value of allowable case temperature for a steel case is 700 K. Aluminum and composite (Kevlar®) cases lose strength rapidly above 39.5 K. Even though a steel case may be able to withstand 700 K, a lower limit may be imposed for a steel case rocket motor because of the adhesive used on the rocket to attach launch lugs or to hold insulation in place. A typical adhesive would begin to lose strength above 400 K. During the coast-to-target stage, allowable structural temperatures can be higher than for the pressurized interval, but the designer still may not want the adhesives used on the system to fail.

To provide some conservatism to the design, typical design practice is to allow less than a 5-deg C temperature rise in the structural parts until motor web time and then to permit the case temperature to rise

gradually to a value just below the point of case strength degradation at the end of the longest coast trajectory.

For composite cases, it should be noted that thermal conductivities of the structural case wall are such that there will be a very significant temperature gradient through the case wall. In fact, the structure is behaving like an insulator in which the case exterior side will not heat up until well after motor operation is over (unless aerodynamic heating is also significant). The critical area of concern for a composite case is heating toward the case interior side because case fiber strength is so dependent on temperature. Consequently, for these case materials the design requirement should be that the case interior temperature should not rise above a specified value by some specified elapsed time.

Although most free flight rockets will not be exposed to severe environments of aerodynamic heating, consideration must also be given to the combined effects of internal (motor heating to the case wall) and external heating to exposed parts. For the hypervelocity rockets, in particular, the combined heating effects can become significant. An approach employed by designers to "uncouple" the effects of combined and external heating is to prescribe that no internal heating penetration to the case wall will occur during powered flight. In this way the combined effects of heating will only be present on the case wall after maximum case stresses have occurred.

Besides the primary thermal design requirement for maintaining case structural integrity, there are usually several design constraints that must be established and assigned priority before proceeding with a thermal analysis. Some of the constraints may be subtle, and some must be traded off with other system design requirements during the preliminary design phase of the rocket. For example, the thermal design of a rocket system might be driven by any one or a combination of the following design constraints on the thermal protection system:

1. Minimum weight cross section of insulation
2. Minimum thickness (so more propellant can be loaded)
3. Compliance with a specific margin of safety on insulation erosion or strength
4. Minimum cost (includes raw materials, fabrication, and insulation)
5. Insulation pyrolysis contribution to minimum signature (electromagnetic wave interference, visible smoke and particulate, afterburning, etc.)
6. Insulation reliability, reproducibility, and service life considerations
7. Chemical and bond compatibility with propellant formulation—i.e., plasticizer migration, etc.
8. Processing and installation constraints.

The relationship between these factors depends greatly upon mission requirements. For a free flight rocket motor, however, it is assumed that high production volume, design simplicity, and minimum cost will provide the guidelines for establishing the ultimate priority on insulation design constraints.

7-7.7 APPROACH TO THERMAL ANALYSIS

Now that the various (considerations have been discussed separately, it is appropriate to discuss the sequential approach employed in conducting a thermal analysis in support of insulation system design for a free flight rocket. The following tasks must be addressed in more or less the order shown, but it is obvious that some of these tasks require interactions and some usually are conducted concurrently:

1. Establish the design requirements and constraints of the system.
2. Select critical areas to analyze such as

a. Case. Specific locations will depend on the propellant grain design. Candidate locations include those areas that become exposed during propellant burn back, those areas subjected to high velocity flow of combustion gases, and those motor cases subjected to severe aerodynamic heating effects. Typical examples are

(1) Case head end and igniter

(2) Case midsection. This area is exposed to tail-off heating only and probably requires no insulation (just the liner used to bond propellant to case).

(3) Aft case. This area may contain propellant slots that burn out to expose the case wall to high-velocity gas flows. (Note that for some designs the slots may be in the forward part of the case.)

   b. Nozzle. Specific areas that merit attention are
     (1) Aft case convergence and nozzle entrance section
     (2) Throat (Establish design approach—eroding versus low-eroding throat insert material.)
     (3) Expansion section.

3. Calculate heating conditions and exposure times for each selected location to be analyzed. This requires calculations from propellant thermochemistry for gas transport properties. Conduct aerodynamic heating analyses to determine external heating conditions.

4. Select candidate insulations to analyze.

5. Obtain thermal and erosion properties for candidate insulations. If the data are not availablr, laboratory and subscale testing of insulations must be conducted to obtain needed information. For example, thermal conductivity}', density, and specific heat of both virgin and char materials are necessary, and empirical data to define the insulation erosion rate as a function of heating conditions are required.

6. Simulate thermal performance of candidate insulations for selected critical locations by using thermal models. Results of the analysis are predictions for temperature versus time at any point in the section analyzed, prediction for erosion and char of insulation.

7. Compare results of thermal analysis with design requirements and constraints.

8. Select insulations to be used and calculate final thicknesses to meet all requirements. Optimize insulation design from a design constraint priority list. This also requires an interaction with the structural designer and the interior ballistics specialist.

7-7.8 ANALYTICAL TECHNIQUES

7-7.8.1 General

Since most thermal processes associated with insulation design and prediction of structural member temperatures are extremely complex and highly transient in nature, thermal simulation computer programs are employed to consider the time-dependent processes. To be most effective, these programs must be calibrated or correlated with experimental data. The experimental data are frequently of two kinds-subscale test data and laboratory characterization data defining the insulation decomposition characteristics. The thermal simulation program is then used to scale insulation performance from the controlled, "calibration" environment of subscale hardware to the rocket motor design conditions of concern. This is accomplished generally by employing the conservation equations of mass, momentum, and energy.

Thermal models will vary in complexity from purely empirical, through the semiempirical, to the complex analytical types. The empirical types may be satisfactory for interpolative use when bounding conditions are known from previous testing. At the other extreme the complex analytical modes are the most difficult to use and interpret, but they are the most genera] and can be most effective for extrapolating data or making *a priori* predictions.

An extensive discussion of analytical techniques for conducting thermal analyses is beyond the scope of this handbook. The reader is directed to the references cited in the subparagraphs that follow for detailed information. Consequently, the discussion will focus briefly on (1) where to find information on nozzle thermal design and (2) the framework of inputs and general approach taken in conducting the most widely accepted complex analytical technique for simulating solid rocket motor thermal protection systems.

7-7.8.2 Nozzle Thermal Techniques

A general nozzle thermal design handbook has been prepared by Ellis, *et al,* for NASA (Ref. 60). This reference provides an excellent overview of nozzle design including thermal considerations. A good summary paper on thermostructural behavior of nozzles is presented in Ref. 61. This paper describes the interaction among nozzle aerodynamic analyses, thermal analyses, and finally structural analyses used to design a nozzle. The aerodynamic design characteristics are further elaborated in Ref. 62.

A semiempirical nozzle erosion prediction model used in the nozzle analysis program discussed in Ref. 63 is an effective technique for predicting nozzle erosion rates and correlating nozzle erosion data for

various design conditions. This technique employs a simplified correlation of the more complex analytical model discussed in par. 7-7.8.3. Erosion rate is defined as a function of the convective heat transfer coefficient, material density, and an effective blowing parameter that is related to the propellant oxidation potential and flame temperature. The effects of throat material thermal conductivity, initial temperature, and surface temperature are approximated.

7-7.8.3 Complex Analytical Techniques

To calculate structural member temperature versus time for any thermal protection component of a free flight rocket (combustion chamber or nozzle wall), a transient thermal analysis program is necessary. Such a computer program simulates the processes of char-forming ablation and erosion while accounting individually for various mechanisms and transient energy absorption processes taking place in a multilayered material undergoing thermal degradation. Thermal response is calculated from finite-difference solutions to the energy equation by incorporating one moving boundary. Both temperature and density gradients are considered as the virgin material is allowed to char and erode. In addition, surface efects such as the fractional blocking of convective heating due to outgassing (blowing) into the boundary layer are considered.

The most comprehensive thermal simulation program employed in the design and analysis of thermal protection systems is described in par. B-2.12, Appendix B. This program, known as the Aerotherm CMA3, also requires as input a set of surface thermochemical data generated from the thermochemistry of the propellant and insulation species. These data are created by first running ACE, an equilibrium surface thermochemistry calculation program described in par. B-2.13, Appendix B.

An overview of the analysis procedure for running CMA is shown in the flowchart of Fig. 7-56. It can be seen that input is required for combustion gas transport properties, gas flow field (both inviscid and viscous), and insulation material properties which are temperature dependent. Chemical, convective, and radiative boundary conditions are calculated as input to the thermal model. A further breakdown of input parameters is listed in Table 7-17. Capabilities of the program are briefly described in par. B-2.12, Appendix B. Outputs are primarily the time-dependent surface recession rate, char rate, and temperature distribution through the composite layers of insulation and structural members.

Although the CMA program requires rather extensive experience for proficient use as a design tool, it provides the most comprehensive and general framework for making *a priori* calculations on thermal and erosion characteristics of rocket motor insulation materials.

7-7.9 SAMPLE THERMAL DESIGN PROBLEM FOR AERODYNAMIC HEATING

7-7.9.1 General

The objective of this paragraph is to present a relatively simple but representative motor case design problem involving aerodynamic heating calculations for a ballistic trajectory that is typical of a free flight rocket. Results of example aerodynamic heating calculations are presented for a rocket case at a point near the forward end of the solid rocket motor where external heating contributions would be greatest to the solid propulsion system. A general schematic of this rocket is shown in Fig. 7-57 where the point analyzed is located 2.26 m downstream of the nose.

The purpose of an aerodynamic heating analysis is to calculate the local enthalpy-based aerodynamic heat transfer (coefficient, recovery enthalpy, and hot wall heat flux as a function of time for a prescribed body location and a predetermined trajectory of the missile. For design purposes, a worst location on the missile and a most severe aerodynamic heating trajectory are selected. The designer should be aware that frequently more than one trajectory can create a set of worst design conditions. For example, a high-velocity, low-altitude. short time-to-target trajectory will cause the highest heat fluxes; however, a high-altitude, lower velocity, long time-to-target trajectory can create the greatest amount of time for external heat to soak into the missile interior. Accordingly, both trajectories should be analyzed during the design phases of a missile. A long-range, ballistic flight was selected for illustration purposes in the sample problem.
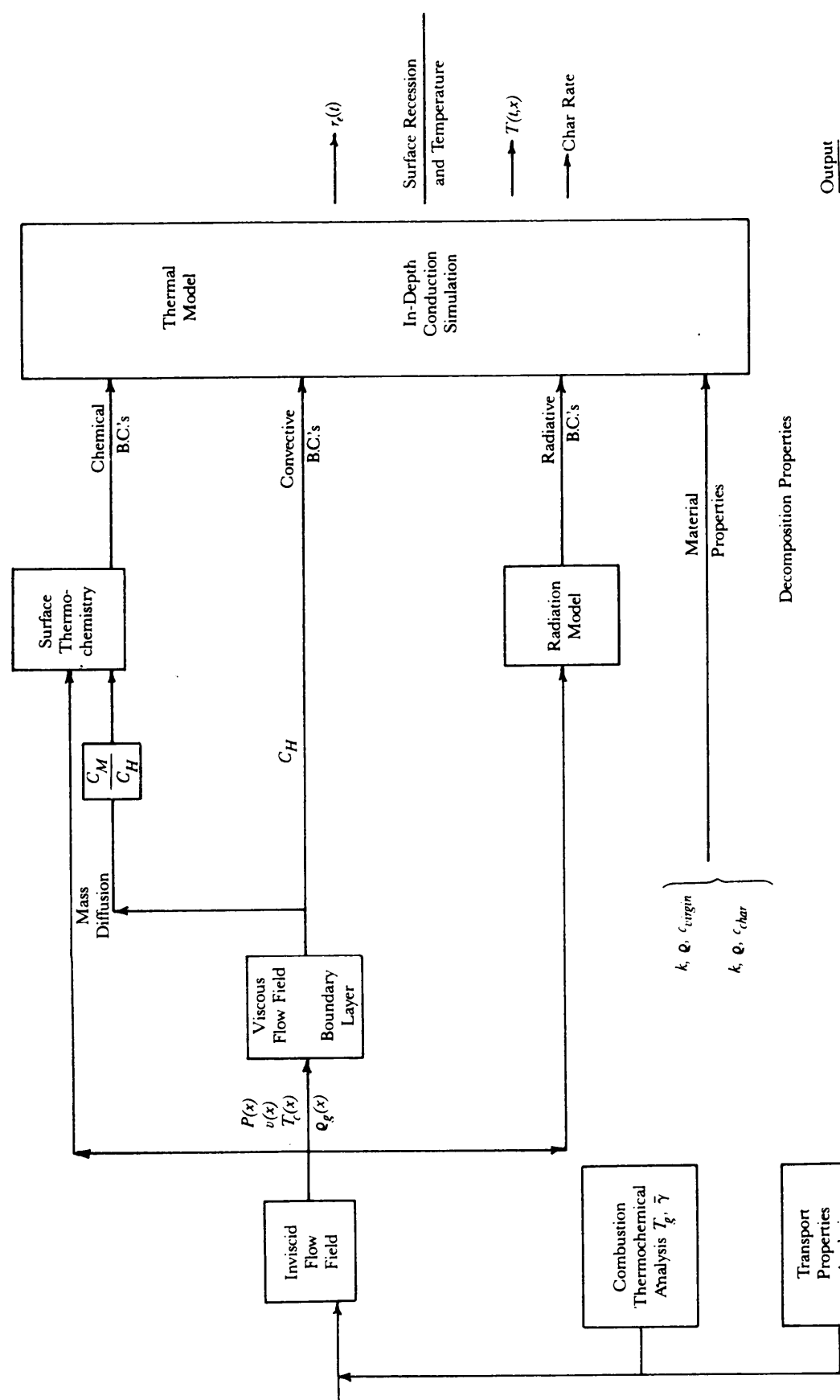
Figure 7-56. Analysis Procedure Flowchart

TABLE 7-17. INPUT PARAMETERS REQUIRED FOR THERMAL ANALYSIS OF CHAMBER AND NOZZLE INSULATION

1. Propellant elemental composition

2. Propellant theoretical flame temperature

3. Combustion chamber operating conditions

4. Motor and nozzle geometry

5. Combustion product radiation properties

6. Surface material elemental chemical composition and constituent makeup

7. Material density

8. Material thermophysical properties (virgin and char):
   a. Specific heat

   b. Thermal conductivity

   c. Surface emissivity

   d. Heat of formation

   e. Decomposition kinetics
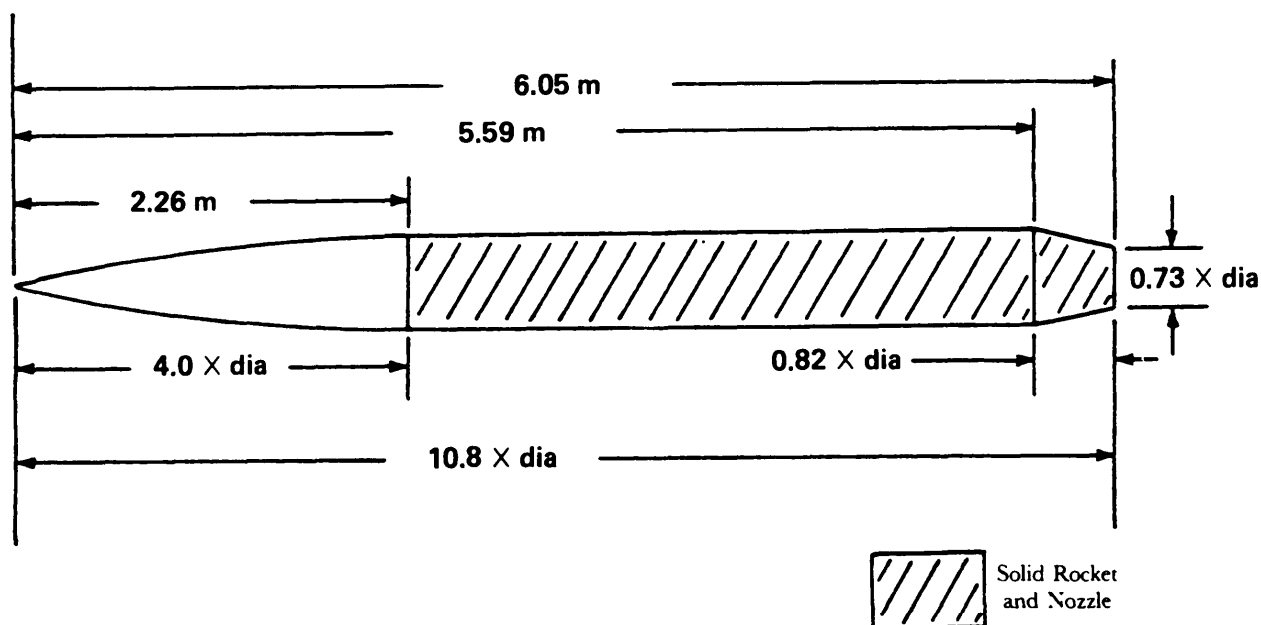
Figure 7-57. Sketch of a Hypothetical Free Flight Rocket Showing Geometry Pertinent to External Heating

The input parameters from a trajectory required to conduct an aeroheating calculation include missile velocity (or Mach number), altitude, and angle of attack as a function of time. The time-dependent output heat transfer coefficients and free stream enthalpies from the aeroheating analysis are then applied as a boundary condition to a multilayered heat conduction program. This program is used to calculate thermal penetration of the external heat (usually radially) into the solid rocket motor components.

Various body shapes, flow fields, heating methods, and thermodynamic properties fo the fluid can be selected to conduct an aerodynamic heating analysis of a rocket motor. The method of analysis selected for the sample problem is discussed in the subparagraphs that follow. More detail on solution equations for several aerodynamic heating calculation techniques can be found in Appendix C.

7-7.9.2 Aerodynamic Heating Calculations

The determination of aerodynamic heating effects at a specified location of a missile requires the repetitive, sequential execution of three primary analytical calculations:

1. Flow field analysis
2. Aerodynamic heating rate calculations
3. Wall temperature (and in-depth) temperature calculation.

The flow field analysis results in the determination of local thermodynamic fluid properties at the edge of the boundary layer around the missile. These properties are then used in the prediction of aerodynamic heating rates by using a selected set of established semiempirical methods. From the predicted aerodynamic heating rates, the wall temperature response can be evaluated. Because the transport properties required in aelodynamic heating predictions are wall temperature dependent, a forward difference numerical technique is employed to perform aerodynamic heating calculations as a function of time.

For the purposes of the sample problem. supersonic flow over a cone was employed to calculate the flow field around the rocket motor. Equilibrium air (real gas) assumptions were used for the determination of the air thermodynamic properties from the standard atmospheric model-i.e.. plessure, density, acoustic velocity, entropy, and enthalpy.

Aerodynamic heating calculations were based on the modified Spaulding-Chi method (see par C-3.5. Appendix C) which considers turbulent. compressible flow over a flat plate. This calculation procedure was selected because experience has shown that this approach is prudent for the analysis of downstream sections of a missile at the solid rocket motor location (Fig. 7-57).

The velocity and altitude versus time upon which aerodynamic heating calculations were based are shown in Fig. 7-58. These flight conditions were calculated for a ballistic trajectory of a missile having the following specifications:

Payload mass = 1135 kg
Propellant mass = 1343 kg
Total vehicle mass = 2925 kg
Motor web time = 15 s
Average chamber pressure = 9.7 MPa
Launch angle = 50 deg (zero length launch rail)
Total flight time = 86 s.

As indicated in Fig. 7-58, maximum velocity was achieved at motor burnout of 15 s. maximum altitude was attained at 43 s and ground impact occurred at 86..5 s. This ballistic trajectory of Mach number and, altitude versus time was used for making the modified Spaulding-Chi heating calculations. In addition a zero angle of attack was assumed for the sample problem.

Results of the aerodynamic heating calculations are shown in Fig. 7-59 where recovery enthalpy i_R and enthalpy-based heat transfer coefficient h are plotted versus time. Both of these parameters attain a maximum value at motor burnout. The heat transfer coefficient experiences a minimum at the time of maximum altitude (43 s) primarily because the density of air is least at the point of maximum altitude. Then, as the missile returns to earth and air density increases again. $\hat{h}$ increases accordingly.
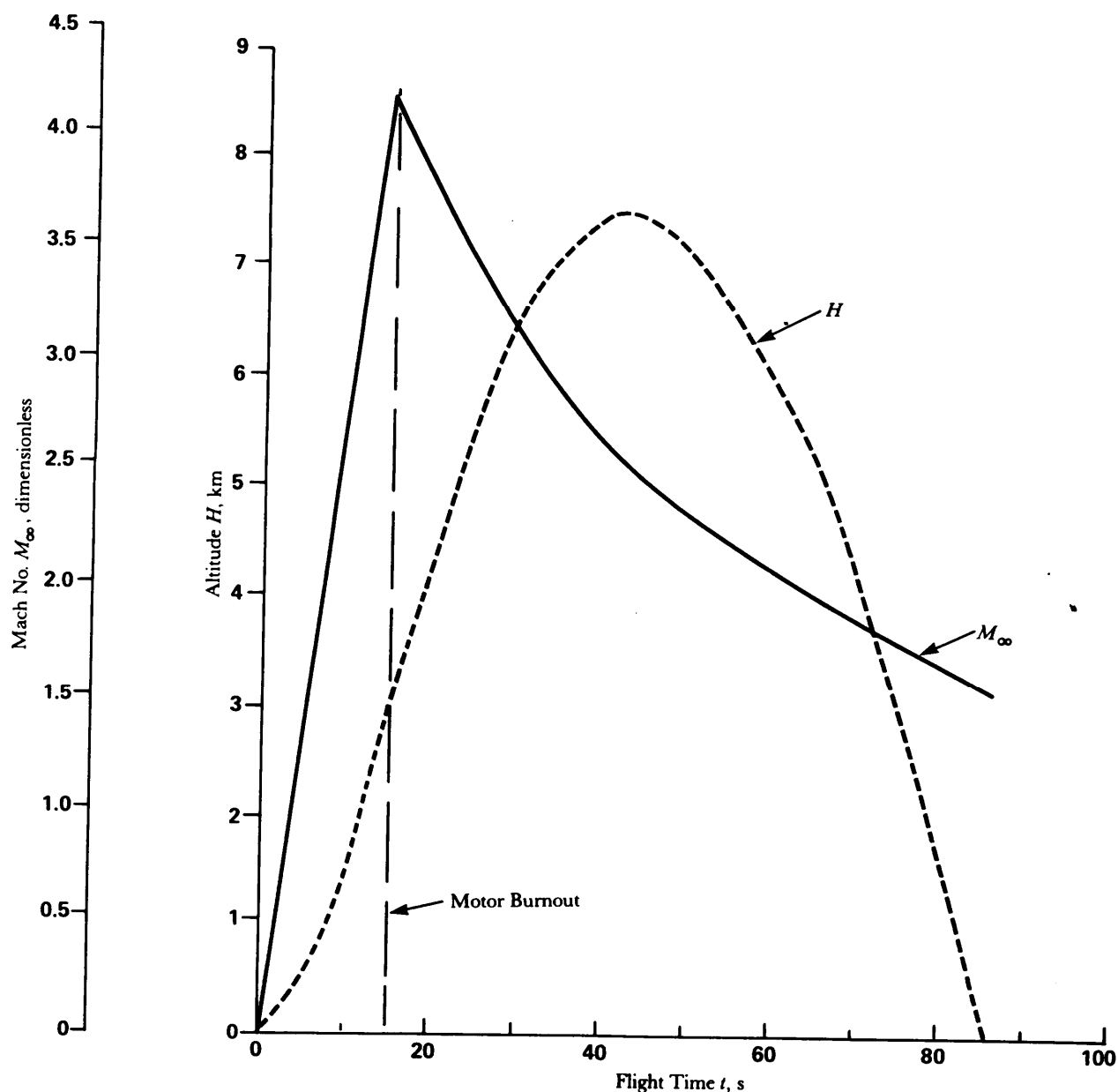
Figure 7-58. Ballistic Trajectory Input for Aerodynamic Heating Analysis

The values of $\hat{h}$ and i_R from Fig. 7-59 are used in the following equation to calculate hot wall heat flux q_{hw} to the motor case wall:

$$q_{hw} = \hat{h} \, (i_R - i_w), \, W/m^2 \qquad (7\text{-}95)$$

where

q_{hw} = hot wall heat flux, W/m^2

$\hat{h}$ = enthalpy-based heat transfer coefficient, $kg/m^2 \cdot s$

i_R = recovery enthalpy, J/kg
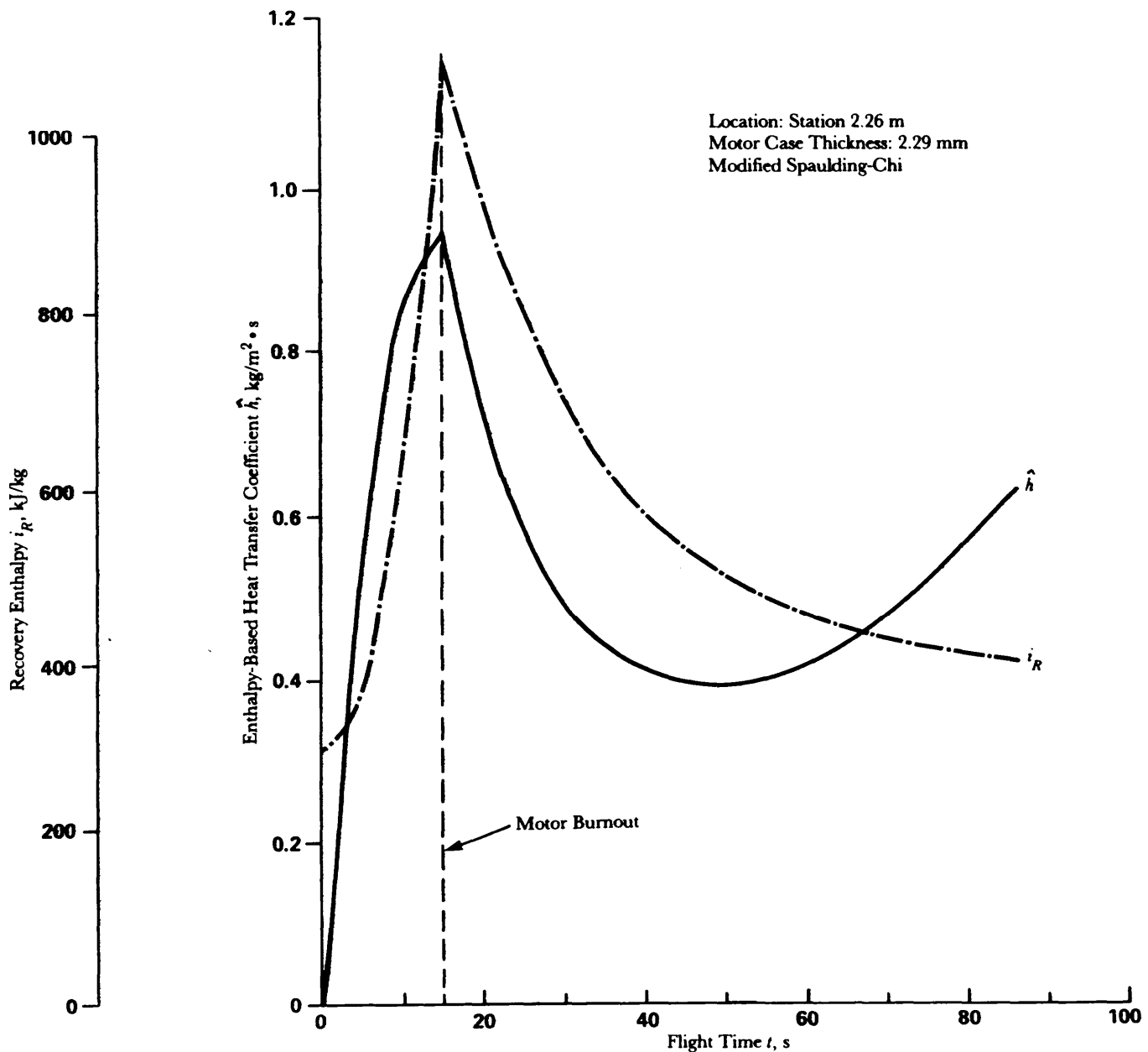
i_w = air enthalpy at wall conditions, J/kg.

Figure 7-59. Heat Transfer Output From Aerodynamic Heating Calculations

Hot wall heat transfer implies that the heated wall temperature is used in Eq. 7-95 to calculate heat flux rather than to assume the wall temperature remains constant at the initial (cold wall) temperature. In the numerical calculation scheme used to obtain q_{hw}, the value of the wall temperature from the previous time step is actually used to calculate heat flux because the present value of the wall temperature is not yet known.

At this point in the analysis a numerical solution technique (heat conduction program) is used to calculate thermal penetration into the rocket motor. Boundary conditions for this heat conduction program are the time-dependent values of i_R and $\hat{h}$ from the aerodynamic heating calculations. Output of the heat conduction program are hot wall heat flux, wall temperature, and thermal penetration into the motor case and internal insulation.

Fig. 7-60 shows the results of the heat conduction calculation for q_{hw} and motor case wall temperature. It can be seen that the maximum heat flux also occurs at motor burnout. Maximum case temperature occurs at about 28 s whereupon the heat flux becomes negative, i.e., $i_w > i_R$, and the motor case is cooled for the remainder of the flight.
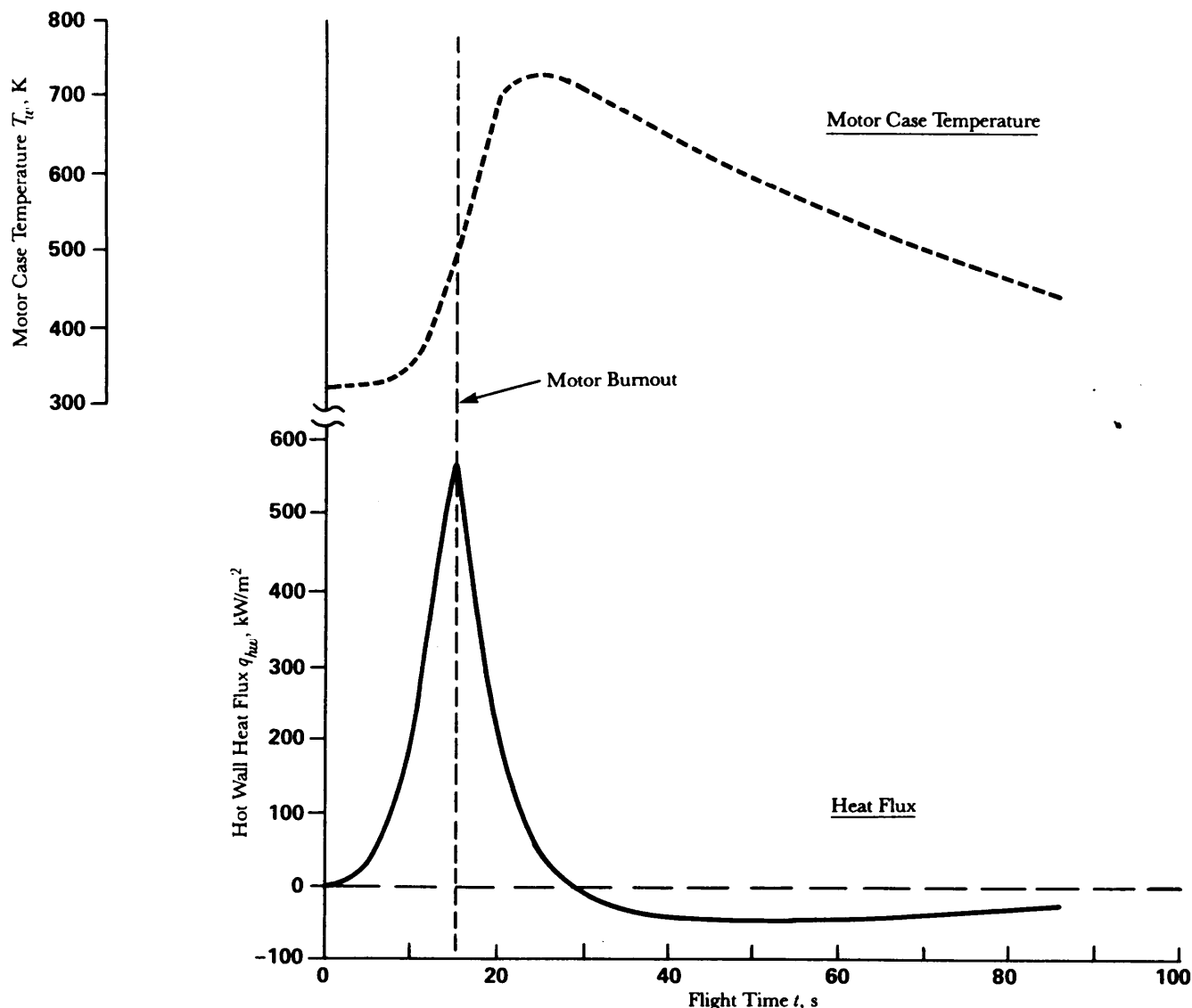
Figure 7-60. Hot Wall Heat Flux and Motor Case Temperature Calculated From Aerodynamic Heating

From a designer's standpoint the two case temperatures of greatest concern are
  1. Maximum case temperature achieved during pressurized motor operation (up to motor burnout)
  2. Maximum case temperature achieved during coast-to-target.
For this sample problem, Fig. 7-60 shows that maximum case temperature during the pressurized interval (motor burn) is 481 K and during the coast interval (after motor burnout), 727 K. Since the case material in the sample problem is steel, and significant case degradation at elevated temperatures does not occur in rapid heating environments below 700 K, the calculated case temperature level of 481 K during motor

operation does not present a design problem. Likewise, during the coast interval following motor burnout when motor case loads have been significantly reduced, the value of 727 K presents no problem. If, however, an aluminum or composite case material had been used in the design, provisions would have to be made for external insulation on the motor case.

Thermal penetration through the case wall into the internal case insulation for various flight times for the sample problem is shown in Fig. 7-61. It can be seen that at the 1.5-s time of motor burnout the thermal wave has only penetrated about 3 mm into the internal case insulation. This should present no design problems. During the coast interval the depth of thermal penetration increases, but it is not a design consideration either because internal heating contributions to internal case insulation are far more influential at motor burnout anti shortly thereafter. Because case stresses are usually so low (flight bending loads) relative to the pressurized case interval, thermal considerations for the case and case insulation are not a high priority design concern during the interval involving coast-to-target.

Note that (his sample problem only illustrates aerodynamic heating considerations. In a real motor design scenario a significant number of similar thermal heat conduction analyses also would be made for the internal heating from combustion gases to establish the required case and nozzle insulation thicknesses. These insulation design conditions were discussed previously in parts of par. 7-7, "Heat Transfer". The reader is also referred to par. 7-7.8, " Analytical Techniques", in which semiempirical and complex analytical thermal protection system design programs are discussed (also see par B-2.12, Appendix B). For some of the extremely high-velocity flight conditions, both internal (rocket motor combustion product) heating and external (aerodynamic) heating must be considered concurrently in the over-all analysis and design of case thermal protection systems. This design approach assures that the motor case and heated structural parts of the missile are maintained within allowable structural/thermal limits for all phases of a flight.

7-8 STRUCTURAL TESTING

Structural members may be of such a form, or loaded in such a manner, as to make calculations of the stresses and strains very difficult. When uncertainties exist concerning the structural integrity, it is usually desirable to verify the structure by subjecting it to a proof test of some sort. This is especially true when the complexity of the structure makes structural modeling difficult.

Structural testing specimens usually are configured for the measurement of strain since this is the most direct way to determine the stress induced by a loading environment. This technique is comparatively easy to use when the stress is fairly uniform over a consider-able length, but it becomes difficult to use when the stress is localized or varies abruptly. Localized stress measurements must then br made over a very short gage length and with great precision. Special strain gages and extensometers have been developed for the testing of such structures. These devices include electrical strain gages; scratch recording strain gages adapted especially for dynamic, vibration, or high-acceleration environments; and magnetic strain gages for rapidly varying strains. Other methods include special lacquers that are used as a brittle coating to reveal crack pattern locations, optical grating methods, and photoelastic methods.

Structural tests are classified as destructive if the test item is permanently deformed or fractured and as nondestructive if the test item is structurally useful after the test. The cost of destructive tests of full-scale motor cases can often be prohibitive. However, destructive testing of properly designed subscale models can be used under certain conditions when care is taken to duplicate the structural behavior and load conditions. However, it is much better to perform structural testing on full-scale devices.

Nondestructive testing includes inspection and hydrostatic proof tests. Inspection tests must be defined in terms of an overall inspection master plan covering all aspects of motor case fabrication. In planning the inspection requirements, particular attention must be given to the design to ensure that proper inspection can be implemented during the fabrication process. For example, this planning ensures that nonmetallic areas do not mask surface or subsurface defects. Inspection tests include magnetic particle and dye penetrant techniques and radiographic and ultrasonic inspections.

The hydrostatic proof test is used to demonstrate the structural integrity of the case for service. The test generally is developed to demonstrate that the case has sufficient structural integrity to sustain the service

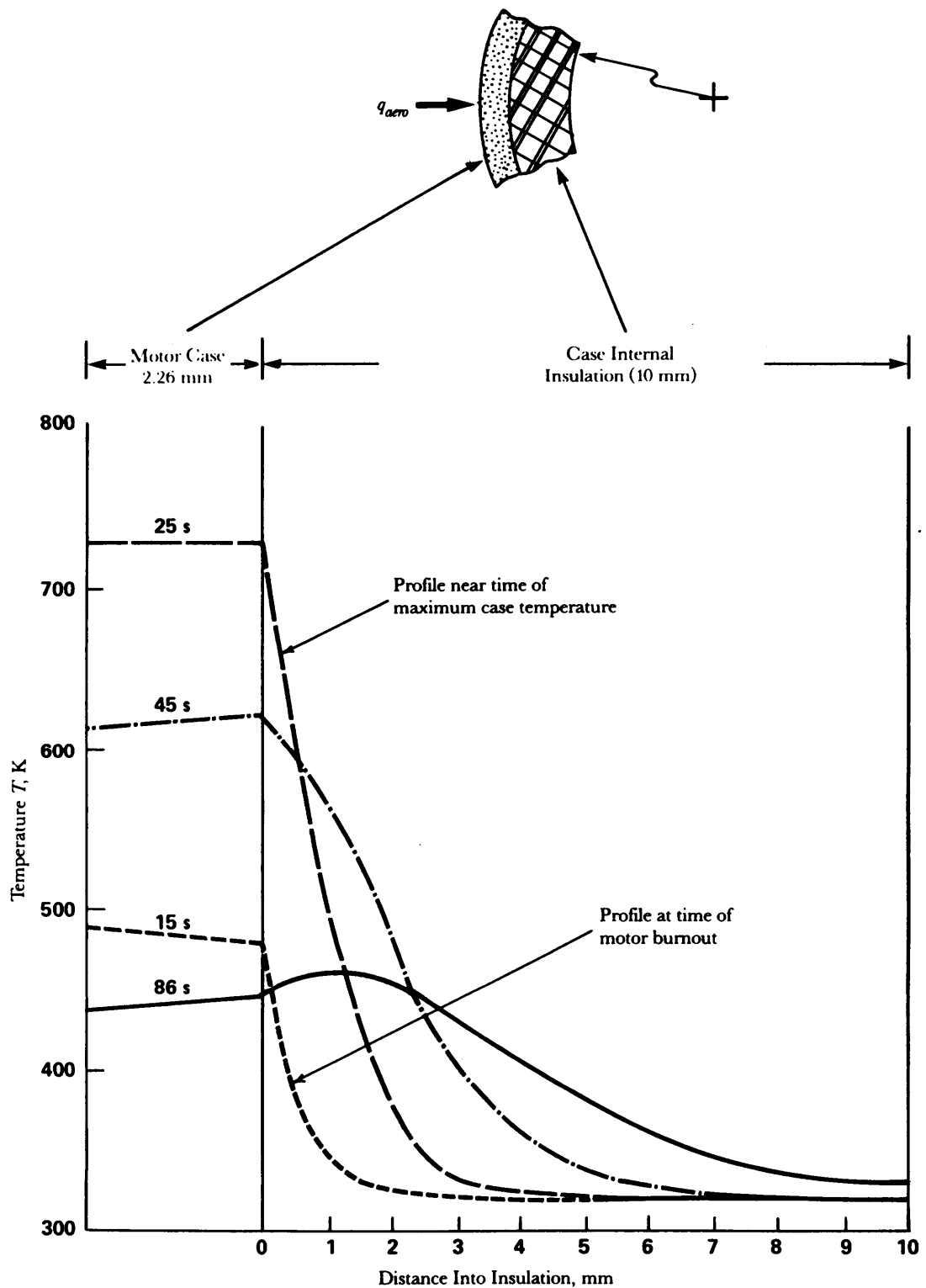Figure 7-61. Temperature Gradient Into Motor Case and Internal Insulation From Aerodynamic Heating for Various Flight Times

pressure cycle. During production, hydrostatic proof tests are used to demonstrate that the cases are suitable for use as motor cases. Test pressure, temperature, external loads, and pressurization rates are evaluated during motor development.

Additional information on testing techniques can be found in Refs. 22 and 64 through 67.

7-9 OTHER STRUCTURAL CONSIDERATIONS

Chapter 3 demonstrates the relationship between structural mass and payload mass when performance (range) is fixed. Savings in structural mass allow additional mass to be used by the payload. However, structural designs to minimize mass have a tendency to increase the cost and, sometimes, to decrease reliability. Therefore, trade-off studies are generally required to evaluate structural concepts versus performance and cost. The cost analysis should include the life cycle costs of research and development, manufacturing, storage, etc. Structural trade-off studies should also include the influence on accuracy since accuracy influences the effectiveness of the system. Trade-off studies to achieve a fixed level of effectiveness at minimum cost may result in simple, low-technology structures. Recent studies of motor cases with simple metal tubing and nonmetallic paper-phenolic and plastic closures demonstrate the advantage of life cycle cost designs over expensive minimum weight case design concepts.

Limiting manufacturing asymmetries to improve accuracy requires careful consideration because excessive demands for symmetry dramatically increase manufacturing costs. The storage of rocket systems is a further consideration since the storage life may be 10 yr or more. During storage, the propellant or case materials may creep and take on a permanent set to create asymmetries that degrade the accuracy. The storage environment requirements and rotation cycle time of a rocket system directly influence the life cycle cost of the rocket system. The service life of a motor can also influence the cost-i.e., if the motor service life is short due to the stress level in the propellant or liner bond, then the service life cycle cost of the rocket system can be high. Careful attention must be given to the mass, cost, and storage life during concept formulation and the preliminary design phase of the structure to ensure that an effective rocket system with a minimum life cycle cost is developed.

REFERENCES

1. S. S. Chin, *Missile Configuration Design,* McGraw-Hill, Inc., New York, NY, 1961, pp. 250-1.

2. G. A. Greathouse and C. J. Wessel, Eds., *Deterioration of Materials, Causes and Preventative Techniques,* Division of Chemistry and Chemical Technology, National Academy of Sciences, National Research Council, Washington, DC, 1954.

3. *The Applicability of Existing Truck and Rail Shock and Vibration Data to Freight Shipment Criteria,* Technical Report No. 58, Vitro Corporation of America , Silver Spring Laboratory, Silver Spring, MD, March 1954.

4. L. E. Lankin, *Packaging Criteria,* Shock and Vibration Bulletin No. 21, Research and Development Board, Department of Defense, Washington, DC, 1955.

5. K. W. Johnson, *Design Criteria for Military Equipment Transported by Common Carrier,* Shock and Vibration Bulletin No. 16, Research and Development Board, Department of Defense, Washington, DC, October 1950.

6. DARCOM-P 706-298, Engineering Design Handbook, *Rocket and Missile Container Engineering Guide,* January 1982.

7. G. E. Weeks and T. L. Cost, "Coupled-Interaction Launch Behavior of a Flexible Rocket and Flexible Launcher", Journal of Spacecraft and Rockets 17, 432-9 (September-October 1980).

8. E. F. Bruhn, *Analysis and Design of Flight Vehicle Structures,* Tri-State Offset Company, Cincinnati, OH, 1965, pp. A8-1-A8-44.

9. R. J. Roar-k and W. C. Young, *Formulas for Stress and Strain,* Fifth Edition, McGraw-Hill Book Company, Inc., New York, NY, 1975, pp. 445-512.

10. J. E. Fitzgerald and W. L. Hufferd, *Handbook for the Engineering Structural Analysis of Solid Propellants,* CPIA Publication 214, Chemical Propulsion Information Agency, Silver Spring, MD, 1971.

11. Joint Munition Effectiveness Manual, *Air-to-Surface Weapons, Effectiveness, Selection, and Requirements(U),* JMEM A-S, Department of Army FM101-50-1, Department of Air Force AFTM61A1-1-l-1, Department of Navy NAVAIROO-130-AS-I, Marine Corp Document FMFM5-2, 1975. (This document is classified CONFIDENTIAL.)

12. MIL-STD-810, *Military Standard Test Environments.*

13. F. Seeley and J. Smith, *Advanced Mechanics of Materials,* Second Edition, John Wiley and Sons, New York, NY, 1967, pp. 76-91.

14. MIL-HDBK-5, *Metallic Materials and Elements for Aerospace Vehicle Structures.*

15. *C. W.* Bert and W. S. Hyler, "Design Considerations in Material Selection for Rocket-Motor Cases", Journal of Spacecraft and Rockets 4,705-15 (June 1967).

16. L. H. Abraham, *Structural Design of Missiles and Spacecraft,* McGraw-Hill Book Company, New York, NY, 1962, pp. 20.5-34.

17. D. V. Rosato and C. S. Grove, Jr., *Filament Winding, Its Development, Manufacture, Applications, and Design,* John Wiley and Sons, Inc., New York, NY, 1964.

18. R. F. Shanley, *Weight Strength Analysis of Aircraft Structures,* Dover Publications, New York, NY, 1960, pp. 160-82.

19. J. E. Fitzgerald and W. L. Hufferd, *JANNAF Solid Propellant Structural Integrity Handbook,* CPIA Publication 230, Chemical Propulsion Information Agency, Silver Spring, MD, 1972.

20. C. E. Hartbower, *User's Requirements of Fracture Mechanics,* CPIA Publication 49B, Chemical Propulsion Information Agency, Silver Spring, MD, 1964, pp. 657-62.

21. *Fracture Toughness Testing and Its Application,* Report ASTM-STP-381, American Society for Testing and Materials, Philadelphia, PA, 1965.

22. Special ASTM Committee on Fracture Testing of High-Strength Materials, "Progress in Measuring Fracture Toughness and Using Fracture Mechanics", Materials Research Standard 4, 107-19 (March 1964).

23. C. F. Tiffany, *Fracture Control of Metallic Pressure Vessels,* Report SP-8040, National Aeronautics and Space Administration, Washington, DC, 1970.

24. W. F. Brown, Jr., and J. E. Srawley, *Plane-Strain Crack Toughness Testing of High-Strength Metallic Materials,* Report ASTM-STP-410, American Society for Testing and Materials, Philadelphia, PA, 1966.

25. V. Weiss, *Aerospace Structural Metals Handbook, Vol. I, Ferrous Alloys,* ASD-TDR-63-741, US Air Force Materials Laboratory, Wright-Patterson AFB, OH, March 1967.

26. V. Weiss, *Aerospace Structural Metals Handbook, Vol. II, Nonferrous Light Metal Alloys,* AS D-TDR-63-741, US Air Force Materials Laboratory, Wright-Patterson AFB, OH, March 1967.

27. B. P. Bardes, Ed., Metals Handbook, Vol. I, *Properties and Selection of Metals,* American Society for Metals, Metals Park, OH, 1961.

28. ASME Handbook, *Metals Engineering Design,* McGraw-Hill, New York, NY, 1958, pp. 3-400.

29. Williams, Landel, and Ferry, "The Temperature Dependence of Relaxation Mechanism in Amorphous Polymers and Other Glass-Forming Liquids", Journal of American Chemical Society 77, 3701-7 (19.5.5).

30. CPIA Publication No. 21, *Solid Propellant Mechanical Behavior Manual,* Chemical Propulsion Information Agency, Johns Hopkins University, Laurel, MD, 1963.

31. A. R. Maykut, "Cost vs Performance in Propulsion System Design", Journal of Spacecraft and Rockets 15, 100-4 (March-April 1978).

32. W. T. Thomson, *Vibration Theory and Application,* Prentice-Hall, Inc., Englewood Cliffs, NJ. May 1965.

33. L. Meirovitch, *Analytical Methods in Vibrations,* The Macmillan Co., New York, NY, 1971, pp. 132-66.

34. C. R. Freberg and E. N. Kember, *Elements of Mechanical Vibration,* John Wiley and Sons, New York, NY, 1955, pp. 141-7.

35. W. Pilkey, *et al., Structural Mechanics Computer Programs,* [University Press of Virginia, Charlottesville, VA, 1974.

36. C. M. Harris and C. E. Creole, *Shock and Vibration Handbook, Vol. I,* McGraw-Hill, New York, NY, 1961, pp. 8-1 to 8-54.

37. P. H. Durgin and E. L. Tilton, *The Effect of Camber and Twist on Wing Pressure Distributions for Mach Numbers from 2 to 7.5, Part I,* Report ASD-TDR-62-557, Aeropropulsion Laboratory, Wright-Patterson AFB, OH, December 1962.

38. P. A. Gaines, *A Method of Determining Aerodynamic-Influence Coefficients From Wind Tunnel Data for Wings at Supersonic Speeds,* Report TND-804, National Aeronautics and Space Administration, Washington, DC, 1961.

39. F. A. Woodward, "Aeroelastic Problems of Low Aspect Ratio Wings, Part II, Aerodynamic Forces on an Elastic Wing in Supersonic Flow", Aircraft Engineering XXVIII, 77-81 (March 1956).

40. V. W; Donato, *Hypersonic Aerothermoelastic Effects on Stability and Control,* Report TR-61-287, Aeropropulsion Laboratory, Wright-Patterson AFB, OH, 1962.

41. E. H. Dowell and H. M. Vos, "Theoretical and Experimental Panel Flutter Studies in the Mach Number Range 1.0 to 5.0", AIAA Journal 3, 2292-304 (December 1965).

42. E. H. Dowell, "Panel Flutter: A Review of the Aeroelastic Stability of Plates and Shells", AIAA Journal 8, 385-99 (March 1970).

43. L. L. Carter and R. O. Stearman, "Some Aspects of Cylindrical Shell Panel Flutter", AIAA Journal 6, 37-43 (January 1968).

44. Schideler, *et al., Flutter at Mach 3, Thermally Stressed Panels and Comparison With Theory for Panels With Edge Rotation Restraint,* Report TND-3498, National Aeronautics and Space Administration, Washington, DC, 1966.

45. J. J. Nichols, *Saturn V, S-IVB Panel Flutter Qualification Test,* Report TND-5439, National Aeronautics and Space Administration, Washington, DC, 1969.

46. E. H. Dowell, *et al., A Modern Course in Aeroelasticity,* Sijthoff and Noordhoff, Alphen aan den Rijn, The Netherlands, 1978, pp. 3-280.

47. H. Schlichting, *Boundary Layer Theory,* McGraw-Hill, New York, NY, 1968, pp. 265-326, 514-16.

48. R. B. Bird, et *al., Transport Phenomena,* John Wiley and Sons, New York, NY, 1960, pp. 426-.5.5.

49. Harris D. Weingold, *ICRPG Turbulent Boundary Layer Nozzle Analysis Computer Program,* Pratt and Whitney Aircraft Company, East Hartford, CT, July 1968.

50. D. E. Bartz, "A Simple Equation for Rapid Estimation of Rocket Nozzles Connective Heat Transfer Coefficients", Jet Propulsion 27, 49-51 (January 1957).

51. Incopera and DcWitt, *Fundamentals of Heat Transfer,* 1st Edition, John Wiley and Sons, New York NY, 1981, pp. 247-459, .541 -672.

52. J. P. Holman, *Heat Transfer,* McGraw-Hill, New York, NY, 1965, pp. 235-98.

53. F. Kreith, *Principles of Heat Transfer,* International Textbook Company, Scranton, PA, 1967, pp. 198-2.50.

54. W. M. Kays and M. E. Crawford, *Convective Heat and Mass Transfer,* McGraw-Hill, New York, NY, 1980, pp. 88-196, 204-36, 275-332.

55. R. Siegel and J. R. Howell, *Thermal Radiation Heat Transfer,* McGraw-Hill, New York, NY, 1981, pp. 8-351.

56. H. S. Carslaw and J. C. Jaeger, *Conduction of Heat in Solids,* Oxford University Press, New York, NY, 1959.

57. V. S. Arpaci, *Conduction Heat Transfer,* Addison-Wesley Publishing Company, Reading, MA, 1966, pp. 17-433.

58. P. J. Schneider, *Temperature Response Charts,* John Wiley and Sons, New York, NY, 1963, pp. 17-28.

59. JANNAF Handbook, *Rocket Exhaust Plume Technology,* Chapter 3, "Rocket Exhaust Plume Radiation", CPIA Publication 263, Chemical Propulsion Information Agency, Johns Hopkins (University, Laurel, MD, May 1980.

60. Russel A. Ellis, *et al., Solid Rocket Motor Nozzles,* NASA SP-8115, June 1975.

61. Laurent Lemoine, "Solid Rocket Nozzle Thermostructural Behavior", AIAA Paper No. 75-1339, AIAA/SAE 11th Propulsion Conference, Anaheim, CA, 29 September - 1 October 1975.

62. 1.. J. Jacques, "Genera] Principles for the Aerodynamic Design of Solid Rocket Nozzles", AIAA Paper No. 7.5-1338, AIAA/SAE 11th Propulsion Conference, Anaheim, CA, 29 September -1 October 1975.

63. G. R. Nickerson, *et al., A Computer Program for the Prediction of Solid Propellant Rocket Motor Performance,* Vols. I, II, and III, Report AFRPL-TR-80-34, Software and Engineering Associates, Santa Ana, CA, April 1981.

64. W. J. McGonnagle, *Nondestructive Testing,* Gordon and Breach Science Publishers, New York, NY, 1966, pp. 16-441.

65. Federal Test Method Standard 151B, *Metals, Test Methods,* Washington, DC, 1971.

66. M. Hetanyi, *Handbook of Experimental Stress Analysis,* John Wiley and Sons, New York, NY, 1950, pp. 28-71, 145-59, 301-635.

67. *Proceedings of the Society for Experimental Stress Analysis,* Addison-Wesley Publishing Co., Reading, MA.

CHAPTER 8

LAUNCHER CONSIDERATIONS

An overview of functions that the launcher may provide for the free rocket is presented. Factors that impose constraints on the launcher from mission definition and operational requirements viewpoints are discussed. Configurational options are Presented with topics relating to the analysis of launcher Performance. The Possible interfaces and interactions between the rocket and launcher are Presented, including mechanical and electrical inter-faces, exhaust impingement, generation of rocket spin, and other design considerations. Launch accuracy is defined, and launch accuracy estimation and measurement are addressed. The effects of rocket flexibility on launch accuracy are presented.

8-1 INTRODUCTION

This chapter provides information necessary to understand the interrelationship between the aerodynamically stabilized free flight rocket and its launching device. Rocket launchers are receiving increased attention at earlier phases of the rocket system design process—a change from past practices. Possible benefits of this approach are improved accuracy and optimization of total system cost. Maturation of the analysis techniques for prediction of launcher and rocket interaction has furthered this increased attention. The purpose of this chapter is to introduce the rocket designer to several launcher-related topics that may influence the design of the rocket.

For a period of time following ignition, the aerodynamically stabilized free flight rocket does not achieve sufficient velocity to provide the necessary aerodynamic stabilizing forces and moments. During this period the launcher provides the forces necessary to overcome the effects of gravity and rocket asymmetry and imbalance. In a real sense the launcher provides initial guidance for the free rocket by producing forces that tend to nullify or reduce the effect of rocket disturbances. When referring to a free rocket, the launch phase is sometimes referred to as the guidance phase.

During the guidance phase the launcher and rocket are both part of an interacting dynamic system. Manufacturing tolerances, mass asymmetries, and other phenomena produce forces normal to the intended path of the rocket. As shown in Chapter 4, many of these normal forces are random in nature. A properly designed launcher is capable of reducing the dispersion inherent in the rocket due to the random accumulation of tolerances and asymmetries (Refs. 1, 2, and 3). The proper selection of launcher structural compliance and control of the launcher motions induced by the rocket can enhance the system accuracy at rocket launch.

8-2 GENERAL

A rocket is primarily a powered air vehicle. As such, it must have some point of departure, or launch point. Rocket launchers have assumed many varied shapes and sizes; the choice depends on system requirements and intended uses. Before launching, the launcher supports the rocket and points it in the desired direction. During the launch phase, the launcher guides the rocket in its first motion and prevents small disturbances from diverting it from the desired path. The launcher can also be used for other purposes such as a packaging and shipping case, a transporter, and for imparting other desired motions (such as spin) to the rocket during the launch phase.

The several functions that a launcher may provide and how the system requirements influence launcher configuration are discussed in the paragraphs that follow.

8-2.1 LAUNCHER FUNCTIONS

There are two primary functions common to all rocket launchers. The first is to support the rocket and to point it in the intended direction of flight, i.e., aiming. The second function is to maintain the

desired aim until the rocket achieves sufficient velocity to operate without additional support, i.e., guidance.

The launcher may be required to provide many other functions that directly contribute to the accomplishment of the free rocket mission. These are discussed in the paragraphs that follow.

8-2.1.1 Environmental Protection and Conditioning

The launcher may be required to protect the rocket from the harsh environments it may encounter; these include meteorologyical and operational environments. Meteorological environments from which the launcher may be required to protect the rocket include rain, hail, and temperature extremes. Operational environments may include shock and vibration; exhaust from previously launched rockets; mud, sand, salt or dirt; as well as electromagnetic, chemical, bacteriologic-al, radiological, and other battlefield environments. The launcher may also be required to condition thermally all the rockets of a given salvo to minimum dispersion due to motor propellant temperature variations.

8-2.1.2 Test and Checkout

The operational readiness of a single rocket or multiple rockets can be tested by connections through the launcher. Electrical continuity, warhead type, condition of gas-generating devices, and internal temperature are some of the rocket readiness parameters the launcher may sense. This information may be displayed for crew considerations or transmitted to automatic equipment for processing.

8-2.1.3 Transportation

Launchers may be required to provide transportation of some form for the rocket. Rockets may be loaded into the launcher at one site, and the combination moved to another site for firing. Some possible forms of transport for the rocket-launcher combination are loading onto another form of conveyance such as a rail car or transport aircraft or towing by another vehicle such as a truck, or the rocket-launcher combination may be an integral part of a tracked or wheeled vehicle. In each case the launcher must provide the means of supporting and restraining the rocket from potentially damaging transportation shocks and vibrations. Such devices, sometimes called marching restraints, may be an integral part of the rocket supports or they may be separate devices installed at loading and removed before firing.

Some systems are mounted on self-propelled, tracked vehicles to provide maximum cross-country capability. The mobility characteristics of the rocket and launcher system are dictated by the system requirements and the rocket characteristics. Many medium and large size rocket systems must be air transportable. In this case, the designer must be conscious of both weight and size.

Aircraft systems are mounted on, or are an integral part of, the aircraft. Size, weight, and aerodynamic (characteristics of the configuration are paramount. A high drag design can slow an aircraft to the point at which range and payload are seriously degraded.

Rocket armament for a tank is also an integral part of its transporter. These systems require serious consideration of the available space within the tank and of the burned gases from the rocket. The launcher designer must provide the means of exhausting the gases, adequate room for the tank crew to operate, and facilities for handling and loading the rockets from within the tank. Considerable ingenuity is required to achieve an acceptable balance of space, weight, and safety for systems that are to be operated in such closely confined spaces.

8-2.1.4 Aiming

The launching device, usually a tube or rail, is supported on an upper carriage through a trunnion connection. This is the joint that provides for the angular elevation and depression of the device (change in quadrant elevation) neccssary to achieve varying ranges for the rocket. If the rocket system is large, a means of assisting the elevation change through gear trains, hydraulic pistons, or other suitable means, may be neccssary. The assist mechanism may be manually operated or may be mechanized for remote contro;, faster operation, or for lessening the burden on the launcher crew.

The launcher rail and upper carriage assembly are mounted on a lower carriage through a vertical pin connection around which it can rotate. This provides for changes in azimuth, or direction of fire.

Manual operations or mechanized means of assisting the motion may be provided. The lower carriage sometimes forms the base of the launcher. It may have wheels mounted to it for towing behind a vehicle; it may be mounted on a wheeled or tracked vehicle as a self-propelled unit; or it may, for small rocket systems, have legs or a base to stand directly on the ground.

Launchers may consist of less than these three basic components- rail, upper carriage, and lower carriage —but, of course, they must always have the rail or another device for supporting or guiding the rocket. For the antitank rocket systems of the M-72 LAW type, for which the launcher is a tube supported on the man's shoulder, the other components do not exist; the man provides the necessary motion for changing azimuth and quadrant elevation. In other systems the carriages may not exist as such, being reduced to nothing more than pinned joints or very simple support members. When the system is self-propelled, the vehicle on which it is mounted may constitute the lower carriage; however, it would not be identifiable as such if the launcher were removed. The particular system and the system requirements will determine how the launch device is to be supported and how the required motions are to be provided.

8-2.1.5 Ignition, Fuze Setting, and Arming

The launcher usually is required to provide the energy source necessary to ignite the rocket motor. The sequence of ignition for multiple rockets may be determined by the launcher. The number of rockets to be fired, accuracy, operational readiness, and warhead mix also may be factors in determining ignition sequence. Arming the rocket and setting the fuze may be performed prior to, during, or after ignition —depending on operational and crew safety considerations. Arming is the remet'al of impediments to the function of the rocket ordnance, including the rocket motor and warhead.

8-2.1.6 Initial Guidance and Spin

The launcher provides the initial guidance of the rocket until it achieves a velocity at which aerodynamic stabilizing forces may be used. The launcher may also be required to spin the rocket to reduce dispersion. Initial guidance and spin requirements and effects are discussed in detail in Chapter 4. Additional information on producing spin is contained in par. 8-3.5, "Rocket Spin Techniques".

8-2.2 SYSTEM CONSTRAINTS ON LAUNCHER

The selection of a launcher design is strongly influenced by considerations other than accuracy. Chapter 1 discussed some of the widely diverse applications of free rockets. Such diversity imposes widely different constraints upon the launcher design.

The degree of launcher mobility is imposed by the mission. By contrast, launchers used for research and development usually are fixed installations, while shoulder-fired antitank rockets are man-portable and, therefore, highly mobile. Further considerations regarding mobility may dictate whether the launcher must be carried, towed, or self-propelled and whether the type of carriage is wheeled, tracked, airborne, or man-portable.

Transportability requirements may impose constraints on launcher size, weight, and external configuration. Transportability constraints are concerned with transporting the launcher as cargo on, or within, a separate vehicle such as a truck or transport aircraft.

Since the rocket and launcher interact as a system during the guidance phase, the accuracy of the launching process is affected by both. A properly designed launcher can alleviate the random variations that are encountered from rocket to rocket. A system trade-off exists between reducing the rocket tolerances and the design, analysis, and manufacture of an optimum launcher. Either of these options may be at the expense of additional costs or other penalties. A trade-off of rocket costs for launcher costs exists when many rockets are fired from one launcher. Rockets are a high density item, and modest cost reductions on the rocket may justify additional launcher expenditures.

8-2.3 LAUNCHER CONFIGURATION

A wide range of configurational options are available to the rocket launcher system designer. In selecting the launcher configuration, the designer must always remain mindful of meeting the system

goals. This paragraph delineates the principal configuration options that are of primary importance to the system and the factors that influence the choice among such options.

8-2.3.1 Tactical Considerations

Operational requirements strong]y affect the selection of the final launcher configuration. The environments in which the launcher will be expected to function must be defined in order to assess properly the configurational options.

Meteorological and climatic considerations include temperature, humidity, and air- and water-borne abrasive and corrosive particles. Operational considerations include the degree of mobility and transportability required, logistic support, storage requirements, deployability, rapidity of response in launching a rocket, serviceability, maintainability, ease of operation, and expected battlefield conditions and survivability. The type of platform on which the launcher is to be placed is a further consideration in determining the launcher configuration. Typical launcher platforms include aircraft and helicopter store installation-points, tracked and wheeled vehicles, fixed installations, tripods, and humans.

8-2.3.2 Control of Aiming

One of the two essential functions of a launcher is supporting and aiming the rocket prior to launch. The launcher configuration is strongly influenced by the mass and mass distribution of the rocket or rockets to be launched and the degree of aiming accuracy desired. Schemes for control of aiming may be categorized as active, passive, or hybrid. A discussion of each scheme follows:

1. Passive control involves the use of the energy inherent within a system and/or its environment along with "natural" feedback to produce a desirable response of the system when acted upon by a disturbance. During guidance of a rocket by launcher constraint, the system consists of both the rocket and the launcher. Passive design techniques will produce launcher motions due to rocket imperfections which will compensate for rocket motions after launch due to these same imperfections. This compensation can either increase or decrease the impact dispersion (see Refs. 1, 2, and 3).

2. Active control of rocket aiming is accomplished by the use of a sensor and an external energy source to drive the system to a desired aim point and maintain this aim during the launch transient period. Active aiming systems are heavier and more expensive than the passive techniques.

3. Hybrid aiming control systems combine the good qualities of both the passive and active systems to achieve the desired result.

In all launcher design problems, passive techniques should be considered first to keep the requirements of an active system to a minimum for cost and weight considerations.

Control of aiming is sometimes referred to as control of launch accuracy. This is correct in the sense that elimination of aiming changes during a fire mission eliminates the dispersion that would have been introduced by such changes. Control of initial aiming primarily influences bias errors. By way of comparison, launcher, guidance techniques (par. 8-3.6) seek to influence precision errors.

Aiming considerations influence the selection of elevation and traverse mechanisms and their power requirements-i.e., manual, electrical, or hydraulic. The use of specific techniques, such as leveling jacks and suspension lockouts, also are influenced by aiming considerations.

8-2.3.3 Research Launchers

A research launcher is one that is designed to perform basic research in rocket technology. Configurationally, research rocket launchers generally consist of the same group of components as other military launchers.

Research launchers generally are constructed as permanent or semipermanent installations. They may provide better rigidity and may be better layed in azimuth and elevation. Weight constraints, rapidity of response, and simplicity of operation requirements may be relaxed since mobility is not a prime requisite.

Research launchers may be highly instrumental for testing purposes and may be required to provide some protection for any sensing and recording devices employed.

8-2.3.4 Tip-Off vs Nontip-Off

This term tip-off refers to the angular momentum acquired by a rocket due to the action of gravity when the forward rocket supports leave the launcher before the aft supports. Nontip-off refers to a rocket launch in which the fore and aft supports are released at the same time. Lip-off is a term applied to the tip-off effect when the launching device is a plane or trough. Lip-off commences when the rocket center of gravity moves off the plane of support. Fig. 8-1 illustrates these terms.

Care must be taken so that the rotation of the rocket due to tip-off will not cause collision of the rocket parts with the launcher. The tip-off effect can be alleviated by increasing the rocket acceleration level or the guidance length. Tip-off acts as a bias in the aiming of a rocket as shown in Chapter 4.

8-2.3.5 Supports

In launching a rocket, the manner in which the launch device (tube or rail) is supported is determined by the consideration of several factors. The launch device must possess sufficient structural strength to support the rocket without significant deformation (sag) and without being excessively heavy. Also the launch device must be sufficiently rigid to avoid excessive vibratory motions and loads, and to avoid contact with the rocket during the launching process. In achieving these goals, the launch device itself may be constructed to provide these requirements or a system of external supports may be used in conjunction with a more lightly constructed tube or rail.

Straight launch rails may use an external truss or frame system for additional strength and stiffness, A helical rail launcher may be attached to a box frame or inside a box tube. Tube launchers may have stiffeners, and support and attaching devices combined (see Fig. 8-2).

A combination of tube and rail design could be affected by forming rails inside the tube during the tube extrusion process. The tube could then be twisted to provide a helical rail.

Smooth bore tube launchers generally are easier to load than rail devices since it is not necessary to mate shoes or lugs to rails. While providing more protection to the rocket, tubes make access to the rocket difficult once it is loaded. Rail launchers can be constructed so that rocket fins can be accommodated in the flight position; tube launchers usually require that the fins be stored and then deployed after the rocket leaves the tube. Finally, there are practical limits to the size of a rocket which may be launched from a tube due to cost, strength, weight, straightness, and stiffness considerations.

8-2.3.6 Types of Launchers

Rockets may be designed and used in an almost unlimited number of ways; consequently, many basic launcher configurations have been developed to support this variety of use. Some of the basic configurational options are presented in this paragraph.

One configurational option is whether the launcher will handle single or multiple rounds. Single-round launchers are meant to launch one rocket. The launcher is then either discarded or reloaded. A multiple-round launcher may launch its rocket from multiple tubes or rails, one for each rocket, or it may launch a rack of several rockets in succession along the same tube or rail.

A container launcher may be a completely assembled rocket system or subassemblies that can be mated and function as a unit. More is said about container launchers in par. 8-3.3.

The intended use of a rocket may require that the launcher be man-portable, transportable by normal weight handling equipment, or airborne. Man-portable launchers are able to be hand carried, assembled, and fired in the field. Launchers may be self-propelled, towed, or attached to some other propelled vehicle such as a jeep, tank, or aircraft.

A zero-length launcher is one that supports the rocket but releases it from constraints immediately upon first rocket motion, i.e., with zero guidance. The rocket must be adequately supported on the launcher and must maintain its aim alignment until it is launched. In practice true zero-guidance-length launchers cannot be achieved; however, guidance lengths of no more than a few millimeters have been achieved. Mechanical considerations generally will dictate the size and length of the attaching devices which, in turn, determine the actual guidance length in zero-length launchers.
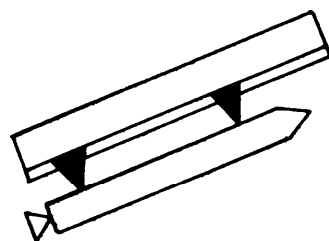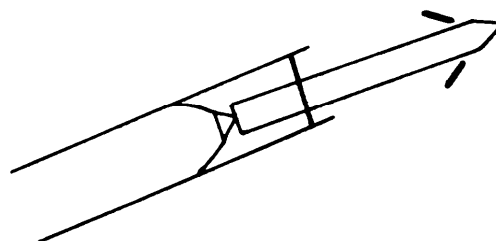
The zero-length launcher attempts to minimize the interaction of the rocket and launcher and, thereby, reduces launch errors. Other consequences of very short guidance lengths may be found in Chapter 4. Figs. 8-3 and 8-4 illustrate some of the combinations of launcher types discussed in this paragraph.
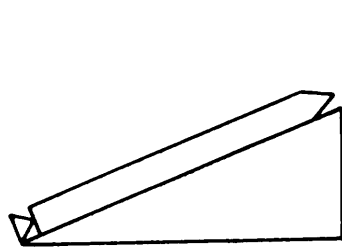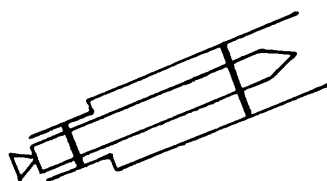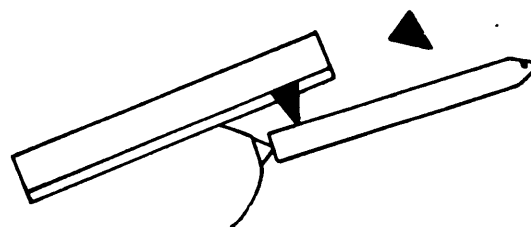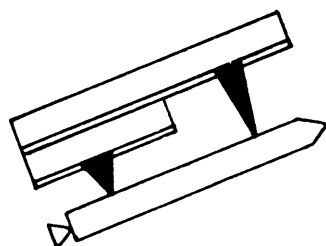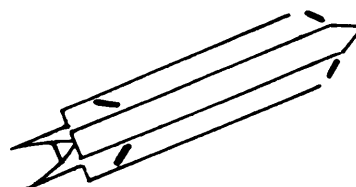
(A) Lip-Off
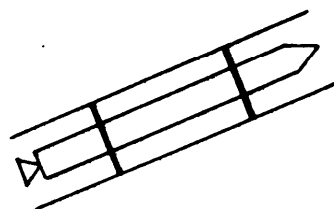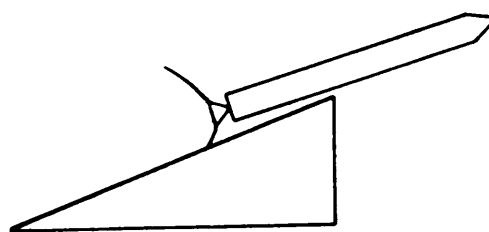
(B) Tip-Off From Tube

(C) Tip-Off From Rail

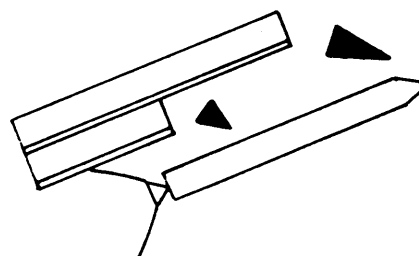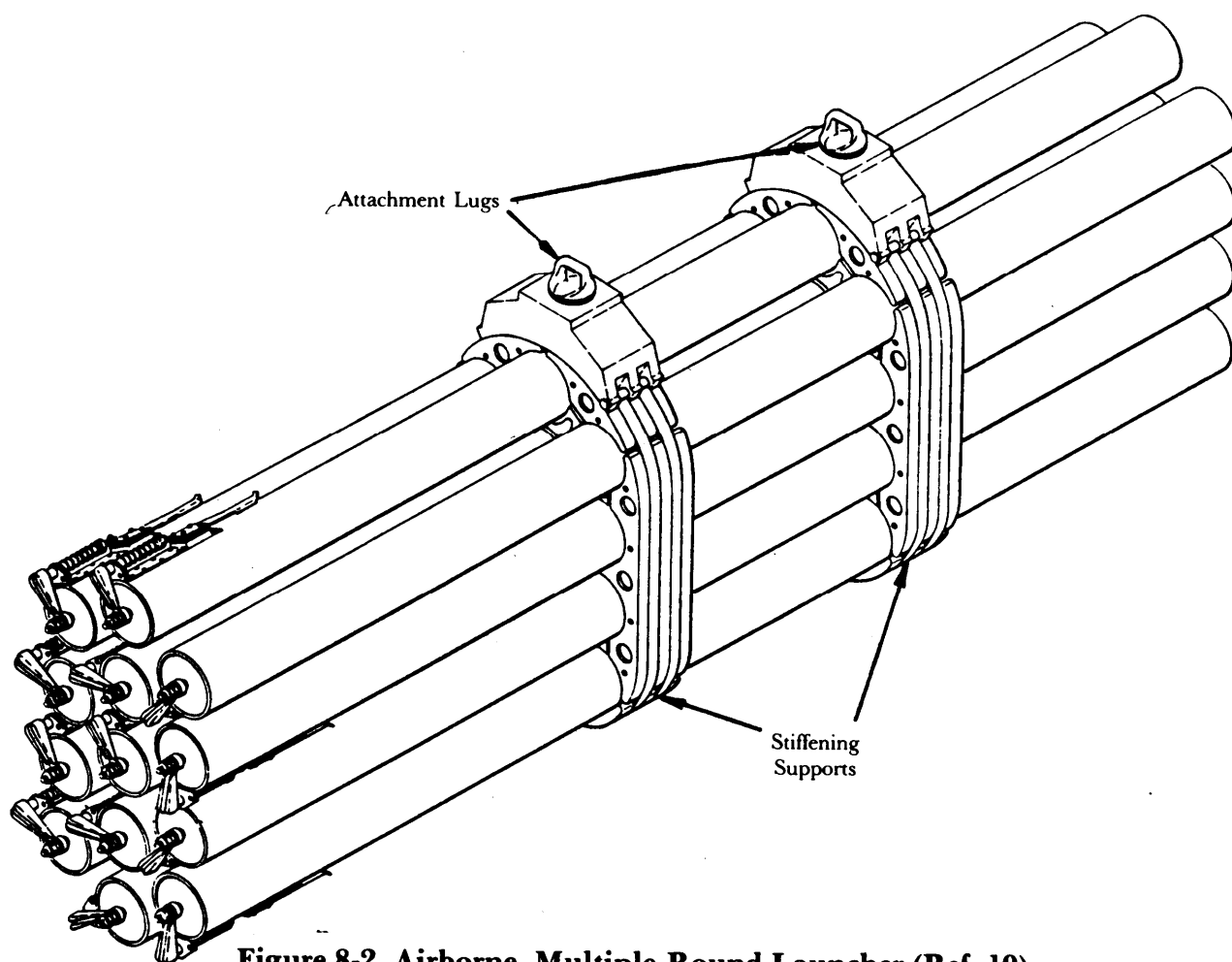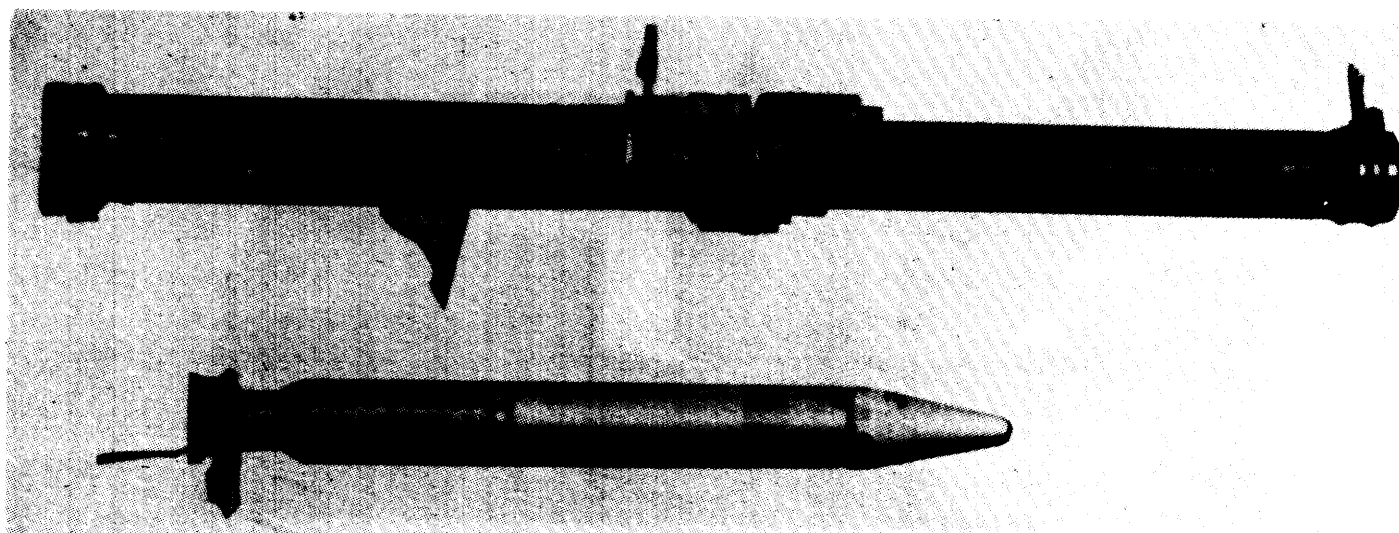(D) Nontip-Off From Tube

(E) Nontip-Off From Rail

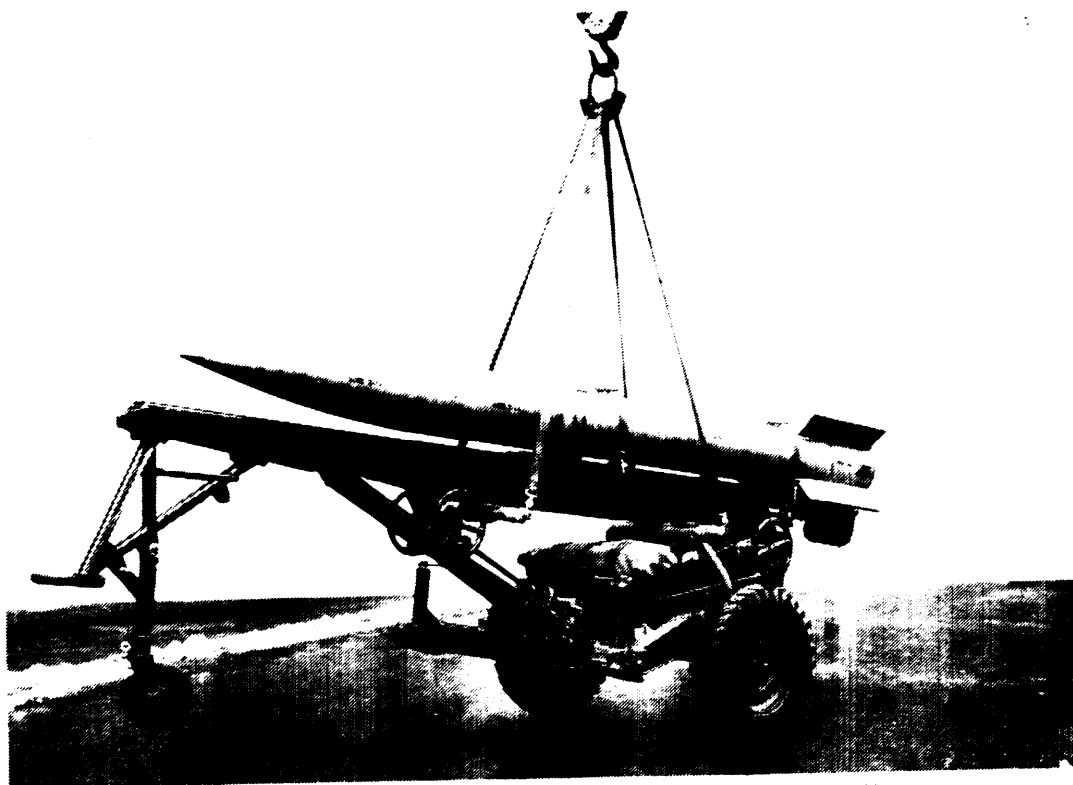**Figure 8-1. Examples of Tip-Off and Nontip-Off From Tubes and Rails**
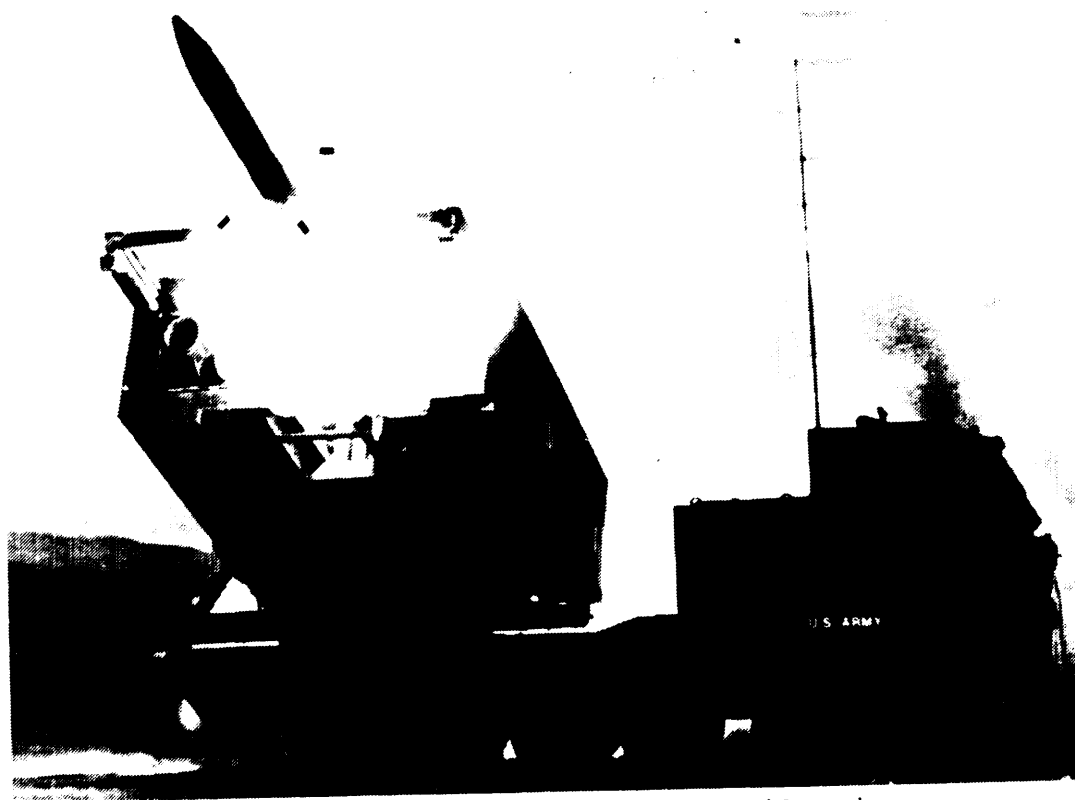
Figure 8-2. Airborne, Multiple-Round Launcher (Ref. 19)

(A) Man-Portable, Single-Round, Container Launcher
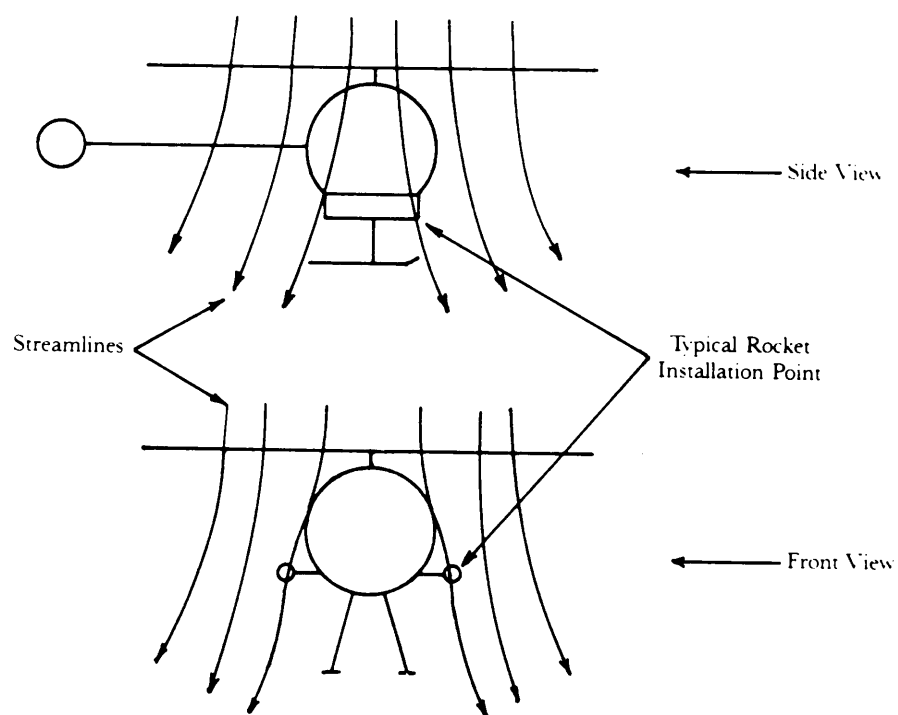
Figure 8-3. Examples of Launcher Types

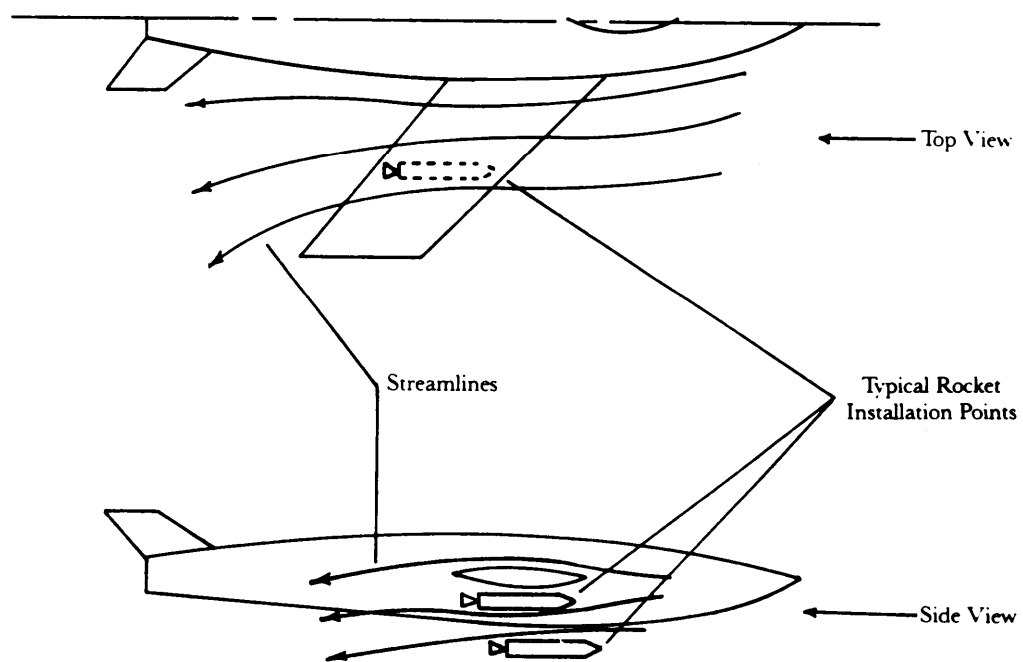(B) Towed, Single-Round Launcher With Helicopter Lift Sling

(C) Self-Propelled, Self-Loading, Multiple-Round Launcher

Figure 8-3. (cont'd)

(A) Rotary Wing

(B) Fixed Wing

Figure 8-4. Typical Aircraft Flow Fields

8-2.3.7 Air-to-Ground Launchers

Airbrrne rockets often are subjected to a more severe launch environment than their ground-launched counterparts. Airborne launchers must be strong to protect the rocket from flight airloads and vibrations, light so as not to overtax the capability of the aircraft, possess minimum frontal area to minimize the degradation in aircraft performance, and often be inexpensive since they may be jettisoned after use.

Airborne rocket launchers often are separate systems that are attached to the aircraft by lugs (see Fig. 8-2). The location of the attach point is often dictated by aerodynamic considerations and the availability of the ailcraft load-carrying structure. For these reasons, the possibility that flexible effects will influence launch accuracy are significant, especially in helicopters. Local airflow effects also act to influence launch accuracy. Fig. 8-4 illustrates typical idealized airflow for a fixed and rotary wing aircraft.

Rotary wing aircraft usually impose the more severe vibration environment on the rocket and launcher. Tqhis affects accuracy by altering the initial conditions for the rocket (see pars. 4-2.3 and 4-3.3). The magnitude and frequency content of the titrations are influenced by aircraft speed, maneuvering, gross payload being carried and its distribution, the installation location of the rocket launcher, and local flow.

Local flow, i.e., airflow in the vicinity of the rocket launcher, affects accuracy in the same manner as ground winds affect a ground launcher (see pars. 4-2.4 and 4-3.4). Factors influencing local flow include those that affect the vibration environment. These factors also include random eddies and turbulence in the area immediately in front of the launch tube.

Most airborne free rockets are tube launched. This protects the rocket while in transit and reduces the local flow effects of those when the rocket exits the tube.

Reduction in launch errors caused by vibration and local flow is realized by selecting a high initial thrust-to-mass ratio. This has the additional advantage of minimizing the exposure of the aircraft to the rocket exhaust.

8-2.4 LAUNCHER ANALYSIS

The selection and design of a launcher system can involve a myriad of trade-offs and compromises. Fig. 8-5 depicts the launch system analysis process. System requirements, physical data, expected disturbance environment, and other considerations are required as inputs to the analysis process. Basically, two types of output information are realized. The first type, such as expected variations in rocket velocity components and attitude rates, relates to system accuracy. The second type—such as configuration options, reaction times, and launcher reliability- influences the physical characteristics of the launcher.

During the launch of a rocket, the launcher provides forces and moments that direct the rocket along the intended path, i.e., launcher initial guidance. Chapter 4 points out that, due to manufacturing and assembly tolerances, no two rockets will require the same history of forces and moments to provide the needed guidance. The launcher must be able to provide a range of guidance forces and moments to accommodate variations in the rocket for which it was designed. Therefore, launcher design analysis should be included as one of the primary factors in the system accuracy improvement phase of development.

A well designed launcher can improve the overall accuracy of the system (Refs. 1, 2, and 3). Fig. 8-6(A) depicts a device analogous to the launcher and rocket system, although much simplified-a rail-type launcher with a center-of-gravity (CG) offset. The figure shows a rod, hinged at its base, allowing a rotational degree of freedom. The rod is further constrained in its motion by a spring (spring 1). The rocket is depicted as a mass that is free to slide along the rod at a point removed from the center of gravity of the mass. The mass is moeved along the rod by spring 2, which is also offset from the center of mass. When spring 2 is released, the rod will tend to rotate away from spring 1 as shown in Fig. 8-6(B). The model might appear as in Fig. 8-6(C) at the instant of mass release. Proper selection of the spring constants and the mass distributions can produce changes in the release direc-
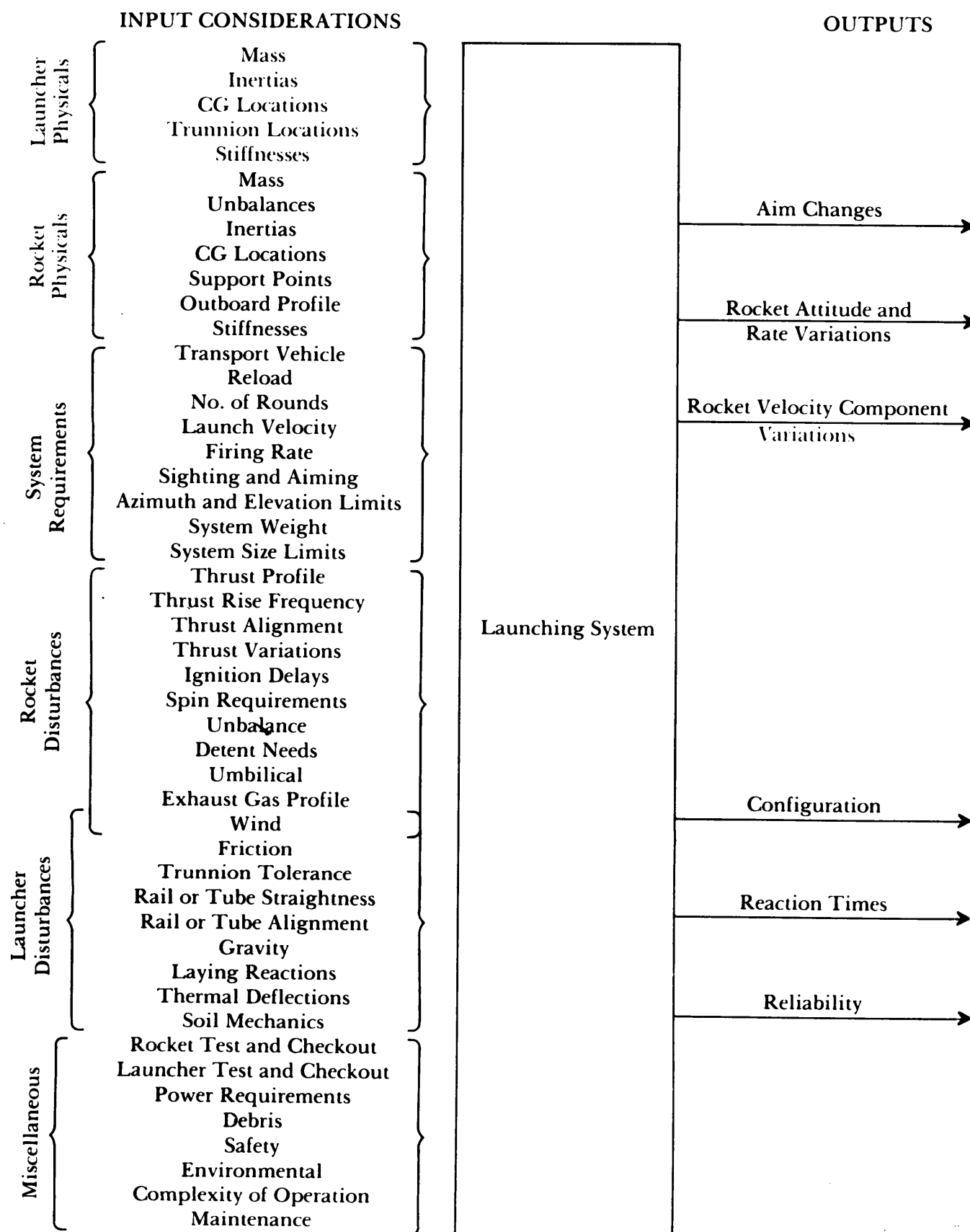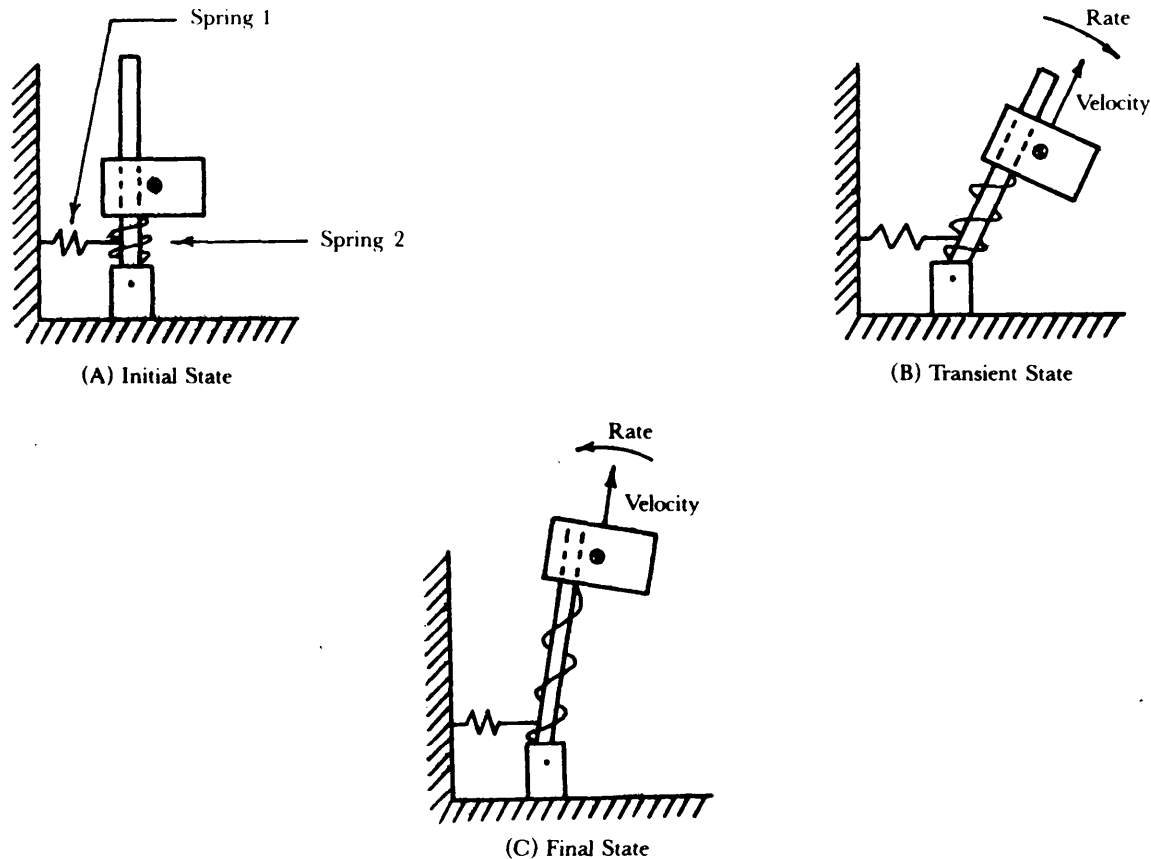
INPUT CONSIDERATIONS

OUTPUTS

Launcher Physicals
- Mass
- Inertias
- CG Locations
- Trunnion Locations
- Stiffnesses

Rocket Physicals
- Mass
- Unbalances
- Inertias
- CG Locations
- Support Points
- Outboard Profile
- Stiffnesses

System Requirements
- Transport Vehicle
- Reload
- No. of Rounds
- Launch Velocity
- Firing Rate
- Sighting and Aiming
- Azimuth and Elevation Limits
- System Weight
- System Size Limits

Rocket Disturbances
- Thrust Profile
- Thrust Rise Frequency
- Thrust Alignment
- Thrust Variations
- Ignition Delays
- Spin Requirements
- Unbalance
- Detent Needs
- Umbilical
- Exhaust Gas Profile

Launcher Disturbances
- Wind
- Friction
- Trunnion Tolerance
- Rail or Tube Straightness
- Rail or Tube Alignment
- Gravity
- Laying Reactions
- Thermal Deflections
- Soil Mechanics

Miscellaneous
- Rocket Test and Checkout
- Launcher Test and Checkout
- Power Requirements
- Debris
- Safety
- Environmental
- Complexity of Operation
- Maintenance

Launching System

OUTPUTS
- Aim Changes
- Rocket Attitude and Rate Variations
- Rocket Velocity Component Variations
- Configuration
- Reaction Times
- Reliability

Figure 8-5. Considerations in the Launcher Analysis Process

Figure 8-6. Two-Degree-of-Freedom Launcher Analog

tion and velocity components that would tend to offset each other. This is passive launch control.

In extending this model to be more analogous to the case faced by the launcher designer, the considerations that follow must be included. The mass, spring constants, and distances from the center of mass to the rod are not precisely known. Each of these parameters, in the rocket analogy, is usually describable only in terms of an expected value and a distribution (see Chapter 4). The designer is now faced with selecting a spring constant that will eject the mass so that the expected value of the direction is along the intended direction of flight. The model may be further refined by the addition of damping, modification of the hinge point, inclusion of articulating rods instead of a single rod, additional or nonlinear springs, etc. Careful analysis of such modifications should result in a design that would substantially reduce the dispersion of the ejection direction (Ref. 2).

As previously stated, the model used for the rocket and launcher system in this example is a decidedly simple one. More elaborate models potentially offer more useful information. This is accomplished by developing an analogous system that more closely resembles the physical system. Another method of elaboration is by increasing the degrees of freedom (DOF) in the model. DOF in this sense is any one of tile number of ways in which the space configuration of a mechanical system may change. The mechanical analog of Fig. 8-6 possesses 2-DOF i.e., rotation of the mass about the hinge and translation of the mass along the rod.

Pats. 4-5.2 and 4-5.3 plesent examples of analogs of physical systems with 6- and 3-DOF, respectively. Generally, the more DOF a model possesses, the closer the model can be made to represent the physical system.

Low-DOF models are useful in that they can aid in defining the basic motions, amplitudes, and magnitudes of forces to be expected. Low-D0F models generally require less knowledge of the system parameters and are useful for parametric and trade-off studies.

High-DOF models provide more detailed information on the forces and motions expected and require that more information about the system be known or estimated. Further, the cause and effect relationships in high-DOF models may be less obvious than they are in 1ow-DOF models.

8-3 INTERFACE CONSIDERATIONS

In considering the rocket and launcher as an interacting system, there are several interfaces and interactions which must be addressed. Interfaces are points at which the rocket and launcher physically react with each other. For the purposes of this paragraph, these interfaces are categorized as being mechanical in nature, electrical in nature, or resulting from the interaction of the rocket and launcher with the rocket exhaust gases.

An example of a mechanical interface would be rocket supports. The device that transmits the motor ignition signal from the launcher to rocket would be an example of an electrical interface. The types of interfaces used affect both the launcher and rocket configurations.

In the subparagraphs that follow several mechanical and electrical interfaces will be defined and discussed. Protective container launchers will be discussed as a class of rocket, and the launcher system and its functions will be defined. The interaction of the rocket and launcher due to exhaust impingement will be explained. The effect of impingement on launcher and rocket motion, accuracy, and other effects will be discussed.

A discusson of launcher and rocket motions resulting from mutual interactions is presented in Chapter 4.

8-3.1 MECHANICAL INTERFACES

Mechanical interfaces between the rocket and launcher are used to accomplish many different functions. Generally, these interfaces restrict the motion of the rocket, such as transportation restraints; induce a desired motion, such as helical rails to provide spin; or protect the rocket from damage, such as a sleeve in a tube launcher. Several mechanical interfaces will be introduced in this paragrah and their intended use or function will be given. Some of the names of these devices have been carried over from artillery application, and their current use for defining a specific mechanism is becoming imprecise.

Mechanical interfaces may be used with both tube- and rail-launched rockets. The trade-off process for the selection of tube- or rail-launched rockets is influenced by many factors. The most influential of these factors is the restraining forces the launcher must supply. Rail launchers usually are required when the rockets are more massive, when mechanical devices are used to induce rocket spin, or when rigidity is required as for long launcher lengths. Tube launchers usually are employed with smaller rockets and usually are from one to several times the length of the rocket. In a tube launcher the rocket may be supported by and move along the total inner surface of the tube without other mechanical interfacing.

A rocket support is any device that carries the weight of the rocket. Sometimes the term rocket support is used to describe a passive element in the launcher system as illustrated in Fig. 8-7(A).

A rail is a bar forming a track along which a rocket slides during launch. The rocket is usually attached to the rail by a shoe that usually grasps the rail in some fashion. These shoes are either fixed to the rocket or are allowed to roll or slide around the rocket circumference. Rails may be twisted into a 'helical spiral to induce rocket spin. Fig. 8-7(C) illustrates the concept of straight and helical rails and shoes. The figure also depicts one form of lug, projection or handle by which something may be grasped, as in Fig. 8-2, or it may be a small projecting part of a larger mechanism as in Fig. 8-7(C).

Both tube and rail launchers may use a device that locks or unlocks a specific movement; such a device is called a detent (see Fig. 8-7(B)).

An umbilical is a servicing electrical and/or fluid line between the launcher or other ground support equipment and the rocket. It is usually disconnected immediately prior to, or at the instant of, ignition, but it also may be disconnected as the rocket moves along the launcher.

(A) Passive Element

(B) Mechanical and Electrical Interfaces (Ref. 19)

(C) Shoes, Rails, and Lugs (Ref. 20)
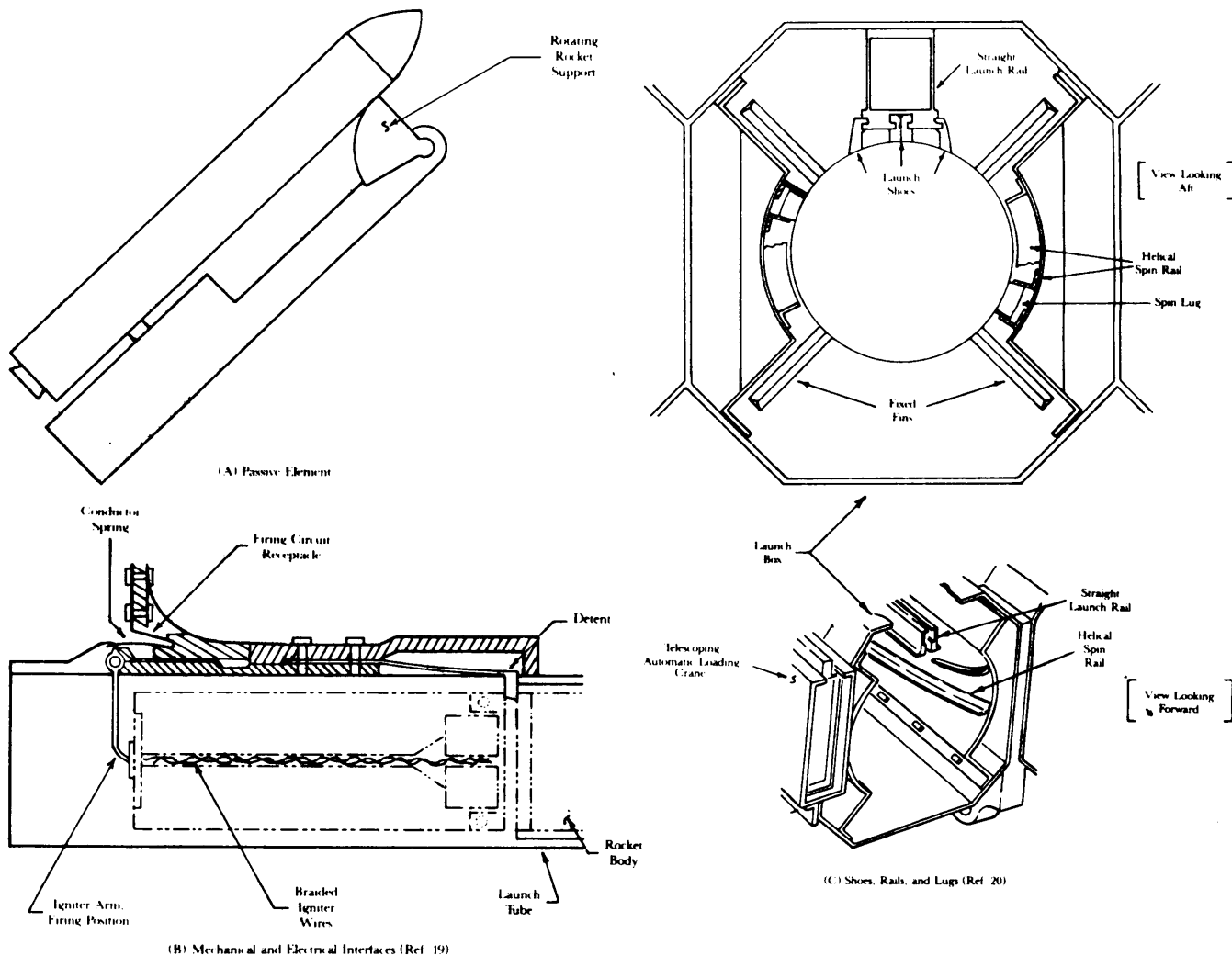
Figure 8-7. Examples of Mechanical Interfaces

Tube launchers may use several devices, subsequently defined, for supporting the rocket in the tube or for protecting the rocket from sliding friction. The term bore-rider, usually passive, refers to any device that literally rides against the inside of the tube. A sabot, usually discarded when free of the tube, is a lightw'eight carrier that positions a subcaliber projectile against a tube and may be used to engage grooves to impart spin. Three parts of a sabot, being discarded, can be seen in Fig. 8-3(C). A bourrelet is a raised band of material spanning the gap between the rocket and the tube. A bourrelet may serve as a gas seal and is usually not discarded after the projectile leaves the tube and in fact may be part of the rocket structure.

other mechanical interfaces serve to protect the rocket by isolating it from the shock and vibration environment of launch or to constrain the rocket while it is being transported in mobile launchers.

8-3.2 ELECTRICAL INTERFACES

The launcher may provide several electrical functions. These functions, described in the paragraphs that follow, may be numerous and varied depending on the particular requirements of the rocket.

Electrical signals and power may be delivered to the rocket through an umbilical. For the purposes of this paragraph, an umbilical is any electrical connection between the rocket and launcher carried by wire or cable. The size and shape of the umbilical and its method of attachment to the rocket are influenced by the amount of current required, number of functions performed, operational and environmental considerations, and method of disconnect. Umbilicals may be disconnected prior to launch

8-14

or as a part of the launch process. The umbilical may move with the rocket until the cable is payed out, at which point the connector is pulled out of the receptacle. An umbilical also may be removed by a lanyard at some point prior to launch. Umbilicals that are large or require strong connectors may be disconnected by explosive bolts or cut by pyrotechnically activated knives or guillotines. If the umbilical is disconnected prior to launch, all further power requirements are placed upon internal rocket power sources such as batteries or gas-powered generator devices.

The most common electrical function provided by the launcher is rocket motor ignition. Fig. 8-7(B) illustrates the principal components of an electrically activated rocket motor ignition system. An electrical connector (not shown) is inserted in the firing circuit receptacle. Simultaneously, the conductor spring is forced down, and a cam-lobe on the igniter arm rotates the arm into contact with the igniter wires that carry the electrical current to the rocket motor.

The launcher may interface with the rocket ordnance to provide safing, arming, and fuze setting functions. Arming is the act of removing safety devices to enable a dangerous device to operate; this action could apply to the operation of the rocket motor or the warhead, or both. An electrical signal may initiate the removal of a safing mechanism from the detonation chain of a warhead or the ignition chain of a rocket motor. Conversely, safing is the act of returning the dangerous device to an inoperable condition. The launcher may be required to provide safing after an aborted fire mission in which the rocket had been previously armed. A fuze is the component that recognizes the optimum time for initiation of the explosive elements leading to the detonation of the warhead and initiates such an action. The launcher may send electrical signals to start a timer in the fuzing device. After the elapse of a predetermined amount of time, the timer emits a signal to detonate the warhead.

The launcher may be used to perform test and checkout functions for the rocket(s) that have been, or are about to be, loaded into it. Equipment associated with the launcher may be used to perform continuity checks of internal wiring, to detect and to display the condition of internal devices such as batteries and gas bottles, and to carry out many other types of checks to determine whether a particular rocket is ready for operation.

With the advent of microprocessors and other low-cost microelectronic devices, the test and checkout interface between the launcher and rocket is becoming more extensive and sophisticated.

8-3.3 CONTAINER LAUNCHERS

Container launchers are a class of launchers which launch the rocket and provide protection from climatic, physical, and mechanical environments during tactical operations, resupply, and storage. The container concept is applicable to all classes of rockets from manually handled and shoulder-fired to mechanically handled and fired from self-propelled launching platforms (Ref. 4).

Protective container launchers are particularly applicable to a rocket system designed to be carried and fired by an individual gunner or to a system that can be mounted manually on a launching platform. Provided the rocket is completely assembled, protective launchers are also applicable to heavier rockets that require weight handling equipment for loading and unloading the mobile launcher. In some instances a rocket might be assembled more easily by a sectionalized, protective launcher than by conventional methods. A protective launcher may be less attractive when the fielded cost of the protective launcher approaches the cost of a reusable launcher and conventional containers. The intended military characteristics of the system must be considered before a decision can be reached on the use of a protective launcher for a particular rocket system.

The advantages of container launchers are several. The rocket is protected from the elements and the shock and vibration of handling and transport, thereby increasing its reliability and useful life expectancy. Handling of rockets is minimized if the container holds several rockets—e.g., external stores on an aircraft or large, mechanically loaded mobile launchers. Test and checkout functions and electrical ignition can be performed by a single interconnect to the container rather than by several interconnects to individual rockets. Container launchers are also attractive as rockets and rocket components, such as microelectronics, become more fragile.

The disadvantages of container launchers include the additional cost, the additional mass of the

protective material and container which must be transported, and the difficulty in visual inspection of the rockets.

8-3.4 ROCKET EXHAUST IMPINGEMENT

The firing of rockets from launchers is accompanied by strong interactions with the walls of the launch tubes and other structural elements. The next two paragraphs will discuss these phenomena and their impact on launcher related topics.

8-3.4.1 Internal Exhaust Impingement

Fig. 8-8 depicts the nozzle exhaust flow in a launch tube that has a gas seal between the rocket body and the tube. The flow experts pressure along the walls of the tube; other consequences of this flow are heating effects and erosion of the tube material. The patterns of impingement and reflected shock waves strongly influence the pressures and temperatures which occur.

Further complitations are introduced because the flow is not exactly axisymmetric, and, therefore, shock impingement points may not be perfectly circular around the circumference of the tube. All of these effects plus the initial ignition transient (shock) can introduce reaction forces and moments that are not precisely deter-minable for each rocket launched.

Two added phenomena can occur when a gap exists between the rocket and the tube as shown in Fig. 8-9. In this case an annual cylinder of space exists between the rocket and the tube, and aspiration
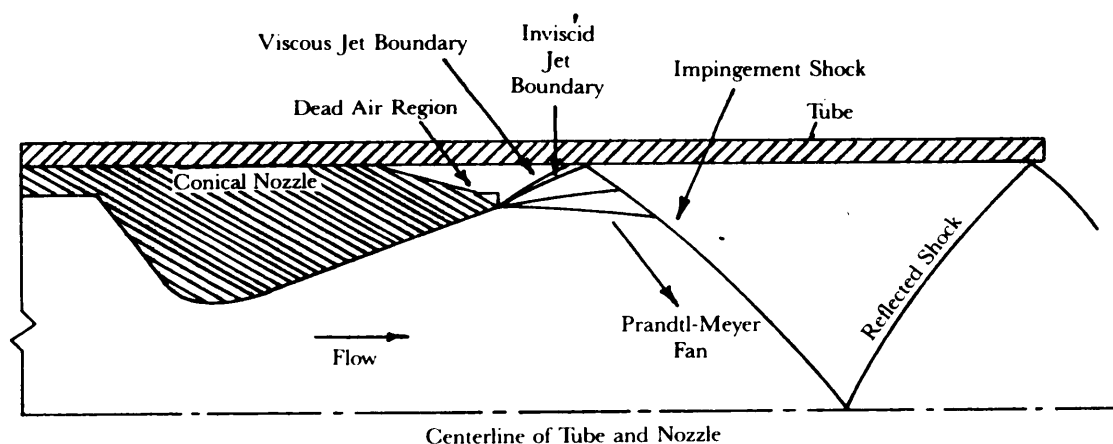
Figure 8-8. Elements of Rocket Plume Interaction With Launch Tube

(A) Exhaust Into Cylindrical Aft-Tube

(B) Exhaust Interacting With Tube Constriction
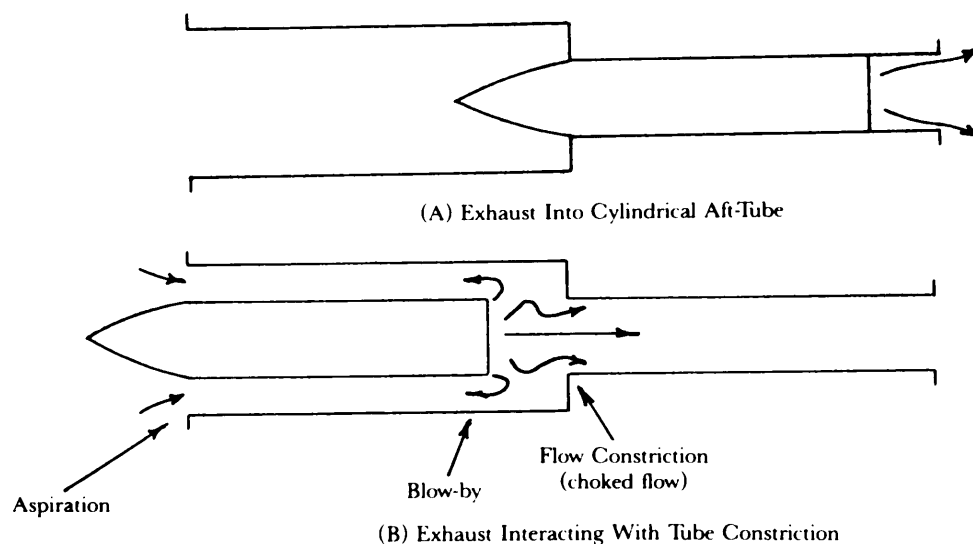
Figure 8-9. Rocket Exhaust Interaction in a Constrictive, Nontip-Off Tube

8-16

or blowby may occur (Refs. 5 and 6). Aspiration is the entraining of air into the front of the launch tube which flows around the rocket and is ejected with the exhaust through the rear of the tube. Blowby occurs when the rocket exhaust encounters adverse pressure gradients and a portion of the exhaust flows upstream, around the rocket, and out the front of the launch tube. Both aspiration and blowby introduce aerodynamic forces and moments on the rocket, These forces affect accuracy by introducing additional motion to the launcher through mechanical interfaces or by translation of the rocket itself if the rocket is free of mechanical interfacing within the tube.

The effect of the flow interactions, the motor ignition shock, the establishment of the shock wave pattern in the launch tube, the movement of the rocket and shock wave pattern through the tube, and the effects of aspiration and blowby generate a time- and position-related pattern of forces and moments which arc transmitted to the launcher. Launcher motion occurs because the launcher cannot instantaneously and exactly respond to these disturbances by applying nullifying forces and moments. The physical configuration of the launcher and its mechanical compliance and damping characteristics determine the degree and extent of the motion encountered.

8-3.4.2 External Exhaust Impingement

For the purposes of this paragraph external impingement occurs when the exhaust gases are not constrained, i.e., the gases may expand freely to atmospheric pressure. Fig. 8-3(C) illustrates external exhaust impingement on a launcher. A further example of external impingement would be a rail-launched rocket for which the rail is supported by an open latticework of simple, structural members. Rocket blast loads is a term sometimes used in referring to external exhaust impingement. The principal effects of external impingement are induced motion of the launcher and erosion of the launcher structure.

In effect, the rocket gases are a high velocity wind flowing around the structure of the launcher. This flow induces aerodynamic forces on the affected launcher components to produce launcher motion,

Rocket exhaust gases have a very high temperature, are very active chemically, and may contain high energy particles of aluminum compounds or other solids. These characteristics produce a highly erosive environment for the affected launcher components. Care must be exercised in the design of such components so that they can withstand the exhaust environment; otherwise, some form of protection must be provided.'

The accuracy of the rocket launch is affected by the degree of exhaust-induced motion. Also exhaust impingement tends to increase the length of time that external forces are being applied to the launcher. Residual vibration of the launcher is of concern in determining the timing of multiple launches. A further concern in multiple launches is insuring that the second and succeeding rockets are not launched into the exhaust environment of a previous rocket.

Two transient exhaust gas phenomena may occur that can affect the accuracy of rockets. The first of these is muzzle blast. As the nozzle exit plane approaches the end of a launch tube (the muzzle), some of the exhaust gas will escape in the direction of rocket motion. The circumferential pattern of this escaped gas is not generally symmetrical. The exhaust gases interact with the aft end of the rocket to alter the local aerodynamics, thereby inducing rocket motions. The second interaction of exhaust gases at launch is known as splash back. Splash back is a pressure propagation affecting the rocket plume and the aft rocket aerodynamics in much the same manner as muzzle blast, except that it occurs for varying distances beyond the nozzle exit point.

8-3.5 ROCKET SPIN TECHNIQUES

Spinning a free flight rocket during its boost phase significantly reduces dispersion at the warhead event; Chapter 4 discusses this technique of dispersion reduction in detail. Par. 4-4.2.6 describes and discusses several spin techniques, their methods of operation, and the consequences of their use. This paragraph discusses the impact and consequences to the launcher of the spin techniques described in Chapter 4.

Methods of inducing spin may be divided into two groups by considering whether the spin is induced by the rocket or by the launcher. The impact of each technique on the launcher is discussed.

Rocket-induced spin usually is accomplished by deflecting the rocket exhaust via jet vanes; by fluted, scarfed, or canted nozzles; or by separate rocket motors. Rocket motors, instead of fins, are selected for producing launch spin because the fins are relatively ineffective during the launch phase and fins are often required to be stowed during launch for packaging and protection consideration. The advantages of rocket-inducted spin arise from the consideration that the launcher may be lighter and less complex as will be seen from the ensuing discussion of launcher-induced spin. This is an overriding consideration in man-mobile or airborne launchers where heavy, mechanically complex launchers have severe limitations. Disadvantages of rocket-induced spin are increased complexity of rocket manufacture and a more severe exhaust erosion environment due to transverse components of exhaust flow.

The most common technique for launcher-induced spin is the helical rail. In this technique, the rocket is constrained to follow a rail that has been formed into a helix. The spin rail may be a separate device, as shown in Fig. 8-7(C), or the launch rail may be formed into a helix, and the functions of launch and spin rails combined. Rails may be extruded on the interior surface of a launch tube, and the tube may be twisted into a helical shape. This method seeks to combine the advantages of tube and rail launchers.

Several unique launcher-induced spin methods have been developed or considered. Two such methods are prespin automatic dynamic alignment (PADA) and spin on straight rail (SOSR). In both of these concepts, prior to ignition, a drive mechanism is used to spin the rocket while on the launcher. SOSR is more fully described in par. 4-4.2.6.2, and PADA is described in par. 4-4.2.6.7.

In launcher-inducted spin systems the launcher must be constructed to accommodate both the spin drive mechanism and the reaction forces during spin-up. Therefore, these launchers must be stronger and heavier than rocket-induced spin launchers. For systems in which the rocket spin is drive by belts or gears, a power source and drive train add additional weight and complexity to the launcher.

8-3.6 LAUNCHER GUIDANCE SCHEMES

During the initial motion along or through the launcher, the rocket produces forces and moments which tend to displace the rocket from its intended path. The launcher must provide forces and moments which tend to cancel or to minimize those produced by the rocket. The action of sensing and providing these reactive forces may be categorized as providing guidance to the rocket.

Guidance may be provided via active or passive sensing of rocket disturbance. Passive launcher guidance, in principal, does not attempt to sense the disturbances directly. Rather, the rocket disturbances are allowed to act on the physical components of the launcher and, thereby, produce launcher motion. The physical components of the launcher are so designed and arranged that, when displaced, they produce an opposing action to minimize the motion or its effect.

Active launcher guidance provides some means of sensing unintended rocket motion and produces a nullifying set of forces on the rocket with a magnitude or duration predetermined by the careful analysis and design of a guidance law. The essential difference is that active guidance uses an external source of energy other than the rocket motor in producing the corrective forces.

Both active and passive guidance techniques seek to influence the precision errors in the rocket weapon system. By way of comparison, active and passive controls of aiming (par. 8-2.3.2) seek to influence system bias errors.

8-3.7 ROCKET FIN CONSIDERATIONS

The size and shape of a rocket fin is determined primarily by aerodynamic considerations. The fin must provide the required stability at tolerable drag levels. Several other factors-such as stability tailoring requirements, packaging, and transportation —influence the final fin shape and sire. Chapter 5 discusses fin application in detail.

Since fins increase the overall diameter of the rocket configuration, stowing—followed by eventual deployment of the fins- is a common technique. Fig. 8-10 illustrates some of the methods in which fins may be stowed and deployed.

Stowing the fins during launch has a beneficial effect on the launcher because it minimizes the size and may allow a simpler structural configuration. Fig. 8-7(C) shows a rocket with fixed fins. In this

(A) Folding Fins

(B) Wrap-Around Fins

(C) Tangential Fins

(D) Pop-Out Fins
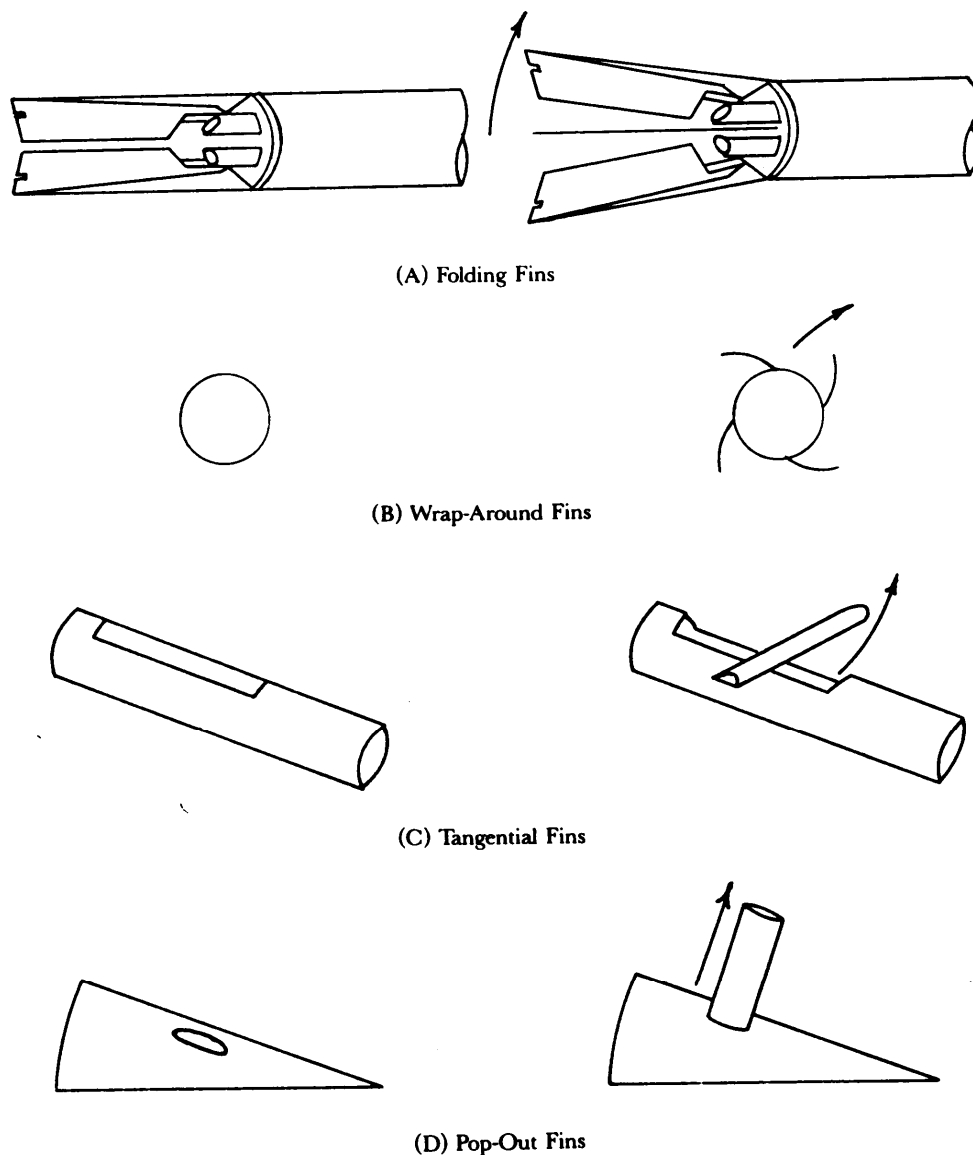
Figure 8-10. Fin Deployment Schemes

technique clearance must be provided for the fins within the launch box. Clearance problems are further complicated if spin is required during the launch phase.

Deployable fins usually are designed so that the overall diameter of the stowed fins does not exceed the overall rocket diameter. This allows the use of cylindrical tubes as launch devices. Rockets also may be more closely spaced in multirocket launchers when the fins are initially stowed.

In most rocket configurations fins are located in the same general area as the motor and nozzle. This competition for space has produced the variety of deployment schemes, illustrated by Fig. 8-10, to be considered.

Fins may be relatively fragile, and any damage to them in the launching process, however slight, may produce unacceptable performance of the rocket.

Fins are usually deployed by a preloaded spring mechanism upon release of a detent device. The release may be initiated by a timed electrical signal or by a trip mechanism as the rocket leaves the launcher. The launch tube may be used as the restraining mechanism, and the fins are deployed as they leave the tube.

8-4 LAUNCH ACCURACY

In Chapter 4, accuraty was defined as the measure of the ability of the rocket system to position the payload at a given point at the warhead event. Pars. 4-2.2 and 4-2.3 defined the prelaunch and launch phases of flight and discussed sources of dispersion and their effects on system accuracy. For the purposes of this paragraph launch-phase accuracy is defined as the measure of the ability of a launcher to position a rocket, at the end of the launch phase of flight. in a specified direction and with a specified angular rate about a transverse rocket axis. This definition is consistent with the principals introduced in par. 4-2.3.

The reader is referred to par. 4-2.1 for a general discusson of error sources and definitions, and to par. 4-4.1 for important considerations in maintaining a balanced approach to the reduction of launcher and rocket errors and dispersion.

8-4.1 MAJOR FACTORS AFFECTING LAUNCH ACCURACY

In general, aiming errors can be discussed in one or more of the following categories:

1. Icomplete knowledge or incorrect determination of the location of the launcher or the target

2. Incomplete knowledge or incorrect determination of the environment to which a given rocket will be subjected during its flight from launcher to target

3. Inability to point precisely the launch device in a predetermined direction. This category is the only one of the three which is universally applied to the launcher (see par. 4-4.6). Rocket pointing errors are influenced by the mechanization of the traversing and elevation elements of the launcher, structural sag in the tube or rail elements, and accuracy of the elevation and azimuth measurement devices. Systematic measurement and testing of the launcher can significanty reduce fixed biases, e.g., a misaligned launch tube with respect to the sighting device. Other pointing error sources, such as asymmetric heat expansion of a launcher due to the sun or previous rocket launches, are not as easily accounted for. However, careful attention to manufacturing procedures and basic structural design can reduce the effect of these random bias errors.

It is useful to approach the launch phase errors by visualizing the rocket and launcher as an interacting system. Each rocket will possess specific thrust and mass characteristics that make it slightly different from the previous, or next, rocket launcher. These characteristics produce differences in acceleration level, static and dynamic imbalance, and thrust misalignment. Movement is induced in the launcher based on the magnitude and orientations of the rocket characteristics, and the dictates of thee launcher design. Proper launch design can result in significant improvement in the accuracy of the overall system at payload disposition.

A balanced approach between launcher design and the rocket dispersion reduction techniques of Chapter 4 allows more flexibility in system accuracy design than the use of the Chapter 4 techniques alone. Fig. 8-5 illustrates the complex interaction of requirements in launcher analysis, of which accuracy is only one. Launcher and rocket costs, operational requirements, and intended application must be considered in providing an effective launcher and rocket system.

8-4.2 LAUNCH ACCURACY ESTIMATION

The analytic estimation of launch accuracy has most often been accomplished by defining the accuracy at the and of the launch phase. Extension of the accuracy estimate to the termination of flight is then accomplished by statistically combining this estimate with independent estimates for the boost and ballistic phases. A second technique involves simulation of the launcher and rocket from ignition to flight termination and the recording of the termination points. The accuracy estimates would then be described by the statistical distribution of the recorded points. Parameters other than those associated with the launcher and rocket—such as ground and ballstic winds and atmospheric variability- should be excluded from the analysis since the are more pertinent to system accuracy than to launch accurary. Chapter 4 pointed out that a statistical (combination of the accuraty results during each flight phase requires statistical independence of the errors among the three flight phases. However, when the level of launch accuracy analysis involves dynamic simulation of the launcher, statistical independence between the launch and boost phases becomes questionable. Chapter 4 showed thrust misalignment

and mass imbalance to be major error sources for both the launch and boost phases. The combination of the launch and boost motions due to these sources may act in a manner that tends either to amplify or to cancel each other in producing burnout dispersion. Improperly accounting for such effects in the statistical combination method may produce overly conservative accuracy estimates.

Refs. 7, 8, and 9 present some typical findings for a multiple-rocket launcher for which the launcher mass is much larger than that of an individual rocket. These results indicate that low cost, accurate, smooth-bore launchers may be feasible, and that the influences of expensive nontip-off guide rails may not be required.

Dynamic simulation of the launch process offers further benefits in the selection of spin rates, in tube versus rail selection, in launcher carriage selection, and in definition of desired structural characteristics for the launcher.

The depth of launcher analysis is influenced by the system design phase. Several factors invite more detailed analysis of launch accuracy prediction to begin earlier in the design phases, namely,

1. The cost of simulation analysis is continuously being reduced through advances in computing machines and equipment.

2. Knowledge of the dynamic behavior of complex launchers continues to advance as evidenced by Refs. 1, 2, 8, 10, 11, and 12.

8-4.3 MEASUREMENT OF LAUNCH ACCURACY

The accuracy of a given rocket or rocket and launcher system can be measured by several methods during actual firings. Such testing involves specifically prepared rockets, launchers, launch sites, and test equipment. Once the basic launch data have been recorded, they must be mathematically processed to account for known sources of error. This processing is known as data reduction. Some random type errors may be estimated and reduced by numerical smoothing, curve fitting, filtering, or other numerical procedures. The final data represent a best estimate of the parameter being measured. These data may be numerically processed further to define derived parameters not directly measured, e.g., angular rate from angle data or velocity and acceleration from position data.

There are three general methods by which launch accuracy is measured, namely,

1. Direct Photographic Method. The rocket is photographed by high-speed motion picture cameras to some point beyond end of guidance. The rocket is photographed against a reference background, and the launch angles are measured directly from the film frames. Two or more cameras are usually employed. vertically oriented cameras photograph the yaw component of launch angle while horizontally oriented cameras photograph the pitch angle. Measurements are taken from each camera frame at the same time sequence. Mallaunch rates are derived by numerically processing this sequence of angular measurements. Rocket launch velocity also can be derived from position readings taken from the film. This is the least expensive method of measurement of rocket angular and velocity data. Unfortunately, inherent inaccuracies in the methods of taking data from film make this method the least accurate for determining mallaunch rates.

2. Optical Lever Method, This technique may employ photographic or other methods for the collection of data. The optical lever refers to a geometric configuration of a camera, a target board, and a mirror affixed to the nose of the rocket. The camera and target board are placed downrange of the launcher and on opposite sides of the intended plane of flight. As the nose of the rocket moves in response to launch dynamics, the camera records sequential positions of the target board which become vsible in the nose-mounted mirror. From this and other data, the rocket angular excursions can be derived. Another version of the optical lever replaces the camera with an illumination source such as a laser. The apparent excursions of the illumination source at the target board position are then recorded, and the rocket nose motion is similarly derived. The optical lever is a highly sensitive method of taking angular rocket data. The construction of the apparatus is relatively expensive and may be subject to considerable risk from malfunctioning rockets. Optical levers may be so sensitive as to record excursions of the nose caused by transverse rocket vibration; this could lead to misinterpretation of launch accuracy if the data were not properly processed (Ref. 13).

3.   Launcher or On-Board Mounted Instrucmentation.   On-Board acceleration sensors may measure the rocket dynamic state and transmit this information by telemetry to rocording equipment (Ref. 14). Alternately, an on-board transmitter may provide a specialized signal that is altered by the rocket motion (Ref. 15). Sensitive reveivers record these altered signals and infer the rocket motion from the type and degree of signal alteration. These on-board techniques require careful attention in order to match the mass and balance of the instrumented rocket with that of the production version of the rocket. The accuracy of launch data is highly dependent on the method of data acquisition, instrument calibration procedures, and careful attention to the interpretation of results.

Ref. 16 provides an overview of the data collection process and prey'ides some acturacy estimates on an automatic tracking laser technique.

8-4.4 FLEXIBLE ROCKET EFFECTS

Flexible rocket effects can influence launch accuracy in several ways. Significant flexible effects arise when the rocket is sufficiently weak in bending with respect to the bending forms and moments to which the rocket is subjected. These effects are most pronounced in very slender rockets, i.e., rockets with a length-to-diameter ratio of approximately 15 or more.

When a rocket is stored with insufficient support along its length for a long time, elastic creeping of the structural and propulsion elements may occur. This tends to cause the rocket to sag and may result in a permanent set to its shape. Such a set would affect rocket static and dynamic balance, thrust alignment, and aerodynamics. Rocket launcher clearances and reaction forces also could be seriously affected. Launch performance degradation would be more pronounced for the unbalanced rockets launched with high spin rates.

Other ways in which the flexible rocket can affect launch accuracy occur during the launch process itself. One such way is the manner in which a rocket is bent due to thrust misalignment as shown in Fig. 8-11. Thrust misalignment produces a force component normal to the missile longitudinal axis. When the rocket is supported at two or more points in the launcher, the rocket will bend in a manner analogous to a simply supported beam with a force acting at one end. In each case, the induced shape of the rocket is dictated by the type of supports employed and their locations. Ref. 17 identifies several other ways in which bending is induced during rocket launch, e.g., transverse frictional force and motor ignition transients.

Rockets rarely will take on a steady deflected shape during the launch and boost phases. Rather, a complex vibration is achieved between the flexible rocket and flexible launcher. A recent analysis (Ref. 18) identified a transverse angular vibration rate at end of guidance as 70 mrad/s for one rocket. These results indicate that flexible effects can influence both the launch process itself and attempts to measure launch accuracy by the methods of par. 8-4.3.
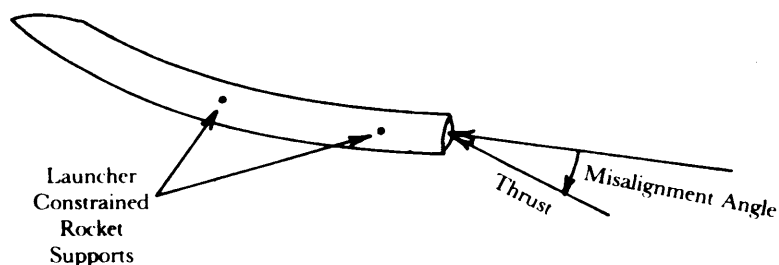
Figure 8-11. Rocket Bending Due to Thrust Misalignment

R E F E R E N C E S

1. J. E. Cochran, Jr., *Launchers as Passive Controllers,* MICOM Report RL-CR-81-2, US Army Missile Command, Redstone Arsenal, AL, 31 December 1980.

2. J. E. Cochran, Jr., *et al., Rocket Launchers as Passive Controllers,* MICOM Report RL-CR-82-2, US Army Missile Command, Redstone Arsenal, Al, 31 December 1981.

3. J. E. Cochran, Jr., and D. E. Christensen, *LauncherlRocket Dynamics and Passive Control,* AIAA Paper 81-1902, AIAA Atmospheric Flight Mechanics Conference, Albuquerque, NM, 19-21 August 1981.

4. C. M. Cornelison and O. R. Stoddard, *Protective Launchers for Missiles and Rockets,* MICOM Report RL-TR-65-2, US Army Missile Command, Redstone Arsenal, AL, May 1965.

5. J. J. Bertin and J. L. Batson, "Experimentally Determined Rocket-Exhaust Flowfield in A Constrictive Tube Launcher", Journal of Spacecraft 12, 711-4 (December 1975).

6. J. J. Bertin and J. L. Batson, "Comparison of Cold-Gas Simulations and Rocket-Launch Data for Constrictive Launchers", Journal of Spacecraft 13,684-91 (November 1976).

7. D. E. Christensen, *Multiple Rocket Launcher Characteristics and Simulation Technique,* MICOM Report TR-RL-76-11, US Army Missile Command, Redstone Arsenal, AL, February 1976.

8. D. E. Christensen and R. L. Richardson, *A Multiple Rocket Launcher Simulation.—Report II,* MIRADCOM Report TL-TR-77-3, US Army Missile Command, Redstone Arsenal, AL, February 1977.

9. D. E. Christensen, "Results of A Multiple Launching Simulation", *Proceedings of the Second Free Flight Rocket Workshop—Volume I,* MIRADCOM Report TF-TR-77-1, US Army Missile Command, Redstone Arsenal, AL, August 1977.

10. W. H. Appich, Jr., and D. E. Tipping, *Free-Rocket Trajectory Errors from Plume-Induced Loading During Tube Launch,* Journal of Spacecraft 14, 614-20, (October 1977).

11. Schmidt, Fansler, and Shear, *Trajectory Perturbations of Fin-Stabilized Projectiles Due to Muzzle Blast,* Journal of Spacecraft 14, 339-44, (June 1977).

12. J. E. Cochran, Jr., *Investigation of Factors Which Contribute to Mallaunch of Free Rockets,* MICOM Report RL-CR-76-4, US Army Missile Command, Redstone Arsenal, AL, October 1975.

13. J. L. Batson, "A Method for Analyzing Optical Lever Data", *Proceedings* of *the Third Annual Free Flight Rocket Workshop,* MIRADCOM Report T-SR-79-12, US Army Missile Command, Redstone Arsenal, AL, October 1978, pp. 266-80.

14. W. Walliser, "The Free Flight Rocket Telemetry Core", *Proceedings of the Second Free Flight Rocket Workship—Volume I,* MIRADCOM Report TF-TR-77-1, US Army Missile Command, Redstone Arsenal, AL, August 1977, pp. 178-94.

15. E. J. Baghdady, "Induced Directional Frequency Modulation Technique for Attitude and Position Real-Time Measurement for Free Flight Rockets", *Proceedings of the Second Free Flight Rocket Workshop— Volume I,* MIRADCOM Report TF-TR-77-1, US Army Missile Command, Redstone Arsenal, AL, August 1977, pp. 195-210.

16. D. B. Brown, "1977 Progress in Data Analysis", *Proceedings of the Second Free Flight Rocket Workshop— Volume I,* MIRADCOM Report TF-TR-77-1, US Army Missile Command, Redstone Arsenal, AL, August 1977, pp. 133-45.

17. J. E. Cochran, Jr., *et al., An Analysis of the Effects of Transverse Vibration on the Attitude Motion of Free Flight Rockets,* MICOM Report RL-CR-80-2, US Army Missile Command, Redstone Arsenal, AL, December 1979.

18. J. E. Cochran, Jr., *et al., Effects of Transverse Bending on the Motion of Free Flight Rockets,*

MIRADCOM Report T-CR-78-21, US Army Missile Command, Redstone Arsenal, AL, September 1978.

19. C. M. Cornelison, *Investigation of Rockets and Launchers for Aircraft Weaponization,* MICOM Report RL-TN-67-6, US Army Missile Command, Redstone Arsenal, AL, August 1967.

20. D. L. Hammock, *Artillery Research Missile Launcher Development Program-Final Report,* NSI Report TR-230-1104, Northrop Services, Inc., Huntsville, AL, July 1972.

BIBLIOGRAPHY

Proceedings of the Second Annual Free Flight Rocket Workshop-Volume I, MIRADCOM Report TF-TR-77-1, US Army Missile Command, Redstone Arsenal, AL, August 1977.

Proceedings of the Third Annual Free Flight Rocket Workshop, MIRADCOM Report T-SR-79-12, US Army Missile Command, Redstone Arsenal, AL, October 1978.

Korst, Butler, and Briski, *Simulation of Jet Plume Interference Effects During Launch Phase of Missiles,* AIAA Paper 79-1292, at AIAA/SAE/ASME 15th Joint Propulsion Conference, Las Vegas, NV, June 1979.

J. L. Batson, *Rocket Exhaust Flow in Tube Launchers,* MICOM Report RL-TR-76-12, US Army Missile Command, Redstone Arsenal, AL, January 1976.

R. R. Morris and J. J. Bertin, *Experimental Study of an Underexpanded, Supersonic Nozzle Exhausting Into An Expansive Launch Tube,* Aerospace Engineering Report 77001, University of Texas at Austin, Austin, TX, January 1977.

G. Batiuk, *A Bibliography of Plume Effects Investigations Conducted by The Army Missile Command,* MICOM Report RF-TR-76-16, US Army Missile Command, Redstone Arsenal, AL, December 1975.

R. R. Maestri and C. A. Kalivretenos, *A Wind-Tunnel Simulation of Rocket/Launcher Interference Effects,* AIAA Paper 71-269, AIAA 6th Testing Conference, Albuquerque, NM, March 1971.

R. J. Prozan and J. K. Lovin, *An Analytic Method for Predicting Rocket Motor Blast Loads on A Launcher,* LMSC Report HREC A712366, Lockheed Missiles and Space Company, Huntsville, AL, October 1965.

R. Coberly, *Miscellaneous Problems in Launcher Dynamics,* RIA Technical Note 38-58, Rock Island Arsenal, Rock Island, IL, November 1958.

R. Coberly, *Design Manual for Launchers,* RIA Technical Note 33-63, Rock Island Arsenal, Rock Island, IL, December 1963 (3 volumes).

M. Stippes, *Final Report on an Analysis of the Motion of Missiles, TAM* Report 210, University of Illinois, Urbana, IL, February 1962.

F. D. Goodson and D. E. Christensen, *Single Degree of Freedom Launcher Model for* LANCE, MICOM Report RL-TN-63-3, US Army Missile Command, Redstone Arsenal, AL, March 1963.

G. A. Wempner and E. V. Wilms, *Multi-Rail Launcher With Six Degrees of Freedom—Final,* UAH Report RR-36, Research Institute, (University of Alabama in Huntsville, Huntsville, AL, September 1966.

G. E. Weeks, and T. L. Cost, *Coupled-Interaction Launch Behavior for a Flexible Rocket and Flexible Launcher,* Journal of Spacecraft 17, 432-9 (September-October 1980).

D. Booker, *Free Flight Rocket Spin Technique Development,* MIRADCOM Report T-TR-78-30, US Army Missile Command, Redstone Arsenal, AL, January 1978.

Denkmann, Hurt, and Beckett, *An Evaluation of Instrumentation for Measuring the Behavior of a*

Rocket Launcher in Laboratory Test and During a Firing, Report No. 4, Dept. of Mechanics, State University of Iowa, Iowa City, IA, July 1961.

A. C. Menius, Jr., Optical Lever Method for Measurement of Orientation of a Spinner Rocket, Report ERD-64/4, Dept. of Engineering Research, North Carolina State College, Raleigh, NC, 1954.

MIL-HDBK-762(MI)

APPENDIX A

ATMOSPHERIC DATA

This appendix presents an overview of the rnore significant sources of atmospheric data available to the rocket designer. Commonly used and availables sources are identified. Some of the relationships most likely to be of interest to the designer are explored. Frequently used data and parameters are provided. References containing additional or more detailed material are cited. The diverse objectives for which aerodynamically stabilized free rockets could be designed are recognized, and thus a wide range of data is presented and referenced.

A-0 LIST OF SYMBOLS

C_s = speed of sound, m/s

e = vapor pressure of water present, Pa

e_s = saturated vapor pressure, Pa

g_0 = 9.80665 m s^2, standard sea level gravitational constant

g_0' = local sea level gravitational constant, m/s^2

$H = \left(\dfrac{g_0'}{g_0}\right) \dfrac{R_0' - Z}{(R_0' + Z)}$, geopotential altitude, m

h = height measured from a level grade around the site, or at the top of heavy vegetation such as wheat, corn, or heavy brush, m

N_A = 6.022169×10^{26} kmol^{-1}, Avogadro's number

P = atmospheric pressure, Pa

P_0 = 101,325 Pa, standard sea level atmospheric pressure

R_0' = local equivalent earth radius, m

RH = relative humidity, %

R^* = 8.31432×10^3 J/kmol·K, universal gas constant

S = 110.4 K, constant in Sutherland's viscosity equation

T = thermodynamic temperature, K

ΔT = lapse rate, K/km

T_i = 273.15 K, ice point temperature

T_v = virtual temperature, K

T_0 = 288.15 K, standard sea level atmospheric temperature

W_{10m} = measured extreme wind speed at 10 m, m/s

$\overline{W}_{10m}$ = measured mean wind speed at 10 m, m/s

W_{h_e} = extreme wind speed at height in question, m/s

$\overline{W}_h$ = mean wind speed at height in question, m/s

Z = geometric altitude, m

β = 1.458×10^{-6} kg/s·m·K$^{1/2}$, constant in Sutherland's viscosity equation

γ = 1.4 dimensionless, ratio of specific heats of air

ρ = atmospheric density, kg/m^3

ρ_0 = 1.2250 kg/m^3, standard sea level atmospheric density

σ_a = 3.65×10^{-10} m, mean collision diameter for air

A-1

A-1 INTRODUCTION

Atmospheric characteristics—especially the speed of sound, density, and wind-are important considerations in the design of rockets. For example, the atmospheric density and the speed of sound are required to compute the aerodynamic forces on the rocket. Wind profiles and wind shear data are necessary for structural design and accuracy studies. Because of the variability of the atmosphere, statistical methods normally are employed for the presentation, analysis, and use of the data. Because of the complexity of atmospheric perturbations, meteorologists have deleloped synthetic standard profiles representing the mean values of available data. In addition, profiles of the deviations of the data from the mean for various latitudes and seasons have been developed.

This Appendix presents an overview of the more significant sources of atmospheric data available to the rocket designer. However, it does not specify how the designer should use atmospheric data in regard to a specific rocket system since the requirements of each system are unique.

A-2 ATMOSPHERIC PROPERTIES

The atmosphere of the earth is a mixture of gases which may be assumed to be dry, to be in hydrostatic equilibrium, and to follow the Ideal Gas Law. The molecular mass and composition may be assumed constant from sea level to 90 km.

A-2.1 BASIC RELATIONSHIPS

In a dry atmosphere, the density p is related to pressure and temperature by the Ideal Gas Law

$$\rho = 3.483676 \times 10^{-3} \frac{P}{T}, \text{ kg/m}^3 \qquad \text{(A-1)}$$

where

P = atmospheric pressure, Pa
T = thermodynamic temperature, K
p = atmospheric density, kg/m^3.

In a moist atmosphere, the relationship of Eq. A-1 still holds if the thermodynamic temperature T is replaced by the virtual temperature T_v

$$T_v = \frac{T}{1 - 0.379 \, (e/P)}, \text{ K} \qquad \text{(A-2)}$$

where

e = vapor pressure of water present, Pa.

If the saturated vapor pressure e_s is used, the vapor pressure e may be determined by

$$e = e_s \frac{RH}{100}, \text{ Pa} \qquad \text{(A-3)}$$

where

RH = relative humidity, %
es = saturated vapor pressure, Pa.

The US Standard Atmosphere, 1976, (Ref. 1) is a dry atmosphere for which Eq. A-1 holds. The moisture conditions in the lower atmosphere were used in the formulations of the US Standard Atmosphere Supplements, 1966, (Ref. 2) and the Range Reference Atmospheres (Ref. 3). For all practical purposes, $T_v = T$ above 5 km.

A-2

MIL-HDBK-762(MI)

Geopotential altitude H is used in the construction of the various standard atmospheres. The relationship between geometric altitude Z and geopotential altitude H is given by

$$H = \left(\frac{g_0'}{g_0} \right) \frac{R_0 Z}{(R_0' + Z)} \ , \text{m} \tag{A-4}$$

where

Z = geometric altitude, m

g_0 = standard sea level gravitational constant, m/s²

g_0' = local sea level gravitational constant, m/s²

R_0' = local equivalent earth radius, m. (Note: This is not the true radius but is a ficticious radius combining both the actual radius and the centrifugal effect of rotation. For further discussion, see Refs. 2 and 4.)

For Z = 30,000 m, H varies from 29,779 m at the equator to 29,937 m at the poles.

Table A-1 presents local gravitational constants and local equivalent earth radii at three latitudes.

TABLE A-1 . REPRESENTATIVE VALUES OF g_0' AND R_0'

Latitude, deg	g_0', m/s²	R_0', m
0 (Equator)	9.78036	6,334,984
45 (~ Paris)	9.80665	6,356,360
90 (Pole)	9.83208	6,377,862

If the temperature changes linearly between two geopotential altitudes, H_1 and H_2, the density p_2 at the top of the layer may be computed from the density p_1 at the bottom of the layer by the relationship

$$\rho_2 = \rho_1 \left(\frac{T_{v1}}{T_{v2}} \right)^{[1 + (0.0341632/\Delta T)]} \ , \text{kg/m}^3 \tag{A-5}$$

where

T_{v1} and T_{v2} = virtual temperature at bottom and top of layer, respectively, K

ΔT = lapse rate, K/km.

The speed of sound C_s may be calculated from the virtual temperature T_v by

$$C_s = 20.04677 \ T_v^{1/2}, \text{m/s.} \tag{A-6}$$

For purposes of computation of values of the US Standard Atmosphere, 1976, it was necessary to establish numerical values for various constants appropriate to the atmosphere of the earth. Table A-2 lists the numerical constants adopted for the necessary computations.

A-2.2 SOURCES OF THERMODYNAMIC DATA

A-2.2.1 US Standard Atmosphere, 1976 (Ref. 1)

The US Standard Atmosphere, 1976, is an idealized, middle latitude, steady-state representation of the atmosphere of the earth from the surface to 1000 km which is assumed to exist during periods of moderate solar activity. This Standard Atmosphere includes a realistic description of the atmosphere above altitudes of conventional aircraft operation. Up to 32 km, the US Atmosphere, 1962, is identical to the US Standard Atmosphere, 1976. The Committee on Space Research (COSPAR) International Atmosphere, which is **used** in Europe, agrees in general with the US Standard Atmosphere, 1976, but has differences in details. The Air Research and Development Command (ARDC) Model Atmosphere, 1959, (Ref. 5) agrees with the US Standard Atmosphere, 1976, up to 20 km altitude.

TABLE A-2. CONSTANTS USED IN CALCULATION OF US STANDARD ATMOSPHERE, 1976 (Ref. 1)

Symbol	Metric Units
P_o	101,325 Pa
ρ_o	1.2250 kg/m^3
T_o	15°C
g_o	9.80665 m/s^2
S	110.4 K
T_i	273.15 K
β	1.458×10^{-6} kg/s·m·K$^{1/2}$
γ	1.40, dimensionless
σ_a	3.65×10^{-10} m
N_A	6.022169×10^{26} kmol^{-1}
R^*	8.31432×10^3 J/ kmol·K

Table A-3 gives US Standard Atmosphere, 1976, values of temperature, pressure, density, and speed of sound for each kilometer of altitude from sea level to 30 km.

The US Standard Atmosphere, 1976, should be used as the primary reference in ballistic studies. A computer subroutine of these data has been made a part of many advanced atmospheric and aerodynamic computer program libraries.

A-2.2.2 US Standard Atmosphere Supplements, 1966

Before' the US Standard Atmosphere, 1976, was published, the Committee on Extension of the Standard Atmosphere (COESA) published the US Standard Atmosphere Supplements, 1966. These supplements to the US Standard Atmosphere, 1962, contain nine atmospheric models that provide idealized representations of tropical, subtropical, temperate, subarctic, and arctic atmospheres from sea level to 120 km. Data are given for each climatic zone for cold (January) and hot (July) periods except for the tropic zone. Generally, the same methods were used in the preparation of these tables as were used in the preparation of the US Standard Atmosphere, 1976. Sea level values of the data are defined along with layers on constant temperature lapse rate.

The US Standard Atmosphere Supplements, 1966, should be used whenever the average difference between climatic zones or between cold or hot conditions is important.

Figs. A-1 through A-5 show representative density profiles from the US Standard Atmosphere Supplements, 1966. Specifically, these figures show mean density deviations from the standard density model established in the US Standard Atmosphere, 1962. These deviations are shown as a function of geopotential altitude H. Profiles for several latitudes and months are shown.

A-2.2.3 Range Reference Atmosphere Documents

In 1960, the Inter-Range Instrumentation Group (IRIG), Meteorologic-al Working Group of the Range Commander's Council, organized the IRIG Rantge Reference Atmosphere Committee with representatives from the US Air Force, US Army, National Aeronautics and Space Administration, US Navy, and the National Oceanographic and Atmospheric Administration to formulate realistic atmospheric models for each of the major missile-test ranges. These models are published in two parts. Part I provides data from the surface to 30 km; Part II, from 2.5 km to 70 km. Monthly tables of thermodynamic quantities, scalar winds, and zonal and meridional wind components are given. At present, 13 Part I and 4 Part 11 models have been published.

These model atmospheres are computed in a manner similar to that used in the US Standard Atmosphere, 1976, except adjustments to the geopotential heights of the standard pressure levels and the temperature lapse rates were determined statistically from measured data at each reference range.

MIL-HDBK-762(MI)

TABLE A-3. TEMPERATURE, PRESSURE, DENSITY, AND SPEED OF SOUND VS GEOPOTENTIAL ALTITUDE: US STANDARD ATMOSPHERE, 1976 (Ref. 1)

Geopotential Altitude, km	Temperature T, K	Pressure P, Pa	Density p, kg/m^3	Speed of Sound c_s, m/s
0	288.1.50	101,325	1.2250	340.29
1	281.650	88,699	1.1116	336.43
2	275.150	79,495	1.0065	332.53
3	268.650	70,108	0.90912	328.58
4	262.150	61,640	,0.81913	324.58
5	2.55.650	54,019	0.73612	320.53
6	249.150	47,181	0.65970	316.43
7	242.650	41,060	0.58950	312.27
8	236.150	35,599	0.52517	308.06
9	229.650	30,742	0.46635	303.79
10	223.150	26,436	0.41271	299.46
11	216.50	22,632	0.36392	295.07
12	216.650	19,330	0.31083	295.07
13	216.650	16,510	0.26548	295.07
14	216.650	14,101	0.22675	295.07
15	216.650	12,044	0.19367	295.07
16	216.650	10,287	0.16542	295.07
17	216.650	8,786.6	0.14129	295.07
18	216.650	7,504.8	0.12068	295.07
19	216.650	6,410.0	0.10307	295.07
20	216.650	5,475.8	0.088035	295.07
21	217.650	4,677.8	0.074874	295.75
22	218.650	3,999.7	0.063727	296.43
23	219.650	3,422.4	0.054280	297.11
24	220.650	2,930.4	0.046267	297.78
25	221.650	2,511.0	0.039466	298.45
26	222.650	2,153.0	0.033688	299.13
27	223.650	1,847.4	0.028777	299.80
28	224.650	1,586.2	0.024599	300.47
29	225.650	1,362.9	0.021042	301.14
30	226.650	1,171.8	0.018012	301.80

A-2.2.4 Military Standard Climatic Extremes, MIL-STD-210

MIL-STD-210 (Ref. 6) provides temperature profiles for high, low, and one-percent risk tempera-
tures at each altitude and the corresponding actual values of density associated with the extreme
temperature values. The table of high and low density values given are based on these temperature
extremes. The negative correlation of density with altitude between the surface and 10 km to 15 km
altitude is neglected, so the use of such profiles may lead to biased results.

A-2.2.5 The NASA/MSFC Global Reference Atmosphere Model—Mod 3

The NASA/MSFC Global Reference Atmosphere Model (Ref. 7) permits generation of mean and
departure profiles of density, temperature, and pressure from 0 to 700 km altitude for any latitude,
longitude, and month.

A-5
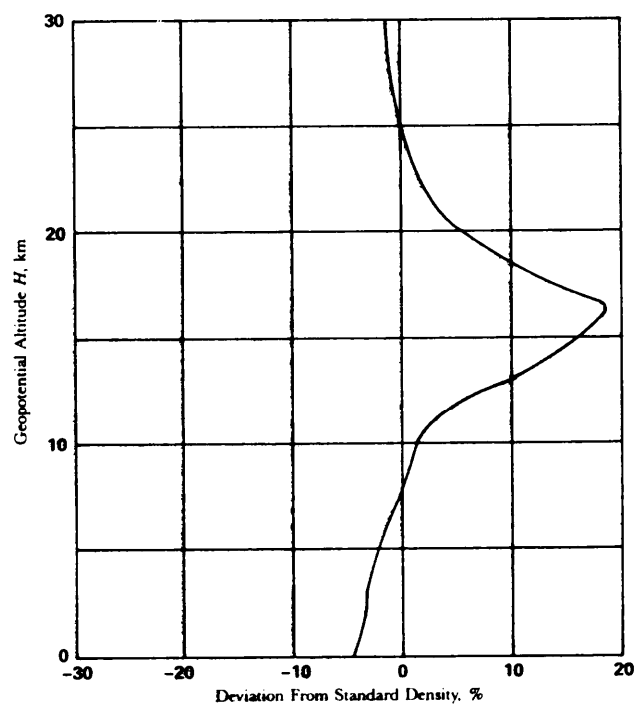
Figure A-1. Density Deviations from the US Atmospheric Model of 1962 at 15°N Latitude
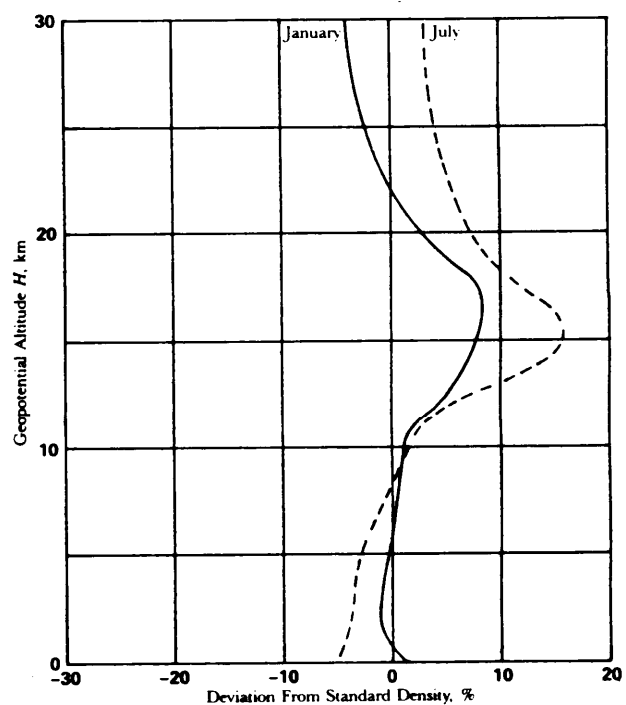
Figure A-2. Density Deviations from the US Atmospheric Model of 1962 at 30°N Latitude
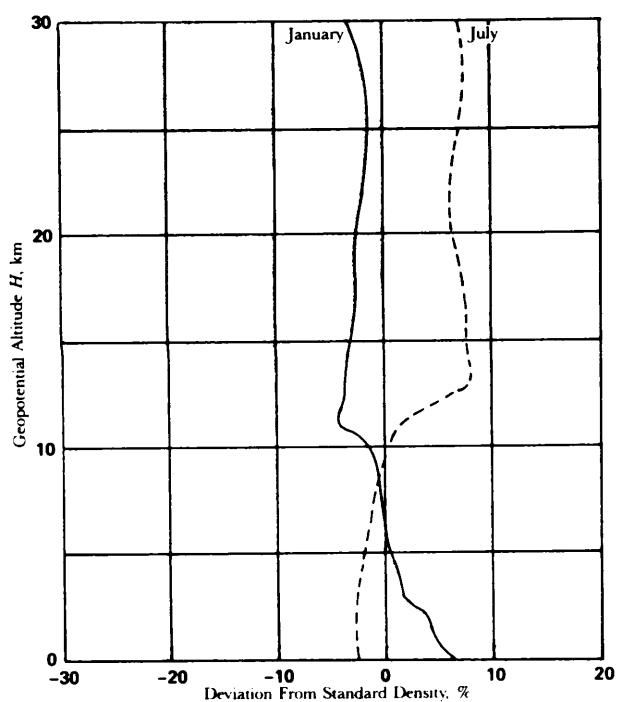
Figure A-3. Density Deviations from the US Atmospheric Model of 1962 at 45°N Latitude
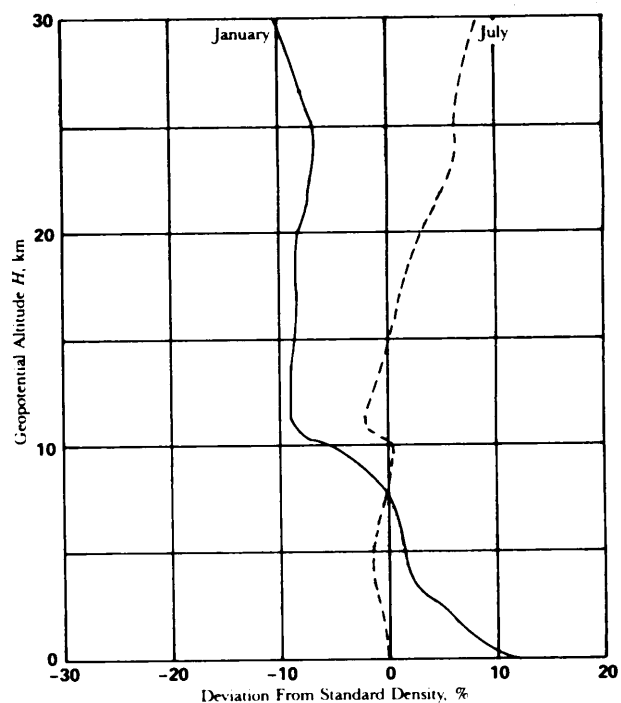
Figure A-4. Density Deviations from the US Atmospheric Model of 1962 at 60°N Latitude

A-6
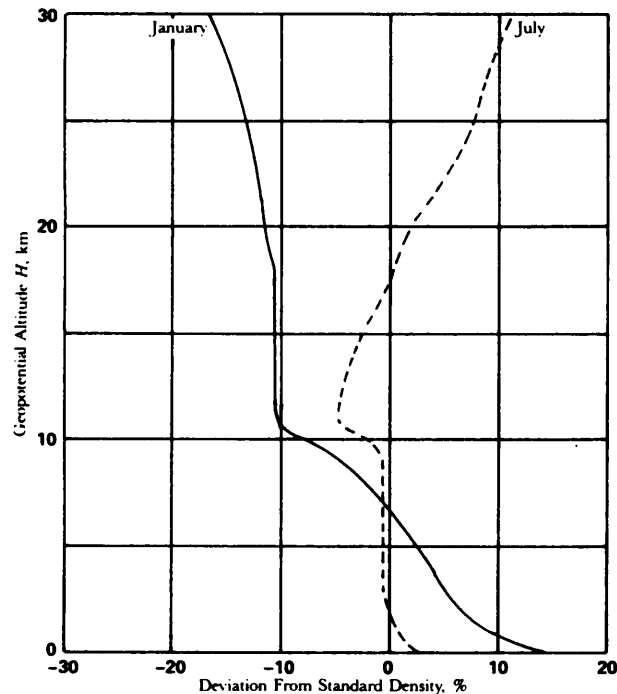
Figure A-5. Density Deviations from the US Atmospheric Model of 1962 at 75°N Latitude

A-2.2.6 Other Regional-Seasonal Atmospheric Data

In 1965, Essenwanger and Dudel (Ref. 8) published tables for 20 density and temperature profiles to 2.5 km altitude derived from radiosonde statistics for tropical, subtropical, temperate, and polar locations. In addition to summer/winter mean conditions, this collection contains seasonal one-sigma profiles.

The Terrestrial Environment (Climatic) Criteria Guidelines for use in Aerospace Vehicle Development (Ref. 9) has tables of density versus altitude at three locations for cold and hot atmospheres. These locations are Kennedy Space Center, FL; and Vanderburg and Edwards Air Force Bases, CA.

A-3 WIND

A-3.1 WIND SPEED

The atmosphere may be divided into three sections, i.e.,

    1. Surface layer (from the ground to 10 m)
    2. Boundary layer (from 10 m to about 2 km)
    3. In-flight layer (above 2 km).

Each of these sections is discussed in the paragraphs that follow.

A-3.1.1 The Surface Layer

Wind in the surface layer (from the ground to 10 m) changes rapidly from zero at the ground surface (or top of the surface roughness layer) to some value at 10 m. The standard height for surface wind measurements is 10 m; therefore, wind speed values at 10 m are available for design use. Extreme wind speed and mean wind speed values are both commonly used in design. Refs. 9 and 10 present additional infornmtion on the use of these design values.

Points on the extreme wind speed profile can be determined from

$$W_{h_e} = 0.93\ W_{10\mathrm{m}} h^{0.03},\ \mathrm{m/s} \tag{A-7}$$

where

W_{h_e} = extreme wind speed at height in question, m/s

W_{10m} = measured (or determined) extreme wind speed at 10 m, m/s

h = height measured from a level grade around the site or at the top of heavy vegetation such as wheat, corn, or heavy brush, m.

The mean wind speed profile below 10 m can be determined from

$$\overline{W}_h = 0.40 \ \overline{W}_{10m} \ h^{0.4}, \ \text{m/s} \tag{A-8}$$

where

$\overline{W}_h$ = mean wind speed at the height in question, m/s

$\overline{W}_{10m}$ = measured mean wind speed at 10 m, m/s.

A-3.1.2 The Boundary Layer

Wind speed in the boundary layer increases with height to about 2 km. At about 2 km, the surface friction no longer has effect on the wind speed, and the wind speed is equal to the geostrophic wind speed.

Eq. A-7 is also valid for determining the extreme wind speed profile above 10 m by using appropriate values of h greater than 10 m.

To determine the mean wind speed profile $\overline{W}_h$ for values above 10 m, the following equation should be used:

$$\overline{W}_h = 0.72 \ \overline{W}_{10m} h^{0.14}, \ \text{m/s}. \tag{A-9}$$

A-3.1.3 The In-Flight Layer

Wind speeds in the in-flight layer are above the effects of surface friction. The wind speed in this layer is a result of the atmosphere pressure field (highs and lows). Wind speeds in this layer are usually presented in the form of wind speed profiles as shown in Fig. A-6.

A-3.2 SOURCES OF WIND SPEED DATA

Wind speed data sources are

1. *Engineering Handbook on the Atmospheric Environmental Guidelines for Use in Wind Turbine Generator Development.* This handbook (Ref. 11) provides discussions on methods of using wind as a design parameter and also provides much data on values of wind speed to use in design. It especially treats effects of local surface features.

2. *Range Reference Atmosphere Documents.* These documents (Ref. 3) contain values of scalar winds and wind components for each of the major missile test ranges.

3. *Military Standard Climatic Extremes,* MIL-STD-210. This document (Ref. 6) provides surface wind speed extremes and also wind profile extreme data.

4. NASA MSFC *Global Reference Atmosphere Model-Mod 3.* This document (Ref. 7) provides worldwide wind profile data.

5. *Terrestrial Environment (Climatic) Criteria Guidelines for Use in Aerospace Vechicle Development.* This document (Ref. 9) includes detailed discussions on designing for wind effects as well as extensive tables of winds for use in design.

A-3.3 WIND SHEAR

Wind shear is the difference between wind speeds in two specific altitude layers. The magnitude of the wind shear varies considerably with the stability of the atmosphere; therefore, consideration of the

A-8
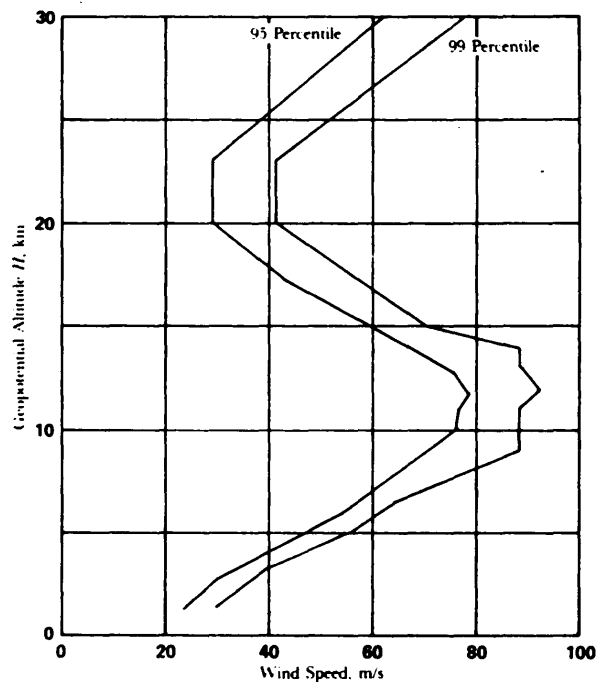
**Figure A-6. Steady-State Scalar Wind Speed
vs Altitude for Two Risk Levels for All
Locations**

atmosphere stability- stable, neutral, or unstable—may be required if wind shear is an important design parameter. Ref. 9 contains a detailed discussion of this subject.

A-3.4 TURBULENCE

Under most conditions, atmospheric winds are fully developed turbulent flows. Spectral methods are particularly. useful in representing the turbulent effects of the wind environment (Refs. 9 and 10).

A-4 ENVIRONMENTAL TEST METHODS

MIL-STD-810, *Environmental Test Methods,* (Ref. 11) establishes uniform environmental test methods for determining the resistance of equipment to the effects of natural and induced environments peculiar to military operations. This material may also be of use in design.

REFERENCES

1. *US Standard Atmosphere, 1976,* Committee on Extension of the Standard Atmosphere (COESA), US Government Printing Office, Washington, DC, October 1976.

2. *US Standard Atmosphere Supplements, 1966,* Committee on Extension of the Standard Atmosphere (COESA), US Government Printing Office, Washington, DC, 1966.

3. *Range Reference Atmosphere Documents,* IRIG Document No. 104-63, published by the Secretariat, Range Commander's Council, White Sands Missile Range, NM. The following reference atmospheres have been published:
   a. Atlantic Missile Range Reference Atmosphere for Cape Kennedy, FL (Part I), 1963.
   b. White Sands Missile Range Reference Atmosphere (Part I), 1964.
   c. Fort Churchill Missile Range Reference Atmosphere for Fort Churchill, Canada (Part I), 1964.
   d. Pacific Missile Range Reference Atmosphere for Eniwetock, Marshall Islands (Part I), 1964.

   e. Fort Greely Missile Range Reference Atmosphere (Part I). 1964.

   f. Eglin Gulf Test Range Reference Atmosphere for Eglin AFB, FL. (Part I). 1965.

   g. Pacific Missile Range Reference Atmosphere for Point Arguello, CA (Part I), 1965.

   h. Wallops Island Test Range Reference Atmosphere (Part I). 1965.

   i. Eastern Test Range Reference Atmosphere for Ascension Island, South Atlantic (Part I), 1966.

   j. Lihue, Kauai, Hawaii Reference Atmosphere (Part I), 1970.

   k. Johnson Island Test Site Reference Atmosphere (Part I), 1970.

   l. Edwards Air Force Base Reference Atmosphere (Part 10), 1972.

  m. Kwajalein Missile Range, Kwajalein, Marshall Islands. Reference Atmosphere (Part I). 1971.

   n. Cape Kennedy. FL, Reference Atmosphere (Part II), 1971.

   o. White Sands Missile Range Reference Atmosphere (Part II), 1971.

   p. Wallops Island Test Range Reference Atmosphere (Part II). 1971.

   q. Fort Greely Missile Range Reference Atmosphere (Part II), 1971.

   r. Pacific Missile Test Center Reference Atmosphere (Part II). November 1975.

4. R. J. List, Ed., *Smithsonian Meteorological Tables,* 6th Revised Edition, Smithsonian Publication No. 4014, Smithsonian Institution Press, Washington, DC. August 1971 (5th reprint).

5. R. A. Minzner, K. S. W. Champion, and H. L. Pond. *The ARDC Model Atmosphere, 1959, Air* Force Surveys in Geophysics NR 115, AFCRC Report TR-59-267. US Air Force Cambridge Research Center, Hanscom Air Force Base, MA, August 1959.

6. MIL-STD-210, *Climatic Extremes for Military Equipment,* 15 December 1973.

7. G. W. Justus, G. R. Fletcher, F. E. Bramling, and W. B. Pace, *The NASA MSFC Global Reference Atmosphere Model—MOD 3 (With Spherical Harmonic Wind Model),* NASA Contractor Report 3256, National Aeronautics and Space Administration, George C. Marshall Space Flight Center, Huntsville, AL, March 1980.

8. O. M. Essenwanger and H. P. Dudel. *Seasonal Models of Air Density, Temperature and Wind Between the Surface and 25 km for Four Geographic Zones,* MICOM Report RR-TR-6508. US Army Missile Command, Redstone Arsenal, AL. May 1965.

9. R. E. Turner and C. K. Hill, Eds., *Terrestrial Environment (Climatic) Criteria Guidelines for Use in Aerospace Vehicle Development 1982 Revision,* NASA Technical Meemoradum 83473, National Aeronautics and Space Administration, George C. Marshall Space Flight Center, Huntsville, AL, May 1982.

10. W. Frost, B. H. Long, and R. E. Turner, *Engineering Handbook on the Atmospheric Environmental Guidelines for Use in Wind Turbine Generator Development,* NASA Technical Paper 1359, National Aeronautics and Space Administration, George C. Marshall Space Flight Center, Huntsville, AL, December 1978.

11. MIL-STD-810, *Environmental Test Methods, 19* July 1983.

A P P E N D I X   B

C O M P U T E R   P R O G R A M S

Selected computer Programs applicable to the design of free flight rockets are Presented and described.

B-1 DISCUSSION

Appendix B contains information concerning computer programs applicable to the design of free flight rockets. Although not exhaustive, the programs represent a sampling of the engineering software available to the rocket designer.

Each program is identified by the most common title, name, or mnemonic. An abstract is included which describes the most prominent and distinguishing features of the program or mathematical method. A reference is cited where more detail can be found. The primary program language is identified with a computer on which the program has been implemented.

Further, the digital computers are classified as being mainframes, minicomputers, or microcomputers. While this common classification is not precise, it does provide some insight into the size, speed, and equipment requirements of the program. The applicable handbook chapters are cited, and an agency is referenced which is knowledgeable in the use of the program.

B-2 PROGRAMS

B-2.1 PROGRAM NAME. AERODRAG

Abstract. The program estimates aerodynamic force and moment coefficients for unguided ballistic rockets. Rocket configurations are limited to ogive-cylinder or cone-cylinder forebodies, conical-flare or conical-coattail afterbodies with in-line wings and/or tail fins which may be deflected. Wing and tail effectiveness includes all interference factors. Body and control surface skin-friction drag is calculated for laminar or turbulent flow. Fin and wing effectiveness includes all interference factors. Fin and wing wave-drag calculations are included. Power-on and power-off estimates of base drag are made, with some estimates being interpolation from data tables based on experiment and theory. Data are confined to the linear region of the coefficient curve with angle of attack. The Mach range is from zero to high supersonic with some restrictions in the transonic region.

Reference. J. C. Craft, *A Digital Computer Program for Estimating Aerodynamic Force Coefficient for Unguided Ballistic Rockets,* MICOM Report RD-TR-69-9, US Army Missile Command, Redstone Arsenal, AL, 30 June 1969.

Machine Implementation:
  Interdata 8/32 (FORTRAN IV)
  Digital Minicomputer.
Applicable Chapters. Aerodynamics and Performance.
Cognizant Organization:
  US Army Missile Laboratory
  US Army Missile Command
  Redstone Arsenal, AL 35898.

B-2.2 PROGRAM NAME. AERODSN

Abstract. The program estimates static stability and damping derivatives at zero angle of attack in the Mach range from zero to 4.5. Rocket configuration with wings and/or tail fins and a conical boattail segment are allowed. Calculations are performed for a "+" roll orientation of fins as opposed to an "X" orientation, and the wings and fins must be in-line with no control surface deflections. A

limited amount of experimental body-alone data are included (ogive-cylinder and cone-cylinder); however, body-alone table input can be selected as an option. The program does not estimate drag.

Reference. W. D. Washington and C. L. Adams, *Computer Program for Estimating Stability Derivatives of Missile Configuration,* MICOM Report RD-76-25, US Army Missile Command, Redstone Arsenal, AL, 13 May 1976.

Machine Implementation:
Interdata 8/32 (FORTRAN IV)
Digital Minicomputer.

Applicable Chapter. Aerodynamics.

Cognizant Organization:
US Army Missile Laboratory
US Army Missile Command
Redstone Arsenal, AL 35898.

B-2.3 PROGRAM NAME. NAVYAERO

Abstract. The program combines theoretical and empirical procedures to compute static and dynamic aerodynamics for missiles, projectiles, and rockets. Reasonably accurate dynamic stability and performance estimates are made for tactical weapons up to Mach number 8 and 180-deg angle of attack. Pointed and blunt-nosed bodies and sharp or blunt wing and fin leading edges are allowed.

References:

F. G. Moore and R. C. Swanson, *Aerodynamics of Tactical Weapons to Mach Number 3 and Angle of Attack 15°; Part I— Theory and Application,* NSWC Report TR-3584, Naval Surface Weapons Center, Dahlgren, VA, February 1977.

F. G. Moore and R. C. Swanson, *Aerodynamics of Tactical Weapons to Mach Number 3 and Angle of Attack 15°; Part II—Computer Program and Usage,* NSWC Report TR-3600, Naval Surface Weapons Center, Dahlgren, VA, March 1977.

F. G. Moore, *et al., Aerodynamic Design Manual for Tactical Weapons,* NSWC Report TR-81-156, Naval Surface Weapons Center, Dahlgren, VA, July 1981.

L. Devon, *Aerodynamics of Tactical Weapons to Mach Number 8 and Angle of Attack 180°; Par-t I, Theory and Application,* NSWC Report TR 80-346, Naval Surface Weapons Center, Dahlgren, VA, October 1980.

Machine Implementation:
CDC 6700 and Interdata 8/32 (both FORTRAN IV)
Digital Mainframe and Digital Minicomputer, respectively

Applicable Chapters. Aerodynamics, Performance, and Accuracy.

Cognizant Organization:
Naval Surface Weapons Center
Dahlgren Laboratory
Dahlgren, VA 22448.

B-2.4 PROGRAM NAME. POINT MASS TRAJECTORY PROGRAMS

Abstract. The cited reference describes two digital computer programs. The first program computes two degree-of-freedom (range and altitude) rocket trajectories that may possess boost, sustain, and coast phases. The second program possesses three degrees of freedom (range, altitude, and flight path angle). Two constant thrust levels and up to three drag tables may be used. Both programs assume a flat earth with altitude variant atmospheric properties. Listings and sample outputs are included in the reference. Operator intervention is required.

Reference. J. Burt, Jr., and M. P. Stamps, *Description of Point Mass and Three-Degree-o/-Freedom Trajectory Programs,* MICOM Report TR-RD-73-31, US Army Missile Command, Redstone Arsenal, AL, 18 September 1973.

Machine Implementation:
   HP 9830A (BASIC)
   Digital Microcomputer.
Applicable Chapter. Performance.
Cognizant organization:
   Systems Simulation and Development Directorate
   US Army Missile Laboratory
   US Army Missile Command
   Redstone Arsenal, AL 35898.

B-2.5 PROGRAM NAME. AER06D

Abstract. This six-degree-of-freedom unguided rocket flight path prediction program is useful in configuration redesign studies, sensitivity analysis, and flight test evaluation of free flight rockets. The standard body-fixed equations of motion of Etkin are used with a fourth order Runge-Kutta numerical integration routine. Rocket motor performance is represented by a thrust table lookup. Atmospheric properties can be input, or computed, by a standard atmosphere routine built into the program. Linear aerodynamics are read into tables as a function of Mach number. Nonlinear aerodynamics can be built in with a system of subroutines.

Reference. W. D. Washington, *A 6D0F Flight Simulation Program for Free Flight Rockets,* MICOM Technical Report RD-82-9, US Army Missile Command, Redstone Arsenal, AL, 12 March 1982.

Machine Implementation:
   Interdata 8/32 (FORTRAN IV)
   Digital Minicomputer.
Applicable Chapter. Performance.
Cognizant Organization:
   US Army Missile Laboratory
   US Army Missile Command
   Redstone Arsenal, AL 35898.

B-2.6 PROGRAM NAME. TRAJ

Abstract. The program computes the flight of aerodynamically and inertially symmetric missiles from initial conditions and tabular representation of aerodynamics. The program is especially efficient for high spin rate projectiles. Nonaxisymmetric thrust may be used.

Reference. B. Barnett, *Trajectory Equations for A Six-Degree-of-Freedom Missile Using a Fixed-Plane Coordinate System,* Technical Report 3391, Mathematical Analysis Division, US Army Armament R&D Command, Dover, NJ, June 1966.

Machine *Implementation:*
   CDC *6000/7000* (FORTRAN IV and FORTRAN 77)
   Digital Mainframe.
Applicable Chapters. Performance and Accuracy.
Cognizant Organization:
   Large Caliber Weapons Systems Laboratory
   US Army Armament R&D Center
   Dover, NJ 07850.

B-2.7 PROGRAM NAME. NUMERICAL FLOW FIELD PROGRAM FOR AERODYNAMIC HEATING ANALYSIS (AERHET)

Abstract. The computer program calculates laminar, transitional, and turbulent aerodynamic heat transfer rates of arbitrary, three-dimensional vehicle configurations at angles of attack in supersonic flows. The program requires 120K of core memory and/or overlay capability.

Reference. H. J. Fivel, Numerical Flow Field Program For Aerodynamic Heating Analysis, Vol. I—Equations and Results, Vol. II—User's Manual, AFFDL Report TR-79-3128, USAF Flight Dynamics Laboratory, Wright-Patterson AFB, OH, December 1979.

Machine Implementation:
   CDC CYBER 75 (FORTRAN IV)
   Digital Mainframe.
Applicable Chapters. Aerodynamics and Structures.
Cognizant Organization:
   US Air Force Flight Dynamics Laboratory
   Wright-Patterson AFB, OH 45433.

B-2.8 PROGRAM NAME. FDL/FSI PARABOLIZED NAVIER-STOKES CODE

Abstract. The program is a factorable, fully implicit finite difference program to solve the parabolized Navier-Stokes equations for supersonic and hypersonic flow about complex vehicle configurations. The program requires a separate blunt body program to generate starting plane data for blunt configurations. Approximately 400K words of core memory required.

Reference. S. P. Shanks, G. R. Srinivasan, and W. E. Nicolet, *AFWAL Parabolized Navier-Stokes Code: Formulation and Users Manual,* AFWAL Report TR-82-2024, USAF Flight Dynamics Laboratory, Wright-Patterson AFB, OH, June 1982.

Machine Implementation:
   CDC CYBER 750, CDC 7600, CRAY (scalar only)
   Digital Mainframes.
Applicable Chapters. Aerodynamics and Structures.
Cognizant Organization:
   US Air Force Flight Dynamics Laboratory
   Wright-Patterson AFB, OH *45433.*

B-2.9 PROGRAM NAME. SUPERSONIC-HYPERSONIC ARBITRARY BODY PROGRAM (S/HABP)

Abstract. The program is capable of calculating the supersonic and hypersonic aerodynamic characteristics of complex, arbitrary three-dimensional shapes. The program consists of a combination of techniques and capabilities including vehicle geometry preparation, calculation of surface pressures using a variety of pressure calculation methods, shielding of one part of a vehicle by another, and calculation of skin-friction forces.

Reference. A. E. Gentry *et al., The Mark IV Supersonic-Hypersonic Arbitrory-Body Program,* AFFDL Report TR-73-159, Three Volumes, USAF Flight Dynamics Laboratory, Wright-Patterson AFB, OH, November 1973.

Machine Implementation:
   CDC CYBER 74, IBM 360, PRIME 550
   Digital Mainframes.
Applicable Chapter. Aerodynamics.
Cognizant Organization:
   US Air Force Flight Dynamics Laboratory
   Wright-Patterson AFB, OH 45433.

B-2.10 PROGRAM NAME. COMPUTER PROGRAM FOR CALCULATION OF COMPLEX CHEMICAL EQUILIBRIUM COMPOSITIONS, ROCKET PERFORMANCE, INCIDENT AND REFLECTED SHOCKS, AND CHAPMAN-JOUGET DETONATIONS—PACK II

Abstract. The program may be used to calculate chemical equilibrium for assigned thermodynamic states, theoretical rocket performance for both equilibrium and frozen compositions during expansion,

incident and reflected shock properties, and Chapman-Jouget detonation properties. These options are available for condensed phase species as well as gaseous phase species. The propellant gas equilibrium chemical composition is determined by minimizing free energy. Minimization of free energy is performed on (1) the Gibbs free energy if the thermodynamic state at a particular location in a rocket is specified in terms of temperature and pressure, and (2) the Helmholtz free energy if the state is specified in terms of temperature and volume (or density).

Reference. S. Gordon and B. J. McBride, *Computer Program for Calculation of Complex Chemical Equilibrium Compositions, Rocket Performance, Incident and Reflected Shocks, and Chapman-Jouget Detonations,* NASA Report SP-273, National Aeronautics and Space Administration, Lewis Research Center, Cleveland, OH, 1971.

Machine Implementation:
Univac 1108 (FORTRAN)
Digital Mainframe.

Applicable Chapters. Propulsion and Structures (Heat Transfer).

Cognizant Organization:
National Aeronautics and Space Administration
Lewis Research Center
Cleveland, OH 44135.

B-2.11 PROGRAM NAME. THE JANNAF STANDARD PLUME FLOW FIELD MODEL (SPF)

Abstract. This program is a two-dimensional or axisymmetric model that predicts the gas-dynamic structure of either purely gaseous or two-phase exhaust plumes below 70 km altitude. The program can be used to calculate the wave structure in plumes implementing characteristic or finite-difference techniques and shock-capturing or shock-fitting procedures. It can also be used to calculate the near-field variable pressure mixing-afterburning region of the plume as well as the constant pressure mixing-afterburning parts of the plume. The program can handle real or ideal gases, solid or free boundaries, and over- or underexpanded nozzles.

Reference. S. M. Dash and H. S. Pergament, *The]ANNAF Standard Plume Flow Field Model (SPF),* MICOM Technical Report RD-CR-82-9, US Army Missile Command, Redstone Arsenal, AL, April 1981.

Machine Implementation:
CDC 7600 (FORTRAN)
Digital Mainframe.

Applicable Chapter. Propulsion.

Cognizant Organization:
US Army Missile Laboratory
US Army Missile Command
Redstone Arsenal, AL 35898.

B-2.12 PROGRAM NAME. CHARRING MATERIAL THERMAL RESPONSE AND ABLATION PROGRAM (CMA3)

Abstract:

The Am-other-m Charring Material Ablation Code (CMA3) is an implicit, finite-difference computational procedure for computing the transient thermal and ablation response of a charring insulation material structure. The program is for one-dimensional bodies that can ablate from a front face and decompose in-depth but can treat a variety of shapes which include planes, cylinders, spheres, and more general thermal "stream-tube" bodies. The program can treat complex systems including a main ablation material, five charring backup materials, and three noncharring material backup structures.

Inputs to CMA include complex tabular surface thermochemical data from ACE, time-dependent convective heat transfer as calculated by BLIMPK, pyrolytic and coking reaction rate coefficients, spe-

cific heat, thermal conductivity, and density as a function of temperature for virgin and char material, nodal position tabulations, thermal contact resistance surface definition, back-side convection coefficients, radiation and convection temperature time-histories, gaseous radiation heating, char swelling parameters, and blowing rate factors for convection coefficient correction.

Reference. C. B. Mayer and M. R. Wool, Users *Manual, Aerotherm Charring Material Thermal Response and Ablating Program, Vols. 1 and 2,* Report AFRPL-TR-70-92, USAF Rocket Propulsion Laboratory, Edwards AFB, CA, April 1970.

Machine Implementation:
Univac 1108 (FORTRAN)
Digital Mainframe.

Applicable Chapter. Structures (Heat Transfer).

Cogniant Organization:
US Air Force Rocket Propulsion Laboratory
Edwards AFB, CA 93523.

B-2.13 PROGRAM NAME. EQUILIBRIUM SURFACE THERMOCHEMISTRY COMPUTER PROGRAM (ACE)

Abstract. The Aerotherm Equilibrium Surface Thermochemistry Computer Program (ACE) computes the equilibrium or mixed frozen/equilibrium thermodynamic state of general chemical systems. Closed (fixed mass) molecular compositions are evaluated from relative elemental quantities. Diffusive-mass flux-dependent states (open system) are defined from surface equilibrium considerations.

Reference. Mitchell R. Wool, Users Manual, Aerotherm Equilibrium Surface Thermochemistry Computer Program, Version 3, Vols. 1 and 2, Report AFRPL-TR-70-93, USAF Rocket Propulsion Laboratory, Edwards AFB, CA, April 1970.

Machine Implementation:
Univac 1108 (FORTRAN)
Digital Mainframe.

Applicable Chapter. Structures (Heat Transfer).

Cognizant Organization:
US Air Force Rocket Propulsion Laboratory
Edwards AFB, CA 93523.

B-2.14 PROGRAM NAME. BOUNDARY LAYER INTEGRAL MATRIX PROCEDURE WITH KINETICS (BLIMPK)

Abstract. The program is a procedure for obtaining numerical solutions of the nonsimilar multi-component laminar and/or turbulent boundary layer with arbitrary equilibrium or nonequilibrium homogeneous or heterogeneous chemical systems, unequal diffusion and thermal diffusion coefficients for all species, radiation absorption and emission, second-order transverse curvature effects, and a variety of surface boundary conditions including intimate coupling with transient charring, ablation energy, and mass balanced plus surfaces of arbitrary catalycities.

Reference. H. Tong *et al., User's Manual, Nonequilibrium Chemistry Boundary Layer Integral Matrix Procedure, Vols. 1 and 2,* AFRPL Report TR-70-92, USAF Rocket Propulsion Laboratory, Edwards AFB, CA, July 1973.

Machine Implementation:
Univac 1108 (FORTRAN)
Digital Mainframe

Applicable Chapter. Structures (Heat Transfer).

Cognizant Organization:
US Air Force Rocket Propulsion Laboratory
Edwards AFB, CA 93523.

B-6

APPENDIX C
HEAT TRANSFER EQUATIONS

Equations are presented for calculating heat conduction, convection, and radiation by finite difference techniques applicable to computer programs of thermal network analyzers. Methods of calculating forced convective heat transfer to two- or three-dimensional shapes are briefly discussed. Empirical data for calculating aerodynamic heating to the exterior of various geometries are discussed.

C-0 LIST OF SYMBOLS

A = surface area normal to heat flow path of nodal element, m^2

A_i = correlation parameter, defined by Table C-1, accounting for change in local body angle, dimensionless

C = contact conductance at interface, $W/m^2 \cdot K$)

C_f = compressible skin-friction coefficient, dimensionless

Cf_i = incompressible skin-friction coefficient, dimensionless

C_N = mass fraction of nitrogen, dimensionless

C_O = mass fraction of oxygen, dimensionless

c_p = specific heat at constant pressure, $J/(kg \cdot K)$

c_{P_1} = specific heat at constant pressure of Node 1, $J/kg \cdot K$

c_v = specific heat at constant volume, $J/kg \cdot K$

D = mass diffusivity, m^2/s

D' = diameter, m

F = radiation shape factor, dimensionless

F_c = parameter for transforming incompressible skin friction to compressible values, dimensionless

F_{R_L} = parameter transforming incompressible length Reynolds number to compressible values, dimensionless

F_{R_θ} = parameter for transforming incompressible momentum thickness Reynolds number to compressible values, dimensionless

g_0 = 9.80665 m/s^2, acceleration due to gravity

H = total specific enthalpy, J/kg

H_{aw} = specific adiabatic wall enthalpy, J/kg

H_d = dissociation specific enthalpy of air, J/kg

H_e = specific enthalpy at edge of boundary layer, J/kg

H_N = specific dissociation enthalpy of nitrogen, J/kg

H_0 = specific dissociation enthalpy of oxygen, J/kg

H_s = stagnation specific enthalpy, J/kg

H_w = wall specific enthalpy, J/kg

H^* = reference specific enthalpy, J/kg

h_{FR} = Fay-Riddell enthalpy-based convection heat transfer coefficient, $kg/m^2 \cdot s$

h_l = laminar convection heat transfer coefficient, $W/m^2 \cdot K$

h_s = stagnation convection heat transfer coefficient, $W/m^2 \cdot k$

h_{sl} = stagnation line convection heat transfer coefficient, $W/m^2 \cdot k$

h_t = turbulent convection heat transfer coefficient, $W/m^2 \cdot k$

k = thermal conductivity, $W/m \cdot K$

k_1 = thermal conductivity of Material 1, $W/m \cdot K$

k_2 = thermal conductivity of Material 2, $W/m \cdot K$

L = heat flow path length, m

$Le = D\rho c_p/k$, Lewis number, dimensionless

l = length, m

l = axial length of Node 1, m

M = Mach number, dimensionless

M_∞ = free-stream Mach number, dimensionless

$Nu = hD'/k$, Nusselt number, dimensionless

$Pr = c_p\mu/k$, Prandtl number, dimensionless

Pr_w = Prandtl number evaluated at wall temperature, dimensionless

p = pressure, Pa

p = modified Newtonian pressure, Pa

p_e = pressure at edge of boundary layer, Pa

p_s = stagnation pressure, Pa

p_∞ = free-stream pressure, Pa

Q = heat flux, w/m^2

Q_{FR} = Fay-Riddell stagnation point heat flow rate, W/m^2

Q_s = stagnation heat flux, W/m^2

$Q_{\Lambda=0}$ = stagnation line heat flux at zero yaw angle, W/m^2

q = heat flow rate, W

q_c = longitudinal conduction heat flow rate, W

q_{fp} = flat plate heat flux, W/m^2

$q_{i1,o2}$ = heat flow rate inside surface of Node 1 to outside surface of Node 2, W

$q_{m1,i1}$ = heat flow rate middle of Node 1 to inside surface of Node 1, W

$q_{m1,m2}$ = heat flow rate middle of Node 1 to middle of Node 2, W

$q_{o2,m2}$ = heat flow rate outside surface of Node 2 to middle of Node 2, W

q_r = radial heat flow rate, W

q_1 = heat flow rate into Node 1, W

q_1 = heat accumulation rate for spherical Element 1, m

q_{12} = heat flow rate from Node 1 to Node 2, W

$Re = \rho u l/\mu$, Reynolds number, dimensionless

Re_L = local compressible Reynolds number based on length L, dimensionless

Re_{L_i} = incompressible Reynolds number based on length L, dimensionless

Re_θ = local compressible Reynolds number based on momentum thickness θ, dimensionless

C-2

Re_{θ_i} = incompressible Reynolds number based on incompressible momentum thickness θ_i, dimensionless

Re^* = Reynolds number based on reference enthalpy, dimensionless

r = radius of sphere, m

r_{cyl} = radius of cylinder, m

r_i = radius measured to inside of a node, m

r_{i1} = radii measured to inside of Node 1, m

r_{i1} = inner radius of Element 1, m

r_{i2} = radii measured to inside of Node 2, m

r_m = radii measured to middle of a node, m

r_{m1} = radii measured to midpoint of Node 1, m

r_{m2} = radii measured to middle of Node 2, m

r_n = nose radius, m

r_o = radii measured to outside of a node, m

r_{o1} = radii measured to outside of Node 1, m

r_{o1} = outer radius of spherical Element 1, m

r_{o2} = radii measured to outside of Node 2, m

S = inverse of Von Karman-Reynolds analogy factor, dimensionless

$St = h/(\rho c_p u)$, Stanton number, dimensionless

T = temperature at time t, K

$\Delta T = (T_1 - T_2)$, temperature difference, deg K

T_b = bulk fluid temperature of source/sink, K

T_e = temperature at edge of boundary layer, K

T_i = temperature at time t for Node i where $i = 1$ or 2, K

T_{i1} = temperature at inside of Node 1, K

T_{m1} = temperature at middle of Node 1, K

T_{m2} = temperature at middle of Node 2, K

T_{o2} = temperature at outside of Node 2, K

T_s = temperature of radiation source/sink, K

T_1 = present temperature, K

T' = temperature at time $t + \Delta t$, K

T'_i = temperature at time $t + \Delta t$ for Node i where $i = 1$ or 2, K

t = time, s

Δt = time increment, s

U = overall heat transfer coefficient, W/K

$(UA)_{m1,m2}$ = overall heat transfer coefficient area product between middle of Node 1 and middle of Node 2, W/K

u = velocity, m/s

u_e = velocity evaluated at boundary layer edge, m/s

u_∞ = free-stream velocity, m/s

$d\left(\dfrac{u}{u_e}\right)$ = differential increment of velocity ratio, dimensionless

V = volume, m^3

V_i = volume of Node i where $i = 1$ or 2, m^3

x = surface distance along body in flow direction, m

x = running length from nose stagnation point, m

x,y,z = coordinate system

Z = compressibility factor, dimensionless

Z_e = compressibility factor based on boundary layer edge conditions, dimensionless

$\gamma = c_p/c_v$, specific heat ratio, dimensionless

$\gamma_\infty = c_p/c_v$, free-stream specific heat ratio, dimensionless

$\delta = \pi/2 - \theta$ body slope, rad

ϵ = emissivity, dimensionless

Θ = longitudinal angle, rad

Θ_{i2} = longitudinal angle measured to inside of Node 2, rad

Θ_m = longitudinal angle measured to middle of Node, rad

Θ_{m1} = longitudinal angle measured to middle of Node 1, rad

Θ_{m2} = longitudinal angle measured to middle of Node 2, rad

Θ_{o1} = longitudinal angle measured to outside of Node 1, rad

Θ_1 = longitudinal angle measured to Surface 1, rad

Θ_2 = longitudinal angle measured to Surface 2, rad

θ = cylindrical wedge angle, rad

θ = local body angle, rad

θ = angular distance around cylinder from stagnation line in a plane normal to cylinder axis, rad

θ = angular distance around a sphere from stagnation point (see Eq. C-48), rad

Λ = yaw or sweep angle, rad

μ = absolute dynamic viscosity, N·s/m^2

μ_e = absolute dynamic viscosity evaluated at edge of boundary layer, N·s/m^2

μ_s = absolute dynamic viscosity of air at stagnation conditions, N·s/m^2

μ_w = absolute dynamic viscosity of air at wall, N·s/m^2

μ^* = absolute dynamic viscosity evaluated at reference enthalpy, N·s/m^2

ρ = density, kg/m^3

ρ_e = density of air at edge of boundary layer, kg/m^2

ρ_s = density of air at stagnation conditions, kg/m^3

ρ_w = density of air at wall, kg/m^3

ρ_1 = density of Node 1, kg/m^3

ρ^* = density of air based on reference enthalpy, kg/m^3

σ = Stefan-Boltzmann constant, W/m^2·K^4

τ_m = Mangler transformation, dimensionless

ψ = latitudinal angle, rad

ψ_{i2} = latitudinal angle measured to inside of Node 2, rad

ψ_{m1} = latitudinal angle measured to middle of Node 1, rad

ψ_{m2} = latitudinal angle measured to middle of Node 2, rad

ψ_{o1} = latitudinal angle measured to outside of Node 1, rad

ψ_1 = latitudinal angle measured to Surface 1, rad

ψ_2 = latitudinal angle measured to Surface 2, rad

C-1 INTRODUCTION

This appendix deals with the development in differential form of heat transfer equations employed in the analyses of external flows and aerodynamic heating associated with the design of a free flight rocket motor.

A free flight rocket designer will probably use automated thermal design programs that incorporate many of the equations presented in this appendix. Consequently, it is beneficial for the designer to develop an understanding of the geometries and equations used in these programs to construct the input and interpret the output properly.

The appendix begins with a discussion of the most important geometric shapes of concern for modeling external flows, namely, cylinders and spheres. It is of interest in aerodynamics heating analyses to evaluate the influence of asymmetries and protuberances on the external surface. Therefore, an understanding of heat conduction in the radial, circumferential, and axial directions of a general cylindrical body is of interenst. Frequently, a singular direction of heat flow dominates, and, therefore, the analyst can by judicious seelection keep the design calculations one-dimensional. Accordingly, equations are presented to describe one-dimensional heat conduction in each of these directions. The differential form of each equation is shown because this best represents a general element of the computerized numerical analysis programs. The equations also include the presence of a contact resistance in the direction of heat flow.

A similar treatment of spherical coordinates is presented because this geometry relates to the nose section of the rocket and to other complex geometries- such as spherical segments, ogives, and cones—in which a radial dimension and two angles are required to define an element of the geometry. General equations for conduction, convection, and radiation in each of the primary directions—radial, longitudinal, and latitudinal-are   presented.

The latter paragraphs of this appendix present many of the various empirical techniques used for calculating aerodynamic heating to the external surfaces of a free flight rocket motor. The calculation sequence is discussed and is followed by a presentation of various calculation techniques. Since external flows are complex, the analyst usually divides the complex geometry of the rocket into a series of simple body shapes including sphere-cone-cylinders, sphere-ogive-cylinders, swept cylinders, and flat plates. Accordingly, equations are presented for aerodynamic heating of these basic shapes. Heat transfer coefficient correlations are presented for laminar and turbulent flow, stagnation point heating, heating to yawed cylinders, flat plates, and the hemispherical distribution of aerodynamic heating. Extensive primary references are listed to provide the analyst with direct source information on the calculation of postshock properties for conical, oblique, normal and parallel shocks, thermodynamic properties, and transport properties of external flows over free flight rockets.

C-2 THERMAL MODELING

This paragraph prevents a general form of modeling heat flow equations. The modeling is applicable to computer programs of thermal network analyzers. The heat flow modes involved include conduction, convection, and radiation. The methods presented express the heat flow as finite difference equations. The models provide geometric and mathematical descriptions of the cylindrical and spherical coordinate options available with the NHEAT program (Ref. 1).

C-2.1 CYLINDRICAL COORDINATE THERMAL MODELING

C-2.1.1 Cylindrical Thermal Storage Model

The general heat storage rate q for thermal model elements of cylindrical geometry is of the form

$$q_1 = \rho_1 c_{p_1} V_1 (T_1' - T_1)/\Delta t, \text{ W} \tag{C-1}$$

where

q_1 = heat flow rate into an element, Node 1, W
V_1 = volume of Node 1, m^3
ρ_1 = density of Node 1, kg/m^3
c_{p_1} = specific heat at constant pressure of Node 1, J/kg·K
T_1' = temperature at $t + \Delta t$, K
T_1 = present temperature, K
Δt = time increment, s.

Note that Eq. C-1 represents the heat being accumulated by an element rather than passing through the element. The temperature difference (T' — T) represents a change in temperature of the element in time At. This is contrasted with the concept of steady heat flow through a medium in which the temperature difference represents a temperature potential.

The nomenclature for cylindrical heat flow elements is shown in Fig. C-1. By use of this nomenclature, the general heat storage rate equation becomes

$$q_1 = \frac{\rho_1 c_{p_1} \left(\dfrac{\ell\theta}{2}\right)(r_{o1}^2 - r_{i1}^2)(T_1' - T_1)}{\Delta t}, \text{ W} \tag{C-2}$$

where

ℓ = axial length of Node 1, m
r_{o1} = radius measured to outside of Node 1, m
r_{i1} = radius measured to inside of Node 1, m
θ = cylindrical wedge angle of Node 1, rad.
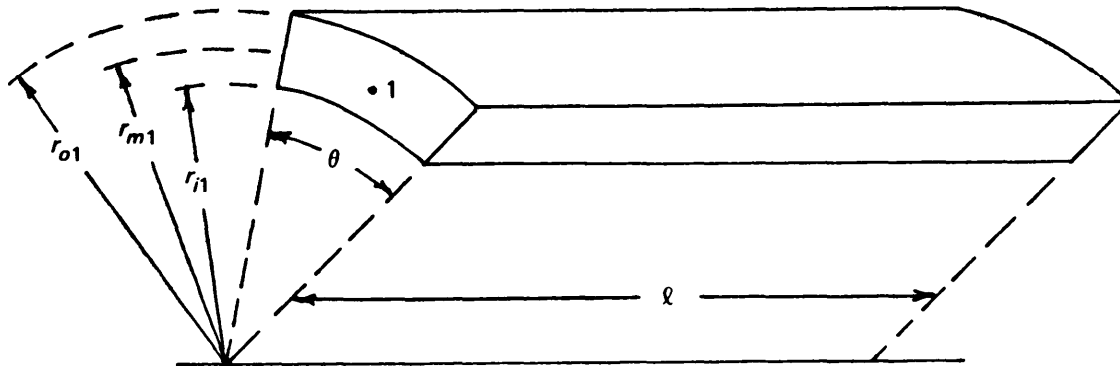
NOTE: On Figures C-1 through C-12, ● denotes the center of the designated surface.

Figure C-1. Cylindrical Heat Storage Model for Node 1

C-2.1.2 Cylindrical Radial Heat Conduction Model

Radial heat conduction between two concentric cylinders of different materials-identified as 1 and 2—through an interface is shown in Fig. C-2. The development of the radial heat flow rate conduction equation is presented here. The steps in the development are applicable to the axial and circumferential equations presented. For a steady heat flow rate

$$q_{m1,m2} = q_{m1,i1} = q_{i1,o2} = q_{o2,m2}, \text{ W}. \tag{C-3}$$
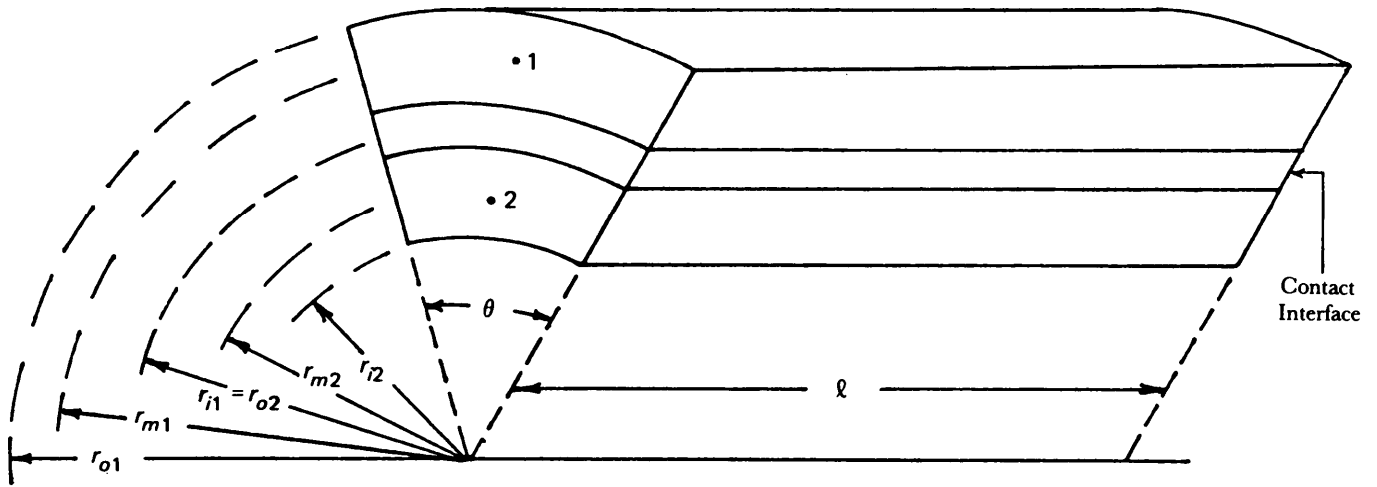
Figure C-2. Cylindrical Radial Heat Conduction Model for Node 1 to Node 2

For the three paths indicated, the heat flow rates are

$$q_{m1,i1} = \frac{k_1 \theta \ell (T_{m1} - T_{i1})}{\ln(r_{m1}/r_{i1})}, \text{ W} \tag{C-4}$$

$$q_{i1,o2} = C r_{o2} \theta \ell (T_{i1} - T_{o2}), \text{ W} \tag{C-5}$$

$$q_{o2,m2} = \frac{k_2 \theta \ell (T_{o2} - T_{m2})}{\ln(r_{o2}/r_{m2})}, \text{ W} \tag{C-6}$$

where

C = contact conductance at interface, W/m²·K
k_1 = thermal conductivity of Material 1, W/m·K
k_2 = thermal conductivity of Material 2, W/m·K
$q_{m1,m2}$ = heat flow rate middle of Node 1 to middle to Node 2, W
$q_{m1,i1}$ = heat flow rate middle of Node 1 to inside surface of Node 1, W
$q_{i1,o2}$ = heat flow rate inside surface of Node 1 to outside surface of Node 2, W
$q_{o1,m2}$ = heat flow rate outside surface of Node 2 to middle of Node 2, W
r_{m1} = radii measured to midpoint of Node 1, m
r_{m2} = radii measured to middle of Node 2, m
r_{i1} = radii measured to inside of Node 1, m
r_{o2} = radii measured to outside of Node 2, m
T_{m1} = temperature at middle of Node 1, K
T_{m2} = temperature at middle of Node 2, K
T_{i1} = temperature at inside of Node 1, K
T_{o2} = temperature at outside of Node 2, K.

The temperature difference between nodes may be written as

$$T_{m1} - T_{m2} = (T_{m1} - T_{i1}) + (T_{i1} - T_{o2}) + (T_{o2} - T_{m2}), \text{ deg K} \tag{C-7}$$

$$T_{m1} - T_{m2} = \frac{q_{m1,m2}}{(UA)_{m1,m2}}, \text{ deg K} \tag{C-8}$$

where

$(UA)ml,m2$ = overall heat transfer coefficient area product between middle of Node 1 and middle of Node 2, W/K.

Solve Eqs. C-4 through C-6 and C-8 for the temperature differences and substitute into Eq. C-7, i.e.,

$$\frac{q_{m1,m2}}{(UA)_{m1,m2}} = \frac{q_{m1,i1}\ln(r_{m1}/r_{i1})}{k_1\theta l} = \frac{q_{i1,o2}}{Cr_{o2}\theta \ell}$$

$$+ \frac{q_{o2,m2}\ln(r_{o2}/r_{m2})}{k_2\theta \ell}, \ K^{-1}. \tag{C-9}$$

Solve Eq. C-9 for $(UA)m1,m2$ and make use of Eq. C-3, i.e.,

$$(UA)_{m1,m2} = \frac{1}{\dfrac{\ln(r_{m1}/r_{i1})}{k_1\theta \ell} + \dfrac{1}{Cr_{o2}\theta \ell} + \dfrac{\ln(r_{o2}/r_{m2})}{k_2\theta \ell}}, \ W/K. \tag{C-10}$$

Then from Eq. C-8

$$q_{12} = \frac{\theta \ell(T_1 - T_2)}{\dfrac{\ln(r_{m1}/r_{i1})}{k_1} + \dfrac{1}{Cr_{o2}} + \dfrac{\ln(r_{o2}/r_{m2})}{k_2}}, \ W. \tag{C-11}$$

where

q_{12} = heat flow rate from Node 1 to Node 2, W
T_1 = temperature at time t for Node 1, K
T_2 = temperature at time t for Node 2, K
θ = cylindrical wedge angle, rad.

C-2.1.3 Cylindrical Circumferential Heat Conduction Model

Circumferential heat conduction in a cylindrical segment between two nodes of different materials and through a contact interface is illustrated in Fig. C-3. The heat flow rate q_{12} between Nodes 1 and 2 is

$$q_{12} = \frac{(T_1 - T_2)}{\dfrac{\theta/2}{k_1\ell\,n(r_o/r_i)} + \dfrac{1}{C\ell\,(r_o - r_i)} + \dfrac{\theta/2}{k_2\ell\,n(r_o/r_i)}}, \ W. \tag{C-12}$$

where

r_i = radius measured to inside of a node, m
r_o = radius measured to outside of a node, m.

C-2.1.4 Cylindrical Axial Heat Conduction Model

Axial heat conduction in a cylindrical segment between two nodes of different materials and through a contact interface is illustrated in Fig. C-4. The heat flow rate q_{12} between Nodes 1 and 2 is

$$q_{12} = \frac{\theta(r_o^2 - r_i^2)(T_1 - T_2)}{\ell/k_1, + 2/C + \ell/k_2}, \ W. \tag{C-13}$$

C-8
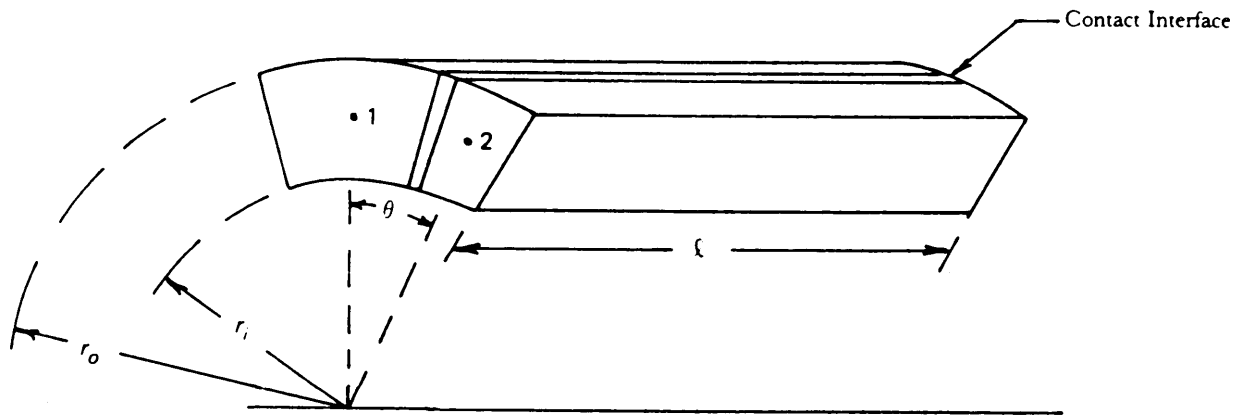
Figure C-3. Cylindrical Circumferential Heat Conduction Model For Node 1 to Node 2
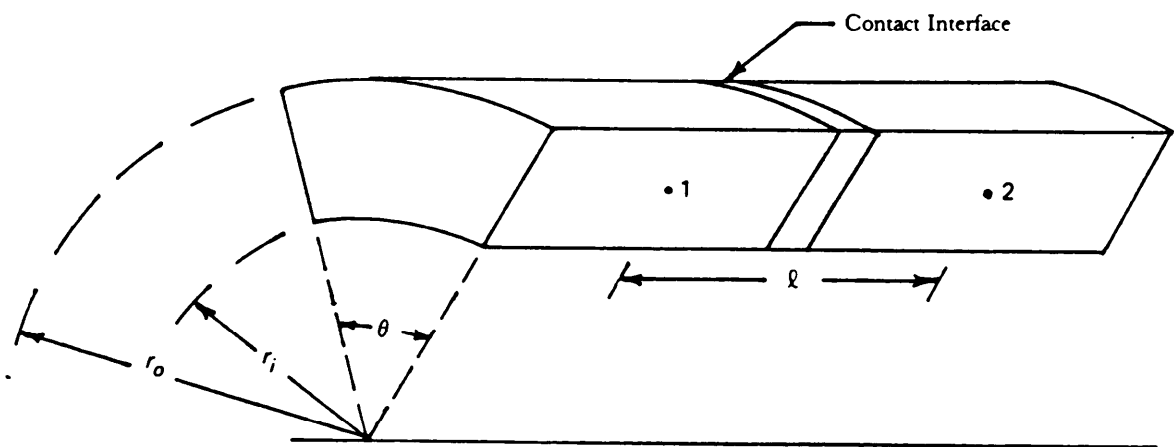
Figure C-4. Cylindrical Axial Heat Conduction Model

C-2.1.5 Cylindrical Heat Convection Model

Convection Heat flow into or out of a cylindrical segment is illustrated in Fig. C-5. The general heat flow

$$q = hA(T_b - T_1), \text{ W} \tag{C-14}$$

where

A = surface area normal to heat flow path of nodal element, m^2
h = convective heat transfer coefficient, $W/m^2 \cdot K$
q = heat flow rate, W
T_b = bulk fluid temperature of source sink, K.

In terms of the nomenclature of **Fig. C-5**

$$q_1 = hr_o\theta\ell(T_b - T_1), \text{ W.} \tag{C-15}$$

C-2.1.6 Cylindrical Heat Radiation Model

Radiation heat flow into or out of a cylindrical segments is illustrated in Fig. C-5. The general heat flow rate q into or out of Node 1 may be expressed as

C-9
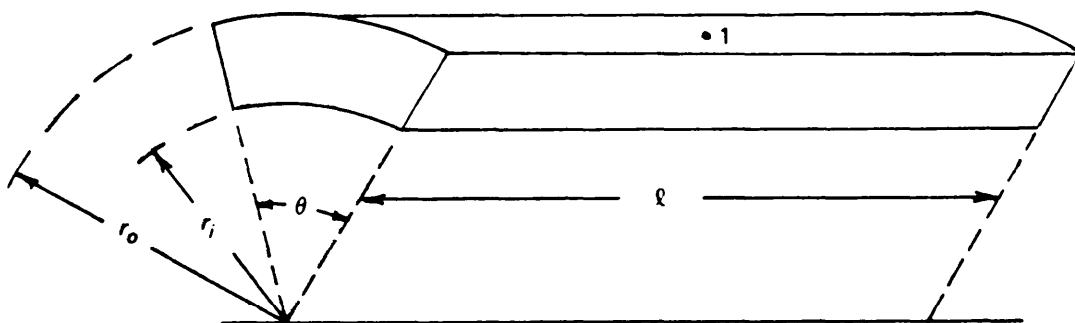
Figure C-5. Cylindrical Heat Convection and Radiation Model

$$-q = \sigma \epsilon F.A(T^4 - T_s^4), \text{ W} \tag{C-16}$$

where

$-q$ = heat flux out of body. W

σ = Stefan-Boltzmann constant. W $m^2 \cdot K^2$

ϵ = emissivity. dimensionless

F = radiation shape factor. dimensionless

T = temperature at time t. K

T_s = temperature of radiation source sink. K.

In terms of the nomenclature of Fig. C-5

$$-q_1 = \sigma \epsilon F r_o \theta l(T_1^4 - T_s^4), \text{ W}. \tag{C-17}$$

C-2.2 SPHERICAL COORDINATE THERMAL MODELING

C-2.2.1 Spherical Thermal Storage Model

The genelal heat storage rate q for thermal model elements of spherical geometry (Fig. C-6) is of the form given by Eq. C-1. i.e..

$$q = \rho c_p V (T' - T) \Delta t, \text{ W}$$

where

c_p = specific heat at constant pressure. J kg·K

q = heat flow rate. W

T' = temperature at time $t - \Delta t$. K

V = volume. m^3

ρ = density. kg m^3.

The nomenclature for spherical heat flow elements is shown in Fig. C-6. The general heat storage rate equation. applying the indicated nomenclature. becomes

$$q_1 = \frac{\rho_1 c_{p_1} \frac{(\psi_2 - \psi_1)}{3}(r_{o1}^3 - r_{i1}^3)(T_1' - T_1)(cos\Theta_1 - cos\Theta_2)}{\Delta t}. \text{ W} \tag{C-18}$$
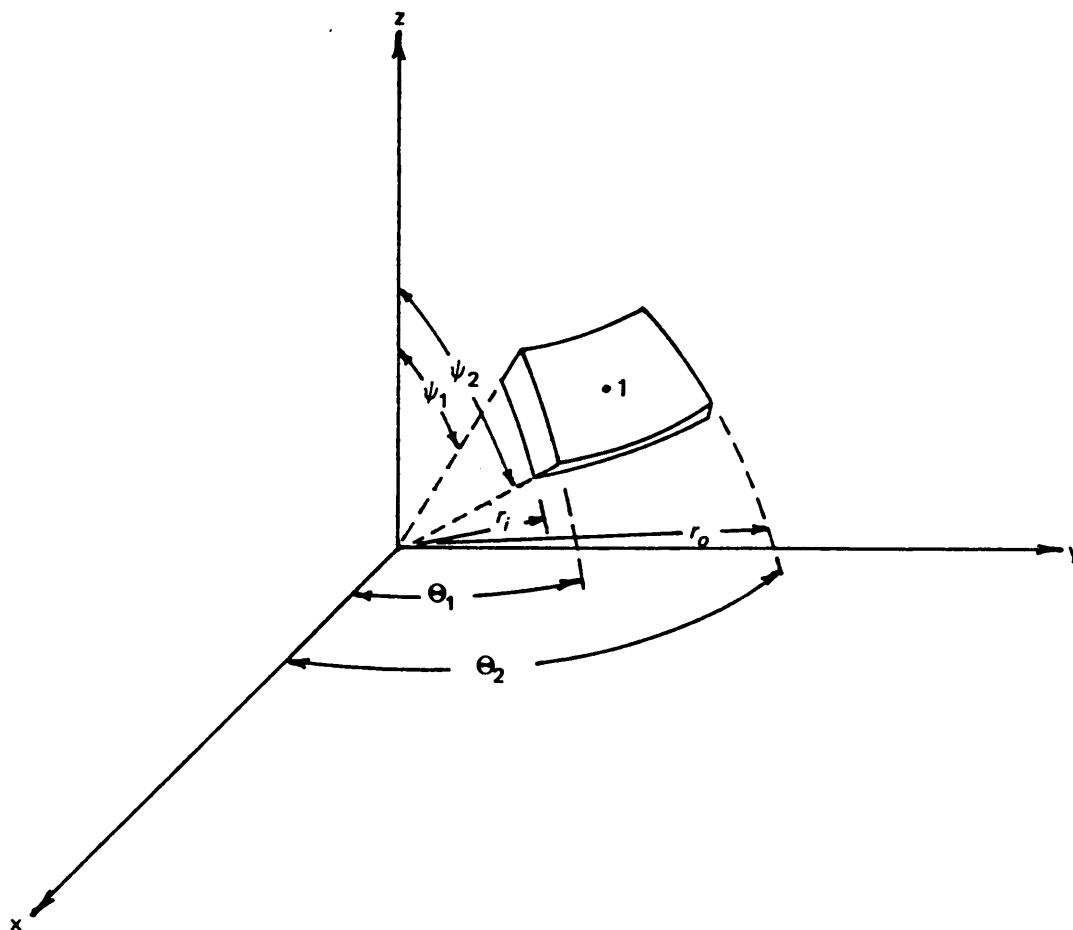
Figure C-6. Spherical Heat Storage Model

where

c_{p_1} = specific heat at constant pressure of spherical Element 1, J/kg·K

q_1 = heat accumulation rate for spherical Element 1, W

r_{o1} = outer radius of spherical Element 1, m

r_{i1} = inner radius of spherical Element 1, m

Θ_1 = latitudinal angle measured to Surface 1, rad

Θ_2 = latitudinal angle measured to Surface 2, rad

ψ_1 = longitudinal angle measured to Surface 1, rad

ψ_2 = longitudinal angle measured to Surface 2, rad.

C-2.2.2 Spherical Radial Heat Conduction Model

Heat flowing radially in a spherical segment can be illustrated as shown in Fig. C-7. The model described here can be used where each layer of the sphere segment is homogeneous and it is desired to calculate heat flow into or out of the segment in the radial direction. The equations can be developed in a manner similar to that described for cylindrical heat flow. Heat flowing radially experiences a change in conduction area proportional to r^2. The heat flow rate q_{12} between Nodes 1 and 2 in Fig. C-7 may be exprcessed as

$$q_{12} = \frac{(\psi_2 - \psi_1)(\cos\Theta_1 - \cos\Theta_2)(T_2 - T_1)}{\dfrac{\left(\dfrac{1}{r_{i1}} - \dfrac{1}{r_{m1}}\right)}{k_1} + \dfrac{1}{Cr_{o1}^2} + \dfrac{\left(\dfrac{1}{r_{i2}} - \dfrac{1}{r_{m2}}\right)}{k_2}} \text{ , W.} \qquad \textbf{(C-19)}$$
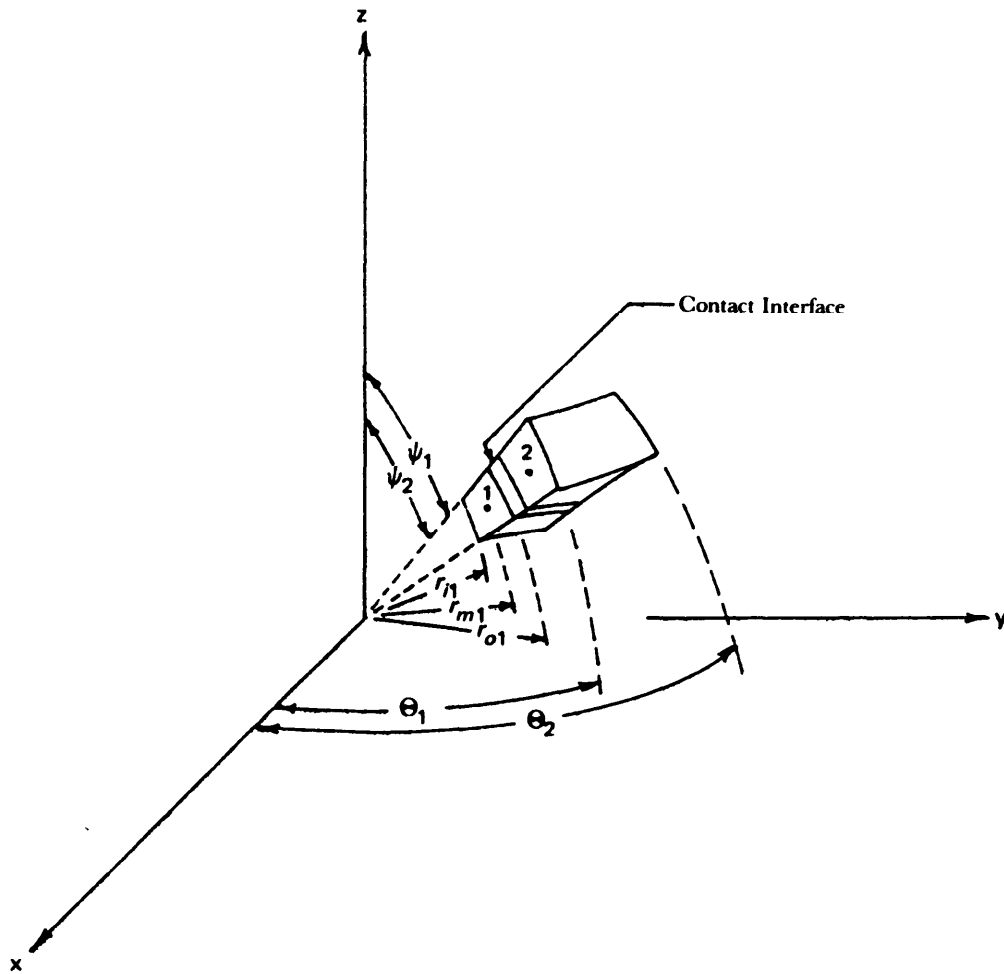
Figure C-7. Spherical Radial Heat Conduction Model

C-2.2.3 Spherical Longitudinal Heat Conduction Model

Heat flow longitudinally in a spherical segment can be modeled as provided by Fig. C-8. The equations for heat flow in the longitudinal direction between Nodes 1 and 2 can be derived similarly to that for flow in the radial direction. Expressions describing the heat flow path length L, the surface area normal to heat flow path .4, and the heat flow rate q_{12} through that area are provided by Eqs. C-20, C-21, and C-22, respectively.

$$L = r_m(\Theta_{m2} - \Theta_{m1}), \text{ m} \tag{C-20}$$

where

L = heat flow path length, m
r_m = radius measured to center of a node, m
Θ_{m1} = longitudinal angle measured to center of Node 1, rad
Θ_{m2} = longitudinal angle measured to center of Node 2, rad.

$$A = \frac{(r_o^2 - r_i^2)}{2} \sin\Theta_m(\psi_2 - \psi_1), \text{ m}^2 \tag{C-21}$$

where

Θ_m = longitudinal angle measured to center of a node, rad.

C-12
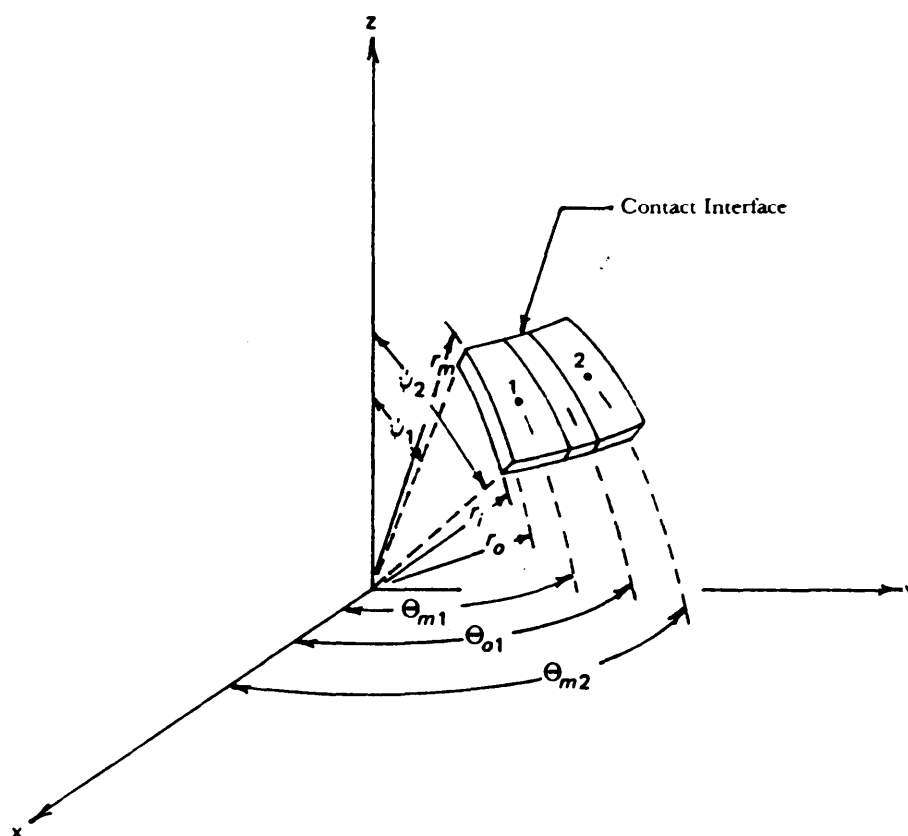
Figure C-8. Spherical Longitudinal Heat Conduction Model

$$q_{12} = [(r_o - r_i)(\psi_2 - \psi_1)(T_2 - T_1)] \div \left\langle \left\{ \frac{\ln[\tan(\Theta_{o1}\ 2)\ \tan(\Theta_{m1}\ 2)]}{k_1} \right\} \right.$$

$$\left. + \left[\frac{C(r_o + r_i)\sin\Theta_{o1}}{2} \right] + \left\{ \frac{\ln[\tan(\Theta_{m2}\ 2)\ \tan(\Theta_{i2}\ 2)]}{k_2} \right\} \right\rangle, W. \tag{C-22}$$

where

Θ_{o1} = longitudinal angle measured to outside of Node 1, rad
Θ_{i2} = longitudinal angle measured to inside of Node 2, rad.

C-2.2.4 Spherical Latitudinal Heat Conduction Model

Heat flow latitudinally in a spherical segment can be modeled as provided by Fig. C-9. Expressions describing the heat flow path length L, the surface area normal to the heat flow path A, and the heat flow rate q12 through that area are provided by Eqs. C-23, C-24, and C-25, respectively.

$$L = r_m\sin\Theta_m(\psi_{m2} - \psi_{m1}), \text{ m} \tag{C-23}$$

where

ψ_{m1} = latitudinal angle measured to center of Node 1, rad
ψ_{m2} = latitudinal angle measured to center of Node 2, rad.

$$A = \frac{(r_o^2 - r_i^2)}{2}(\Theta_2 - \Theta_1), \text{ m}^2. \tag{C-24}$$
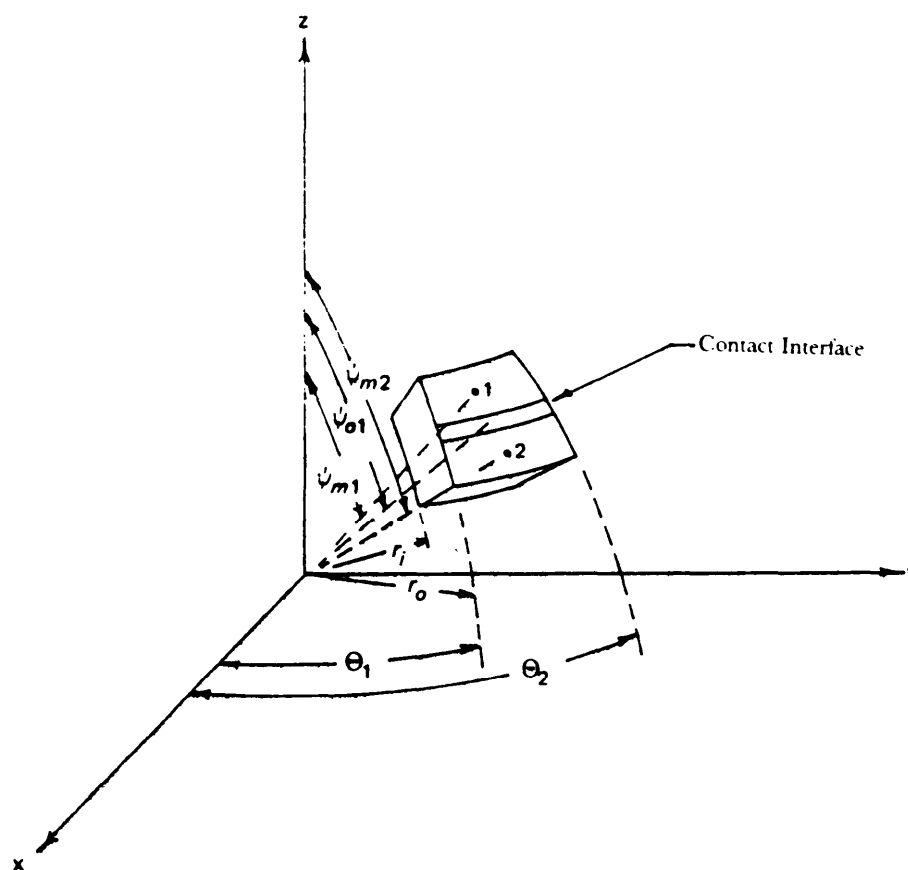
Figure C-9. Spherical Latitudinal Heat Conduction Model

$$q_{12} = \frac{(r_o - r_i)(T_2 - T_1)}{\dfrac{(\psi_{o1} - \psi_{m1})}{k_1 \ln\left[\dfrac{\tan(\Theta_2/2)}{\tan(\Theta_1/2)}\right]} + \dfrac{2}{c(r_o - r_i)(\Theta_1 - \Theta_2)} + \dfrac{(\psi_{i2} - \psi_{m2})}{k_2 \ln\left[\dfrac{\tan(\Theta_2/2)}{\tan(\Theta_1/2)}\right]}} , \text{W}. \qquad \text{(C-25)}$$

where

ψ_{i2} = latitudinal angle measured to inside of Node 2, rad

ψ_{o1} = latitudinal angle measured to outside of Node 1, rad.

C-2.2.5 Spherical Heat Convection Model

Convection heat flow rate in the radial direction through a spherical segment is illustrated in Fig. C-10. The confection heat flow rate q_1, into or out of Node 1, is also derived by Eq. C-14, i.e.,

$$q_1 = hA(T_b - T_1), \text{W}.$$

In terms of the nomenclature of Fig. C-10, this expression for convection heat transfer becomes

$$q_1 = hr_{o1}^2 (\cos\Theta_1 - \cos\Theta_2)(\psi_2 - \psi_1)(T_b - T_1), \text{W}. \qquad \text{(C-26)}$$

C-2.2.6 Spherical Heat Radiation Model

Radiation heat flow rate in the radial direction through a spherical segment is illustrated by Fig. C-10 The radiation heat flow rate q_1, into or out of the surface of Node 1, is by Eq. C-16

C-14
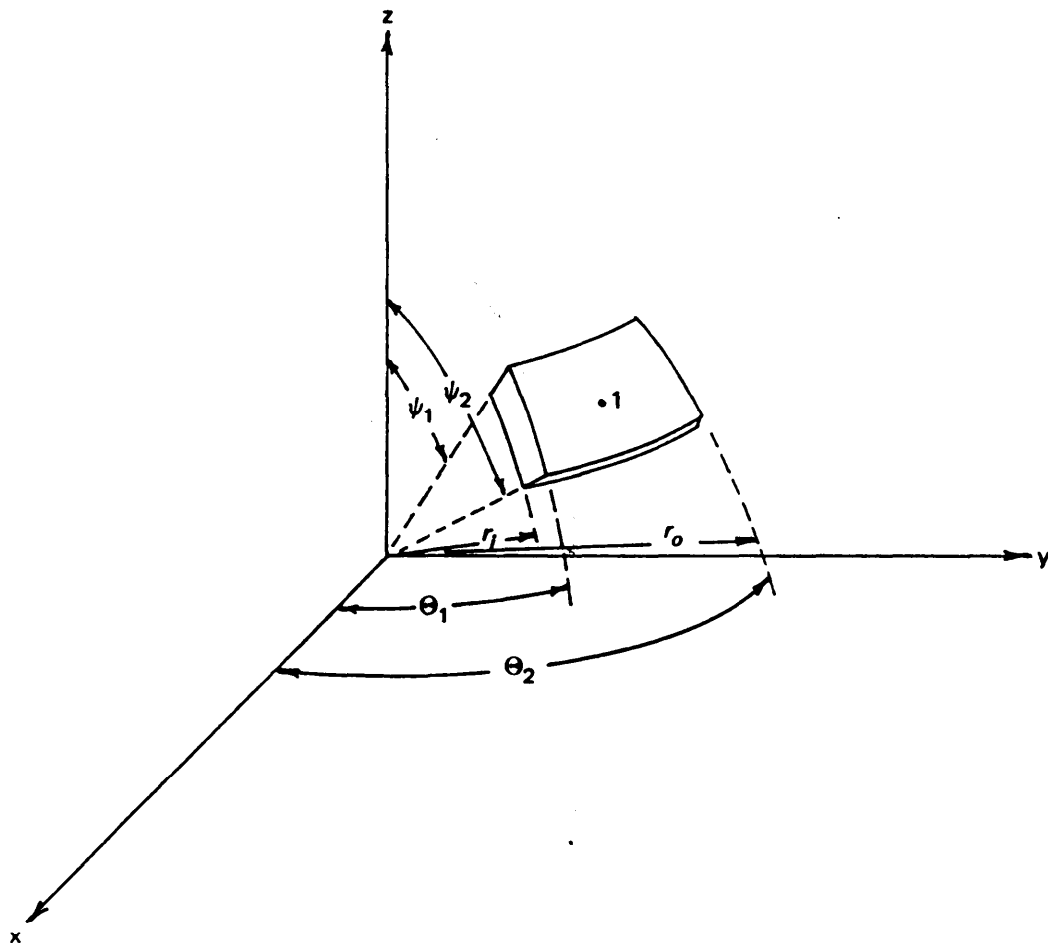
Figure C-10. Spherical Heat Convection and Radiation Model

$$q_1 = \sigma \epsilon F A (T_1^4 - T_s^4), \text{ W.}$$

In terms of the nomenclature of Fig. C-10, the expression for radiation heat transfer becomes

$$q_1 = \sigma \epsilon F r_{o1}^2 (\cos\Theta_1 - \cos\Theta_2)(\psi_2 - \psi_1)(T_1^4 - T_s^4), \text{ W.} \tag{C-27}$$

C-2.2.7 Spherical Modeling for Nonhomogeneous Spherical Elements

C-2.2.7.1 General

In some special cases it may be desirable to model thermal elements in spherical coordinates to allow latitudinal heat flow (Ref. 2). The detailed study, described in Ref. 2, modeled heat flow in elements of spherical slices as shown in Fig. C-11. Particular packaging configurations may require development of particular equations or the use of one of the general coordinate finite element computer programs to solve for heat transfer characteristics.

C-2.2.7.2 Derivation of Area, Volume, and Heat Transfer Equations for a Spherical Slice

The spherical slice shown in Fig. C-11 is defined by the angles ψ_1, ψ_2, Θ_1 and Θ_2, and the radii r_i and r_o. These angles and radii are defined specifically by Fig. C-12 in which
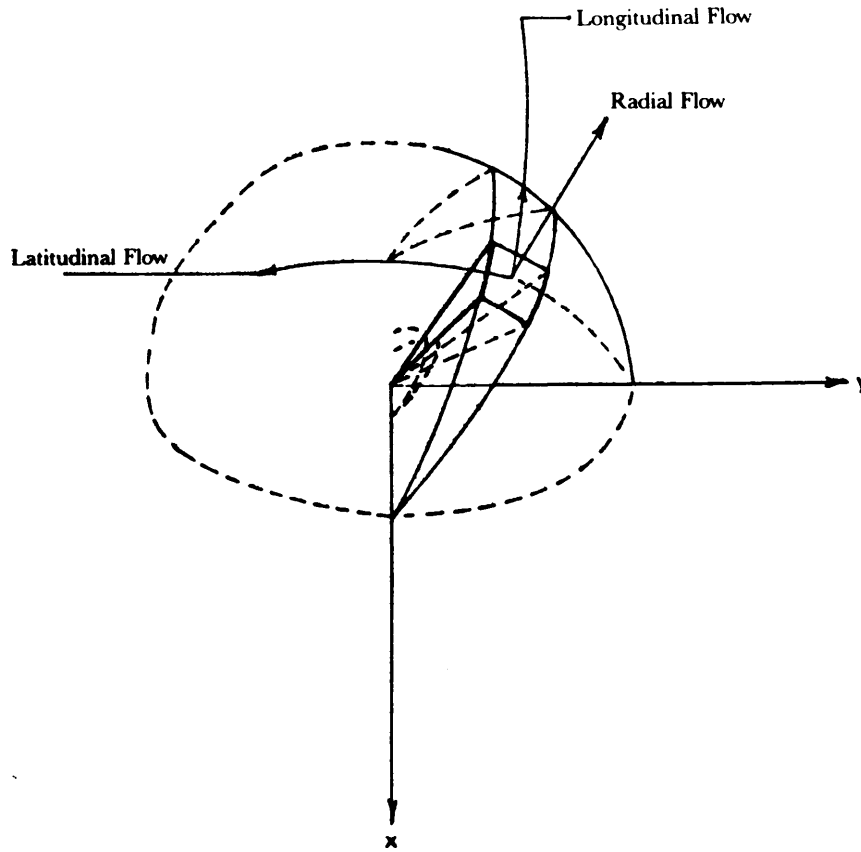
Figure C-11. Spherical Slice Model

$$-\frac{\pi}{2} \leq \psi_1 \leq \psi_2 < \frac{\pi}{2}$$

$$0 < \Theta_1 < \Theta_2 < \pi$$

$$0 \leq r_i < r_o.$$

The surface area integral is

$$A = \int_{\psi_1}^{\psi_2} \int_{\Theta_1}^{\Theta_2} r_o^2 \sin\Theta d\Theta d\psi, \text{ m}^2 \qquad \text{(C-28)}$$

which may be integrated directly since the three coordinates are independent of each other as follows:

$$A = r_o^2 (\cos\Theta_1 - \cos\Theta_2)(\psi_2 - \psi_1), \text{ m}^2. \qquad \text{(C-29)}$$

The volume integral of a concentric slice is

$$V = \int_{r_i}^{r_o} \int_{\psi_1}^{\psi_2} \int_{\Theta_1}^{\Theta_2} r_o^2 \sin\Theta d\Theta d\psi dr, \text{ m}^3 \qquad \text{(C-30)}$$

which, upon integration, gives

$$(r_o^3 - r_i^3)(\cos\Theta_1 - \cos\Theta_2)(\psi_2 - \psi_1)/3, \text{ m}^3. \qquad \text{(C-31)}$$

The basic conduction equation is given by

C-16

NOTE:
These are not spherical coordinates.
Θ = longitudinal angle
ψ = latitudinal angle
r is measured from origin.
$r_o = r_i + dr$
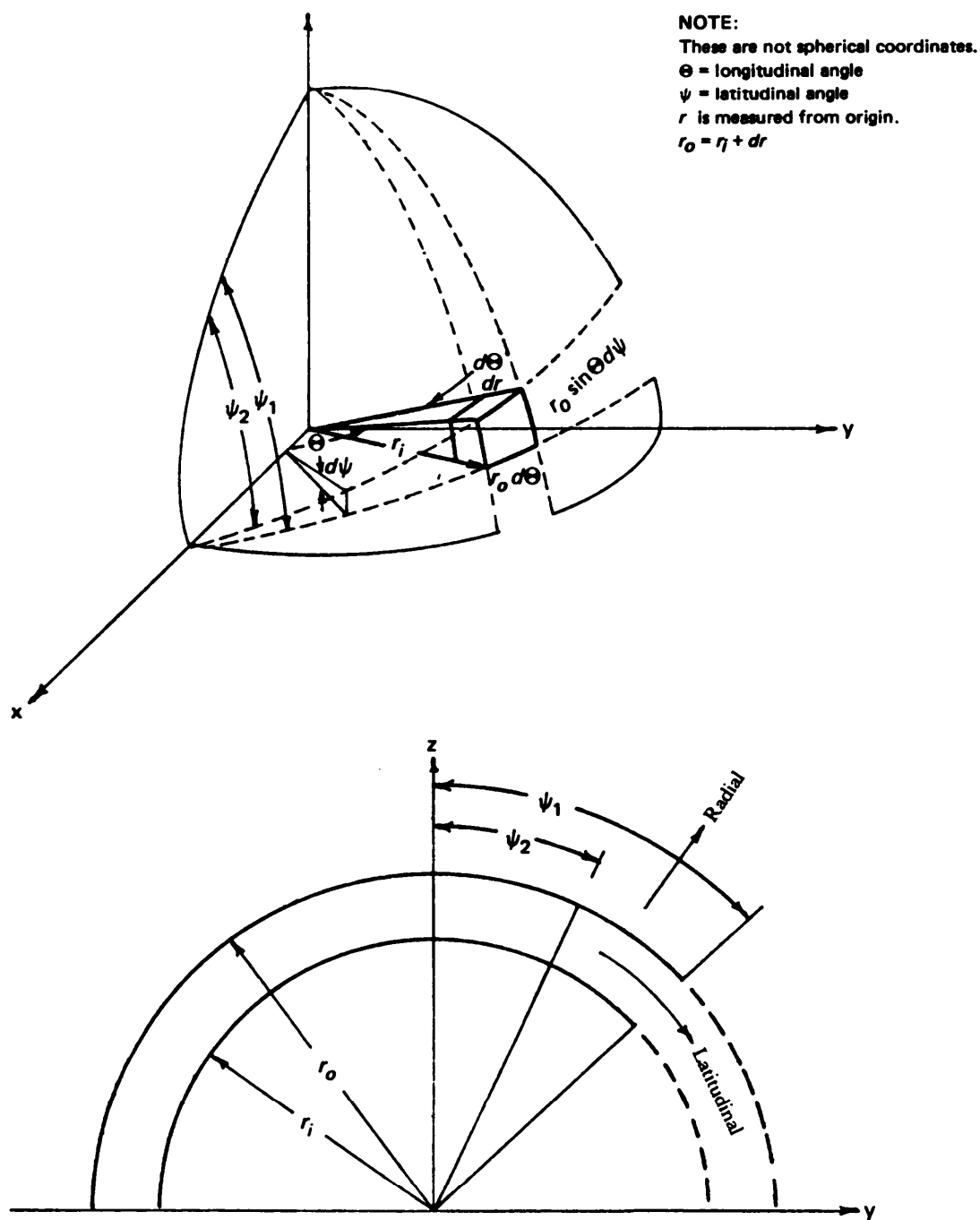
Figure C-12.   Spherical Slice Coordinate System

$$dq = k\frac{dA}{d\ell}\Delta T, \text{ W} \tag{C-32}$$

where

$\Delta T = (T_1 - T_2)$, the temperature difference between Nodes 1 and 2, deg K

dA = element of area, m^2

$d\ell$ = element of conductive path length, m

dq = resultant heat flow, W.

Setting up the conduction heat rate transfer q, in the radial direction yields

$$dA = r^2\sin\Theta d\Theta d\psi, \text{ m}^2$$
$$d\ell = dr, \text{ m}$$

where
r = **radius of sphere, m**

and by substituting these expressions into Eq. C-32, we have

$$q_r\int_{r_i}^{r_o}\frac{dr}{r^2} = k\Delta T\int_{\psi_1}^{\psi_2}\int_{\Theta_1}^{\Theta_2}\sin\Theta d\Theta d\psi, \text{ W} \qquad \text{(C-33)}$$

where
q_r = radial heat flow rate, W

which may be integrated to give

$$q_r = k\Delta T\left(\frac{r_i r_o}{r_o - r_i}\right)(\cos\Theta_1 - \cos\Theta_2)(\psi_2 - \psi_1), \text{ W}. \qquad \text{(C-34)}$$

Setting up the conduction heat transfer rate q_c in the latitudinal direction yields

$$dA = rd\Theta dr, \text{ m}^2$$
$$d\ell = r\sin\Theta d\psi, \text{ m}$$

and, by substituting these expressions into Eq. C-32.

$$q_c\int_{\psi_1}^{\psi_2} d\psi = k\Delta T\int_{\Theta_1}^{\Theta_2}\int_{r_i}^{r_o}\frac{drd\Theta}{\sin\Theta}, \text{ W} \qquad \text{(C-35)}$$

where
q_c = latitudinal conduction heat flow rate, W

which may be integrated to give

$$q_c = \left[\frac{k\Delta t(r_o - r_i)}{(\psi_2 - \psi_1)}\right]\ln\left[\frac{\tan(\Theta_2/2)}{\text{ran}(\Theta_1/2)}\right], \text{ W}. \qquad \text{(C-36)}$$

Eqs. C-34 and C-36 maybe replaced by Eqs. C-19 and C-25, respectively, where conduction occurs between spherical nodes of different materials or a contact resistance occurs between elements.

C-3 FORCED CONVECTION HEAT TRANSFER TO ROCKET MOTOR EXTERNAL SURFACES

The effects of aerodynamic heating rates to the external surface of a rocket motor influence the design of the vehicle external and internal thermal protection systems. This paragraph presents many of the empirical techniques used for calculating external, forced convection, and heat transfer (aerodynamic heating) to rocket motor surfaces. These calculations arc performed in a series of steps as follows:

1. The aerodynamic heating to a complex body is analzyed by dividing the body into simple shapes —i e., sphere-cone-cylinders, sphere-ogive-cylinders, swept cylinders, flat plates, etc.

2. Local surface pressures are obtained for each shape based on body geometry, attitude, free stream Mach number using two-dimensional flowfield methodologies such as the modified Newtonian (Ref. 3), Tangent Wedge and Parallel Shock, (Refs. 4 and 5), Tangent Cone, (Refs. 6 through 13) and Prandtl Meyer Expansion (Ref. 14) Theories.

3. A normal, parallel, oblique or conical shock is selected as applicable for each body shape for calculating postshock flow conditions. Schlieren - or shadowgraph-measured shock structure definition can be used if available for selecting the correct shock shape. The postshock total pressure/enthalpy are isentropically expanded to the selected local body pressure to obtain the other local boundary layer edge properties.

4. The boundary layer edge properties, free stream properties, and postshock properties are used in empirical aerodynamic heating calculations for the different vehicle shapes.

5. Steps 1 through 4 are repeated for selected time intervals along the rocket motor trajectory.

Heat transfet to an axisymmetric spherical stagnation point can be calculated using the method of Fay and Riddell (Ref. 14). The distribution around a sphere or ogive to the sonic point (approximately 30 deg off the nose) can be calculated using Lees' distribution method for laminar flow (Ref. 15). The Lees, Detra, and Hidalgo (Ref. 16) hemisphere method provides a method for calculating turbulent heating from the sonic point rearward on a sphere or ogive. The heat flux aft of the sphere-cone or sphere-ogive junction can be calculated by using the method of Eckert (Ref. 17) for laminar flow and Spalding and Chi (Ref. 18) for turbulent flow. The heating rate to flat plates and cylinders at small angle of attack can also be calculated using the Eckert or Spalding and Chi methods. The heat transfer to a swept leading edge provided by rocket motors at large angles of attack can be predicted by using the theory of Beckwith and Gallagher (Ref. 19) for either laminar or turbulent flow.

The methods of Fay and Ridden; Lees; Lees, Detra, and Hidalgo; Eckert; Spalding and Chi; and Beckwith and Gallagher are presented in the subparagraphs that follow. The laminar method of Sayano and Greenwald (Ref. 20) is sometimes preferred to that of Beckwith and Gallagher for laminar heating to a yawed cylinder. This method is also presented.

The prediction of the thermal characteristics of weapons operating in high-speed flight requires knowledge of certain thermodynamic and transport properties for air. Several methods for calculating these properties and comparisons to measured data are presented in Ref. 21. Ref. 22 presents properties of air which are useful in calculating the thermal characteristics of air.

The concept of stagnation point and stagnation line aerodynamic heating theories is discussed in texts such as Refs. 23 and 24.

'I-his paragraph presents methods of estimating the forced convection heat transfer to the surface of various configurations. Methods are presented for laminar and turbulent boundary layers.

C-3.1 SPHERICAL STAGNATION POINT HEATING

The essential equations of stagnation heating based on the theory of Fay and Riddell are

$$Q_{FR} = \frac{Nu}{\sqrt{Re}} \sqrt{\rho_w \mu_w \left(\frac{du_e}{dx}\right)} \left(\frac{H_s - H_w}{Pr_w}\right), \text{W/m}^2 \tag{C-37a}$$

$$h_{FR} = Q_{FR} / (H_s - H_w), \text{kg/m}^2 \cdot \text{s} \tag{C-37b}$$

where
h_{FR} = Fay-Riddell enthalpy-based convection heat transfer coefficient, kg m^2·s
H_s = stagnation specific enthalpy, J kg
H_w = wall specific enthalpy, J kg
Nu = Nusselt number, dimensionless

Re = Reynolds number, dimensionless

Q_{FR} = Fay-Riddell stagnation point heat flow rate, W·m²

Pr_w = Prandtl number at wall temperature, dimensionless

u_e = velocity evaluated at boundary layer edge, m·s

x = surface distance along body in flow direction, m

μ_w = absolute dynamic viscosity of air at wall, N·s·m²

ρ_w = density of air at wall, kg/m³

$$\frac{Nu}{\sqrt{Re}} = 0.76 \left[Pr_w \left(\frac{\rho_s \mu_s}{\rho_w \mu_w} \right) \right]^{0.4} \left[1 + (Le^{0.52} - 1) \left(\frac{H_d}{H_s} \right) \right], \text{dimensionless} \qquad \text{(C-38)}$$

H_d = dissociation specific enthalpy of air, J/kg

Le = Lewis number, dimensionless

μ_s = absolute dynamic viscosity of air at stagnation conditions, N·s·m²

ρ_s = density of air at stagnation conditions, kg/m³

and

$$\frac{du_e}{dx} = \frac{1}{r_n} \sqrt{\frac{2(p_s - p_\infty)}{\rho_s}} \text{ , for a sphere and } M_\infty > 1.22, \text{ s}^{-1} \qquad \text{(C-39)}$$

$$= \frac{1}{2r_n} \sqrt{\frac{2(p_s - p_\infty)}{\rho_s}} \text{ , for a cylinder and } M_\infty > 1.12, \text{ s}^{-1} \qquad \text{(C-40)}$$

$$= \frac{u_\infty}{r_n} (1.5 - 0.378\, M_\infty^2 - 0.02625\, M_\infty^4), \text{ for a sphere and}$$
$$M_\infty \leq 1.22, \text{ s}^{-1} \qquad \text{(C-41)}$$

$$= \frac{u_\infty}{r_n} (2.0 - 0.782\, M_\infty^2 - 0.328\, M_\infty^4), \text{ for a cylinder and}$$
$$M_\infty \leq 1.12, \text{ s}^{-1} \qquad \text{(C-42)}$$

where

r_n = nose radius, m

M_∞ = free-stream Mach number, dimensionless

p_s = stagnation pressure, Pa

p_∞ = free-stream pressure, Pa

u_∞ = free-stream velocity, m/s.

The dissociation specific enthalpy H_d of air is

$$H_d = C_O H_O + C_N H_N, \text{ J/kg} \qquad \text{(C-43)}$$

where

C_O = mass fraction of oxygen, dimensionless

C_N = mass fraction of nitrogen, dimensionless

H_O = 15.4351×10⁶ J·kg, specific dissociation enthalpy of oxygen

H_N = 33.62411×10⁶ J·kg, specific dissociation enthalpy of nitrogen.

C-3.2 LEES' HEMISPHERICAL DISTRIBUTION, LAMINAR FLOW

Lees' heating distribution over a sphere for an ideal gas in laminar flow is

$$\frac{q}{Q_s} = \frac{h}{h_s} = \frac{2\theta\sin\theta\left[\left(1 - \frac{1}{\gamma M_\infty^2}\right)\cos^2\theta + \frac{1}{\gamma M_\infty^2}\right]}{\sqrt{D(\theta)}}, \text{dimensionless} \tag{C-44}$$

where

$$D(\theta) = \left(1 - \frac{1}{\gamma M^2}\right)\left[\theta^2 - \frac{\theta\sin(4\theta)}{2} + \frac{1 - \cos(4\theta)}{8}\right]$$

$$+ \frac{4}{\gamma M^2}\left[\theta^2 - \theta\sin(2\theta) + \frac{1 - \cos(2\theta)}{2}\right], \text{dimensionless} \tag{C-45}$$

Q_s = stagnation heat flux, W/m²
h_s = stagnation convection heat transfer coefficient, W/m²·K
M = Mach number, dimensionless
γ = free-stream specific heat ratio, dimensionless
θ = local body angle, rad

where the subscript s denotes the stagnation condition determined by any suitable method, e.g., Fay-Riddell.

C-3.3 DETRA-HIDALGO HEMISPHERICAL DISTRIBUTION, TURBULENT FLOW

The Detra and Hidalgo heating distribution over a sphere for an ideal gas in turbulent flow is

$$Q = (H_{aw} - H_w)\left(\frac{0.029}{Pr^{2/3}}\right)\left(\frac{\mu_e}{x}\right)\left(\frac{\rho_e u_e x}{\mu_e}\right)^{0.8}[1.037f(\delta)^{0.2}]$$

$$\left[1 + 0.58\left(\frac{H_e}{H_T}\right)\right], \text{W/m}^2 \tag{C-46}$$

where $f(\delta)^{0.2}$ is evaluated by

$$f(\delta)^{0.2} = \sum_{i=1}^{3} A_i \delta^i, \text{dimensionless} \tag{C-47}$$

where the A_i are given in Table C-1, and

$$\delta = \pi/2 - \theta, \text{body slope, rad} \tag{C-48}$$

where

x = running length from nose stagnation point, m
H = total specific enthalpy, J/kg
H_{aw} = specific adiabatic wall enthalpy, J/kg
δ = local body slope, rad
μ_e = absolute dynamic viscosity evaluated at edge of boundary layer, N·s/m²
ρ_e = density of air at edge of boundary layer, kg/m³
θ = angular distance around a sphere from stagnation point, rad.

MIL-HDBK-762(MI)

TABLE C-1. COEFFICIENTS OF EXPANSION FOR
$$f(\delta)^{0.2}$$

i	For $\delta < 25$ deg A	For $\delta \geq 25$ deg A
1	1.03754	0.96451
2	0.0043776	0.01107
3	-0.6187×10^{-4}	0.842558×10^{-4}

C-3.4 ECKERT LAMINAR FLAT PLATE HEATING METHOD

Eckert's laminar flat plate heating expression for the convection heat transfer coefficient h_l is

$$h_l = \frac{3768}{Pr^{2/3}}\left(\frac{\rho^* u_e}{\sqrt{Re^* \tau_m}}\right)c_p, \ W \cdot m^2 \cdot K \tag{C-49}$$

where

$Re^* = \rho^* = u_e x \ \mu^*$, Reynolds number evaluated at reference conditions, dimensionless. The reference conditions are obtained from the reference specific enthalpy H^* and the edge pressure p_e.

ρ^* = density of air based on reference enthalpy, kg·m^3

μ^* = absolute dynamic viscosity evaluated at reference enthalpy, N·s·m^2

τ_m = Mangler transformation, dimensionless

and

$$H^* = H_e = 0.5(H_w - H_e) + 0.22\,(H_{aw} - H_e), \ J \ kg \tag{C-50}$$

where

H_e = specific enthalpy at edge of boundary layer, J·kg.

For geometries other than a flat plate, the dimensionless Mangler transformation τ_m, may be interpreted as

$\tau_m = 1$, for a flat plate

$\tau_m = 2$, for a cylinder

$\tau_m = 3$, for a cone.

C-3.5 MODIFIED SPALDING-CHI METHOD

The modified heating calculations due to Spalding and Chi refer to real-gas heat transfer for a turbulent boundary layer flow.

Cary (Ref. 25) investigated a large body of skin-friction and heat-transfer data (two-dimensional and conical) obtained in high-speed wind-tunnel flows to evaluate which of the more promising engineering prediction methods most accurately and consistently correlates the data.

Cary's general approach was to compare flat-plate experimental data with analytical prediction methods and to transform the data to the incompressible plane (according to each prediction scheme) and then to compare the transformed data with classical incompressible predictions. The Spalding and Chi method, using Von Karman-Reynolds analogy, was shown to give the best predictions based either on length or momentum thickness Reynolds number when the proper virtual origin was specified.

The dimensionless parameters F_c, $F_{R\theta}$, and F_{R_L}, respectively, are used to transform from the incompressible flow skin-friction coefficient C_f, incompressible momentum thickness Reynolds number Re_{θ_i}, and incompressible length Reynolds number Re_{L_i}, to corresponding compressible values as follows:

C-22

$$C_{f_i} = (1\ 2)F_cC_f, \text{ dimensionless} \tag{C-51}$$

$$Re_{\theta_i} = F_{R_\theta}Re_\theta, \text{ dimensionless} \tag{C-52}$$

$$Re_{L_i} = F_{R_L}Re_L, \text{ dimensionless} \tag{C-53}$$

where

C_f = compressible skin-friction coefficient, dimensionless

Re_θ = local compressible Reynolds number based on momentum thickness θ, dimensionless

Re_L = local compressible Reynolds number based on length L, dimensionless.

These parameters are functions of Mach number, ratio of wall-to-total enthalpy, and recovery factor only. The parameters F_c, F_{R_θ} F_{R_L} are calculated using Eqs C-54 through C-58 as follows:

$$F_c = \frac{1}{Z_eT_e}\int_0^1\left[\left(\frac{1}{ZT}\right)^{1\ 2}d\left(\frac{u}{u_e}\right)\right]^{-2}, \text{ dimensionless} \tag{C-54}$$

where

$ZT = f(H, p_e)$, K (Ref. 21) $\tag{C-55}$

p_e = pressure at edge of boundary layer, Pa

T_e = temperature at edge of boundary layer, K

Z = compressibility factor, dimensionless

Z_e = compressibility factor based on boundary layer edge conditions, dimensionless

$d\frac{u}{u_e}$ = differential increment of velocity ratio, dimensionless

$$H = H_w + (H_{aw} - H_w)\left(\frac{u}{u_e}\right) - (H_{aw} - H_e)\left(\frac{u}{u_e}\right)^2, \text{ J kg} \tag{C-56}$$

$$F_{R_\theta} = \left(\frac{H_{aw}}{H_w}\right)^{0.\ \ 2}\left(\frac{H_e}{H_w}\right)^{0.\ 02}, \text{ dimensionless} \tag{C-57}$$

$$F_{R_L} = F_{R_\theta}\ F_c, \text{ dimensionless.} \tag{C-58}$$

The compressible skin-friction coefficient C_f and Stanton number St are calculated using Eqs. C-59 and C-60, respectively.

$$(1\ 2)C_fF_c = (1\ 2)\exp\left\langle\sum_{i=1}^{10}A_i\left\{\ln\left[F_{R_L}\left(\frac{Re_L}{\tau_m}\right)\right]\right\}^{i-1}\right\rangle, \text{ dimensionless} \tag{C-59}$$

$$ST = \frac{C_{f_i}}{2F_cS}, \text{ dimensionless} \tag{C-60}$$

where

S = inverse of the Von Karman-Reynolds Analogy Factor, a factor showing the similarity between the transport of mass, heat, and momentum, dimensionless

and the A_i values, found in Table C-2, are constants.

TABLE C-2. COEFFICIENTS FOR THE 31 MODIFIED SPALDING-CHI METHOD

i	I
1	9.2808635
2	-4.7340248
3	$6.6858663 \times 10^{-}$
4	$-4.1876614 \times 10^{-2}$
5	$-5.5054577 \times 10^{-4}$
6	2.8367291×10^{-4}
7	$-2.1249608 \times 10^{-5}$
8	8.0162000×10^{-7}
9	$-1.5900985 \times 10^{-8}$
10	$-1.3236350 \times 10^{-10}$

C-3.6 LAMINAR CIRCUMFERENTIAL HEATING ON A YAWED CYLINDER

The method presented here is the Beckwith and Gallagher laminar windward circumferential heating calculations for a cylinder. The convection heat transfer coefficient h_l at some circumferential angle θ is related to the Fay-Riddell stagnation line convection coefficient h_s as follows:

$$\frac{h_l}{h_s} = \left(\frac{p}{p_s}\right)^{\frac{3\gamma-1}{2\gamma}} \left\{ 2\left(\frac{p}{p_s}\right)\left[\frac{2}{\gamma}\left(1 - \frac{p_\infty}{p_s}\right)\right]^{1/2} \right\}^{-1/2}$$

$$\times \left\{ \frac{2}{\gamma}\left(\frac{p_s}{p}\right)^{\frac{5\gamma-3}{2\gamma}} (\sin\theta\cos\theta)\left(1 - \frac{p_\infty}{p_s}\right)\left\{\frac{2}{\gamma-1}\left[\left(\frac{p_s}{p}\right)^{\frac{\gamma-1}{\gamma}} - 1\right]\right\}^{-1/2}$$

$$+ \frac{p}{p_s}\left\{\left(\frac{2}{\gamma-1}\right)\left[\left(\frac{p_s}{p}\right)^{\frac{\gamma-1}{\gamma}} - 1\right]^{1/2} \left[\int_0^\theta \left(\frac{p}{p_s}\right)^{\frac{3\gamma-1}{2\gamma}} d\theta\right]^{-1} \right\}, \text{ dimensionless}$$

$$(C\text{-}61)$$

and the modified Newtonian pressure p is

$$\frac{p}{p_s} = 1 - \left(\frac{p_\infty}{p_s}\right)(\cos\theta)^2 + \frac{p_\infty}{p_s} \text{ , dimensionless} \qquad (C\text{-}62)$$

where

θ = angular distance around cylinder from stagnation line in a plane normal to cylinder axis, rad

p_s = stagnation line pressure, N·m^2

By use of Eqs. C-61 and C-62, the local stagnation line heat transfer coefficient ratio may be computed for a range of $0 \leq \theta \leq 80$ deg. The Fay-Riddell stagnation line convection coefficient is equal to 0.707 times the Fay-Riddell stagnation point convection coefficient. The stagnation point convection coefficient is provided by Eq. C-37b.

C-3.7 TURBULENT STAGNATION LINES HEATING ON A YAWED CYLINDER

The Beckwith and Gallagher turbulent, real-gas yawed cylinder stagnation line heat flux is

$$h_{SL} = 0.0323 \left(\frac{1}{Pr^{2/3}}\right) \left(\frac{u_\infty \sin\Lambda}{\mu_s}\right)^{0.6} (\rho^* \mu^*)^{0.8} \left(\frac{du_e}{dx}\right)_{x=0}^{0.2}, \, W/m^2 \cdot K \qquad \text{(C-63)}$$

where

$$\left(\frac{du_e}{dx}\right)_{x=0} = \frac{1.414}{r_{cyl}} \left\{ \left(\frac{p_e - p_\infty}{\rho_e}\right) \right\}^{1/2}, \, s^{-1} \qquad \text{(C-64)}$$

h_{SL} = stagnation line convection heat transfer coefficient, $W/m^2 \cdot K$
r_{cyl} = radius of cylinder, m
x = distance from stagnation line, m
Λ = yaw (sweep) angle, rad

and the superscript * indicates that the parameters are to be evaluated at Eckert's reference enthalpy and edge presssure (see par. C-2.4).

A second method of stagnation line heating estimation is the method of Sayano and Greenwald. The method is based on the Fay-Riddell spherical stagnation heating q_{fr} described in par C-2.1. The method is defined by the empirical relationship

$$\frac{Q_s}{Q_{\Lambda=0}} = \left(\frac{Q_{fp}}{Q_{\Lambda=0}}\right)(\sin^2\Lambda) + \cos^{1/5}\Lambda, \text{ dimensionless} \qquad \text{(C-65)}$$

where

$$Q_{\Lambda=0} = 0.707 Q_{FR}, \, W/m^2 \qquad \text{(C-66)}$$

Q_s = stagnation heat flux on a yawed cylinder, W/m^2
Q_{FR} = Fay-Riddell spherical stagnation point heat flux, W/m^2
Q_{fp} = flat plate heat flux, W/m^2
$Q_{\Lambda=0}$ = cylinder heat flux at zero sweep (zero yaw), W/m^2.

R E F E R E N C E S

1. V. A. Dauro, *Heat Transfer and Fluid Flow Computer Program (NHEAT)*, NSI Memorandum M9230-78-05, Northrop Services, Inc., Huntsville, AL, December 1978.

2. W. W. Boyle *et al., Nuclear Waste Disposal Mission Analysis,* NSI Report TR-223-1874, Northrop Services, Inc., Huntsville, AL, November 1977.

3. L. L. Trimmer, *Equations and Charts for the Evaluation of Forces on Spherically Blunted Cones by Newtonian Theory,* AEDC Report TR-66-16, ARO, Inc., Arnold Air Force Station, TN, April 1966.

4. Ames Research Staff, *Equations, Tables and Charts for Compressible Flow,* NACA Report 1135, National Advisory Committee for Aeronautics, Washington, DC, 1953.

5. P. V. Marrone, *Normal Shock Waves in Air Equilibrim Composition and Flow Parameters for Velocities form 26,000 to 50,000 ft s,* CAL Report No. AG-1729-A-2, Cornell Aeronautical Laboratory, Buffalo, NY, August 1962.

6. J. L. Sims, *Tables for Supersonic Flow Around Right Circular Cones at Zero Angle of Attack,* NASA SP-3004, National Aeronautics and Space Administration, Washington, DC, 1964.

7. J. L. Sims, *Tables for Supersonic Flow Around Right Circular Cones at Small Angle of Attack<* NASA SP-3007, National Aeronautics and Space Administration, Washington, DC, 1964.

8. Z. Kopal, *Tables of Supersonic Flow Around Cones,* MIT Technical Report No. 1, Massachusetts Institute of Technology, Cambridge, MA, 1947.

9. Z. Kopal, *Tables of Supersonic Flow Around Yawing Cones,* MIT Technical Report No. 3, Massachusetts Institute of Technology, Cambridge, MA, 1947.

10. D. J. Jones, *Tables of Inviscid Supersonic Flow About Circular Cones at Incidence, y = 1.4, Part I and Part II,* AGARDograph 137, The Advisory Group for Aerospace Research ad Development, NATO, Neuilly-Sur-Seine, France, November 1969.

11. J. L. Sims, *Supersonic Flow Around Right Circular Cone Tables for Zero Angle of Attack,* ABMA Report No. DA-TR-11-60, US Army Ballistic Missile Agency, Redstone Arsenal, AL, 1960.

12. J. N. Cleary, *An Experimental and Theroetical Investigation of the Pressure Sistribution and Flow Fields of Blunted Cones at Hypersonic Mach Numbers,* NASA TN-D-2969, National Aeronautics and Space Administration, Ames Research Center, Moffett Field, CA, 1965.

13. A. M. Morrison *et al., Handbook of Inviscid Sphere—Cone Flow Fields and Pressure Distributions: Vol. I,* NSWC/WOL TR-75-45, National Surface Weapons Center, White Oak Laboratory, Silver Spring, MD, December 1975.

14. J. A. Fay and F. R. Riddell, "Theory of Stagnation Point Heat Transfer in Dissociated Air", Journal of Aeronautical Science 25, No. 2, 73-97 (February 1958).

15. L. Lees, "Laminar Heat Transfer Over Blunt-Nosed Bodies at Hypersonic Flight Speeds", Jet Propulsion 26, 259-69 (April 1956).

16. L. Lees, h. W. Detra, and H. Hidalgo, *Generalized Heat Transfer Formulae and Graphs,* Avco Everett Research Report 72, Avco Everett Research Laboratory, Everett, MA, March 1960.

17. E. R. G. Eckert, "Engineering Relations for Heat Transfer and Friction in High Velocity Laminar and Turbulent Boundary Layer Flow Over Surfaces With Constant Pressure and Temperature", Transactions of the ASME 78, 1273-83 (August 1959).

18. D. B. Spalding and S. W. Chi, "The Drag of A Compressible Turbulent Boundary Layer on A Smooth Flat Plate With and Without Heat Transfer", Journal Fluid Mechanics 18, 1 and 117-43 (January 1964).

19. I. E. Beckwith and J. J. Gallagher, *Local Heat Transfer and Recovery Temperatures on A Yawed Cylinder at Mach Number 4.15 and High Reynolds Number,* NASA TR-R-104, National Aeronautics and Space Administration, Washington, DC, 1961.

20. Shoichi Sayano and G. F. Greenwald, "Approximate Method for Calculating Heat Transfer to Yawed Cylinders in Laminar Flow", Journal of Spacecraft and Rockets 10, No. 2, 157-9 (February 1973).

21. C. F. Hansen, *Approximation for the Thermodynamic and Transport Properties of High Temperature Air,* NASA TR-R-50, National Aeronautics and Space Administration, Washington, DC, 1959.

22. *W. E. Moeckel and K. C. Weston, Composition and Thermodynamic Properties of Air in Chemical Equilibrium,* MACA RN-4265, National Advisory Committee for Aeronautics, Washington, DC, april 1958.

23. F. Kreith, *Principles of Heat Transfer, Third Edition,* Harper and Row, New York, NY, 1973, pp. 517-24.

24. SAE Committee, AC-9, Aircraft Environmental Systems, *SAE Aerospace Applied Thermodynamics Manual, Second Edition,* Society of Automotive Engineers, Inc., 1969, pp. 66-93, 127-258.

25. A. M. Cary, Jr., and M. H. Bertran, *Emergency Prediction of Turbulent Sken Frictions and Heat Transfer in High-Speed Flow,* NASA TN-D-7507, National Aeronautics and Space Administration, Washington, DC, July 1974.

B I B L I O G R A P H Y

Richard D. Neuman, G. L. Burke, J. R. Hayes, and A. B. Lewis, *The Analysis of Aerodynamic Heating to Supersonic Missilies,* AIAA Short Course on Missile Aerodynamics, American Institute of Aeronautics and Astronautics, 1633 Broadway New York, NY 10019, August 1982.

INDEX

Committee on Extension of the Standard Atmosphere
(COESA), A-4
Committee on Space Research (COSPAR), A-3
Component constraints, in comcept selection, 2-4, 2-5
Compressibe flow skin friction, C-22, C-23
Computer codes
  design programs, B-1 through B-6
    heat transfer, C-5
Concept selection, 2-1 through 2-2, 2-4 through 2-7
Contact conductance, C-8
Conduction, C-6
  spherical model latitudinal, C-13
Confidence intervals, definition, 4-57
Configuration management, 2-28
Container launcher, 8-5
  defined, 8-15
Continuity equation, 6-12
Control of launch accuracy. *See* Aiming, control of
Cure temperature, 7-35
Cylinders, C-5
Cylindrical
  anial heat conduction model, C-8
  circumferential heat conduction model, C-8
  coordinates, thermal modeling, C-6
  heat Convection model, C-9
  heat radiation model, C-9
  radial heat conduction model, C-6
  segment, in thermal modeling, C-8
  thermal storage model, C-5, C-6

D

Deflection error probable, definition, 4-60
Degree of freedom, definition, 8-12
DeLaval. *See* Nozzle
Density, atmospheric, A-2 through A-6
  measureing devices, 2-19, 2-20
  reationship, 6-17 through 6-18
Design, process, the four steps, 2-24
  documentation, 2-24 through 2-25
Detent, definition, 8-13
Dispersion reduction
  definition, 4-24
Dispersion reduction factor, definition, 4-30
Drag
base, 5-43, 5-50 through 5-55
  boattail, 5-51 through 5-52, 5-54
  coefficient, 5-43, 5-44, 5-51, 5-54, 5-55
  fin, 5-55
  flare, 5-51
  power-ff, 5-51 through 5-52
  power-on, 5-52 through 5-54
  ringtail effect, 5-56
  fiction, 5-43, 5-49, 5-50
  system design, 2-12, 2-13
  tatal, 5-55, 5-56
  wave, 5-43, 5-44 through 5-49
    boattail, 5-47, 5-51, 5-52, 5-53
    conical frustum, 5-48
    fin, 5-48, 5-49
    flare, 5-48, 5-49

  forebody, 5-44 through 5-47
  Me'plat, 5-46
  midbody, 5-47
  ogites, 5-45
  split petal, 5-52
  zero lift, 5-43, 5-44
Dynamic aiming, definition, 4-46
Dynamic imbalance
  effect of launch error, 4-19
  related to inertias, 4-53
Dynamic pressure, 5-9, 6-23
Dynamics system design, 2-14 through 2-17
  simulation, 2-14
  trajectory analysis. 2-14

E

Earth radius, local equivalent, A-3
Edge pressure, C- 19, C-21, C-22
Effective exhaust velocity, 6-6
Enthalpy, 6-15 through 6-17, 6-32. *See* also Specific
  enthalpy
  dissociation, C-20
  reference, C-22
Equations of motion
  six degree of freedom, 4-49, 4-51
  three degree of freedom, 4-53
  pitch plane, 4-54
  linearized, 4-22, 4-54
Equation of state. *See* Ideal gas equation
Erosion. *See* Nozzle erosion and Erosive burning
  (coefficient, 6-36
Erosive burning, 6-32, 6-36
Errir budget, in system design, 2-16
Error source, definition, 4-5
Error sources
  ballistic phase, 4-5, 4-11 through 4-14,
    4-22, 4-23
  boost phase, 4-5, 4-9 through 4-11, 4-22
  effects of, 4-14 through 4-17
  launch phase, 4-5, 4-7, 4-8, 4-17
  prelaunch phase, 4-5, 4-6, 4-17 through 4-21
  preliminary design, 2-2, 2-6, 2-7, 2-14 through 2-16
Errors
  bias, 2-14, 4-5
  precision, 2-14, 4-5
  random, definition, 4-5
Exhaust impingement, 8-16, 8-17
Expansion deflection nozzle, 6-21
External configuration, 5-1 through 5-9
  bodies of revolution, 5-10
  necked-down centerbody, 5-13
  nose cylinder, 5-11, 5-12, 5-13
  noses. *See* Forebody configuration

F

Failure
  brittle, 7-61
  ductile, 7-61

STANDARDIZATION DOCUMENT IMPROVEMENT PROPOSAL

INSTRUCTIONS

1. The preparing activity must complete blocks 1, 2, 3, and 8. In block 1, both the document number and revision letter should be given.

2. The submitter of this form must complete blocks 4, 5, 6, and 7.

3. The preparing activity must provide a reply within 30 days from receipt of the form.

NOTE: This form may not be used to request copies of documents, nor to request waivers, or clarification of requirements on current contracts. Comments submitted on this form do not constitute or imply authorization to waive any portion of the referenced document(s) or to amend contractual requirements.

I RECOMMEND A CHANGE:	1. DOCUMENT NUMBER MIL-HDBK-762(MI)	2. DOCUMENT DATE (YYMMDD) 900717

3. DOCUMENT TITLE
Design of Aerodynamically Stabilized Free Rockets

4. NATURE OF CHANGE (Identify paragraph number and include proposed rewrite, if possible. Attach extra sheets as needed.)

5. REASON FOR RECOMMENDATION

6. SUBMITTER

a. NAME (Last, First, Middle Initial)	b. ORGANIZATION	
c. ADDRESS (Include Zip Code)	d. TELEPHONE (Include Area Code) (1) Commercial (2) AUTOVON (If applicable)	7. DATE SUBMITTED (YYMMDD)

8. PREPARING ACTIVITY

a. NAME U.S. Army Missile Command	b. TELEPHONE (Include Area Code) (1) Commercial (205) 876-6980	(2) AUTOVON 746-6980
c. ADDRESS (Include Zip Code) Commander, U.S. Army Missile Command, ATTN: AMSMI-RD-SE-TD-ST, Redstone Arsenal, AL 35898-5270	IF YOU DO NOT RECEIVE A REPLY WITHIN 45 DAYS, CONTACT: Defense Quality and Standardization Office 5203 Leesburg Pike, Suite 1403, Falls Church, VA 22041-3466 Telephone (703) 756-2340 AUTOVON 289-2340	

DD FORM 1426 89 OCT